Indian Institute of Metals Series

A. K. Tyagi
Raghumani S. Ningthoujam *Editors*

Handbook on Synthesis Strategies for Advanced Materials

Volume-II: Processing and Functionalization of Materials

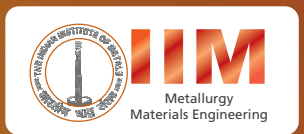

Springer

Indian Institute of Metals Series

About the Book Series:

The study of metallurgy and materials science is vital for developing advanced materials for diverse applications. In the last decade, the progress in this field has been rapid and extensive, giving us a new array of materials, with a wide range of applications, and a variety of possibilities for processing and characterizing the materials. In order to make this growing volume of knowledge available, an initiative to publish a series of books in Metallurgy and Materials Science was taken during the Diamond Jubilee year of the Indian Institute of Metals (IIM) in the year 2006. Ten years later the series is now published in partnership with Springer.

This book series publishes different categories of publications: textbooks to satisfy the requirements of students and beginners in the field, monographs on select topics by experts in the field, professional books to cater to the needs of practicing engineers, and proceedings of select international conferences organized by IIM after mandatory peer review. The series publishes across all areas of materials sciences and metallurgy. An eminent panel of international and national experts acts as the advisory body in overseeing the selection of topics, important areas to be covered, and the selection of contributing authors.

More information about this series at https://link.springer.com/bookseries/15453

A. K. Tyagi · Raghumani S. Ningthoujam
Editors

Handbook on Synthesis Strategies for Advanced Materials

Volume-II: Processing and Functionalization of Materials

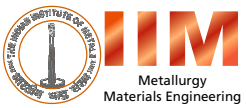

Springer

Editors
A. K. Tyagi
Chemistry Division
Bhabha Atomic Research Centre
Mumbai, Maharashtra, India

Homi Bhabha National Institute
Mumbai, Maharashtra, India

Raghumani S. Ningthoujam
Chemistry Division
Bhabha Atomic Research Centre
Mumbai, Maharashtra, India

Homi Bhabha National Institute
Mumbai, Maharashtra, India

ISSN 2509-6400 ISSN 2509-6419 (electronic)
Indian Institute of Metals Series
ISBN 978-981-16-1802-4 ISBN 978-981-16-1803-1 (eBook)
https://doi.org/10.1007/978-981-16-1803-1

Series Editor's Preface

The Indian Institute of Metals Series is an institutional partnership series focusing on metallurgy and materials science and engineering.

About the Indian Institute of Metals

The Indian Institute of Metals (IIM) is a premier professional body (since 1947) representing an eminent and dynamic group of metallurgists and materials scientists and engineers from R&D institutions, academia, and industry, mostly from India. It is a registered professional institute with the primary objective of promoting and advancing the study and practice of the science and technology of metals, alloys, and novel materials. The institute is actively engaged in promoting academia–research and institute–industry interactions.

Genesis and History of the Series

The study of metallurgy and materials science and engineering is vital for developing advanced materials for diverse applications. In the last decade, the progress in this field has been rapid and extensive, giving us a new array of materials, with a wide range of applications and a variety of possibilities for processing and characterizing the materials. In order to make this growing volume of knowledge available, an initiative to publish a series of books in metallurgy and materials science and engineering was taken during the Diamond Jubilee year of the Indian Institute of Metals (IIM) in the year 2006. IIM entered into a partnership with Universities Press, Hyderabad, and, as part of the IIM book series, 11 books were published, and a number of these have been co-published by CRC Press, USA. The books were authored by eminent professionals in academia, industry, and R&D with outstanding background in their respective domains, thus generating unique resources of validated expertise

of interest in metallurgy. The international character of the authors' and editors has enabled the books to command national and global readership. This book series includes different categories of publications: textbooks to satisfy the requirements of undergraduates and beginners in the field, monographs on selected topics by experts in the field, and proceedings of selected international conferences organized by IIM, after mandatory peer review. An eminent panel of international and national experts constitutes the advisory body in overseeing the selection of topics, important areas to be covered, in the books and the selection of contributing authors.

Current Series Information

To increase the readership and to ensure wide dissemination among global readers, this new chapter of the series has been initiated with Springer in the year 2016. The goal is to continue publishing high-value content on metallurgy and materials science and engineering, focusing on current trends and applications. So far, four important books on state of the art in metallurgy and materials science and engineering have been published and, during this year, three more books are released during IIM-ATM 2021. Readers who are interested in writing books for the Series may contact the Series Editor-in-Chief, Dr. U. Kamachi Mudali, Former President of IIM and Vice Chancellor of VIT Bhopal University at ukmudali1@gmail.com, vc@vitbhopal.ac.in or the Springer Editorial Director, Ms. Swati Meherishi at swati.meherishi@springer.com.

About the Three Volumes of Handbook on Synthesis Strategies for Advanced Materials

The Handbook on "Synthesis Strategies for Advanced Materials" is aimed to provide information on (i) Variety of synthetic methods to prepare advanced materials (stable and metastable hitherto unknown materials, chemically and crystallographically designed materials and assemblies) and their structure, micro-structure, and morphology; and (ii) Functional properties like soft to hard, insulators to superconductors, crystalline to amorphous like glass or polymeric, nano- to thin films to bulk single crystals. Keeping in mind the interests of students and young researchers, and senior faculty members, the basic concepts of synthesis, processing and materials aspects, and their recent developments are covered in three volumes.

The Editors Dr. A.K. Tyagi, Director, Chemistry Group, and Dr. S.R. Ningthoujam, Scientific Officer-F, Chemistry Group, from Bhabha Atomic Research Centre have meticulously edited the three volumes with 20 each chapters for Vols. I and II, and 18 chapters for Vol. III. These chapters have been prepared by the editors as well as well-experienced authors from academia, R&D, and industry. This handbook will

be a treasure for those who are interested in learning everything about advanced materials and pursue a career and study in the area of advanced materials. The editors and authors are gratefully acknowledged for their excellent chapters covering wide range of information on the subject matter.

Dr. U. Kamachi Mudali
Editor-in-Chief
Series in Metallurgy and Materials Engineering

Preface

The ever-developing human civilization thrives on materials which may be of technological, health, environmental, or geological relevance. The development of materials has, thus, been a constantly evolving process both in nature as well as by human efforts. Over the time immemorial, a continuous evolution of materials for fulfillment of needs of healthy living or advanced lifestyle has been witnessed and that makes the twenty-first century a century of materials. This is recognized by the surge in advanced materials in engineering, electronics, and communications as well as in healthcare, medicine, and societal sectors. The fascinating and ever-growing world of materials extends from soft materials to super-hard materials, insulators to superconductors, extended solids to molecular solids, self-assembled materials, catalysts, materials with tailored thermal expansion, composites and hybrid materials, materials with multifunctionality, ceramics and glasses, metals–alloys–intermetallics, drugs and drugs delivery systems, polymers, bio-materials, nuclear materials, optical materials, fast ionic conductors, soft and hard magnets, etc. Still the quest of humanity for developing better and more efficient materials remains never ending. The development of materials depends on the ability to synthesize them, or to find a more cost- and energy-efficient synthesis methodology or design newer materials with appropriate constituents and functionalities to make them usable. Thus, the synthesis methods play a pivotal role in the materials research. Although the synthesis or synthetic materials chemistry originated just after the Stone Age, the understanding of chemistry and physics of materials with the progress of time only could lead to discovery of newer materials as well as the targeted materials for desired purposes. This in turn resulted in the development of state-of-art synthesis procedures. Further, new functional materials are also being designed by interplay of synthesis methodologies, crystallographic structures, morphologies, and dimensionality for desired functional properties. Many a times, thermodynamics and kinetic parameters are controlled to overcome the barriers to achieve the desired materials. Thus, the methodologies for synthesis of materials became multidisciplinary which include the approaches from chemists, biologists, physicists, metallurgists, and engineers. This has been witnessed as the development of several unconventional synthetic routes that involve

parameters such as extremely high temperature, high pressure, radiation, mechanical attrition and unusually reactive intermediates. Some non-traditional synthesis routes have also been developed that follow a gentle chemical reaction favoring an intermediate or alternate pathway to bypass hindrance to reach the targeted material or utilizing the memory of the materials to introduce functionalities. The unconventional synthesis methodologies play important roles in the direction of many new and metastable materials which otherwise were not possible to prepare. Similarly, the multifunctional materials, i.e., the materials which can perform two or more synergistic or antagonistic functionalities are being achieved by judicious adoption of synthesis methods. In addition, varieties of soft chemical methods have emerged that play important roles in the field of functional materials, in particular medicine and healthcare products to design materials for desired technological applications. Thus, the material synthesis assumes an unprecedented role in this endeavor and remains as a challenge as well as an opportunity to chemists and materials scientists. The synthesis methods and their scopes have been discussed in varieties of monographs as well as compilations and proceedings from time to time. Usage for various synthetic methods for preparation of newer and exotic materials as well as recent modifications and their potentials as handy information is essentially a need for researchers in today's times and that has been achieved in this present compilation *Handbook on Synthesis Strategies for Advanced Materials*, Volumes I, II, and III.

This handbook series on *Synthesis Strategies for Advanced Materials* is aimed to provide information on varieties of synthetic methods being adopted by researchers to prepare different kinds of advanced materials covering from the viewpoints of structure, micro-structure and morphology of materials, stable and metastable hitherto unknown materials, chemically and crystallographically designed materials and assemblies, as well as from the viewpoints of functional properties like soft to hard, insulators to superconductors, crystalline to amorphous like glass or polymeric, nano- to thin films to bulk single crystal. These have been achieved by adoption, alteration, or judicious selection of synthesis methods. Keeping in mind the interests of students and young researchers, and senior faculty members, the basic concepts of synthesis, processing, and materials aspects and their recent developments are covered in three volumes, namely Volume-I: *Techniques and Fundamentals*, Volume-II: *Processing and Functionalization of Materials*, and Volume-III: *Materials Specific Synthesis Strategies.* Each volume is made independent by taking care of minimal overlap of the topics. Volume-I is primarily focused on the principles and procedures of various synthesis methods. The basic principles and scope/limitations of various synthetic methods, like solid-state reaction to gentle molecular aggregation methods and chimie douce, synthesis under high temperature, hot-injection method, polyol method, metal-organic frameworks, electrochemical method, mechanochemistry, hydro/solvothermal reaction, high-pressure and high-temperature reactions, arc melting, induction heating, melt-quench method, ion-exchange process, microwave and visible to gamma radiations, green methods of synthesis, thermolysis, bio-inspired synthesis, etc., are discussed along with the inputs from authors' hands on experience and expertise. In Volume-II, various processing methodologies for preparation of various types of functional materials or functionalization of materials by

chemical, structural, or microstructural alterations are presented. This volume covers the processing of nanomaterials, porous or sintered materials, composite materials, low-dimensional like 1D to 2D materials, thin films, single crystals, template method, self-assembly, biomaterials, inkjet printing, 3D printing, size and shape engineering, etc., in a lucid manner. Volume-III is focused on the synthesis aspects of materials like hybrid inorganic–organic, metal oxide frameworks, intermetallics, hydrides, borides, carbides, nitrides, phosphides, silicide, selenides, fluorides, various biomaterials, materials for sensors and detectors, optical materials, carbon-based materials, colloids, noble gas compounds, lithium based ceramics, materials with unusual oxidation state, organo-selenium and platinum compounds, silicon-based materials, and lithium-based ceramics. The evolution and state-of-the-art synthesis methods for practical requirements as well as new concepts with most recent literatures dealing with their synthesis are presented in this volume. These volumes are expected to serve as handy guides for synthesis and processing of advanced materials of wide range and category.

The editors are immensely thankful to all the authors for their rich contributions toward this book. Although due efforts have been taken to make the book as error-free as possible, some may have crept in as unnoticed. We shall be thankful to the readers for bringing such unintentional errors to our notice. Finally, we sincerely hope that our efforts will be of use to both new and experienced researchers in the field.

Mumbai, India
November, 2021

A. K. Tyagi
Raghumani. S. Ningthoujam

Contents

About the Editors

Dr. A. K. Tyagi obtained his M.Sc. (Chemistry) degree in 1985 from Meerut University, Meerut, Uttar Pradesh, India and joined 29th batch of BARC Training School, Mumbai in the same year. After completing one year orientation course, he joined Chemistry Division, Bhabha Atomic Research Centre (BARC), Mumbai in 1986. Presently, he is Director, Chemistry Group, BARC, Mumbai, and a Senior Professor of Chemistry at Homi Bhabha National Institute (HBNI), Mumbai. His research interests are in the field chemistry of materials, which includes functional materials, nanomaterials, nuclear materials, energy materials, metastable materials, hybrid materials and structure-property correlation. He has published more than 600 papers in journals, several books and has supervised 30 Ph.D. students.

He was awarded Ph.D. by Mumbai University, Mumbai in 1992. He did postdoctoral research at Max-Planck Institute for Solid State Research (MPI-FKF), Stuttgart, Germany during 1995–1996 on a Max-Planck Fellowship. Subsequently, he regularly visited MPI-FKF, Stuttgart as a visiting scientist. In addition, he has also visited Institute of Superior Technology, Portugal; Institute for Chemical Process and Environmental Technology, Ottawa, Canada; Dalhousie University, Halifax, Canada; Moscow State University, Moscow, Russia; Institute for Materials, Nantes, France; University of Malay, Malaysia; National Institute of Materials Science, Tsukuba, Japan; National University of Singapore, Singapore; Royal Institute of Technology, Stockholm, Sweden; Rice University, Houston, USA;

Shanghai, China; University of Valencia, Valencia, Spain; Weizmann Institute of Science, Israel; University of Queensland, Brisbane, Australia; US-Air Force Research Lab, Dayton, USA, Institute for Studies of Nanostructured Materials, Palermo, Italy and iThemba Labs, Cape Town, South Africa.

In recognition of his significant contributions to the field of chemistry of materials, he has been conferred with many prestigious awards, such as Dr. Lakshmi award by the Indian Association of Solid State Chemists and Allied Scientists (2001); Rheometric Scientific-Indian Thermal Analysis Society Award (2002); Gold Medal of Indian Nuclear Society (2003); Materials Research Society of India's Medal (2005); Chemical Research Society of India's Bronze Medal (2006); DAE-Homi Bhabha Science and Technology Award (2006); IANCAS-Dr. Tarun Datta Memorial Award (2007); Rajib Goyal Prize in Chemical Sciences (2007); RD Desai Memorial Award from Indian Chemical Society (2008) and DAE-SRC Outstanding Research Investigator Award (2010); CRSI-Prof. CNR Rao National Prize in Chemical Sciences (2012); ISCB Award for Excellence in Chemical Sciences (2013); MRSI-ICSC Materials Science Senior Award (2014); Coastal Chemical Research Society's Award (2014); Platinum Jubilee Lecture Award in Materials Science from Indian Science Congress Association (2015); Metallurgist of the Year Award (2017), from Ministry of Steel, Government of India; Chemical Research Society of India's Silver Medal (2018); Materials Research Society of India's Prof. CNR Rao Prize in Advanced Materials (2018); JNCASR's National Prize in Solid State and Materials Chemistry (2018) and Acharya PC Ray Memorial Award from Indian Science Congress Association (2020).

He is an elected Fellow of the Indian Academy of Sciences (FASc); National Academy of Sciences, India (FNASc); Maharashtra Academy of Sciences (FMASc); Royal Society of Chemistry, UK (FRSC) and Asia Pacific Academy of Materials.

Dr. Raghumani S. Ningthoujam obtained M.Sc. in Chemistry from Manipur University, Imphal, Manipur, India in 1994. He was awarded Ph.D. in Chemistry from IIT Kanpur in area of superconductivity, electron transport and magnetic properties of nanostructured transition metal nitrides in 2004. He joined BARC (Bhabha Atomic Research Centre), Mumbai as Scientific Officer (D) in 2006 after completion of Dr. K. S. Krishnan Research Associate Fellowship. Presently, he is working in area of Luminescent and Magnetic Nanomaterials and their applications in sensors, imaging, diagnosis and therapy. He did Post-Doctoral Fellowship at University of Victoria, Canada in the area of quantum dots. Presently, he is Scientific Officer (F) at Chemistry Division, BARC, Mumbai. He is recognized for Guideship of Ph.D. at Homi Bhabha National Institute (HBNI), Mumbai and Mumbai University, Mumbai. Many research scholars and students finished their projects under his guidance. He has published about 150 papers in the refereed journals, five review articles and four book chapters. In recognition of his significant contributions to the chemical science, he has been awarded DAE-Scientific & Technical Excellence Award in 2012 and Young Achiever Award, SSPS 2010. He has been elected as a Fellow, The National Academy of Sciences, India (FNASc) in 2016 and Fellow, Maharashtra Academy of Sciences (FMASc) in 2013.

Chapter 1
Shape Forming and Sintering of Ceramics

R. K. Lenka, P. K. Patro, and T. Mahata

Abstract Ceramic materials at large are inorganic compounds (oxides, borides, carbides, and nitrides) having high melting temperature and inherent brittleness. Because of these properties the state-of-the-art melting and casting methodologies are not applicable for shape forming of ceramic materials. Further, conventional machining of ceramics is also difficult due to their brittle nature. Therefore, powder metallurgy route is usually adopted for making ceramic body of near net shape. Initially green shapes are formed and subsequently sintered to get the product of desired density and microstructure. The packing of ceramic powders need to be uniform throughout the green shape in order to avoid warping or cracking of the shape during sintering. For achieving uniform packing, the powder particles must flow significantly to fill every space and contours. Different ceramic shape forming techniques have been evolved based on convenience, reproducibility, and state of feed material. Dry powder pressing is the most common among these. Various additives are mixed with powders to make the feed material in paste form or suspension form which shows good plasticity and flowability. In the green shapes, powder particles are in physical contact without any bonding. Upon firing the green compact, a coherent, predominantly a solid structure is formed due to mass transfer through a process called sintering. Decrease in surface free energy is the driving force for the process. Mass transfer is the basis to fill the pores and a resultant dense coherent mass with definite microstructure is obtained. Mass transfer takes place due to the difference in chemical potential between two regions. There are different pathways through which mass transfer takes place. Sintering techniques are generally classified based on diffusion pathway and type of applied field/heating to assist in sintering. This chapter deals with the various techniques of ceramic shape forming, sintering techniques, mechanism of sintering, and factors affecting sintering. At the end the future directions of ceramic shape forming and sintering have been discussed.

R. K. Lenka (✉) · P. K. Patro · T. Mahata
Powder Metallurgy Division, Bhabha Atomic Research Centre, Vashi Complex, Navi Mumbai 400703, India
e-mail: rklenka@barc.gov.in

P. K. Patro · T. Mahata
Homi Bhabha National Institute, Mumbai 400094, India

A. K. Tyagi and R. S. Ningthoujam (eds.), *Handbook on Synthesis Strategies for Advanced Materials*, Indian Institute of Metals Series,
https://doi.org/10.1007/978-981-16-1803-1_1

Keywords Consolidation techniques · Shape forming · Sintering phenomena · Sintering mechanism · Assisted sintering

1.1 Introduction

Ceramic materials are being used since ancient times for different applications due to its higher strength and non-corrosive nature. In date to day life traditional ceramics like potteries, porcelains, cement, glass, etc. are being used. Advance ceramics or engineering ceramics are being explored in recent times to mitigate the challenges offered to develop materials of enhanced functional properties. These ceramics are being used for electrical, optical, magnetic, nuclear, thermal, chemical, and biological applications [1–4]. Among these advanced ceramics which finds its technological application needs stringiest compositional control, processing condition, shape forming methodology, and sintering conditions to meet the functional requirement. This needs expertise in the field of advanced ceramic fabrication technology with a combination of a good understanding of solid-state chemistry and physics. Based on the end applications, one particular ceramic material may have to go through several processing conditions. Material availability, specific properties, and fabrication technique are three corners of the product triangle. However, availability of the material or synthesis of the material in desired phase is a matter of concern. Once the phase pure material is developed, the role of fabrication technique is to prepare desired shape and size for the intended application. Here, processing of ceramics is required to get a near net structure which need to be sintered for further densification. During sintering, dimension of the green shape decreases appreciably leading to stress and defects in the material. Raw material quality and pre-processing are required to minimize the dimensional change and defect annihilation.

Ceramic materials due to its higher melting temperature cannot be shaped like metals via melting and casting methods. Hence powder metallurgy route is adopted for shape forming of ceramics followed by sintering. Shape forming in ceramics is undoubtedly the key stage in the manufacturing of any ceramic component; this not only determines its geometry but also its functional requirement. The functional properties are in turn influenced by the properties of the raw materials [5]. Broadly ceramics show mixed bonding behavior, a combination of covalent and ionic bonds. This determines the type and selections of consolidation techniques which will be more appropriate to arrive at a component with desired properties. Before finalizing a consolidation technique, physical and chemical characterization of powder particles are carried out first followed by the selection of additives required for powder processing and shape forming technique.

Shaping alone does not circumvent the purpose. The desired functional properties like mechanical property, electrical property, optical property, magnetic property, catalytic property are prominent in the dense structure. Intrinsic properties such as thermal expansion, elastic modulus, and melting temperature do not depend on the

microstructure of the sintered body. However, electrical properties, magnetic properties, dielectric properties, mechanical properties depend on the microstructure [6]. In a sintering process, coherent and preferentially a solid structure is achieved on heating the green compact at high temperatures. Strong inter particle bonding is developed with decrease in the inter particle space by diffusional mass transport. With progress of sintering temperature and time different microstructure is developed. Based on the microstructural development, different stages of sintering are assigned and mechanism for the same has been evolved. The factors that influence sintering process are sintering temperature, heating rate, atmosphere, pressure, composition, and non-stoichiometry; hence influence the product quality [7, 8]. All these aspects will be covered in this chapter.

1.2 Important Characteristics of Ceramic Feed Material for Shape Forming

The starting powder characteristics (physical and chemical) have significant influence on the consolidation and sintering processes. The most important characteristics are phase purity, particle shape, size, and distribution. For achieving a good sintered product it is desirable to have a uniform and more closed powder packing in the green compact which is guided by the powder quality. Chemical composition and purity are of utmost importance in processing advance ceramics. A small change in the chemical composition or presence of impurity largely influences the functional property of the ceramic products. For example, transparency in magnesium aluminate ceramics decreases drastically with the incorporation of a small amount of impurity [9]. LiF addition to the magnesium aluminate spinel increases the transparency as it helps in removing the impurities at the grain boundaries. Apart from impurity, phase purity of the starting powder is also ensured to achieve desired properties.

Surface area of the powder is an important parameter which influences the sinterability and densification. Particle agglomeration is a phenomenon which retards sinterability. As the particles obtained from various processes are generally submicron in size there is a tendency to agglomerate during preparation steps. This agglomeration can be avoided in the wet chemical synthesis route by adding suitable dispersant. In a powder mass the particles can be a primary particles or particle agglomerate. Primary particle is the smallest unit with definite boundary/surface. It cannot be further broken down by forces like ultrasonication, grinding etc. Primary particles are bonded together by weak forces and form agglomerates. Hence, interconnected porosities remain there within an agglomerate. Based on the strength of the agglomerates, it can be soft or hard. The soft agglomerates are likely to be broken down into primary particles by repeated milling or pressing. Particle is in general the smallest unit that moves in a medium or the smallest unit that is transferred. Schematic diagram of primary particle, porosity, and agglomerates is shown in Fig. 1.1. From the picture, it can be seen that isolated pores do exist in the primary particle and continuous pores

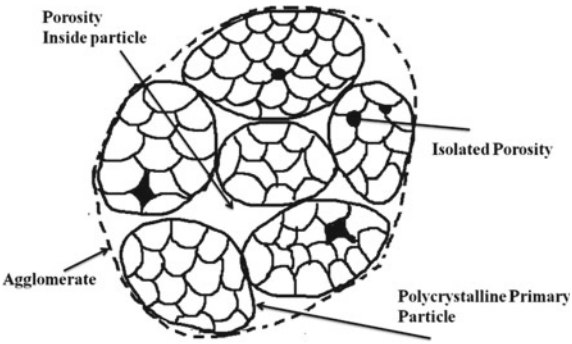

Fig. 1.1 Schematic diagram of agglomerate showing particles and porosity

in the inter particle space. Another term commonly used is aggregate, which is a large size (1–50 μm) hard agglomerate. Aggregates are difficult to break by ultrasonication and even by ball milling, hence avoided in the powder metallurgical processes. Non-uniform and preferential sintering takes place at certain regions in the aggregate which leads to non-uniform densification.

Ceramics are divided into two categories, namely, crystalline materials and amorphous materials. In crystalline materials, there is a long range repeated rearrangement of atoms in three dimensions. The smallest unit of the crystalline material is called crystallite or grain. When the primary particle is a single crystallite, it is called a single crystal. When a primary particle constitutes lots of crystallites separated by boundaries called grain boundaries, this particle is called a polycrystalline material. This grain boundary region is a highly disordered area where there is a random arrangement of atoms. Grain size may vary from nanometer range to micron range. In polycrystalline materials when the grains are in nanometer range, these are called nanocrystalline materials. These nanocrystalline materials show distinct advantages due to finer grains, and higher grain boundary area to grain area. For example, superplasticity of Ni_3Al alloys decreases from 1050 to 650 °C when the grain size changes from 6 μm to 50 nm [10]**.** Many of the properties like hardness, strength, ductility, thermal conductivity, electrical conductivity are influenced by the nanocrystalline nature of the materials [11]**.** Amorphous materials like glasses and cements do not have either long range repeated arrangement of atoms or they have distinct grain boundaries. Hence, they offer different kinds of mechanical, thermal, and electrical properties.

In many of the shape forming methods, powders are often granulated to increase the flowability which in turn gives uniform green density, reproducible property, and improved productivity. Within a granule, a high packing density is obtained. The need of granulation is experienced while compacting nano-powders. Low flowability of nano-powders in the die filling step leads to inhomogeneous powder packing. Therefore, nano-powders need to be granulated before going for any shape forming process. Some of the defects in the pressing of nano-powder are end capping, chipping, non-uniform densification along the uniaxial pressure direction. For ceramics, both dry and wet granulation methodologies are adopted depending on the nature of powder.

As the starting powder has significant influence on the shape forming methods, its physical and chemical characterization is done first. Based on the properties, further processing method is decided.

1.2.1 Physical Characteristics

Measurement of particle size and distribution: Different methods have been used to measure the particle size of the powders. Microscopy is being used to see the particle size and shape. If the particle size is more than ~1 μm optical microscope is used to observe the size. For lower size particles down to ~1 nm, electron microscope is used. Due to higher resolution, degree of agglomeration is also observed from the electron micrographs. For measuring the average particle size and distribution, the image analysis tools are used where a large number of image files can be processed in a small-time scale.

Sedimentation method is also used for size measurement. Principle of particle size measurement using sedimentation of powder particle through a liquid medium is based on Stokes law. When a powder is falling in a viscous medium, it attains a constant velocity called terminal velocity defined by the weight of the particle and viscosity of the medium. In this method powder is put on a liquid surface and concentration of particles at a particular height is measured with time. This gives information about the size and particle fraction. Sedimentation method has its own limitation. When the size of the particle comes down to nanometer range, the particle follows Brownian motion, and erroneous sedimentation result is obtained.

The most common method used for particle size measurement is based on light scattering. The principle of particle size measurement based on light scattering is based on Raleigh scattering theory, Mie theory and Fraunhofer diffraction theory. When light falls on a particle dispersed in a medium, the scattering angle is inversely proportional to the size of the particle. One to two monochromatic light sources are used for scattering experiment and the intensity of light are measured at different angles. Measurement of scattered light at a certain angle defines the particle size and intensity of light defines the population. Particle sizes from 0.1 to 1000 μm can be measured by light scattering method. Brownian motion of smaller particle lower than 0.1 μm when dispersed in a liquid limits the use of most intensively used light scattering method for measuring the size. For nano particles, intensity of the scattered light at a particular angle changes with time. This change in intensity of the scattered light is monitored and particle size information is calculated from Stokes-Einstein equation. This is the basis of particle size measurement of nano particles via dynamic light scattering.

Particle size can also be measured from the broadening of the x-ray diffraction peak pattern.

This broadening is calculated from the full width at half maximum (FWHM). Instrument broadening and residual stress in the sample also contribute to the broadening phenomena. Suitable methods are utilized to calculate the broadening due to sample only and the other factors are subtracted from the measurement. It can be mentioned here that the size measured by x-ray line broadening is the crystallite size. Hence, the value measured here will be always lowest compared to size measured by other methods. For most of the nano-materials, crystallite size is equal to particle size when there is no agglomeration between the particles.

Surface area: Measurement of surface area is based on the principle of nitrogen adsorption on the particle surface. Powder sample is degassed at 200–300 °C and equilibrated with nitrogen gas at different pressure keeping sample at liquid nitrogen temperature. Adsorption-desorption isotherm from the surface area measurement gives an idea of pores inside the particles. Results from particle size analysis, surface area measurement, and X-ray line broadening can be correlated to get information about primary particles, agglomerates, and extent of agglomeration.

1.2.2 Chemical Characteristics

Chemical characterization of powders before shape forming includes compositional characterization, phase characterization, and surface characterization. Compositional characterization of the powder includes the determination of chemical composition and the impurity analysis in the sample. Phase characterization includes the phase formation and crystal structure determination. Surface characterization includes the determination of composition at the surface and oxidation state of the element on the powder surface.

1.2.2.1 Chemical Characterization

Powder composition has been analyzed by atomic absorption spectroscopy (AAS) and inductively coupled plasma atomic emission spectroscopy (ICP-AES). The sample is dissolved in suitable acid or alkali medium and the elemental composition is measured from the absorption or emission spectra. Many ceramics are not soluble with any of the solvents. Hence it is difficult to analyze the samples by these above methods. X-ray fluorescence spectroscopy is often used to analyze the elemental composition of ceramics. Solid samples can be analyzed directly without dissolving in a medium. As the analysis is very fast, it is widely used for compositional analysis at the first site. Detection limit of this method is poor compared to AAS, hence impurity analysis is more preferred in AAS. Another method of analyzing composition is by DC arc method. DC arc is being used to excite the sample from solid state to vapor

form. Once the sample is vaporized, its absorption spectra are recorded for elemental analysis. Apart from these, techniques like neutron activation analysis (NAA), energy dispersive spectra (EDS), and electron energy loss spectroscopy (EELS) are used for impurity analysis.

1.2.2.2 Phase Characterization

The phase purity of the material is confirmed by analyzing the X-ray diffraction pattern of the sample at room temperature. Phase evolution of the sample at high temperatures is analyzed by heating the sample at high temperature and simultaneously taking the diffraction data. Apart from the phase information, the lattice structure can be refined from the diffraction data. Similar to x-ray diffraction, neutron diffraction experiments are used for phase and structural characterizations of materials. As neutrons interact more with low Z elements, polymer samples are extensively studied via neutron diffraction experiments. Due to coupling of magnetic field with neutrons, magnetic domains are well characterized by neutrons. However, due to less availability of neutron source, this method is limited to laboratory experiments only.

1.2.2.3 Surface Characterization (Compositional)

As decrease in surface free energy is the driving force for sintering, surface characterization has immense influence in the sintering process. Surface compositions and defect concentration on the surface are important. Techniques like auger electron spectroscopy, x-ray photo electron spectroscopy, Fourier-transform infrared spectroscopy (FTIR), Raman spectroscopy are used to know the surface composition and oxidation state of different elements. Combined with surface area data, this surface information has vital role in defining surface diffusion mechanism and hence the sintering mechanism.

1.3 Role of Additives in Ceramic Green Shape Formation

There are four categories of ceramic shape forming processes, which are largely classified based on the quantity of water/solvent in the ceramic bodies and pressure applied for shape forming. These are (i) dry shaping (ii) semi dry pressing (iii) plastic forming and (iv) semi-liquid shaping as shown in Fig. 1.2. In dry pressing, no water/solvent is mixed with the powder and very high pressure is required. As water content increases, pressure required for shape forming decreases [12, 13]. Table 1.1 compares the details about three major shape forming methods, namely, dry pressing, extrusion and slip casting. Comparison is made with respect to complexity of shaping, cost of production, production rate, industrial adoption of the process, etc.

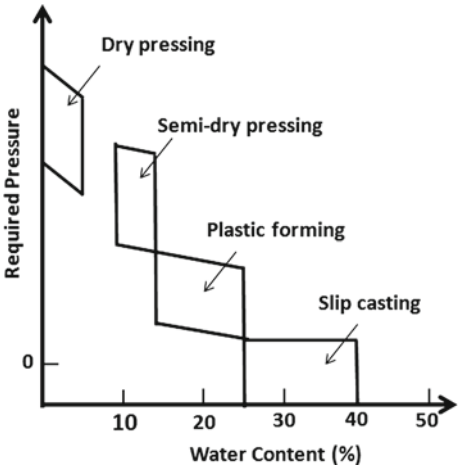

Fig. 1.2 Water content versus required pressure in different shape forming process

Table 1.1 Comparisons of three major shape forming methods

	Dry pressing	Extruding	Slip casting
Average moisture content	5 wt%	17 wt%	28 wt%
Green density	High	Medium-high	Low
Green deformability	Low	Medium	High
Mold/die material	Rigid or Elastic	Rigid	Rigid
Mold/die porosity	No	No	Yes
Shrinkage after sintering	Low	Medium	High
Drying ability	High	Low	Low
Geometry of shaped article	Simple	Quite complex	Complex
Productivity	High	High	Low
Automation level	High	High	Low
Specific production cost	Medium	Low	High

Powder packing density in the green shape should be uniform in order to achieve sintered body with uniform density and microstructure. Depending on the shape forming method ceramic powder is mixed with essential additives in a definite ratio. The common additives include solvent, binder, plasticizer, dispersant, and lubricant.

The combination of additives that are to be used depends on the shape forming methodology. Each additive has specific roles in green shape forming as described below.

Binders: Binders are long chain polymer molecules either soluble in water or in organic liquid. Binder when added with powder in small concentration creates bridges between the particles and provides handling strength in the green body formed by pressing dry powders. Binders are also added in the powder granulation step. The granules are often used as feed material for powder compaction. Binders are used in high concentration to provide flexibility in the feed material for shape forming through processes like extrusion and injection molding. When used in high concentration, binder burn out (BBO) step becomes critical in subsequent processing. Temperature, holding time, heating rate, and atmosphere are judiciously chosen in the binder burn out step. Some of the water soluble binders are polyvinyl alcohol (PVA), polyvinylpyrrolidone, poly acrylic acid, polyethylene glycol, methyl cellulose, starch, and dextrins**.** Binders commonly used in organic medium are polyvinyl butyral (PVB), poly methyl methacrylate (PMMA), ethyl cellulose, etc.

Plasticizers: Plasticizers are usually of low molecular weight organic substances and used to soften the binder in the dry or near dry state. Plasticizer is most commonly used in tape casting process and the role is to increase the flexibility of the green body. Plasticizers must be soluble in the same liquid which dissolves the binder. The plasticizer molecules interact with the polymer chains of the binder softens the chain alignment and reduce the Van der Waals bonding. Some commonly used plasticizers are ethylene glycol, polyethylene glycol (PEG), glycerol, dimethyl phthalate, and di-butyl phthalate.

Dispersant/De-flocculent: This is essentially used in slurry-based shape forming methods such as slip casting and tape casting. Dispersants are used to stabilize the slurry by increasing the repulsion between the particles. The viscosity of slurry is strongly influenced by the addition of small concentration of dispersant. Addition of dispersant helps in getting a slurry with high solid content. In aqueous-based slurry, some of the dispersants are sodium silicate, sodium carbonate, calcium carbonate, and magnesium sulphate. The most commonly used commercial dispersant in organic solvents are menhaden fish oil, glyceryl trioleate, oleic acid, sodium polyacrylate, ammonium polyacrylate, sodium succinate, and sodium citrate. Sometimes these dispersants leave impurity in the ceramic body, however, their quantity is so small that it does not affect the functional properties.

Lubricants: It reduces the friction between the powder and the die during compaction or shaping. This not only increases the life of the die but also gives a smooth surface to the compact. A dilute lubricant solution is applied over the die surface which are exposed to the powder. These lubricants are removed at higher temperatures. Lubricants play important role in die compaction, extrusion, and injection molding process. Commonly used lubricants are stearic acid, stearates, waxy substances, and carboxymethyl cellulose.

Solvents: The primary role of the solvent lies in the dissolution of the additives and formation of a homogenous distribution of powder in it. This gives fluidity to the slurry. Choice of additives depends on the solvent or vice versa. Aqueous medium is mostly used for making slurry for slip casting and extrusion. The commonly used organic solvents are methanol, ethanol, isopropanol, acetone, methyl ethyl ketone (MEK), chlorinated hydrocarbons (tri-chloroethylene), toluene, and xylene. Based on the cost of organic solvents and associated health issues, aqueous solvent is most preferred.

1.4 Green Shape Forming Techniques

1.4.1 Shape Forming Processes Staring with Dry Powders

There are two types of dry powder-based shaping methods (a) Uniaxial die pressing (Hydraulic Pressing) and (b) Isostatic Pressing. Homogenous powder filling in the die cavity is essential to get a uniform green density. In both types of pressing methods granulated powder (or spray dried powder) is usually used. As solvent is not used, no dimensional change is expected in the green compact. A better dimensional control can be achieved by this dry powder pressing methodology.

1.4.1.1 Uniaxial Die Pressing

In this process granulated powder is allowed to flow into a hardened steel die/mold followed by uniaxial pressing. Powder inside the die is pressurized and kept at desired pressure for some time before releasing the pressure. The same press is being used for ejecting the compact from the die. Normally the die materials used are either hardened steel or tungsten carbide. Pressing action can be done by movement of either single punch (top or bottom) or both punches. Accordingly, these are called as single acting or double acting uniaxial pressing. Schematic of single acting and double acting die pressing is shown in Fig. 1.3. Double action press is better than the single action press in getting a fairly uniform density product. This becomes more significant when the desired shape has large length to diameter ratio.

Sometimes binder is added during dry pressing of the powder which helps in retaining its shape after the compaction and gives handling strength to the compact. The binder is chosen in such a way that it leaves the system upon heating without any traces. Binder is removed at a temperature around 300–500 °C. Binder burnout schedule and sintering atmosphere are defined accordingly. This method of shape forming is normally automated to a large extent for mass production of the components in industries. A simple grinding or polishing of the compact may result in a ready to use product. However, this technique is not used for complicated shapes.

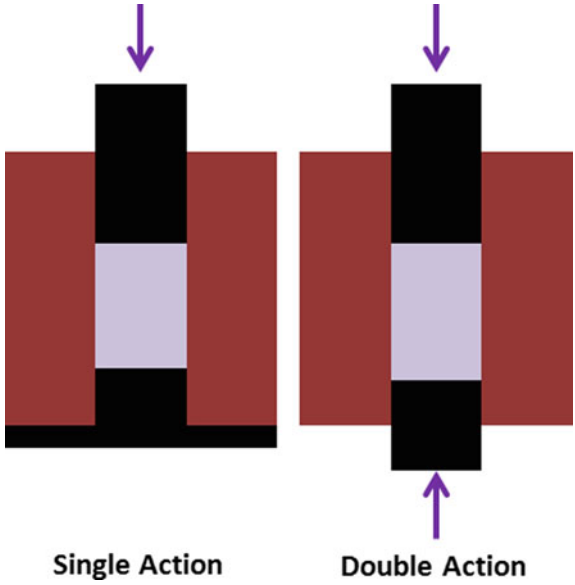

Fig. 1.3 Single and double action die pressing

After compaction, the green body must be ejected from the die. During die ejection the green body is released from compression at high pressure to very low pressure gradually and then pushed out of the mold. The primary force to be overcome during die ejection is that of wall friction which depends on the roughness of the die wall and lubrication applied. For walls with a scale of roughness larger than the diameter of the powder, the wall friction is essentially the same as the internal friction of the powder. If the wall has a scale of roughness smaller than the diameter of the powder, the wall friction is controlled by particle-wall friction [14]. Wall friction can be decreased by lubricants applied to the wall prior to pressing. Common lubricants like steric acids, stearates, and various waxy substances can be used to minimize the particle-die wall friction [15].

The common defects observed in this process are delaminations, end capping, or ring capping. However, use of proper die tooling, selection of pressure, powder granulation, proper lubrication, and powder filling reduces these common defects. For example, making a pellet using fine/nano-powder directly may cause end capping and sometimes cracks. Here, pre-compaction of the powder and granulation annihilates these defects.

1.4.1.2 Cold Isostatic Pressing (CIP)

In cold isostatic pressing method of shape forming, powders are filled in a flexible mold (e.g., a rubber membrane or a metallic can) that is subjected to isostatic, external pressure. The rubber mold is filled with powder and is then submerged in a pressure

vessel filled with oil. The fluid is pressurized and the fluid pressure is isostatically transmitted to the powder.

Normally cold isostatic pressing is of two types (a) Wet bag CIP and (b) Dry bag CIP as shown in Fig. 1.4a and b. In Wet bag CIP, the rubber mold is filled with powder and is then submerged in the pressure vessel. This type of CIP is used for shaping complicated shapes and large jobs with extremely high applied pressure (10^4–10^5 psi). The disadvantage of a wet bag CIP is the possible contamination of the job with the pressurizing fluid. A leak during compaction or removal of job in the rubber mold will lead to contamination of the compact with the oil. It is not suitable for near net shaping, labor intensive, and has low production rate. Hence usually this type of CIP is limited to R&D laboratories and academic institutes. In dry bag CIP the mold is fixed in the pressure vessel; powder filling and compacting takes place within the pressure vessel. The advantages of this type of CIPs are high production rate in an automatic to semi-automatic systems, free from fluid contamination, capability of pressing near net-shaped compacts, and less labor intensive. The disadvantages of dry bag CIP systems are smaller size of compact formation capability and have a lower pressure capability compared to wet CIP systems [16]. These systems are very much suited for industries with larger production cycle.

Compression, holding, and decompression cycle is followed precisely to achieve sound green compact. As the pressure is isostatic the compact achieves uniform density. The advantages of isostatic pressing over die compaction are uniform hydrostatic pressure, no friction with die wall, and complex shape formation with uniform density.

1.4.2 Shape Forming Using Ceramic Paste

1.4.2.1 Extrusion

In extrusion, a powder is mixed with solvent, binder, and lubricant to make stiff dough. Green shapes are formed by pushing the pastes continuously through a die. Due to higher hardness of ceramics, erosion of the die walls decreases the die life. Hence, it is a general practice to use lubricating agent while preparing the dough. Die is typically made of hardened steel or tungsten carbide.

Industrially, the process is usually carried out by a screw-fed extruder connected to an electric motor. This process can be used to produce long extrudates. Because of the high shear rates imposed upon the ceramic paste it flows through the die and upon leaving the die it solidifies into the desired shape as the paste is no longer under shear. Before it completely solidifies, the extrudate is cut periodically to give green bodies of definite length [17]. The schematic of extrusion process is shown in Fig. 1.5. Extrusion is a continuous process with high production rate and low production cost. However, the products have limited complexity in shape and have uniform cross-sectional area. Ram driven by hydraulic press is also used for extrusion press. But these are semi-continuous processes, dough is filled in the die periodically. Solvent

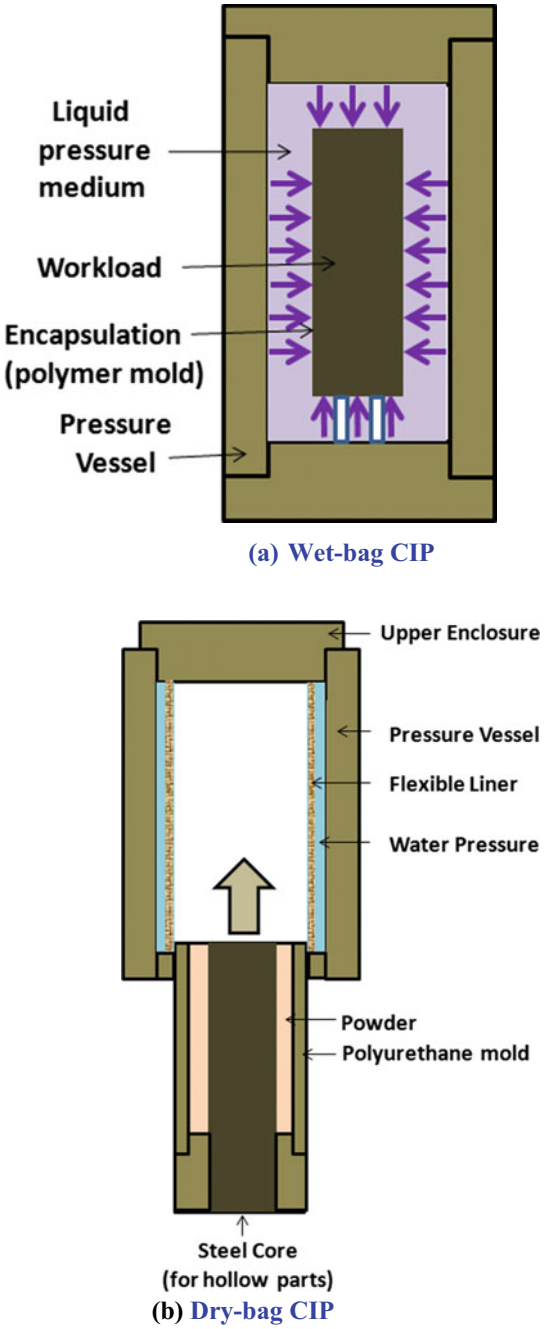

Fig. 1.4 Schematic of cold isostatic pressing **a** Wet bag CIP. **b** Dry bag CIP

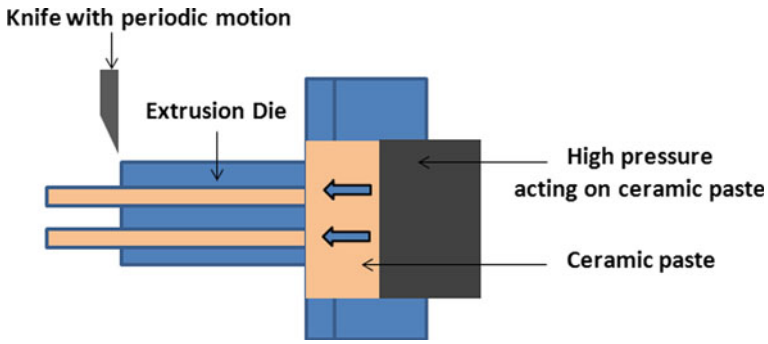

Fig. 1.5 Schematic of an extruder machine

drying and binder burn out is a critical step before firing the components. Therefore, binders and additives are judiciously chosen in an extrusion process.

1.4.2.2 Injection Molding

Ceramic injection molding is the most versatile technique in which the ceramic powders are converted into a green shape through an organic vehicle. This technique is similar to polymer processing where a thermoplastic polymer which softens upon heating and hardens on cooling is used. This thermoplastic polymer is used as binder in injection molding process. In ceramic injection molding normally the ceramic powder is added to the thermoplastic polymer (binder) along with other organic materials to achieve the desired rheological properties. The total organic component may be as high as 40% of the total mix. Here the plastic mass is first heated and then forced into a cavity when the desired softening of the mass is achieved. It was then allowed to cool in the mold so that the organic component hardens. In this process a typical shrinkage of 15–20% makes it difficult in achieving the desired dimensions unless vigorous optimization in powder processing, polymer type, quantity of organic polymer, and molding conditions are carried out [18].

Binder burnout is a crucial step in injection molding technology. Decomposition or evaporation behavior of binder, decomposition temperature, and impurity content affect the product quality. When this binder leaves the molded product, rearrangement of particles takes place. Hence removal rate or kinetics of decomposition essentially affects the product quality. A schematic of the ceramic injection molding is shown in Fig. 1.6. Split mold is used for shape forming through injection molding as complicated shapes are difficult to come out of the mold. Proper joining of the two splits of the mold is essential to hold the powder with the thermoplast at high temperature and high pressure. This technique has the capability of manufacturing complex shapes with dimensional accuracy. The limiting factors are a high capital and tooling cost. Non-uniform solidification and removal of organic matter prior to the initiation of sintering are also the limitations of this method [12].

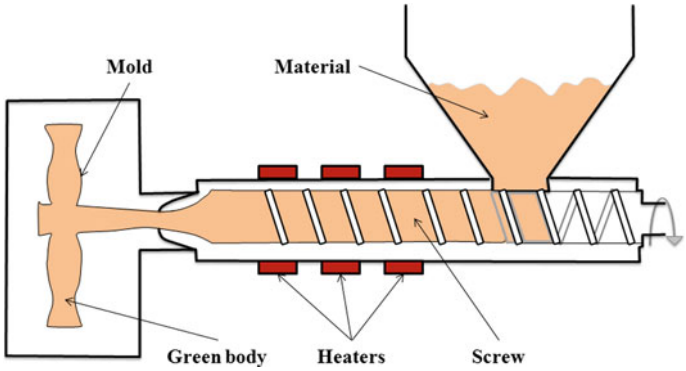

Fig. 1.6 Schematics of an injection molding machine

1.4.3 Shape Forming Using Ceramic Slurry

In this type of shape forming processes, ceramic powders are dispersed in a solvent for the preparation of the slurry. The slurry formation involves (a) wetting the solid particle surface with the liquid (i.e., replacing solid-vapor interracial area with solid-liquid interfaces), (b) breaking down agglomerates, and (c) controlling particle surface charge to prevent flocculation or re-agglomeration. To optimize dispersion and stability, dispersants, also known as deflocculants are often added to the slurries [19]. Deflocculants prevent dispersed particles from re-agglomerating in the slurry by keeping particle-particle separation distances sufficiently large such that the short range Van der Waals attractive forces that hold particles together are negligible. Particle stabilization in a slurry is achieved by steric effect of the dispersant or the electrostatic effect of the dispersant with respect to the charge of the particles. The preferential adsorption of large deflocculant molecules on the particle surfaces separates the particles by steric effect. Electrostatic stabilization is achieved by forming electrical double layer around the particles that results in repulsion between particles of similar surface charges [20].

Two major types of slurry-based shape forming processes are

(a) Slip casting/pressure casting
(b) Tape casting.

1.4.3.1 Slip Casting

Slip casting is an old and well-established technique which uses precisely shaped porous molds for casting. It normally utilizes relatively cheap plaster of Paris molds. This process is extensively used in white-ware and lab-ware ceramic fabrication industries. This technique is usually selected for production of complicated shapes that cannot be achieved by simple pressing. In slip casting the slurry is poured into a porous mold that removes the liquid by capillary force through the pores and leaves

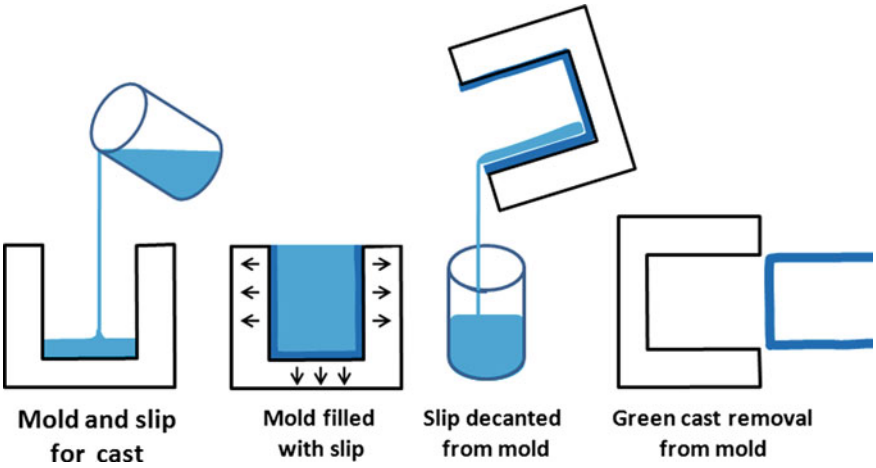

Fig. 1.7 Schematic of slip casting process using a plaster of Paris mold

a powder compact in the mold. Once a sufficient thickness is achieved, the remaining slip is poured out and the cast is allowed to dry. Once the cast is sufficiently dried it shrinks and easily comes out of the mold. The schematic of slip casting process is shown in Fig. 1.7. Another variation of slip casting is filter-pressing. Here, pressure is applied on the slurry to enhance the fluid flow through the pores of the filter. Instead of a plaster of Paris mold a durable resin mold is used. Both the capillary action of the porous mold and pressure applied to the slurry accelerate the casting process [21]. Figure 1.8 shows the schematic of the pressure slip casting process. In slip casting and filter-pressing homogeneous distribution of particles in the slurry plays an important role to ensure high green density. Slurry rheology becomes an important parameter in determining the quantity of additives (dispersant, solvents, etc.) in order to ensure good repeatability in different slip batches [22].

The solvents used in slip casting are usually classified into two major groups: (i) aqueous and (ii) organic. Most traditional ceramic industries are aqueous based. When there is a possibility of reaction between powder particles with aqueous medium, organic solvents are preferred. As there is higher cost attached to the organic solvents, its use is restricted to the casting of high-performance ceramics in industries.

1.4.3.2 Tape Casting

Tape casting is a process in which slurry consisting of ceramic powder, binder, plasticizer, and solvent is poured onto a flat substrate and then evenly spread using casting knife alternatively known as doctor-blade. The solvent subsequently evaporates resulting in a ceramic tape which can be peeled off from the flat substrate (glass/polished granite/silicone-coated mylar film) for further processing. Figure 1.9 shows the schematic of tape casting process. The equipment used for casting the

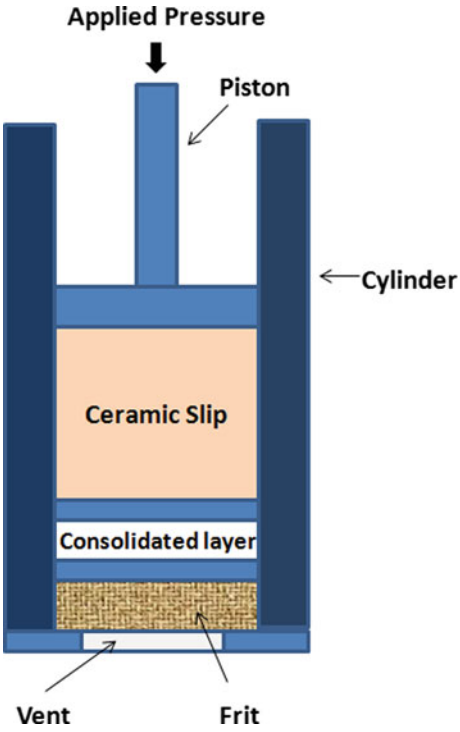

Fig. 1.8 Schematic of Pressure slip casting

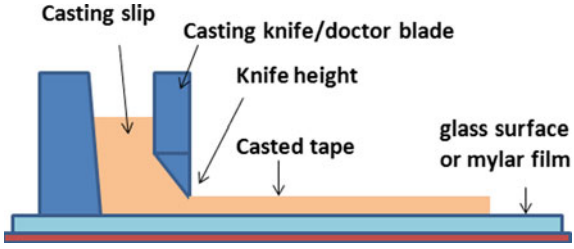

Fig. 1.9 Schematic of tape casting process

tape is called doctor-blade tape caster. It can be a moving blade type or moving bed type. For lab scale fabrication process moving blade type systems are used where normally the tape is casted on a fixed glass or granite surface. In a moving bed type tape casting system which is normally employed for regular production in an industry, the bed (silicone-coated mylar film) is moved at certain speed keeping the doctor-blade constant. These systems are usually accompanied with an in-situ dryer so that the casted tape can be stored in a film roll immediately.

The tape thickness can be controlled by adjusting the gap between the substrate and blade. Both water and organic-based slurry formulation can be done and powder can have moderate to high packing factor. Some solvents or other constituents might be carcinogenic and care must be taken during drying and debinding steps. Quality

of tape is very sensitive to slurry composition and ambient conditions (temperature and humidity) of the lab [23].

In a tape casting slurry normally both binder and plasticizer are added to the solvent. The solvents can be either water or organics like alcohols, ketones etc. In some cases an azeotropic mixture of solvents is used and the commonly azeotropic mixture used is ethanol-methyl ethyl ketone [24]. In the azeotropic mixture the drying rate of the solvent is controlled. When the amount of binder is less it generates crack in the tape and excess binder may result in tapes with many voids. With increase in binder, the green tape strength increases but this leads to a decrease in green tape density. Most commonly used binders are ethyl cellulose, poly vinyl alcohol (PVA) and poly vinyl-butaral (PVB). Glycerine, diethyl oxalate, poly ethylene glycol (PEG), and di-butyl pthalate (DBP) are the most commonly used plasticizer in the process of tape casting. It is difficult to handle either nano-powders or large micron size particles (>50 μ) for tape casting. Slurry rheology will be difficult to adjust for these types of powders. Tape-casted products find applications mainly in capacitors and piezo actuators (either in manolayer or multilayer forms) porous substrate for filter applications, solid oxide fuel cell, etc.

1.5 Sintering Phenomenon

Sintering is a process in which a green compact is heat treated at high temperatures to give a coherent and preferentially solid structure as a result of strong bonding between the particles [6]. Coherent bonding between the particles leads to decrease in porosity in the green compact. These strongly bonded structures generate different microstructures. Some of the properties that depend on microstructure are mechanical strength, dielectric strength, electrical conductivity, etc. which improves upon sintering. All pre-compaction technologies discussed earlier generate near net shape. This only offers handling strength in the compact and deprives of required functional properties which depends on density. Hence sintering not only gives strength but also influences some of the microstructural and density dependant properties. The driving force for sintering process is the decrease in surface free energy of the system. There is a large change in the surface area of the particles which leads to decrease in surface free energy of the system. Particles lose its identity in sintering and inter particle pores are closed by the mass transfer from particles to pores. Chemical potential at a point depends on surface free energy and chemical composition. Mass transfer takes place due to the chemical potential difference between two points [25]. There are different pathways through which mass transfer takes place. The various mass transport phenomena are surface diffusion, viscous flow, plastic flow, vapor transport, volume diffusion, and grain boundary diffusion [26]. Mass transfer takes place through the solid state diffusion process primarily. Sintering is predominately discussed for solid state sintering of crystalline materials. Other two types of sintering are liquid phase sintering and reaction sintering where an added liquid phase or reactive phase enhances the mass transport process.

In the sintering processes, intra particle and inter particle pores close and bonding between particles take place. Therefore, change in dimension occurs during sintering of ceramics. Precise dimensional control in sintering is essential. If highly compressible powder is used as initial powder, a large dimensional change is expected. The ultimate goal in sintering lies in densification with limited shrinkage and free of defects. However, impurity from binders, plasticizers, dispersants, and additives generate defects in the dense structure. As sintering is an irreversible process, defects remain to the end. Similarly, in-homogeneity in the green compact is reflected in the final structure as a defect. Hence in getting a finished product with precise dimension free of defects, a lot of parameters have to be taken care.

Sintering takes place in stages and transport of mass is the phenomena that guides sintering. If spherical model of sintering is considered, first the particles come in contact followed by neck formation. Neck growth is the next step in sintering where separation between particles comes down. With increase in neck size, interconnected porosity decreases and at certain stage only isolated pores are formed. In the final stage, these isolated pores are closed. This whole process is pictorially represented in Fig. 1.10.

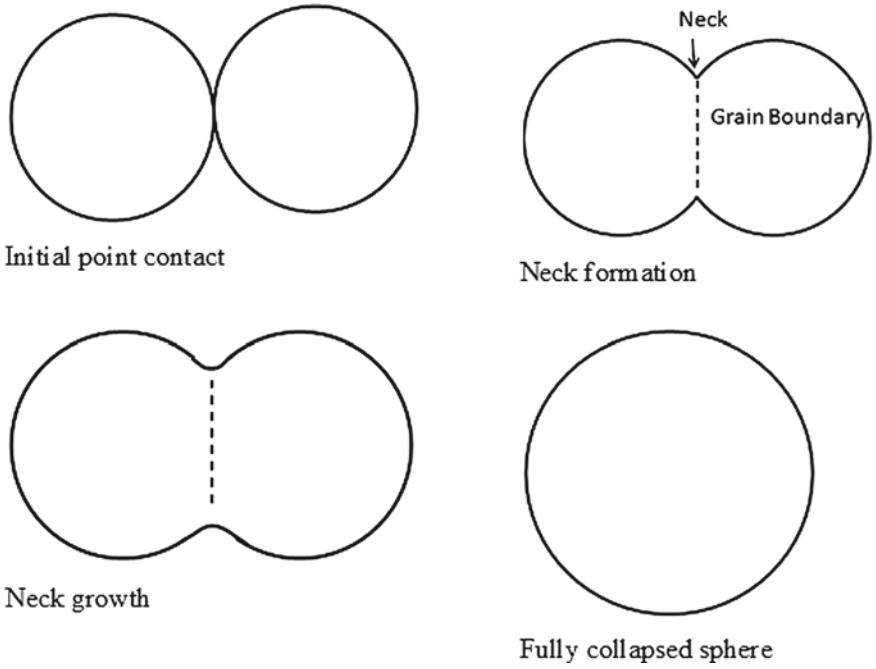

Fig. 1.10 Inter particle bonding during sintering

1.5.1 Different Energy Terms in Sintering

In the solid-state sintering of polycrystalline materials grain and grain boundaries are developed upon densification. Scanning electron micrograph of a sintered material is shown in Fig. 1.11 reflecting distinct grains separated by grain boundaries. The grains can be considered as single crystals within which the atomic arrangements are regular in three dimensions. At the grain boundaries there is discontinuity in the repeated pattern. Atomic positions at the grains and grain boundaries are schematically presented in Fig. 1.12. These atomic positions can be visualized through a high resolution transmission microscope (TEM). It can be observed that the misfits between two grains are not constant. This misfit is measured in terms of misfit angle as shown in Fig. 1.13. Based on the misfit angle grain boundaries are assigned as small angle and large angle grain boundaries. A lot of mechanical properties depend upon this orientation of the grain and grain boundaries. The deviation of atomic position from the perfect lattice leads to a higher energy-state. This is the origin of grain boundary energy. Grain boundary energy is correlated with excess volume of an interface which can be calculated from the knowledge of grain boundary crystallography. Anisotropy in the grain boundary energy is measured from the dihedral angle at triple lines and using Herring equation at triple junctions. Grain boundary energy dictates the distribution and population of grain boundary [27]. Grain boundary energy is related to the energy of two surfaces that make up the boundary.

Surface energy (γ) is the energy required to create a new surface and defined by

$$\gamma = {}^{dG}/_{dA}$$

dG is the change in free energy of the surface due a small change in area dA.

Surface free energy is similar to surface tension. Surface tension is the force per unit length in all directions on the surface. Whereas surface energy is the

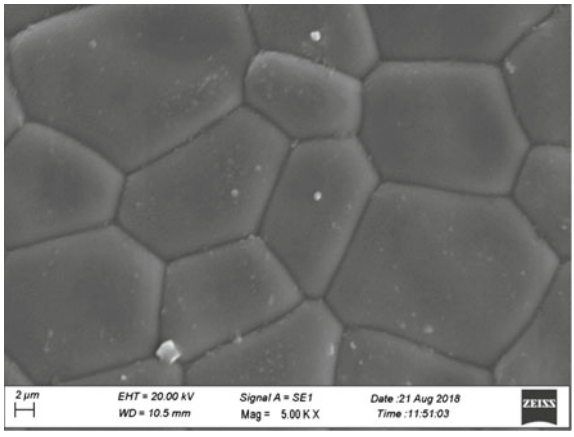

Fig. 1.11 SEM picture of sintered ytterbium iron garnet showing grain and grain boundary

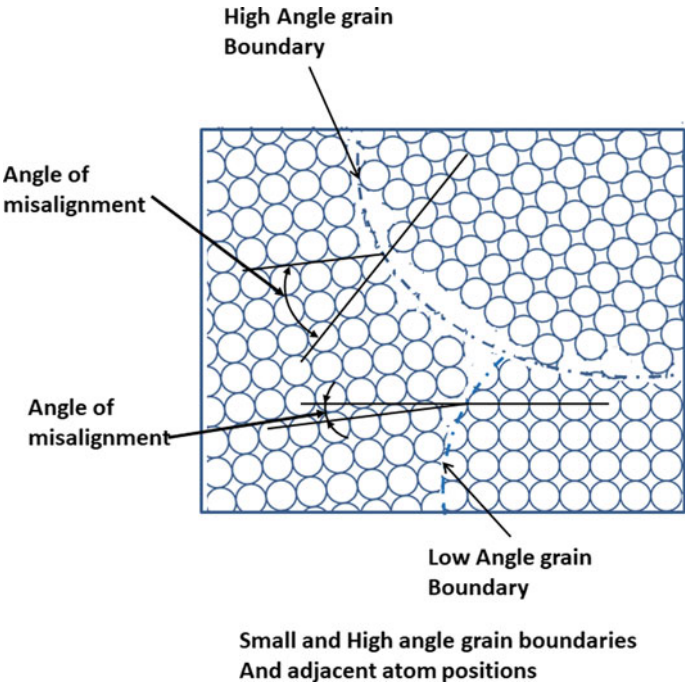

Fig. 1.12 Pictorial presentation of atomic arrangements in a grain and grain boundary

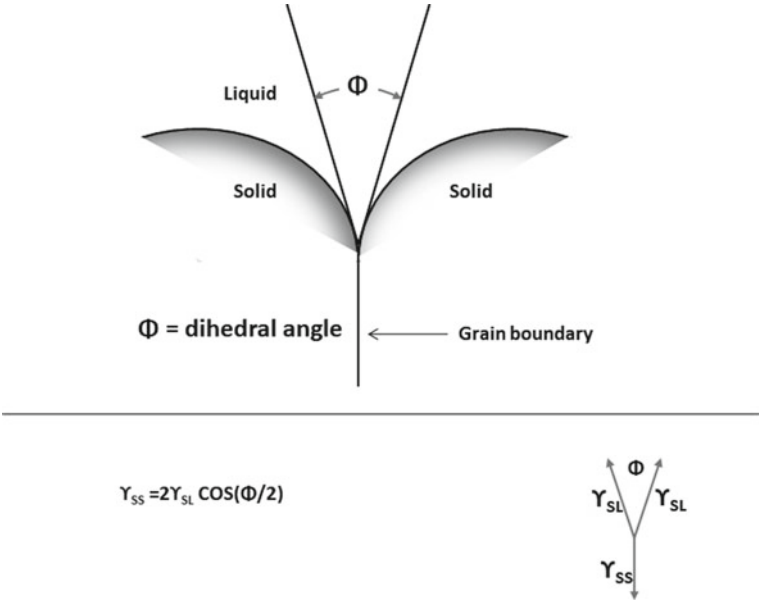

Fig. 1.13 Representation of the dihedral angle and energy balance at the triple point

energy required to create a new surface. Assume a molecule inside a liquid droplet. It is homogenously surrounded by other molecules by cohesive forces. However, molecules at the surface are attached to the molecules inside the bulk by cohesive forces from inside. But have unbalanced forces on the top. This creates stress on the surface [28].

1.5.2 Sintering and De-Sintering Phenomena

During sintering the value of grain boundary energy to surface energy detects sintering. The process in which more decrease in the overall free energy occurs that path is favored. Pore structure surrounded by three grains is shown in Fig. 1.13. At the junction of pore surface with the grain boundaries, all the forces are balanced. Solid vapor interface tension is balanced by the grain boundary energy as per the following equation

$$\gamma_{gb} = 2\gamma_{sv} \cos\left(\psi/2\right)$$

where γ_{gb} is the specific grain boundary energy, γ_{sv} is the specific surface free energy and ψ is the dihedral angle. The angle between the tangents to adjacent pair of boundaries is called dihedral angle.

During sintering, surface free energy decreases due to decrease in surface area. As grain boundary area also changes during sintering the overall free energy change in the system is presented as

$$\Delta E = \gamma_{sv} \cdot \Delta A_{sv} + \gamma_{gb} \cdot \Delta A_{gb}$$

where ΔA_{sv} is the change in surface area and ΔA_{gb} is the change in grain boundary area.

The relative ratio of grain boundary energy to surface free energy predicts whether grain growth is more favorable or not.

Grain growth is an associated phenomenon with densification when the sintered mass is further heat treated after achieving full densification. In this process, grain size increases and grain boundary area decreases. Grain coarsening is another competitive phenomenon which often retards densification process. Figure 1.14 shows the pictorial representation of the rearrangement of grains in densification, grain growth, and coarsening process. Sometimes pores are entrapped in the intergranular region and within a grain. Pores remain in the sintered material and cannot be eliminated even after increasing the sintering temperature [29]. Rearrangement of pores only takes place without any significant change in pore volume. In coarsening, larger pores are developed at the expense of the smaller pores and the average pore size increases. Mass transport takes place predominantly through surface diffusion or

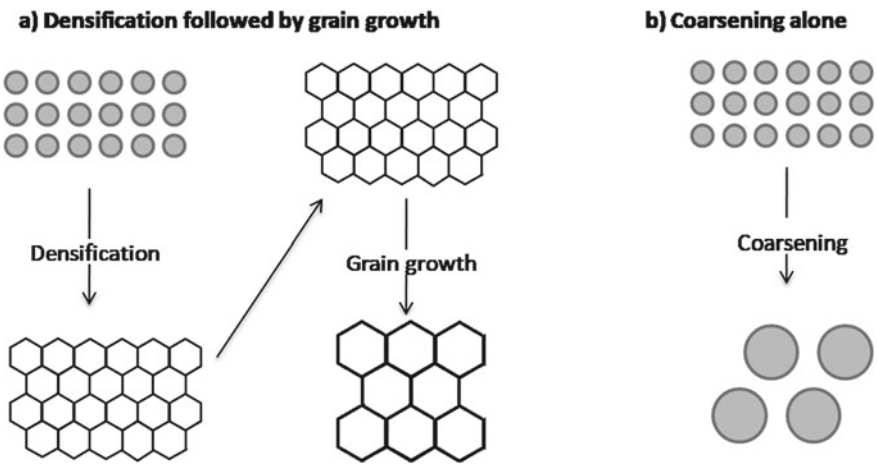

Fig. 1.14 Pictorial presentation of densification, grain growth, and coarsening

evaporation-condensation mechanism. Eventually there is a decrease in surface area without any dimensional change and no decrease in pore size [30]. In a coarsening process pore coordination number is high and particle coordination number is low. Reverse is the case for densification process [31]. Hence large grains and small pores encourage densification. In a sintering process if coarsening and densification take place simultaneously, the shape and size of pore and grain size are difficult to predict**.** In the sintering of fine ThO_2 powders from sol-gel method, near theoretical density is observed at a sintering temperature of 1200 °C. On further increase in the sintering temperature a decrease in overall density is observed [32]. At a sintering temperature of 1800 °C, 90% of the theoretical density is obtained. This is attributed to the increase in grown growth and formation of inter-granular pores.

1.5.3 Driving Force for Sintering

In the sintering process, free energy of the system decreases due to different phenomena. Three factors are responsible for the decrease in free energy, namely, decrease in curvature of the particle surface, applied pressure, and chemical reaction in the sintered mass [33]. There is a large decrease in surface area associated with decrease in surface curvature of the particles. Hence there is an overall decrease in the surface free energy of the system. Surface free energy can be correlated to surface chemical potential which is the surface or interfacial energy per unit particulate mass. Chemical potential at a point depends on chemical composition (volume free energy), surface free energy, and strain free energy. According to Gibbs-Thomson equation the surface chemical potential is inversely proportional to particulate radius.

$\mu(r) - \mu(\infty) = 2\ K\Omega/r$
$\mu(r)$ = surface chemical potential of radius r
$\mu(\infty)$ = surface chemical potential of flat surface
K = surface free energy
Ω = molecular volume
r = particle radius.

For smaller particles or particles with curved surface offers higher chemical potential. Curved surfaces tend to flatten in order to reduce this chemical potential difference.

In many of the ceramic systems surface free energy change is sufficient to cater the densification process. However, slow diffusion of mass in some advanced ceramics makes it difficult to sinter. Non-oxide ceramics are difficult to sinter through conventional method, due to involvement of many non-densifying processes. Applied pressure during sintering has advantages of formative mass transfer for densification. At the contact point the stress generated is a combination of tension, shear, and compression [34]. Chemical potential in the stress and strain region is different and this difference favors mass transport. Hence, carbides (SiC, B_4C, and TiC), nitrides (Si_3N_4), and borides (ZrB_2, HfB_2) are sintered via hot pressing or hot isostatic pressing method [35–37]. Particle rearrangement and creep mechanism are the added factors contributing to the sintering mechanism. Chemical reaction where there is a large change in free energy associated, also favors sintering. In the reaction sintering, phase formation and densification take place simultaneously. The exothermic heat of reaction is utilized for both purposes. This change in free energy is highest among the other driving forces. However, its advantages cannot be utilized due to lack of control over the grain growth. Non-uniform grain size affects the physical properties of the advanced ceramics where microstructure plays an important role.

1.5.4 Mass Transport Mechanism

There are various factors responsible for the sintering process. However, actual sintering process is associated with transport of atoms, ions, and molecules via defects. In a crystalline material there are regions of imperfection where the lattice positions are not regular. These defects are point defects, line defects, and planar defects. Point defects are more common in crystalline materials. Intrinsic defects like Frenkel defects and Schottky defects are formed due to inherent abnormalities in the lattice positions. Extrinsic defects are formed due to non-stoichiometry, atmosphere, and dopant addition. As intrinsic defect concentration is very low, it cannot affect much to the mass transport mechanism. Extrinsic defect like temperature, atmosphere, and dopant concentration controls the mass transport, hence the sintering mechanism. For example, doping of Y_2O_3 in Ce_2O_3 generates oxygen vacancies as a charge compensation process. If diffusion of oxygen vacancy is the rate limiting step, the addition of Y enhances the sintering process. It is observed that Y_2O_3 doping

level less than 0.5 mol % enhances oxygen conductivity and sintering rate [38]. It is not definite to assign a single mechanism responsible for sintering. Hence, it is difficult to tailor the sintering process, and ultimately control of microstructure.

Sintering takes place due to the transport of matter through different mass transport processes and sintering mechanism defines the transport mode by which densification takes place. In the sintering process, pores are considered as bunch of vacancies. Transport of mass takes place using these vacancies [6]. Figure 1.15 shows the different mass transport phenomena visualized at a junction of three contacting particles. Different mass transport processes associated with sintering phenomena are namely surface diffusion, lattice diffusion from the surface, vapor transport, grain boundary diffusion, lattice diffusion from the grain boundary, and plastic flow. Broadly all mass transport phenomena fall into two categories, namely, surface transport and bulk transport. Processes like grain boundary diffusion, lattice diffusion from the grain boundary, and plastic flow where transfer of mass takes place to the porous region enhance densification. Plastic flow is more prominent in case of a metallic powder system. However, the other three processes such as surface diffusion, lattice diffusion from the surface, and vapor transport, though lead to neck growth does not contribute to densification. Hence these processes are called non-densifying processes. The above phenomena are discussed for polycrystalline materials. However, similar mechanism is not valid for amorphous materials like glasses where viscous flow of materials along with particle deformation contributes to sintering and densification.

Diffusion is the major means of mass transport during sintering. Three major diffusion processes are lattice diffusion, grain boundary diffusion, and surface diffusion. Point defects move through the bulk of the lattice, hence the name lattice diffusion. Point defects like vacancies and interstitial positions take part in the diffusion mechanism. Atom from a normal site jumps to the nearby vacant site, the vacant site move in the opposite direction to a normal site. When some atoms are there in the interstitial positions, they also participate in the diffusion process. They act in a similar

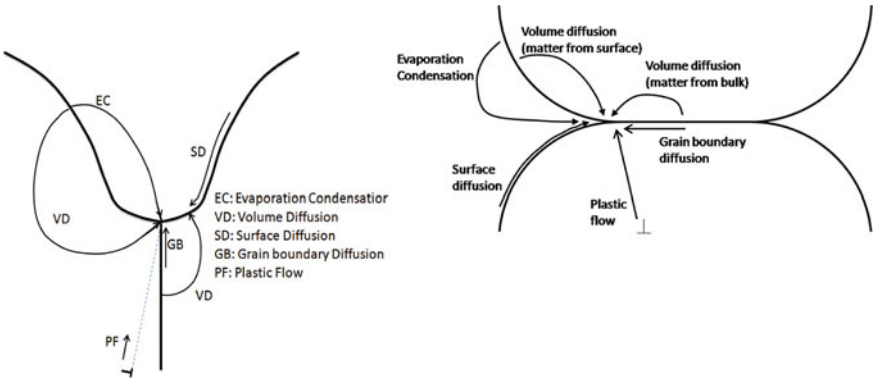

Fig. 1.15 Mass Transport processes at the contact point between three particles

way as a vacancy for mass transport. A regular atom may exchange its position with an interstitial atom or interstitial atom may move from one interstitial position to another interstitial position.

In a polycrystalline material grain boundary separates the crystals, i.e., regions of regular lattice sites. Hence, it is the highly defective or irregular region between the lattices and more facilitates mass transport through diffusion. A typical width of a grain boundary is limited to ~1 nm. For fine particles (nano-materials), the area covered by grain boundary is higher. Hence grain boundary diffusion will be more prominent in nano-materials.

When transfer of mass or vacancies takes place along the particle surface it is called surface diffusion phenomena. Like grain boundaries, surface of a polycrystalline material is not perfect and associated with defects, vacancies, ad-atoms, terraces, and kinks. Hence the diffusion process is assumed to be similar to grain boundary diffusion limited to ~1 nm thickness over the crystal surface. Unlike grain boundaries, one side of the surface is free with less number of neighboring atoms. Hence, it is easier for the atoms to migrate through the defects and have lower activation energy for the diffusion process. As activation energy is less, surface diffusion is prominent in the lower temperature region. Population of surface defect sites and their migration are temperature-dependent and atmosphere-dependent process. Surface diffusion takes place at low temperature region till the surface defects are consumed. In this process transfer of mass takes place from surface to surface without affecting any shrinkage. Hence this does not favor densification. As it is a low temperature process rapid heating at low temperature minimizes surface diffusion effect for densification.

Viscous flow is essentially a major mass transport process in amorphous material. In case of amorphous materials like glass and polymers, viscosity decreases with temperature then flow of material under applied stress takes place. Sintering of an amorphous material is different from a polycrystalline material. As there is no grain boundary, the two particles sintering phenomena or the neck formation process does not exist. The effective viscosity is inversely proportional to the volume diffusion coefficient.

Evaporation-condensation is another mass transport phenomenon where relocation of atoms from a surface to a nearby surface takes place through pores. The net result is the decrease in surface area without densification. As population of atoms on a convex surface decreases with increase over concave surface, atoms number on the surface decrease. This mode of transport depends on temperature and equilibrium vapor pressure and is defined by Arrhenius equation. Fine powder with high surface area and high vapor pressure favors evaporation-condensation phenomena as a major transport process.

When transport of matter takes place through the lattice interior it is either by viscous flow or volume diffusion. Mass transport via dislocation structure is called plastic flow. Though neck growth is facilitated by both surface and bulk transport process, their role is different with respect to sintering. Processes like volume diffusion, grain boundary diffusion, and plastic flow, where mass transfer from bulk interior to neck takes place and facilitate densification. Role of plastic flow is limited to low temperatures only. Viscous flow is more prominent in metals where liquid phase

is formed at the grain boundary. There are different theories altogether for validating a sintering process. Different geometrical models are assigned to these theories. Sintering process is modeled with temperature pressure and different dopants with respect to different mass transport mechanisms.

1.5.5 Stages of Sintering

Green compact formed by different shape forming methods is heat treated at a specific temperature, under desired atmosphere and heating rate. Initially the powder particles are packed in a definite manner. Loose powders when come close to each other during compaction adhere each other via weak forces in random orientations. A particle with an average coordination number ~7 is obtained initially. With progress of sintering the bonding between the particles grows and grain boundary is generated. This grain boundary developed has some associated grain boundary energy which is a function of crystal orientation at the boundary. As crystal orientation at the grain boundary, particle coordination and surface energy change with the progress of sintering, particle rotation takes place to minimize the change and increase the packing density [39, 40]. New contacts develop due to these changes. Particle coordination as high as ~14 is observed at the latter stages of sintering. In the sintering process with time or density of the compact, it undergoes distinct microstructural changes. Based on this changes three stages have been assigned as the initial stage, intermediate stage, and final stage of sintering. In each stage, there is a certain change in surface energy, contact between particles, porosity, and pore volume apart from microstructural changes. Microstructural changes in a sintering process are pictorially shown in Fig. 1.16.

1.5.5.1 Initial Stage

This is the first stage of sintering where neck formation between the particles takes place and neck growth with other contacting particles are independent of each other. Initial step is limited to neck growth up to 0.4–0.5 of the particle radius. Growth at neck region is associated with material deposits at the neck. In this process, gradient in the curvature decreases and surface becomes smoother. Surface curvature gradient facilitates mass transfer to the sinter bond position [41, 42]. Linear shrinkage around 3–5% is observed in this stage along with a marginal increase in the density. Initial neck growth is associated with the transfer of mass through diffusion, vapor transport, viscous flow, and/or plastic flow. Both surface and grain boundary diffusions become prominent when size of the particles decreases. Shrinkage takes place with formation of new neck and decrease in inter particle space. It has been observed that lower grain boundary energy favors grain growth instead of neck growth.

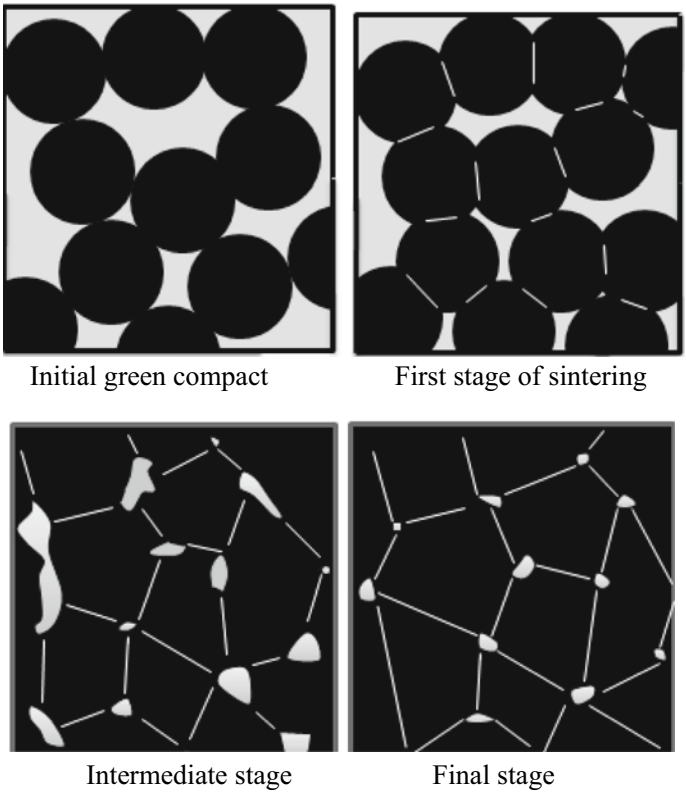

Fig. 1.16 Microstructural changes in the sintering process

1.5.5.2 Intermediate Stage

Initial stage is limited to neck formation and a small neck growth. In the intermediate stage the major change includes densification, rounding of pores, and grain growth [43]. As curvatures are smoothened in the beginning of the second stage the surface energy change is the driving force in this stage [44]. With neck growth, stable pores are generated at the grain edges. These cylindrical pores around the grain edges are continuous and distributed. At the end of the second stage, pore rounding takes place and pores are isolated at the grain corners. Both coordination number of pores and grains are frozen. This transformation from second to third stage can be visualized from Fig. 1.17. Now this continuous pore structure changes to discrete ones. Rate of densification is inversely proportional to the cube of the grain size. Hence, smaller is the grain size, larger is the densification rate. Though all mass transport means contributes in the intermediate stage, grain boundary diffusion, and volume diffusion caters to densification. Pores adhere to the grain boundary annihilates rapidly. As grain boundary is an effective path for mass transport, pore structure is largely

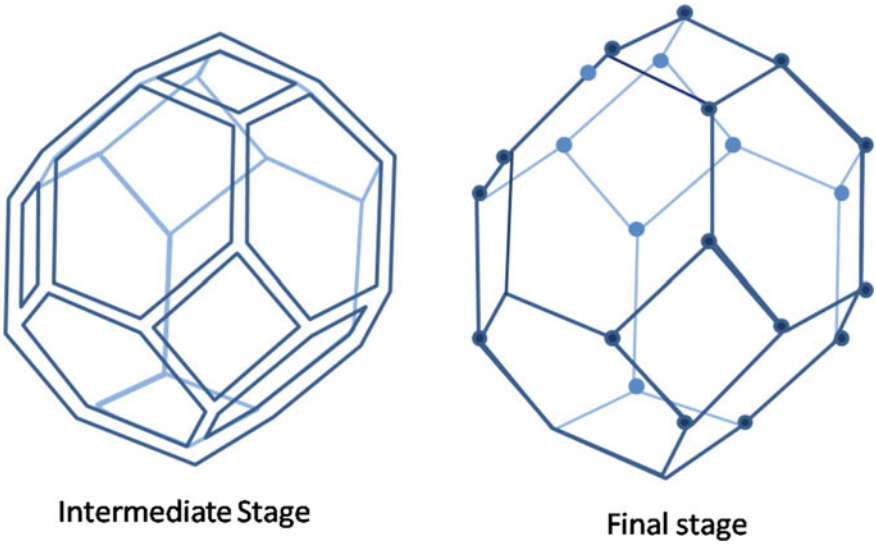

Fig. 1.17 Change in pore morphology from intermediate to final stage of sintering

affected. Small pores are annihilated and big pores are enlarged. Though surface transport is active, but it does not contribute to densification. It only helps in migration of pores during grain growth and rounding of pores. This stage is associated with maximum in densification and linear shrinkage. Density reaches to a value of ~90% of the theoretical value.

1.5.5.3 Final Stage

Third stage is quite important in getting full density in the material. In the final stage densification is very slow. Final stage starts when continuous cylindrical pores break into discrete pores. These pores are adherent to the grain corners. Coarsening is a competing phenomenon with densification in this stage. Pores may either attach to the grain boundary or may stay inside the grains. Spherical shape of pores is visualized if the pore is inside the grain. Lenticular pore structure is generated when pores are attached to the grain boundaries. As densification, grain growth, and pore shrinkage rate are different, it's uncertain to predict the final density. If pores are isolated from the grain boundary due to higher grain growth rate compared to pore mobility, densification rate decreases due to long range volume diffusion. If pores are attached to the grain boundary, annihilation or shrinkage takes place via surface diffusion or evaporation-condensation. In general, pore mobility is less compared to grain boundary motion leading to decrease in grain growth [45]. Larger pores cannot remain adherent to moving grain boundary for a larger time and move inside the

grain interior. There is always a scope in changing the grain boundary energy by doping and getting near theoretical density in materials.

1.6 Assisted Sintering Processes

1.6.1 Liquid Phase Sintering

Previously the sintering mechanism via solid-state diffusion was discussed. However, in some cases the solid-state diffusion is very slow and densification requires very high temperature. A small amount of additive phases are introduced to form a liquid phase which enhances densification by increasing the diffusion rate of the species and simultaneously enhancing grain growth. This has been practiced long back for the fabrication of glass-bonded ceramics and potteries. However, the actual theory has been extensively studied while working on tungsten heavy alloys during 1930s. Cobalt is the minor liquid forming phase for low temperature processing of these WC alloys [46, 47]. Magnesium oxide addition to alumina [48], bismuth oxide addition to zinc oxide varistors [49], and Al-Si addition into calcium stabilized zirconia system [50] are some of the examples of liquid phase sintering in ceramic systems. In many of the technical ceramics a small glassy phase is observed at the grain boundary as seen from the high resolution transmission electron microscopy [51, 52]. So it is believed that liquid phase enhances sintering in many ceramic systems.

Sintering rate is influenced by the surface tension of the liquid formed. Once liquid is formed at the boundaries, its effect on sintering depends on (1) solubility of the solid particles in the liquid, (2) wetting properties of the liquid for the solid, and (3) diffusivity of the solid particles in the liquid medium [47]. In the liquid medium, diffusion of solid particles will be higher compared to a solid-state diffusion process. Here, the capillary force of the liquid medium favors the liquid to cover the solid particle surfaces and enter into the porous region. Compressive capillary stress generated by the liquid phase enhances the sintering process, though grain coarsening is a drawback. Agglomerated powder particle surfaces dissolve in the liquid phase. In liquid phase sintering, the liquid phase should form a eutectic phase with the solid phase. Solubility of the solid in the liquid medium or the reverse case ultimately influences the liquid phase sintering. Limited densification is achieved when the solid has lower solubility in the liquid and liquid has limited solubility in solid. Cases where the solid has extensive solubility in the liquid, densification is more favored. In case, liquid has more solubility in solid, its effect is detrimental to densification and leads to swelling of the mass with abnormal grain growth. A mixed effect of swelling and densification is observed when solid has good solubility in liquid and vice versa. Hence, we need to have a good choice of the liquid phase forming additive in a definite proportion to encourage the densification process.

Liquid phase sintering is divided into two types based on the existence of liquid phase during sintering. When the liquid phase formed remains whole through the

sintering process, it is called persistent liquid phase sintering. This liquid phase solidifies at the grain boundaries as an amorphous phase or a crystalline phase. Most of the liquid phases sintering mechanism are discussed based on persistent liquid phase sintering. In the other case, liquid phase disappears at the end of the sintering process either via incorporation into the grains through reaction or evaporation at elevated temperatures. In the liquid phase sintering of aluminum nitride with CaF_2 additive, $CaAl_{12}O_{18}$ liquid phase is formed which transforms to $CaAl_2O_4$ phase at higher temperatures. This is called transient liquid phase sintering [53].

Prior to the formation of liquid phase, solid-state sintering of the compact takes place. Initial contact between the particles forms a rigid framework. Subsequently, liquid phase is formed at the grain interfaces. Similar to solid-state sintering liquid phase sintering also progresses through stages. The three stages are (1) rearrangement (2) solution precipitation, and (3) final stage sintering. This is pictorially presented in Fig. 1.18. Volume of the liquid phase formed due to the additive phase detects the particle rearrangement. At a higher level of liquid phase content, more rearrangement of particles takes place leading to full density. On the other hand at a lower level of liquid phase, rigid solid to solid bond formation inhibits sintering.

In the first stage of liquid phase sintering the driving force is the capillary force exerted by the liquid on the solid surface. Materials from the grain surface start dissolving in the liquid. Grains shrink and rearrangement of grains takes place. When solid-liquid surface energy is lower compared to solid-vapor surface energy, a good wettability is observed. Liquid enters into the porous intergranular space. This grain rearrangement step may contribute a major part in the densification process. However, initial solid-state sintering forms a rigid bond and inhibits further rearrangement.

The second stage of liquid phase sintering starts when the rearrangement process comes down and solubility effect predominates. In this solution precipitation stage solid solubility of the smaller grain surface is more compared to the larger size grains. Mass transport from the smaller size grains takes place, hence their population decreases. Another event occurs in parallel called grain shape accommodation, where grains are flattened along the neighboring faces and this increases the packing density. Some more pores are filled by grain shape accommodation. The final step is a very slow process where pores are removed from the liquid phase. In some cases, residual pores enlarge due to trapped gases leading to swelling of the compact. Coarsening of the microstructure also continues in the third stage. Dwelling in the final stage is crucial in deciding the sintered microstructure. This less control over the microstructure is the biggest disadvantages of a liquid phase sintering. This leads to decrease in many mechanical properties of the material. Advantages like lower sintering temperature, faster sintering, full densification in material systems with slow solid-state diffusion rate, etc. are associated with a liquid phase sintering process.

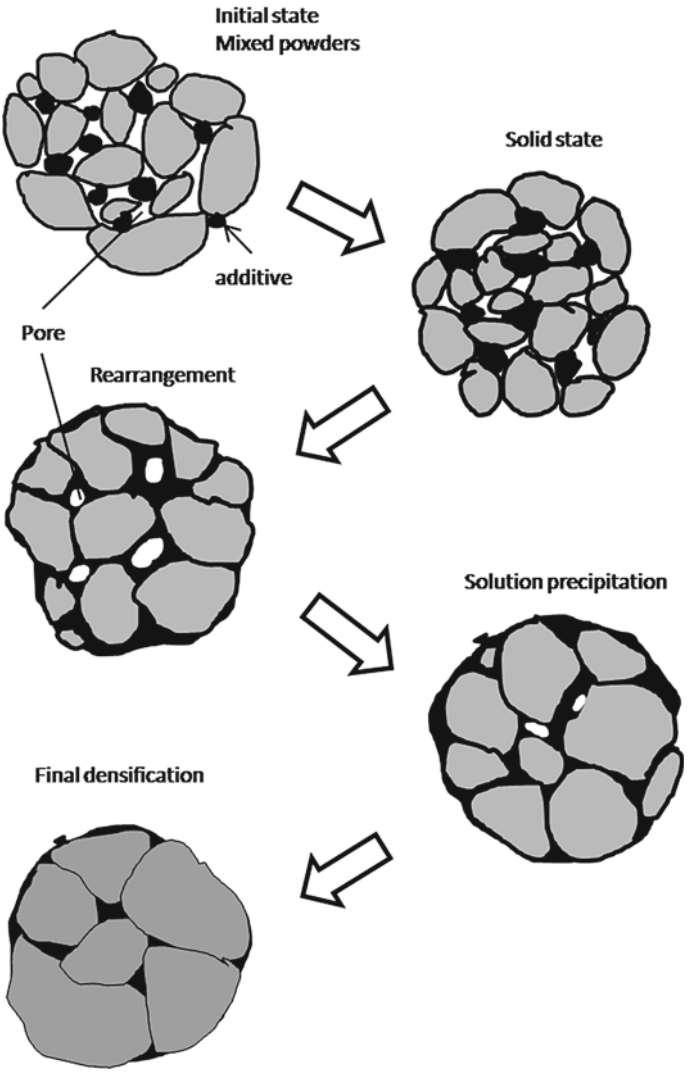

Fig. 1.18 Pictorial presentation of liquid phase sintering

1.6.2 Hot Pressing

In hot pressing process both external pressure and temperature are applied simultaneously for densification process. It is carried out by placing either powder or a compacted preform into a suitable die and applying uniaxial pressure while keeping the entire system at an elevated temperature. This can be done either in a controlled atmosphere or in vacuum. Hot pressing method is suited to relatively simple shapes and more useful for non-oxide ceramics more specifically covalent bonded ceramics

where it is extremely difficult to obtain the near theoretical density by conventional sintering process. Some materials either decompose or evaporate before achieving near theoretical density. Hot pressing is used for such materials to get full density at lower sintering temperature. In hot pressing, densification can be achieved at relatively lower temperature which results in fine-grained microstructure, better mechanical and functional properties [54, 55]. Die tooling in hot pressing is very important as the die has to withstand high pressure and high temperature (usually > 1000 °C). Hence, materials with high creep resistance are suited for this kind of applications. Further, the coefficient of thermal expansion of the die material should be less than the material whose shape forming has to be carried out. Else during cooling there is a chance that the compact may break due to the compressive stress from the die.

Graphite is the most commonly used die material due to its lower cost, ease of machinability and high creep resistance. Graphite is the best choice for pressing refractory materials, where the operating temperatures vary from 1000 to 2500 ° C.Graphite exhibits a gradual increase in strength, almost double the room temperature strength at 1500 °C. However, due to oxidation of graphite above 500 °C, either vacuum or inert atmosphere is required for protection. Therefore, suitable containment such as high vacuum chamber and pumping system is essential. The limitations for graphite die are the low operating pressure and interaction with some powders. In hot pressing of most ceramics, the die life can be increased by applying boron nitride powder coating to the graphite die to prevent the reaction with the powder. Other die materials that can be used for high temperature hot pressing are SiC, WC, etc. But the cost and machining challenges limit its use for specific high end applications only. Multi-cavity die can also be used in order to increase the number of products in one cycle. Figure 1.19 shows schematic picture of a vacuum hot pressing machine. Hot pressing technique is extensively used for consolidation of SiC [56, 57], B_4C [58, 59], di-boride-based ultra-high temperature materials like ZrB_2, HfB_2,TiB_2, etc. [37, 60, 61], oxides like BeO [62], MgO [63] and thermoelectric materials like $FeSi_2$, Bi_2Te_3, etc. [64, 65].

1.6.3 Hot Isostatic Pressing (HIP)

Hot isostatic pressing technique involves sintering of a compact at high temperature and high pressure. In this process the compact can be either made impermeable to the pressurized gas (where powder compacts are first sintered to remove surface connected porosity; sinter hipping) or encapsulated in a gas-tight container. Powders are usually encapsulated in a metallic container but sometimes in glass. Initially the container is evacuated; the powder is out-gassed to avoid contamination of the materials by any residual gas during the consolidation stage and sealed-off. Further the compact is subjected to isostatic pressure. Figure 1.20, shows the schematic of the hot isostatic pressing (HIP). The application of high inert gas pressures (usually Ar) at elevated temperatures results in the removal of internal voids and creates a strong metallurgical bond throughout the material. As densification occurs, the

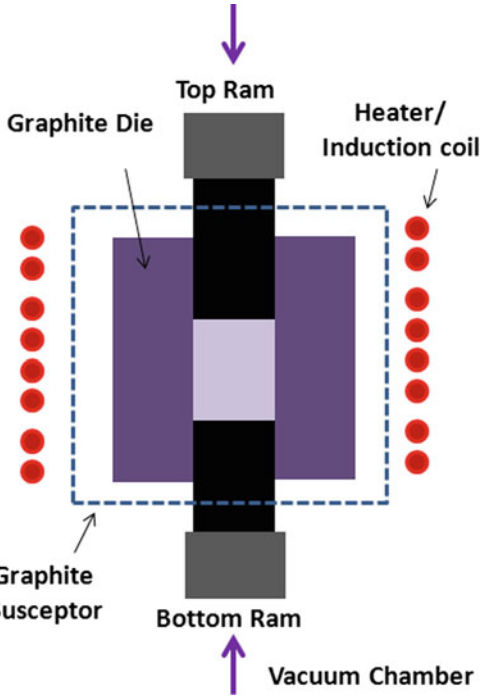

Fig. 1.19 Schematic of vacuum hot pressing

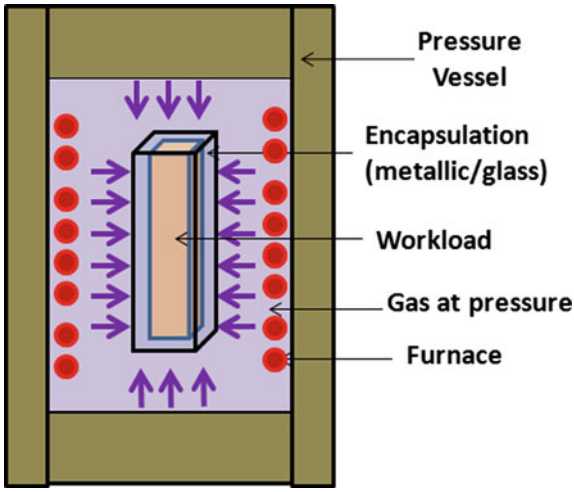

Fig. 1.20 Schematic of hot isostatic pressing

powder compact shrinks. The external metal or glass envelope shrinks with it to the same extent in all the directions due to the isostatic pressure. Thus the densifying powder is formed into the same shape as that of the envelope. This result is a clean homogeneous material with a uniformly fine grain size and a near theoretical density. The technique requires considerable financial investment as the pressure vessel has to withstand the internal gas pressure and allow the powder to be heated to high temperatures. Similar to cold isostatic pressing, only semi-finished products are produced, either for subsequent working to smaller sizes, or for machining to finished dimensions. The use of hot isostatic pressing leads to additional densification and increased strength in ceramics. Specific advantages of HIP technique for shape forming are reduction in porosity, uniform microstructure, near net shape (more than 80% material utilization), complex shaping, and improved mechanical properties of the product. Broader applications of HIP technique include consolidation of metal/alloy/ceramic powder, near net shape forming, diffusion bonding of dissimilar materials, cladding, and component repair [66]. Literature indicates that many transparent polycrystalline ceramics [67, 68] like magnesium aluminate [69, 70], zinc sulfide [71–73], Nd-YAG [74, 75], PLZT [76] have been successfully prepared using HIP by many research groups.

1.6.4 Field Assisted Sintering

Field Assisted Sintering Technology (FAST) alternatively known as Spark Plasma Sintering (SPS) is a relatively new sintering technology in the field of materials science and engineering. This process is similar to hot pressing process; however, instead of an external heating source a pulsed electric current is passed through the pressing mold and sample. Typically current in the range of 5000–10,000 A is applied across the sample. When current passes through the sample, granular boundaries of the initial powder particles are heated up and creates an electric field with a plasma effect. Schematic of the spark plasma sintering setup is shown in Fig. 1.21.

In this sintering technology, a very rapid heating cycle and short process time is achieved which leads to suppressed grain growth. Materials with novel properties can be prepared by this process which cannot be achievable in conventional sintering technique [77]. Typical electrical pulse, duration, and strength play a pivotal role in realizing the SPS effect. Electric field induces microstructural evolution through complex multi-physical phenomena take place at the surfaces and interfaces.

Several mechanisms have been suggested to explain the influence of external field on the materials like field-induced ponderomotive forces, generation of defects like Frenkel pairs, localized heating pairs around grain boundaries, etc. As a consequence of ultra-high heating rate, field assisted sintering process can readily alter the mass transport phenomena in ceramics and promote chemical reactions, phase transformation, microstructural evolution, densification, and grain growth [78]. Some of the products and components prepared through this technique are diamond and cubic BN-WC/Co composites for cutting tool applications [79], ZrO_2-HAP composites for

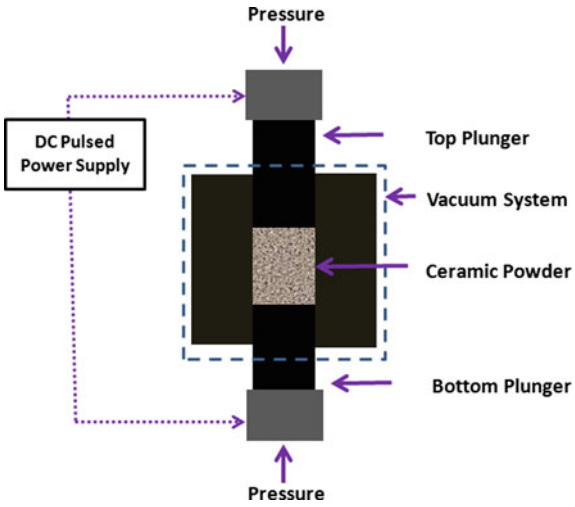

Fig. 1.21 Schematic diagram of the SPS process

biomaterials [80], magnesium aluminates as transparent ceramics [81], (K_x Na_{1-x}) NbO_3 piezoceramics [82], layered ternary carbides and nitrides based MAX phases [83], etc.

1.6.5 Microwave Sintering

Conventional microwave heating is being extensively used for heating/processing of foods, rubber, polymers, and laboratory synthesis. Nowadays this has also been used for sintering of ceramics [84]. The electromagnetic radiation interacts with the material and heats the sample internally. The dipoles and charge species align in the direction of the applied electromagnetic wave. As the sign of the electromagnetic wave changes, polarity change. In this process, heating of the sample takes place due to internal resistance of the material. A material can be transparent, opaque, or absorbent to the microwave radiation depending on the dielectric properties of the material. Higher the loss tangent more is the interaction of the electromagnetic radiation with matter and hence more heating of the substrate. This loss tangent is related to the conductivity, magnetic permittivity of the material, and frequency of microwave. The imposed power per unit volume of a material is proportional to the loss tangent and square of the electric field strength as per the following relation.

$$P = \pi . E_0^2 . f . \varepsilon_o . \varepsilon_r^{'} . \tan\delta$$

where E_0 is the amplitude of the electric field, f is the frequency, ε_o is the permittivity in vacuum, ε_r is the relative permittivity and tan δ is the loss tangent.

In conventional sintering process indirect heating (radiation heating) from the heating elements is used to heat the sample. However, microwave heating takes place throughout the sample. The advantages of microwave sintering compared to conventional sintering are high energy efficiency and short sintering time. Thus, grain growth of the sintered body is restricted. Many engineering properties are improved due to finer grains in the sintered materials. It has also been reported that microwave sintering improves dielectric and ferroelectric properties in ceramics owing to fine grain structure [85]. However, in some cases rapid sintering results in entrapment of gases and contaminants.

Although there is clarity in microwave heating mechanism, the role of microwaves in sintering process is not clear. One of the theories indicates that microwave enhances grain boundary diffusion thus favoring densification [86, 87]. Another theory tells about the large thermal gradient generated between the surface and the grain interior which results in large gradient in defect concentration [88]. This concentration gradient generated is the driving force for mass transport and densification. Some functional ceramics which can be processed through microwave sintering are SiC [89], B_4C [90], WC [91], ZrO_2-Y_2O_3 [92], hydroxyapatites [93], strontium barium niobate (SBN) [85], etc.

Ceramics such as SiC absorb microwave energy more efficiently at room temperature. However, materials such as alumina, magnesia, and silica are transparent to microwave at room temperature. But these materials begin to couple with microwave at elevated temperature. In case of microwave transparent materials the sample is placed in a cage of susceptor material (usually graphite) which is an absorbent of microwave. Figure 1.22 shows the schematic diagram of the microwave sintering setup. Sample is placed inside the SiC susceptor and microwave generated from magnetron is imposed on the susceptor. Radiation heat from the susceptor heats the sample.

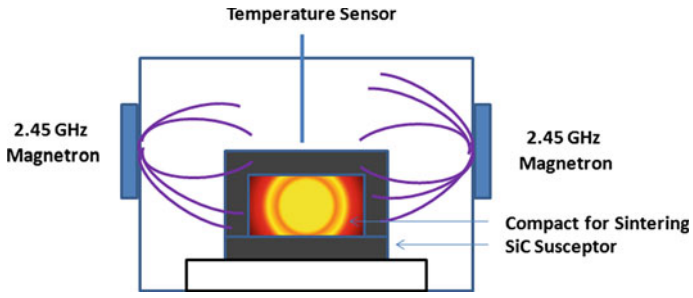

Fig. 1.22 Schematics of the microwave heating set-up

1.6.6 Reactive Sintering

In a reactive sintering, reactive process (combustion reaction) is carried out along with sintering and densification. Combustion reaction is initiated within the powder mixture and this exothermic reaction proceeds spontaneously. The exothermic heat produced is utilized for sintering. Once this exothermic reaction is initiated, it proceeds on its own without any external heat. This reactive process is also known as self-propagating high temperature reaction (SHS), self combustion, and gasless combustion reaction. One example of reaction synthesis is the fabrication of B_4C components. A mixture of boric acid and carbon is heated initially to start the combustion process [94]. Similar to combustion process, the maximum achievable temperature called adiabatic temperature can be calculated theoretically [95]. In this calculation it is assumed that the process is adiabatic and there is no heat loss to the surrounding. Adiabatic temperature depends on the thermodynamic parameters like heat of reaction, enthalpy of melting, heat capacity of the reactants and products.

Reaction sintering is a self-sustaining and self-propagating combustion reaction. Hence the velocity of the combustion wave depends on the heat transport rate of the reaction zone. However, reaction rate can be controlled with the addition of inert materials. Mixture of two components mixed intimately when heated, one of the components melts and forms a eutectic with the other component. As the wave front proceeds, product is formed at the tail. Reaction rate and product quality depend on the initial powder size. Homogenously mixed powder with both phases inter connected has a good control over the reaction rate. By two ways reaction sintering is different from liquid phase sintering (1) liquid forming component ratio is almost half of the reactant and (2) liquid phase is not segregated separately at the grain boundaries. However, the advantages of enhanced mass transport through the liquid medium are achieved in this process. Reaction sintering is mostly used for the production of SiC and SiC composites [96, 97]. A preform of SiC and graphite powder is prepared first through the pressing method. Molten silicon is infiltrated into the preform to produce SiC components. As reactive sintering process requires large control over many variables, it is not practiced in industry.

1.6.7 Additive Manufacturing in Ceramics

Additive manufacturing (AM) alternatively known as Solid Freeform Fabrication (SFF), Rapid Prototyping (RP), or 3D printing has the potential not only to change the way of conventional industrial manufacturing processes but also have demonstrated broad range of products with complex geometry. It is the process of manufacturing objects by depositing layer upon layer, from 3D model data, as opposed to subtractive manufacturing methodologies, such as traditional machining. Schematic of a 3D

printing machine is shown in Fig. 1.23. Here the feedstock is typically fed into the system as powder or granules (some time as paste or suspension also) and the desired object shape is built up layer by layer [98, 99]. Sintering of the powder particle is facilitated by the laser beam from the top. AutoCAD programme is used to draw the product with exact dimensions. Feed material is deposited in the places as designed in the AutoCAD drawing. Depending on the form of feedstock and the consolidation technique different terminologies are used for additive manufacturing as listed in Table 1.2.

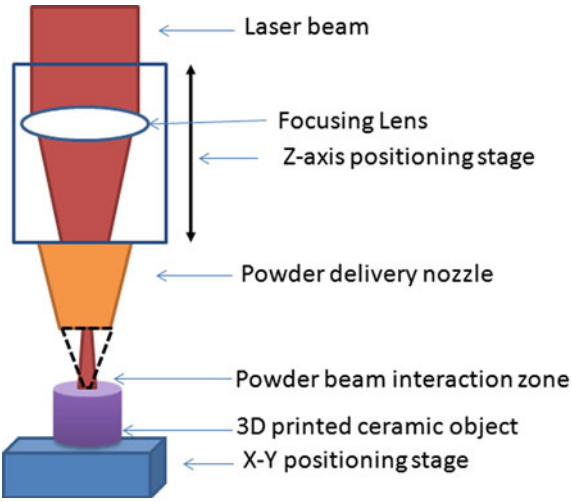

Fig. 1.23 Schematic diagram of a 3D printing machine

Table 1.2 Ceramic additive manufacturing technologies

Feedstock form	Additive manufacturing technologies type	Abbreviation used
Slurry-based	Stereolithography	SL
	Digital light processing	DLP
	Two-photon polymerization	TPP
	Inkjet printing	IJP
	Direct ink writing	DIW
Powder-based	Three-dimensional printing	3DP
	Selective laser sintering	SLS
	Selective laser melting	SLM
Bulk solid-based	Laminated object manufacturing	LOM
	Fused deposition modeling	FDM

In the field of additive manufacturing of ceramics, all the efforts are being made to address the technical challenges associated with either obtaining porous components or fully dense monolithic components. Accordingly it is further categorized as (1) technologies not capable of producing dense structures, (2) technologies capable of producing fully dense monolithic ceramic bodies with restriction in dimension, and (3) technologies capable of producing fully dense monolithic ceramic bodies without restriction in dimension [100, 101]. The additive manufacturing technology enables the production of complex-shaped porous structures with precise control on dimension, shape, and amount of pores. Thus, it is opening up completely new fields of research and applications which was not possible with any of the traditional manufacturing technologies. Another application of this technique is to develop reproducible fine filigree structures, which are not possible by any other ceramic shaping techniques. The additive manufacturing technique is being extensively used in the field of dental ceramics [102], hydroxyapatite scaffolds for bone implant applications [103], zirconia impellers [101], and more recently in the field of solid oxide fuel cells [104].

1.7 Factors Affecting Sintering

Sintering is aimed at getting a dense product of desired shape, size, and density with necessary functional properties. As many factors affect sintering at different stages, their role has to be meticulously monitored. These factors are powder quality (size and distribution, degree of agglomeration), powder packing, additives (composition, impurity, liquid phase), temperature/heating rate, atmosphere, external field, and applied pressure. Sintering is largely influenced by the interaction of particles, pores, grain boundaries, impurity, and atmosphere.

Particle size effect: Size of the initial particles influences some of the mass transfer processes at different stages of sintering. Smaller size particles will have higher interface contacts per unit volume, hence higher diffusion rate is expected. Surface diffusion and grain boundary diffusion processes depend on particle sizes. Volume diffusion is less dependent on particle size whereas viscous flow doesn't depend on size at all. Lastly, evaporation-condensation has moderate sensitivity to change in particle sizes. Finer particles show higher sintering activity due to higher surface area, more unbalanced surface forces, pores associated with higher energy per unit volume, and high surface curvature. Sintering time for different particle sizes of same system is better explained by Herring [25].

Particle size distribution influences the pore size distribution and hence the transport mechanism. In the final stage of sintering wide initial particle size distribution influences much on densification. It offsets the balance between pinning and separation of grain boundaries from pores, allowing grain growth to initiate in sintering resulting in a lower final density [27]. However, as large number of small particles are there in a wide particle size distribution, early sintering benefits are obtained. But this benefit is nullified if sintering is carried out for a longer sintering time and

high sintering temperatures [28, 30]. When mono-sized particles are taken, higher density can be achieved with minimal in-homogeneity and control over grain growth during sintering. In this case no grain boundary curvature is observed between grains of equal size. Similarly, grain size also influences the densification rate. Grain sizes inside the particle have different grain boundary areas per unit volume. Polycrystalline materials with more number of grain boundaries have better mass transport mechanism and favors fast sintering [31]. Particle shape influences surface area per unit volume, responsible for accelerating sintering process in case of non-spherical particles. However, these non-spherical particles generate low green density also. This porosity in the particles decreases the sintered density.

Particle packing: The journey of microstructural development with time is decided by arrangement of initial powders in the compact. In-homogeneity due to small packing defects and random packing arrangements are the sources of disorder. Generation of differential sintered regions surrounded by large pores is observed due to this disorder apart from flaws [6]. Similarly, when there is a wide initial pore size distribution, mostly it hinders densification in the final stages of sintering. In random packing of particles, different particles will have different coordination number. Two particles with different coordination number will sinter differently. Lower density is observed for particles with lower coordination compared to particles with more number of touching neighbors. Hence, better sintered microstructures are expected for homogenous green microstructure.

When sintering proceeds, neck growth takes place and simultaneously new contact points are generated due to shrinkage. Due to this changing coordination number, the generated torque inside the microstructure favors particle motion. Some of the existing sinter bonds rupture to accommodate the unbalanced force and particle motion. When mono-sized powder is taken, initially they have sufficient number of contacts which do not favor much for repack. New contacts are developed without any broken bonds; this helps to generate a homogenous microstructure.

Green density: Better green density is essential in getting good sintered density. When green density is more, there will be more initial particle contacts and initial pore sizes will be smaller. Sintering needs less shrinkage or densification to get full density with more dimensional control. Green density gradient also should be minimum in compacts to avoid any defects in the product. Minimum 40–50% green density is essential to get a full density. Lower green density compacts lead to particle bonding with long chain, grain growth, and open pore structure with little shrinkage.

Porosity: If the particle size distribution is over a wide range, then the adhered pore will also be over a wide range. In the intermediate stage stable pore structure is developed which controls the sintering rate. Due to higher affinity of a pore with the grain boundary, pore remains attached to it [35]. Pores are mostly attached to the larger grains in the latter part of sintering process. The equilibrium dihedral angle formed by the intersection of grain boundary with pore influences the sintering curve and for systems with very high dihedral angle, pore closure is not favorable. In some occasions, there is overall decrease in porosity and increase in pore size.

When a pore is developed, the grain boundary is also extended, consequently the system energy also increases. The relative size of pores compared to the size of grains also matters. Very big pores are difficult to remove. As a thumb rule if the pore size is half or less than the grain size, the pore is removed during densification [36]. These phenomena are more prominent in agglomerates or poorly consolidated samples with sintering difficulties. Hence particles with narrow pore size distribution and high packing density favors densification. In case of agglomerates, cluster of small particles sinter rapidly and independently. This preferential sintering generates regions of high density with pores in the inter particle space between the clusters [105]. Smaller intra agglomerate pores close first leaving behind large pores in the inter agglomerate region. Hence a bimodal pore size distribution is generated in the agglomerates. This bimodal pore size distribution can be avoided by increasing green density with applied pressure.

As pore tries to spheroidize at high temperatures, pore shape greatly influences the densification mechanism. Elongated pores generated during uniaxial compaction shrinks in the direction perpendicular to the compression axis and leads to anisotropic shrinkage. It is observed that more number of pores are attached to the grain faces of largest grains and at the grain corners for the smallest grains. From the observation it can be concluded that grain growth takes place when pore is attached to the grain faces and pore closure takes place when it is attached to the grain corners [94]. Late in the densification process, rapid grain growth takes place as pinning effect from the residual pores diminishes. Hence for a homogenious green structure, uniform grain size and pore size distribution delay the onset of grain growth to a higher density. Pore has a binding energy to the grain boundary and this energy increases with porosity. This increases the system energy equivalent to the newly created interface area compared to separate pore and boundary areas. As pore reduces the total grain boundary area, the system energy is lower for pores occupying grain edges. Large grain size to pore size leads to breakaway at the time of grain growth. Surface transport processes govern pore mobility whereas transport across grain boundary governs grain boundary mobility and both are associated with some activation energies sensitive to temperature. In the final stage of sintering if sufficient mobility developed in the pores they can migrate with the grain boundaries to avoid the breakaway.

Temperature and heating rate: There are four competitive phenomena like pore shrinkage, grain growth, pore growth, and densification in the sintering process that control the final microstructure. For uniform microstructure small pores with narrow size distribution are essential during microstructural development. Microstructural defects are generated in the early stages of sintering and grow at high temperatures [95]. Here temperature is an important parameter in sintering. At a relatively high temperature when the compact has achieved around ~90% of the theoretical density, increase in the temperature increases the rate of grain growth instead of densification, i.e., rate of grain growth is more than the rate of densification. By suitably adjusting temperature-time profile one can control the grain growth during the final stage of densification.

Heating rate not only affects sintering but also influences final microstructure. Surface diffusion dominates sintering at low temperatures and bonding between particles takes place without densification. At high temperatures, densification is a predominant phenomenon apart from grain growth and grain coarsening. One should be careful about the goal of sintering; its sinter bonding without densification or without grain growth. To reduce the low temperature effects ultra-high heating rate is practiced. This improves densification and controls grain growth. Temperature difference is a driving force for sintering when ultra-high heating rates is imposed [96, 97]. In the large compacts poor heat transfer is an issue while going for high heating rates. As a consequence of large thermal gradient cracks or defects are developed.

Applied pressure: Pressure is applied either in shape forming method or during sintering due to some added benefits. In many of the shape forming methods pressure is applied on the powder before sintering. Pressure helps in decreasing porosity and increasing dislocation population in the green compacts [46]. Density, coordination number, and contact size increase with high compaction pressure and with reduced neck growth. This essentially leads to densification with less shrinkage, i.e., good dimensional control. Most of the industrial products are prepared through die compaction where dimensional control is achieved by using powder of larger size, low temperature sintering, high compaction pressure, short sintering time for simple structures.

There are certain conditions like low sintering temperature (decomposition issue), coarse powder, composite materials, etc. which requires external pressure during sintering. Through conventional sintering approach it is difficult to achieve the desired functional properties related to density. Pressure removes some of the sintering difficulties and good sintered density could be achieved for larger particles, at low sintering temperature and short sintering time. The residual porosity in the solid-state sintering is eliminated due to the applied pressure. Concentrated stress is developed at the contact regions for compressed particles. Hence, factors like particle size, pressure, temperature, and compact density influences pressure assisted sintering. At a small inter particle contact, large stress is developed and with growth of this contact region stress reduces. Pores do not carry stress, hence the actual pressure experienced is much higher than the pressure applied [47, 48]. Hence, actual stress can be correlated with the applied stress by using the fractional density.

Powder packing with wide distribution of particles will have more contact points. Hence higher effective pressure will be experienced on the particles. This will lead to more densification. In a study it has been observed that particles with bimodal particle size distribution gives better sintered density compared to uniform size of particles under similar pressure assisted sintering conditions [49]. However, in case of uniaxial pressing, the contact along the pressure direction is higher compared to perpendicular direction, which leads to non-uniform densification. Grain growth is also an issue in the pressure assisted sintering. With the increase in pressure, packing/coordination increases, hence densification also. This implies to the prior onset of grain growth and increase in grain size for pressure assisted sintering compared to traditional sintering.

Impurity/contamination: Impurity generated during sintering like moisture, carbonaceous materials, and entrapped gases influences sintering rate. For example, cemented carbides when sintered above an alumina support, Al_2O_3 reacts with carbides. The reaction product having a higher vapor pressure generates pores in the sintered mass.

Vacancy has a great role in the mass transport mechanism and its absolute concentration depends on impurity content and dopant addition. Apart from this, temperature and stoichiometry change the equilibrium vacancy concentration. For example, when oxygen vacancy concentration increases in oxide system, densification rate increases. Cations have higher mobility than oxide ion, so conditions favoring formation of oxygen vacancies increases the sintering rate [51]. Sometimes this impurity or dopant forms inclusion which enhances the final stage of sintering by impeding the grain growth.

Sintering is affected by rate of grain growth and adherence of the pores with the grain boundary. Grain growth is related to the grain boundary mobility and in ionic solids it is influenced by dopants and their volume. Similarly, impurities also segregate at grain boundaries and control the grain boundary mobility and pore mobility. Doping 0.1 wt % MgO in Al_2O_3 influences the rate of grain growth and densification in the final stage of sintering. MgO interacts with CaO impurity and lowers the grain boundary mobility. Hence, slow moving pores adhere to the moving grain boundaries during the final stage of sintering [52]. Exaggerated grain growth due to glassy phase formed by CaO segregated at the grain boundaries is hindered by MgO addition. Grain boundary mobility can be altered by suitably doping at the grain boundaries also. This inturn minimizes the grain growth which finally alters the sintered density [39, 53].

Atmosphere: Atmosphere not only influences sintering but also affects some of the important properties in the sintered mass. Removal of organics used for shape forming is essential at low temperatures to avoid any side reactions. Hence proper environment has to be monitored for organic removal at low temperature. For example, during sintering of cemented carbides or nitrides proper protective environment is required for stabilization of the phase. Insoluble gases are entrapped during sintering of alumina and degrade the optical properties, hence its sintering is carried out in hydrogen or vacuum. Some of the materials either decompose or show volatization before getting full density. Proper atmosphere is maintained to avoid these issues. Some of the atmosphere generates defects responsible for mass transport in sintering. For example, ionic material when sintered in desired environment generates vacancies responsible for better sintering rate. Sintering atmosphere should be chosen so that it should not affect the environment and human life also.

In the sintering of advance ceramics, vacuum is mostly preferred, as it provides clean and non-reactive environment. However, evaporation at high temperature is an issue in vacuum sintering. Sintering rate is influenced by excess vacuum which alters the diffusion kinetics. Similarly, sintering atmosphere influences different mechanisms responsible for sintering. For example, while sintering NiO at 700 °C in oxygen there is less densification with greater surface area loss [44]. This clearly shows that surface transport is the dominant process for sintering. However, when

Ar is used as sintering atmosphere more dense product is obtained with lesser change in surface area suggesting bulk transport is responsible for sintering.

External field/factors: In the conventional sintering either electrical resistance heating or burning of combustible gas is used to increase the temperature. However, in novel sintering technology other fields like microwave, plasma, DC arc, and laser are being implemented solely or in combination with conventional heating technique to improve sintering. For example, many dielectrics are sintered in a hybrid furnace where initial heating is carried out by conventional resistance heating followed by microwave heating. Dielectric properties of the material interact with the microwave and generate heat inside the sample. These external fields are applied for short period at high temperatures. Hence better microstructural control could be attained. Similarly nano structured carbides, nitrides, and borides are prepared using spark plasma sintering. In the hot pressing condition a pulse DC in the sample increases the instantaneous temperature of the sample. Apart from the change in surface energy, diffusion coefficient and chemical potential of particles and grains facilitate densification.

1.8 Common Defects in Ceramic Sintering and Sintering Approaches

In a sintering process the prime objective is to achieve desired density, strength, functional properties, control over dimensions, and microstructure. In reality, the sintering studies from the lab experiments and theoretical calculations differ from industrial practices. Laboratory experiments are carried out with small scale and well-defined furnace heating. In actual, the availability of furnace construction material, heating element, environment, contamination, etc. used in industry are different from lab practices. In theoretical studies, many of the assumptions like mono size powder distribution, powder sphericity, and uniform heating do not match with the actual conditions. In practice, many process variables are manipulated to get some improved properties. However, these variables create some other difficulties. Often it is being argued to decrease the particle size to increase the diffusion rate by changing the surface area to volume ratio. Higher shrinkage in the smaller size particles offers challenge in getting precise dimensional control. Apart from dimensional control, contamination, cost, and health hazards are the added disadvantages. Sintering time can also be increased to achieve good density. More sintering time implies more shrinkage and grain growth. Hence less control over microstructure and less dimensional reproducibility. It also adds extra cost to the product. Similarly, increase in the sintering temperature gives some unwanted phenomena like decomposition and evaporation apart from added cost and energy. High temperature sintering implies higher shrinkage, distortion, and warpage which need additional cutting and polishing step. Grain growth is another detrimental aspect of high temperature sintering. Furnace life time also decreases for prolonged use of it at high temperatures. Improvement in initial green density is practiced to improve densification. But this leads to wear in the

die components due to higher friction between walls and powder. Gradient in green density can be observed for components with complicated shape and components with large variation in length to width. This density variation is reflected in form of warpage in the final densification. Sintering aids are introduced when densification in conventional sintering is difficult due to various reasons. However, products prepared using sintering aids lead to distortion and grain growth. As there is no control over the grain growth some of the mechanical properties like toughness and ductility are degraded.

Few parameters have to be checked meticulously to achieve products of desired intension. One is a dimensional parameter, getting reproducible component with less variation in dimension. Forming methods are mainly responsible for dimensional variation in the components. The defects in the forming are amplified in the sintering step. Hence uniformity in the packing during shape forming step has to be carefully inspected first if dimensional reproducibility is an issue followed by inspecting the sintering schedule. Friction from the sintering support, gravity induced creep, and non-uniform heating also contributes to the variation in the dimensions [45]. Lower sintering temperature is preferred for impeding dimensional changes. At the same time, higher green density is preferred to lower shrinkage. Other scenarios where dimensional changes expected are (1) sintering involving liquid phase (2) binder assisted techniques like slip casting and injection molding having lower packing density and subsequent more shrinkage and (3) nano scale systems with lower packing density with an overall shrinkage of around 20–25%.

Green density gradient is the greatest culprit for dimensional irregularity. Low density regions or regions of lower packing density shrinks more and responsible for wrap. In die compaction, non-uniform density regions are developed due to wall friction with the powder. Hence isotropic green microstructure developed by injection molding and iso-pressing shows uniform shrinkage and less dimensional distortion. Pore developed in uniaxial pressing also alters the uniformity in shrinkage. Compact mass from uniaxial pressing shows flat pores in the pressing direction and elongated pores in the perpendicular direction. Spheroidization of pores during sintering results in enlargement of pores in the pressing direction and shrinkage in the perpendicular direction. For low green density structure or bigger compact gravity plays an important role and shrinkage gradient is generated in the gravitational direction. Dimensional change due to anisotropy generated by uniaxial compaction can be minimized by use of low compact pressure and graded particle size distribution. High fluidity generated by formation of liquid phase also contributes to sagging of the structure. This can be avoided by judicious use of liquid phase forming component. A residual force is generated by the support on which the compact is placed during shrinkage. In the lower part retarded shrinkage is observed. Hence use of smooth surface nullifies the retardation effect of the support. Both gravitational force and retardation from the surface together induce distortion for massive components [41]. As we move from top to bottom the cumulative pressure favors axial compaction and a radial flaw.

Dimensional irregularity is also generated due to temperature gradient in a furnace. Shrinkage takes place in the hotter region at a faster rate and cooler region is distorted due to differential shrinkage between the hotter and cooler region. For a distorted

component the warpage developed shows bend toward the hotspot. Such situation can be avoided by placing the compact at the center of the furnace and maintaining a slower heating rate in the lower temperature region. Error in the measurement of temperature and time contributes to differential shrinkage. A small variation of temperature at a high temperature region has more shrinkage error. However, at high temperatures a small variation in time has less effect on shrinkage error. The trend is opposite in the low temperature region. It can be concluded that the shrinkage error is less at low temperature and longer time.

In the initial stages the compact has low strength. With progress of sintering, sintering stress is developed; at the same time inter particle bonding takes place. In a situation where the compact has not attained enough strength, the sintering stress generates cracks. This crack propagates in the latter stages of sintering. To overcome this issue slow heating rate is preferred where sufficient sinter bonding develops which resists the defect generation from stress or shrinkage. Strength is lowered in materials having weak inter particle bonds and large grains [42, 43]. Higher ductility and higher toughness are achieved for highly dense materials. Higher thermal conductivity is obtained for highly dense materials with coarse grain structure and thermal properties are reduced by porosity.

Final density, microstructure, defects, flaws all depend on green microstructure and are enhanced during densification. Use of small powders with narrow size distribution and uniform packing can avoid such situations to a larger extent. Binder and lubricants used for shape forming need to be removed initially else will be trapped in the sintered product. This issue is more prominent in case of nano-powders where sintering starts well before the binder burnout temperature of organics. Residual carbonaceous materials affect density, porosity, phase, and many physical properties also. For non-oxide ceramics sintering atmosphere play an important role. For example, to prevent silicon loss in the sintering of SiC, a combination of vacuum and residual gas environment solves the evaporation problem. Shadowing is a common problem when two components are very different in size and placed in the same furnace. The radiation heat is blocked by the large component and the small component experience less heat. However, increase in the sintering time compensates for this non-uniform heating effect.

In some transient liquid phase sintering fast heating rate is required to minimize the surface diffusion at low temperatures. However, this will have adverse effects like incomplete binder removal and non-uniform heating. For large components, slow heating rate is advisable to reduce the thermal stress which generates crack at low temperatures. Similarly, cooling rate has to be very fast in case where impurity segregation is an issue. During solidification, porosity developed decreases strength of the materials.

In a furnace, support material role is equally important in holding the compact during sintering without deformation and preventing the compacts to join with each other. The support should be rigid and inert to the compact during the sintering cycle, neither it should react with the compact nor should evolve any impurity. Alumina is widely used as support up to 1800 °C in oxidizing, inert, or vacuum environment. However its use is limited to 1500 °C in reducing and carburizing environment.

Reduction of alumina takes place in carburizing environment above 1500 °C. Hence for high temperature operation in reducing environment one can think of refractory like molybdenum and tantalum. Similarly, for ultra-high temperature ceramics like titanium diboride, hafnium diboride the choice of support materials is limited.

There are certain instances where the stoichiometry or chemistry of the material changes during sintering either due to evaporation, decomposition, or atmosphere. In such situations the material is packed with special materials inside the support to retain the chemistry. For example sintering of beta alumina components or lithium titanium-based components have to be sintered in a bed of the respective powders to maintain the chemistry.

1.9 Case Study of Sintering Cycles

Two case studies are discussed here in which how sintering approaches are adopted in oxide and non-oxide ceramics will be discussed.

Sintering of SiC components: SiC is among the advance ceramic materials having excellent corrosion resistance, high temperature stability, chemical resistance to many systems, excellent mechanical strength, high wear resistance, etc. This non-oxide ceramic is used for heat exchangers, gas turbines, chemical reactors, nuclear reactors, space shuttles, and many protective coating applications. Hence SiC is required in different dimensions with tailored functional properties to suit these applications. Conventional sintering is not advisable in these covalently bonded compounds due to slower diffusion process and requires additives for sintering. In the latter stage of sintering, lower solid-vapor surface energy in comparison to grain boundary energy inhibits pores closure and favors grain growth. Hence both high temperature and high pressure are used during sintering. Sintering aids like C, B, Al, B_4C, Y_2O_3, Al_2O_3, TiO_2, and few rare earth oxides are used to assist sintering at a lower temperature and pressure. When solid-state sintering aids like C, B, Al, and B_4C are used, the grain surface-boundary energy is decreased which enhances the diffusional mass transport. A mixture of boron and carbon additives is used in practice where boron prevents the low temperature surface diffusion and carbon decrease the evaporation loss of Si at high temperatures. Carbon reacts with the surface SiO_2 to form SiC at high temperature. Increasing the carbon content in SiC increases the conductivity, which is useful for cutting the component through EDM wire cutting. Near theoretical density is achieved at a sintering temperature around 2100 °C. Heating schedule up to 1700 °C is carried out in vacuum to avoid the oxidation of SiC. Afterward the atmosphere is maintained as inert to avoid the evaporation loss. Use of fine powders of silicon carbide raw material and decrease in dwelling time at the maximum sintering temperature helps to control over the grain size.

Liquid phase sintering of SiC is also tried with additives like Y_2O_3, Al_2O_3, CaO, and Sm_2O_3. The additive forms a liquid phase with SiC and enhances the diffusion process. Some of the nuclear applications do not require boron as an additive, for these applications other additives like Al_2O_3-Y_2O_3 mixture can be used. Some components which requires very high strength have to be sintered at low temperatures with minimal liquid phase forming additives. In such cases, pressure assisted sintering schedule is preferred. Novel sintering techniques like spark plasma sintering and flash sintering techniques are employed along with pressure to further reduce the sintering temperature.

Sintering of alumina: Alumina is among the commonly used refractory for high temperature applications and electronic applications. Surface diffusion at low temperature is the issue in sintering alumina, though grain boundary diffusion via vacancy motion manipulates sintering. Ionic compounds like alumina are sensitive to oxygen ion mobility. Sintering aids like MgO or NiO in small quantities are used to enhance densification and retard grain growth. Rate controlled sintering schedule is optimized for getting near theoretical density. Initial small size powders with narrow size distribution are required to have lower sintered grain size. From room temperature to 1200 °C first sintering rate is maintained to decrease the surface diffusion phenomena. Slow heating rate is maintained between 1200 °C and 1300 °C to effectively observe the liquid phase sintering. Again fast heating rate is maintained to the sintering temperature of 1600 °C, to avoid the grain growth. In this rate controlled sintering, density close to theoretical density is obtained with a grain size of 2 μm. For high temperature applications the use of additives has to be minimized, else they will change the mechanical properties. Sintering difficulties increases with decrease in the additive content. Hence balance in the composition is essential for end user applications.

1.10 Future Directions in Shape Forming and Sintering

Over decades there has been significant progress both in theories and practices on shape forming and subsequent sintering of ceramics. This drive is motivated due to the demand of materials or components of desired properties for medical, space, nuclear, strategic, and energy applications. In a powder metallurgy process, every step is inter dependant and hence the success in manufacturing a component remains in the selection of appropriate processing technique in each step. Development of new techniques and improvement in the existing techniques through modeling and simulation will continue to take place to cater the stringent requirement in dimensional control of the components. Over the last decade more thrust has been given on sintering under external stress, novel sintering processes, sintering of nano particles, and constrained sintering like sintering of layers, sintering of composites, and subsequent microstructural evolution. Some improvement in the product quality is achieved by changing sintering schedules, like two-step sintering, flash sintering,

etc. In the theoretical side, multiscale models and microstructure-based models have been studied extensively.

Sintering process is aimed at developing controlled microstructure choosing right kind of sintering technique and sintering equipments. Microstructural evolution and its co-relation with grain boundary structure in both solid-state sintering process and liquid phase sintering process have been a topic of intense investigation these days. Only diffusional mass transfer could not explain the solid state reaction mechanism. Meaningful co-relation between theoretical prediction and experimental investigation is obtained for a solid state sintering process when interface reaction is incorporated as a plausible mass transfer process apart from diffusional mass transfer. Grain growth is a major concern in the liquid phase sintering process and it depends on the equilibrium grain boundary structure. Solid-liquid interface structure and grain boundary mobility contribution can be studied extensively to explain the abnormal grain growth in liquid phase sintering process.

Sintering process is influenced by powder characteristics (such as shape, size, size distribution, surface chemistry), temperature, external field, environment, and chemistry of sintering aids. It is important to know how the external fields influence fundamental sintering parameters such as chemical potential gradients, diffusion coefficients leading to enhanced mass transport. As sintering phenomenon takes place in multiple length scale there will be a lot of research interest in multiscale material modeling to understand the process.

Constrained sintering is an issue for multilayer and composite systems. Minor phase in a composite system may sinter faster or slower with respect to the matrix. Over all sintering rate and localized sintered density need to be further studied to decrease the gap between the theoretical and experimental results. In a multilayer system, densities at the intermediate time need to be evolved. At this situation the substrate and layers are not fully constrained. Geometrical changes at different stages of sintering process need an extensive study.

Sintering becomes more complex and challenging when it comes to nano-materials. In case of nano-materials retaining the nanostructure in the sintered body is utmost important. Agglomeration of nanoparticles is a common phenomenon which leads to differential sintering and grain growth. Pinning of grain boundary also affects the sintering process in nano-materials. Sintering stress is developed due to this nonhomogenous densification which affects the sintering kinetics. Research interest in densification and microstructure evolution in nano-materials will be continued both in experiment and modeling directions.

New sintering techniques have been evolved where other forms of energy are used apart from thermal energy. These include pressure assisted sintering (e.g., hot pressing, hot isostatic pressing), and field assisted sintering (spark plasma sintering, flash sintering, and microwave sintering). Distribution of temperature, pressure, or applied field has positive effects on the sintering process. There remains a scope to development large components using these field assisted sintering techniques using meso-scale modeling and design of equipments.

Sintering is associated with large shrinkage in different directions. Lot of stress is generated during sintering that may lead to failure of the components. This is more

prominent in sintering of complex shapes. Modeling of stress distribution during sintering can be useful in understanding the process and sintering rate or component design can be suitably modified to avoid failure.

Additive manufacturing will remain an evolving field particularly in making miniature components and complex shapes. A slurry-based, powder-based, or bulk solid-based feed stocks are being used for this process. A deep understanding of the powder properties, slurry rheology, binder bur out, ceramic to laser interaction, and sintering under thermal gradient is required. However, the process is highly localized and the dynamics of sintering is quite different. Hence more focus is required to make the process more convenient.

1.11 Conclusion

Ceramic products with desire shape and functional properties are used for advance applications. Ceramic powders are shaped into desired dimensions and sintered at required temperature for getting near theoretical density. Ceramic shape forming and sintering are interdependent. Based on the end application, density and microstructure is fixed first. To achieve the desired properties, shape forming is chosen accordingly. Different factors affecting sintering are discussed in this chapter. Different mass transport phenomena responsible for the sintering process are discussed. There is positive effect of different fields like microwave, DC arc, plasma, etc. on sintering. There is an evolution of new sintering technologies with time. Additive manufacturing is the recent one in which complex as well miniature ceramic structures could be prepared.

References

1. Mahata T, Nair SR, Lenka RK, Sinha PK (2012) Int J Hydrogen Energy 37:3874–3882
2. Costa AL, Esposito L, Medri V, Bellosi A (2007) Adv Eng Mater 9:307–312
3. Palanki B (2015) Nat Sci 7:10–17
4. Cláudia Ângela Maziero Volpato LGDAG, Fredel MC, Bondioli F (2011) Application of Zirconia in dentistry: biological, mechanical and optical considerations. In: Sikalidis C (ed) Advances in ceramics—electric and magnetic ceramics, bioceramics, ceramics and environment
5. Mullainathan RVAS (2013) Asian J Chem 25:S449–S454
6. Veringa HJ (1993) J Mater Sci 28:2757–2762
7. Guo Y, Ran R, Shao Z, Liu S (2011) Int J Hydrogen Energy 36:8450–8460
8. Jojo N, Shongwe MB, Tshabalala LC, Olubambi PA (2019) SILICON 11:2689–2699
9. Rubat du Merac M, Reimanis IE, Smith C, Kleebe H-J, Müller MM (2013) Int J Appl Ceram Technol 10:E33–E48
10. Mukherjee AK, Mishra RS (2001) Superplasticity. In: Buschow KHJ, Cahn RW, Flemings MC, Ilschner B, Kramer EJ, Mahajan S, Veyssière P (eds) Encyclopedia of materials: science and technology. Elsevier, Oxford, pp 8977–8981

11. Mayo MJ (1998) Nanocrystalline ceramics for structural applications: processing and properties. In: Chow G-M, Noskova NI (eds) Nanostructured materials: science & technology. Springer, Netherlands, Dordrecht, pp 361–385
12. Barry Carter MGNC (2007) Ceramic materials science and engineering. Springer
13. Rahaman MN (2007) Ceramic processing. Taylor & Francis Group, New York
14. Dynys FW, Halloran JW (1983) J Am Ceram Soc 66:655–659
15. Ross JDJ, Pollock HM, Guo Q (1991) Powder Technol 65:21–35
16. Koizumi MNM (1992) Isostatic pressing technology and applications. New York
17. Handle F (2007) Extrusion in ceramics. Springer, Leipzig
18. Brook RJ (1996) Processing of ceramics part-I. VCH Verlagesesellschaft mbH, Weinheim
19. Lange FF (1989) J Am Ceram Soc 72:3–15
20. Hunter RJ (1988) Zeta potential in colloid science. Academic Press, San Diago
21. Fennelly TJ, Reed JS (1972) J Am Ceram Soc 55:381–383
22. Tallon C, Limacher M, Franks GV (2010) J Eur Ceram Soc 30:2819–2826
23. Descamps M, Moreau G, Mascart M, Thierry B (1994) J Eur Ceram Soc 13:221–228
24. Boch P, Chartier T, Huttepain M (1986) J Am Ceram Soc 69:C-191–C-192
25. Herring C (1950) J Appl Phys 21:301–303
26. Rahaman MN (2003) Ceramic processing and sintering. CRC Press
27. Chappell JS, Ring TA, Birchall JD (1986) J Appl Phys 60:383–391
28. Ting JM, Lin RY (1995) J Mater Sci 30:2382–2389
29. Kun Woo S, Young Woo L, Myung Seung Y, Dong-Seong S, Young Hwan K (1994) J Nucl Mater 209:263–269
30. German RM (1992) Acta Metall Mater 40:2085–2089
31. Slamovich EB, Lange FF (1990) J Am Ceram Soc 73:3368–3375
32. Morgan CS, McCorkle KH, Powell GL (1973). In: Kuczynski GC (ed) Sintering and related phenomena. Springer, US, Boston, MA, pp 293–299
33. Kang S-JL (2005) Sintering: densification, grain growth, and microstructure. Butterworth-Heinemann, Oxford
34. Friedrich WSAE (1982) Crystal Res Technol 17:1061–1070
35. Patterson BR, Liu Y, Griffin JA (1990) Metall Trans A 21:2137–2139
36. Zheng J, Reed JS (1989) J Am Ceram Soc 72:810–817
37. Neuman EW, Fahrenholtz WG, Hilmas GE (2019) Int J Appl Ceram Technol 16:1715–1722
38. Tavafoghi Jahromi MJTM (2009) J Achiev Mater Manuf Eng 34:130–136
39. Rahaman MN, Manalert R (1998) J Eur Ceram Soc 18:1063–1071
40. Exner HE (1979) Principles of single phase sintering. Freund Publishing House
41. Raman R, German RM (1995) Metall and Mater Trans A 26:653–659
42. Wilcox PD, Cutler IB (1966) J Am Ceram Soc 49:249–252
43. Passmore EM, Spriggs RM, Vasilos T (1965) J Am Ceram Soc 48:1–8
44. Boškovic SB, Ristić MM (1972) Sov Powder Metall Metal Ceram 11:755–759
45. Geiger FVAM (1990) Powder Met Intern 22
46. German RM (1976) Metall Trans A 7:1879–1885
47. Mocellin A (1983) Stress assisted hot formation of ceramics. In: Riley FL (ed) Progress in nitrogen ceramics. Springer, Netherlands, Dordrecht, pp 253–272
48. Kakar AK, Chaklader ACD (1967) J Appl Phys 38:3223–3230
49. Li EKH, Funkenbusch PD (1993) Metall Mater Trans A 24:1345–1354
50. Atkinson HV, Davies S (2000) Metall Mater Trans A 31:2981–3000
51. Poisl WH, Chaklader ACD (1993) J Am Ceram Soc 76:1177–1184
52. Liu Y, Patterson BR (1993) Metall Trans A 24:1497–1505
53. Behera SK, Cantwell PR, Harmer MP (2014) Scripta Mater 90–91:33–36
54. Farahbakhsh I, Ahmadi Z, Shahedi Asl M (2017) Ceram Int 43:8411–8417
55. Deng J, Zhao J, Li Y, Song W (2008) Ceram Int 34:1361–1366
56. Šajgalík P, Sedláček J, Lenčéš Z, Dusza J, Lin HT (2016) J Eur Ceram Soc 36:1333–1341
57. Abhijit Ghosh AKG, Fotedar RK, Dey GK, Suri AK (2009) Microstructural studies of hot pressed silicon carbide ceramic. In: Ceramics in nuclear applications, pp 113–122

58. Angers R, Beauvy M (1984) Ceram Int 10:49–55
59. Koval'chenko MS, Tkachenko YG, Koval'chuk VV, Yurchenko DZ, Satanin SV, Kharlamov AI (1990) Sov Powder Metall Metal Ceram 29:523–526
60. Chakraborty S, Debnath D, Mallick AR, Das PK (2014) Int J Refract Metal Hard Mater 46:35–42
61. Monteverde F (2008) J Mater Sci 43:1002–1007
62. Carniglia SC, Johnson RE, Hott AC, Bentle GG (1964) J Nucl Mater 14:378–394
63. Vieira JM, Brook RJ (1984) J Am Ceram Soc 67:450–454
64. Qu X, Lü S, Hu J, Meng Q (2011) J Alloy Comp 509:10217–10221
65. Bohra AK, Bhatt R, Singh A, Bhattacharya S, Basu R, Meshram KN, Sarkar SK, Bhatt P, Patro PK, Aswal DK, Muthe KP, Gadkari SC (2018) Mater Des 159:127–137
66. Atkinson HV (1991) Hot isostatic pressing. Adam Higer, Bristol
67. Johnson R, Biswas P, Ramavath P, Kumar RS, Padmanabham G (2012) Trans Indian Ceram Soc 71:73–85
68. Xiao Z, Yu S, Li Y, Ruan S, Kong LB, Huang Q, Huang Z, Zhou K, Su H, Yao Z, Que W, Liu Y, Zhang T, Wang J, Liu P, Shen D, Allix M, Zhang J, Tang D (2020) Mater Sci Eng Rep 139:100518
69. Shimada M, Endo T, Saito T, Sato T (1996) Mater Lett 28:413–415
70. Cohen S, Ratzker B, Sokol M, Kalabukhov S, Frage N (2018) J Eur Ceram Soc 38:5153–5159
71. Ramavath P, Biswas P, Johnson R, Reddy GJ, Laxminarayana P (2014) Trans Indian Ceram Soc 73:299–302
72. Yashina EV, Gavrishchuk EM, Ikonnikov VB (2004) Inorg Mater 40:901–904
73. Li C, Xie T, Kou H, Pan Y, Li J (2017) J Eur Ceram Soc 37:2253–2257
74. Lee S-H, Kupp ER, Stevenson AJ, Anderson JM, Messing GL, Li X, Dickey EC, Dumm JQ, Simonaitis-Castillo VK, Quarles GJ (2009) J Am Ceram Soc 92:1456–1463
75. Zhang W, Lu T, Ma B, Wei N, Lu Z, Li F, Guan Y, Chen X, Liu W, Qi L (2013) Opt Mater 35:2405–2410
76. Clasen EBABMWR (2003) Improved preparation of transparent PLZT ceramics by electrophoretic deposition and hot isostatic pressing. In: 27th annual cocoa beach conference on advanced ceramics and composites: B: Ceramic engineering and science proceedings, pp 169–174
77. Laxmanan A (2012) Sintering of ceramics-new emerging techniques, Intech, Janeza Trdine 9, 51000 Rijeka, Croatia
78. Jha SK, Phuah XL, Luo J, Grigoropoulos CP, Wang H, García E, Reeja-Jayan B (2019) J Am Ceram Soc 102:5–31
79. Echeberria VMJ, Sánchez JM, Bourgeois L, Barbier G, Hennicke J, Kneringer PRAHW G (ed) Proceedings of 16th international plansee seminar, 2005, pp 434–448
80. Shen ZJ, Adolfsson E, Nygren M, Gao L, Kawaoka H, Niihara K (2001) Adv Mater 13:214–216
81. Frage N, Cohen S, Meir S, Kalabukhov S, Dariel MP (2007) J Mater Sci 42:3273–3275
82. Souza CA, Eiras JA, Lente MH (2016) Ferroelectrics 499:47–56
83. Ghosh NC, Harimkar SP (2012) Consolidation and synthesis of MAX phases by Spark Plasma Sintering (SPS): a review. In: Low IM (ed) Advances in science and technology of Mn+1AXn phases, pp 47–80. Woodhead Publishing
84. Agrawal D (2006) Trans Indian Ceram Soc 65:129–144
85. Patro PK, Kulkarni AR, Gupta SM, Harendranath CS (2007) Phys B Condens Matter 400:237–242
86. Agrawal DK (1998) Curr Opin Solid State Mater Sci 3:480–485
87. Rybakov KI, Olevsky EA, Krikun EV (2013) J Am Ceram Soc 96:1003–1020
88. Żymełka D, Saunier S, Goeuriot D, Molimard J (2013) Ceram Int 39:3269–3277
89. Ahmadbeygi S, Khodaei M, Nemati A, Yaghobizadeh O (2017) J Mater Sci: Mater Electron 28:5675–5685
90. Katz J, Blake R, Petrovic J, Sheinberg H (1988) MRS proceedings, pp 219
91. Zafar S, Sharma AK (2014) Mater Charact 96:241–248

92. Goldstein A, Travitzky N, Singurindy A, Kravchik M (1999) J Eur Ceram Soc 19:2067–2072
93. Bose S, Dasgupta S, Tarafder S, Bandyopadhyay A (2010) Acta Biomater 6:3782–3790
94. Xu A, Solomon AA (1987) The effects of grain growth on the intergranular porosity distributions in hot-pressed and swelled UO2. In: Pask JA, Evans AG (eds) Ceramic microstructures '86: role of interfaces. Springer, US, Boston, MA, pp 509–518
95. Ohji T, De Jonghe LC (1994) J Am Ceram Soc 77:1685–1687
96. Beruto D, Botter R, Searcy AW (1989) J Am Ceram Soc 72:232–235
97. Young RM, McPherson R (1989) J Am Ceram Soc 72:1080–1081
98. Chen Z, Li Z, Li J, Liu C, Lao C, Fu Y, Liu C, Li Y, Wang P, He Y (2019) J Eur Ceram Soc 39:661–687
99. Ian Gibson DWR, Stucker B (2010) Additive manufacturing technologies: 3D printing, rapid prototyping, and direct digital manufacturing, 2nd edn. Springer, New York
100. Li Yang HM (2017) 28th Annual international solid freeform fabrication symposium—an additive manufacturing conference, 2017, pp 653–679
101. Zocca A, Colombo P, Gomes CM, Günster J (2015) J Am Ceram Soc 98:1983–2001
102. Lian Q, Sui W, Wu X, Yang F, Yang S (2018) Rapid Prototyp J 24:114–119
103. Kumar A, Kargozar S, Baino F, Han SS (2019) Front Mater 6.
104. Du Y, Fatoba OS (2019) ECS Trans 91:277–283
105. Rhodes WH (1981) J Am Ceram Soc 64:19–22

Chapter 2
Growth of Single Crystals for Nuclear Radiation Detection

Mohit Tyagi and S. C. Gadkari

Abstract Single crystals are the vital components for the technology development having various applications in industries including semiconductors, electronics, watch, detectors, medical diagnostics, homeland security, etc. The performance characteristics of single crystals usually change with increasing the dimensions. A systematic approach and strategy are essential to grow large size single crystals with desired properties. This chapter briefs the challenges in the growth of large size single crystals for radiation detection applications. The growth of single crystals from melts strongly depends on the thermal properties of the material, stoichiometric ratio of the constituent oxides, dopant concentration, growth ambient, etc. In addition to the effects of crystal growth parameters on their properties, an approach to further improve the performance characteristics has been discussed in details.

Keywords Single crystal · Czochralski technique · Scintillator · Co-doping · Defects · Annealing

2.1 Introduction

2.1.1 Crystalline Structure

A material is usually found in three states: solid, liquid and gas; however, plasma and Bose–Einstein condensate have also been considered as the state of matters in the modern science. In the gaseous state the molecules are moving at high speeds and situated at large distances. Due to the attraction, molecules begin to come closer if the temperature of the system is reduced. The liquid state is eventually formed

M. Tyagi (✉)
Technical Physics Division, Bhabha Atomic Research Centre, Mumbai 400 085, India
e-mail: tyagi@barc.gov.in

Homi Bhabha National Institute, Mumbai 400 085, India

S. C. Gadkari
Department of Atomic Energy, Raja Ramanna Fellow, Mumbai, India

A. K. Tyagi and R. S. Ningthoujam (eds.), *Handbook on Synthesis Strategies for Advanced Materials*, Indian Institute of Metals Series,
https://doi.org/10.1007/978-981-16-1803-1_2

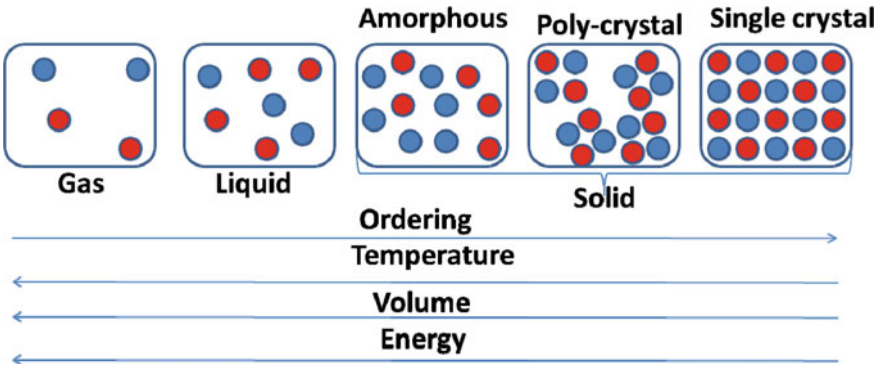

Fig. 2.1 The different states of matter

after cooling down where the molecules are in denser state and the energy of the system is reduced to favor the stability of the state. A more energetically favored ordered state can be achieved by further reducing the temperature. Molecules are in relatively fixed position and cannot move freely in the solid state. This arrangement in solids can be ordered either in a long range or in a random manner which are called crystalline and amorphous/glass materials respectively (Fig. 2.1). In polycrystalline materials several crystallites are separated by grain boundaries across which their relative orientation may different (random). In the long-range ordering, position and surrounding of any atom can be known if we know the position of one atom even if these atoms are situated far away. However, reducing the temperature is necessary to form the solid state; it is not the sufficient condition to form crystals. The formation of an ordered state from a disordered state introduces a barrier to the formation of the first tiny crystal. The formation of this first baby crystal is called nucleation [1]. This barrier leads to the liquid state to be cooled even below its freezing temperature. The liquid state below its freezing temperature is called supercooled, and this occurrence is called supercooling [2]. The nucleation and supercooling are the most important phenomena for growing single crystals which have been described in more details in the next sections.

2.1.2 History

The crystallization of materials has been occurring in nature, and it has been carried out even by human beings over the long ages. It was usually expressed as condensation or coagulation before the 17th century. Various crystals like quartz, gem-stones etc. have been formed in the nature, while the transformation of sea water to salt can be considered as the oldest method of crystallization by human. Bohm has nicely compiled the history of crystal growth in details [3]. The crystallization of various salts has been described in a Roman literature "Naturalishistoria" written well before

the Christian era. An article by the alchemist Geber in 12th century is considered to be the oldest article about the preparation and purification of various materials [3]. Some of the important events towards the modern era of crystal growth are listed as below [3]:

- In the 17th century the theory of crystallographic structure and crystal angle was suggested with the help of snow crystals. [Kepler (1611) and Hooke (1665)] [4, 5].
- The role of impurities and growth rate in the formation of crystals from solution was observed experimentally by Boyle (1666—1672) [6].
- The supercooling of water and heat of crystallization in ice formation was observed in 18th century (Fahrenheit 1724) which is one of the fundamental theories for the crystallization [7].
- In 19th century, the idea of periodic structure was introduced and Bravais (1849) derived the 14 lattice types. The crystal structure could be well understood after the invention of Laue X-ray diffraction [8].
- The start of modern large size crystal growth era can be considered to be started after the growth of large ruby crystal by Verneuil (1902–1904) using his flame fusion method which is still adopted by various industries [9].
- The hydrothermal solution growth of large size quartz crystals, otherwise occurring naturally, by Spezia (1905–1909) encouraged to generate nature-like conditions in laboratories [10].
- Czochralski (1918) and Kyropoulos (1926) modified Nacken (1915–1916) method to grow single crystals from melts by using a cooled rod or seed and pulling crystal from melts [11–13].
- Bridgman (1923–1925) introduced the melt to be freezed in the crucible by lowering it to a lower temperature zone and this method was extensively used to grow large size alkali halide crystals [14, 15].
- Burten Cabrera and Frank (BCF) gave a revolutionary generalized theory for the crystal growth [16].
- The large size germanium crystal was pulled from the melt by Teal and Little (1950) [17].
- The concept of constitutional supercooling was established by Rutter and Chalmers (1953) to achieve the inclusion-free single crystal growth [18].
- Bundy, Hall, Strong and Wentorf (1955) synthesized diamond in laboratory [19].
- The growth of sapphire crystals (Al_2O_3) on industrial scale by Verneuil method (1977) [20].
- The development of scintillator crystals starts from the invention of NaI(Tl) by Hofshtadter followed by the invention of $PbWO_4$, $Bi_4Ge_3O_{12}$ and Lu_2SiO_5 [21].

2.1.3 Applications

Most of the properties of any material can be realized the best in their single crystalline form. The absence of grain boundaries makes single crystals as the most suitable choice in numerous applications. The anisotropic properties of single crystal

also make it possible to study the dependence of various properties indifferent directions of propagation in materials which is otherwise not possible in any other form. The industrial applications of single crystals increased manifold during the world war and has been growing continuously after that. The single crystals have a vast range of studies from academic research to the advanced technologies including ICs, detectors, turbine blades, etc. and therefore have become the vital component of the technology development. Semiconductor industries have the maximum share applications of crystals. Single crystal silicon is used in almost all electronic equipment [22]. It is also used in solar panel fabrications, radiation detectors and as a substrate for various applications. Single crystals of metals or metal-alloys have the best electrical and thermal properties in single crystalline form and are therefore useful in various applications having extremely high temperature and force, e.g., jet engine turbine blades [23]. The wide transparent regions of single crystal insulators find applications in various devices like electro-optical, acousto-optical, fiber optics, laser hosts, non-linear optics, scintillation detectors, etc. Single crystalline diamonds are also now being synthesized in laboratories for various applications in extreme conditions of temperature and pressure [24].

This chapter mainly emphasizes the synthesis and properties of single crystals of scintillating materials used in the radiation detection applications. The scintillating materials are characterized with the emission of visible light when irradiated with higher energy radiations like x-ray, gamma or with charged particles like electrons, alpha, etc. [25]. The single crystalline form of such materials is preferable especially in the spectrometry. The single crystals are rich in electrons which interact with the radiation and could transmit the emitting light from the bulk without any scattering losses from grain boundaries. The single crystalline form ensures the light output to be proportional to the deposited energy which leads to the distinct photo-peak unlike that observed in glasses or liquid scintillators. The excellent energy resolution makes it possible to identify different radio-nuclides by radiation detectors based on single crystals [26]. Therefore, the single crystalline form is essential for the spectrometry applications. The single crystal scintillators have major applications in homeland security, medical imaging, high energy physics experiments, oil well logging, nuclear industries, etc.

The applications of single crystals are continuously increasing beyond the academic interests, which have made them to be one of the most vital components of the current technology development. The single crystal of materials which can perform under extreme conditions like high temperature in advanced reactors, high luminosity in advanced accelerators, high flux in advanced synchrotron beam lines, etc. are continuously attracting various research groups to work in collaboration with the industries.

2.2 Growth of Single Crystals

2.2.1 Basic Concept

As mentioned earlier, to bring an ordered state to disordered state does not require any thermodynamic barrier, e.g., melting ice into water. In general, the liquid state can be transformed in to more ordered solid state by decreasing the temperature. However, lowering the temperature to transform liquid state into more ordered solid state is not the sufficient condition and the molecules need to overcome a thermodynamic barrier to forma first tiny aggregate unit usually called nuclei and the process is known as the "Nucleation" [27]. This temperature region where the state is still in the liquid form even below its freezing temperature is called supercooling[28]. For example, water may not freeze into ice even below −20 °C in the absence of any seed crystal. The nuclei usually considered to be spherical for various energy calculations. For smaller radii of nuclei, the surface energy term dominates while attraction volume energy dominates as the radii increases. The competition between surface and volume energies decides a critical radius for the nuclei corresponding to the inflection point that indicates the minimization of the energy and stability of the phase. In the presence of impurities, surface, interface dust, etc., the energy required for the nucleation is reduced by the contact angle and the nucleation takes place heterogeneously or it may occur homogenously in a few cases which obviously requires overcoming a higher energy barrier [27]. The rate of nucleation not only depends on the thermodynamic barrier but the kinetic barrier also plays a role as the temperature of the system decreases that consequently slows down the nucleation rate. An increase in the degree of supercooling limits the kinetic motion of the molecules. The energetically favorable nuclei grow further and eventually the growth starts. In a similar manner as of the nucleation, the growth rate also attains a maximum and limited by the atomic mobility in a more viscous melt with decreasing the temperature further (Fig. 2.2) [29].

Therefore, the transition from liquid to solid state is mainly governed by the balance of internal energy and a transformation from disordered to ordered state.

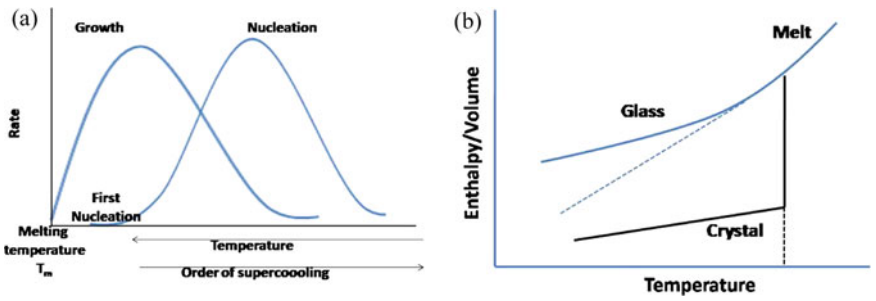

Fig. 2.2 Temperature dependence of **a** nucleation and growth rates and **b** Enthalpy/volume [30]

The Gibbs free energy can be defined to include both the terms as G = H–TS, where temperature dependent term describes the disordering called entropy and H represents the internal energy called enthalpy and behaves like the volume [29]. The enthalpy decreases similar to the volume of the system with decrease in temperature. While decreasing the temperature of liquid state, if the cooling rate is significantly high, it does not allow sufficient time for the nucleation. Further a fast cooling rate will lead the melt to more and more viscous state and then the liquid in due course transforms into a rigid glass phase. However, on the other hand, if cooling rate is kept slow that allows the nucleation to take place the enthalpy drops sharply and liquid transform into the crystalline phase [29].

2.2.2 Various Methods and Techniques

The growth of a crystal is basically attaining a long-range order from the randomly moving molecules. A single crystal is characterized by the absence of any grain boundary and requires the growth of only a single grain. Depending on the application and requirement of size, the crystals could be grown from vapor, melt or solution. Various growth methods and techniques are listed in Table 2.1.

Different growth techniques have some advantages and disadvantages over other techniques. Melt growth techniques are the most preferred ones to grow large size single crystals. Although the crystals grow at much faster rate when grown from the melt as compared to the solution growth, the melt growth is limited to only materials that melt congruently. In addition to the application and size of the crystal, thermal properties like expansion, conductivity, viscosity, chemical stability and requirement of composition, size and quality are the major factors to decide a technique which should be used to grow single crystals of a particular material [31]. Majority of single crystals used in various applications including the most extensively used semiconductors are grown using melt growth techniques. We are mainly focusing on scintillator single crystals in this chapter, which are mostly grown from melts using the Czochralski or Bridgman techniques [32]. In the Bridgman technique, a

Table 2.1 Crystal growth methods and techniques

Melt growth techniques	Solution growth techniques	Vapor growth techniques
Czochralski (CZ)	Aqueous solution	Direct synthesis (DS)
Bridgman	Travelling heater (THM)	Physical vapor transport (PVT)
Floating zone	Solute solution diffusion (SSD)	Chemical vapor transport (CVT)
Verneuil	Solvent evaporation (SE)	Solid phase reaction
	Temperature difference under controlled vapor pressure (TDM-CVP)	
	Hydrothermal synthesis	

crucible containing the melt is lowered from a zone at a higher temperature to the zone at a temperature lower than the melting point through a temperature gradient. In the other scheme called the Czochralski technique (CZ), the crystals are grown by pulling the melt to a lower temperature zone. The crucible is kept stationary, while the position of solid-melt interface shifts into the hot zone. The use of an oriented seed allows the growth along a specific crystallographic direction in this technique. The ambience of growth chamber can be also selected according to the material and crucible properties. The possibility to observe seeding and growth process in the CZ technique enables to take corrective measures in real time during the growth process unlike the Bridgman technique. In this chapter the single crystal scintillators grown by the CZ technique are mainly discussed. In this technique, the powders of constituent metal-oxides are mixed in their respective stoichiometric molar ratio and filled in a suitable crucible to melt through inductive or resistive heating. A seed crystal, mounted on a suitable seed holder and a seed road attached to the weighing load cell, is brought in contact with the melt. The speed of lowering the seed has to be also optimized based on the properties of melt which is kept in thermal equilibrium with the rotating seed. The seed may be the single crystal of the same material to be grown or an iso-structural material for better nucleation and minimization of dislocations and other defects propagating from the seed. The weight signal is used to adjust the heater power such that there is no growth and the melt maintain the state. This complete process is called "seeding". This first key step decides the fate of whole growth run and therefore considered as one of the most crucial steps. The growth is progressed thereafter by withdrawing the seed crystal with an optimized rate. The growth rate is increased in a controlled manner to slowly increase the diameter to a desired value. The maximum diameter is usually attained to the half of the crucible diameter [33].

The growth is eventually completed after achieving the desired length. The crystal/melt interface is snapped off by either through rapid lifting or by raising the melt temperature. The grown crystal is subsequently cooled slowly to the room temperature (Fig. 2.3) [34].

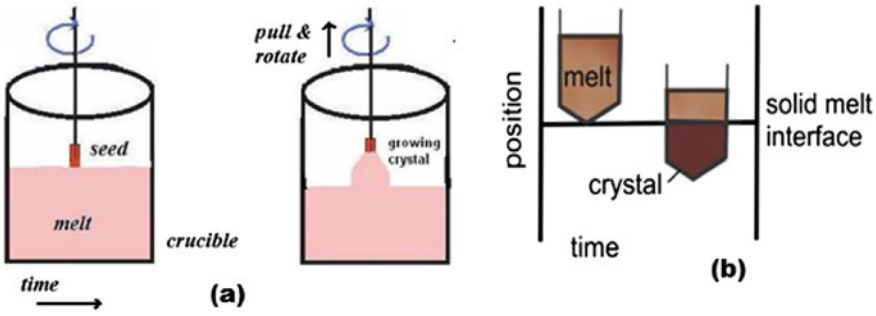

Fig. 2.3 Schematic diagram of **a** Czchrolaski and **b** Bridgman technique to grow single crystals from melts [34]

A typical CZ crystal puller is mainly consisting of a power supply, suitable crucible, a growth chamber to provide housing for crucible, thermal shield and controlled ambient, a mechanism for pulling, rotation and weighing the crystal and a computer controlled system. An iridium crucible is generally used for the growth of materials with high melting temperatures. Therefore, the growth chambers need to be closed to provide suitable ambient for the crucible material containing high temperature melts. The main input parameters for a computer based close-loop control systems are height and diameter of the crystal parts like seed, shoulder, cylindrical and tail portions, pull rate, rotation rate, solid and melt densities, and translation height for crystal detachment. The difference between the mass growth rates calculated from the input parameters and measured in the real time generates an error signal to provide a feedback for the power supply. When the growth rate is slow the negative error signal would lead to the lowering of power while in case of a faster growth rate the power (hence temperature) would be increased due to a positive feedback from the error signal. The system may be put in the automatic control when the error signal reaches close to zero. Inputs on the proportion and integration terms decide how to respond with the power changes and mainly governed by the thermal inertia and temperature oscillations stirring in the melt. This real-time feedback and corrective measures make the CZ technique the most useful for various single crystals specially required in larger sizes.

2.2.3 Challenges and Strategies

Although the mechanism of crystal growth from melts seems very simple but one has to face numerous challenges in growing device quality single crystals. Each single crystal needs to comply for some specific criteria before being used them in any application. Single crystals for laser applications require insignificant absorption coefficient and negligible refractive index variation, while single crystal scintillators for radiation detection require high light output, fast radiative decay, high radiation hardness and absence of afterglow. The devices based on single crystalline semiconductors like c-Si and Ge desires high resistivity and long carrier life time [34]. Since the crystal growth is a high temperature process, it needs a systematic optimization of various parameters to achieve good quality crystals having the desired properties.

The selection of various growth parameters significantly varies from material to material and strongly depends upon the material properties along with the dimensional and quality requirements. The main properties of materials, to decide the growth parameters, include thermal conductivity of solid and liquid phases, melt viscosity and microstructure, chemical properties, anisotropy in thermal expansion, difference in solubilities of dopant in liquid and solid phases, etc. Therefore, any small change in the material needs multiple trial growth runs to optimize various growth parameters. The control of growth parameters is usually governed by adjusting the power rather than the temperature which is difficult to monitor. Some materials have higher tendencies to grow in glassy phase and therefore require a very slow

growth rate for the crystallization [33]. The difference in ionic radii of constituents and dopants lead to a low segregation and the concentration varies in the melt and solid phases [35]. The presence of strong cleavage planes makes the crystal prone to cracking along particular planes and therefore requires the growth to be carried out using a seed oriented in a specific direction.

The shape of the solid-melt interface is one of the most important parameters that determine the stability of the growth process. A slightly convex shape toward the melt prevents an unpredictable detachment of the growing crystal. The presence of strain and dislocations also depends on the shape of the solid-melt interface. Based on the density, viscosity and conductivity of the melt, the rotation and pulling rates are adjusted for the required interface shape [36].

There are various kinds of heat flows and convective currents in the melt during the growth process which include gas and melt convection, solid and liquid heat conduction and the heat of fusion [36]. Heat from the melt and the latent heat of crystallization are required to be conducted through the growing crystals for a stable growth. The various heat flows mainly depend on the thermal conductivities of melt and solids and governed by radial and axial temperature gradients. The thermal gradients could be optimized by the geometry of growth station, dimension and material of the seed holder, flow and pressure of ambient gas, diameter of seed and crystal, etc. [37].

The pull rate of crystals is related to the growth rate which varies from few tenths of mm/h to a few of cm/h from material to material. The growth rate is basically limited by the thermo-elastic properties of the crystal, segregation of dopants/impurities and the generation and propagation of defects. Metals that have higher thermal conductivities for releasing the heat of crystallization can be pulled at a much faster rate which is usually limited by the thermal gradient above the solid-melt interface [32].

The axial temperature gradient has to be optimized based on the radius of crystal, the heat loss from the crystal, thermal expansion coefficient and the breaking strain of the crystal. A small value of anisotropy in thermal expansion and thermal conductivity can also cause crystal cracking during the growth or annealing. The growth should preferably be along the axis that has the smallest thermal expansion coefficient to minimize the cracking problem during the growth and cooling of the crystal. The cooling rate of the grown crystal also depends on the breaking strain, thermal expansion coefficients and the crystal diameter [32].

The differences in vapor pressures of constituent oxides make selective evaporative losses and lead to stoichiometric variations during the growth. The variation from the stoichiometry in the grown crystal and in the melt (left over charge after the growth) causes cracking and coloration in the grown crystals. The most volatile component is usually compensated in the starting powder to avoid variation from the stoichiometric ratio [35].

The oxide crystals usually have defect centers related to the oxygen sublattice. These defect centers can be controlled by selecting appropriate growth ambience and after growth annealing treatment. The exchange of cations also causes to the antisite defects in some oxide crystals which can be compensated with the appropriate co-doping in some cases [38]. Since the growth process usually takes 7–10 days to get a

crystal with a decent size, sometimes there are unpredictable parameters which may cause the crystal yield to be less than 100% in most of the cases.

2.3 Characterization Techniques

2.3.1 Thermal and Structural Characterization

The phase formation and melting/solidification behavior are the essential properties that need to be known before planning any crystal growth experiment. The temperature variations of material properties are generally studied by Differential thermal analysis (DTA) experiments. In this technique, the difference between the temperatures of two crucibles (reference and sample) is measured as a function of time to measure endothermic/exothermic reaction or phase change. The DTA of a compound, that melts congruently, would have a single sharp peak. A material which decomposes before its melting temperature or have multiple peaks corresponding to more number of phases cannot be grown from melt growth methods. The crystalline or glassy nature of transition can also be observed from the DTA plots [39].

The X-ray powder diffraction (XRD) is used to identify the phase formed during material synthesis and after the crystal growth. The structural parameters of the crystal, grain size, texture, residual stress, presence of foreign phase, etc. can be obtained by analyzing the XRD pattern [40]. The regular pattern of atoms in a crystalline solid lead to constructive interference between reflected x-rays corresponding to certain angles satisfying the Bragg condition ($2d\sin\Theta = n\lambda$). The pattern of a single crystal has single peak corresponding to a single plane. The powder samples have randomly oriented numerous crystals, and therefore the pattern is consisted of multiple peaks (Fig. 2.4).

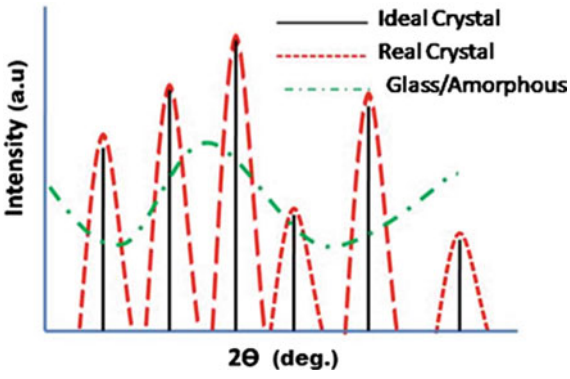

Fig. 2.4 XRD patterns of perfect crystal, real crystal and glass/amorphous

The perfection of crystallinity and presence of any strain or mosaicity in the single crystal scan be measured by recording the rocking curve using a triple axis high resolution XRD (HR-XRD) employing a well collimated X-ray beam. The orientation of a single crystal is determined from the symmetry of projections measured by the Laue techniques [40].

2.3.2 Electronic And Optical Characterization

The fraction of incident light transmitted through a sample is measured using a double beam UV/VIS spectrophotometer for transmission/absorption properties [41].

$$\text{Transmittance (\% T)} = \text{Light passing through a sample} \big/ \text{Incident light}$$

$$\text{Absorbance (A)} = -\log(\%\text{T} \big/ 100)$$

The value and nature of the band gap can be calculated by applying a power law equation on the fundamental absorption edge data. In addition to the near edge fundamental absorption with urbach tail, atypical absorption spectrum represents various features in the crystal arising due to the absorption from high lying energy levels, excitons, impurities and free carriers also. The radiation hardness of a scintillator crystal is calculated from the radiation induced absorption by measuring absorption spectra before and after the irradiation.

The emission followed by the absorption is called luminescence and measured using either a photoluminescence spectrometer (UV–VIS excitation) or a radioluminescence setup (X-ray excitation) [42]. The wavelength dependent emitted intensity and the distribution of intensity that causes luminescence are called emission spectrum and excitation spectrum respectively. The time spent in the excited state, i.e., life-time of the excited state is measured as the luminescence decay time. These are the important parameters to be determined for any scintillator crystal and the emitted light wavelength should match with the available photo-sensors efficiencies, and the emission decay should be fast enough to handle higher count rates of incident radiation. The excitation spectrum represents the presence of bands corresponding to the excited states of activator ions in forbidden band gap and their position relative to the conduction band edge. The excited states of the activator should not be very close to conduction band to minimize the thermal ionization of excited carrier to conduction band and should not be very far as well to minimize the available sites for trap centers. The temperature dependence of luminescence helps to understand the electronic band structures and describes the activation energy for thermal quenching of the emission. Time resolved photo-luminescence helps to identify the excited states that contribute to the different components of the emission decay times [42]. The presence of long-lived trap centers may result in the afterglow of the emission which can be measured using a fast shutter to stop the irradiation of the excited light and measuring the remaining emitted light as a function of time.

The presence of defect structure in the materials can be probed by measuring the thermally stimulated luminescence (TSL) or optically stimulated luminescence (OSL) [43]. The excited charge carriers are trapped in the defect centers present in the crystal scintillators due to various imperfections. These trapped carriers are excited thermally or optically which consequently recombine to emit photons that are measured by suitable photo-sensors. The position of these trap centers in the forbidden gap can be calculated by plotting the temperature as a function of emitted intensity, called a glow-curve. The intensity of the stimulated light is proportional to the deposited dose of radiation in the dosimeter materials [43].

2.3.3 Scintillation Properties

The main characteristics for ideal scintillator crystals are high effective atomic number, high light output, fast decay, high mechanical, chemical and radiation hardness, emission matching with photo-sensors and energy proportionality. As there is no single material that fulfils all the criteria, different single crystal scintillators are used as radiation detector in different applications. For examples, medical imaging like PET requires fast coincidence timing resolution while high energy physics experiments require high density and high radiation hardness [21]. Therefore, the grown single crystals need to be characterized for their scintillation properties useful for a particular application before developing devices based on them [44]. For basic scintillation characterizations, the single crystals are usually coupled with photo-sensors like PMT, photodiodes or SiPM using optical grease due to the variation in refractive indices. All other surfaces of the single crystal except the surface to be coupled with photo-sensors need to be covered with some kind of reflector like Teflon tape, Spectral on hemisphere or reflecting paint to collect the maximum number of photons generated from high energy radiation. The output of photo-sensor is subsequently fed to a setup consisting of a pre-amplifier, a shaping (spectroscopic) amplifier and a multi channel analyzer (MCA). The pulse-height spectrum (PHS) represents counts (on ordinate y-axis) as a function of the MCA output voltage proportional to the number of photons which are proportional to the deposited energy (the pulse height, on abscissa, x-axis). The radiation interacts via three processes: photoelectric absorption, Compton scattering and pair production which are observed in the pulse-height spectrum. The dominance of these processes is mainly governed based on the interacting medium and the energy of the incident radiation. The photo-peak represents the full energy deposition peak. Therefore, the x-axis representing the energy describes the light output of any scintillator crystal corresponding to the position of the photo-peak. Light output (ph/MeV) can be defined as the number of photons generated per unit energy deposition. The relative position of the photo-peak that was measured with a known scintillator like BGO or NaI:Tl gives the relative light output of a scintillator [25]. A higher light output leads to better statistics and better energy resolution to identify the radio-nuclides having close energies. The energy resolution is defined as the ratio of full width at half maxima (FWHM) to the energy. Ideally, the light

output should be proportional to the deposited energy but most of the single crystals have non-proportionality which affects their energy resolution and therefore need to be investigated for this deviation to understand the basic scintillation mechanism in addition to the performance of devices.

The kinetics of scintillation is mainly characterized by measuring the scintillation decay times using the anode pulse fed to a fast oscilloscope or using a complex Thomas-Bollinger setup based on time correlated single photon counting [45]. The scintillation decay time of an excited state limits the application of a scintillator crystal in high count rate (high activity) applications. The presence of multi-components in the exponential decay times makes it possible to discriminate various kinds of excitations, e.g., alpha, gamma, etc. if the ratio of different decay components depends on the mode of excitation.

Based on the applications, other scintillation properties like coincidence timing resolution, pulse-shape discrimination, etc. can be measured by using standard nuclear electronics modules or advanced digitizers [25].

2.4 Improvement of Performance Characteristics

A systematic approach to grow single crystals of a promising scintillating garnet material and a strategy based on defect engineering to improve its scintillation characteristics is briefed in this section. Some of the results have been represented from our articles published in J. Phys D: Appl. Phys. 46 (2013) 475302 and Phys Stat Solidi-Rapid Research Letters 9 (2015) 530 with the proper permission [46, 47] (Fig. 2.5).

2.4.1 Material Designing and Dopant

Metal-oxide single crystals, having a garnet structure, usually have high density to stop high energy radiation, broad transmission range to accommodate suitable dopant and transmit the emitted light, and have significantly improved mechanical, radiation and chemical resistance. These host materials can be doped with an activator ion Ce^{3+} which has efficient and fast emission originating from the allowed transition between 5d to 4f states and therefore makes it a suitable choice as a dopant in scintillating crystals with trivalent cations. Crystal field due to the surrounding legend ions, dominantly, affects the splitting and positioning of 5d states and therefore resulting in a broad range of emission wavelengths of Ce^{3+} ions depending on the host lattice. An extensive investigation was carried out on the multi-component garnet compounds by combinatorial band gap engineering approach. The results of these comprehensive studies found Ce doped $Gd_3(GaAl)_5O_{12}$ crystals having very promising scintillation properties [49]. These materials crystallize in a cubic structure where the Gd/Ce is dodecahedrally coordinated with oxygen in the D_2 point

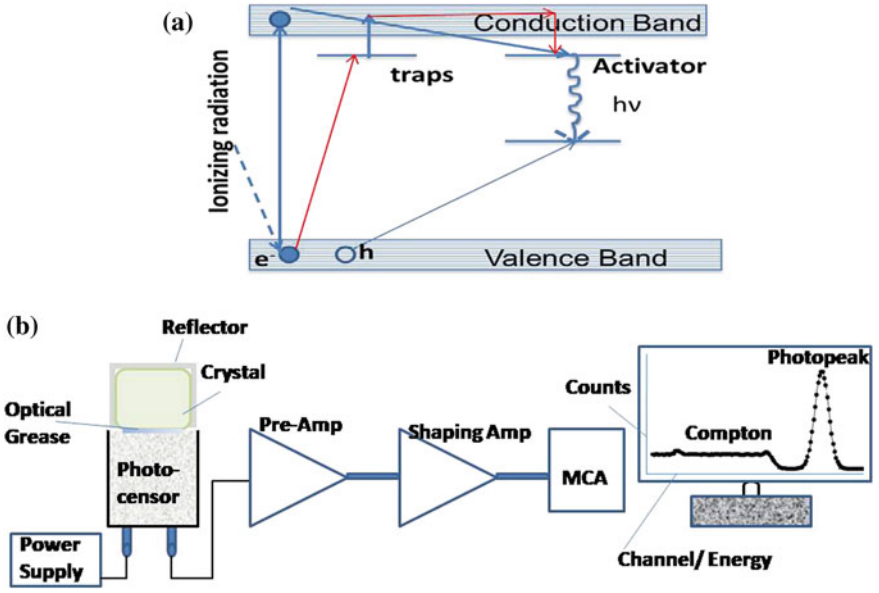

Fig. 2.5 **a** A schematics of basic scintillation process and **b** characterization setup with a typical pulse-height spectrum

group symmetry while Ga and Al cations are in octahedral and tetrahedral configurations with oxygen ions as shown in Fig. 2.6a. This symmetry splits the 5d level of Ce^{3+} in 5 sublevels where three sublevels having higher energies are buried in the conduction band and two sublevels reside in the forbidden band gap region. A larger Ga ion (0.62 Å) et al. (0.54 Å) sites induces a compression on the adjacent Gd/Ce ions, coordinated with oxygen in dodecahedral, and therefore consequently changes the crystal field splitting of Ce 5d levels. It subsequently leads to a change in the position of the lowest excited 5d level with respect to the conduction band and causes the blue shift (towards lower wavelength) in the emission as shown in Fig. 2.6b. Therefore, with the help of material engineering the relative position of the conduction band and Ce $5d_1$ level can be optimized to provide an adequate gap for minimizing the room temperature thermal ionization of excited charge carriers [48]. However, the gap should not be too high to accommodate more trap centers. This material engineering should consequently result in an enhancement of the radiative recombination to increase the scintillation light output. The ratio of Ga:Al was optimized to be 3:2 for the best combination of light yield and decay kinetics [49].

Due to the high melting temperature, the Czochralski technique was used to grow single crystals of Ce doped $Gd_3Ga_3Al_2O_{12}$ (henceforward will be represented as GGAG only). An automatic diameter-controlled crystal puller system was used along with starting charges prepared by mixing the constituent metal-oxides of Gd_2O_3, Al_2O_3, Ga_2O_3 in respective stoichiometric molar ratio and doped with 0.2 at% CeO_2. Several crystal growth experiments were carried out as per the following details:

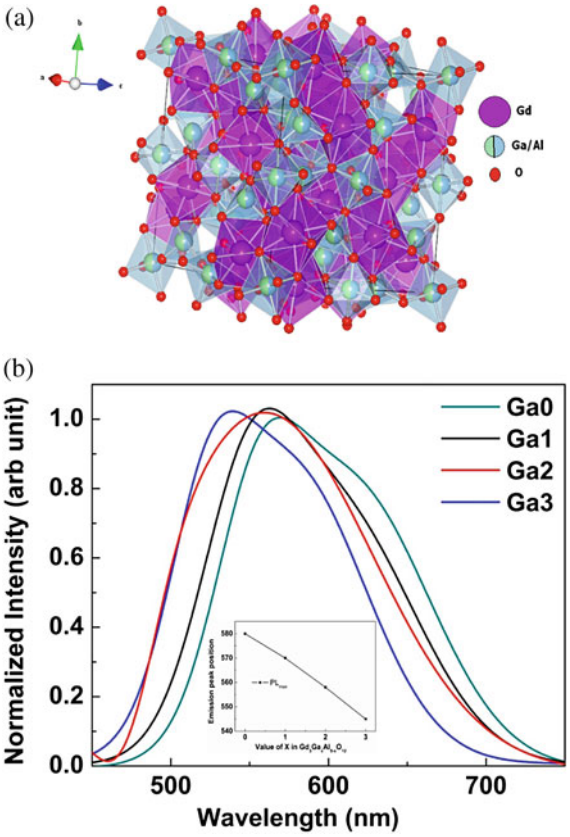

Fig. 2.6 **a** The crystal structure of $Gd_3(Ga, Al)_5O_{12}$ and **b** the shifting of Ce^{3+} emission with respect to Ga concentration [46] [Reproduced with the permission from "IOP Publishing"]

- As-prepared powder pressed in the form of pellets and loaded in a crucible.
- The mixed powder sintered at 1400 °C to pre-synthesize the phase before growing the crystal.
- Partial oxygen pressure maintained in the growth chamber by flowing nitrogen and air to avoid oxidation of iridium crucibles.
- To avoid the oxidation of Iridium crucible and Ce^{3+} ions, Argon gas was constantly flown during the growth in a closed chamber.
- After loading the as-prepared or pre-synthesized material, the crucible was heated to about 50 °C more than the melting temperature for homogenizing the melt.
- In initial growth runs, a single crystal seed, prepared from the $Y_3Al_5O_{12}$ (YAG), was used to pull some single crystalline chunk. Later, an un-oriented GGAG seed was prepared and used to grow larger single crystals.

Initially, due to the higher density (~6.5 g/cc), the loaded material was not sufficient to provide an appropriate melt height for the required thermal gradient and growth could not be initiated. Therefore, the initial material was pressed into pellets to load in a larger quantity and melted and reloaded after cooling. The process was

Fig. 2.7 Single crystals grown **a** in the first attempt and **b** after the optimization of various parameters

repeated to attain the required melt height. However, to avoid any stoichiometric deviation due to higher evaporative losses of Ga_2O_3, an excess amount was taken accordingly and initial material was also prepared in multiple batches. In initial growth attempts the seed got melted during the optimization of power and the crystal could be grown from the iridium seed holder. The grown crystal was found to have multiple cracks with poorly controlled diameter. A seed was cut perpendicular to the growth axis and used in next growth runs. A good quality single crystal could be grown after multiple attempts as shown in Fig. 2.7b. The poor quality in the lower region may be assigned to the deviation from stoichiometry due to different evaporative losses of constitute oxides. The diameter control was improved significantly after the optimization of growth parameters. The solid-melt interface was found to be nearly flat. The optimized parameters, for a successful growth run after multiple trial runs, are listed in Table 2.2.

The effect of co-doping and growth ambient has been discussed in the next sections.

Table 2.2 Crystal growth parameters

Melting temperature	1850 °C
Pull rate	1 mm/h
Rotation rate	10–20 rpm
Initial chamber pressure	1×10^{-5} mbar
Ar gas pressure	1100 mbar
Temperature gradient	30–50 °C/cm
Cooling rate	20–30 °C/h

2.4.2 *Effect of Co-Doping*

Single crystals usually have point defects including cation or anion vacancy centers. Additionally, the materials, having a garnet structure, usually have antisite defects also (such as Lu_{Al} in $Lu_3Al_5O_{12}$, LuAG). These defect centers play a crucial role in the luminescence efficiency and decay kinetics of these materials. Similar to the ratio of Ga:Al cations as shown in Fig. 2.6b, the aliovalent and/or codopants of different ionic radii may also modify the crystal field affecting the transitions in Ce ions and have an effect on the scintillation properties consequently. The codoping may also affect the defect structure of single crystals. Therefore, in addition to Ce activators, the single crystals were grown with various co-dopants. The significant changes were observed in calcium (Ca) and boron (B) codoped crystals as discussed in the following paragraphs.

The absorption spectra recorded for differently codoped crystals are presented in Fig. 2.8. The forbidden band gap of GGAG crystals was found to be $\geq$5.8 eV. The dominating absorption bands observed at 440 and 340 nm can be assigned to the transitions from 4f ground state to the 5d excited states located in the forbidden band gap. The narrow absorption bands at 274 and 310 nm and increased absorption in the lower wavelength region can be assigned to the transitions of Gd^{3+} ions. The small difference between these transitions to Ce^{3+} states indicates a larger possibility of resonant transfer from Gd^{3+} to Ce^{3+} ions. Calcium (Ca) codoping was found to significantly increase the absorption at lower wavelengths near the absorption edge resulting in suppression of the absorption band at 340 nm corresponding to Ce^{3+} 4f-5d_2 higher energy transitions. This can be assigned to the occurrence of the additional energy levels of Ca^{2+}. Boron (B) codoping induces a slight improvement of the transmission in the lower wavelength region near the absorption edge. However, no additional lower energies (in the visible region) absorption bands were observed due to these co-dopants and therefore indicating the absence of any additional defects in codoped crystals. The transitions from the excited $^5d_1$ state of Ce^{3+} results in an emission band consisting of two bands at 520 nm and 565 nm corresponding to the splitting up of the ^{4}f ground state into $^4F_{5/2}$ and $^4F_{7/2}$ states. The emission spectrum was observed to be unaffected with the co-doping. This indicates that there is no considerable change in the band gap, crystal field, or the relative position of Ce excited states due to the codopants. Therefore, the effect of codoping should be mainly assigned to the modification of the defect structure of crystal.

The effect of co-doping on the scintillation light output is shown in Fig. 2.9. The pulse-height spectra were recorded using a Cs^{137} source. The position of the photo-peak describes the relative light output. Ca codoping decreased the light output significantly, while B codoping was found to increase the light output of GGAG:Ce crystals. The absolute light outputs of GGAG:Ce and Ca and B codoped crystals were measured as 47,000 ph/MeV, 32,460 ph/MeV and 52,000 ph/MeV, respectively[46]. The B codoping significantly improves the energy resolution also, from 9 to 7.8%, measured at 662 keV gammas. The effect of codoping on scintillation kinetics of these crystals by gamma excitation and measured at room temperature is represented

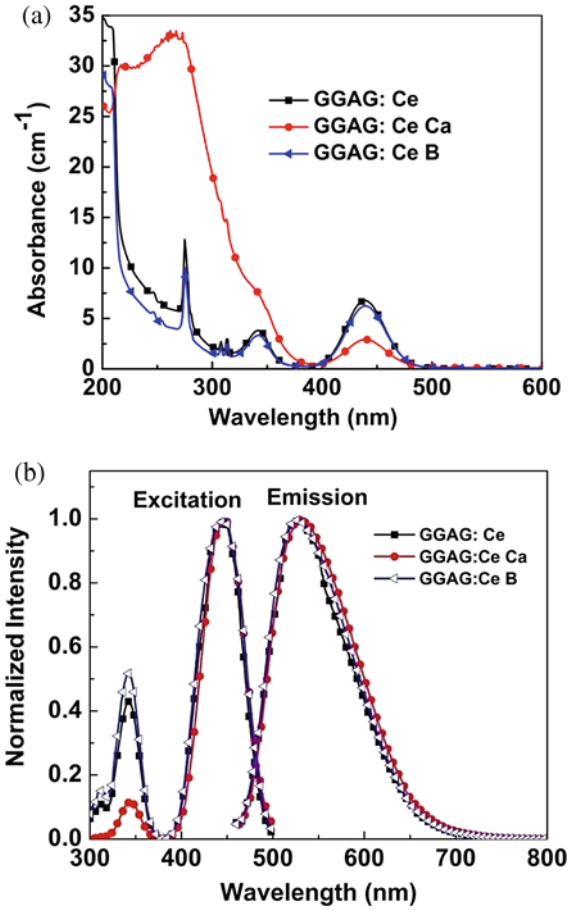

Fig. 2.8 The effect of codoping on **a** absorption and **b** excitation and emission spectra of a GGAG:Ce crystal [46] [Reproduced with the permission from "IOP Publishing"]

in Fig. 2.9b. The decay curve consists of mainly two components and indicates the presence of more than one mechanism for the de-excitation. The decay curves were fitted exponentially having two decay components and the obtained values are listed in Table 2.3. While the Ca codoping accelerates the scintillation rise and decay times, no considerable effect was observed with the B codoping.

However, the co-doping did not have any significant effect on the photoluminescence (PL) decay times. The difference between intrinsic PL and scintillation decay time can be attributed to an energy transfer mechanism that plays a significant role when electrons are excited deep into the conduction band by higher energy gamma excitations in scintillation decay time measurements.

These results suggest that the co-doping affects the defect structure of the crystal. The possible effects of codoping on defect structures may be envisaged as given below [Reproduced with the permission from "IOP Publishing"]:

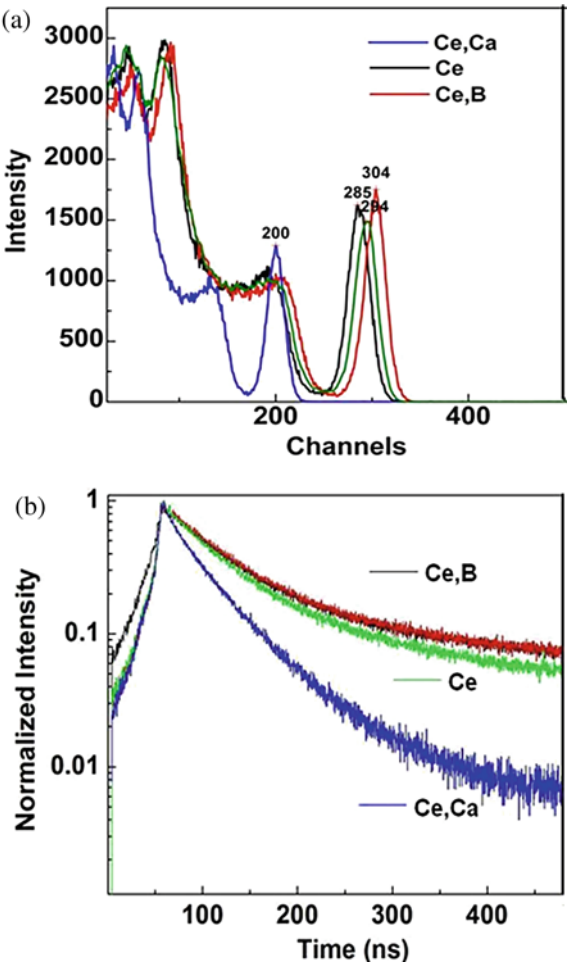

Fig. 2.9 Effect of codoping on **a** relative scintillation light output and **b** scintillation decay time of GGAG:Ce crystal measured using a Cs^{137} source. The light output is on a scale where a reference BGO light output was set at channel 100 [46] [Reproduced with the permission from "IOP Publishing"]

Table 2.3 The fitted values of scintillation rise (τ_r) and decay times (τ_1 and τ_2) and their relative ratios for differently codoped crystals

Composition	τ_r(ns)	τ_1(ns) (R%)	τ_2(ns) (R%)
GGAG:Ce	8	52 (74%)	335(26%)
GGAG:Ce, Ca	6	44 (76%)	260(24%)
GGAG:Ce, B	8	58 (75%)	350(25%)

(1) The Ca co-doping introduces a few additional energy levels or traps in the forbidden band gap as confirmed by the absorption spectrum. These levels provide a non-radiative bypass path for relaxing the excitation, thus affecting the energy transfer from Gd^{3+} to Ce^{3+} and consequently quenching the light output together with reducing the decay time. The Ca ions have a larger ionic

radii (1.0 Å) and lower valence state (2+) which cause increasing the concentration of cation vacancies and hole trap centers by replacing smaller cations Gd^{3+} (ionic radius 0.94 Å), Ga^{3+} (0.62 Å) or Al^{3+} (0.54 Å). The lower valence state of Ca may also enhance the formation of optically inactive Ce^{4+} ions in place of the efficiently emitting Ce^{3+} ions. In addition, the charge transfer from O^{2-} to Ce^{4+} increases the absorption at higher energies, as observed in the absorption spectrum [46].

(2) The co-doping with B^{3+} that has a much smaller ionic radius of (0.27 Å), may readily fit into interstitial sites and therefore may act as competing electron trap centers due to excessive charge. This consequently causes a decrease in the trap centers related to the oxygen vacancies and improves the transmission at higher energies as revealed in the absorption spectrum. Therefore, the excitation in a higher Ce^{3+} excited state also increases and eventually leads to a better light output [46].

(3) The creation of defects in anion sublattices related to trapped holes at interstitial oxygen (O^-) or trapped electrons at oxygen vacancies (F or F^+) may also be affected which could be further investigated by the post growth annealing treatment [47].

2.4.3 Growth Ambient and After Growth Treatment

In addition to the defect centers related to the anion sublattice, the tendency of multi-valence state of activator Ce ions (+3 or +4) can also be influenced with the growth ambient, pre-growth and after-growth annealing. Therefore, single crystals were grown and annealed under different conditions and the scintillation properties were studied. The single crystal grown from a pre-synthesized material (sintered at 1400 °C) was found to have poor absorption at characteristics Ce^{3+} bands suggesting the presence of Ce^{4+} ions in the material used for the growth. Therefore, crystal growth experiments were planned with as-mixed powders of constituent metal-oxides without any sintering. Since boron codoping was found to improve the scintillation performance, single crystals of GGAG:Ce (0.2 at%) codoped with B (0.2 at%) were grown using the Czochralski technique in a partial oxygen ambient (90% N_2 + 10% air) and in flowing argon (Ar) in separate experiments.

Figure 2.10a exhibits absorption spectra recorded for the crystals grown in varying conditions. In addition to the characteristics Ce^{3+} absorption bands at 340 and 445 nm, the presence of optically inactive Ce^{4+} ions can be inferred from an increased absorption at higher energies due to the charge transfer transition from O^{-2} to Ce^{4+} ions below 300 nm. The presence of cerium ions in the tetravalent state (+4) was found to be maximum in crystals grown from a material synthesized in air which consequently leads to the lesser light output.

The absorption near the fundamental edge is slightly higher in crystals grown in a partial oxygen ambient compared to that measured for the crystals grown in argon. However the characteristic absorbance bands at 345 and 445 nm due to Ce^{3+} ions are

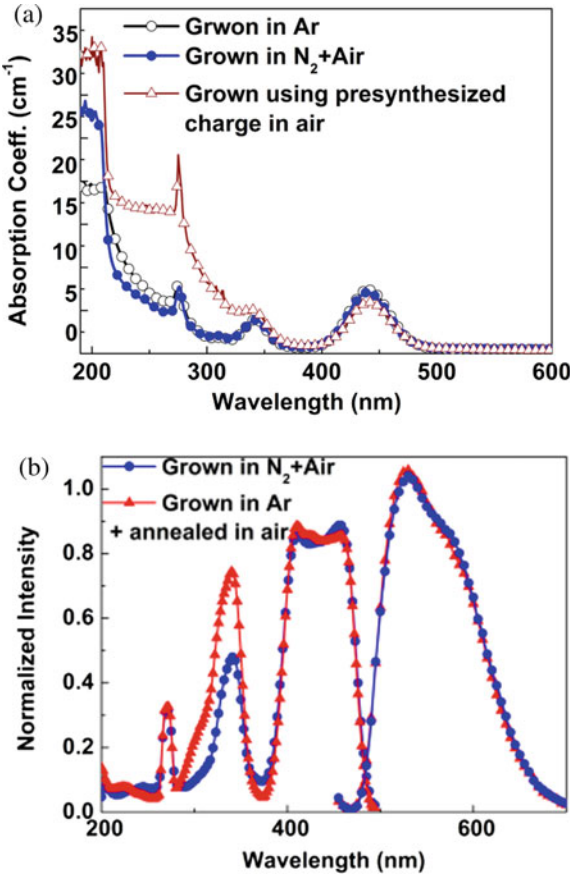

Fig. 2.10 **a** The absorption spectra of GGAG:Ce, B crystals grown using pre-synthesized charge in air (—Δ—), in partial oxygen pressure (—•—) and in argon ambient (—o—). **b** The photoluminescence excitation and emission spectra of GGAG:Ce, B crystals grown in partial oxygen pressure (—•—), and annealed in air after the growth in argon ambient (—▲—) [47] [Reproduced with the permission from "Wiley–VCH Verlag GmbH & Co. KGaA"]

similar in these crystals and therefore the scintillation properties can be compared for these two crystals grown in different ambient conditions. Figure 2.10b shows the effect of the growth ambient on PL excitation and emission spectra of a GGAG:Ce, B crystal. The relative intensity of higher energy excitation band is suppressed in the crystals grown in partial oxygen due to a higher absorption near the fundamental absorption region as shown in Fig. 2.10a.

The effect of growth ambient and after-growth annealing treatments on scintillation light output and decay time are shown in Fig. 2.11. The scintillation light output was found to increase and decay-time becomes faster after annealing. The crystals grown in argon ambient and annealed in air were found to have the highest light yield. On the other hand, a crystal grown in a partial oxygen ambient did not show any change after the annealing in air or vacuum at 1000 °C for 10 h. The light yield improved from 54,000 ph/MeV for crystals grown in partial oxygen ambient to more than 60,000 ph/MeV for the crystals grown in argon and annealed in air after the growth. The energy resolution also improved to 5.8% at 662 keV for the

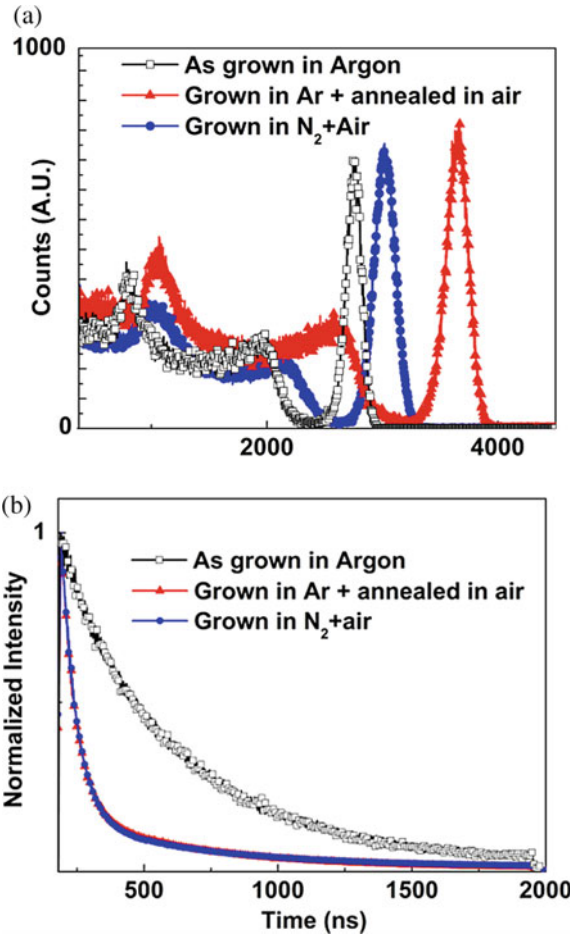

Fig. 2.11 The pulse-height spectra and scintillation decay time measured for a ^{137} Cs gamma source using a GGAG:Ce, B crystal grown in partial oxygen (–•–), argon ambient (—□—), and annealed in air after the growth in argon ambient (—▲—) [47] [Reproduced with the permission from "Wiley–VCH Verlag GmbH & Co. KGaA"]

annealed crystals. The best value for the energy resolution of about 4.7% is reported for a GGAG crystal having 1% Ce and coupled with APD (Hamamatsu S8664-010). However, the scintillation decay time was not significantly different for these two types of crystals.

The post-growth annealing treatment did not make any significant change in the absorption spectrum suggesting that the effect of annealing is not responsible for the change in the valence state of cerium from 4+ to 3+. Therefore the change in the valence state and crystal field splitting cannot be considered for improving the light output in crystals grown in Ar ambient and annealed in air. Since these crystals were grown in different ambient conditions, the defect centers may play a major role for any change in optical or scintillation properties. The crystals grown in argon are more prone to have defect centers related to the anion sub-lattices which can be generated either due to oxygen vacancies (F or F^+) or presence of interstitial

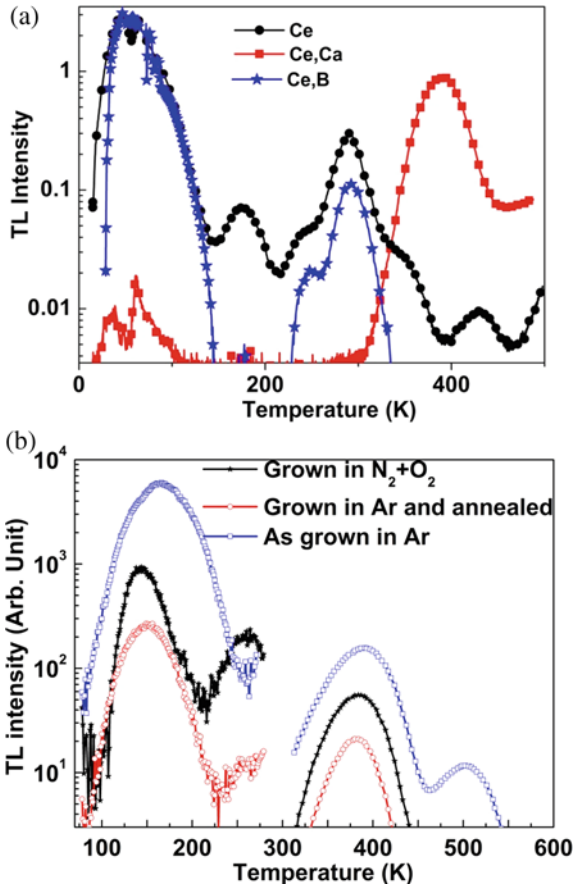

Fig. 2.12 **a** Effect of codoping and **b** growth ambient/after-growth annealing on the thermo-luminescence properties of GGAG:Ce crystal [47] [Reproduced with the permission from "Wiley–VCH Verlag GmbH & Co. KGaA"]

oxygen (O^-). Annealing in air decreases the concentration of these defect centers that consequently increases the light output and makes the decay faster.

Thermo-luminescence measurements were performed to understand the defect structure in crystals grown under varying conditions (Fig. 2.12). The thermo-luminescence measurements below room temperatures and at elevated temperatures were performed respectively in a liquid nitrogen cryostat and in conventional thermo-luminescence measurement set-up. The size and weight of the samples for TL measurements were kept the same, and the TL glow curves were normalized for the luminescence intensity and its temperature dependence. Therefore the intensity of glow peaks can be considered proportional to the concentration of trap centers.

The codoping with Ca greatly reduced the shallow charge traps. However, new deeper traps dominated at 390 K in the Ca codoped crystals. The co-doping with boron also had a significant effect on the TL glow curve by eliminating the 200 K trap and the deeper traps above room temperature.

The crystals grown in argon ambient had a higher concentration of defect centers that was reduced significantly after the annealing of crystals in air. The glow peak at 550 K completely diminished after the annealing of crystals in air and therefore can be assigned to oxygen vacancies. The trap centers in the as-grown crystals grown in argon ambient compete with other electron trap centers like antisite defect centers etc., which affected the light output of these materials. An absence of glow peaks around 250 K also indicates elimination of this kind of trap centers in the crystal grown in Ar ambient. The post-growth annealing of crystals in air reduced the concentration of trap centers related to oxygen sublattices which already had a lesser concentration of other trap centers. Consequently, the crystals grown in argon and annealed in air will have the least concentration of defect centers and therefore improved scintillation properties.

2.5 Conclusion and Future Outlook

In summary, a systematic approach has to be adopted for growing single crystals of multi-component garnets having promising scintillation properties of radiation detection. With a better understanding of underlying processes, the scintillation performance characteristics could be further tailored with the help of appropriate selection of co-dopants. An optimization of growth ambient and after-growth annealing treatments can be also made useful for further modification of the defect structure of single crystals in a favorable manner to achieve a higher light output and better energy resolution. The defect centers related to the oxygen sub-lattice, caused by the reducing growth ambient, may compete with the formation of other trap centers having detrimental effects on scintillation properties. The concentration of trap centers related to the oxygen vacancies/interstitials may be subsequently reduced by the after-growth annealing treatment in an appropriate ambient. This chapter demonstrated that this scheme could eventually improve the performance characteristics of GGAG crystals but it can be successfully adopted for other oxide scintillators as well.

References

1. Pound GM, La Mer VK (1952) Kinetics of crystalline nucleus formation in supercooled liquid tin. J Am Chem Soc 74(9) 2323
2. Dorsey NE (1938) Supercooling and freezing of water. J Res Natl Bur Stand 20:799–809
3. Bohm J (1985) The history of crystal growth. Acta Physica Hungarica 57(3-4):161–178
4. Kepler J (1611) Strenaseu de nivesexangula. Frankfurt/Main
5. Hooke R (1665) Micrographia. London
6. Boyle R (1972) An essay about the origine and virtues of gems (1672). Repr. Hafner New York
7. Fahrenheit DG (1724) Experimenta & observationes de congelationeaquae in vacuo.Phil Trans Royal Soc (London) 33:78–84
8. Bravais A (1849) Etudes cristallographiques. Paris

9. Verneuil A (1904) Memoire sur la reproduction artificielle du rubis par fusion. Ann Chim et Phys (Paris) 3:20–48
10. Spezia G, Atti R (1909) Sullaccrescimento del quarzo. Accad Sci Torino 44:95–107
11. Nacken R (1916) "Kristallz"Z. Instrumentenkunde 36:12–20
12. Czochralski J (1918) EinneuesVerfahrenzurMessung der Kristallisationsgeschwindigkeit der Metalle. Z phys Chem 92:219–221
13. Kyropoulos S (1926) Ein Verfahren zur HerstellunggroBerKristalle. Z. anorg, u. allg. Chem 154:308–313
14. Bridgman PW (1923) The compressibility of thirty metals as a function of pressure and temperature. Proc Am Acad Arts Sci (Boston) 58:165–242
15. Bridgman PW (1925) Certain physical properties of single crystals of tungsten, antimony, bismuth, tellurium, cadmium, zinc, and tin Proc Am Acad Arts Sci (Boston) 60:303–383
16. Burton WK, Cabrera N, Frank FC (1949) Role of dislocations in crystal growth Nature 163:398–399
17. Teal GK, Little JB (1950) Growth of germanium single crystals. Phys Rev 25:6, and Bull Am Phys Soc 78:647
18. Rutter JW, Chalmers B (1953) A prismatic substructure formed during solidification of metals Can J Phys 31:1–39
19. Bundy FP, Hall HT, Strong HM, Wentorf RH (1955) Man-made diamonds. Nature (London) 176:51–55
20. Nassau K, Verneuil AVL (1972) The man and the method. J Cryst Growth 13/14:12–18
21. Lecoq P, Gektin A, Korzhik M (2016) Inorganic scintillators for detector systems. Springer
22. Fisher G, Seacrist MR, Standley RW (2012) Silicon Crystal Growth and Wafer Technologies. Proc IEEE 100:1454–1474
23. Onyszko A, Kubiak K, Sieniawski J (2009) Turbine blades of the single crystal nickel based CMSX-6 superalloy. J Achieve Mater Manufact Eng 32(1):66–69
24. Sumiya H (2012) High Pressure Synthesis of Defect-free Single Crystal Diamond. J Jpn Assoc Crys Growth 39:164–169
25. Knoll GF (2010) Radiation detection and measurement, 4th ed. Wiley. ISBN 978-0470131480
26. Nikl M, Vedda A, Laguta VV (2010) Single-crystal scintillation materials. In: Springer handbook of crystal growth. Springer, Berlin
27. Vekilov PG (2010) Nucleation. Cryst Growth Des 10(12):5007–5019
28. Schülli TU et al (2010) Nature 464:1174–1177
29. Brice JC (1986) Crystal growth processes. Blackie & Son Ltd., Glasgow and London
30. Varshneya A (1994) Fundamentals of inorganic glasses. Academic Press
31. Rosenberger F (1979) Fundamentals of crystal growth. Springer Series in Solid-State Sciences, Berlin
32. Brice JC (1973) The growth of crystals from liquids. North Holland Publishing Company, Amsterdam
33. Hurle DTJ (2004) Crystal growth-from fundamentals to technology. In: Muller G, Metois JJ, Rudolph P (eds) Elsevier, Amsterdam
34. Tyagi M, Growth and characterization of scheelite crystals. VDM Verlag, Germany
35. Brandle CD (2004) Czochralski growth of oxides. J Cryst Growth 264:593–604
36. Bottaro A, Zebib A (1989) Three dimensional thermal convection in Czochralskimelt. J Cryst Growth 97:50–58
37. Muiznieks A, Krauze A, Nacke B (2007) Convection phenomena in large melts including magnetic fields. J Cryst Growth 303:211–220
38. Bunch JM (1977) Phys Rev B 16:724–730
39. Gallagher PK (2001) Thermal Analysis: further developments. In: Encyclopedia of materials: science and technology
40. Warren BE (1969) X-ray diffraction. New York. ISBN 0-486-66317-5
41. Wahlstrom EE (1969) Optical crystallography, 4th edn. John Wiley & Sons, New York
42. Winefordner JJD, Schulman SG, O'haver TC (1972) Luminescence spectrometry in analytical chemistry.Wiley-Interscience, New York

43. Khan FM (2003) The physics of radiation therapy. Lippincott Williams &Wilkins
44. Korzhik M, Gektin A (2016) Engineering of scintillation materials and radiation technologies. Springer Proceedings in Physics
45. Bollinger LM, Thomas GE (1976) Measurement of the time dependence of scintillation intensity by a delayed coincidence method. Rev Sci Instrum 32:751–767
46. Tyagi M, Meng F, Koschan M, Donnald SB, Rothfuss H, Melcher CL (2013) Effect of codoping on scintillation and optical properties of Ce doped $Gd_3Ga_3Al_2O_{12}$ scintillators. J Phys D Appl Phys 46:475302–475314
47. Tyagi M, Singh AK, Singh SG, Desai DG, Patra GD, Sen S, Gadkari SC (2015) Improvement of the scintillation properties of $Gd_3Ga_3Al_2O_{12}$:Ce, B single crystals having tailored defect structure. Phys Stat solidi-Rapid Res Lett 9:530–534
48. Kamada K et al (2011) Composition Engineering in Cerium-Doped (Lu, $Gd_)3$(Ga, $A_l)_{5O}12$ Single-Crystal Scintillators. Cryst Growth Des 11(10):4484–4490
49. Kamada K et al (2011) Scintillator-oriented combinatorial search in Ce-doped (Y, $Gd_)3$(Ga, $A_l)_{5O}12$ multicomponent garnet compounds. J Phys D-Appl Phys 44:505104–505112

Chapter 3
Techniques for Thin Films of Advanced Materials

K. R. Sinju, A. K. Debnath, and Niranjan S. Ramgir

Abstract With the advent of nanoscience and nanotechnology, there has been an upsurge in the synthesis, characterization, and application of numerous functional materials. This has been attributed predominantly to the enhanced surface area to volume ratio and ease of control over the surface functionalities requisite for targeted applications. The numerous functionalities and tailor made properties are obtained by careful choice of process parameters involved in different synthesis strategies. Thin film deposition techniques have become the obvious choice of synthesis as it is possible to envisage the desired control in the resulting advanced materials. In order to introduce the novel functionalities in these advanced materials, the thin film deposition techniques have been modulated, upgraded, and even developed. The present chapter focuses on the recent advancement in the thin film techniques that have been utilized effectively to realize advanced materials for targeted applications. Each technique has been discussed elaborately explaining the basic principle and importantly highlighting the novel functionalities introduced, its merits and demerits citing advanced materials synthesized using the same.

Keywords Thin films · Advanced materials · Metal oxide semiconductor · Nanoscience · Nanotechnology

3.1 Introduction

With the advent of nanoscience and nanotechnology there has been an upsurge in the synthesis of novel functional materials or the so-called advanced materials. This upsurge has demanded the development of novel techniques like vapor phase growth using furnaces, Langmuir Blodgett (LB), and Self assembled monolayers (SAM) or modulation of existing conventional techniques. In order to sustain the growth in this field, various conventional thin film deposition techniques have been upgraded or modified so as to achieve possibility of advanced material synthesis. Films having the

K. R. Sinju · A. K. Debnath · N. S. Ramgir (✉)
Technical Physics Division, Bhabha Atomic Research Centre, Mumbai 400 085, India
e-mail: ramgirns@barc.gov.in

A. K. Tyagi and R. S. Ningthoujam (eds.), *Handbook on Synthesis Strategies for Advanced Materials*, Indian Institute of Metals Series,
https://doi.org/10.1007/978-981-16-1803-1_3

thickness less than 1 μm are generally referred to as thin films. They are alternatively defined as the films having the thickness at which the material possess the properties that are markedly distinct from its bulk counterparts. Thin film deposition techniques have a good blend of process parameters that can effectively be used to realize advanced materials. The beginning of the advanced material may be assigned to the observation of two dimensional electron gas (2DEG) observed in metal oxide semiconductor field effect transistor (MOSFETs) synthesized using the conventional C-MOS technique mainly thin film techniques [1]. Herein, electrons are confined to a 2D plane probably because of a Schottky barrier that exist between metal and oxide (MOSFET), or different semiconductors (heterostructures) [2]. This has marked the growth in synthesis of such and other allied materials that now arrive to the recent discoveries of 2-D nanostructures such as graphene and metal dichalcogenides like MoS_2 [3, 4].

Nanotechnology is an advanced and fast growing technology and has gained enormous attention due to its noticeable performance in science and thereby all disciplines of human life. It deals with the materials, devices, and other structures having at least one dimension in the size from 1 to 100 manometers. At this scale quantum effects are noticeable and have been explored for their usage in various device applications. Accordingly, various synthesis routes have been developed and reported for nanomaterials. Thin films have its own great role in the nanoscience and accordingly, have found unique applications such as antireflection coatings [5], reflection coating for mirrors [6], corrosion or oxidation protection coatings, sensors for liquid or gaseous chemicals, SQUID, and semiconductor industry [7]. For the realization of novel advanced materials, the conventional thin film deposition techniques become an important part of the set of tools used for their synthesis or fabrication [8]. For examples, to realize nanowires using top down approaches, the thin film of the required materials is first deposited using thin film techniques (like thermal evaporation, sputtering) and later etched out (like deep anisotropic etch, Inductively coupled plasma (ICP), reactive ion etch (RIE), anisotropic wet etch and metal assisted etch (MAE)) in controlled manner to realize different nanomorphologies [9–11]. Same is the case with the growth of different nanoforms using the bottom-up approaches. Herein, again the conventional thin film techniques like thermal evaporation, e-beam deposition and sputtering, are employed to realize the seed layer of catalyst that are later grown using the vapor–liquid–solid (VLS) mechanism [12, 13]. Thus, it is evident that the thin film techniques form the backbone to various strategies or methodologies required for the reproducible and repeatable synthesis of various advanced materials. The main dependence on the thin film techniques is attributed mainly to its great potential for scale up required for batch or bulk production crucial for commercial viability.

The aim of the present chapter is to provide the state of the art of the thin film techniques that have been used and modulated where required realizing advanced materials and describing the novel thin films techniques that have been recently introduced for the same. Care has been taken to provide basic introduction to the techniques covering the working principles and then elaborating their utility in realizing the novel materials citing results from the literature. The chapter ends briefing

the important advancement in the field and discussing the future prospects. Growth of advanced materials using thin film techniques is a wide field and it is difficult to incorporate all the important findings. Although attempts were made to include all the important advancement, it is possible to miss some of them.

3.2 Basic Introduction and Fundamentals of Thin Film Techniques

Thin film refers to a coating or formation of a film on a substrate that is few nanometers to 100 μm thick [14, 15]. The controlled synthesis of material in the thin film form is the most fundamental step in numerous fields including optical electronics, microelectronics, communication, catalysis, and energy [16, 17]. Film deposition in general involves processes such as impingement, desorption, nucleation and growth, coalescence of islands and eventually development of continuous film structure [18]. The nucleation step is very important as it governs microstructure and crystallinity of the resulting film. In chemical synthesis, nucleation is considered to be a physical reaction that occurs when the components in a solution precipitate out, forms nuclei which eventually attracts more precipitate. For physical methods, there are mainly three modes of film growth given as follows:

(i) Island or Volmer—Weber growth
(ii) Layer by Layer or Frank—Van der Merve growth and
(iii) Mixed or Stranski—Krastanov growth

Island growth occurs when the atoms or ions of precursors are more strongly bound to each other. This bond is stronger than the one between atoms and the substrate. Further growth results in the merging of the islands into a continuous film. Deposition of alkali halides, metals on insulators show this type of mechanism. Normally it is a slow diffusion process. In layer by layer growth film atoms are more bound to substrate rather than each other. First a complete monolayer is formed and then the second layer begins. It is a fast diffusion processes and results in high crystalline quality. In mixed growth, initially film growth takes place as per layer by layer model and then it forms three dimensional islands.

The techniques of thin film deposition are often classified into three main categories namely.

1. Physical deposition (e.g., chemical vapor deposition, thermal evaporation, molecular beam epitaxy, sputtering, atomic layer deposition, etc.) and
2. Chemical deposition (electro chemical deposition, Langmuir–Blodgett films and self-assembled monolayers) and
3. Organic monolayers

The sub-classifications of the techniques are given in Table 3.1.

Table 3.1 Sub classifications of the thin film deposition techniques

Physical deposition	Chemical deposition	Organic monolayers
• **Evaporation technique** – Vacuum thermal evaporation – Electron beam evaporation – Laser beam evaporation – Arc evaporation – Molecular beam epitaxy – Ion plating evaporation • **Sputtering technique** – DC sputtering – RF sputtering	• **Sol—gel technique** • **Chemical bath deposition** • **Spray pyrolysis** • **Plating** – Electro plating – Electroless deposition • Chemical vapor deposition(CVD) • Low pressure chemical vapor deposition(LPCVD) • Plasma enhanced chemical vapor deposition(PECVD) • Atomic layer deposition(ALD)	• **Langmuir-Blodgett** • **Self assembly**

3.3 Physical Deposition Techniques

Physical deposition is a purely physical process involving high temperature vacuum evaporation that is considered as the common/general technique for the thin film deposition. There are basically three steps involved in the physical vapor deposition namely evaporation from the source, transport, and condensation of the evaporants on the substrates. Depending upon the methodology employed for the evaporation of the material from the source following methods have been adopted; Thermal, Electron beam, Molecular beam, Laser, or Sputtering.

3.3.1 Thermal Evaporation

The technique involves vaporization of the source material at an elevated temperature under controlled conditions, such as pressure, substrate temperature, and quantity of material, to form thin film with desired thickness. The material vapor condenses in the form of thin film on the substrate surfaces kept in vacuum at a pressure of ~10^{-6} torr. At this pressure, the mean free path of the vapor atom is nearly similar to vacuum chamber dimension implying that the particles travel in straight line from the evaporation source to substrate. The average energy of the vapor atoms reaching on the substrates is low, ~few tens of eV, and has a strong effect on the adhesion and morphology of the resulting film. Here, source of material has to be taken in metal boats, filaments, etc. Generally Tungston (W), Tantalum (Ta), and Molybdenum (Mo) are used as heating resistance materials which have been attributed to their high melting points of 3380, 3000, and 2620 °C, respectively. The vapor pressure at the evaporation temperature (1000–2000 °C) comes to zero. The resistance heated evaporation has some unique features over the other thin film deposition methods, such as

- Simple, robust, and in widespread use
- Can be used for pure atomic elements including both metals and non-metals.
- There is a wide choice for substrates such as semiconductor wafers, solar cells, and optical components.
- Process is carried out in high vacuum and therefore could be used to achieve films with high purity.
- Higher deposition rate such as 1000 monolayers per sec can be achieved [19].
- Damage to the substrate during deposition can be minimized.
- The source of material can be solid in any shape or form
- When deposition is not desired, the particular areas can be avoided from the deposition by suitable masks.
- Common evaporent materials are Au, Ag, Sn, Cr, Sb, Ge, PdS, KCl, and $PbCl_2$.

The method also has some limitations such as

- Can only achieve the temperature about 1800 °C, hence not possible to deposite materials with high melting points
- Poor step coverage because of the shadowing effect
- Forming alloys can be difficult
- After deposition post annealing may be required especially for oxide films.

Using this simple method of thin film deposition various advanced functional materials have been deposited by employing careful choice of process parameters. For example, Zhang et al. realized high-quality topological insulator Bi_2Se_3 thin film [20]. The precursor powders were evaporated from Mo boat and deposited on the single crystal Si(100) substrate. Wang et al. reviewed the progression of fabrication of efficient metal halide based perovskite solar cells (PSC) by thermal evaporation [21]. Liu et al. has reported dual-cell thermally evaporated PSCs with high power conversion efficiency (PCE) of 15.4% [22]. Some of the device structure and performance of PSCs with the perovskite layer deposited by thermal evaporation method are listed in Table 3.2.

For gas sensing application, using thermal evaporation researchers were able to fabricate various nano-morphologies with improved response kinetics. For example; Navale et al. fabricated ZnO hierarchical nanostructures for NO_2gas sensor [27]. In particular, they could fabricate nanorods and bunch of nanowires on glass substrate by thermal evaporation method. The chemi-resistive sensor films were able to respond to the lease quantity such as 1 ppm of NO_2 gas at 200 °C. Some of the advanced metal oxide semiconductor (MOS) films realized using thermal evaporation and their sensing properties are listed below in Table 3.3.

Another important application is in the field of batteries. In particular, for deposition of solid electrolyte interface (SEI) coating between the electrolyte solution and lithium with no direct contact. The formation of SEI using various materials such as LiF [32], Li_3N [33], Li_2O [34], and carbon based materials [35] has been reported. Hwan et al. deposited LiF on Li surface by thermal evaporation and demonstrated it to be best material for protecting the lithium surfaces [36]. LiF's wide electrochemistry

Table 3.2 Device structure and performance of PSCs with the perovskite layer deposited by thermal evaporation method

Device structure	V_{OC} (V)	I_{sc} (mA/cm^2)	FF	PCE (%)	Active area (cm^2)	Refs
FTO/SnO_2/$MAPbI_3$/spiro-OMeTAD/Au	1.08	19.18	0.738	15.28	0.08	[23]
FTO/C_{60}/$MAPbI_3$/CuPc/Au	1.04	18.91	0.7811	15.33	0.08	[24]
ITO/PEDOT:PSS/polyTPD/$MAPbI_3$/$PCBM_{60}$/Au	1.07	17.9	0.57	10.9	0.95	[25]
FTO/TiO_2/$CsPbIBr_2$/Au	0.959	8.7	0.56	4.7	–	[26]

I_{sc}—Short circuit current, FF—Fill factor, V_{oc}—Open circuit potential

Table 3.3 Advanced MOS films and their sensing properties

MOS	Gas	Concentration (ppm)	Response time (s)	Recovery time (s)	Operating Temp. (°C)	Ref
SnO_2	NO_2	1	10	123	200	[28]
CuO	H_2S	0.1–0.4	60	90	200	[29]
Fe modified SnO_2	H_2S	10	98	90	225	[30]
ZnO modified CuO	H_2S	5	6	30	200	[31]

stability window and negligible solubility in most electrolytes and an ability to regulate the surface tension [37] leads to its widespread usage. The most stable cycling performance was achieved for the cell with 300 nm thick LiF layer. In industrial application, the thermal evaporation techniques have been widely used. Pan et al. fabricated Sb_2S_3 solar cell with an overall efficiency of 1.76 and used for device fabrication [38].

More importantly, the technique has also found its utility in the position control growth of various nanomorphologies like nanorods and nanowires realized using vapor phase growth [39]. In particular, using thermal evaporation a thin coating of ~5 nm of seed layers (e.g., Au, Ag) has been deposited on to the substrate followed by annealing that results in the uniform distribution of seed layer on the substrate which are then subjected to nanowires growth [40–42]. Additionally, this technique is also used with other approaches like nanosphere lithography and phase shift lithography to realize accurate position control of the nanostructures [43, 44].

Over all the thermal evaporation method offers advantages over deposition techniques that includes

- Uniform coating can be realized on the substrate
- Process is solvent free
- Good control over the deposition rates thereby film thickness;
- Simple and easy to operate
- Good quality films having good adhesion to the substrate can be obtained
- Suitable for scale up device fabrication for the industry application.

3.3.2 Electron Beam Evaporation

Electron beam evaporation technique is yet another simple and commonly used technique for the deposition of thin films. Herein, the intensive beam of electrons emitted from a filament falls on the target vaporizing it under vacuum environment. A high difference of potential (kV) is used to accelerate emitted electrons towards an anode (source of material). A strong magnetic field is often applied to bend and

enhance the effective trajectory of the electron beam and allow it to fall on the source of material. The technique offers some advantages which are listed below

- Electron beam is focused on a specific area on the crucible that allows the control over the evaporation rate
- High melting point (above 1800–3300 °C) materials can be deposited by e-beam evaporation.
- Alloys could be congruently deposited i.e., without dissociation of constituent elements which are suited for reactive evaporation (for oxides, nitrides, etc.)
- Contamination from the crucible is less.
- High quality films can be obtained.
- High deposition rate of 50–500 nm/min.

The technique also has fewer disadvantages like at high energy (>10 keV), the incident electron beam could cause X-ray emission and importantly the deposition equipment is costly. Large categories of materials can be prepared by electron beam evaporation technique such as oxides [45], semiconductors [46], metals and even molecular materials [47]. The films of advanced materials prepared using e-beam techniques have found tremendous applications in various fields such as saturable absorber in Q-switched ytterbium doped fiber laser [48], fuel cell electrodes [49], solar cells [50], optical, and photoconductive studies [51]. Now, MEMS (micro electro mechanical systems) technology has been used for the structural and device fabrication of the devices. It merges at the nano-scale into nano-electromechanical systems and nanotechnology. Normally, crystalline silicon or polycrystalline thin films and more recently amorphous silicon (a-silicon) have been used as the structural material in MEMS applications [52]. E-beam evaporation is a good choice for formation of a-silicon thin films for MEMS applications. Michael et al. studied the a-silicon thick film (>10 μm and ultra-smooth) deposited by e-beam evaporation for MEMS application [53]. Joseph et al. have demonstrated the applicability of ultra-smooth a-silicon thin film (<500 nm) in MEMS applications [54]. The inherent tensile stress is found to be doubled, and surface roughness is found to be reduced. Thus, a-Si thin film deposited by e-beam evaporated is demonstrated to be a potential candidate for low thermal budget MEMS applications.

E-beam technique has also been found useful for several bio-applications. For example, Gnanavel and his co-workers [55] have demonstrated that the HA (hydroxyapatite) films deposited by e-beam evaporation on bio inert metal namely Ti-13Nb-13Zr (near β titanium alloy) exhibited excellent bioactivity. This work is of particular significance and desired to realize HA ceramics bone implants. For other application like corrosion resistance novel compositions were realized using e-beam method viz., TiO_2, $Ti_{0.41}W_{0.59}O_x$ [56, 57]. Other interesting applications of e-beam is in the development of electrochromic (EC) materials. In EC materials application of a small voltage causes a significant variation of the optical state (darkness/lighten). Accordingly, they have found promising relevance's in the field of antiglare automobile rear-view mirrors, optical displays, energy efficient smart windows, etc. [58–60]. Tungsten oxide (WO_2) is one of the smart materials among the electrochromic materials that has high coloration efficiency, stability, and contrast ratio along with low power

consumption and excellent memory effects [61, 62]. Eevecan et al. fabricated tungsten oxide thin films using e-beam evaporation that exhibited good electrochromic properties for use in electrochromic devices. Karaca et al. [63] have found that the inclusion of gold/poly (3,4-ethylenedioxythiophene)/platinum (Au/PEDOT/Pt) microtubes into WO_3 resulted in an increase in optical modulation by 26% with improved response times (t_b: 13.83 and t_c:19.25 s) and electrochromic stability.

Although e-beam is considered to be a good approach for the synthesis of metal and alloy coatings, it is not good for ceramics due to charge build up on the ceramic target. Accordingly, for deposition of ceramics usually sputtering techniques have been employed. However, this technique itself is very expensive and needs high vacuum environment. Because of their resistance to mechanical shock ceramic oxides, nitrides and carbides (e.g. BeO, Al_2O_3, AlN, SiC/Si) are attractive for application in protective coating materials [64]. Using e-beam evaporation Yushkov and coworkers were able to deposit alumina coating on using a fore vacuum plasma cathode electron source [65]. Ceramic is a dielectric (insulating) material, and during the deposition process, the negative charged electrons gets accumulated on the ceramic surface giving it a high negative potential. This causes electron beam to reflect and deflect, consequently no further deposition could take place. The solution to this problem could be provided by the fore vacuum pressure plasma cathode electron beam source. Electron beam generated by this kind of source, typically of energy up to 20 keV, current upto 1A, and under residual gas pressure of ~75 mTorr could lead to plasma that provides excellent neutralization of the electronic charge accumulated on the ceramic surface. As a result, a good functional ceramic coating of alumina from its bulk alumina ceramic is obtained. Importantly, the ceramic target material evaporation rate was found to be up to 4.2 g/h, which is high as compared to other vacuum coating methods. The film deposition rates of ~18 μm/h could also be achieved [66]. The e-beam method offers several advantages over other techniques such as high material utilization efficiency, good control over evaporation rate, possibility of depositing high melting point (above 1800 °C) materials, and alloys without dissociation of constituent elements.

3.3.3 Laser Beam Evaporation (Pulsed-Laser Deposition)

Pulsed-laser deposition (PLD) is another technique that allows the stoichiometric transfer of complex materials such as $YBiO_3$ and Ag_2S_3 onto the substrates [67]. The laser ablation method allows good control over films thickness and could be used effectively to obtain films of easily decomposable compounds or nano-layered structures [68]. In this technique, the ablation of the material to be deposited is achieved employing high power pulsed laser beam that is focused on the target. The target is to be melted, evaporated, and ionized by high power laser beam. Different laser sources are being used to ablate the target material, and the most common laser sources are Nd-YAG laser, KrF (248 nm), and XeCl (308 nm). When the laser beam strikes the target material, it produces the plume which could deposit on various substrates. The

created plume may contain neural- and ground-state atoms and ionized species. The deposition can be carried out in ultrahigh vacuum or background gas like oxygen or nitrogen [69]. The film quality is governed by various process parameters such as laser wavelength, pulsed duration, repetition rate energy, ambient gas pressure, and substrate temperature [70, 71]. The technique has some advantages over the other physical deposition systems because of its fast deposition rates and capability to grow films under oxygen or other environments. Some of the advantages are listed below

- Material displaced is deposited onto the substrate without decomposition
- This method is highly preferred when complex stoichiometries are required.
- High quality of thin films
- Ease of operation and reproducibility
- Films do not required post-deposition annealing.

The technique also suffers from drawbacks like the target is ablated to form "chunks" and thus the main challenge is to minimize the chunkse-beam evaporation.

PLD has been demonstrated a good technique to control the surface polarity of the ZnO films [72]. Surface polarity has a strong influence on the material properties especially the optoelectronic and chemical properties [73]. The thickness of MgO layer can be tuned to get the different polarity of ZnO surface. In particular, for MgO thicknesses <2 nm and >3 nm results in O-polar and Zn-terminated polar surface respectively. PLD has been effectively used to realize novel nanomaterials like $CuSbS_2$, [74] multi-walled carbon nanotubes (MWCNTs) decorated CdO nanoparticles, [75] and Au NPs in TiO_2 [76].

3.3.4 Epitaxial Growth Techniques

Epitaxial growth technique have been largely used in the fabrication of electronic circuits which is attributed to the compositional uniformity, good control, and understanding of the growth parameters. Several epitaxial techniques have been used for the growth of epilayers of III-V, II-IV compound semiconductors, and other materials. The most commonly used among them are liquid phase epitaxy (LPE), vapor phase epitaxy (VPE), molecular beam epitaxy (MBE), chemical beam epitaxy (CBE), and atomic layer epitaxy (ALE).

3.3.4.1 Liquid Phase Epitaxy

LPE is an excellent method to realize thin layers of group III-V, II-IV, and IV-VI compounds [77]. This method is flexible for device applications and in the fabrication of the device structures such as hetrostructure laser diodes, gundiodes, pin-photodiodes, avalanche photodiodes, integrated bipolar transister laser circuits, and

rare earth doped injection lasers. In LPE, the films usually grow from metallic solutions onto a crystalline substrate. The solvent contains a small quantity of solute example, as in Ga for epitaxial growth of GaAs layers which is transported towards the liquid–solid interface. There are three kinds of LPE growth techniques: tipping, dippind, and sliding. In tipping techniques, the substrate is placed tightly at the upper end of a graphite boat while the growth solution is placed at the lower end. Tipping of the substrate is performed to bring the solution into contact. The furnace is then slowly cooled, and an epitaxial layer is grown on the substrate. The growth is terminated by tipping the furnace back to its original position. The solution remains on the film surface is removed by wiping and dissolving in a suitable solvent. The apparatus used for tipping and dipping techniques is very simple and easy to operate. For multilayers growth, sliding technique using multi bin graphite boat is used. The growth is usually carried out in an atmosphere of hydrogen.

3.3.4.2 Vapor Phase Epitaxy

VPE is a technique used for the growth of III-V compound semiconductors. As the name indicates vapor phase epitaxy, the growth is carried out by vapourizing the source material. Inorganic or organic materials which reacts with the other materials to form the compound semiconductors on the substrate. Growth is controlled by the partial pressures of each of the components of the source materials. There are two different forms of vapor phase epitaxy growth (i) chloride VPE and (ii) hydride VPE.

In chloride VPE, GaAs has been grown successfully using an $AsCl_3$-Ga-H_2 system and PCl_3-In-H_2 system has been used to grow InP. The advantages of trichloride VPE arises from the fact that $AsCl_3$ and PCl_3 can be distilled into very pure liquids and the fact that AsH_3, and PH_3 are not used. In hydride VPE, the growth of GaAsP was first demonstrated using the group V hydride arsine (AsH_3) and phosphine (PH_3). These are added to gas flows containing the group III metal chlorides and or InCl which are formed by reaction of HCl gas with liquid Ga and In sources. Both the source reactions and the deposition reactions are done inside a hot walled quartz reactor. The major advantages of hydride VPE are that epitaxial growth on large wafers and on multiple wafers is possible simultaneously.

3.3.4.3 Molecular Beam Epitxy (MBE)

MBE is a technique that is used for the deposition of thin film compound semiconductrors, metals, and insulators. It is a mono crystal film growth technique and a commercial production technique for compound semiconductor materials such as GaAs. In MBE, beams of atoms and molecules direct on to a crystal surface. It works under ultrahigh vacuum and hence produced extremely pure material film. The beam pressure is extremely low that the molecular flow regime is maintained, and the incident fluxes can be controlled rapidly and efficiently by simple shutters or needle valves. The evaporated elements (atoms/molecules) travel straight to the

substrate without interacting with each other or the gases present in the chamber. This is because of their long mean free path involved in the deposition process. Under appropriate conditions of beam flux and substrate temperature, epitaxial film is formed. This technique is widely used to produce superlattice structures having multilayer with single layer thickness of ~10 Å.

Recently semiconductor/superconductor hybrids have gained a great attention wherein the interface governs the induced superconducting gap. Krogstrup et al. have studied the epitaxial growth of semiconductor–metal core–shell nanowires [78]. They demonstrated a new route for controlled electrical contacts to nanostructures enabling device designing for topological and gate-controlled superconducting electronics. Their choice of material was epitaxial InAs/Al grown with single-plane interfaces. At the boundaries of different topologies, quasiparticles have been found to exist. Such quasiparticles—"Majorana modes"—can be formed in semiconductors nanowires (NWs) coupled to conventional superconductors. So far, conventional methods have shown some unexpected low-energy states below the proximity-induced superconducting gap. The disorder in the semiconductor/superconductor (SE/SU) interface is attributed to be the source of such soft gap. The device performance has also been found to increase together with interface quality. Kronstrup et al. have studied the electrical properties of Al/InAs hybrid. To investigate the superconducting properties of the Al film, four terminal devices were fabricated on a 90 nm diameter with a 13 nm full shell, as illustrated in Fig. 3.1a,b. Figure 3.1c depicts the temperature dependence of the four-terminal resistance.

The Al shell has a normal state resistance of ~50 Ω for temperature above 1.6 k, showing a gradual transition to the superconducting zero-resistance state, which is

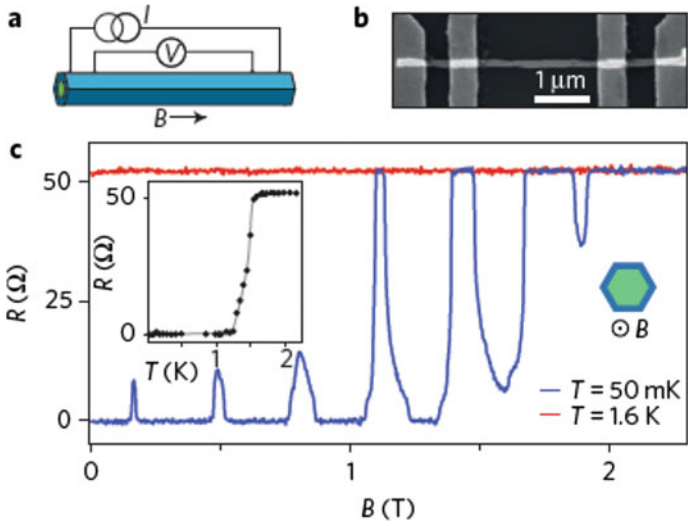

Fig. 3.1 A schematic illustration of the four-terminal device made from a full-shell Al/InAs nanowire with a 13 nm thickness of Al, **b** SEM image of the device, and **c** measurement of four-terminal resistance as a function of magnetic field. Reprinted with permission from P. Krogstrup et al., Nature Mater. 14 (2015) 400–406, Copyright © 2015 Springer Nature Publishing AG [78]

fully developed by 1.3 K. For temperature below the superconducting transition, Al induces superconducting gap into the InAs by virtue of proximity effect.

MBE has also been demonstrated as a tool to grow catalyst-free nanostructures. For example, Tchoe et al. demonstrated a catalyst free growth of coaxial nanorod heterostructures of InAs/InGaAs on large-area graphene layers [79]. Interestingly, the nanorods on the graphene exhibited homogeneous composition. They used combination of the technique namely CVD and MBE for the fabrication of nanostructures. Graphene has high mechanical strength and flexibility. The large-area graphene layers were prepared by CVD as a substrate for InAs/InGaAs coaxial nanorod heterostructures growth.

Among other Group III nitrides, indium nitride (InN) has some promising features such as excellent electron mobility (4400 $cm^2V^{-1}s^{-1}$ at 300 K) [80], small direct band gap of 0.65 eV [81]. Accordingly, it could be a good candidate for long wavelength optoelectronic devices like photodiodes, optical sensors, and band solar cells. For the fabrication of a heterojunction solar cell, the combination of InN with Si can form a hetrojunction. In order to minimize the resistance between both cells, establishing a tunnel junction between InN and Si is required. For this a favorable way is to grow InN directly on Si without any buffer layer which still remains a daunting challenge. Use of nanowires (NWs) could possibly overcome this problem, as the lattice mismatch strain can relax through the NW sidewalls because of their small foot-print. Weiszer et al. have studied the systematic growth of self-assembled and position-controlled InN nanowires (NWs) on Si (111) substrates by plasma-assisted MBE without using a buffer layer [82]. For device fabrication, two factors are important (i) growth of NWs with a defined diameter and length at a specific position in a reproducible way, and (ii) structures should not suffer from statistical in homogeneities in NW morphology. Authors achieved this with the help of an additional pre structured Ti-mask on top of the substrate and is called position-controlled or selective area growth (SAG). For the nanowire growth substrate temperature, growth time and III/IV flux ratio are found to be major factors. With substrate temperature of 480 °C, growth time of 90 min, and III/IV flux ratio of $1{:}10^{-3}$homogeneous InN NWs with a maximum aspect ratio were successfully grown.

HgCdTe has been used in IR detectors for a decade attributed to its excellent performance advantage and technical maturity. The near perfect lattice match with HgCdTe makes $Cd_{0.96}Zn_{0.04}Te$ (CZT) ideal substrates for fabricating high performance infrared focal plane arrays (IRFPAs). However, low mechanical strength and thermal conductivity, high cost, and poor quality pose serious limitations [83]. Gu et al. have demonstrated alternative substrate namely GaSb for epitaxial growth of HgCdTe films with lower Etch Pit Density (EPD) and higher minority carrier lifetime than other conventional substrates.

Tanaka et al. have studied photoluminescence (PL) of ZnTe/ZnMgTe multiple quantum well structures (MQW) deposited on ZnTe [84]. PL properties of MQW structures strongly depend on the well widths and Mg content in the barrier layer as they affect the quantum energy levels formed in the ZnTe well layer and the crystallinity of epilayers. In ZnTe/ZnMgTe MQWs, it was found that a carrier escape out of the ZnTe quantum well is a dominant origin for thermal quenching and the

design of QW structures with a higher barrier was found to be crucial to obtain PL at higher temperature. The MQW structures with an adequate well width and Mg content showed PL at room temperature, which demonstrate a potential for pure-green LEDs.

All the above studies clearly indicates that MBE is a versatile technique among the other deposition technique. However, one has to keep in mind that being a slow process it may not be useful for mass production in industrial applications.

3.3.5 Sputtering

Sputtering technique is mostly used for depositing metal and oxide films by controlling the crystalline structure and surface roughness. In sputtering, a voltage is applied between the target material (cathode) and the substrate (anode) placed in a vacuum chamber. Initially the plasma is created by ionizing a sputtering gas (Ar) which bombards the target and sputters off the material, which eventually gets deposited onto the substrates. The sputtering is referred to as the process in which the momentum transfer between the sputter gases and target atoms causes removal of material to be deposited. One of the reasons for the popularity of the technique is the possibility of depositing the materials with very high melting points with a complete composition transfer from the target. This technique is widely used for depositing metal and oxide films by controlling the crystalline structure and surface roughness. One of the important parameter of the process is the sputtering yield 'S' which refers to the number of atoms ejected per incident ion. It takes the values typically in the range of 0.01 and 4. The yield is a strong function of the target material its mass and composition, binding energy, sputter power, nature of the incident ion, and the overall geometry. For accelerating ions the plasma is maintained between target and substrate. Magnetrons giving very strong electric and magnetic fields are generally employed to confine plasma close to the target surface and accordingly, the technique is referred to as the magnetron sputtering. In magnetic field, electrons follow helical paths increasing the effective electron path length thereby causing more ionization of the gases. DC power sources are employed for depositing metals and referred to as DC sputtering herein sputtering target and the substrate are held in parallel plate configuration. More often RF sources (13.56 MHz) are used to avoid charge build-up on the insulating targets and is referred to as RF sputtering. The quality of the films is easily controllable by careful choice of process parameters namely base vacuum, sputter gas and its pressure, sputter power, target, and substrate temperature [85].

This technique is a good choice for the synthesis of advanced materials. These days, supercapacitors have been developed for the applications in electronic devices, portable power sources, and electric vehicles. They offer the advantages of high charging and discharging efficiency, long cycle life time than that of batteries, high power density, and low sensitivity to temperature. Some of the active materials for supercapacitors includes carbon materials [86, 87], metals oxides like MnO_x, NiO, RuO_2, and Co_3O_4 [88–91]. Among these active advanced materials, a manganese

oxide (MnO_2) is found to be promising electrodes in supercapacitors (SC) [92]. The research has thus focused on one dimensional (1-D), two-dimensional (2-D) metal oxide nano-structured materials, which can have superior electro chemical performance [93]. MnO_3 has high theoretical specific capacitance (C_{SP}~1370 F/g), easy preparation, low toxicity, and low cost. The electrochemical properties of SCs depend on the morphology and structure of the active material, electrical contact with current collectors, amounts of cations, and exposed surface area. For 1-D nanostructured morphologies such as nanorods, nanowires, and nanoflakes, the sufficiently high surface area and shorter diffusion paths for electron/ion transfer helps to realize high capacitance [94, 95]. Fabrication of such a nanostructure has been developed by many methods such as sol–gel, electrochemical deposition, chemical reduction, thermal decomposition, and precipitation with use of polymer binders and additives [96, 97]. These binders and additive fused with active materials and reduced the capacitance of super capacitor [98]. This implies that an effective way to fabricate binder free, low cost, high quality, and contamination free nanostructure is employing PVD techniques, particularly sputtering.

Recently, transition metal nitrides, such as VN, Mo_2N, TiN, CrN, and NbN, based supercapacitors have been studied [99–103]. Prakash et al. have studied the tungsten nitride thin film electrode deposited by reactive sputtering for supercapacitor devices [104]. Among various transition metal nitrides, tungsten nitrides (W_2N) are more attractive for SCs because of tunable electrical conductivity, high melting point, and excellent chemical and thermal stability with superior mechanical properties.

Other advanced materials are thermoelectric materials that have gained tremendous attraction. These are the materials that converts waste heat into electricity directly and reversibly employing Seebeck and Peltier effects and accordingly have promising applications in power generation and cooling [105, 106]. Somdock et al. studied the bismuth telluride (Bi_2Te_3) compound for thermoelectric application [107]. Bi_2Te_3 is an anisotropic material wherein the material property varies with structure and orientation. Somdock et al. have synthesized Bi_2Te_3 film on the (00l) plane wherein the thermo electric properties were found dependent on the orientation of (00l) plane and chemical composition. Among the deposition techniques sputtering is a good option for the highly oriented (00l) seed layer and stoichiometric thin film of Bi_2Te_3. In order to get the preferred orientation plane the substrate temperature plays a key role. Le et al. found out that the film with preferred orientation of (00l) layers having lowest surface energy can be achieved in the temperature range of 220–380 °C [108]. Nuthongkum et al. found out that the working pressure plays a significant role for composition control and improve thermoelectric properties of Bi-Te thin film [109]. The thermoelectric properties of the Bi_2Te_3 thin films fabricated by sputtering have been compared in Table 3.4.

Orientation of bismuth telluride thin film, carrier concentration (n), electrical conductivity (σ), carrier mobility (μ), and power factor (PF).

Another application of sputtering technique is in the fabrication of electrochromic devices. Gomes et al. have reported indium-zinc oxide (IZO) film deposition with a ceramic IZO target onto using RF and DC sputtering [113]. Further, Gomes et al. reported that IZO films could be achieved possessing low sheet resistance (‘20 Ω/sq)

Table 3.4 Thermoelectric properties of the Bi_2Te_3 thin films fabricated by sputtering

Sample	Orientation	n (cm^{-3}) × 10^{20}	σ (s/cm)	S (μV/K)	μ (cm^2/Vs)	PF ($W/Mk^{2)}$	Refs.
Bi_2Te_3	(00l)	7.87	14.9	−76	118.0	8.62×10^{-3}	–
	(00l) + (015)	1.3	952.4	−55	45	2.75×10^{-4}	[110]
	(00l) + (015)	0.51	549.5	−128	67.2	9×10^{-4}	[111]
	(00l) + (015)	6.94	710	−75	6.39	4×10^{-4}	[112]

and 80% optical transmittance in visible part of the spectrum and the electrical stability above eight months. Baptista et al. have reviewed about the evolution of magnetron sputtering process for industrial applications [114]. PVD processes have the higher energy consumption as compared to that of CVD processes. The DC source is the most commonly used source in magnetron sputtering. The combination of RF and MF (microwave frequency) sources led to a new technique namely Dual Anode Sputtering (DAS) with reduced heat load in the substrate.

3.4 Chemical Techniques for Thin Film Deposition

This refers to the technique that involves use of chemicals or solution to realize the thin films. In particular, at a solid surface the fluid precursor undergoes a chemical change leaving a solid layer. This type of techniques have attracted much attention owing to numerous advantages that includes low cost, ease of synthesis, and potential for scale up for commercial deployability. Depending upon the phase of the precursor, the technique is further classified into following techniques.

3.4.1 Sol–Gel Method

Sol–gel process refers to a method for material synthesis from solutions, in which there is a change from a liquid state to a gel state through polycondensation reaction. A sol is a stable dispersion of colloidal particles or polymers in a solvent. A gel consists of a 3-D continuous network of the sol particles, which encloses a liquid phase [115].

Bahuguna et al. reviewed about the sol–gel techniques for the thin film growth. There are several advantages of a sol–gel method over the other thin film deposition methods [116]. These include significant ease of coating the complex shapes, cost effective owing to the requirement of smaller quantities of the material. Importantly, the process is feasible at room temperature with possibility of getting the desired morphology careful choice of the reaction condition. This method also has fewer drawbacks like gel drying, extreme volume shrinkage during gelation, removal of

Table 3.5 List of materials, nanostructure grown by sol–gel method, and their applications

Material	Nanostructure	Applications	Refs.
b/Tourmaline/TiO_2	Nanotubes	Photocatalysis	[117]
Silver doped titanium oxide	Thin film	Gas sensing	[118]
Yttrium iron garnet (YIG)	Thin film	Spintronics	[119]
Erdoped SnO_2	Nanoparticles	Photoluminescence	[120]
$Sr_2Bi_4Ti_5O_{18}$ (SBTi) and Nd-modified SBTi (SBNT)	Thin film	Ferroelectrics	[121]

the redundant residuals, and the occurrence of pores. Leitzke et al. described the low temperature and cost effective synthesis of amorphous WO_3 films on ITO/PET flexible substrate [117] to be used as a working electrodes in flexible electrochromic devices. Table 3.5 provides examples of material with nanostructure and applications.

3.4.2 Spray Pyrolysis

Spray pyrolysis is another approachable technique for the thin film deposition. Herein the thin film is deposited by spraying a solution onto a hot surface facilitating the reaction of the constituents forming a chemical compound to be deposited. The chemical reactants are so chosen that the undesired products are volatile and automatically do not form the part of the film composition. Generally, it forms an aerosol droplets comprising of metallic salts solution or colloidal solution which are consequently heated in a furnace (thermolysis) wherein they undergo to different stages before forming a thin film. First, microporous particles with defined phase composition are formed, followed by formation of solid particles, and finally sintering of these particles to form a thin film coating on the substrate.

The technique offers numerous advantages over other synthetic techniques. First, it has simple equipment so it is easy to handle. Secondly, it does not require high-quality reagents or compositions. By varying the chemical conditions, additives, concentration of the precursors, it is possible to get a good control over the morphology and size of resulting particles. It has some disadvantages also that include possibility of the oxidation of the reactants and difficulty for scale-up. However, the technique has demonstrated good potential to realize novel advanced materials for applications in the field of superconductor powders, multicomponent ceramics, catalysts, electrode materials, energy storage, and conversion. For example, Yoon et al. have reported a facile one-pot spray pyrolysis method for the preparation of SnO_2 spheres having 3-D interconnected and size-tunable trimodal (micro-, meso, and macro-scale) pores [122]. This was achieved by employing sacrificial templates of macroscale polystyrene spheres and mesoscale-diameter long carbon nanotubes (CNTs). Figure 3.2 shows the schematics of the process for the formation of SnO_2 nanospheres with trimodal porosity [123]. The resultant spheres with different modal

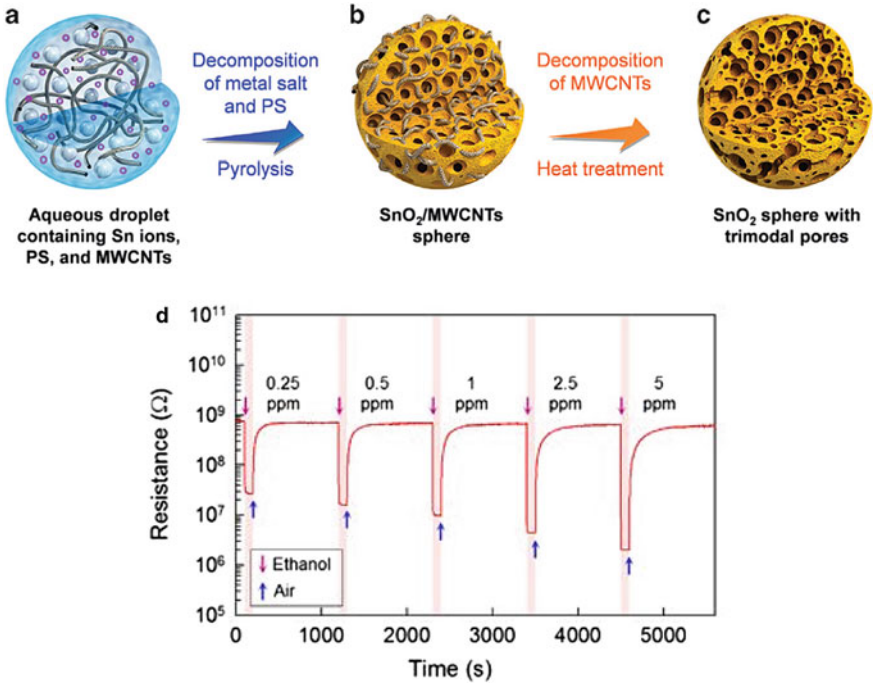

Fig. 3.2 Schematic representation of the steps involved in the formation of SnO_2 nanospheres with trimodal (3 M) porosity. **d** Dynamic gas-sensing transients of the 3 M-SnO_2 spheres to 0.25–5 ppm of ethanol at 400 °C. Reprinted with permission from J.-W. Yoon et al. NPG Asia Materials 8(2016) e244. Copyright © 2016 Springer Nature Publishing AG [123]

pores (sizes ~3, 20, and 100 nm) have shown unprecedentedly high response to ppb levels of ethanol (Fig. 3.2). From the figure, it is evident that the SnO_2 spheres with trimodal porosity exhibited remarkable sensor response towards ethanol.

Another interesting application of the spray pyrolysis method has been found in the development of anode materials for application in lithium ion batteries (LIBs). Park et al. have investigated cobalt hydroxychloride [$Co_2(OH)_3Cl$] as anode material for LIBs [124]. For this, the cobalt chloride salt solution was spray coated during which ultrafine nanocrystals with spherical geometry were formed. The $Co_2(OH)_3Cl$ powder exhibited high thermal stability below 220 °C and superior electrochemical properties than $CoCl_2$: $(H_2O)_2$ and CoO deposited using the similar process. Superior electrochemical properties are attributed to the spherical shape of $Co_2(OH)_3Cl$ powders. In particular, the discharge capacity of bare $Co_2(OH)_3Cl$ powders is found improved. Besides, it acts as a buffer layer for large volume changes during cycling.

Very recently, Leng et al. have critically reviewed spray pyrolysis as a versatile synthetic technology to realize powdered materials and thin films for potential application in energy storage and conversion [125]. As shown in Fig. 3.3, using

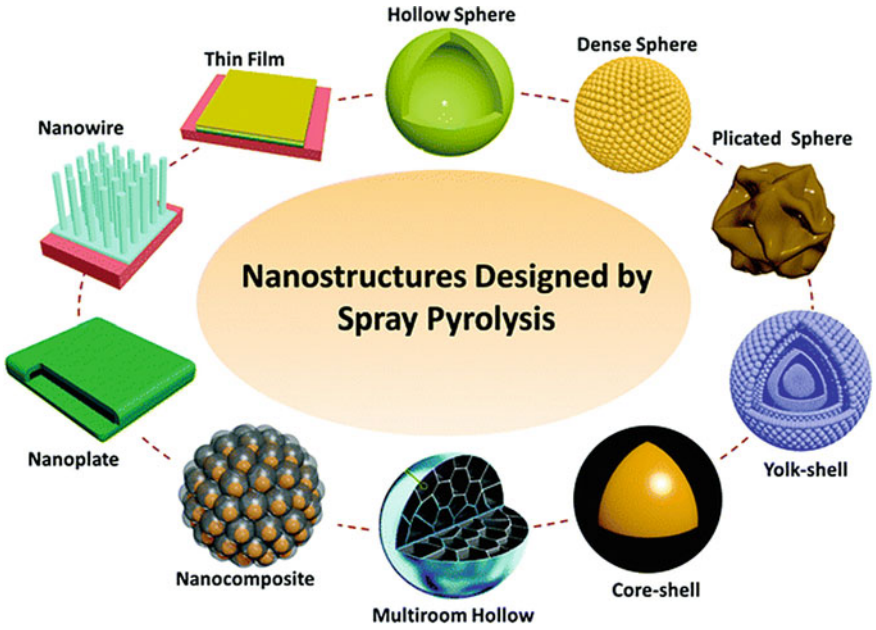

Fig. 3.3 Different nanostructures designed by spray pyrolysis. Reprinted with permission from J. S. Cho et al. Nano Energy, 2016, 26, 466–478. Copyright © 2016, Elsevier [126]

spray pyrolysis different nanostructured products like hollow or dense spheres, yolk–shell, or core–shell structures, composite materials and thin films were successfully synthesized [126].

3.4.3 Chemical Bath Deposition (CBD)

Chemical bath deposition (CBD) technique is a well-suited technique to produce thin films for large area applications. It involves mainly two steps, nucleation and growth. In this technique, the substrate to be deposited is generally immersed in a solution containing the precursors. Accordingly, the choice of substrate and the solution parameters like composition, temperature and duration, are found to play a crucial role in determining the quality of the thin film. Importantly, CBD is known to give well adherent, stable, and uniform coatings on the substrates. Kim et al. have studied the hierarchical interconnected nickel cobalt sulfide ($NiCo_2S_4$) nanosheets deposited on a flexible stainless steel foil [127]. These interconnected $NiCo_2S_4$ nanosheets as electrodes have shown a specific capacitance of 1155 F/g at 10 mV/s with superior cycling stability retaining 95% of capacity up to 2000 cycles. Guo et al. studied the coercivity enhancement of sintered Nd-FeB magnets realized by CBD of $TbCl_3$. The coercivity was observed to increase from 11.89 to 14.72 kOe without any reduction

of reminiscence and excellent thermal stability [128]. This coercivity enhancement is attributed to the formation of a core–shell structure with the (Pr, Nd, Tb)$_2$Fe$_{14}$B phase surrounding the (PrNd)$_2$Fe$_{14}$B phase.

3.4.4 Chemical Vapor Deposition (CVD)

Chemical vapor deposition (CVD) as the name suggest is a process in which the chemical interaction takes place between the precursors molecules in the vapor phase and the corresponding product as solid material gets deposited as thin film or collected in powder form. The process is often carried out inside a flow reactor wherein the precursors are activated (thermal, photo, or plasma energy) leading to deposition on the substrate surface to produce the desired film. This process has been adapted in the semiconductor industry especially for the fabrication of device and importantly for protective coatings on precision machine parts.

Metal organic frame works (MOFs) are class of compounds that comprises metal ions or clusters coordinated to organic ligands to give 1-, 2-, and 3-D structures that are often porous. They have disruptive potential in microelectronics. Suitable film deposition methods are crucial for MOFs. The films fabricated by solvent based processes often face corrosion and contamination risks. Stassen et al. demonstrated CVD process to achieve high quality zeolitic imidazolate framework films of ZIF-8, with a uniform and controlled thickness, even on high-aspect ratio features [129]. Later MOF-CVD integrated on microelectronics devices by lithography. Solvothermal transformation of metal oxides to generate 2-D and 3-D MOF patterns have also been studied extensively [130, 131]. Formation of pinholes, rough films, and homogeneous nucleation in solution faced risk by solvothermal method. Stassen et al. demonstrated that these problems could be avoided by employing combined MOF-CVD approach wherein the organic linker is supplied as a vapor instead of in-solution. Figure 3.4 shows the SEM image of the deposited zif-8-coated silicon pillar array

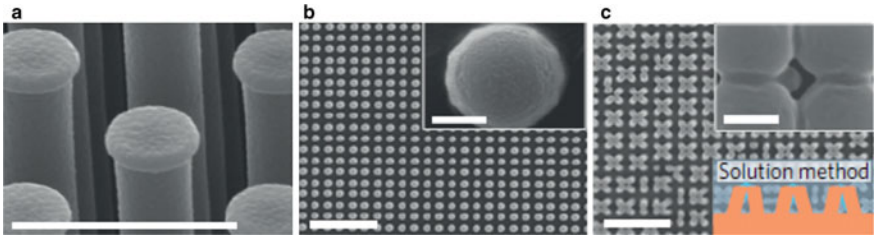

Fig. 3.4 SEM image of **a** ZIF-8-coated silicon pillar array, **b** MOF-CVD coated PDMS pillars, and **c** identical PDMS pillars after conventional processing of ZIF-8. Reprinted with permission from I. Stassen et al. Nature Mater. 15(2016)304–310 Copyright © 2016 Springer Nature Publishing AG [129]

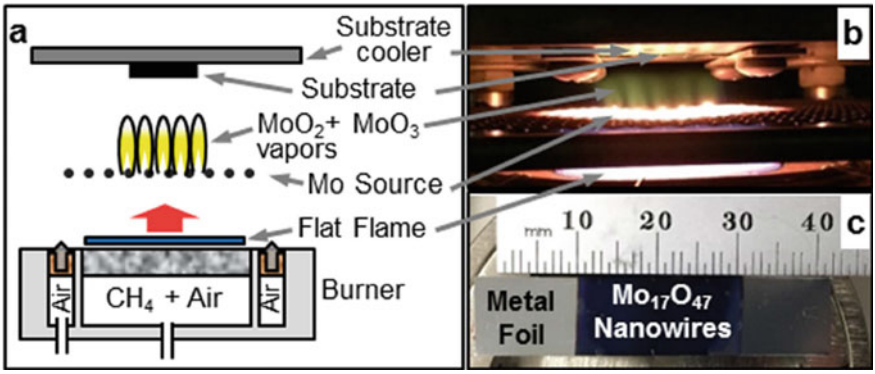

Fig. 3.5 Description of the flame vapor deposition process. **a** Schematic, **b** photograph of flame vapor deposition setup, and **c** photograph of metal foil substrate with dark blue deposit consisting of $Mo_{17}O_{47}$ nanowire-arrays. Reprinted with permission from Allen et al. Nature Sci. Rep.6 (2016) 27,832. Copyright © 2016 Springer Nature Publishing AG [132]

exhibiting a homogeneous coverage of pillars, MOF-CVD coated PDMS pillars and identical PDMS pillars after conventional processing of ZIF-8.

$Mo_{17}O_{47}$ nanowires as active materials are employed as conductive supports for batteries and related applications. Generally, $Mo_{17}O_{47}$ nanowires are synthesized by electrically-heated CVD under vacuum conditions. Allen et al. demonstrated an alternative way based rapid atmospheric flame vapor deposition (FVD) to grow $Mo_{17}O_{47}$ nanowire-arrays on metal foil substrates. The nanowires could be obtained with faster growth rate and were of high-purity, thinner, longer, and densely packed [132]. The FVD synthesis conducted at atmospheric pressure in the flow of hot gaseous combustion products from a flat CH_4-air flame with no enclosing walls or chamber as shown schematically in Fig. 3.5. The synthesis relies on the flame to provide the heat and oxidizing gases required to evaporate and degenerate molybdenum oxide vapors from a solid molybdenum source that is placed above the flame. The vapors then deposit onto a substrate.

As compared to electrically-heated vacuum deposition methods, FVD synthesis allows the total concentration of MoO_x vapors to be larger, resulting in denser nucleation of nanowires with smaller diameters, and faster axial growth rates thereby assuring higher aspect ratio and surface area. In addition, a benefit of this approach is that the partial pressure of oxygen in the synthesis environment can be directly controlled over many orders of magnitude through control over the ratio of CH_4 (fuel) and air (oxidizer) supplied to the flame. The FVD method can be scaled up for large-scale area deposition on to substrate, and the atmospheric operation of the FVD synthesis is less energy-intensive than maintaining a vacuum.

Liu et al. have demonstrated the vapor–solid growth of $Mo_xW_{1-x}Te_2$ nanobelts by facile CVD method [133]. They adopted one-step CVD method, in which Mo (W) and Te precursor are both evaporated during the heating, transported by carrier gas, deposited on the substrate, and reacting with each other finally. In general, there

are two proposed mechanisms for the growth of nanobelts, including the vapor–liquid-solid (VLS) and vapor–solid (VS) growth, respectively. In general, the CVD process begins with the vapor precursors and ends with solid products, and there is no liquid involved in the growth. For a typical VS growth, the solid is evaporated at high temperature, transported by carrier gas, and deposited on the substrate at lower temperature. For this reason Liu et al. said that $Mo_xW_{1-x}Te_2$ nanobelts are governed by VS mechanism. They emphasized that the H_2 carrier gas played a significant role for the nanobelt growth.

Zhang et al. demonstrated highly ordered arrays of WS_2 grown by low pressure CVD (LPCVD) [134]. Figure 3.6 shows the LPCVD synthesis of WS_2 on sapphire grown with jagged edges under pure Ar gas flow and flakes synthesized under mix Ar and H_2 flow [135].

Some of the advantages of CVD are listed below.

- High growth rates
- Possible to deposit materials which are otherwise hard to evaporate
- High reproducibility
- Epitaxial growth of films
- Formation of films at low-temperature.

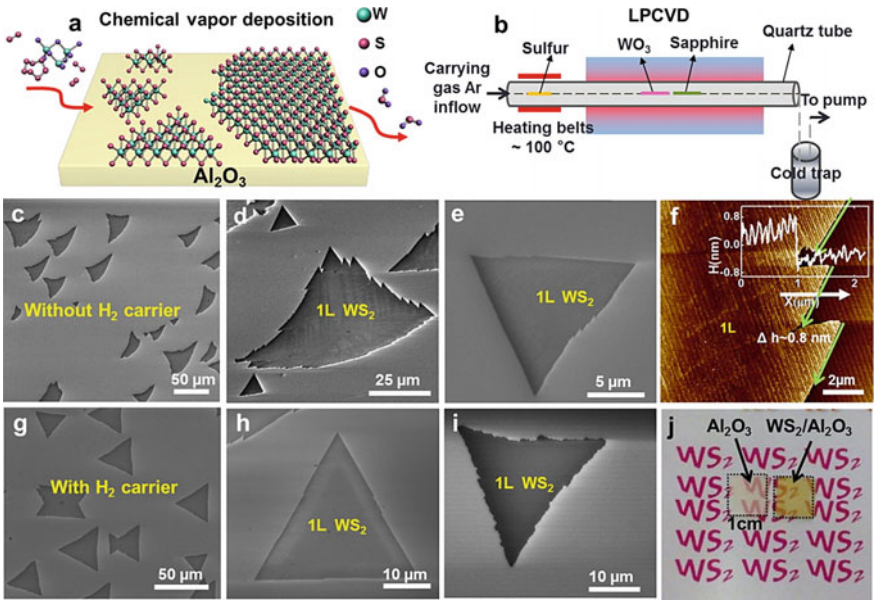

Fig. 3.6 LPCVD synthesis of WS_2 on sapphire. **a** Schematics of the chemical reaction, **b** Experimental setup, **c**, **d**, **e** SEM images of jagged edge WS_2 flakes. **f** Corresponding AFM characterization of the monolayer nature. **g**, **h**, **i** SEM images of WS_2 flakes, **j** Photograph of bare sapphire and monolayer as-grown WS_2. Reprinted with permission from Zhang et al. ACS Nano. 7 (2013)8963–8971, Copyright © 2019 American Chemical Society [135]

CVD also suffers from some of the disadvantages as listed below.

- Not possible for some materials for which no suitable chemical reactions are known
- Not suitable for complex materials also.

3.4.5 Atomic Layer Deposition

Atomic layer deposition (ALD) is a sub-class of CVD and considered to be an advanced deposition technique that employs sequential gas phase chemical processes to realize thin films [136]. Most common ALD processes involves two chemicals called precursors which reacts with the material surface in a sequential and self-limiting manner [137]. A thin film with atomic scale accuracy gets formed on the surface slowly via repeated and sequential exposure to the precursors. A single exposure to all of the precursors is referred to as ALD cycle and the maximum amount of material deposited, i.e., growth per cycle is governed by precursor-surface interactions. The thickness of the material on any arbitrarily complex and large substrates can easily be controlled by careful choice of ALD cycles. The rate of adsorption (R) per unit of surface area is directly proportional to the sticking probability (S), and the incident molar flux (F) given as follows:

$$R = S * F. \tag{3.1}$$

Herein, S changes continuously reaching to zero at saturation. Depending upon the nature of adsorption and reaction mechanism involved, ALD are often classified into but not limited to Thermal, Plasma, Photoassisted, Catalytic, and Metal (elimination) ALD processes. The technique has been widely exploited for polymer surface functionalization, catalytic surfaces, MOS devices, formation of composite structures, and advanced nano morphologies [138, 139]. Using ALD it is possible to grow films to an atomically specified thickness and even multilayer structures. Additionally, it typically involves relatively low temperatures which is advantageous for soft substrates, such as organic and/or biological samples and a catalyst, which is thermochemically favored [140].

Zacharias et al. have demonstrated growth of ultra-long single-crystal $ZnAl_2O_4$ spinel nanotubes using the Kirkendall effect [141]. In particular, they demonstrate the transformation of nanowires into nanotubes using interfacial solid-state reaction of core–shell ZnO–Al_2O_3 nanowires. For this pre-synthesized ZnO nanowires were coated with a alumina layer (10 nm) using ALD at 200 °C followed by annealing at 700 °C in air for 3 h. The high temperature annealing results in interfacial solid-state reaction or kirkendall effect and subsequent diffusion. Employing similar process various nanotubes and hollow nanoparticles have been synthesised [142]. It has been demonstrated that using the ALD along with the kirkendall effect it is possible to introduce superior functionality by design. For example, Guder et al. have shown the

successful conversion of smooth nonpolar ZnO nanowire surfaces to zigzagged high-index polar surfaces as shown in Fig. 3.7 [143]. The resultant zigzagged nanowires with inherent defect-rich high-index polar surfaces exhibited a superior ozone sensing property in particular significantly higher sensitivity (ppb level) as compared to that of nanowires with smooth surfaces and ZnO–ZnO core–shell nanowires.

Superparamagnetism has found profound applications in the field spintronics and bio-applications [144, 145]. It is usually observed in small magnetic nanoparticles, wherein the thermal fluctuations cause magnetization to flip randomly. A transition from superparamagnetism to ferromagnetism usually takes place when the size of the particle is increased. Hence, preparation of supermagnetic oxide thin film instead of nanoparticle is a great challenge. Zhang et al. have successfully synthesized superparamagnetic and ferromagnetic Fe_3O_4 thin films with angstrom level thickness control using ALD [146]. These films exhibited a superparamagnetic behavior with blocking temperature of 210 K which upon post-annealing in H_2/Ar at 400 °C exhibited ferromagnetism. The low-energy growth and self-limiting surface reactions are ideal for the superparamagnetic film depositions.

The technique was also employed effectively to realize carbon nanotubes (CNT) forest [147]. CNT forests or fibres were grown using conformal and active catalyst nanoparticles that can be obtained on concave geometries and/or inner surfaces

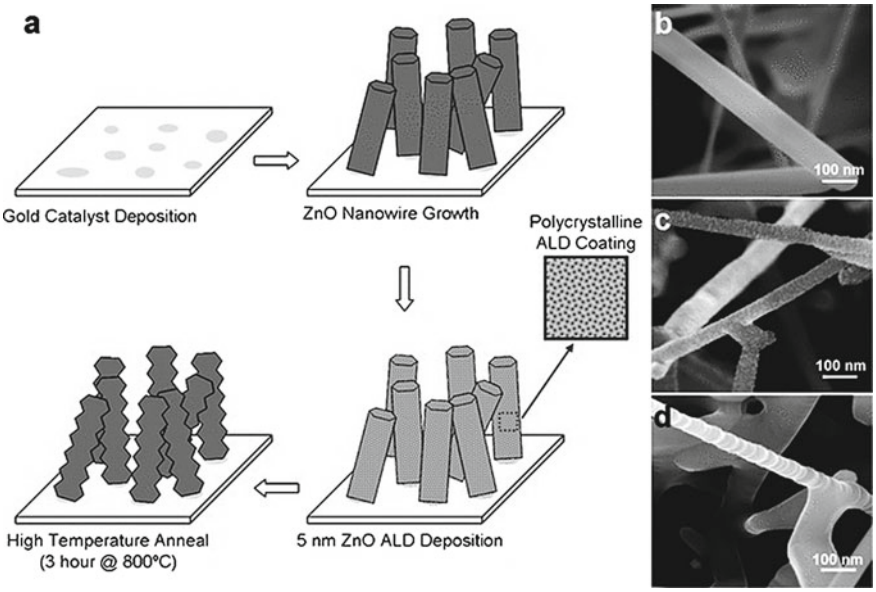

Fig. 3.7 **a** Schematic representation of transformation process of smooth nanowires to zigzagged nanowires. Smooth ZnO nanowires are first coated with thin ZnO layer with subsequent annealling at 800 °C for 3 h in air. SEM images of **b** as-grown nanowires; **c** 5 nm ALD ZnO-coated ZnO core–shell nanowires; **d** ZnO nanowires with zigzagged high-index polar surfaces. Reprinted with permission from F. Güder et al. Small 2012, 8 (21), pp. 3307–3314. Copyright © 2000–2019 by John Wiley & Sons, Inc [143]

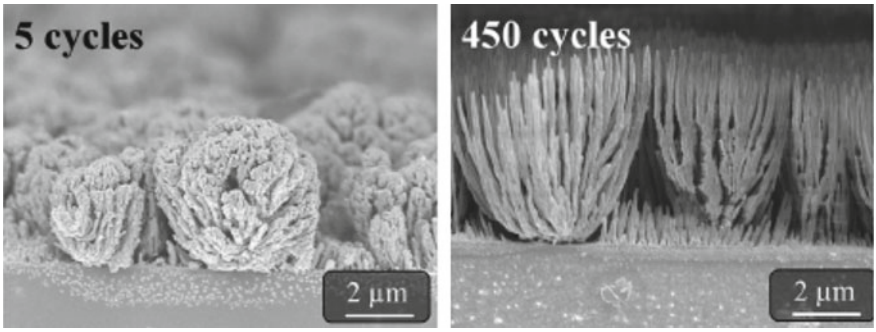

Fig. 3.8 SEM cross section image of 3D nanostructure on the glass substrate formed by applying 5 and 450 silica cycles, respectively. Dose time of TDMAS is 20 ms and plasma dose time is 6 s. Reprinted with permission from M. Zieger et al. Mater. Today Chem. 10 (2018) 112–119. Copyright © 2019, Elsevier [148]

of porous structures using ALD. Zieger et al. demonstrated a new method to generate 3D silver-silica nanostructures using plasma-enhanced ALD of silica with tri(dimethylamino)silane (TDMAS) and oxygen plasma as precursors [148]. For this method, Ag nanoparticles were used as templates, during the deposition of silica, the repeatable process of the formation of metastable silver oxides and their decomposition is involved, leading to strong side reactions and the formation of 3D silver-silica hybrid-nanostructures as shown in Fig. 3.8. This method is known as metastable ALD (MS-ALD). The 3D nanostructures have promising applications in the field of energy harvesting, photo-catalysis, and sensing [149–151].

There are also several disadvantages involved in the use of ALD processes, namely, high cost of the instrument, relatively slower deposition rates, and chemical limitation on the substrate to be used. For example, biological substrates cannot be used owing to there sensitivity towards heat and fast decomposition rates [152].

3.5 Organic Monolayers

This is a novel thin film deposition technique used for realization of organic thin films onto the substrate using chemisorbed organic molecules [153]. The ease with which different functional groups can be anchored, and the technique is highly useful to modify and protect surfaces for desired applications like organic electronic or bioelectronics, wearable, and smart electronics [154–156]. Depending upon the mode of transfer or formation of thin films, the technique is further classified into Self-assembly (SAM) and Langmuir Blodgett (LB) techniques [157].

3.5.1 Langmuir–Blodgett Technique (LB)

One of the daunting challenges in materials science is to achieve designer materials (tailor made) for a specific device application [158]. Langmuir–Blodgett (LB) technique is a good choice for achieving the goal in engineering the molecules which would be building blocks in molecular electronics. It allows highly ordered and ultra-thin growth of organic films. In this method, a one molecule thick layer (Langmuir monolayer) spread at the air–water interface is transferred onto a solid substrate by dipping. A multilayer film can easily be obtained by meagre repetition of the process several times. Herein, first the spreading of insoluble, non-volatile substances is carried out on the surface of a clean liquid having high surface tension, e.g., water. This causes the formation of the insoluble monolayer over the surface. For the molecules possessing a hydrophilic head and a long hydrophobic tail the spreading occurs when molecules are attracted to the water more than themselves. When the surface is sufficiently broad to accommodate all the molecules that are spread, a Langmuir mono layer or one molecule thick film is said to be formed.

These days, researchers are focusing on the single walled carbon nanotubes (SWCNT) since it has much potential in the field of molecular engineering. The chirality of SWCNTs is responsible for its semiconducting or metallic characteristics, and accordingly, it becomes challenging to control the electrical property of SWCNT—based devices (Fig. 3.9). G. H. Nam et al. have studied the modulation of the semiconducting behavior in the CNT LB films based devices by controlling the effective channel dimension [159]. The aligned assembly of a monolayer SWCNT bundle have shown anisotropic electrical properties. In the devices that are formed, the channel dimensions is demonstrated to govern the gating effects. It was further shown that a drastic decrease in the metallic pathway thereby enhancing the semiconducting behavior can be induced by meagre shrinkage of the channel dimension. Using LB, it is possible to grow SWCNT film which is uniform, aligned, and with high packing density.

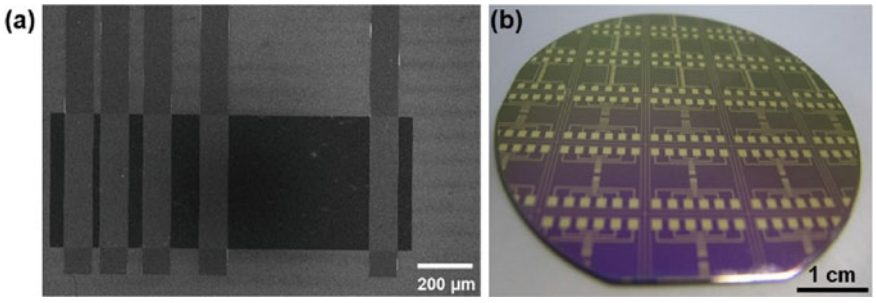

Fig. 3.9 **a** SEM image and **b** Photograph of SWCNT LB film based-devices on 2-inch silicon wafer. Reprinted with permission from G. H. Nam et al. Appl. Surf. Sci. 481 (2019) 540–544, Copyright © 2019, Elsevier [159]

Ziade et al. have described how the LB technique can be used to experimentally determine the thermal interface conductance between polymers and solid substrates [160]. It is a challenge to directly probe the thermal interface conductance between polymers and inorganic materials due to the low thermal conductivity of most polymers. Thickness of the polymer film is important to isolate the thermal interference conductance, and it should be in the order of few nanometres. The LB technique offers a way to repeatedly deposit nanometer-thick films at different phases with a varying degree of chain ordering [161, 162]. Using LB Ziade et al. have grown nanometer-thick films of poly(vinyl acetate) (PVAc) on Si and Au substrates in two distinct states: Liquid condensed (Lc) and Liquid expanded (Le). They used the frequency domain thermo reflectance for thermal conductivity and thermal interface conductance measurements. PVAc films exhibited higher thermal conductivity than bulk and the thermal interface conductance between PVAc and gold, and between PVAc and silicon, were ~90 and 70 MW/m^2K for both the Le and Lc states, respectively. Moreover, the thermal conductivity of the LB films was up to two times the value for bulk PVAc, with the Le phase exhibiting higher thermal conductivity than the Lc phase.

Figure 3.10 shows the total interface conductance ($G_{measured}$) as a function of film thickness for the Lc and Le phases on Si (circles) and Au (squares).

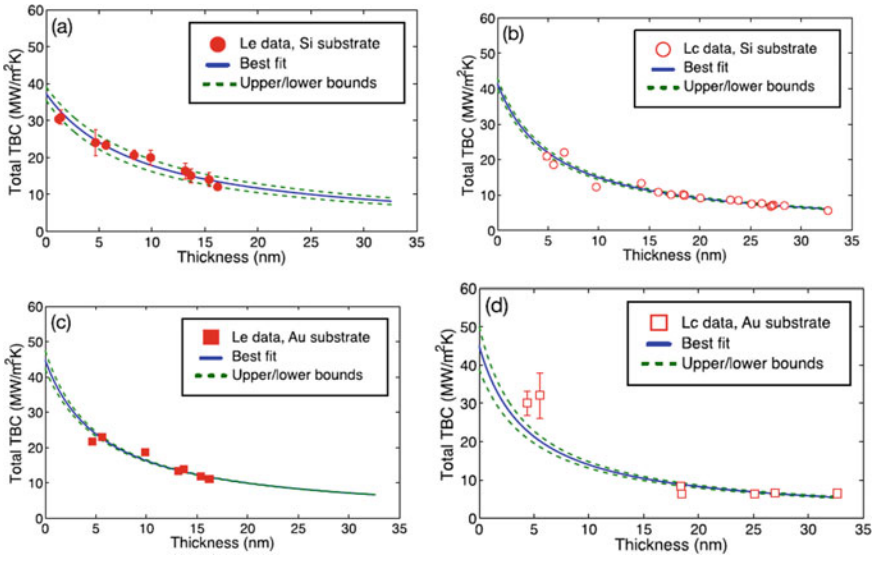

Fig. 3.10 Total interface conductance ($G_{measured}$) as a function of film thickness for the Lc and Le phases on Si (circles) and Au (squares). The solid blue line is the best fit curve to the mean measured values, while the dashed green lines are the best fit curves for the upper and lower values of the error bars. Reprinted with permission from E. Ziade et al. Appl. Phys. Lett. 107, 221603 (2015), Copyright © 2015 AIP Publishing LLC [160]

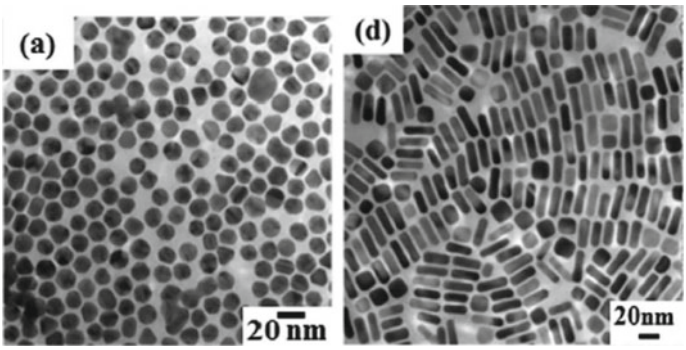

Fig. 3.11 TEM images of gold nanospheres and gold nanorods in LB film. Reprinted with permission from Y. H. Wu et al. Coll, Surf. A 532(2017) 213–221, Copyright © 2019, Elsevier

Another application of LB techniques is in alignment of technological important nanomaterials namely gold nanoparticles. The unique physical, chemical, electrical, and optical properties exhibited by Au nanoparticles have led to their use in industrial and biomedical fields. These nanoparticles can easily be grown into different shapes and sizes [163–166]. Different methods of synthesis namely laser ablation, vapor deposition, electrochemical reaction, and chemical reduction have been investigated to get more characteristic properties. For example; Wu et al. have studied surface enhanced plasmon effects by gold nanospheres and nanorods in LB films [167]. Figure 3.11 shows the TEM image of the gold nanoparticles and nanorods by LB technique. It was found that the film formation using LB raised the red-shift of a plasmon band of nanorods to ~1000 nm. LB helped to realize high coverage and particle density that provided larger enhancement factors with a potential for utilization as photosensitizers and chemo- and biosensors.

LB technique, however, suffers from some demerits like it is a slow process to fabricate thick film, drying time is required after each layer, mechanical and chemical stability of the films is rather poor, and it requires a clean room [167].

3.5.2 Self-Assembled Monolayers (SAMs)

Self-assembled monolayers (SAMs) refers to the close-packed 2-D molecular assemblies of organic molecules that are formed spontaneously on the surfaces by chemisorption. Self assembly involves a chemical interaction like covalent bonding between adsorbed molecules and the surface. The growth of organic SAMs takes place via the spontaneous adsorption from solution onto the substrates like SiO_2 and metal [168]. Although, being just few nanometers in thickness but they can significantly maneuver the surface properties. And accordingly, they have been developed as a powerful molecular platform for interface engineering [169, 170]. SAMs comprise of three main parts: an anchor or head group, a linker and a terminal group.

For example, an α,ω-functionalized alkane, has a head (α) group which is linked with an alkyl chain to a terminal (ω) group [171]. The head groups usually have a specific affinity for a substrate that results in selective formation of chemical bonds with surface atoms of the substrate. Examples include thiolates on gold, silanes on SiO_2, and phosphonic acids on metal oxides. Owing to inter-chain van der Waals interactions that becomes stronger with chain length, the alkyl chains play a critical role in the ordered supramolecular structure formation. The chemical structure of the terminal/surface or tail group determines the surface properties of the SAMs. The structure and properties of resulting SAMs are determined from the chemical composition, monolayer thickness and packing density and molecular ordering and crystallinity. Moreover these can easily be controlled by chemical modification of the anchor group, the terminal group and the linker in and variation of the conditions for adsorption and reaction. Accordingly, they have found application in various fields including molecular electronics [172], control of wetting and adhesion [173], molecular recognition [174], nanofabrication [175], and patterning to realize complex shapes [176–178], and biosensors [179, 180].

Using the principles of SAMs various stable nanoclusters so-called monolayer protected clusters (MPCs) have been realised [181]. The monolayers provides the means not only to control the size, shape, location, and position control but also the structural, morphological, and optoelectronic properties of the resulting nanomaterials [182]. Accordingly, these MPCs have found profound application in numerous fields such as gas sensors [183], bio sensors [184], drug delivery [185], molecular electronics [186, 187], electrocatalyst [188], and study of advanced physics [189].

3.6 Hybrid Approaches for Thin Film Deposition

With the advancement in nanoscience and nanotechnology, there has been an upsurge in the development of novel methodologies that can be effectively employed so as to realize a position and aspect ratio control growth or synthesis of nanostructures. Herein, also the thin film techniques have demonstrated their excellent applicability to realize the desired pattern configurations important for particular applications. For example, using thermal evaporation or spin coating (polystyrene spheres) the seed layer is provided for the growth of nanostructures using either hydrothermal or vapor phase depositions [190]. Bent et al. have demonstrated a unique way to fabricate 3D structures with dimensions down to the nanoscale using combination of ALD and SAM techniques [191]. In particular, a patterned resist, typically a SAM or a polymer can be employed area-selective film deposition through ALD and results in lateral patterning. Importantly, high degree of packing and hydrophobicity of the SAMs forms a means to block growth by ALD. Figure 3.12 summarizes the different steps involved in the fabrication of the patterned thin films using microcontact printing and selective ALD.

In order to realize organic–inorganic hybrid thin films a multiple source based thermal evaporation technique has been effectively employed [192]. Herein, hybrid

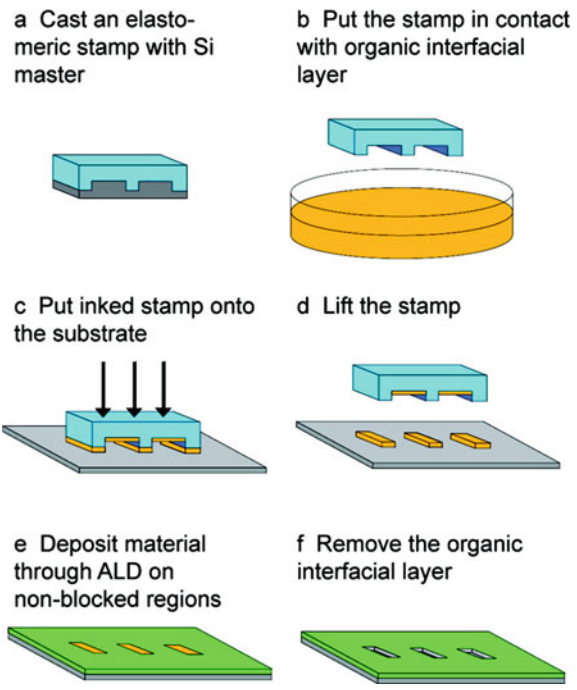

Fig. 3.12 Schematics of the steps to achieve patterned thin films using microcontact printing and selective ALD. Reprinted with permission from X. Jiang et al. J. Phys. Chem. C 2009, 113, 41, 17613–17625, Copyright © 2019 American Chemical Society [191]

films were deposited by thermal evaporation employing a different source each for the organic and inorganic components. Use of different sources enables different power conditions for the two components. Using the approach several hybrid films like copper phthalocyanine (CuPc)/TiOx multilayers [193], phthalocyanato tin(IV) dichloride ($SnCl_2Pc$)/cadmium(II) selenide [194], CuPc/PbTe [195], and 8-hydroxyquinoline aluminum (Alq)/MgF_2 [196], have been achieved.

3.7 Non-conventional Thin Film Techniques

Several non-conventional thin film techniques have also been employed for realizing films for desired applications. Chuang et al. reported a novel ultrasound-assisted supercritical argon electroplating process (US-SC-Ar) with no additives to produce copper metal coatings [197]. Ultrasound applied to electroplating process creates cavitation phenomena resulting in particle de-agglomeration, enhanced mass transfer, increased nucleation rates and thus, cleaner deposits with finer grain sizes [198, 199]. Introduction of ultrasound accelerates metal ion mobility, yielding densely-packed structures with finer grains and better aesthetic finish. Temperature of 35 °C, pressure of 2500 psi, current density of 5 A/dm^2, and acoustic power density of 0.094 W/cm^3, produced coatings with enhanced mechanical and corrosion behavior

compared to those produced by conventional or silent SC-Ar processes. Chuang et al. demonstrated a novel method of fabrication for the high aspect ratio NiP nanowires using blind-hole anodic aluminium oxide (AAO) templates by supercritical (sc)-CO_2 electroless plating method (SC-ELP) [200]. Using the method 1D NiP nanowires with relatively high AR were easily obtained.

Huet et al. demonstrated a reproducible and scalable way to realize high quality graphene film on thin Cu substrates using a pressure-controlled CVD [201]. Using the technique single-layer graphene with millimeter-size domains crucial for various device applications was easily obtained.

3.8 Transfer of Thin Films from One Substrate to Another

There are certain applications like optoelectronics and high frequency/power electronics that demands the transfer of thin films from one substrate to another [202]. Herein the films with desired properties are first grown on to the substrates (single crystal) and later are removed and transferred onto the foreign substrates like silicon, polycrystalline metal, glass, and transparent plastics for achieving the device configuration [203]. For instance, single crystal nitride films can easily be grown onto crystalline substrates while it is very difficult to grow them onto polycrystalline or amorphous substrates. Accordingly, the films grown onto the crystalline substrates demands their release and transfer to suitable foriegn substrates to realize device application. Generally, the films are first deposited onto the buffer layers such as aluminium nitride (AlN), galium nitride(GaN), aluminium oxynitride (AlON), graphite, graphene, hexagonal boron nitride (h-BN), and ZnO [204, 205]. The release and transfer of the films is then achieved employing thermal, chemical, and mechanical techniques. For example, Kobayashi et al. have reported the successful transfer of the multiple quantum well structures grown onto h-BN buffer substrate using mechanical force and indium sheet as an adhesive layer for the transfer onto the foreign substrates [206].

3.9 Future Prospects and Conclusion

From the above discussion it is evident that with advancement in nanoscience and nanotechnology, thin film techniques both conventional and un-conventional have evolved to cope up with this increasing field. Thin film techniques offering advantages like flexibility of precursors, control over process parameters, possibility of bulk production, excellent compatibility with CMOS technique and above all cost have not only sustained the advancement but also contributed enormously for synthesis novel functional advanced materials. Besides, these techniques have paved the way for realizing a complete device with industrially acceptable standards. Importantly, the advanced materials synthesised have demonstrated an excellent, enhanced, and

desired functionalities. To achieve these most of the techniques have to undergo course correction and some have to be used in conjunction with other. All these points clearly illustrate the fact that the thin film techniques are the fundamental backbones for not only the synthesis of advanced material but also in realizing a potential, complete, and commercially acceptable devices. Thus, thin film techniques have hold the promise for the present and are expected to contribute enormously for future device applications also.

Acknowledgements One of the authors, KRS, would lilke to thank CSIR-UGC fellowship for JRF. The authors also thank the support from Dr. K. P. Muthe and Dr. T. V. C. Rao, TPD, BARC.

References

1. Jiang C, Tsui DC, Weimann G (1988) Appl Phys Lett 53:1533
2. Aoki H (2011) 1.05 - Integer Quantum Hall Effect, in Reference Module in Materials Science and Materials Engineering, Comprehensive Semiconductor Science and Technology, 1, 175–209
3. Berger C, Song Z, Li T, Li X, Ogbazghi AY, Feng R, Dai Z, Marchenkov AN, Conrad EH, First PN, de Heer WA (2004) J Phys Chem B 108:19912–19916
4. Novoselov KS, Falko VI, Colombo L, Gellert PR, Schwab MG, Kim K (2012) Nature 490:192–200
5. Wahyuningsih S, Fadillah G, Hidayat R, Ramelan AH (2016) Procedia Chem 19:632–637
6. Yamadan Y, Kitamura S, Miura M, Yoshimura K (2015) Solar energy mater. Solar Cells 141:337–340
7. Li J, Zhou Y-H, Zhu W-Q, Zhang J-H, Zhang Z-L (2019) Mater Sci Semi Proc 93:201–207
8. Hill DJ, Cahoon JF (2017) Mater Matt 12:1
9. Hobbs RG, Petkov N, Holmes JD (2012) Chem Mater 24(11):1975–1991
10. Pan C, Luo Z, Xu C, Luo J, Liang R, Zhu G, Wu W, Guo W, Yan X, Xu J, Wang ZL, Zhu J (2011) ACS Nano 5:6629–6636
11. Pennelli G (2009) Microelectron Eng 86:2139–2143
12. Ramgir NS, Subannajui K, Yang Y, Grimm R, Michiels R, Zacharias M (2010) J Phys Chem C 114:10323–10329
13. Subannajui K, Ramgir N, Grimm R, Michiels R, Yang Y, Müller S, Zacharias M (2010) Cryst Growth Des 10:1585–1589
14. Chopra KL, Major S, Pandya DK (1983) Thin Solid Films 102:1–46
15. Chopra KL (1969) Thin film phenomena. McGraw-Hill, OCLC 499963884, p 864
16. Shanthi E, Pandya DK, Chopra KL (1978) Transparent conducting coatings for solar cells. Sun: Mankind's Future Source Energy 2:698–702
17. Major S, Chopra KL (1988) Indium-doped zinc oxide films as transparent electrodes for solar cells. Solar Energy Mater 17:319–327
18. Chopra KL (1983) Thin film device applications. Springer, ISBN, p 9780306412974
19. Faadam SF, Mustafa MH, Hussein A, AlRazak, Shihab AS (2019) Energy Procedia 157:635–643
20. Zhang M, Li LV, Wei Z, Guo C, Yang X (2014) Mater Lett 123:87–89
21. Wang S, Li X, Wu J, Wen W, Qi Y (2018) Curr Opin Electron Chem 11:130–140
22. Liu M, Johnston MB, Snaith HJ (2013) Nature 501:395–398
23. Ke W, Zhao D, Cimaroli AJ, Grice CR, Qin P, Liu Q, Xiong L, Yang Y, Fang G (2015) J Mater Chem A 3:24163–24168

24. Ke W, Zhao D, Grice CR, Cimaroli AJ, Fang G, Yang Y (2015) J Mater Chem A 3:23888–23894
25. Malinkiewicz O, Carmona CR, Soriano A, Bandiello E, Camacho L, Nazeeruddin MK, Bolink HJ (2014) Adv Energy Mater 4:1400345
26. Ma Q, Huang S, Wen X, Green MA, Ho-Baillie AWY (2016) Adv Energy Mater 6(7):1502202
27. Navale YH, Navale ST, Ramgir NS, Stadler FJ, Gupta SK, Aswal DK, Patil VB (2017) Sens Actuators B 251:551–563
28. Ingole SM, Navale ST, Navale YH, Bandgar DK, Stadler FJ, Mane RS, Ramgir NS, Gupta SK, Aswal DK (2017) J Coll Interface Sci 493:162–170
29. Ramgir NS, Ganapathi SK, Kaur M, Datta N, Muthe KP, Aswal DK, Gupta SK, Yakhmi JV (2010) Sens Actuators B 151:90–96
30. Ramgir NS, Datta N, Kumar S, Ganapathi SK, Patil UV, Karmakar N, Kaur M, Debnath AK, Kothari DC, Aswal DK, Gupta SK (2015) Mater Chem Phys 156:227–237
31. Datta N, Ramgir NS, Kaur M, Ganapathi SK, Debnath AK, Aswal DK, Gupta Sen SK (2012) Actuators B 166–167:394–401
32. Xu K (2014) Chem Rev 114:11503–11618
33. Park K, Yu BC, Goodenough JB (2016) Adv Energy Mater 6:1502534
34. Abouimrane A, Cui Y, Chen Z, Belharouak I, Yahia HB, Wu H, Assary R, Curtiss LA, Amine K (2016) Nano Energy 27:196–201
35. Bie Y, Yang J, Wang J, Zhou J, Nuli Y (2017) Chem Comm 53:8324
36. Yang J-H, Myong SY, Lim KS (2014) IEEE Electron Device Lett 35:102–104
37. Zhu Z, Tang Y, Lv Z, Wei J, Zhang Y, Wang R, Zhang W, Xia H, Ge M, Chen X (2018) Angew Chem 57(14):3656–3660
38. Pan G, Wang D, Gao S, Gao P, Sun Q, Liu X, Zhou Z, Sun Y, Zhang Y (2019) Sol Energy 182:64–71
39. Fan HJ, Werner P (2006) M. Zacharias. Small 2:700–717
40. Kim DS, Scholz R, Gösele U, Zacharias M (2008) Small 4:1615–1619
41. Subannajui K, Wongchoosuk C, Ramgir NS, Wang C, Yang Y, Hartel A, Cimalla V, Zacharias M (2012) J Appl Phys 112:034311
42. Ramgir NS, Subannajui K, Yang Y, Grimm R, Michiels R, Zacharias M (2010) J Phys Chem C 114(23):10323–10329
43. Subannajui K, Güder F, Zacharias M (2011) Nano Lett 11(9):3513–3518
44. Youn SK, Ramgir NS, Wang C, Subannajui K, Cimalla V, Zacharias M (2010) J Phys Chem C 114:10092–10100
45. Nistor M, Gherendia F, Perrière J (2018) Mater Sci Semi Proc 88:45–50
46. Merkel JJ, Sontheimer T, Rech B, Becker C (2013) J Crystal Growth 367:126–130
47. Schulz U, Terry SG, Levi CG (2003) Mater Sci Eng A 1–11
48. Ahmad MT, Muhammad AR, Haris H, Rahim HRA, Zakaria R, Ahmad H, Harun SW (2019) Optik 182:241–248
49. Raso MA, Carrillo I, Navarro E, Garcia MA, Mora E, Leo TJ (2015) Int J Hydro Energy 40:11315–11321
50. Chen J, Shen H, Zhai Z, Li Y, Yi Y (2018) Appl Surf Sci 433:271–278
51. Tanusevski A, Poelman D (2003) Solar Energy Solar Cells 80:297–303
52. Chang S, Sivoththaman S (2006) J Micromech Microeng 16(7):1307
53. Michael A, Kwork CY, Wang P, Kazuo O, Varlamov S (2015) J MEMS 24(6):1951–1959
54. Joseph J, Singh SG, Vanjari SRK (2017) Mater Lett 197:52–55
55. Gnanavel S, Ponnuswamy S, Mohan L, Kalisz M, Grobelny M, Kaczmarek D, Domaradzki J, Mazur M, Wojcieszak D (2017) Appl Surf Sci 421:185–190
56. Kalisz M, Grobelny M, Kaczmarek D, Domaradzki J, Mazur M (2017) D. Wojcieszak. Appl Surf Sci 421:185–190
57. Mazur M, Kalisz M, Domaradzki J, Grobelny M, Wojcieszak D, Kaczmarek D, Poniedziatek A (2016) Surf Coat Tech 307:502–596
58. Mortimer RJ, Dyer AL, Reynolds JR (2006) Displays 27(1):2–18
59. Yang P, Sun P, Mai W (2016) Mater Today 19(7):394–402

60. Deb SK (1992) Sol Energy Mater Sol Cells 25:327–338
61. Yang L, Ge D, Zhao J, Ding Y, Kong X, Li Y (2012) Sol Energy Mater Sol Cells 100:251–257
62. Kostis I, Vasilopoulou M, Soultati A, Argitis P, Konofaos N, Douvas AM, Vourdas N, Papadimitropoulos G, Davazaoglou D (2013) Microelectron Eng 111:149–153
63. Karaca GY, Eren E, Cogal GC, Uygun E, Oksuz L, Oksuz AU (2019) Opt Mater 88:472–478
64. Zaenchkovsky PV, Makarov OY (2009) Proc Voronezh State Technical University 7
65. Yushkov YG, Oks EM, Tyunkov AV, Zolotukhin DB (2019) Cer Inter 45:9782–9787
66. Oks EM, Tyunkov AV, Yushkov YG, Zolotukhin DB (2017) Surf Coat Tech 325:1–6
67. Tveryanovich YS, Razumtcev AA, Fazletdinov TR, Tverjanovich AS, Borisov EN (2018) Thin Solid Films 666:172–176
68. Fokina SV, Borisov EN, Tomaev VV, Tumkin II, Tveryanovich YS (2016) Solid State Ionics 297:64–67
69. Jilani S, Abdel-wahab MS, Hammad AH (2017) Advance deposition techniques for thin film and coating, Intech Open Access Book Chapter 8
70. Lowndes DH, Geohegan DB, Puretzky AA, Rouleau CM (1996) Science 273(5277):898–903
71. Ashfold MNR, Claeyssens F, Fuge GM, Henley SJ (2004) Chem Soc Rev 33(1):23–31
72. Luo CQ, Ling FCC, Rahman MA, Phillips M, Ton-That C, Liao C, Shih K, Lin J, Tam HW, Djurišić AB, Wang SP (2019) Appl Surf Sci 483:1129–1135
73. Kato H, Miyamoto K, Sano M, Yao T (2004) Appl Phys Lett 84:4562–4564
74. Shaji S, Vinayakumar V, Krishnan B, Johny J, Sharma Kanakkillam S, Flores Herrera JM, Sepulveda Guzman S, Avellaneda DA, Castillo Rodriguez GA, Aguilar Martinez JA (2019) Appl Surf Sci 476: 94–106
75. Mwafy EA, Mostafa AM (2019) Opt Laser Tech 111:249–254
76. Bricchi BR, Ghidelli M, Mascaretti L, Zapelli A, Russo V, Casari CS, Terraneo G, Alessandri I, Ducati C, Bassi AL (2018) Mater Des 156:311–319
77. Farag AAM, Ashery A, Zaki AH, Hussein Mourad M (2019) Chin J Phys 59:83–91
78. Krogstrup P, Ziino NLB, Chang W, Albrecht SM, Madsen MH (2015) Nat Mater 14:400–406
79. Tchoe Y, Jo J, Kim M, Yi GC (2015) NPG Asia Mater 7:e206
80. Chang YL, Li F, Fatehi A, Mi Z (2009) Nanotech 20:345203
81. Wu J, Walukiewicz W, Shan W, Yu KM, Ager JW, Haller EE, Lu H, Schaff WJ (2002) Phys Rev B 66:1257
82. Weiszer S, Zeidler A, Mata M, Stutzmann M (2019) J Cryst Growth 510:56–64
83. Gu R, Antoszewski J, Lei W, Madni I, Umana-Membrenao G, Faraone L (2017) J Cryst Growth 468:216–219
84. Tanaka T, Ohshita H, Saito K, Guo Q (2018) Superlattices Microstruct 114:192–199
85. Zhu H, Dong Z, Niu X, Li J, Wan M, Shen K, Mai Y (2019) Appl Surf Sci 465:48–55
86. Lee YJ, Park HW, Park S, Song IK (2012) Curr Appl Phys 12(1):233–237
87. Mao L, Zhang K, Chan HSO, Wu J (2012) J Mater Chem 22(1):80–85
88. Kumar A, Sanger A, Kumar A, Kumar Y, Chandra R (2016) Electrochim Acta 222:1761–1769
89. Kim JY, Lee SH, Yan Y, Oh J, Zhu K (2012) RSC Adv 2:8281–8285
90. Hu CC, Chang KH, Lin MC, Wu YT (2006) Nano Lett 6:2690–2695
91. Park S, Kim S (2003) Electrochim Acta 89:516–522
92. Yang L, Hauqing X, Jing L, Jifen W (2013) Mater Lett 102:30–32
93. Sanger NA, Malik VK, Chandra R (2018) Int J Hydro Energy 43:11141–11149
94. Liu J, Essner J, Li J (2010) Chem Mater 22:5022–5030
95. Yu L, Zhang G, Yuan C, Lou XW (2013) Chem Comm 49:137–139
96. Reddy RN, Reddy RG (2004) J Power Sources 132:315–320
97. Toupin M, Brousse T, Belanger D (2004) Chem Mater 169:3184–3190
98. Gomez J, Kalu EE (2013) J Power Sources 230:218–224
99. Hou X, Li Q, Zhang L, Yang T, Chen J, Su L (2018) J Power Sources 396:319–326
100. Gao B, Xiao X, Su J, Zhang X, Peng X, Fu J (2016) Appl Surf Sci 383:57–63
101. Shah SIU, Hector AL, Owen JR (2014) J Power Sources 266:456–463
102. Wang P, Wang R, Lang J, Zhang X, Chen Z, Yan X (2016) J Mater Chem 4:9769–9776
103. Wei B, Mei G, Liang H, Qi Z, Zhang D, Shen H (2018) J Power Sources 385:39–44

104. Prakash R, Kumar A, Pandey A, Kaur D (2019) Int J Hydro Energy 44:10823–10832
105. Shang H, Ding F, Li G, Wang L, Qu F, Zhang H, Dong Z, Zhang H (2017) J Alloys Compd 726:532–537
106. Yamauchi K, Takashir M (2017) J Alloys Compd 698:977–983
107. Somdock N, Kianwimol S,Harnwunggmoung A, Sakulkalavek A, Sakdanuphab R (2019) J Alloys Compd 773:78–85
108. Le PH, Liao CN, Luo CW, Leu J (2014) J Alloys Compd 615:546–552
109. Nuthongkum P, Sakdanuphab R, Horprathum M, Sakulkalavek A (2017) J Electron Mater 46(11):6444–6450
110. Kim DH, Byon E, Lee GH, Cho S (2006) Thin Solid Films 510:148–153
111. Kim DH, Lee GH (2006) Mater Sci Eng B 131:106–110
112. Huang H, Luan WL, Tu ST (2009) Thin Solid Film 517:3731–3734
113. Gomes L, Marques A, Branco A, Araujo J, Simoes M (2013) Displays 34:326–333
114. Baptista A, Silva FJG, Porteiro J, Miguez JL, Pinto G, Fernandes L (2018) Proc Manufact 17:746–757
115. Mahmood A, Naeem A, In Recent Applications in Sol-Gel Synthesis, Ch. 9, Sol-Gel-Derived Doped ZnO Thin Films: Processing, Properties, and Applications, 169–193. https://doi.org/10.5772/67857
116. Bahuguna G, Mishra NK, Chaudari P, Kumar A, Singh R (2016) Res J Chem Sci 6(7):65–72
117. Leitzke CW, Cholant CM, Landarin DM, Lucio CS, Krüger LU, Gündel A, Flores WH (2019) Thin Solid Films 683:8–15
118. Nataraj JR, Bagali PY, Krishna M, Vijayakumar MN (2018) Mater Today Proc 5:10670–10680
119. Garcia RP, Delgado A, Guerra Y, Hernandez EP (2015) Mater Lett 161:384–386
120. Sambasivam, Kim SB, Jeong JH, Choi BC, Lim KT, Kim SS, et al (2010) Curr Appl Phys 10:1383–1386
121. Cui L, Hu YJ (2009) Phys B 404:150–153
122. Yoon JW, Choi SH, Kim JS, Jang HW, Kang YC, Lee JH (2016) NPG Asia Mater 8:244
123. Yoon JW, Choi SH, Kim JS, Jang HW, Kang YC, Lee JH (2016) NPG Asia Mater 8:e244
124. Park GD, Ko YN, Kang YC (2014) Conf Proc A Proc Energy (4) 5785
125. Leng J, Wang Z, Wang J, Wu HH, Yan G, Li X, Guo H, Liu Y, Zhang Q, Guo Z (2019) Chem Soc Rev, Advance Article, https://doi.org/10.1039/C8CS00904J
126. Cho JS, Won JM, Lee J-K, Kang YC (2016) Nano Energy 26:466–478
127. Kim D-Y, Ghodake GS, Maile NC, Kadam AA, Lee DS, Fulari VJ, Shinde SK (2017) Sci Rep 7:9764
128. Guo S, Zhang X, Ding G, Chen R, Lee D, Yan A (2014) J Appl Phys 115:17A754
129. Stassen I, Styles M, Grenci G, Gorp HV, Vanderlinden W, Feyter SD, Falcaro P, Vos DD, Vereecken P, Ameloot R (2016) Nat Mater 15:304–310
130. Stassen, Campagnol N, Fransaer J, Vareeckan P, Vos DD, Ameloot R (2013) Cryst Eng Commun 15:9308–9311
131. Khaletskaya K, Turner S, Tu M, Wannapaiboon S, Schneemann A, Meyer R, Ludwig A, Tendeloo GV, Fischer RA (2014) Adv Func Mater 24:4804–4811
132. Allen P, Zhou L, Zhao C, Zhao C, Rao PM (2016) Nat Sci Rep 6:27832
133. Liu SJ, Zou YC, Shi XL, Li QZ, Yang YZ, Liu WD, Chen Z-G, Zou J (2019) J Alloys Compd 777:926–930
134. Zhang S, Wang J, Lu Y, Hou W, Cao K, Guo S, Wang Z, Wang L (2019) Chem Phys 523:106–109
135. Zhang Y, Zhang YF, Ji QQ, Ju J, Yuan HT, Shi JP, Gao T, Ma DL, Liu MX, Chen YB, Song XJ, Hwang HY, Cui Y, Liu ZF (2013) ACS Nano 7:8963–8971
136. Miikkulainen V, Leskelä M, Ritala M, Puurunen RL (2013) J Appl Phys 113(2):021301
137. Mackus J, Adriaan M, Schneider JR, MacIsaac C, Baker JG, Bent SF (2018) Chem Mater 31(4):1142–1183
138. George SM (2010) Chem Rev 110(1):111–131
139. Kim H (2003) J Vacuum Sci Tech 21(6):2231
140. Pang C, Lee C, Suh K-Y (2013) Appl Poly Sci 130(3):1429–1441

141. Fan HJ, Knez M, Scholz R, Nielsch K, Pippel E, Hesse D, Zacharias M, Gçsele U (2006) Nat Mater 5:627
142. Fan HJ, Gçsele U, Zacharias M (2007) Small 3:1660–1671
143. Güder F, Yang Y, Menzel A, Wang C, Danhof J, Subannajui K, Hartel A, Hiller D, Kozhummal R, Ramgir NS, Cimalla V, Schwarz UT, Zacharias M (2012) Small 8:3307–3314
144. Nam JM, Thaxton CS, Mirkin CA (2003) Science 301:1884
145. Hoffmann C, Mazari E, Lallet S, Borge RL, Marchi V, Gosse C, Gueroui Z (2013) Nat Nanotech 8:199–205
146. Zhang Y, Liu M, Zhang Y, Chen X, Ren W, Ye ZG (2015) J Appl Phys 117(17):17C743
147. Chen B, Zhang C, Esconjauregui S, Xie R, Zhong G, Bhardwaj S, Cepek C, Robertson J (2014) J Appl Phys 115:144303
148. Zieger M, Yuksel S, Goerke S, Cialla-may D, Hubner U, Wang D, Schmidt H, Schaaf P (2018) Mater Today Chem 10:112–119
149. Na JS, Gong B, Scarel G, Parsons GN (2009) ACS Nano 3:3191
150. Langer A, Knez M, Muller F, Gosele U (2008) Appl Phys A 93:399
151. Park JY, Choi SW, Lee JW, Lee C, Kim SS (2009) J Am Ceram Soc 92:2551
152. Leskelä M, Ritala M (2003) Angew Chem 42(45):5548–5554
153. Lingenfelser D, Hess P (2007) J Phys Chem C 111(26):9250–9254
154. Arias AC, MacKenzie JD, McCulloch I, Rivnay J, Salleo A (2010) Chem Rev 110:3–24
155. Rivnay J, Owens RM, Malliaras GG (2014) Chem Mater 261:679–685
156. Huang L, Hu X, Chi L (2015) Langmuir 31:9748–9761
157. Moehwald H, Brezesinski G (2016) Langmuir 32:10445–10458
158. Oliveira ON Jr (1992) Braz J Phys 22:2
159. Nam GH, Kim KS, Park SH, Kim HS, Ahn DH, Kim JH, Lee JH (2019) Appl Surf Sci 481:540–544
160. Ziade E, Goni M, Sato T, Czubarow P, Schmidt AJ (2015) Appl Phys Lett 107:221603
161. Manyes SG, Domenech O, Sanz F, Montero MT, Hernandez-Borrell J (2007) Biochim Biophys Acta 1768:1190
162. Albrecht O, Gruler H, Sackmann E, Albrecht O, Gruler H, Sackmann E (1978) J Phys France 39:301
163. Mafuné F, Kohno J, Takeda Y, Kondow T, Sawabe H (2001) J Phys Chem B 105:5114–5120
164. Manna A, Imae T, Yogo T, Aoi K, Okazaki M (2002) Coll Int Sci 256:297–303
165. Santos IP, Gomez D, Pérez-Juste J, Liz-Marzán LM, Mulvaney P (2004) Phys Chem Chem Phys 6(21):5056–5060
166. Sharma J, Tai Y, Imae T (2008) J Phys Chem C 112:17033–17037
167. Wu YH, Imae T, Ujihara M (2017) Coll Surf A 532:213–221
168. Greene JE (2015) Appl Phys Rev 2:011101
169. Liu D, Miao Q (2018) Mater Chem Front 2:11–21
170. Dong H, Jiang L, Hu W (2012) Phys Chem Chem Phys 14:14165
171. Ulman A (1996) Chem Rev 96:1533
172. Maheshwari P, Mukherjee S, Bhattacharya D, Sen S, Tokas RB, Honda Y, Basu S, Padma N, Pujari PK, Appl ACS (2015) Mater Interfaces 7:10169
173. Laibinis PE, Whitesides GM, Allara DL, Tao YT, Parikh AN, Nuzzo RG (1991) J Am Chem Soc 113:7152–7167
174. Noyhouzer T, Mandler D (2011) Anal Chim Acta 684:1–7
175. Schwartz DK (2001) Annu Rev Phys Chem 52:107–137
176. Seong JK (2007) Nanoscale Res Lett 2:519–545
177. Aslam M, Mulla IS, Vijayamohanan K (2001) Langmuir 17(24):7487–7493
178. Mizuno H, Buriak JM (2009) J Am Chem Soc 130(52):17656–17657
179. Smith RK, Lewis PA, Weiss PS (2004) Prog Surf Sci 75:1–68
180. Gao Y, Koumoto K (2005) Cryst Growth Des 5:1983–2017
181. Templeton AC, Wuelfing WP, Murray RW (2000) Acc Chem Res 33:27–36
182. Colangelo E, Comenge J, Paramelle D, Volk M, Chen Q, Lévy R (2017) Bioconjugate Chem 28(1):11–22

183. Saha K, Agasti SS, Kim C, Li X, Rotello VM (2012) Chem Rev 112(5):2739–2779
184. Sekhar PK, Ramgir NS, Bhansali S (2008) J Phys Chem C 112(6):1729–1734
185. Rana S, Bajaj A, Mout R, Rotello VM (2012) Adv Drug Delivery Rev 64:200–216
186. Park J, Pasupathy AN, Goldsmith JI, Chang C, Yaish Y, Petta JR, Rinkoski M, Sethna JP, Abruña HD, McEuen PL, Ralph DC (2002) Nature 417:722
187. Gittins DI, Bethell D, Schiffrin DJ, Nichols RJ (2000) Nature 408(6808):67–69
188. Pietron JJ, Murray RW (1999) J Phys Chem B 103(21):4440–4446
189. Halperin WP (1986) Rev Mod Phys 58(3):533–606
190. Youn SK, Ramgir N, Wang C, Subannajui K, Cimalla V, Zacharias M (2010) J Phys Chem C 114(22):10092–10100
191. Jiang X, Bent SF (2009) J Phys Chem C 113(41):17613–17625
192. Mitzi DB (2001) Chem Mater 13(10):3283–3298
193. Akada J, Awaji H, Koshioka M, Nakajima A, Nevin WA (1992) Appl Phys Lett 61:2184
194. Imanishi Y, Ishihara S, Hamada T (1998) Mol Cryst Liq Cryst 315:111
195. Lee H, Kang Y, Choi B, Jeong J, Tabata H, Kawai T (1999) J Korean Phys Soc 34:S64
196. Tokito S, Sakata J, Taga Y (1994) Appl Phys Lett 64(11):1353–1355
197. Chuang H, Sanchez J (2019) Mater Lett 243:54–57
198. Tudela I, Zhang Y, Pal M, Kerr I, Cobley A (2014) Surf Coat Tech 259:363–373
199. Coleman S, Roy S (2014) Chem Eng Sci 113:35–44
200. Chuang HC, Chang TS, Sanchez J (2019) Mater Lett 236:657–660
201. Huet B, Raskin J-P (2017) Chem Mater 298:3431–3440
202. Ningthoujam RS, Gajbhiye NS (2015) Prog Mater Sci 70:50–154
203. Cho CY, Lee SJ, Hong SH, Park SC, Park SE, Park Y, Park SJ (2011) Appl Phys Express 4:012104
204. Ahn J-H, Kim H-S, Lee KJ, Jeon S, Kang SJ, Sun Y, Nuzzo RG, Rogers JA (2006) Science 314(2006):1754–1757
205. Rogers DJ, Hosseini Teherani F (2007) Appl Phys Lett 91:071120
206. Kobayashi Y, Kumakura K, Akasaka T, Makimoto T (2012) Nature 484:223–227

Chapter 4
Inkjet Printing of Nanomaterials and Nanoinks

O. D. Jayakumar and A. K. Tyagi

Abstract Research on nanomaterials has become a fascinating branch of science in recent years as it offers tremendous opportunities for surprising discoveries due to the size-dependent properties of nanoparticles. The properties of nanoparticles completely differ from their corresponding bulk counterparts and gradually changes with size and shape, and hence find extensive applications in new advanced smart and intelligent technologies. Development of new dimensional-dependent advanced materials needs novel and controlled synthsesis methods and advanced characterization techniques, in addition to new theories and models, to explain the experimental observations posing challenges to the scientists and engineers. This article focuses mainly on yet another new method of synthesis and fabrication of some inorganic materials using chemistry of nanoink development and its subsequent inkjet printing to form nanostructures. It provides balanced and brief coverage of the fundamentals and processing techniques with regard to the above synthesis routes and characterization techniques. It also gives a first-hand information about the recent technology of 3D printing. This chapter is written with an intention to serve as a general introduction to nonmaterial's synthesis by nanoink printing methods. The article ends with the future of inkjet printing technology and by introducing 4D printing where 4th dimension is time.

Keywords Nanomaterials · Nanoink · Inkjet printing · Magnetic materials · Semiconductors

O. D. Jayakumar · A. K. Tyagi (✉)
Chemistry Division, Bhabha Atomic Research Centre, Mumbai 400085, India
e-mail: aktyagi@barc.gov.in

O. D. Jayakumar
e-mail: ddjaya@barc.gov.in

A. K. Tyagi
Homi Bhabha National Institute, Mumbai 400094, India

A. K. Tyagi and R. S. Ningthoujam (eds.), *Handbook on Synthesis Strategies for Advanced Materials*, Indian Institute of Metals Series,
https://doi.org/10.1007/978-981-16-1803-1_4

4.1 Overview of Printing Technology

4.1.1 Introduction

The process of positioning of an ink droplet of miniature volume that is correlated with an image, on a pre-treated substrate, is called Digital printing. This printing process, can be used for the low-cost deposition of functional or non-functional materials, on preferred locations on a substrate with diameters in μm range, which nearly matches with nozzle diameter. The minimum volume of the ink droplets that can be printed can be as small as picolitre. Inkjet printing technique is an advanced digital fabrication process for the modern flexible electronics because of many reasons like:

1. Inkjet printing deposits required materials selectively drop-by-drop on a substrate by a non-contact method.
2. It is a low-cost method and needs only small working space.
3. It is suitable for industrial production of prototypes.
4. Minimum wastage of ink.
5. It can print different structures and thin films, which are key for organic electronics.

The process of direct printing of advanced functional materials has emerged as an alternative technology to conventional integrated circuit (IC) development particularly in developing cost-effective flexible electronics. Among few direct printing techniques [1–3], Drop-On-Demand (DOD) inkjet printing is being rapidly growing as an attractive patterning technique for large field of applications like organic electronics [1], nanotechnology [2], flexible electronics [2] and tissue engineering [3]. Inkjet printing technique, a non-contact and digitally controlled technique, is based on the ejection of ink drops through fine nozzle directly to a pre-decided position. Inkjet printing can produce and repeatedly dispense spheres of ink with diameters in μm range. Figure 4.1 shows different kinds of materials and devices that can be printed using printing technologies. Inkjet printing is commercially classified as continuous and Drop-On-Demand (DOD). DOD is further mainly subdivided as thermal and piezoelectric. Further subdivisions are given in Fig. 4.2. Continuous inkjet printing is very useful in industrial environment because its printing speed is quite high. Further, the printing nozzle does not easily get clogged as the ink droplets are continuously generated and volatile inks are allowed to dry rapidly. In spite of these advantages, continuous inkjet printing suffers from some major disadvantages like (1) low resolution due to the high-speed of printing; (2) only charged inks can be printed; and (3) high cost of maintenance.

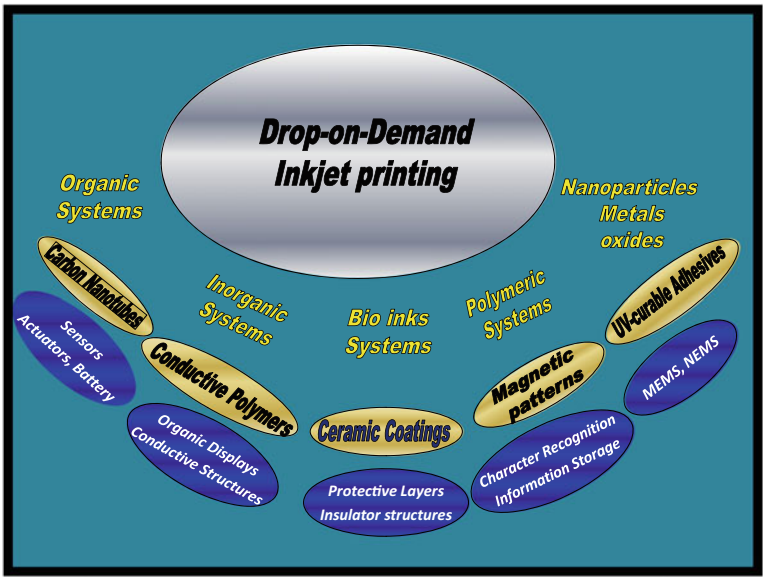

Fig. 4.1 The typical examples of inkjet printing technology

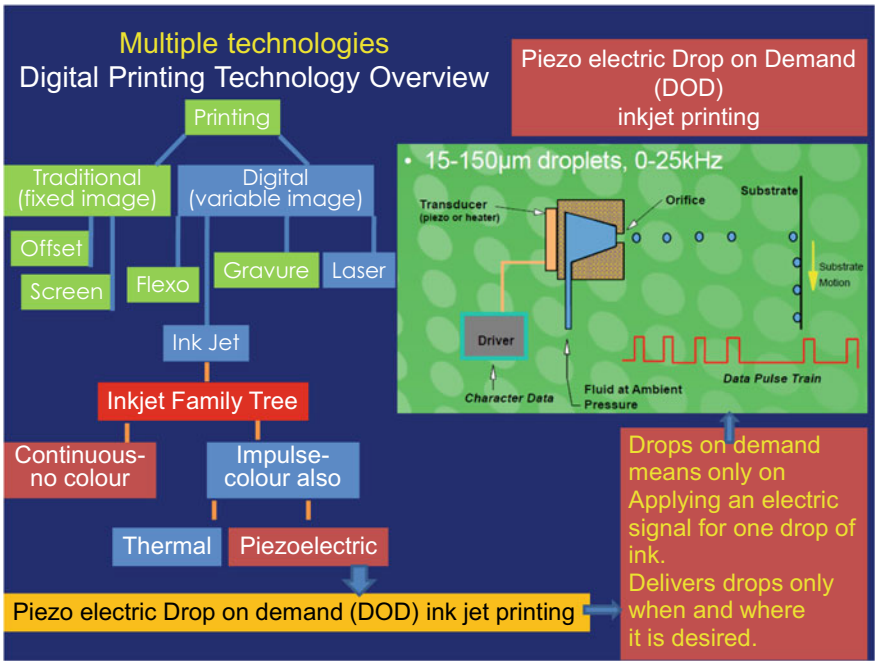

Fig. 4.2 Different kinds of printing technologies

4.1.2 Drop-On-Demand Inkjet Printing

It works on a simple principle of whenever the user needs a drop of ink to be placed on a substrate, the control mechanism communicates with the inkjet head by sending a signal to print one drop (=one signal). While both thermal and piezo electric inkjet printing rely on printing drops of ink on to the substrate, how the drops are ejected from the nozzles of inkjet cartridge is what differentiates the two, i.e. thermal [4, 5] and piezoelectric [6, 7].

4.1.3 Thermal Inkjet Printer

The technology of thermal inkjet printing involves a process of heating rapidly the ink in the chamber to a temperature in the range of 250–350 °C to create vapours of ink which creates bubble, and hence, a pulse to force the ink droplets out through the nozzle. The bubble collapses once the ink drop comes out through the nozzle. The collapse of bubble forces the ink to refill again. The advantage of thermal inkjet printer is that its nozzle density is high, and hence small ink volume (100–200 picolitres) can be dispensed.

4.1.4 Piezo Inkjet

Unlike continuous mode, DOD does not involve recirculation of the ink; hence, colour printing can be done. A further advantage is higher integration, as it is possible to have larger number of channels which give more coverage area. Piezoelectric inkjet printers use the inverse piezoelectric effect, which causes certain crystalline materials (e.g. PZT) to change shape when a voltage is applied across them. In printers used for commercial applications, the voltage pulse frequency n ranges from 1 to 20 kHz. Pressure waves are generated because of piezo electric effect, and travel through the ink channel, and droplets are generated at acoustic frequencies [8]. Thus, a small electrical pulse makes the crystal contract slightly, squeezing ink out of the nozzle onto the substrate (Fig. 4.3).

One more classification of Piezoelectric mode is binary and greyscale printing**.** Every pixel on the substrate follows binary choice, i.e. presence or absence of ink. Greyscale inkjet technology works in the same as binary inkjet but has the ability to fire a range of drop sizes—up to 16 different sizes.

The piezoelectric inkjet printing technique can be applied to a wide range of material dispensing applications, such as bio-medical materials [9], metal inks [10] and polymers [11] and oxides [12]. The additive process of DOD with direct-write ability in a non-contact deposition mode can be done without masks, which leads to cost-savings, contamination-free efficient use of materials and waste elimination.

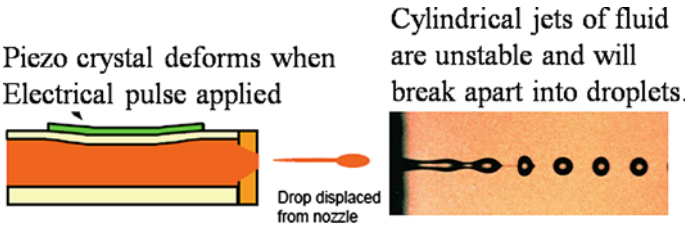

Fig. 4.3 Mechanism of ejection of ink drop from a nozzle

The past few years have seen growing applications, especially in developing organic transistors [13], light emitting diodes [14], ceramics [15] and biopolymer arrays [16]. It is now routinely used to form polymer and organic LEDs [16] for flexible display applications, to fabricate electronic circuits and for the controlled deposition of nanoparticles [17]. Further, the method is suitable for fabricating DNA microarrays as well as for depositing SAMs or proteins. In view of the low cost compared to other physical methods and no material waste, inkjet printing technology is now being deployed commercially in solar cell manufacturing process. Majority of companies now make use of inkjet printing technology in the production of second generation thin film solar cells, and numerous groups are exploring the possibilities for even third generation solar cell production.

4.1.5 Rheology of Inks for Inkjet Printing

The ink must be highly stable and shelf-life of ink should be high. Secondly, the 'ink' has to meet required viscosity and surface tension, so that the ink can be printed freely without clogging of nozzles. Also, the solvent used for making ink must have low volatility to avoid clogging. These properties of ink should be in such a way as to print repeatedly and reliably to obtain the best printed pattern. The surface tension of the ink must be around 30 mN/m, and the ink pressure should be low so as to prevent dropping of the ink from the nozzle [18]. Particle size and structure of the ink particle at both molecular- and nano-scale will affect as the solubility and chemical and environmental stability of the ink. The ink droplets with diameter in the microscale should have enough kinetic energy to exceed the interfacial energy that holds them to the liquid meniscus in the nozzle. The viscosity of ink must be low enough to allow the channel to be refilled as fast as possible in ~100 μs [19]. Printing of ink with high-viscosity is difficult as the power generated by the piezoelectric and heater membrane is limited [20].

4.2 Applications

The scope of inkjet printing technology is vast, and it can solve many ranges of problems in different fields including industrial and commercial applications. Inkjet printing process has the advantage of skipping many steps in the manufacturing process at the time of production. Inkjet printing process can develop novel advanced smart and intelligent materials that can have newer applications. It can produce new materials with superior functionality that have previously been unfeasible. Few important applications of inkjet and devices are listed below.

Inkjet printing technique has been used for developing microlenses [21], waveguides [22], rechargeable Li ion battery [23], Smart Bandage for Wireless Monitoring of Chronic Wounds [24], Zero-power sensors for large-scale RFID-integrated smart skins [25] and Large Area Multifunctional Smart Windows [26].

4.3 An Introduction to 3D Inkjet Printing

The very recent emergence of 3D printing technology has got significant attention because it can be used for printing 3D structured materials for making next generation smart, intelligent and wearable functional devices. 3D printed health monitoring devices, implantable and biomimetic devices [27] for individual needs and robotics got scientific community's attention. Novel devices of complicated structures are developed by layer-by-layer printing following the digital 3D model of devices [28–38]. The another positive functional advantage of using the 3D printing method for fabricating flexible electronic devices is that it can be used to fabricate devices with necessary properties for individual as well as for company customers on demand. The aforementioned many positive advantages of 3D printing technology for fabricating smart and intelligent flexible devices make this technology as the future.

For example, 3D printed devices made by fused deposition modelling follows pasting of various microelectronic devices and components and connecting with circuit elements like resistors, capacitors and inductors. In another type of the 3D printing, the 3D model of the product, generated by computer-aided design, can be 3D printed layer-by-layer to obtain the final product. The important advantage of this method over other methods is its ability of delivering a final finished product without any further processing, like heating or melting or else fusion of metals or plastics.

4.4 Highlights of Our Results On DOD Inkjet Printing

The advent of 3D printing fabrication process for development of devices by building parts layer-by-layer has led to interest in fabrication of devices by inkjet printing technique by printing different parts and circuits of devices by layer-by-layer assembly

too. There are only few reports of inkjet printing of inorganic materials and patterns compared to printing of organic materials and devices [39].

Here, we present our efforts in making some inorganic inks and their subsequent inkjet printing in the form of patterns like dots, lines, junctions and films on different substrates to make their oxide form after proper heat treatment to study their magnetic and sensing properties.

The synthesis of transition metals [TM]-doped wide band gap semiconductors has attracted scientific attention, because of their application in spintronic devices with improved performance, less power requirement and increased speeds, than the conventional charge-based devices. TM-doped ZnO [40–42] have recently attracted great interest among many semiconductor host materials that have been investigated for spintronic applications being ideal systems for spintronic and functional devices. The structural, physical and chemical properties of TM-doped ZnO are influenced by method of synthesis, synthesis conditions and TM dopant concentrations in host ZnO that will influence the observed magnetic properties too. DOD printer can be used for developing ZnO and TM-doped ZnO microstructure patterns like dots, lines, junctions and films using solvent-based inks on different substrates like Si, plastic and polyimide using inkjet printing technology, which are important for the applications of spintronics-based devices. Magnetic and structural properties of inkjet printed films have been studied by taking 2% Mn-doped ZnO film as a representative film [39]. The printed 2% Mn-doped ZnO film showed fast UV sensing capability along with ferromagnetism. Among all films, $Zn_{0.97}Mn_{0.02}Al_{0.01}O$ showed the enhanced ferromagnetism due to extra carriers generated from Al [43].

Figure 4.4 depicts schematic steps followed for inkjet printing and processing of films and patterns of formulated ZnO, 2% Mn-doped ZnO and 2% Co-doped ZnO inks on the preheated substrate. During the drying at ~200 °C followed by heating at 400–500 °C for 30 min, the solvent escapes from the substrate leaving metal oxide structure on the substrates. Figure 4.4 also depicts the photos of formulated ZnO-based inks and their printed patterns.

The ZnO and doped ZnO inks were prepared by dissolving corresponding precursors in low-cost solvents as reported by us elsewhere [39, 44]. However, inks of metal nanoparticles were prepared by dispersing nanoparticles of Au, Cu and Ag (prepared by a solvo-thermal method of heating acetate or chloride precursor in ethylene glycol at 140 °C for 2 h followed by washing) in printable solvent after surface modification of metal nanoparticles.

Crystalline films of oxide structures were inkjet printed on n-type Si (001) with preferred c-axis (002) orientation (Fig. 4.5) by 3-pass printing of 0.25 M inks, with intermittent heating at 400 °C for 30 min, 1-pass after another, after printing and drying. No evidence for any impurities of manganese or cobalt oxides has been seen by XRD [39, 44]. XRD analysis of (002) peaks, using the Scherer equation and also SEM images, yields an average crystallite size of ~25 nm for ZnO-based samples. Critical analysis of XRD patterns of doped ZnO exhibited peak position shift to lower angles proving the volume increase of ZnO because of the substitution of Mn^{2+}/Co^{2+} in ZnO lattice [39, 44].

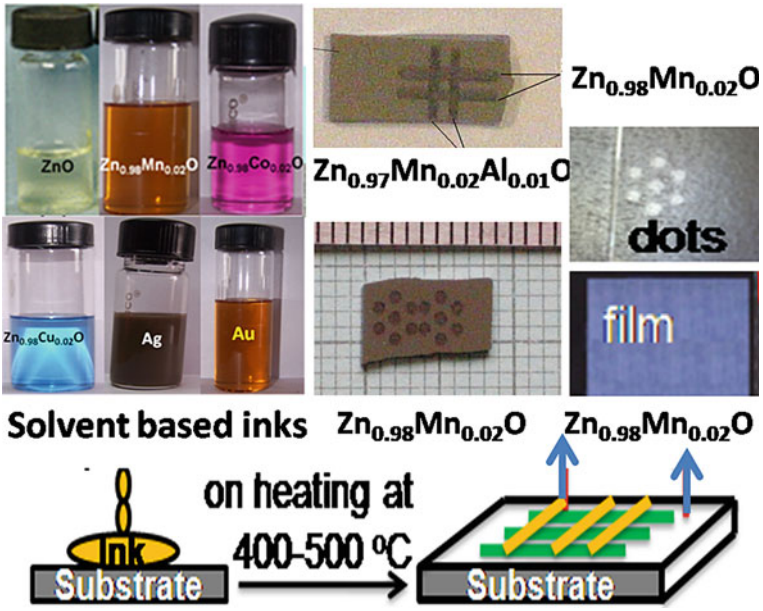

Fig. 4.4 Typical schematic steps followed for developing different inkjet printed patterns of ZnO base formulations. (Refs. [39, 44])

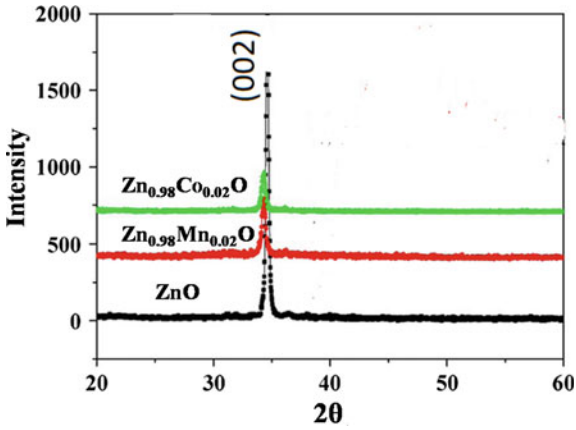

Fig. 4.5 XRD patterns of ZnO, 2% Mn-doped ZnO and 2% Co-doped ZnO [39, 44]

Films with different thickness have been developed by printing different number of passes, layer-by-layer, subsequent to drying and heating after each pass of printing. For 1- and 2-pass inkjet printed films of all the three inks, the film thickness was 40 and 80 nm, respectively. The 3-pass inkjet printed films of these materials were of 130 nm film thickness.

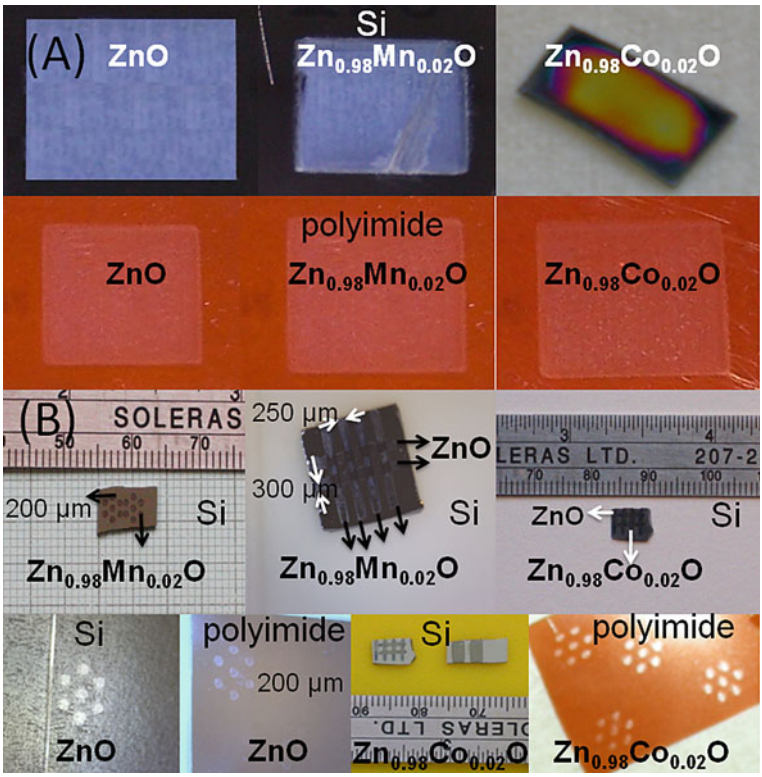

Fig. 4.6 Inkjet printed structures (films and different patterns like dots, lines and junctions) of ZnO, 2% Mn-doped ZnO and 2% Co-doped ZnO. (Refs. [39, 44])

Figure 4.6 shows the 3-pass and 1-pass inkjet printed films and patterns developed on silicon and polyimide substrates of ZnO, 2% Mn-doped ZnO and 2% Co-doped ZnO, respectively. All films were annealed for 30 min at 400 °C after printing. Figure 4.6B shows dots (~200 μm diameter), lines of ZnO, 2% Mn-doped ZnO and 2% Co-doped ZnO with width between 150 and 400 μm and junctions of widths 250 and 300 μm (Fig. 4.7).

Magnetic properties of inkjet printed films of ZnO, 2% Mn-doped ZnO and 2% Co-doped ZnO are well explained elsewhere [39, 44]. Figure 4.8a and b depict the magnetization (M) vs Field (H) for 6 lines of $Zn_{0.98}Mn_{0.02}O$ and $Zn_{0.97}Mn_{0.02}$ $Al_{0.01}O$, respectively. It is clear from magnetic data that the doping of 1% Al in $Zn_{0.98}Mn_{0.02}O$ caused an increase in magnetic properties of $Zn_{0.97}Mn_{0.02}$ $Al_{0.01}O$ which may be due to the extra charge carriers due to trivalent Al [43]. However, the magnetic moment of 14 dots of $Zn_{0.98}Mn_{0.02}O$ (Fig. 4.9) was found to be significantly higher than the inkjet printed films of $Zn_{0.98}Mn_{0.02}O$ (Fig. 4.6A). This is surprising and needs further systematic studies.

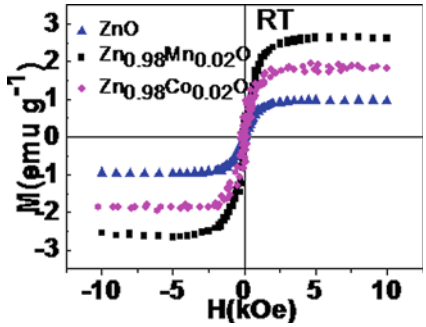

Fig. 4.7 Magnetization versus field plot of ZnO, 2% Mn-doped ZnO and 2% Co-doped ZnO films. (Refs. [39, 44])

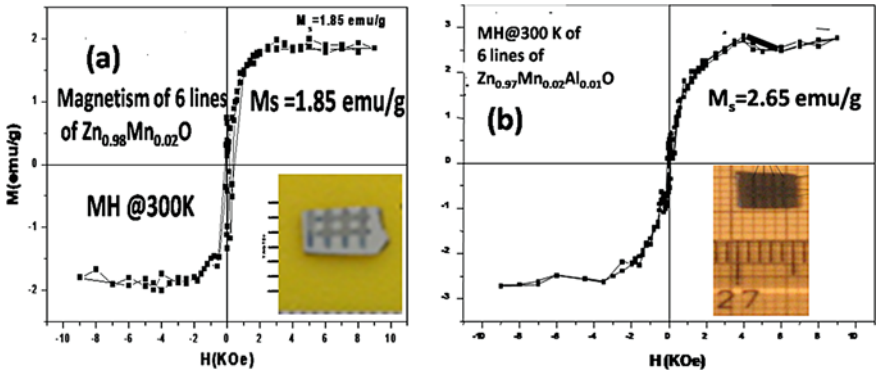

Fig. 4.8 **a** Image of printed lines (6 lines) of 2% Mn-doped ZnO and its MvsH curve. **b** Image of 6 lines of printed $Zn_{0.97}Mn_{0.02}$ $Al_{0.01}O$ and its MvsH curve

Fig. 4.9 Printed image of 14 dots of 2% Mn-doped ZnO and its MvsH curve

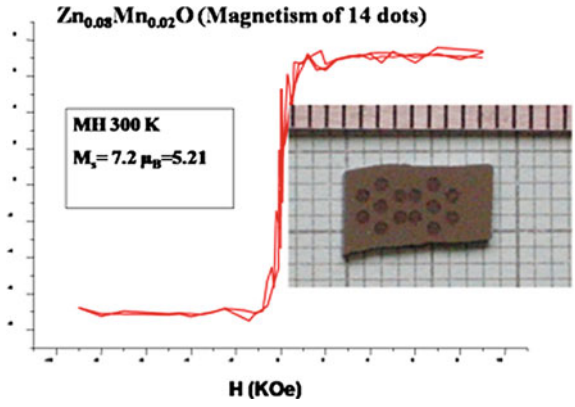

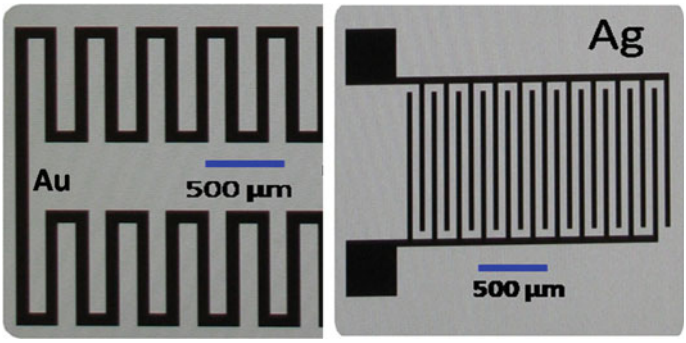

Fig. 4.10 Inkjet printed electrodes using Au and Ag nano-particle inks

In our earlier studies [39] of 2% Mn-doped ZnO made by inkjet printing, we have reported on the bifunctional properties of the same. The response of UV light on 3-pass inkjet printed ZnO and $Zn_{0.98}Mn_{0.02}O$ films developed on Silicon by heating in presence of air at 400 °C was measured using a Tektronix 7503 oscilloscope. The UV response of these films with 130 nm thickness on Silicon substrate was measured by keeping the film in UV light of 365 nm wavelength emitted by an LED. We have observed a fast decay time of ~0.52 ms for the $Zn_{0.98}Mn_{0.02}O$ film while ZnO film decayed in 0.60 ms [39]. In addition, the $Zn_{0.98}Mn_{0.02}O$ film showed more photocurrent compared to pristine ZnO film. The short decay time and fast response to UV light exhibited by ferromagnetic $Zn_{0.98}Mn_{0.02}O$ film compared to diamagnetic film of pristine ZnO needs detailed investigation.

The increased UV response of inkjet printed $Zn_{0.98}Mn_{0.02}O$ film encouraged us to develop a prototype of UV sensor using $Zn_{0.98}Mn_{0.02}O$ film. The processing scheme followed for the development of UV sensor is shown in Fig. 4.10. The inkjet printed $Zn_{0.98}Mn_{0.02}O$ film is printed over the Si substrate which was pre-printed with two gold electrodes. The UV response of ZnO film is shown by an LED (indicator) as well as the resistance change. When the ZnO film is irradiated by UV light (363 nm), the photocurrent developed in the circuit lights up indicator. At the same time, the resistance of ZnO film decreases from ~8 Mega Ohm to ~0.5 Mega Ohm as shown in Fig. 4.10.

4.5 Conclusions

A brief introduction to 2D and 3D inkjet printing and its versatility of applications is given in this chapter. DOD inkjet printed structures of ZnO, 2% Co-doped ZnO and 2% Mn-doped ZnO were developed on Silicon and polyimide substrates, by using their solvent-based inks. The 2% Mn-doped ZnO film on Si substrate showed UV sensing ability along with enhanced ferromagnetism. This paves the way for

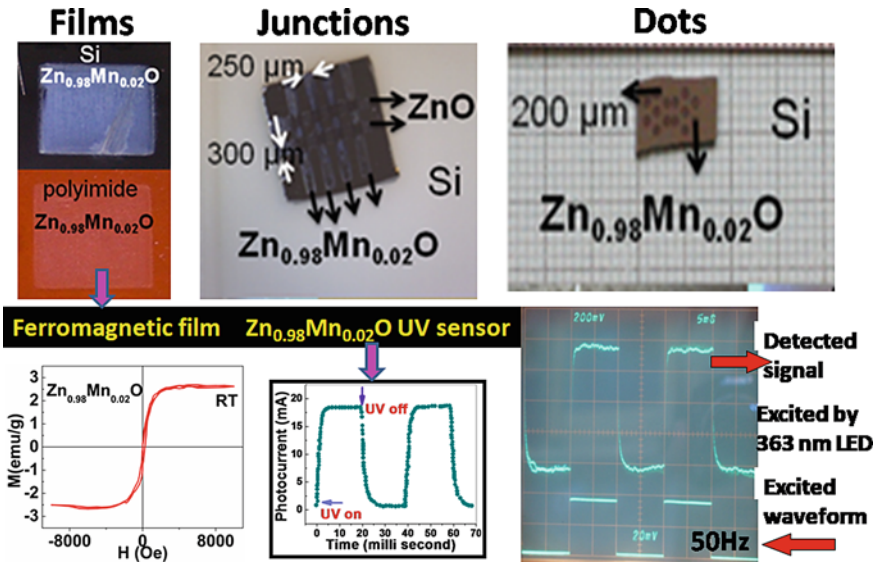

Fig. 4.11 Magnetic and UV sensing properties of 2% Mn-doped ZnO (Refs. [39, 44])

multifunctional devices. The chapter ends with the introduction to 4D printing, the future for new material synthesis Figs. 4.11 and 4.12.

4.6 Future Scope

The future and the demand of additive manufacturing process are very promising in many fields ranging from food to medical. Future may see business centres, disaster sites and even every home with the 3D printing device.

4D printing, the futuristic future

The process of self-transforming a 3D printed object into a new structure with new functionality due to the external stimuli like temperature, light or environmental change over a period of time is called 4D printing. Or simply 4D printing is creating a material after 3D printing with time as 4th dimension. Hence, the **breakthrough about 4D Printing is its ability of changing the shape of a structure made by 3D Printing technology over a time period**. The shape of 4D printed object is obtained from 3D printed shape. The difference between 3D printing and 4D printing is 4D printing makes use of programmable software and parameters like temperature, light, pressure, etc. This is similar to a non-living object in 3D shape change its 3D shape over a period of time into a 4D shape with new structure.

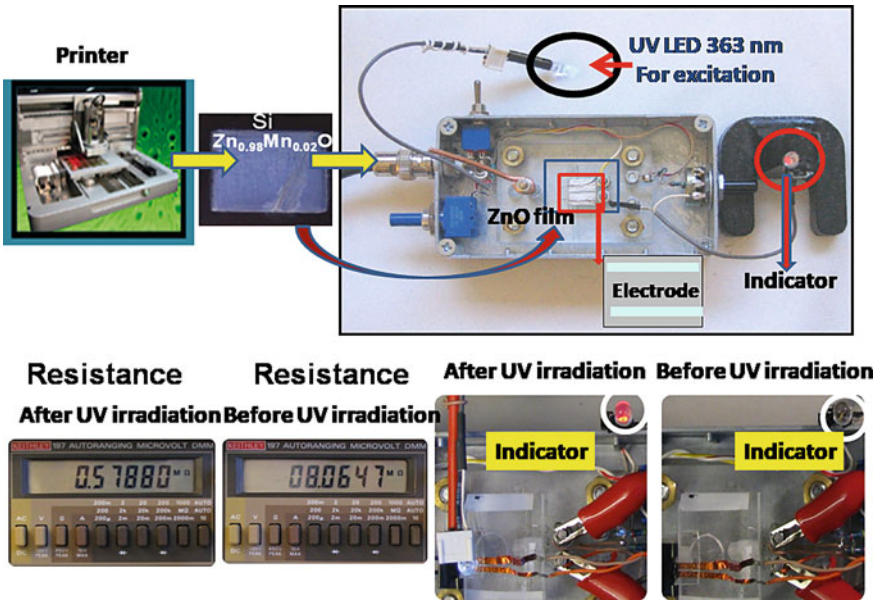

Fig. 4.12 The scheme followed for the development of a UV sensor using ZnO film and a prototype of UV sensor

Acknowledgements We place on record, our deepest gratitude to Prof. K. V. Rao, Department of Materials Science and Engineering, KTH-Royal Institute of Technology, Stockholm SE10044, Sweden for his invaluable support, guidance and motivation.

References

1. Amruth, Luszczynska B, Dupont BGR, Sieradzki Z (2017) Display and imaging 2:339
2. Raut NC, Al-Shamery K (2018) J Mater Chem C 6:1618
3. Kim YK, Park JA, Yoon WH, Kim J, Jung S (2016) Biomicrofluidics 10:064110
4. Patent US3857049 A, 1974
5. Patent US4243994 A, 1981
6. Patent US4500895 A, 1985
7. Patent US3747120 A, 1973
8. Derby B (2010) Annu Rev Mater Res 40:395
9. Li J, Rossignol F, Macdonald J (2015) Lab Chip 15:2538
10. Park YG, An HS, Kim JY, Park JU (2019) Sci Adv 5(eaaw284):2844. https://doi.org/10.1126/sciadv.aaw2844
11. Wolfer T, Bollgruen P, Mager D, Overmeye L, Korvink JG (2014) Procedia Technol 15:521
12. Shao F, Wan Q (2019) J Phys D Appl Phys 52:143002
13. Matsui H, Takeda Y, Tokito S (2019) Org Electron 75:105432
14. Feng C, Zheng X, Xu R, Zhou Y, Hu H, Guo T, Ding J, Ying L, Li F (2020) Org Electron 85:105822
15. Derby B (2011) J Eur Ceram Soc 31:2543

16. de Gans BJ, Schubert US (2004) Langmuir 20(18):7789
17. Wang Y, Guo H, Chen JJ, Sowade E, Wang Y, Liang K, Marcus K, Baumann RR, Feng ZS (2016) ACS Appl Mater Interfaces 8(39):26112
18. Menard E, Meitl MA, Sun YG et al (2007) Chem Rev 107:1117
19. Calvert P (2001) Chem Mater 13:3299
20. de Gans BJ, Schubert US (2003) Macromol Rapid Commun 24:659
21. Sanchez EA, Waldmann M, Arnold CB (2011) Appl Opt 50:1974
22. Klestova A, Cheplagin N, Keller K, Slabov V, Zaretskaya G, Vinogradov AV (2018) Adv Opt Mater 1801113
23. Gu Y, Wu A, Sohn H, Nicoletti C, Iqba Z, Federici JF (2015) J Manufact Process 20:198
24. Farooqui MF, Shamim A (2016) Sci Rep 6:28949
25. Cook BS, Le T, Palacios S, Traille A, Tentzeris MM (2013) IEEE Microwave Mag 14:103
26. Cai G, Darmawan P, Cheng X, Lee PS (2017) Adv Energy Mater 7:1602598
27. Vukicevic M, Mosadegh B, Min JK, Little SH (2017) JACC: Cardiovasc Imaging 10:171
28. Guo S-Z, Qiu K, Meng F, Park SH, McAlpine MC (2017) Adv Mater 29:1701218
29. Zarek M, Layani M, Cooperstein I, Sachyani E, Cohn D, Magdassi S (2016) Adv Mater 28:4449
30. Ota H, Emaminejad S, Gao YJ, Zhao A, Wu E, Challa S, Chen K, Fahad HM, Jha AK, Kiriya D, Gao W, Shiraki H, Morioka K, Ferguson AR, Healy KE, Davis RW, Javey A (2016) Adv Mater Technol 1:1600013
31. Wu SY, Yang C, Hsu W, Lin L (2015) Microsyst Nanoeng 1:15013
32. Yamamoto Y, Harada S, Yamamoto D, Honda W, Arie T, Akita S, Takei K (2016) Sci Adv 2:e1601473
33. Yang H, Qi D, Liu Z, Chandran BK, Wang T, Yu J, Chen XD (2016) Adv Mater 28:9175
34. Xu Y, Wu X, Guo X, Kong B, Zhang M, Qian X, Mi S, Sun W (2017)Sensors 17:1166
35. MacDonald E, Wicker R (2016) Science 353:6307:aaf2093
36. Rim YS, Bae S-H, Chen H, de Marco N, Yang Y (2016) Adv Mater 28:4415
37. Sirringhaus H, Kawase T, Friend RH, Shimoda T, Inbasekaran M, Wu W, Woo EP (2000) Science 290:2123
38. Muth JT, Vogt DM, Truby RL, Mengüç Y, Kolesky DB, Wood RJ, Lewis JA (2014) Adv Mater 26:6307
39. Jayakumar OD, Tyagi AK (2011) J Mater Chem 21:12246
40. Jayakumar OD, Salunke HG, Kadam RM, Mohapatra M, Yaswant G, Gopalakrishnan IK (2006) Nanotechnology 17:1278
41. Jayakumar OD, Gopalakrishnan IK, Kulshreshtha SK (2006) Adv Mater 18:1857
42. Jayakumar OD, Sudakar C, Vinu A, Asthana A, Tyagi AK (2009) J Phys Chem C 113:4814
43. Wu Y, Voit W, Belova LM, Rao KV (2009) Mater Res Soc Symp Proc (2009) 1161:1161–103–22
44. Jayakumar OD, Sudarsan V, Tyagi AK (2011) Nanosci Nanotechnol Lett 3:136

Chapter 5
Particle Size and Shape Engineering for Advanced Materials

R. S. Ningthoujam and A. K. Tyagi

Abstract Advanced Materials are the materials whose properties/characteristics are superior over the traditional materials for a particular application. Materials can be obtained by preparation of new methodology or modifications of existing materials. Materials consist of many particles with varying size ranging from nanometer to micron. On the basis of arrangement of atoms/ions in particles, materials can be grouped into three: amorphous, liquid crystal, and crystalline materials. Particles can be generated by three ways: natural, man-made industrial processes, and laboratory synthesis or modification of existing ones. Examples of natural particles include sea spray, mineral composites, volcano ashes, etc. Examples of man-made industrial processes include cooking smokes, diesel exhaust, welding fumes, industrial effluents, sandblasting, etc. Laboratory synthesis or modification of existing ones are performed for a particular purpose or many purposes, which include metal, non-metals, alloys, semiconductors, insulators, composites, etc. Particle size and shape are important parameters for a particular application. In this chapter, engineering of particle size and shape will be discussed. The changes in chemical and physical properties as a function of particle size and shape will also be discussed. Mechanisms behind the formation of particles in solid, liquid, and gas phases are included.

Keywords Advanced materials · Crystalline · Amorphous · Liquid crystalline · Size and shape of particles · Chemical and physical properties · Mechanism

R. S. Ningthoujam (✉) · A. K. Tyagi
Chemistry Division, Bhabha Atomic Research Centre, Mumbai 400085, India
e-mail: rsn@barc.gov.in

Homi Bhabha National Institute, Mumbai 400094, India

A. K. Tyagi
e-mail: aktyagi@barc.gov.in

A. K. Tyagi and R. S. Ningthoujam (eds.), *Handbook on Synthesis Strategies for Advanced Materials*, Indian Institute of Metals Series,
https://doi.org/10.1007/978-981-16-1803-1_5

5.1 Introduction

Advanced Materials are the materials whose properties/characteristics are superior over the traditional materials for a particular application. Advanced materials can be obtained by preparation of new methodology or modifications of existing materials. Let us take an example. Gold is one of the inert materials as well as non-toxic elements in environment. However, pure gold is difficult to be used as jewelry since it is extremely soft in the as-cast and annealed states [1]. Thus, it is alloyed with a little amount of Cu, Ag, Pd, or Ni as impurity to impart desired hardness. Depending on the amount of above impurities, its color changes from reddish yellow (pure) to greenish yellow (Ag) and red (Cu). Pure gold has particle size of micron, and thus it could not be used for ultra-sensing in biological applications (biosensors, diagnosis, biotechnological environmental monitoring, and wellness monitoring). It requires changes in its particle size and shape up to nano-region (0D, 1D, or 2D). After preparation of such nanoparticles, post-processing, such as patterning of nanoparticles in the form of films and surface modification or functionalization with proper ligands/molecules/antibody, is necessary [2–4]. In case of catalysis, catalytic properties of gold particle change with size, shape (spherical, nanorods, nanowires, prism, star, and hollow structures), and dielectric medium [5–7]. Every particle can have interesting properties, which are suitable for a particular application, but every particle may not be useful in different areas of application. Engineering aspects are necessary to make material for a particular application. The advanced materials can be of following types: metals, semiconductors, insulators, composites, magnetic, ferroelectric, piezoelectric, shape memory, thermo-chromic, photochromic, magneto-rheological, smart materials [8–10]. The interesting functional property of material for a particular application can be brought by engineering shape, size, hollowness, porosity, defects, or combination with other material through modification of synthesis procedure and post-processing after getting the initial material. The technological advantages bring a strategy to revolutionize materials for industrial and societal needs. Collaboration among R and D sectors and industrial partnership is need of the hour to design new materials for advanced applications. These advanced materials may be used by a company for launching a new product, which has many features or superior properties that satisfy many customers, so that company achieves profitability goals. The company has to follow regulatory compliance and sustainability [11].

Scientists, academicians, and engineers need to start innovative ideas, which are required for present and future scopes in the areas of environmental friendliness, sustainability, security, prevention of pathogenic microbes, energy, and high value-added markets.

Existence of advanced materials is a result of demand for a particular application in early stage and up to certain times, and it may become obsolete after sometime if the new development arises due to conditions or environment or time. New development may arise due to serendipity or rational modifications of existing materials or technology. Let us discuss a few examples.

There are many allotropes of carbon. Diamond is one of the allotropes of carbon, which is an electrical insulator, and it has high hardness and high thermal conductivity. It has been used for cutting and polishing tools and anvil-cells for high pressure applications [12–14]. The chemical bond of C atom to surround 4 C atoms is covalent bond (sp^3 hybridization). Usually, diamonds are found naturally in earth's crust. Depending on the demand of users, its color needs to be modified. A fancy-colored diamond is in high demand by purchasers. Only 0.01% of natural diamonds are colored. This color can be introduced by incorporation of defects, addition of impurities such as N, B, and other elements. This can be achieved by synthesis process. Many synthesis methods have been developed in terms of economic viability or industrial ways. So far, a large-scale production of artificial diamond is not achieved. The cost of synthesis of diamond is exorbitant, but its demand in market is high. We would like to bring to the notice of researchers that advanced synthesis method is required to meet its demand or requirement in market. Concept of materials science can bring a new synthesis procedure for diamond in economical ways.

Initially, the graphite was considered as the best material for electrical and thermal conductivities as well as chemical and thermodynamic stabilities. Because of these interesting properties, it is useful in electronic products such as batteries, solar panels, and electrodes as well as refractories in high temperature material processing applications in absence of oxygen [15–17]. Carbon (C) atom in graphite has chemical bonding with surrounding 3 C atoms in same layer by covalent bond (sp^2 hybridization) and has hexagonal closed packing structure. Between the layers, there are van der Waals forces, which impart lubricant property to graphite. Each layer is known as graphene, which was later isolated in 2004.

Two new types of hollow C molecules are a closed case (known as buckyballs, C_{60}, C_{70}) and a cylinder (nanotubes). In 1985, C_{60} (fullerene) was prepared by vaporization of the graphite rods using laser in an inert atmosphere of helium gas [18–21]. That was the first report for preparation of nanosized carbon molecule. The fullerene molecules range from C_{36} to C_{176} with respective diameter of 0.5–1.2 nm. The C_{60} has diameter of 0.7 nm. The C_{60} molecule has alternate single and double bonds (=C–C=C–) to form hollow sphere with 20 hexagonal and 12 pentagonal faces just like in soccer ball. This molecule can donate and accept electrons in the reaction. Because of this, these are used in many applications such as batteries, catalysts, and nanoelectronics [22]. The addition and substitution reactions can take place on the surface of C_{60} sphere, and thereby, many derivatives have been prepared. These derivatives are used in many applications including biosensors. With addition of alkali metals (M = Li, K, Cs, Rb) to form M_3C_{60}, it exhibits superconductivity up to 45 K [23].

In 1991, carbon nanotubes were prepared by carbon arc discharge, which was similar to those used to prepare fullerene molecules [24–26]. There are two types of carbon nanotubes. One type is considered as single-wall carbon nanotubes (SWCNTs), which is composed of halves of fullerene cage attached to ends of a tube or a hollow cylinder and flat graphene (2D), which is rolled up into nanometer-sized hollow cylinder. SWCNTs exhibit the ballistic transport rather than conducting electricity via electron transport and fast ionic movement along hollow tube. Another

type of CNTs is multi-walls carbon nanotubes (MWCNTs), which have multiple layers of carbons over inner layer. Among layers, there are van der Waals forces. C atoms undergo a mixing of sp^2 and sp^3 hybridizations. Such carbon nanotubes show the enhanced field emission properties and have been used as tips for STM (scanning tunneling microscopes) and AFM (atomic force microscopy) [27]. It has high thermal conductivity, high electrical conductivity, high tensile strength, and high Young's modulus of elasticity. Because of the above properties, it brings advance scopes in different areas of materials science. Such small-size nanotubes are used in medical sciences as nanosensor, nono-emitter, etc.

Many researchers were thinking to develop carbon fibers and single-layer plane graphene without rolling since 1960s [28–30]. In the graphite intercalation compounds, the graphene layers can function as either acceptor of electrons from or donation of electrons to the intercalated species. Typical examples are mentioned here. K-graphite (KC_8) is a donor graphite compound, whereas Br-graphite is an acceptor compound. With progress of materials science, new allotrope of carbon, say graphene (atomic layers), was prepared by mechanical exfoliation of small mesas of graphite in 2004. The graphene is a 2D material with a few layers of sp^2-sp^2 chemical bonds. It has interesting properties such as high electric conductivity, high thermal conductivity, like a metallic nature, and strong ambipolar electric field effect (electron and hole concentrations of $10^{13}/cm^2$), and room temperature mobility of 10,000 cm^2/Vs. Now, graphene and their derivatives and nanocomposites have been prepared by different synthesis routes or post-processing or modifications.

These are some of the new developments of materials for different applications. Au nanostructures of spherical, rod, hollow, cage, star shapes, and various sizes, and with combination with others (Ag, Fe_3O_4, SiO_2) in the form of composite, and core–shell nanostructures have been developed by different synthesis routes [31–38].

Magnetic nanoparticles have been used as catalysts, nanocarriers for drug, contrast agents in magnetic resonance imaging (MRI), heat-generators in hyperthermia-based treatment, magnetic-based separation for bacteria, toxic ions/compounds, etc. [39–51]. For every device or application, specific synthesis strategies and post-processing are required so that this can be utilized in economic and environmentally friendly ways. Surface functionalization or modification of particles with suitable functional group(s) is important in designing materials for specific purposes.

Ceramic materials such as glass fibers, Al_2O_3, YPO_4, YVO_4, lanthanide-doped vanadates and phosphates, oxides, and intermetallic compounds as FePd, FePt, NbTi, Cu-Zn, VN, MoN, SiC, TiN, BN, $Fe_{6.3}Cr_{2.5}Co_{12}$, FeCrAl, γ'-Ni_3(Al, Ti), $Al_xCoCrCuFeNi$, and $Al_XFe_{1.5}CrMnNi_{0.5}$ ($x = 0.3, 0.5$) are important in high temperature and extreme environment, and used as crucibles, coating, tools, heating element, and superconducting materials [52–63].

Preparation of different shapes of ceramics is one of the challenges to materials scientists. Polymers are important in imparting durability, lightweight, and flexible properties of materials. Composites/hybrids are important materials which can have superior functionalities than individual ones. Biomaterials are materials, which are used in health care. Laser-based synthesis, fabrication, fine tuning techniques, atomic layer deposition, high purity single crystal preparation, and 3D/4D printings are

important areas in materials science. In addition to above materials, engineering of size, shape, hollowness, and dimensionality of particles, and post-processing will be required to design new materials. Advanced materials can be categorized into the following on the basis of performance [11, 64–66]:

1. High performance materials (ceramics, alloys, carbon-based materials, lightweight material having stability under high temperature, high pressure, high radiation or extreme conditions)
2. Energy materials (fuel cells, batteries, solar photovoltaic)
3. Additive (additive manufacturing, 3D/4D printing)
4. Nano (Nanomaterials, nanostructures, nano-engineering)
5. Semiconductor-based integrated circuits (Computer, mobile, robotics)
6. Biomaterials (drug delivery and repairing of DNA/RNA through nanocarriers, replacement of bones, teeth)
7. Smart materials (sensors, actuators, materials that sense and react to environmental conditions or stimuli, say mechanical, chemical, electrical, or magnetic signals)
8. Environmental materials (Materials for recovery, or reuse or substitutions, environment friendly, harmless to environment, eco-friendly)
9. Surface coatings (surface coating, surface engineering over materials or particles, thin films to enhance stability, multi-utilities)
10. Metalwork (metals processing technology)
11. Joints (welding, brazing)
12. Durability-Flexibility (polymers, rubber, resistance to any fatigue, thermal)
13. Multifunctional (hybrids, composites, core–shell materials)
14. Green materials (economic way of research, environmental friendly)

Light-amplification (Laser-related cutting, drilling, down and upconversion photonics, laser-based devices in electro-optics, magneto-optics, health care, industry, security, laser surface cleaning or treatment, chemical reactions, patterning, fine tuning/marking, communication, printing, lithography, sensors, guiding, heat-generation, melting, vaporization).

5.2 Different Types of Particles in Materials Science

Particle in materials science is an entity of atoms, and its size can range from nanometer to micron. Its properties are generally different from individual atoms or molecules. It can move in free space or liquid medium, but it is restricted inside solid. It can have vibrations and rotations of molecules or chemical bonds of atoms due to absorption of energy from surrounding. Particles can be generated by three ways: natural, man-made industrial processes, and laboratory synthesis or modification of existing ones. Examples of natural particles are sea spray, mineral composites, volcano ashes, etc. Bioinspired synthesis of nanoparticles such as Fe_3O_4, Ag, and naturally formed nanoparticles such as Fe_3O_4 in living cells (magnetotactic bacteria)

are also reported [67, 68]. The bioinspired synthesis of particles is also considered as green chemistry route. Examples of incidental particles are man-made industrial processes, which include cooking smokes, diesel exhaust, welding fumes, industrial effluents, sandblasting, etc. Engineering particles are the prepared particles for a particular purpose or many purposes, which include metal, non-metals, alloys, semiconductors, insulators, composites, etc. The particles in laboratory synthesis or modification of existing ones can be generated by two approaches: Bottom-up and Top-down approaches [51]. On the basis of arrangement of atoms in particles, they can be grouped into three: Amorphous, liquid crystal, and crystalline materials (Figs. 5.1 and 5.2). Amorphous material does not have a long order of atoms (isotropic in properties). Here, the diameter (d) of spherical particle is assumed as size. Examples of amorphous materials are many plastic, polymers, papers, etc. A liquid crystal is a state of matter having properties between those of conventional liquid and those of solid crystal. They can be used as liquid in which molecules have proper orientations. Examples of liquid crystals are solutions of soap and detergents, biological membranes, and cell membranes. DNA and many polypeptides can form liquid crystal. Crystalline materials can be grouped into two categories, namely, single and polycrystalline materials. In single crystal, atoms are arranged in perfect order. It means that there are no grain boundaries (Fig. 5.3). Grain boundary is space

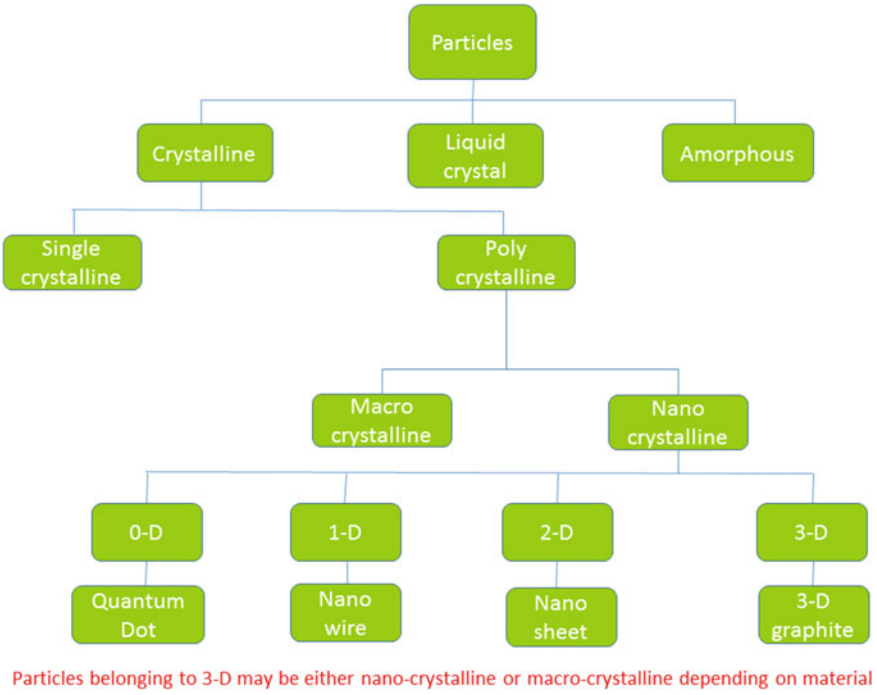

Fig. 5.1 Types of particles on the basis of arrangement of atoms/ions

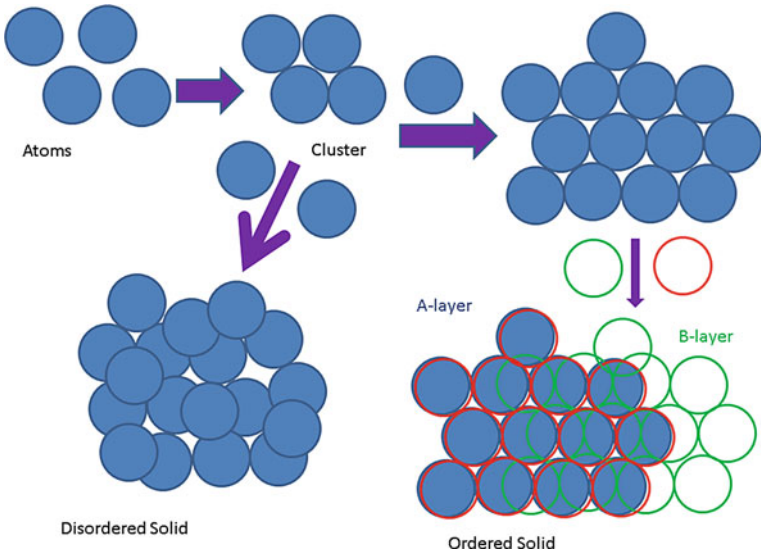

Fig. 5.2 Evolution of particle from atoms through cluster. Particles are of two types: Disordered and ordered solid. In ordered solid: different layers of A, B, and C types can form A (simple packing), AB (hexagonal closed packing), or ABC (face-centered cubic closed packing or cubic closed packing) in a particular crystal structure

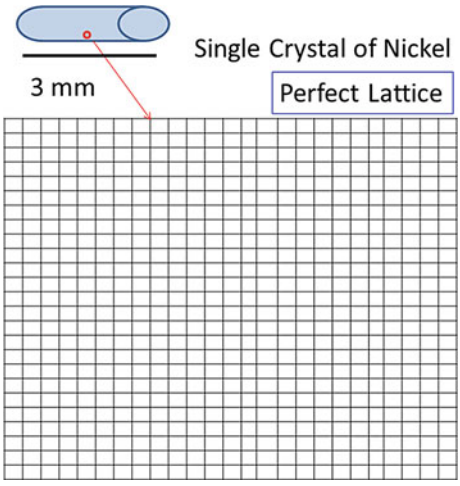

Fig. 5.3 In a single crystal, arrangement of atoms/ions in lattice is perfect (2D representation). A schematic part of single crystal having length of 3 mm is shown

between grains or particles. In grain boundary, atomic density is less than the bulk or grain [69]. In case of polycrystalline materials, there are grain boundaries between grains. Polycrystalline materials can be further grouped into two: macrocrystalline and nanocrystalline materials (Figs. 5.4 and 5.5). In case of macrocrystalline, size of

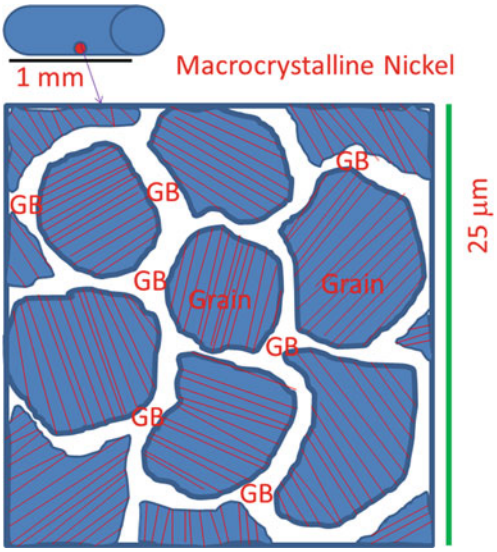

Fig. 5.4 In a macrocrystaline, arrangement of atoms/ions in lattice forms grains (2D representation). Between grains (G), there is a grain boundary (GB). Space of GB is not much significant as compared to that of G. The orientation of a particular grain is different from neighboring ones. A schematic part of macrocrystaline having length of 1 mm is shown

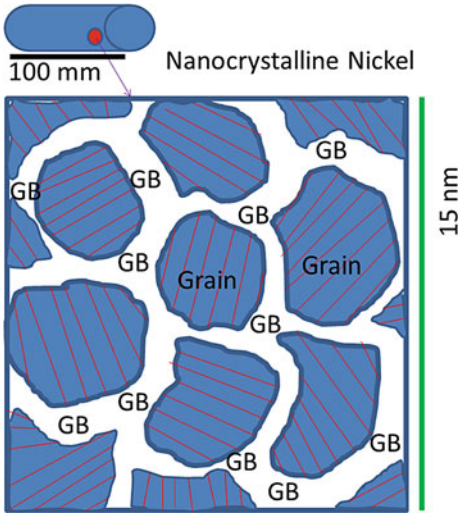

Fig. 5.5 In a nanocrystaline, arrangement of atoms/ions in lattice forms grains (2D representation). Between grains (G), there is a grain boundary (GB). Space of GB is significant as compared to that of G. The orientation of a particular grain is different from neighboring ones. A schematic part of nanocrystaline having length of 100 nm is shown

grain is from submicron to a few microns (d >> 100 nm). Examples of macrocrystalline materials are highly crystalline particles of ceramics, alloys, metals, composites, etc. In case of nanocrystalline, size of grain is in nanometer range (1–100 nm). Depending on confinement of electrons or atoms, nanocrystalline can be grouped into four categories, namely: 0D, 1D, 2D, and 3D. Examples of 0D, 1D, 2D, and 3D materials are quantum dots, nanowires, nanosheets, and nanostars (or nanotetrapods), respectively [70]. The atomic/ionic arrangement in lattice of a particular structure

can be of simple (A-type), hexagonal close packing (hcp, AB-type), or cubic closed packing (ccp, ABC-type) (Fig. 5.2).

Four types of synthesis methods for materials are generally found: (1) Dried powder-based synthesis, (2) Liquid/Solution-based synthesis, (3) Gas-based synthesis, and (4) Thin film-based synthesis. In case of dried powder-based synthesis, the precursors are ground or mixed without using any liquid (water or oil), and then heated or pressurized or combined form of heat-treatment and pressure is used or excitation is done using suitable light (UV, visible, and IR) or laser or irradiation with γ-rays, β-rays, α-rays or neutron sources or any kind of external uncharged or charged particles.

This includes the preparation of oxides by the solid-state reaction, the preparation of alloys by arc melting, polymerization of monomers under irradiation, light- or laser-induced synthesis, etc. Now, how to change size and shape of particles? In case of liquid-based synthesis, the precursors are generally dissolved in water or oil or mixture of water and oil into molecular and ionic forms, and then compounds or materials are precipitated out. It may be further carried out for post-processing, say, heat-treatment. This includes the precipitation, co-precipitation, sol-gel route, micro-emulsion route, hot-injection route, hydrothermal route, crystallization, etc. Now, how to change size and shape of particles? In case of gas-based synthesis, atoms or ions or molecules are brought to gaseous formation, and reaction among them occurs in gaseous state to form cluster or particles. This includes the formation of molecules of compounds or particles in stars, ionosphere, exosphere, magnetosphere, etc. Here, the roles of absorption of UV light, x-rays, γ-rays, electromagnetic waves (electric and magnetic fields), or uncharged particles are important. Even in laboratory, the particles are prepared in gaseous form using time of flight mass spectrometer, plasma synthesis, etc. The role of environment, such as inert gases, cooling process, condensation, and presence of electromagnetic waves, can tune size and shape of particles. In case of thin film-based synthesis, gaseous forms of atoms or ions or molecules are condensed on a substrate, or molecules in liquid form are deposited on substrate. This includes chemical and physical vapor deposition (CVD, PVD) and molecular beam epitaxy (MBE), mono- or poly-layered deposition of long chain fatty acids or surfactants on substrate from liquid medium, etc. In subsequent sections, different methods to tailor the size and shape of particles of advanced materials will be discussed. Engineering of particles means the preparation of desired particles followed by processing such as fabrication, surface modification, design, or construction, so that properties/characteristics of products are superior over the traditional materials for a particular/targeted application. Such engineered products or advanced materials can have impact in different areas such as (i) Energy technologies, (ii) Conversion of greenhouse gases such as CO_2 to methane or methanol or ethanol or any derivative, (iii) Transportation, (iv) Information Technology, (v) Catalysts including photocatalysts, (vi) Health care, (vii) Biomaterials, (viii) Biotechnology, (ix) Structural materials, (x) Robotics, (xi) Food processing, (xii) Material science, (xiii) Sensors including biosensors, (xiv) Cosmetic technology, (xv) Nuclear energy, (xvi) Alternative source of fuel (H_2) produced from various processes such as splitting of H_2O or fuels $CH_4/C_2H_6/C_3H_8$, (xvii) Production of energy or electricity

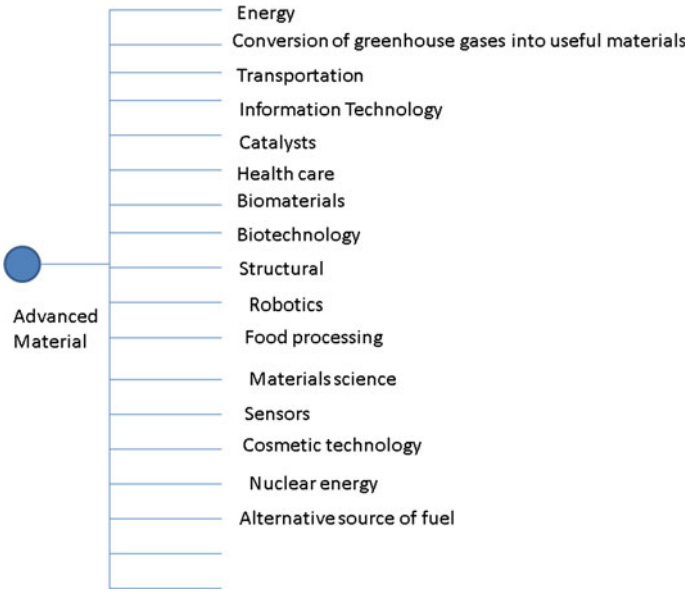

Fig. 5.6 Use of engineered products or advanced materials in different areas

through wind or tidal waves, (xviii) Space science and technology, (xix) Carrier in drug delivery, (xx) Effective drug design, (xxi) Solar cells or photovoltaics or fuel cells or batteries, (xxii) Efficient light emitter materials, (xxiii) High data storage devices, (xxiv) Sustainable environment, (xxv) Surface and polymer sciences, (xxvi) Processing of papers and inks, (xxvii) 3D/4D printing, and (xxviii) Mechanical, civil, and metallurgical areas (Fig. 5.6). However, it is not possible to cover all areas in this chapter.

5.3 Need for Different Sizes of Particles and Shapes in Advanced Materials

This aspect can be emphasized by several examples. Suppose, the particles are useful in drug carrier in living body, and then, shape of particles must be spherical and size of particles should be 100–300 nm (micelles, liposomes, polymers) or smaller size <50 nm (Fe_3O_4 or SiO_2). Micelles, liposomes, and many polymers are amorphous in nature, whereas Fe_3O_4 particles are crystalline and SiO_2 is amorphous [71, 72]. Micelles or liposomes have water-soluble and oil-soluble structural components. If drug molecules are water soluble, these can be conjugated with water-soluble component, whereas if drug molecules are oil soluble, these are conjugated with oil-soluble component. Drug release kinetic is based on temperature, pH of environment, or other type of counter interaction (positive and negative polar groups). If

particles are useful in replacement of teeth, bone, shape of particles can vary from spherical, nanowires, or nanorods. Even particle size can vary from nanometer to micron. Particles can be amorphous or crystalline. Materials such as hydroxyapatite (HA = $Ca_{10}(PO_4)_6(OH)_2$), titanium, alloys (Ti-Al-V, Ti-Al-V-Li), composites of tri-calcium phosphate (TCP = $Ca_3(PO_4)_2$), Al_2O_3, ZrO_2 are used as biomaterials for replacement of teeth or bone [73]. Porous scaffold biomaterials have been used as templates for tissue regeneration, so that damaged tissues after surgical procedures can be regenerated. This engineering is very important for application. HA and TCP scaffolds have characteristic properties such as high mechanical stiffness (Young's modulus), hard brittle surface, and very low elasticity as well as highly biocompatibility. These have chemical and structural similarity to the microenvironment of native bone. Thus, these are used in dental and orthopedic surgery to coat metallic implant surfaces to improve implant integration with host bone. Sometimes, these have limitation in shaping for implantation, and even new bone formed in a porous HA or TCP scaffold cannot sustain the mechanical loading needed for remodeling. Also, degradation of scaffold occurs with time or different pH medium (5–8). Nowadays, synthetic polymers, such as poly-l-lactic acid (PLLA), poly-dl-lactic-co-glycolic acid (PLGA), polystyrene, and polyglycolic acid (PGA), have been used as scaffold materials for tissue engineering [74]. Many composites have been fabricated with a tailored architecture. Naturally occurring biomaterials, such as collagen, various proteoglycans, and chitosan, have been used in tissue engineering, such as the regeneration of damaged tissue due to injury or surgery, with incorporation of a proper antibacterial, anti-fungal, or anti-virus materials. Ag or TiO_2 nanoparticles have been used for protection from microbes such as bacteria, fungus, or virus [75, 76]. For cartilage and cardiovascular repair, composites of naturally occurring polymer with synthetic polymer have been used. It needs a purpose or any targeted point for materials. Sometimes, porous carbon fibers have been used as scaffold in tissue engineering to enhance mechanical strength. Hollow Au and Ag nanoparticles with size less than 100 nm have been used as drug carrier as well as heat generator under NIR laser excitation (photothermal) or reactive oxygen generator under NIR laser excitation (photodyanamics) [77]. The drug is loaded inside the core. This concept has been used to cure tumor through blood–brain barrier.

In case of photocatalysts, a light absorber is necessary. In order to perform light absorption in UV, visible, and NIR, materials are varied. This is based on band gap engineering. The particles with appropriate size and shapes can have high absorption cross-section. It also calls for designing different types of materials. Anatase TiO_2 nanoparticles can absorb the UV light, and after N doping, it can absorb light in the visible range [78]. Quantum dots (QDs) in general show absorption spectrum from UV to visible, since it can have discrete absorption peaks along with lowest energy absorption peak. Sometimes, QDs can absorb light from UV-to-Visible-NIR range, which cover almost entire solar spectrum. PbS QDs can show absorption in visible range, and PbSe QDs can show absorption in visible-NIR range. Bulk PbS and PbSe have band gaps of 0.41and 0.26 eV, respectively [79]. When shape of particle changes from the nanosized spherical to nanorod, a variation in absorption band is observed. When heterostructures of metal–semconductor, semiconductor I (lower

band gap)–semiconductor II (higher band gap), semiconductor I (lower band gap)–semiconductor II (higher band gap)–semiconductor I, semiconductor I (lower band gap)–semiconductor II (higher band gap)–semiconductor III (different band gap from I or II) are produced, improvement in absorption cross-section as well as band gap tuning can be brought [80]. Multi-well heterostructures are essential for absorption of light from UV-visible-NIR, in case of conversion of solar light to the electricity or heat. Conservation of energy or production of H_2 from water splitting and solar light using proper photocatalysts is up most important for today and tomorrow society in sustainable environment. Synthesis and fabrication of particles in powders and thin films are important steps to achieve proper target or goal.

The possible sizes and shapes of particles from materials are shown (Fig. 5.7). In spherical particles, particle size can be increased by heat-treatment, because diffusion or chemical reaction is faster at higher temperature. Sizes 2–5 nm, 10 nm, 100 nm, 1 μm, 10 μm can be obtained. Particles with disc type can be converted into rod by increasing length. Tube-type particles can be prepared by using template method.

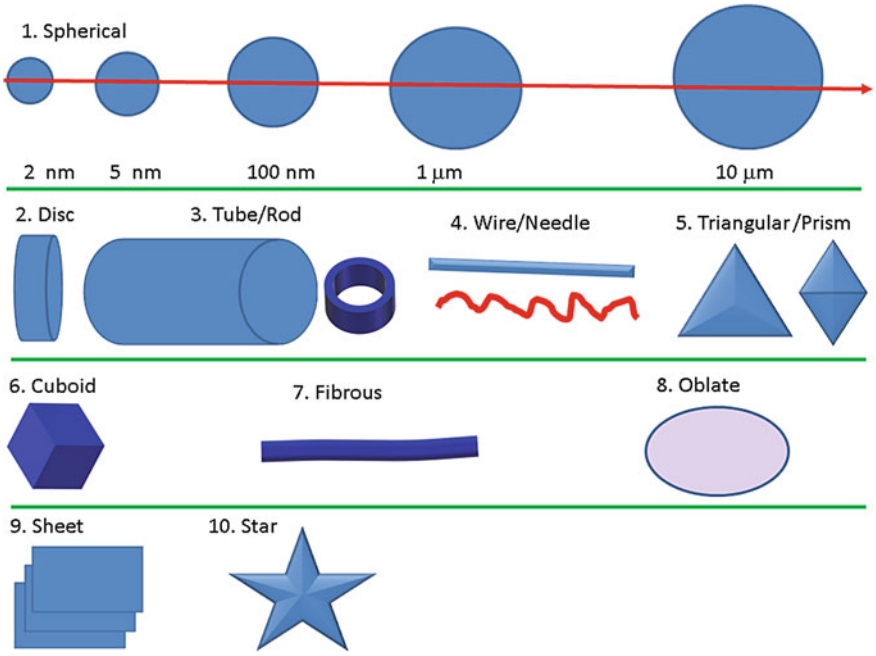

Fig. 5.7 The regular size and shape of particles can be obtained from different materials. 1. In spherical particles, particle size can be increased by heat-treatment because diffusion or chemical reaction is faster at higher temperature. Size 2–5 nm, 10 nm, 100 nm, 1 μm, 10 μm can be obtained. 2 and 3. Particles with disc type can be converted into rod by increasing length. Tube-type particles can be prepared by using template method. In this, template will be removed by heating or dissolution after formation of material. Different shapes such as (4) needle, wire, (5) triangular, prism, (6) cuboid, (7) fibrous, (8) oblate, (9) sheet, (10) star, etc., can be prepared by chemical or physical methods

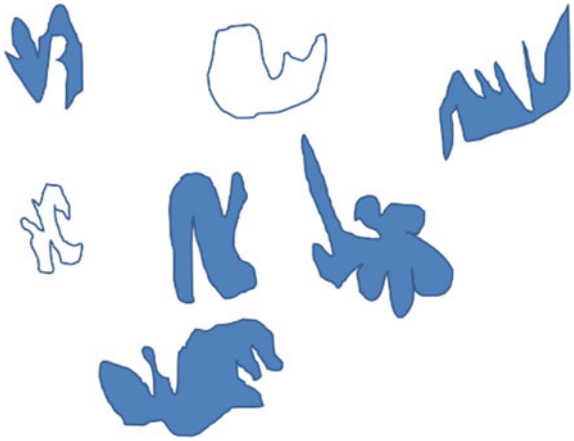

Fig. 5.8 Many particles having irregular shapes

Different shapes such as needle, wire, triangular, prism, star, cuboid, oblate, fibrous, sheet, etc., can be prepared by chemical or physical methods. Those are highly regular. However, many particles having irregular shapes are obtained (Fig. 5.8). In this, determination of shape and size is very difficult. Sometimes, many nanostructures of hollow, core–shell structure, dispersion of small-size particles in core surrounded by shell or dispersion of particles in another phase or hybrid are obtained from synthesized particles and nature (Fig. 5.9).

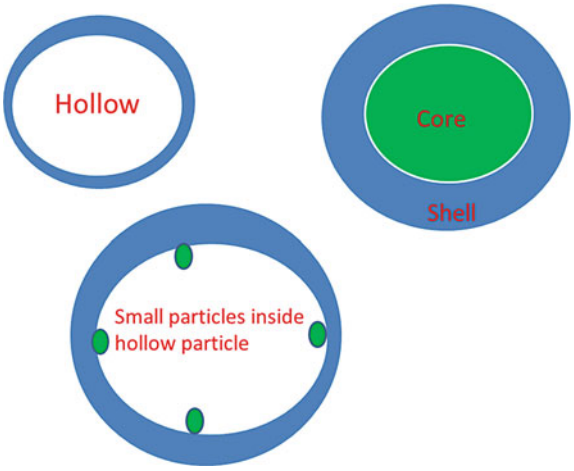

Fig. 5.9 Many nanostructures of hollow, core–shell structure, dispersion of small-size particles in core surrounded by shell

5.4 The Role of Nanosized Particles in Advanced Materials and Recent Advances in Nanoscience and Nanotechnology

When atoms or ions come closer with or without external forces, they can form molecule (Fig. 5.2). For example, H atoms prefer to form molecule, whereas He atoms prefer to exist independently. Many atoms or ions prefer to form molecule after gaining or loosing electrons or balancing with counter ions so that they stabilize at lower energy. The group of molecules can form cluster. With further addition of atoms or ions or molecules, cluster can exist as independent entity since size increases. Generally, sizes of atoms or ions vary from 0.3 to 2.2 angstrom (10^{-10} m = 1 Å). Sizes of smaller clusters are in the range of 5–10 Å. The smaller-sized clusters can be dissociated into atoms or ions or molecules if binding energy among them is weak. The larger-sized cluster in the range of 20–100 Å can exist as solid, in which their binding energy is strong. The binding energy is related to lattice energy in case of solid. The solid means the rigid structure, in which movement of atoms or ions is restricted, but only vibrations of chemical bonds can take place. Usually, atoms or ions in solid are arranged in a highly ordered microscopy structure (in x-, y-, and z-axes) forming lattice. In few cases, disorder in arrangement of atoms or ions is found. They are divided into two groups: crystalline and amorphous solids when atoms or ions are arranged in order and disorder, respectively. The larger-sized clusters are known as nanosized particles. Nanosized particles exhibit the different properties such as magnetic property, electrical resistivity, catalytic property, hardness, thermal and chemical stabilities, etc., as compared to their bulk counterpart. Here, bulk counterpart means micron-sized particle. 1 micron is equal to 1000 nm. The chemical bonding among atoms or ions will be of ionic bonding (electrostatic), covalent bonding (sharing of electrons), metallic bonding. Generally, they are very stable in solid form. There are other solids, which are possible under high pressure and low temperature. Molecules such as Ar, H_2, CCl_4, CO_2, N_2, I_2, HCl, H_2O, NH_3 can form solids, and the chemical bonds are of London dispersion forces, electric dipole–dipole interaction, and hydrogen bonding [81, 82].

Science dealing with nanosized particles (1–100 nm) is known as nanoscience. Thus, all branches of science, such as biology, chemistry, physics, and engineering, and their interface branches such as microbiology, biotechnology, environment, etc., are interrelated after evolution of nanoscience. This brought many interesting applications in different areas such as pharmaceutical (new design of drug, minerals, formulation), health care (drug delivery, treatment and diagnosis), agriculture (control of disease, crop protection, better seeds, livestock productivity), water treatment (safe use, purification, removal of toxics), diseases (removal of bacteria, virus, and fungus, early detection), energy storage (solar power, wind power), environment (preparation of compounds using green chemistry route), data storage (a few terabytes), cosmetics (protection from fungus in homes, cars, and bus using Ag-TiO_2, protection from UV lights coming from sun), robotics, computer, information, ceramic industry, glass industry, metal industry, day-to-day uses, etc. Technology dealing with application

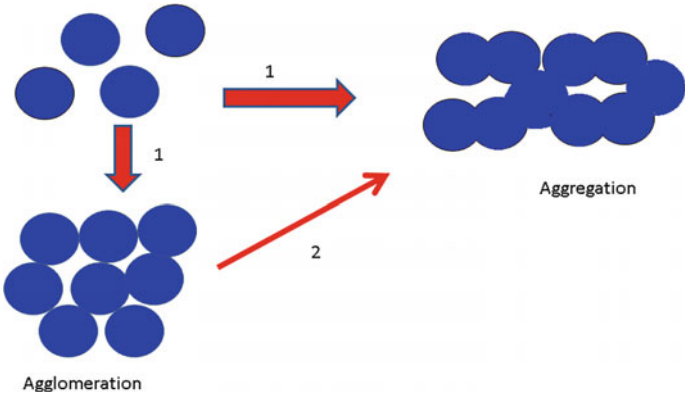

Fig. 5.10 Schematic representation of aggregation and agglomeration of small-sized particles

of nanomaterials is known as nanotechnology. In view of this, we need to understand basic concept of nanoscience, development, and its applications in society.

In case of structural materials, there are variations in physical properties with decrease in particle size or dimension (3D to 2D to 1D to 0D). Many physical and chemical observations of materials are observed with respect to particle size and shape; and these are discussed here.

5.4.1 Aggregation and Agglomeration

When small-sized particles are prepared in aqueous medium, attractive forces, such as dipole–dipole interaction, though electric or magnetic or both forces arise, and thus, they get agglomerated and with longer time, get aggregated (Fig. 5.10). Agglomeration can be minimized by dispersion of particles in another medium having capping agents and followed by ultrasonication. Agglomeration has weak bonds between particles. In case of aggregation, it is difficult to separate particles. There are many other ways to reduce aggregated particles using digestion method. Such aggregated or agglomerated particles have different properties from those particles having monodispersed nature.

5.4.2 Atomic Structure in Lattice

In single crystal, defects of atoms in lattice sites are negligible. Thus, it is perfect lattice in 3D directions. In case of polycrystalline materials, there are two types of lattice due to particle size [69]. One type of polycrystalline materials is microcrystalline, where particle size is of the order of microns. Here, one particle can have many

grains (G), and in between grains, there is a grain boundary (GB). Size of GB is so small as compared to that of G (Fig. 5.4). Thus, effect of GB in properties is minimum. Another type is nanocrystalline, where particle size is of the order of nanometers (d = 1–100 nm) (Fig. 5.5). Here, effect of GB is high. In 1–2 nm size, effect of GB can change chemical and physical properties. Even, density of GB is almost same as G in 1 nm-sized particle. Atomic density in one site (A) is different from another (B) or (C) site (Fig. 5.11). The grains or crystallites are arranged in different orientations in neighbor. Many dangling bonds on the surface of particle arise if small-size particles are prepared in inert atmosphere. Number of dangling bonds can be minimized using suitable surfactant/capping agent. Such dangling bonds can change chemical and physical properties. In ambient or oxygen atmosphere, such dangling bonds are very reactive to form oxide layer over particles (Fig. 5.12). If exposure is longer, it can form core@shell particles (here shell is oxide layer). With further decrease in particle size, stability decreases. At extreme decrease in particle size, it becomes amorphous or disorder in atomic arrangement or cluster of atoms.

Porosity is also an important parameter to measure void or empty spaces in a material (soils, particles prepared in lab, and natural particles). In prepared particles of carbon and silica, size of pores can vary from 1–2 nm (microporous) to 50 nm (mesoporous). Their atomic structures are different from single crystal lattice. Layered

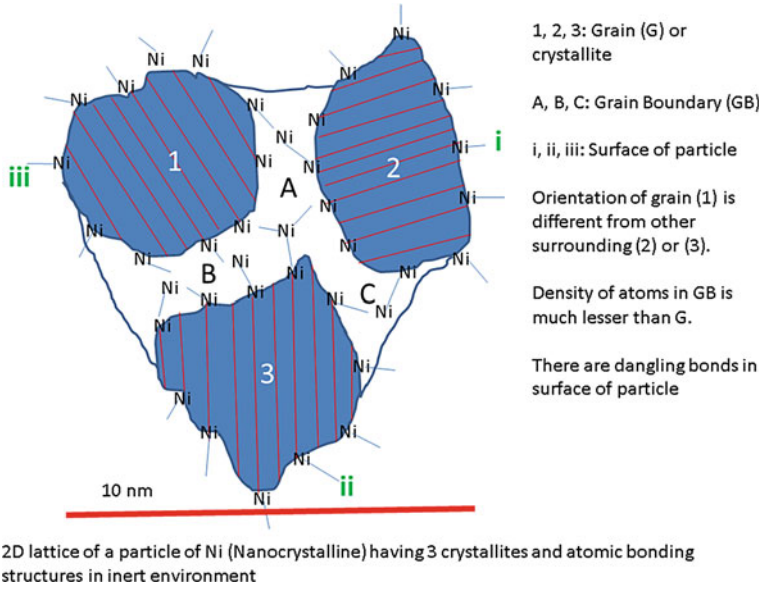

Fig. 5.11 2D lattice of a particle of Ni (Nanocrystalline) having three crystallites and atomic bonding structures in an inert environment. Magnetic properties of Ni will vary with decrease in particle size due to effects from surface dangling, lattice defects, and grain boundary.

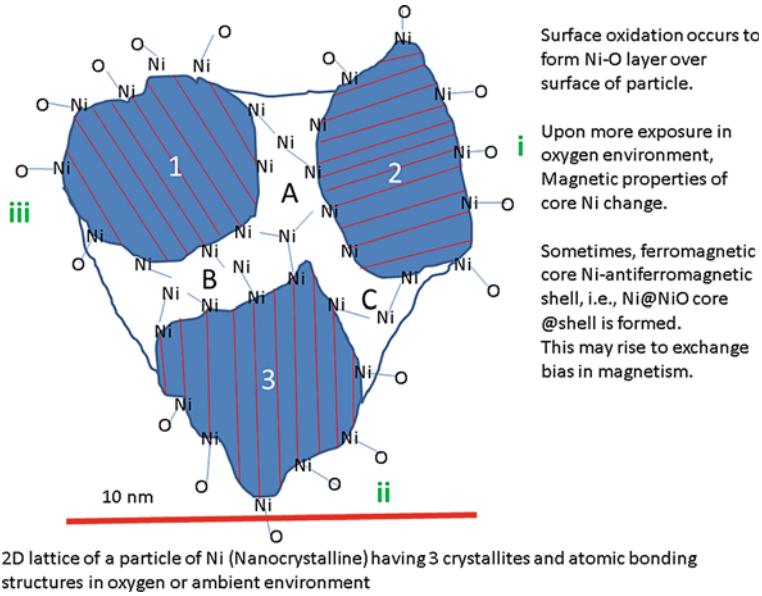

Fig. 5.12 2D lattice of a particle of Ni (Nanocrystalline) having three crystallites and atomic bonding structures in an oxygen or ambient environment. Magnetic properties of Ni will vary with decrease in particle size due to effects from surface dangling, surface oxide layer, lattice defects, and grain boundary. Ni (ferromagnetic)@NiO (antiferromagnetic) heterostructure can be defined after long exposure in an oxygen or ambient environment

structured compounds have different atomic structures as compared to their corresponding other phase. These materials have potential applications such as removal of toxic ions or gases, drug delivery, battery, catalysts, ion-exchange, etc.

5.4.3 Magnetic Properties

Types of magnetic materials include ferromagnetic or ferrimagnetic, antiferromagnetic, paramagnetic, and diamagnetic materials [83]. In case of ferromagnetic or ferrimagnetic material, they have spontaneous magnetization, Curie temperature (ferromagnetic to paramagnetic transition, T_c), coercivity (H_c), retentivity (M_r), and saturation magnetization (M_s). In case of antiferromagnetic material, they show the magnetic transition known as Neel's temperature (antiferromagnetic to paramagnetic transition, T_N). In case of paramagnetic materials, magnetization value is very small and magnetization decreases with increase of temperature following Curie law. Magnetic field can influence magnetization of ferromagnetic and antiferromagnetic materials, but its effect will be less in paramagnetic material. In diamagnetic material, moment is negative and small; and under applied magnetic field, its spin tries

to oppose magnetic field. These types can be distinguished on the basis of ratio of magnetization to applied magnetic field with temperature ($\chi = M/H$ vs. T) (Fig. 5.13). Intrinsic magnetic properties of materials do not change in case of macrocrystalline particles (size of 1–10 μm).

When size of particle reduces to nanometer range, their magnetic properties are different from intrinsic properties. First, ferromagnetic material will be discussed. In micron-sized particles, particles are considered as multi-domain, where magnetic domains have spins and surrounded by domain walls (Fig. 5.14). Because of presence of domain walls, it has coercivity (H_c) and magnetic retentivity (M_r), saturation magnetization; and it shows the hysteresis loop upon changing magnetic fields in opposite directions (+ve and –ve directions) at large values of 2–3 T [83]. With decrease in particle size, the saturation magnetization decreases, and on further decrease in particle size, it does not achieve saturation magnetization, and even does not have H_c or M_r. In such situation, particles are so small that without magnetic field, it does not have magnetization just like paramagnetic nature. Such particles are considered as superparamagnetic particles, in which individual particle is assumed as a single domain (Fig. 5.14).

In an assembly of single-domain particles, there is a product of volume (V) and anisotropic constant (K) (KV = particle energy or anisotropy energy), which is much less than that of room temperature energy (kT). It changes the direction of magnetization of a particle from one easy direction to the opposite within 10^{-9} s [84–86]. Net moment becomes zero. In case of normal paramagnetic materials, such as (Na, K), K is zero. In superparamagnetic particles, K is not zero, but the particles behave

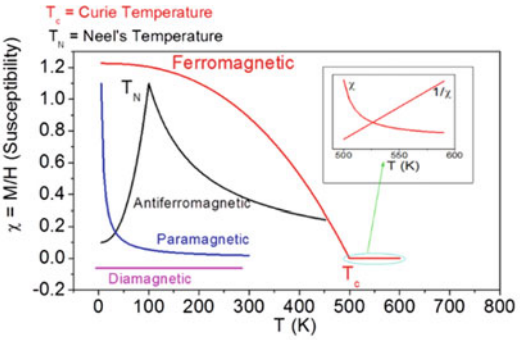

Magnetic susceptibility- temperature curves for different types of magnetic materials

Fig. 5.13 Schematic representation of magnetic susceptibility–temperature curves for different types of magnetic materials: Paramagnetic, diamagnetic, ferromagnetic, and antiferromagnetic behavior can be observed. Paramagnetic substance shows the decrease in susceptibility with temperature, i.e., it follows the Curie Law. Diamagnetic substance has negative susceptibility. Ferromagnetic substance shows the ferromagnetic to paramagnetic transition (T_c), known as Curie temperature. Inset shows the behavior of susceptibility above T_c. Antiferromagnetic substance shows antiferromagnetic to paramagnetic transition (T_N), known as Neel's temperature

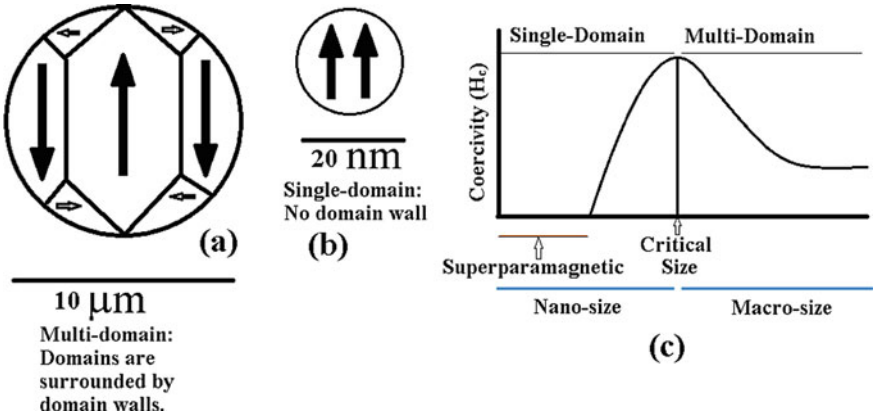

Fig. 5.14 Schematic representation depicting **a** multi-domain, **b** single domain, and **c** H_c versus particle size

as paramagnetic because anisotropic energy (KV) is dominated by the surrounding energy. Every domain or particle can have high moment of 10^3–10^5 μ_B on the basis of chemical formula of atoms or molecule. Thus, the term 'super' is added to paramagnetic as prefix. The relaxation time (τ) is the average time to decay the magnetization value to 1/e of its initial one as given by

$$\frac{1}{\tau} = f_0 e^{-\frac{KV}{kT}} \tag{5.1}$$

In case of high temperature T (kT >> KV), the time-scale of thermal relaxation is much faster than the experimental time window (1–50 s), net moment becomes zero and it becomes superparamagnetic (Fig. 5.15). In case of very low temperature T (kT << KV), the relaxation time is very slow as compared to experimental time window, it shows magnetic moment, and thus, it can show the ferromagnetic behavior. The temperature at which thermal relaxation is equal to experimental time window is known as the blocking temperature (T_b), and above this, it behaves as superparamagnetic, and below this, it behaves as ferromagnetic. The T_b value decreases with decrease in particle size.

The coercivity (H_c) of ferromagnetic materials decreases with decrease in particle size. However, there are two different variations in H_c (Fig. 5.14) [83]. With decrease in particle size in polycrystalline ferromagnetic materials (multi-domain region), there is an increase of H_c, and it reaches the highest value when size of particle becomes single domain or critical size (each particle acts as single domain), and then decrease in H_c is found with further decrease in particle size. H_c becomes zero when particles are so small. These particles are considered as superparamagnetic particles, in which relaxation of magnetization is so fast (10^{-9} s). The direction of magnetization varies from easy direction 0–180° within 10^{-9} s.

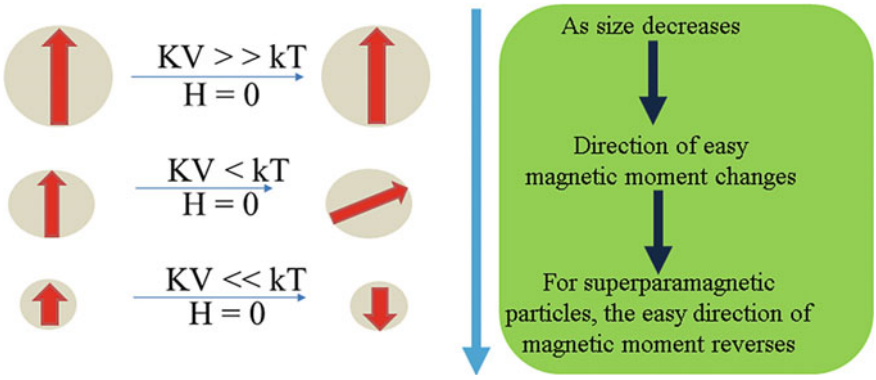

Fig. 5.15 Schematic diagram depicting change in easy direction of magnetic domain with decrease in particle size in room temperature (kT, k is Boltzmann constant). K and V represent anisotropic constant and volume of particle, respectively

There is a decrease in ferromagnetic to paramagnetic transition (Curie temperature, T_c) with decrease of particle size. This is due to decrease in exchange interaction in magnetic structure. E.g., Bulk $MnFe_2O_4$ has T_c at 570 °C and saturation magnetizations (M_s) at 110 and 80 emu/g at 10 and 300 K, respectively [87]. With decrease in particle size down to 5 nm, their Ms and Tc are found to decrease. This is known as finite size effect of nanoparticles on magnetic properties.

Apart from particle size effect on magnetic thermal relaxation of superparamagnetic particles, contribution of surface dangling bonds in small-sized particles must be considered. Even defects in lattice are also associated in small-size particles. Thus, whenever magnetic properties of small-size particles are discussed, effect of small size (KV), surface dangling bonds, and defects in lattices are required (Fig. 5.11). The effect from surface oxidation or chemical-absorption of gases such as CO_2, H_2, H_2O, CO_3^{2-} is also required in small-size particles if experiment is performed in ambient atmosphere (Fig. 5.12). Such ferromagnetic core will be surrounded by antiferromagnetic oxide layer or paramagnetic spins arose from surface or lattice. Sometimes, exchange bias behavior from ferromagnetic@antiferromagnetic interface interaction may arise [88]. Also, cation distribution in ferrites, hexaferrites, and garnet compound needs to be considered during interpretation of magnetic properties [83, 89].

When shape of particles changes from spherical to rods or needle or any shape, the coercivity of ferromagnetic materials increases. This is due to enhancement in magnetocrystalline anisotropic constant (K_{eff}) [83].

There is a decrease of magnetization (emu/g) of ferromagnetic materials with decrease in particle size. The bulk magnetization of Fe_3O_4 at room temperature is 90 emu/g and particles of 8–30 nm size have 30–70 emu/g [90–93]. With change in shape from spherical to rods or needle in particles, there is an enhancement of magnetization in nanosized particles.

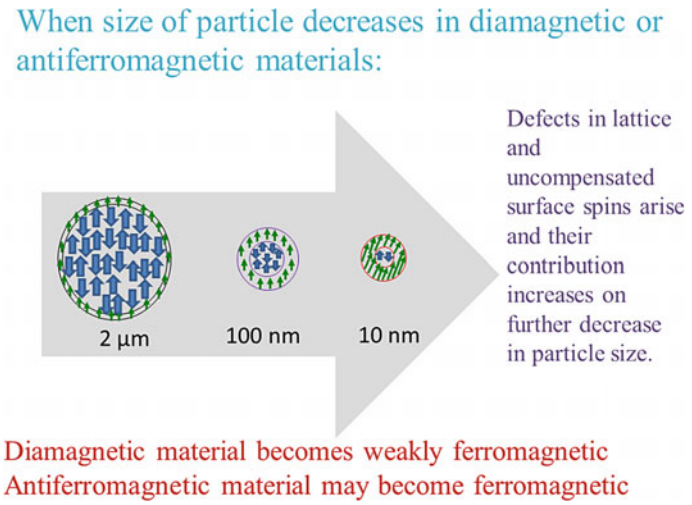

Fig. 5.16 Schematic diagram depicting change in spin structure in diamagnetic and antiferromagnetic particle when size of particle decreases

Now, what behaviors can be seen in antiferromagnetic materials upon decreasing particle size? It can show three types of behavior: (1) reduction in T_N and amount of paramagnetic character may be increased, (2) finite size effect on T_N (in case of antiferromagnetic material) or T_C (in case of ferromagnetic material), and (3) change from antiferromagnetic to ferromagnetic behavior (Fig. 5.16) [94, 95]. Diamagnetic particles become a weak ferromagnetic character (bulk ZnO particles are diamagnetic at room temperature and exhibit a weak ferromagnetic in case of small-sized particles due to localized ordering of uncompensated spins which come from defects in lattice) (Fig. 5.16) [51, 96]. In case of paramagnetic materials, the effect of particle size will be less.

5.4.4 Electrical Resistivity Property

There is an increase of metallicity with reduction in dimension in case of 3D (graphite) to 2D (graphene) in carbon allotropes. Diamond shows insulating behavior and has the highest electrical resistivity as compared to carbon nanotubes, graphite, and graphene in carbon allotropes.

The electrical resistivity (ρ) of elemental metals such as Ag, Au, Cu, Ni, Sn, Gd increases with decrease in particle size [69, 97]. This is due to association of grain boundaries (gb) and surface effect associated in nanocrystalline materials. The electron mean free path decreases with decrease in particle size. It is to be noted that one particle of nanocrystalline material composes of many small crystallites/grains (g), and in between crystallites, there are grain boundaries. Different orientations

of crystallites or lattices are observed in a particle. The path of electrons is not disturbed in crystallite region due to order of atoms/ions, but is disturbed by grain boundaries. Thus, mean free path of electrons decreases in nanocrystalline materials as compared to bulk or single crystal. Thus, electric resistivity follows the same trend. The electron scattering is more in case of nanocrystalline materials as compared to that of microcrystalline materials (Fig. 5.17).

At room temperature, additional resistivity in nanosize particles is related to $\rho_0 \times \lambda/d$, where parameters such as ρ_0, λ, and d are the room temperature resistivity, mean free path of electron-phonon scattering, and length scale, respectively [98]. Here, length scale is related to the wire width or grain size which can add surface and grain boundary scattering. These are important in choosing suitable elemental wire for downscaling of integrated circuits. 10 nm wide Cu interconnect lines have higher resistivity than that of bulk.

Electron mean path values of Ag, Cu, Au, and Ni are 53.3, 39.9, 37.7, and 5.87 nm, respectively, at room temperature [99]. The room temperature resistivity values of Ag, Cu, Au, and Ni are 1.587, 1.678, 2.214, and 6.98 μΩ-cm, respectively. Thus, Ag is the best conductor among these. In same length scale (d), the product of $\rho_0 \times \lambda$ will have minimum value for Ni as compared to others. Thus, Ni will have good conductor for downscaling of integrated circuits.

At low temperature, electrical resistivity (ρ_T) for clean metal is given by:

$$\rho_T = \rho_e + \rho_i \tag{5.2}$$

where ρ_e and ρ_i represent the resistivity arising from the elastic and inelastic scattering, respectively. The ρ_e arises from impurities, defects, or disorder and is

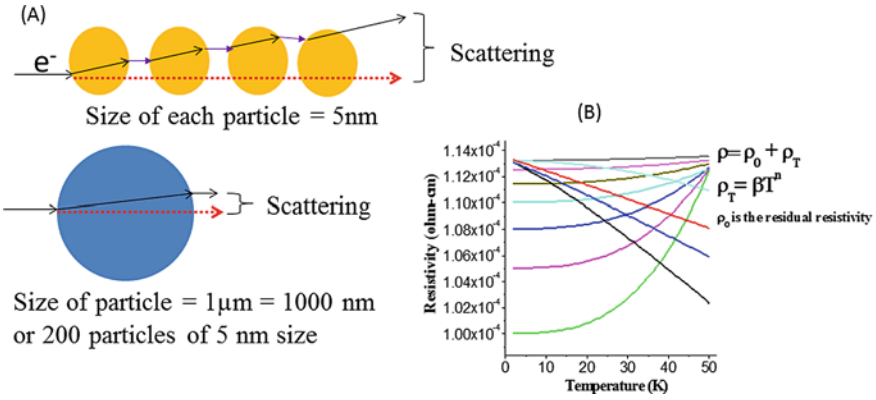

Fig. 5.17 **a** A schematic view of simple understanding of the scattering of an electron when it travels a fixed distance in a micron-size crystal and a nanocrystal. **b** Schematic representation of electrical resistivity versus temperature at low temperature for clean and dirty elemental metals. Curves are the simulated data representation

considered as the residual resistivity (ρ_0). The ρ_i arises from the electron-electron (e-e), electron-phonon (e-ph), and/or electron-magnon (e-m) effects and is proportional to the term βT^n ($2 \leq n \geq 5$ for $T \leq 0.25\theta_D$, and the θ_D is the Debye temperature of metal [100–102]. Thus, electrical resistivity (ρ_T) for clean metal can be written as

$$\rho_T = \rho_0 + \beta T^n \tag{5.3}$$

The ρ-T behavior is shown in (Fig. 5.17). Resistivity increases with temperature. It shows the positive coefficient of resistivity. With increase in value of ρ_0, the behavior in ρ_T-T curve is also shown. The curve is almost a straight line when system becomes highly dirty due to the presence of impurities, defects, or disorder. Then, resistivity decreases with increase in temperature. The nature of curve is like a semiconductor behavior.

5.4.5 *Optical Property*

Only when particle size of semiconductor is less than exciton Bohr radius, its band gap is found to be more than that of bulk. This is due to the quantum confinement effect. Those particles below exciton Bohr radius show the enhancement of band gap with decrease of particle size. Discrete peaks below the minimum absorption energy peak (E_{min}) are generally observed in QDs. The wavelength corresponding to E_{min} increases with increase of size in QDs. It is to be noted that one emission peak is observed at near to E_{min}. The wavelength corresponding to E_{min} in absorption spectrum is slightly less than that corresponding to emission peak. The absorption and emission peaks related to surface defect of semiconductor are generally broad.

Band gap of QDs can be explained by taking formation of molecule from atoms/ions [55]. During formation of molecule, the bonding and anti-bonding orbitals (BMO and AMO) are formed with a particular energy gap (ΔE). With addition of atoms/ions to the molecule, it forms a cluster by reduction of chemical potential of system. With further addition of atoms/ions, formation of QDs in semiconductor starts. Discrete energy levels arise in BMO and AMO. This discrete energy levels come closer when particle size is reaching critical size, known as the exciton Bohr's radius. For particle size above Bohr's radius, it behaves as normal semiconductor (valence and conduction bands). Evolution of QDs from atoms/ions is shown in Fig. 5.18. It is to be noted that the attractive and repulsive forces arise with addition of atoms/ions to the system.

QDs are considered as 0D. In QDs, band gap increases with decrease of particle size. In case of PbSe, bulk has the band gap of 0.26 eV, but QDs with sizes of 2, 4, and 6 nm have the band gaps of 2.06, 1.07, and 0.77 eV, respectively [103]. This happens when crystalline particle size is less than the exciton Bohr radius of material. It is to be noted that bulk PbSe has the exciton Bohr's radius (46 nm). Those particle sizes less than this 46 nm show the blue shift in band gap as compared with the bulk value. Many discrete energy absorptions can be seen in addition to minimum

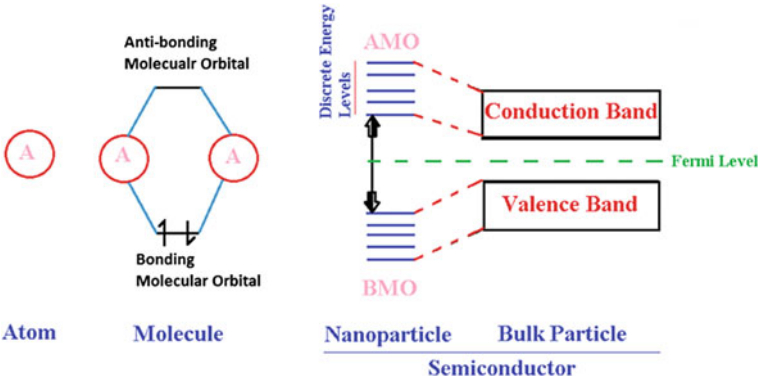

Fig. 5.18 Evolution of QDs from atoms/ions along with bulk semiconductor. AMO and BMO in nanoparticles can be considered as conduction band and valence band of semiconductor, respectively

energy absorption. This is known as the quantum confinement effect in the solid-state communities. TEM micrographs of PbSe particles prepared at 140 °C with waiting time (W_t) of (a) 0.5, (b) 2, (c) 5, (d) 10, and (e) 30 min, and (f) schematic representation of monomers, cluster, and QDs of PbSe are shown in Fig. 5.19. Since the particle size for $W_t = 0.5$ min is too small, its size could not be determined exactly. The particle sizes for $W_t = 2$, 5, 10, and 30 min are found to be 4.1, 5.1, 5.4, and 6.3 nm, respectively. The UV-Visible-NIR spectra of PbSe samples prepared at (a) room temperature (22 °C), (b) 80 °C, and (c) 100 °C with different W_t are shown in Fig. 5.20. PbSe QDs prepared at 180 °C with $W_t = 15$ min show the absorption bands at 675, 1110, 1452, 1715, 2118, and 2397 nm. These are assigned to the discrete levels due to quantum confinement. With increase in W_t at a particular temperature or heating temperature, minimum absorption peak is found to shift to longer wavelength suggesting increase in size of QDs. Magic-sized cluster is obtained for sample prepared at room temperature. Samples prepared at 80, 100, and 180 °C show the behavior of QDs. Figure 5.21 shows the photoluminescence (PL) of PbSe sample prepared at (a) room temperature (22 °C), (b) 80 °C, and (c) 100 °C with different W_t after excitation at 600 nm CW laser (HeNe), and (d) PL decay of PbSe QDs having emission peak at 1300 nm and excitation wavelength at 600 nm. Data are fitted with monoexponential equation. At room temperature, emission peak at 790 nm is obtained. With different waiting times, peak does not shift indicating the presence of magic-size particles. PL spectra of sample prepared at 80 °C for different W_t times show that there are shifts in emission peak at longer wavelength with increase in W_t indicating particle size effect in QDs. Emission peaks at 1078, 1257, and 1360 nm for $W_t = 45$, 60, 120, and 180 min, respectively, are observed. PL spectra of sample prepared at 100 °C for different $W_t = 10$, 15, 30, and 60 min show peaks at 1127, 1215, 1363, and 1481 nm, respectively.

The lifetime values for QDs having emission peaks at 1300 and 1535 nm are obtained to be 1.3 and 1.0 μs, respectively.

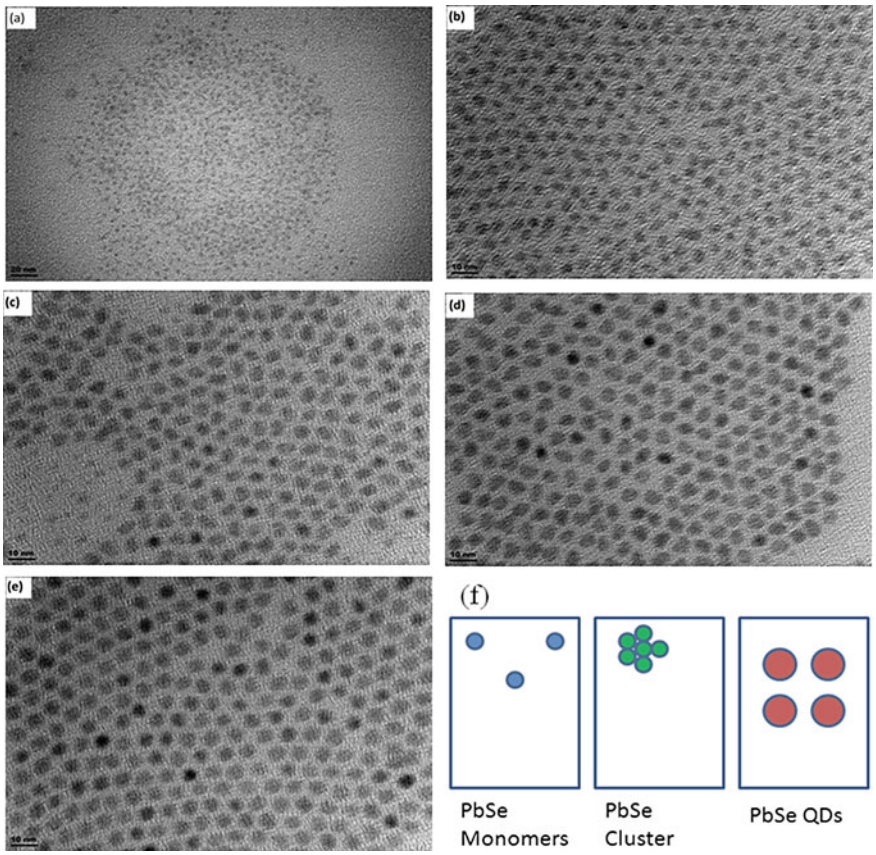

Fig. 5.19 TEM images of PbSe particles prepared at 140 °C with waiting time (W_t) of **a** 0.5, **b** 2, **c** 5, **d** 10, and **e** 30 min. **f** Schematic representation of monomers, cluster, and QDs of PbSe. Reproduced with permission from PCCP Owner Societies and RSC Publications as a co-author of this paper [103]

As compared to bulk, the quantum yield of emission from QDs can be increased to 80–95%. Generally, luminescence intensity is improved with decrease of particle size in QDs and peaks are sharp. This is opposite to bulk or micron-sized particles because non-radiative from surface effect is associated.

QDs of PbSe nanoparticles are prepared by injecting Se-TOP into Pb-oleate in 1-Octacence, which was kept at 80–170 °C [103]. With different waiting time at a particular temperature, size of QDs can be varied. Instead of Se-TOP, when Se-TDP (TDP = tris(diethylamine)-phoshphine) is added to Pb-oleate in 1-Octacence, which was kept at 170 °C, it forms PbSe of nanorods [104]. Depending on the ratio of Pb and Se, the different lengths of nanorods are prepared. With increase of waiting time, length of nanorods increases (Fig. 5.22), and also absorption peak shifts to longer wavelength with increase in length (Fig. 5.23).

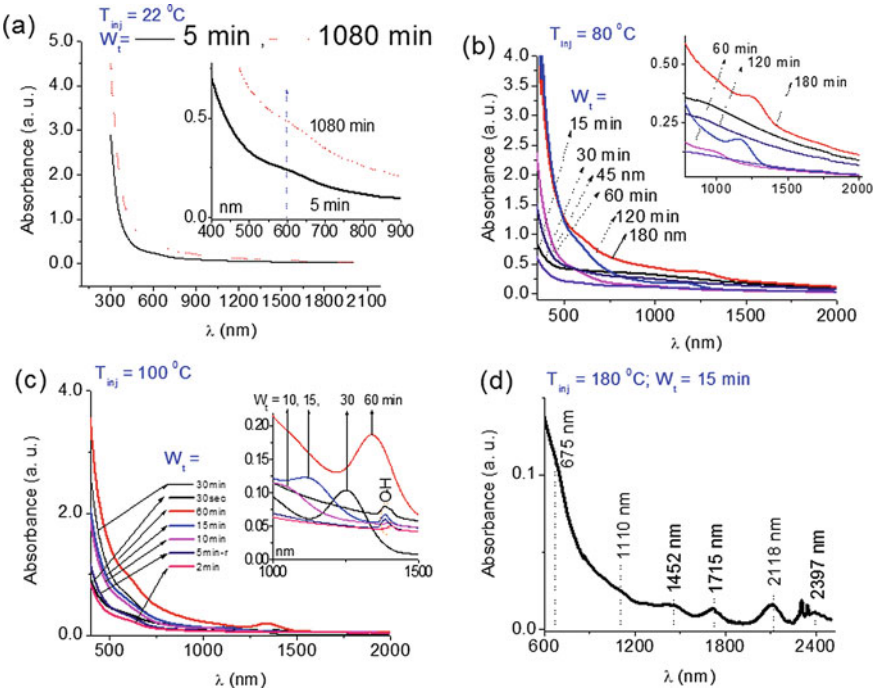

Fig. 5.20 The UV-Visible-NIR spectra of PbSe samples prepared at **a** room temperature (22 °C), **b** 80 °C, and **c** 100 °C with different waiting times (W_t, minutes). **d** PbSe QDs prepared at 180 °C with $W_t = 15$ min show the absorption bands at 675, 1110, 1452, 1715, 2118, and 2397 nm, which are assigned to the discrete levels due to quantum confinement. Reproduced with permission from PCCP Owner Societies and RSC Publications as a co-author of this paper [103]

Many shapes of PbSe nanoparticles can be prepared using noble metal nanoparticles (Au, Ag, or Pd) as seed. Here, concentrations of the seed and precursors are varied. Various shapes such as quantum dots, cubes and stars of nanostructures are prepared. The yield is very high (Fig. 5.24) [105].

It is to be noted that excitons are the imaginary quasiparticles produced by pairing of an electron (from the conduction band) and a hole (from the valence band), due to Coulombic interaction [55]. It forms H-like atom states with diameter significantly larger than the unit cell length. The exciton radius (R_b) can be calculated from the effective masses of electron (m_e*) and hole (m_h*) and dielectric constant of medium (ε), and their relation is given below:

$$R_b = \frac{h^2}{e^2}\left(\frac{1}{m_e^*} + \frac{1}{m_h^*}\right) \tag{5.4}$$

As the band gap of nanoparticle semiconductor (E_g) is more than the bulk ($E_g(R \rightarrow \infty)$) due to the quantum confinement effect (QCE), their relationship

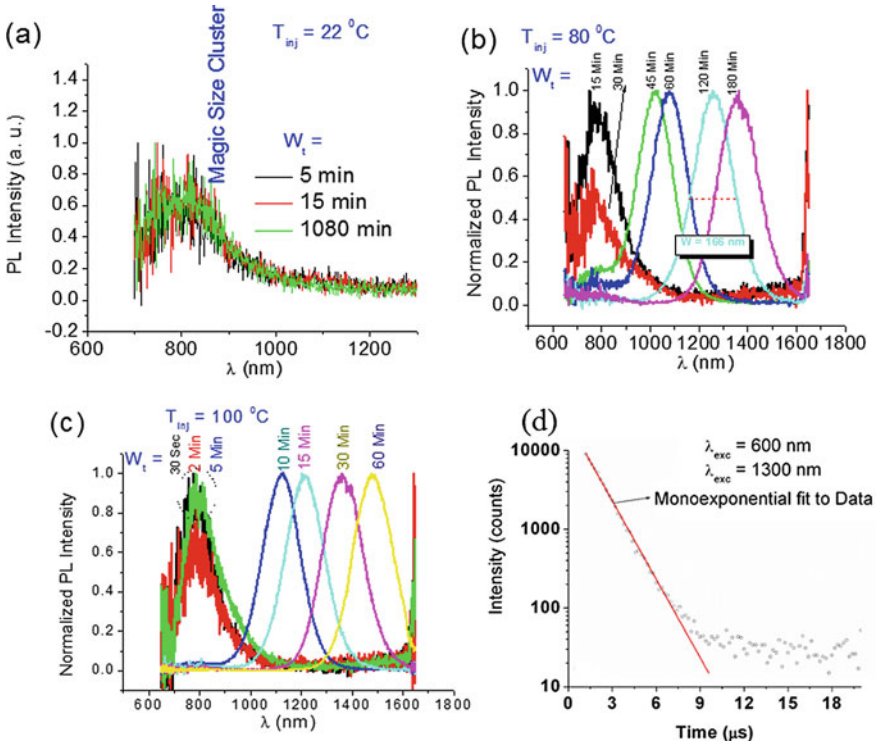

Fig. 5.21 PL spectra of PbSe sample prepared at **a** room temperature (22 °C), **b** 80 °C, and **c** 100 °C with different waiting times (W_t, minutes). **d** Luminescence decay of PbSe sample having emission peak at 1300 nm. Data are fitted with monoexponential equation. Excitation wavelength is fixed at 600 nm. Reproduced with permission from PCCP Owner Societies and RSC Publications as a co-author of this paper [103]

is given below:

$$E_g = E_{g(R\to\infty)} + \frac{h^2}{8R^2}\left(\frac{1}{m_e^*} + \frac{1}{m_h^*}\right) \tag{5.5}$$

where R is the radius of particle size assuming it to be a spherical particle.

Even particle size of material slightly greater than that of the exciton Bohr radius can show the quantum confinement when particles are dispersed in another dielectric medium or core–shell formation. For example, SnO_2 has the exciton Bohr radius of 2.4 nm, which is too small. Thus, it is difficult to prepare QDs of SnO_2. But SnO_2 having particle sizes of 3 and 5 nm can show quantum confinement when dispersed in TiO_2, SiO_2, or Y_2O_3 matrix [106–110].

There is a report on increase of band gap for MoS_2 with reduction of dimension from 3D ($\Delta E = 1.23$ eV, bulk) to 2D layers ($\Delta E = 1.88$ eV, monolayer) [111].

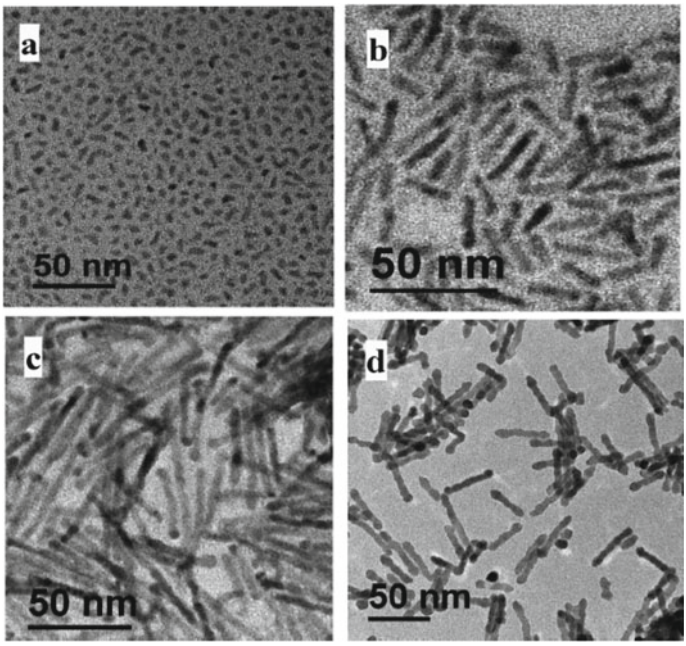

Fig. 5.22 TEM images of different growth times/waiting times: **a** $W_t = 30$ s, d = 3.9 nm; **b** $W_t = 2$ min, d × L = 3.8 × 21 nm^2; **c** $W_t = 4$ min, d × L = 4.1 × 44 nm^2; and **d** $W_t = 8$ min, d × L = 5.7 × 35 nm^2. (d is diameter of the rods and L is the length of the rods). Reproduced with permission from ACS Publications [104]

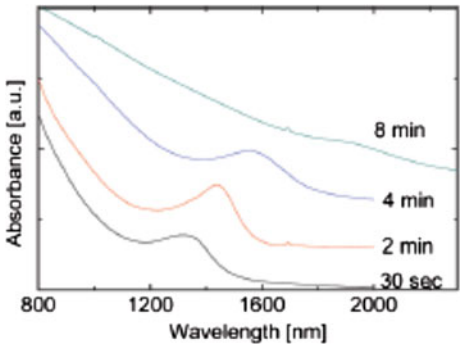

Fig. 5.23 Absorption spectra of different growth times/waiting times: **a** 30 s, d = 3.9 nm; **b** $W_t = 2$ min, d × L = 3.8 × 21 nm^2; **c** $W_t = 4$ min, d × L = 4.1 × 44 nm^2; and **d** $W_t = 8$ min, d × L = 5.7 × 35 nm^2. (d is diameter of the rods and L is the length of the rods). Reproduced with permission from ACS Publications [104]

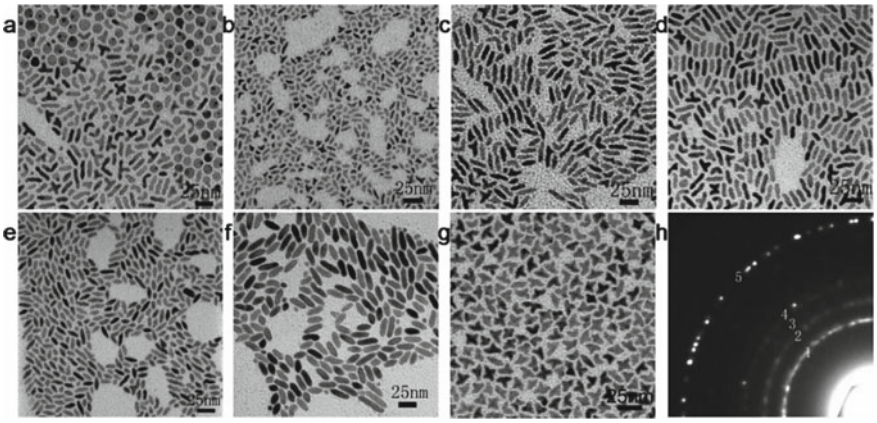

Fig. 5.24 TEM images of and transmission electron diffraction from PbSe nanocrystals: **a**–**d**, **g** Reactions carried out at 125–135 °C, **e**, **f** reaction carried out at 155 °C. **a** Final products as a mixture of Au-Fe_3O_4 seeds and PbSe nanorods. PbSe nanorods extracted at **b** 4, **c** 7, **d** 9 min waiting time, **e** 30 s, and **f** 90 s waiting time after selenium injection. **g** TEM image of branched PbSe nanocrystals produced after 8 min of reaction at 125–135 °C using ½ the quantity of seed particles used for the samples shown in (**a**)–(**f**). **h** Electron diffraction pattern of the final products in (**a**). Reproduced with permission from ACS Publications [105]

In case of carbon allotropes, graphite belongs to 3D type having semiconducting property with narrow band gap of 40 meV, whereas graphene belongs to 2D having semi-metallic property [112]. Their properties in 2D and 3D are largely different even though chemical formula of molecule is same.

In metallic systems such as Ag, Au, and CuS nanoparticles, surface plasmon resonance (SPR) spectrum is observed [113]. In case of nanorods, two SPR peaks corresponding to diameter of rod (at lower wavelength, which is similar to spherical nanoparticles) and length (at longer wavelength due to longitudinal polarization effect) are observed.

5.4.6 Bulk Density of Materials

Nanocrystalline materials have lower temperature to achieve 95–99% theoretical density as compared to coarse micron-sized particles [69]. The TiO_2 nanocrystalline 12 nm shows enhanced densification as compared to 13 μm at same temperature of heat-treatment, say at 900 °C. The pore or void density is less in case of nanocrystalline TiO_2 as compared to that in micron particles. This is confirmed by enhanced decrease of a positron annihilation lifetime in case of nanocrystalline sample (about 390 ps) as compared to that in micron particles (about 420 ps). Doping of Y in nanocrystalline TiO_2 enhances densification, but their grain size decreases.

With increase of consolidation pressure up to 3 GPa, nanocrystalline Fe particles (6–10 nm) show additional broadening in sextet spectrum of Mossbauer recorded at 77 K [69]. One sextet is fitting with α-Fe in perfect lattice and broadening comes from Fe atoms in grain boundary. This is due to increase in grain boundary percentage, and simultaneously, percentage of pore or void present in lattice decreases. The broadening in peak decreases after annealing nanocrystalline Fe at 500 °C for a few hours in vacuum. In this way, size of particles increases to bulk. This is also proved by positron annihilation data of nanocrystalline Ni (in which two lifetime data (183 and 291 ps) are observed and corresponding to the presence of vacancies or pores of two different types).

Absorption of H_2 occurs in case of Pd [69]. Nanocrystalline Pd has more storing capacity of H_2 as compared to single crystalline Pd. This is due to presence of grain boundaries in nanocrystalline Pd. Usually, H_2 molecules or atoms occupy interstitial sites of Pd (tetrahedral and octahedral sites) in case of single crystal, and occupy interstitial sites as well as grain boundaries in case of nanocrystalline.

5.4.7 Variation in Properties from Single Layer to Multilayer/Heterstructures/Superlattice

With change from single layer to multilayer or heterostructure (–A/B/A/B/A–), luminescence intensity can be improved. This happened in LEDs such as GaN/InN or GaN/AlN heterostructures as compared to pure GaN, InN, or AlN [100, 114]. In heterostructures, photo-catalytic property can be improved due to tuning of band bending at Fermi energy [78].

Even, giant magnetoresistance (GMR) is observed in such as multilayer or superlattice system of Fe/Cr/Fe or Fe/Mn/Fe, Co/Cr/Co, Co/Mn/Co, and enhancement in GMR is observed with increase of multilayers [115–117]. Each layer has 5–20 Å thickness. This provides higher data storage capacity. Schematic diagram show the resistivity drop in the presence of a few Tesla (Fig. 5.25). Fe or Co is ferromagnetic and Cr or Mn is antiferromagnetic in nature. Without magnetic field, antiferromagnetic coupling between Fe and Cr occurs, and thus resistance is very high. In the presence of magnetic field, all spins in Fe and Cr are parallel to each other, and thus, resistance is dropped significantly.

5.4.8 Evolution of Multifunctional Materials by the Formation of Core–Shell or Composite or Hybrid

In case of noble metals such as Ag and Au, these are often found in rocks, rivers, ponds, muds, etc., and their intrinsic properties do not change much. However, in case of Fe and Co, they do not exist freely in nature. They are highly oxidized and form

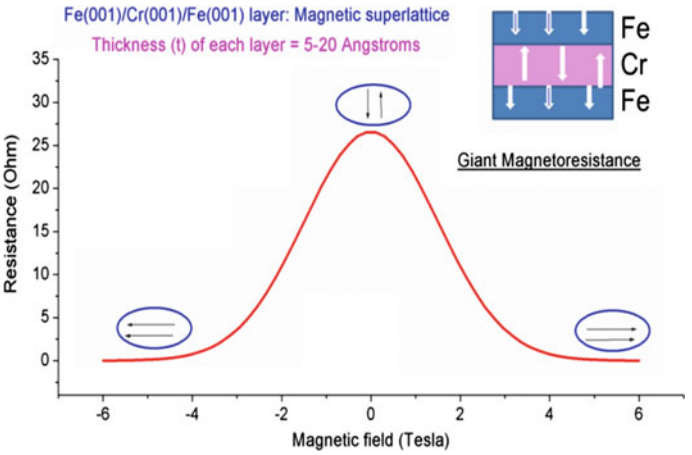

Fig. 5.25 Resistivity versus Magnetic field in Fe(001)/Cr(001)/Fe(001) layer: magnetic superlattice. This is redrawn from Ref. [115–117]

oxides in ambient atmosphere. Even, some oxides such as Fe_3O_4 are slightly stable as compared to pure Fe, but they are less stable than that of α-Fe_2O_3 [93, 118]. It means that unstable phase can form core–shell formation in native oxygen or ambient environment. With time, they are converted to stable phase. For example, Fe_3O_4 particles are converted to α-Fe_2O_3 with time or by heating. This can be represented by core–shell model: Fe_3O_4 (t = 0 s), Fe_3O_4@α-Fe_2O_3 (t = 30 days), α-Fe_2O_3 (1 year).

When there is a decrease of particle size down to nanometer, the chemical and physical properties of materials change. The chemical stability is less than that of bulk. Even in inert atmosphere, percentage of surface dangling bonds increases with decrease in particle size, and thereby their magnetic properties are varied: decrease in magnetization and Curie temperature. Increase of surface dangling bonds can form ferromagnetic core@antiferromagnetic shell that is confirmed by exchange bias in coercivity study [119].

With decrease of particle size in noble metals such as Ag and Au, electron density of states at the surface of particles is different from their bulk. They result in the surface plasmon resonance (SPR) effect [113].

Intentional addition of shell or conjugation of another material can change properties of particle. Even co-doping to host can improve properties in terms of luminescence and magnetic properties. Examples are SnO_2@SiO_2, SnO_2-SiO_2, SnO_2-TiO_2, Au@UNPS (UCNP = unconversion nanoparticles), AVO_4:RE, APO_4:RE, $NaYF_4$:RE, and their core shell (shell = same host material or another material; RE = rare-earth) [106–110, 120–137]. Luminescence intensity is generally improved in case of core@shell structures. AVO_4:RE@AVO_4, AVO_4:RE@SiO_2, $NaYF_4$:RE@$NaYF_4$ have more luminescence intensity as compared to that

of core counterpart. The hybrid of magnetic and luminescence nanoparticles such as CaF_2:Eu-Mn@Fe_3O_4, YVO_4:Eu @Fe_3O_4, UNPS@Au@Fe_3O_4, $NaErF_4$:Tm@$NaYF_4$:Yb, $CaMoO_4$:Tb@Fe_3O_4, $Mn_{0.5}Fe_{2.5}$@YVO_4:Eu^{3+} show interesting properties as compared to individual materials [36, 120, 122, 123, 133, 134]. These materials have potential for bio-imaging and therapy under AC magnetic field and under NIR laser excitation. This can bring multi-functional materials after conjugation of two or more materials having different properties.

5.4.9 Change in Crystal Structure or Crystallinity with Reduction in Particle Size

In general, crystallinity decreases with decrease in particle size in nanosized range. With decrease of particle size, stability of a phase or crystal structure changes [138]. Metal bulk cobalt (Co) exits into two forms, HCP and FCC phases. With decrease of particle size to 10 nm, a new phase ε-Co (structurally related to the β phase of Mn) is formed.

In bulk form, insulator alumina (Al_2O_3) exits in α-form. However, with decrease of particles, another crystal structure of γ-form is formed [139–141]. This is due to increase of surface area with decrease of particle size. This surface energy is taking main role in formation of γ-form.

5.4.10 Induced Electric Field or Induced Magnetic Field Study

MoS_2 (bulk) and MoS_2 nanosheets are semiconductors. Upon applying electric field, bulk MoS_2 can be brought to superconducting at 9.4 K [142].

5.4.11 Thermodynamic Properties (Excess Enthalpy, Melting Point) with Decrease in Particle Size

Generally, surface energy is higher in case of small-sized particles as compared to bulk particles. Because of this, their chemical and physical properties are different from bulk. The excess enthalpy of SnO_2 increases with decrease of particle size [143]. The melting point decreases with decrease in particle size of material [69].

5.4.12 *Surface Functionalization, Processing, and Finishing for a Particular Application*

Surface functionalization is necessary to get desired products. For biomedical application, proper surface functionalization is required, so that particles become highly dispersible in water, have longer stability in the blood flow, become specific to target, have chemical stability, and are highly biocompatible. For ceramic application, material should be highly stable at higher temperature [54]. For purpose of smart materials, it should have high sensitivity at any change of pH, temperature or pressure or moisture or gases. In this, proper fabrication and engineering aspect is necessary [144]. For coating materials, nitrides, carbides, borides, and oxides can be used [53, 100, 145]. For covering precious materials, light materials having carbon or aluminum matrix can be used. Since carbon nitrides and boron nitrides are very light, stable, and have high mechanical stability, they are used as bullet protecting materials [146]. They are usually inert to other materials. Dynamic impact resistance tests of these nitrides exhibit that the wearable electronic textile (WET) absorbs all the impact energy.

For coloring of materials with golden color, TiN can be coated over material [53, 100]. For making of drilling machine and ultra-hard materials, nitrides and carbides are used [53, 100]. Carbon nitrides and WC are used for such purposes. LaB_6 has been used as electron emitter in electron microscopy [53, 100]. Silicon nitride and carbon nitrides are used as tip in atomic force microscopy [53, 100]. For solder materials, lead-free materials containing Sn, In, Zn, Cu, Bi, Ag have been used [147]. For cosmetic purpose in paint or face makeup and skin protection, TiO_2, Ag, and ZnO nanoparticles are added as additive [148]. For battery, many nanoparticles of carbon-based materials, 2D materials, Li- and Na-based materials are used, and show the better quality of battery in terms of capacity, reuse through recharge and discharge, and longer life time [149].

5.5 Determination of Particle Size Distribution

The following statistical terms will be useful in consideration for particle size and shape distribution.

5.5.1 *Gaussian or Normal Distribution (Mean, Median, and Mode)*

Gaussian distribution is commonly considered as normal distribution and is a form of continuous probability distribution for a real-values random variable. Its probability density function (f_x) is defined by [150–152]:

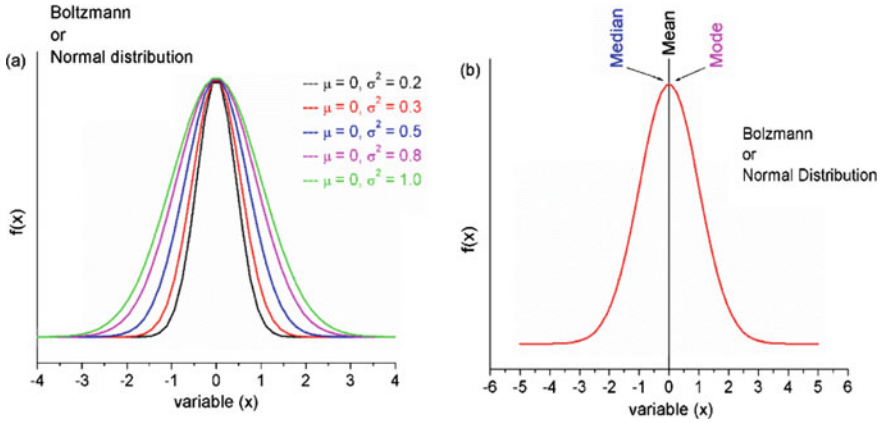

Fig. 5.26 **a** The probability density function f(x) with variable (x) following normal distribution. **b** Positions of mean, median, and mode in distribution. All the curves are the simulated data representation

$$f(x) = \frac{1}{\sigma\sqrt{2\pi}} e^{-\frac{1}{2}\left(\frac{x-\mu}{\sigma}\right)^2} \tag{5.6}$$

where μ is the mean of expectation of the distribution and σ is the standard deviation and its square value (σ^2) is called the variance of the distribution. 'x' is variable value.

Figure 5.26(a) shows the probability density function f(x) with variable (x) following normal distribution. From this, it is observed that distribution function is different for various variance values (σ^2) even though mean value is same ($\mu = 0$). Figure 5.26b shows the positions of mean, median, and mode in distribution. Mean is arithmetic average of the data. Median is a value in particle size, and it divides the population accurately into two equal halves, and this value is in between 50% above and 50% below distribution. Mode is the most common value of the frequency distribution, and it is assigned to the highest point of the frequency curve.

Figure 5.27a shows the particle size distribution function f(x) or number of particles with variable (x) or particle size (D, nm), which follows the normal distribution. Here, mean, median, and mode have same value, i. e., 10 nm. Figure 5.27b shows bimodal distribution of particles and both (depicted as '1' and '2') follow normal distribution. The variable x or change in particle size is exactly same (i.e., '1' has 6–14 nm and difference is 8 nm; '2' has 14–22 nm and difference is 8 nm). Mean is average of '1' and '2' distributions and this is assigned with 14 nm. However, there is no particle. Also, the particle size distributions in '1' and '2' are 49% and 51%, respectively. After removing 1% from '2,' median is obtained. The exact position is not provided. The mode is assigned to '2' since it has higher population as compared to '1.' In case of '1' having 6–14 nm and '2' having 14–26 nm, the mean is 16 nm, and median is assigned above mean (not exact value); and mode is assigned to '2'

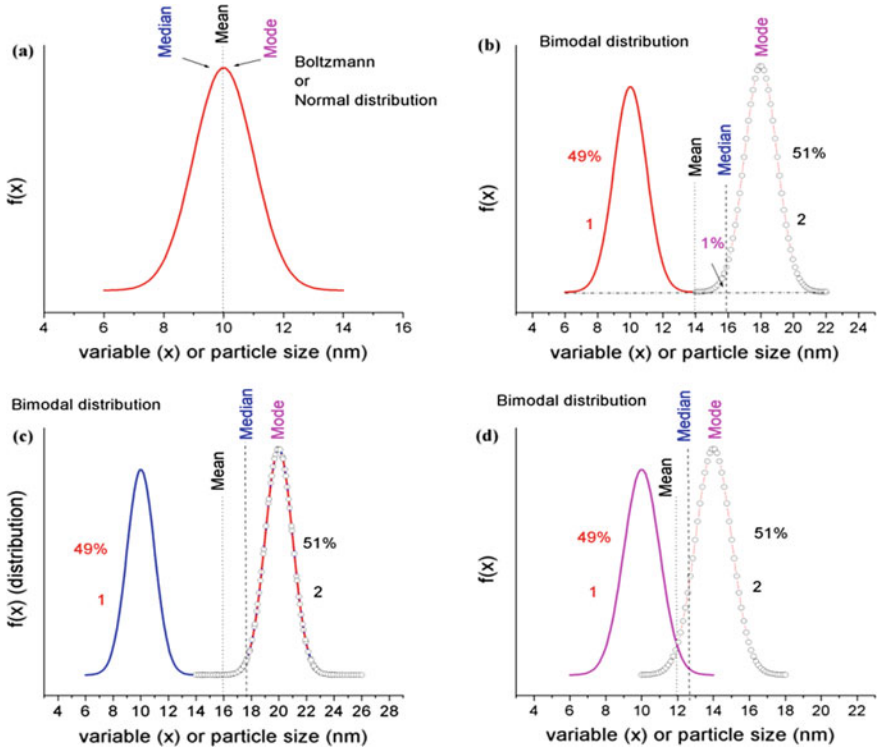

Fig. 5.27 **a** The particle size distribution function f(x) or number of particles with variable (x) or particle size (D, nm), which follows the normal distribution. **b** bimodal distribution of particles and both (depicted as '1' and '2') follow normal distribution. The variable x or change in particle size is exactly same (i.e., '1' has 6–14 nm and difference is 8 nm; '2' has 14–22 nm and difference is 8 nm). **c** bimodal distribution of particles and both (depicted as '1' and '2') follow normal distribution. The variable x or change in particle size is exactly same (i.e., '1' has 6–14 nm and difference is 8 nm; '2' has 14–26 nm and difference is 12 nm). (d) bimodal distribution of particles and both. There is overlapping of both curves. All the curves are the simulated data representation

(Fig. 5.27c). In both Fig. 5.27b and c, there is no overlapping in both '1' and '2.' In Fig. 5.27d, there is overlapping, the mean is 12 nm, which has particle. From these, it can be possible to have a number of particle size distributions, such as tri-modal, etc.

5.5.2 *Log-Normal Distribution*

In general, particle size distribution is not exactly normal or Boltzmann. There is randomization in distribution [150–154]. This is usually calculated using log-normal distribution, and its probability density function (f_x) is defined by:

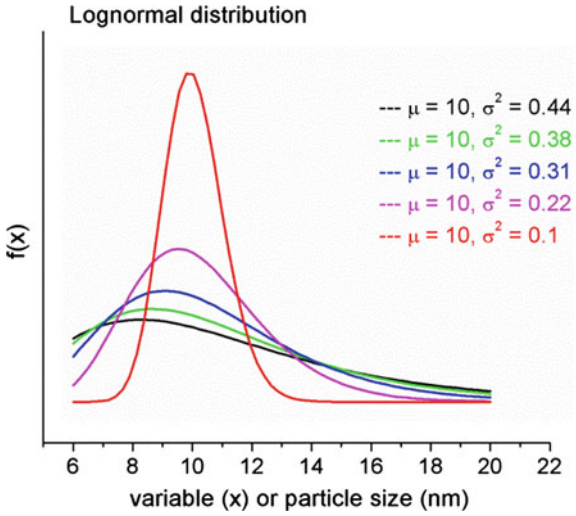

Fig. 5.28 The log-normal distribution curves for different values of mean and variance

$$f(x) = \frac{1}{x\sigma\sqrt{2\pi}} e^{-\frac{1}{2}\left(\frac{\ln(x/\mu)}{\sigma}\right)^2} \tag{5.7}$$

where μ is the mean or expectation of the distribution and σ is the standard deviation and its square value (σ^2) is called the variance of the distribution. 'x' is variable value. Exact calculations of mean, median, variance, and mode are slightly different from those of normal distribution. Figure 5.28 shows the log-normal distribution curves.

5.5.3 *Other Distributions*

In addition to normal or log-normal distribution, many equations are used to analyze particle size and shape of particles of inorganic, organic, minerals, food, and biomaterials. Details can be found in many literatures [152–159].

5.5.4 *Aspect Ratio, Regular, and Irregular Shapes*

The size and shape of particles prepared in laboratory may vary from spherical to rod, hollow, star, prism, disc, needle, triangular, tube, fibrous, etc. [155–162]. It is not so easy to calculate mean, median, and mode using normal or log-normal distribution when shape changes from spherical to others. Many mineral particles are available in nature and are used in various industries in catalysis, as fillers, in coatings, as absorbers, etc. It is required to control particle size and shape for the

performance and properties of materials. Even after dispersion in liquid, the rheological properties of dispersions depend on analysis of size and shape of particles. For use of particles as biomaterials, it requires size and shape of particles, chemical and photo-stability, biocompatibility, mechanical stability, microenvironment, etc. Many techniques are used to see morphology of particles using sedimentation method (Stoke's law), Laser light scattering/projected area (Fraunhofer), Laser light scattering/particle volume (Mie-theory), Photon correlation spectroscopy/translational diffusion, surface area using BET technique, electron microscopy, DLS (Dynamic light scatterings) techniques, etc. Still many variations in size and shape of particles are obtained. Surface area measurement has limitations because even pores available in particles can provide additional surface area apart from surface of particles.

In disc shape, there are diameter and thickness. With increase of thickness, it becomes rod shape. In such cases, ratio of major length to minor length can provide aspect ratio. This is an important parameter in mechanical, rheological, magnetic properties, etc. Aspect ratio (AR):

$$AR = \frac{L_{Major}}{L_{Minor}} \tag{5.8}$$

Regular-shaped particles are of spherical, disc, rod, sheet, hollow, core–shell, needle, star, rigid fibrous, triangular, oblate, tube, etc. For rod-, needle-, or wire-shaped particles, there are two axes such as minor and major axes. The volume of spherical particle by taking minor length as diameter can be calculated. Then, number of equivalent volumes of spherical particle with minor length as diameter present in rod, needle, and wire can be approximately calculated. Even, when shape becomes oblate, star, prism, or triangular, such equivalent volumes can be used, so that approximate value of equivalent volume of a particular-shaped particle can be compared with others. In case of hollow or tube, inner and outer volume calculations can help in finding equivalent volume. However, when shapes do not have a proper regular, it is difficult to use equivalent volumes. Instead, surface area measurement, small angle neutron scattering, small angle x-rays scattering, and image software will help in proper calculation of volume.

5.6 Mechanism

Mechanism behind the formation of nucleation and growth of particles in different media [69, 163–171]:

(A) Solid State Phase
(B) Liquid State Phase
(C) Gas State Phase
(D) Single-crystal growth from S-L phases.

5.6.1 Solid State Phase

In solid state, the molecules or atoms in a particle are closely packed together and have chemical bonding through ionic, covalent bond, or metallic bond [172]. Generally, they are rigid, but atoms in solid are under constant vibration. They can undergo chemical reaction either by heating or changing environment. For example, oxidation of iron piece occurs in ambient atmosphere. In case of decomposition of $CaCO_3$, it requires heat to produce CaO (solid) and CO_2 (gas). Two types of chemical reactions are observed: Homogeneous and Heterogeneous reactions. In homogenous, phase transformation occurs from one solid to solid or liquid or gas (S-S, S-L, S-G). In case of heterogeneous, different species (reactants or products) are involved. Mechanisms involved in the solid-state reaction can include the following [163].

1. Phase Change, 2. Formation of Phase Boundaries or Interface, 3. Rate Process Changes, 4. Nucleation, 5. Growth, 6. Diffusion.

5.6.1.1 Phase Change

In case of phase change, homogeneous and heterogeneous types of phase changes occur. Homogeneous type of phase changes is S-S, S-L, and S-G phase transformations. Example of S-S phase transformation is polymorphic transformation (diamond to graphite, graphite to graphene, graphite to carbon-nantube). Example of S-L phase transformation is melting (diamond melts at 4000 °C in inert atmosphere). Example of S-G phase transformation is sublimation (naphthalene sublimes at 80 °C at standard atmospheric temperature, sublimations of ammonium chloride, camphor, iodine, and anthracene). In case of heterogeneous transformation, different species of reactant or product are associated. Table 5.1 will provide the possible ways of heterogeneous

Table 5.1 The possible ways of heterogeneous transformation [163]

Ways or types	Reactants	Products	Reactions/examples
Decomposition or disproportionates	A→	B +C:S +S S +G G +G	$3AuCl \rightarrow 2Au + AuCl_3$ $CaCO_3 \rightarrow CaO + CO_2$ $NH_4Cl \rightarrow NH_3 + HCl$
Combination or synthesis	A + B→	C: S	$MgO + A1_2O_3 \rightarrow MgAl_2O_4$ $MgO + SiO_2 \rightarrow MgSiO_3$
Replacement or substitution	A + B→	C +D:S +S S +G	$Cu + AgCI \rightarrow CuCI + Ag$ $BaCO_3 + TiO_2 \rightarrow BaTiO_3 + CO_2$
Sequential or consecutive	A→	B → C	(i) $La_2O_3 + 11A1_2O_3 \rightarrow 2\ LaAlO_3 + 10A1_2O_3$ (ii) $2LaAlO_3 + 10A1_2O_3 \rightarrow LaAl_{11}O_{18}$

transformation. Here, symbols such as A, B, C, D are used to represent reactants or products. S, L, G stand for solid, liquid, and gas phase, respectively.

5.6.1.2 Formation of Phase Boundaries or Interface

When solid particles of different phases (A and B reactants) are mixed using pestle mortar, it imparts close proximity. The possible interactions from mixing are: (1) no reaction at room temperature or a slight higher temperature, i.e., it needs activation energy (ΔE) for formation of interface (C). (2) it starts the formation of interface (C) due to fast diffusion of atoms or ions of A and B at room temperature or higher temperature. With time at particular temperature (higher than that required for formation of interface), the size of interface increases. If amount of A is more in terms of atomic percentage than that of B, some part of A remains as unreacted after completion of reaction between A and B in case of AB chemical formula. In some cases, it so happened that B atoms or ions are homogeneously or heterogeneously mixing with A atoms depending on types of chemical compounds or stoichiometry (AB, A_nB, AB_n ($n = 2–12$)) formed. (3) In case, A site is highly stable in terms of chemical bonding even at higher temperature (i.e., inert). It is difficult to react with B atoms or ions. When there is a presence of vacancies in the lattice of A, the chemical stability of A decreases. Atoms or ions of B site can enter the interstitial sites or void or pores of A site, and reaction starts at small region of A site to form interface inside A site. (4) Either of A or B site or both have very small-sized particles (nanosized). The reaction for formation of interface occurs at lower temperature than normal reaction temperature, because small-sized particles have large surface area as well as less chemical and thermal stability. (5) In some case, if A is highly stable, but B decomposes to other species (solid or gas or liquid or S-S, S-G, or S-L) at slightly higher temperature, reaction for formation of interface can be enhanced if one or more species after decomposition of B starts reaction with A site. This is due to atomic level interaction between A and species at different environment. Interface region of A and B to form new compound (C) at the first stage is known as nucleus and the process is known as nucleation. (6) The presence of impurities in A or B site or both may change the formation mechanism for interface. The size of interface can be increased with extent increase of time under temperature or pressure or radiation and this is considered as growth. The possible interactions from mixing of reactants are represented by schematic diagram (Fig. 5.29). The density of compound (C) can be increased by annealing compacted portion (pallet) of compound at higher temperature ($T = 0.7–0.8\ T_m$; T_m = melting point of compound C). This process is known as sintering. By changing partial pressure of reaction medium or by changing environment through addition of alkaline or acidic material/gases or by variation of pressure or temperature, the various reaction pathways for formation of compounds including metastable phases can be produced.

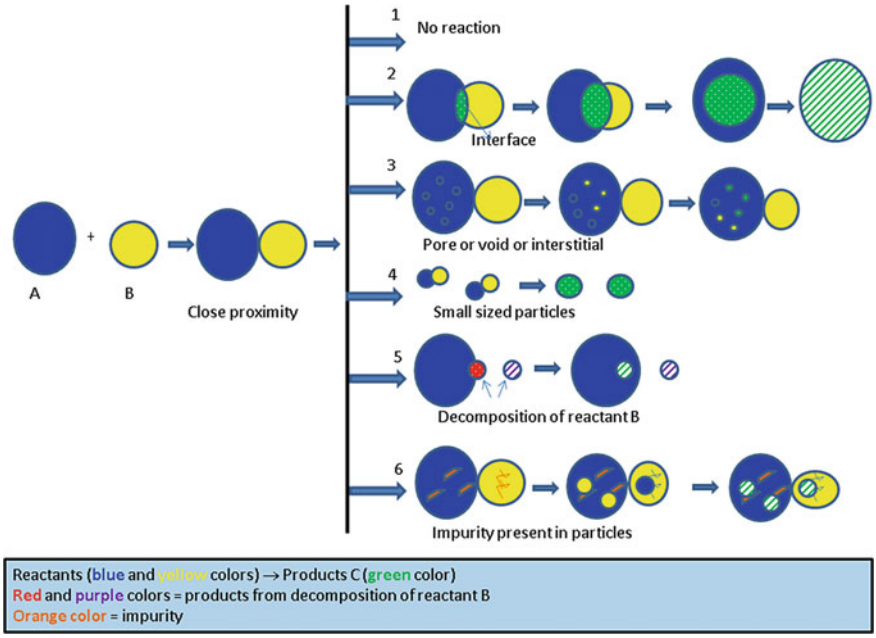

Fig. 5.29 Schematic representation depicting the possible interactions from mixing of reactants or particles. Details are provided in main text

5.6.1.3 Rate Process Changes

The rate equation for homogenous reaction in gaseous system can be expressed

$$A_s \rightarrow B_s \tag{5.9}$$

The rate equation is

$$r = {}^{-d[A]}/_{dt} = k[A] \tag{5.10}$$

[A] is concentration of reactant A. k is a reaction rate coefficient. The free energy (G_A) of reactant is less than that of activation energy (G^*), and that of product (G_B) is less than that of reactant.

$$\Delta G = RT\ln K^* \tag{5.11}$$

where K^* is equilibrium constant.

In case of solid-state reaction, rate equation is defined by [163].

$$\text{rate} = {}^{dn_i}/_{dt}\left({}^{1}/_{V_t}\right) \tag{5.12}$$

where n_i is initial moles and V_t is the volume of solid/interface/compound formation at time t.

In case of heterogeneous reaction, rate equation is complicated depending on type of reaction. It may associate various activation energies such as initial, intermediate and final.

5.6.1.4 Nucleation and Growth

In solid-state reaction, nucleation starts at surface of particles where chemical reaction between particles of reactants occurs. With time, growth of new particles starts if sufficient reactants are present.

5.6.1.5 Diffusion

Diffusion in solid-state reaction involves one or more of the following: the interchange of atoms or ions, vacancy hopping, movement of interstitial sites, and exchange due to decomposition or pressure and temperature gradient. The Fick's law can be applied in diffusion [163]:

1. First law:

$$J = {}^{-Ddc}/_{dx} \tag{5.13}$$

   where J is total number of jumps and D is diffusion coefficient for a process. Dc/dx is change in concentration with distance x.
2. Second law:

$$[dc/dt]_x = d\{Ddc/dx\} \tag{5.14}$$

$$(dc/dt\}_x = D(d^2c/dx^2) \tag{5.15}$$

The temperature-dependent diffusion coefficient (D) can be expressed using Arrhenius equation:

$$D = D_o \exp(-E/kT) \tag{5.16}$$

The diffusion rate in solid-state reaction can be related by the following:

$$\text{Rate} = kt^n \tag{5.17}$$

where n = 0.5, 1.0, 2.0, 3.0, or fraction.

Sometimes, the flux is used to make solid-state reaction at lower temperature. The flux has a low temperature melting point, which is lower than solid-state reaction temperature. The flux carries one or more of reactant components to reaction zone. Final product does not react with flux added.

In solid-state reaction, nucleation, growth, coarsening, sintering, and the formation of grain boundaries between particles are associated.

5.6.2 Liquid State Phase

Evolution of particles from liquid state is generally known as solidification [169, 170]. Another term is precipitation, which is generally referred to ionic compounds. The precipitation occurs when ionic product of opposite charged ions (anions and cations) is more than that of solubility product. With further increase of ionic product, it becomes supersaturated. Once supersaturation state is reached, the solid product can be observed by our eye. The solubility product of ionic compound is fixed at a particular temperature and it varies slightly with temperature.

Example, 'C' is compound formed by A^+ (cation) and B^- (anion). The dissolution of C takes place in a solvent if its solvation enthalpy is greater than its lattice enthalpy.

$$C(s) \rightleftharpoons A^+(\text{aq}) + B^-(aq) \tag{5.18}$$

$$K_{sp} = \left[A^+\right]\left[B^-\right] \tag{5.19}$$

Compounds such as NaCl, $BaSO_4$, $CaMoO_4$, $Fe(OH)_3$, Fe_3O_4, MFe_2O_4 (M = Zn, Mn), A_2O_3 (A = Y, Y, Gd), APO_4 (A = Y, La, Gd), $NaYF_4$, CdS, PbSe, ZnO, SnO_2, TiO_2, AVO_4 (A = Y, La, Gd), can be prepared from the corresponding sources of positive and negative ions. Precipitation is faster if opposite charges have high concentrations in solutions. Ag, Ni, Au, Pd, FePt, FePd particles can be prepared from the respective ions in solution. This is a solidification process. Sometimes, the term precipitation is used. The term precipitation belongs to solidification. The condensation of atoms or ions or vapors into solid is also considered as solidification. In air atmosphere, condensation of water vapor occurs due to gravitation forces or cooling process, and finally, many types of precipitation such as ice pellets, drizzle, sleet, snow, rain, hail, and graupel can occur. In sea, different types of precipitation occur in different zones due to surrounding environment and depths.

Ionic compounds such as AgCl, AgBr, and AgI have the solubility products (K_{sp}) of 1.77×10^{-10}, 5.35×10^{-13}, and 8.52×10^{-17}, respectively [173]. There is a decrease in solubility product with change of negative counterpart Cl^- to Br^- to I^-. Thus AgI is sparingly soluble in water. In the same strength of solution of such ionic compound, the precipitation of AgI will be faster. The K_{sp} can be calculated from the electrochemical reduction potentials. For example, the K_{sp} of AgI at 25 °C can be calculated from electrochemical reduction potentials:

Equations	Reactions	Reduction potential half-reaction (E^o, V)
i	$AgI_{(s)} + e \rightarrow Ag_{(s)} + I^-$	0.15
ii	$I_{2(s)} + 2e \rightarrow 2I^-$	0.54
iii	$Ag^+ + e \rightarrow Ag_{(s)}$	+0.80

The dissolution of AgI in water can take place:

$$AgI_{(s)} \rightleftharpoons Ag^+_{(aq)} + I^-_{(aq)} \tag{5.20}$$

Here,

$$K_{sp} = \left[Ag^+\right]\left[I^-\right] \tag{5.21}$$

From equations (i) and (ii), the complete reduction potential (E^o) can be calculated as:

Equations	Reactions	Reduction potential half-reaction (E^o, V)
iv	$AgI_{(s)} + e \rightarrow Ag_{(s)} + I^-$	0.15
v	$Ag_{(s)} \rightarrow Ag^+ + e$	0.80
(iv) + (v)	$AgI_{(s)} + e \rightarrow Ag_{(s)} + I^-$	$E^o = -0.95$ V

Using the Nernst equation,

$$E_{cell} = E^o - (0.0591/n)\ \log K_{sp} \tag{5.22}$$

Here $n = 1$.

Or, $0 = -0.95 - (0.0591/1)\log K_{sp}$.
Or, $\log K_{sp} = 0.95/(-0.0591)$.
Or, $\log K_{sp} = -16.07$.
$K_{sp} = 8.52 \times 10^{-17}$.

The process of the precipitation can be explained by nucleation and growth of particles. Mechanisms behind the formation of nuclei and growth of particles in unprotected and protected systems in solution can be discussed here. The solution comprises of solute dissolved in a solvent. The precipitation can occur when ionic product is more than solubility product or monomers come closer in proximity to make stable nuclei. E.g., precipitation of AgCl can occur in water when product of Ag^+ and Cl^- pair ions is more than that of solubility product at a particular temperature. The solubility product of AgCl at 300 K is 1.77×10^{-10}. Ag^+ ion and Cl^- ion come closer to form AgCl molecule or monomer. These molecules or monomers will form nucleus. If chemical potential of AgCl molecule or monomer is higher in nucleus as compared to that in solution, nucleus will dissolve to solution. On the other hand, if chemical potential of AgCl molecule or monomer is lower in

nucleus compared to that in solution, the nucleus is stable. With time, AgCl molecules or monomers will come closer to nucleus, and subsequently, growth of particle starts. Here, uncontrolled growth may take place. The size of nucleus will be in 2–5 nm. After growing, size of particle may increase from a few nm to a few microns. The agglomeration or aggregation can take place depending on electrostatic interaction or H-bonding or electric or magnetic dipole–dipole interaction. Usually, particles can be separated in agglomeration under ultrasonication or by changing polarity or pH of medium. In case of aggregation, it is difficult to remove individual particles using many techniques.

Various types of solidification will occur from different sources (Table 5.2). Many attractive forces are associated during solidification. Force of attraction follows Induced dipole–induced dipole attraction < dipole–dipole attraction < H-bonding < ionic or covalent bonding [81, 82].

Broadly, three types of nucleation such as homogeneous, heterogeneous, and unusual one (in which mixture of them depending on pH, temperature, and environment) are found in solution. In homogenous nucleation, nuclei are formed uniformly in a liquid, whereas, heterogeneous nucleation takes place in the presence of foreign substance (impurities, container, grain boundaries, etc.). Classical nucleation can be valid in case of spherical particles. In case of formation of hollow, thin film, and different shapes of particles, it did not follow classical nucleation theory.

Table 5.2 Various types of solidification [81, 82]

Sources	Types of attractive forces/bonding among atoms or ions or molecules	Examples
Molecules with non-polar	London dispersion force is a temporary attractive force, which arises from induced dipole–induced dipole attraction. This is possible in non-polar molecules coming closer in such a way that the electrons in two adjacent atoms get displaced and make temporary dipole molecule	Ar, Xe, CO_2, I_2, N_2, Cl_2
Molecules with polar	Dipole–dipole interaction	HCl, NH_3,
Molecules with polar	Hydrogen bonding	H_2O, H_2S, HF,
Molecules with polar	Ionic bonding	$[Ni(NH_3)_6]Cl_2$,
Atoms	Metallic bonding	Ni, Co, Sc, Gd, Ag, Au, Pt, Pd, FePt, metallic alloys
Atoms	Covalent bonding	Graphite, graphene, carbon nanotubes, fullerenes, carbon fibers, Sulfur (S_6, S_8), phosphorus (P_4)
Ions	Ionic bonding	NaCl, MgO, Al_2O_3

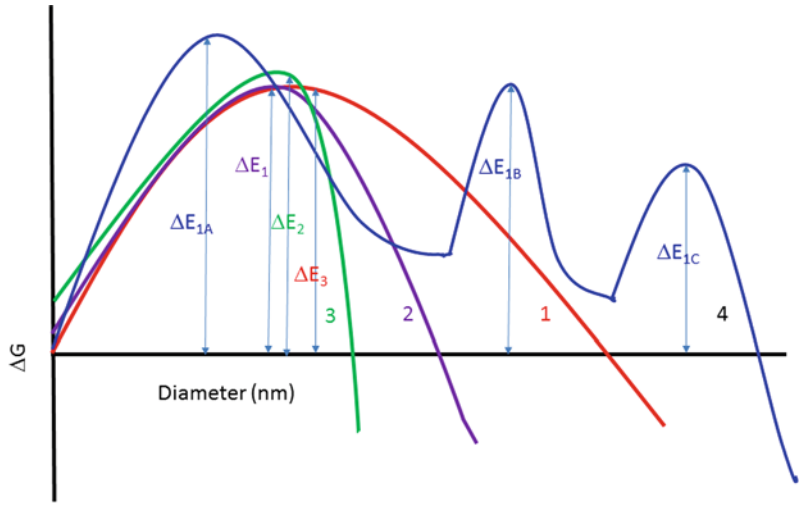

Fig. 5.30 Schematic representation depicting different reaction pathways to prepare particles: path 1, 2, or 3 can form single phase in plot of free energy changes versus diameter of particles. Path 4 can form metastable phases along with final product

The various reaction pathways for formation of products and metastable phases are shown in Fig. 5.30 [163–171]. Classical and non-classical types of nucleation and growth of particles are available [169, 170]. Activation energy required to occur a chemical reaction has higher than that of reactants or products. Product has lower energy than that of reactants in general. In case of metastable formation, intermediate activation energy is associated. In path 1, 2, or 3, particles of single phase are formed from reactant molecules or ions or monomers in solution. Here, monomers come closer and form cluster, and then finally nuclei are formed at critical diameter where activation energy exists. When chemical potential of monomer is more in nuclei as compared to that in the solution, nuclei will start dissolution. When chemical potential of monomer is less in nuclei as compared to that in solution, nuclei will start growing and finally product will be formed. Path 4 shows metastable phase formation before the final product formation.

5.6.3 Gas State Phase

In gas state synthesis, target material is fixed in closed vacuum chamber [69, 168]. This was bombarded by high temperature Ar or plasma Ar^+ gases, some atoms are detached from target to form cluster. The cluster is carried by cold Ar gases to the deposited place or the suitable substrate. Magnetron sputtering or vacuum chamber deposition is a system for this. In this way, nanoparticles of Ag, Au, Pd, Pt, Co, Ni can be prepared. If two more targeted sources are used, alloys, core@shell, composites can be prepared. FePd, FeAl, FePt, CoPt, SmCo, YCo_5, can be prepared. Core-shell, hybrid, oxides, nitrides, sulfides such as Pd@MgO, CuO, TiO_2, PbS, Fe_3N can be prepared by using different atmospheres. Post-processing and finishing help in designing materials for different applications. Different density of nanoparticles can be prepared by pressure-induced cold condensation/compaction. These nanostructures are useful in many applications in catalytic, photo-catalytic, plasmonic, gas-sensing, bio-sensing, anti-corrosion areas, etc.

5.6.4 Single-Crystal Growth

Single crystals are crystals having high degree of perfect lattice. Dislocation or defects are least in case of single crystals as compared to others such as polycrystals [69, 174]. To grow a crystal, it needs to attain a state of supersaturation, followed by process of nucleation. The growth of crystals can be done from melt, vapor, and solution. The growth of crystal from solid is difficult. Different techniques are reported to produce single crystals. Every technique has advantages and disadvantages for the preparation of a particular material. Single crystals can be prepared by different methods (Fig. 5.31).

Crystal growth from the melt is the process of crystallization of fusion. Here, polycrystalline material is melted, and crystallization starts from a melt on cooling the liquid from its freezing point. The chance of contamination with impurities is less and the rate of growth is generally more than that of other possible methods. Different methods for crystal growth from melt include Bridgmann, Czochralski, Vernuil, Zone melting, Kyropoulos, and Skull melting methods.

Crystal growth from vapor is performed by two routes: Chemical and physical transport methods. In chemical transport method, chemical precursors in the form of molecules of halide is transported, and it gets decomposed in the growth area and deposition of particles on suitable substrate occurs. In physical transport method, polycrystalline material (known as target material) gets converted into vapor or gas using Plasma source of Ar^+ or other heater; and gases of targeted atoms are transported to cooler area, where single crystal seed of a particular crystallographic direction (say, [100, 110, 111]) is kept. In this way, growth of single crystal takes place on single crystal seed.

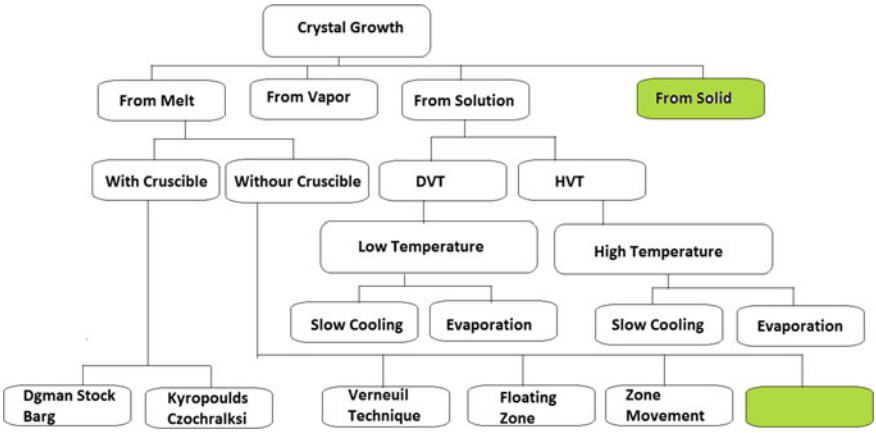

Fig. 5.31 Different methods to prepare single crystals of metallic, semiconductors, oxides and sulfides, halides

Crystal growth from solution takes place from solution, where material required for the growth dissolve in a particular solvent such as water or organic solvent, and either evaporation of solvent takes place or slow cooling takes place or temperature gradient takes place. This is considered as the low temperature solution growth. There is a process of preparation of single crystals using high temperature solution growth. In this, material or reactants are dissolved in water or a particular solvent and transferred into a closed reaction chamber, which is non-reactive in reaction process such as Teflon container. This Teflon container is closed and kept in stainless steel container, which sustains a high pressure and temperature. When temperature is provided, the vapor pressure is increased. When it reaches the critical point of solvent, the dielectric constant changes. Water at normal condition has dielectric constant of 78 and decreases to 5–10, at or above critical point. Dissolution of compound having ionic bonding decreases at higher temperature and pressure, since dielectric constant is less than that at normal condition. Those compounds having covalent bonding did not dissolve in water at normal condition and these can dissolve at critical point of water. The supersaturation of ions for the formation of inorganic compound is faster at critical point as compared to that at normal condition; and thus crystallization process is different under high pressure and high temperature. This method is known as solvothermal method. If water is used as solvent, this is considered as hydrothermal method.

There are many difficulties to prepare single crystals of high Tc-compounds and compounds having many different elements, because in melt technique, different reactants/elements have different melting points. It is not easy to prepare single crystals from solid. Recently, the preparation of single crystal from amorphous phase of solid is reported [171]. Here, a suitable laser source is heated at the spot of amorphous phase, and then crystallization starts below melting point. In this way, many shapes of single crystals can be prepared.

5.7 Conclusions

Size and shape engineering of particles is important in order to get desired material so that these can be useful for a particular application. Classification of particles in terms of crystallinity or arrangement of atoms/ions is provided. Atomic structures in single crystals, macro-crystalline, and nanocrystalline materials are shown. Atomic structure in nanocrystalline materials suggests the high contribution of grain boundaries with respect to grain. The properties of materials changes with variation in size and shapes of particles in nano-range. Higher bulk density material can be achieved by using nanocrystalline material as compared to that using macro-crystalline material. Band gap in QDs can be increased by decrease in particle size. Electrical resistivity is more in case of nanocrystalline material as compared to that of macro-crystalline material. This is due to the contribution of grain boundaries in nanocrystalline material. In terms of magnetic property, superparamagnetic particles can be generated by decrease of particle size in ferromagnetic material. Particle size distributions are associated during preparation of particles or in natural available materials. Their fitting equations are provided here. Lastly, mechanisms for the formation of polycrystalline or single crystal particles in solid, liquid, gas media are discussed.

References

1. Fischer-Bühner J (2005) Hardening of low-alloyed gold. Gold Bull 38:210–131
2. Pingarrón JM, Yáñez-Sedeño P, González-Cortés A (2008) Gold nanoparticle-based electrochemical biosensors. Electrochim Acta 53:5848–5866
3. Lertvachirapaiboon C, Baba A, Ekgasit S, Thammacharoen S, Shinbo K, Kato K, Kaneko F (2011) Gold nanoparticles synthesis used for sensor applications. In: Conference proceedings of ISEIM2011, pp 395–397
4. Priyadarshini E, Pradhan N (2017) Gold nanoparticles as efficient sensors in colorimetric detection of toxic metal ions: a review. Sens Actuators, B Chem 2:888–902
5. Yue J, Feliciano TJ, Li W, Lee A, Odom TW (2017) Gold nanoparticle size and shape effects on cellular uptake and intracellular distribution of siRNA nanoconstructs. Bioconjug Chem 28:1791–1800
6. He Y, Liu J-C, Luo L, Wang Y-G, Zhu J, Yingge Du, Li J, Mao SX, Wang C (2018) Size-dependent dynamic structures of supported gold nanoparticles in CO oxidation reaction condition. PNAS 115:7700–7705
7. Bond GC (1972) The catalytic properties of gold potential applications in the chemical industry. Gold Bull 5:11–13
8. Stephen A, Hashmi K (2007) Gold-catalyzed organic reactions. Chem Rev 107:3180–3211
9. Callister WD (2009) Material science and engineering: an introduction, 6th edn. John Wiley & Sons, Inc, New Delhi
10. Curlee TR, Das S (1991) Advanced materials: information and analysis needs. Butterworth-Heinemann Ltd., Resources Policy, pp 316–331
11. Advanced materials and applications: tackling new R&D and engineering challenges. Elsevier. https://www.elsevier.com/data/assets/pdf_file/RD-Solutions_CH. https://www.elsevier.com/rd-solutions/industry-insights/chemicals/ty/download-form-rd-and-engineering-challenges
12. Shenderova OA, Shames AI, Nunn NA, Torelli MD, Vlasov I, Zaitsev A (2019) Review article: synthesis, properties, and applications of fluorescent diamond particles. J Vac Sci Technol B 37:030802

13. Li H, Cheng S, Li J, Song J (2015) A review on the low-dimensional and hybridized nanostructured diamond films. J Nanomater 692562
14. Schwander M, Partes K (2011) A review of diamond synthesis by CVD processes. Diam Relat Mater 20:1287–1301
15. Li Y, Lu Y, Adelhelm P, Titirici M-M, Hu Y-S (2019) Intercalation chemistry of graphite: alkali metal ions and beyond. Chem Soc Rev 48:4655–4687
16. Sengupta R, Bhattacharya M, Bandyopadhyay S, Bhowmick AK (2011) A review on the mechanical and electrical properties of graphite and modified graphite reinforced polymer composites. Prog Polym Sci 36:638–670
17. Chung DDL (2002) Review graphite. J Mater Sci 37:1475–1489
18. Kroto HW, Heath JR, O'Brien SC, Curl RF, Smalley RE (1985) C_{60}: buckminsterfullerene. Nature 318:162–163
19. Gokhale MM, Somani RR (2015) Fullerenes: chemistry and its applications. Mini-Rev Org Chem 12:355–366
20. Nimibofa A, Newton EA, Cyprain AY, Donbebe W (2018) Fullerenes: synthesis and applications. J Mater Sci Res 7:22–36
21. Goel A, Howard JB, Sande JBV (2004) Size analysis of single fullerene molecules by electron microscopy. Carbon 42:1907–1915
22. Yadav BC, Kumar R (2008) Structure, properties and applications of fullerenes. Int J Nanotech Appl 2:15
23. Haddan RC (1992) Electronic structure, conductivity, and superconductivity of alkali metal doped C_{60}. Acc Chem Res 25:127
24. Iijima S (1991) Helical microtubules of graphitic carbon. Nature 354:56–58
25. Saeed Ibrahim K (2013) Carbon nanotubes–properties and applications: a review. Carbon Letters 14:131–144
26. Ghosh S, Sood AK, Kumar N (2003) Carbon nanotube flow sensors. Science 299:1042–1044
27. Saitoa Y, Uemura S (2000) Field emission from carbon nanotubes and its application to electron sources. Carbon 38:169
28. Novoselov KS, Geim AK, Morozov SV, Jiang D, Zhang Y, Dubonos SV, Grigorieva IV, Firsov AA (2004) Electric field effect in atomically thin carbon films. Science 306:666–669
29. Boehm H-P, Setton R, Stumpp E (1994) Nomenclature and terminology of graphite intercalation compounds. Pure Appl Chem 66:1893–1901
30. Coroş M, Pogăcean F, Măgeruşan L, Socaci C, Pruneanu S (2019) A brief overview on synthesis and applications of graphene and graphene-based nanomaterials. Front Mater Sci 13:23–32
31. Ishida T, Murayama T, Taketoshi A, Haruta M (2020) Importance of size and contact structure of gold nanoparticles for the genesis of unique catalytic processes. Chem Rev 120(2):464–525
32. Van Thai P, Abe S, Kosugi K, Saito N, Takahashi K, Sasaki T, Kikuchi T (2019) Size/shape control of gold nanoparticles synthesized by alternating current glow discharge over liquid: the role of pH. Mater Res Express 6:095074
33. Huang T, Cheng J, Bian D, Zheng Y (2016) Fe–Au and Fe–Ag composites as candidates for biodegradable stent materials. J Biomed Mater Res B: Appl Biomater 104:225–240
34. Lee YH, Polavarapu L, Gao N, Yuan P, Xu Q-H (2012) Enhanced optical properties of graphene oxide Au nanocrystal composites. Langmuir 28:321–326
35. Yamaguchi A, Koinkar P, Furube A (2019) PMMA-BN composites incorporated with Au nanoparticle fabricated by laser ablation. IOP Conf Ser J Phys Conf Ser 1230:012099
36. Soni AK, Joshi R, Singh BP, Singh NN, Ningthoujam RS (2019) Near infrared- and magnetic-field-responsive $NaYF_4:Er^{3+}/Yb^{3+}@SiO_2@AuNP@Fe_3O_4$ nanocomposites for hyperthermia applications induced by fluorescence resonance energy transfer and surface plasmon absorption. ACS Appl. Nano Mater. 2:7350–7361
37. Hanawa T (2012) Research and development of metals for medical devices based on clinical needs. Sci Technol Adv Mater 13:064102
38. Ferrando R, Jellinek J, Johnston RL (2008) Nanoalloys: from theory to applications of alloy clusters and nanoparticles. Chem Rev 108:845–910

39. Sharma KS, Ningthoujam RS, Dubey AK, Chattopadhyay A, Phapale S, Juluri RR, Mukherjee S, Tewari R, Shetake NG, Pandey BN, Vatsa RK (2018) Synthesis and characterization of monodispersed water dispersible Fe_3O_4 nanoparticles and in vitro studies on human breast carcinoma cell line under hyperthermia condition. Sci Rep 8:14766
40. Joshi R, Perala RS, Srivastava MBP, Singh BP, Ningthoujam RS (2020) Heat generation from magnetic fluids under alternating current magnetic field or induction coil for hyperthermia-based cancer therapy: Basic principle. J Radiat Cancer Res 10:156–164
41. Thorat ND, Patil RM, Khot VM, Salunkhe AB, Prasad AI, Barick KC, Ningthoujam RS, Pawar SH (2013) Highly water dispersible surface functionalized LSMO nanoparticles for magnetic fluid hyperthermia application. New J Chem 37:2733
42. Shete PK, Patil RM, Ningthoujam RS, Ghosh S, Pawar SH (2013) Magnetic core shell structures for magnetic fluid hyperthermia therapy application. New J Chem 37:3784–3792
43. Dalal M, Greneche J-M, Satpati B, Ghzaiel TB, Mazaleyrat F, Ningthoujam RS, Chakrabarti PK (2017) Microwave absorption and the magnetic hyperthermia applications of $Li_{0.3}Zn_{0.3}Co_{0.1}Fe_{2.3}O_4$ nanoparticles in multiwalled carbon nanotube matrix. ACS Appl Mater Interf 9:40831–40845
44. Akbarzadeh A, Samiei M, Davaran S (2012) Magnetic nanoparticles: preparation, physical properties, and applications in biomedicine. Nanoscale Res Lett 7:144
45. Guo T, Lin M, Huang J, Zhou C, Tian W, Yu H, Jiang X, Ye J, Shi Y, Xiao Y, Bian X, Feng X. The recent advances of magnetic nanoparticles in medicine. J Nanomater 2018. Article ID 7805147, 8 p
46. Gloag L, Mehdipour M, Chen D, Tilley RD, Gooding JJ (2019) Advances in the application of magnetic nanoparticles for sensing. Adv Mater 31:1904385
47. Sun X, Sun S (2017) Preparation of magnetic nanoparticles for biomedical applications. Biomed Nanotechnolo 1570:73–89
48. Singamaneni S, Bliznyuk VN, Binek C, Tsymbal EY (2011) Magnetic nanoparticles: recent advances in synthesis, self-assembly and applications. J Mater Chem 21:16819–16845
49. Majeed J, Pradhan L, Ningthoujam RS, Vatsa RK, Bahadur D, Tyagi AK (2014) Enhanced specific absorption rate in silanol functionalized Fe_3O_4 core—shell nanoparticles: study of Fe leaching in Fe_3O_4 and hyperthermia in L929 and HeLa cells. Colloids Surf B 122:396–403
50. Gajbhiye NS, Bhattacharyya S, Balaji G, Ningthoujam RS, Das RK, Basak S, Weissmuller J (2005) Mössbauer and magnetic studies of MFe_2O_4 (M = Co, Ni). Hyperfine Interact 165:153
51. Ningthoujam RS, Vatsa RK, Kumar A, Pandey BN (2012) Functionalized magnetic nanoparticles: concepts, synthesis and application in cancer hyperthermia. In: Banerjee S, Tyagi (AK), Chap 6, pp 229–260. Elsevier Inc, USA
52. Denry I, Holloway JA (2010) Ceramics for dental applications: a Review. Materials (Basel) 3:351–368
53. Ningthoujam RS (2017) Synthesis, characterization of borides, carbides, nitrides and their applications. In: Banerjee S, Tyagi AK (eds), Materials under extreme conditions: recent trends and future prospects, Chap 10, pp 337–376. Elsevier Inc, USA
54. Mishra R, Ninghthoujam RS (2017) High temperature ceramics. In: Banerjee S, Tyagi AK (eds), Materials under extreme conditions: recent trends and future prospects, Chap 11, pp 377–410. Elsevier Inc., USA
55. Ningthoujam RS, Singh LR, Sudarsan V, Singh SD (2009) Energy transfer process and optimum emission studies in luminescence of core–shell nanoparticles: YVO_4:Eu–YVO_4 and surface state analysis. J Alloys Compd 484:782–789
56. Ningthoujam RS, Shukla R, Vatsa RK, Duppel V, Kienle L, Tyagi AK (2009) Gd_2O_3:Eu^{3+} particles prepared by glycine-nitrate combustion: phase, concentration, annealing, and luminescence studies. J Appl Phys 105:084304
57. Yaiphaba N, Ningthoujam RS, Singh NS, Vatsa RK (2010) Luminescence properties of redispersible Tb^{3+}-doped $GdPO_4$ nanoparticles prepared by an ethylene glycol route. Eur J Inorg Chem 2010:2682–2687
58. Ningthoujam RS (2012) Enhancement of photoluminescence by rare earth ions doping in semiconductor host. In: Rai SB, Dwivedi Y (2012), Chap 6, pp 145–182. Nova Science Publishers Inc, USA

59. Meetei SD, Singh SD, Singh NS, Sudarsan V, Ningthoujam RS, Tyagi M, Gadkari SC, Tewari R, Vatsa RK (2012) Crystal structure and photoluminescence correlations in white emitting nanocrystalline ZrO_2:Eu^{3+} phosphor: effect of doping and annealing. J Lumin 132:537–544
60. Singh LR, Ningthoujam RS, Sudarsan V, Singh SD, Kulshreshtha SK (2008) Probing of surface Eu^{3+} ions present in ZnO: Eu nanoparticles by covering ZnO: Eu core with Y_2O3 shell: luminescence study. Lumin 128:1544
61. Ningthoujam RS, Sudhakar N, Rajeev KP, Gajbhiye NS (2002) Electrical resistivity study of La, B doped nanocrystalline superconducting vanadium nitride. J Appl Phys 91:6051
62. Ningthoujam RS, Gajbhiye NS (2008) Magnetic study of single domain ε-Fe_3N nanoparticles synthesized by precursor techniques. Mater Res Bull 43:1079
63. Sharma S, Gajbhiye NS, Ningthoujam RS (2010) Effect of annealing on magnetic properties of FePd and FePdPt nanoparticles. AIP Conf Proc 1313:125
64. Grant P (2013) New and advanced materials: chemistry input into the manufacturing of novel materials and future trends in food manufacturing. This review has been commissioned as part of the UK Government's Foresight Future of Manufacturing Project. The views expressed do not represent policy of any government or organization
65. Advanced Materials. Nabertherm GmbH Bahnhofstr. 20 28865 Lilienthal, Germany. https://www.nabertherm.com
66. Featherston C, O'Sullivan E (2014) A review of international public sector strategies and roadmaps: a case study in advanced materials. © Centre for Science Technology and Innovation, Institute for Manufacturing, University of Cambridge 17 Charles Babbage Road, Cambridge, CB3 0FS, UK March, 2014
67. Chen L, Bazylinski DA, Lower BH (2010) Bacteria that synthesize nano-sized compasses to navigate using earth's geomagnetic field. Nat Edu Knowl 3(10):30
68. de la Rica R (2016) Bioinspired synthesis of nanomaterials. In: Bhushan B (eds) Encyclopedia of nanotechnology. Springer, Dordrecht
69. Gleiter H (1989) Nanocrystalline materials. Prog Mater Sci 33:223
70. Alivisatos AP (1996) Semiconductor clusters, nanocrystals, and quantum dots. Science 271:933
71. Pandey H, Rani R, Agarwal V (2016) Liposome and their applications in cancer therapy, Braz Arch Biol Technol 59:e16150477
72. Ghazanfari MR, Kashefi M, Shams SF, Jaafari MR (2016) Perspective of Fe_3O_4 nanoparticles role in biomedical applications. Biochem Res Int 7840161
73. Hassan MN, Mahmoud MM, AbdEl-Fattah A, Kandi S (2016) Microwave-assisted preparation of nano-hydroxyapatite for bone substitutes. Ceram Int 42:3725
74. Lu L, Peter SJ, Lyman MD, Lai H-L, Leite SM, Tamada JA, Uyama S, Vacanti JP, Langer R, Mikos AG (2000) In vitro and in vivo degradation of porous poly(DL-lactic-*co*-glycolic acid) foams. Biomaterials 21:1837
75. Wang L, Hu C, Shao L (2017) The antimicrobial activity of nanoparticles: present situation and prospects for the future. Int J Nanomed 12:1227–1249
76. Kubacka A, Diez MS, Rojo D, Bargiela R, Ciordia S, Zapico I, Albar JP, Barbas C, Martins dos Santos VAP, Fernández-García M, Ferrer M (2014)Understanding the antimicrobial mechanism of TiO_2-based nanocomposite films in a pathogenic bacterium. Sci Rep 4:4134
77. Yao C, Zhang L, Wang J, He Y, Xin J, Wang S, Xu H, Zhang Z (2016) Gold nanoparticle mediated phototherapy for cancer. J Nanomater 2016:5497136
78. Cheng X, Yu X, Xing Z, Yang L (2016) Synthesis and characterization of N-doped TiO_2 and its enhanced visible-light photocatalytic activity. Arab Jo Chem 9:S1706
79. Kang I, Wise FW (1997) Electronic structure and optical properties of PbS and PbSe quantum dots. J Opt Soc Am B 14:1632–1646
80. Nikolić BK. Heterojunctions, interfacial band bending, and 2DEG formation. http://www.wiki.physics.udel.edu/phys824
81. NCERT CBSE Class XII, Chemistry text book (2020). New Delhi, India
82. https://www.unf.edu/~michael.lufaso/chem2046/2046chapter12.pdf

83. Cullity BD, Graham CD (2008) Introduction to magnetic materials, 2nd edn. Publisher, John Wiley and Sons, USA
84. Gajbhiye NS, Ningthoujam RS, Weissmuller J (2004) Mössbauer study of nanocrystalline ε-$Fe_{3-x}Co_xN$ system. Hyperfine Interact 156:51
85. Ningthoujam RS, Umare SS, Sharma SJ, Shukla R, Kurian S, Vatsa RK, Tyagi AK, Tewari R, Dey GK, Gajbhiye NS (2008) Magnetic and Mössbauer studies on nanocrystalline $Co_{1-x}Li_xFe_2O_4$ (x = 0, 0.2). Hyperfine Interact 184:227
86. Ningthoujam RS, Gajbhiye NS (2010) Magnetization studies on ε- $Fe_{2.4}Co_{0.6}N$ nanoparticles. Mater Res Bull 45:499
87. Chen JP, Sorensen CM, Klabunde KJ, Hadjipanayis GC, Devlin E, Kostikas A (1996) Size-dependent magnetic properties of $MnFe_2O_4$ fine particles synthesized by co-precipitation. Phys Rev B 54:9288
88. Radu F, Zabel H (2008) Exchange bias effect of ferro-/antiferromagnetic heterostructures. In: Zabel H, Bader SD (eds) Magnetic heterostructures. Springer tracts in modern physics, vol 227. Springer, Berlin, Heidelberg
89. Upadhyay C, Verma HC, Anand S (2004) Cation distribution in nanosized Ni–Zn ferrites. J Appl Phys 95:5746
90. Barick KC, Sharma A, Shetake NG, Ningthoujam RS, Vatsa RK, Babu PD, Pandey BN, Hassan PA (2015) Covalent bridging of surface functionalized Fe_3O_4 and YPO_4: Eu nanostructures for simultaneous imaging and therapy. Dalton Trans 44:14686–14696
91. Bhattacharya S, Roychowdhury A, Tiwari V, Prasad AI, Ningthoujam RS, Patel AB, Das D, Nayar S (2015) Effect of biomimetic templates on the magneto-structural properties of Fe_3O_4 nanoparticles. RSC Adv 5:13777–13786
92. Ghosh R, Pradhan L, Devi YP, Meena SS, Tewari R, Kumar A, Sharma S, Gajbhiye NS, Vatsa RK, Pandey BN, Ningthoujam RS (2011) Induction heating studies of Fe_3O_4 magnetic nanoparticles capped with oleic acid and polyethylene glycol for hyperthermia. J Mater Chem 21:13388
93. Jadhav NV, Prasad AI, Kumar A, Mishra R, Dhara S, Babu KR, Prajapat CL, Misra NL, Ningthoujam RS, Pandey BN, Vatsa RK (2013) Synthesis of oleic acid functionalized Fe_3O_4 magnetic nanoparticles and studying their interaction with tumor cells for potential hyperthermia applications. Colloids Surf B 108:158–168
94. Kisan B, Shyni PC, Layek S, Verma HC, Hesp D, Dhanak V, Krishnamurthy S, Perumal A (2014) Finite size effects in magnetic and optical properties of antiferromagnetic NiO nanoparticles. IEEE Trans Magn 50:2300704
95. Tiwari SD, Rajeev KP (2005) Signatures of spin-glass freezing in NiO nanoparticles. Phys Rev B 72:104433–104442
96. Garcia MA, Merino JM, Fernández Pinel E, Quesada A, de la Venta J, Ruíz González ML, Castro GR, Crespo P, Llopis J, González-Calbet JM, Hernando A (2007) Magnetic properties of ZnO nanoparticles. Nano Lett 7:1489–1494
97. Zeng H, Wu Y, Zhang J, Kuang C, Yue M, Zhou S (2013) Grain size-dependent electrical resistivity of bulk nanocrystalline Gd metals. Progr Nat Sci Mater Int 23 :18–22
98. Gall D (2020) The search for the most conductive metal for narrow interconnect lines. J Appl Phys 127:050901
99. Gall D (2016) Electron mean free path in elemental metals. J Appl Phys 119:085101
100. Ningthoujam RS, Gajbhiye NS (2015) Synthesis, electron transport properties of transition metal nitrides and applications. Progr Mater Sci 50:50–154
101. Sudhakar N, Ningthgoujam RS, Rajeev KP, Nigam AK, Weissmuller J, Gajbhiye NS (2004) Effect of La, B doping on the electrical resistivity and magnetic susceptibility of nanocrystalline vanadium nitride. J Appl Phys 96:688
102. Ningthoujam RS, Gajbhiye NS (2010) Electron-electron interaction effect and resistivity maximum in nanocrystalline and ordered superconducting γ-Mo_2N. Int J Nanotechnol 7:932
103. Ningthoujam RS, Gautam A, Padma N (2017) Oleylamine as reducing agent in syntheses of magic-size clusters and monodisperse quantum dots: optical and photoconductivity studies. Phys Chem Chem Phys 19:2294–2303

104. Koh W-K, Bartnik AC, Wise FW, Murray CB (2010) Synthesis of monodisperse PbSe nanorods: a Case for oriented attachment. J Am Chem Soc 132:3909–3913
105. Yong K-T, Sahoo Y, Choudhury KR, Swihart MT, Minter JR, Prasad PN (2006) Shape control of PbSe nanocrystals using noble metal seed particles. Nano Lett 6:709–714
106. Ningthoujam RS, Sudarsan V, Godbole SV, Kienle L, Kulshreshtha SK, Tyagi AK (2007) SnO_2:Eu^{3+} nanoparticles dispersed in TiO_2 matrix: improved energy transfer between semiconductor host and Eu^{3+} ions for the low temperature synthesized samples. Appl Phys Lett 90:173113
107. Ningthoujam RS, Sudarsan V, Kulshreshtha SK (2007) SnO_2: Eu nanoparticles dispersed in silica: a low temperature synthesis and photoluminescence study. J Lumin 127:747
108. Ningthoujam RS, Sudarsan V, Vinu A, Srinivasu P, Ariga K, Kulshreshtha SK, Tyagi AK (2008) Luminescence properties of SnO_2 nanoparticles dispersed in Eu^{3+} doped SiO_2. J Nanosci Nanotech 8:1489
109. Ningthoujam RS, Vatsa RK, Vinu A, Ariga K, Tyagi AK (2009) Room temperature exciton formation in SnO_2 nanocrystals in SiO_2: Eu matrix: quantum dot system, heat-treatment effect. J Nanosci Nanotech 9:2634
110. Ningthoujam RS (2010) Generation of exciton in two semiconductors interface: SnO_2:Eu-Y_2O_3. Chem Phys Lett 497:208
111. Gusakova J, Wang X, Shiau LL, Krivosheeva A, Shaposhnikov V, Borisenko V, Gusakov V, Tay BK (2017) Electronic properties of bulk and monolayer TMDs: theoretical study within DFT framework (GVJ-2e Method). Phys Stat Sol 214:1700218
112. García N, Esquinazi P, Barzola-Quiquia J, Dusari S (2012) Evidence for semiconducting behavior with a narrow band gap of Bernal graphite. New J Phys 14:053015
113. Jain PK, Huang X, El-Sayed IH, El-Sayed MA (2007) Review of some interesting surface plasmon resonance-enhanced properties of noble metal nanoparticles and their applications to biosystems. Plasmonics 2:107–118
114. Verma J, Verma A, Protasenko V, Islam SM, Jena D (2014) 12—Nitride LEDs based on quantum wells and quantum dots. Materials, technologies and applications, pp 368–408. © 2014 Woodhead Publishing Limited
115. Thompson SM (2008) The discovery, development and future of GMR: The Nobel Prize 2007. J Phys D Appl Phys 41:093001
116. Grünberg P, Schreiber R, Pang Y, Brodsky MB, Sowers H (1986) Layered magnetic structures: evidence for antiferromagnetic coupling of Fe layers across Cr interlayers. Phys Rev Lett 57:2442
117. Baibich MN, Broto JM, Fert A, Nguyen Van Dau F, Petroff F, Etienne P, Creuzet G, Friederich A, Chazelas J (1986) Giant magnetoresistance of (001)Fe/(001)Cr magnetic superlattices. Phys Rev Lett 61:2472
118. Joshi R, Singh BP, Ningthoujam RS (2020) Confirmation of highly stable 10 nm sized Fe_3O_4 nanoparticles formation at room temperature and understanding of heat-generation under AC magnetic fields for potential application in hyperthermia. AIP Adv 10:105033
119. Hu Y, Du A (2011) Surface-anisotropy and training effects of exchange bias in nanoparticles with inverted ferromagnetic-antiferromagnetic core-shell morphology. J Appl Phys 110:033908
120. Joshi R, Perala RS, Shelar SB, Ballal A, Singh BP, Ningthoujam RS (2020) Super bright red upconversion in $NaErF_4$: 0.5% Tm@ $NaYF_4$: 20% Yb nanoparticles for anti-counterfeit and bioimaging applications. ACS Appl Mater Interf
121. Soni AK, Yadav KK, Singh BP, Joshi R, Chakraborty S, Chakravarty R, Nagaraja NK, Singh DK, Kain V, Dash A, Ningthoujam RS (2020 Smart YPO_4:Er–Yb nanophosphor for optical heating, hyperthermia, security ink, cancer endoradiotherapy, and uranyl recovery. ACS Appl Nano Mater
122. Parchur AK, Kaurav N, Ansari AA, Prasad AI, Ningthoujam RS, Rai SB (2013) CaMoO4: Tb@Fe_3O_4 hybrid nanoparticles for luminescence and hyperthermia applications. AIP Conf Proc 1512:184

123. Ningombam GS, Ningthoujam RS, Kalkura SN, Singh NR (2018) Induction heating efficiency of water dispersible $Mn_{0.5}Fe_{2.5}O_4$@YVO_4:Eu^{3+} magnetic-luminescent nanocomposites in acceptable AC magnetic field: haemocompatibility and cytotoxicity studies. J Phys Chem B 122:6862–6871
124. Wangkhem R, Yaba T, Singh NS, Ningthoujam RS (2018) Red emission enhancement from $CaMoO_4$:Eu^{3+} by co-doping of Bi^{3+} for near UV/blue LED pumped white pcLEDs: energy transfer studies. J Appl Phys 123:124303
125. Dalal M, Das A, Das D, Ningthoujam RS, Chakrabarti PK (2018) Studies of magnetic, Mössbauer spectroscopy, microwave absorption and hyperthermia behavior of Ni-Zn-Co-ferrite nanoparticles encapsulated in multi-walled carbon nanotubes. J Magn Magn Mater 460:12–27
126. Soni AK, Joshi R, Jangid K, Tewari R, Ningthoujam RS (2018) Low temperature synthesized $SrMoO_4$:Eu^{3+} nanophosphors functionalized with ethylene glycol: a comparative study of synthesize route, morphology, luminescence and annealing. Mater Res Bull 103:1–1
127. Mallick A, Mahapatra AS, Mitra A, Greneche JM, Ningthoujam RS, Chakrabarti PK (2018) Magnetic properties and bio-medical applications in hyperthermia of lithium zinc ferrite nanoparticles integrated with reduced graphene oxide. J Appl Phys 123:055103
128. Parchur AK, Ansari AA, Singh BP, Hasan TN, Syed NA, Rai SB, Ningthoujam RS (2014) Enhanced luminescence of $CaMoO_4$: Eu by core@shell formation and its hyperthermia study after hybrid formation with F_e3_O4: cytotoxicity assessment on human liver cancer cells and mesenchymal stem cells. Integr Biol 6:53–64
129. Ningombam GS, Singh NR, Ningthoujam RS (2017) Controlled synthesis of CaWO4:Sm3+ microsphere particles by a reverse-micelle method and their energy transfer rate in luminescence. Colloids Surf A 518:249–262
130. Chakravarty R, Chakraborty S, Ningthoujam RS, Nair KVV, Sharma KS, Ballal A, Guleria A, Kunwar A, Sarma HD, Vatsa RK, Dash A (2016) Industrial-scale synthesis of intrinsically radiolabeled ^{64}CuS nanoparticles for use in positron emission tomography (PET) imaging of cancer. Ind Eng Chem Res 55:12407–12419
131. Ningthoujam RS, Sharma A, Sharma KS, Barick KC, Hassan PA, Vatsa RK (2015) Roles of solvent, annealing and Bi^{3+}co-doping on the crystal structure and luminescence properties of YPO_4:Eu^{3+} nanoparticles. RSC Adv 5:68234–68242
132. Chakraborty S, Sharma KS, Rajeswari A, Vimalnath KV, Sarma HD, Pandey U, Ningthoujam JRS, Vatsa RK, Dash A (2015) Radiolanthanide-loaded agglomerated Fe_3O_4 nanoparticles for possible use in the treatment of arthritis: formulation, characterization and evaluation in rats. J Mater Chem B 3:5455–5466
133. Singh LP, Jadhav NV, Sharma S, Pandey BN, Srivastava SK, Ningthoujam RS (2015) Hybrid nanomaterials YVO_4:Eu/Fe_3O_4 for optical imaging and hyperthermia in cancer cells. J Mater Chem C 3:1965–1975
134. Singh LP, Srivastava SK, Mishra R, Ningthoujam RS (2014) Multifunctional hybrid nanomaterials from water dispersible CaF_2:Eu^{3+}, Mn^{2+} and Fe_3O_4 for luminescence and hyperthermia application. J Phys Chem C 118:18087–18096
135. Phaomei G, Ningthoujam RS, Singh WR, Loitongbam RS, Singh NS, Rath A, Juluri RR, Vatsa RK (2011) Luminescence switching behavior through redox reaction in Ce^{3+} co-doped $LaPO_4$:Tb^{3+} nanorods: Re-dispersible and polymer film. Dalton Trans 40:11571
136. Phaomei G, Singh WR, Singh NS, Ningthoujam RS (2013) Luminescence properties of Ce^{3+} co-activated $LaPO_4$:Dy^{3+} nanorods prepared in different solvents and tunable blue to white light emission from Eu^{3+} co-activated $LaPO_4$:Dy^{3+}, Ce^{3+}. J Lumin 134:649–656
137. Thorat ND, Khot VM, Salunkhe AB, Ningthoujam RS, Pawar SH (2013) Functionalization of $La_{0.7}Sr_{0.3}MnO_3$ nanoparticles with polymer: studies on enhanced hyperthermia and biocompatibility properties for biomedical applications. Colloids Surf B Biointerf 104:40–47
138. Puntes VF, Krishnan KM, Alivisatos AP (2001) Colloidal nanocrystal shape and size control: the case of cobalt. Science 291:2115–2117
139. Gregory PJ, Ross M, Douglas MS, William F, Steve F (1992) Reactive laser ablation synthesis of nanosize alumina powder. J Am Ceram Soc 75:3293–3298

140. McHale JM, Auroux A, Perrotta AJ, Navrotsky A (1997) Surface energies and thermodynamic phase stability in nanocrystalline aluminas. Science 277:788–791
141. Kumar PM, Borse P, Rohatgi VK, Bhoraskar SV, Singh P, Sastry M (1994) Synthesis and structural characterization of nanocrystalline aluminium oxide. Mater Chem Phys 36:354–358
142. Taniguchi K, Matsumoto A, Shimotani H, Takagi H (2012) Electric-field-induced superconductivity at 9.4 K in a layered transition metal disulphide MoS_2. Appl Phys Lett 101:042603
143. Ningthoujam RS, Mishra R, Das D, Dey GK, Kulshreshtha SK (2008) Excess enthalpy and luminescence studies of SnO_2 nanoparticles. J Nanosci Nanotech 8:4176
144. Qiu X, Shuwen Hu (2013) "Smart" materials based on cellulose: a review of the preparations, properties, and applications. Materials 6:738–781
145. Calnan S (2014) Applications of oxide coatings in photovoltaic devices. Coatings 4:162–202
146. Wang S, Xuan S, Liu M, Bai L, Zhang S, Sang M, Jiang W, Gong X (2017) Smart wearable Kevlar-based safeguarding electronic textile with excellent sensing performance. Soft Matter 13:2483–2491
147. Salmela O (2007) Acceleration factors for lead-free solder materials. IEEE Trans Compon Packag Technol 30:700
148. Chiari-Andréo BG, de Almeida-Cincotto MGJ, Oshiro Jr JA, Taniguchi CYY, Chiavacci LA, Isaac VLB (2019) Nanoparticles for cosmetic use and its application. In: Grumezescu AM (ed) Nanoparticles in pharmacotherapy, pp 113–146. William Andrew Publishing
149. Palomares V, Casas-Cabanas M, Castillo-Martinez E, Han MH, Rojo T (2013) Update on Na-based battery materials. A growing research path. Energy Environ Sci 6:2312
150. Thomas JC (1987) The determination of log normal particle size distributions by dynamic light scattering. J Colloid Interf Sci 17:187
151. Basic principles of particle size analysis (2014) Malvern Instruments Worldwide Sales and service centres in over 65 countries. https://www.malvern.com/contact
152. Lyon A (2000) Why are normal distributions normal? Brit J Phil Sci 65:621–649
153. Fredlund MD, Fredlund DG, Ward Wilson G (2000) An equation to represent grain-size distribution. Can Geotech J 37:817–827
154. Bayvel LP, Jones AR (1981) Methods of measuring particle size distribution,electromagnetic scattering and its applications. ©Applied Science Publishers Ltd
155. Podczeck F (1997) A shape factor to assess the shape of particles using image analysis. Powder Technol 93:47–53
156. Gantenbein D, Schoelkopf J, Matthews GP, Gane PAC (2011) Determining the size distribution-defined aspect ratio of rod-like particles. Appl Clay Sci 53:538–543
157. Wilhelm LR, Suter DA, Brusewitz GH (2004) Physical properties of food materials. Chapter 2 in food & process engineering technology, pp 23–52. St. Joseph, Michigan: ASAE. © American Society of Agricultural Engineers (Rev Aug 2005)
158. Ankamwar B (2012) Size and shape effect on biomedical, applications of nanomaterials, Intech, © 2012 Ankamwar, licensee InTech
159. Cho Y, Shin J-H, Costa A, Kim TA, Kunin V, Li J, Lee SY, Yang S, Han HN, Choi I-S, Srolovitz DJ (2014) Engineering the shape and structure of materials by fractal cut. PNAS 111:17390–17395
160. Takashimiz Y (2016) New parameter of roundness R: circularity corrected by aspect ratio. Prog Earth Planet Sci 3:2
161. Jiang XC, Zeng QH, Chen CY, Yu AB (2011) Self-assembly of particles: some thoughts and comments. J Mater Chem 21:16797
162. Merkus HG (2009) Particle size, size distributions and shape. In: Particle size measurements. Particle technology series, vol 17. Springer, Dordrecht
163. Ropp RC (2003) Mechanisms and reactions in the solid state. Elsevier Science, Solid state chemistry, pp 129–189
164. Miura H (2020) Crystal growth hysteresis in spiral growth. Cryst Growth Des 20:245–254
165. Chen H, Li M, Zheyu Lu, Wang X, Yang J, Wang Z, Zhang F, Chunhui Gu, Zhang W, Sun Y, Junliang Su (2019) Multistep nucleation and growth mechanisms of organic crystals from amorphous solid states. Nat Commun 10:3872

166. Cubillas P, Anderson MW. Synthesis mechanism: crystal growth and mucleation. In: Čejka J, Corma A, Zones S (eds). Copyright © 2010 Wiley-VCH Verlag GmbH & Co. KGaA
167. Zachmann HG (1973) Theory of nucleation and crystal growth of polymers in concentrated solutions. Macromol Microsymp XII and XIII 79–96
168. Grammatikopoulos P, Steinhauer S, Vernieres J, Singh V, Sowwan M (2016) Nanoparticle design by gas-phase synthesis. Adv Phys X 1:81–100
169. Zhaohui Wu, Yang S, Wei Wu (2016) Shape control of inorganic nanoparticles from solution. Nanoscale 8:1237–1259
170. Lee J, Yang J, Kwon SG, Hyeon T (2016) Nonclassical nucleation and growth of inorganic nanoparticles. Nat Rev Mater 1:16034
171. Savytskii D, Knorr B, Dierolf V, Jain H (2016) Demonstration of single crystal growth via solid-solid transformation of a glass. Sci Rep 6:23324
172. Kittel C (2004) Introduction to solid state physics, 8th edn. John Wiley and Sons, USA
173. CRC Handbook of chemistry and physics, 87th edn
174. Seevakan K, Bharanidharan S (2018) Different types of crystal growth methods. Int J Pure Appl Math 119:5743–5758

Chapter 6
Synthesis of Porous Materials

Deepak Tyagi and K. Bhattacharyya

Abstract This chapter deals with the different types of porous materials, their synthesis and their characterization of the pores. The different porous materials could be broadly grouped into three types of artificially created pores. The microporous and mesoporous materials are discussed in detail here with their synthesis strategies and characterization techniques in this chapter along with the broad classification of different types of porous materials and their generic properties.

Keywords Porous materials · Porous metals · Microporous materials · Mesoporous materials · Characterization techniques

6.1 Introduction

A porous medium or a porous material could be described as a material that possesses pores (voids). The non-porous structural part of the material is often called the "matrix" or "frame". The pores are typically filled with a fluid (liquid or gas). The skeletal material is generally solid, however foam structures also nicely depict porous media. Right from the beginning of the earth the solids have their pores in them which are useful for the different physical, biological and transport phenomena. A tree leaf (with a stomata), a shell with pores, a bone joint, a honey comb, a pumice stone, a wall made of stones/bricks, etc., all have pores of different sizes, shapes, magnitudes and are used for different purposes [1, 2]. The materials without voids are termed as non-porous materials and are better defined as the materials whose density is close to its theoretical density calculated from its atomic structure. Examples for the nonporous

D. Tyagi (✉) · K. Bhattacharyya (✉)
Chemistry Division, Bhabha Atomic Research Centre, Mumbai 400085, India
e-mail: dtyagi@barc.gov.in

K. Bhattacharyya
e-mail: kaustava@barc.gov.in

K. Bhattacharyya
Homi Bhabha National Institute, Mumbai 400094, India

A. K. Tyagi and R. S. Ningthoujam (eds.), *Handbook on Synthesis Strategies for Advanced Materials*, Indian Institute of Metals Series,
https://doi.org/10.1007/978-981-16-1803-1_6

materials are forged metals, alloys, sintered carbide cutting tools, glass (without air bubbles) silicon wafers and gem-quality diamonds, etc. However, all materials have small holes about the size of an atom. It is impossible to remove them so we wouldn't call these small holes "pores" (though this may be debatable) however if the pores are of lower than the atomistic size and they do not contribute to their theoretical density they could be ignored. Therefore, essentially non-porous materials are denser and do not absorb well and do not allow much air/liquid (fluid) to flow through. The materials through which fluid can pass are called porous materials. The materials through which fluid can't pass are called non-porous materials.

Now the next question is could all the materials with pores be termed as porous materials? Technically the answer is no. Usually the porous materials are those where the pores usually add to the property enhancement for the designer, or they are usually termed as defects. Therefore, the porous materials should have two essential characteristics to be termed as porous materials: (a) they should have lot of voids (pores); (b) the pores are intended explicitly to accomplish the desired index of the material property under the research.

6.2 Types of Pores

In a porous material there can be different types of pores. The division of pores could be made on different basis sets.

6.2.1 Accessibility and the Shape of the Pores

A porous material may contain pores like cavities, channels, interstices that are deeper than they are wide. The porous materials can be described by pores, as well as the cell/pore walls as seen in Fig. 6.1.

Accessibility:

A	Closed pores
B, C, E, F, G	Open pores
B, F	Blind pores (dead-end or saccate)
E	Through pores

Shape:

C	Cylindrical open
F	Cylindrical blind
G	Roughness
B	Ink-bottle-shaped
D	Funnel shaped

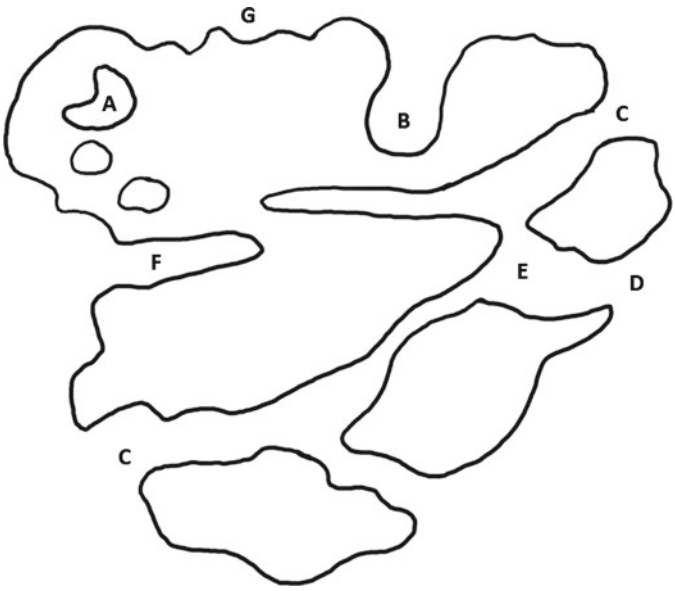

Fig. 6.1 Different types of Pores

6.2.2 Size of the Pores

Pore size is important for different applications. International Union of Pure and Applied Chemistry (IUPAC) has designated three pore size regimes that could be associated with the designated isotherm for the physisorption experiments (like N_2 adsorption-desorption experiments) and their associated transport mechanisms:

(a) **Microporous**—The pore size is smaller than 2 nm, which is comparable to the size of molecules. The transport phenomenon is dominated by mainly activated transport.

(b) **Mesoporous**—The pore size is between 2 and 50 nm. The pore size is either same order or smaller than the typical mean free path length of typical fluid. Transport mechanisms that may be occurring are Knudsen diffusion and surface diffusion. Multilayer adsorption and capillary condensation may also contribute.

(c) **Macroporous**—The pore sizes are larger than 50 nm, i.e. the pores are larger than the mean free path length of fluid. Transport phenomenon is dominated by bulk diffusion and viscous flow.

6.2.3 Ordering of the Pores

The pores that are formed in the solid matrix could be ordered with a specific ordering or could be present randomly. The ordered mesoporous systems are like MCM-41, SBA-15, etc. MCM-41 has one-dimensional hexagonal porous structure and SBA-15 is hexagonal three-dimensional ordered structure. Anatase TiO_2 has random microporous structures.

6.2.4 Type of Pore Dimension

The pores present in the solid matrix could be one dimensional, two dimensional or three dimensional which definitely affects the transport phenomena of the fluids inside them. MCM-4 has one-dimensional hexagonal pore, SBA-15 has three-dimensional hexagonal pores, MCM-48 has three-dimensional cubic pores, etc. Several zeolites have two-dimensional pore systems.

i. Natural and artificial pores
Porous solids include two types of porous structures, i.e. natural and artificial porous structures. Natural porous solid could be found universally such as in bones of animal and human beings, plant leaves, wood, sponge, coral, etc. The artificial porous materials are the materials that are synthesized intentionally with the formation of a particular type of pore and could again be segmented into three different divisions:

   (a) **Porous Metal**: This is rather a new genre of scientific materials that is used for its functional and structural properties [3–5]. The porous metals are light weight and possess the properties both of metals like ductility, conductivity (electrical), etc., in general along with the other properties like low bulk density, greater surface area, lesser thermal conductivity, better penetrability, mechanical damping, electromagnetic shielding, noise attenuation, etc. There can be different types of porous metals that are designated according to their synthesis methods like (a) Powder Sintering; (b) Fibre Sintering; (c) Metal Casting; (d) Metal deposition; (e) Direct Solidification; (f) Composite formation.

   (b) (b)**Porous Ceramic**: These comprise of heat-resistant ceramic materials ranging from metal oxides to chalcogenides to phosphates, aluminates, etc. The pore size mostly ranges between angstrom to millimetre in units and usually the materials are thermally stable [6, 7]. Usually the characteristics of the ceramic porous materials are: (a) good chemical stability, (b) rigidity and specific strength and (c) good thermal stability. At times the hydrothermal stability is poor however that may vary from the way they are synthesized and the shape of them. The porous ceramic could be again divided broadly into two types upon the synthetic route: (a) **Soft**

Templating: If the templates are utilized directly from long-chain micelles and post synthesis these micellar medium are thermally removed to obtain the desired pore size and the structure; (b) **Hard Templating**: Using the soft templated porous ceramics as the basis of templates and removal of the soft templates post synthesis usually with HF or NaOH depending on the type of the soft template used. Here for the hard templating the walls of the soft template would be used to form the pores and the pores of the soft template will be utilized for the matrix of the hard-templated porous ceramic. It could also be distributed in another two classes (c) honeycomb ceramics and (d) ceramic foam [7–9].

(c) **Porous Foam:**These foams are usually polymer materials covered with several large pores [10, 11] and made up of either resin (phenolic formaldehyde resin, epoxy resin) or polystyrene materials (polyvinyl chloride, polyurethane, polyethylene, urea-formaldehyde, etc.).The large pores present in the above materials are usually occupied with gaseous moiety. The volume ratio of gas-filled pores to that of solid polymer defines its density. They could be classified according to their density and rigidity. (a) **Density**: According to density there are three different types viz. low, moderate and high foaming materials. Density for low foamed (high density) polymers is more than 0.4 g/cc, moderate foamed in between (0.1–0.4) gm/cc and high foamed (low density) less than 0.1gm/cc. The expansion ratio for low (<1.5), medium (1.5–9.0) and high (>9.0) foaming materials. (b) **Rigidity**: According to rigidity, there are three different categories rigid, semi-rigid and flexible foams [11] which are classified according to their glass transition temperature (GTT) [defined as the temperature required for melting the polymeric crystal foam]. The rigid foam is crystalline and rigid at room temperature (RT) and has high GTT (>RT). The flexible foam has low GTT (<RT) and the semi-rigid has GTT in between these two. Usually resins (phenol-formaldehyde resin, epoxy resin) polystyrene, polycarbonate rigid polymers whereas porous rubber, elastic polyurethane are flexible ones. Polyvinyl Chlorides and polyolefin can have both. The general features of polymer foams are: (a) low relative density; (b) very good heat insulation; (c) good sound insulation; (d) and sound specific strength.

6.3 Synthesis of Porous Metallic Materials

Porous materials including porous metals require certain degree of porosity in them and certain degree of strength in the matrix.

6.3.1 Sintering

One of the processes commonly utilized is the sintering to form the porous materials. The sintering process for the porous powder ingredients is displayed by the following mechanism: The atoms in the connecting area of the different powders will diffuse from their parent crystal lattice (~$0.4T_m$) (Melting Temperature) and form preliminary bonding between each other. Next at (~$0.5T_m$) is signified by the migration of the surface atoms in the adjoining convex area of powders nearby to produce a sintering neck. The different methods for synthesis of diverse porous materials via sintering could be accounted as follows:

(a) Sintering of Powders: The powder sintering is signified by sintering of a mixture of metal powders and pore-forming organic materials. The sintering process is emphasized by the disintegration of the pore-forming organics followed by the atomistic diffusion of metallic materials producing spongy and porous metal. Different metallic powders utilized are Aluminium, Molybdenum, Mo-alloy, Tungsten, W-alloys, etc., and their combinations.

(b) Loose Sintering: This process is exemplified by using powders without pelletization (i.e. without applying pressure to them). The surface tension and the capillary effect between the different powder materials is the source of contact between them whilst sintering. The major caution for this process is the mould materials so utilized should possess higher thermal strength and should not take part in the reaction or react with the powders. Further higher porosity could be attained via utilizing pore former organics. Examples are Cu-Sn alloy and Ni-diaphragm (utilized in Alkaline Batteries/Fuel cell).

(c) Activated Sintering: Usually for synthesizing porous metals possessing higher melting point requires either higher temperature or higher sintering time. These metals usually require certain type of activation to reduce either the energy for sintering or time of sintering. An activator so employed for an activated treatment however could lower the sintering temperature or time. Fundamentally the activator lowers down the thermodynamic activation energy of the process and improves the kinetics of the system by enhancing the reaction rate. The proposed activation could be achieved using physical or chemical methods. The physical means that could be employed would be using and additional force field which would thereby lower the activation energy by supplying extra energy like (a) Magnetic Field, (b) Vibrational Energy (c) Radiation (High energy Radiation), etc. The Chemical activation may be achieved by using a supplement material that produces an intermediate step whose oxidation/reduction releases high energy and mass which could be then subsequently utilized to lower the final activation barrier and formation of porous material by the loss of the additional mass. Hydrides, reactive gases, certain trace elements, peroxides, etc., are often utilized as these activating materials. Mechanistically the activated sintering phenomenon is largely centered around the volume diffusion of the activator and the defects created by the activators leading to porosity. However, around the grain boundary the surface diffusion could not

be completely ruled out. The alteration in diffusion coefficient for the defect sites/ vacancies and metal atoms could lead to faster migration of the metal atoms thereby enhancing the kinetics of the system.

(d) Electric Flash Sintering: The metal powders with high melting point could be allowed before a high frequency A/C (alternating current) or D/C (direct current) flash or spark discharge. The small discharge emanating from the A/C or D/C source is for a very small time (15–30 s) however produces a very high energy instantaneously and thereby the metals do not get enough time to quench thoroughly leading to formation of pores inside and thereby a porous material. Usually, porous refractory materials are made by this technique.

(e) Sintering in Liquid Phase: The diffusion of the metal atoms/defects in a liquid phase is usually faster if equated with the respective solid phase. This simple technique could be utilized as the basis to form porous alloy materials with one of the metal with lower melting point. The surface tension and the tension in boundary of the solidus-liquidus eutectic mixture could be used as a common driving force. Porous Cu-Sn alloys are usually subjected to this type of treatment.

(f) Sintering of Slurry Using Foaming Agents: The metal in powder form, required foaming agents, organic chemicals (leading to formation of gaseous material upon degradation) are mixed together to form a semi-solid slurry. Subsequently upon sintering the slurry leads to formation of high porous metals. Metals with lower melting points are usually utilized like Be, Ni, Fe, Cu, Al, etc. Alloys like stainless steel or bronze, etc., are subjected to such treatment to obtain good degree of porosity.

The physico-chemical properties, agglomeration rate (particle size), surface entity and the phase property of the composition are directly dependent on the sintering temperature. Ideally $0.5T_m$ is taken a good sintering temperature as rule of thumb, though it varies from system to system. However, depending on the different physical properties like malleability, strength, and porosity of the metal required along with the required mechanical strength of the metal in question sintering temperature could be varied from 0.6 to $0.8T_m$. Utmost care should be taken for sintering the metals that are prone to oxidation. They should be sintered in either an inert atmosphere or in a reducing atmosphere. Usually the sintering time should be optimized considering into fact the properties that are required and holding time should be determined experimentally. For porosity factor, the shape of the pore and the type of the pore also depend on the sintering time. The different sintering atmospheres could be differentiated in the following ways:

(a) Oxidizing Conditions (O_2 (high purity), H_2O (steam), Air (usually where pure O_2 is not required).
(b) Reducing Conditions (H_2 (high purity), NH_3 (decomposed), CO (lower reducing atmosphere), H_2 and CO combination
(c) Neutral/Inert Conditions (N_2, Ar, He, vacuum)
(d) Carburizing Conditions (Carbon Monoxide, Methane and other hydrocarbons)
(e) Nitriding Conditions (Ammonia and Nitrogen).

The reductive, oxidative or neutral conditions are relative and vary from system to system. One should understand that a sintering atmosphere oxidative for a system could be neutral or different for other systems. Usually for the porous materials the condition (reductive, oxidative, etc.) are done in presence of a gaseous entity which enhances pore formation. Equivalently certain pore-forming agents are also added during the sintering process which releases good amount of gases in the reducing or oxidizing conditions leading to formation or pores of certain type and ensuring high degree of porosity in the metals.

The addition of pore-forming agents (PFAs) is usually utilized for metals with high porosity. These PFA's should neither react with the concerned metal nor should absorb water or decompose at room temperature or reaction conditions. The PFAs are decomposable when heated and should not leave any residue in the metals that could act as impurity. Inorganic salts possessing lower melting point are employed as PFA viz. camphor, urea, acid carbonates and ammonium chloride. Pore enhancers and natural cellulose may also be used additionally.

6.3.2 Fibre Sintering

The general process to synthesize porous metals via fibre sintering process are threading, felting and sintering [4]. Metallic fibres with particular known dimensions (length, diameter, and length-diameter ratio) are aligned to the felt and further calcined under reducing conditions resulting in porous fibres. Different alloys like Ni–Cr alloy, stainless steel, Cu, Ni, etc., with a broad range of porous structure are prepared by this method. Porous metals obtained from fibre sintering possesses certain gains in the form of higher compression resistance, better elasticity and better toughness.

6.3.2.1 Electrode Plating with Porous Metal Fibres

The Ni-base plate commonly utilized in the battery industry are porous metallic fibre electrodes. It is manufactured using different approaches like:

(a) A uniform mixture of metal fibres and fibre felt is prepared (diameter to length ratio) and thereby calcined in reducing medium to acquire a porous matrix. Metallic plated organic fibre is calcined, cut and drawn to manufacture the fibres.
(b) The reductive sintering of metal plated fibres is attained through thermally decomposing the organic or via direct thermal decomposition of metallic plated fibres.
(c) The metallic carbonyl compounds are decomposed thermally for the continuous production metallic fibre base plate.

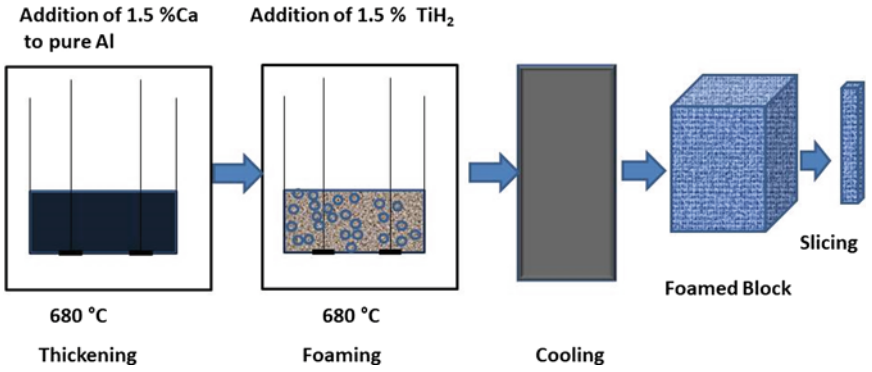

Fig. 6.2 Representation of Metallic Melt Foaming using hydride PFA for porous metal foam

(d) PFA along with binder Ni powder and Ni-slurry are employed in a simple technique.

6.3.3 Metallic Melt Foaming

Pore foaming agent (PFA) which releases gaseous material (Fig. 6.2) on thermal decomposition is added to the metallic melt after optimization of the viscosity. The foaming of the melt is caused by the thermal decomposition of the added foaming agent which expands and is cooled thereby [12, 13].

Metal hydrides powders that decompose at low temperature(~400–500 °C) like—hydrides of Ca, Mg, Ti, Zr and Er are essentially employed as PFA. Different metals and alloys formed by this method possess lower melting point viz. Al-alloys, Al, Pb, Sn and Zn.

6.3.4 Introduction of Gases to Metallic Melt

Stream of gas bubbles of air, CO_2 or inert gases are introduced from the bottom molten metal with an optimized viscosity as shown in Fig. 6.3. The metallic foam formed should be stable and non-brittle in the course of this process. The solid stabiliser particles along with the metal forms are heated to a melting temperature above the metal liquidus and then gas is introduced from bottom to form cell bubbles. On cooling down from the liquidus to solidus of the metal foam with required pores is acquired [12, 13].

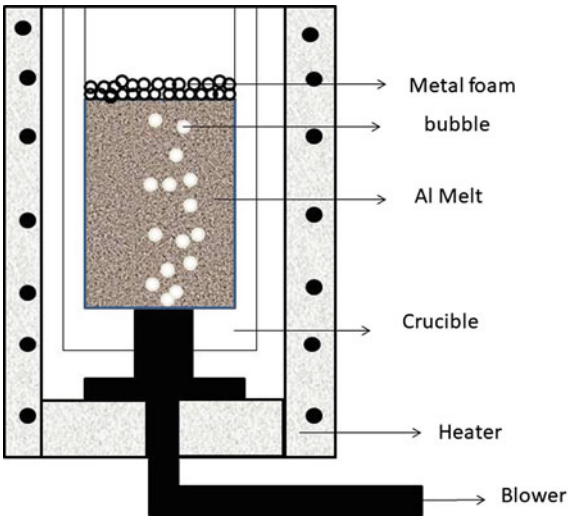

Fig. 6.3 Gas introduction into the metal liquidus from below to produce porous metal foam

6.3.5 Infiltration Casting

The pores or interfaces which are created by the inorganic/organic materials or hollow spheres with lower density are loaded up in the mould. The infiltration of the metal in the molten state occurs through the interspaces. On dissolution of these pileups by the thermal process porous metals are produced. Heat resistance and soluble inorganic materials could be used as the pileup like aluminium hollow balls, NaCl, puffing clay particles, fired clay balls, sand balls, glass ball foams. Depending on the kinetics of the infiltration and solidification certain polymers could be accepted as the substrate and subsequently be pressurized with required pressure. The synthesis of metals like Al, Mg, Zn, Pb, Sn and cast iron with high porosity in spongy form is established by this method.

6.3.6 Metal Deposition

The metal deposition could be achieved through Physical or Chemical means or by Electrode position to attain porous metal. One of the physico-chemical method is vapour deposition depending on the way it is performed. In the physical vapour deposition method, the materials are usually heated under strong vacuum to the vapour state by using either Electric Arc, Electron Beam or Resistance heating and subsequently are dispersed over a porous substrate. The evaporized metal in vapour state is deposited over a polymer surface forming a film of metal few multilayer thick. The film thickness is proportional to that of the vapour density and time of deposition. Finally, the porosity in the metal film would be obtained by degenerating

the polymeric porous substrate in the required atmosphere (reductive/oxidative) at a particular temperature. Organic materials, polymers like polyester, polyurethane, etc,. could be used as the polymeric base discussed above. The metals that could be used in the vapour deposition technique are Cu, Ni, Zn, Al, Mo, Ti, Fe, etc. The alloy of the different metals could also be made depending on the precursors used and the time of alloying. Another way of deposition is evaporating the metal vapour under inert atmosphere in lieu of vacuum. The porous structure formed by the deposited vapour formed mainly by resistive heating. The presence of the inert atmosphere leads to the collision between the metal atoms and that of the inert gas molecules as they lose kinetic energy differentially and reassemble in the form of a cluster, subsequently the growth mechanism is followed as cluster growth to produce a film of metal. Thereby growth of porous metal film is dependent on the gravitational force of the metal vapour atoms carried by the inert carrier gas. The rate of migration and diffusion in the lower temperature also plays a role in the formation of the porosity in this technique. Usually, highly porous metal thin films are produced in this fashion.

6.3.6.1 Electrodeposition

This is a method of electrodeposition of metal ions present in the electrolyte over a foam polymer substrate and thereby decomposition of the polymer leads formation of porous metal. Electrodeposition method leads to formation of highly uniform porous metal surfaces. The substrate used could be organic foams like polyurethane, polyester, vinyl polymer and styrene polymers and polyamides. An initial pretreatment to eradicate the surface impurities, oil and closed pores is accomplished using an alkali/acid solution. The materials/substrate not electrically conductive are made conductive using techniques like evaporation plating, ion plating, chemical plating, conductive gluing, conductive resin coating and slurry coating. Then electroplating is conducted either by the traditional methods, pulse current method to lower polarization. Different porous metals like Cu, Sn, Pb, Fe, Au, Ni, Pt, Pd, Al, Cd Cr, Zn, Ag, Hg, Tl, Ga, Co, In and several metallic alloys are produced.

6.3.7 New Methods for Directional Porous Metals

GASAR (A Russian word meaning- Gas Reinforced): Solid gas eutectic solidification is a new improved technique for synthesis of porous metals using their eutectic point. Generically, it is more of a casting method in which a metal in liquid state with some dissolved gas (like H_2-gas dissolved in the liquid metal) is solidified near its eutectic temperature (possessing a lower co-melting point). The differential solubility of dissolved gas moiety H_2 in the solid metal as compared to the liquid metal plays a pivotal role. Therefore, it serves the dual purpose that the metal solidification and the pores introduction at the eutectic temperature. The eutectic point of a metal is its state property and mainly depends on the total pressure of the system. The porosity

in the system can be tuned by altering the hydrogen pressure in required cavity. The temperature of the liquid metal has a great effect on the solubility of hydrogen. Therefore, melting temperature of the metal should be tuned so that it can be utilized for the eutectic point of the metal. If not regulated properly it could lead to certain different phases of the metal with undesirable properties. The pore size is controlled by the cooling rate, GASAR is applied for the production of metals with high porosity like Co, Cr, W, Cu, Mg, Al, Ni, Mo, Be and alloys like stainless steel, steel, bronze, etc., with a desired pore [14].

6.4 Synthesis of Porous Ceramic Materials

The term *"Molecular sieves"* was suggested by McBain (1932) for the materials demonstrating specific adsorption characteristics. He proposed that for a material to be a molecular sieve, it must have separate components of a mixture based on molecular sizes and shape differences. We have walked a long way where the porous materials are synthesized with required properties performing specific tasks which could be well correlated with their structural attributions. Due to various properties of zeolite molecular sieves such as Lewis and Bronsted acidity, shape selectivity, etc., these materials find a broad range of applications different industrial processes. Zeolites have now become a synonymous name in petrochemical and fine chemical industries. A lot of research has been invested to understand their structure, formation, and their effective properties. This chapter will describe the generic viewpoints required in their synthesis, the characterization techniques required to study their characteristics and their utilization both in the research domain and industry. The ability of the molecular sieves to separate various molecules based on their pore size, hydrophobic and hydrophilic nature has been utilized extensively. For example, a number of zeolites are now used routinely as drying agents, in gas purification and in separation processes involving hydrocarbons [15]. Zeolites are also utilized on large scale in detergent industries as additives where they act as ion exchangers and adsorbents [16]. Zeolites and zeo-type materials because of their high acidity, shape selectivity, regenerability and thermal stability are used in petrochemical industry, olefin oligomerization and select to forming, dewaxing and MTG (methane to gasoline) processes[17, 18]. For example, Zeolite-A is used in separation process of n-paraffins from branched paraffins, Zeolite–X and Zeolite–Y are employed as cracking catalysts in petrochemical industries [8], and TS-1 is used in oxidation reactions of paraffins, olefins, alcohols, etc. [19] They also serve as large surface area and porous support to load certain active species. The zeolite-type materials, with their definite pore structure act as a perfect host, to encapsulate a number of nanosized materials, like nanosized metals, metal oxides, semiconducting materials, complexes and dyes, etc. [20–23] These materials are also employed in treatment of waste water, in nuclear effluent treatment and in soil enrichment [15, 24]. Classification for the molecular sieves is represented below (Fig. 6.4).

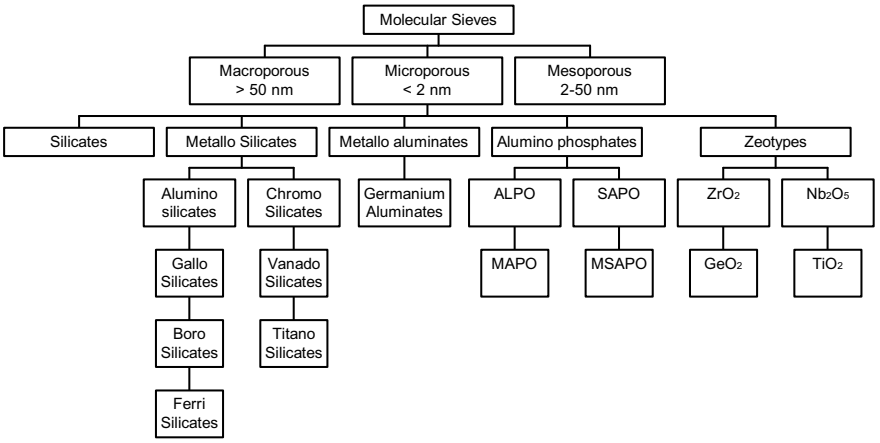

Fig. 6.4 Classification of molecular sieves based on chemical ingredients

6.4.1 Microporous Materials

6.4.1.1 Zeolites and Zeotypes

(a) Zeolite

Alex Fredrik Cronstedt, a Swedish geologist, discovered Zeolite (1756) as a rock. The zeolitic material was gathered from a copper mine and was detected to discharge heavy amount of steam on heating. The steam came from the adsorbed water inside the mineral structure. The zeolite term was coined from the Greek word "boiling stone". Synthesis of zeolites was first performed in 1930s and was found to have substantial demand in large scale petroleum industries for catalytic cracking purpose in 1960s. These zeolitic materials were also found to be very important in the laundry industry and have exchanged the phosphate compounds which incremented their importance in 1970s. Zeolites are classically produced with crystals and crystal aggregates in the micron range. Lately there have been number of approaches for the synthesis of nanocrystalline zeolites with crystal sizes ranging from few nm to 100 nm such as silicalite, ZSM-5, beta-mordenite and faujasite by different groups.

The basic structure for all zeolites generally involves an Alumino-silicate framework which includes a tetrahedral arrangement of silicon cations (Si^{4+}) along with that of aluminium cations (Al^{3+}) where each metal ion is bonded to four oxygen anions (O^{2-}). Every O^{2-} ion of the Si-O and Al-O bonds is connected to the two cations (Si^{4+} and Al^{3+}) and is shared between the two tetrahedra. The resultant macromolecular three-dimensional structure is made up of SiO_2 and AlO_4 tetrahedral building blocks. A three-dimensional structure of silicate or aluminate tetrahedra with a Si:O ratio of 1:2 was formed where every tetrahedron comprises a Si/Al cation bonded with four O_{2-} anions [25]. Certain Si^{4+} ions are exchanged with Al^{3+}

ions, which results in total negative charge in the tetrasilicate framework, present over the O^{2-} anion bonded to Al^{3+} cation. The counter ions like metals from group IA and IIA (Na^+, K^+ or Ca^{2+}, Sr^{2+}, Ba^{2+}, Li^+, Mg^{2+}) balance the negative charge of the zeolitic network [25]. Mostly these ions are present on the zeolitic external surface bounded in the alumina-silicate structure with weak electrostatic bonds [26, 27]. These replaceable mobile counter ions/molecules present in the non-framework structure are present in the three-dimensional pores and the cavities resulting from the three-dimensional tetrahedral framework. Such molecules like water molecules found in these cavities make the zeolites hydrated at room and lower temperatures. The generic stoichiometric formulation of zeolites is $[(Li, Na, K)_a (Mg, Ca, Sr, Ba)_d (Al_{(a+2d)}Si_{n-(a+2d)}O_{2n})]\cdot mH_2O$ [25, 28].

Zeolitic crystal structure could be differentiated mainly into "two types of motifs"- primary building motif (PBM) and secondary building motif (SBM) (Fig. 6.5). The main and the primary building motif are the $(SiO_4)^{4-}$ and $(AlO_4)^{5-}$tetrahedra (Fig. 6.5). A spatial arrangement of two- and three-dimensional simple geometric forms are produced by sharing oxygens of the primary motifs with adjacent tetrahedra to form the secondary building motif. These secondary building motifs could be present in diverse shape like single rings, double rings, polyhedral, etc., or may even be present in more complex units formed by different ways of cross linking to yield various distinctive channels and cage structures. Unit cell of a Zeolite definitely contains definite number of secondary building motifs which could then be extended in the three-dimensional regime. The non-chiral secondary building motifs could comprise almost 16 terminal atoms. The number of atoms of the SBM are calculated with the primary assumption that a unit cell should possess integer atoms and

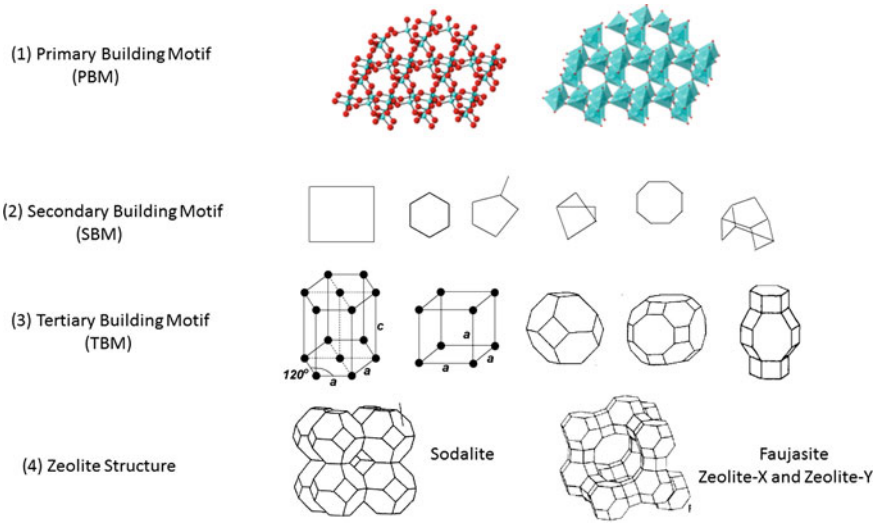

Fig. 6.5 Different moieties used for making the framework structure of a Zeolite (1) PBM—the $(SiO_4)^{4-}$ or $(AlO_4)^{5-}$tetrahedra (2) SBMs and (3) TBMs and (4) the representative zeolitic assembly

same single framework (Fig. 6.5). Along with the above-defined PBMs and SBMs, double rings, can crinite cages and alpha cavities may also be present in the zeolites. These are called tertiary building motifs TBMs (Fig. 6.5). The TBM's are found in diverse framework structures and can be a potent tool for understanding interrelations between the different frameworks. They can definitely be chiral in nature and are not used to build the complete framework [29]. The PBMs are defined by the rings that can accommodate the required number of tetrahedrons. A ring is designated after the number of tetrahedrons that are present in the ring. Therefore, n-tetrahedrons will be representing as a ring of n. Zeoliticnetwork is commonly made of tetrahedrons (4, 5, 6, 8, 10, or 12) whereas rings consisting of higher tetrahedrons (like 14–20) are also found in literature [30, 31]. A zeolitic network with odd-numbered ring (3, 7, or 9) are quite unusual [32, 33]. The pore size in a zeolite is governed by the particular framework ring size. The pore entrance known as a window.

(b) Zeotypes

The basic (primary) building blocks of zeotypes are tetrahedral made of either SiO_4 or AlO_4, and all the tetrahedra share corners. The arrangement of the building blocks is periodic (crystalline) and therefore possess particular symmetry. There are primary or basic building motifs which are mainly Tetrahedron and then present are the secondary or composite building motifs having polymeric structures which are mainly interconnection of the tetrahedral shared corners with the O-atoms, like (rings, prisms, etc.) and finally tertiary building units like larger cages. Different types of soft templated methods are applied for synthesis of hollow zeolitic superstructures. They include pickering stabilized colloids, interfacial techniques with non-miscible solvents and fast crystallization from droplets. Literature report established on single-step emulsion-based technique mainly stabilized using micellar materials like Fe-based metal-organic frameworks (MOFs) cubic crystals into a three-dimensional hollow superstructure. However, hollow zeotypes are rare and synthesis of them are really tough. Other than MOFs, hollow SAPO-34 and APO-34 materials exhibit macroporous internal structures. Chabazite zeolite, a very good catalyst for methanol to olefins and for separation of CO_2 and H_2 from other gases, also shows similar macroporous hollow porous structure.

6.4.2 Formation of Zeolites

Zeolites can be of two types: (i) Naturally occurring in form of minerals and (ii) Synthetic that are produced commercially for specific uses for research purpose.

6.4.2.1 Natural Zeolites

Most of the natural zeolites are found in the craters formed after the volcanic eruption and have to mined to extract them. These are formed when the volcanic ash produced by lava from volcanic eruptions come in contact with sea or lake water. The chemical reaction between these aluminosilicates and the salts present in water leads to natural zeolite formation.

Therefore, the principal factors determining the formation of natural zeolite are:

(i) Type of volcanic matter (lava or ash) reaching water.
(ii) Type of contact water (sea water or lake/ground water).
(iii) Ratio and concentration of the various salts.
(iv) pH of water.

These factors involved in the formation of a zeolite are the reason that each natural zeolite has unique properties. It was further established by researchers that formation of zeolite may take place under any of combinations of the following conditions: hydro-geo thermal systems, waterbody or soil alkaline/saline in nature, exposed water bodies with low-temperature, sediments under the deep-sea, burial diagenesis. The formation of reasonably pure deposit of zeolite are obtained from the rapid cooling of the volcanic ashes in the saline, alkaline lakes [34]. There are about 40 naturally occurring zeolites forming in both volcanic and sedimentary rocks. As per US Geological survey, the most mined zeolites are Chabazite [$Al_2S_{14}O_{12}{\cdot}6H_2O$], Clinoptilolite [$(Na, K, Ca)_{2\text{-}3}Al_3(Al, Si)2Si_{13}O_{36}{\cdot}12H_2O$] and mordenite [$A_{l2}Si_{10}O_{24}{\cdot}7H_2O$].

6.4.2.2 Synthetic Zeolites

In addition to the naturally occurring zeolites, many synthetic zeolites were synthesized by different methods for specific applications. The best known are zeolite A (used as laundry detergent), zeolite X and Y (Faujasites, used for cracking) and ZSM-5 (Pentasil zeolite used as petroleum catalyst).

The first synthetic zeolite was reported by St Claire Deville (1862) as production of levynite [35]. However, modern zeolite synthesis has its origin from the works of Richard Barrer and Robert Milton (1940s). Research study of Barrer consisted of transformation of existing minerals at elevated temperature (~300 °C) using highly concentrated salt solutions [36] whereas Milton utilized highly reactive synthons (aluminosilicate gels), enabling the reactions to be carried out under relatively mild conditions. This led to discovery of zeolite A and B along with 20 other Zeolites by Milton and his co-workers [37]. In the sixties, the range of reactants was further broadened and quaternary ammonium cations were included. Another breakthrough was the introduction of organic constituents, which led to discovery of many new phases like zeolite beta, ZSM-5, etc.

General route of zeolite synthesis includes sluggish crystallization of silica-alumina gel with alkali and organic templates. In addition to the variation in structure, the zeolites can also be synthesized by incorporating variety of other atoms (heteroatoms like Ge, Fe, Ga, B, Zn, Ti and Sn, etc.) which gives rise to interesting properties. A brief account of the two most commonly used methods for zeolite synthesis, i.e. Sol-Gel method and Hydrothermal method is given below.

6.4.2.3 Sol-Gel Process

Exceedingly condensed and branched polymers are synthesized by hydrolysis and condensation of metal alkoxides which could be termed as prevalent precursors for sol-gel processing. The functionality of the metal usually guides interconnection in the polymers like Si, having coordination number 4 could result in many branched framework structure.

The sol to gel conversion is guided by hydrolysis and condensation reactions for the precursors. A typical hydrolysis reaction may be exemplified below (with Si-OR):

$$\mathrm{Si\,(OR)_4 + n\,H_2O = (HO)_n - Si\,(OR)_{4-n} + ROH.}$$

Where R is Alkyl Group for metal alkoxide precursors. The metal is completely hydrolysed when $n = 4$. Partial hydrolysis is observed if $n \neq 4$. The condensation is signified by liberation of a H_2O/ROH from partially hydrolysed molecule. The general reaction is represented as:

$$\mathrm{(OR)_{4-n}Si(OH)_n + (HO)_n\,Si(OR)_{4-n} = (OR)_{4-n}(OH)_{n-1}Si - O - Si(HO)_{n-1}(OR)_{4-n} + H_2O.}$$

The maximization of metal-metal linkage through oxygen (M-O-M) bonds occurs through condensation and thereby minimises the terminal –OH group by internal condensation. These monomers bind together forming rings, and thereby generating required three-dimensional structures. The dense structural network is formed by condensation of the hydroxyl groups outside.

The product properties are mainly governed by the composition of reaction mixture, overall pH, reaction temperature, seeding time, time taken for reaction and the type of templates used. The beauty of the sol-gel process is the easy incorporation of other elements like metals and metal oxides.

6.4.2.4 Hydrothermal Process

Hydrothermal synthesis of zeolite can be presented by following simple steps:

1. Silica and alumina-containing reactants (amorphous in nature) are mixed with a cation source, usually in a basic medium.
2. Heating reaction mixture (>100 °C) in a hydrothermal autoclave.

3. The reactants continue to be in amorphous form (induction period) post that the crystallization starts.
4. Slowly all the amorphous material is replaced by an approximately equal mass of zeolite crystals.
5. These zeolite crystals are recovered by filtration, followed by washing and drying [38].

Silicon and aluminium which make the microporous framework are introduced in their amorphous oxide forms. The amorphous oxides possess Si-O and Al-O bonds and these bonds are converted to Si-O-Al bonds in the hydrothermal reaction with a mineralizing agent (commonly an alkali metal hydroxide). As only few new bonds are formed for the zeolite from their precursor oxides the free energy change for production of zeolite is pretty less. Various detailed mechanisms have been proposed for the synthesis, e.g. Condensation polymerization of polygonal and polyhedral anions, linkage of polyhedral, etc.

6.4.3 Mesoporous Materials

The 1990s saw the development of an innovative field in porous materials post the advent of new plethora of materials possessing ordered mesoporous structures which were designed using soft templated surfactants along with silicates and alumino-silicates to obtain the desired size of mesopores and its properties. Utilizing the surfactant route not only gave larger mesopores but also the control to engineer them along with the amorphous framework structure which being distinctly different from the crystalline zeolitic framework It was for the first time that Kuroda et al. informed Kanemite mesoporous material (FSM-16) formed through the hydrothermal method for synthesis of silicates [39]. An ordered material possessing pores diameter (2–4 nm) with very high surface area (~900 m^2g^{-1}) was reported by this research group with the optimized reaction conditions [40]. However, by the same time, Mobil scientists reported a new group of mesoporous materials, labelled M41S [41], which had 1-D hexagonal pores (MCM-41) and showed several similarities with FSM-16. The M41S family consists of three members viz. one dimensional hexagonal MCM-41, 3-D cubic MCM-48, and thermally unstable MCM-50. Thereafter various silica and alumino-phosphate based mesoporous materials such as, HMS [42], MSU-1 [43], KIT-1 [44], LUM-1 [45], SBA-n [46], HMA [47], UHM-1 [48], etc., have been reported in the literature (Table 6.1) and the field has been of intense research from the point of view of fundamental and as well as applied work. The extensive work and growing importance on these mesoporous materials have been reported in several review articles. These mesoporous materials have several advantages, which make them superior to the microporous molecular sieves and the main features are as follows:

1 Tunable pore sizes (2–10 nm).
2 Large number of internal hydroxyl groups, 30–50% (surface).

Table 6.1 Overview of mesoporous molecular sieves

Mesophase name	Silica source	Template	Reaction conditions	Medium	Pore size (nm)	Pore dimension
MCM-41	Fumed silica	Alkyltrimethylammonium halides	Hydrothermal synthesis	Basic	2–10	1D
FSM-16	Layered silicate	Alkyltrimethylammonium halides	Ambient temperature	Basic	2–10	1D
HMS	TEOS	Primary amines	Ambient temperature	Neutral	2–10	1D
MSU-1	TEOS	Poly(ethylene oxides)	Ambient temperature	Neutral	2–15	1D
LMU-1	TEOS	Alkyltrimethylammonium halides	Hydrothermal synthesis	Basic	2–10	1D
SBA-15	TEOS	Ethylene oxide Block copolymers	Thermal synthesis	Acidic	5–30	1D
HMA	–	Alkyltrimethylammonium halides	Hydrothermal synthesis	Basic	2–10	1D
MCM-48	TEOS	Alkyltrimethylammonium halides	Hydrothermal synthesis	Basic	2–10	3D
KIT-1	Colloidal Silica	Alkyltrimethylammonium halides	Hydrothermal synthesis	Basic	2–10	3D
SBA-1	TEOS	Alkyltriethylammonium halides	Lower temperature (273 K)	Acidic	2–10	3D
SBA-16	TEOS	Ethylene oxide Block copolymers	Ambient temperature	Acidic	5–10	3D

MCM = Mobil Composition Material; FSM-16 = Folded Sheet Mechanism number 16; HMS = Hexagonal Mesoporous Silica; MSU-1 = Michigan State University number 1; SBA-n = Santa Barbara University (n = 1, 2, 3, 6, 11, 12, 15, 16); LMU-1 = Ludwing-Maximilians-Universitat # 1; HMA = Hexagonal Mesoporous Aluminophosphate; KIT-1 = Korea Advanced Institute of Science and Technology number 1 (Reference taken from Thesis of Kaustava Bhattacharyya)

3 High internal surface area (600–1500 m^2g^{-1}).
4 Hydrophilic and hydrophobic nature.
5 Good thermal stability (~1200 K).
6 Different pore geometry.

Owing to these characteristics, the mesoporous materials could generate several promising new prospects in catalysis, particularly for conversion of bulkier molecules in several processes, for instance as a cracking catalyst in petrochemical refineries, as well as in the area of advanced materials, where they are used as hosts to accommodate various semiconducting materials, dyes and complex nanoparticles. The importance of these materials can simply be realized from the large number of research papers and review articles [37–51], that appeared on this subject during the late 90s.

6.4.3.1 Formation Mechanism

Generally, the hydrothermal synthesis of zeolites involves mixing of the silica, alumina, alkali/alkaline earth metal ions and an organic template molecule, followed by crystallization in an autoclave for several hours. The most outstanding feature and the novel idea of replacing the organic (single molecule) template by assemblies of cationic surfactant molecules was first demonstrated and reported systematically by the Mobil scientists [41]. Depending on the gel composition and synthesis conditions, the material achieved may consist of a hexagonal MCM-41, cubic MCM-48 or a thermally unstable MCM-50 structure. Mainly three ingredients are required for synthesizing these mesoporous materials. These are, silica source, a structure-directing agent in the form of surfactant and a solvent which is generally water. The final product is obtained after ageing of the gel at about 383 K or by continuously stirring the gel at room temperature for several hours or days. The solid material obtained is thoroughly washed with distilled water, dried and finally calcined at 823 K first in nitrogen and then in oxygen to remove the surfactant. These mesostructured materials thus obtained can be synthesized from various sources of silica such as fumed silica, tetraethyl orthosilicate, sodium silicate, colloidal silica and also by using different kinds of surfactants, viz. cationic, anionic, neutral, gemini [49].

6.4.3.2 Various Mechanisms Proposed

Quite a series of synthesis mechanisms are projected to demonstrate the evolution of the mesoporous materials viz. liquid crystal templating (LTC) mechanism, cooperative templating (CT) mechanism, neutral templating (NT) mechanism and folded sheet (FS) mechanism.

In these mesoporous materials formation, surfactant has major role and depending upon the water to surfactant ratio, temperature, etc., the surfactant molecules tend to organize themselves into aggregates with different shapes, basically called micelles. The scientists from the Mobil group were the first to propose the formation mechanism, (Liquid Crystal Templating (LTC) mechanism) [41]. It was assumed that a liquid crystalline hexagonal mesophase is formed through self-organization of the surfactant molecules (cationic head groups, S^+) followed by surrounding and condensation of the silicate anions (I^-) present in the reaction mixture. It results into inorganic polymer formation, which attains the surfactant mesophase shape.

The surfactant is removed by burning off through calcination, and the resultant is hollow inorganic silicate cylinders which are present in a hexagonal arrangement.

This mechanism was not accepted by many groups and subsequently another mechanism was suggested by the Mobil group. According to this mechanism, when anionic silicate is added to the cationic surfactant it initiates the formation of hexagonal liquid crystalline phase and the subsequent steps were the same as depicted in the first path. This mechanism got support from a number of research groups [50].

Furthermore, Chen et al. suggested that initially micelles are formed in rod shape and a random manner. These micelles interact with anionic silicates via electrostatic

interaction to give polymerized silica monolayers over the micellar surface [51, 52]. The silica-coated micelles then spontaneously arrange themselves into long hexagonal arrays. The driving force for the process was believed to cause further condensation of the silicate species.

Stucky and coworkers proposed the Cooperative Templating (CT) mechanism which was closely related to their earlier proposed lamellar-hexagonal phase transformation mechanism [53, 54]. This mechanism involves the following three steps: (i) Strong interaction of Silicate polyanions with surfactant cationic groups at silica-surfactant interface. (ii) Silicate polymerization takes place at the interface. (iii) Lamellar phase is transformed into cubic or hexagonal material. The generally accepted scheme for synthesis of MCM-41 is presented in Fig. 6.6 which matches with the different propositions proposed by different groups.

Tanev and Pinnavaia suggested a neutral templating (NT) mechanism. These neutral surfactants include polyethylene oxides and primary amines, where both the head and the tail groups of the surfactant are neutral [55]. The mesoporous silicates prepared using this method were designated as HMS and MSU. The NT mechanism is governed by hydrogen bonding due to the neutral surfactants present in this case, While LCT and CT mechanisms are governed by electrostatic interaction. The silicate source in this case is tetraethyl orthosilicate (TEOS).

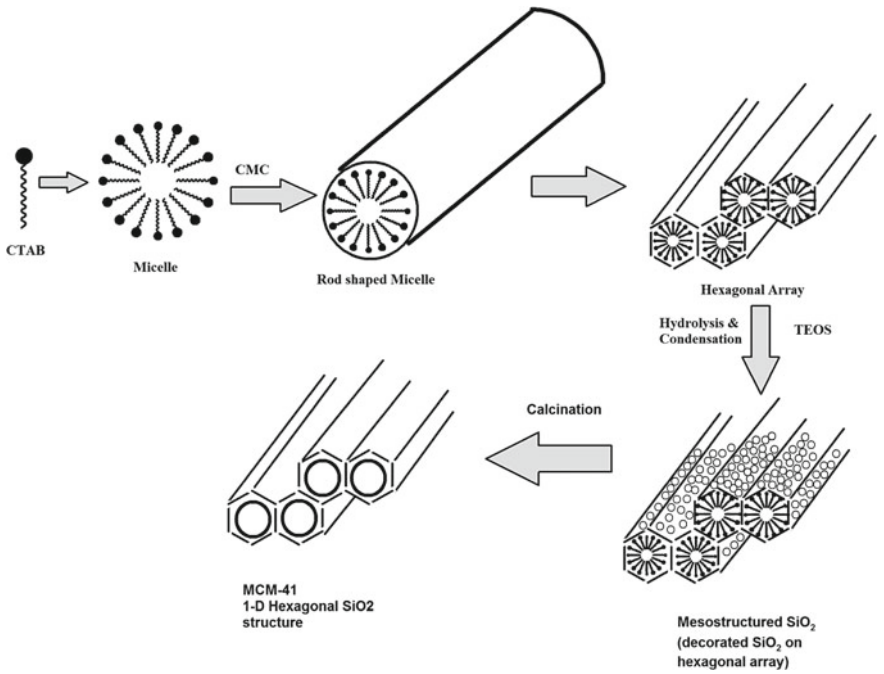

Fig. 6.6 Suggested mechanism for synthesis of MCM-41; CTAB (cationic surfactant), CMC signifies critical micelle concentration where the spherical micelle forms rod-shaped TEOS (tetra ethyl ortho silicate)

TEOS interacts with head group of the surfactant amine through H-bonding. This silica-surfactant complex is amphiphilic in nature and contains bulky head groups. The presence of these bulky moieties enhances the chances of formation micelles in the form of rods. These rods tend to organize themselves into hexagonal packing. Following which, the silanol groups undergo condensation and form rigid silica walls.

6.4.3.3 Mesoporous MCM-48 and MCM-41

The advancement of mesoporous M41S materials can be recalled as a very strong innovation in the field of zeolite and materials science. Three subgroups of the M41S family have been reported: (i) MCM-41, (ii) MCM-48 and (iii) MCM-50 as described earlier [41].

Though most of the studies and the research work in the field have been concentrated and related to MCM-41, the reason being ease in the preparation of MCM-41 [56, 57]. However, the MCM-48 with three-dimensional pore structure has a number of advantages over the one-dimensional MCM-41 and this has been well demonstrated in studies relating to loading of various guest species, catalytic activity, etc. [58, 59].

6.4.3.4 Synthesis Parameters

Following are some of the important parameters which govern the formation of high quality MCM-48 and MCM-41 samples: (i) the nature of surfactants, (ii) surfactant-silica ratio, (iii) duration of synthesis, (iv) pH, (v) crystallization time and (vi) temperature, etc. A brief discussion of some of these parameters is given below.

(a) **Nature of Surfactant**
The pore size of the mesoporous material can be tuned by using a suitable surfactant of a particular chain length. It has been reported that each additional –(CH_2)– unit increase the pore size by around 0.3 nm. For example, pore size of MCM-41 increased from 3.16 to 4.80 nm by increasing the chain length of the surfactant from C_{12} ($C_{12}H_{25}(CH_3)_3N^+Br^-$) to C_{22} ($C_{22}H_{45}(CH_3)_3N^+Br^-$) [60]. Furthermore, additional swelling agents like trimethyl benzene also help to increase the size of the pores [41].

(b) **Silica Source and Surfactant-Silica Ratio**
The variation in the surfactant to silica ratio also yields mesoporous materials of different structures. Thus, the change in the surfactant to silica ratio results in the formation of MCM-41 ($\leq$0.5), MCM-48 (>0.5–1.5) and MCM-50 ($\geq$1.5) structures [61]. For MCM-41 the silica source which is generally used is fume silica whereas for MCM-48 tetraethyl orthosilicate (TEOS) is used as a silica source.

(c) **Crystallization Conditions**
The crystallization of MCM-48/MCM-41 has been studied at different temperatures ranging from ambient temperature to 423 K. Generally, it is found that for an optimized gel composition at a pH of about 11.0–11.5, a well-ordered structure is formed from 373 to 383 K. For temperatures below or above limit, disordering in the structure along with presence of other phases is detected. For MCM-48 and MCM-41 crystallization time of about 24 and 72 h are found to give an ordered structure. Increase in the crystallization time particularly for MCM-48 samples leads to transformation of its structure to mixed structure of (MCM-48 and MCM-50) and finally into a lamellar structure.

(d) **Removal of Surfactants**
As discussed earlier, the surfactants are removed from the pores by the calcination step. This step affects the crystallinity and ordering of the mesoporous material prepared. The process of calcination is done in a controlled manner where the sample is first heated in nitrogen and then in oxygen. In order to avoid or reduce the loss in crystallinity, alternative template removal processes have been developed, where the sample is washed thoroughly before calcination with mixture of HCl/ethanol or various heptane/ethanol mixtures containing dil. HNO_3 so as to remove a part of the surfactant in the process [62, 63].

6.4.4 Application of Mesoporous Molecular Sieves

Mesoporous molecular sieves have applications very much similar to zeolites and zeo-type materials. Some of the applications of mesoporous materials are discussed below.

6.4.4.1 Acid Catalyst

All siliceous mesoporous materials have rather poor catalytic activity because of the surface silanol groups present. Therefore, the substitution of silica by trivalent atoms like Aluminium, Iron, Gallium, etc., in the mesoporous molecular sieves framework is widely attempted to generate the acidic sites within these materials and detailed study of which has been presented in an article by Tuel et al. [64]. Thus the mild acidity of mesoporous materials with large pores due to incorporation of such heteroatom has increased their catalytic applications, such as acetylation, [65] alkylation [66], esterification [67], Diels-Alder reactions [68], hydrogenation [69], hydrosulfurization and hydrodesulfurization [70], isomerization [71], polymerization [72], coupling [73] and in petrochemical reactions such as cracking/hydroprocessing of cumene and hydrocracking of vacuum gas oil [74]. For example, Pt/Al-MCM-41 helped for isomerization of n-paraffin's to is paraffin's [75]. Al-MCM-41 was utilized for Friedel-Crafts alkylation of paraffins, benzene, napthanlene, toluene, etc., using olefins and alcohols as alkylating agents and their activity was found to be better

than their microporous counterparts [66]. NiMo-MCM-41 showed very good results for mild hydrocracking of vacuum gas oil leading to high yields of mild distillates of diesel, kerosene, naptha and C_1-C_4 gases. B-MCM-41 homologue has been used in Prins reaction [66]. MCM-41 bearing large pores have also been found suitable as acidic catalyst for a number of reactions involving bulky molecules for example, alkoxylation of tetraphydropyran, acylation of 2-methoxynaphthalene, etc. [76–79].

6.4.4.2 Base Catalyst

The mesoporous materials especially those containing a trivalent heteroatom have applications as base catalyst also. In this case, an alkali ion or an organic molecule like amine, etc, compensate the trivalent atom's negative charge. The process of imparting basicity can be implemented by cation exchange [80, 81], impregnation [81], or organic molecules functionalization as a part of treatment after the synthesis [82, 83], or alternatively by direct incorporation in the gel during the hydrothermal synthesis [84, 85]. Following are few examples of these approaches: Na^+ and Cs^+ ion-exchanged Al-MCM-41 samples have been reported by Kloetstra and co-workers [80, 81]. Temperature programmed desorption of CO_2 was used to evaluate the basic strength of these materials and the material exhibited good activity as well as selectivity for the Knoevenagel condensation of benzyladehyde with ethyl acetoacetate and o-methylation to form napthol. Brunel et al. reported functionalization of MMS surfaces by alkoxysilanes using the process of grafting [83] and these materials exhibited strong basicity, which is required for certain reactions like Michael reactions and transesterification. Introduction of such organic amines during gel synthesis was reported by Macauaric [84]. Recently, Jaenicke et al. have grafted organic amine on MCM-41 and used it for formation of monoglycerides from lauric acid and glycidol [82]. Miller and coworkers reported basic heterogenous mesoporous materials synthesized through cross-linking of lyotropic liquid crystals [86]. It was found to be good catalyst for Knoevengel condensation of ethyl cynoacetate with benzaldehyde. Besides this, MCM-41 supported sulfated zirconia, mono and dimetallic catalysts have also been reported [87, 88].

6.4.4.3 Redox Catalyst

Electro neutrality of the silica framework is maintained by introducing tetravalent cations in it and therefore it can be used as a redox catalyst. Thus, a number of transition metal ions such as Sn^{4+}, Zr^{4+}, Ti^{4+}, V^{4+}, etc., have been introduced in the silicate framework and are used as redox catalysts [42, 89]. The redox behaviour of these mesoporous molecular sieves has enabled the process of larger bulky molecules of various paraffins, olefins and alcohols, etc., for selective oxidation. For example, Ti-MCM-41 and Ti-MCM-48 catalysts had been utilized for epoxidation of 1-hexene by H_2O_2 [90, 91]. Ti-HMS showed good catalytic properties for oxidation of 2, 6 di-t-butylphenol to the corresponding quinone and for the hydroxylation of benzene

to phenol. Zr-MS was used for aniline to azoxibenzene oxidation and epoxidation of cyclohexene in presence of H_2O_2 by Tuel and Gontier [92]. V-MCM-41 was extensively used for oxidation of organics such as cyclodecane, 1-napthol, phenol, cyclohexene and other bulky aliphatic and aromatic compounds [93]. Sn-MCM-41 showed selective oxidation and hydroxylation for aromatics [89]. Abdel and Pinnavia used Sn substituted mesoporous molecular sieves for lactide ring-opening reactions and to produce poly (l-lactic acid) [94]. Mo and Ni MCM-41 catalysts were used for hydrosulfurization of thiophene [95]. Cr containing mesoporous silica is used to catalyse reactions involving various organic substrates. Recently a few lanthanides and actinides ions have been incorporated in the siliceous framework and found to be active for oxidation of certain organic substrates.

6.4.4.4 Molecular Host

The mesoporous materials have larger pores as equated to microporous zeolitic materials and the pore size distribution is narrow and tuneable in this case. Therefore, these materials have found a wider application in intrapore chemistry as compared to the previously used microporous materials [96]. Active research in the areas that include fundamental studies of sorption and phase transition of water, gases and organics in confined spaces has been studied by many research groups [97, 98]. Recently, adsorption behaviour studies for benzene and cyclohexene have been carried out and have been compared with the microporous zeolites [99, 100]. Mesoporous materials have been ion exchanged with various metal ions and complexes and these hybrid materials have been used for various catalytic and photocatalytic reactions [101–103]. Another area where these mesoporous materials have been employed extensively is as host to accommodate nano-scale metal, metal oxides, semiconductor clusters etc. [104, 105]. The mesoporous materials have also been extensively used to encapsulate various other guest molecules such as complexes, heteropolyacids, dyes, enzymes, polymers, fullerenes, carbon nanotubes, carbon wires and polyaniline filaments, etc., and such hybrid materials have been used for various fundamental and industrial research studies [106, 107]. Thus, discovery of mesoporous materials has led to a new era in the field of inclusion chemistry.

6.4.4.5 Adsorption and Separation

These materials have the potential to be used as a very good adsorbent owing to their hydrophobic/hydrophilic nature and at the same time a large-sized pore structure. For example, it has been possible to entrap bulkier molecules like fullerenes in MCM-41 [108]. Thus, these materials can be used as selective adsorbents in separation techniques such as high-performance chromatography and critical fluid chromatography [109]. They are also used for removing VOCs (volatile organic compounds) from the gaseous emissions from the industries [110]. Mesoporous solids are also used for separation of biological molecules. Further, these mesoporous solids can also be

used for heavy metal ions (Ag, Hg, Pb U, etc.) recovery from wastewater. Therefore, these materials can be effectively utilized for various environment or pollution control-related reactions [111, 112].

6.4.5 Hard Templating Method (Nano-Casting)

In this strategy of preparation of porous materials, hard templates, e.g. silica, etc., are used as the structure-directing agents. This method is used for synthesis of materials that are cannot be synthesized or difficult to be synthesized by soft templating methods, e.g. porous carbon and metal oxides.

The basic steps involved here are similar to soft template synthesis, i.e.

a. Preparation of the template
b. Synthesis of the desired material by using template
c. Template removal.

This method is analogous to the metallurgical process of "casting", only the scale is minimized to nanometric scale, therefore it is also called as "Nanocasting" [113]. Here the template act as mould and after removal of the mould we get a replica of the desired material.

The main advantage of this method is better shape and size control, pore regularity and crystallinity [114–116]. However, the removal of template is often difficult as compared to the soft templates. Mesoporous carbon [117, 118] and mixed oxides [114, 115] have been prepared by this method using mesoporous silica templates. The hard template pores are filled with the precursor and the precursor is thermally converted to the desired product within the pores. Commonly used precursors are: sucrose for carbon and metal salts for MOX. In the final step, the desired porous material is obtained by removal of the template.

Mesoporous silica is one of the most widely used and attractive material as hard template due to its superior properties like well-defined structure and even pore distribution, large surface area, low toxicity, high thermal stability and good compatibility with other materials [119]. As discussed in the earlier part of this chapter, these properties of the mesoporous silica can be tuned by its synthesis conditions (pH of the synthesis conditions, temperature, nature of structure-directing agents, etc.). Thermal and chemical stability is another advantage of silica which leads to better crystallinity of the end product as compared to the soft template method. The basic ideology of casting and that of nano-casting are portrayed in Fig. 6.7.

The limitation associated with these templates is their removal, since it involves leaching with reactive chemicals like HF and NaOH which are not environment friendly and sometime they may react with the end product as well. Another disadvantage is that it is a very time-consuming method as the preparation of the template itself takes a lot of time.

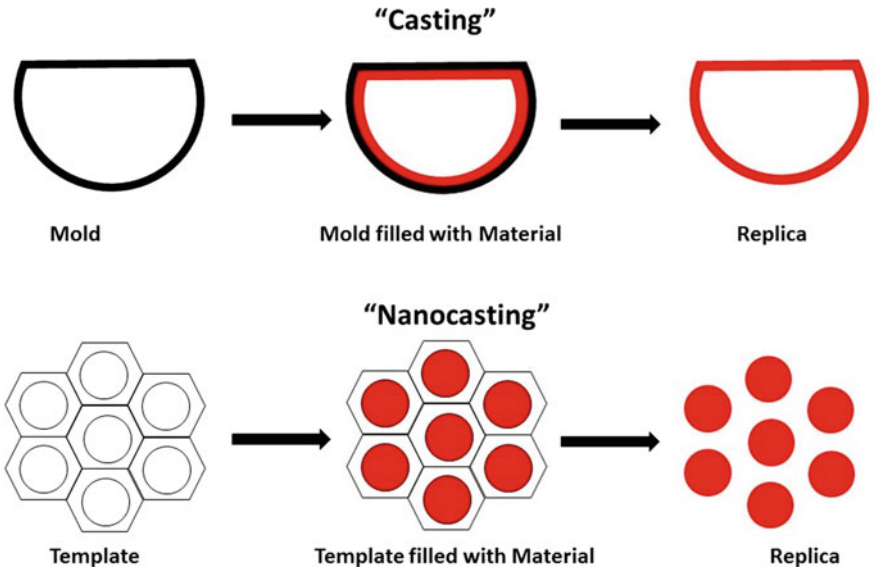

Fig. 6.7 Schematic representation of casting and nanocasting

6.4.5.1 Mesoporous Carbon Preparation by Hard Templating Method

Carbon-based materials have a wide range of applications due to their unique properties like high surface area and tunable porosity. Some of the possible applications include energy conversion and storage, sensors gas separation, water purification, biomedical and as catalyst support for production of various bulk and fine chemicals. Porous carbon-based materials which are suitable for application in various important technologies can be divided into many categories, e.g. activated carbon-based (granules/fibers), graphene-based, CNT-based, ordered porous carbon, etc.

Activated carbon is the major fraction of porous carbon used in different technologies, which is generally microporous in nature. It has pores consisting of graphene layers (hydrophobic in nature) and surface functional groups (generally hydrophilic in nature). It can be prepared by methods like physical activation, chemical activation, or combination of both chemical and physical activation, carbonization of polymeric materials and carbonization of carbon precursors using metal salts. All these methods have been conventionally used to prepare porous carbon. In general, the inherent advantage of activated carbon as porous carbon lies in low cost of production as compared to other types of porous carbon.

However, preparation of ordered porous carbon and porous carbon with uniform pores is difficult as compared to silica because the structure evolution in carbon is more complicated as compared to silica. Therefore, soft templating methods that are used for preparation of porous silica, cannot be used for preparation of porous carbon. For carbon, hard templating route or nanocasting route is employed.

Three basic steps involved in the process are:

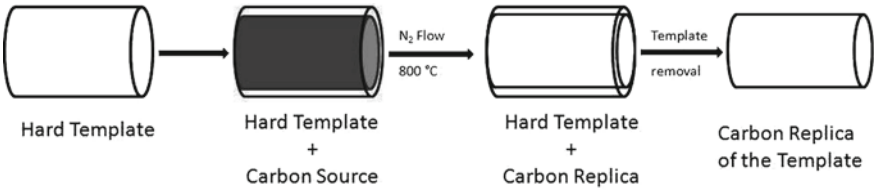

Fig. 6.8 Synthetic Strategy for the porous carbon support by Nanocasting

(i) Impregnation of template with carbon precursor, i.e. formation of precursor template composite.
(ii) Carbonization of precursor by heating in inert atmosphere.
(iii) Removal of the template.

This can be presented in Fig. 6.8.

6.4.5.2 Preparation of Metal Oxides (MO_X) Using Hard Templating Method

Ordered mesoporous transition metal oxides have numerous advantages over their bulk and nano-sized counterparts. The superior properties like high surface area, open pores, tuneable pore size and morphology, stability make them a suitable candidate for several applications in catalysis, adsorption, drug delivery, sensors, lithium ion batteries and supercapacitors [119–123].

The three basic steps involved in this case are:

(i) Introduction of metal oxide precursor in the template
(ii) Conversion of precursor to oxide by decomposition or reduction.
(iii) Removal of the template.

For preparation of porous metal oxides, mesoporous silica is the most frequently used as hard template due to its superior properties as discussed earlier. Furthermore, the surface silanol (Si-OH) groups lead to better interaction between silica and metal precursors which results into better replication of the porous structure. However, the silica-based templates need to be removed by using hydrofluoric acid or sodium hydroxide, which limits their applicability for preparation of oxides that react with either solution, e.g. ZnO, MgO, Al_2O_3. For example, hard template synthesis of mesoporous ZnO using silica can be attained only when the pH of the potassium hydroxide solution used to remove silica is adjusted to 12 [124].

Other templates like mesoporous carbon, etc., have also been employed for porous metal oxide synthesis. The limitation in case of carbon materials arise due to poor surface wetting properties [120, 125, 126]. This issue can be overcome by surface functionalization of carbon using oxidizing agents. Another issue in this case is mesoporous structure retention during template removal since high temperature combustion is required to remove carbon.

6.5 Characterization for Different Types of Pores

The use of porous materials in form of charcoal, clay and mortar, etc., and their properties can be dated back to various ancient civilizations. However, the related general principles of capillarity, diffusion, and fluid flow were developed much later in the nineteenth century. Several methods were proposed or developed for quantifying porosity, most common being by the adsorption of different fluids or gases. Porosity can be simply defined as the faction of empty (void) volume over the total volume. However, measurement of porosity is not as simple as its definition, as the empty space can be of different length scales in different materials (few nanometres to centimetres). Therefore, it is impossible to have a single method that covers this range. The different techniques that are used could be broadly be divided into four types as represented in the below Table 6.2 and are classified in the order of the pores sizes that they can characterize. Also, it is to be mentioned that different techniques have their own fundamental assumptions and hence may give different results. Therefore, a combination of different techniques may give a better understanding of the pore structure of the porous materials.

6.5.1 Adsorption Techniques

6.5.1.1 Surface Area Analysis

The surface area possessed by solid oxide catalyst is important not only for adsorption process but also for catalytic activity. The gas adsorption-desorption techniques are generally used to measure the surface area and pore size distribution of solid materials. BET (Brunauer-Emmett-Teller) method [127] is the most common method for determination of surface area, involves the following equation:

$$\frac{p}{v\,(p_0 - p)} = \frac{1}{v\,m\,C} + \frac{C-1}{vm\,C}\left(\frac{p}{p_0}\right) \tag{6.1}$$

where

p Adsorption equilibrium pressure
p_o Saturation vapour pressure of adsorbate at the adsorption temperature
v_m Volume of adsorbate required for monolayer coverage
v Volume of adsorbate adsorbed at p
C Constant related exponentially to the heat of adsorption in the first layer (q_1) and heat of liquefaction of adsorbate (q_L) ; $C = e^{(q_1 - q_L)/RT}$

The constant C determines the shape of the isotherm. The higher the value of C, the more the isotherm tends to type-II, which is desirable for accurate determination of surface area. A plot of $p/(p_o - p)$ versus v relative pressure p/p_o yields a straight

Table 6.2 Showing the different techniques to detect the different types of pores. Macroporous—>50 nm, Mesoporous—(2–50) nm, Microporous—<2 nm; All Micro + Meso + Macro; Capillaries—>1000 nm

Sl. no.	Characterization tool	Techniques	Pore range
1	Optical and electromagnetic radiation	Optical microscopy	Macroporous
		Scanning electron microscope (SEM)	Mesoporous and macroporus
		Transmission electron microscope (TEM)/high resolution TEM	Microporous and mesoporous
		Atomic force microscope	Mesoporous and macroporus
		Scanning tunnelling microscope (STM)	Microporous and mesoporous
		Small angle X-ray scattering (SAXS)	All
		X-ray tomography	Capillaries
2	Fluid and adsorption based	N_2, He, Xe-adsorption	All
		CO_2-adsoprtion	All
		Hg-porosimetry	Mesoporous and macroporus
		He-pycnometry	All
		Water porosimetry	All
3	Nuclear techniques	NMR microscopy	Capillaries
		NMR relaxation	Mesoporous and macroporus
		Small angle neutron scattering (SANS)	All
		Positron annihilation spectroscopy (PAS)	Microporous and mesoporous
4	Others	Thermal porometry	Mesoporous and macroporus
		Mechanical tracing	Capillaries

line, where the slope $S = (C - 1)/v_m C$ and intercept $I = 1/v_m C$. From this, v_m can be calculated as follows.

$$v_m = \frac{1}{S + 1} \tag{6.2}$$

Using the volume of adsorbate required for monolayer coverage (v_m) and cross-sectional area of the adsorbates molecule, we can calculate the specific surface area of the sample by following equation:

$$S = \frac{v_m N_A A_m}{W \times 22414} \times 10^{-20}\ (\mathrm{m}^2/\mathrm{g}) \tag{6.3}$$

where

S Specific Surface Area.
N_A Avogadro's number
v_m Monolayer volume in ml at STP
W Weight of the sample (g).
A_m Mean cross-sectional area occupied by adsorbate molecule which is 16.2 $Å^2$ for nitrogen at 77 K.

For many practical purposes, the BET equation is generally fitted to the data over a range $p/p_o = 0.05-0.3$ as at higher p/p_o values complexity arising due to the adsorption of multilayer and/or due to condensation within the pores. Prior to surface area determination, samples are subjected to a pre-treatment at 300 °C for nearly 5 h under vacuum, this step removes impurities such as moisture. An adsorption isotherm gives better understanding of the surface area and porosity of a material. Adsorption isotherm is constructed by plotting adsorbate quantity versus relative pressures at a constant temperature, it is obtained by successive addition of the adsorbate and subsequent measurement of the equilibrium pressure. In the same manner, desorption isotherms are acquired by calculating the removed gas quantities from the sample upon lowering of relative pressure. The adsorption isotherms can be categorized into five types viz. Type I or Langmuir isotherms show concave curve to the P/P_0 axis and the amount of adsorbate approaches a limiting value as P/P_0 approaches 1. Type I isotherms are characteristic of microporous materials which have small external surfaces, some examples are molecular sieve zeolites and activated carbons. In this type of materials, accessible micropore volume governs the limiting uptake of adsorbate.

Type II isotherms are characteristic of a nonporous or macroporous material. In this type of isotherm, we get unhindered monolayer as well as multilayer adsorption. There is a point on this isotherm where the linear central part of the isotherm starts, this point usually indicates the completion of monolayer coverage.

Type III isotherms are convex to the P/Po axis. Type III isotherms are very rarely obtained (example is adsorption of water vapor on nonporous carbons). The absence of a distinct point (as in case of type II) on type III isotherm is due to strong adsorbate-adsorbate interactions (Fig. 6.9).

Type IV isotherms are characteristic of mesoporous materials. The initial part of the isotherm is similar to that of type II and it has a steep slope at higher relative pressures. The adsorption and desorption isotherms don't follow the same path in this case and thus give a hysteresis loop due to capillary condensation in mesopores. The shape of this hysteresis curve gives idea about the shape of the pores.

Type V isotherms are rare, like that of type III. The only difference is that pores in this case are in the range of mesopore.

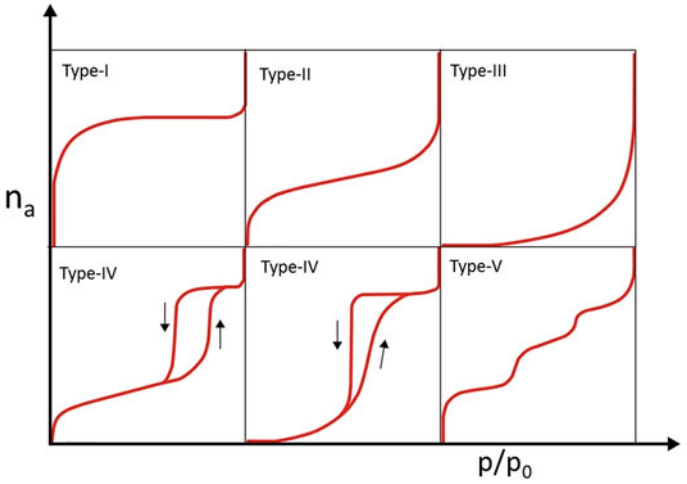

Fig. 6.9 Different adsorption Isotherms

6.5.1.2 Pore Volume and Pore Radii

The total pore volume is measured when quantity of vapour adsorbed when relative pressure is near to unity and thereby the pores are filled with liquid adsorbate. With the approximation of absence of macropores in the solid the isotherm remains horizontal in the range of $P/P_0 = 1$ where the measurement of pore volume could be well accepted. In the event of the occurrence of macropores there is a steep increment of the isotherm close to $P/P_0 = 1$ and in the limiting presence of macropores it exhibits a complete vertical rise in the isotherm. However, once there is a reliable acceptance of limiting adsorption the total pore volume could be measured under the sample kept under isothermal conditions. It is considered to be a complete equilibrium between the formation of the gaseous $N_2(V_{ads})$ and liquid $N_2(V_{liq})$ and V_{liq} is calculated using the Eq. (6.4).

$$V_{liq} = \frac{P_a V_{ads} V_m}{RT} \tag{6.4}$$

where, respectively Pa and T denotes ambient Pressure and temperature, and Vm represents molar volume of the liquid adsorbate (34.7 cm^3/mol for nitrogen).

The total pore volume and surface area has very less contribution from the pores that are filled below a relative pressure of 1, thereby average pore size could also be estimated from the pore volume. For example, taking into consideration a cylindrical pore geometry (type A hysteresis), the average pore radius r_p can be represented as

$$r_P = \frac{2V_{liq}}{S} \tag{6.5}$$

6.5.1.3 Pore Size Distribution

Statistical plot for pore volume distribution versus pore size is called a pore size distribution plot. The desorption isotherm is given more importance as compared to that of the adsorption isotherm for the distribution plot as the desorption isotherm for equivalent amount of gas volume shows lower relative pressure, consequently possessing lower free energy state. The thermodynamic stability is established via the desorption branch isotherm. However, in typical cases possessing the hysteresis in the type -IV- IUPAC the adsorption branch accepted for pore size distribution. Primarily N_2 gas is utilized as the adsorbate gas, however along with it, He and Xe are also known as adsorbate gases. The Eq. (6.6) is derived with N_2 taken as a adsorbate. Pore size calculation of a mesoporous material is made by assuming a cylindrical pore structure using the Kelvin Eq. (6.6)

$$r_k = \frac{-2\gamma V_m}{RT\,\mathrm{lh}(\mathrm{P}/\mathrm{P}_{\tilde{0}})} \tag{6.6}$$

where

y	the surface tension of nitrogen at its boiling point (8.85 ergs/cm^{2}at 77 K).
V_m	the molar volume of liquid nitrogen (34.7 cm^3/mol).
R	gas constant (8.314 × I0^{7}ergs/deg/mol).
T	boiling point of nitrogen (77 K).
P/Po	relative pressure of nitrogen.
r_K	the Kelvin radius of the pore.

Using the appropriate constants for nitrogen, Eq. (6.6) reduces to

$$r_k\left(\overset{\circ}{\mathrm{A}}\right) = \frac{4.15}{\log\left(P_0/P\right)} \tag{6.7}$$

r_k = Kelvin pore radius for condensation at relative pressure of *P/P*o. There is a definite adsorption that occurs before condensation Since, prior to condensation, r_k is not the genuine pore radius. Some additional term is added to it. The actual pore radius r_p is given by

$$r_p = r_k + t \tag{6.8}$$

$$t\left(\overset{\circ}{\mathrm{A}}\right) = \left[\frac{13.99}{\log(P_0/P)}\right]^{1/2} \tag{6.9}$$

where t is the thickness of the adsorbed layer. This statistical t can be considered as 3.54 ($V_{ads}N_m$) in which 3.54 Å is the thickness of one nitrogen molecular layer and

V_{ad}/V_{mis} the ratio of the volume of nitrogen adsorbed at a given relative pressure to the volume adsorbed at the completion of a monolayer for a nonporous solid of the same composition as the porous sample. A more convenient method for estimating t was proposed by de Boer in the form of Eq. (6.9) and is accessible for pore size distribution calculations. The pore size calculation is basically done by the BJH (Barrett-Joyner-Halenda) method.

6.5.2 Small Angle X-Ray Scattering (SAXS)

The numerical nanoscale density variance is measured by a low (below 5° θ) angle X-Ray scattering technique namely Small-angle X-ray scattering (SAXS). Average particle size distribution, ascertaining pore size, resolving pore shape and size for monodispersed macromolecules, determine space between partially ordered materials, etc., are obtained by SAXS instrument. This could be understood effectively by inspecting the elastic scattering behaviour of X-Rays when passed through a material and recording the scattering phenomena a small X-Ray angles. The scattering intensity could be signified by the spatial Fourier transform of the electron density fluctuation in a sample where the assumed microstructures may be nearly estimated as constant electron density. The particle morphology would be obtained indirectly with a required fitting with certain models. The finely divided solids show definitive interference effects in certain cases whilst are negligible in others as shown previously in the literature. The alteration in the packing type leads to different scattering patterns which may be represented by the radial distribution function as compared to that of polydispersity. However, within the limit of prod, if absence of oscillations is detected in scattered intensity, the systematic lowering of intensity is accredited to the effect of polydispersity in nano-particle size distribution. In SAXS scattered intensity is represented as a function of the magnitude of scattering vector "q" where $q = 4\,\pi \sin(\theta)/\lambda$ ($2\,\theta$ is the angle between the incident beam and the detector measuring the scattered intensity, and λ is the wavelength of the radiation). In the intermediate and the high region, the scattering intensity is proportional to q^{-4}. The assumptions for that are taken into consideration are: (a) Scattering is from equi-axial materials (like sphere, cube or disc with aspect ratio ~1); (b) nanoparticles are assumed to possess polydispersity in size, but not in shape. The scattering intensity I (q) can be expressed

$$I(q) = C \int_{R_{\min}}^{R_{\max}} P(q, R)\, N(R)\, (V(R))^2\, dR \tag{6.10}$$

where, P(q, R)—structure factor of the particle; R—Characteristic length, R; N(R)—size distribution.

However, for spherical nano-particles. A modified Debye-Bueche function is adapted in order to optimise the structure factor as shown below in (6.11)

$$P(q, R) = \left[1 + \frac{2^{1/2}}{3} q^2 R^2\right]^{((D_s-6)/2)} \tag{6.11}$$

The constant in Eq. (6.11) was chosen with an assumption of the structure factor of a perfect sphere, where R- radius of sphere and D- surface fractal dimension of the sphere. V(R) is volume of the sphere; and N(R) represents pore radii distribution. The N(R) can be expressed as

$$N(R) = \frac{1}{\sqrt{2\pi\sigma^2}} \exp\left[-\frac{[(R - R_0)]^2}{2\sigma^2}\right] \tag{6.12}$$

R_0 and σ are two parameters of the distribution which are related to the mean.

6.5.3 Mercury Porosimetry

Porosimetry is another analytical technique used for quantification of a porous material in terms of pore diameter, total pore volume, etc. It involves the introduction of a non-wetting liquid into the pores of the material to be examined by applying positive excess hydrostatic pressure. The applied pressure has an inverse relation with the radius of the pore. Therefore, the pore size can be determined by external pressure needed to force the liquid into a pore against the opposing force of the liquid's surface tension. This behaviour of a non-wetting liquid was first described by E. W. Washburn in 1921 and therefore the equation governing is known as Washburn equation.

Mercury is most commonly used because it is not wetting, non-reactive for most of the surfaces and it does not penetrate pores by capillary action. The surface tension of liquid mercury is very high therefore it tends to contract its volume into a form with the least surface area. Therefore, the entry of mercury into the pores is facilitated by application of pressure and this pressure has inverse relation with the opening of the pore [128].

6.5.3.1 Calculation of the Pore Size Distribution

It is assumed that as the pressure is increased, mercury enters pores in decreasing order of size. Thus, if ΔV is the volume intruded between P and P+ΔP, it will equal the volume of pores with radii between r and r-Δr,

$$r = \frac{2\sigma \cos\theta}{P} \quad \text{(Washburnequation)} \tag{6.13}$$

where σ is the surface tension and Θ is the contact angle. This gives a volumetric distribution of pore sizes.

6.6 Conclusion

This chapter includes an intense description of the synthesis and the characterization of the different microporous and the mesoporous materials. This will act as a good guideline for the students and the researchers to understand the different strategies for synthesis and understanding the properties of the different microporous and the mesoporous substances.

References

1. Gibson LJ, Ashby MF (1977) Cellular solids: structure and properties. Cambridge University Press, Cambridge, UK
2. Banhart J, Baumeister J, Weber M (1997) Metal foams near commercialization. Met Powder Rep 4:38–41
3. Zhu ZG (1999) Physics 24:84–88
4. Nakajima H, Hyun SK, Ota K, Murakami K (2001) Coll Surf 179:209–214
5. Zeng HM (1993) General Introduction high technology and materials. China Science and Technology Press
6. Wang LX, Ning QJ, Yao ZC (1998) Development of porous ceramic materials. Bull Chin Cer Soc 1:5–41
7. Scheffler M, Colombo P (2005) Cellular ceramics. Wiley-VCH, Wein Hein
8. Montanaro L, Zorand Y, Fantozzi F, Negro A (1998) Cermaic foams by powder processing. J Eur Cer Soc 18:1339–1350
9. Hirschfeld DA, Li TK, Liu DM (1996) Processing of porous ceramic oxide. Key Eng Mat 115:65–80
10. Zhang YL, Li CD (2000) Primary introduction to polymer foams. Zhejiang science and Technology Press, Hangzhou
11. Wu XY, Ju JY (2002) Polymer foams formation. Chemical Industry Press, Beijing
12. Banhart J (2000) JOM 52:22–27
13. Banhart J (2006) Adv Eng Mat 8:781–794
14. Peisheng L, Guo-Feng C (2014) Porous materials processing and applications, Elsevier Science, Burlington. ISBN: 9780124077881
15. Breck DW (1974) Zeolite molecular sieves. Wiley, New York
16. Rabo JA, Pellet RJ, Coughlin PK, Shamshon ES (1989) Zeolites as catalysts and detergent builders. In: Karge HG, Weitkamp J (eds), vol 1. Elsevier, Amsterdam
17. Dartt CB, Davis ME (1994) Catal Today 19:151
18. Venuto PB (1994) Microporous Mater 2:297
19. Perego C, Carati A, Ingallina P, Mantegazza MA, Bellussi G (2001) Appl Catal A 221:63
20. Stucky GD, Dougall JEM (1990) Science 247:669
21. Schulz-Ekloff G (1991) Stud Surf Sci Catal 69:65
22. Sachtler WMH (1993) Acc Chem Res 26:383
23. Suib SL, Kostapapas A, Psaras D (1984) J Am Chem Soc 106:1614
24. Szostak R (1989) Molecular sieves; principles of synthesis and identification. van Nonstrand Reinhold, NewYork

25. Armbruster T, Gunter ME (2001) Crystal structure of natural zeolites. In: Bish DL, Ming DW (eds) Natural zeolites: occurrence, properties, applications, vol 45, pp 1–68. Mineralogical Society of America, Geochemical Society
26. Farkaš A, Rožić M, Barbarić-MikočevićJ Ž (2005) Hazard Mat B 117:25–33
27. Widiastuti N, Wu H, Ang HM, Zhang D (2011) Desalination 277:15–23
28. Hashimoto S (2003) J Photochem Photobio C: Photochem Rev 4:19–49
29. Baerlocher Ch, McCusker L, Olson DH (2007) Atlas of zeolite framework types, 6th edn. Elsevier Publishing co, Amsterdam
30. Estermann M, McCusker LB, Baerlocher C, Merrouche A, Kessler H (1991) A synthetic gallophosphate molecular sieve with a 20-tetrahedral-atom pore opening. Nature 352:320–323
31. Wessels T, Baerlocher C, McCusker LB, CreyghtonJ EJ (1999) Am Chem Soc 121:6242–6247
32. McCusker LB, Grosse–Kunstleve RW, Baerlocher C, Yoshikawa M, Davis ME (1996) Microporous Mater 6:295–309
33. Robrig C, Gies H (1995) Angew Chem Int Ed 34:63–65
34. Hay RL (1986) Pure Appl Chem 58:1339–1342
35. de St Claire Deville H (324) Compt Rend Se´ances Acad Sci 54:324
36. Barrer RM (1948) J Chem Soc 127
37. Milton RM (1989). In: Occelli ML, Robson HE (eds) Zeolite synthesis, vol 398, p 1. ACS Symp Series
38. Cundy CS, Cox PA (2005) Microporous Mesoporous Mater 82:1–78
39. Yanagisawa T, Shimizu T, Kuroda K, Kato C (1990) Bull Chem Soc Jpn 63:988
40. Inagaki S, Fukushima Y, Kuroda K (1993) J Chem Soc Chem Commun 680
41. Kresge CT, Leonowicz ME, Roth WJ, Vartuli JC, Beck JS (1992) Nature 359:710. (b) Beck JS, Vartuli JC, Roth WJ, Leonowicz ME, Schmidtt KD, Chu CTW, Olson DH, Sheppard EW, McCullen SB, Higgins JB, Schlenker JL (1992) J Am Chem Soc 114:10834
42. Tanev PT, Chibwe M, Pinnavaia TJ (1994) Nature 368:321
43. Bagshaw SA, Prouzet E, Pinnavaia TJ (1995) Science 269:1242
44. Ryoo R, Kim JM, Ko CH, Shin CH (1996) J Phys Chem B 100:17718
45. Behrens P, Glaue A, Haggenmuller C, Schechner G (1997) Solid State Ionics 101–103:255
46. Zhao D, Feng JL, Huo Q, Melosh N, Fredrickson GH, Chmelka BF, Stucky GD (1998) Science 279:548; (b) Zhao D, Huo Q, Feng JL, Chmelka BF, Stucky GD (1998) J Am Chem Soc 120:6024
47. Kimura T, Sugahara Y, Kuroda K (1997) Chem Lett 983; (b) Mohapatra SK, Shaoo B, Keune W, Selvam P (2002) Chem Commun 1466
48. Zhao D, Luan Z, Kevan L (1997) J Chem Soc Chem Commun 1009
49. Huo Q, Margolese DI, Ciesla U, Demuth DG, Feng P, Gier TE, Siger T, Firouzi A, Chmela BF, Schuth F, Stucky GD (1994) Chem Mater 6:1176
50. Chen CY, Burkett SL, Li HX, Davis ME (1993) Microporous Mater 2:27
51. Cheng CF, He H, Zhou W, Cheng CF. Klinowski J (1995) Chem Phys Lett 244:117
52. Cheng CF, Luan Z, Klinowski J (1995) Langmuir 11:2815
53. Monnier A, Schuth F, Huo Q, Kumar D, Margolese D, Maxwell R, Stucky GD, Krishnamurthy M, Petroff P, Firouzi A, Janicke M, Chmelka BF (1993) Science 261:1299
54. Firouzi A, Kumar D, Bull LM, Besier T, Seiger P, Huo Q, Walker SA, Zasadzinki JA, Glinka C, Nickol J, Margolese D, Stucky GD, Chmelka BF (1995) Science 267:1138
55. Tanev PT, Pinnavaia TJ (1996) Science 267:865
56. Pera ML, Dejoz A, Fornes V, Rey F, Vazquer MI, Lopez Nieto JM (2001) Appl Catal A 209:155
57. Auvray X, Petipas C, Anthore R, Rico I, Lattes A (1989) J Phys Chem 93:7458
58. Koyano KA, Tatsumi T (1996) J Chem Soc Chem Commun 145
59. Pu SB, Kim JB, Seno M, Inui T (1997) Microporous Mesoporous Mater 10:25
60. Kruk M, Jaroniec M, Sakamoto Y, Terasaki O, Ryoo R, Ko CH (2000) J Phys Chem B 104:292
61. Stucky GD, Monnier A, Schuth F, Huo Q, Margolese D, Kumar D, Krishnamurty M, Petroff P, Firouzi A, Janicke M, Chmelka BF (1994) Mol Cryst Liq Cryst 240:187
62. Schmidt R, Akporiaye D, Stocker M, Ellestad O (1994) Stud Surf Sci Catal 84:61

63. Kawi S, Lai MW (1998) Chemtech 26
64. Tuel A (1999) Microporous Mesoporous Mater 27:151
65. Gunnewegh EA, Gopie SS, van Bekkum H (1995) J Mol Catal A 153:25
66. Armengol EA, Cano ML, Corma A, Garcia H, Navarro MT (1995) J Chem Soc Chem Commun 519
67. Dimitriu E, OnTrong D, Kaliaguine S (1997) J Catal 170:150
68. Onka M, Yamasaki R (1998) J Catal 171:259
69. Wang J, Huang L, Chen H, Li Q (1995) Catal Lett 38:33
70. Ziolek M, Nowak I (1997) Zeolites 18:356; Chen M, Kumta F, Saita T, Komatsu T, Yashima T (1999) Appl Catal A 183:199
71. Seo G, Kim N-H, Lee YH, Kim JH (1999) Catal Lett 57:209
72. Climent MJ, Corma A, Lopez G, Iborra S, Primo J (1998) J Catal 175:70
73. Aromengol E, Corma A, Garcia H, Primo J (1999) Eur J Org Chem 1915
74. Reddy KM, Song C (1996) Catal Today 31:137
75. Girgis MJ, Tsao YP (1996) Ind Eng Chem Res 35:386
76. Kloestra KR, van Bekkum HJ (1995) Chem Res S-26
77. Climent MJ, Corma A, Iborra S, Navarro MT, Primo J (1996) J Catal 161:783
78. Hitz S, Prins R (1997) J Catal 168:194
79. Sakata Y, Uddin MA, Muto A (1999) J Anal Appl Pyrol 51:135
80. Kloestra KR, van Bekkum H (1995) J Chem Soc Chem Commun 1005
81. K.R. Kloestra, M. van Laren, and H. van Bekkum, *J. Chem. Soc., Faraday Trans.* 93 (1997) 1211
82. Jaenicke S, Chuah GK, Lin XH, Hu XC (2000) Microporous Mesoporous Mater 35–36:143
83. Brunel D, Cauvel A, Fajula F, Renzo D (1995) Stud Surf Sci Catal 97:173
84. Macquarrie DJ (1966) Chem Commun 1961
85. Mdoe JEG, Clark JH, Macquarrie DJ (1998) Synlett 6:625
86. Miller SA, Kim E, Gray DH, Gin DL (1999) Angew Chem Int Ed 38:3021
87. Konhevnikov IV, Sinnema A, Jansen RJJ, Pamin K, van Bekkum H (1995) Catal Lett 30:241
88. Long R, Yang RT (1998) Catal Lett 52:91
89. Das TK, Chaudhari K, Chandwadkar AJ, Sivasanker S (1995) J Chem Soc Chem Commun 2495; Zhang W, Pinnavaia TJ (1996) Catal Lett 38:261
90. Corma A, Navarro MT, Pariente JP (1994) J Chem Soc Chem Commun 147
91. Zhang W, Pinnavaia TJ (1996) Catal Lett 38:261
92. Tuel A, Gontier S (1997) Stud Surf Sci Catal 105:1085
93. Reddy KM, Moudrakovski A, Sayari A (1994) J Chem Soc Chem Commun 1059
94. Abdel-Fattah TM, Pinnavaia TJ (1996) J Chem Soc Chem Commun 665
95. Cui J, Yue Y, Sun Y, Dong W, Gao Z (1997) Stud Surf Sci Catal 105:69
96. Biz S, Occelli ML (1998) Catal Rev Sci Eng 40:329
97. Elder KJ, Reynolds PA, Trouw F, White JW (1996) Chem Phys Lett 249:438
98. Marler B, Oberhagemann U, Vortmann S, Gies H (1996) Microporous Mater 6:375
99. Sahasrabudhe A, Mitra S, Tripathi AK, Mukhopadhyay R, Gupta NM (2003) Phys Chem Chem Phys 5:3066
100. Flego C, Carati A, Perego C (2001) Microporous Mesoporous Mater 44–45:733
101. Bhattacharyya K, Varma S, Tripathi AK, Vinu A, Tyagi AK (2011) Chem Eur J 17:12310–12325
102. Bhattacharya K, Tripathi AK, Dey GK, Gupta NM (2005) J Nanosci Nanotech 5:790–796
103. Bhattacharya K, Varma S, Kumar D, Tripathi AK, Gupta NM (2005) J Nanosci Nanotech 5:797–805
104. Wu CG, Bein T (1994) Science 264:1757; (b) Science 266:1013
105. Ryoo R, Kim JM, Ko CH, Shin CH (1996) J Phys Chem 100:17718
106. Liu C, Shan Y, Yang X, Ye X, Wu Y (1997) J Catal 168:35
107. Kozhevnikov IV, Sinnema A, Jansen RJJ, Pamin K, van Bekkum H (1995) Catal Lett 30:241
108. Piwonski I, Zaljac J, Jones DJ, Roziere J, Partyka S (1998) J Mater Chem 8:17
109. Grun M, Kurganov AA, Schacht S, Schuth F, Ugner KK (1996) J Chromatogr A 740:1

110. Zhao XS, Ma Q, Lu GQ (1998) Energy Fuels 12:1051
111. Vidya K, Dapurkar SE, Selvam P, Badamali SK, Gupta NM (2001) Microporous Mesoporous Mater 50:173
112. Vidya K, Dapurkar SE, Selvam P, Badamali SK, Kumar D, Gupta NM (2002) J Mol Catal A 181:91
113. Lu A-H, Schüth F (2006) Adv Mater 18:1793–1805
114. Tian BZ, Liu XY, Yang HF, Xie SH, Yu CZ, Tu B, Zhao DY (2003) Adv Mater 15:1370–1374
115. Jiao F, Harrison A, Jumas JC, Chadwick AV, Kockelman W, Bruce PG (2006) J Am Chem Soc 128:5468–5474
116. Lai XY, Li XT, Geng WC, Tu JC, Li JX, Qiu SL (2007) Angew Chem 119:752–755
117. Han B-H, Zhou W, SayariJ A (2003) Am Chem Soc 125:3444–3445
118. Tyagi D, Scholz K, Varma S, Bhattacharya K, Mali S, Patil PS, Bharadwaj SR (2012) Int J Hydrogen Energy 37:3602–3611
119. Deng X, Chen K, TüysüzChem H (2017) Mat 29:40–52
120. Ren Y, Ma Z, Bruce PG (2012) Chem Soc Rev 41:4909–4927
121. Davis ME (2002) Nature 417:813–821
122. Taguchi A, Schüth F (2005) Microporous Mesoporous Mater 77:1–45
123. Polarz S, Antonietti M (2002) Chem Comm 22:2593–2604
124. Lepoutre S, Julián-López B, Sanchez C, Amenitsch H, Linden M, Grosso D (2010) J Mater Chem 20:537−542
125. Roggenbuck J, TiemannJ M (2005) Am Chem Soc 127:1096–1097
126. Roggenbuck J, Schäfer H, Tsoncheva T, Minchev C, Hanss J, Tiemann M (2007) Microporous Mesoporous Mater 101:335–341
127. Brunauer S, Emmett P, Teller E (1938) J Am Chem Soc 60:309
128. Klobes P, Munro RG. Porosity and specific surface area measurements for solid materials. NIST Publication

Chapter 7
Synthesis of Highly Ordered Nanoporous Anodic Aluminium Oxide Templates and Template-Based Nanomaterials

S. Boominatha sellarajan and Subir Kumar Ghosh

Abstract Fabrication of ordered arrays of nanodots, nano-pillars and nanotubes require a suitable mould before-hand to mimic the pattern. Nanoporous anodic aluminium oxide (AAO) templates having pores with long-range order are ideal fabrication tool for the synthesis of such nanostructures for applications in high-end technological and biomedical devices. In this chapter, various synthetic routes for the fabrication of barrier-type oxide layer to nanoporous to ultra-nanoporous ordered AAO templates having pore dimensions of 10–50 nm with porosity 3–45% have been discussed. Depending on the type of electrolytes used, temperature and anodizing voltage, the evolution of pore diameter and cell structure have been covered in detail. Extensive discussions on the synthesis of self-ordered nanoporous AAO membrane, effect of anodization conditions on pore parameters was limited to H_2SO_4 electrolyte. Special attention was given on the synthesis strategies of fabrication of self-ordered ultra-nanoporous AAO membrane with pore sizes <20 nm. Efforts have also been made to cover the viable synthetic route for large-scale production of self-supporting porous AAO (PAAO) templates to mitigate future technological demands. Various techniques that have been adopted to synthesize various nanomaterials (nanorod, nanodot, nanotube, etc.) using PAAO template as mould and diverse applications of these nanostructures have also been covered.

Keywords Porous anodic aluminium oxide (PAAO) template · Ultra-nanoporous AAO · Hard anodization · Pulse anodization · Nanomaterials synthesis · Bio-applications

S. Boominatha sellarajan
Department of Mechanical Engineering, Indian Institute of Technology Madras, Chennai 600036, India

S. K. Ghosh (✉)
Materials Processing and Corrosion Engineering Division, Bhabha Atomic Research Centre, Mumbai 400 085, India
e-mail: sghosh@barc.gov.in

Homi Bhabha National Institute, Mumbai 400 094, India

A. K. Tyagi and R. S. Ningthoujam (eds.), *Handbook on Synthesis Strategies for Advanced Materials*, Indian Institute of Metals Series,
https://doi.org/10.1007/978-981-16-1803-1_7

7.1 Introduction

Porous anodic aluminium oxide (PAAO) membrane is unique because of its highly ordered honeycomb-like structure consisting of a close-packed array of columnar hexagonal cells/pores. Such novel structures have attracted tremendous attention to both scientific as well as a technological community because of their capability to synthesize self-sustained micrometre to nanometer dimensions materials [1–9]. Utilizing bottom-up approach, a simple PAAO template-assisted synthesis technique allows one to grow nanostructured materials such as nanowires [10, 11], nanorods [12], nanotubes [13, 14], nanodots [15–20], anti-dot arrays [18, 21–23] easily. Several porous materials have been considered as templates for synthesizing the nomaterials such as polymer track membranes [24–27], self-organized anodized nanoporous membranes of Al [1, 15, 28–39], Ti [34, 40–46], Si [47, 48], Zr [49] and Hf [50], zeolites [51, 52], porous mica [53, 54], nanoporous polymer glasses [55, 56] and other materials. Among these, polymer track and PAAO membranes are considered to be commercially viable because of ease of fabrication and tunable porous structure formation. However, the PAAO membrane is superior to the polymer membranes due to the following advantages: (i) high chemical resistance, (ii) high thermal resistance up to 1000 °C (i.e., polymer membrane can be stable up to ~200 °C), (iii) tuneable pore parameters such as diameter, interpore distances and density via electrochemical anodization process conditions and (iv) stable pore parameters during the post anodization process unlike deformation of pore sizes may occur in polymer membrane during the post-processes such as nanostructure growth, etc. Moreover, PAAO membranes are rather inexpensive and template-based synthesis of nanomaterials is rather faster in comparison to lithographic (photo, X-ray, ion-beam and interference) techniques (a top-down approach) in fabricating highly ordered nanomaterials since the later process is highly time-consuming and requires very expensive sophisticated equipment's. On the other hand, the electrochemical anodization process is a simple, cost-effective, easy to scale-up and capable of producing highly ordered long-range nanoporous structures even in the scale of centimetres. It is believed that the sensitivity of the nano-size effect on materials properties is strongly influenced by the membranes with uniform/regular cylindrical pore structures. For this reason, the commercial PAAO membranes obtained by traditional methods that exhibit a three-dimensional pore structure with a large pore size distribution, i.e., it does not have near-monodisperse pore sizes along the length, are not desirable to fabricate high-quality nanomaterials. Therefore, the optimization of process parameters to obtain PAAO membranes with monodisperse pore diameters along the length of the pores with uniform physical and chemical properties on the surface and walls of the pores is very important. Due to these reasons, the last couple of decades, extensive investigations have been done and still, the research is continuing on the synthesis of structurally advanced PAAO membranes, understanding the porous structure formation mechanism [39, 57–60], tuning the pore diameters while retaining the ordered structure [30, 32, 33, 38, 57, 61], scaling up of technology [3,

5, 61–65], etc. These PAAO membranes and template-based fabricated nanomaterials find application in technologically efficient [15] for a compact, high density and highly sensitive magnetic [10] and electronic devices [3, 8, 39, 61, 62, 64], biosensors [64], gas sensors [66], bio-filtration [67, 68] and also in photonics[69] devices.

In general, two typical methods are followed for the synthesis of PAAO membranes: (i) a pretreatment or pre-texturing techniques via imprint or electron beam lithography, optical diffraction grating, atomic force microscope scanning probe, focused ion beam and polystyrene beads followed by anodization process [15, 70–73] and (ii) two-step anodization process for the self-organized porous alumina membranes [28, 38, 73–75]. The pre-texturing processes are very expensive, time-consuming and are only responsible for controlling the initial sites of pore formation to achieve the ordered AAO membranes. However, the critical factors of controlling the growth of pores and arrangements with respect to each other are controlled by the anodization process itself, i.e., the collective anodizing parameters such as electrolyte solution, pH, concentration, temperature and applied potential or current density. Due to these constraints, the synthesis of self-ordered nanoporous AAO membrane using the self-organized two-step method has become very popular. Details of AAO template fabrication, mechanism and several parameters dependent pore structure variations, template-based several nanomaterials fabrication and their applications have been reviewed previously [4, 5, 16, 39, 62, 76–82]. However, these reviews mostly covered AAO template fabrication from three major acids such as sulfuric acid (H_2SO_4) [38, 83, 84], oxalic acid ($H_2C_2O_4$) [28, 75, 85, 86], and phosphoric acid (H_3PO_4) [28, 60, 87, 88] covering pore diameters in the range 30–500 nm. In the recent past, in addition to these three acids, several other acids have been explored to produce porous alumina templates with a wide variety of pore structures [5, 28, 75]. However, in industries, sulfuric acid has been chosen as the most common electrolyte for the synthesis of the highly ordered PAAO membranes with various structures due to its low-cost, relative ease of handling and capability to synthesize very small pore diameter [29, 32, 36, 38, 61]. This has led to the investigation of synthesis of ultra-small nanoporous($\leq$20 nm) AAO membranes and thereby fabrication of ultrafine nanoarrays which ultimately assisted to investigate the quantum confinement effect and other size-dependent properties [6, 39, 64, 65, 67, 72, 79, 80]. In this chapter, a brief summary of different strategies adopted to synthesize PAAO membranes with self-ordered pore patterns, pore formation mechanism, highly ordered ultra-small PAAO membrane formation with large porosity and template-based strategies of formation of different nanomaterials will be covered.

7.2 Anodic Aluminium Oxide (AAO)

Formation of a passive oxide layer on the metal surface is very common which is sometimes dense and tightly bound that prevents further oxidation under ambient conditions. For example, a thin oxide layer forms spontaneously on the Al surface, so-called “alumina (Al_2O_3) layer” under the service environment. This layer thickness

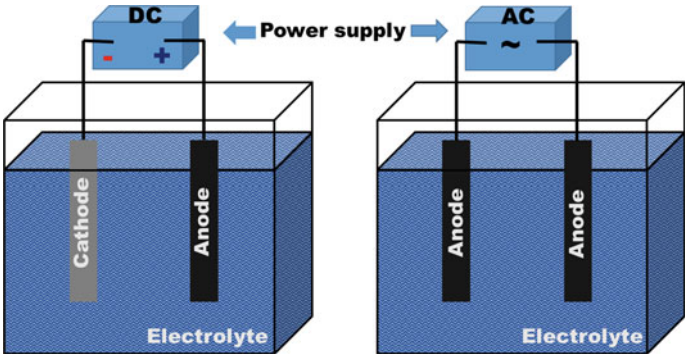

Fig. 7.1 Experimental set-up for anodizing with DC (left) and AC (right). *Source* Connected to electrodes inside the electrolyte medium

depends directly on the humidity of the air or the composition of the water/electrolyte. However, many years ago in 1857, Buff [89] realized artificial growth of compact and thick soluble porous oxide or insoluble non-porous oxide layer on Al by an anodizing process in which Al metal was oxidized by immersing in the electrolyte (e.g., acid for porous and base for nonporous layers) and connected anodically with a current source either DC or AC as shown in Fig. 7.1. In most cases, a DC source was used and oxide layers were formed due to the movement of the anions of the electrolyte to the anode in the presence of an electric field. This led to the formation of one to two-thousandths of a millimetre-thick oxide layer on Al via "anodization process" for better corrosion resistance behaviour of Al and its alloys in diverse service environments. Since then, this kind of thick anodic oxide layers on Al eventually are used as protection against corrosion and wear, dielectrics in Al capacitors, decorative purposes and the ability of colouring after incorporation of organic or metallic pigments, electrical insulation, thermal resistance, and biocompatible coatings, etc. [1, 90].

7.2.1 Types of AAO

With the progressive development of both anodic oxide layer growth on Al surface from a variety of electrolytes and with the advent of the electron microscopy, Keller and his co-workers in the year 1953 [91] first reported the formation of self-organized hexagonal nanoporous and barrier types of alumina layer attached to Al substrates in acidic medium. Later in the 1990s, Masuda et al. [92] for the first time was successful in fabricating self-sustained, highly ordered anodic aluminium oxide (AAO) membrane/template by anodization process from a simple acidic solution. With subsequent extensive research work in this field [15, 70–75, 92] led to the conclusion that during anodization process, Al tends to form two kinds of AAO

layer: (a) the nonporous or barrier-type and (b) the porous oxide layer depending upon the anodizing condition and parameters [74].

7.2.1.1 Nonporous AAO

A flat, nonporous insulating barrier oxide layer is formed, when Al is anodized in near neutral (pH > 5) or basic and non-aggressive electrolytes at ambient temperatures under high current efficiency conditions. This thin oxide layer is highly uniform in thickness and relatively compact, hard and wear-resistant and behaves as an electrical insulator; such layers are called barrier-type AAOs (named as BAAO). These layers can be grown as either amorphous or crystalline structures depending upon anodizing electrolyte used or anodization conditions [93]. Table 7.1 summarizes various anodizing electrolytes and their conditions used for the synthesis of BAAOs. Amorphous type BAAO is reported when Al is directly anodized in electrolyte solutions such as ammonium adipate [94, 95] and borate [96]. Whereas, the crystalline type of AAO is formed when the Al surface first reacts with hot water to deposit a hydrous oxide layer and subsequent anodization to deposit a barrier oxide layer under the hydrous layer [93]. The resulting amorphous BAAO layer density is reported to be 3.2 g cm^{-3} which is relatively lower in comparison to the density of crystalline

Table 7.1 Summary of anodization conditions for the non-porous barrier aluminium oxide layer

Non-acids	Concentration	pH	Anodization current density/formation voltage/electrolyte temp	References
Ammonium adipate	150 g L^{-1}	6.44	140 V, 65 °C	Oh et al. [94], Chang et al. [95]
Ammonium borate	5 wt%	–	20 A m^{-2}/300 V, 23 °C	Shimizu et al. [96]
Sodium borate	2.2 M	7	5 mA cm^{-2}	Thompson [1], Uchi et al. [93]
Sodium chromate	0.1 M	10	50 A.m^{-2}/125 V	Wood et al. [97]
Sodium hydroxide	0.01, 0.03 and 0.1 M	–	3–100 mA cm^{-2}/20–200 V	Moon et al. [98]
Sodium molybate	0.1 M	9.4	175 V	Thompson et al. [90]
Sodium phosphate	0.1 M	9.4	50 A m^{-2}/168 V	Thompson [1], Wood et al. [97]
Sodium sulphate	0.1 M	5.8	50 A m^{-2}/44 V	Wood et al. [97]
Sodium tungstate	0.1–0.00001 M	7.5	5 mA cm^{-2}/285–860 V	Thompson [1], Thompson et al. [90]

BAAO of ~3.5–3.8 g cm^{-3}. It may be noted that the density of crystalline BAAO is very close to bulk γ-alumina and is reported to have a significant fraction of void volume [90].

7.2.1.2 Porous AAO (PAAO)

Unlike BAAOs, the porous-type AAO (named as PAAO) layers are formed in acidic and aggressive electrolytes at low temperature and the growth of pore formation is rather complex. Structurally the porous alumina consists of 10–100 nm thick nonporous oxide (i.e., barrier layer) over the Al surface that forms during the initial stages of the anodization process in an acidic electrolyte. Further, with progress in anodization duration, it exhibits deep pores with diameters varying between 5 and 700 nm and lengths up to several microns. On microscopic observation, it is now clear that a very thin barrier-type oxide layer is first formed underneath each vertically grown pores on top of Al surface during anodization process, i.e., a barrier-type oxide layer is sandwiched between the pores and the Al surface. This kind of porous oxides can have highly disordered to a long-range self-organized nanoporous structure having a wide range of aspect (length/pore diameter) ratios. It is also established that irrespective of the formation of a type of AAO layer, the typical oxide growth kinetics are mainly initiated due to commensurate egress of Al^{3+} ions from the Al matrix and ingress of the O^{2-}or OH^{-} ions from electrolyte solutions into the electrolyte/oxide/metal interfaces under potentiostatic or galvanostatic anodizing conditions. It is now established that BAAO type layer formation is a prerequisite at the initial stages of PAAO growth [90], hence, we will limit our discussion on BAAO to the extent needed. However, the growth mechanisms of these two different oxide layers are quite different and are discussed below.

7.2.2 Growth Mechanism of AAO

Let us consider the case of BAAO layer growth under potentiostatic conditions. Upon switching on the cell voltage, the resultant current density (j) decreases exponentially with time (t) because of the progressive growth of insulating oxide layer thickness as shown in the schematic representation in Fig. 7.2. This *j versus t* plot dictates the oxide layer growth behaviour with time and ultimately limits the maximum BAAO layer thickness. Similarly, under galvanostatic growth of BAAO layers, the voltage across the cell is increased linearly with time, resulting in the formation of uniform and thick oxide layer. Once oxide films thicken further, rise in voltage stops and show plateau behaviour with time. At this high voltage region, the oxide thickening ceases with the occurrence of a dielectric breakdown associated with visible sparking on the anode surface. In the linear region of the voltage–time curve, the Faradic efficiency is 100% [90] and with the progress of oxide film thickness, the current efficiency decreases because of the limited supply of oxidizing ions (O^{2-} and OH^{-}). It is

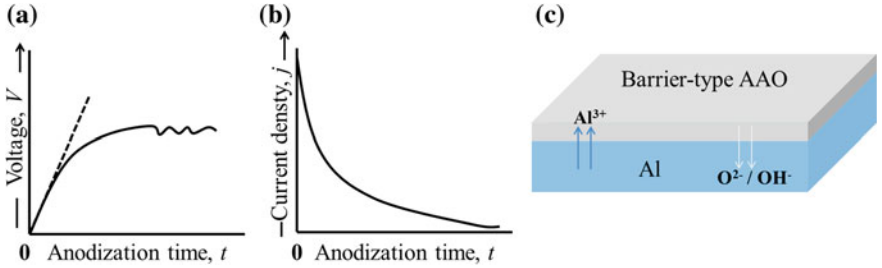

Fig. 7.2 Schematic diagram of barrier-type alumina formation in **a** galvanostatic conditions, **b** potentiostatic conditions and **c** BAAO film on Al surface. Reprinted with permission from Ref. [5]. Copyright 2014, American Chemical Society

now established that the thickness of the BAAO layer grown under potentiostatic or galvanostatic conditions, is proportional to the applied voltage or the resultant voltage attained to maintain the current density. However, in all these anodization processes, the basic mechanism of BAAO growth lies in the migration of Al^{3+} ions outwards from the aluminium/oxide (Al/O) interface and the inward motion of O^{2-} and OH^{-} ions from the oxide/electrolyte (O/E) interface [90] as shown in Fig. 7.2c. The outward migrated Al^{3+} ions get oxidised at the O/E interface [74].

Higher current efficiency in case of BAAO formation could be attributed to the contributions from oxidation at Al/O and O/E interfaces simultaneously [76]. It is to mention here that the current efficiency, greater than 60% is necessary to form BAAO type layer formation even when partial current is in the utilization of PAAO type layer formation [90]. In general, the PAAO layers are synthesized in acidic medium either by potentiostatic (Fig. 7.3a) or galvanostatic (Fig. 7.3b) conditions. A thin barrier oxide, BAAO is formed on top of the Al surface during the initial anodization process. As a result, anodizing current density demonstrates a formation of high electrical resistance via oxide growth by indicating a steep drop to a low value after the initial surge (Fig. 7.3a) and simultaneous increase of voltage (Fig. 7.3b) with time is shown in Fig. 7.3 of region "I". However, within no time, BAAO starts dissolving in the electrolyte at O/E interface, hence, decreasing the rate of fall (increase) of current density (voltage). This leads to the non-uniform dissolution of BAAO layer and causes minor cracks/flaws at O/E interface as shown in the schematic representation of Fig. 7.3 in region "II". These cracks/flaws provide an electric path, i.e., pore initiates and high current density flows which allows further oxide growth/dissolution kinetics. On the other hand, the non-uniform thickening of the BAAO layer may cause the local concentration variation of anions, i.e., a local increase in the electric field, E, at a relatively thin layer region. In region III, a steady-state pore formation is recognized, however, the descending pore density due to the superimposing of pores with the neighbouring one attributes the small reduction in the resultant current density versus time in Fig. 7.3a. Moreover, the barrier oxide layer thickness is determined by the dynamic rate balance between oxide formation (i.e., at the Al/O interface) and oxide dissolution (at O/E interface). Hereto, the oxide layer

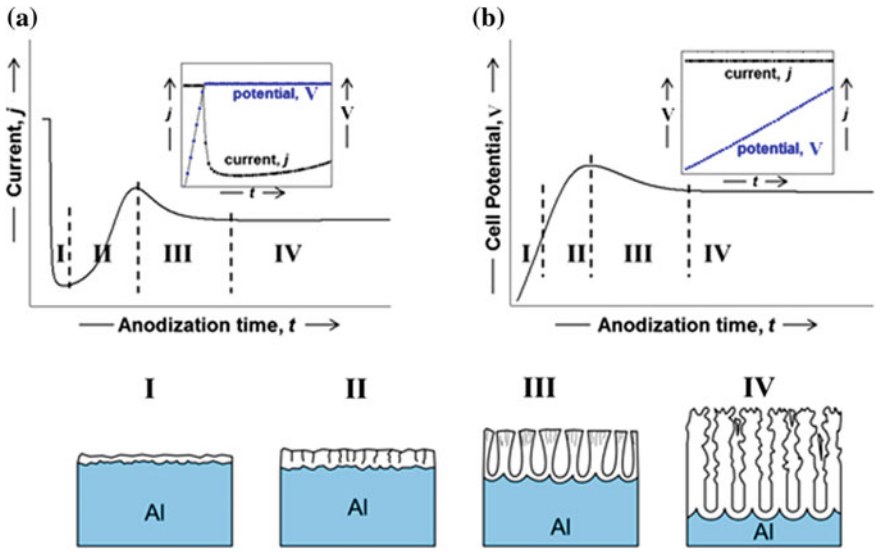

Fig. 7.3 Schematic diagram of the kinetics of porous AAO growth in **a** potentiostatic and **b** galvanostatic conditions: **a** Current (j) − time (t) curves for potentiostatic anodization (i.e., V = constant) and **b** Potential (V) − time (t) curve for galvanostatic anodization (i.e., j = constant). Inset: Represents I: formation of thin BAAO layer on Al; II: initiation of pore nucleation; III: the growth of regular pore pattern; and IV: formation of the PAAO structure on Al. Reprinted with permission from Ref. [5]. Copyright 2014, American Chemical Society

formation at the pore bottom is similar to BAAO formation assisted by the inward migration of O^{2-} and OH^{-} ions. However, the dissolution of the previously grown oxide layer at the pore base (O/E interface) is mainly governed by the applied electric field-assisted distribution of reacting ions associated with outward migration of Al^{3+} ions. This process is called field-assisted dissolution (FAD) of BAAO at the O/E interface [74] which nucleates a regular pattern of pores as can be seen in the region "III" (inset of Fig. 7.3). With further progress in time, the porous layer consisting of uniform pores grows perpendicular to the Al surface as shown in Fig. 7.3 region IV. The thickness of the porous alumina layer depends on the anodization time and the chemical reactions involved at the two interfaces for the formation of PAAO layers are written as [74]:

At the Al/O interface:

$$Al \rightarrow Al^{3+}_{(ox)} + 3e^{-} \tag{7.1}$$

$$2Al^{3+}_{(ox)} + 3O^{2-}_{(ox)} \rightarrow Al_2O_3 \tag{7.2}$$

At the O/E interface:

$$2Al^{3+}_{(ox)} + 3O^{2-}_{(ox)} \rightarrow Al_2O_3 \tag{7.3}$$

$$2H_2O_{(l)} \rightarrow O^{2-}_{(ox)} + OH^{-}_{(ox)} + H^{+}_{(aq)} \tag{7.4}$$

$$2O^{2-}_{(ox)} \rightarrow O_{2(g)} + 4e^{-} \tag{7.5}$$

$$4OH^{-}_{(ox)} \rightarrow O_{2(g)} + 2H_2O + 4e^{-} \tag{7.6}$$

$$Al_2O_3 + 6H^{+}_{(aq)} \rightarrow 2Al^{3+}_{(ox)} + 3H_2O_{(l)} \tag{7.7}$$

$$Al^{3+}_{(ox)} \rightarrow Al^{3+}_{(aq)} \tag{7.8}$$

It is now understood that the pore deepening process is determined by the steady-state equilibrium between the rate of nonporous oxide formation on Al and the rate of dissolution of aluminium oxide at discrete points. The chemical reactions Eqs. 7.2 and 7.3 correspond to the anodic oxide formation at Al/O and O/E interfaces respectively and the reaction Eq. 7.7 represents hydrogen ion-assisted previously formed oxide dissolution catalyzed by local Joule heating [5, 74, 75, 90–99] and applied potential. This FAD mechanism favours a direct ejection of Al^{3+} ions from the Al/O interface to the electrolyte through the oxide layer as described in reaction Eq. 7.8 [74]. Therefore, the net current efficiency (η_j) associated with the AAO growth is decreased by reactions Eqs. 7.5–7.8 for porous-type AAO. The current efficiency for the PAAO forming layer is ~53% [1, 90, 96] which is much lower in comparison to BAAO layer formation. This can be explained by the Pilling-Bedworth ratio (PBR) [100], i.e., the ratio of the molar volume of the grown oxide to molar volume of the consumed metal in the oxide formation process. The PBR for BAAO type layer formation is reported to be ~1.7, for the growth of highly uniform oxides on Al surface, keeping Al/O and O/E interfaces flat.

On the other hand, in the case of PAAO type layer formation, PBR ~0.9 is reported at the initial stage, and this value rises to 1.22–1.45 for highly ordered PAAO formation [74] irrespective of the electrolyte. The resultant structure becomes porous consisting of pores perpendicular to the Al surface as shown in Fig. 7.3 region IV. Based on [34] these mechanisms, the overall BAAO layer dissolution reaction at O/E interface is written as:

$$Al_2O_3 + nH_2O_{(l)} \rightarrow 2Al^{3+}_{(aq)} + (3 - n - x)O^{2-}_{(ox)} + xOH^{-}_{(ox)} + (2n - x)3H^{+}_{(aq)} \tag{7.9}$$

In the case of disordered pore formation, the rate of oxygen evolution is thought to depend on the applied voltage and dictates the pore parameters. However, the attainment of long-range regular porous structure and the control over the pore size and the cell size is determined by the anodizing parameters, such as pH, nature of the electrolyte, applied voltage or current density and bath temperature that will be discussed in the next few sections of this Chapter. The overall comparison of

Table 7.2 Comparison of BAAO and PAAO type layer formation, property and applications

Parameters/conditions	BAAO	PAAO
Electrolytes used	Near-neutral and non-aggressive	Acidic and aggressive
Maximum layer thickness under potentiostatic condition	Directly proportional to the applied potential (V)	Current density (j) (i.e., the total amount of charge) involved in the electrochemical reaction
Oxide layer growth rate	Decreases almost exponentially with time	Decreases linearly with time
Current efficiency (η_j)	Nearly 100%	Less than BAAO, typically 60%
Pilling–Bedworth Ratio	≈1.7 for the highly uniform oxide layer	<1 at the initial barrier oxide formation, which facilitates the pore initiation either by FAD or H^+ assisted at O/E interface ~1.22–1.45 for self-ordered PAAO
Layer property	Highly uniform in thickness and relatively compact	A porous structure consisting of vertically/slanting aligned pores grown on top of thin and compact BAAO layer attached to Al base
Applications	Corrosion, wear resistance in the automobile industry, etc.	Catalytic, optical and template-based nanomaterials/nanostructured fabrication and their related nanotechnology

BAAO and PAAO type layer formation, properties of AAO layers and applications are summarized in Table 7.2.

7.3 Synthesis of Self-ordered Nanoporous AAO Structure

Formation of PAAO structure followed by anodization of Al is of one kind but the size of pores and their distribution across the surface and orientation is very important for scientific investigations and device fabrication. Therefore, synthesis of AAO structure with self-ordered pore patterns with uniform pore structure is desirable unlike the staggered distribution of pores with different sizes and pattern. The properties of PAAO layers such as the oxide film thickness, porosity, other structural parameters (pore size, interpore distance) and hardness are strongly influenced by the anodization process parameters (i.e., electrolyte type and concentration, applied voltage/current density, temperature and time). Based on the film growth rate (thickness per unit time) and its hardness property, the traditional anodization process in the industry

was technically classified as mild or soft and hard anodization. Both techniques were used for obtaining the PAAO layer on Al [89, 91, 101, 102]. These two anodization processes of Al are defined as follows:

(i) **Hard Anodization**: When Al is anodized at high current density/potential at low temperature (−1 to 10 °C) in concentrated acids yielding a porous/semi-porous, thick (10–110 μm) and harder oxide coating (hardness ~65 HRC) is called as "*hard-anodization* (HA) process" [101, 102]. The low electrolyte temperature promotes a reduction in chemical dissolution rate of the oxide layer and pore nucleation sites during surface reconstruction and the applied high current density/voltage increases the overall alumina thickness as well as the pore-wall thickness between the neighbouring pores (low porosity). This type of oxide films has been practiced as corrosion and wear-resistant coatings in manufacturing industry applications (pistons, cylinders and hydraulic gears) for several decades. It provides black plating services to military standard spec Mil-A-8625 [103]. Industrially, the HA process is superior to mild anodization due to its performance level and versatility, producing heavy and durable coatings for abrasive wear applications requiring a larger build-up.

(ii) **Mild Anodization**: AAO coatings with moderate porosity when prepared at relatively low current density/potential under high or near room temperature (≥20 °C) and mild acid contents for a long anodization time is called as "*mild-anodization* (MA) process". Typical industry-based anodization (MA) conditions are 15% H_2SO_4 at 20 °C and 12 A/sq. ft. for different anodization time based on the requirement of the alumina thickness (0.5–7 μm) [89, 104–107]. This kind of oxide coating has smaller pore-wall thickness than the HA AAO porous layer and the resultant pores are used as a base for primers, bonding agents and organic coatings for excellent colour dyeing applications.

These two processes are differentiated by the anodic layer thickness and their hardness parameters. Since the pores formed in the porous alumina membrane prepared either by classical HA or classical MA processes possess non-uniform distribution of pores along with several micro-cracks on top of the surface that are not suitable for the synthesis of nanostructures. It should be mentioned here that since decades researchers avoid chromic acid anodization due to its carcinogenic effect, i.e., the usage of Cr(VI) ions [107–109] and have not been considered here for discussion.

7.3.1 Modified Mild Anodization (MMA) Process

Mild anodization (MA) has become famous since 1953 because of PAAO structure formation due to Kellers et al. [91] revolutionary work. However, the MA process had some inherent shortcomings due to very poor reproducibility in forming long-range self-ordered pore patterns and in growing high aspect ratio channels. Later in 1995, Masuda and Fukuda pioneered an advanced "*two-step anodization technique*" more suitable for synthesizing PAAO templates with highly long-range ordered hexagonal

pore arrangements with uniform pore diameters [92]. The first step involves porous pattern formation in an electrolyte under applied potential/current density and at low temperature followed by the controlled dissolution of the AAO layer formed retaining the initial defects on the surface. In the second step, anodization is carried out under identical conditions of the first step for the growth of pores starting from the previous step defects sites to inside AAO/Al layer. Post second anodization, a suitable chemical etching reveals nice long-range self-ordered porous pattern on the surface of the AAO layer attached to Al substrate. This process is called "*modified mild anodization*" (MMA). The typical growth rate of PAAO under MMA condition is ~2–10 $\mu m\, h^{-1}$ which is rather low in comparison to conventional MA and HA processes. Furthermore, this process is also found to be simple and cost-effective to produce an ordered pore formation compared to the one fabricated by the pre-patterned texture formation on Al surface using the focused ion beam milling, scanning probe scraping, or hard SiC moulding followed by a single-step anodization process.

Self-ordering of such porous structure is normally estimated from pore parameters (a) pore size/diameter (D_P); (b) interpore spacing/periodicity (D_{int}) and or (c) the porosity ($P \sim (D_P/D_{int})^2$) values which are controlled by careful selection of the anodizing electrolyte (type and concentration) and the operating parameters (applied current density/potential, electrolyte temperature, anodization time) employed. Therefore, this self-assembled pore formation occurs only in a narrow anodizing condition, i.e., more specific to acidic electrolytes called, "*self-ordering regime*". Typically, the following acids were extensively used for the fabrication of highly ordered porous alumina membrane via two-step anodization of aluminium and typical self-ordered regimes are:

(a) Sulfuric [19–25 V; $D_{int} = 50$–65 nm at 1–3 °C]
(b) Oxalic [30–60 V; $D_{int} = 105$ nm at 1–15 °C]
(c) Phosphoric [195 V; $D_{int} = 500$ nm at 1 °C]

In recent years, several other inorganic/organic acids such as malonic [58], selenic [110, 111], acetylene di-carboxylic [112], glutaric [113], α-ketoglutaric [113], acetonedicarboxylic (β-ketoglutaric acid) [113], squaric [114], etidronic [115, 116], phosphonic [117] and phosphonoacetic acids [118] have also been explored to synthesize the self-ordered PAAO membranes. Among these, etidronic acid was found as one of the self-ordering electrolytes which extends the D_{int} [530–670 nm] under anodization conditions of applied potential [145–310 V] and temperature [0–60 °C] [115, 116].

Figure 7.4 shows the schematic view (a–b) and SEM images of long-range ordered porous AAO, (c) top surface, (d) cross-section view of AAO with narrow pore channels, and (e) bottom surface, respectively. Figure 7.5a, b schematically defines various pore parameters such as growth rate (R_{ox} = AAO layer thickness/anodization time), barrier layer thickness (t_b), pore wall thickness (t_w), pore diameter (D_p), interpore distance ($D_{int} = D_p + 2t_w$) for a perfect hexagonal pore arrangement. It should be mentioned here that there are other pore parameters involved in estimating the regularity and higher orderings such as porosity (P), pore density (n) which are derived from D_p and D_{int}. As mentioned earlier, the magnitude of these pore parameters

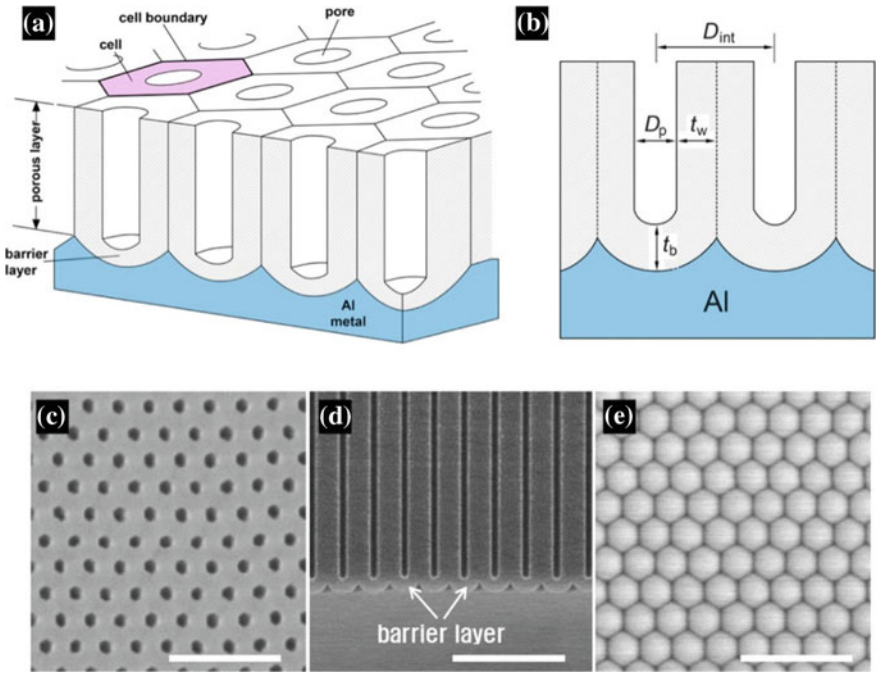

Fig. 7.4 Schematic structure of **a** porous anodic aluminium oxide (AAO) on Al foil and **b** cross-sectional view. **c**–**e** SEM images of porous AAO, showing top surface, barrier layer, and bottom surface, respectively. Scale bars are 1 μm. Reprinted with permission from Ref. [5]. Copyright 2014, American Chemical Society. Panels (c-e) were reprinted with permission from Ref. [31]. Copyright 2006 Springer Nature

is extremely influenced by the anodization conditions, such as the anodic potential/current density, nature of acid, concentration and temperature of electrolyte and the first anodization time.

Figure 7.5 shows a schematic representation of the two-step anodization process followed for the synthesis of long-range ordered PAAO membrane. For a two-step anodization process, a high purity Al (99.999%) passes through an initial anodization process under a potentiostatic or galvanostatic conditions followed by a chemical etching step (typically with 1.8 wt% chromic acid / 7.0 wt% phosphoric acid at 60 ºC) that selectively etch the freshly grown yet irregularly shape porous patterned alumina layer without damaging the Al substrate, ensuring a hexagonally ordered and textured surface obtained for a 2nd anodization process. This textured surface is acting as nucleation sites for the pore growth positions during the 2nd anodization process since pore nucleation favourably occurs at these defect sites. Generally, the 2nd anodization process is carried out under identical conditions similar to the first anodization process. The final thickness /required pore-channel length of the AAO membrane could be achieved by suitably controlling the 2nd anodization process duration. It should be mentioned here that the pore parameters are strongly influenced

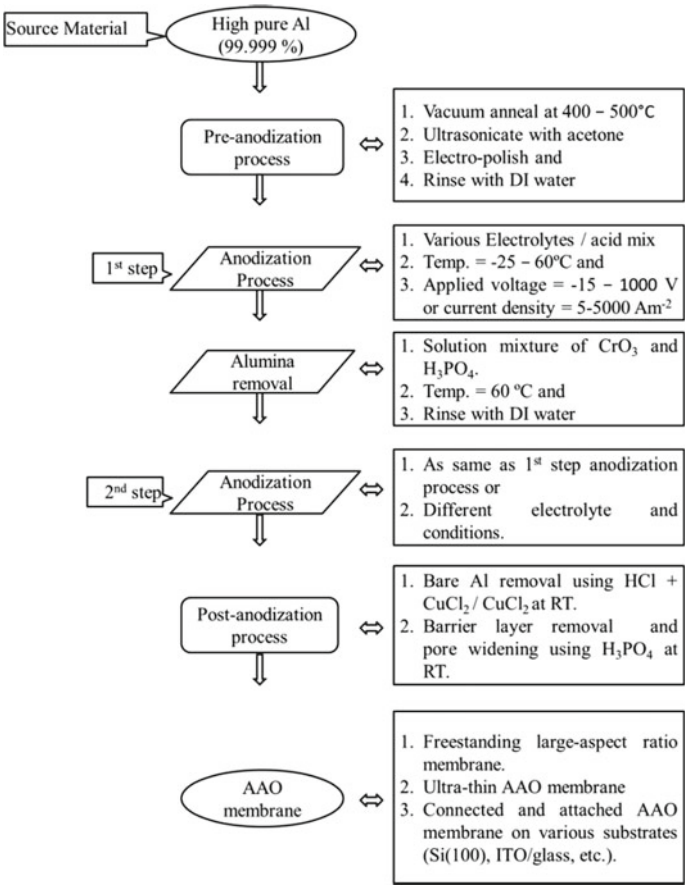

Fig. 7.5 Schematic representation of the preparation steps of PAAOs by using a two-step anodization process

by the applied potential/current density and electrolyte temperature. However, the pore size can further be adjustable by post-anodization processing while immersing the AAO membrane in dilute phosphoric acid at room temperature without changing its interpore distance (D_{int}). Based upon the thickness and substrate used for the AAO membrane, further, it is classified as free-standing or ultra-thin alumina membrane and connected/attached alumina membrane, as mentioned in Fig. 7.5. The fabrication of PAAO membranes with a long-range self-ordered nanoporous structure and high pore regularity depends on the following factors such as:

(i) Sample purity, i.e., typically Al of 99.999% whereas aluminium alloys are used for industrial MA and HA processes for automobile and other applications. It should be mentioned here that the alloying element causes different dissolution rates and diverge the oxide formation mechanism which causes non-uniform

pore formation and micro-cracks. Therefore, it is necessary to use high purity Al for long-range ordered PAAO fabrication for nanotechnology applications.

(ii) Pretreatment processes such as annealing and electropolishing/NaOH etching of Al, which helps to reduce the mechanical stress and grain growth for long-range ordering and to generate a smoother surface with small etch pits which act as pore nucleation sites, respectively, and

(iii) A very longer first anodization duration (~5–48 h) leads to achieving a larger domain size with uniform pore distribution at the pore bottom due to the coalescence of neighbouring smaller pores and reduces the final pore density (~10^{10}–10^{12} cm^{-2}).

In the next few Sections, as a case study, the self-ordered PAAOs formation in H_2SO_4 electrolyte under different anodizing parametric conditions is discussed to demonstrate mechanistic aspects of controlling pore parameters to obtain a self-ordered regime zone. It is the H_2SO_4 electrolyte that is reported so far PAAO structure with the smallest pore sizes [32, 36, 61, 119] among all the acids considered for synthesizing self-ordered porous pattern.

7.3.2 Synthesis of Self-ordered PAAOs with Small Pore Sizes

It is now understood that there are two important anodizing parameters that govern predominantly the pore parameters while self-ordered pore formation in AAO membranes. These are anodizing potential and electrolyte temperature. Therefore, a special emphasis is given here on the anodization conditions as a function of anodization potential as well as electrolyte temperature for synthesizing self-ordered small and ultra-small PAAOs via two-step anodization of Al in H_2SO_4 based electrolytes.

A simple two-step anodization procedure was employed on Al (99.99%) to obtain a self-organized PAAO membrane in 0.3 M H_2SO_4 electrolyte. The spatial features of pore ordering and hexagonal arrangements of the AAO membranes are intensively characterized by 2D or 3D Fast Fourier Transform (FFT) of the FESEM images of top-surface PAAO membranes/attached oxide layer. It converts the FESEM surface images to the resultant lattice points obtained for the structural periodicity in the inverse space. The FFT images are produced using the image processing software WSxM (http://www.wsxm.es) [120]. The FFT patterns such as disc, ring and six-distinct points (six-fold symmetry) strongly depend on the arrangements of pore periodicity/pore regularity, i.e., pore distribution across the plane of the PAAO layers. The resultant FFT pattern signifies about the pore arrangements and shapes in XY-plane as:

(a) Disc shape FFT pattern corresponds to a disordered pore structure (both size and periodicity)

(b) Ring shape FFT pattern represents ordered periodicity with non-uniform pore size, and

(c) Six distinct points or six-fold symmetry FFT pattern indicates the highly ordered arrangements of pores.

Therefore, the top surface FESEM images of PAAOs for a selected area (~1.16 μm^2) and its 3D-FFT images are considered here for the discussion to elucidate the influence of anodization potential and electrolyte temperature on the regularity of self-ordered pore formation. Moreover, the estimated average pore size and the interpore distance values are also discussed in the below Sects. 3.3 and 3.4.

7.3.3 *Effect of Anodizing Potential on Pore Regularity*

The top surface morphology of PAAO membranes fabricated under second anodization at three different anodization potentials (15, 19 and 25 V) at a constant electrolyte temperature (3 °C) is shown on the left side of Fig. 7.6. The corresponding 3D-FFT plot is also shown on the right side of the figure for the quantitative analysis on pore regularity and/or pore ordering of PAAOs. It is evident that with an increase in anodizing potential (15–25 V), the pore ordering is significantly improved from the irregular pore formation to an ordered hexagonal array as evident by the FFT pattern transition from the ring shape to the hexagon. Here, the ring structure signifies for

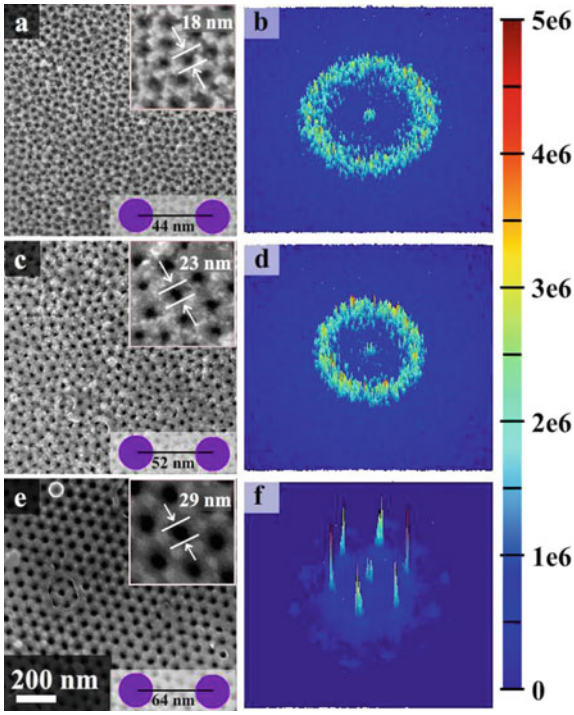

Fig. 7.6 FESEM micrographs and 3D FFT images of AAO thin membranes prepared at 3 °C for voltages of **a**, **b** 15 V, **c**, **d** 19 V and **e**, **f** 25 V. Reprinted with permission from Ref. [38]. Copyright 2016, Microporous and Mesoporous Materials

the poor ordering among pores consisting of short-range domains and non-sharp boundaries (see Fig. 7.6b, d), whereas the enhancement in the ordered domain size or the uniformity in repeating pore structure depicted by six distinct high-intensity peaks arranged in the form of a hexagon (see Fig. 7.6f), as reported by Sulka et al. [121]. This enhancement in pore ordering at higher anodization potential (e.g. 25 V) could be attributed by the improved interpore spacing, which further reduces the net pore density. This is evidenced by the reduced ring diameter of the FFT images with an increase in anodization potential as shown in Fig. 7.6, i.e., the interpore distance between two neighbouring nanopores is inversely proportional to the ring diameter [38, 59, 61, 121]. The estimated average pore size (D_p) and interface pore spacings (D_{int}) from FESEM image analysis are depicted in Fig. 7.6 as 18 nm (44 nm), 23 nm (52 nm) and 29 nm (64 nm) for three different anodizing potentials (15, 19 and 25 V), respectively [38]. This study clarifies that the pore ordering highly depends on the applied anodization potential at constant electrolyte temperature and the best pore regularity was obtained at 25 V in 0.3 M H_2SO_4 medium at 3 °C.

7.3.4 Effect of Anodizing Temperature on Pore Regularity

The pore-ordering as a function of electrolyte temperature (1–15 °C) while keeping the anodization potential at 25 V constant was studied in detail in 0.3 M H_2SO_4 electrolyte [38]. Top-view FESEM images of PAAO membranes prepared at different electrolyte temperatures along with corresponding 3D-FFT images are shown in Fig. 7.7. It is well known that the electrolyte temperature directly influences the diffusion of ionic species such as (Al^{3+} or O^{2-}/OH^- or $SO_4{}^{2-}$). This leads to relatively increase in current density due to enhanced dissolution of the oxide layer at a constant applied potential. Ultimately it contributes to the enhanced oxide growth rate as well as oxide dissolution at the pore wall edges at the top AAO surfaces as indicated by an arrow in Fig. 7.7i and corroborated with the previous reports by Aerts et al. [122, 123]. As a result, the pore sizes were enhanced without affecting the interpore distances. Moreover, the hexagonal symmetry which represents the domain size of self-ordered hexagonal arranged pores was noticed to effectively increase till 3 °C and then deteriorated with further increase in temperature due to enhanced etching rate [38]. In general, the size of the ordered domain in PAAO should follow an empirical relation with time as described by a formula, $R = Bt^n$, where R is the radius of the domain, B is a temperature-dependent parameter and n ranges between 0.5 and 0.4. However, Almasi et al. [124] reported an increase in domain size as a linear function of bath temperature for temperature below 17 °C whereas it drastically reduced for temperature above 20 °C. This kind of non-linear behaviour in the domain size may occur due to different oxide growth rates at different temperatures at a constant potential.

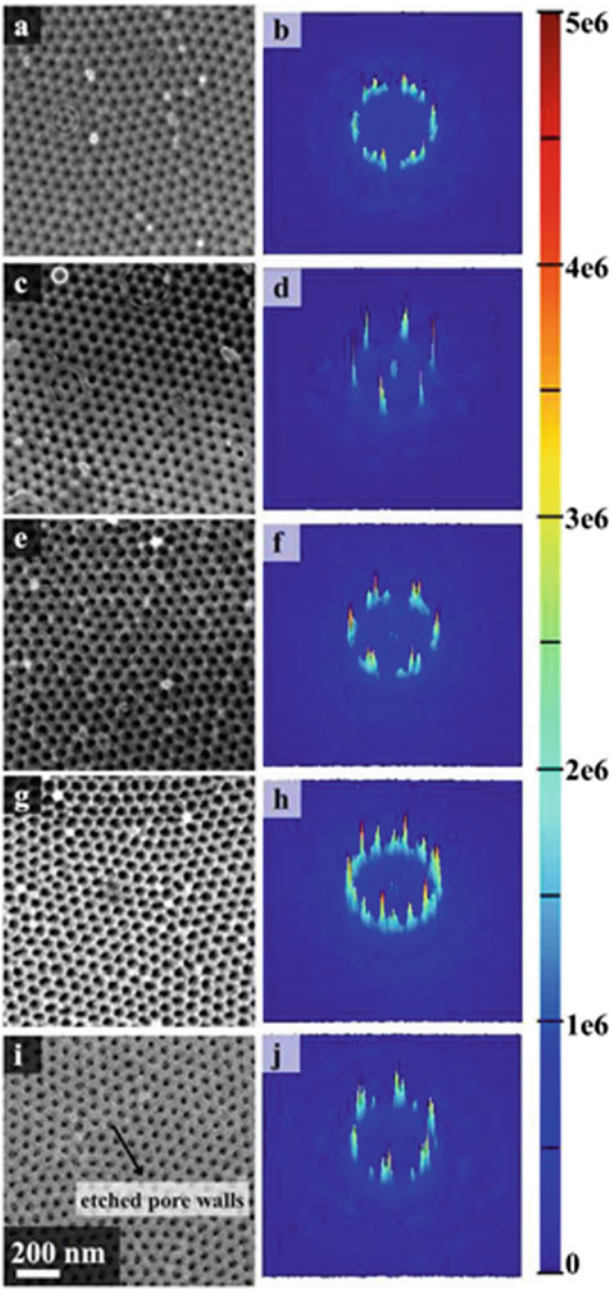

Fig. 7.7 FESEM micrographs and 3D FFT images of AAO thin membranes prepared at 25 V for bath temperatures of **a**, **b** 1, **c**, **d** 3, **e**, **f** 7, **g**, **h** 10 and **i**, **j** 15 °C. Reprinted with permission from Ref. [38]. Copyright 2016, Microporous and Mesoporous Materials

7.3.5 *Pore Diameter, Inter-Pore Distance and Growth Kinetics*

Figure 7.8a, b show the average interpore distance and pore diameter estimated from two-step anodization process of Al as a function of electrolyte temperature at a constant anodization potential in 0.3 M H_2SO_4 [38]. At constant potential, the following observations were made; (i) the interpore distance does not vary much with temperature, however, (ii) the temperature assisted oxide dissolution significantly etches out the inner wall of the pores thereby increases the pore diameter. It is well known that the pore parameters in AAO membranes are strongly dependent on the applied potential as supported by the literature data [74]. Similarly, the estimated interpore distance values were found to be increased from 42 ± 3 nm to 64 ± 3 nm with an increase in the anodization voltage from 15 to 25 V at a given temperature could be attributed to variation in diffusion layer thickness at the Al/E interface [86]. It is well known that the diffusivity and reactivity of ions in solution increase with the rise in temperature and this ultimately enhances the chemical dissolution of Al_2O_3 film on Al. This enhanced dissolution, therefore, etches out preferentially the larger surface area inner wall of the pores in comparison to limited surface area pore base. In addition to the electrolyte temperature, the pore diameter also increases with increase in anodizing voltage. Hence, an enlargement in pore diameter with the rise in temperature followed by a saturation tendency at a higher temperature was noticed (as shown in Fig. 7.8b) in contrast to the previous literature [123] which reported a monotonous increase of pore diameter with temperature. It is now inferred that the pore nucleation pattern on the Al surface is essentially dictated by the applied potential and the combined effect of potential and temperature facilitates unidirectional pore propagation along the Al base via dissolution. Therefore, the self-ordered nanoporous domain structure is a resultant influence of the composition of the electrolyte, anodizing potential and temperature. Moreover, the net current

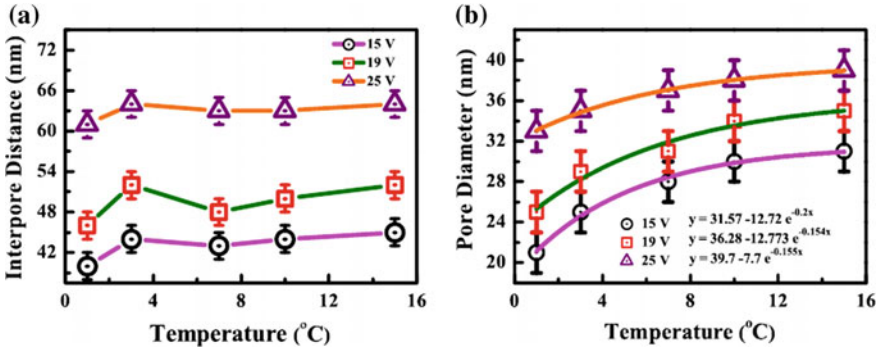

Fig. 7.8 Variation of pore parameters of AAO membrane as a function of electrolyte temperature: **a** inter-pore distance and **b** pore diameter when the voltage is constant at 15, 19 and 25 V, respectively. Reprinted with permission from Ref. [38]. Copyright 2016, Microporous and Mesoporous Materials

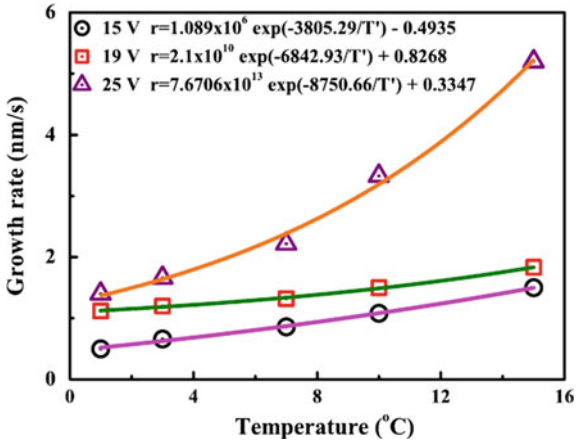

Fig. 7.9 The variation of growth rate as a function of temperature for anodizing potentials of 15, 19 and 25 V. Reprinted with permission from Ref. [38]. Copyright 2016, Microporous and Mesoporous Materials

density/high electric field strength at the pore bottom [30, 125, 126] can also impact on the pore growth kinetics or the oxide layer thickness, hence the pore regularity could be controlled.

For detailed analysis, the steady-state current density data during constant potential anodization was considered to correlate with the oxide growth rate, R_{ox} (nm/s). A 3D surface profilometer was extensively used to measure the oxide layer thickness for the given anodization time. Figure 7.9 shows the exponential nature of the AAO membranes growth rate with electrolyte temperature at different voltages [38]. It becomes more prominent at 25 V due to greater influence in growth kinetics. On the other hand, the electrolyte temperature alone has a noteworthy influence on the pore growth rate apart from the kind of electrolyte and anodizing potential due to increased oxide dissolution at the pore bottom as well as the pore edges. This not only increases the pore diameter but also increases the pore lengthening. As a result, at a higher temperature, the overall thickness of AAO membranes increases. A modified Arrhenius equation [127, 128] was used to fit the experimental growth rate data and temperature (Fig. 7.12) as

$$R_{ox} = A \cdot \exp^{-E_a/RT'} + c \tag{7.10}$$

where E_a is the activation energy, R is the gas constant (8.314 J/mol K), T' (=T + 273.15) is the bath temperature in K, c is a constant and A is a field dependent coefficient. In 0.3 M H_2SO_4 medium, for the given applied potentials 15, 19 and 25 V, the E_a values calculated are 31.6, 56.9 and 72.8 kJ/mol, respectively [38], which corroborates nicely with Han and Shen [87] results reported earlier in H_3PO_4 medium. Due to difference in electrolyte type and the voltage applied, a slight difference in activation energy values could be noticed.

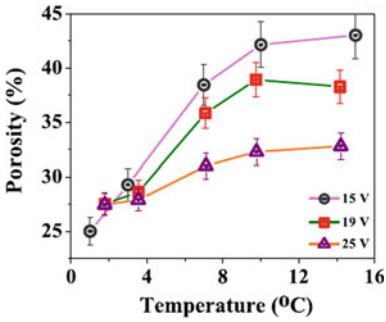

Fig. 7.10 Variation of porosity of ordered AAO membranes in the temperature range 1–15 °C for anodizing potentials 15, 19 and 25 V. Reprinted with permission from Ref. [38]. Copyright 2016, Microporous and Mesoporous Materials

7.3.6 Porosity

Porosity (P) of the porous structure is an important characteristic parameter that defines the pore density and it is estimated from primary pore parameters such as D_p and D_{int}($P \propto (D_p/D_{int})^2$). Figure 7.10 shows the variation of porosity as a function of electrolyte temperature at different anodizing potentials. It is noticed that irrespective of the anodization potential, the porosity is found to be nearly constant ~28% for anodizing temperature up to 3 °C. However, with an increase in temperature, the porosity increased from 28 to 45% at 15 V, 26–41% at 19 V and 26–33% at 25 V, respectively [38]. The porosity values were saturated at higher anodizing temperatures due to temperature-assisted oxide dissolution at the pore walls without affecting the interpore distances at a constant potential, as discussed earlier [30]. On the other hand, interesting results obtained that the porosity values were found to be decreased with the increase in applied potential from 15 to 25 V for a given temperature. This could be explained by the significant effect on pore parameters (i.e., interpore distance and pore size) which are strongly influenced by the applied voltage than the electrolyte temperature. This particular effect is more prominent in the calculated higher porosity value of PAAO membranes fabricated at lower anodizing potentials 15 and 19 V in comparison to 25 V at elevated temperatures. It is worth mentioning that Nielsch et al. [28] proposed 10% porosity (P) is a pre-requisite for obtaining self-ordering in pore patterns regardless of the specific anodizing conditions and pore diameter is mainly governed by the applied voltage. On the contrary, several subsequent investigations reported self-ordering of pores can occur in a wide range of the porosity values from 8 to 45% [61] depending upon anodizing conditions [30] corroborating present data.

7.3.7 Modified Hard Anodization (MHA) Process

During HA process, it is very difficult to maintain a stable anodization condition above the breakdown or burning of alumina potential (i.e., 27 V for sulfuric acid)

due to unwarranted corrosive attack associated with other side reactions under a high electric field. As a result, non-uniform or irregular porous alumina films are formed without long-range order for nanotechnology applications. Moreover, this kind of PAAO layers exhibit poor mechanical strength due to incorporation of the high density of cracks and structural defects which makes them difficult to handle. To overcome these difficulties, Lee and other group [5, 30, 31, 125, 129–131] have developed a modified HA (MHA) process in various electrolytes and successfully synthesized stable PAAO layers for real-life applications. It is noted that unlike conventional HA process (10-90 V for sulfuric acid), the MHA process differs substantially in applied voltages (40-70 V for sulfuric, 120-160 V for oxalic and 195-210 V for phosphoric acids) and oxide film structures [5, 31, 129]. Conventional HA process provides a compact, thick and locally bulged surface with several cracks consisting of non-uniformed pores of porous alumina coating [101, 102] contrary to MHA process which avoids burning effect by adopting several strategies during anodization process, as given below [30, 31, 125, 129, 130]. Moreover, the conventional HA process displays a large current density whereas the MHA process shows a nearly exponential decay in current density in current-voltage transient behaviour that could be attributed to a combination of both ionic and electronic current density in the latter case. There are of course a few advantages and disadvantages of the MHA process in forming porous AAO structures:

Advantages:

(i) Very high growth rate (~50–100 $\mu m\ h^{-1}$) [5, 31, 129] unlike MMA process (~2–5 $\mu m\ h^{-1}$) [5, 38, 75, 132].
(ii) Self-ordered porous AAO structure with thick oxide wall thickness.

Disadvantages:

(i) Due to very high applied potential, a large amount of localized Joule heat generates and makes the dissolution process extremely faster. The typical Joule heating is ~2–4 orders of MMA processes that stimulate hasty dissolution of the oxide layer at the pore bottom (O/E interface) causing uneven stress development leading to the local breakdown of the alumina layer.
(ii) Very little control over the pore parameters of the synthesized PAAO structure.
(iii) Very poor reproducibility and reliability of PAAO fabricated from a given electrolyte.

To overcome these difficulties in MHA and to make it commercially viable and faster process several methodologies were adopted:

- Aged electrolyte solution [30, 125, 131]
- Effective removal of Joule heat by using a combination of voltage ramping and cooling plate attached to Al substrate during anodization process [5, 31, 129, 130] and

- Electrolyte to act as a coolant by the addition of organic solvents such as ethanol, ethylene glycol that lowers the freezing point of the electrolyte, hence effectively removes the localized Joule heat generated during the anodization process [5, 36, 69, 118, 119].

Even after adopting all these techniques, the local burning effect or the oxide dissolution rate at the harsh MHA conditions was not fully solved. Further to that, a thin (~300 nm) protective alumina layer was formed before the MHA process using a different MMA process. This effectively prevented the anode from electrochemical dissolution at the harsh MHA process which exhibited good reproducibility and reliability [5, 31, 129, 130]. On solving a local heating problem during MHA, the PAAO layer with a non-uniform porous structure containing bulged surface transforms into a long-range self-ordered porous structure with a uniform pattern and high mechanical strength layer. Note that its overall density and hardness reduce substantially in comparison to BAAO layer formed during conventional HA process [101, 102]. Lee et al. [5, 31, 129, 130] has succeeded in the formation of highly ordered PAAO membranes with a very high growth rate (~50–100 $\mu m\ h^{-1}$) using MHA process.

Several researchers [5, 30, 31, 122, 125, 129–131] have made considerable efforts to utilize MHA technique for the synthesis of the new self-ordering regime to obtain a wide-range of Dint. The resultant alumina layers provided stable and well-ordered pore structures with relatively larger Dint values under different operating regimes. Lee et al. [5] have recently summarized these self-ordering voltages for the fabrication of PAAOs and their corresponding interpore distance under MMA and MHA conditions in three major electrolytes, such asH_2SO_4, $C_2H_2O_4$ and H_3PO_4, as shown in Fig. 7.11. This indicates that the applied voltage in MHA processes is higher than the MMA processes, hence the former results in higher pore growth rate (~50 $\mu m\ h^{-1}$) in comparison to MMA (2–6 $\mu m\ h^{-1}$) processes for the same electrolyte. Apart from this, the MHA process significantly increases the interpore distances without disturbing the pore diameter. As a result, the overall porosity value is found to be reduced to ~3.3% [5, 31, 129, 130]. It should be mentioned here that similar to MMA process, the pore parameters such as pore diameter, interpore distances, barrier layer thickness are highly dependent upon the anodization voltage, V. In Table 7.3, the relevant pore parameters obtained under MMA and MHA anodization conditions are compared

7.3.8 Synthesis of Self-ordered PAAO Nanostructure by Pulse Anodization (PA)

Self-ordered PAAOs formed by anodization of Al become a popular template system in the development of functional nanostructures. As discussed earlier, two main groups of anodization of Al are; modified mild anodization (MMA) and modified hard anodization (MHA) and then the combined effect of MMA-MHA promotes a new sub-group, called "*pulse anodization*" (PA). It is now clear that the MMA

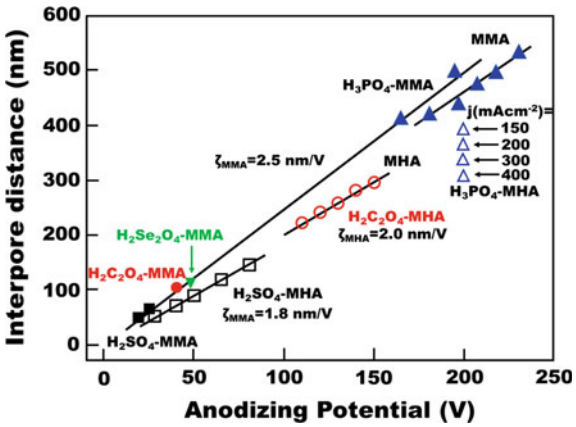

Fig. 7.11 Self-ordering regimes in MMA (filled symbols) and MHA (open symbols) by using H_2SO_4 (black symbols), $H_2C_2O_4$ (red symbols), H_2SeO_4 (green symbol), and H_3PO_4 (blue symbols). The black solid lines represent the linear regressions of the data with correlation parameters of $\zeta_{MMA} = 2.5$ nm V^{-1} and $\zeta_{MHA} = 1.8$–2.0 nm V^{-1}. Data for H_3PO_4-MHA (△) show current density (j) dependence of the interpore distance (D_{int}) at a fixed anodizing potential (195 V). Reprinted with permission from Ref. [5]. Copyright 2014, American Chemical Society

process is slow, but it produces self-ordered and uniform tubular pore structures in a narrow window of anodization conditions. Whereas, MHA process enables faster oxide growth (i.e., ~25–35 times than the MA), with a larger interpore distance and forms a new set of self-ordering anodization conditions.

Further, in the PA process, the advantages of MMA and MHA processes were combined and applied in sequential order. It allows one to design the pulse sequences purposely that results in continuous tailoring of the internal pore structure as well as the composition of the anodic oxide. Multi-segmented PAAO layers can be obtained by different combinations of MHA and MMA regimes, hence, resultant PAAOs may have different pore sizes and interpore distances along the pore channels.

PAAOs with periodically modulated pore diameters along the pore length have been synthesized by applying several anodization strategies. Lee et al. [130] first could able to tailor the PAAOs pore structure using a combination of modified HA and MA processes. This study makes a new revolution in the pore structural engineering of PAAOs and called as pulse anodization (PA) process. Here, with a controlled duration of self-ordered MMA and MHA conditions, the corresponding MMA and MHA pore structures were achieved alternatively along the length of the vertical pores. For example, the fabrication of PAAOs with periodically modulated pore diameters is shown in Fig. 7.12 for anodization carried out in H_2SO_4 at MMA and MHA potentials of 25 V and 35 V, respectively. Figure 7.12a shows the schematic of a typical pulse anodization (PA) process, where the MMA and MHA conditions are applied to achieve continuously by the periodic pulses consisting of a low-applied voltage pulse ($V_{MMA} = 25$ V) followed by a high voltage pulse ($V_{MHA} = 35$ V), respectively. During PA in a given electrolyte, the pore structures were periodically

Table 7.3 Comparison of MMA and MHA processes

Conditions/Pore parameters	Modified Mild Anodization			Modified hard anodization		
Applied voltage/current density	Less than a breakdown/burning voltage			Greater than the breakdown/burning voltage		
Anodization setup	The special cooling system of the Al substrate is not required			The special cooling system of Al is required to remove local heat during HA in addition to electrolyte cooling		
Pre-treatment	Surface cleaning and no protective layer required			The thin protective oxide layer on aluminium to control the reaction heat during HA		
Oxide growth rate	Linear, below 10 μm/h			Nonlinear, 5–35 times higher than MA, 50–100 μm/h		
Barrier layer thickness	Linearly dependent on the applied potential, 1.2 nm/V			0.6–1.0 nm/V		
Pore diameter, D_p	0.9 nm/V			0.4 nm/V		
Inter-pore distance, D_{int}	2.5 nm/V			1.8–2.0 nm/V		
Porosity (P)	10–45%			~3%		
Pore density (n)	10^9–10^{12} pores/inch^2			Lesser than MA		
Self-ordering	Voltage (V)	D_p (nm)	D_{int} (nm)	Voltage (V)	D_p (nm)	D_{int} (nm)
H_2SO_4	25	6–30	65	40–70	15–30	90–140
$C_2H_2O_4$	40–45	30–60	100	120–150	49–59	220–300
H_3PO_4	195	100–300	300–500	195–235 V/150–400 mA cm^{-2}	80–140	400–550

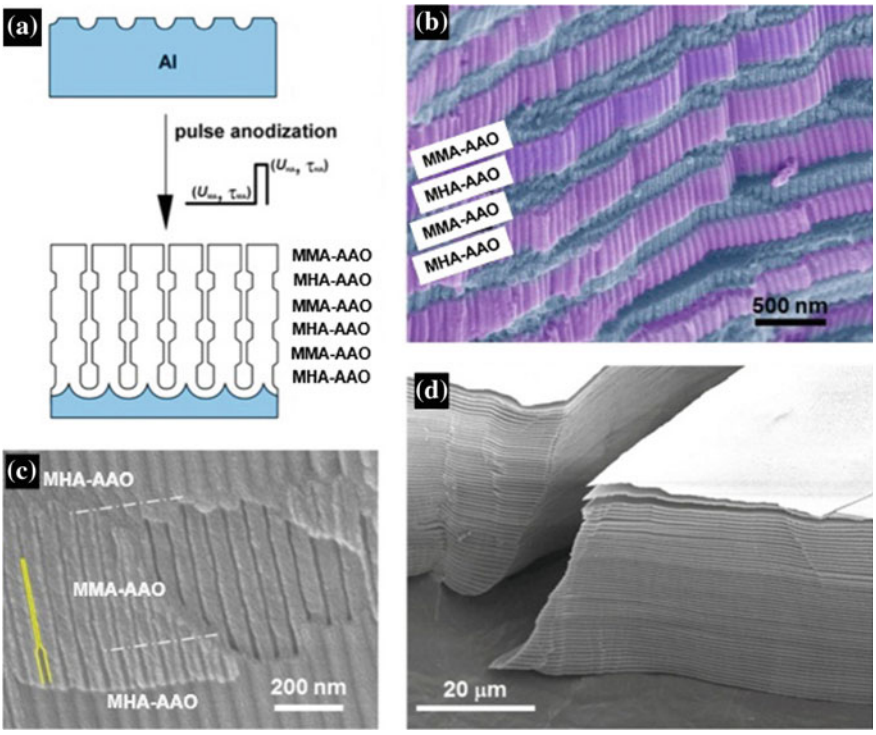

Fig. 7.12 **a** Scheme for the preparation of porous AAOs with modulated pore diameters by pulse anodization (PA). **b** False-coloured SEM image of AAO formed by H_2SO_4 PA. PAAO slabs formed by MMA and MHA pulses are indicated by MMA-AAO and MHA-AAO, respectively. **c** SEM image showing modulated pore diameter. **d** SEM image of 3D stacks of MMA-AAO slabs, obtained by selective removal of MHA-AAO slabs by chemical etching. Reproduced with permission from Ref. [130]. Copyright 2008, Springer Nature

modulated due to the variation in the current density of each MMA and MHA pulse conditions and the schematic is shown in Fig. 7.12a.

Since the current density at MMA is lower than the MHA process, a layered structure of smaller pore diameter followed by a larger pore diameter are alternatively arranged in the formed PAAOs, whereas the thickness of each anodized segment is determined by the pulse durations ($t_{MHA} = 120$ s and $t_{MHA} = 0.5$ s) as shown in Fig. 7.12b, c [130]. Apart from this, various anodization techniques have also been used to modulate the pore structures via PA process: (i) combination of two different MHA voltages [133], (ii) sequentially changing the electrolytes under same anodizing current density [60], or anodizing potential [88], etc.

Table 7.4 Summary of recent self-ordered small and ultra-small nanoporous anodic alumina membrane using H_2SO_4

Con. H_2SO_4	Additives Ethylene Glycol (wt.%)	Anodization voltage, V (V)	Electrolyte temp., T_E, (°C)	Pore diameter, D_p (nm)	Interpore distances, D_{int}(nm)	Porosity, P (%)	References
10 wt%	0	6–18	3	6.8–19.34	20.47–58.25	–	Zhang et al. [32]
0.3 M	0	15–25	1–15	22–39	42–64	24–43	Sellarajan et al. [38]
0.3 M	0	25	0–3	43–50	62–65	37–44	Syed et al. [61]
10 wt%	0–90	19	0	19–16	50	14.1–9.5	Martín et al. [36]
10 wt%	50	19	5 -15	21–12	50	17.6–5.2	Manzano et al. [119]
10 wt%	50	15–19	-15	21–25	37–47	34–27	Syed et al. [61]

7.4 Synthesis of Ultra-Small Pore Diameter PAAOs

Studies on low dimensional nanostructures have attracted to enhance the material properties due to their quantum confinement effects which are useful to explore the quantum phenomenon and integrate quantum devices [39, 134]. For most of the materials, this quantum regime could be achieved for structures below 15 nm [36, 39, 61, 64, 119]. Therefore, it is important to fabricate nanostructures within the desired range to understand and explore the confinement effect. Porous anodic alumina membrane with pore sizes less than 15 nm have been achieved in MMA conditions [36, 39, 61, 64, 119]. Several synthesis strategies have been employed to fabricate highly ordered arrangement of self-ordered ultra-small pore arrays via a simple two-step anodization process. In this context, the basic understanding of the MMA conditions concerning the pore parameters followed by the strategies employed for the ultra-small pore formation via a two-step anodization process is given below:

- The interpore spacing, (D_{int}) is exclusively controlled by the applied potential [28, 75, 132], whereas the pore size, D_p is governed by both applied potential and electric field strength (E) at the O/E growth front due to balance between oxide formation and dissolution rate [30]. This oxide layer formation-dissolution rate at the pore bottom also depends on the localized temperature resulted by the Joule heating as well as by the electrolyte temperature.
- It is reported [30] that self-ordering in PAAO membrane is improved due to change in porosity ($P \propto (D_p/D_{int})^2$) and the ratio ($D_p/D_{int}$) is a function of electric field strength (E) during anodization and maintains an inverse relationship at constant applied voltage.

- The D_p is subjected to widening process due to the solubility nature of alumina in the acidic electrolyte during anodization thereby relatively changes the film porosity without altering the interpore distances. The AAO dissolution process is found to be temperature-dependent and a dynamic process, i.e., the diffusion of reactants from the electrolyte to pore walls and vice versa.

Therefore, the velocity of the reactants or ions (v) is directly proportional to the electric field strength (E), zeta potential (ξ) and the dielectric constant (ε) of the electrolyte and maintains an inverse relationship to the viscosity coefficient (η) of the electrolyte [33] as described in the following equation in steady-state condition during the self-ordering process:

$$v = \frac{\varepsilon \xi E}{4\pi \eta} \tag{7.11}$$

According to this equation, the electric field strength (E) is inversely proportional to dielectric constant ε of the aqueous electrolyte. Hence low ε leads to higher E and hence smaller magnitude of D_p/D_{int} under a given potential. It is also clear that low ε associated with high η would lead to decrease in velocity of ions under a given anodizing condition which effectively can reduce the pore-wall widening in a self-ordered regime and results in the smaller magnitude of D_p/D_{int}. With the following new strategies, the ordered porous AAO having ultra-small pore diameters have been fabricated in MMA process utilizing altered anodizing conditions such as [36]:

- By decoupling the D_p/D_{int} ratio by applying high electric field strength (E) at the pore-bottom via reduction of dielectric constant (ε) of the electrolyte. This was obtained by the addition of a highly water-soluble organic solvent such as ethylene glycol with low dielectric constant ($\boldsymbol{\varepsilon}_{\mathbf{ethyleneglycol}} = 41.1$) than water ($\boldsymbol{\varepsilon}_{\mathbf{water}} = 72$ at 20 °C).
- By decreasing the dissolution rate through the addition of an organic solvent in the acidic medium which ultimately moderates the aggressiveness of the electrolyte, i.e., the reactivity of the O^{2-} and OH^- ions gets reduced for dissolution of pore wall [33] during anodization.
- By decreasing the anodizing temperature and voltage compared to MHA self-ordered regime so that overall PAAO growth rate gets suppressed. This is achieved by mixing of ethylene glycol in the electrolyte which ultimately decreases the freezing point of water $\leq$0 °C. Apart from this, the viscosity of the electrolyte increases with the addition of ethylene glycol that lowers the temperature thereby reducing the ionic diffusion according to Eq. (7.11).

Several attempts have been made for the fabrication of ultra-small pore diameters in PAAO membranes are summarized in Table 7.4. The PAAO membranes having ultra-small pore diameters in the range 6–19 nm and interpore distance of 20–58 nm obtained at lower anodization potential (6–18 V) in 10% H_2SO_4 electrolyte at 3 °C are shown in Fig. 7.13 [32]. It is well known that in MMA conditions, the D_p and D_{int} follow a linear relationship with applied anodization potential, (i.e., $D_p \propto V =$

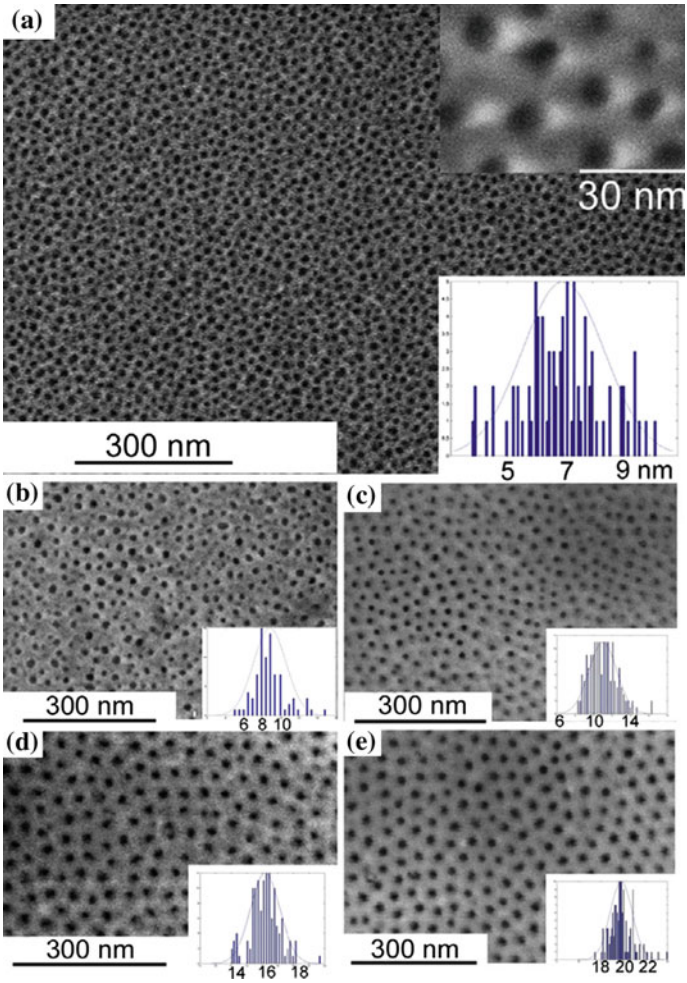

Fig. 7.13 Plane-view FESEM micrographs of the PAAO membranes. The periodic pore arrangements with pore diameters of **a** 6.8 nm, **b** 8.6 nm, **c** 11.12 nm, **d** 16.38 nm and **e** 19.34 nm are obtained under anodizing potentials of 6 V, 8 V, 12 V, 16 V and 18 V, respectively. The inset histograms show the Gaussian distributions of the pore diameters for the five samples. Two magnified figures are inset in **a** for clarity. Reprinted with permission from Ref. [32]. Copyright 1990, Nanotechnology

kV, and $D_{\text{int}} \propto V = \zeta V$) with the proportionality constants k ~ 0.9–1.25 nm V^{-1} and ζ ~ 2.5 nm V^{-1}. At lower anodization potentials (2–18 V), Zhang et al. [32] reported a similar proportionality coefficient for the pore diameter, i.e., k = 0.9666 nm V^{-1} but with slightly different coefficient for cell diameter or interpore separation, i.e., ζ = 2.97 nm V^{-1}. This particular phenomenon was attributed to the difference in pore formation mechanism in comparison to self-ordered regime obtained at high applied

potentials in MMA conditions. Here, at lower applied potential (<5 V), the barrier layer grows at a very slow rate just after pore nucleation within the first 20 s, unlike moderate high voltage MMA conditions where the barrier layer thickness grows very fast as mentioned earlier in Sect. 3.7. From Fig. 7.13, it should be mentioned here that the fabricated AAO membranes using simplest H_2SO_4 electrolyte via a two-step anodization process at low applied voltages have restricted quantitative characteristics pore parameters with a hexagonal symmetry, pore ordering and larger domain size for nanotechnology applications.

Fabrication of high-aspect ratio (i.e., length-to-diameter ratio ~3300) PAAO membranes with self-ordered ultra-small pore diameter <14 nm was successfully demonstrated by Martin et al. [36] by anodizing Al in electrolyte containing ethylene glycol (0–90wt%) in 10wt.% sulfuric acid at 19 V and 0 °C. A systematic decrease in pore diameter from 19 to 14 nm without affecting the interpore distance (~50 nm) was reported with the gradual addition of ethylene glycol into H_2SO_4 electrolyte. Thus, it led to a gradual decrease in porosity of the film from 14.1 to 7.1%. It was also demonstrated that the gradual increase of ethylene glycol into sulfuric acid decreased the pore growth linearly. As shown in Fig. 7.14a–c, an electrolyte containing 50wt% ethylene glycol shows the formation of ordered PAAO membranes having the smallest pore diameter of ~14 nm with a porosity of 7.1% after two-step anodization process. A close look into Fig. 7.14a shows the ultra-small PAAO membrane consists of poly-domain smaller ordered zones resulting a ring shape FFT image as shown in the inset of Fig. 7.14a. This study opens up a new scope for preparing ordered arrays with high-aspect ratio of one-dimensional (1D) quantum nanostructures via PAAOs that could be integrated into quantum devices.

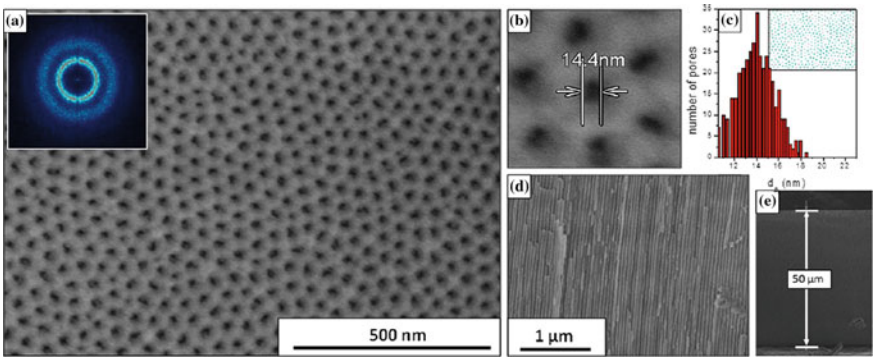

Fig. 7.14 SEM micrographs of the PAAO anodized in the presence of 50 wt % of ethylene glycol. **a** Large view where the polydomain structure can be seen (magnification: 100000×); the inset corresponds to the Fourier transform (FT) of an image taken at 50000×. **b** High-magnification SEM micrograph of the hexagonal cell from which the pore diameter has been directly measured. **c** Pore diameter distribution diagram obtained from the digitally analyzed image shown in the inset. **d** Detailed view of the cross-section where the parallel pore walls can be clearly seen. **e** The total thickness of one of the templates (~50 µm). Reprinted with permission from Ref. [36]. Copyright 2013, Chemical Society

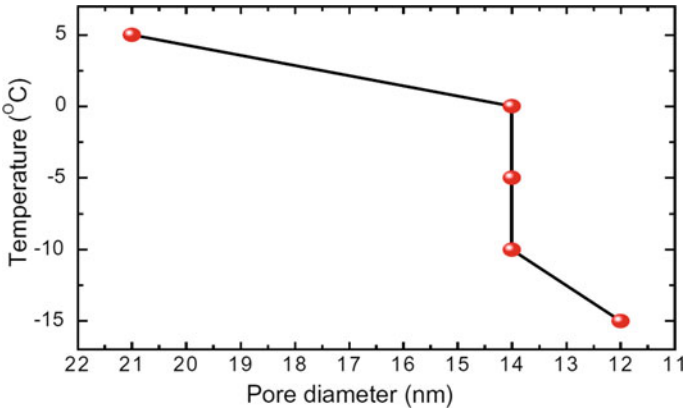

Fig. 7.15 Anodization temperature as a function of the pore diameter. The whole set anodization was performed in 50wt.% ethylene glycol containing 10wt.% H_2SO_4 electrolyte. Reprinted with permission from Ref. [119]. Copyright 2014, Microporous and Mesoporous Materials

Recently, the effect of electrolyte temperature (+15 to −15 °C) in 10% H_2SO_4 + 50% ethylene glycol electrolyte on various pore parameters was investigated by Manzano et al. [119]. The variation of pore diameter with electrolyte temperature is shown in Fig. 7.15. They obtained a high aspect ratio (>1000) ultra-small PAAO membrane with pores of 12 nm in diameter even at 19 V and −15 °C. In this study, the investigators nicely played with the electrolyte viscosity and dielectric constant. At low temperature (below freezing point of water, −15 °C), the electrolyte viscosity increases and addition of ethylene glycol (50 wt%) decrease the dielectric constant. Therefore, in effect, the diffusion rate of the ionic species decreases resulting in narrow pore formation.

Very recently, Syed et al. [61] have also demonstrated the successful fabrication of self-ordered AAO membranes at 15 and 19 V in 10% H_2SO_4 + 50% ethylene glycol at −15 °C. The FESEM images of AAOs prepared are shown in Fig. 7.16. The obtained average D_p and pore regularity parameters are in the range of 23–27 nm and ~10^8 after post anodization process using 5% H_3PO_4. It should be mentioned here that the post-anodization process includes removal of unreacted Al followed by barrier layer etching along with the widening of the pore wall using H_3PO_4. This leads to an increase in the average pore diameter without affecting the interpore distances, hence the porosity value is also increased, i.e., the obtained porosity was in the range 31–35%.

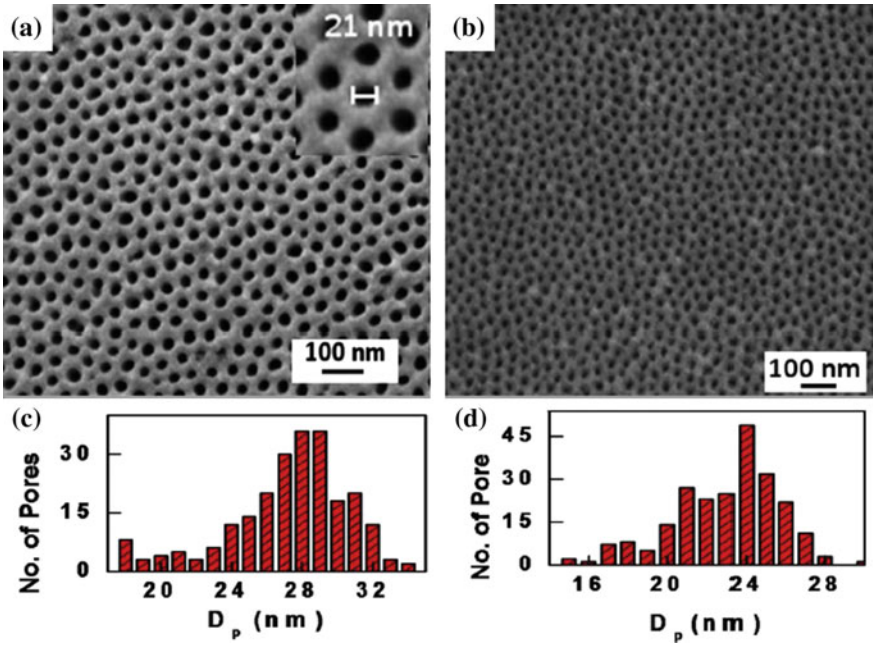

Fig. 7.16 FESEM image of PAAOs prepared in 10% H_2SO_4 + 50% glycol at − 15 °C. **a** 19 V; inset shows typical hexagonal cell pattern and **b** 15 V, respectively. **c**, **d** Pore size distribution of (**a**), and (**b**). Reprinted with permission from Ref. [61]. Copyright 2018, Microporous and Mesoporous Materials

7.5 Self Standing PAAO Membrane Formation

Previous sections have covered about the synthesis of nanoporous and ultra-nanoporous AAO structure on Al substrate by different techniques. However, for applications, the preparation of the self-supporting/free-standing AAO membranes/templates that are separated from the untreated bare Al substrate is required and the removal of the base Al layer is another challenging task. Several techniques have been attempted to detach the PAAO membrane from the bare Al such as:

- **Electrochemical Etching**: The electrochemical reduction either by exponential decay linear/gradual or step-wise decrease in applied potential/current density at the last stage of anodization process [35], which leads to thinning down the barrier layer thickness effectively without affecting the other pore parameters.
- **Dry Etching**: Selective dissolution of Al substrate chemically followed by the controlled removal of bottom side barrier oxide layer by using dry etching with the help of Ar^+ ion beam [29], BCl_3 reactive ions [135] and focused ions beams of Ga^+ [136]. This process also may not influence the pore diameter. However, the dry-etching processes are rather expansive and time-consuming.

- **Wet Chemical Etching**: Wet-chemical route using H_3PO_4 solution [137] for suitable etching of Al and the attached oxide layer is another alternative. However, the wet-chemical process might enlarge the pore size due to the pore-wall etching mechanism.

Among these techniques, wet-chemical etching is preferred and very common due to its simplicity, faster and inexpensive processes for removal of Al as well as barrier oxide layer with controllable pore size using an H_3PO_4 solution and is considered here for discussion.

Before removal of the barrier layer, the unreacted bare-Al film first dissolves using $CuCl_2$ solution as mentioned in Fig. 7.5. However, the most critical step in the fabrication of a self-sustained AAO template is the pore opening just after the removal of barrier oxide layers by a wet chemical process. As mentioned earlier, H_3PO_4 acid is used to etch the bottom cap alumina layer. This process is time-consuming and depends mainly on the etchant concentration, temperature and the uniformity of the barrier layer (locally). At first, it dissolves the oxide layer to thin down the barrier alumina from the centre of the hemisphere structure [137]. Once the pore opens up with the thin barrier layer, the migration of solution inside the pores would induce isotropic chemical etching throughout the alumina film, i.e., simultaneous etching on the inner pore walls and the exposed AAO surface kept inside the etchant bath. Therefore, the pore size could be tuned by controlling the etching rate and time in this wet-chemical process, without affecting the pore density and D_{int}. The samples used here are prepared by the self-ordered PAAO membrane at 25 V and 3 °C in H_2SO_4.

FESEM images of PAAO membranes after the removal of bare Al followed by the barrier oxide layer at different etching time, i.e., 20–30 min at room temperature are shown in Fig. 7.17. With the progressive increase in etching time, the barrier layers are seen to thin down with opening up of pores from the center of each pore on the PAAO membrane and thereby increases the pore size. At 20 min of H_3PO_4 etching time, an average pore size of 25 nm was obtained, whereas, these pore sizes were further widened with longer duration etching i.e., 35 ± 4 to 45 ± 4 nm for 25 and 30 min, respectively. At 30 min of etching time, the disintegration of the honeycomb network structure on the PAAO surface has been seen to be initiated as shown in Fig. 7.17c. This reveals that the pore walls can be fully etched by prolonging etching time, and the upper boundary limits of the etching time may vary with the pore characteristics parameter, for this case the upper boundary time is as <30 min. Therefore, the porous AAO membranes were etched for the time interval of 20–28 min to produce 25–45 $\pm$ 4 nm pore size.

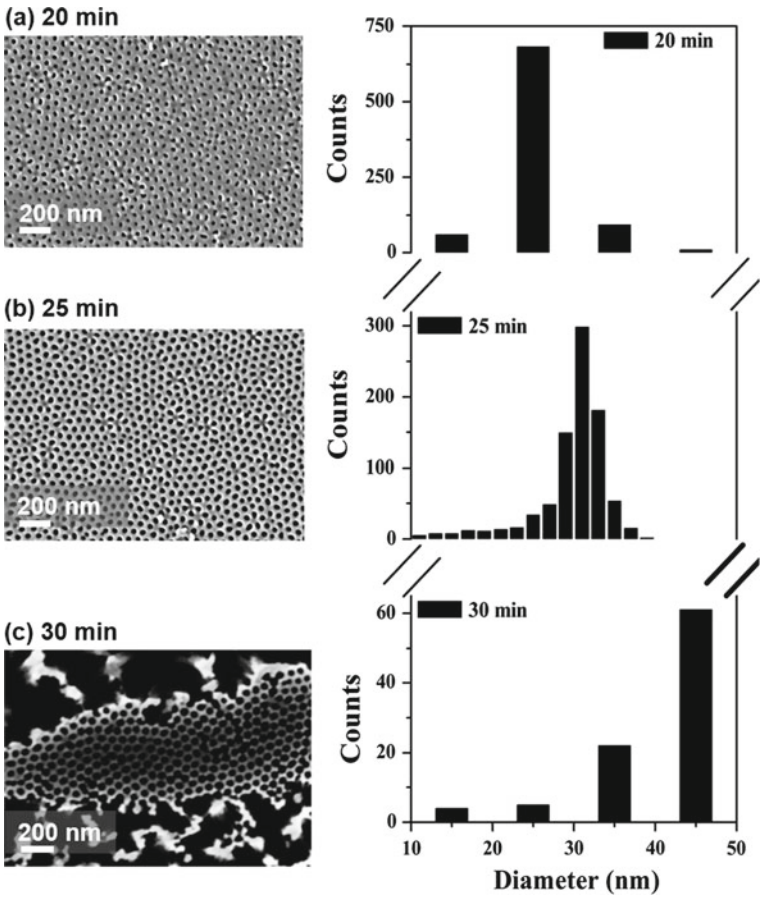

Fig. 7.17 FESEM image of AAO membranes after widening the pores in H_3PO_4 solution at RT for **a** 20, **b** 25 and **c** 30 min; images are having the scale bar of 200 nm. The corresponding pore size distribution is shown in the right column

7.6 PAAO Template Based Nanomaterials Fabrication

In this section, suitable surface modification of these synthesized PAAO templates followed by fabrication of various nanostructures (NSs) and their potential applications are discussed. In general, the functionalities and the properties of the materials differ if one or more of their dimensions are reduced between 100 and 1 nm from its bulk form (three-dimensional or 3-D). This is called the 'nanosize regime' and are classified as (i) thin films/antidot arrays (two-dimensional, or 2-D; one of the dimension is confined to nm), (ii) nanowires/nanotubes (one-dimensional, or 1-D; two of the dimensions are confined to nm) and (iii) nanoparticles/quantum dots (zero-dimensional, or 0-D; three of the dimensions are confined to nm). The existence of

nanoporous channels inside the PAAO membrane helps to act like mould to fabricate the desired dimension of nanomaterials by controlling the pore filling process. The main advantages of the PAAO template approach are:

(a) A non-lithography approach for patterning of nanoarrays via a simple and low-cost process. Pore structures are arranged parallel to each other and their size and separation can be properly adjusted by anodization conditions.
(b) Highly stable in chemical over a wide pH range (3–9) and temperature upto 1000 °C without degradation of pore parameters.
(c) High surface area (180–250 $m^2\ g^{-1}$), high pore density (10^{10}–10^{12} pores cm^{-1}); and are robust and biocompatible.
(d) Post deposition, AAO membranes can easily be dissolved selectively in an acidic or basic solution due to its amphoteric nature and helps to fabricate the free-standing highly ordered NSs for over a large area with high throughput.

Through-hole AAO membranes used for nanostructure synthesis:

(a) Synthesis of large/small-aspect ratio nanowires (rods)/nanotube (rings) arrays via chemical (liquid/gas) phase mechanism.
(b) Evaporation or sacrificial masks: synthesis of ordered nanodot and nanohole (antidot) arrays via gas-phase deposition and etching respectively.

Various materials like metals, semiconductors, polymers, carbon nanotubes, biomaterials, proteins can be grown inside the pores of porous AAO membrane either by gas phase and wet-chemical process.

Bottom-up Techniques: The pore filling of PAAO membrane is normally done by a bottom-up approach. Two important methods are normally practised to grow nanomaterials, that are classified as dry and wet processes. The dry process includes the physical vapour deposition, chemical vapour deposition, molecular beam epitaxy, pulsed laser deposition techniques, etc. It should be mentioned here that similar to lithography process, these dry processes also require sophisticated equipment to grow nanostructured materials in the gas-phase environment. Wet-chemical processes include sol–gel, hydrothermal, electroless and electrodeposition methods which are very simple, hence, used to grow nanostructures at low cost within a short period and allows one to fabricate ordered arrays of nanowires (NWs), nanotubes (NTs) and nanodots (NDs) structures [133–136, 138–140].

Figure 7.18 represents the schematic view for the scopes of PAAOs in mimicking various nanostructures: 3D (nanopore arrays), 2D (films of antidot arrays), 1D (nanowire/tubes) and 0D (nanodot arrays), and different kinds of materials and fabrication techniques used to fulfil the applications.

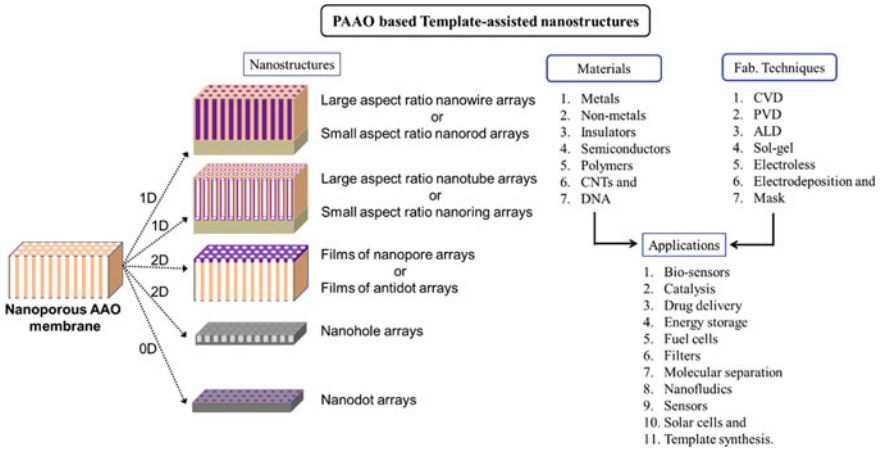

Fig. 7.18 The schematic view represents the PAAO-based template-assisted nanostructures developed for emerging nanotechnology applications

7.6.1 Fabrication of Nanomaterials

7.6.1.1 Nanorod and Nanotubes

Large aspect ratio nanowire/tube arrays were fabricated by electroless and electrodeposition processes [10–12, 133, 136, 138–140] through the channels of the porous metallized alumina membranes having variable pore diameters and the inter-pore distances. The electroless process being an autocatalytic reduction reaction helps the metal nucleation to start anywhere on the exposed surface of pore walls or pore bottom. Since the deposition starts from the pore walls and proceeds inwardly, electroless deposition often grows nanowires or nanotubes concerning deposition time. The major advantage of this method is, it does not require an electrically conductive surface or the deposited material. Hence, a large variety of materials has been grown as nanowires or nanotube arrays within the pores of the PAAO membrane [13, 14, 66, 133, 136, 138–140]. On the other hand, the electrochemical reduction of the ions of one or more metals requires a bottom electrode, which is normally obtained by metalizing one surface of PAAO membrane by PVD technique. This pore bottom metallized surface forces unidirectional growth of metals through the nanochannels of an insulating alumina membrane. Figure 7.19 shows the schematic representation of template-assisted electrodeposition for the preparation of nanowire arrays. It should be mentioned here that the unwanted electrically conducting surfaces and the chemically reactive surfaces must be masked from the electrolytes by using a suitable insulating material. Due to higher and uniform filling rate inside the nanopores of an AAO membrane, solid nanowires have been grown [10–12], however, one can tune the growth morphology either rod or tube and properties of these materials by suitably adjusting the pH, applied current density and chemical composition of the

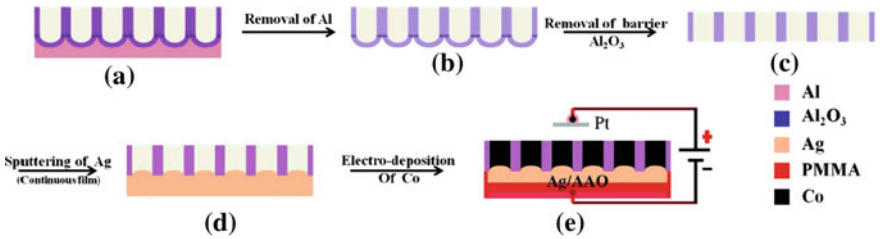

Fig. 7.19 Schematic view of the template-assisted electro-deposition process for the growth of uniform and high-aspect nanowire arrays

electrolyte [10–12]. The length of the nanorods or nanotubes can be adjusted by simply controlling deposition time.

7.6.1.2 Nanodot and Antidot Arrays

Fabrication of nanodot array requires ultrathin PAAO membranes to get rid of shadow effect while deposition. The ultra-thin alumina membrane, so-called UTAM (i.e., thickness ≤100 nm) have been fabricated via two-step anodization process which is then transferred to a variety of optically flat substrates such as mirror-polished Si suitably to obtain base support. This Si supported UTAM membrane then serves as a shadow mask for the fabrication of a highly ordered array of nanodots [16, 18, 21–23, 67] by sputtering or other physical vapour deposition technique. Using this technique, high-quality nanodot array of different materials (i.e., metallic, magnetic and semiconductor) has been fabricated [13, 15, 17–20, 65, 135]. The schematic presentation of process steps to fabricate ordered nanodot arrays via vapour phase deposition is shown in Fig. 7.20. During the deposition process, the sputtered materials are

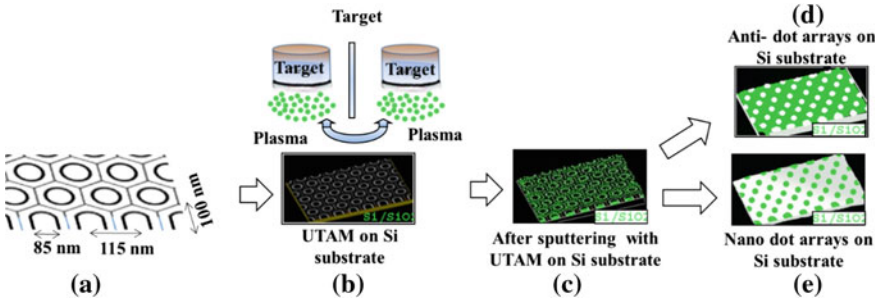

Fig. 7.20 Schematic view of synthesis of nanodots and antidot arrays on Si substrate using gas phase deposition process: **a** Highly ordered ultra-thin alumina membrane, **b** UTAM transferred on Si substrate and ready for sputter deposition process, **c** sputtered particles on UTAM/Si substrate, **d** antidot arrays formed on the top surface of the alumina membrane and **e** ordered nanodot arrays after removal of the alumina membrane on Si substrate

entered through nanopores of the mask and formed nanodot arrays on the flat base surface. At the same time, the coated materials on the top of the membrane formed an antidot array. Therefore, the ordered nanodot arrays were prepared on Si substrate after suitably dissolving the alumina membrane in NaOH solution. At the same time, the films deposited over the porous surface result in antidot nanoarray structures, as shown in Fig. 7.20d. These structures have been used to investigate the reversal magnetization process as a function of size and separation in perpendicular magnetic recording media applications (FePt, CoPt, etc.) [16, 18, 21–23, 67]. Similarly, the Si nanohole arrays have been fabricated by reactive-ion-etching while serving UTAM as etching mask/sacrificial layer, in which the bottom surface is etched through the nano-channel arrays [70, 71]. This technique replaces conventional photolithography and electrochemical etch methods.

As shown in Fig. 7.21, AAO membrane serves as the evaporation mask to prepare customized plasmonic nanoarrays such as nanodot, nanocluster, nano-island by electron beam evaporation using varying membrane surface morphology and deposition conditions [17, 19, 20, 65]. Figure 7.21a1–a8 displays the Ag and Al nano-island arrays with different sizes produced with ultrathin hexagonal PAAO membranes and their extinction spectra as a function of the quantum size effect. This reveals that the

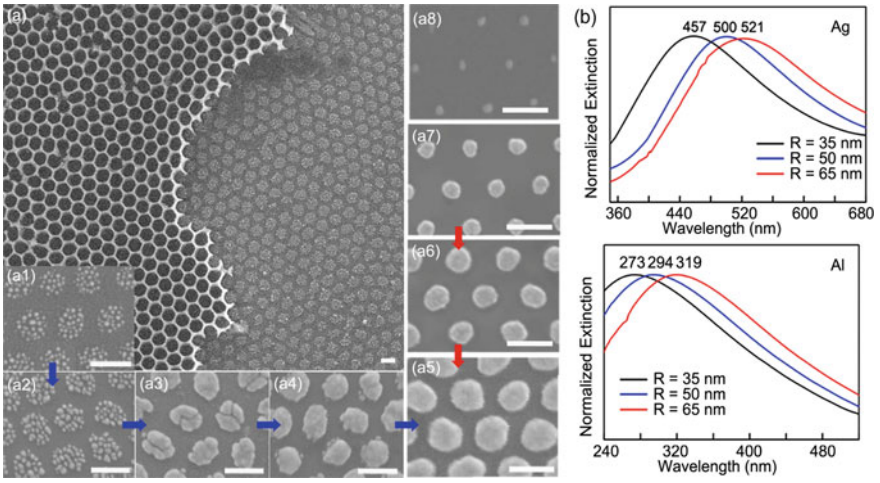

Fig. 7.21 Fabrication of plasmonic nanoarrays by adopting the AAO membranes as masks: **a** SEM images of the patterned plasmonic nanoarrays fabricated by electron evaporation utilizing ultrathin AAO as masks. The large-area SEM image exhibits the patterned silver cluster nanoarray fabricated with a ~100 nm thick AAO mask. (a1)–(a5) Evolution of the plasmonic nanoarrays during evaporation with alayer thickness of 5 nm, 10 nm, 20 nm, 40 nm, and 60 nm, respectively. (a5)–(a7) 60 nm thick metallic nano-islands fabricated by adopting the AAO masks with $d = 65$ nm, 50 nm and 35 nm, respectively. (a8) Ultra-small nanodots fabricated by partial removal of the AAO barrier layer and the etching time for the AAO mask is $t_1 = 1200$ s and $t_2 = 1400$ s. **b** UV–V is spectra of the Ag and Al plasmonic arrays from (a5)–(a7) on the quartz substrate. The scale bars in the SEM images are 100 nm. Reproduced with permission from Ref. [19]. Copyright 2017 IOP Publishing

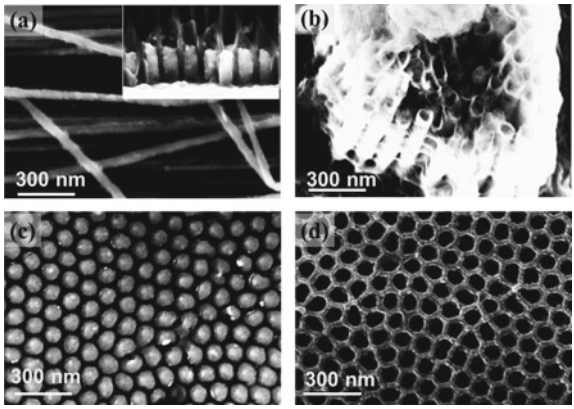

Fig. 7.22 Template assisted magnetic Co nanostructure arrays: **a** electrode posited nanowires; **b** nanotubes; **c** sputter deposited nanodots and **d** nanostructured anti-dots. Inset in **a** shows a small-aspect ratio electrodeposited nanowires embedded inside PAAOs

localized surface plasmon resonance (LSPR) can be tuned precisely by varying the nanoarrays size and distances. These nanostructures and their reduced size offer an opportunity to investigate the quantum confinement effect, i.e., surface plasmon resonance is highly sensitive. Moreover, the advantage of using these structured arrays in various applications such as imaging, sensing and catalysis as well as novel quantum devices due to the increased surface-to-volume ratio [19, 65].

Figure 7.22 shows the template-assisted growth of various Co nanostructures: (a–b) electrodeposited nanowires/nanotube arrays and (c–d) sputter deposited nanodots and antidot arrays through the pores of porous alumina membrane prepared by two-step anodization process [10–12, 17, 18, 20, 23].

7.6.2 Applications

(1) **Filtration and separation**: Freestanding PAAOs of through-hole membranes with various pore sizes have been used to separate chemical species for bio-applications [67, 68, 141].

(2) **Metal oxide nanostructures**: Atomic layer deposition techniques have been successfully employed to grow metal oxides within the pores of porous AAO, such as zinc oxide [65, 142], titanium oxide and silicon oxides [143–146]. These hybrid nanostructure oxides find potential applications in energy storage (coaxial nanowire ultra-capacitors) [9], energy conversion (photovoltaics), chemical sensing [62–64, 78, 80, 81], photocatalysis [142], photoelectrochemistry [142] and cell culture [65, 78–82, 147, 148].

(3) **Template assisted carbon-based nanostructures**: Chemical vapour deposition (CVD) process have been utilized to fabricate different carbon-based structures within the pores of the porous AAO membranes: (i) vertically aligned carbon nanotubes based alumina membrane prepared from the metal catalyst at the pore bottom of the AAO membrane via electrodeposition process

followed by CVD process [62, 149], (ii) diamond-like-carbon (a mixture of graphite and diamond phase) have been homogeneously grown over the inside pores and also outside porous AAO surface via CVD process [149] and (iii) Ultra-nanocrystalline diamond films have been demonstrated grown on the top surface of the AAO membrane by CVD process [150, 151]. These carbon-based composites have been attracted for their improved mechanical, electrical properties with the biocompatibility and chemical resistivity behaviour that can be functionalized with various chemical groups and suitably applied for numerous biomedical applications [149–151].

(4) **Functionalized PAAO Membranes**: To make the PAAO nano-channels biocompatible, suitable functionalization has been done. Such as n-heptylamine plasma polymer (HAPP) coatings have been synthesized using plasma-enhanced chemical vapour deposition process to functionalize the nanoporous channels of AAO membrane. The HAPP coatings on the AAO surface lead to subsequent functionalization of amino or other chemical groups. These functionalized AAO surfaceshave been utilized for various separation and drug delivery applications [62, 65, 149].

(5) **Biomedical applications**: Nanoporous PAAOs have found applications in implant modifications [151], cell culture substrates (neuronal, connective tissue cells, epithelial cells, muscle cells, blood cells, etc.), immune isolation and drug delivery applications in biotechnology and medicine [4, 6, 62–64, 67, 78, 80, 81, 149, 152, 153]. Recent past, Aw et al. [8] have reviewed the progress in PAAOs application based on their structural factors and biocompatibility studies.

(6) **Biosensors**: Due to the unique properties of PAAOs such as (i) the possibilities like immobilization of target molecules on nanopores and (ii) the enhanced optical properties, it plays an important role in chemical sensors and biosensors. Recently, Sriram et al. [63] and Santos et al. [154] have summarized the utilization of PAAOs as chemical and biosensors via optical (luminescence, plasmon resonance, reflectance, interferometer and scattering effect) and electrochemical (voltammetric, amperometric, impedance, capacitive, resistive and conductive effect, etc.) sensors.

(7) **Quantum Efficiency**: Hsu et al. [155] have shown recently the morphologically manipulated wavelength tunability (i.e., blue shift) and external quantum efficiency (i.e., ~2.7×10^{-2}%) in the silicon quantum dots (Si-QD) doped Si-rich SiO_x metal–oxide–semiconductor light-emitting diode (MOSLED) which was fabricated within the nanoporous PAAO membrane to spatially confine the size of silicon quantum dots (Si-QDs) embedded in silicon oxide (SiOx) during synthesis.

7.7 Summary

Synthesis strategies of fabrication of self–ordered PAAOs with nanoporous and ultra-nanoporous pore sizes with dimensions in the range of 10–50 nm have been discussed based on MMA, MHA and pulse anodization technique mainly in H_2SO_4 electrolyte. Various advantages and disadvantages of MA and HA processes have also been covered. Modified mild anodization is found to be most cost-effective for large scale production of PAAOs. The detailed mechanism of BAAO layer formation followed by field-assisted selective dissolution of the oxide layer, the formation of pore nucleation and subsequent pore growth along the oxide layer was discussed. In H_2SO_4 medium, the pore diameter is strongly dependent on anodizing voltage, temperature and but the interpore distance is strictly dependent on the applied potential. The self-ordered regime in H_2SO_4 medium is 25 V at 3 °C. Addition of low dielectric constant solvent like ethylene glycol into H_2SO_4 electrolyte led to the formation of ultra-nanoporous PAAOs with a pore diameter of ~12–15 nm at a lower anodizing temperature below the freezing point of water. Post anodization, fabrication of self-sustained PAAOs with precise pore diameters via controlled dissolution of Al and underneath BAAO layer has also been demonstrated. During this stage, one can even control over the pore size. Utilization of PAAOs and template-based fabrication of various nanomaterials by controlling synthetic processing techniques and application of these nanostructured materials were discussed.

References

1. Thompson GE (1997) Porous anodic alumina: fabrication, characterization and applications. Thin Solid Films 297(1–2):192–201
2. Corma A (1997) From microporous to mesoporous molecular sieve materials and their use in catalysis. Chem Rev 97(6):2373–2420
3. He Z, Yao L, Zheng M, Ma L, He S, Shen W (2010) Enhanced humidity sensitivity of nanoporous alumina films by controlling the concentration and type of impurity in pore wall. Phys E 43(1):366–371
4. Ingham CJ, ter Maat J, de Vos WM (2012) Where bio meets nano: The many uses for nanoporous aluminum oxide in biotechnology. Biotechnol Adv 30(5):1089–1099
5. Lee W, Park S-J (2014) Porous anodic aluminum oxide: anodization and templated synthesis of functional nanostructures. Chem Rev 114(15):7487–7556
6. Hernández-Eguía LP, Ferré-Borrull J, Macias G, Pallarès J, Marsal LF (2014) Engineering optical properties of gold-coated nanoporous anodic alumina for biosensing. Nanoscale Res Lett 9(1):414
7. Bellemare J, Carignan L-P, Sirois F, Menard D (2015) Etching the oxide barrier of micrometer-scale self-organized porous anodic alumina membranes. J Electrochem Soc 162(4):E47–E50
8. Aw MS, Bariana M, Losic D (2015) Nanoporous anodic alumina for drug delivery and biomedical applications. In: Losic D, Santos A (eds) Nanoporous alumina, 219. Springer International Publishing, Cham, pp 319–354
9. Zhao H, Liu L, Lei Y (2018) A mini review: functional nanostructuring with perfectly-ordered anodic aluminum oxide template for energy conversion and storage. Front Chem Sci Eng 12(3):481–493

10. Sellarajan B, Kulkarni PD, Krishnan M, Barshilia HC, Chowdhury P (2013) Magnetic properties of ordered bi-layer nanowire arrays with different Co crystallographic structures. Appl Phys Lett 102(12):122401
11. Kulkarni PD, Sellarajan B, Krishnan M, Barshilia HC, Chowdhury P (2013) Anisotropic magnetic properties of bi-layered structure of ordered Co nanowire array: micromagnetic simulations and experiments. J Appl Phys 114(17):173905
12. Sellarajan B, Nagaraja HS, Barshilia HC, Chowdhury P (2016) Effect of shape and magnetocrystalline anisotropies in ordered Co nanorod arrays with smaller diameter. J Magn Magn Mater 404:197–204
13. Meng G et al (2009) A general synthetic approach to interconnected nanowire/nanotube and nanotube/nanowire/nanotube heterojunctions with branched topology. Angew Chem Int Ed 48(39):7166–7170
14. Meng G, Jung YJ, Cao A, Vajtai R, Ajayan PM (2005) Controlled fabrication of hierarchically branched nanopores, nanotubes, and nanowires. PNAS 102(20):7074–7078
15. Masuda H, Yasui K, Nishio K (2000) Fabrication of ordered arrays of multiple nanodots using anodic porous alumina as an evaporation mask. Adv Mater 12(14):1031–1033
16. Lei Y, Cai W, Wilde G (2007) Highly ordered nanostructures with tunable size, shape and properties: a new way to surface nano-patterning using ultra-thin alumina masks. Prog Mater Sci 52(4):465–539
17. Chowdhury P, Sellarajan SB, Krishnan M, Barshilia HC (2012) Fabrication of magnetic nanodot arrays using ultrathin alumina membrane (UTAM). AIP Conf Proc 1447:357–358
18. Rahman MT, Shams NN, Lai C-H (2009) Nonlithographic fabrication of 25 nm magnetic nanodot arrays with perpendicular anisotropy over a large area. J Appl Phys 105(7):07C112
19. Hao Q, Huang H, Fan X, Hou X, Yin Y, Li W, Si L, Nan H, Wang H, Mei Y, Qiu T, Chu PK (2017) Facile design of ultra-thin anodic aluminum oxide membranes for the fabrication of plasmonic nanoarrays. Nanotechnology 28(10):105301
20. Sellarajan B, Saravanan P, Ghosh SK, Nagaraja HS, Barshilia HC, Chowdhury P (2018) Shape induced magnetic vortex state in hexagonal ordered cofe nanodot arrays using ultrathin alumina shadow mask. J Magn Magn Mater 451:51–56
21. Rahman MT et al (2009) Controlling magnetization reversal in Co/Pt nanostructures with perpendicular anisotropy. Appl Phys Lett 94(4):042507
22. Rahman MT, Shams NN, Wang DS, Lai C-H (2009) Enhanced exchange bias in sub-50-nm IrMn/CoFe nanostructure. Appl Phys Lett 94(8):082503
23. Rahman MT, Shams NN, Lai CH, Fidler J, Suess D (2010) Co/Pt perpendicular antidot arrays with engineered feature size and magnetic properties fabricated on anodic aluminum oxide templates. Phys Rev B 81(1):014418
24. Rao V, Amar JV, Avasthi DK, Charyulu RN (2003) Etched ion track polymer membranes for sustained drug delivery. Radiat Meas 36(1–6):585–589
25. Kravets L, Dmitriev S, Dinescu G, Lazea A, Satulu V (2009) Effect of plasma treatment on polymer track membranes. Plasma Process Polym 6(S1):S796–S802
26. Balakin AA, Buido EA, Markin MI, Novikova LI, Baldwin MA (2010) Polymer track membranes for atmospheric pressure field extraction of ions from liquid solutions. J Electrost 68(1):96–100
27. Kravets LI, Dmitriev SN, Satulu V, Mitu B, Dinescu G (2014) Structure and electrochemical properties of track membranes with a polymer layer obtained by plasma polymerization of acetylene. J Phys Conf Ser 516:012006
28. Nielsch K, Choi J, Schwirn K, Wehrspohn RB, Gösele U (2002) Self-ordering regimes of porous alumina: the 10 porosity rule. Nano Lett 2(7):677–680
29. Xu T, Zangari G, Metzger RM (2002) Periodic holes with 10 nm diameter produced by grazing Ar^+ milling of the barrier layer in hexagonally ordered nanoporous alumina. Nano Lett 2(1):37–41
30. Ono S, Saito M, Ishiguro M, Asoh H (2004) Controlling factor of self-ordering of anodic porous alumina. J Electrochem Soc 151(8):B473

31. Lee W, Ji R, Gösele U, Nielsch K (2006) Fast fabrication of long-range ordered porous alumina membranes by hard anodization. Nat Mater 5(9):741–747
32. Zhang F, Liu X, Pan C, Zhu J (2007) Nano-porous anodic aluminium oxide membranes with 6–19 nm pore diameters formed by a low-potential anodizing process. Nanotechnology 18(34):345302
33. Chen W, Wu J-S, Xia X-H (2008) Porous anodic alumina with continuously manipulated pore/cell size. ACS Nano 2(5):959–965
34. Su Z, Zhou W (2008) Formation mechanism of porous anodic aluminium and titanium oxides. Adv Mater 20(19):3663–3667
35. Chowdhury P, Sellarajan SB, Krishnan M, Raghuvaran K, Barshilia HC, Rajam KS (2012) In Situ electrochemical thinning of barrier oxide layer of porous anodic alumina template. Adv Sci Lett 5(1):253–257
36. Martín J, Manzano CV, Caballero-Calero O, Martín-González M (2013) High-aspect-ratio and highly ordered 15-nm porous alumina templates. ACS Appl Mater Interfaces 5(1):72–79
37. Kikuchi T, Nakajima D, Nishinaga O, Natsui S, Suzuki R (2015) Porous aluminum oxide formed by anodizing in various electrolyte species. Curr Nanosci 11(5):560–571
38. Sellarajan B, Sharma M, Ghosh SK, Nagaraja HS, Barshilia HC, Chowdhury P (2016) Effect of electrolyte temperature on the formation of highly ordered nanoporous alumina template. Microporous Mesoporous Mater 224:262–270
39. Sulka GD, Brzózka A, Zaraska L, Wierzbicka E, Brudzisz A (2017) AAO templates with different patterns and channel shapes. In: Bettotti P (ed) Submicron porous materials. Springer International Publishing, Cham, pp 107–156
40. Choi J, Wehrspohn RB, Lee J, Gösele U (2004) Anodization of nanoimprinted titanium: a comparison with formation of porous alumina. Electrochim Acta 49(16):2645–2652
41. Macak JM, Sirotna K, Schmuki P (2005) Self-organized porous titanium oxide prepared in Na_2SO_4/NaF electrolytes. Electrochim Acta 50(18):3679–3684
42. Raja KS, Misra M, Paramguru K (2005) Formation of self-ordered nano-tubular structure of anodic oxide layer on titanium. Electrochim Acta 51(1):154–165
43. Mohan L, Viswanathan S, Anandan C, Rajendran N (2015) Corrosion behaviour of tetrahedral amorphous carbon (Ta-C) filled titania nano tubes. RSC Adv 5(113):93131–93138
44. Mohan L, Anandan C, Rajendran N (2015a) Electrochemical behaviour and effect of heat treatment on morphology, crystalline structure of self-organized TiO_2 nanotube arrays on Ti–6Al–7Nb for biomedical applications. Mater Sci Eng C 50:394–401
45. Mohan L, Anandan C, Rajendran N (2015b) Effect of plasma nitriding on structure and biocompatibility of self-organised TiO_2 nanotubes on Ti–6Al–7Nb. RSC Adv 5(52):41763–41771
46. Mohan L, Anandan C, Rajendran N (2016) Drug release characteristics of quercetin-loaded TiO_2 nanotubes coated with chitosan. Int J Biol Macromol 93:1633–1638
47. Leïchlé T, Bourrier D (2015) Integration of lateral porous silicon membranes into planar microfluidics. Lab Chip 15(3):833–838
48. Karbassian F (2018) Porous silicon. In: Ghrib TH (ed) Porosity—Process, technologies and applications. InTech
49. Tsuchiya H, Macak JM, Ghicov A, Taveira L, Schmuki P (2005) Self-organized porous TiO_2 and ZrO_2 produced by Anodization. Corros Sci 47(12):3324–3335
50. Tsuchiya H, Schmuki P (2005) Self-organized high aspect ratio porous hafnium oxide prepared by electrochemical anodization. Electrochem Commun 7(1):49–52
51. Kusakabe K, Kuroda T, Murata A, Morooka S (1997) Formation of a Y-type zeolite membrane on a porous r-alumina tube for gas separation. Ind Eng Chem Res 36(3):649–655
52. Wenten IG, Dharmawijaya PT, Aryanti PTP, Mukti RR, Khoiruddin K (2017) LTA zeolite membranes: current progress and challenges in pervaporation. RSC Adv 7(47):29520–29539
53. Pandey K, Dwivedi MM, Sanjay SS, Asthana N (2017) Development of mica-based porous polymeric membrane and their application. Ionics 23(1):113–120
54. Jin P, Mukaibo H, Horne LP, Bishop GW, Martin CR (2010) Electroosmotic flow rectification in pyramidal-pore mica membranes. J Am Chem Soc 132(7):2118–2119

55. Müller R, Anders N, Titus J, Enke D (2013) Ultra-thin porous glass membranes—An innovative material for the immobilization of active species for optical chemosensors. Talanta 107:255–262
56. Barascu A, Kullmann J, Reinhardt B, Rainer T, Roggendorf H, Syrowatka F, Enke D (2015) Porous glass membranes with an aligned pore system via stretch forming in combination with thermally induced phase separation. Glass Phys Chem 41(1):73–80
57. Choi DH, Lee PS, Hwang W, Lee KH, Park HC (2006) Measurement of the pore sizes for anodic aluminum oxide (AAO). Curr Appl Phys 6:125–129
58. Lee W, Nielsch K, Gösele U (2007) Self-ordering behaviour of nanoporous anodic aluminum oxide (AAO) in malonic acid anodization. Nanotechnology 18(47):475713
59. Belwalkar A, Grasing E, Vangeertruyden W, Huang Z, Misiolek W (2008) Effect of processing parameters on pore structure and thickness of anodic aluminum oxide (AAO) tubular membranes. J Membr Sci 319(1–2):192–198
60. Liu S, Tang S, Zhou H, Fu C, Huang Z, Liu H, Kuang Y (2013) Fabrication of AAO films with controllable nanopore size by changing electrolytes and electrolytic parameters. J. Solid State Electrochem 17(7):1931–1938
61. Syed R, Sen D, Mani Krishna KV, Ghosh SK (2018) Fabrication of highly ordered nanoporous alumina membranes: probing microstructures by SAXS, FESEM and AFM. Microporous Mesoporous Mater 264:13–21
62. Aramesh M, Cervenka J (2014) Surface modification of porous anodic alumina for medical and biological applications. In: Nanomedicine. One Central Press (OCP), Manchester, UK, pp 439–467
63. Sriram G, Patil P, Bhat MP, Hegde RM, Ajeya KV, Udachyan I, Bhavya MB, Gatti MG, Uthappa UT, Neelgund GM, Jung H-Y, Altalhi T, Madhuprasad, Kurkuri MD (2016) Current trends in nanoporous anodized aluminaplatforms for biosensing applications. J Nanomater 1753574
64. Santos A, Balderrama VS, Alba M, Formentín P, Ferré-Borrull J, Pallarès J, Marsal LF (2012) Nanoporous anodic alumina barcodes: toward smart optical biosensors. Adv Mater 24(8):1050–1054
65. Fan X, Hao Q, Qiu T, Chu PK (2020) Improving the performance of light-emitting diodes via plasmonic-based strategies. J Appl Phys 127(4):040901
66. Sadeghian RB, Kahrizi M (2007) A novel miniature gas ionization sensor based on freestanding gold nanowires. Sens Actuators A 137(2):248–255
67. Kumeria T, Rahman MM, Santos A, Ferré-Borrull J, Marsal LF, Losic D (2014) Structural and optical nanoengineering of nanoporous anodic alumina rugate filters for real-time and label-free biosensing applications. Anal Chem 86(3):1837–1844
68. Zhang S, Wang Y, Tan Y, Zhu J, Liu K, Zhu J (2016) Anodic aluminum oxide with fine pore size control for selective and effective particulate matter filtering. Mater Res Express 3(7):074004
69. Lee HJ, Kim DN, Park S, Lee Y, Koh W-G (2011) Micropatterning of a nanoporous alumina membrane with poly(ethylene glycol) hydrogel to create cellular micropatterns on nanotopographic substrates. Acta Biomater 7(3):1281–1289
70. Masuda H, Yamada H, Satoh M, Asoh H, Nakao M, Tamamura T (1997) Highly ordered nanochannel-array architecture in anodic alumina. Appl Phys Lett 71(19):2770–2772
71. Masuda H (2005) Highly ordered nanohole arrays in anodic porous alumina. In: Ordered porous nanostructures and applications. nanostructure science and technology. Springer, Boston, MA
72. Masuda H, Abe A, Nakao M, Yokoo A, Tamamura T, Nishio K (2003) Ordered mosaic nanocomposites in anodic porous alumina. Adv Mater 15(2):161–164
73. Masuda H, Nishio K (2006) Synthesis and applications of highly ordered anodic porous alumina. In: Adachi M, Lockwood DJ (eds) Self-organized nanoscale materials. nanostructure science and technology. Springer, New York, NY
74. Li F, Zhang L, Metzger RM (1998) On the growth of highly ordered pores in anodized aluminum oxide. Chem Mater 10(9):2470–2480

75. Jessensky O, Müller F, Gösele U (1998) Self-organized formation of hexagonal pore arrays in anodic alumina. Appl Phys Lett 72(10):1173–1175
76. Zehetbauer MJ, Zhu YT (eds) (2009) Bulk nanostructured materials. Wiley-VCH, Weinheim
77. Poinern GEJ, Ali N, Fawcett D (2011) Progress in nano-engineered anodic aluminum oxide membrane development. Materials 4(3):487–526
78. Poinern GEJ, Le XT, O'Dea M, Becker T, Fawcett D (2014) Chemical synthesis, characterisation, and biocompatibility of nanometre scale porous anodic aluminium oxide membranes for use as a cell culture substrate for the vero cell line: a preliminary study. BioMed Res Int 1–10
79. Jani AMMd, Losic D, Voelcker NH (2013) Nanoporous anodic aluminium oxide: advances in surface engineering and emerging applications. Prog Mater Sci 58(5):636–704
80. Santos A, Kumeria T (2015) Nanoporous anodic alumina for optical biosensing. In: Losic D, Santos A (eds) Nanoporous Alumina, 219. Springer International Publishing, Cham, pp 219–247
81. Reddy SM (2017) Membrane technologies for sensing and biosensing. In: Cesar Paixão TRL, Reddy SM (eds) Materials for chemical sensing. Springer International Publishing, Cham, pp 75–103
82. Yen M-L, Hsiao H-M, Huang C-F, Lin Y, Shen Y-K, Tsai Y-L, Chang C-W, Yen H-J, Lu Y-J, Kuo Y-W (2017) Aluminum templates of different sizes with micro-, nano- and micro/nano-structures for cell culture. Coatings 7(11):179
83. Sulka GD, Parkoła KG (2006) Anodising potential influence on well-ordered nanostructures formed by Anodisation of aluminium in sulfuric acid. Thin Solid Films 515(1):338–345
84. Sulka GD, Parkoła KG (2007) Temperature influence on well-ordered nanopore structures grown by anodization of aluminium in sulfuric acid. Electrochim Acta 52(5):1880–1888
85. Kashi MA, Ramazani A, Rahmandoust M, Noormohammadi M (2007) The effect of PH and composition of sulfuric-oxalic acid mixture on the self-ordering configuration of high porosity alumina nanohole arrays. J Phys Appl Phys 40(15):4625–4630
86. Sulka GD, Stępniowski WJ (2009) Structural features of self-organized nanopore arrays formed by anodization of aluminum in oxalic acid at relatively high temperatures. Electrochim Acta 54(14):3683–3691
87. Han XY, Shen WZ (2011) Improved two-step anodization technique for ordered porous anodic aluminum membranes. J Electroanal Chem 655(1):56–64
88. Zaraska L, Jaskuła M, Sulka GD (2016) Porous anodic alumina layers with modulated pore diameters formed by sequential anodizing in different electrolytes. Mater Lett 171:315–318
89. Buff H (1857) Ueber das electrische Verhalten des Aluminiums. Annalen der Chemie und Pharmacie 102(3):265–284
90. Thompson GE, Skeldon P, Shimizu K, Wood GC (1995) The compositions of barrier-type anodic films formed on aluminium in molybdate and tungstate electrolytes. Philos Trans R Soc A: Math Phys Eng Sci 350(1692):143–168
91. Keller F, Hunter MS, Robinson DL (1953) Structural features of oxide coatings on aluminum. J Electrochem Soc 100(9):411
92. Masuda H, Fukuda K (1995) Ordered metal nanohole arrays made by a two-step replication of honeycomb structures of anodic alumina. Science 268:1466–1468
93. Uchi H, Kanno T, Alwitt RS (2001) Structural features of crystalline anodic alumina films. J Electrochem Soc 148(1):B17
94. Oh H-J, Park G-S, Kim J-G, Jeong Y, Chi C-S (2003) Surface roughness factor of anodic oxide layer for electrolytic capacitors. Mater Chem Phys 82(2):331–334
95. Chang J-K, Lin C-M, Liao C-M, Chen C-H, Tsai W-T (2004) Effect of heat-treatment on characteristics of anodized aluminum oxide formed in ammonium adipate solution. J Electrochem Soc 151(3):B188
96. Shimizu K, Thompson GE, Wood GC (1981) The duplex nature of anodic barrier films formed on aluminium in aqueous borate and borate-glycol solutions. Thin Solid Films 85:53–59
97. Wood GC (1996) A model for the incorporation of electrolyte species into anodic alumina. J Electrochem Soc 143(1):74

98. Moon S-M, Pyun S-I (1999) The formation and dissolution of anodic oxide films on pure aluminium in alkaline solution. Electrochim Acta 44:2445–2454
99. Zhu X-F, Song Y, Liu L, Wang C-Y, Zheng J, Jia H-B, Wang X-L (2009) Electronic currents and the formation of nanopores in porous anodic alumina. Nanotechnology 20(47):475303
100. Pilling NB, Bedworth RE (1923) The oxidation of metals at high temperatures. J Inst Met 29:529–591
101. Csoḱn P (1964) Some observations on the growth mechanism of hard anodic oxide coatings on aluminium. Trans IMF 42(1):312–320
102. Lichtenberger-Bajza E, Donony A, Csokfáah P (1960)Untersuchung der Struktur und anderer Eigenschaften von durch anodische Oxydation auf Aluminium erzeugten Hartoxydschichten. Mater Corros 11(11):701–707
103. Osborn JH (2014) Understanding and specifying anodizing. OMW Corporation. www.omwcorp.com
104. Balaraju JN, Srinivasan A, Yoganandan G, William Grips VK, Rajam KS (2011) Effect of Mn/Mo incorporated oxide layer on the corrosion behaviour of AA 2024 alloy. Corros Sci 53(12):4084–4092
105. Yoganandan G, Bharathidasan T, Soumya Sri M, Vasumathy D, Balaraju JN, Basu BJ (2015) Effect of anodized oxide layer aging on wettability of Alkyl Silane coating developed on aerospace aluminum alloy. Metall Mater Trans A 46(1):337–346
106. Yoganandan G, Premkumar KP, Balaraju JN (2015) Evaluation of corrosion resistance and self-healing behavior of zirconium–cerium conversion coating developed on AA2024 alloy. Surf Coat Technol 270:249–258
107. Yoganandan G, Balaraju JN, Low CHC, Qi G, Chen Z (2016)Electrochemical and long term corrosion behavior of Mn and Mo oxyanions sealed anodic oxide surface developed on aerospace aluminum alloy (AA2024). Surf Coat Technol 288:115–125
108. Slunder CJ, Pray HA (1946) Modified chromic acid anodizing process for aluminium. Ind Eng Chem 38(6):592–596
109. Elabar D, La Monica GR, Santamaria M, Di Quarto F, SkeldonandG P, Thompson E (2017) Anodizing of aluminium and AA 2024-T3 alloy in chromic acid: effects of sulphate on film growth. Surf Coat Technol 309:480–489
110. Nishinaga O, Kikuchi T, Natsui S, Suzuki RO (2013) Rapid fabrication of self-ordered porous alumina with 10-/sub-10-nm-scale nanostructures by selenic acid anodizing. Sci Rep 3:1
111. Kikuchi T, Nishinaga O, Natsui S, Suzuki RO (2014) Self-ordering behavior of anodic porous alumina via selenic acid anodizing. Electrochim Acta 137:728–735
112. Kikuchi T, Nishinaga O, Natsui S, Suzuki RO (2014) Fabrication of anodic nanoporous alumina via acetylenedicarboxylic acid anodizing. ECS Electrochem Lett 3(7):C25–C28
113. Nakajima D, Kikuchi T, Natsui S, Suzuki RO (2014) Growth behavior of anodic oxide formed by aluminum anodizing in glutaric and its derivative acid electrolytes. Appl Surf Sci 321:364–370
114. Kikuchi T, Yamamoto T, Natsui S, Suzuki RO (2014) Fabrication of anodic porous alumina by squaric acid anodizing. Electrochim Acta 123:14–22
115. Kikuchi T, Nishinaga O, Natsui S, Suzuki RO (2015) Fabrication of self-ordered porous alumina via etidronic acid anodizing and structural color generation from submicrometer-scale dimple array. Electrochim Acta 156:235–243
116. Takenaga A, Kikuchi T, Natsui S, Suzuki RO (2016) Exploration for the self-ordering of porous alumina fabricated via anodizing in etidronic acid. Electrochim Acta 211:515–523
117. Akiya S, Kikuchi T, Natsui S, Sakaguchi N, Suzuki RO (2016) Self-ordered porous alumina fabricated via phosphonic acid anodizing. Electrochim Acta 190:471–479
118. Takenaga A, Kikuchi T, Natsui S, Suzuki RO (2015) Self-ordered aluminum anodizing in phosphonoacetic acid and its structural coloration. ECS Solid State Lett 4(8):P55–P58
119. Manzano CV, Martín J, Martín-González MS (2014) Ultra-narrow 12nm pore diameter self-ordered anodic alumina templates. Microporous Mesoporous Mater 184:177–183
120. Horcas I, Fernández R, Gómez-Rodríguez JM, Colchero J, Gómez-Herrero J, Baró AM (2007) A software for scanning probe microscopy and a tool for nanotechnology. Rev Sci Instr 78:013705

121. Sulka GD, Stroobants S, Moshchalkov V, Borghs G, Celis J-P (2002) Synthesis of well-ordered nanopores by anodizing aluminum foils in sulfuric acid. J Electrochem Soc 149(7):D97
122. Aerts T, Jorcin J-B, De Graeve I, Terryn H (2010) Comparison between the influence of applied electrode and electrolyte temperatures on porous anodizing of aluminium. Electrochim Acta 55(12):3957–3965
123. Aerts T, Dimogerontakis T, De Graeve I, Fransaer J, Terryn H (2007) Influence of the anodizing temperature on the porosity and the mechanical properties of the porous anodic oxide film. Surf Coat Technol 201(16–17):7310–7317
124. Kashi MA, Ramazani A (2005) The effect of temperature and concentration on the self-organized pore formation in anodic alumina. J Phys D Appl Phys 38(14):2396–2399
125. Chu SZ, Wada K, Inoue S, Isogai M, Katsuta Y, Yasumori A (2006) Large-scale fabrication of ordered nanoporous alumina films with arbitrary pore intervals by critical-potential anodization. J Electrochem Soc 153(9):B384
126. Ono N, Kitamura K, Nakajima K, Shimanuki Y (2000)Measurement of Young's modulus of silicon single crystal at high temperature and its dependency on boron concentration using the flexural vibration method. Jpn J Appl Phys 39(Part 1, No. 2A):368–371. https://doi.org/10.1143/JJAP.39.368
127. Patermarakis G, Diakonikolaou J, (2012) Mechanism of aluminium and oxygen ions transport in the barrier layer of porous anodic alumina films. J Solid State Electrochem 16(9):2921–2939
128. Patermarakis G, Lenas P, Karavassil C, Papayiannis G (1991) Kinetics of growth of porous anodic Al_2O_3 films on Al metal. Electrochim Acta 36:709–725
129. Schwirn K, Lee W, Hillebrand R, Steinhart M, Nielsch K, Gösele U (2008) Self-ordered anodic aluminum oxide formed by H_2SO_4 hard anodization. ACS Nano 2(2):302–310
130. Lee W, Schwirn K, Steinhart M, Pippel E, Scholz R, Gösele U (2008) Structural engineering of nanoporous anodic aluminium oxide by pulse anodization of aluminium. Nat Nanotechnol 3(4):234–239
131. Chu S-Z, Wada K, Inoue S, Isogai M, Yasumori A (2005) Fabrication of ideally ordered nanoporous alumina films and integrated alumina nanotubule arrays by high-field anodization. Adv Mater 17(17):2115–2119
132. O'Sullivan JP, Wood GC (1970) The morphology and mechanism of formation of porous anodic films on aluminium. Proc R Soc A: Math Phys Eng Sci 317(1531):511–543
133. Esmaeily AS, Venkatesan M, Razavian AS, Coey JMD (2013) Diameter-modulated ferromagnetic CoFe nanowires. J Appl Phys 113(17):17A327
134. Hicks LD, Dresselhaus MS (1993) Effect of quantum-well structures on the thermoelectric figure of merit. Phys Rev B 47(19):12727–12731
135. Yan B, Pham HTM, Ma Y, Zhuang Y, Sarro PM (2007) Fabrication of *in situ* ultrathin anodic aluminum oxide layers for nanostructuring on silicon substrate. Appl Phys Lett 91(5): 053117
136. Liu N et al (2008) Focused-ion-beam-based selective closing and opening of anodic alumina nanochannels for the growth of nanowire arrays comprising multiple elements. Adv Mater 20(13):2547–2551
137. Lillo M, Losic D (2009) Pore opening detection for controlled dissolution of barrier oxide layer and fabrication of nanoporous alumina with through-hole morphology. J Membr Sci 327(1–2):11–17
138. Schlorb H, Haehnel V, Khatri MS, Srivastav A, Kumar A, Schultz L, Fahler S (2010) Magnetic nanowires by electrodeposition within templates. Phys Status Solidi B 247(10):2364–2379
139. Yin AJ, Li J, Jian W, Bennett AJ, Xu J (2001) Fabrication of highly ordered metallic nanowire arrays by electrodeposition. Appl Phys Lett 79(7):1039–1041
140. She G, Mu L, Shi W (2209) Electrodeposition of one-dimensional nanostructures. Recent Patents Nanotechnol 3(3):182–191
141. Lee KP, Mattia D (2013) Monolithic nanoporous alumina membranes for ultrafiltration applications: characterization, selectivity–permeability analysis and fouling studies. J Membr Sci 435:52–61
142. Najma B, Kasi AK, Kasi JK, Akbar A, Bokhari SMA, Stroe IR (2018) ZnO/AAO photocatalytic membranes for efficient water disinfection: synthesis, characterization and antibacterial assay. Appl Surf Sci 448:104–114

143. Yao Z, Wang C, Li Y, Kim N-Y (2015) AAO-assisted synthesis of highly ordered, large-scale TiO_2 nanowire arrays via sputtering and atomic layer deposition. Nanosc Res Lett 10(1):166
144. Cremers V, Puurunen RL, Dendooven J (2019) Conformality in atomic layer deposition: current status overview of analysis and modelling. Appl Phys Rev 6(2):021302
145. Elam JW, Xiong G, Han CY, Wang HH, Birrell JP, Welp U, Hryn JN, Pellin MJ, Baumann TF, Poco JF, Satcher JH (2006) Atomic layer deposition for the conformal coating of nanoporous materials. J Nanomater 2006:1–5
146. Chiou C-J, Chiu S-P, Lin J-J, Chou Y-C (2015) Effects of atomic scale imperfection at the interfaces of $CoSi_2$ and Si (100) on Schottky Barrier contacts. CrystEngComm 17(23):4276–4280
147. Popat KC, Chatvanichkul K-I, Barnes GL, Latempa TJ, Grimes CA, Desai TA (2007) Osteogenic differentiation of marrow stromal cells cultured on nanoporous alumina surfaces. J Biomed Mater Res Part A 80A(4):955–964
148. Weber H, Baxan N, Paul D, Maclaren J, Schmidig D, Mohammadzadeh M, Hennig J, von Elverfeldt D (2011) Microcoil-based MRI: feasibility study and cell culture applications using a conventional animal system. Magn Reson Mater Phys Biol Med 24(3):137–145
149. Aramesh M, Shimoni O, Fox K, Karle TJ, Lohrmann A, Ostrikov K, Prawer S, Cervenka J (2015) Ultra-high-density 3D DNA arrays within nanoporous biocompatible membranes for single-molecule-level detection and purification of circulating nucleic acids. Nanoscale 7(14):998–6006
150. Tsai H-Y, Liu H-C, Chen J-H, Yeh C-C (2011)Low cost fabrication of diamond nano-tips on porous anodic alumina by hot filament chemical vapor deposition and the field emission effects. Nanotechnology 22(23):235301
151. Zhan H, Garrett DJ, Apollo NV, Ganesan K, Lau D, Prawer S, Cervenka J (2016)Direct fabrication of 3D graphene on nanoporous anodic alumina by plasma-enhanced chemical vapor deposition. Sci Rep 6(1):19822
152. Santos A, Aw MS, Bariana M, Kumeria T, Wang Y, Losic D (2014)Drug-releasing implants: current progress, challenges and perspectives. J Mater Chem B, 2(37):6157–6182
153. Yamaguchi A, Hotta K, Teramae N (2009) Optical waveguide sensor based on a porous anodic alumina/aluminum multilayer film. Anal Chem 81(1):105–111
154. Santos A, Kumeria T, Losic D (2013) Nanoporous anodic aluminum oxide for chemical sensing and biosensors. Trends Analytic Chem 44:25–38
155. Hsu W-L, Cheng C-H, Wu C-L, Pai Y-H, Lin G-R (2017) Nano-porous MOSLEDs with spatially confined Si quantum dots buried in anodic aluminum oxide membrane. IEEE J Sel Top Q Electron 23(5):1–7

Chapter 8
Synthesis Aspects of Nanoporous and Quasi-One-Dimensional Thin Film Architecture Photoelectrodes for Artificial Photosynthesis

Rajini P. Antony

Abstract Artificial photosynthesis is a promising concept (soon to be realized) where one can use natural resources such as sunlight and water for converting energy to hydrogen and then to electricity. This is achieved by employing functional materials which can generate photogenerated electrons and holes which facilitates hydrogen generation and water oxidation, respectively. In this respect appropriate materials should be chosen, which possess good visible light absorption, suitable band position straddling with water oxidation and reductions potentials, chemically/photochemically stable and earth abundant. Hence, transitions metal oxides like TiO_2, Fe_2O_3, $BiVO_4$, WO_3, etc. are generally explored to this end. However, all these materials have limitations with respect to recombination of charge carriers, diffusion lengths and conductivity. To overcome these limitations, different strategies have been adopted such as doping, nanostructuring and making hetero-junctions. Because of the short penetration depth of photons into the bulk and the short mean free paths of charge carriers, for a conventional semiconductor, a single atomic layer of semiconductor is insufficient to absorb the solar flux, typically of the order of a few micrometres are required to absorb a significant fraction of light. Thus, a high percentage of charge carriers recombine in the oxide bulk before diffusing to the semiconductor surface, resulting in poor surface reaction kinetics. The issue can be addressed to a certain extent by manipulating the semiconductor morphology—for example, quasi-one-dimensional morphologies such as nanotubes, nanorods and nanoporous structures can improve photoelectrochemical performance. This is because the electron transport down the length of the tube/rod is increased in comparison with a collection of nanoparticles, while the distance holes must travel to reach the semiconductor/liquid interface is relatively small (the upper limit is half of the tube wall thickness). Thus, the radius of the semiconducting material should be tuned to the minority carrier collection length and the length should be adjusted for optimal light absorption. Moreover, the idea of an inexpensive approach of constructing of

R. P. Antony (✉)
Water and Steam Chemistry Division, BARC Facilities, Indira Gandhi Centre for Atomic Research, Kalpakkam 603 102, India
e-mail: rajiniantony@igcar.gov.in

A. K. Tyagi and R. S. Ningthoujam (eds.), *Handbook on Synthesis Strategies for Advanced Materials*, Indian Institute of Metals Series,
https://doi.org/10.1007/978-981-16-1803-1_8

photoelectrode assembly includes the development of one-dimensional nanostructured photoelectrodes, electrocatalyst and finally constructing the tandem cell can reduce the overall cost of the device. The advancement of nanotechnology has enabled scientific community to engineer nanostructured materials with enhanced electronic, catalytic and surface properties. In view of this, the present chapter provides an idea of the fabrication of nanostructured thin films by different inexpensive synthetic routes which can be scaled up for commercial devices.

Keywords Thin films · Photoanodes · Photocathodes · Photoelectrochemical water splitting · Nano-architectured photoelectrodes

8.1 Introduction

Solar to energy conversion by utilizing earth abundant resources is the urgent requirement for energy researchers in the context of depletion of fossil fuels, global warming and environmental pollution [1]. Natural photosynthesis is considered to be the main energy supply in the earth, where plants produce carbohydrates using carbon dioxide and water. Under optimum conditions maximum conversion efficiency that can be achieved is 7%, but only ~1% is the average conversion efficiency from the plants during its entire life span. Artificial photosynthesis (AP) is a promising concept, where the idea is to mimic natural photosynthesis process, and one can use natural resources such as sunlight and water for converting solar energy to hydrogen and related hydrocarbons and then to electricity [2]. This is achieved by employing functional materials which can produce photogenerated electrons and holes, and facilitates hydrogen generation and water oxidation, respectively. However, the major issues associated with the AP systems are the difficulty in fabricating an efficient device which can compete with the existing fossil fuel system with respect to cost and scale up. Thus, much improvement is required for an AP device and a faster research is vital pertaining to material development, cell construction and long-term running of the device. Similar to natural photosynthesis process, the AP involves absorption of light, charge carrier generation and separation followed by catalytic reactions. Thus, in the context of immediate energy requirement, one should look for realizing efficient AP devices, the fundamental and mechanistic understanding of the processes, energetics involved, and cost-effectiveness and up-scaling possibility of the device in terms of practical application.

Photoelectrochemical (PEC) water splitting is a category of AP, where visible light active semiconductors and sunlight are utilized for splitting water under applied bias/no bias generating oxygen and hydrogen in separate compartments [2–5]. A PEC cell consists of a photoanode and a photocathode where water oxidation and reduction reactions occur, generating oxygen and hydrogen gas, respectively. The overall reaction involved is given by following equations

$$4H^+ + 4e^- \leftrightarrow 2H_2,\ E^0_{red} = 0\ \text{V versus NHE} \tag{8.1}$$

$$2H_2O + 4H^+ \leftrightarrow O_2,\ E^0_{ox} = -1.229\ \text{V versus NHE} \tag{8.2}$$

Overall water splitting process can be expressed as

$$2H_2O + 2H_2 + O_2 \cdots E^0_{cell} = 1.229\ \text{V versus NHE} \tag{8.3}$$

The Gibbs free energy change involved in the overall water splitting reaction is given by the equation

$$\Delta G = -nFE \tag{8.4}$$

When the cell voltage is 1.23 V at standard temperature (298 K) and concentration (1 mol/L, 1 bar) the value of ΔG is + 237 kJ/mol showing that the water splitting reaction uphill. A schematic representation of the water oxidation and reduction process using a photoanode and photocathode is shown as Fig. 8.1a, b. The overall water splitting experimental set up is pictorially given in Fig. 8.1c where optimized photocathode and photoanode are used for water splitting reaction. In real situation, one has to apply a potential higher than 1.23 V due the over potentials involved.

The main challenge faced by the PEC system is with respect to photoelectrode materials used, where a combination of efficient light absorption, charge separation, and transport are the key factors to be achieved. Other aspects include abundant availability, low toxicity and long-term stability. Different systems have been explored to this end which includes molecular[4] and semiconductor [3]-based materials. In these, semiconductor-based materials are of utmost interest which have great potential scope for commercialization due to its earth abundance, photo-stability, suitable band edge straddling with water redox levels and good visible light absorption capability. Several significant achievements have already been realized in the material development aspect; however, working optimization of the devices is still lagging. Several questions to be addressed in the material context are as follows:

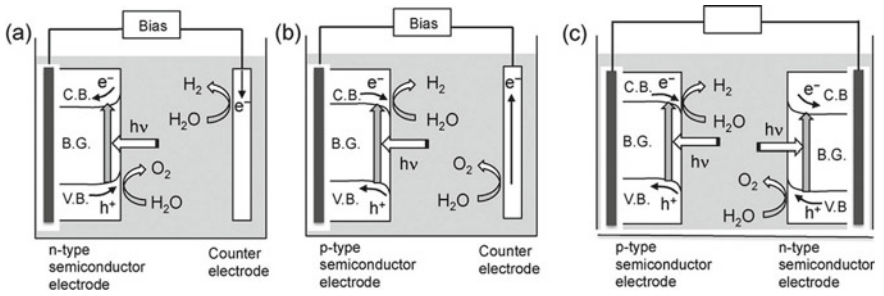

Fig. 8.1 photoelectrochemical water splitting systems using **a** *n* type semiconductor photoanode, **b** *p*-type semiconductor photoanode and **c** tandem device. Image taken with copy right permission from Elsevier [6]

1. How to improve the visible light absorption or light trapping ability of the material?
2. Can it be improved by engineering the surface structure of the material?
3. What are the modifications to be made to minimize the charge carrier recombination and maximize the charge separation?
4. Whether single materials serve the purpose of improving all these criteria or it is required to use heterojunctions?

A practical solution to the above questions can help one to come up with a promising system which can be utilized to make a commercial PEC device for efficient energy conversion. The following section discusses main features of semiconducting materials which can be used as photoelectrodes in PEC systems. The chapter then focuses on the key requirement for the morphological modification using different synthesis strategies followed by a discussion on most common synthesis strategies adopted for fabrication of quasi-one-dimensional nanostructure based photoanodes.

8.2 Desired Features of Photoelectrodes Used for Photoelectrocatalysis

As discussed in the previous section, the appropriate materials to be chosen should possess good visible light absorption, suitable band position straddling with water oxidation and reduction potentials, chemically/photochemically stable and earth abundant [6, 7]. A pictorial representation of an overall water splitting device using quasi-one-dimensional nanostructured photoelectrodes is shown in Fig. 8.2a, where the device is composed of a photoanode and photocathode separated by a proton ion conducting membrane. Both photoelectrodes are coated with electrocatalysts to improve the charge transfer kinetics involved in hydrogen and oxygen evolution reactions. Thus, transitions metal oxides like TiO_2 [8–11], Fe_2O_3 [12–15], $BiVO_4$ [16–19] and WO_3 [20–23] are generally explored as photoanodes and the band edge straddling with water redox levels are schematically shown in Fig. 8.2b. Also, the theoretical photocurrents that can be achieved by each semiconducting material is limited by its band gap and the values are graphically shown in Fig. 8.3 [3]. Though the band edge straddling is suitable for water splitting, these materials have limitations with respect to recombination [3, 24], diffusion lengths [18, 25–27] and conductivity [15, 28]. To overcome these limitations, different strategies have been adopted such as doping [29], nanostructuring [12, 30–34] and making heterojunctions [19, 35–37]. For a conventional photoelectrode, due to the large penetration depth of photons into the bulk and the short mean free paths of charge carriers, a single atomic layer of semiconductor is insufficient to absorb the solar flux efficiently and a too thick layer will prevent the photogenerated charge carriers from reaching the surface for reactions. Thus, when a bulk electrode is used a high percentage of charge carriers

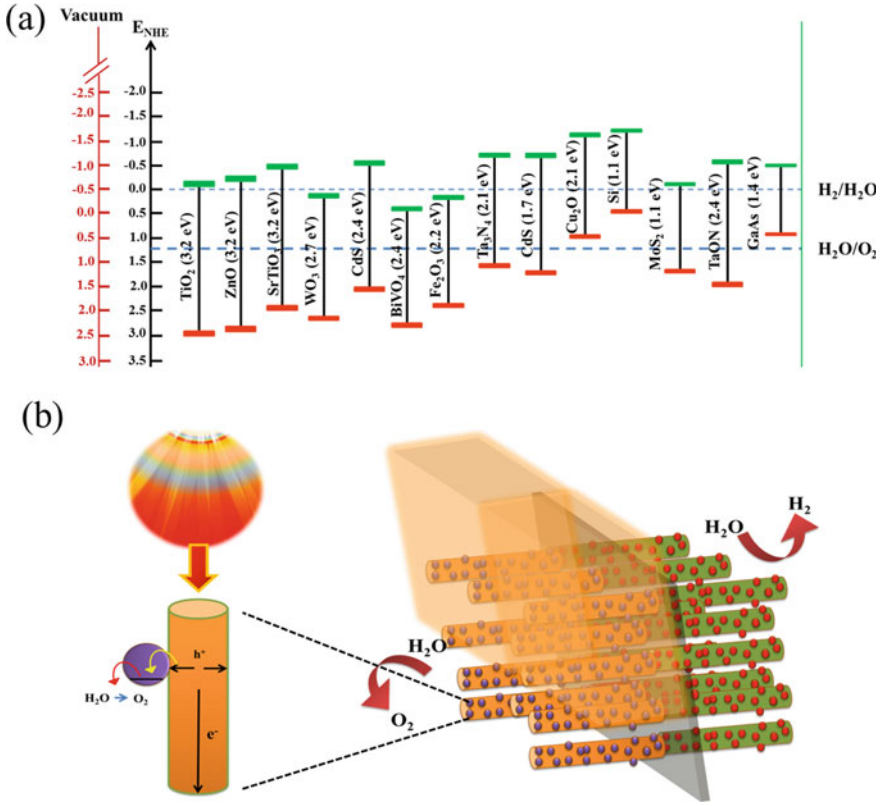

Fig. 8.2 **a** Conduction and valence band straddling of semiconductors with water reduction and oxidation potentials and **b** typical pictorial illustration of an AP-based PEC device where the photoelectrodes are composed of Q-one-dimensional architecture. The zoomed portion shows the orthogonal separation and transport of photogenerated electrons and holes

recombine in the oxide bulk before diffusing to the semiconductor surface, resulting in poor surface reaction kinetics.

The above issues can be addressed to a certain extent by manipulating the semiconductor morphologies like quasi-one-dimensional (Q-one-dimensional) structures such as nanotubes, nanorods and nanoporous structures. These structures can improve transport properties of the device because the electron transport down the length of the tube/rod is increased in comparison with a collection of nanoparticles [3, 26]. In addition, the physical dimensions are similar to that of the charge carrier diffusion length to enable photogenerated charge carriers to reach the surface easily from the exciton generation point [38–40]. In other words, the distance with which holes must travel to reach the semiconductor/liquid interface is relatively small; the upper limit is half of the diameter of the one-dimensional structure. Thus, improvement in both the transport properties and orthogonal charge separation by one-dimensional structures can enhance the overall efficiency of the device. The fundamental issues posed

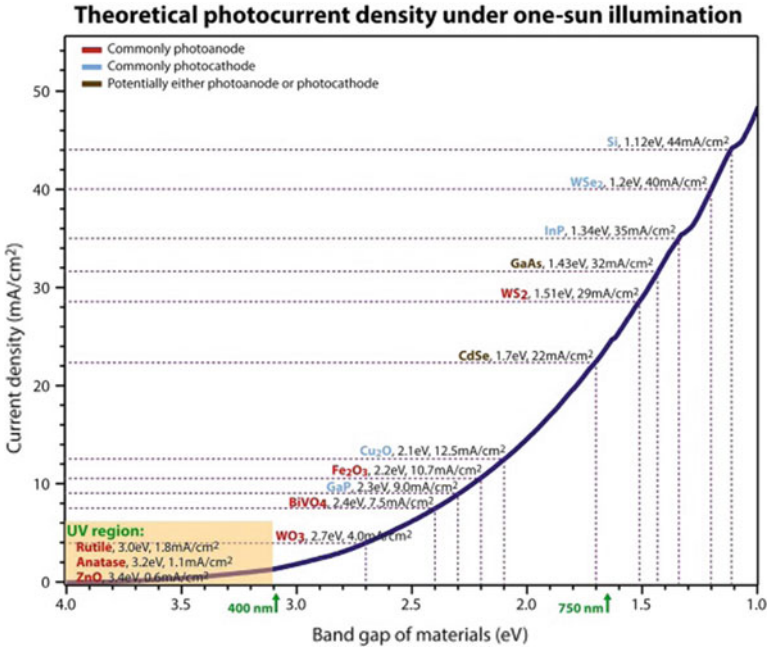

Fig. 8.3 Graph showing the theoretical photocurrent density achieved different semiconductor materials under 1 sun illumination conditions. Reproduced with copyright permissions from ACS chemistry of materials [3]

by the notoriously shorter hole diffusion length of the metal oxide-based electrode can, therefore, be overcome by fabricating nanostructures having dimensions lesser than twice the diffusion length of the material used.

Based on the above discussions, it is now clear that the dimensions of the semiconducting material should be tuned to optimize the minority carrier collection length and light absorption for achieving higher efficiencies in the commercial devices. Moreover, the idea of inexpensive photoelectrode assembly mainly includes the development of one-dimensional nanostructured photoelectrodes, electrocatalyst and finally constructing the tandem cell. The advancement of nanotechnology has enabled scientific community to engineer nanostructured materials with enhanced electronic, catalytic and surface properties [26, 28, 41–44]. Different forms of one-dimensional nanostructures have attracted the attention recently in the field of energy storage and conversion devices. The family of one-dimensional nanostructures consist of systems such as nanotubes [45], nanowires [46], nanorods [47] and nanofibers [48]. For developing these one-dimensional nanostructures, different strategies are generally adopted which include nucleation and growth, self-assembly or self-organization and size reduction from two dimensions [26, 43, 44, 49]. In view of these aspects, a basic idea of the Q-one-dimensional nanostructures is discussed in next section.

8.3 Quasi-One-Dimensional Nanostructures

The word "nano" is a term indicating a fraction of 1 billionth of a quantity. Materials which have dimensions in these regimes have shown extraordinary physical, chemical, electronic and mechanical properties [26, 28, 41–44]. Excellent reviews and books are available in the literature where detailed reports in which nanostructuring of a material and related improvement in physical and chemical properties [26, 42–44, 49–52]. The classical examples are carbon nanotubes and fullerenes which are the breakthroughs [53] in the field of nanoscience and technology. Following these inventions, extensive research has been carried out on these carbon materials with respect to its morphological, physico-chemical and mechanical properties. Later many inorganic-based one-dimensional nanomaterials were developed by various researchers [49, 53, 54] and rigorous researches were conducted and still on-going for controlling the size and shape of the materials and understanding its changes in physico-chemical behaviour with respect to the bulk materials. For this advanced microscopic and spectroscopic tools have been developed, which enabled the researcher to unveil the physics and chemistry of these nanomaterials.

One important parameter which distinguishes different types of nanomaterials is its dimensionality aspect. A material is considered to be of nanometer size when at least one of its dimensions is confined to less than 100 nm. Thus, the nanomaterials are classified into 0-D, one-dimensional, two-dimensional and three-dimensional nanomaterials. In the case of 0-D materials the confinement is in the three directions, for one-dimensional materials the confinement is in the two directions and for the two-dimensional structure the confinement is on 1 direction. Another subtype of the class of nanomaterials are quasi-one-dimensional structure where the confinement is in two directions and weak confinement in the third direction due to the axial direction and are having interesting applications and expected to play and major role in the form of interconnects and individual structures in electronic and optical-based devices [44, 49]. Thin films-based nanotubes, nanorods, nanowires and nanofibers belong to these classes of materials and are pictorially represented in Fig. 8.4 [44]. These quasi-one-dimensional nanostructures have shown good performance as photoelectrodes in AP device compared to other nanostructures.

The present chapter does not intend to give a comprehensive idea of fabrication of quasi-1D nanostructure, rather focussing on the methodologies adopted commonly for the fabrication of quasi-1D thin film to be used as photoelectrodes in artificial photosynthesis devices. Thus, the chapter mainly discusses selective and the most widely adopted synthesis techniques used for the fabrication quasi-1D nanostructured thin films which are expected to improve the efficiency compared to particulate nanostructured thin films. Each section discusses the basic technique and instrumentation involved in fabricating the quasi-1D nanostructures and nanoporous structures followed by advantages and disadvantages of the respective technique. Selected results on the performances of the photoelectrodes fabricated by the technique, for the water splitting application, are also summarized in each section.

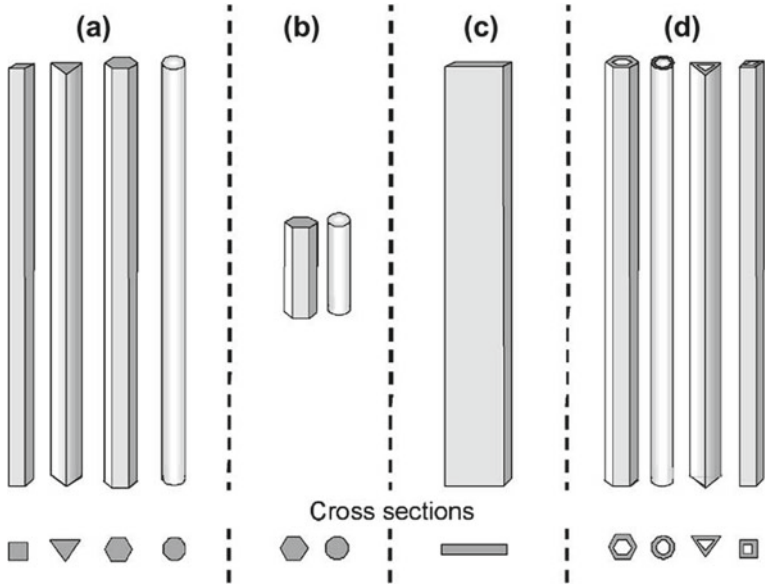

Fig. 8.4 Schematic representation of different types of one-dimensional nanostructures which include **a** nanowires or nanofibers, **b** nanorods, **c** nanobelts or nanoribbons and **d** nanotubes. These structures typically have one dimension in the nanometer regime and the second dimensions in few hundreds of nanometres. Reproduced with the copyright permission form Elsevier [44]

8.4 Role of Quasi-One-Dimensional Photoelectrodes in Improving the Efficiency of the Photoelectrodes

8.4.1 Improvement in the Light Absorption

Light absorption efficiency of the photoelectrode directly affects the performance of the photovoltaic/PEC devices. Implementing the surface texture on the surface of the photoelectrode thin film can enhance the light trapping and absorption. It is well understood that the nanomaterials having dimensions less than 100 nm are transparent to light as the dimensions are lesser than the wavelength of the light. The light absorption can be improved by incorporating three-dimensional texturization on the surface of the photoelectrode. This can be realized by using arrays of nanowires, nanorods, nano pillars and nanotubes. By a series of experimental and theoretical studies by *Katzenberg and Korsten* et al. showed that Si nanowire array improved the efficiency of the solar to light conversion [42]. Thus, light absorption of the materials should be improved by modifying the dimensions of the materials under investigation. Here, the one-dimensional structures have an advantage of having longer axial lengths and enable improved scattering of light thereby the neighbour one-dimensional structure can absorb the light efficiently. In the case of nanotubular

structures, the light absorption can be further enhanced by the multiple scattering and absorption of light when the light traps inside the tube. The light harvesting efficiency (LHE) is calculated from the reciprocal of the absorption length as given by Eq. 8.5 [18]

$$\mathrm{LHE}(\lambda) = 1 - 10^{-\mathrm{A}(\lambda)} \tag{8.5}$$

where A is the absorption at particular wavelength, λ.

Other advantages of one-dimensional structures are higher charge carrier mobility, superior mechanical strength and mechanical flexibility compared to other dimensional materials, which can prevent the cracking of the devices as well as its use in flexible devices.

8.4.2 Improvement in the Carrier Collection Efficiency

An important aspect in the AP devices is the carrier collection efficiency. A properly designed quasi-one-dimensional nanostructure can also enhance the photo generated carrier collection efficiency. Normally for efficient light absorption, the material should possess sufficient thickness to have maximum absorption, whereas for better carrier collection efficiency, the material should be thin to minimize the minority carrier travel distance. Thus, there is a competition in light absorption and charge carrier efficiency. This effect becomes pronounced in the case of semiconducting polycrystalline materials which are facing the notorious issue of "shorter diffusion length". For example, the hole diffusion length of the Fe_2O_3 photoanodes is reported to be in the range of 5–20 nm while a film thickness of a few hundreds of nm are required for good light absorption [55, 56]. Hence, it is an important requirement that the dimensions of the material to be tuned in such a way that maximum hole transfer should be achieved either by increasing the hole diffusion length of the material or by nanostructuring process. To minimize these issues, self-organized structures of one-dimensional nanostructures are proposed, where charge carrier collection occurs perpendicular to the light absorption. Experimental studies on nanopillar structures of materials having shorter diffusion length showed an improved light absorption and charge collection efficiency, which lead to the production of highly efficient photoelectrodes with earth abundant materials using a low-cost production technology [18, 36].

Many researchers have adopted different synthesis strategies for fabricating Q-one-dimensional nano-architectured thin films of pristine, doped, composite and heterojunctions-based semiconductors to improve the conductivity, hole diffusion length, light absorption and charge separation. The following section provides a brief idea about classic techniques adopted for the fabrication of thin film photoelectrodes.

8.5 Conventional Synthesis Methods Adopted for Fabrication of Nanostructured Thin Film Photoelectrodes

The present section essentially gives a brief idea of the conventional and cost-effective techniques used for the fabrication of thin film photoelectrodes. A number of techniques are discussed in detail covering the basic principle, instrumentation, and selected photoelectrochemical results for photoelectrodes fabricated by respective technique for having a better insight on each route and its influence in increasing the PEC activity.

8.5.1 Drop Casting

Drop casting technology is nothing but dropping the solution on the substrate followed by evaporation of the solvent leading to the formation of thin films. The method is a very simple route for fabrication thin films photoelectrodes where easily evaporating solvents are employed for making the precursor solution.

When considering the fabrication of thin film photoelectrodes using this technique, normally precursor of photoelectrode materials are dissolved in a suitable solvent (should be evaporated at moderately faster rate; systems such as ethanol–water mixture, ethanol and any other easily evaporating solvents/ mixture) and is dropped onto the conducting substrates, thereafter subjected to calcination at desired temperature for crystallization and adhesion. An alternate way of fabricating thin film photoelectrode using the same methodology is to disperse the semiconductor nanoparticles in an appropriate solvent, drop casting followed by calcination at high temperature for improving the adhesion of the nano particulate thin film onto the substrate. The drop casting method is generally used for the preliminary evaluation of the performance of the novel materials, where the homogeneity of the thin film is not critical. Cluster-modified photocathodes were fabricated by drop casting technique by *Hou* et. Al. using Mo_3S_4 clusters and H terminated p-Si electrode which demonstrated the water splitting capability with an over potential of 400 mV [57]. *Zhao* and co-workers studied the water oxidation activity of drop casted monoclinic WO_3 photoanode and reported a photocurrent density of 3.8 $mAcm^{-2}$ at 1.36 V versus RHE in 0.1 Na_2SO_4 with a Xenon lamp illumination [58]. *Lionet* and co-workers reported the PEC activity of MIL-101(Fe) photoanode fabricated by drop casting route [59]. All these studies show that the present fabrication route can be used as a preliminary technique to evaluate the solar water splitting activity of novel materials. The main advantages and disadvantages of the technique are listed below.

Advantages

1. Quick and accessible method to fabricate thin films in relatively small area
2. No waste of precursor solution during synthesis

3. Can be used for the preliminary performance evaluation of the novel materials fabricated.

Disadvantages

1. Non-uniform film thickness or internal structure (surface roughness) due to the different evaporation rates across the substrate or change in concentration even under best conditions
2. Difficult to control the thickness of the film
3. Cannot be used in large area film synthesis.

8.5.2 Spin Coating

Spin coating is one of the most commonly adopted techniques for the fabrication of thin films due to the ease of handling and quality of the film. The technique is widely applied in organic electronics, nanotechnology and semiconductor industries. This is because; the technique can generate films of varying thicknesses (from few nm to several micrometres) with good uniformity, and is essential for electronic devices. The spin coating process involves dropping of the precursor solution or ink onto the desired substrate, similar to the drop casting technique. The drop casted substrate is then rotated at a high speed (decided by rotations per minute, rpm), thereby spreading the ink uniformly all over the substrate. The substrate to be coated is normally fixed on the rotor with the help of vacuum. During the rotation period, the solvent evaporates and the desired material coating is achieved on the substrate uniformly. The thin films thus formed are subjected to calcination for crystallization. The pictorial representation of the fabrication steps of the thin film photoelectrode using this technique is as shown in Fig. 8.5. Along with the drop casting technique, spin coating technique is considered as the benchmark for the research and industrial level fabrications. The thickness of the spin-coated film is dependent on the rotation speed, viscosity of the solution used, and the time of rotation. The parameter which decides the thickness of the film is governed by the following Eq. (8.6).

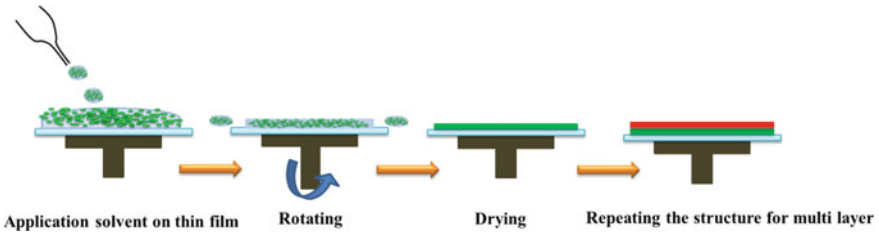

Fig. 8.5 Schematics representation of fabrication of thin films by spin coating route

$$t = \left(\frac{1-\rho A}{\rho A_0}\right) \cdot \left(\frac{3\eta m}{2\rho A_0 \omega^2}\right)^{\frac{1}{3}} \tag{8.6}$$

where t is the thickness of the film, ρ_A = density of volatile liquid, η= viscosity of solution, m = rate of evaporation and ω is the angular velocity. Thus, the thickness of the film is inversely proportional to the square root of the angular velocity as shown in Eq. (8.7) and can be used as a simpler route Eq. (8.6) to calculate the thickness of the film.

$$t \propto \frac{1}{\sqrt{\omega}} \tag{8.7}$$

Thus, spin-coated films having thickness in the nanometer regime is generally fabricated under high rpm. This dependence allows the precise control of the film thickness.

In the same way, the concentration of the ink also governs the film thickness, where at low concentration range; the film thickness will have a linear dependency, whereas at higher concentration a nonlinear relationship will develop due to the increased viscosity of the ink. The spin coating duration also affect the thickness of the film and generally the duration of the rotation is kept in the range of 30–60 s for common solvents such as water, isopropyl alcohol, ethanol and methanol when solvents such as ethylene glycol and glycerol (high viscous solvents) are used a longer spin duration is required to achieve similar thicknesses.

The spin coating technique is also an effective way of constructing three-dimensional nanoporous films having a controllable thickness, which has shown very good performance in PEC devices. This is generally achieved by incorporating high molecular weight sacrificial polymers such as polyvinyl pyrollidone [60–62] or poly vinyl alcohol [63, 64] into the precursor solution for spin coating and the nanoporous structure is thus achieved by repeated spin coating–annealing steps. The porosity of the film in this case can also be varied by changing the amount of polymer incorporated. Thus, the light absorption and catalytic efficiency can be varied by changing the porosity of the thin films fabricated using this technique.

Parmar and co-workers reported the fabrication of $BiVO_4$-based photoanodes using spin coating technique where the Mo, W co-doped $BiVO_4$ photoanode showed a water oxidation photocurrent of 2.38 $mAcm^{-2}$ at 1.23 V versus RHE [65]. *Biswas and Baeg* fabricated W doped $FeVO_4$ photoanodes by layer by layer deposition by spin coating having a photocurrent density of 0.4 $mAcm^{-2}$ [66] Fabrication of $CuWO_4$ photoanode through spin coating was reported by *Zhang* et al. which demonstrated a photocurrent of 1.5 mA cm^{-2} in phosphate buffer [67]. A layer by layer porous gradient Mo:$BiVO_4$ was fabricated by *Antony* et al. by repeated spin coating route and PVP was used a sacrificial polymer to introduce porosity in thin film [68]. The resultant photoanode could generate a photocurrent of ~1.74 $mAcm^{-2}$ at 1.23 V versus RHE in 0.5 M Na_2SO_4. *Quinonero* et al. have used the spin coating technique to fabricate La and Ce doped $BiVO_4$ photoelectrode and reported an increase in the

photocurrent with doping process [69]. All these studies point towards the impression that the spin coating route for the fabrication of photoelectrode is an efficient method to have preliminary evaluation of the PEC performance of novel photoelectrodes fabricated. In addition, in case of porous thin films fabricated by this route, where sacrificial polymers are employed, and the water oxidation performance is promising and the technique can be up scaled for commercialization. Few advantages and disadvantages of the current technique are given below.

Advantages

1. Simple and cost-effective technique
2. Good reproducibility of the technique due to high rotation speed, air flow and drying
3. Good uniformity of the spin-coated film
4. Good control over the thickness of the film
5. Multilayer deposition can be achieved.

Disadvantages

1. Technique cannot be applied for large surface area coating
2. Wastage of the precursor during deposition
3. Faster drying of the film leads to lesser molecular disordering, thus resulting a lower performance of the device
4. Relatively lower throughput.

8.5.3 Dip Coating

Dip coating is an easy, simple and controlled process where the substrate of interest is dipped in a precursor solution with precise withdrawal rate under controlled conditions of temperature and pressure. The thickness of the film formed is mainly decided by the withdrawal speed, amount of precursor in the solution and the viscosity of the solution. During the withdrawal of the substrate, the solution homogeneously spreads on the substrate surface due to the combined effect of viscous drag and capillary rise. After withdrawal of the substrate, the drying process of the film can be done by conventional thermal/UV/or IR techniques. The coating thickness can be calculated by the Landau–Levich equation [70] (Eq. 8.8) as given below.

$$h = 0.94.\frac{(\eta.v)^{2/3}}{\gamma_{LV}^{1/6}(\rho.g)^{1/2}} \tag{8.8}$$

where h = coating thickness, η = viscosity, γ_{LV} = liquid–vapour surface tension, ρ = density and g = gravity. A schematic representation of the dip coating technique is shown in Fig. 8.6 where different steps involved in the dip coating process leading to the formation of thin films are picturized. For an efficient coating, the whole

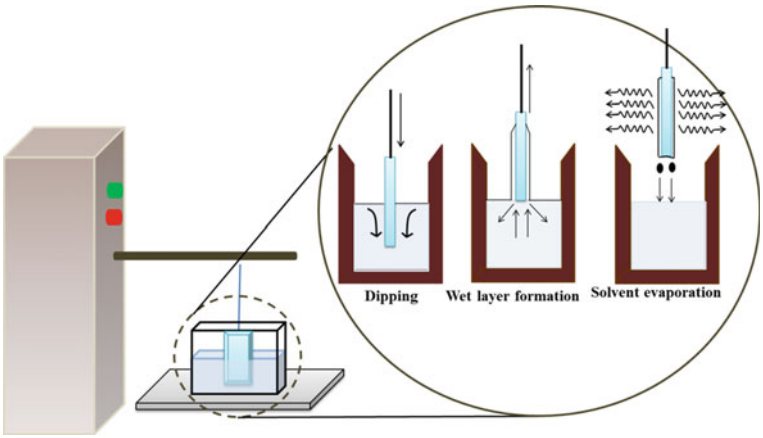

Fig. 8.6 Schematic representation of conventional dip coating unit. The zoomed portion shows different process happening during the dipping and withdrawal of the substrate leading to the formation of thin film electrodes

experimental facility should be kept on a vibration free table to ensure the film thickness homogeneity formed at each deposition step.

Dip coating technique was applied for the fabrication of WO_3 photoanodes by *Hilliard* et al. and the PEC studies showed a photocurrent of 0.6 $mAcm^{-2}$ in potassium phosphate buffer [23]. Similarly, Mo doped $BiVO_4$ photoanodes fabricated using this technique showed an efficient water oxidation photocurrent of 1.9 $mAcm^{-2}$ which is a promising value for researchers to use this technique and material for commercial application [71]. In a parallel publication, it was reported that sol gel dip coating route can be adopted to fabricate $BiVO_4$ films for photoanode application showing a photocurrent value of 2.1 $mAcm^{-2}$ under 300 W Xenon lamp illumination (phosphate buffer—pH = 7) [72]. *Landsmann* et al. adopted a dip coating strategy to fabricate reproducible, and scalable particle based photoanode system employing $LaTiO_2N$ with a maximum photocurrent density of 2.52 mA/cm^2 at 1.23 V versus RHE under 1 sun illumination [73]. Efficient solar water splitting performance was observed for highly aligned $Cu_2O/CuO/TiO_2$ core/shell nanowire array photocathode, where TiO_2 is coated on Cu_2O/CuO by a dip coating route [46]. Thus, photoanodes fabricated by this method is proved to show good water oxidation behaviour and can be adopted for a large-scale electrode fabrication. Some of the merits and demerits of the dip coating technique is listed below.

Advantages

1. Easy and simple technique
2. Minimal wastage
3. Uniform film coating can be achieved
4. Large area coating can be achieved
5. Very thin layers can be generated.

Disadvantages

1. Technique results in coating on both side
2. No control over the surface roughness
3. Time consuming process
4. Requirement of clean room
5. Proper training and optimization is required for getting a high-quality film
6. A good dip coating machine is normally expensive.

8.5.4 Doctor Blading

Doctor blading is a widely accepted thin film fabrication technique which is applied for large-scale fabrication. In this process, well-dispersed slurry containing the nanomaterials of interest is applied on the substrate to be coated which is kept under vacuum for adhesion. The blade helps to spread the slurry homogenously on to the substrate. A constant relative movement between substrate and the blade with a specific distance (typically 10–500 μm) enable the formation of thin wet film. The thickness of the film can be controlled by adjusting the gap between the blade and the substrate. A schematic representation of the doctor blading technique is shown in Fig. 8.7a. The wet thickness of the film is generally half of the gap between the blade and the substrate and is influenced by the substrate surface energy, surface tension and viscosity of the coating solution. The dried film thickness as a result of doctor blading can be calculated by the empirical relation given below in equation [74] (8.9)

$$d = \frac{1}{2} g\left(\frac{c}{\rho}\right) \tag{8.9}$$

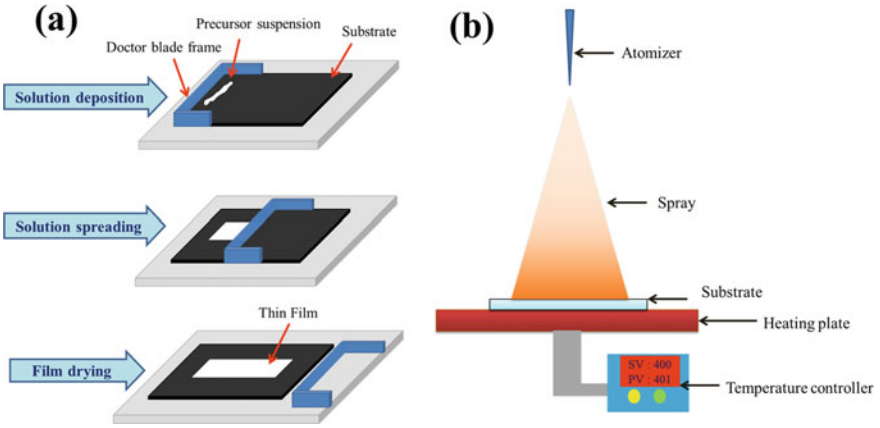

Fig. 8.7 Pictorial illustration of **a** doctor blading technique and **b** spray coating technique

where d is the dried film thickness, g the gap width between the blade and the substrate, c the concentration of the precursor solution in gcm^{-3} and ρ the density of the material in the precursor solution in gcm^{-3}. Doctor Blading technique is widely used for the fabrication of TiO_2-based photoanodes for dye sensitized solar cells (DSSC) [75–77]. Doctor Blading technique was employed to fabricate $BiVO_4$ thin film on FTO glass by *Mohamed* and co-workers employing an ionic liquid medium [78]. *Franking* et al. have fabricated doped hematite photoanodes by doctor blading route and demonstrated a post-doping strategy for improving the efficiency [12].

Advantages

1. Simplest and low-cost printing methods for the fabrication of semiconducting coating
2. Can be used for large-scale film development
3. Less than ~5% loss of materials
4. Good uniformity.

Disadvantages

The process is relatively slow, leading to a chance of aggregation of materials at high precursor concentration.

8.5.5 Spray Coating

Spray coating is an easy and promising technique which can be used as a large-scale thin film fabrication technique. The method is generally employed either in the solution coating mode where the precursor is dissolved in a suitable solvent and sprayed or in the solid form where the coating is done at a temperature above which the precursor of interest is decomposed. The technique can be applied for the fabrication of a variety of nanomaterials such as dense and porous thin films, multi-layers and powders. The instrumental set up for a spray pyrolysis unit is relatively simple and cost-effective. Typically, a spray pyrolysis unit consists of a precursor solution, atomizer, substrate onto which the film has to be deposited, heater for a desired substrate temperature, and a temperature controller to adjust the temperature. A schematic representation of the simple spray pyrolysis unit is shown in Fig. 8.7b. The role of an atomizer is to create a spray of the precursor solution having droplet size varying in the range of a few nanometers to micrometres. This enables one to tune the morphology and dimensions of the films fabricated. For this, different types of atomizers are employed, which are generally pneumatic or ultrasonic-based atomizers. Usually, three processes are involved in the spray deposition process.

1. **Atomization** of precursor taken in a suitable solvent which is realized by compressed air, electrostatic mode or ultrasonically. The formation and the size of the aerosols thus formed influence the morphology and porosity of the thin films.

2. **Transportation of aerosols** is the next process which is normally carried out with the help of gravitation, electrical or by thermoelectric methods. During this transportation, the solvent in the aerosols is evaporated leading to a decrease in the size of the droplet. The droplets then precipitate on the substrate when the concentration of the precursor in the droplet exceeds the solubility limit.
3. **Decomposition of the precursor** is the final step, where the precipitate is decomposed leading to the desired product depending on the temperature of the substrate.

When the spray generated from atomizers hit on the substrate, the atom loses its energy, spreads on the substrate and interacts with the adsorbed atoms. This will lead to the formation of islands and merge to form continuous film. The technique can be used for the fabrication of nanomaterials in the powder form, thin films and multilayer films for various applications. Different types of spray pyrolysis systems have been developed which includes, ultrasonic spray pyrolysis [79], plasma assisted spray pyrolysis [80] and flame pyrolysis [81]. The qualities of the thin films are varied with the experimental conditions such as type of precursor, precursor concentration, and temperature of the substrate, drop size and the time of deposition.

Many researchers have attempted fabricating photoelectrodes for AP device using this technique as it is easily scalable for fabricating large area electrodes. Mesoscopic leaflet type α-Fe_2O_3 thin films was fabricated by ultrasonic spray pyrolysis (USP) technique and the PEC water oxidation activity was reported to be 1 $mAcm^{-2}$ at 1.23 V versus RHE [82]. Later in 2006 *Cesar* et al. fabricated translucent hematite thin films by USP technique and an improved response was reported with Si doping [15]. Fabrication of a different system like ZnO-based structures are explored using spray pyrolysis technique for application as photoanode in DSSC [83]. In a similar way, spray pyrolysis route was adopted to fabricate doped [84], heterojunctions [79] and derivative of hematite structures [85] for the obtaining efficient photoanodes for AP device. A cold spray technique was adopted by *Haisch et.al.* to fabricate WO_3 and TiO_2 thin films for water and methanol oxidation reactions [86].

Advantages

1. Layer thickness can be tuned
2. Large area fabrication can be achieved
3. The coating by this method is independent of the substrate morphology
4. Effective tool to fabricate metal oxide thin films
5. Cost-effective.

Disadvantages

1. Non-uniformity in the film
2. Nonstoichiometry and defects in the film
3. Use of inorganic precursors is limited; generally, organic precursors are more favourable for spray coating as they have low volatility and require low deposition temperatures.

All the above-mentioned techniques are conventional synthesis technologies for the fabrication of thin film photoelectrodes which leads to the formation of nanostructured and nanoporous thin films based on the modified conditions with respect to instrumentation and precursor compositions. Most of these techniques though while possessing advantages related to simplicity, cost-effectiveness and good accessibility yield photoelectrodes which are inefficient with respect to light absorption and charge separation. In the upcoming section of the present chapter, some basic knowledge, experimental methodology and selected efficiency results of the quasi-1D photoelectrode fabricated by different routes is discussed.

8.6 Synthesis Strategies for the Fabrication Quasi-One-Dimensional Thin Films

8.6.1 Hydrothermal/Solvothermal

Hydrothermal synthesis is the most widely and popularly used synthesis technique for the fabrication of nanomaterials nowadays. The term hydrothermal is of geological origin, first used by Sir Rodrick Murchison, a British geologist, who explained the behaviour of water at high temperature and pressure, which can bring changes in the earth crust leading to the formation of rocks and minerals [87]. The synthesis procedure has been defined by Byrappa and Voshimura as any heterogeneous chemical reaction in the presence of an aqueous or non-aqueous solvent above room temperature and pressure greater than 1 atm in a closed system [88]. Based on the solvents used in the system, the technique can be defined as ammono-thermal [89–91], glycothermal [92–94], alcohothermal [95–97], supercritical hydrothermal [98–100], etc. and hence the technique can also be named as solvothermal synthesis. Each parameter employed in this synthesis technique has a specific role in the formation of nanomaterials. The role of temperature is to increase the kinetics of the product formation and thermodynamic stability. Another parameter is pressure which influences the solubility and recrystallization process and stability of the product. Generally, hydrothermal syntheses are conducted without agitation and under isothermal and isobaric conditions.

The general synthesis strategy of the nanomaterials in the powder form by hydrothermal route is already given in detail in other chapters. In the present chapter, we are trying to discuss the extension of this synthesis route for the fabrication of nanostructured thin films on conducting glasses, which can be used as photoelectrodes after calcination at the desired temperature. For fabricating thin films, normally the substrate to be coated is immersed in the solution and kept for hydrothermal reaction. A schematic representation of fabrication of photoelectrodes by hydrothermal route is shown in Fig. 8.8. It is a two-step process, where the first step is the fabrication of amorphous one-dimensional nanorod array at controlled temperature and

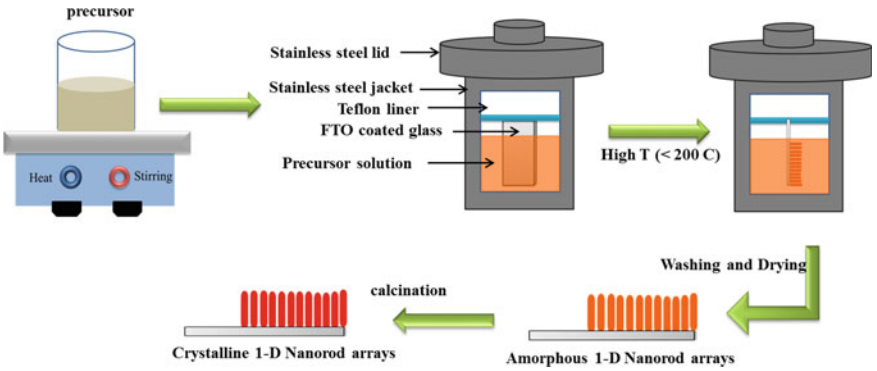

Fig. 8.8 Synthesis steps involved in the fabrication of 1 dimensional semiconductor thin films for photoelectrode preparation by hydrothermal route

pressure, followed by the second step of calcination of the amorphous thin films leading to the formation of photoelectrodes.

A classic example of fabrication of photoelectrodes by hydrothermal route is the synthesis of one-dimensional nanorod arrays of hematite on fluorine doped tin oxide (FTO) glass which was first reported by *Vyssires* et al. in 2000 [101] and later the technique was explored by many researchers for fabrication hematite-based photoelectrodes for solar water oxidation [29, 102, 103]. Cleaned FTO glasses are inserted into Fe precursor a solution with structure directing agent (urea) and kept for hydrothermal reaction [47]. Typically, in the first step of reaction, FeOOH nanorods on FTO/ITO glass are formed at a temperature of ~90 °C, followed by high temperature annealing (550–700 °C) for fabricating crystalline red hematite-based electrode which can be used directly as photoanodes in solar energy conversion devices. The methodology is now widely adopted by various researchers in the field of artificial photosynthesis [102]. Necessary modifications in experimental parameters such as alternative structure directing agents (sodium nitrate) [104], temperature, time of reaction, incorporation of dopants (Ti [102], Sn [105], etc.) are the latest approaches employed to improve the efficiency of the hematite-based photoanodes. Other semiconducting one-dimensional nanostructures such as ZnO [106, 107], TiO_2 [108], and their heterojunctions with Fe_2O_3 are explored using this synthesis technique. Typical surface and cross-sectional morphology of the hematite thin films developed by this route is shown in Fig. 8.9b, c with nanorod diameter of 50 nm and typical length of 500 nm. The photocurrent response of the Fe_2O_3–Fe_2TiO_5 heterojunctions fabricated by hydrothermal route by *Prince* et al. is shown in Fig. 8.9c, d [36]

Numerous studies are available in the literature which discusses the fabrication of photoelectrodes using hydrothermal route. Table 8.1 gives an idea of the variety of Q-1D semiconductors-based photoelectrodes fabricated by hydrothermal method and their typical performance towards water splitting.

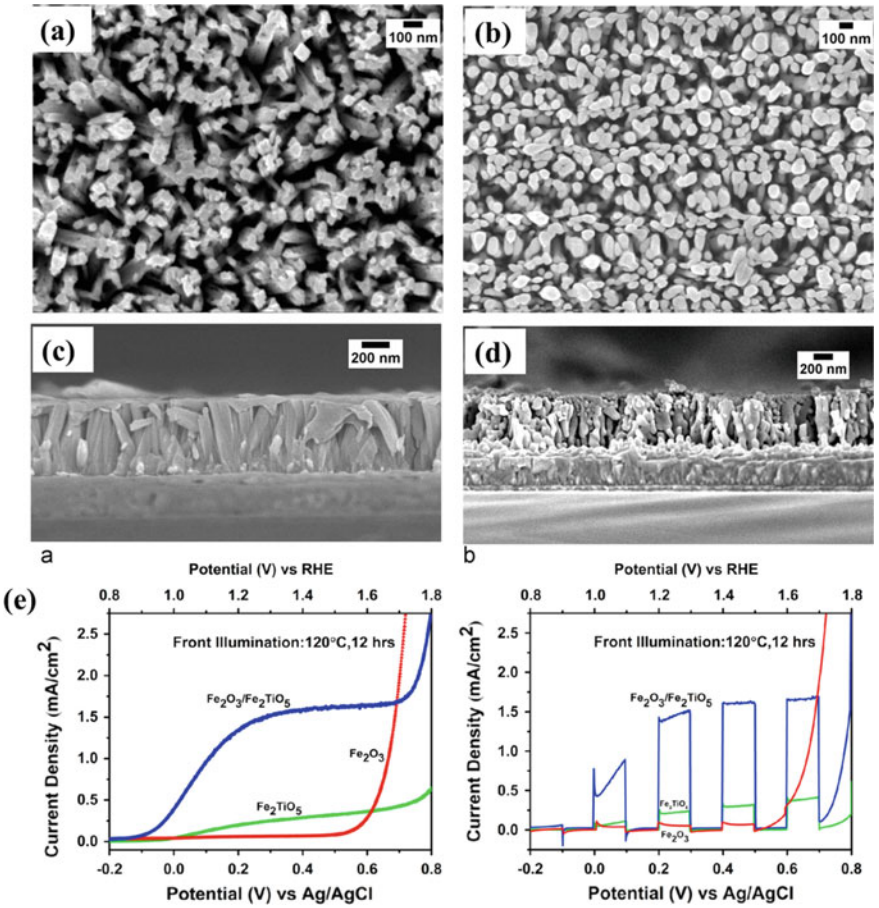

Fig. 8.9 Typical FESEM images showing surface view of the **a** amorphous FeOOH nanowires, **b** Fe_2O_3 nanowires formed after annealing FeOOH nanowires, cross-sectional view of **c** FeOOH nanowires (length ~500 nm) and **d** Fe_2O_3 nanowires fabricated by hydrothermal route and **e** The photocurrent response of Fe_2O_3–Fe_2TiO_5 heterojunctions fabricated by hydrothermal route. Image reproduced with permission from Elsevier [36]

Advantages

1. Easy control of the size and shape of the nanomaterials by changing the temperature, solvent concentration and type, precursor type and time of reaction
2. The synthesis technique can be up scaled to large-scale synthesis.

Disadvantages

1. Expensive autoclaves
2. Careless handling such as uncontrolled temperature, crack in the autoclaves and use of unsuitable solvents can lead to explosion.

Table 8.1 Table showing the PEC performance of photoanodes grown by hydrothermal method

Material	Photocurrent (1.23 V vs RHE)	Electrolyte used	References
Ti-doped-Fe_2O_3 nanorod arrays	0.72	1 M NaOH	Vayssieres et al. [102]
CoPi-modified-Fe_2O_3 nanorod arrays	0.27	1 M KOH	Fu et al. [13]
S-doped hematite nanorod arrays	0.1	1 M KOH	Varghese et al. [109]
Sn-doped-Fe_2O_3 nanorod arrays	~1	1 M NaOH	Annamalai et al. [105]
Single crystalline α-$(Fe_{0.99}Sn_{0.01})_2O_3$	0.74	1 M NaOH	Antony et al. [110]
post-growth Ti doping of a-Fe_2O_3	~0.4	1 M KOH	Franking et al. [12]
Dendritic Au/TiO_2 nanorod arrays	~2.32	1 M KOH	Kong [111]
Ti-doping + oxygen vacancies in hematite	2.25	1 M NaOH	Mor et al. [112]
Flame processed Ti-doped-Fe_2O_3 nanorod arrays	~1.5	1 M NaOH	Macak [113]
Mn-doped hematite nanorod arrays	1.6	1 M NaOH	Gurudayal et al. [47]
Silica encapsulation in Sn doped hematite nanorod arrays	1.36	1 M NaOH	Huan [114]
Low temperature activated Sn-Fe_2O_3 nanorod arrays	0.1	1 M NaOH	Yang [115]
titanium dioxide interlayer that serves as passivation layer and dopant source for hematite (a-Fe_2O_3) nanoarray	2.5	1 M KOH	Luo et al. [34]
Hematite nanorod array in a plasmonic gold nanohole array pattern	~1	1 M NaOH	Hoyer [116]
Ti doped hematite nanorod	2.28	1 M NaOH	Takahashi et al. [117]
α-Fe_2O_3/GIO	0.8	1 M NaOH	Shinde et al. [118]
rutile TiO_2 nanorods	0.5	1 M NaOH	Formhals [119]
Branched TiO_2 nanorods	1	1 M KOH	Mor et al. [108]
TiO_2 Nanorod Arrays Decorated with CdSe	−0.015	0.1 M NaOH	Bang and Kamat [10]
Branched TiO_2 nanoarrays sensitized with CdS quantum dots	4 at 0 V versus RHE (hydrogen generation current)	1 M KOH	Taylor [120]
Branched TiO_2 Nanorods	~1	1 M KOH	Cho et al. [30]

(continued)

Table 8.1 (continued)

Material	Photocurrent (1.23 V vs RHE)	Electrolyte used	References
Fluorine-doped hierarchical porous single-crystal rutile TiO_2 nanorods	0.9	1 M KOH	Han et al. [121]
N-modified TiO_2 nanowire arrays	0.5	1 M KOH	Reneker and Yarin [122]
Rutile TiO_2 nanowires	~0.75	1 M KOH	Hwang et al. [9]
two-dimensional $ZnIn_2S_4$ Nanosheet/one-dimensional TiO_2 Nanorod Heterostructure Arrays	0.6	0.35 M Na_2SO_3 and 0.24 M Na_2S (pH 11.5)	Huang et al. [123]
Fe_2O_3/Fe_2TiO_5 heterojunction nanorods	1.4	1 M NaOH	Bassi et al. [36]
Fe_2TiO_5 nanorods	~0.5	1 M NaOH	Bassi et al. [36]

3. Toxic and corrosive solvents create damage to autoclave
4. Inability to observe the growth of the nanocrystals.

8.6.2 Electrochemical Anodization

Electrochemical anodization is a well-known technique for the fabrication of metal oxide nanotube arrays, mainly of valve metals such as Ti, Al, Si and Zr. Valve metals are the class of metals which allows the current to flow only in one direction (analogy to the rectifying behaviour of a diode). The technique is simple and easy to do in a normal laboratory with the help of a DC power supply which can go up to an applied DC voltage of 60 V. This synthesis method enables one to fabricate self-organized, highly ordered nanotubes arrays having dimensions in the nano-regime with narrow size distribution. For energy conversion applications, TiO_2 nanotube arrays (TNTA) are promising among other quasi-one-dimensional materials because of its straddling band edge positioning with respect to water oxidation and reduction potentials. Though the first report on fabrication of porous TiO_2 is by *Zwilling* et al. [36], synthesis of TNTA by anodization of Ti foil was reported by *Grims* and co-workers [108, 109]. Later optimization of the nanotube lengths, diameter and wall thickness was done by varying the time of anodization, electrolyte concentration and applied potential by various research groups working in this field. The electrolyte composition is an important parameter in the formation of TNTAs. Thus, the discussion on this synthesis method will be mainly based on the TNTA. The experimental setup for the synthesis of TNTA is shown in Fig. 8.10a. A two-electrode system is employed, in which Ti foil or Ti metal coated substrates are used as anode with a counter electrode (cathode, normally Pt foil) kept at specific separation of about 1–2 cm. The electrolyte used for anodization is generally fluoride-based organic/aqueous electrolyte.

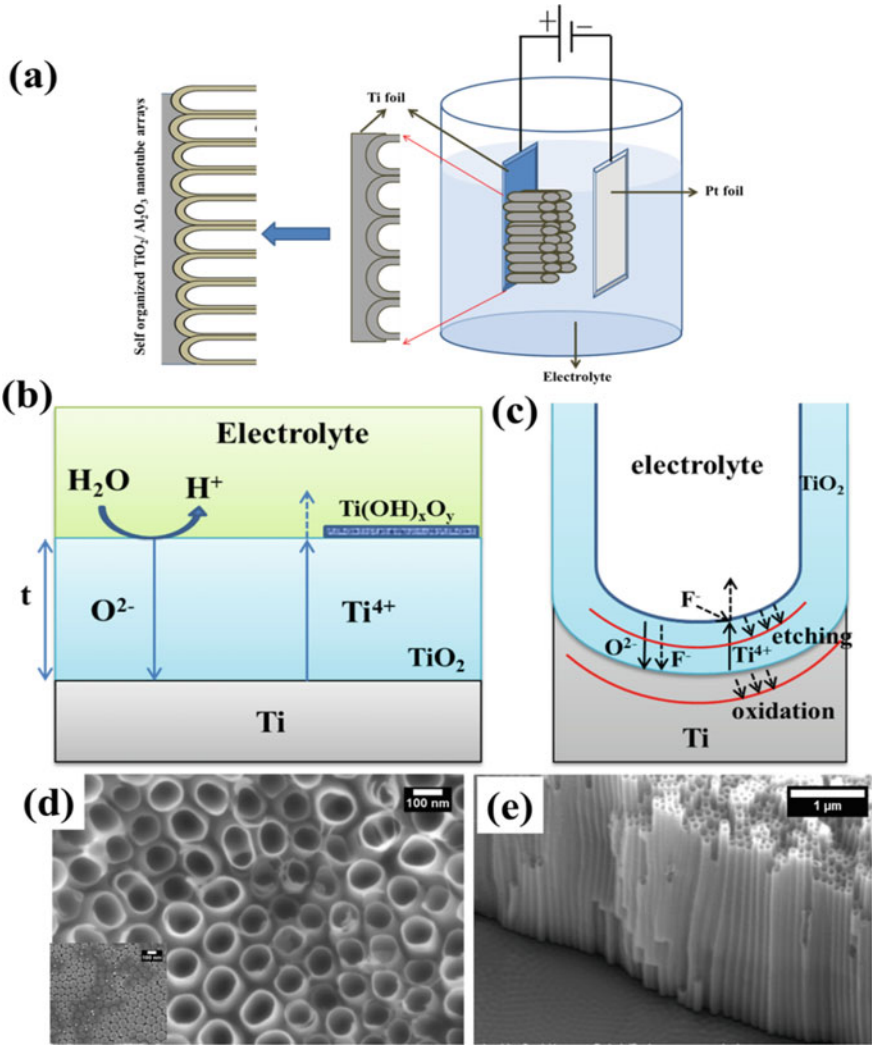

Fig. 8.10 **a** Experimental setup used for electrochemical anodization of valve metals, **b** Oxide formation mechanism of Ti metal under potentiostatic condition, **c** mechanism showing the formation of nanotube in presence of fluoride ion, **d** FESEM image of surface view of TNTA (inset shows the back side view of the TNTA revealing the hemispherical active area and **e** the cross-sectional FESEM view of TNTA showing the self-organized formation of TNTA (the dimples on the Ti metal is clearly visible where imprint of hemispherical area was present)

For this, the basic mechanism behind the formation of TNTAs should be understood first. The formation mechanism of nanotube by anodization in the case of Ti foils is similar to the case of anodic porous alumina. The main processes that occur during electrochemical anodization are the following.

First step is the formation of oxide layer with the help of an external field in the presence of O_2 and OH^- followed by the movement of metal oxide-metal interface layer towards inside of the metal by the reaction of anions formed with the Ti metal. At the same time transfer of Ti^{4+} ions takes place and these move outwards to metal–metal oxide interface and reach the metal oxide-electrolyte interface with the help of an electric field. Thus, oxide formation and chemical dissolution are the two competing processes that are involved in the formation oxide layer on the Ti substrate. The experimental setup and processes involved are schematically represented as in Fig. 8.10a, b. The overall chemical reactions involved are given as follows:

$$2H_2O \rightarrow O_2 + 4H^+4e^- \tag{8.10}$$

$$Ti + O_2 \rightarrow TiO_2 \tag{8.11}$$

The process thus creates a passivation layer on Ti substrate and becomes a corrosion resistant coating. The trend shows a change when anodization is conducted in fluoride containing electrolytes. It is well studied on the behaviour of passivated titanium metal when subjected to fluoride containing electrolyte [110–114]. The stable oxide layer is attacked by the fluoride ions in the electrolyte leading to the formation of $[TiF_6]^{2-}$ complexes in the solution. The chemical reaction is shown as given below.

$$TiO_2 + 6F^- + 4H^+ \rightarrow [TiF_6]^{2-} + 2H_2O \tag{8.12}$$

$$Ti + 6F^- \rightarrow [TiF_6]^{2-} \tag{8.13}$$

Initially, the field assisted attack of fluoride ions on anode occurs locally leading to formation pits in the nanometer scale on the surface. The presence of H^+ and F^- ions increases the chemical dissolution current density. Consequently, the applied field is equally shared by the pores formed and continuous growth of the pore is assisted by an equifield mechanism. Thus, the hemispherical area becomes the active site for the oxide formation and chemical dissolution. At equilibrium, the rate of oxide formation and chemical dissolution will be same and continuous growth of nanotube will occur towards the metal oxide-metal interface. The pictorial representation of the formation of nanotube arrays, where an equifield hemispherical active area plays a major role is shown in Fig. 8.10c. This behaviour is generally inferred from the current density transient recorded during the anodization. During the commencement of the reaction, the current density recorded as a function of time (constant potential) is high as the metal substrate is exposed to the electrolyte with a constant potential applied between the electrodes Ti metal reacts with oxygen and hydroxyl ions leading to the formation

oxide layer on the metal and thus a drastic decrease in the current density. Thereafter, there is a competition between the field assisted oxidation and dissolution and due to this a hump is visible in the current density transient. When equilibrium is attained the current density becomes constant and thus indicating continuous formation of nanotubes. The surface, bottom and cross-sectional views of the nanotube arrays thus prepared are shown in the FESEM images given in Fig. 8.10d, e. The potential window applied for the formation of nanotubes by anodization also depends on the electrolyte employed.

Numerous reports are available in the literature where photoelectrode made of electrochemical anodization route is investigated for its water oxidation activity. Nanotube arrays of oxides of valve metals have used as photoanodes in solar water oxidation among which the most commonly used are TiO_2, WO_3, Ta_2O_5 and Fe_2O_3 nanotube arrays. Selected results are tabulated in Table 8.2 where the achieved photocurrent values are listed for each type of photoanodes employed.

Advantages

1. Simple and highly reproducible with the same quality of metal foils
2. Dimensions of the self-organized arrays can be tuned by changing the anodization parameters
3. Utilization of cost-effective electrolyte.

Disadvantages

1. The technique cannot be applied for the synthesis of all metal oxide nanotubes
2. Peeling off of the nanotube is observed when anodized for longer time and during sonication for longer time.
3. Though the synthesis of nanotube arrays is pretty easy by anodization process, the film transfer to a transparent substrate is a tedious procedure when it comes to device application.
4. Fabrication nanotube arrays by anodization of Ti thin films on conducting glass are a challenge as the process involves deposition of Ti layer on conducting substrates, anodization od deposited films till all the Ti reacts to form TNTA. A problem observed in this case is the peeling of the Ti metal coating during anodization and incomplete oxidation of Ti metal at the conducting glass-metal interface leading. The peeling off issue should be addressed by selecting a deposition technique which can produce an adhesive metal thin film on FTO/ITO glasses.

8.6.3 Electrodeposition

The electrodeposition technique is a process by which single/composite thin films can be fabricated on to preferred substrates by means of electrical energy. The process is carried out either in a two-electrode or a three-electrode configuration.

Table 8.2 Table showing the water oxidation activity of the photoelectrodes fabricated by electrochemical anodization technique

Material	Photocurrent (1.23 V vs RHE)	Electrolyte used	References
TiO_2 nanotube arrays	5	1 M KOH	Shankar et al. [8]
N doped TiO_2 nanotube arrays	~0.3	1 M KOH	Choi et al. [131]
Micron-Length Highly-Ordered Titania Nanotube Arrays	30	1 M KOH	Shankar et al. [8]
Black TiO_2 nanotube arrays	~3.5	1 M NaOH	Zhang et al. [132]
Reduced TiO_2 nanotube arrays	0.73	1 M NaOH	Kang et al. [11]
hierarchical TiO_2 nanotube arrays	1.59	1 M KOH	Bedford and Steckl [133]
Plasmonic Gold Nanocrystals Coupled with Photonic Crystal on TiO_2 Nanotube	~2	1 M KOH	Lepcha et al. [134]
Vertically Aligned WO_3 Nanowire Arrays	1.43	0.1 M Na_2SO_4	Mao et al. [135]
2 electrode system ($TiO_{2-x}C_x$ Nanotubes as anode and Pt/TiO_2 Nanotubes as a Cathode	2–2.8 at −0.4 V versus AgAgCl	1 KOH	Croce et al. [136]
Sulphur treated TiO_2 nanotube arrays	2	0.1 M KOH	Einert et al. [137]
multi-anodized TiO_2 nanotube arrays	~5	0.5 M KOH	Jung et al. [138]
p-type Zn-doped a-Fe_2O_3 nanotube arrays	0.04	1 M NaOH	Qi et al. [25]
Self-Assembled Hematite (r-Fe_2O_3) Nanotube Arrays	<0.1	1 M NaOH	Saveh-Shemshaki et al. [139]
Ultrathin r-Fe_2O_3 Nanotube Arrays	~1	1 M NaOH	Sander and Tan [140]
L-cysteine @ Fe_2O_3 nanostructure	~8	1 M NaOH	Lee et al. [141]
Ta_3N_5 Nanorod Arrays	~4	0.5 M Na2SO4	Han et al. [142]
W-doped Ta_2O_5 nanotube arrays	~1	1 M KOH	Li et al. [143]
Porous Ta_3N_5 nanotubes	7	0.1 M $K_4[Fe(CN)_6$ and 0.1 mM $K_3[Fe(CN)_6]$(pH = 7.5)	Kim et al. [144]

(continued)

Table 8.2 (continued)

Material	Photocurrent (1.23 V vs RHE)	Electrolyte used	References
TaON nanotube arrays	~2	1 M KOH	Kim et al. [145]
Ta_3N_5 Nanotube Photoanodes with subnitrides	~6	1 M KOH	Yoon et al. [146]
Hybrid tungsten trioxide-titanium dioxide (WO_3-TiO_2) nanotube	2	1 M KOH	Lai and Sreekantan [22]
Hierarchical WO_3–TiO_2 nanotube arrays	0.6	1 M NaOH	Shi et al. [147]
Anodically Grown WO_3 Electrodes	8	1 M H_2SO_4	Cristino et al. [20]

Figure 8.11 shows a schematic of an electrodeposition system which utilizes 3-electrode systems for fabricating nanostructured thin films. The substrate normally used as the working electrode will be conducting glasses (FTO/ITO), conducting

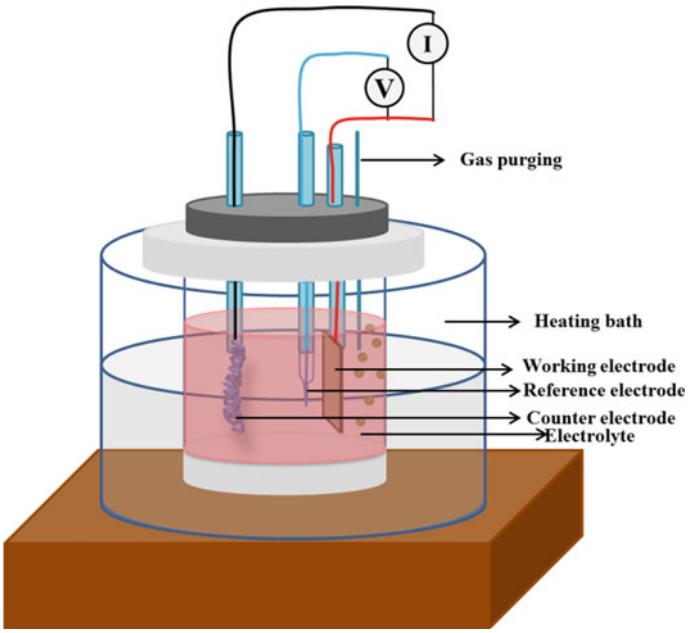

Fig. 8.11 Schematic presentation of electrodeposition setup used for the fabrication of nanostructured thin films

plastics, metal coated glass substrates and metallic substrates. Different electrochemical techniques such as pulse electrodeposition, chronoamperometry, chronopotentiometry and cyclic voltammetry are employed for the synthesis through this route. The salt solution of the metal to be deposited is generally used as the electrolyte. The substrates used for fabricating Q-one-dimensional structures can be template-assisted electrodeposition where a template like anodic alumina is used or a template-less deposition where intrinsic anisotropic crystallographic structure of the target material can be utilized. Fabrication of the one-dimensional metal oxide nanostructures using template assisted electrodeposition can be achieved by removal of the template followed by annealing under oxygen rich atmosphere to convert the metal to metal oxide. Direct oxide deposition is also achieved by the electrodeposition route [115–117].

When electrodeposited photoelectrode are used for solar water oxidation nanoporous $BiVO_4$ photoanodes are the classic example of electrodes fabricated by electrodeposition route, which was reported for the very first time *Choi*'s research group in 2014 [17]. The anodes showed a typical photocurrent density of ~2.5 $mAcm^{-2}$ at an applied bias of 1.23 V in 0.5 M Na_2SO_4. *Shinde* and co-workers fabricated hierarchical hematite (α-Fe_2O_3) nanopetals-based photoelectrodes by pulse reverse electrodeposition and demonstrated the solar water oxidation activity [118].

The advantages of these techniques are as follows:

1. Low cost
2. Environmentally friendly
3. Low energy consumption
4. Easy to handle
5. High growth rate at low temperatures
6. Good control over the film thickness, size and shape of the nanostructures.

Disadvantages

1. Substrate adhesion is an issue
2. Not all metal oxides can be fabricated by this route.

8.6.4 Electrospinning

Electrospinning is an alternative and efficient technique to fabricate one-dimensional nanostructures, mainly nanofibers and nanotubes. The first electrospinning apparatus is demonstrated by *A. Formhals* and later it was patented in 1929 [119]. Thereafter in 1960s *G Taylor* presented research findings, explaining the physics involved in the electrospinning process [120]. In 2000s, *Reneken and Yarin* made investigations on electrospinning polymer solution and clarified the theory behind the formation of such fibres [121, 122]. Later this idea was transferred to other materials and their derivatives such as carbon fibres and inorganic nanowires, nanofibres and nanotubes [123, 124]. A schematic representation of the electrospinning unit is given

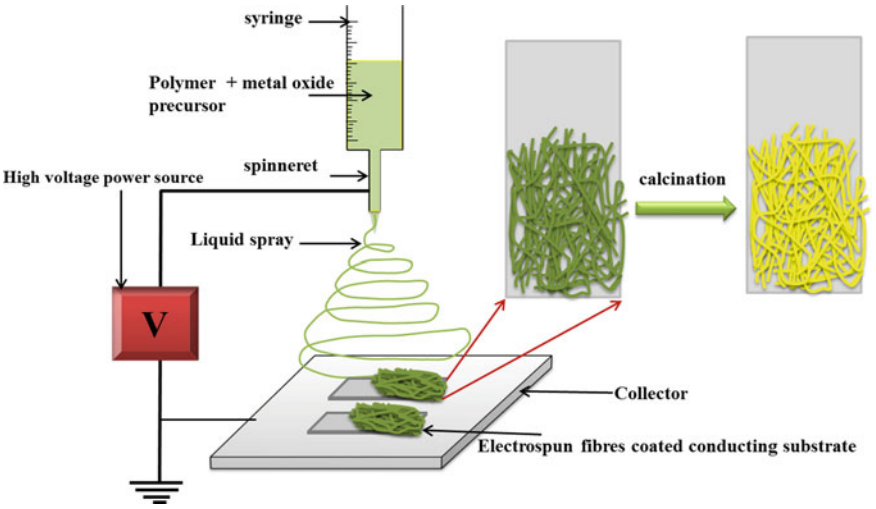

Fig. 8.12 **a** Schematics of the instrumentation setup used for electrospinning of polymers, metal oxides and carbon fibres, **b** typical SEM image of the metal oxide nanowires fabricated by electrospinning and **c** Carbon nanofibers fabricated by electrospinning followed by Ar annealing

in Fig. 8.12. The instrument for electrospinning consists of three main units (a) a high voltage power supply, (b) solvent dispensing syringe with metallic needle and (c) a grounded collector. For the fabrication of electrospun fibres, high molecular weight polymers generally poly vinyl pyrollidone (PVP) [18], polyvinyl alcohol (PVA) [125] and poly vinyl acetate [126] are used for preparing viscous solvent which will be filled in the syringe connected to the metallic needle. The needle is connected with the one lead, and the counter lead is connected to the grounded collector which is normally aluminium foils or any other conducting substrates selected based on the application of interest. In the case of preparation of photoelectrode, normally FTO/ITO coated glass substrates or heavily doped silicon substrates are employed. A high voltage, typically in the range of a few kV to 30 kV, is applied using the high voltage power supply. When a high voltage is applied to the viscous solution, the electric field is generated between the spinneret (metallic needle) and the collector. Consequently, a droplet is formed at the tip of the needle and when the electrostatic force overcomes the surface tension of the viscous liquid, the droplet is deformed to a Taylor cone and start emitting the liquid in the form of a jet from the needle tip. Due to the electric field and the surface tension effect, the jet stream starts whipping and the solvent dries subsequently. This lead to the formation of fine fibres having diameter varying from few micrometres to nanometres deposited on the conducting collector. The diameter of the electrospun fibres depends on the viscosity of the solution used and is experimentally confirmed by *Baumgarten* [127] and *He* [128] and the relation is given by the following Eq. (8.14)

$$d \approx \eta^{0.5} \tag{8.14}$$

Similarly, the diameter of the fibres formed is also dependent on the applied potential as given below

$$d \approx E^{-0.5} \tag{8.15}$$

These electrospun nanostructures find wide application in the field of sensors [162, 163], drug delivery [164], medical implants [165], environmental cleaning [166], energy conversion [18, 63, 167] and storage applications [168, 169]. Coming back to artificial photosynthesis point of view, the electrospun one-dimensional semiconductor-based nanostructures have shown promising improvement in the performance when used as photocatalyst and photoelectrodes. Recently, the electrospinning technique was adopted to fabricate the hematite hollow nanofibers-based photoanodes by *Einert* and co-workers [170] using PVP as sacrificial polymer demonstrating a photocurrent density of 3.4 μAcm^{-2}. Fabrication of $BiVO_4$ photoanodes by electrospinning approach is another effort done by various researchers. Nanoporous Mo-$BiVO_4$ photoanodes are by fabricated by *Antony* et al. and investigated the effect of doping and porosity in improving the charge separation and hole diffusion length [18]. Similarly, *Jung* et al. fabricated Mo-$BiVO_4$ photoanodes by electrospinning route and a photocurrent of ~0.175 $mAcm^{-2}$ is reported for the best sample [171]. Recently, nanostructured g-C_3N_4/$BiVO_4$ composite films were prepared by Wang and co-workers and demonstrated the photoelectrochemical characteristics with an excellent improvement in water oxidation performance on C_3N_4 loading [19]. In the case of hematite systems, very few reports are available where electrospinning route is adopted as a technique to fabricate hematite photoanodes for solar water oxidation. Si and Ti doped hematite nanostructured films are fabricated by *Santangelo* et al. and PEC water oxidation performance was investigated [63]. Mesoporous functional hematite nanofibrous photoanodes were fabricated and the photocurrent density was reported to 0.55 $mAcm^{-2}$ with a light intensity of 900 $mWcm^{-2}$ [172]. An improved PEC water oxidation activity was observed for electrospun ZnO/TiO_2 nanostructures [158]. Electrospun black titania nanofibers showed a water oxidation activity with photocurrent of 0.2 $mAcm^{-2}$ at 1.23 V versus RHE [167].

Advantages

1. Complex hierarchical structures can be fabricated
2. Tuning of the nanofiber diameters is possible by optimizing the solvent and instrument parameters
3. Can be used for large-scale synthesis of one-dimensional nanostructures
4. Can make high aspect ratio and large surface area materials
5. Nanostructures will have narrow size distribution
6. Simple and cost-effective technique
7. Highly reproducible.

Disadvantages

1. Usage of variety of polymers and solvents are limited
2. Sometimes the metal oxides nanofibers are brittle after calcination process which limits the performance
3. Inferior performance of the filters fabricated by electrospinning technique
4. Inefficiency in fabricating nanostructures with dimensions less than 20 nm.

8.6.5 Template Assisted (TA) Growth

Template assisted growth is another promising route commonly adopted for the fabrication of one-dimensional ordered arrays. Different types of inorganic and organic templates are explored to this end, and anodized alumina membranes (AAM) and etched polycarbonate membranes are the most commonly used as templates for growing one-dimensional structures. Other templates which are used for the synthesis of one-dimensional structure are electrochemically etched silica and mesoporous materials [173–175]. Fabricating one-dimensional arrays using AAM is known as a hard-templating route wherein there is a good control over composition, size and dimensions of the nanostructures. The technique is generally combined with electrodeposition, atomic layer deposition (ALD), thermal decomposition and chemical vapour deposition. Polystyrene beads and life radiation track etched polycarbonate membranes are another class which comes into the soft template category and is relatively flexible for fabricating inverse opal semiconductor photoelectrode structures [176]. This type of fabrication is generally termed as opal template assisted nanostructure growth. In this, controlled and uniform deposition of colloidal particles is employed leading to highly ordered and close-packed multi-layered films. The deposition is normally conducted either by dip coating or a spin coating route. These films now can be used as templates for growing semiconductor nano architectures. Generally, polystyrene (PS) beads are used for the preparation of soft templates and the substrates used are FTO/ITO-based conducting glasses and Si substrates which are the most common substrates used for the fabrication of photoelectrodes.

The photovoltaic activity of periodically aligned ZnO hemisphere crystals was studied *Kim* et al. and was fabricated by photolithographic TA growth [177]. *Kim* et al. studied the photoelectrochemical activity of vertically aligned Cu_2ZnSnS_4 nanorod arrays fabricated by TA route [178]. Similarly, TA method was adopted for fabricating photoelectrode which includes hematite [179, 118, 180], $BiVO_4$ [181] and CIGS [178]-based system (Fig. 8.13).

Advantages

1. Easy fabrication of one-dimensional nanostructured arrays and porous nanostructured assembly
2. Good control over the dimensions by using templates having different diameter and length
3. The technique can be hyphenated with high temperature synthesis technique due to the high temperature stability of AAM.

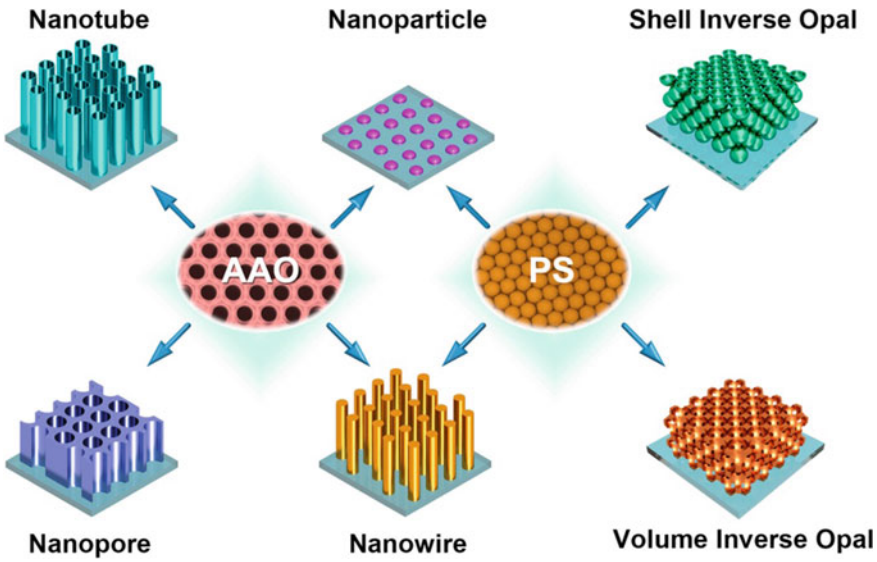

Fig. 8.13 Schematic illustration of template-assisted fabrication of nanostructured materials based on anodized aluminium oxide (AAO) and self-assembled opal templates. Reproduced with permission from Elsevier. Copyright 2015 [182]

Disadvantages

1. Difficulty in removing the templates selectively after synthesis
2. Low yield of materials
3. Predominantly polycrystalline materials are synthesized by this technique.

8.6.6 Chemical Vapour Deposition

Chemical vapour deposition is a well-known technique, which involves the conversion of gaseous molecules to solid form possessing different dimensions. The technique basically involves different steps and as listed as follows:

1. Introduction of reactant gas molecules in combination with inert gas into the reaction chamber, where the substrate to be deposited is situated
2. Mass transfer of the reactants to the substrate from the main flow region
3. Adsorption of the molecules on the reaction site of the substrate
4. Reaction, nucleation and growth of the one-dimensional structures by reaction among the molecules to form an array in the form of thin film
5. Desorption of the by-products from the reaction
6. Flushing the inert gas and removal of the unreacted gaseous products and by-products from the reaction chamber.

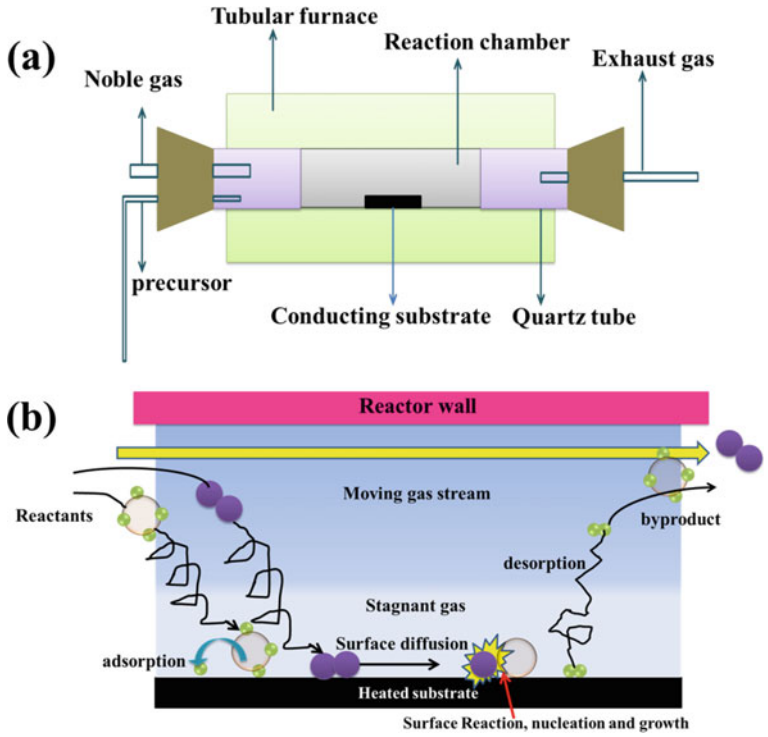

Fig. 8.14 **a** Schematic of instrumental setup for CVD reaction and **b** pictorial representation of mechanism involved in conventional CVD reaction

The pictorial representation of the CVD synthesis process and the mechanism involved is shown in Fig. 8.14a, b [183]. Generally, volatile reactant mixtures are placed in the reaction chamber, where a controlled release is ensured using a mass flow controller. Crystallinity of the material is achieved by heating the substrate to the desired temperature during the course of deposition. Highly oriented and high quality one-dimensional structured thin films can be achieved using CVD technique. Using hard template such as AAO is a simple and straight forward approach to fabricate one-dimensional nanostructure [184, 185]. In this case, the template should be kept as the substrate to be deposited and after CVD growth, the template is etched out by suitable chemical process. Another approach is to initiate the nucleation and growth by means of a catalyst. This technique is classified based on the phases involved in the reaction process and is defined as vapour–liquid–solid growth (VLS), solution-liquid–solid growth (SLS) or vapour–solid growth (VS) [183]. In both these cases usually, metal nanoparticle is used as the nucleation catalysts and the semiconductor to be grown are introduced in the vapour phases. The size of the metal nanoparticle decides the diameter of the nanowire grown. A large variety of materials can be fabricated using different forms of CVD techniques for wide range of applications.

The variations of CVD technique includes plasma enhanced CVD (PECVD), metal organic CVD (MOCVD), laser induced CVD (LICVD), ALD, etc.

CVD technique is successfully employed to fabricate Q-one-dimensional thin film photoelectrodes for AP device. Nanostructured anatase–rutile TiO_2 heterojunctions-based photoelectrodes are fabricated using pulsed pressure MOCVD technique, and the most active samples were reported to have a photocurrent density of ~1.2 $mAcm^{-2}$ at 1.23 V versus RHE [37]. A direct liquid injection CVD method was adopted by Archana and co-workers to fabricate $BiVO_4$ thin film photoelectrode to use as photoanode [186].

Advantages

1. Uniform step coverage
2. Good control over structure and composition as the stoichiometry of the formed material is controlled by control on the flow rate of the precursor
3. Good reproducibility
4. Epitaxial film formation and ability to fabricate abrupt junctions
5. The pressures in CVD allows to grow three dimensional structures with large aspect ratios
6. Higher deposition rate due to higher flow rates
7. Simple and can be scaled up to several substrates
8. Ultra-high vacuum is not necessary
9. Change in the type of precursor is easy
10. High purity films can be prepared.

Disadvantages

1. High temperature
2. CVD precursors are often hazardous and toxic and hence the deposition process may involve evolution of toxic and corrosive gases
3. The precursors need to be volatile at room temperature
4. Some metal organic precursors used as CVD precursors are very expensive
5. Complex processes
6. The films are usually deposited at high temperatures in some derivatives of the CVD and hence the type of substrate which can be used in CVD process is restricted. Also, difference in thermal expansion coefficient of materials can lead to stress in the films deposited thereby causing a mechanical instability in the film.

8.6.7 Atomic Layer Deposition

Atomic layer deposition technique also known as atomic layer epitaxy (ALE) or atomic layer chemical vapour deposition (ALCVD) is an advanced synthesis technique for the fabrication of nanostructured thin films for applications such as PEC [9, 187, 188], photovoltaics [189] and electrocatalysis [190–193]. For fabrication

of thin films by ALD route, different steps are involved similar to the conventional CVD process. The schematic representation of the ALD growth of the nanostructures is shown in Fig. 8.15. In the first step of ALD process, excess of precursor A is introduced into the reaction chamber where the substrate to be deposited is situated. Chemisorption of A at the surface, till a monolayer formed is the second step. Excess of A is removed by an inert gas purging during the third step. Thereafter precursor B is introduced for the adsorption and chemical reaction with adsorbed precursor A (step 4). Finally, in step 5 the unreacted precursors and the by products are flushed out by inert gas leaving an ALD coated thin film on the desired substrate. In contrast to CVD technique, in the case of ALD, when one monolayer is formed, adsorption of precursor is stopped. Thus, the growth of the thin film is independent of the precursor pulse time. Other conditions to be satisfied in ALD technique are.

1. Precursor should be stable at the decomposition temperature, in order to prevent the decomposition of the film formed after chemisorption.
2. Reaction rates should be very high to avoid long saturation pulse time.

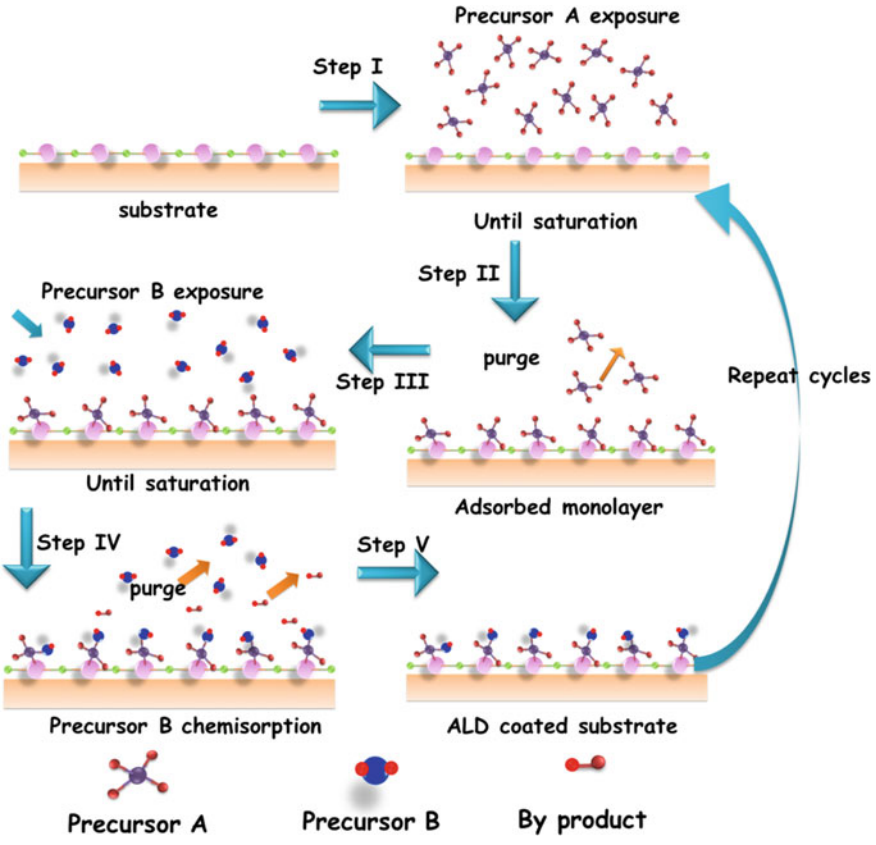

Fig. 8.15 Typical synthesis steps involved in Atomic Layer Deposition technique

The technology is now widely used in the manufacture of novel thin films of metal oxides, as well as passivation layer for minimizing the surface state recombination in photovoltaic and photoelectrochemical water splitting. In 2008 *Hammann* et al. developed ALD coated TiO_2 on templated substrate and proved the ability of same as photoanode in DSSC [189]. WO_3 nanostructured thin film electrodes was fabricated by Liu et al. using ALD technique which demonstrated efficient solar water oxidation performance [194]. APCVD grown quasi-one-dimensional nano structures of hematite could generate a photocurrent up to 2.3 $mAcm^{-2}$ at 1.23 V versus RHE, is a new bench mark material developed by *Graetzel* and co-workers, and is a highly efficient photoanode developed by this route [15] (Fig. 8.16a, b). Later, numerous researches have been carried out to study the physic chemical processes behind ALD fabricated photoelectrodes. Ultrathin hematite photoanodes were fabricated by *Klahr* and colleagues to study the effect in solar water oxidation and physico-chemical processes behind that [189]. Plasma enhance ALD route was adopted by *Kot* et al. to

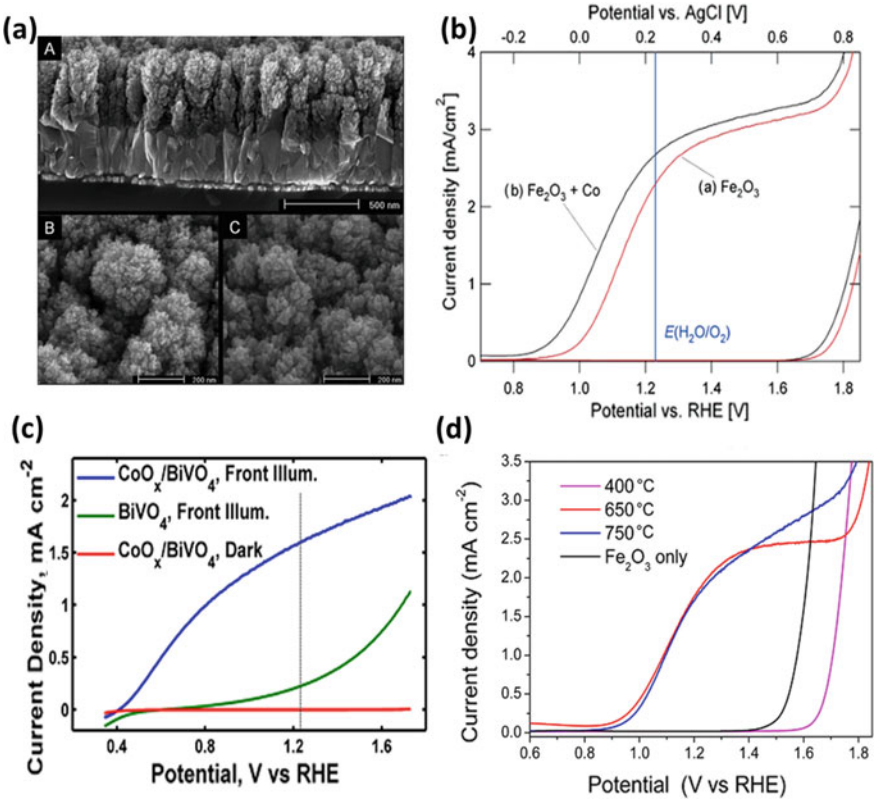

Fig. 8.16 **a** cross-sectional and surface view of ALD grown thin film [15], **b** the PEC response of ALD grown films[15], **e** CoO_x catalyzed $BiVO_4$ photoanode [196] and **f** ultrathin TiO_2 layer on hydrothermally grown hematite photoanode [191]. Reproduced with permission from American chemical society. Copyright 2015

fabricate titanium oxynitride films which is a promising candidate as photoanode in AP device [195]. Lin and co-workers use ALD route to fabricate p-type hematite and successfully introduce n-p junction in hematite films for an improved water oxidation performance [187]. ALD technique is also used as an efficient route to passivate the photoanodes to minimize the surface recombination of charge carriers. ALD-coated passivation layer of ZnO–TiO_2 on CuO nanofiber was developed by *Kim* et al. and the hydrogen evolution current density was up to -4.1 $mAcm^{-2}$ [48]. The coating served the role of both co-catalysts as well as a protecting layer for CuO. Ultrathin Al_2O_3 coating on hematite single crystals are deposited using ALD technique by *Jiao* et al. and the photoelectrochemical was improved with respect to water oxidation onset potential and photocurrent compared to pristine hematite electrode [86]. Cobalt oxide catalytic layer on $BiVO_4$ photoanode was deposited by ALD route by *Lichterman* and co-workers [196]. The resultant ALD-CoO_x/$BiVO_4$ assembly showed an improved PEC performance compared to the pristine $BiVO_4$ photoanode (Fig. 8.16c). *Li* and co-workers used ALD technique to coat ultrathin TiO_2 layer on hydrothermally grown hematite photoanode which showed a better charge separation and an improvement in the photocurrent. Their studies also revealed that the role of thickness of ALD coating in minimizing the charge recombination through a surface state intermediate charge transfer process (Fig. 8.16c) [191].

Advantages

1. Nanometer level control over film thickness
2. Low defect density of the films fabricated
3. Excellent repeatability for the thin films fabricated
4. Good control over the heterojunctions, doping and multilayer processes
5. Excellent adhesion of the thin films.

Disadvantages

1. The ALD precursors are generally costly and storage needs expensive set up
2. Limited precursors are available due to reactivity
3. Longer processing time to fabricate thin films
4. The substrate size with this technology is limited to $15 \times 15 \times 15$ cm
5. Not every material can be coated with this technique
6. Thermal decomposition of the precursor is allowed.

8.7 Conclusions and Future Scope

Artificial photosynthesis is an important field of research which utilizes earth abundant sunlight and water for energy conversion process, to satisfy the future requirement where humankind will have a crucial dependence on natural and renewable energy resources. The concept of utilizing artificial material especially earth abundant semiconducting materials for energy conversion in the form of photoelectrodes for water splitting is a promising route to achieve this. When the photoelectrodes are

in the nanostructured form especially in the Q-one-dimensional structure it attains excellent enhancement in the device efficiency. However, the efficiency of the devices using these materials is not yet to the commercialization level, and hence extensive researchers is being carried out all over the world to come up with an efficient device. This chapter tried to give a brief insight of the different strategies for the synthesis of Q-one-dimensional materials which are commonly adopted to reduce the cost of the materials and can stand as a collective reference for beginners or young researchers to improve their knowledge on synthesis methods used in this field. Elaborate schematics and images have been included to provide the readers a visual feel on the appearance of the nanostructures as well as the various steps involved in the different nanostructure fabrication processes. Most of the techniques described in the chapter, except advanced technologies like ALD and CVD (which are generally available only in research institutes or manufacturing industries), can be adopted in college or university level experiments for the fabrication of photoelectrodes.

Acknowledgements Authors acknowledge Dr. Bevita K Chandran, Research fellow NTU Singapore, for her involvement in pointing out and correcting the discontinuity, technical errors and grammatic mistakes in the book chapter at its different stages of preparation. Author is thankful to Mr Rajendra Vikhram Singh, SO/C, Chemistry Division, BARC, for his help in correcting subsections of book chapter.

References

1. Su J, Vayssieres L (2016) A place in the sun for artificial photosynthesis? ACS Energy Lett 1:121–135
2. Bard AJ, Fox MA (1995) Artificial photosynthesis: solar splitting of water to hydrogen and oxygen water splitting. Acc Chem Res 28:141–145
3. Liu C, Dasgupta NP, Yang P (2014) Semiconductor nanowires for artificial photosynthesis. Chem Mater 26:415–422
4. Gust D, Moore TA, Moore AL (2009) Solar fuels via artificial photosynthesis. Acc Chem Res 42:1890–1898
5. Gratzel M (1981) Artificial photosynthesis: water cleavage into hydrogen and oxygen by visible light. Acc Chem Res 14:376–384
6. Abe R (2010) Recent progress on photocatalytic and photoelectrochemical water splitting under visible light irradiation. J Photochem Photobiol C Photochem Rev 11:179–209
7. Sivula K, Van De Krol R (2016) Semiconducting materials for photoelectrochemical energy conversion. Nat. Rev. Mater. 1
8. Shankar K et al (2007) Highly-ordered TiO_2 nanotube arrays up to 220 um in length: Use in water photoelectrolysis and dye-sensitized solar cells. Nanotechnology 18
9. Hwang Y, Hahn C, Liu B, Yang P (2012) Photoelectrochemical properties of TiO_2 nanowire arrays: a study of the dependence on length and atomic layer deposition coating. ACS Nano 6:5060–5069
10. Bang JH, Kamat PV (2010) Solar cells by design: photoelectrochemistry of TiO_2 nanorod arrays decorated with CdSe. Adv Funct Mater 20:1970–1976
11. Kang Q et al (2013) Reduced TiO_2 nanotube arrays for photoelectrochemical water splitting. J Mater Chem A 1:5766
12. Franking R et al (2013) Facile post-growth doping of nanostructured hematite photoanodes for enhanced photoelectrochemical water oxidation. Energy Environ Sci 6:500–512

13. Fu L, Yu H, Zhang C, Shao Z, Yi B (2014) Cobalt phosphate group modified hematite nanorod array as photoanode for efficient solar water splitting. Electrochim Acta 136:363–369
14. Kment S et al (2017) Photoanodes based on TiO_2 and α-Fe_2O_3 for solar water splitting—superior role of 1D nanoarchitectures and of combined heterostructures. Chem Soc Rev 46:3716–3769
15. Cesar I, Kay A, Martinez JAG, Grätzel M (2006) Translucent thin film Fe_2O_3 photoanodes for efficient water splitting by sunlight: nanostructure-directing effect of Si-doping. J Am Chem Soc 128:4582–4583
16. McDonald KJ, Choi K-S (2012) A new electrochemical synthesis route for a BiOI electrode and its conversion to a highly efficient porous $BiVO_4$ photoanode for solar water oxidation. Energy Environ Sci 5:8553
17. Kim T, Choi KS (2014) Nanoporous $BiVO_4$ photoanodes with dual-layer oxygen evolution catalysts for solar water splitting. Science 343:990–994
18. Antony RP et al (2016) Electrospun Mo-$BiVO_4$ for efficient photoelectrochemical water oxidation: direct evidence of improved hole diffusion length and charge separation. Electrochim Acta 211:173–182
19. Wang Y, Sun J, Li J, Zhao X (2017) Electrospinning preparation of nanostructured g-C_3N_4/$BiVO_4$ composite films with an enhanced photoelectrochemical performance. Langmuir 33:4694–4701
20. Cristino V et al (2011) Efficient photoelectrochemical water splitting by anodically grown WO_3 electrodes. Langmuir 27:7276–7284
21. De Tacconi NR et al (2006) Nanoporous TiO_2 and WO_3 films by anodization of titanium and tungsten substrates: influence of process variables on morphology and photoelectrochemical response. J Phys Chem B 110:25347–25355
22. Lai CW, Sreekantan S (2013) Preparation of hybrid WO_3-TiO_2 nanotube photoelectrodes using anodization and wet impregnation: improved water-splitting hydrogen generation performance. Int J Hydrogen Energy 38:2156–2166
23. Hilliard S et al (2017) Mesoporous thin film WO_3 photoanode for photoelectrochemical water splitting: a sol–gel dip coating approach. Sustain Energy Fuels 1:145–153
24. Janáky C, Rajeshwar K (2017) Current trends in semiconductor photoelectrochemistry. ACS Energy Lett 2:1425–1428
25. Qi X, She G, Wang M, Mu L, Shi W (2013) Electrochemical synthesis of p-type Zn-doped α-Fe_2O_3 nanotube arrays for photoelectrochemical water splitting. Chem Commun 49:5742
26. Han N, Ho JC, Wang F (2011) One-dimensional nanostructured materials for solar energy harvesting. Nanomater Energy 1–14
27. Wheeler DA, Wang G, Ling Y, Li Y, Zhang JZ (2012) Nanostructured hematite: synthesis, characterization, charge carrier dynamics, and photoelectrochemical properties. Energy Environ Sci 5:6682
28. Zhang Z, Senz S (2013) One-dimensional semiconductor nanostructure growth with templates. Wiley 1–18
29. Bassi PS, Chiam SY, Barber J, Wong LH (2014) Hydrothermal grown nanoporous iron based titanate, Fe_2TiO_5 for light driven water splitting. ACS Appl Mater Interfaces 6(24):22490–22495
30. Cho I, Chen Z, Forman A, Kim D, Rao P, Jaramillo T, Zheng X (2011) Branched TiO_2 nanorods for photoelectrochemical hydrogen production. Nano Lett 11:4978–4984
31. Bhat SSM, Jang HW (2017) Recent advances in bismuth-based nanomaterials for photoelectrochemical water splitting. Chemsuschem 10:3001–3018
32. Li Y, Nagato K, Delaunay J-J, Kubota J, Domen K (2014) Fabrication of highly ordered Ta_2O_5 and Ta_3N_5 nanorod arrays by nanoimprinting and through-mask anodization. Nanotechnology 25:014013
33. Sun X, Li Q, Jiang J, Mao Y (2014) Morphology-tunable synthesis of ZnO nanoforest and its photoelectrochemical performance. Nanoscale 6:8769–8780
34. Luo Z, Wang T, Zhang J, Li C, Li H, Gong J (2017) Dendritic hematite nanoarray photoanode modified with a conformal titanium dioxide interlayer for effective charge collection. Angew. Chemie - Int. Ed. 56:12878–12882

35. Ye L, Wang D, Chen S (2016) Fabrication and enhanced photoelectrochemical performance of MoS_2/S-Doped g-C_3N_4 heterojunction film. ACS Appl Mater Interfaces 8:5280–5289
36. Bassi PS, Antony RP, Boix P, Fang Y, Barber J, Wong LH (2016) Crystalline Fe_2O_3/Fe_2TiO_5 heterojunction nanorods with efficient charge separation and hole injection as photoanode for solar water oxidation. Nano Energy 22:310–318
37. Gardecka A, Bishop C, Lee D, Corby S, Parkin I, Kafizas A, Krumdieck S (2018) High efficiency water splitting photoanodes composed of nano-structured anatase-rutile TiO_2 heterojunctions by pulsed-pressure MOCVD. Appl Catal B Environ 224:904–911
38. Gärtner WW (1959) Depletion-layer photoeffects in semiconductors. Phys Rev 116:84–87
39. Kennedy JH, Frese KW (1978) Photooxidation of water at α-Fe_2O_3 electrodes. J Electrochem Soc 125:709–714
40. Kay A, Grave D, Deo Malviya K, Ellis D, Dotan H, Rothschild A (2017) Wavelength dependent photocurrent of hematite photoanodes: reassessing the hole collection length. J Phys Chem C 121:28287–28292
41. Fan HJ, Werner P, Zacharias M (2006) Semiconductor nanowires: from self-organization to patterned growth. Small 2:700–717
42. Fan Z, Ho JC, Huang B (2013) One-dimensional nanostructures for energy harvesting. One-Dimens Nanostruct Princ Appl 1–12
43. Comini E, Baratto C, Faglia G, Ferroni M, Vomiero A, Sberveglieri G (2009) Quasi-one dimensional metal oxide semiconductors: preparation, characterization and application as chemical sensors. Prog Mater Sci 54:1–67
44. Barth S, Hernandez-Ramirez F, Holmes JD, Romano-Rodriguez A (2010) Synthesis and applications of one-dimensional semiconductors. Prog Mater Sci 55:563–627
45. Tan LK, Liu X, Gao H (2011) Vertically standing, highly ordered, and dimension and morphology controllable TiO_2 nanotube arrays via template-assisted atomic layer deposition. J Mater Chem 21:11084
46. Huang Q, Kang F, Liu H, Li Q, Xiao X (2013) Highly aligned Cu_2O/CuO/TiO_2 core/shell nanowire arrays as photocathodes for water photoelectrolysis. J. Mater Chem A 1:2418–2425
47. Gurudayal CS, Kumar MH, Bassi PS, Seng H, Barber J, Wong LH (2014) Improving the E FFI ciency of hematite nanorods for photoelectrochemical water splitting by doping with manganese. ACS Appl Mater Interfaces 6:5852–5859
48. Kim M, Yoon H, Ohm T, Jo H, An S, Choi S, Park H, Al-Deyab S, Min B, Swihart M, Yoon S (2017) Nanotextured cupric oxide nanofibers coated with atomic layer deposited ZnO–TiO_2 as highly efficient photocathodes. Appl Catal B Environ 201:479–485
49. Xia Y, Yang P, Sun Y, Wu Y, B Mayers, Gates B, Yin Y, Kim F, Yan H(2003) One-dimensional nanostructures: synthesis, characterization, and applications. Adv Mater 15:353–389
50. Zhang J, Wu J, Xiong Q (2013) One-dimensional semiconductor nanowires: synthesis and raman scattering. In: T. Zhai T, Yao J (eds) One-dimensional nanostructures. https://doi.org/10.1002/9781118310342.ch7
51. Lu JG, Chang P, Fan Z (2006) Quasi-one-dimensional metal oxide materials-Synthesis, properties and applications. Mater Sci Eng R Rep 52:49–91
52. Shi X, Zhou W, Ma D, Ma Q, Bridges D, Ma Y, Hu A (2015) Electrospinning of nanofibers and their applications for energy devices. J Nanomater 2015:140716
53. Wang ZL (2008) Splendid one-dimensional nanostructures of zinc oxide: a new nanomaterial family for nanotechnology. ACS Nano 2:1987–1992
54. Tian J, Zhao Z, Kumar A, Boughton RI, Liu H (2014) Recent progress in design, synthesis, and applications of one-dimensional TiO_2 nanostructured surface heterostructures: a review. Chem Soc Rev 43:6920–6937
55. Warren S, Voïtchovsky K, Dotan H, Leroy C, Cornuz M, Stellacci F, Hébert C, Rothschild A, Grätzel M (2013) Identifying champion nanostructures for solar water-splitting. Nat Mater 12:842–849
56. Kennedy JH, Frese KW (1978) Photooxidation of water at c-FeO Electrodes 125:709–714
57. Hou Y, Abrams B, Vesborg P, Björketun M, Herbst K, Bech L, Setti A, Damsgaard C, Pedersen T, Hansen O, Rossmeisl J, Dahl S, Nørskov J, Chorkendorff (2011) Bioinspired molecular

co-catalysts bonded to a silicon photocathode for solar hydrogen evolution. Nat Mater 10:434–438
58. Zhao J, Olide E, Osterloh FE (2014) Enhancing majority carrier transport in WO_3 water oxidation photoanode via electrochemical doping. J Electrochem Soc 162:H65–H71
59. Lionet Z, Kamata Y, Nishijima S, Toyao T, Kim T, Horiuchi Y, Lee S, Matsuoka M (2018) Water oxidation reaction promoted by MIL-101(Fe) photoanode under visible light irradiation. Res Chem Intermed 44–8:4755–4764
60. Antony R, Bassi P, Abdi F, Chiam S, Ren Y, Barber J, Loo J, Wong L (2016) Electrospun Mo–$BiVO_4$ for efficient photoelectrochemical water oxidation: direct evidence of improved hole diffusion length and charge separation. Electrochim Acta 211:173–182
61. Lin YP, Lin SY, Lee YC, Chen-Yang YW (2013) High surface area electrospun prickle-like hierarchical anatase TiO_2 nanofibers for dye-sensitized solar cell photoanodes. J Mater Chem A 1:9875
62. Wang X, He G, Fong H, Zhu Z (2013) Electron transport and recombination in photoanode of electrospun TiO_2 nanotubes for dye-sensitized solar cells. J Phys Chem C 117:1641–1646
63. Santangelo S, Frontera P, Pantò F, Stelitano S, Marelli M, Patanè S, Malara F, Dal Santo V, Antonucci P (2017) Effect of Ti-or Si-doping on nanostructure and photo-electro-chemical activity of electro-spun iron oxide fibres. Int J Hydrogen Energy 42:28070–28081
64. Kumar P, Sundaramurthy J, Sundarrajan S, Babu V, Singh G, Allakhverdiev S, Ramakrishna S (2014) Hierarchical electrospun nanofibers for energy harvesting, production and environmental remediation. Energy Environ Sci 7:3192–3222
65. Parmar KP, Kang HJ, Bist A, Dua P, Jang JS, Lee JS (2012) Photocatalytic and photoelectrochemical water oxidation over metal-doped monoclinic $BiVO_4$ photoanodes. Chemsuschem 5:1926–1934
66. Biswas SK, Baeg JO (2013) Enhanced photoactivity of visible light responsive W incorporated $FeVO_4$ photoanode for solar water splitting. Int J Hydrogen Energy 38:14451–14457
67. Zhang H, Yilmaz P, Ansari JO, Khan FF, Binions R, Krause S, Dunn S (2015) Incorporation of Ag nanowires in $CuWO_4$ for improved visible light-induced photoanode performance. J. Mater. Chem. A 3:9638–9644
68. Antony RP, Zhang M, Zhou K, Loo SCJ, Barber J, Wong LH (2018) Synergistic effect of porosity and gradient doping in efficient solar water oxidation of catalyst-free gradient Mo:$BiVO_4$, ACS Omega 33:2724–2734
69. Quiñonero J, Lana-Villarreal T, Gómez R (2016) Improving the photoactivity of bismuth vanadate thin film photoanodes through doping and surface modification strategies. Appl Catal B Environ 194:141–149
70. Landau L, Levich B (1988) Dragging of a liquid by a moving plate. Dyn Curved FrontXVII:141–153
71. Rohloff M, Anke B, Zhang S, Gernert U, Scheu C, Lerch M, Fischer A (2017) Mo-doped $BiVO_4$ thin films—high photoelectrochemical water splitting performance achieved by a tailored structure and morphology. Sustain Energy Fuels 1:1830–1846
72. Hilliard S, Friedrich D, Kressman S, Strub H, Artero V, Laberty-Robert C (2017) Solar-water-splitting $BiVO_4$ thin-film photoanodes prepared by using a sol-gel dip-coating technique. ChemPhotoChem 1:273–280
73. Landsmann S, Surace Y, Trottmann M, Dilger S, Weidenkaff A, Pokrant S (2016) Controlled design of functional nano-coatings: reduction of loss mechanisms in photoelectrochemical water splitting. ACS Appl Mater Interfaces 8:12149–12157
74. Joshi M, Butola BS (2013) 14—Application technologies for coating, lamination and finishing of technical textiles. In: MLBT-A Gulrajani (ed) Woodhead publishing series in textiles. Woodhead Publishing, pp 355–411. https://doi.org/10.1533/9780857097613.2.355
75. Ito S, Ha N, Rothenberger G, Liska P, Comte P, Zakeeruddin S, Péchy P, Nazeeruddin M, Grätzel M (2006) High-efficiency (7.2%) flexible dye-sensitized solar cells with Ti-metal substrate for nanocrystalline-TiO_2 photoanode. Chem Commun 38:4004–4006
76. Bai Y, Han C, Chen X, Yu H, Zong X, Li Z, Wang L (2015) Boosting the efficiency of quantum dot sensitized solar cells up to 7.11% through simultaneous engineering of photocathode and photoanode. Nano Energy 13:609–619

77. Li K, Luo Y, Yu Z, Deng M, Li D, Meng Q (2009) Low temperature fabrication of efficient porous carbon counter electrode for dye-sensitized solar cells. Electrochem commun 11:1346–1349
78. Mohamed EA, Zahran ZN, Naruta Y (2017) Simple preparation of highly active water splitting FTO/$BiVO_4$ photoanode modified with tri-layer water oxidation catalysts. J Mater Chem A 5:6825–6831
79. Hussain S, Hussain S, Waleed A, Tavakoli M, Yang S, Rauf M, Fan Z, Nadeem M (2017) Spray pyrolysis deposition of $ZnFe_2O_4/Fe_2O_3$ composite thin films on hierarchical three-dimensional nanospikes for efficient photoelectrochemical oxidation of water. J Phys Chem C 121:18360–18368
80. Kozhukharov S, Tchaoushev S (2013) Spray pyrolysis equipment for various applications. J Chem Technol Metall 48:111–118
81. Kavitha R, Meghani S, Jayaram V (2007) Synthesis of titania films by combustion flame spray pyrolysis technique and its characterization for photocatalysis. Mater Sci Eng B 139:134–140
82. Duret A, Grätzel M (2005) Visible light-induced water oxidation on mesoscopic α-Fe_2O_3 films made by ultrasonic spray pyrolysis. J Phys Chem B 109:17184–17191
83. Dhamodharan P, Manoharan C, Bououdina M, Venkadachalapathy R, Ramalingam S (2017) Al-doped ZnO thin films grown onto ITO substrates as photoanode in dye sensitized solar cell. Sol Energy 141:127–144
84. Bedoya-Lora F, Hankin A, Holmes-Gentle I, Regoutz A, Nania M, Payne D, Cabral J, Kelsall G (2017) Effects of low temperature annealing on the photo-electrochemical performance of tin-doped hematite photo-anodes. Electrochim Acta 251:1–11
85. Guo Y, Zhang N, Wang X, Qian Q, Zhang S, Li Z, Zou Z (2017) A facile spray pyrolysis method to prepare Ti-doped $ZnFe_2O_4$ for boosting photoelectrochemical water splitting. J Mater Chem A 5:7571–7577
86. Haisch C, Schneider J, Fleisch M, Gutzmann H, Klassen T, Bahnemann D (2017) Cold sprayed WO_3 and TiO_2 electrodes for photoelectrochemical water and methanol oxidation in renewable energy applications. Dalt Trans 12811–12823
87. Murchison RI (1839) The Silurian system, founded on geological researches in the counties of Salop, hereford, radnor, montgomery, caermarthen, brecon, pembroke, monmouth, gloucester, worcester, and stafford: with descriptions of the coalfields and overlying formations (Murray J)
88. Yoshimura M, Byrappa K (2008) Hydrothermal processing of materials: past, present and future. J Mater Sci 43:2085–2103
89. Wu H, Hunting J, Uheda K, Lepak L, Konkapaka P, Disalvo F, Spencer M (2005) Rapid synthesis of gallium nitride powder. J Cryst Growth 279:303–310
90. Thomas T, Guo X, Shi J, Lepak L, Chandrashekhar M, Li K, Disalvo F, Spencer M (2011) Gallium nitride powders: mechanism of ammonothermal synthesis, ball-mill assisted rare earth doping and uniform electrophoretic deposition. J Cryst Growth 316:90–96
91. Li B, Xie Y, Huang J, Qian Y (1999) Synthesis by a solvothermal route and characterization of $CuInSe_2$ Nanowhiskers and nanoparticles. Adv Mater 11:1456–1459
92. Crystallized H, Tio A, Lim D, Cho S (2015) Glycothermal synthesis and photocatalytic properties of highly crystallized anatase TiO_2 nanoparticles 15:6193–6200
93. Kim BK, Lim DY, Riman RE, Nho JS, Cho SB (2003) A new glycothermal process for barium titanate nanoparticle synthesis. J Am Ceram Soc 86:1793–1796
94. Chaianansutcharit S, Mekasuwandumrong O, Praserthdam P (2006) Effect of organic solvents on iron oxide nanoparticles by the solvothermal method. Cryst Growth Des 6:40–45
95. Hong Z, Shan, Cao Y, Deng JF (2002) A convenient alcohothermal approach for low temperature synthesis of CuO nanoparticles. Mater Lett 52:34–38
96. Zhang Y, Si R, Liao C, Yan C, Xiao C, Kou Y (2003) Facile alcohothermal synthesis, size-dependent ultraviolet absorption, and enhanced CO Conversion activity of ceria nanocrystals. J Phys Chem B 107:10159–10167
97. Lu Z, Qian L, Xu W, Tian Y, Jiang M, Li Y, Sun X, Duan X (2016) Dehydrated layered double hydroxides: alcohothermal synthesis and oxygen evolution activity. Nano Res 9:3152–3161

98. Mousavand T, Takami S, Umetsu M, Ohara S, Adschiri T (2006) Supercritical hydrothermal synthesis of organic-inorganic hybrid nanoparticles. J Mater Sci 41:1445–1448
99. Aymonier C, Loppinet-Serani A, Reverón H, Garrabos Y, Cansell F (2006) Review of supercritical fluids in inorganic materials science. J Supercrit Fluids 38:242–251
100. Kawasaki S, Xiuyi Y, Sue K, Hakuta Y, Suzuki A, Arai K (2009) Continuous supercritical hydrothermal synthesis of controlled size and highly crystalline anatase TiO_2 nanoparticles. J Supercrit Fluids 50:276–282
101. Vayssieres L, Beermann N, Lindquist S-E, Hagfeldt A (2001) Controlled aqueous chemical growth of oriented three-dimensional crystalline nanorod arrays: application to Iron(III) oxides. Chem Mater 13:233–235
102. Fu Z, Jiang T, Liu Z, Wang D, Wang L, Xie T (2014) Highly photoactive Ti-doped α-Fe_2O_3 nanorod arrays photoanode prepared by a hydrothermal method for photoelectrochemical water splitting. Electrochim Acta 129:358–363
103. Li Q, Antony RP, Wong LH, Ng DHL (2015) Promotional effects of cetyltrimethylammonium bromide surface modification on a hematite photoanode for photoelectrochemical water splitting. RSC Adv 5:00142–100146
104. Jeon TH, Moon G, Park H, Choi W (2017) Ultra-efficient and durable photoelectrochemical water oxidation using elaborately designed hematite nanorod arrays. Nano Energy 39:211–218
105. Annamalai A, Shinde P, Jeon T, Lee H, Kim H, Choi W, Jang J (2016) Fabrication of superior α-Fe_2O_3 nanorod photoanodes through ex-situ Sn-doping for solar water splitting. Sol Energy Mater Sol Cells 144:247–255
106. Yang X, Wolcott A, Wang G, Sobo A, Fitzmorris R, Qian F, Zhang J, Li Y (2009) Nitrogen-doped ZnO nanowire arrays for photoelectrochemical water splitting. Nano Lett 9:2331–2336
107. Guo M, Diao P, Cai S (2005) Hydrothermal growth of perpendicularly oriented ZnO nanorod array film and its photoelectrochemical properties. Appl Surf Sci 249:71–75
108. Liu J, Yu X, Liu Q, Liu R, Shang X, Zhang S, Li W, Zheng W, Zhang G, Cao H, Gu Z (2014) Surface-phase junctions of branched TiO_2 nanorod arrays for efficient photoelectrochemical water splitting. Appl Catal B Environ 158–159:296–300
109. Bemana H, Rashid-Nadimi S (2017) Effect of sulfur doping on photoelectrochemical performance of hematite. Electrochim Acta 229:396–403
110. Li S, Cai J, Liu Y, Gao M, Cao F, Qin G (2018) Tuning orientation of doped hematite photoanodes for enhanced photoelectrochemical water oxidation. Sol Energy Mater Sol Cells 179:328–333. https://doi.org/10.1016/j.solmat.2017.12.028
111. Su F, Wang T, Lv R, Zhang J, Zhang P, Lu J, Gong J (2013) Dendritic Au/TiO_2 nanorod arrays for visible-light driven photoelectrochemical water splitting. Nanoscale 5:9001
112. Pu A, Deng J, Li M, Gao J, Zhang H, Hao Y, Zhong J, Sun X (2014) Coupling Ti-doping and oxygen vacancies in hematite nanostructures for solar water oxidation with high efficiency. J Mater Chem A 2:2491
113. Cho IS, Han HS, Logar M, Park J, Zheng X (2016) Enhancing low-bias performance of hematite photoanodes for solar water splitting by simultaneous reduction of bulk, interface, and surface recombination pathways. Adv Energy Mater 6:1–9
114. Li M, Yang Y, Ling Y, Qiu W, Wang F, Liu T, Song Y, Liu X, Fang P, Tong Y, Li Y (2017) Morphology and doping engineering of Sn-doped hematite nanowire photoanodes. Nano Lett 17:2490–2495
115. Ling Y, Wang G, Wang H, Yang Y, Li Y (2014) Low-temperature activation of hematite nanowires for photoelectrochemical water oxidation. Chemsuschem 7:848–853
116. Li J, Cushing S, Zheng P, Meng F, Chu D, Wu N (2013) Plasmon-induced photonic and energy-transfer enhancement of solar water splitting by a hematite nanorod array. Nat Commun 4:1–8
117. Wang D, Chen H, Chang G, Lin X, Zhang Y, Aldalbahi A, Peng C, Wang J, Fan C (2015) Uniform doping of titanium in hematite nanorods for efficient photoelectrochemical water splitting. ACS Appl Mater Interfaces 7:14072–14078
118. Yoon K, Lee J, Kim K, Bak C, Kim S, Kim J, Jang J (2014) Hematite-based photoelectrochemical water splitting supported by inverse opal structures of graphene. ACS Appl Mater Interfaces 6:22634–22639

119. Fàbrega C, Andreu T, Tarancón A, Flox C, Morata A, Calvo-Barrio L, Morante J (2013) Optimization of surface charge transfer processes on rutile TiO_2 nanorods photoanodes for water splitting. Int J Hydrogen Energy 38:2979–2985
120. Su F, Lu J, Tian Y, Ma X, Gong J (2013) Branched TiO_2 nanoarrays sensitized with CdS quantum dots for highly efficient photoelectrochemical water splitting. Phys Chem Chem Phys 15:12026
121. Fang W, Huo Z, Liu P, Wang X, Zhang M, Jia Y, Zhang H, Zhao H, Yang H, Yao X (2014) Fluorine-doped porous single-crystal rutile TiO_2 nanorods for enhancing photoelectrochemical water splitting. Chem. - A Eur. J. 20:11439–11444
122. Hoang S, Guo S, Hahn NT, Bard AJ, Mullins CB (2012) Visible light driven photoelectrochemical water oxidation on nitrogen-modified TiO_2 nanowires. Nano Lett 12:26–32
123. Liu Q, Lu H, Shi Z, Wu F, Guo J, Deng K, Li L (2014) 2D $ZnIn_2S_4$ nanosheet/1D TiO_2 nanorod heterostructure arrays for improved photoelectrochemical water splitting. ACS Appl Mater Interfaces 6:17200–17207
124. Mor GK, Shankar K, Paulose M, Varghese OK, Grimes CA (2005) Enhanced photocleavage of water using titania nanotube arrays. Nano Lett 5:191–195
125. Varghese OK, Paulose M, Shankar K, Mor GK, Grimes CA (2005) Water-photolysis properties of micron-length highly-ordered titania nanotube-arrays. J Nanosci Nanotechnol 5:1158–1165
126. Antony RP, Mathews T, Dash S, Tyagi AK, Raj B (2012) X-ray photoelectron spectroscopic studies of anodically synthesized self aligned TiO_2 nanotube arrays and the effect of electrochemical parameters on tube morphology. Mater Chem Phys 132:957–966
127. Kong D-S (2008) The influence of fluoride on the physicochemical properties of anodic oxide films formed on titanium surfaces. Langmuir 24:5324–5331
128. Mor GK, Shankar K, Paulose M, Varghese OK, Grimes CA (2006) Use of highly-ordered TiO_2 nanotube arrays in dye-sensitized solar cells. Nano Lett 6:215–218
129. Macak JM, Sirotna K, Schmuki P (2005) Self-organized porous titanium oxide prepared in Na_2SO_4/NaF electrolytes. Electrochim Acta 50:3679–3684
130. Huang H-H (2003) Effect of fluoride and albumin concentration on the corrosion behavior of Ti–6Al–4V alloy. Biomaterials 24:275–282
131. Shankar K, Tep KC, Mor GK, Grimes CA (2006) An electrochemical strategy to incorporate nitrogen in nanostructured TiO_2 thin films: modification of bandgap and photoelectrochemical properties. J Phys D Appl Phys 39:2361–2366
132. Cui H, Zhao W, Yang C, Yin H, Lin T, Shan Y, Xie Y, Gu H, Huang F (2014) Black TiO_2 nanotube arrays for high-efficiency photoelectrochemical water-splitting. J. Mater. Chem. A 2:8612–8616
133. Zhang Z, Wang P (2012) Optimization of photoelectrochemical water splitting performance on hierarchical TiO_2 nanotube arrays. Energy Environ Sci 5:6506
134. Zhang Z, Zhang L, Hedhili MN, Zhang H, Wang P (2013) Plasmonic gold nanocrystals coupled with photonic crystal seamlessly on TiO_2 nanotube photoelectrodes for efficient visible light photoelectrochemical water splitting. Nano Lett 13:14–20
135. Su J, Feng X, Sloppy JD, Guo L, Grimes CA (2011) Vertically aligned WO_3 nanowire arrays grown directly on transparent conducting oxide coated glass: Synthesis and photoelectrochemical properties. Nano Lett 11:203–208
136. Mohapatra SKSK, Misra M, Mahajan VKVK, Raja KSKS (2007) Design of a highly efficient photoelectrolytic cell for hydrogen generation by water splitting: application of $TiO_{2-x}C_x$ nanotubes as a photoanode and Pt/TiO_2 nanotubes as a cathode. J Phys Chem C 111:8677–8685
137. Shin SW, Lee JY, Ahn K-S, Kang SH, Kim JH (2015) Visible light absorbing TiO_2 nanotube arrays by sulfur treatment for photoelectrochemical water splitting. J Phys Chem C 119:13375–13383
138. Gong J, Lai Y, Lin C (2010) Electrochemically multi-anodized TiO_2 nanotube arrays for enhancing hydrogen generation by photoelectrocatalytic water splitting. Electrochim Acta 55:4776–4782

139. Thomas J, LaTempa TJ, Feng X, Paulose M, Grimes CA (2009) Temperature-dependent growth of self-assembled hematite (α-Fe2O3) nanotube arrays: rapid electrochemical synthesis and photoelectrochemical properties. J Phys Chem C 113:16293–16298
140. Mohapatra SK, John SE, Banerjee S, Misra M (2009) Water photooxidation by smooth and ultrathin α-Fe_2O_3 nanotube arrays. Chem Mater 21:3048–3055
141. Qiu P, Yang H, Song Y, Yang L, Lv L, Zhao X, Ge L, Chen C (2018) Potent and environmental-friendly L-cysteine @ Fe_2O_3 nanostructure for photoelectrochemical water splitting. Electrochim Acta 259:86–93
142. Li Y, Takata T, Cha D, Takanabe K, Minegishi T, Kubota J, Domen K (2013) Vertically aligned Ta_3N_5 nanorod arrays for solar-driven photoelectrochemical water splitting. Adv Mater 25:125–131
143. Grigorescu S, Bärhausen B, Wang L, Mazare A, Yoo J, Hahn R, Schmuki P (2015) Tungsten doping of Ta_3N_5-nanotubes for band gap narrowing and enhanced photoelectrochemical water splitting efficiency. Electrochem commun 51:85–88
144. Khan S, Zapata M, Baptista D, Gonçalves R, Fernandes J, Dupont J, Santos M, Teixeira S (2015) Effect of oxygen content on the photoelectrochemical activity of crystallographically preferred oriented porous Ta_3N_5 nanotubes. J Phys Chem C 119:19906–19914
145. Banerjee S, Mohapatra SK, Misra M (2009) Synthesis of TaON nanotube arrays by sonoelectrochemical anodization followed by nitridation: a novel catalyst for photoelectrochemical hydrogen generation from water. Chem Commun 7137. https://doi.org/10.1039/b912549c
146. Wang L, Zhou X, Nguyen NT, Hwang I, Schmuki P (2016) Strongly enhanced water splitting performance of Ta_3N_5 nanotube photoanodes with subnitrides. Adv Mater 28:2432–2438
147. Momeni MM, Ghayeb Y, Davarzadeh M (2015) Single-step electrochemical anodization for synthesis of hierarchical WO_3-TiO_2 nanotube arrays on titanium foil as a good photoanode for water splitting with visible light. J Electroanal Chem 739:149–155
148. Yang S (2004) Multispectra method for error reduction of the quantized fourier modulus in the iterative fourier transform algorithms used for phase retrieval. Opt Eng 43:713
149. Hoyer P (1996) Formation of a titanium dioxide nanotube array. Langmuir 12:1411–1413
150. Takahashi K, Limmer SJ, Wang Y, Cao G (2005) Growth and electrochemical properties of single-crystalline V_2O_5 nanorod arrays. Jpn J Appl Phys 44:662–668
151. Shinde PS, Go GH, Lee WJ (2012) Facile growth of hierarchical hematite (α-Fe_2O_3) nanopetals on FTO by pulse reverse electrodeposition for photoelectrochemical water splitting. J Mater Chem 22:10469
152. Formhals A (1934) US Patent 1975504. D01D5/00
153. Taylor G (1969) Electrically driven jets. Proc R Soc A Math Phys Eng Sci 313:453–475
154. Han T, Reneker DH, Yarin AL (2007) Buckling of jets in electrospinning. Polymer (Guildf). 48:6064–6076
155. Reneker DH, Yarin AL (2008) Electrospinning jets and polymer nanofibers. Polymer (Guildf). 49:2387–2425
156. Huang Z-M, Zhang Y-Z, Kotaki M, Ramakrishna S (2003) A review on polymer nanofibers by electrospinning and their applications in nanocomposites. Compos Sci Technol 63:2223–2253
157. Xue J, Xie J, Liu W, Xia Y (2017) Electrospun nanofibers: new concepts, materials, and applications. Acc Chem Res 50:1976–1987
158. Ramos P, Flores E, Sánchez L, Candal R, Hojamberdiev M, Estrada W, Rodriguez J (2017) Enhanced photoelectrochemical performance and photocatalytic activity of ZnO/TiO_2 nanostructures fabricated by an electrostatically modified electrospinning. Appl Surf Sci 426:844–851
159. Ganesh VA, Dinachali SS, Nair AS, Ramakrishna S (2013) Robust superamphiphobic film from electrospun TiO_2 nanostructures. ACS Appl Mater Interfaces 5:1527–1532
160. Baumgarten PK (1971) Electrostatic spinning of acrylic microfibers. J Colloid Interface Sci 36:71–79
161. He J, Wan Y, Yu J (2004) Application of vibration technology to polymer electrospinning. Int J Nonlinear Sci Numer Simul 5:253

162. Kim I, Rothschild A, Lee B, Kim D, Jo S, Tuller H (2006) Ultrasensitive chemiresistors based on electrospun TiO_2 nanofibers. Nano Lett 6:2009–2013
163. Wang J, Sun X, Yang Y, Huang H, Lee Y, Tan O, Vayssieres L (2006) Hydrothermally grown oriented ZnO nanorod arrays for gas sensing applications. Nanotechnology 17:4995–4998
164. Choi J, Yang BJ, Bae GN, Jung JH (2015) Herbal extract incorporated nanofiber fabricated by an electrospinning technique and its application to antimicrobial air filtration. ACS Appl Mater Interfaces 7:25313–25320
165. Zhang Y, Chwee TL, Ramakrishna S, Huang ZM (2005) Recent development of polymer nanofibers for biomedical and biotechnological applications. J Mater Sci Mater Med 16:933–946
166. Bedford NM, Steckl AJ (2010) Photocatalytic self cleaning textile fibers by coaxial electrospinning. ACS Appl Mater Interfaces 2:2448–2455
167. Lepcha A, Maccato C, Mettenbörger A, Andreu T, Mayrhofer L, Walter M, Olthof S, Ruoko T, Klein A, Moseler M, Meerholz K, Morante J, Barreca D, Mathur S (2015) Electrospun black titania nanofibers: influence of hydrogen plasma-induced disorder on the electronic structure and photoelectrochemical performance. J Phys Chem C 119:18835–18842
168. Mao X, Hatton T, Rutledge G (2013) A review of electrospun carbon fibers as electrode materials for energy storage. Curr Org Chem 17:1390–1401
169. Croce F, Focarete ML, Hassoun J, Meschini I, Scrosati B (2011) A safe, high-rate and high-energy polymer lithium-ion battery based on gelled membranes prepared by electrospinning. Energy Environ Sci 4:921
170. Einert MOstermann R, Weller T, Zellmer S, Garnweitner G, Smarsly B, Marschall R (2016) Hollow α-Fe_2O_3 nanofibres for solar water oxidation: improving the photoelectrochemical performance by formation of α-Fe_2O_3/ITO-composite photoanodes. J Mater Chem A 4:18444–18456
171. Jung H, Chae SY, Kim H, Min BK, Hwang YJ (2016) Electrospun Mo-doped $BiVO_4$ photoanode on a transparent conductive substrate for solar water oxidation. Catal Commun 75:18–22
172. Saveh-Shemshaki N, Latifi M, Bagherzadeh R, Malekshahi Byranvand M, Naseri N, Dabirian A (2016) Synthesis of mesoporous functional hematite nanofibrous photoanodes by electrospinning. Polym Adv Technol 27:358–365
173. Sander MS, Tan L-S (2003) Nanoparticle arrays on surfaces fabricated using anodic alumina films as templates. Adv Funct Mater 13:393–397
174. Lee J, Yoon S, Oh SM, Shin C-H, Hyeon T (2000) Development of a new mesoporous carbon using an HMS aluminosilicate template. Adv Mater 12:359–362
175. Han Y-J, Kim JM, Stucky GD (2000) Preparation of noble metal nanowires using hexagonal mesoporous silica SBA-15. Chem Mater 12:2068–2069
176. Li L, Zhai T, Zeng H, Fang X, Bando Y, Golberg D (2011) Polystyrene sphere-assisted one-dimensional nanostructure arrays: synthesis and applications. J Mater Chem 21:40–56
177. Kim K, Song H, Nam S, Kim S, Jeong H, Kim W, Jung G (2012) Fabrication of an efficient light-scattering functionalized photoanode using periodically aligned ZnO hemisphere crystals for dye-sensitized solar cells. Adv Mater 24:792–798
178. Kim J, Yang W, Oh Y, Kim J, Moon J (2017) Template-directed fabrication of vertically aligned Cu_2ZnSnS_4 nanorod arrays for photoelectrochemical applications via a non-toxic solution process. J Alloys Compd 691:457–465
179. Shi X, Zhang K, Shin K, Moon J, Lee T, Park J (2013) Constructing inverse opal structured hematite photoanodes via electrochemical process and their application to photoelectrochemical water splitting. Phys Chem Chem Phys 15:11717–11722
180. Zhang K, Shi X, Kim JK, Lee JS, Park JH (2013) Inverse opal structured α-Fe_2O_3 on graphene thin films: enhanced photo-assisted water splitting. Nanoscale 5:1939
181. Ma M, Kim J, Zhang K, Shi X, Kim S, Moon J, Park J (2014) Double-deck inverse opal photoanodes: efficient light absorption and charge separation in heterojunction. Chem Mater 26:5592–5597

182. Yew R, Karuturi SK, Tan HH, Jagadish C (2017) Nanostructured photoelectrodes via template-assisted fabrication. In: Semiconductors and semimetals, vol 97. Elsevier Inc.
183. Pierson HO (2008) CVD processes and equipment. Handb Chem Vap Depos 108–146. https://doi.org/10.1016/b978-081551432-9.50008-5
184. Sui Y, Acosta D, González-León J, Bermúdez A, Feuchtwanger J, Cui B, Flores J, Saniger J (2001) Structure, thermal stability, and deformation of multibranched carbon nanotubes synthesized by CVD in the AAO template. J Phys Chem B 105:1523–1527
185. Shi J, Sun C, Starr MB, Wang X (2011) Growth of titanium dioxide nanorods in 3D-confined spaces. Nano Lett 11:624–631
186. Archana PS, Shan Z, Pan S, Gupta A (2017) Photocatalytic water oxidation at bismuth vanadate thin film electrodes grown by direct liquid injection chemical vapor deposition method. Int J Hydrogen Energy 42:8475–8485
187. Lin Y, Xu Y, Mayer M, Simpson Z, McMahon G, Zhou S, Wang D (2012) Growth of p-type hematite by atomic layer deposition and its utilization for improved solar water splitting. J Am Chem Soc 134:5508–5511
188. Klahr BM, Martinson ABF, Hamann TW (2011) Photoelectrochemical investigation of ultrathin film iron oxide solar cells prepared by atomic layer deposition. Langmuir 27:461–468
189. Hamann TW, Martinson ABF, Elam JW, Pellin MJ, Hupp JT (2008) Atomic layer deposition of TiO_2 on aerogel templates: new photoanodes for dye-sensitized solar cells. J Phys Chem C 112:10303–10307
190. Pickrahn K, Park S, Gorlin Y, Lee H, Jaramillo T, Bent S (2012) Active MnO_x electrocatalysts prepared by atomic layer deposition for oxygen evolution and oxygen reduction reactions. Adv Energy Mater 2:1269–1277
191. Li X, Bassi PS, Boix PP, Fang Y, Wong LH (2015) Revealing the role of TiO_2 surface treatment of hematite nanorods photoanodes for solar water splitting. ACS Appl Mater Interfaces 7:16960–16966
192. Nardi KL, Yang N, Dickens CF, Strickler AL, Bent SF (2015) Creating highly active atomic layer deposited NiO electrocatalysts for the oxygen evolution reaction. Adv Energy Mater 5:1500412
193. Li H, Shao Y, Su Y, Gao Y, Wang X (2016) Vapor-phase atomic layer deposition of nickel sulfide and its application for efficient oxygen-evolution electrocatalysis. Chem Mater 28:1155–1164
194. Liu R, Lin Y, Chou L, Sheehan S, He W, Zhang F, Hou H, Wang D (2011) Water splitting by tungsten oxide prepared by atomic layer deposition and decorated with an oxygen-evolving catalyst. Angew Chem 123:519–522
195. Kot M, Henkel K, Das C, Brizzi S, Kärkkänen I, Schneidewind J, Naumann F, Gargouri HSchmeißer D (2017) Analysis of titanium species in titanium oxynitride films prepared by plasma enhanced atomic layer deposition. Surf Coat Technol 324:586–593
196. Lichterman M, Shaner M, Handler S, Brunschwig B, Gray H, Lewis N, Spurgeon J (2013) Enhanced stability and activity for water oxidation in alkaline media with Bismuth Vanadate photoelectrodes modified with a cobalt oxide catalytic layer produced by atomic layer deposition. J Phys Chem Lett 4:4188–4191

Chapter 9
Synthesis Strategies and Applications of Metallic Foams and Hollow Structured Materials

Ashis Kumar Satpati

Abstract The porous materials or foams are becoming ubiquitous in various research fields as they find applications in several important modern devices. The porous nano structures may be considered as a generalised name of foams which are generated from both metallic and non-metallic components. Present chapter however discussed primarily on the metallic foams. After a brief account of the history of the generation of metallic foams, the synthesis procedures have been discussed, the chapter has been organised by describing various synthesis procedures of metallic foams, which leads to the variation in their properties. Since porous nano structure materials have wide varieties of applications, only some of the important application are presented in the chapter. In addition to the nano porous foams, the metallic foam with macro porous structures have widespread large scale commercial applications, which has been discussed in brief. Some of the important applications of porous nano structures materials in alternate energy technology, sensors and biosensors and bio-regenarative medicines are included in the present chapter. Apart from the metallic foams, non-metallic foams are also very important and associated its signature with various scientific and technological applications; however, the detailed discussion on the non-metallic foams are made out of the scope of the present chapter with only a small discussion on the graphene foams, which has accrued an important place in various scientific inventions, has been mentioned towards the end of the chapter.

Keywords Porous structure · Metal foam · Hollow structure · Porous noble metal nanostructures (PNMNs) · Transition metal chalcogenides · Hard template · Soft template · Self-template · Electrodeposition · Gas template · Kirkindall effect · Li ion battery · Supercapacitor · Fuel cell · Water splitting · Sensors · Commercial applications · Regenerative medicines

A. K. Satpati (✉)
Analytical Chemistry Division, Bhabha Atomic Research Centre, Mumbai 400085, India
e-mail: asatpati@barc.gov.in

Homi Bhabha National Institute, Mumbai 400094, India

A. K. Tyagi and R. S. Ningthoujam (eds.), *Handbook on Synthesis Strategies for Advanced Materials*, Indian Institute of Metals Series,
https://doi.org/10.1007/978-981-16-1803-1_9

9.1 Introduction

The metallic foam was created accidentally through combustion experiments by Tappan et al., at Los Alamos National Laboratory. While Professor Tappan was carrying a burning-rate experiment in 2005 to investigate the decomposition behaviour of iron complex with nitrogen-rich ligands, namely, ammonium tris[bi(tetrazolato)-amine] ferrate(III). While igniting a small pellet of the metal complex, with the expectation that the complex material would either be exploded or it might burn slowly. However, he observed that the smoke filled the reaction chamber due to which it was impossible to record the progress of the decomposition of the material. While opening up the reaction vessel to clean for the next set of experiments he found the resulted materials with long columnar structure. With curiosity he characterised the materials to find that the mysterious column of materials was basically a foam composed mostly with iron metal. The porous materials were having the pore diameters in the range from 10 to 20 nm, which were exceptionally good characteristics for metallic foam. This has been considered as one of the first well reported metallic foam. The metallic foams have several advantages, "One huge advance with metal foams could be getting a real base metal like nickel to behave more like platinum or palladium" [1–11].

In older literature, porous metallic materials are in use in the name of powder metallurgy (PM) materials and served various important purposes due to their high surface area and superior mechanical properties. For the selection of materials to form the PM, the most common examples are bronze, nickel and nickel-base alloys. As non-ferrous metals, copper, aluminium, gold, niobium, tantalum, silver, zirconium and titanium are fabricated into porous materials, from powder [12]. In order to obtain the materials of required shape and sizes, PM materials undergo various types of separations like, sieving, ultrasonic separations, after which the materials undergo several compaction techniques or sintering processing. In addition to the compaction and sintering, the materials are produced through the metallurgical procedures like, centrifugal slurry casting, metal injection moulding, extrusion, direct tapping method gravity filling of shaped moulds and wet powder spraying to fabricate the materials in usable forms [12].

Major progress has been made later in the direction of developments of improvised metals and alloys with suitable pores and surface areas superior to the PM materials, which are named as metallic foams also called as cellular metals having properties step ahead compared to the PM materials. Foams find superior application due to the high porosity, low specific weight combined with excellent mechanical properties [12]. It has been a challenging task for the materials scientists to design suitable synthesis protocols to generate PM materials, foams or cellular metals with high and controllable pore structures. The combustion synthesis procedure is an age-old synthesis technique to generate porous structured materials [13–17].

In some of the literatures published earlier the synthesis of metal foam has been mentioned with the combination of foaming agent along with molten metal [18]. The foaming agent was reported as the powders of metal hydrides, which are decomposed

and formed gases when heated to a temperature above 400 °C. When the foaming agents come in contact with the molten metal, instant decomposition takes place. The homogeneous distribution of the gas-forming particles all along the melts is not possible due to the insufficient time of contact. This has resulted in the difficulty in controlling the overall reaction and thus controlling the resulted product. Metal foams are also synthesised from the metal melts for the metal of low melting points and the utilisation of the eutectic composition further decrease the process temperature [5].

Metal foams are known for their interesting properties having ultra-low density arises through their highly porous organised network structure. In older literatures the documented density values of porous structures are between 0.5 and 1 g/cm [3] which have been improved significantly with the density for metallic foams as low as 10 mg/cm [1, 1]. The porous nano structure materials are capable in absorbing significant amount of strain. The stress–strain dependency indicates that the foam materials has the capacity to absorb large amount of energy [19]. The porous or hollow nano structures having excellent properties like, large pore volume, high specific surface areas, high capacity for loading, possibility of various functionalisation, which leads to their applications in, a few of them are named as lithium-ion batteries [20–26], catalysis [27–31], drug delivery [32–36], sensors [37–40], water treatment [41–45], and dye-sensitized solar cells [46, 47].

9.2 Synthesis Procedures Porous Materials

The combustion synthesis process is the conventional route of synthesising of metallic foams. The combustion synthesis procedures are carried out either in solid state or in aqueous solution. The solid state synthesis procedure generally proceeds as self-propagating process, thus calling them as the self-propagating high temperature synthesis procedure [14, 48]. The synthesis is carried out without the use of any external combustion agents. The simple chemical reaction used to represent the combustion process is represented in Eq. 9.1.

$$A + B + G = Product + G\prime \tag{9.1}$$

Where A is the metal, which also can be functioned as the fuel, B can be a metal or metallic oxide (e.g., Ni, $Ni(NO_3)_2$, Fe_2O_3), which act as the fuel. G is the gasifying agent, and these are metal hydrides and carbonates, which on heating liberate gases like, hydrogen, carbon di-oxide or carbon monoxide. Teflon, borax etc. are also used as the gasifying agents. Porous metal, bi-metal, metal carbide and silicide are formed as product in the solid state combustion synthesis. The combustion synthesis without the use of gasifying agents were also used, be practised, which however generated the porous structure with only about 30–50% porosity. Use of the gasifying agents during the synthesis process improved the porosity in the material over 85%. The combustion process is carried out through the templating or non-templating routes. Mixing of the reactants are very important in the generation of homogeneous porous structures as

the products. The reactants in the nano particles improves the surface kinetics of the combustion reaction, thus the delay in the ignition process substantially reduced due to the utilisation of nano particles as reactants. Though the reactant particles with nano meter size shown better kinetics and also generates hierarchical structures, it is sometime detrimental in generating the quality of the porous materials. The use of Al nano particle for the synthesis of NiAl bimetallic system generated the inferior quality of products. This was explained to be due to the excessive generation of Al_2O_3 passive layer over the Al nano particle surface due to the fast surface kinetics of the Al nano particles. The problem has been eliminated through the use of organic passivating agents over the Al nano particle surface, additionally the passivating agents act as gasifying agents during the combustion synthesis. $C_{13}F_{27}COOH$ was used as the passivating and also as the gasifying agent over the Al nano particle surface for the synthesis of Ni foam [49]. The optimisation of the pore forming agents or the gasifying agent is important, the excess use of these reagents though generates porous materials with higher pore volume, the mechanical stability and the continuity in the generation of the foams impedes. The energy for the combustion synthesis process are provided from the mechanical, chemical, electrical or from the lasers.

In the solution combustion route of synthesis, the metal precursors, which are in the form of nitrates dissolved in water along with the fuels (glycine, citrate, urea etc.), sometime complexing agents are also added in the mixture. The mixture is heated in open air hot plate for complete evaporation first, and then the mixture undergoes ignition especially through the decomposition of nitrates. The porous materials thus synthesised has the advantage over the solid state synthesis as the reactants are mixed well up to the molecular level of mixing. The perovskite type of complex oxides could be synthesised using the solution based combustion synthesis procedures [50]. Depending upon the requirements, the solution based synthesis process has been augmented through the sol–gel synthesis, utilisation of micelles, vesicles templates for generating porous structures with controlled porosity, which are discussed in the later parts of the chapter.

For better control over the pore size and their distributions, the porous materials are synthesised through the templating routes. In the template synthesis protocol, the metallic foams are synthesised using a polymeric template, and metal is deposited over the template. Several inorganic materials and organic polymers are used as template. Easily available polymers like melamine, plastic polymer, polyurethane, polydimethylsiloxane are very commonly utilised in the synthesis process [51]. In the template route of synthesis, the self-assembly has an important role in generating nano structured materials with controlled porous structures. The sizes of the pores and their distributions are important factors in determining the properties of porous structured materials which would enhance the performance of the materials in various applications. The assembling of nano structured materials generates various new chemical, electrical, electronic, magnetic and optical characteristics. The combinations of high surface area and fast charge transport are the most important parameters for their advanced scientific applications. According to their pore sizes, porous nanomaterials are branched out into three different categories: microporous

(pore size < 2 nm), mesoporous (2 nm < pore size < 50 nm), and macroporous (pore size > 50 nm) materials.

Among various porous materials the porous noble metal nanostructures (PNMNs) having ordered or non-ordered structures, attracted the scientists to investigate in their catalytic properties applicable in various important fields [52–55]. In electrochemical catalysis, most of the catalytic systems require porous materials with different pore structure for efficient catalytic applications. The porous materials with large effective pore volumes in the form of electrodes have the advantages from the enhanced surface area, higher electron transfer rate and the efficient mass transfer process through the pores. There are several reports dealing with the PNMNs, generated through plenty of different synthetic procedures. Different synthesis strategies generated several different ordered or non-ordered porous nano structures and the materials generated sometime are named as nano foams, aerogels, hollow structures etc. Such materials have applications in sensors and catalysis [20]. The synthesis procedures of such ordered and non-ordered nano structures are discussed in the following section of the chapter.

9.2.1 Synthesis of Ordered Porous Nano Structures Through Template Route

Various templating routes are adopted for the synthesise of ordered PNMNs, among them the hard templates and the soft templates routes are practiced the most as these routes are the most effective in the synthesis of ordered porous nanostructures.

9.2.1.1 Synthesis of PNMNs Using Hard Template Route

The hard templates, which include the assembled colloidal crystals, mesoporous silica, alumina membranes, zeolites, have been extensively utilised for the synthesis of several ordered porous nanostructures of metals [56, 57] oxides [58, 59] and other compositions [60, 61], such templates provide the porous structures with controlled morphologies. It is worth mentioning that the generation of the mesoporous templates with the retention of morphology without any deformation is extremely important task. Generally, the non-uniformity in the porous structures arises through the collapse of the pore volume when the chemical procedures are applied to generate the porous materials. The synthesis protocol following the hard template route has been the most widespread used method to generate ordered porous materials consisting of metals, metal oxides and carbon, with well distributed porous structures and defined morphologies [62, 63].

There are three major steps in the synthesis protocol to synthesise the materials, with the first step as the synthesis of sacrificial template having ordered porous structure, then in the second step, incorporation of composite materials inside the

template and finally removal of the sacrificial template. Highly ordered mesoporous or macroporous materials like; KIT-6, MCM-48, MCM-41, and SBA-15 produce the well-ordered nano structure with highly ordered pores. Controlling the pore parameters would generate PNMNs with properties suitable to include various functionalities for targeted applications. The electrochemical deposition, electroless deposition, chemical processing, ammonia treatment and hydrogen reduction process could be included in the generation and modulation of materials through hard templating route.

The 3D close packed crystals of silica and latex having long range ordered structure generate materials with ordered distribution of pores [64, 65]. Additionally, different functional groups, like; $-NH_2$, $-SH$, and $-COOH$, could be grafted in this process of synthesis. Such inclusion of functional groups enhances the applicability of the nano porous materials. The thiol functional groups are useful in the incorporation of gold nano particles (AuNPs) inside the pores, later through the electroless deposition of metals and heat treatments and finally removal of the sacrificial template generates the free standing porous gold metal nano porous structures [66]. Similar synthesis procedure has been adopted to fabricate the porous nano structures of AuNPs and Au/Pt bi metallic nano porous materials [67, 68].

The electrochemical deposition processes combining with the hard templating process generate efficient routes in the synthesis of porous structured materials with well-defined and controlled pore structure, additionally the electrochemical method of synthesis is fast and better controllable through modulation of deposition parameters. It was demonstrated about the deposition of ordered porous structure using electrochemical deposition with varying metal composition [69].

9.2.1.2 Soft Template Method of Synthesise of PNMNs

The controlled pore structure also could be synthesised through the soft template routes, and the process of the synthesis is diverse in generating the nano structures [70]. As soft templates, the amphiphilic molecules like surfactants and amphiphilic block copolymers are used in the generation of the templates. Such molecules generate the self-assembled structure called micelles in solution at a concentration slightly higher than the critical micelle concentration (CMC). At even higher concentration of the surfactants, the surfactant molecules form the lyotropic liquid crystals (LLCs) phases. Both the micelles and the LLCs are utilised in the synthesis of porous nano structures. Attard and co-workers have developed the synthesis protocols for the mesoporous platinum nano particles (PtNPs) through chemical and also through electrochemical deposition routes utilising the LLCs as the templates. The porous nano structure with pores size less than 4 nm has been reported which are synthesised using the soft template route [71, 72].

On contrary to the LLCs route of synthesis protocol, the micelle assembly route requires low concentration of the surfactants, sometimes prove to be advantageous alternative to synthesise mesoporous metal nano structures. Yamauchi and co-workers established the new approach, through the generation of micelle assembly through electrochemical route, for assembling mesoporous Pt-based films and the

deposition was carried out at a constant potential [73–75]. Li et al. demonstrated the electrochemical deposition of Au films with mesoporous structure with controlled porous assembly using micellar soft templates [76]. The nano structure of porous Pt nano rods are reported with the 6–8 nm pore sizes using electrochemical deposition procedures [77]. In addition to the electrochemical deposition process, soft templates are used for the generation porous structure through the chemical reduction process where Pt-based nano porous structures are generated [78, 79].

In a different synthesis approach the well-ordered mesoporous nano structures were generated through the solution based reduction using di-block copolymer Pluronic F127 soft templates [80]. The block copolymers (BCPs) are a branch of polymers where the two or more homopolymers coexists, the template preparation using the BCPs has the flexibility to generate well-ordered nano structure with the additional advantage of self-degradable nature of the polymers, and thus the use of block copolymers produces the facile approach of synthesising the porous nano structure [81].

9.2.2 Synthesis of Non-ordered Porous Nano Structures

After discussion about the ordered porous nano structure, the class of compound with non-ordered porous nano structure are discussed here, which are more ubiquitous in nature compared to the ordered porous structures. The non-ordered materials could be made with large specific surface area, better mass and charge transport property which are the essential elements to function the materials as efficient catalyst. The design strategy has been modified in the direction to generate materials with non-ordered pores for the noble and non-noble metal nano structures and their utilisation in various catalytic processes [82]. Several different strategies adopted in synthesising non-ordered nano structures are discussed in the following sections.

9.2.2.1 Synthesis of Nanofoams Using Dealloying Strategy

Dealloying is one of the effective way to generate porous nano foams, in this process the active component of the alloy is selectively etched out through the chemical, electrochemical or sometime utilising the chemical and electrochemical routes together. Generation of Raney nickel is an age old material generated through the dealloying process, discovered by Murray Raney in the year 1926 [83]. The de-alloying process involves two main steps, the dissolution of the active materials out of the alloy and the surface diffusion of the other material to form the aggregate. Through the de-alloying process, the gold nano structure was formed through the selectively etching out the Ag and Cu from the alloy of Au, Ag and Cu [84].

At this juncture, it is to be mentioned that the chemical etching process has some inherent drawbacks as it is challenging to have control over the process, the atoms at the surface of the materials are highly active towards the etching process and undergo

random dissolution during the chemical etching step. For better control of the dissolution process, stabilising agents and surfactants are required to be added along with the etching agents to get the materials with controlled characteristics. In one of the initial reports, Shao et al. reported the generation of porous/hollow palladium copper nano particle (Pd/Cu NPs) utilising the electrochemical dealloying procedures, the porous structure was then used to fabricate core–shell nano structure with monolayer Pt as the shell [85]. The resulting core–shell nano structure was applied as the electrocatalysts, which showed 14-fold improvement in the ORR activity over the commercially available Pt/C catalysts. Such enhancement is observed to be due to the Pt monolayers at the shell and the synergistic effect from the core of the catalyst.

9.2.2.2 Synthesis Through the Kinetically Controlled Reduction Method

Synthesis of kinetically controlled materials generated nano structures of facile properties suitable for catalytic activities. In a report by Eswaramoorthy and co-workers, the kinetically controlled reduction process using $NaBH_4$ and generation of noble metal-based nanosponges with significantly high surface area was discussed [86]. Through the selected concentrations of metal precursor and the reducing agents, various kinetically controlled PNMNs of 3D network structures could be formed. It was also applied with the bi-metallic and tri-metallic nano sponges which were utilised as the electrocatalysts in ethanol and methanol oxidation processes [87–89]. The kinetic controlled reduction process has been extended for the non-noble materials as well [90–92]. Such kinetic controlled mechanism of reduction process involving the $NaBH_4$ as the reducing agent which is an efficient procedure to generator nano sponges within a very short time at room temperature; however, due to the fast process kinetics the controlling of the shape, size of the nano structures is limited. Through the modification in the synthesis strategy like lowering of temperature, scavenging the kinetics and slowing down of the network generation process the overall control of the porosity and sizes have been reported to be improved [93].

9.2.2.3 Synthesis of Non-ordered Porous Nano Structures Through Dynamic Templates

In addition to the kinetically controlled synthesis procedures, the non-ordered porous materials are synthesised through soft templates using surfactants. For the synthesis of Pt based porous network materials, cetyltrimethylammonium bromide (CTAB) dispersed in water and chloroform phases was successfully used [94].

Electrochemical deposition procedures have been applied using the gas bubble dynamic template, for the generation of porous nanostructures with controlled and uniform pore size and distribution. The pioneering work by Liu et al., revealed the electrodeposition of 3D foam films of non-noble based metals like, Cu, Sn, and

CuSn alloys in acidic solution [95, 96]. In this synthesis procedure the metal electrochemical deposition process is accompanied by the hydrogen evolution process, where H_2 molecule evolves as gas bubbles after reduction of H^+ ions, these gas bubbles act as the dynamic template for the simultaneous deposition of metal nano particles, the 3D porous nano structures at the surface of the electrode is generated through these gas bubble templating route [96]. The electrochemical deposition technique for the generation of porous nano structures is relatively green method of synthesis compared to the other chemical template based synthesis procedures. The process is simple as it does not require the preparation of the soft template and its removal after the synthesis procedure. The H_2 template method has been utilised for the synthesis of 3D noble metal ion foams are Au [97], Ag [98], Pt [99], Pd [100], using direct electrochemical deposition procedure. In addition to the single metals, bi-metallic nanostructures are also formed through the direct electrochemical deposition procedure [101, 102]. The indirect electrochemical deposition procedures involve the formation of 3D PNMNs through galvanic replacement recation [103–105]. Underpotential deposition procedure is another method of electrochemical deposition process through which the porous nano structure could be formed [106] which is associated with processes like, electrochemical dissolution and reduction process [107–109]. This synthesis protocol could be adopted with plenty numbers of modulations, where the morphology of the metal foams could be tuned with the variation of deposition potential, deposition time, electrolyte compositions and modification of the condition of the synthesis procedures, the process allows to introduce various functionalities in the porous materials.

9.2.2.4 Synthesis of Non-ordered Porous Nano Structures Through Self-Assembly Method

Metal nano sponges are synthesised through the self-assembly derived route, using surfactant self-assembly and capping agent, citrate ions have the versatile role as capping agent; however, it is challenging to have the well-controlled nano porous structure. The solution compositions and the type of electrolyte influences the texture of the materials to a great extent. Zhang et al. have investigated the impact of electrolytes by introducing the halide ions (F^-, Cl^-, Br^-, and I^-) over the synthesis of porous AuNPs [110]. The resulting nano sponges of AuNPs are shown in Fig. 9.1. The difference in the affinities of halide ions with the AuNPs impact critically in tuning the porous structure of sponge-like Au nano materials. During the synthesis procedure, the citrate ions linked with the surface of AuNPs are replaced by the halide ions, the replacement process is different which strongly depends on the affinity between the halide ions and AuNPs. The replacement step modulates the fusion and aggregation behaviours of the AuNPs, which resulted the generation of nanosponges with different morphologies.

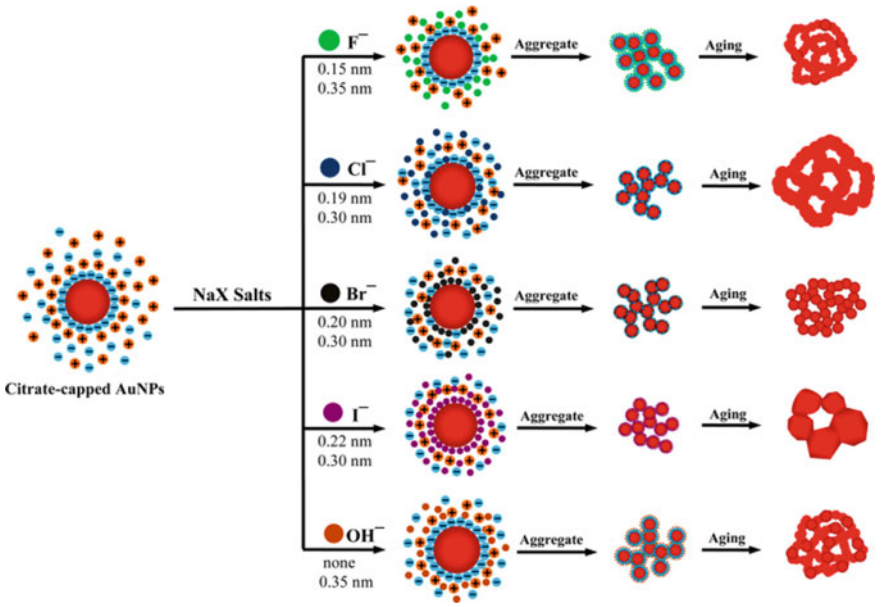

Fig. 9.1 The schematics, depicting the effects of halide ions on the AuNPs and formation of sponge-like Au nanostructures. Reprinted with permission from Ref. [110]. Copyright 2014 American Chemical Society

9.2.3 Hollow Nanostructured Materials

Like the metal nano foam or the nano sponges, the hollow metallic nanostructures are also included in the class of compounds of porous nano structures which are important in terms of their versatile applicabilities [36, 111]. The hollow nano structures have the advantage of having the distinctive combination of two or more surfaces. Hollow nano structure consists of the internal surface and the external surfaces along with the pores on the wall of both the surfaces. The morphologies of all these pores, and surfaces could be tuned for generating optimum properties from such materials. Such materials are advantageous for electrocatalysis and many other catalytic applications. These materials are divided into two categories, simple and complex nano structures. Depending on the number of the outer shells, the hollow nano structures are classified as single, double and multi-shell. The porous hollow nano structures are generally synthesised through the template based method and also through the self-templating methods like galvanic replacement and the Kirkendall effect. Such materials have unique characteristics, like, finely tuned morphology, porous outer walls, hollow interior walls, the composition may also be tuneable. The synthesise procedures of the hollow sphere materials are discussed in the following sections.

The hard templating protocol of synthesis of hollow nano structure is one the most used methods of synthesis, and the methods are effective and simple to carry

out [112]. The process of the synthesis involves four major steps: (a) formation of the hard template, generally the chemically removable are used for such purposes (b) modification of the surface of the template through chemical modification; (c) development of the distinct structure over the surface of the chemically modified template (d) selective removal of the template present inside the nano structure. Finally, the hollow nano structures are formed using the hard templating technique. Similar to the generation of PNMNs through the hard template route, the hard templating can be made by using polymer, silica template and carbon based template for the generation hollow nano structures.

In the polymer based hard template methods, the template is essentially formed through the covalent linkage between the polymer chains [113]. Some of the polymer chains commonly used for making the template are poly (methyl methacrylate) (PMMA) and polystyrene (PS), the most important benefits of using such polymer based templates is the easy removal of the template, which can be achieved by dissolving it in organic solvent or through the easy thermal treatment. Li et al. have reported the hard template synthesis of nearly monodispersed PMMA double shelled hollow spheres and SiO_2 core in double shell hollow spheres [114].

Silica template-based methods are the most important hard template route of synthesis of hollo nano structure with the morphological uniformity and tunable particle size, and it is also one of the cost effective method of synthesis procedure [115]. The SiO_2 spheres with high nondispersive nature are obtained using the classical sol–gel method of synthesis, where the silicon alkoxides condensed in water/alcohol mixture with the addition of ammonia [115]. Jang et al. have used the synthesis protocol in synthesising TiO_2 hollow spheres hard-template with controlled numbers of shell [116]. The method was also used for the synthesis of hematite (α-Fe_2O_3) spindles with a SiO_2 layer, through which the ellipsoidal α-Fe_2O_3@SiO_2 core–shell particles were formed [117]. The α-Fe_2O_3@SiO_2 particles were used as the hard template, and the hydrothermal procedures were adopted for the synthesis of shell-by-shell polycrystalline SnO_2. Finally, the SiO_2 template was removed, and the double-shelled hollow SnO_2 nanococoons with portable α-Fe_2O_3 spindles were generated.

Carbon based hard template methods are also adopted for the synthesis of complex hollow structures, and porous carbon hard templates have the additional advantages as they could sorb various chemical species easily, which would facilitate the shell formation process [118]. The transition metal oxides, such as α-Fe_2O_3, Co_3O_4, NiO, CuO and ZnO with multi-shelled hollow microspheres were reported to be formed using the synthesis technique. The numbers of shells in the core shell structures are determined from the rate at which the metal ions fed during the synthesis process.

In contrast with the hard template method of synthesis, the soft template based synthesis procedures has the advantage as it is easy to refill the hollow space inside and also easy to encapsulate with the dispersed functional species. Based on the strategies used in the synthesis process, the soft template method can be classified into three categories, (a) emulsion templating, (b) vesicle/micelle templating and (c) gas bubble templating. In both the emulsion and micelle based techniques, the parameters such as the surfactant concentrations, pH, and electrolyte concentration are important

in modulating the templating conditions. In the gas bubble template procedures gas bubbles dispersed over the liquid phase are used as the soft templates. The gas bubble emulsions are formed using sonication, gas blowing, chemical reactions, etc. Using the micro-emulsion approach, the Au hollow nano structures having wall thickness between 2 and 6 nm and the inner diameter between 20 and 40 nm are reported to be formed [119]. Several micelles or vesicles have also been employed as soft templates for the synthesis of different hollow nanostructures [120–122].

The self-templating method of the synthesis of hollow sphere materials is important as it requires less numbers of synthesis steps which leads to the reduction in the production cost. Two important self-template based synthesis strategies such as galvanic replacement and the Kirkendall effect have been discussed in the following part of the chapter.

9.2.4 Synthesis of Hollow Nano Structure Using Galvanic Replacement

The galvanic replacement reactions are effective in generating hollow nano structures by replacing the sacrificial templates of the original metal or metal oxide. The replacement processes are determined by the difference in redox potentials of the two metals. The Au hollow nanostructures are formed from AgNPs [123], using the method, several other research groups later utilised as the synthesis strategy to synthesise hollow nano structure for several important applications. The galvanic replacement strategy has been utilised using Ag as sacrificial agent in the Au, Pd, Pt, and multimetal compositions to synthesise the hollow nanostructures, with geometries such as spherical nanoshells [124], core–shell nano particles [125], nanodots [126], nanocages [127], nanotubes [128], nanoframes [129], and nanodendrites [130].

In the synthesis process, initially the replacement procedure starts at specific sites, where the surface energies are relatively large and then a seamless hollow nanostructure is formed. For example, in case of Au–Ag alloy, Ag dissolves out from the surface and simultaneously migrate to Au shell which may be called as alloying. Later the Ag atoms at the shell are selectively further dissolved to form hollow walled nano structure. The suggested mechanism is applicable in sacrificial templates as long as there is enough difference in the reduction potential of two metals. Oxides are also used as the template to synthesis the hollow nano structures, Cu_2O is used as template for the synthesis of polyhedral hollow structure of Au [131]. In an another important example of such synthesis procedure, Pt was spontaneously deposited at the Mn_3O_4 nano particles surface by the galvanic replacement procedure between Mn_3O_4 and $[PtCl_6]$ [132]. This new approach of synthesis provided an important procedure to load metal nano catalystsover metal oxide surfaces to improve the catalytic process through the generation of hybrid nano composites.

9.2.5 Kirkendall Effect

Apart from the various approaches as discussed to generate the hollow nano porous structures, the Kirkendall effect is very effective to produce the nanostructures in broad range of materials. In the synthesis process utilising the Kirkendall effect, a net inward diffusion is generated due to the difference is ionic diffusion rates of the core and shell materials, which leads to the nucleation of voids at the core/shell interface and the void generation leads to the formation of hollow structured material. Solid bridges are formed between the core and the shell, which facilitates the transportation of core materials outward for the generation of the hollow structure. The Kirkendall effect is a unique self-templating synthesis strategy for the generation of nanostructures with high yield, high crystal quality, and uniform size and shape, of metal oxides [133–137], metal chalcogenides [138–146] metal phosphines [147–149] alloys [150–152] and compound nanocrystals [153–156].

The Kirkendall synthesis strategy has been utilised to generate solid palladium nanocrystals into hollow palladium nanocrystals, which has been achieved through the insertion and extraction of phosphorus. The Kirkendall cavitation procedure when repeated several times gradually inflate the hollow metal nanocrystals, which would produce the nano shells of targeted thickness. The generation of hollow palladium nano crystals is shown in Fig. 9.2 [158].

9.2.6 Foams of Metal Chalcogenide

The layered transition metal chalcogenides (TMCs) nanostructures are emerging as important materials due to their exceptional chemical and physical characteristics, which are not present in other nanostructured materials, the properties are sometimes superior even to graphene. TMCs exhibit various anisotropic characteristics which ranged from the electron mobility, magnetism, intercalation of species, catalytic activity, and optical properties [159–166]. TMCs exist in two crystallographic structures; as in octahedral (1 T) and trigonal prismatic (2H). The versatile physicochemical properties of transition metals generated through the varied characteristics from metallic to semi-metallic or semiconducting with the variation in the composition and crystallographic structure. The TMC, MoS_2 is known for its unique properties of possibility of nano porous, and layered structures lead to its excellent applications in optoelectronics, and electrochemical energy harvesting and storage [167–171]. The modulation of the shape and sizes of the TMCs generate interesting electrical, electronic, optical, catalytic properties leads to several important applications. As the synthesis procedures, the bottom-up chemical synthetic approaches, chemical vapour deposition (CVD), mechanical/chemical exfoliations are some of the popular synthesis routes which have been adopted to synthesise TMCs [172–175]. The uniform mesoporous foam of MoS_2 has been synthesised using the $(NH_4)_6Mo_7O_{24}$, where wet impregnation method was used to homogeneously coat

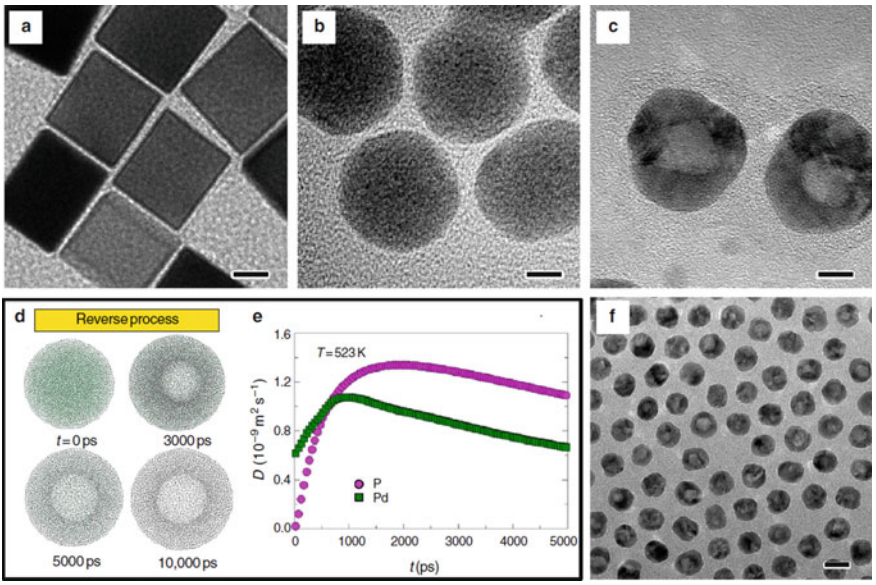

Fig. 9.2 Transformation of solid Pd nanocubes into Pd hollow nanocrystals with hollow interiors. **a–c** TEM images of Pd nanocubes, Pd-P intermediates, and hollow Pd nanospheres, respectively. Scale bars in (**a** to **c**) are 5 nm. **d** Snapshots of a Pd nanocrystal at different simulation time. **e** Instantaneous diffusion coefficients D of Pd and P atoms during the simulation. **f** TEM images of hollow Pd nanospheres at a low magnification. Scale bar in **f** is 20 nm, Reprinted with permission from Ref. [158]. Copyright 2017 Springer Nature

the compound onto the pre-synthesized SiO_2 nano spheres. The surface chemical reaction using CS_2 at the SiO_2 surface converted the Mo precursor into vertically aligned MoS_2 layers around the SiO_2 nanospheres. The mesoporous MoS_2 foam thus formed were recovered through the etching of the SiO_2 template with an HF solution [176, 177]. Through another simple synthesis strategy, the hydrothermal reaction between sodium molybdate and thiourea with P123 as a surfactant at the reaction temperature of 200 °C. The interconnected and porous 3D honeycomb-like constructions of nano structure with pore size varied from 50 nm to hundreds of nanometres of MoS_2 nanosheets were synthesised. Other than MoS_2, VSe_2 nanosheets were synthesised from of vanadyl acetylacetonate ($VO(acac)_2$) as a precursor for V [178]. For the synthesis of WSe_2, nano porous structures trioctylphosphine oxide (TOPO) is injected rapidly into the solution containing $W(CO)_6$ in TOPO, the diameter of the WSe_2 nano discs are reported to be 5.8 nm and the later is sized in the ranges of 2.5 to 9.7 nm, and the size variation could be modulated through the variation in the molar ratio between metal precursor and the surfactant [179].

Carbonaceous composites of TMCs

The hetero-structure between carbon and TMC have applications in energy research owing to the enhanced surface area and reduced mean free path of diffusion for the

charges, which results in the enhancement in the electrochemical performance. The hollow carbonaceous core is synthesised through multistep change in the compositional and subsequent etching process, over the hollow carbonaceous core, the 2D layered TMCs are grown using a seed-mediated growth method [180].

In an another synthesis procedure, cube-shaped α-Fe_2O_3 is synthesised with dimensions of 500 nm using co-precipitation method over the cube-shaped α-Fe_2O_3 smooth polydopamine layer is generated. Afterwards by the utilisation of the carbonisation route in nitrogen atmosphere, the core–shell α-Fe_2O_3@PDA is transformed into α-Fe_2O_3@C nanocubes. Thereafter the α-Fe_2O_3 core is etched out with the HCl treatment and the carbon nanoboxes were obtained. Over the carbon nano boxes, MoS_2 nanosheets are grown by solvothermal reaction, thus producing C@MoS_2 nanoboxes. Using a similar method of synthesis, three-layered TiO_2@C@MoS_2 tubular shaped nanowires are generated [181].

For further increase the conductivity and also to improve the catalytic performance of the TMCs, TMCs-CNT/Graphene nano structure are synthesised. Inside the 2D layered TMCs, highly conducting materials such as carbon nanotubes (CNT), graphene, and conductive polymers are incorporated [182, 183]. The incorporation of graphene sheets has improved the electrical conductivity, flexibility, and chemical robustness of TMCs. The presence of oxygen containing functional groups like $–COO^-$, –COOH, and –COH on rGO assist as sites for the nucleation of MoS_2 due to their high chemical interactions with Mo precursors. The MoS_2/rGO hybrid nanosheets are synthesised through the solvothermal protocols [182].

In order to further improve the catalytic performance of the material, the TMCs-Noble Metals nano porous composite materials are synthesised. The growth of the metal nano crystals are succeeded over the large surface area MoS_2 nanosheets using the precursors of K_2PtCl_4, K_2PdCl_4, $HAuCl_4$, or $AgNO_3$ through the chemical, photochemical reduction or electroless deposition techniques [184–187]. Using mild reducing agents in combinations of surfactants, such as sodium citrate, PVP and CTAB, are beneficial in preferential incorporation of noble metal inside the TMCs sheets by controlling the kinetics of the processes [184].

9.2.7 Synthesis of Porous Structure Through Electrospinning Route

The electrospinning effect was first explained by Lord Rayleigh in 1882, and he explained the typical characteristics of the charged droplets and reported about the maximum amount of charges that a liquid droplet could be able hold after which the charged droplet would be ejected in the form of a liquid jet [188]. Electrospinning technique can be considered as different variant of the electrospraying; in both the techniques high voltage was applied to eject the liquid jets [189]. However, there is significant difference between the two techniques in terms of the viscosity and viscoelasticity of the liquid used and their ejection with the application of high

voltages. In case of electrospraying process, the jet introduced the liquids in the form of droplets, whereas in the case of electrospinning the liquid jet is ejected in continuous mode without breaking.

Electrospinning technique has been utilized to fabricate nanofibers from ranges of materials. The polymers can be electropsun, and the nano porous network structure can be formed. Self-assembled molecules may also be electrospun to form several different structures. Several nano fibres could be formed through electrospinning method using sol–gel jet [190].

In metal nano foams synthesis, metal nano particles at high concentration is used as the dispersion media or spinnable media. As an example of this method of synthesis, Ag nanoparticles (40 ± 5 nm) were dispersed in ethylene glycol with the metal loading of about 50 weight % [191]. The Ag nano fibres are synthesised by electrospinning the solution first, then annealing at 150 °C in air, the average diameter of the Ag nanofibers using this procedure was obtained as 338 ± 35 nm. The important limiting factor of the process is the inability to increase the metal nano particle loading. Electrospinning is also utilised for the synthesis of ceramic nanofibers, though it is difficult to carry the electrospinning using the ceramic melts as it requires very high temperature for the melting [192, 193]. The electrospinning of ceramic materials is reported using aged sol, using this procedure, ceramic fibres of very high density are formed. The silica fibres are obtained using the sol–gel procedures of uniform viscosity [194]. TiO_2 nanofibers of anatase phase contained of fused TiO_2 nanoparticles of diameter 10 nm with voids between adjacent nanoparticles could be formed using the method of synthesis [195].

9.3 Applications of Porous Structured Materials

The porous materials or foams have widespread commercial applications which are utilised since long time which includes filtration devices, battery electrodes, self-lubricated bearings, structural components, diesel soot filtrations and flow control devices [196]. Foams are known to have excellent properties of absorption of energy, finds important applications in fabrication of sound, pressure and vibration dampening components and used for such purposes in several industries [197, 198]. As an important application of energy absorption, the German automotive supplier Karmann uses aluminium foam in the construction of bulkhead and the rear seat wall for their convertible cars. The foam materials used for such purposes are reported to be up to 10 times stiffer than the conventional steel parts with 30–50% less weight. Porous materials are finding very important applications in developing several energy storage materials either in the form of Li ion battery or supercapacitor [199]. In the following section the applications of the porous nano structured materials are mentioned in brief in the field of energy harvesting and storage, sensors, large scale industrial use and in biomedical applications.

9.3.1 Use of Foams in Li Ion Battery and Supercapacitors

In the verge of rapid industrial developments and increasing wealth of modern societies requires the development along with the sustainability and the environment friendliness [200]. The world fossil fuel consumption in 2018 was 11,743.6 million tons of oil equivalent (Mtoe), which accounts for the 84.7% of the world's energy consumption [201]. With the pace of developments, the fossil fuel combustion is set to increase further, and it is projected that by the year 2040 the expected fossil fuel consumption would be 17,651 Mtoe. It is therefore required to enhance the consumption of the renewable energy, and it is targeted to use the renewable energy by 20% of the total energy consumptions. Utilisation of renewable and clean energy requires efficient storage system, Lithium (Li)-ion batteries (LIBs) has proven track record as an efficient energy storage system due to their high specific energy, high power density, and acceptable environmental friendliness. Among all the electrochemical energy storage systems, LIBs has the largest share, as estimated in the year 2018 about 86% of the total energy stored are in the form of LIBs [202].

Current collector is an important component in energy storage devices. As current collector, Ni foam is best suited to be used in Li ion battery and it is used for the efficient transport of charges both from the cathode and the anode side of the Li ion battery. The superior property of 3D Ni foam over the conventional films or sheets has been utilised for enhancement in the performance of Li ion battery in terms of enhancing the capacity at higher current rates. The redox reaction at the junction of the frame of the Ni foam and the active materials is beneficial in improving the capacity. The 3D structure and the incorporation of the active material significantly reduce the diffusion length of the transport of charges, which is the important factor in higher rate capability. Additionally, the use of Ni foam reduces the swelling of the active materials on prolonged charge and discharge cycles [203]. Due to such advantages, Ni foam was used as current collector in Li ion battery. The application of Ni foam in holding the active $CoSn_2$ material used in Li ion battery is shown in Fig. 9.3. It

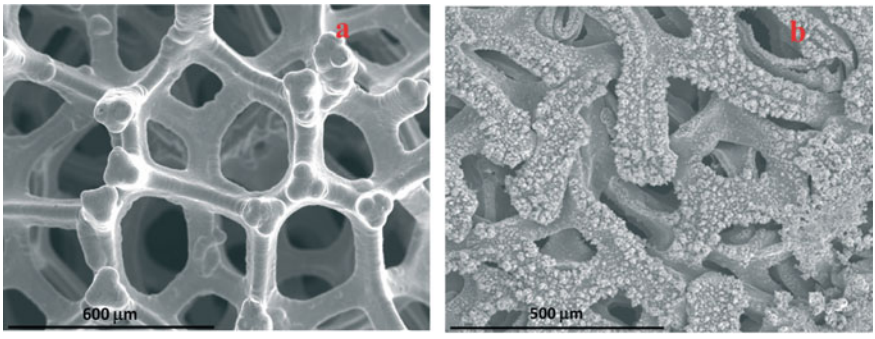

Fig. 9.3 The SEM micrographs of electrodes. **a** Nickel foam before electrodeposition of cobalt and tin. **b** After electrodeposition of Co–Sn alloy. Reprinted with permission from Ref. [204] Copyright 2013 Royal Society of Chemistry

was shown that the $CoSn_2$ evenly deposited over the Ni foam surfaces, due to such coexistence of the active material and the current collectors the efficiency of the charge transport in expected to enhance significantly, which has been reflected from the enhanced rate capability of the materials through depositing materials directly over the Ni foam current collectors [204–206].

However, there are several challenges in the use of metal foams as current collectors for Li-ion batteries because the conventional metal foam based current collectors usually has low tolerance in long term charging or discharging, especially at high voltages. Though Ni foam is very well suited as current collector in Ni/MH battery [207], it is vulnerable to corrosion when the foam parts come in contact with the electrolyte materials of Li-ion battery [208]. In order to improve the corrosion resistance of Ni foam, NiCrAl alloy foam was reported to use as the current collector for lithium iron phosphate ($LiFePO_4$) based battery system. The $LiFePO_4$ is a promising material due to its low toxicity, high safety, available at low cost, excellent cycle life, high structural stability, and large theoretical capacity (170 mA h g^{-1}); however, the kinetics of the material is quite slow. Application of Ni foam or NiCrAl alloy foam improves the kinetics of $LiFePO_4$, which has reflected in the enhancement of the rate capability [209]. Similar to the Li ion battery, metallic foams are applied in other secondary battery electrodes like, Zn air battery, Li oxygen battery and other secondary battery systems [210, 211].

Like Li ion battery, supercapacitor is a potential energy storage device becoming more popular in recent times. Supercapacitor is also called as pseudocapacitor or ultracapacitor and is a highly efficient in storing charges. In conventional capacitors, the charge is stored through the electrostatic interactions, whereas in supercapacitor the charge is stored through both redox process and the electrostatic process. Due to the involvement of the redox process, supercapacitors are called as the pseudocapacitor. The fast discharge process in supercapacitor leads to the enhanced gravimetric power density compared to the rechargeable batteries, additionally the supercapacitors can sustain significantly higher numbers of charge and discharge cycles compared to the rechargeable batteries. Supercapacitor devices are finding applications in automobiles, small buses, electric drives, UPS, active filters, traction devices etc. The energy storage through the regenerative braking is an important application in automobile industry, and supercapacitors are used for this purpose for short term energy storage. The redox process in the supercapacitor is mainly associated at the surfaces of the materials therefore the requirement of materials with high surface area are essential for the constructions of supercapacitor electrodes [212–216].

The current collector function as the electrical linking between the active materials of supercapacitor with the external terminals. The redox processes essentially occur at the surfaces of the active electrode materials which requires efficient transport of charges from the active electrode materials to the output terminals through the current collectors; therefore, the current collectors must provide good electrical contact with the active electrode materials [217]. Current collectors with porous nano structures serves the purpose of effective transport of charge without increasing the mass loading of the device. The porous nano structures with three dimensional geometry have the advantage of having large contact areas with the active materials, which

reduced the requirements of the ions to diffuse the long distances thereby promotes the transport of charges [218–221]. The improvement in the design aspects and making better contact between the active materials and current collectors enhances the charge storage capacity without increasing the material loading [222, 223].

The porous nano structure with controlled pore size is important for the active electrode material. Pore sizes should be optimum for the electrolytes to seep in for accessing the redox sites and also should have good numbers of redox sites. It is to be noted that the unutilised pores are responsible for the decrease in the volumetric capacitance of the porous materials. The carbon based porous materials along with metal oxides with porous nano structures have shown significant improvement in the capacitive property [213]. The mesoporous Co_3O_4 has shown the enhanced ion transport properties, which leads to the enhancement in the capacitive behavior [214]. Wu et al. have formed the hollow nano structured $Ni(OH)_2$ with porous walls; the electrodes fabricated using the porous $Ni(OH)_2$ provide more efficient paths for the interaction between the electrode materials, and the electrolyte and the capacitance increased significantly [215]. The porous nano tube structure of TiO_2 was fabricated as support material, within that the Co or Ni oxides are deposited as redox active substrate, the combination of porous nano structure of TiO_2 and the redox active Co and Ni oxides has improved the charge storage capacity [216].

9.3.2 Application of Porous Nano Structures in Fuel Cell Technologies

Nano porous structure finds important applications in fuel cells, considered to be the most important energy conversion technology. Generation of efficient materials for the electrodes in fuel cells are very important technological challenge, generally noble metal based catalytic materials are widely used as both cathode and anode for the catalytic hydrogen evolution process and also for the catalytic oxidation of small molecules or in the oxygen reduction [224, 225]. The key requirement of the electrode materials is to have high electrochemically active surface area (ECSA) and conductivity. The PNMNs serve both the purposes well. Porous nano structure reduced the mass of the noble metal catalysts, thus reducing the overall cost of the catalytic system.

PNMNs are directly used both as the cathode and the anode material for catalytic electrochemical processes in the fuel cell. Most importantly, PNMNs can be used without any support, thus eliminating the use of carbon support in the fuel cell applications. These materials can be directly applied as self-supported nano catalysts for both the cathodic and anodic electrochemical reactions of fuel cells, which can eliminate the use of the conventional carbon support to the electrode, thus avoids the drawbacks of the carbon supported catalysts. Applications of some of the PNMNs used as the active electrode in the fuels cell research are discussed in the following section.

As anode materials PNMNs are utilised for the oxidation of small molecules like methanol, ethanol, and formic acid as fuels in the fuel cell. Xiao et al. reported the synthesis of hierarchically porous Au-Pt nanostructures, where the porous Pt nano structures are decorated over the surface 3D AuNPs [226]. The nano structured materials have shown excellent catalytic activity for the methanol oxidation reaction. Due to the nano porous structure, the mass transfer property has been significantly improved. The porous nano structure also reduced the tolerance to the intermediate species generated due to the oxidation of methanol, which are otherwise detrimental to the catalytic property of the materials. As a non-noble metal, Ni was incorporated in Pt-Ni–P hybrid system and the porous nano structure of the system was fabricated through the template assisted electrodeposition route. The materials showed promising results with the additional benefits of decrease in the noble metal requirements [227]. In a recent study, Sesu et al. reported the Cu-Ni@rGO foams for the enhancement in the methanol oxidation reaction. The self-propagation combustion method was utilised for the synthesis of the non-noble metal based foam nano structure and rGO was also incorporated for improvement in the conductivity and surface area further [228].

Several non-noble metal foams are being utilised for the catalytic oxidation of methanol, in a recent study adopting the self-combustion technique, low density Co–Cu-Bi ternary foams with three dimensional structures was synthesised and the catalytic efficiency for the methanol oxidation has been improved significantly. The catalysis poisoning effect, which is common with the noble metal based catalysts, has been reduced significantly in this system, the catalytic activity reported to be retained at 50% even after 10 h of operation [229, 230].

As the ethanol oxidation electrode, Pd based aerogels are reported to increase the efficiency significantly compared with the commercially available Pd/C catalytic system. The Pd aerogels have shown the electrochemical surface area (ECSA) values significantly improved for the various Pd aerogels as reported by Liu et al. [231] Ni foam as current collector or catalysts support is almost unavoidable in making efficient electrodes. Apart from the function as current collector, Ni foams are used for the deposition of active catalysts materials, as an example Au nano particles in the form 3D nano structure are electrochemically deposited over Ni foam substrate [16, 232–234]. The catalytic system has been efficient for ethanol oxidation reaction with significant improvement in the efficiency.

Oxidation of formic acid is also an important reaction utilised as the anode process in fuel cell. The nanoporous Pd-Cu alloys catalysts were reported to be fabricated using the de-alloying method of synthesis, and the catalysts electrodes were fabricated using the porous Pd-Cu based nano structures [235]. Compared to the nanoporous Pd alone the catalytic activity using nanoporous Pd-Cu system was improved significantly. Cherevko et al. developed high surface area Pd foams through the electrochemical deposition route with the roughness factors over 1000 and the specific surface area of 60 m^2/g, the catalysts has shown high activity towards ethanol oxidation reaction [100].

The porous nano structures are also utilised as cathode materials for the Oxygen Reduction Reaction (ORR) at cathode. The ORR is one of the most technological

challenge in fuel cell fabrication, which arises due to the complexity in the reduction process of oxygen. The requirement of an efficient catalyst is thus very important for efficient running of the cathode reaction in fuel cell. The porous nano structure of foams were utilised for the catalytic reduction of oxygen at the cathode. Investigations revealed that the porous self-supporting network structures enhanced the electrochemical performance by about 2–3 times than that of the commercially available standard Pt/C catalytic system. In the report by Strasser et al., the Pt-Ni bimetallic porous materials are synthesised, the porosity induced catalytic performance was investigated, it was observed that porosity below 10 nm is beneficial, and at higher pore size, remarkable drop in the catalytic performance observed [236].

Oxygen evolution reaction (OER) plays a crucial role in electrolysers, solar cells and photoelectrochemical water splitting process [237–241]; however, the sluggish electron transfer kinetics of the process is of considerable concern [242–247]. The porous nano structured materials have excellent applications in the oxygen evolution reactions (OER). Building hierarchical hollow structures thus holds promise for more efficient electrocatalysts, which can render large surface area, better electronic conductivity and porosity for electrochemical processes [248–250]. Great efforts have been devoted to develop such porous and hollow nanostructure, which can, not only enhance the desired activity but also impart new functionalities [249–253].

In a work reported from our group has focused on the synthesis of porous nano structure of $Ni_xCo_{3-x}O_{4-y}$ nanocages through a simple metal organic frame work (MOF) template based fabrication route for non-stoichiometric Ni-Co metal oxide nanocages with mesoporous structure [254]. The redox centres rich in Ni and Co have shown as efficient catalysts for the oxygen evolution reaction. The influence of different compositions of $Ni_xCo_{3-x}O_{4-y}$ nanocages on their structural and chemical characteristics is investigated along with tuning of the electrocatalytic OER process. The SEM images of the nano cages with different ratios of Ni and Co along their schematic representations are shown in Fig. 9.4. In the nano cage structure, the best catalytic activity was observed with Ni:Co ratio of 1:1. The combined effect of 3D porosity, rich redox centres, oxygen vacancies associated non-stoichiometry and high electrochemical surface area (ECSA) has resulted in achieving a higher catalytic current at a lower onset potential, faster OER kinetics and a facile mass transport during oxygen evolution. Such synergistic behaviour imparts exceptional catalytic activity to $Ni_xCo_{3-x}O_{4-y}$ porous nanocage system as a cost effective and viable oxygen evolution catalyst.

Hydrogen evolution reaction (HER) is the process through which hydrogen is generated from water through electrolysis process. It is essential to have of earth abundant catalysts in place of the noble metal catalytic system and has generated the interest in research in the development of materials for the HER. Among several non-noble metal catalytic system, the molybdenum di-sulphide (MoS_2) has shown promising results in generating hydrogen from water through electrolysis [255–261]. The MoS_2 with porous or layered nano structure has the advantage of having multiple reaction sites, and better access to the electrolytes over its surfaces. The conductivity of the MoS_2 is important and 1 T phase serve the purpose better. The surface area and the charge transport property of MoS_2 further improved through making composite

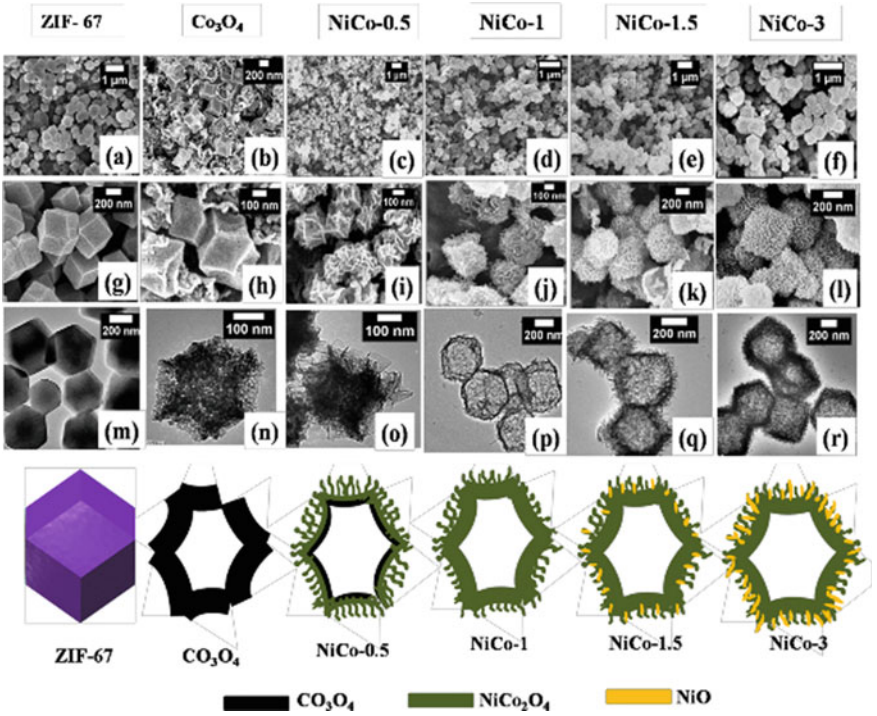

Fig. 9.4 **a** to **f** FESEM images of the MOF derived catalysts, **g** to **l** magnified FESEM image of the MOF derived catalysts, and **m** to **r** TEM images of the respective MOF derived catalysts. The schematic shown in the bottom of Fig. 9.4 represents the evolution of the $Ni_xCo_{3-x}O_{4-y}$ catalyst when Ni is loaded in different concentration, Ni/Co = 0, 0.5, 1, 1.5 and 3. Reprinted with permission from Ref. [254] Copyright 2016Wiley-VCH GmbH

with graphene oxide (GO) or reduced graphene oxides (rGO). In our investigation we have observed that the enhanced mass transfer through the fast exchange of protons from the medium and the functional groups of GO in MoS_2/GO composite shown improved catalytic activity. The schematic representation of the proton exchange process between the medium and the functional groups of GO is shown in Fig. 9.5 [182]. The TEM image and the scanning electrochemical microscopy (SECM) scan of the catalysts surface are also shown in Fig. 9.5. The TEM image showing the layered structure of the composite. The SECM imaging indicates the current response from the catalyst surface originating from the catalytic hydrogen evolution process. The image shows several areas from which high HER current response could be generated.

The foams with porous structure having large surface areas are especially advantageous in utilisation of electrocatalytic or photocatalytic splitting water to generate hydrogen and oxygen [262–264]. For photoelectrochemical water splitting the porous network materials are replacing the conventional indium tin oxide (ITO) or fluorine doped tin oxide (FTO) as the electrode substrates, which has improved the charge

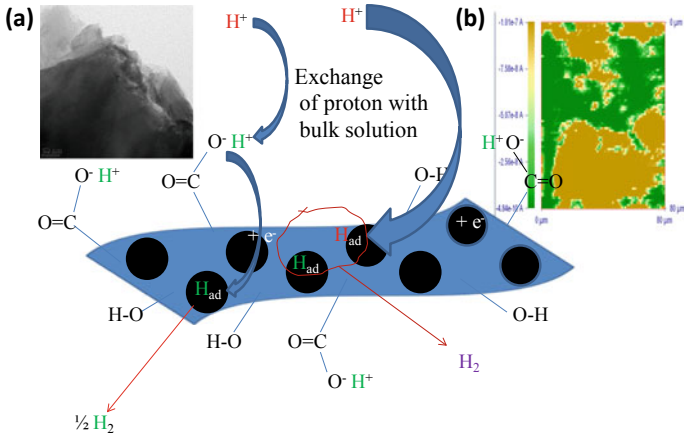

Fig. 9.5 The Schematic representation of the mechanism of the proton transfer process in the MoS_2/GO composite during the HER process; Inset **a** the TEM image of the layered structure of the composite and **b** The SECM image of showing the HER current response over the composite modified electrode surface. Reprinted with permission from Reference [182]. Copyright 2017 American Chemical Society

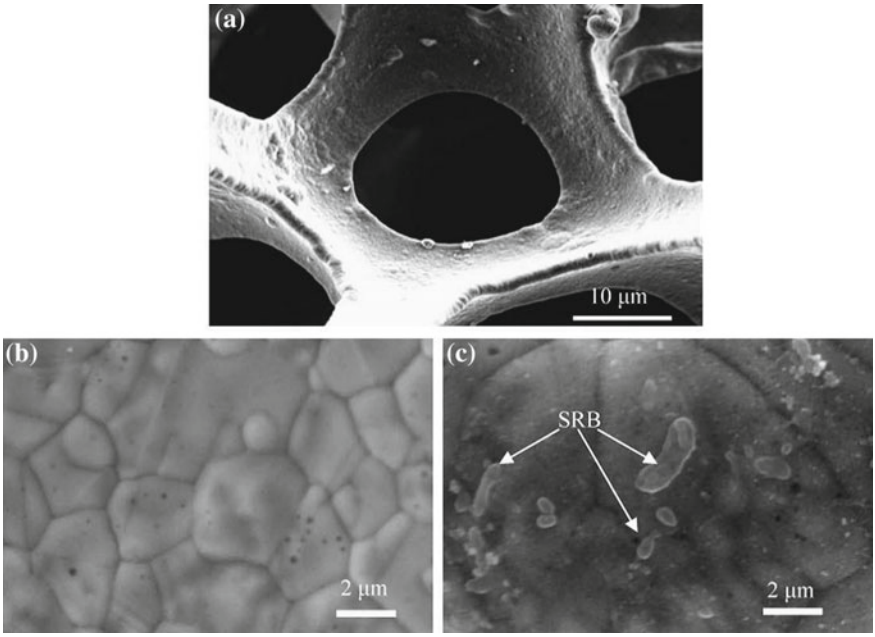

Fig. 9.6 SEM images of foam Ni (**a**), antibody-functionalized foam Ni incubated without (**b**) and with (**c**) SRB culture. Reprinted with permission from Ref. [293]. Copyright 2010 Elsevier

transfer property of the cathodes and anodes. The Ni and Fe foams are the better choice for loading the active materials to fabricate the anodes and cathodes for water splitting experiments.

9.3.3 Application of Porous Structures in Electrochemical Sensors and Biosensors

The design and development of electrochemical sensors are fascinating in terms of their portability and onsite applications [265–267]. Construction of the electrodes with suitable electrode materials is the most important part in the development of sensors. The porous nano structure materials with their unique properties of high surface area, faster transport of charge and the ability to be functionalised with suitable functional groups are important factors making them suitable in developing the sensors. PNMNs are generally best suited for the modification of electrodes in developing electrochemical sensors and biosensors, owing to their enhanced charge transfer properties in addition to other properties common to all porous materials. Several PNMNs modified electrodes were explored in developing electrochemical sensors for the small molecule, toxins, drugs, using enzyme, non-enzyme based sensors, DNA sensors, immunosensors etc.

9.3.3.1 Application of Porous Nano Structure in Non-Enzyme Based Sensor

The non-enzyme based sensor offers easy operation, storage and have better long term usability compared to the enzyme based sensors. Metal foam or the nano porous materials offers great supports as the electrode materials for the non-enzyme based sensors. Juska et al. have developed the Cu nano dendrite foams based array sensors for the detection of glucose. They have demonstrated the enhanced catalytic activity of the electrochemically deposited Cu foams based miniaturised electrodes as the electrode materials for the efficient non enzymatic oxidation of glucose. The array electrodes offered sensitivity much superior to the related literature reports along with the typical characteristics of the non-interference from the chloride ions, which is an important interfering agent in glucose sensing [268]. Similarly, the gold nano rods decorated over the Ni foams are applied for the enhanced electrochemical signal from glucose, the copper oxide nano wire over the copper foams are also reported for the glucose sensing. In addition to the copper foams, the gold foams are also found to be suitable for the electrochemical sensing of glucose [269–271]. Metal and graphene based composite foams are also reported for the non-enzyme based sensing of glucose [272, 273]. Other than glucose, the metal nano-porous structures and foams are utilised for the sensing of H_2O_2, several drugs and biomolecules [274].

Denuault et al. have constructed mesoporous Pt microelectrodes to utilise the quasi-hemispherical diffusion with large effective electroactive area for the high sensitive detection of H_2O_2 over a wide range of concentrations [275]. Furthermore, well-defined nanoporous PtNi alloy nanowires [276] and 3D nano porous gold film [277] were fabricated through the dealloying method of synthesis. Both the materials showed a remarkable enhancement in the electrocatalytic activity for H_2O_2 sensing. Additionally, Chung et al. have constructed 3DAu nano-dendrites through electrodeposition of Au using a gas bubble dynamic template method [278]. The porous Au nanostructures with ultrahigh surface area were used as the sensor substrate for the advanced detection of As(III) at ultralow concentration.

9.3.3.2 Application of Porous Nano Structure in Enzyme-Based Biosensors, DNA Sensor and Immunosensors

The coupling of enzymatic actions with the electrochemical sensors enables the appropriate detection of target molecules through the utilization of combined effect of the high specificity of the enzymes with the high sensitivity of electrochemical signals generated through porous materials [129, 279]. Several nanomaterials with variation in sizes, shapes, and compositions have been prepared and employed as advanced porous electrode materials for the immobilisation of enzymes; thus, the electrochemical enzyme based biosensors were fabricated. PNMNs with high pore volume and large surface area, which increase the enzyme loading and also has the capacity to protect the enzyme from the surrounding environment. Pariente et al. developed lactate oxidase-based biosensors by fabricating porous Au material with rough surfaces [280, 281]. The sensor used hydroxyl-methyl ferrocene as the redox active agent, and the analytical method developed using the modified electrode could sensitively detect lactate with the detection limit of 21.5 μM and sensitivity of 1.49 $\mu A\ mM^{-1}$. Additionally, Chen et al. [282] and Huang et al. [283] used Au nanostructure based electrode fabricated from the dealloying technique and used as sensor for the development of glucose sensor, where glucose oxidase enzyme was used as modifier. The enzyme based biosensor has the advantage of the superior activity in terms of specific interaction with the analytes and the inherent fast response; however, the enzyme based sensors have the issues like high cost and instability with minor variation in the experimental conditions [284].

The sensing of the biomolecules based on the electrochemiluminescence (ECL) is an important analytical methods utilises the luminescence signal from a standard redox probe with the application of suitable potential. However, the ECL based detection has the issues like weak and broad signal, and intermittent loss in signal strength, the application of porous nano materials improves the signal strength of ECL based detection [285]. The modification of Ni-foam with NiO nano structure has been utilised in the ECL based detection of glucose of in serum sample, where the ECL signal could be enhanced and stabilised [286].

DNA biosensor sensors are known for their high specificity and extremely high sensitivity up to the femtomolar concentration, which leads to their applications in

genoassay, suitable for the clinical diagnosis, forensic and the environmental analysis. Gold has special application in DNA based sensors due to their compatibility; gold in the form of nano porous structure is termed as the nano porous gold (NPG) and is very well suited for the electrochemical DNA biosensor [287, 288]. The electrochemical DNA biosensor fabricated using the NPG electrodes has been utilised for the determination of retinoic acid receptor α(PML/RARα) fusion genes in the case of acute promyelocytic leukemia, where the electrochemical signal from the methylene blue (MB) is used for the detection. The signal was typically enhanced by about 10 times especially due to the use of NPG modified electrode. Mehrgardi et al. have used the NPG as the electrode in DNA biosensor where ferrocene carboxylic acid was used as the redox probe. In this case the redox probe, ferrocene carboxylic acid was attached covalently on the top of the probe DNA, and the signal is generated while the probe DNA undergo hybridization when comes in contact with the target DNA. The significant enhancement of the electrochemical signal due to the NPG electrode leads to the development of detection strategy up to the detection of single base pair mismatch in DNA [289].

The early detection of the microorganisms is extremely important in deciding the treatment procedures in all diseases, which guide the medical system for the early decision on treatments with minimal use of antibiotics. Immunosensing is an important procedure in detecting the microorganisms responsible for various illnesses [290]. The porous nano structures are used in the fabrication of electrodes in the immunosensing applications. The porous gold films are utilised as the electrode materials in developing label free immunosensor for the determination of C-reactive protein, the resistance signal was generated from electrochemical impedance spectroscopy measurement for the impedance based sensor [291].

Additionally, the copper foam nano wire arrays are utilised in developing the electrochemical immunosensor for prostate specific antigen. [292] It was also reported about the immunosensors for the sulphate reducing bacteria (SRB) using Ni foam and gold nanoparticles as the substrate, which provides effective trapping platform for the bacteria. The sensor was utilised in the detection through the impedometric detection techniques [293]. The typical structure of the Ni foam used in the immunosensing purposes of SRB and the Ni foam modified with rabbit antibody used for the sensing of SRB along with the SRB embedded over the sensors substrate are shown in Fig. 9.4. The instant decrease in the charge transfer resistance form the electrochemical impedance measurements was utilised in the determination of SRB.

In a recent study the metal–organic framework (MOF) based Ni foam supported three-dimensional (3D) immunosensor was constructed and utilized for the specific recognition of troponin (I), acardiac biomarker. Ni was amine functionalised, which was interfaced with the biologically active materials anti-troponin (I), the sensor electrode was thus fabricated and utilised. Analytical measurements were carried out using impedance measurements by electrochemical impedance spectroscopy. The sensor generated high sensitive measurements procedures with limit of detection 13 fg/mL with improved specificity [294].

9.3.4 Applications Porous Materials in Concentrating Solar Power (CSP)

Solar energy is the most abundant renewable resource available on Earth. About 430 EJ (1 EJ = 10^{19} J) of sunlight energy impact on the Earth per hour, which is much more than the total annual world energy consumption [295]. There are several methods targeted to harvest solar energy into usable form, out of which the one of the important solar energy harvesting protocol is through the high temperature thermochemical storage, which can be utilised in large scale. This process contains a heliostat field and a solar receiver generally located on the top of a tower, due its presence over a top of a tower such plants are called as tower plants. The heliostats are mirrors with large dimensions, which are used for the reflection of sunlight and concentrate it on the receiver placed at the centre [296].

The solar receivers are the heat exchangers, used for the transformation of concentrated solar energy into thermal energy by heating up a fluid, the hot fluid flows through the radiation absorber components. Metallic foams are best suited as the receiver materials for the solar energy concentrators, the porous structure helps to expose large area materials by allowing the solar radiation to enter inside the materials, also the high temperature corrosion of such materials could be reduced through the utilisation of bi-metallic foams. Ni foams has been used as the receiver materials, and the bi-metallic foam of Ni with Al reduces the corrosion at high temperature [297–299].

The solar heat is also stored through the redox processes, and the materials placed as the receiver can be utilised for receiving the solar radiation along with conversion and storage through the redox processes. The foams of cobalt oxide are best suited for such purposes. Agrafiotis et al. have reported the use of porous foams of Co_3O_4 with good structural stability, which does not show any significant loss of redox activity after 30 cycles [300, 301]. However, due to high cost and scarcity, and also the known toxicity of Co, several other metal are incorporated with Co_3O_4 such as Mn, Fe, Ni, Cu and Zn to reduce the requirement of Co for the purpose, at the same time keeping the capacity of the material unchanged. The Mn-doped Co oxides showed that the material performed better as the density of energy storage was decreased with the incorporation of Mn with Co_3O_4 [302]. However, with low Fe concentrations (about 5%), the long term cyclability of the materials along with density of energy storage turn out to be high [303]. The Co_3O_4 based foams used for the high temperature redox process, and the device form of the materials before after use are shown in Fig. 9.7 [304, 305].

9.3.5 Commercial and Large Scale Applications of Foams

The porous structure with macroscopic pores is having several industrial applications. There are large number of manufacturing technologies for the synthesis

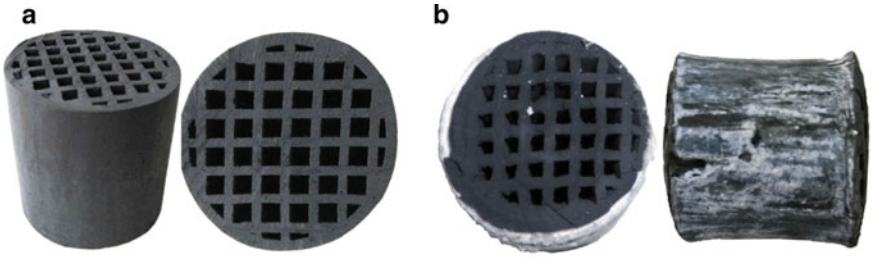

Fig. 9.7 **a** Picture of Co_3O_4/Al_2O_3 with 90/10 wt. % based honeycombs (freshly made before use). **b** the sample after 104 cycles. Reprinted with permission from Ref. [305]. Copyright 2016 Elsevier

of foams, sponges and porous materials with macroscopic pores. The commercial synthesis process utilises the powder metallurgy route or the melting route for the large scale generation of such materials. The direct and indirect foaming methods are also utilised for the large scale synthesis of foams which are very well described in the literature [306–308]. The porous materials offer important applications in the automotive industry, in the electric car, as the lightweight construction becoming mandatory. Additionally, the safety is another important factor, where a light and effective crash protection system is essential. The example of such application is shown in Fig. 9.8, where the metal foam is sued as the crash protector. Metal foam parts developed by the Technical University Berlin and Pohltec are shown in the prototype of an ultra-light electric vehicle developed in the frame of the European Project Evolution [309]. In another example Alulight manufactures the metallic foam shock absorber and manufacture millions of such units for high end vehicles, the per unit mass requirements of such foams is significantly low, only about 7 g of mass is used per device. Exploiting the property of high energy absorption capability of the metallic foams, Foamtech (Daegu, Korea) provided crash elements for a guardrail at the Massan-Chanwon Bridge in Korea. The Al-foam as a protection element in A-pillars was investigated for its suitability in the crash protection [310]. The Al-foam reinforcement for the A-pillar of a Ford passenger car provides an improvement of 30% in crash energy absorption achieved with only a 3% increase in the weight [311].

In addition to the structural material and shock absorbing applications, metallic foams have application in silencers, mufflers, diesel, particulate filters, support for the selective catalysis reduction, etc [312]. Several companies like Exxentis (Wettingen, Switzerland) and Mott Corporation (Farmington, CT, USA) manufacture filters for the gas filtration and liquid filtration [313], several other manufacturing companies have products in their line for catalyst carrier, filtration fluid control or anti-sloshing purposes [314]. The nonporous gold foams have important applications as catalysts [315]. Pictures of the components used in filtration and different functional components are shown in Fig. 9.9.

Due to the high stability at high temperatures good thermal conductivity and excellent surface area, metallic foams have important applications in heat exchangers

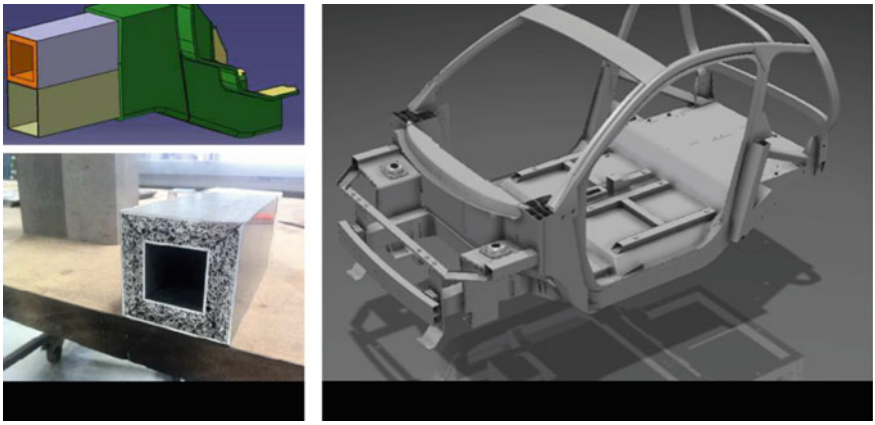

Fig. 9.8 Crash absorber box of the electric car prototype in the frame of the European Project Evolution made with rectangular Al-profiles filled with Al-foam; and CAD design of the body in white. (product of Cidaut, Valladolid, Spain, Pinningfarina, Cambiano, Italy and Pohltec metal foam, Collogne, Germany). Reprinted with permission from Ref. [309]. Copyright 2016 MDPI AG

Fig. 9.9 Pictures a large number of filters from Alantum, Korea, Reprinted with permission from reference [309]. Copyright 2016 MDPI AG

used as passive cooling devices [316, 317]. The pictures of different heat exchangers from M-pore, Germany [318], are shown in Fig. 9.10.

For application even in larger scale metallic foams have application as structural materials in several constructions, as an example the foam from Alusion used the

Fig. 9.10 Diverse types of heat exchangers based on Al- and Cu-foams manufactured by M. pore and Mayser GmbH, Reprinted with permission from Reference [309]. Copyright 2016 MDPI AG

entrance of a souterrain and a bell tower monument, the pictures of such structures are shown in Fig. 9.11.

Fig. 9.11 Translucent entrance of a souterrain and bell tower monument made of Alusion foam, Reprinted with permission from Reference [309]. Copyright 2016 MDPI AG

9.3.6 Application of Foams in Regenerative Medicines

The regenerative tissue engineering is an important application where porous nano foams works in the regeneration and controlling the growth of human tissues having large defects. The porous scaffold required to be placed at the defect sites to provide mechanical stability and promote the cell growth. The porous foams are used as the scaffolding structural materials, and the pores are utilised for (a) allowing and controlling cell attachment, migration and infiltration; (b) they provide improved nutrient and transport of metabolite to and from the cells respectively; (c) also facilitate vascular infiltration; and (d) control the orientation of extracellular matrix molecules produced and laid down by cells [319–321]. Electrospun generated collagen nano porous materials are applied for the nerve regeneration [322]. The 3D nanofibril scaffolds fabricated through an improvised electrospinning technique has been reported to regulate the proliferation and critical functions of rabbit corneal cells, and the investigation has demonstrated the suitability of the technique in the treatment of injuries of ocular tissues [323].

As a material of choice titanium is the most widely used materials for orthopaedic implants, dental implants, and hip replacements. The biocompatibility of titanium is one of the best, in spite of having very good stability some titanium implants fails. For the improvement in the life time of titanium based implants, the surfaces of such materials are modified with porous nano structures. Self-assembling peptide has been used as potential templates for nanofabrication in bio regeneration, direct mineralisation of hydroxyapatite [324, 325]. The self-assembled nanofibers of lipopeptide have been used as bio-regenerative materials, coated over the Ti-6Al-4 V foam bone implant. It was reported that the nanofibers occupied the nano pores of the metallic foam with the bioactive matrices encapsulating the cells for their growth. The nanofibers in the implants facilitate the mineralization of hydroxyapatite, which facilitates the bone formation without deformities [326–328].

Dental caries is one of the most widespread infectious diseases in the world. Currently, it has been handled through replacement of decayed part along with implantations of some materials [329]. With the advancement of the tissue engineering, it has been targeted to generate the hole tooth using tissue growth through nano structured scaffolding and incorporation of stem cells.

With the advancement of the stem cell research and the tissue engineering the cardiac tissue regeneration through the self-assembled systems has shown promising results in the engineered growth of cardiac tissue. As reported by Lee et al. [330] the self-assembled nano structure of peptides works as scaffold for the embryonic stem cells for mice. It was reported that the self-assembly of peptide scaffold provides supports and promote vascularization. The foams provide the large surface area and porosity for the cells to attach, migrate and communicate while growing, generate a suitable platform for the cell engineering, collagen based nano structured scaffold has been investigated for the engineered cardiac tissue growth [331–333].

9.4 Graphene Foam

This book chapter has focused mainly on the metallic foam; however, a small introduction about the graphene foam has been mentioned at this part of the book chapter due to the impulse it has been created in the research fields. In non-metallic foams, the polyurethane (PU) foam has significant commercial applications. It is worth mentioning that the PU foam is being synthesised from the natural sources showing superior properties mechanical properties [334–337].

The 2-dimentional graphene (2D graphene) was synthesised in 2004 and has opened up new research domain worldwide. The fascinating properties of graphene like the large surface area, high thermal conductivity and also the electrical conductivity has led to its several applications in medical, engineering, energy, sensing and environmental related fields [338]. The 2D graphene sheet however undergoes severe deformation in properties due to the agglomeration arises due to the strong π-π interaction between the graphene sheets. The generation of macroscopic object from the 2D graphene sheets would reduce the issues related to the agglomeration, additionally it would provide mechanical strength and enhance the applicability due to the 3D network structure in 3 dimensional graphene (3D graphene).

The 3D graphene assemblies are synthesised through the solution based gelation of graphene oxide sheets, after the gelation process assemblies are subjected to the chemical reduction process or pyrolysis [339–341]. In addition to the solution based synthesis, chemical vapour deposition or powder metallurgy routes have been utilised for the synthesis of 3D graphene, which might be used for the large scale applications also [342–344]. There are several applications of 3D graphene based foams which includes Electronic devices [345–347], energy storage devices [348, 349], Electrocatalytic applications [350–352] to sensors [353–356], and thermal managements [357–359].

For its application in electrochemical sensor, the 3D porous structure has several attractive features well suited in the electrochemical sensor applications. A large electroactive surface area makes the access of the analyses through several channels. The good mechanical strength and the exceptionally good conductivity leads to its application as free standing electrode without the requirements of any support. Additionally, the possibility of the formation of composites with several other metallic and non-metallic substances will generate highly sensitive and selective analytical methods based on 3D graphene. 3D graphene can undergo several types of functionalisation, it can be attached with biologically active molecule like enzymes, and it has wide electrochemical potential window, capable in monitoring the electrochemical oxidation and reduction of several analytes [356, 360]. In our recent investigation the 3D graphene composites of noble metals like Pt, Pd, Au and Ag, which were named as Pt/3D-G, Pd/3D-G, Au/3D-G, Ag/3D-G respectively, were utilised in the investigation of HER activity [352]. The catalytic current of the respective noble metals Pt, Pd, Au and Ag are increased significantly while their presence as composite with 3D graphene. The schematic representation of the synthesis of the catalytic system and the comparison of the catalytic activity are shown in Fig. 9.12. It can be seen that

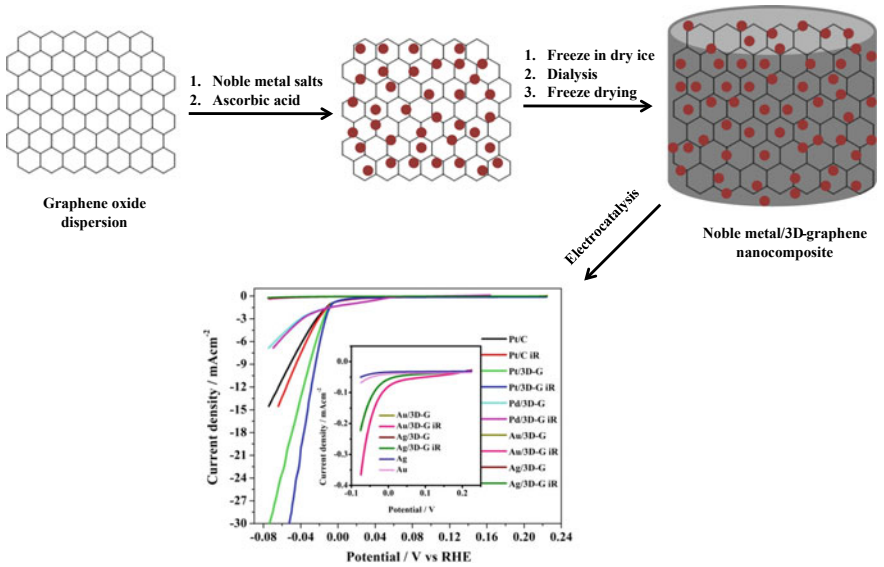

Fig. 9.12 The schematic representation of the synthesis process and the evaluation of the catalytic activity of the 3D-G and Pt, Pd, Au, Ag composites (Pt/3D-G, Pd/3D-G, Au/3D-G, Ag/3D-G, respectively). Reprinted with permission from Ref. [352], Copyright 2019 Elsevier

the HER catalytic response from the Pt/3D-G is higher than the commercially available Pt/C catalytic system. For the overall comparison of the catalytic responses, the plots with and without the iR compensations are shown. High conducting and porous network of graphene sponge provides the excellent charge transfer and diffusion of ions through highly porous materials, which improve the HER catalytic activity in addition to proving support to the noble metal nano particles in improving the stability of the catalysts.

Graphene foam composites are utilised in the next generation super capacitors, and the graphene at the gelation state which are known as the graphene hydrogels are utilised for the enhancement of the super-capacitive property of due to excellent interfacial surface area [361–365]. Graphene hydrogels have improved interconnections among various graphene sheets. The effective acquaintances of graphene hydrogels with the metal oxide redox active materials further improves the charge storage property of such composite materials. In bio-regeneration the 3D graphene foams are serving as promising candidate by mimicking in vivo environments. The nano structural scaffolds of 3D graphene provides easy access for the efficient cell attachment, proliferation, and differentiation during the regenerative medical applications. The efficient mass and the charge transport through the porous graphene 3 dimensional structures provides the physical and chemical stimulations to cells for the required growth [366].

9.5 Summary

In this book chapter, the brief history of the porous metal nano structure has been discussion citing some of the initial journal publications and books. The porous materials used to be practiced in the name powder metallurgy materials, and a brief introduction about that has been included in the chapter. The book chapter then primarily discussed about the metallic foams and hollow nano structures, which are most sought-after materials, finding several important applications. The strategy for the conventional synthesis along with some of the templated synthesis protocols are discussed. The hollow nano structured materials are a special type of porous structured materials finding important applications in sensors and in catalysis. The process of the transport of charges through the inner and out spheres make the hollow nano structured materials special. The discussion about the synthesis procedure through self-templating route and electrospinning is some of the non-conventional synthesis process should be explored further, would find several important applications of the materials synthesised using such routes. The porous or layered transition metal chalcogenides are important class of materials being discussed as an alternate to the graphene, and the materials have enormous potential in catalysis. Applications of porous nano structured materials starting from the reachargeable battery, supercapacitor, fuel cell technology are presented. The applications in sensors and biosensors are discussed in the line of non-enzymatic and enzymatic routes utilising metallic foams. In biomedical field, foams are utilised in tissue engineering as regenerative medicines, and the field is expected grow further to support several modern medical treatment protocols. In addition to the meso or nano porous structures, the forms with macrospores have important large scale industrial applications, and some related examples are presented in the book chapter. Though present book chapter has focused on the metallic foams, a brief account of the graphene foams is presented towards the end of the chapter. The research potential in graphene foam is large enough to sought interest in another chapter mentioning the synthesis strategy and application of the composites of graphene foam. Overall, the author has discussed a brief account of the porous structured materials in the chapter, though several related researches are missed out. Consideration has been given to the topic which are futuristic and strategically advance in the synthesis protocols and applications. The author is hopeful that the content of the book chapter finds significant interest among the fellow researches.

Acknowledgements The author thanks Prof. A. K. Tyagi, Director, Chemistry Group, Bhabha Atomic Research Centre for his encouragement, support, and guidance in writing the book chapter. The author also thanks Shri. Abhishek Sharma for his help in assembling the references.

References

1. Tappan B, Huynh M, Hiskey M, Chavez D, Luther E, Mang J, Son S (2006) Ultralow-density nanostructured metal foams: combustion synthesis, morphology, and composition. J Am Chem Soc 128:6589–6594
2. Halford, B (2006) Whipping up metal foams. Chem Eng News 84, 32–32
3. Peng Y, Liu H, Li T, Zhang J (2020) Hybrid Metallic Foam with Superior Elasticity, High Electrical Conductivity, and Pressure Sensitivity. ACS Appl Mater Interfaces 12:6489–6495
4. Benito P, de Nolf W, Nuyts G, Monti M, Fornasari G, Basile F, Janssens K, Ospitali F, Scavetta E, Tonelli D (2014) role of coating-metallic support interaction in the properties of electrosynthesized Rh-based structured catalysts. ACS Catal 4:3779–3790
5. Allioux FM, Merhebi S, Ghasemian MB, Tang J, Merenda A, Abbasi R, Mayyas M, Daeneke T, O'Mullane AP, Daiyan R, Amal R (2020) Bi-Sn catalytic foam governed by nano-metallurgy of liquid metals. Nano Lett
6. Egaña A, Sanz O, Merino D, Moriones X, Montes M (2018) Fischer-Tropsch Synthesis Intensification in Foam Structures. Ind Eng Chem Res 57:10187–10197
7. Duraiswamy S, Khan, SA (2010) Plasmonic nanoshell synthesis in microfluidic composite foams. Nano letters, 10, 3757–3763
8. Ji J, Cui X, Zhu Y, Lai L, Zhao X, Zhang Y, Zhang L (2016) Tailoring the electrode interface with enhanced electron transfer for high-rate lithium-ion battery anodes. Ind Eng Chem Res 55:6643–6648
9. Li Z, Liu Z, Sun H, Gao C (2015) Superstructured assembly of nanocarbons: fullerenes, nanotubes, and graphene. Chemical reviews, 115, 7046–7117
10. K I, S (2012) Rigid polyurethane foams from cardanol: synthesis, structural characterization, and evaluation of polyol and foam properties. ACS Sustainable Chemistry & Engineering, 1, 232–242
11. Wang K, Feng G, Liang C, Xia Y, Zhang J, Gan Y, Huang H, Tao X, Zhang W (2018) Green and low-temperature synthesis of foam-like hierarchical porous carbon from CO2 as superior lithium storage material. ACS Applied Energy Materials 1:7123–7129
12. Yefimov, N (2009) Handbook of non-ferrous metal powders: technologies and applications; Elsevier
13. Du R, Jin X, Hübner R, Fan X, Hu Y, Eychmüller A (2020) Engineering Self-Supported Noble Metal Foams Toward Electrocatalysis and Beyond. Adv Energy Mater 10:1901945
14. Hunt EM, Pantoya ML, Jouet RJ (2006) Combustion synthesis of metallic foams from nanocomposite reactants. Intermetallics 14:620–629
15. Vijayan S, Narasimman R, Prabhakaran K (2016) A carbothermal reduction method for the preparation of nickel foam from nickel oxide and sucrose. Mater Lett 181:268–271
16. Philip MR, Narayanan TN, Kumar MP, Arya SB, Pattanayak DK (2014) Self-protected nickel–graphene hybrid low density 3D scaffolds. Journal of Materials Chemistry A, 2, 19488–19494
17. Vijayan S, Narasimman R, Prudvi C, Prabhakaran K (2014) Preparation of alumina foams by the thermo-foaming of powder dispersions in molten sucrose. J Eur Ceram Soc 34:425–433
18. Akiyama S, Ueno H, Imagawa K, Kitahara A, Nagata S, Morimoto K, Nishikawa T, Itoh M (1989) Foamed metal and method of producing same. European Patent 01986:210
19. Jiang W, Wu N, Wang X, Chi Y, Zhang Y, Qiu X, Hu Y, Li J, Liu Y (2015) Dysbiosis gut microbiota associated with inflammation and impaired mucosal immune function in intestine of humans with non-alcoholic fatty liver disease. Scientific reports, 5, 8096
20. Zhu C, Du D, Eychmüller A, Lin Y (2015) Engineering ordered and nonordered porous noble metal nanostructures: synthesis, assembly, and their applications in electrochemistry. Chem Rev 115, 8896–8943
21. Li Y, Luo J, Hu X, Wang X, Liang J, Yu K (2015) Fabrication of TiO2 hollow nanostructures and their application in Lithium ion batteries. J Alloy Compd 651:685–689
22. Wei W, Du P, Liu D, Wang H, Liu P (2017) Facile mass production of porous SnO2 hollow nanospheres as high performance anode material in lithium-ion batteries. Mater Lett 196:191–193

23. Yi Y, Lee G-H, Kim J-C, Shim H-W, Kim D-W (2017) Tailored silicon hollow spheres with Micrococcus for Li ion battery electrodes. Chem Eng J 327:297–306
24. Guo M, Zhang X, Bai Z, Ye J, Meng W, Song H, Wang Z (2017) Hollow SnNi@ PEO nanospheres as anode materials for lithium ion batteries. Int J Hydrogen Energy 42:15290–15298
25. Wang Z, Zhou L, Lou XW (2012) Metal oxide hollow nanostructures for lithium-ion batteries. Advanced materials, 24, 1903–1911
26. Zou S, Xu X, Zhu Y, Cao C (2017) Microwave-assisted preparation of hollow porous carbon spheres and as anode of lithium-ion batteries. Microporous Mesoporous Mater 251:114–121
27. Wu S, Shen X, Zhu G, Zhou H, Ji Z, Chen K, Yuan A (2016) Synthesis of ternary Ag/ZnO/ZnFe2O4 porous and hollow nanostructures with enhanced photocatalytic activity. Appl Catal B 184:328–336
28. Krajczewski J, Kołątaj K, Kudelski A (2016) Enhanced catalytic activity of solid and hollow platinum-cobalt nanoparticles towards reduction of 4-nitrophenol. Appl Surf Sci 388:624–630
29. Dong W, Zhang L, Li B, Wang L, Wang G, Li X, Chen B, Li C (2016) Preparation of hollow multiple-Ag-nanoclustes-C-shell nanostructures and their catalytic properties. Appl Catal B 180:13–19
30. Mahmoud MA, Saira F, El-Sayed MA (2010) Experimental evidence for the nanocage effect in catalysis with hollow nanoparticles. Nano letters, 10, 3764–3769
31. Prieto G, Tüysüz H, Duyckaerts N, Knossalla J, Wang GH, Schüth F (2016) Hollow nano-and microstructures as catalysts. Chem Rev 14056–14119
32. Yang J, Li F, Li M, Zhang S, Liu J, Liang C, Sun Q, Xiong L (2017) Fabrication and characterization of hollow starch nanoparticles by gelation process for drug delivery application. Carbohydrate polymers, 173, 223–232
33. Yi Z, Wang K, Tian J, Shu Y, Yang J, Xiao W, Li B, Liao X (2016) Hierarchical porous hydroxyapatite fibers with a hollow structure as drug delivery carriers. Ceram Int 42:19079–19085
34. Zhu Y, Ikoma T, Hanagata N, Kaskel S (2010) Rattle-type Fe3O4@ SiO2 hollow mesoporous spheres as carriers for drug delivery. Small 6:471–478
35. Cheng K, Sun S (2010) Recent advances in syntheses and therapeutic applications of multifunctional porous hollow nanoparticles. Nano Today 5:183–196
36. An K, Hyeon T (2009) Synthesis and biomedical applications of hollow nanostructures. Nano Today 4:359–373
37. Wang T, Kou X, Zhao L, Sun P, Liu C, Wang Y, Shimanoe K, Yamazoe N, Lu G (2017) Flower-like ZnO hollow microspheres loaded with CdO nanoparticles as high performance sensing material for gas sensors. Sens Actuators, B Chem 250:692–702
38. Han B, Liu X, Xing X, Chen N, Xiao X, Liu S, Wang Y (2016) A high response butanol gas sensor based on ZnO hollow spheres. Sens Actuators, B Chem 237:423–430
39. Yan Y, Liu J, Zhang H, Song D, Li J, Yang P, Zhang M, Wang J (2012) Self-assembly of hierarchical ZnSnO3-SnO2 nanoflakes and their gas sensing properties. Transactions of Nonferrous Metals Society of China, 22, 2451–2458
40. Jia X, Yue F, Chen X, Pan H-B, Liu W-G, Liu J-Y (2014) One-pot controlled synthesis of single-crystal α-Fe 2 O 3 hollow nanostructure and its gas sensing properties. RSC Adv 4:42899–42904
41. Kalantari M, Yu M, Noonan O, Song H, Xu C, Huang X, Xiang F, Wang X, Yu C (2017) Rattle-type magnetic mesoporous hollow carbon as a high-performance and reusable adsorbent for water treatment. Chemosphere 166:109–117
42. Xu J-S, Zhu, Y-J (2012) γ-Fe2O3 and Fe3O4 magnetic hierarchically nanostructured hollow microspheres: preparation, formation mechanism, magnetic property, and application in water treatment. Journal of colloid and interface science, 385, 58–65
43. Vickers NJ (2017) Animal communication: when i'm calling you, will you answer too? Current biology, 27, R713-R715
44. Cao J, Mao Q, Shi L, Qian Y (2011) Fabrication of γ-MnO 2/α-MnO 2 hollow core/shell structures and their application to water treatment. J Mater Chem 21:16210–16215

45. Fei J, Cui Y, Yan X, Qi W, Yang Y, Wang K, He Q, Li J (2008) Controlled preparation of MnO2 hierarchical hollow nanostructures and their application in water treatment. Adv Mater 20:452–456
46. Chauhan R, Shinde M, Kumar A, Gosavi S, Amalnerkar DP (2016) Hierarchical zinc oxide pomegranate and hollow sphere structures as efficient photoanodes for dye-sensitized solar cells. Microporous Mesoporous Mater 226:201–208
47. Han G, Wang M, Li D, Bai J, Diao G (2017) Novel upconversion Er, Yb-CeO2 hollow spheres as scattering layer materials for efficient dye-sensitized solar cells. Sol Energy Mater Sol Cells 160:54–59
48. Shcherbakov V, Merzhanov A (1998) Structure formation in porous materials produced by gravity-sensitive SHS
49. Jouet RJ, Warren AD, Rosenberg DM, Bellitto VJ, Park K, Zachariah MR (2005) Surface passivation of bare aluminum nanoparticles using perfluoroalkyl carboxylic acids. Chem Mater 17:2987–2996
50. Erri P, Nader J, Varma A (2008) Controlling combustion wave propagation for transition metal/alloy/cermet foam synthesis. Adv Mater 20:1243–1245
51. Jiang B, He C, Zhao N, Nash P, Shi C, Wang Z (2015) Ultralight metal foams. Scientific reports, 5, 13825
52. Yang S, Luo X (2014) Mesoporous nano/micro noble metal particles: synthesis and applications. Nanoscale 6:4438–4457
53. Biener J, Nyce GW, Hodge AM, Biener MM, Hamza AV, Maier SA (2008) Nanoporous plasmonic metamaterials. Adv Mater 20:1211–1217
54. Guo DJ, Ding Y (2012) Porous nanostructured metals for electrocatalysis. Electroanalysis 24:2035–2043
55. Kloke A, von Stetten F, Zengerle R, Kerzenmacher S (2011) Strategies for the fabrication of porous platinum electrodes. Adv Mater 23:4976–5008
56. Shin HJ, Ko CH, Ryoo R (2001) Synthesis of platinum networks with nanoscopic periodicity using mesoporous silica as template. J Mater Chem 11:260–261
57. Lu L, Eychmüller A, Kobayashi A, Hirano Y, Yoshida K, Kikkawa Y, Tawa K, Ozaki Y (2006) Designed fabrication of ordered porous Au/Ag nanostructured films for surface-enhanced Raman scattering substrates. Langmuir 22:2605–2609
58. Lai X, Li X, Geng W, Tu J, Li J, Qiu S (2007) Ordered mesoporous copper oxide with crystalline walls. Angew Chem Int Ed 46:738–741
59. Jiao F, Jumas J-C, Womes M, Chadwick AV, Harrison A, Bruce PG (2006) Synthesis of ordered mesoporous Fe3O4 and γ-Fe2O3 with crystalline walls using post-template reduction/oxidation. J Am Chem Soc 128:12905–12909
60. Hoffmann C, Thieme S, Brückner J, Oschatz M, Biemelt T, Mondin G, Althues H, Kaskel S (2014) Nanocasting hierarchical carbide-derived carbons in nanostructured opal assemblies for high-performance cathodes in lithium–sulfur batteries. ACS Nano, 8, 12130–12140
61. Zhou M, Wu HB, Bao J, Liang L, Lou XW, Xie Y (2013) Ordered macroporous BiVO4 architectures with controllable dual porosity for efficient solar water splitting. Angew Chem Int Ed 52:8579–8583
62. Stein A, Li F, Denny NR (2008) Morphological control in colloidal crystal templating of inverse opals, hierarchical structures, and shaped particles. Chem Mater 20:649–666
63. Ryoo R, Joo SH, Jun, S (1999) Synthesis of highly ordered carbon molecular sieves via template-mediated structural transformation. The Journal of Physical Chemistry B, 103, 7743–7746
64. Jiang P (2004) Surface-Templated Nanostructured Films with Two-Dimensional Ordered Arrays of Voids. Angew Chem Int Ed 43:5625–5628
65. Lu L, Eychmueller A (2008) Ordered macroporous bimetallic nanostructures: design, characterization, and applications. Accounts of chemical research, 41, 244–253
66. Jiang P, Cizeron J, Bertone JF, Colvin VL (1999) Preparation of macroporous metal films from colloidal crystals. J Am Chem Soc 121:7957–7958

67. Lu L, Capek R, Kornowski A, Gaponik N, Eychmüller A (2005) Selective fabrication of ordered bimetallic nanostructures with hierarchical porosity. Angew Chem 117:6151–6155
68. Lu L, Randjelovic I, Capek R, Gaponik N, Yang J, Zhang H, Eychmüller A (2005) Controlled fabrication of gold-coated 3D ordered colloidal crystal films and their application in surface-enhanced Raman spectroscopy. Chem Mater 17, 5731–5736
69. Wang D, Luo H, Kou R, Gil MP, Xiao S, Golub VO, Yang Z, Brinker CJ, Lu Y (2004) A general route to macroscopic hierarchical 3D nanowire networks. Angew Chem Int Ed 43:6169–6173
70. Yamauchi Y (2013) Field-Induced alignment controls of one-dimensional mesochannels in mesoporous materials. J Ceram Soc Jpn 121:831–840
71. Yamauchi Y, Sugiyama A, Morimoto R, Takai A, Kuroda K (2008) Mesoporous platinum with giant mesocages templated from lyotropic liquid crystals consisting of diblock copolymers. Angew Chem Int Ed 47:5371–5373
72. Attard GS, Bartlett PN, Coleman NR, Elliott JM, Owen JR, Wang JH (1997) Mesoporous platinum films from lyotropic liquid crystalline phases. Science 278:838–840
73. Wang H, Jeong HY, Imura M, Wang L, Radhakrishnan L, Fujita N, Castle T, Terasaki O, Yamauchi Y (2012) Electrochemical design of mesoporous Pt–Ru alloy films with various compositions toward superior electrocatalytic performance. Chem A Eur J, 18, 13142–13148
74. Li C, Wang H, Yamauchi Y (2013) Electrochemical deposition of mesoporous Pt–Au alloy films in aqueous surfactant solutions: towards a highly sensitive amperometric glucose sensor. Chemistry–A European Journal, 19, 2242–2246
75. Wang H, Wang L, Sato T, Sakamoto Y, Tominaka S, Miyasaka K, Miyamoto N, Nemoto Y, Terasaki O, Yamauchi Y (2012) Synthesis of mesoporous Pt films with tunable pore sizes from aqueous surfactant solutions. Chem Mater 24:1591–1598
76. Li C, Dag Ö, Dao TD, Nagao T, Sakamoto Y, Kimura T, Terasaki O, Yamauchi Y (2015) Electrochemical synthesis of mesoporous gold films toward mesospace-stimulated optical properties. Nat Commun 6, 1–8
77. Li C, Sato T, Yamauchi Y (2013) Electrochemical synthesis of one-dimensional mesoporous Pt nanorods using the assembly of surfactant micelles in confined space. Angew Chem 125:8208–8211
78. Ataee-Esfahani H, Liu J, Hu M, Miyamoto N, Tominaka S, Wu KC, Yamauchi Y (2013) Mesoporous metallic cells: design of uniformly sized hollow mesoporous Pt–Ru particles with tunable shell thicknesses. Small 9:1047–1051
79. Li C, Imura M, Yamauchi Y (2014) A universal approach to the preparation of colloidal mesoporous platinum nanoparticles with controlled particle sizes in a wide range from 20 nm to 200 nm. Phys Chem Chem Phys 16:8787–8790
80. Li C, Sato T, Yamauchi Y (2014) Size-controlled synthesis of mesoporous palladium nanoparticles as highly active and stable electrocatalysts. Chem Commun 50:11753–11756
81. Bates, F. S.; Fredrickson, G. H. Block copolymer thermodynamics: theory and experiment. *Annual review of physical chemistry* **1990**, *41*, 525–557.
82. Tappan BC, Steiner SA III, Luther EP (2010) Nanoporous metal foams. Angew Chem Int Ed 49:4544–4565
83. Raney M Method for producing Finely Divided Nickel, US Pat., 16281901927
84. Erlebacher J, Aziz MJ, Karma A, Dimitrov N, Sieradzki K (2001) Evolution of nanoporosity in dealloying. Nature 410:450–453
85. Shao M, Shoemaker K, Peles A, Kaneko K, Protsailo L (2010) Pt monolayer on porous Pd−Cu alloys as oxygen reduction electrocatalysts. J Am Chem Soc 132:9253–9255
86. Krishna, K. S.; Sandeep, C. S.; Philip, R.; Eswaramoorthy, M (2010) Mixing does the magic: a rapid synthesis of high surface area noble metal nanosponges showing broadband nonlinear optical response. ACS nano, 4, 2681–2688
87. Xiao M, Feng L, Zhu J, Liu C, Xing W (2015) Rapid synthesis of a PtRu nano-sponge with different surface compositions and performance evaluation for methanol electrooxidation. Nanoscale 7:9467–9471
88. Zhu, Z.; Zhai, Y.; Zhu, C.; Wang, Z.; Dong, S. Bimetallic alloy nanowires and nanosponges: A comparative study of peroxidase mimetics and as enhanced catalysts for oxygen reduction reaction. Electrochemistry communications, 36, 22–25

89. Zhu, C.; Guo, S.; Dong, S. Rapid, general synthesis of PdPt bimetallic alloy nanosponges and their enhanced catalytic performance for ethanol/methanol electrooxidation in an alkaline medium. Chemistry–A European Journal 2013, 19, 1104–1111.
90. Zhu, C.; Wen, D.; Leubner, S.; Oschatz, M.; Liu, W.; Holzschuh, M.; Simon, F.; Kaskel, S.; Eychmüller, A (2020) Nickel cobalt oxide hollow nanosponges as advanced electrocatalysts for the oxygen evolution reaction. Chemical communications, 51, 7851–7854
91. Zhu Z, Zhai Y, Dong S (2014) Facial synthesis of PtM (M= Fe Co, Cu, Ni) bimetallic alloy nanosponges and their enhanced catalysis for oxygen reduction reaction. ACS Appl Mater Interfaces 6:16721–16726
92. Zhu C, Wen D, Oschatz M, Holzschuh M, Liu W, Herrmann AK, Simon F, Kaskel S, Eychmüller A (2015) Kinetically controlled synthesis of PdNi bimetallic porous nanostructures with enhanced electrocatalytic activity. Small 11:1430–1434
93. Tang, S.; Vongehr, S.; Wang, Y.; Cui, J.; Wang, X.; Meng, X. Versatile synthesis of high surface area multi-metallic nanosponges allowing control over nanostructure and alloying for catalysis and SERS detection. *Journal of Materials Chemistry A***2014**, *2*, 3648–3660.
94. Yang, S.; Hong, F.; Wang, L.; Guo, S.; Song, X.; Ding, B.; Yang, Z (2020) Ultrathin Pt-based alloy nanowire networks: synthesized by CTAB assistant two-phase water− chloroform micelles. The Journal of Physical Chemistry C, 114, 203–207
95. Shin HC, Liu M (2005) Three-dimensional porous copper–tin alloy electrodes for rechargeable lithium batteries. Adv Func Mater 15:582–586
96. Shin HC, Dong J, Liu M (2003) Nanoporous structures prepared by an electrochemical deposition process. Adv Mater 15:1610–1614
97. Cherevko S, Chung C-H (2011) Direct electrodeposition of nanoporous gold with controlled multimodal pore size distribution. Electrochem Commun 13:16–19
98. Cherevko, S.; Chung, C.-H (2012) Impact of key deposition parameters on the morphology of silver foams prepared by dynamic hydrogen template deposition. Electrochimica acta, 55, 6383–6390.
99. Ott, A.; Jones, L. A.; Bhargava, S. K. Direct electrodeposition of porous platinum honeycomb structures. Electrochemistry communications2011, 13, 1248–1251
100. Cherevko S, Kulyk N, Chung C-H (2012) Nanoporous palladium with sub-10 nm dendrites by electrodeposition for ethanol and ethylene glycol oxidation. Nanoscale 4:103–105
101. Liu J, Cao L, Huang W, Li Z (2012) Direct electrodeposition of PtPd alloy foams comprised of nanodendrites with high electrocatalytic activity for the oxidation of methanol and ethanol. J Electroanal Chem 686:38–45
102. Ojani, R.; Hasheminejad, E.; Raoof, J. B (2010) Hydrogen evolution assisted electrodeposition of bimetallic 3D nano/micro-porous PtPd films and their electrocatalytic performance. international journal of hydrogen energy, 39, 8194–8203
103. Shahbazi, P.; Kiani, A. Nanoporous Ag and Pd foam: Redox induced fabrication using electrochemically deposited nanoporous Cu foam with no need to any additive. *Electrochimica acta*, *56*, 9520–9529.
104. Yin, J.; Jia, J.; Zhu, L (2010) Macroporous Pt modified glassy carbon electrode: Preparation and electrocatalytic activity for methanol oxidation. International journal of hydrogen energy, 33, 7444–7447
105. Xiong L, Huang Y-X, Liu X-W, Sheng G-P, Li W-W, Yu H-Q (2013) Three-dimensional bimetallic Pd–Cu nanodendrites with superior electrochemical performance for oxygen reduction reaction. Electrochim Acta 89:24–28
106. Huang, J. F (2008) 3-D nanoporous Pt electrode prepared by a 2-D UPD monolayer process. Electroanalysis: An International Journal Devoted to Fundamental and Practical Aspects of Electroanalysis, 20, 2229–2234
107. Zhong G, Liu A, Chen X, Wang K, Lian Z, Liu Q, Chen Y, Du M, Lin X (2011) Electrochemical biosensor based on nanoporous gold electrode for detection of PML/RARα fusion gene. Biosens Bioelectron 26:3812–3817
108. Huang, W.; Wang, M.; Zheng, J.; Li, Z (2010) Facile fabrication of multifunctional three-dimensional hierarchical porous gold films via surface rebuilding. The Journal of Physical Chemistry C, 113, 1800–1805

109. Nagaraju, D.; Lakshminarayanan, V (2009) Electrochemically grown mesoporous gold film as high surface area material for electro-oxidation of alcohol in alkaline medium. The Journal of Physical Chemistry C, 113, 14922–14926
110. Zhang Z, Li H, Zhang F, Wu Y, Guo Z, Zhou L, Li J (2014) Investigation of halide-induced aggregation of Au nanoparticles into spongelike gold. Langmuir 30:2648–2659
111. Skrabalak, S. E.; Chen, J.; Sun, Y.; Lu, X.; Au, L.; Cobley, C. M.; Xia, Y. Gold nanocages: synthesis, properties, and applications. Accounts of chemical research 41, 1587–1595
112. Wang, X.; Feng, J.; Bai, Y.; Zhang, Q.; Yin, Y. Synthesis, properties, and applications of hollow micro-/nanostructures (2016) Chemical reviews, 116, 10983–11060.
113. Brun, N.; Yu, S.-H.; White, R. J (2014) Porous hydrothermal carbon materials, nanoparticles, hybrids and composites. Porous carbon materials from sustainable precursors, 156.
114. Li G, Shi Q, Yuan S, Neoh K, Kang E, Yang X (2010) Alternating silica/polymer multilayer hybrid microspheres templates for double-shelled polymer and inorganic hollow microstructures. Chem Mater 22:1309–1317
115. Han, L.; Liu, H.; Cui, P.; Peng, Z.; Zhang, S.; Yang, J. Alloy Cu 3 Pt nanoframes through the structure evolution in Cu-Pt nanoparticles with a core-shell construction. *Scientific reports***2014**, *4*, 6414.
116. Hwang SH, Yun J, Jang J (2014) Multi-shell porous TiO2 hollow nanoparticles for enhanced light harvesting in dye-sensitized solar cells. Adv Func Mater 24:7619–7626
117. Lou XW, Yuan C, Archer LA (2007) Double-walled SnO2 nano-cocoons with movable magnetic cores. Adv Mater 19:3328–3332
118. Lai X, Li J, Korgel BA, Dong Z, Li Z, Su F, Du J, Wang D (2011) General synthesis and gas-sensing properties of multiple-shell metal oxide hollow microspheres. Angew Chem Int Ed 50:2738–2741
119. Zimmermann C, Feldmann C, Wanner M, Gerthsen D (2007) Nanoscale gold hollow spheres through a microemulsion approach. Small 3:1347–1349
120. Zhang X, Li D (2006) Metal-compound-induced vesicles as efficient directors for rapid synthesis of hollow alloy spheres. Angew Chem Int Ed 45:5971–5974
121. Bastakoti BP, Inuoe M, Yusa S-I, Liao S-H, Wu KC-W, Nakashima K, Yamauchi Y (2012) A block copolymer micelle template for synthesis of hollow calcium phosphate nanospheres with excellent biocompatibility. Chem Commun 48:6532–6534
122. Liu Q, Liu H, Han M, Zhu J, Liang Y, Xu Z, Song Y (2005) Nanometer-sized nickel hollow spheres. Adv Mater 17:1995–1999
123. Sun Y, Mayers BT, Xia Y (2002) Template-engaged replacement reaction: a one-step approach to the large-scale synthesis of metal nanostructures with hollow interiors. Nano Lett 2:481–485
124. Gilroy KD, Farzinpour P, Sundar A, Hughes RA, Neretina S (2014) Sacrificial templates for galvanic replacement reactions: design criteria for the synthesis of pure Pt nanoshells with a smooth surface morphology. Chem Mater 26:3340–3347
125. Song HM, Anjum DH, Sougrat R, Hedhili MN, Khashab NM (2012) Hollow Au@ Pd and Au@ Pt core–shell nanoparticles as electrocatalysts for ethanol oxidation reactions. J Mater Chem 22:25003–25010
126. Wang C, Wang Y, Xu L, Shi X, Li X, Xu X, Sun H, Yang B, Lin Q (2013) A galvanic replacement route to prepare strongly fluorescent and highly stable gold nanodots for cellular imaging. Small 9:413–420
127. Lu, X.; Au, L.; McLellan, J.; Li, Z.-Y.; Marquez, M.; Xia, Y. (2003) Fabrication of cubic nanocages and nanoframes by dealloying Au/Ag alloy nanoboxes with an aqueous etchant based on Fe (NO3) 3 or NH4OH. *Nano letters*, *7*, 1764–1769
128. Chen Z, Waje M, Li W, Yan Y (2007) Supportless Pt and PtPd nanotubes as electrocatalysts for oxygen-reduction reactions. Angew Chem Int Ed 46:4060–4063
129. Wan D, Xia X, Wang Y, Xia Y (2013) Robust synthesis of gold cubic nanoframes through a combination of galvanic replacement, gold deposition, and silver dealloying. Small 9:3111–3117
130. Zhang, G.; Sun, S.; Cai, M.; Zhang, Y.; Li, R.; Sun, X (2003) Porous dendritic platinum nanotubes with extremely high activity and stability for oxygen reduction reaction. *Scientific reports*, *3*, 1–8.

131. Fang, J.; Lebedkin, S.; Yang, S.; Hahn, H (2011) A new route for the synthesis of polyhedral gold mesocages and shape effect in single-particle surface-enhanced Raman spectroscopy. *Chemical communications*, *47*, 5157–5159.
132. Kim, K. W.; Kim, S. M.; Choi, S.; Kim, J.; Lee, I. S (2012) Electroless Pt deposition on Mn3O4 nanoparticles via the galvanic replacement process: electrocatalytic nanocomposite with enhanced performance for oxygen reduction reaction. ACS nano, *6*, 5122–5129
133. Nakamura, R.; Tokozakura, D.; Nakajima, H.; Lee, J.-G.; Mori, H. Hollow oxide formation by oxidation of Al and Cu nanoparticles. *Journal of applied physics*, *101*, 074303.
134. Railsback, J. G.; Johnston-Peck, A. C.; Wang, J.; Tracy, J. B. Size-dependent nanoscale Kirkendall effect during the oxidation of nickel nanoparticles. *ACS nano*, *4*, 1913–1920.
135. Peng S, Sun S (2007) Synthesis and characterization of monodisperse hollow Fe3O4 nanoparticles. Angew Chem 119:4233–4236
136. Niu, K.-Y.; Park, J.; Zheng, H.; Alivisatos, A. P (2013) Revealing bismuth oxide hollow nanoparticle formation by the Kirkendall effect. *Nano letters*, *13*, 5715–5719.
137. Cabot A, Puntes VF, Shevchenko E, Yin Y, Balcells L, Marcus MA, Hughes SM, Alivisatos AP (2007) Vacancy coalescence during oxidation of iron nanoparticles. J Am Chem Soc 129:10358–10360
138. Zhang G, Wang W, Yu Q, Li X (2009) Facile one-pot synthesis of PbSe and NiSe2 hollow spheres: Kirkendall-effect-induced growth and related properties. Chem Mater 21:969–974
139. Wang W, Goebl J, He L, Aloni S, Hu Y, Zhen L, Yin Y (2010) Epitaxial growth of shape-controlled Bi2Te3− Te heterogeneous nanostructures. J Am Chem Soc 132:17316–17324
140. Cabot A, Smith RK, Yin Y, Zheng H, Reinhard BM, Liu H, Alivisatos AP (2008) Sulfidation of Cadmium at the Nanoscale. ACS Nano 2:1452–1458
141. Tan, H.; Li, S.; Fan, W. Y (2008) Core− Shell and Hollow Nanocrystal Formation via Small Molecule Surface Photodissociation; Ag@ Ag2Se as an Example. The Journal of Physical Chemistry B, 110, 15812–15816
142. Wang Y-L, Cai L, Xia Y-N (2005) Monodisperse spherical colloids of Pb and their use as chemical templates to produce hollow particles. Adv Mater 17:473–477
143. Gao J, Zhang B, Zhang X, Xu B (2006) Magnetic-Dipolar-Interaction-Induced Self-Assembly Affords Wires of Hollow Nanocrystals of Cobalt Selenide. Angew Chem 118:1242–1245
144. Cabot A, Ibáñez M, Guardia P, Alivisatos AP (2009) Reaction regimes on the synthesis of hollow particles by the Kirkendall effect. J Am Chem Soc 131:11326–11328
145. Tang, Y.; Ouyang, M (2007)Tailoring properties and functionalities of metal nanoparticles through crystallinity engineering. *Nature materials*, *6*, 754–759
146. Yin, Y.; Erdonmez, C. a. Cabot, S (2006) Hughes and AP Alivisatos. Adv. Funct. Mater, *16*, 1389–1399
147. Wang J, Johnston-Peck AC, Tracy JB (2009) Nickel phosphide nanoparticles with hollow, solid, and amorphous structures. Chem Mater 21:4462–4467
148. Henkes AE, Vasquez Y, Schaak RE (2007) Converting metals into phosphides: a general strategy for the synthesis of metal phosphide nanocrystals. J Am Chem Soc 129:1896–1897
149. Chiang, R.-K.; Chiang, R.-T (2007) Formation of hollow Ni2P nanoparticles based on the nanoscale Kirkendall effect. *Inorganic chemistry*, *46*, 369–371.
150. Jana, S.; Chang, J. W.; Rioux, R. M (2003) Synthesis and modeling of hollow intermetallic Ni–Zn nanoparticles formed by the Kirkendall effect. *Nano letters*, *13*, 3618–3625
151. González E, Arbiol J, Puntes VF (2011) Carving at the nanoscale: sequential galvanic exchange and Kirkendall growth at room temperature. Science 334:1377–1380
152. Sun, Y.; Xia, Y. Shape-controlled synthesis of gold and silver nanoparticles. *science***2002**, *298*, 2176–2179.
153. Tian, L.; Yang, X.; Lu, P.; Williams, I. D.; Wang, C.; Ou, S.; Liang, C.; Wu, M (2008) Hollow single-crystal spinel nanocubes: The case of zinc cobalt oxide grown by a unique Kirkendall effect. *Inorganic chemistry*, *47*, 5522–5524
154. Cao H, Qian X, Wang C, Ma X, Yin J, Zhu Z (2005) High symmetric 18-facet polyhedron nanocrystals of Cu7S4 with a hollow nanocage. J Am Chem Soc 127:16024–16025

155. Liang X, Wang X, Zhuang Y, Xu B, Kuang S, Li Y (2008) Formation of CeO2− ZrO2 solid solution nanocages with controllable structures via Kirkendall effect. J Am Chem Soc 130:2736–2737
156. Zhang F, Shi Y, Sun X, Zhao D, Stucky GD (2009) Formation of hollow upconversion rare-earth fluoride nanospheres: nanoscale kirkendall effect during ion exchange. Chem Mater 21:5237–5243
157. Peng Q, Sun X-Y, Spagnola JC, Saquing C, Khan SA, Spontak RJ, Parsons GN (2009) Bi-directional kirkendall effect in coaxial microtube nanolaminate assemblies fabricated by atomic layer deposition. ACS Nano 3:546–554
158. Tianou, H.; Wang, W.; Yang, X.; Cao, Z.; Kuang, Q.; Wang, Z.; Shan, Z.; Jin, M.; Yin, Y (2007) Inflating hollow nanocrystals through a repeated Kirkendall cavitation process. Nature communications, 8, 1–9
159. Xu J, Zhang J, Zhang W, Lee CS (2017) Interlayer Nanoarchitectonics of Two-Dimensional Transition-Metal Dichalcogenides Nanosheets for Energy Storage and Conversion Applications. Adv Energy Mater 7:1700571
160. Cao X, Tan C, Zhang X, Zhao W, Zhang H (2016) Solution-processed two-dimensional metal dichalcogenide-based nanomaterials for energy storage and conversion. Adv Mater 28:6167–6196
161. Han, J. H.; Kwak, M.; Kim, Y.; Cheon, J. Recent advances in the solution-based preparation of two-dimensional layered transition metal chalcogenide nanostructures. *Chemical reviews*, *118*, 6151–6188.
162. Kibsgaard, J.; Chen, Z.; Reinecke, B. N.; Jaramillo, T. F. Engineering the surface structure of MoS 2 to preferentially expose active edge sites for electrocatalysis. *Nature materials* 2012, *11*, 963–969.
163. Jaramillo, T. F.; Jørgensen, K. P.; Bonde, J.; Nielsen, J. H.; Horch, S.; Chorkendorff, I. Identification of active edge sites for electrochemical H2 evolution from MoS2 nanocatalysts. *science* 2007, *317*, 100–102.
164. Nicolosi, V.; Chhowalla, M.; Kanatzidis, M. G.; Strano, M. S.; Coleman, J. N. Liquid exfoliation of layered materials. *Science* 2013, *340*.
165. Coleman JN, Lotya M, O'Neill A, Bergin SD, King PJ, Khan U, Young K, Gaucher A, De S, Smith RJ (2011) Two-dimensional nanosheets produced by liquid exfoliation of layered materials. Science 331:568–571
166. Chhowalla, M.; Shin, H. S.; Eda, G.; Li, L.-J.; Loh, K. P.; Zhang, H. The chemistry of two-dimensional layered transition metal dichalcogenide nanosheets. *Nature chemistry* 2013, *5*, 263–275.
167. Acerce M, Akdoğan EK, Chhowalla M (2017) Metallic molybdenum disulfide nanosheet-based electrochemical actuators. Nature 549:370–373
168. Mak, K. F.; He, K.; Shan, J.; Heinz, T. F. Control of valley polarization in monolayer MoS 2 by optical helicity. *Nature nanotechnology* 2012, *7*, 494–498.
169. Zeng, H.; Dai, J.; Yao, W.; Xiao, D.; Cui, X (2009) Valley polarization in MoS 2 monolayers by optical pumping. Nature nanotechnology, *7*, 490–493.
170. Lee, J.; Wang, Z.; Xie, H.; Mak, K. F.; Shan, J. Valley magnetoelectricity in single-layer MoS 2. *Nature materials***2017**, *16*, 887–891.
171. Radisavljevic, B.; Radenovic, A.; Brivio, J.; Giacometti, V.; Kis, A. Single-layer MoS 2 transistors. *Nature nanotechnology***2011**, *6*, 147–150.
172. Withers, F.; Yang, H.; Britnell, L.; Rooney, A.; Lewis, E.; Felten, A.; Woods, C.; Sanchez Romaguera, V.; Georgiou, T.; Eckmann, A. Heterostructures produced from nanosheet-based inks. *Nano letters* 2014, *14*, 3987–3992.
173. Finn, D. J.; Lotya, M.; Cunningham, G.; Smith, R. J.; McCloskey, D.; Donegan, J. F.; Coleman, J. N. Inkjet deposition of liquid-exfoliated graphene and MoS 2 nanosheets for printed device applications. *Journal of Materials Chemistry C* 2014, *2*, 925–932.
174. Li J, Naiini MM, Vaziri S, Lemme MC, Östling M (2014) Inkjet printing of MoS2. Adv Func Mater 24:6524–6531

175. Varrla E, Backes C, Paton KR, Harvey A, Gholamvand Z, McCauley J, Coleman JN (2015) Large-scale production of size-controlled MoS2 nanosheets by shear exfoliation. Chem Mater 27:1129–1139
176. Deng, J.; Li, H.; Wang, S.; Ding, D.; Chen, M.; Liu, C.; Tian, Z.; Novoselov, K.; Ma, C.; Deng, D (2017) Multiscale structural and electronic control of molybdenum disulfide foam for highly efficient hydrogen production. Nature Commun, 8, 1–8
177. Wang J, Liu J, Chao D, Yan J, Lin J, Shen ZX (2014) Self-assembly of honeycomb-like MoS2 nanoarchitectures anchored into graphene foam for enhanced lithium-ion storage. Adv Mater 26:7162–7169
178. Zhao W, Dong B, Guo Z, Su G, Gao R, Wang W, Cao L (2016) Colloidal synthesis of VSe 2 single-layer nanosheets as novel electrocatalysts for the hydrogen evolution reaction. Chem Commun 52:9228–9231
179. Jin H, Ahn M, Jeong S, Han JH, Yoo D, Son DH, Cheon J (2016) Colloidal single-layer quantum dots with lateral confinement effects on 2D exciton. J Am Chem Soc 138:13253–13259
180. Yu XY, Hu H, Wang Y, Chen H, Lou XW (2015) Ultrathin MoS2 nanosheets supported on N-doped carbon nanoboxes with enhanced lithium storage and electrocatalytic properties. Angew Chem 127:7503–7506
181. Wang, S.; Guan, B. Y.; Yu, L.; Lou, X. W. Rational design of three-layered TiO2@ Carbon@ MoS2 hierarchical nanotubes for enhanced lithium storage. *Advanced materials*2017, *29*, 1702724.
182. Kumar, S.; Sahoo, P. K.; Satpati, A. K. Electrochemical and SECM investigation of MoS2/GO and MoS2/rGO nanocomposite materials for HER electrocatalysis. *ACS omega*2017, *2*, 7532–7545.
183. Li Y, Wang H, Xie L, Liang Y, Hong G, Dai H (2011) MoS2 nanoparticles grown on graphene: an advanced catalyst for the hydrogen evolution reaction. J Am Chem Soc 133:7296–7299
184. Zeng Z, Tan C, Huang X, Bao S, Zhang H (2014) Growth of noble metal nanoparticles on single-layer TiS 2 and TaS 2 nanosheets for hydrogen evolution reaction. Energy Environ Sci 7:797–803
185. Shi, Y.; Huang, J.-K.; Jin, L.; Hsu, Y.-T.; Yu, S. F.; Li, L.-J.; Yang, H. Y. Selective decoration of Au nanoparticles on monolayer MoS 2 single crystals. *Scientific reports*2013, *3*, 1839.
186. Kim, J.; Byun, S.; Smith, A. J.; Yu, J.; Huang, J. Enhanced electrocatalytic properties of transition-metal dichalcogenides sheets by spontaneous gold nanoparticle decoration. The journal of physical chemistry letters 2013, *4*, 1227–1232
187. Huang, X.; Zeng, Z.; Bao, S.; Wang, M.; Qi, X.; Fan, Z.; Zhang, H. Solution-phase epitaxial growth of noble metal nanostructures on dispersible single-layer molybdenum disulfide nanosheets. Nature communications 2013, *4*, 1–8
188. Rayleigh LXX (1882) On the equilibrium of liquid conducting masses charged with electricity. The London, Edinburgh, and Dublin Philosophical Magazine and Journal of Science 14:184–186
189. Electrostatic Spraying of Liquids. Von A. G. Bailey, Research Studies Press LTD Taunton, Somerset/John Wiley & Sons Inc, New York (1988) 197 Seiten, 24,75 $. Phys Unserer Zeit 1989(20):160–160
190. Xue J, Wu T, Dai Y, Xia Y (2019) Electrospinning and Electrospun Nanofibers: Methods, Materials, and Applications. Chem Rev 119:5298–5415
191. Jang J, Hyun BG, Ji S, Cho E, An BW, Cheong WH, Park J-U (2017) Rapid production of large-area, transparent and stretchable electrodes using metal nanofibers as wirelessly operated wearable heaters. NPG Asia Materials 9:e432–e432
192. Panda P (2007) Ceramic nanofibers by electrospinning technique—A review. Trans Indian Ceram Soc 66:65–76
193. Fridrikh, S. V.; Jian, H. Y.; Brenner, M. P.; Rutledge, G. C (2003) Controlling the fiber diameter during electrospinning. *Physical review letters*, *90*, 144502.
194. Geltmeyer J, De Roo J, Van den Broeck F, Martins JC, De Buysser K, De Clerck K (2016) The influence of tetraethoxysilane sol preparation on the electrospinning of silica nanofibers. J Sol-Gel Sci Technol 77:453–462

195. Li D, Xia Y (2003) Fabrication of Titania Nanofibers by Electrospinning. Nano Lett 3:555–560
196. Steigert, S. Porous sintered metal for soot filtration. *In Proceedings of 2004 Powder Metallurgy World Congress,* compiled by European Powder Metallurgy Association, Bellstone Shrewsbury, UK,**2004**, *4*, 195–200.
197. Farber, J., Bojack, A., Stoiber, M., Plankensteiner,; A., G., H., Schneidereit, H. Molybdenum hollow sphere structures for high temperature applications. *In Proceedings of 2004 Powder MetallurgyWorld Congress ,* compiled by European Powder Metallurgy Association, Bellstone Shrewsbury, UK 2004, *4*, 131–135.
198. Waag, U., Stephani, G., Farber, J., Venghaus, H.,; Bingel, G. Cellular structures based on metallic hollow spheres – mechanical and acoustical properties. *In Proceedings of 2004 Powder Metallurgy WorldCongress ,* compiled by European Powder Metallurgy Association, Bellstone Shrewsbury, UK 2004, *4*, 143–148.
199. Zhou G, Xu L, Hu G, Mai L, Cui Y (2019) Nanowires for Electrochemical Energy Storage. Chem Rev 119:11042–11109
200. Chen, H.; Ling, M.; Hencz, L.; Ling, H. Y.; Li, G.; Lin, Z.; Liu, G.; Zhang, S. Exploring chemical, mechanical, and electrical functionalities of binders for advanced energy-storage devices. *Chemical reviews*2018, *118*, 8936–8982.
201. BP Statistical Review of World Energy; BCP, 2019. https://www.bp.
202. *com/en/global/corporate/energy-economics/statistical-review-ofworld-*
203. *energy.html* (**accessed Aug 20, 2019**).
204. Fan, E.; Li, L.; Wang, Z.; Lin, J.; Huang, Y.; Yao, Y.; Chen, R.; Wu, F. Sustainable recycling technology for li-ion batteries and beyond: Challenges and future prospects. *Chemical Reviews*2020.
205. Sa Q, Wang Y (2012) Ni foam as the current collector for high capacity C-Si composite electrode. J Power Sources 208:46–51
206. González, J. R.; Nacimiento, F.; Alcántara, R.; Ortiz, G. F.; Tirado, J. L. Electrodeposited CoSn 2 on nickel open-cell foam: advancing towards high power lithium ion and sodium ion batteries. *CrystEngComm*2013, *15*, 9196–9202.
207. Mukanova A, Jetybayeva A, Myung S-T, Kim S-S, Bakenov Z (2018) A mini-review on the development of Si-based thin film anodes for Li-ion batteries. Materials Today Energy 9:49–66
208. Arthur TS, Bates DJ, Cirigliano N, Johnson DC, Malati P, Mosby JM, Perre E, Rawls MT, Prieto AL, Dunn B (2011) Three-dimensional electrodes and battery architectures. MRS Bull 36:523
209. Fukunaga H, Kishimi M, Matsumoto N, Ozaki T, Sakai T, Tanaka T, Kishimoto T (2005) A nickel electrode with Ni-coated 3D steel sheet for hybrid electric vehicle applications. J Electrochem Soc 152:A905
210. Yao M, Okuno K, Iwaki T, Kato M, Tanase S, Emura K, Sakai T (2007) LiFePO4-based electrode using micro-porous current collector for high power lithium ion battery. J Power Sources 173:545–549
211. Luo, W.-B.; Chou, S.-L.; Zhai, Y.-C.; Liu, H.-K. Self-assembled graphene and LiFePO 4 composites with superior high rate capability for lithium ion batteries. *Journal of Materials Chemistry A*, *2*, 4927–4931.
212. Xu K, Loh A, Wang B, Li X (2018) Enhancement of Oxygen Transfer by Design Nickel Foam Electrode for Zinc− Air Battery. J Electrochem Soc 165:A809
213. Xu, J.-J.; Chang, Z.-W.; Yin, Y.-B.; Zhang, X.-B. Nanoengineered ultralight and robust all-metal cathode for high-capacity, stable lithium–oxygen batteries. *ACS central science*, *3*, 598–604.
214. Pham, V. H.; Dickerson, J. H. Reduced graphene oxide hydrogels deposited in nickel foam for supercapacitor applications: toward high volumetric capacitance. *The Journal of Physical Chemistry C*, *120*, 5353–5360.
215. Fernández JA, Tennison S, Kozynchenko O, Rubiera F, Stoeckli F, Centeno T (2009) Effect of mesoporosity on specific capacitance of carbons. Carbon 47:1598–1604

216. Zheng, M.-b.; Cao, J.; Liao, S.-t.; Liu, J.-s.; Chen, H.-q.; Zhao, Y.; Dai, W.-j.; Ji, G.-b.; Cao, J.-m.; Tao, J. Preparation of mesoporous Co3O4 nanoparticles via solid− liquid route and effects of calcination temperature and textural parameters on their electrochemical capacitive behaviors. *The Journal of Physical Chemistry C*, *113*, 3887–3894.
217. Wu, M.-S.; Wu, J.-F. Nickel hydroxide electrode with porous nanotube arrays prepared by hydrolysis and cathodic deposition for high-performance supercapacitors. *Journal of power sources*, *240*, 397–403.
218. Liu S, Sun S, You X-Z (2014) Inorganic nanostructured materials for high performance electrochemical supercapacitors. Nanoscale 6:2037–2045
219. Wang, Q.; Zhang, Y.; Jiang, H.; Meng, C. In-situ grown manganese silicate from biomass-derived heteroatom-doped porous carbon for supercapacitors with high performance. *Journal of colloid and interface science*, *534*, 142–155.
220. Jing, C.; Song, X.; Li, K.; Zhang, Y.; Liu, X.; Dong, B.; Dong, F.; Zhao, S.; Yao, H.; Zhang, Y. Optimizing the rate capability of nickel cobalt phosphide nanowires on graphene oxide by the outer/inter-component synergistic effects. *Journal of Materials Chemistry A***2020**, *8*, 1697–1708.
221. Simon, P.; Gogotsi, Y.: Materials for electrochemical capacitors. In *Nanoscience and technology: a collection of reviews from Nature journals*; World Scientific, ; pp 320–329.
222. Zhang, Y.; Wang, C.; Jiang, H.; Wang, Q.; Zheng, J.; Meng, C. Cobalt-nickel silicate hydroxide on amorphous carbon derived from bamboo leaves for hybrid supercapacitors. *Chemical Engineering Journal*2019, *375*, 121938.
223. Zhao, J.; Zou, X.; Sun, P.; Cui, G. Three-Dimensional Bi-Continuous Nanoporous Gold/Nickel Foam Supported MnO 2 for High Performance Supercapacitors. *Scientific reports*2017, *7*, 1–8.
224. Zhou, R.; Meng, C.; Zhu, F.; Li, Q.; Liu, C.; Fan, S.; Jiang, K. High-performance supercapacitors using a nanoporous current collector made from super-aligned carbon nanotubes. *Nanotechnology*2010, *21*, 345701.
225. Pilathottathil S, Thayyil MS, Pillai M, Jemshihas A (2019) Role of a Printed Circuit Board Copper Clad Current Collector in Supercapacitor Application. J Electron Mater 48:5835–5842
226. Bianchini C, Shen PK (2009) Palladium-based electrocatalysts for alcohol oxidation in half cells and in direct alcohol fuel cells. Chem Rev 109:4183–4206
227. Jung N, Chung DY, Ryu J, Yoo SJ, Sung Y-E (2014) Pt-based nanoarchitecture and catalyst design for fuel cell applications. Nano Today 9:433–456
228. Xiao, S.; Xiao, F.; Hu, Y.; Yuan, S.; Wang, S.; Qian, L.; Liu, Y. Hierarchical nanoporous gold-platinum with heterogeneous interfaces for methanol electrooxidation. *Scientific reports*2014, *4*, 4370.
229. Ding, L.-X.; Wang, A.-L.; Li, G.-R.; Liu, Z.-Q.; Zhao, W.-X.; Su, C.-Y.; Tong, Y.-X. Porous Pt-Ni-P composite nanotube arrays: highly electroactive and durable catalysts for methanol electrooxidation. *Journal of the American chemical society* 2012, *134*, 5730–5733.
230. Catherin Sesu D, Patil I, Lokanathan M, Parse H, Marbaniang P, Kakade B (2018) Low Density Three-Dimensional Metal Foams as Significant Electrocatalysts toward Methanol Oxidation Reaction. ACS Sustainable Chemistry & Engineering 6:2062–2068
231. Sesu, D. C.; Marbaniang, P.; Ingavale, S.; Manohar, A. C.; Kakade, B. Bi-Co-Cu Metal Oxide Foam as Significant Electrocatalyst for Methanol Electrooxidation. *ChemistrySelect* 2020, *5*, 306–311.
232. Liu W, Herrmann AK, Geiger D, Borchardt L, Simon F, Kaskel S, Gaponik N, Eychmüller A (2012) High-performance electrocatalysis on palladium aerogels. Angew Chem Int Ed 51:5743–5747
233. Sharma P, Radhakrishnan S, Khil M-S, Kim H-Y, Kim B-S (2018) Simple room temperature synthesis of porous nickel phosphate foams for electrocatalytic ethanol oxidation. J Electroanal Chem 808:236–244
234. Tammam RH, Touny A, Abdesalam ME, Saleh M (2018) Mesoporous NiPh/carbon fibers nanocomposite for enhanced electrocatalytic oxidation of ethanol. J Electroanal Chem 823:128–136

235. Vyas AN, Desai MA, Phase DM, Saratale RG, Ambekar JD, Kale BB, Pathan HM, Sartale SD (2019) Nickel nanoparticles grown by successive ionic layer adsorption and reaction method for ethanol electrooxidation and electrochemical quartz crystal microbalance study. New J Chem 43:2955–2965
236. Hatamie A, Rezvani E, Rasouli AS, Simchi A (2019) Electrocatalytic Oxidation of Ethanol on Flexible Three-dimensional Interconnected Nickel/Gold Composite Foams in Alkaline Media. Electroanalysis 31:504–511
237. Xu C, Liu Y, Wang J, Geng H, Qiu H (2012) Nanoporous PdCu alloy for formic acid electrooxidation. J Power Sources 199:124–131
238. Gan, L.; Heggen, M.; O'Malley, R.; Theobald, B.; Strasser, P. Understanding and controlling nanoporosity formation for improving the stability of bimetallic fuel cell catalysts. *Nano letters***2013**, *13*, 1131–1138.
239. Graetzel M (1981) Artificial photosynthesis: water cleavage into hydrogen and oxygen by visible light. Acc Chem Res 14:376–384
240. Bard AJ, Fox MA (1995) Artificial photosynthesis: solar splitting of water to hydrogen and oxygen. Acc Chem Res 28:141–145
241. Turner JA (2004) Sustainable hydrogen production. Science 305:972–974
242. Lewis NS, Nocera DG (2006) Powering the planet: Chemical challenges in solar energy utilization. Proc Natl Acad Sci 103:15729–15735
243. Herrero, C.; Quaranta, A.; Leibl, W.; Rutherford, A. W.; Aukauloo, A. Artificial photosynthetic systems. Using light and water to provide electrons and protons for the synthesis of a fuel. *Energy & Environmental Science***2011**, *4*, 2353–2365.
244. Kanan MW, Nocera DG (2008) In situ formation of an oxygen-evolving catalyst in neutral water containing phosphate and Co2+. Science 321:1072–1075
245. Blakemore JD, Schley ND, Olack GW, Incarvito CD, Brudvig GW, Crabtree RH (2011) Anodic deposition of a robust iridium-based water-oxidation catalyst from organometallic precursors. Chem Sci 2:94–98
246. Gong M, Li Y, Wang H, Liang Y, Wu JZ, Zhou J, Wang J, Regier T, Wei F, Dai H (2013) An advanced Ni–Fe layered double hydroxide electrocatalyst for water oxidation. J Am Chem Soc 135:8452–8455
247. Parent AR, Crabtree RH, Brudvig GW (2013) Comparison of primary oxidants for water-oxidation catalysis. Chem Soc Rev 42:2247–2252
248. Katsounaros I, Cherevko S, Zeradjanin AR, Mayrhofer KJ (2014) Oxygen electrochemistry as a cornerstone for sustainable energy conversion. Angew Chem Int Ed 53:102–121
249. Liu S, Zheng L, Yu P, Han S, Fang X (2016) Novel Composites of α-Fe2O3 Tetrakaidecahedron and Graphene Oxide as an Effective Photoelectrode with Enhanced Photocurrent Performances. Adv Func Mater 26:3331–3339
250. Liu S, Hu L, Xu X, Al-Ghamdi AA, Fang X (2015) Nickel cobaltite nanostructures for photoelectric and catalytic applications. Small 11:4267–4283
251. Lou XW, Archer LA, Yang Z (2008) Hollow micro-/nanostructures: Synthesis and applications. Adv Mater 20:3987–4019
252. Zhang, Q. I. lee, JB Joo, F. Zaera, Y. Yin. *Acc. Chem. Res* 2013, *46*, 1816–1824.
253. Du J, Qi J, Wang D, Tang Z (2012) Facile synthesis of Au@TiO2 core–shell hollow spheres for dye-sensitized solar cells with remarkably improved efficiency. Energy Environ Sci 5:6914–6918
254. Yin H, Tang H, Wang D, Gao Y, Tang Z (2012) Facile synthesis of surfactant-free Au cluster/graphene hybrids for high-performance oxygen reduction reaction. ACS Nano 6:8288–8297
255. He L, Liu Y, Liu J, Xiong Y, Zheng J, Liu Y, Tang Z (2013) Core-Shell Noble-Metal@ Metal-Organic-Framework Nanoparticles with Highly Selective Sensing Property. Angew Chem 125:3829–3833
256. Antony RP, Satpati AK, Bhattacharyya K, Jagatap BN (2016) MOF derived nonstoichiometric NixCo3− xO4− y nanocage for superior electrocatalytic oxygen evolution. Adv Mater Interfaces 3:1600632

257. Hou Y, Zhang B, Wen, Z, Cui, S, Guo, X, He Z, Chen J (2014) A 3D hybrid of layered MoS/nitrogen-doped graphene nanosheet aerogels: an effective catalyst for hydrogen evolution in microbial electrolysis cells
258. Pan, L. F.; Li, Y. H.; Yang, S.; Liu, P. F.; Yu, M. Q.; Yang, H. G (2014) Molybdenum carbide stabilized on graphene with high electrocatalytic activity for hydrogen evolution reaction. Chemical communications, 50, 13135–13137
259. Yan Y, Ge X, Liu Z, Wang J-Y, Lee J-M, Wang X (2013) Facile synthesis of low crystalline MoS 2 nanosheet-coated CNTs for enhanced hydrogen evolution reaction. Nanoscale 5:7768–7771
260. Merki D, Hu X (2011) Recent developments of molybdenum and tungsten sulfides as hydrogen evolution catalysts. Energy Environ Sci 4:3878–3888
261. Yan Y, Xia B, Xu Z, Wang X (2014) Recent development of molybdenum sulfides as advanced electrocatalysts for hydrogen evolution reaction. ACS Catal 4:1693–1705
262. Lv, R.; Robinson, J. A.; Schaak, R. E.; Sun, D.; Sun, Y.; Mallouk, T. E.; Terrones, M (2015) Transition metal dichalcogenides and beyond: synthesis, properties, and applications of single- and few-layer nanosheets. Accounts of chemical research, 48, 56–64
263. Li, Z.; Dai, X.; Du, K.; Ma, Y.; Liu, M.; Sun, H.; Ma, X.; Zhang, X (2016) Reduced Graphene Oxide/O-MWCNT hybrids functionalized with p-Phenylenediamine as high-performance MoS2 electrocatalyst support for hydrogen evolution reaction. The Journal of Physical Chemistry C, 120, 1478–1487
264. Zhou H, Yu F, Sun J, He R, Chen S, Chu C-W, Ren Z (2017) Highly active catalyst derived from a 3D foam of Fe (PO3) 2/Ni2P for extremely efficient water oxidation. Proc Natl Acad Sci 114:5607–5611
265. Kaplan, A.; Korin, E.; Bettelheim, A. Macrocellular iron foams: characterization and facile conversion into water splitting photoanodes. *RSC advances***2012**, *2*, 9376–9379.
266. Yu H, Quan T, Mei S, Kochovski Z, Huang W, Meng H, Lu Y (2019) Prompt Electrodeposition of Ni Nanodots on Ni Foam to Construct a High-Performance Water-Splitting Electrode: Efficient, Scalable, and Recyclable. Nano-Micro Letters 11:41
267. Walcarius, A.; Minteer, S. D.; Wang, J.; Lin, Y.; Merkoçi, A. Nanomaterials for bio-functionalized electrodes: recent trends. *Journal of Materials Chemistry B***2013**, *1*, 4878–4908.
268. Zhu C, Dong S (2014) Energetic Graphene-Based Electrochemical Analytical Devices in Nucleic Acid, Protein and Cancer Diagnostics and Detection. Electroanalysis 26:14–29
269. Zhu, C.; Yang, G.; Li, H.; Du, D.; Lin, Y. Electrochemical sensors and biosensors based on nanomaterials and nanostructures. *Analytical chemistry***2015**, *87*, 230–249.
270. Juska VB, Walcarius A, Pemble ME (2019) Cu Nanodendrite Foams on Integrated Band Array Electrodes for the Nonenzymatic Detection of Glucose. ACS Applied Nano Materials 2:5878–5889
271. Shen N, Xu H, Zhao W, Zhao Y, Zhang X (2019) Highly responsive and ultrasensitive non-enzymatic electrochemical glucose sensor based on Au foam. Sensors 19:1203
272. Li, Z.; Chen, Y.; Xin, Y.; Zhang, Z. Sensitive electrochemical nonenzymatic glucose sensing based on anodized CuO nanowires on three-dimensional porous copper foam. *Scientific reports***2015**, *5*, 1–8.
273. Liu, W.; Wu, X.; Li, X. Gold nanorods on three-dimensional nickel foam: a non-enzymatic glucose sensor with enhanced electro-catalytic performance. *RSC advances***2017**, *7*, 36744–36749.
274. Khosroshahi, Z.; Karimzadeh, F.; Kharaziha, M.; Allafchian, A. A non-enzymatic sensor based on three-dimensional graphene foam decorated with Cu-xCu2O nanoparticles for electrochemical detection of glucose and its application in human serum. *Materials Science and Engineering: C***2020**, *108*, 110216.
275. Liu Q, Zhong H, Chen M, Zhao C, Liu Y, Xi F, Luo T (2020) Functional nanostructure-loaded three-dimensional graphene foam as a non-enzymatic electrochemical sensor for reagentless glucose detection. RSC Adv 10:33739–33746
276. Zhao F, Sun T, Geng F, Chen P, Gao Y (2019) Metal-organic frameworks-based electrochemical sensors and biosensors. Int J Electrochem Sci 14:5287–5304

277. Evans SA, Elliott JM, Andrews LM, Bartlett PN, Doyle PJ, Denuault G (2002) Detection of hydrogen peroxide at mesoporous platinum microelectrodes. Anal Chem 74:1322–1326
278. Liu L, Scholz R, Pippel E, Gösele U (2010) Microstructure, electrocatalytic and sensing properties of nanoporous Pt46Ni54 alloy nanowires fabricated by mild dealloying. J Mater Chem 20:5621–5627
279. Huan TN, Ganesh T, Kim KS, Kim S, Han S-H, Chung H (2011) A three-dimensional gold nanodendrite network porous structure and its application for an electrochemical sensing. Biosens Bioelectron 27:183–186
280. Zhai, D.; Liu, B.; Shi, Y.; Pan, L.; Wang, Y.; Li, W.; Zhang, R.; Yu, G. Highly sensitive glucose sensor based on Pt nanoparticle/polyaniline hydrogel heterostructures. *ACS nano***2013**, *7*, 3540–3546.
281. Wang, Y.; Shao, Y.; Matson, D. W.; Li, J.; Lin, Y. Nitrogen-doped graphene and its application in electrochemical biosensing. *ACS nano***2010**, *4*, 1790–1798.
282. Gamero M, Pariente F, Lorenzo E, Alonso C (2010) Nanostructured rough gold electrodes for the development of lactate oxidase-based biosensors. Biosens Bioelectron 25:2038–2044
283. Szamocki R, Reculusa S, Ravaine S, Bartlett PN, Kuhn A, Hempelmann R (2006) Tailored mesostructuring and biofunctionalization of gold for increased electroactivity. Angew Chem Int Ed 45:1317–1321
284. Chen L, Fujita T, Chen M (2012) Biofunctionalized nanoporous gold for electrochemical biosensors. Electrochim Acta 67:1–5
285. Qiu H, Xue L, Ji G, Zhou G, Huang X, Qu Y, Gao P (2009) Enzyme-modified nanoporous gold-based electrochemical biosensors. Biosens Bioelectron 24:3014–3018
286. Sarma AK, Vatsyayan P, Goswami P, Minteer SD (2009) Recent advances in material science for developing enzyme electrodes. Biosens Bioelectron 24:2313–2322
287. Cai, W.-R.; Zhang, G.-Y.; Lu, K.-K.; Zeng, H.-B.; Cosnier, S.; Zhang, X.-J.; Shan, D. Enhanced electrochemiluminescence of one-dimensional self-assembled porphyrin hexagonal nanoprisms. *ACS applied materials & interfaces***2017**, *9*, 20904–20912.
288. Kamyabi MA, Moharramnezhad M (2020) A highly sensitive ECL platform based on GOD and NiO nanoparticle decorated nickel foam for determination of glucose in serum samples. Anal Methods 12:1670–1678
289. Rho, S.; Jahng, D.; Lim, J. H.; Choi, J.; Chang, J. H.; Lee, S. C.; Kim, K. J. Electrochemical DNA biosensors based on thin gold films sputtered on capacitive nanoporous niobium oxide. *Biosensors and bioelectronics***2008**, *23*, 852–856.
290. Hu, K.; Lan, D.; Li, X.; Zhang, S. Electrochemical DNA biosensor based on nanoporous gold electrode and multifunctional encoded DNA− Au bio bar codes. *Analytical chemistry***2008**, *80*, 9124–9130.
291. Ahangar LE, Mehrgardi MA (2012) Nanoporous gold electrode as a platform for the construction of an electrochemical DNA hybridization biosensor. Biosens Bioelectron 38:252–257
292. Leva-Bueno, J.; Peyman, S. A.; Millner, P. A review on impedimetric immunosensors for pathogen and biomarker detection. *Medical Microbiology and Immunology***2020**.
293. Chen, X.; Wang, Y.; Zhou, J.; Yan, W.; Li, X.; Zhu, J.-J. Electrochemical impedance immunosensor based on three-dimensionally ordered macroporous gold film. *Analytical chemistry***2008**, *80*, 2133–2140.
294. Chen, Z.-A.; Lu, W.; Bao, C.; Niu, Q.; Cao, X.; Wang, H.; Yao, R.-X. Copper (II) 1, 4-naphthalenedicarboxylate on copper foam nanowire arrays for electrochemical immunosensing of the prostate specific antigen. *Microchimica Acta***2019**, *186*, 758.(297)Wan, Y.; Zhang, D.; Wang, Y.; Hou, B. A 3D-impedimetric immunosensor based on foam Ni for detection of sulfate-reducing bacteria. *Electrochemistry communications***2010**, *12*, 288–291.
295. Palanisamy, S.; Senthil Raja, D.; Subramani, B.; Wu, T.-H.; Wang, Y.-M. Label-Free Bimetallic In Situ-Grown 3D Nickel-Foam-Supported NH2-MIL-88B (Fe2Co)-MOF-based Impedimetric Immunosensor for the Detection of Cardiac Troponin I. *ACS applied materials & interfaces***2020**, *12*, 32468–32476.

296. Fend T (2010) High porosity materials as volumetric receivers for solar energetics. Opt Appl 40:271–284
297. Romero M, González-Aguilar J (2014) Solar thermal CSP technology. Wiley Interdisciplinary Reviews: Energy and Environment 3:42–59
298. Xiao X, Jia H, Pervaiz S, Wen D (2020) Molten Salt/Metal Foam/Graphene Nanoparticle Phase Change Composites for Thermal Energy Storage. ACS Applied Nano Materials 3:5240–5251
299. Romero M, Steinfeld A (2012) Concentrating solar thermal power and thermochemical fuels. Energy Environ Sci 5:9234–9245
300. Michailidis, N.; Stergioudi, F.; Omar, H.; Missirlis, D.; Vlahostergios, Z.; Tsipas, S.; Albanakis, C.; Granier, B. Flow, thermal and structural application of Ni-foam as volumetric solar receiver. *Solar energy materials and solar cells***2013**, *109*, 185–191.
301. Agrafiotis, C.; Roeb, M.; Schmücker, M.; Sattler, C. Exploitation of thermochemical cycles based on solid oxide redox systems for thermochemical storage of solar heat. Part 2: Redox oxide-coated porous ceramic structures as integrated thermochemical reactors/heat exchangers. *Solar Energy***2015**, *114*.
302. Carrillo, A. J.; González-Aguilar, J.; Romero, M.; Coronado, J. M. Solar energy on demand: A review on high temperature thermochemical heat storage systems and materials. *Chemical reviews***2019**, *119*, 4777–4816.
303. Carrillo AJ, Moya J, Bayón A, Jana P, de la Peña O'Shea VA, Romero M, Gonzalez-Aguilar J, Serrano DP, Pizarro P, Coronado JM (2014) Thermochemical energy storage at high temperature via redox cycles of Mn and Co oxides: Pure oxides versus mixed ones. Sol Energy Mater Sol Cells 123:47–57
304. Block T, Knoblauch N, Schmücker M (2014) The cobalt-oxide/iron-oxide binary system for use as high temperature thermochemical energy storage material. Thermochim Acta 577:25–32
305. Agrafiotis, C.; Roeb, M.; Sattler, C. Exploitation of thermochemical cycles based on solid oxide redox systems for thermochemical storage of solar heat. Part 4: Screening of oxides for use in cascaded thermochemical storage concepts. *Solar Energy***2016**, *139*, 695–710.
306. Karagiannakis G, Pagkoura C, Halevas E, Baltzopoulou P, Konstandopoulos AG (2016) Cobalt/cobaltous oxide based honeycombs for thermochemical heat storage in future concentrated solar power installations: Multi-cyclic assessment and semi-quantitative heat effects estimations. Sol Energy 133:394–407
307. Baumeister, J.; Weise, J. Metallic foams. *Ullmann's Encyclopedia of Industrial Chemistry***2000**.
308. Ashby, M. F.; Evans, A.; Fleck, N. A.; Gibson, L. J.; Hutchinson, J. W.; Wadley, H. N. Metal foams: a design guide-Butterworth-Heinemann, Oxford, UK, ISBN 0–7506–7219–6, Published 2000, Hardback, 251 pp., $75.00. *Materials and Design***2002**, *1*, 119.
309. Banhart J (2001) Manufacture, characterisation and application of cellular metals and metal foams. Progress in materials science, *46*, 559–632
310. García-Moreno F (2016) Commercial applications of metal foams: Their properties and production. Materials 9:85
311. Kretz, R.; Gotzinger, B. Energy absorbing behaviour of aluminium foams: head impact tests on an a-pillar of a passenger car. *MIT Verlag Publishing(Germany)***2001**, 17–24.
312. Hanssen A, Stöbener K, Rausch G, Langseth M, Keller H (2006) Optimisation of energy absorption of an A-pillar by metal foam insert. Int J Crashworthiness 11:231–242
313. Kim, S.; Lee, C.-W. A review on manufacturing and application of open-cell metal foam. *Procedia Mater. Sci***2014**, *4*, 10.1016.
314. Mott Corporation. Available online: http://www.mottcorp.com/products/ (accessed on 24 July 2015).
315. Paserin, V.; Marcuson, S.; Shu, J.; Wilkinson, D. S. The chemical vapor deposition technique for Inco nickel foam production–manufacturing benefits and potential applications. *Cellular Metals and Metal Foaming Technology***2003**, 31.
316. Wittstock A, Zielasek V, Biener J, Friend C, Bäumer M (2010) Nanoporous gold catalysts for selective gas-phase oxidative coupling of methanol at low temperature. Science 327:319–322

317. Lu, T.; Stone, H. A.; Ashby, M. Heat transfer in open-cell metal foams. *Acta materialia***1998**, *46*, 3619–3635.
318. Evans, A. G.; Hutchinson, J.; Ashby, M. Multifunctionality of cellular metal systems. *Progress in materials science***1998**, *43*, 171–221.
319. M-pore http://www.m-pore.de/. Accessed on 24 July 2015
320. Li, S.; de Wijn, J. R.; Li, J.; Layrolle, P.; de Groot, K. Macroporous biphasic calcium phosphate scaffold with high permeability/porosity ratio. *Tissue engineering***2003**, *9*, 535–548.
321. Karande, T. S.; Ong, J. L.; Agrawal, C. M. Diffusion in musculoskeletal tissue engineering scaffolds: design issues related to porosity, permeability, architecture, and nutrient mixing. *Annals of biomedical engineering***2004**, *32*, 1728–1743.
322. Madaghiele M, Salvatore L, Sannino A (2014) Tailoring the pore structure of foam scaffolds for nerve regeneration. Elsevier, In Biomedical Foams for Tissue Engineering Applications, pp 101–128
323. Prabhakaran MP, Vatankhah E, Ramakrishna S (2013) Electrospun aligned PHBV/collagen nanofibers as substrates for nerve tissue engineering. Biotechnol Bioeng 110:2775–2784
324. Kim JI, Kim JY, Park CH (2018) Fabrication of transparent hemispherical 3D nanofibrous scaffolds with radially aligned patterns via a novel electrospinning method. Sci Rep 8:1–13
325. Hartgerink JD, Beniash E, Stupp SI (2001) Self-assembly and mineralization of peptide-amphiphile nanofibers. Science 294:1684–1688
326. Dickerson MB, Sandhage KH (2008) Naik RR Protein-and peptide-directed syntheses of inorganic materials. Chem Rev 108, 4935–4978
327. Spoerke ED, Anthony SG, Stupp SI (2009) Enzyme directed templating of artificial bone mineral. Adv Mater 21:425–430
328. Sargeant TD, Guler MO, Oppenheimer SM, Mata A, Satcher RL, Dunand DC, Stupp SI (2008) Hybrid bone implants: self-assembly of peptide amphiphile nanofibers within porous titanium. Biomaterials 29:161–171
329. Dewle A, Pathak N, Rakshasmare P, Srivastava A (2020) Multifarious fabrication approaches of producing aligned collagen scaffolds for tissue engineering applications. ACS Biomater Sci Eng 6:779–797
330. Liang YX, Cheung SW, Chan KC, Wu EX, Tay DK, Ellis-Behnke RG (2011) CNS regeneration after chronic injury using a self-assembled nanomaterial and MEMRI for real-time in vivo monitoring. Nanomed Nanotechnol Biol Med 7, 351–359
331. Narmoneva DA, Vukmirovic R, Davis ME, Kamm RD, Lee RT (2004) Endothelial cells promote cardiac myocyte survival and spatial reorganization: implications for cardiac regeneration. Circulation 110:962–968
332. Geng X, Liu B, Liu J, Liu D, Lu Y, Sun X, Liang K, Kong B (2018) Interfacial tissue engineering of heart regenerative medicine based on soft cell-porous scaffolds. J Thoracic Disease, 10, S2333
333. Laflamme MA, Chen KY, Naumova AV, Muskheli V, Fugate JA, Dupras SK, Reinecke H, Xu C, Hassanipour M, Police S, O'Sullivan C (2007) Cardiomyocytes derived from human embryonic stem cells in pro-survival factors enhance function of infarcted rat hearts. Nat Biotech 25, 1015–1024
334. Wang Y, Haider HK, Ahmad N, Xu M, Ge R, Ashraf M (2006) Combining pharmacological mobilization with intramyocardial delivery of bone marrow cells over-expressing VEGF is more effective for cardiac repair. Journal of molecular and cellular cardiology, 40, 736–745
335. Biermann U, Friedt W, Lang S, Lühs W, Machmüller G, Metzger JO, Rüsch gen. Klaas M, Schäfer HJ, Schneider MP (2000) New Syntheses with Oils and Fats as Renewable Raw Materials for the Chemical Industry. Angewandte Chemie (International ed. in English), 39, 2206–2224
336. Petrovic Z (2008) Polyurethanes from vegetable oils. Polym Rev 48:109–155
337. Tan S, Abraham T, Ference D, Macosko CW (2011) Rigid polyurethane foams from a soybean oil-based polyol. Polymer 52:2840–2846
338. Suresh KI (2013) Rigid polyurethane foams from cardanol: synthesis, structural characterization, and evaluation of polyol and foam properties. ACS Sustainable Chemistry & Engineering 1:232–242

339. Novoselov KS, Fal VI, Colombo L, Gellert PR, Schwab MG, Kim K (2012) A roadmap for graphene. Nature, 490, 192–200
340. Xu X, Guan C, Xu L, Tan YH, Zhang D, Wang Y, Zhang H, Blackwood DJ, Wang J, Li M, Ding J (2019) Three Dimensionally Free-Formable Graphene Foam with Designed Structures for Energy and Environmental Applications. ACS nano, 14, 937–947
341. Wang C, Kim J, Tang J, Kim M, Lim H, Malgras V, You J, Xu Q, Li J, Yamauchi Y (2020) New strategies for novel MOF-derived carbon materials based on nanoarchitectures. Chem 6:19–40
342. Obraztsov A, Obraztsova E, Tyurnina A, Zolotukhin A (2007) Chemical vapor deposition of thin graphite films of nanometer thickness. Carbon 45:2017–2021
343. Sha J, Gao C, Lee SK, Li Y, Zhao N, Tour JM (2016) Preparation of three-dimensional graphene foams using powder metallurgy templates. ACS nano, 10, 1411–1416
344. Obraztsov AN (2009) Making graphene on a large scale. Nature Nanotechnol 4, 212–213
345. Yousefi N, Lu X, Elimelech M, Tufenkji N (2019) Environmental performance of graphene-based 3D macrostructures. Nat Nanotech 14, 107–119
346. Meng Y, Zhao Y, Hu C, Cheng H, Hu Y, Zhang Z, Shi G, Qu L (2013) All-graphene core-sheath microfibers for all-solid-state, stretchable fibriform supercapacitors and wearable electronic textiles. Adv Mater 25, 2326–2331
347. Wang Y, Wang L, Yang T, Li X, Zang X, Zhu M, Wang K, Wu D, Zhu H (2014) Wearable and highly sensitive graphene strain sensors for human motion monitoring. Adv Func Mater 24:4666–4670
348. Bera KP, Haider G, Usman M, Roy PK, Lin HI, Liao YM, Inbaraj CRP, Liou YR, Kataria M, Lu KL (2018) Trapped Photons Induced Ultrahigh External Quantum Efficiency and Photoresponsivity in Hybrid Graphene/Metal-Organic Framework Broadband Wearable Photodetectors. Adv Func Mater 28:1804802
349. Balci O, Kakenov N, Karademir E, Balci S, Cakmakyapan S, Polat EO, Caglayan H, Özbay E, Kocabas C (2018) Electrically switchable metadevices via graphene. Sci Adv 4, eaao1749
350. Phare CT, Lee Y-HD, Cardenas J, Lipson M (2015) Graphene electro-optic modulator with 30 GHz bandwidth. Nat Photonics 9:511–514
351. Chai G-L, Qiu K, Qiao M, Titirici M-M, Shang C, Guo Z (2017) Active sites engineering leads to exceptional ORR and OER bifunctionality in P, N Co-doped graphene frameworks. Energy Environ Sci 10:1186–1195
352. Tang C, Li BQ, Zhang Q, Zhu L, Wang HF, Shi JL, Wei F (2016) CaO-templated growth of hierarchical porous graphene for high-power lithium–sulfur battery applications. Adv Func Mater 26:577–585
353. Kumar S, Sahoo PK, Sharma A, Satpati AK (2020) Insight into the catalytic performance of HER catalysis of noble metal/3D-G nanocomposites. Electrochimica Acta, 333, 135467
354. Yun J, Lim Y, Jang GN, Kim D, Lee S-J, Park H, Hong SY, Lee G, Zi G, Ha JS (2016) Stretchable patterned graphene gas sensor driven by integrated micro-supercapacitor array. Nano Energy 19:401–414
355. Goossens S, Navickaite G, Monasterio C, Gupta S, Piqueras JJ, Pérez R, Burwell G, Nikitskiy I, Lasanta T, Galán T (2017) Broadband image sensor array based on graphene–CMOS integration. Nat Photonics 11:366–371
356. Han T, Jin J, Wang C, Sun Y, Zhang Y, Liu Y (2017) Ag Nanoparticles-Modified 3D Graphene Foam for Binder-Free Electrodes of Electrochemical Sensors. Nanomaterials 7:40
357. Dong X, Wang X, Wang L, Song H, Zhang H, Huang W, Chen P (2012) 3D graphene foam as a monolithic and macroporous carbon electrode for electrochemical sensing. ACS applied materials & interfaces, 4, 3129–3133
358. Pawar PB, Saxena S, Badhe DK, Chaudhary RP, Shukla S (2006) 3D Oxidized graphene frameworks for efficient nano sieving. Scientific reports, 6, 21150.
359. Ramirez S, Chan K, Hernandez R, Recinos E, Hernandez E, Salgado R, Khitun A, Garay J, Balandin A (2017) Thermal and magnetic properties of nanostructured densified ferrimagnetic composites with graphene-graphite fillers. Mater Des 118:75–80

360. Hu X, Xu W, Zhou L, Tan Y, Wang Y, Zhu S, Zhu J (2014) Tailoring graphene oxide-based aerogels for efficient solar steam generation under one sun. Advanced materials, 29, 1604031
361. Zhou M, Zhai Y, Dong S (2009) Electrochemical sensing and biosensing platform based on chemically reduced graphene oxide. Analytical chemistry, 81, 5603–5613
362. Patil U, Lee SC, Kulkarni S, Sohn JS, Nam MS, Han S, Jun SC (2015) Nanostructured pseudocapacitive materials decorated 3D graphene foam electrodes for next generation supercapacitors. Nanoscale 7:6999–7021
363. Chen J, Sheng K, Luo P, Li C, Shi G (2012) Graphene hydrogels deposited in nickel foams for high-rate electrochemical capacitors. Advanced materials, 24, 4569–4573
364. Maiti UN, Lim J, Lee KE, Lee WJ, Kim SO (2014) Three-dimensional shape engineered, interfacial gelation of reduced graphene oxide for high rate, large capacity supercapacitors. Adv Materi (Deerfield Beach, Fla.), 26, 615–619, 505
365. Xu Y, Lin Z, Zhong X, Huang X, Weiss NO, Huang Y, Duan X (2008) Holey graphene frameworks for highly efficient capacitive energy storage. Nature communications, 5, 1–8
366. Feng X, Chen W, Yan L (2015) Reduced graphene oxide hydrogel film with a continuous ion transport network for supercapacitors. Nanoscale 7:3712–3718
367. Amani H, Mostafavi E, Arzaghi H, Davaran S, Akbarzadeh A, Akhavan O, Pazoki-Toroudi H, Webster TJ (2018) Three-dimensional graphene foams: synthesis, properties, biocompatibility, biodegradability, and applications in tissue engineering. ACS Biomater Sci Eng 5:193–214

Chapter 10
Exfoliation Routes to the Production of Nanoflakes of Graphene Analogous 2D Materials and Their Applications

N. Padma

Abstract In the past decade, with the discovery of graphene, two-dimensional (2D) graphene analogous materials like nanolayers of transition metal dichalcogenides (TMDCs), monoelemental Xenes (like phosphorene, antimonene etc.) and MXenes (like Ti_2C, Mo_2C etc.) have attracted much attention owing to their high mobility of charge carriers, accompanied by other useful and unique electronic, optical, and mechanical properties. The thickness-dependent electronic properties of these materials demand isolation of the nanolayers from their corresponding bulk layered solids. An attempt is made in this chapter to discuss the exfoliation of some of these nanolayers and their thickness identification, with a brief description of their structure and band energy diagrams. Layer isolation is generally carried out by mechanical exfoliation or by liquid phase exfoliation (LPE). While the former does not result in scalable production that is required for various device applications, the latter offers improvement in this aspect The yield and the efficiency of dispersion of the nanoflakes in the LPE method depend on the choice of good solvents, i.e., the solvents having matching surface energy with that of the material to be exfoliated. The mechanism governing such surface energy-dependent exfoliation is discussed. Since most of these good solvents exhibit high boiling points hindering the device performance, the discussion is also made on the exfoliation by cosolvent method where a mixture of two low boiling point so-called bad solvents is used. Alkali metal ion and surfactant intercalation methods that are employed to improve the concentration of the dispersion are also mentioned here. Identification of the layer thickness and verification of the thickness-dependent electronic properties by some of the techniques like optical microscope, atomic force microscope (AFM), Raman and photoluminescence (PL) spectroscopy etc. are highlighted. The potential applications of these graphene analogous layered materials in the areas of nanoelectronics, photovoltaic devices, supercapacitors, etc. are briefed.

Keywords 2D materials · Mechanical exfoliation · Liquid exfoliation · Layer thickness · Thickness identification

N. Padma (✉)
Technical Physics Division, Bhabha Atomic Research Centre, Mumbai 400085, India
e-mail: padman@barc.gov.in

A. K. Tyagi and R. S. Ningthoujam (eds.), *Handbook on Synthesis Strategies for Advanced Materials*, Indian Institute of Metals Series,
https://doi.org/10.1007/978-981-16-1803-1_10

Abbreviations

D	Dimensions
L	Layer
LPE	Liquid Phase Exfoliation
TMDCs	Transition metal dichalcogenides
CMOS	Complementary metal oxide semiconductor
MOSFET	Metal oxide semiconductor field-effect transistor
GO	Graphene oxide
RGO	Reduced graphene oxide
BP	Black phosphorous
HSP	Hansen's solubility parameters
LED	Light emitting diode
FET	Field-effect transistors
NMP	N-methyl pyrrolidone
DMF	Dimethyl formamide
IPA	Isopropyl alcohol
DMSO	Dimethyl sulfoxide
AFM	Atomic force microscope
PL	Photoluminescence
ITO	Indium tin oxide
FTO	Fluorine doped Tin oxide
HTL	Hole transporting layer
P3HT	Poly 3-hexyl thiophene
PCBM	Phenyl-C61-butyric acid methylester
PDMS	Poly dimethylsiloxane
EDLC	Electric double layer capacitance
VBM	Valence band maximum
CBM	Conduction band minimum
IL	Ionic liquid
SC	Supercritical
SCF	Supercritical fluid
PANI	Polyaniline

10.1 Introduction

Ever-increasing societal demands for the high performing appliances related to low power electronic devices, sensors, and health-related equipment, energy sectors, etc., which require faster transport of data and processing capabilities, have been constantly moving the technology world towards miniaturisation of the devices. This motive to scale down the devices has accelerated the global development in nanotechnology in the last three decades. Nanotechnology is basically a field in

materials science dealing with nanomaterials having at least one dimension in the nanometers scale, offering advantage of providing a large surface to volume ratio. When two dimensions are limited in size, one-dimensional nanowires are formed whereas restriction in all the three dimensions results in 0D quantum dots. When dimension is restricted to only one side, it results in two-dimensional materials. The continuous scaling down process using conventional silicon-based electronic devices has reached a limit due to various reasons such as short channel effects caused by degradation in electrostatic control, processing and economic limitations, etc. [1]. Apart from miniaturisation of the devices, wearable equipment such as roll-up displays, bendable mobile phones, e-skin applications, etc. have begun to take an important place in our daily life. These applications require stable and reliable performance after many cycles of bending and stretching. This demands the employment of materials exhibiting high mechanical flexibility. Therefore, developing the next-generation electronic and optoelectronic devices strongly demand new materials with different dimensionality, functionality, mechanical strength and flexibility, especially high performing semiconductors exhibiting excellent transport property and good sensitivity to incident photons.

Though layered materials have been of scientific interest for the past 150 years, only for the past one decade, their potential for advanced technological applications has been recognised, after the discovery of graphene in 2004 by Novoselov and Geim and after the awarding of Nobel prize to them in 2010 [2]. Even though the word graphene was coined by Boehm in 1962, Geim's group was able to practically isolate a monolayer of graphene from the van der Waals solid only in 2004 [3]. Graphene is basically a two-dimensional (2D) material with carbon atoms in a single sheet, possessing unique properties such as high optical transmittance of about 97.7%, a high charge carrier mobility of around 200,000 cm^2/Vs, high thermal conductivity and excellent mechanical flexibility with Young's modulus of about 0.5–1 TPa [4]. In a layered crystal, the electronic wavefunction exceeds in three dimensions while in the 2D layers, there is a strong quantum confinement of electrons with their wave functions constrained to adopt a two-dimensional form. This imparts the 2D materials with new electronic band structures and with unique and fascinating physical/electrical/electronic properties [5–7]. The above-mentioned interesting properties of graphene have been usefully exploited for technological development in next-generation devices in the areas of electronics, optoelectronics, energy storage applications, etc. The disadvantage of graphene lies in the fact that it lacks intrinsic bandgap making it unsuitable for certain logic applications like transistors requiring high ON/OFF ratio. Band gap engineering, like functionalisation, doping, introducing defects etc., has been adapted to open a band gap in graphene without considerable modification of the pristine sheet. Unfortunately, during such processes, the conductivity of graphene reduces drastically [8–12].

The success and the exotic performance observed in this material have fuelled increasing interest and intense effort to search for alternative 2D materials having more versatility, tunability, flexibility and functionality. 2D materials are defined to be those one atom thick sheets isolated from bulk as free-standing layers and do not need a substrate to exist. Often, layers with up to 10 atom thick sheets are also considered as

2D sheets [13]. Classical physics predictions hinted that lattice thermal fluctuations do not allow 2D materials to be thermodynamically stable at finite temperatures [14]. Interestingly, a closer examination and finer studies of graphene revealed the presence of ripples, which were found to distorting the 2D lattice. This was considered to be making graphene sheets 3D like, thereby resolving the controversy over 2D materials.

2D materials basically possess neutral atoms covalently or ionically bonded with their neighbours in a plane/layer while the layers are held together by van der Waals coupling along the third axis. The weak van der Waals energies (~40–70 meV) allow the facile exfoliation of these layers from their parent bulk material [7, 15]. This search towards new materials has forced the research community to turn towards more exotic layered materials like silicene, germanene, hexagonal boron nitrides (hBN) and transition metal dichalogenides (TMDCs) etc. Some, like graphene, have truly extraordinary properties like tensile strength 200 times greater than steel combined with high flexibility, astonishingly high conductivity, tremendous energy storage capacity etc. These planar materials exhibit different electronic structures and hence varying band gaps depending on their thickness and stacking order [7, 12, 15, 16]. In many of the TMDCs, there is a transition from indirect band gap in the bulk to direct band gap in the monolayer. Such thickness and stacking order-dependent band gaps and photoluminescence make these materials usable in the optoelectronic devices. Larger interlayer spacing, high specific capacity and power density make them highly suitable for flexible energy storage applications [16].

Layered materials cover a wide range of materials including clays, layered oxides, halides, carbides, nitrides, hydroxides, phosphates, phosphonates, etc. apart from the above-mentioned TMDCs and mono-elemental materials. Though most of these materials are binary layered compounds, ternary compounds can also be possible ($CuSbS_2$) candidates [7, 14, 17]. Layered materials can be further classified depending on the nature of interaction between the layers. This interaction is governed by hydrogen bonds, interstitial cations or van der Waals forces. This chapter will be dealing with graphene and other van der Waals-based graphene analogous inorganic layered materials, their nanoflakes production, characterisation and some of their applications such as field-effect transistors (FETs), photovoltaic and energy storage devices, etc.

10.2 Classes, Structure of 2D Materials and Their Band Structures

In this section, a brief overview of the structure of some of the commonly used 2D materials will be shown. It is well known that the energy band structure is an important factor through which knowledge about the properties of a solid-state material can be acquired. The electronic band structures are mostly represented along the high symmetry points (Γ-M–K-Γ) in the Brillouin zone [18]. Though this chapter will

not deal with theoretical band structure calculations, a brief mention of the same for some of these common graphene analogous materials will be made.

10.2.1 Graphene

Graphene, the father of 2D materials, is an atomically thin single-layer sheet of sp^2 hybridised carbon atoms arranged in a honeycomb lattice with adjacent π–π stacked layers having a spacing of 0.34 nm and held together by weak van der Waals force (Fig. 10.1). The corresponding Brillouin zone and the band structure are shown in Fig. 10.1c, d, respectively [8]. The four valence electrons of each of the carbon atom are exactly enough to fill all of the bonding electronic orbitals [11, 17]. The homogenous electron distribution allows graphene to be chemically very stable. Graphene exhibits a semi-metallic property with zero band gap, but with density of states zero at its Fermi level. Electronic bands cross the Fermi level at the six corners of the two-dimensional hexagonal Brillouin zone, making the dispersion relation (the change of electron energy of a band within the Brillouin zone) linear or conical at these points. This causes the electrons or holes to behave like relativistic particles with zero effective mass making this material highly conductive. The electrons and holes are called the Dirac Fermions and the six corners of the Brillouin zone as the Dirac points [13, 14].

10.2.2 Transition Metal Dichalcogenides (TMDCs)

Layered metal oxides, double hydroxides, layered silicates or clays and mica are the well-known examples of layered materials [7]. Transition metal trichalocgenides like NbX_3, TiX_3, TaX_3 (X = S, Se or Te), transition metal dihalides like $MoCl_2$, metal halides like $CrCl_3$, $PbCl_4$, transition metal oxides such as TiO_2, Nb_3O_8, V_2O_5, MoO_3, MnO_3, WO_3 and hexagonal boron nitride (h-BN) etc. are the different families of 2D materials where metal oxides are considered to be falling into the category of 2D family only modestly. Group III-VI materials like InSe, GaS etc. and group V-VI chalcogenides such as Bi_2Te_3 and Sb_2Se_3 are tending to become prominent members in the layered materials family.

Transition metal dichalocogenides (TMDCs) of the form MX_2, where M is a transition metal element from group 4 to group 10 (M = Mo, W, Re, Ti, Ta etc.), and X represents a chalcogen element (S, Se or Te) are the most focussed class of layered materials. TMDCs with M=group 4–7 are mostly layered structures while some with group 8–10 M atoms are found in non-layered structure [17, 19]. The metal atoms provide four electrons to fill the bonding states of TMDCs such that the M and X atoms are in the oxidations states of + 4 and −2, respectively [19]. The termination of the surface layers with the lone pair electrons of the chalcogen atoms and the absence of the dangling bonds ensure the stability of these layers to reactions

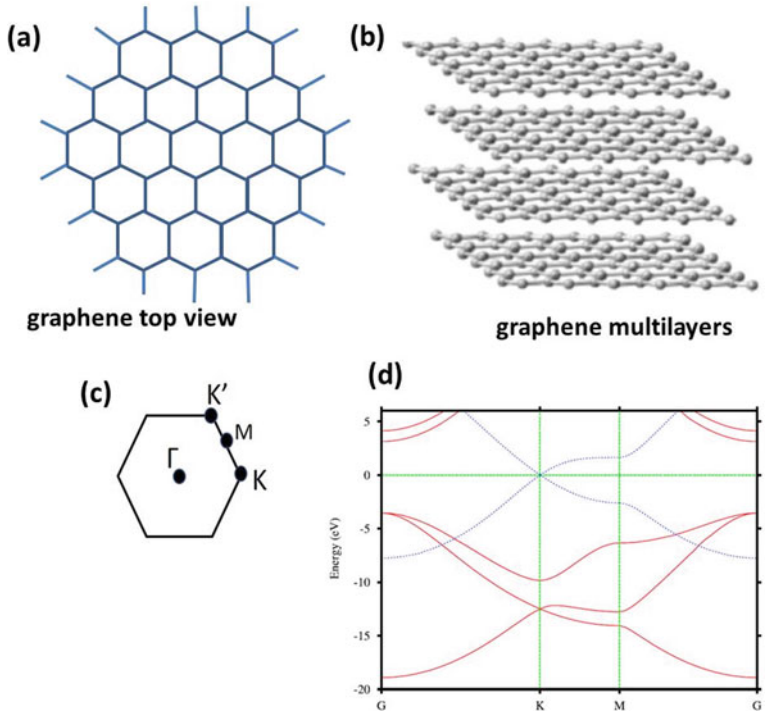

Fig. 10.1 **a** graphene top view, **b** multilayer graphene or graphite (Guo, Y.; Wei, Y.; Li, H. and Zhai, T. Layer Structured Materials for Advanced Energy Storage and Conversion. Small. 2017. 1,701,649(1–22). Copyright Wiley–VCH Verlag GmBH & Co. KGaA. Reproduced with permission), **c** typical Brillouin zone of graphene and **d** band structure of graphene, solid red lines are σ bond and dotted blue lines are π bonds (d—"Reprinted (figure) with permission from (Boukhvalov D. W.; Katsnelson M. I.; Lichtenstein A. I.; Phys. Rev. B.,77, 035,427, 2008). Copyright (2018) American Physical Society")

against species in the environment. TMDCs occur as 40 different types depending on the combination of chalcogen (S, Se or Te) and transition metal among which MoS_2 is the most common and well-studied material [7, 17]. The structures of some of these TMDCs are shown in Fig. 10.2.

The metal atoms in the layered TMDCs are mainly sandwiched between two layers of chalcogen atoms through covalent bonding, forming X-M-X units with the tri-layer like structure. The combined trilayer is considered to be a monolayer in TMDCs with adjacent such layers held by van der Waals force [12, 19]. The inherent weakness of the van der Waals forces in these materials can cause the mutual sliding of the adjacent layers and introduce stacking faults, thereby resulting in different stacking sequences. Therefore, the MX_2 solids crystallise in different polymorphs depending on the varying stacking orders and the metal coordination, with the latter being either trigonal prismatic or octahedral. Varying stacking sequences modify the crystal symmetry, which, in turn, alters the coulomb interaction between the layers

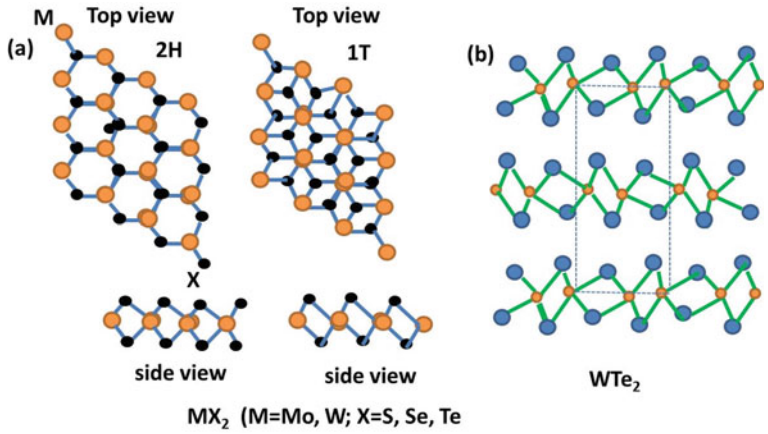

Fig. 10.2 Structure of TMDCs—**a** 2H and 1 T structure of MX_2 (M = Mo, W, and X = S, Se) in top and side views and **b** side view of WTe_2

leading to different interlayer distances [20]. The different types of stacking of a bilayer of MoS_2 are shown in Fig. 10.3a. Bilayer, which is the first multilayer with van der Waals interaction, can be considered to exist in five possible high-symmetry stacking order along the z axis, almost exhausting all conceivable combinations, as explained here: (1) AA—eclipsed stacking with atoms of the same type being superimposed, i.e., M over M and X over X of the two layers, (b) AA'—eclipsed with one atom type above the other (M over X), (c) A'B–M atoms superimposed and the X atoms in the top layer over the hexagon centres in the bottom layer, (d) AB'—X atoms are superimposed and the M atoms in the top layer over the hexagon centres of the bottom layer, (e) AB—X atoms in the top layer over the M atoms in the bottom layer and M atoms in the top layer over the hexagon centres of the bottom layer [20–25]. Interestingly, one stacking can be changed to another by simply sliding the layers horizontally and/or by rotation around the vertical axis. Varying the stacking sequence also forms an additional pathway to tune the optical and electronic properties where the band gap can be easily tuned by varying the twist angle [26]. For example, the band gap of a bilayer MoS_2 varies from 1.49 to 1.62 eV for twist angles of 0 and 30º between the two layers. This change is attributed to the effect of interlayer coupling, which varies with the angle between the two layers [24, 26].

The TMDC layers exist in different electronic structures such as the 1T, 2H or 3R phases, where the numbers indicate the number of X-M-X units in the unit cell and T, H and R represent the trigonal, hexagonal and rhombohedral configurations, respectively (Fig. 10.3b) [12, 17–19]. The 2H phase has hexagonal symmetry with two layers per repeat unit with trigonal prismatic metal coordination, the 3R phase has rhombohedral symmetry with three layers per repeat unit and trigonal prismatic coordination, the 1T phase has tetragonal symmetry with one layer per repeat unit and octahedral coordination [12]. Natural or synthetic MX_2 crystals generally exist in two different polytypisms, namely, the 2H or 3R phase, both with trigonal prismatic

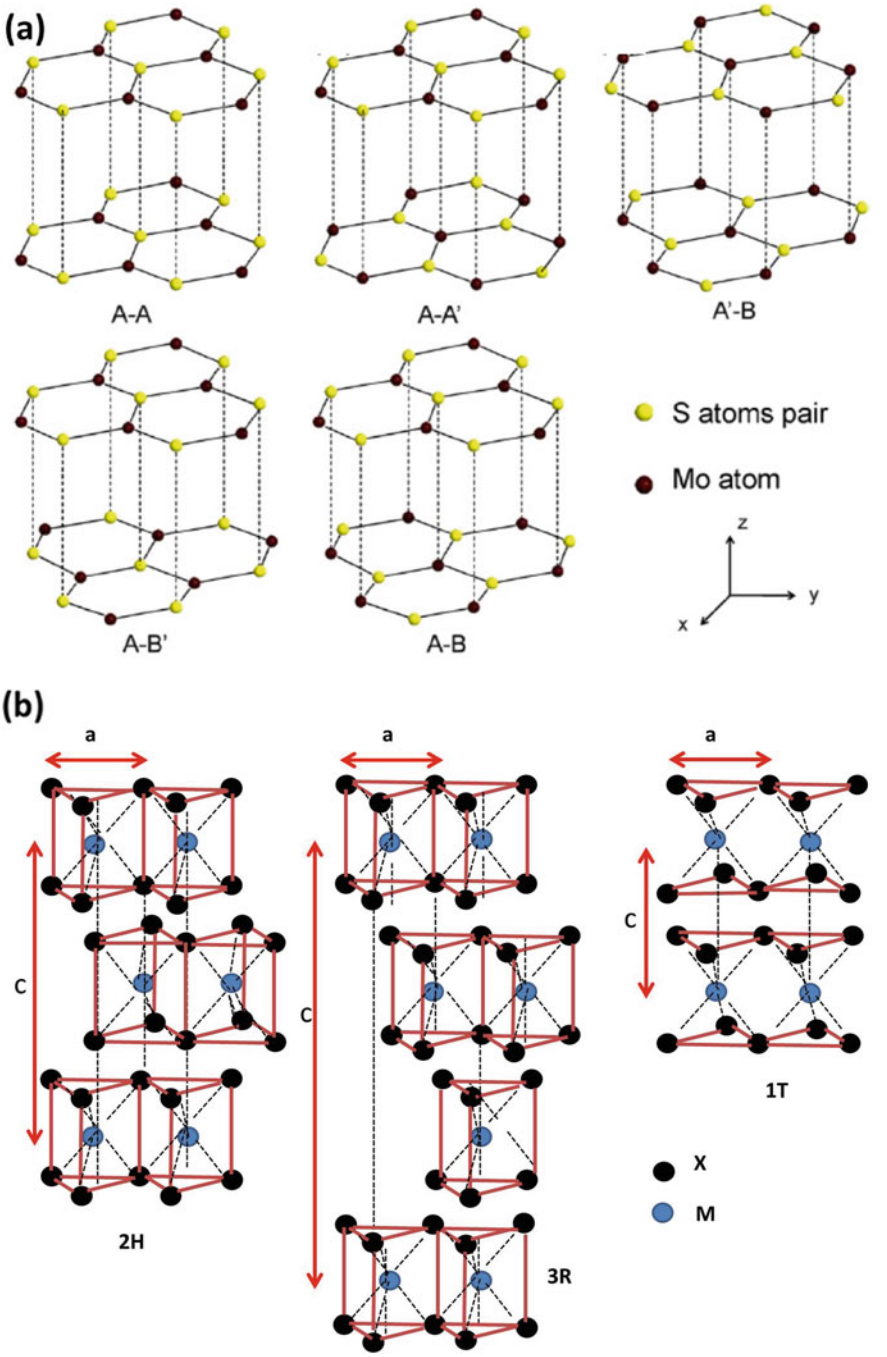

Fig. 10.3 **a** Different stacking of MoS_2 (Reprinted (adapted) with permission from (J. Phys. Chem. C, 2012, 116, 21,556). Copyright (2019) American Chemical Society") and **b** different polymorphism-2H, 1T and 3R structures

coordination [19, 20]. In both phases, the M atom in one layer is aligned above the X atom in the layer beneath, but with a different lateral registry. The X atoms are fully eclipsed in the 2H phase while they are staggered in the 3R phase with one X being eclipsed by the Mo atom above and the second one being located below the hexagonal hollow site [20, 22]. In the case of hexagonal MoS_2, the 2H MoS_2 and 1 T MoS_2 phases are mainly formed in multilayer and monolayers, respectively, where the 2H MoS_2 is a semiconductor and 1 T MoS_2 is metallic. Among them, the most stable configuration is the semiconducting 2H phase where the A layer is rotated by 60º with respect to A' layer with inversion symmetry [5, 20, 27]. If one of S atoms is shifted out of order, the structure is denoted as metallic 1 T-MoS_2 [28, 29]. Similar to MoS_2, $MoSe_2$, WS_2 and WSe_2 also have a hexagonal crystal structure, in which Mo and W are found to be in trigonal prismatic coordination with sulphur atoms, and hence similar stacking order [18, 30].

Though most of the TMDCs show such similarities in their structures, they simultaneously exhibit minor variations also. For example, while most of the TMDCs have hexagonal symmetry with trigonal prismatic coordination, $MoTe_2$ and WTe_2 have the distorted octahedral coordination [18, 19, 31, 32]. Depending on the coordination and oxidation state of the metal atoms or doping of the lattice, TMDCs can be metallic, semiconducting or semi-metallic and even superconductors [7, 12, 17, 19]. The type of coordination and the phase preferred by the TMDCs depend on the d electron count of the transition metal [19]. Group 4TMDCs with d^0 transition metal centres adopt octahedral structure. Group 5 TMDCs with d^1 electron count are seen in octahedral and in trigonal prismatic structure. Group 6 TMDCs with d^2 electrons are found primarily in trigonal prismatic phase and group 7 TMDCs with d^3 electrons are in a distorted octahedral structure. All group X TMDCs with d^6 transition metal centres adopt in octahedral structure. This difference in the transition metal's coordination environment and its d electron count is mainly responsible for the difference in their electronic properties. The non-bonding d bands are located within the gap between the bonding (σ) and antibonding (σ^*) bands of the M-X bonds. These d bands are either degenerate or they are split depending on whether the transition metals are octahedrally coordinated or with trigonal prismatic coordination, respectively. Difference in the filling of these bands from group 4 to group 10 species is observed reflecting in change in their electronic properties. When the orbitals are partially filled, as found for 2H-$NbSe_2$, 1 T-ReS_2, they exhibit metallic conductivity. When the orbitals are fully occupied, as for 2H-MoS_2, 1 T-HfS_2 etc., they become semiconductors. Though the electronic structure is majorly decided by the metal atoms, the change in the same is also observed for the change in the chalcogen atoms. Mainly, decrease in the band gap is observed for increasing atomic number of the chalcogen atoms. For example, the band gap reduces gradually from 1.3 to 1.0 eV in the order 2H MoS_2 > 2H-$MoSe_2$ > 2H-$MoTe_2$. For change in chalcogen atoms from S to Te, the electronegativity decreases and the orbital radii increase. Due to these changes, the effect of ligand field of the chalcogen atoms on the metal atom d states becomes more and more prominent. This leads to broadening of the d bands and hence decreases in band gap. Difference in the semiconducting nature was also observed for different chalcogen atoms, where MoS_2 shows *n*-type behaviour,

$MoSe_2$ is bipolar and $MoTe_2$ exhibits *p*-type. Among the *n*-type MoS_2 and WS_2, the carrier density is reported to be higher in MoS_2 [33]. Similarly, the bond length M–M, where M is the transition metal, is similar for MoS_2 (3.16) and WS_2 (3.15), and it is slightly larger for WSe_2 (3.28). Also, the interlayer gap is higher for WSe_2 than that for WS_2 due to the larger size of Se atoms [34]. Such variations imply that many of these TMDCs are yet to be explored thoroughly.

While the band structure of most of the semiconducting TMDCs (MoS_2, WS_2 etc.) is similar, as shown by first principles and tight binding approximations as well as measured using many spectroscopic techniques, they differ from that of the zero band gap graphene [18, 30, 32, 33]. A typical case of MoS_2 is discussed here. The occupation of the sub-lattices by Mo and S atoms at different planes, unlike that of the C atoms in graphene, lifts the degeneracy in the electronic structure at K (K') point in the Brillouin zone while the existence of this degeneracy was responsible for Dirac-cone like dispersion relation in graphene [15]. Band structure calculations of MoS_2 shown in Fig. 10.4 reveal the indirect band gap of bulk MoS_2 where the bottom of the conduction band lies at the midpoint along Γ – K symmetry lines and top of the valence band is located at Γ point. Several groups have predicted and observed a transition from the indirect-band gap to a direct band gap at the K point of the Brillouin zone for thinning of the flake thickness from bulk to a monolayer, with the conduction band bottom and the valence band top getting located at same point K in the wave vector axis for monolayer. The first principle calculations carried out by different groups on the electronic structure of bulk and the monolayer MoS_2 shows that the density of states around Fermi level is due to molybdenum d states [12, 18, 19, 26, 32]. The conduction band states at the K point were suggested to be composed of strongly localised d orbitals of the Mo atoms. Since Mo atoms are located in the middle of S-Mo-S structure, they experience minimum interlayer coupling. Hence layer thinning makes K states remain unaffected. However, the states near the Γ point are predicted to be due to the presence of strong hybridisation between the Mo *d* orbitals and the antibonding p_z orbitals of the chalcogen atoms. They are subjected to strong interlayer coupling and hence become sensitive to layer thinning [5, 18, 26, 35]. The transition from indirect to direct band gap with layer thickness reduction is said to be due to the quantum confinement and to the change in this hybridisation happening at the Γ point [12, 15, 19]. Similar transition from indirect to direct band gap is also shown in Fig. 10.4 for WS_2 and $MoSe_2$ [12, 18].

Among these TMDCs, ReS_2 and $ReSe_2$ have attracted special attention because of their interesting electronic properties different from that of MoS_2. They stand out from other TMDCs due to their distorted 1T crystal structure (Fig. 10.5) with triclinic unit cell where Re atoms are displaced from the hexagonal lattice and form diamond chains along the b axis [31, 36–42]. The distorted structure is explained as follows: Compared with the 2H structure of classical TMDCs, an additional valence electron in Re atom impacts energy balance by forming covalent bonding between the neighbouring Re atoms. This leads to the formation of Re chains along the b-axis of the crystal. The superlattice structure of Re chains thus formed tends to distort the crystal from the more symmetric 1T phase, drastically reducing its symmetry. The low crystal symmetry results in highly anisotropic optical and electrical transport

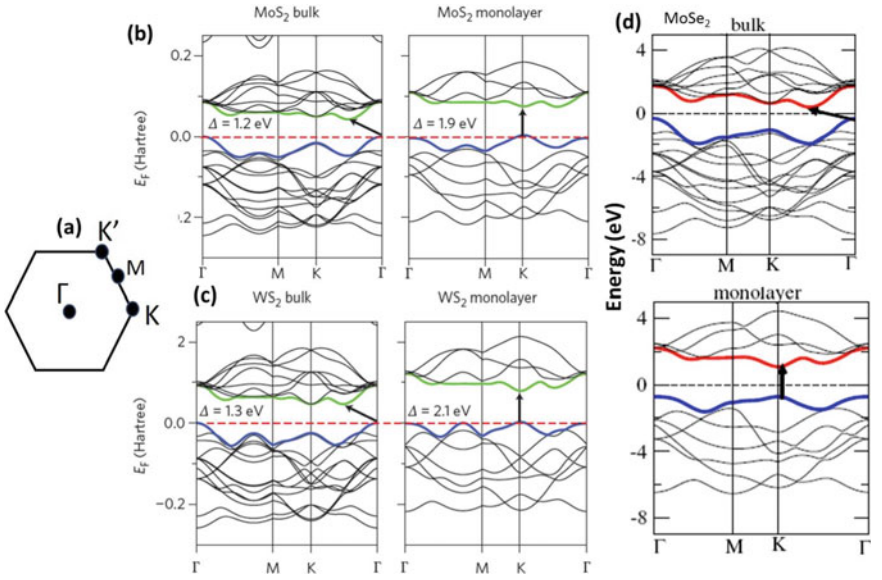

Fig. 10.4 **a** Brillouin zone for hexagonal lattice of MoS_2, band structure calculations of **b** MoS_2 and **c** WS_2 **b** and **c**—Reproduced with permission from Springer Nature [12], and **d** $MoSe_2$ (Reproduced with permission from Springer Nature [18])

properties, adding an additional degree of freedom for applications in sensor and electronic devices. The distorted structure tends to weaken the interlayer coupling preventing an ordered stacking of the layers and minimising the overlap of the wavefunctions. Therefore, unlike MoS_2, bulk ReS_2 and $ReSe_2$ electronically behave like a decoupled monolayer due to weak interlayer interaction, maintaining the direct band gap of around 1.5 eV from bulk to monolayer [36–38]. In pristine ReS_2, the valence band maximum is determined by 5d orbitals of the Re atoms and 3p orbitals of the S atoms. The conduction band minimum is composed of 5d orbitals of the Re atoms. Like MoS_2, ReS_2 is also an *n*-type semiconductor with its Fermi level about 0.07 eV below the bottom of the conduction band.

Density functional theory calculations predict a interlayer coupling energy as low as 18 meV per unit cell, which is about 8% of that observed for MoS_2 [36, 37]. Due to this, though the band structure of most of the TMDCs is similar, it varies clearly for ReS_2. A typical band structure calculation shown in Fig. 10.6a reveals the decoupled nature of ReS_2. The figure shows a very small change in band gap when thinned down from bulk to monolayer. But recently, some studies have contradicted this conclusion and suggested the existence of significant interlayer coupling in ReS_2 and also in $ReSe_2$ [39, 40]. A very recent study by Gehlman et al. indicated the indirect band gap nature of bulk ReS_2 [39]. Interestingly, their GW-based calculations suggest that transition to direct band gap occurs for bilayer ReS_2, while it becomes indirect again for monolayer, making the former better for device applications than the latter. The typical band structure calculations shown by them are given in Fig. 10.6b along

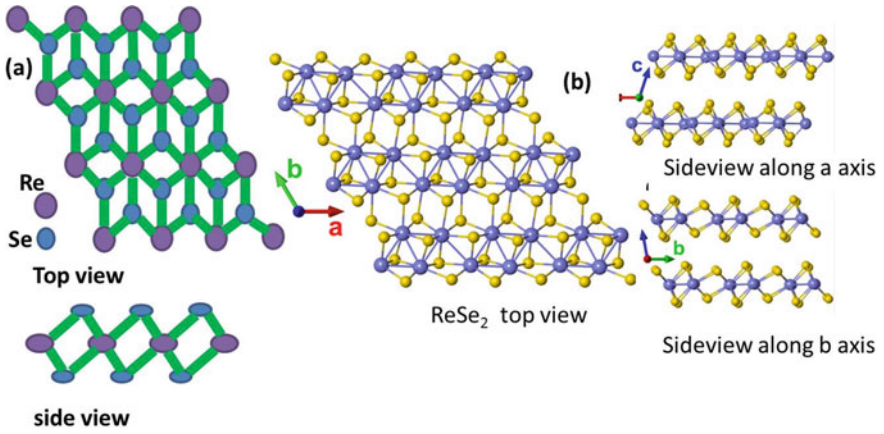

Fig. 10.5 **a** Top and side views of undistorted $ReSe_2$, **b** top and side views of distorted $ReSe_2$ ("Reprinted (adapted) with permission from (Nano Lett, 2017, 17, 3202). Copyright (2018) American Chemical Society")

with the 3D *k*-space with positions of the selected directions in Fig. 10.6c. They have also concluded that the indirect band gap is only very faintly observed, which could be the reason why some studies found indications of both direct and indirect band gap.

10.2.3 Monoelemental Graphene Analogous Materials

Another class of 2D materials, closely related to graphene, are the zero-band gap semi-metallic mono-elemental 2D X-enes made of group IVA elements, i.e., silicene, germanene, stanene etc. when X = Si, Ge, Sn, respectively. Their large interatomic distances result in up and down buckling of the atoms about a honey-comb lattice. Unlike carbon, group IVA silicon, germanium or stannum do not have allotropic layered structures that can be exfoliated into monolayers [17]. Their freestanding 2D layers are not very stable, as their 3D cluster formation is more favoured. To date, 2D nanosheets of silicene, germanene and stanene have been grown only on certain metallic substrates while their freestanding form is yet to be realised [11, 17]. Several allotropes and compounds of group 3 (Boron) and 5A elements in the Periodic Table (phosphorous, arsenic, antimony and bismuth) have also been identified as potential members of graphene analogous materials where theoretical predictions have shown them to exhibit 2D like characteristics. However, like silicene and germanene, hexagonal boron (borophene) nanosheets are theoretically predicted to be unstable in the freestanding form and can be stabilised only by the interaction with the substrate.

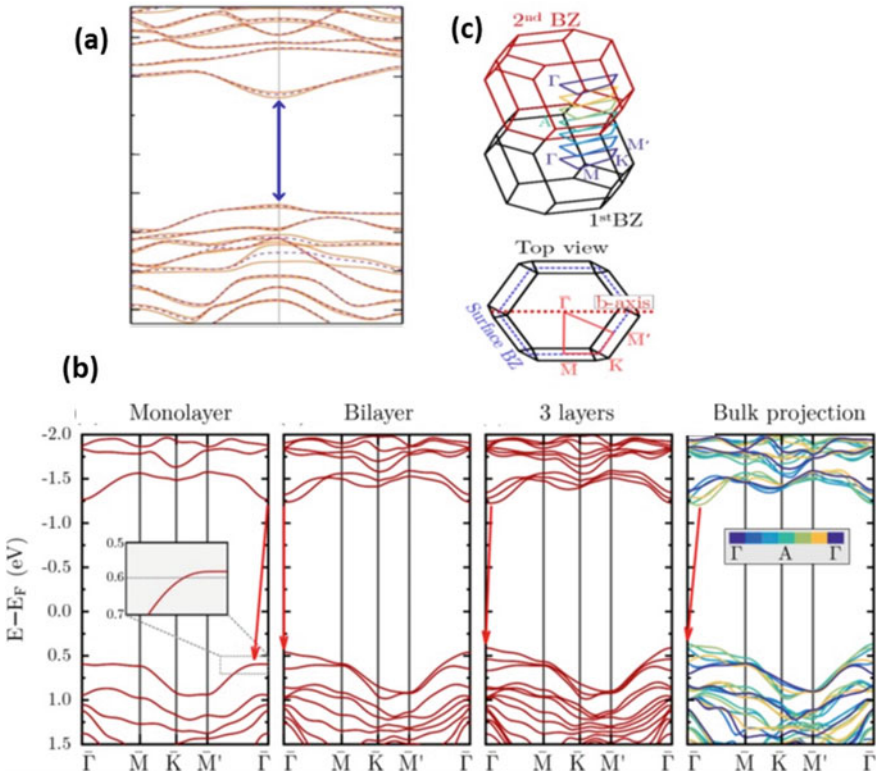

Fig. 10.6 **a** Calculated band structure showing direct band gap for bulk ReS_2 (Reproduced with permission from Springer Nature [36], **b** band structure showing indirect to direct band gap with layer thickness and c) Brillouin zone representation for band structure shown in Fig. 10.6b ("Reprinted (adapted) with permission from (Nano Lett. 2017, 17, 5187). Copyright (2018) American Chemical Society")

These elemental 2D materials possess simple composition and structure but offer a huge treasure of electronic properties. Though they all share similar buckled honeycomb like structure, they vary in their electronic structures and properties significantly. Phosphorous has a stable allotrope in the layered fashion called black phosphorous (BP), which is thermodynamically more stable than the red and white phosphorous [17]. According to various reports, Phosphorene, a 2D analogue of black phosphorous (BP), is the only elemental semiconducting 2D material with the theoretical and experimental investigations revealing the band gap to be direct for the bulk as well as monolayer and ranging from 0.36 to around 1.8 eV [11, 43, 44]. The top view of a typical monolayer phosphorene with thickness around 2.1 Å. is shown in Fig. 10.7a while the side view of the multilayers structure is shown in Fig. 10.7b. The single layer black phosphorous consists of two atomic planes with P atoms having sp^3 orbitals hybridisation and a lone pair of electrons. Due to the out of plane orbitals, the overlap between the lone pair electrons in adjacent layers leads to interlayer van

der Waals interactions [44]. This results in two kinds of P–P bonds where the shorter one connects the nearest atoms in the same plane and the longer one connects P atoms located in the top and bottom of the layer, with anisotropic bond angles caused by puckered structure. Each P atom has three equidistant (2.18 Å) nearest neighbours, two in-plane and one out of plane at bond angles of 99° and 103°, respectively. This arrangement gives rise to armchair (AC) and zig-zag (ZZ) configurations along the x and y directions, leading to highly anisotropic mechanical, electrical, optical and thermal properties within *ab* plane. For multilayers, the AB stacked layers of sp^3 hybridised phosphorous are at an interlayer distance of 5.2–5.3 Å. This relatively larger spacing, as compared with that of graphene, is due to its puckered structure as well as the AB stacking in the unit cell [17, 44]. Such large spacing makes the phosphorene layers held together by a weak van der Waal interaction (~20 meV $atom^{-1}$) and hence can be easily separated. Due to its *p*-type behaviour with large hole mobility > 1000 cm^2/Vs, its tunable band gap with near/mid-infrared region absorption and its orientation-dependent properties, phosphorene was considered as the most suitable material for nanoelectronics, photonics, optoelectronics like photovoltaic devices and LEDs, high-frequency electronics operating in multi GHz frequency range, sensing and energy storage applications [11, 44].

A few groups have carried out band structure predictions of bulk and few layer phosphorenes using the first-principle calculations, where at Γ point, the conduction band and the valence band consist of a mixture of s and p orbitals (p_z component) [44, 45]. This is different from graphene whose bands are solely composed of p_z orbitals. Cai et al. have carried out systematic band structure calculations for bulk BP as well as for layer thickness varying from 5 layers to 1 layer. The former along with the corresponding Brillouin zone representation is shown in Fig. 10.8a and b, respectively, and the latter is shown in Fig. 8c [45]. The variation of band gap is plotted as a function of number of layers in Fig. 8d.

The disadvantage with phosphorene is that the mono or few layer thick phosphorene is highly reactive and hence degrades within a few hours in air. Very recently,

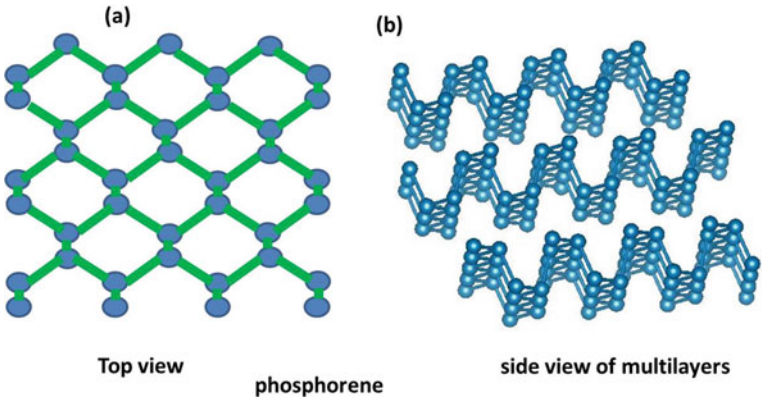

Fig. 10.7 **a** Top view of monolayer phosphorene and **b** side view of multilayer phosphorene

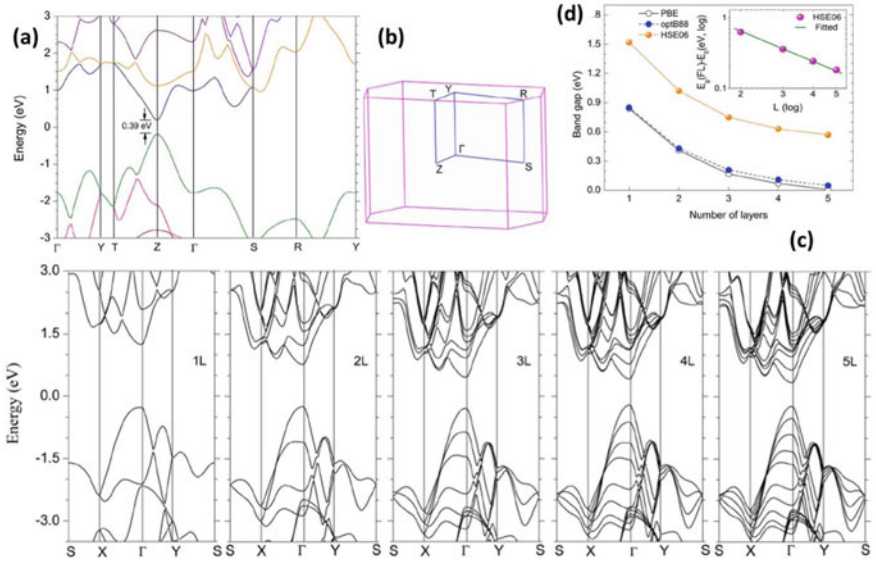

Fig. 10.8 Electronic band structure calculations of black phosphorous **a** bulk, **b** corresponding Brillouin zone, **c** for different layer thickness from monolayer (1L) to 5 layers (5L), **d** Variation of band gap with layer thickness. Reproduced with permission from Springer Nature [45]

arsenene and antimonene are the two new members of group VA elements with indirect band gaps, joining the 2D family. They were predicted to show a buckling structure different from that of phosphorene. With reducing thickness up to monolayer, their band gap was expected to be opening up to 2.49 and 2.28 eV, respectively, for As and Sb. In contrast to phosphorene, antimonene was recently predicted to exhibit good stability in air [46, 47]. The top view of a monolayer antimonene and the side view of the multilayer antimonene stacking are shown in Fig. 10.9. Theoretical calculations have shown that antimonene can transform from semi-metal in the bulk form to a topological insulator when the number of layers is below 22 and

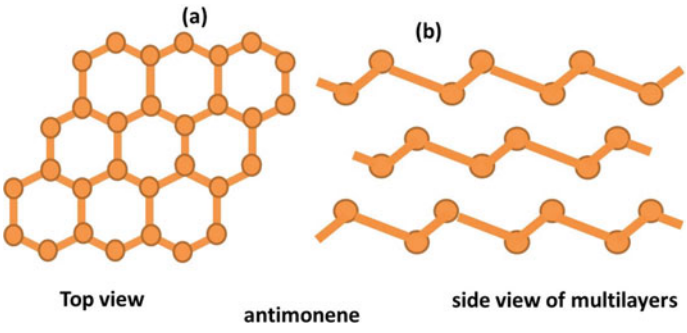

Fig. 10.9 **a** Top view and **b** side view of multilayers of antimonene

becomes semiconducting with an indirect band gap of 2.28 eV, exhibiting high hole and electron mobilities, when thinned down to one atomic layer [48]. Though reports on theoretical predictions are multiplying very fast, experimental studies on the same are still scarce.

All 2D monoelemental materials are buckled/puckered except graphene enabling the applied electric field perpendicular to the surface to produce a potential difference on lattice sites above and below the plane. Therefore, the applied electric field can act as a parameter to tune the electronic structure of these 2D materials [11]. The interest in theoretically predicting 2D form of different materials was also recently extended to group 6 elements (S, Se, Te) of the Periodic Table, named as selenene for Se and tellurene for Te. The studies on these materials are in infancy and mostly at theoretical stage.

10.2.4 MXenes

Apart from the above-mentioned layered materials, transition metal carbides/carbonitrides/nitrides of the form of the MXenes (first reported by Gogotsi's group), where M is a transition metal (Ti, V, Cr, Nb etc.) and X is carbon or nitrogen, are emerging to gain primary importance [4, 17, 49–53]. They are of the form $M_{n+1}X_n$ derived from $M_{n+1}AX_n$ precursors where A refers to mostly group IIIA or IVA elements (Al, Si, Sn, In etc.), and n = 1, 2 or 3 (Fig. 10.10) MAX precursors basically possess hexagonally close-packed strongly bonded MX layers held together by weakly bonded A layers. MAX phase cannot be exfoliated into layers due to chemical bonding by A layer. But upon etching with hydrofluoric acid (HF), A layers are etched away as they are highly reactive, leaving behind the MXene layers. Structures of some of the MXenes are shown in Fig. 10.10 b–d. During this synthesis, functional groups like -OH, -F or -O get attached to MXene layers (Fig. 10.10e) which would be influencing their physical and chemical properties. Due to their excellent structural stability, flexibility and high electrical conductivity, they are useful for many applications like supercapacitors, Lithium-ion batteries, oxygen evolution reaction, electromagnetic interference shielding, transparent conductive coatings, etc. MXenes nanosheets are reported to be highly useful for applications in water purification with a water permeance of around 1000 Lm^{-2} h^{-1} bar^{-1}, much higher than that for most of the membranes studied under 90% rejection rate [50].

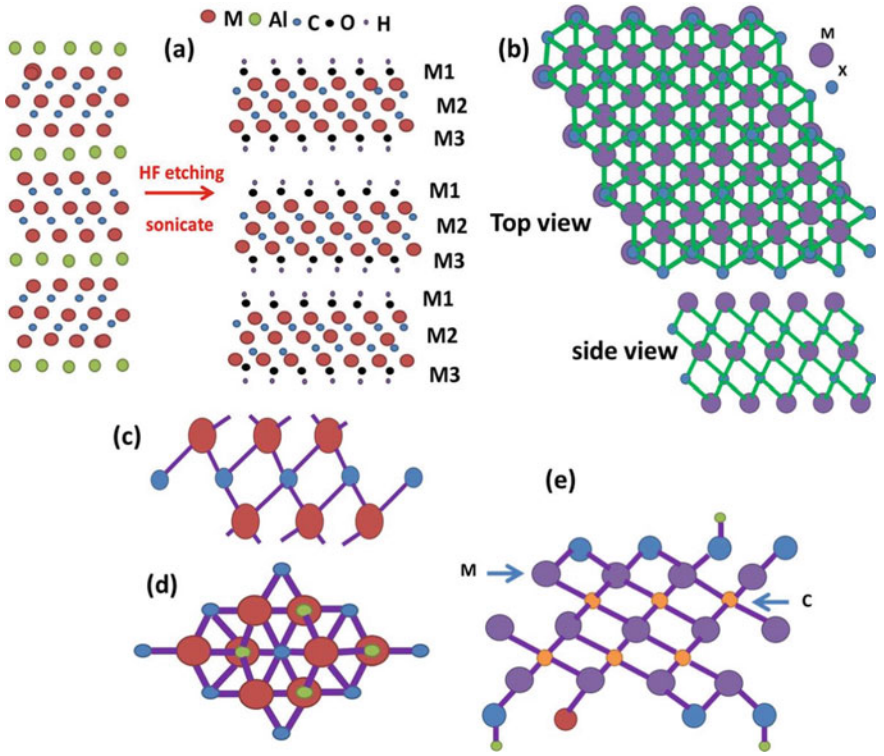

Fig. 10.10 **a** Schematic showing formation of MXene layers from MAX precursors, **b**–**d** structures of some of the MXenes, **e** Structure of MXene with surface termination groups

10.3 Synthetic Routes to 2D Layers

The process of thinning down of the bulk materials to a few/multi layers is called exfoliation. The main reason to exfoliate these layered solids into thinner sheets is to increase the accessible surface area. For surface-active and catalytic materials as well as for devices depending on the reactivity at the surface, like gas sensing, such exfoliation assures an increase in efficiency. Additionally, the strong layer thickness-dependent electronic properties emphasise the necessity for developing strategies to produce reliable and high-quality ultrathin sheets of these 2D materials from their bulk counterpart. The success of exfoliation is gauged by the layer thickness, lateral dimensions, size dispersity, crystal quality, etc. The synthesis of 2D nanosheets is mainly based on two major approaches, namely, top-down and bottom-up strategies. The nanosheets are exfoliated from the 3D bulk by mechanical or chemical methods in the former. In the latter case, they are prepared starting from the basic building blocks which upon chemical reactions complete the formation of covalently linked large area 2D sheets. Some of the commonly methods relevant to bottom-up approach

are chemical vapour deposition (CVD), pulsed laser deposition (PLD), sputtering method, atomic layer deposition (ALD), physical vapour deposition (PVD), etc. In this chapter, we will be reviewing the different exfoliation routes in the top-down approach for the production of nanosheets of the layered materials.

10.3.1 Top-Down Approach

Over the decade, many methods have been attempted to exfoliate thin layers down up to monolayer thickness, from bulk layered solids. Such exfoliation resulted in high aspect ratio flakes with large surface area, enough to process them for device applications and other surface-related activities.

10.3.1.1 Mechanical Exfoliation

Scotch Tape-Based Mechanical Exfoliation

Mechanical exfoliation of graphene from graphite using scotch tape, that was the first one to be attempted, has allowed the production of flakes in which many novel properties were discovered [2, 3, 54]. The success observed in graphene has allowed this method to continue to be the primary route for producing ultra-thin flakes. Due to the strong in-plane and weak out of plane bonding, layered materials can be sheared parallel or expanded normal to the in-plane direction. This can overcome the van der Waals forces and result in a process called exfoliation, producing nanometer or even atomically thin sheets or nanosheets. Figure 10.11 illustrates the various steps involved in the mechanical cleavage method using adhesive tape. In mechanical exfoliation, the competition between the intersheet van der Waals forces in a layered solid and that between the substrate and the outermost sheet plays a crucial role in efficient thinning of the solids [54]. Typically, a well-cleaned SiO_2/Si substrate is used for transferring the flakes. The adhesive tape is contacted with the bulk crystal and then removed such that multi-layered flakes are transferred onto the tape. During the few times repetitive process of contacting the flake loaded tape with fresh tape, the flake thickness reduces with each contact. After considerable thinning of the flakes, the adhesive tape is brought in contact with the substrate and peeled off, leaving the high quality ultra-thin single-crystal flakes on the substrate, suitable for fundamental studies. Many materials like MoS_2, ReS_2, WSe_2, TaS_2, $TaSe_2$, BP etc. have been successfully exfoliated into thin sheets using this method and have been employed for developing FETs, phototransistors etc. [35, 37, 56–61]. One main disadvantage of this method is that it leaves contaminants from the adhesive tape. Some studies have introduced an additional step where the substrates with flakes are dipped in acetone for about 5 min, in order to remove the residues of the tape [61].

Some studies have reported the use of polydimethylsiloxane (PDMS) stamps to transfer flake onto the substrate instead of the adhesive tape, in order to avoid the

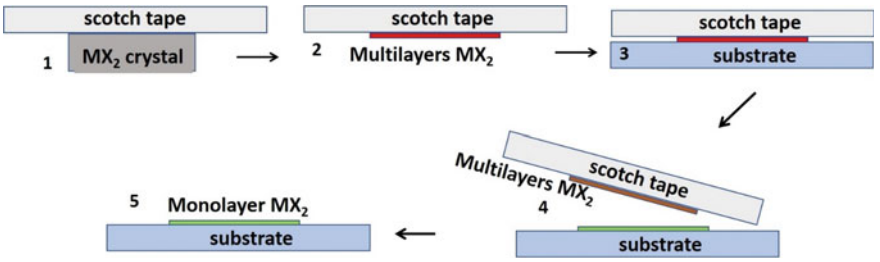

Fig. 10.11 Schematic of the steps involved in mechanical exfoliation

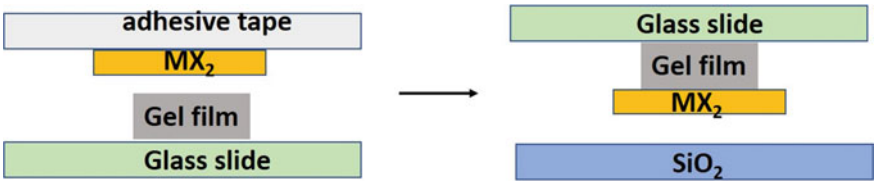

Fig. 10.12 Schematic of steps involved in gel mediated mechanical exfoliation

contaminants from the adhesive tape [62]. Another study has used a gel film as an intermediate step in mechanical exfoliation [63]. Here, they have fixed a gel film on a glass slide, carefully removing the air trapped between the two. They have then brought the tape with exfoliated flake in contact with the gel film such that the flakes are transferred onto the latter. The gel film with the flakes is now pressed against the SiO_2/Si substrate such that the flakes are available on the SiO_2 substrate. They have claimed that with this method, they have obtained large area flakes, free of contaminants from adhesives, better than that with the scotch tape. A schematic depicting this procedure is shown in Fig. 10.12.

Metal-Assisted Mechanical Exfoliation

A useful modification in mechanical exfoliation is metal-assisted exfoliation, especially Au facilitated mechanical cleavage from the bulk, which has been attempted by some groups [64, 65]. This method has reportedly brought about improvement, producing large size flakes. A schematic showing the various steps mentioned above is shown in Fig. 10.13.

Javey group has deposited gold film of thickness about 100–150 nm on bulk MX_2 crystals. Due to the strong bonding occurring between gold and the chalcogen atom in the top-most layer, much stronger than the van der Waals forces existing between the layers, this layer was selectively cleaved using a thermal tape, which was later brought into contact with the SiO_2/Si substrate. The tape was then removed by heating the substrate at about 130ºC and the residues further cleaned by exposing

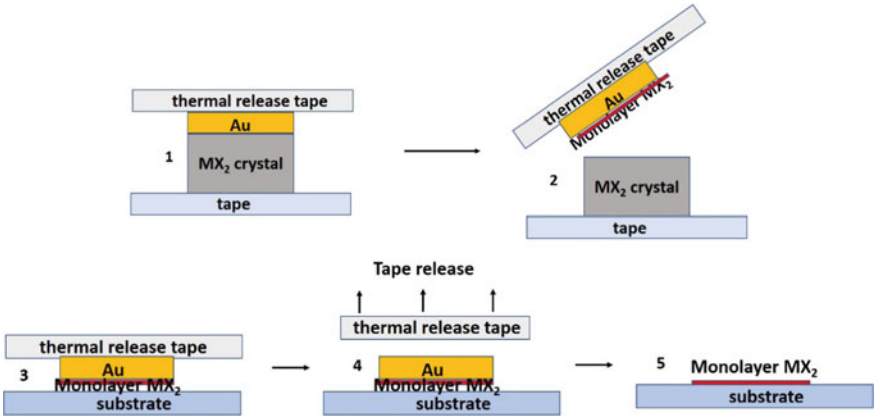

Fig. 10.13 Schematic of various steps involved in Au-mediated mechanical exfoliation

the substrate to mild O_2 plasma, taking care not to etch away the gold. The gold film is later etched using KI/I_2 wet etch, which does not affect the flakes underneath. After further cleaning with acetone and isopropyl alcohol, large area flakes are obtained for further processing for device applications. Another study has reported a similar procedure using nickel and copper-assisted exfoliation in the place of gold film [64].

Ottaviano et al. have recently modelled the mechanical exfoliation by the scotch tape peeling off process as random vertical exfoliation and lateral fragmentation phenomena and demonstrated a relation between the number of iterations in the scotch tape peeling and the layer thickness transferred on the substrates. They have taken into account the layer–layer interaction (which is always the same) and the layer–tape interaction (which is different from layer–layer interaction) in their modelling. They report that the occurrence of monolayers becomes most probable by the second peeling itself. They also mentioned that by increasing the number of iterations, the lateral dimension decreases drastically [57].

One of the disadvantages of the mechanical exfoliation is that it suffers from difficulties in reproducibility since the quality of flakes produced is subject to human skills thereby resulting in random errors at every step [66]. It also does not allow systematic control over the layer thickness and size. Most importantly, for practical applications of these materials to act as active materials for displays, solar cells, energy storage and water splitting applications etc., large-scale production of 2D nanosheets is required. The yield of 2D materials by mechanical exfoliation is very low making it unsuitable for large-scale production and hence for the above-mentioned applications [4, 12, 66].

10.3.1.2 Liquid Phase Exfoliation (LPE)

Liquid phase exfoliation of layered materials, where the bulk layered solids are exfoliated in liquids mostly under ultrasonication, is a highly promising route for large-scale production of 2D nanosheets. LPE basically involves three steps—(1) dispersion of the bulk material in a liquid medium, (2) exfoliation of the nanosheets by the use of ultrasonic waves and (3) purification and isolation of the exfoliated sheets. LPE method permits hybrids and composites by simple mixing of the dispersions of the two materials [52, 67, 68]. Large area thin films can also be formed by coating the resultant dispersions by spray coating, inkjet or screen printing, spin coating, doctor blading, etc.

Ultrasonic Waves

To overcome the van der Waals forces or electrostatic interactions binding the layers in 2D solids, a sufficiently large input energy is necessary, which is provided by ultrasound waves [7, 69–73]. Ultrasound is basically the sound wave transmitted through any material (solid, liquid or gas) possessing elastic properties. As the acoustic wavelengths are much longer than the molecular dimensions, no direct interaction takes place between the sound waves and the chemical species in the liquid. When ultrasound of frequency above 20 kHz is transmitted through a liquid, they produce alternating high- and low-pressure cycles, depending on the frequency. During the low-pressure cycle, high-intensity small vacuum bubbles are created, which oscillate with the alternating pressure cycle. Such oscillating bubbles can accumulate ultrasonic energy, thereby growing to a certain size (typically tens of μm) by rectified diffusion and coalescence. As they grow beyond a certain size, they collapse during a high pressure cycle, subsequently releasing the concentrated energy stored in the bubble within a very short time (with a heating and cooling rate of $> 10^{10}$ Ks^{-1}). This process is called cavitation. A schematic of the process of bubble formation, their growth and implosion are shown in Fig. 10.14.

This implosion creates a high temperature and high pressure of about 5000 K and 1000 bar locally along with a high-speed liquid jet. During implosion, the speed of the bubbles' wall exceeds that of the sound in the gaseous interior, thereby creating shock waves with shear and normal force. These forces overcome the attractive interactions taking place between the layers, thereby resulting in breaking of the bulk into fine particles and to efficient delamination of the nanosheets. The defects produced either in the edge or in the basal planes during prolonged exposure to ultrasound result in providing surface polarity to the nanosheets, thereby improving the dispersibility of the same in the liquids. The schematic showing the delamination of the layered material into nanosheets due to the shear and compressive forces produced by the shock waves is shown in Fig. 10.15.

Ultrasound sonication can be performed using a variety of designs, such as bath sonicators, direct immersion ultrasonic horns and flow reactors. The delamination

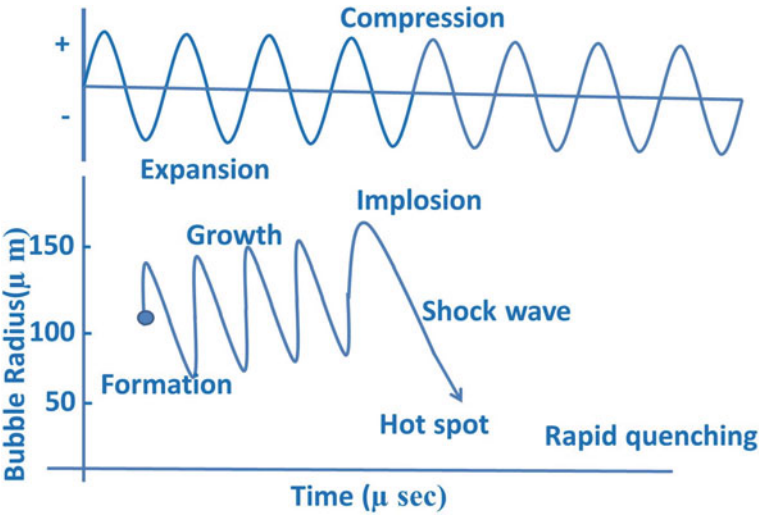

Fig. 10.14 Schematic representation of transient acoustic cavitation

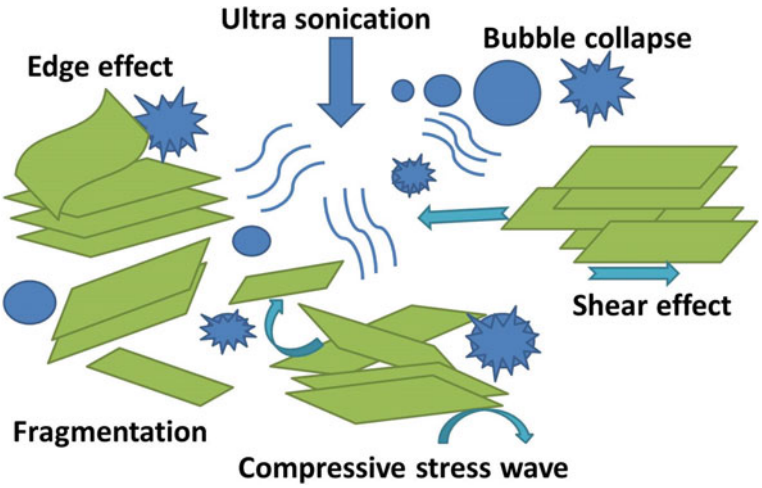

Fig. 10.15 Schematic showing the cavitation induced exfoliation of flakes

efficiency depends on the solvent density, pressure, sonication probe shape, ultrasound frequency, etc. Increasing the density and or the pressure of the solvent is said to increase the cavitation threshold. Cavitation occurs under the frequency range of tens of Hz to tens of MHz. Beyond this frequency range, intrinsic viscosity of the liquids prevents the occurrence of cavitation. Under ultrasonic exfoliation, flakes of size ranging from 50 nm to about 10 μm can be produced. Increasing the ultrasonic time was found to enhance the yields of exfoliated sheets, though increasing time would

cause more defects and reduce the lateral dimensions of the flakes. Coupling ultrasonication with magnetic stirring was observed to expedite exfoliation in graphene, resulting in a yield of around 95% [4].

LPE Using Organic Solvents

There are various ways to carry out LPE involving oxidation, surface passivation by solvents and use of intercalation compounds. One of the methods applied much earlier was to oxidise the layered crystals and then disperse them in suitable solvents. For example, graphene was exfoliated from graphite by ultrasonication using Brodie's, Staudenmaier's or Hummer's method [7, 73]. Here, graphite was treated with sulphuric acid and potassium permanganate resulting in addition of hydroxyl and epoxy groups. This caused graphene sheets to turn hydrophilic allowing easy intercalation of water, leading to well-exfoliated graphene oxide layers and stabilised against reaggregation due to the negative surface charge, yielding a concentration up to 1 mg/ml. But this procedure disrupts the electronic structure of graphene where the graphene oxide (GO) produced exhibited loss of conductivity. The functional groups were then removed by reducing the GO to produce the reduced graphene oxide (RGO). The disadvantage of this method is that a large number of holes and sp^3 defects are produced during the oxidation and the removal of functional groups. Additionally, interfering heteroatomic species like S and metal-containing impurities like K, Mn etc. can get covalently attached to the nanosheets altering their properties [4, 68].

Ultrasonic-based exfoliation can also be carried out by using appropriate solvents where the bulk material is dispersed in a suitable solvent. The basic requirements for a solvent to be suitable are that (1) it should efficiently be able to delaminate the flakes from the bulk to the highest concentration possible and (2) it should prevent reaggregation of the exfoliated flakes and stabilise the same for the longest duration possible. Re-aggregation of the exfoliated sheets is prevented generally by solvation where a good solvent prevents this re-aggregation while a bad solvent allows the same, as shown in Fig. 10.16 [7, 12, 74].

It is a common fact that the interfacial tension between a solid and a liquid plays a crucial role in the interaction between the two. An ideal solvent will minimise the potential energy between the two adjacent layers in a solid to overcome the van der Waals forces between them and offer a balancing solid-nanosheet attractive force to stabilise the dispersion of the nanosheets in the liquid [67, 68, 74–76]. The energy required to exfoliate the layers depends on the surface energy, which is the energy per unit area required to overcome the van der Waals forces to peel off two layers apart. Coleman's group demonstrated exfoliation of graphite into graphene with concentrations up to 0.01 mg/ml using the solvent N-methyl pyrrolidone (NMP) for dispersing graphite layers. They took the cue from the fact that carbon nanotubes could be efficiently exfoliated in solvent like NMP, as demonstrated in an earlier study, brought about by the excellent interaction between the solvent and the nanotubes. Though they could also obtain success using some other solvents like N–N-dimethylacetamide

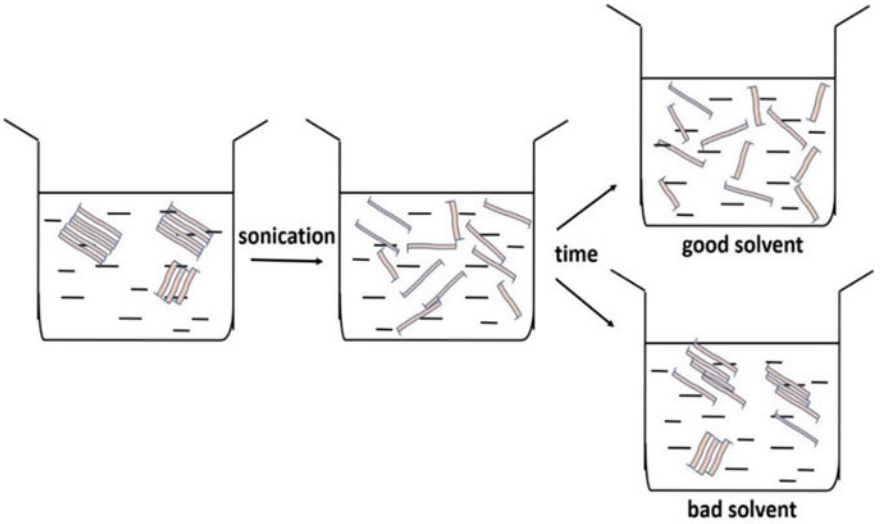

Fig. 10.16 Schematic showing liquid phase exfoliation under ultrasonication, with good and bad solvents

(DMA), γ-butyrolactone (GBL), 1,3-dimethyl-2-imidazolidinone (DMEU) etc., they concluded the best result to be with NMP. They observed that the surface energy of NMP that is around 70 mJ/m^2 was matching well with that of graphene (68 mJ/m^2). Such an observation led to the investigation of the mechanism responsible for higher efficiency of certain solvents. They suggested that the exfoliation is maximum when the net energetic cost is minimum. The detailed explanation offered by them for exfoliation of graphene is as follows [4, 74–76]:

It can be stated that the mechanism governing the exfoliation of 2D materials in liquid is based on solution thermodynamics. Assuming the entire dispersion to be a solution, the free energy of mixing (ΔG_{mix}) is given by [76]

$$\Delta G_{mix} = \Delta H_{mix} - T\Delta S_{mix} \tag{10.1}$$

where ΔH_{mix} is the enthalpy of mixing and ΔS_{mix} is the entropy of mixing. Though large ΔS_{mix} will result in negative ΔG_{mix}, favouring thorough mixing, the large size of 2D nanosheets will lead to smaller ΔS_{mix}. Alternately, by minimising the enthalpy of mixing, better dispersions can be obtained. The energy balance, expressed as the enthalpy of mixing (per unit volume), can be given by the following expression [4, 73, 75]:

$$\Delta H_{mix}/V_{mix} = 2/T_{flake}(\sqrt{E_{sur}^{G}} - \sqrt{E_{sur}^{sol}})^2\varphi \tag{10.2}$$

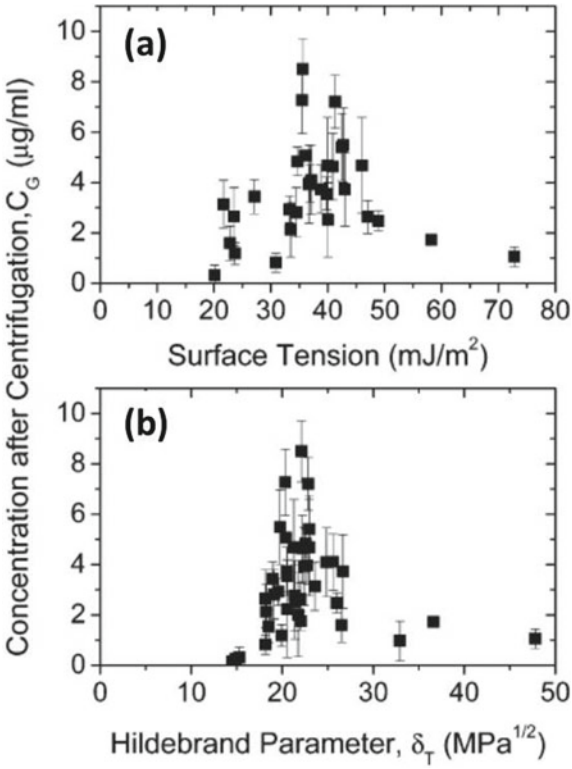

Fig. 10.17 Concentration of exfoliated graphene obtained for various solvents with **a** different surface tension and **b** Hildebrand solubility parameter ("Reprinted (adapted) with permission from Langmuir, 2010, 26(5), 3208). Copyright (2018) American Chemical Society")

where E_{sur}^{G} and E_{sur}^{sol} are the surface energy or surface tension of graphene and the solvent respectively, T_{flake} is the thickness of the graphene flake and φ is the graphene volume fraction. The surface energy is correlated to surface tension, γ, by the expression $\gamma = E_{sur}^{sol}\text{-T}\,S_{sur}^{sol}$ where S_{sur}^{sol} is the surface entropy of the solvent having a universal value of around $0.1\text{mJK}^{-1}\ \text{m}^{-2}$. Coleman group exfoliated graphene in a variety of solvents and observed that maximum yield was obtained for those with surface tension around 40–50 mJ/m^2, equivalent to surface energy of about 70 mJ/m^2 (Fig. 10.17a). This shows that the enthalpy of mixing is minimum when the surface energies of the solvent and the material are very close. Therefore, it was suggested that the lower the difference between the surface energy of the solvent and that of the layered solid, the better was the efficiency and yield of the exfoliation. But it was also pointed out that using surface tension alone could not be justified as differences in concentration of graphene for solvents with similar surface tension were also observed.

Coleman group used the solubility theory, where the solubility of a molecular solute is said to closely depend on its cohesive energy density $E_{C,T}/V$. Here, $E_{C,T}$ is the total molar cohesive energy and V is the molar volume of the solvent. The Hildebrand solubility parameter, δ_T, which is the square root of cohesive energy density, $\sqrt{E_{C,T}/V}$, was also used for solvent screening (Fig. 10.17b). Again, different solvents with

similar Hildebrand solubility parameters were observed to yield different efficiency of exfoliation.

It was realised later that considering only the surface energy factor was not sufficient and that the use of Hildebrand solubility parameter to screen the solvents was only a weak approximation as this parameter was mainly valid for non-polar solvents. In order to widen the range of solvents including the polar solvents, the criterion was further widened. It is well known that in a solvent–solute system, the intermolecular interaction can be divided into three components of the cohesive energy—polar (P), dispersive (D) and hydrogen bonding (H) components. The square root of each of these components is a Hansesn's solubility parameter, δ_i. The expression relating the three components with δ_T is as given below [4, 74, 76]:

$$\delta_T^2 = \delta_D^2 + \delta_P^2 + \delta_H^2 \tag{10.3}$$

Hansen has suggested the enthalpy of mixing to be.

$$\frac{\Delta H_{mix}}{V} \approx [(\delta_{D,S} - \delta_{D,G})^2 + (\delta_{P,S} - \delta_{P,G})^2/4 \ + (\delta_{H,S} - \delta_{D,S})^2/4]\phi \tag{10.4}$$

where the subscripts S and G represent the solvent and graphene, respectively. This expression now indicates that for maximum dispersion of the solute in the solvent, all the three solubility parameters of the solvent have to be close to those of the solute.

It was reported that graphene was exfoliated more efficiently in NMP than in pyridine though the latter had closer Hansen's solubility parameters. The above expressions are generalised for a solvent and a molecular solute while graphene is a layered nanomaterial. For such materials, interaction with the solvent takes place at well-defined surfaces. Because of this reason, the use of surface energy-based Hansen like solubility parameters would be more appropriate, considering surface energy also to be divided into polar, dispersive and hydrogen bonding components. However, such solubility parameters are available only for very few solvents while Hansen's solubility parameters are available for more than 1000 solvents. Surface tension components of the mixtures are not accessible even if those of the individual solvents are available. Estimating precisely the surface tension of the 2D layers is a difficult task. Because of these reasons, the screening of the solvents is carried out using the latter, where the concentration of graphene sheets is plotted as a function of δ_D, δ_P, and δ_H as shown in Fig. 10.18.

As per the second criterion for a good solvent, high dispersions for a long duration should be obtained, preventing re-aggregation. This necessitates the wetting of the exfoliated layers by the solvent, by causing surface modification if necessary, thereby blocking the process of re-aggregation. Spontaneous wetting of the solvent on the solid surface (2D layer) occurs when the spreading coefficient $S_{SOL/2D}$ is positive [4]. The spreading coefficient is given by the expression as shown below:

$$S_{SOL/2D} = \gamma_{2D} - \gamma_{SOL} - \gamma_{2D/SOL} > 0 \tag{10.5}$$

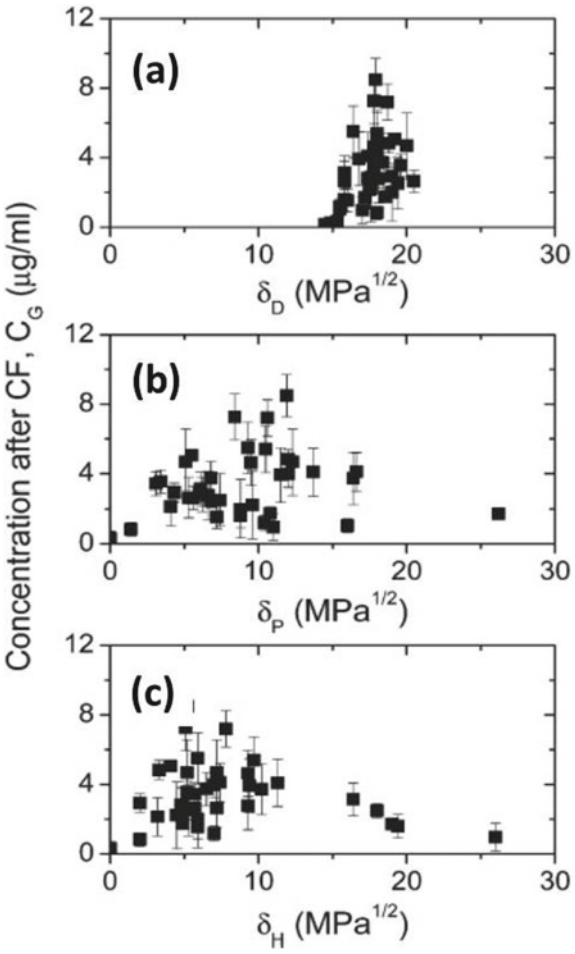

Fig. 10.18 Concentrations of exfoliated graphene (dispersibility) tested for various solvents as functions of Hansen solubility parameter for **a** dispersive, **b** polar and **c** hydrogen bonding components. ("Reprinted (adapted) with permission from (Langmuir, 2010, 26(5), 3208). Copyright (2018) American Chemical Society")

where γ_{SOL} is the surface energy of the solvent, γ_{2D} is the surface energy of the 2D material and $\gamma_{2D/SOL}$ is the solvent/2D layer interfacial energy. The above expression can be rearranged as follows:

$$\gamma_{2D} > \gamma_{SOL} + \gamma_{2D/SOL} \tag{10.6}$$

Texter proposed that the best solvent that would maintain the dispersions by wetting thoroughly would satisfy this inequality. The extent of wetting of the solvent on the layer surface can be estimated using the Young's equation given by.

$$\gamma_{2D/SOL} = \gamma_{2D} - \gamma_{SOL}\cos(\theta) \tag{10.7}$$

where θ is the contact angle that the solvent makes at the solid surface and which can be measured. γ_{SOL} can be available from the literature and since γ_{2D} will remain the same irrespective of the solvent used, the interfacial energy and hence the wettability of the solvent can be estimated from the measured contact angle. It has to be noted that for a given 2D layer, the term $\gamma_{2D/SOL}$ is not tunable. Recently, Ajayan group proposed a universal method to identify good solvents for all 2D materials like graphene, MoS_2, WS_2, h-BN, $MoSe_2$, TaS_2, SnS_2, etc. based on surface tension components [68]. They obtained precise surface tension components of more than 40 solvents by detecting minute tension changes using commercial equipment. They determined the polar and dispersive components of the surface tension for each solvent. Since determining the absolute value of the surface tension of 2D materials is difficult, they obtained the ratio of the polar and dispersive components by combining OWRK (Owen Wendt, Rabel and Kaelble) theory with Young's equation—0.471 for graphene, 0.563 for WS_2, 0.449 for MoS_2 and 0.450 for h-BN. They also noticed that apart from exfoliation, surface tension also had a role in the dispersibility. By plotting the dispersibility with surface tension components ratio, a strong correlation between the dispersibility and the ratio of the components was observed, with the dispersibility peaking when the ratio matches with that of the 2D materials (Fig. 10.19). For example, the polar/dispersive component ratios of the best solvents for exfoliation of graphene and WS_2 were found to be around 0.48 and 0.52, respectively, which are close to the values 0.471 and 0.563 for graphene and WS_2, respectively.

The concentrations obtained using these methods were found to be very low with the flakes existing as mostly multilayer stacks and only with few monolayer sheets, thereby requiring large improvement in the same. A simple explanation for low concentration could be that the solvent radicals get attached to the basal plane of the nanosheets and become a nucleation site for other solvent molecules, thereby stabilising the flakes in the dispersion [4]. Coleman group attempted to increase in sonication time and obtained improvement in the concentration of the graphene flakes from 0.05 mg/ml to around 1 mg/ml. They had observed that the concentration scaled well with square root of the sonication time (Fig. 10.20). Unfortunately, the flake dimensions were also found to reduce with increasing sonication time as $t^{-1/2}$, probably due to sonication induced scission, along with generation of new defects [75, 77].

They also attempted size selected exfoliation of graphene by conducting controlled centrifugation [78]. Here, they successively reduced the centrifugation speed from 4000 to 500 rpm in various steps. Between each step, they removed the supernatant and added NMP to the sediment to proceed with the centrifugation. They observed that the flake length at higher centrifugation speed is much smaller than that at lower speed. They did another study on the yield of MoS_2 where they varied the initial mass and the starting concentrations of the same ranging from 5 to 200 mg/mL in NMP [79]. They observed the dispersion concentrations to scale linearly with the starting concentration. Their sonication time-dependent yield measurements revealed that after 23 h sonication, the concentration was about 3.2 mg/mL, which increased to 40 mg/mL after 140 h sonication. They also carried out controlled centrifugation measurements, similar to that carried out for graphene in their previous study. Though

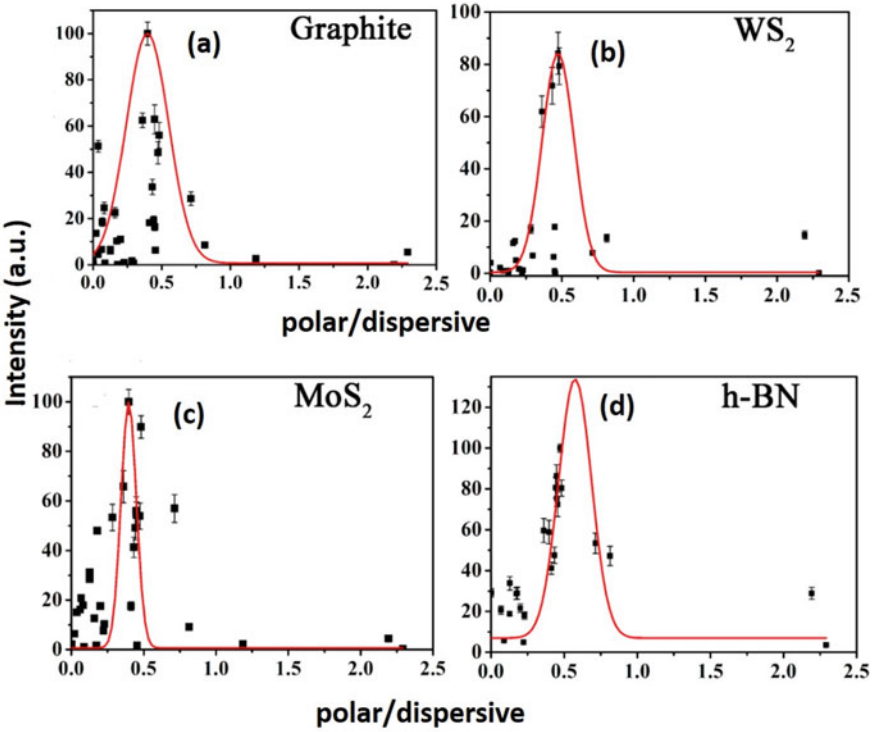

Fig. 10.19 Dispersion for **a** graphene, **b** WS_2, **c** MoS_2 and **d** h-BN. ("Reprinted (adapted) with permission from (Nano Lett. 2015, 15, 5449). Copyright (2018) American Chemical Society")

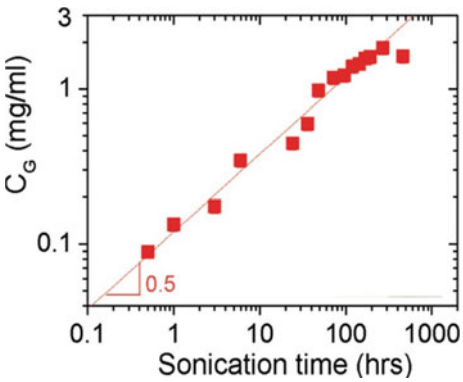

Fig. 10.20 Concentration of exfoliated and dispersed graphene sheets in NMP solvent, as a function of sonication time—("Reprinted (adapted) with permission from (Accounts of Chemical Research, 2013, 46, 14). Copyright (2018) American Chemical Society")

the reduction in the flake size with sonication time showed a similar relationship as observed for graphene, concentration of the dispersion did not show a dependency on square root of sonication time, as observed for graphene. This suggests that the exfoliating kinetics to be varying for different materials. They made an attempt to explain the variation of flake thickness with its size as follows: At high concentrations, large flake size will have a relatively small volume of the solvent, which could be driving aggregation phenomenon such that the volume of the solvent per flake increases to an appropriate level. Similar observations were also made for carbon nanotubes [80, 81]. A relationship between the dispersed concentration and the mean flake dimensions was suggested as below [79]:

$$C \infty < w >< t > / < L >^2 \tag{10.8}$$

where L is the length, w is the width and t is the thickness. This suggested that at high concentrations, large-sized flake should become thicker than those dispersed with lower concentrations. By lowering the concentration, though the flakes had become marginally thinner, they had also become smaller in size. Hence such a direct correlation could not be proved. Qiao et al. have investigated the effect of varying the ultrasonic power on the yield of exfoliation of MoS_2 in NMP solvent [77]. A monotonic increase in concentrations of the flakes with ultrasonic power was not observed. Rather, the maximum concentration was found at an optimum value of 320 W, which decreased with further increase in the power. The size of MoS_2 flakes was around 300 nm with narrow size distribution.

Experimental results on exfoliation studies as well as from inverse gas chromatography measurements reveal the surface energy of h-BN, MoS_2, WS_2 and $MoSe_2$ to be in the range 65–75 mJ/m^2, which is similar to that of graphene (65–120 mJ/m^2). This suggests that inorganic layered compounds can also be exfoliated through liquid phase method [12]. Shen et al. have made efforts to identify best solvents for exfoliation of MoS_2, WS_2, $MoSe_2$ etc. [68]. Lee et al. have reported a yield of 0.3 mg/mL of MoS_2 nanosheets of thickness in the range 3–17 nm with the lateral dimensions around 1 μm, when exfoliated in N-vinyl-2-pyrrolidone using probe sonication [82]. Bourlinos and his group used electron-withdrawing fluorine group-based compounds as organic solvent and demonstrated successful exfoliation. They proposed that apart from surface energy, donor–acceptor interaction between the solvent and the layered material also could be influencing the exfoliation [83]. Hanlon et al. have exfoliated black phosphorous (BP) in the solvent N-cyclohexyl-2-pyrrolidone (CHP) and in NMP, even in ambient conditions [84]. They have claimed size-selective exfoliation through controlled centrifugation. For exfoliating BP, apart from the criteria mentioned earlier for other 2D materials, the solvent must also form a solvation shell acting as a barrier to oxygen and water. Kang et al. investigated structural stability of BP flakes after exfoliation in NMP and concluded that this solvent enhances stability towards ambient conditions [85]. They compared exfoliation yield of BP in different solvents like NMP, acetone, chloroform, hexane, isopropyl alcohol and dimethylformamide (DMF). Among these, they obtained the highest yield with NMP solvent.

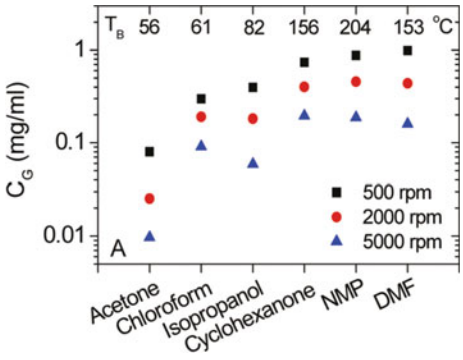

Fig. 10.21 Concentrations of exfoliated graphene for different solvents and centrifugation rate (Reprinted (adapted) with permission from (J. Phys. Chem. C, 2011, 115, 5422). Copyright (2018) American Chemical Society")

Ren et al. also exfoliated BP flakes in NMP and the yield was good enough that they could coat a film of these flakes on ITO (indium tin oxide) and demonstrate a three-electrode photoelectrochemical cell [86]. Best performance in exfoliation of BP in terms of yield for various solvents was reported in the order formamide > dimethylsulfoxide (DMSO) > DMF, NMP, IPA > ethanol, methanol > acetone > tetrahydrofuran (THF), water [66, 85].

Some studies mention that liquid exfoliation of ReS_2 in organic solvents is scarcely attempted as there are not many solvents, which have matching surface energy for this 2D material [37].

Liquid phase exfoliation was modified by changing the liquid from the high boiling point solvents like NMP, DMF etc. to the low boiling point solvents like methanol, ethanol, isopropyl alcohol, acetone, etc. This was because (1) solvents like NMP were toxic and could pose safety issues and (2) as they are high boiling point, they did not evaporate easily, thus remaining on the surface of the exfoliated flakes and hindering the use of these flakes in practical applications [51]. Coleman group has also demonstrated exfoliation of graphene in low-boiling point solvents like chloroform, isopropanol, acetone along with cyclohexanone, NMP and DMF. Concentrations of graphene for various solvents under different centrifugation rates are shown in Fig. 10.21 [87].

The study showed that they could exfoliate in isopropanol and chloroform to a concentration of 0.5, 0.2 and 0.07 mg/ml at centrifugation rates of 500, 2000 and 5000 rpm, respectively. Acetone showed poorer results with yield of 0.08, 0.025 and 0.01 mg/ml for 500, 2000 and 5000 rpm, respectively. They obtained these results at a sonication time of around 30 min only. They also observed that these dispersions remained stable up to about 80% even after 100 h. The average size of the flakes was around 1×0.35 μm and about 10 layers. Choi et al. could exfoliate graphene in a volatile solvent, propanol, to a concentration of about 1 mg/mL [88]. The advantage of using these volatile solvents is that they can become ready for use in device applications without the solvent sticking on them as well as prevention of restacking of the flakes when deposited on a substrate, ensured by the fast evaporation of the solvents.

LPE Using Cosolvent Method

Due to the disadvantages of using high-boiling point solvents and that of the low boiling point poor solvents, Zhou et al. arrived at an improvement in LPE using cosolvency method where they have used a mixture of two poor solvents in which the nanosheets exhibit poor exfoliations individually [89]. As discussed before, the dispersibility of a material in a liquid is predicted by Hansen's solubility parameters (HSP). Though they are mostly employed for single solvents, Zhou et al. have extended these HSP parameters to a mixture of solvents in which each of the three HSP parameters for a solvent mixture is a linear function of composition as given below:

$$\delta_{blend} = \Sigma \phi_{n,comp} \delta_{n,comp} \tag{10.9}$$

where ϕ is the volume fraction for each composition. Using this expression, in combination with Eq. 10.4, the solubility of various nanolayered materials in different solvent mixtures can be estimated, thereby allowing the engineering of an ideal solvent mixture for each 2D material. Zhou et al. have employed alcohol and water mixture to exfoliate different graphene analogous systems like MoS_2, WS_2 and BN. They have investigated the efficiency of exfoliation of each of these materials by varying the volume fractions of ethanol in water where the HSP of water are—δ_D 15.5 $MPa^{1/2}$, δ_P 16 $MPa^{1/2}$and δ_H 42.3 $MPa^{1/2}$ and that of ethanol are—δ_D 15.8 $MPa^{1/2}$, δ_P 8.8 $MPa^{1/2}$and δ_H 19.4 $MPa^{1/2}$. The photograph below shows that high concentrations of dispersed flakes are obtained for MoS_2 at 45%, WS_2 at 35% and BN at 55% (Fig. 10.22). The major advantages in using these liquids are that they are of low cost, easily volatile so that they do not hinder the fabrication and performance of the devices and are toxic free. Though the concentrations of 0.032 and 0.018 mg/mL obtained for WS_2 and MoS_2, respectively, were much lower than that reported by Coleman using high-boiling point solvents, these results provided positive indications that such unharmful and low-cost methods can be used for exfoliations.

Halim et al. have shown successful exfoliation of graphene and MoS_2 in different alcohols and water mixture with weight fraction of alcohols varying from 0 to 100% of each of them [90]. They observed maximum exfoliation occurring for IPA was at around 30% in water. They have attempted to explain the mechanism behind such cosolvent-based exfoliation in their study. They have suggested that the alcohol molecules in the mixture behave similar to surfactant molecules due to their tendency to aggregate in water. While they mix macroscopically well with water, they tend to microscopically form aggregates to hide their hydrophobic groups. This aggregate formation is similar to micelle formation in surfactants varying only with the degree of hydrophobicity. While the highly hydrophobic surfactants mostly have around 1% critical micelle concentrations, alcohols require a much higher concentration with weight percentage around multiples of 10 to form their aggregates. In the case of tetra-butyl alcohol, these aggregations were found to vary with the concentration and their size could be as large as around 40 Å. These aggregates are highly mobile

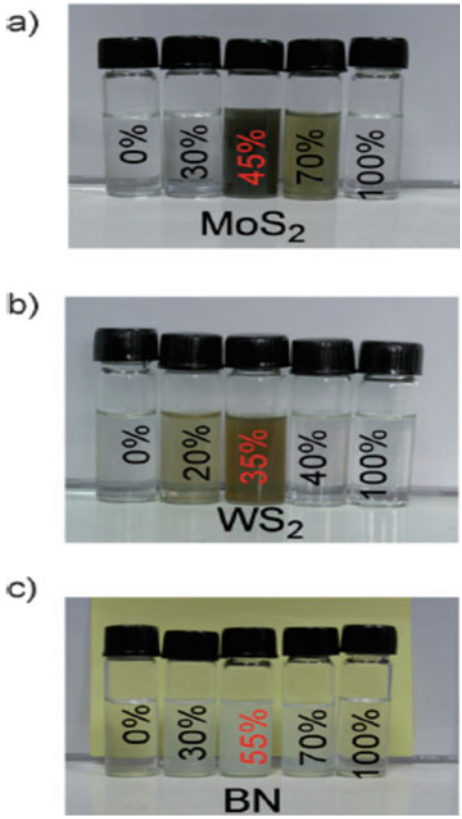

Fig. 10.22 Photograph showing various concentrations of dispersed flakes at different combinations of ethanol/water mixtures for **a** MoS_2, **b** WS_2 and c) BN (Zhou, K. G.; Mao, N. N.; Wang, H.X.; Peng, Y. and Zhang, H. L. A Mixed-Solvent Strategy for Efficient Exfoliation of Inorganic Graphene Analogues. Angew. Chem. Int. Ed. 2011. 50.10839. Copyright Wiley–VCH Verlag GmBH & Co. KGaA. Reproduced with permission)

and they fluctuate. As most of the nanoflakes are hydrophobic, the non-polar ($-CH_3$) groups interact with the surface of the nanoflakes while the polar (-OH) groups point out and interact with water thereby solvating the entire system. The optimum weight fraction of alcohol arises due to the fact that with increase in the same, the competition between aggregate formation and dispersion of flakes occur, where the addition of too much alcohol would allow mainly aggregates formation and prevent them from settling on the layer surface. This would result in lesser exfoliation and dispersion. This could be the reason behind the observation of different critical concentrations for different alcohols, i.e., 80% for methanol, 50% for ethanol, 30% for isopropyl alcohol and 10% for tetrabutyl alcohol. They have also observed that the peak exfoliation yield is increasing with the molecular weight of the alcohols with minimum for methanol and maximum for tetrabutyl alcohol suggesting that the cosolvent molecular size has an influencing role in exfoliation. They correlated this observation with steric repulsion, with the larger size offering higher steric repulsion and hence better dispersion. When two nanolayers are separated by less than a critical distance of around 5 Å, the attractive forces between the layers are strong enough to expel the trapped molecules. But if their separation increases beyond this critical

distance due to the larger size of the cosolvent molecules penetrating between or intercalating the layers, the weakened attractive forces are unable to expel the trapped molecules, thereby improving dispersion and stability. Yao et al. have employed a transfer technique where they have initially grinded the bulk TMDC powders in NMP and further have sonicated the same in ethanol/water mixture to obtain a yield of around 26 mg/mL [91]. Wang et al. have attempted a novel technique to pre-treat the bulk powders in liquid nitrogen followed by sonication in alcohol/water mixture. They claimed that such pre-treatment aided in the initial peeling off of the layers from the bulk [92].

LPE Using Supercritical Fluid (SCF)

Gulari's group developed a new method using supercritical fluids (SCF) to exfoliate nanoflakes of layered silicates [93]. Supercritical fluids, the substances in the middle state between gas and liquid phase and becoming fluid state above their critical temperature, share the properties of both the phases. They have much more empty space than ordinary liquids and are highly compressible. As a result, the density and the strength of the solvent can be tuned to change them from gas-like to liquid-like state, just by applying pressure, temperature etc. Such tunability, accompanied with low interfacial tension, excellent wetting of the surfaces and high diffusion coefficients, make them best-suited solvents for penetrating between the layers for exfoliation. Rangappa et al. and some others have used supercritical ethanol and DMF to exfoliate graphene nanosheets from graphite crystals [94]. Here typically, the initial bulk powder was dispersed initially in a solvent and the dispersion is subjected to high temperature and pressure in a stainless steel reactor. Pu et al. recently modified slightly where they have used supercritical CO_2 (SC CO_2) to exfoliate graphene instead of using supercritical organic solvents [95]. This method offers a simple and clean route to exfoliate graphene in large quantities. Following this path, Qi et al. have exfoliated MoS_2 using a green route using ethanol and water with SC CO_2 [96]. Here, they have dispersed MoS_2 in an aqueous solution of ethanol and subsequently exposed them to CO_2 under supercritical condition. Due to the compatibility of SC CO_2 with ethanol, two phases were formed, i.e., SC CO_2–ethanol and MoS_2–water. Initially, due to hydrophobic properties of MoS_2, they disperse at the interface of water and SC CO_2–ethanol. The pickering emulsion droplets are formed due to the synergetic effect of SC CO_2, ethanol and high-speed mechanical stirring. The SC CO_2 can also intercalate between the MoS_2 layers and weaken the van der Waals forces between the adjacent layers. Ethanol molecules are carried along with CO_2 molecules and get inserted between the layers, thereby weakening the van der Waals further. Under continuous high-speed stirring, the existing shear force between the SC CO_2 and MoS_2–water phases forces the exfoliation of the MoS_2 sheets layer by layer.

Though liquid exfoliation using organic solvents is insensitive to ambient conditions and hence environment friendly, it suffers from a low yield. Different methods of liquid exfoliation were focused on to increase the yield.

Ion Intercalation-Based Exfoliation

As said in the above sections, the first step in exfoliation is to weaken the attractive force between the adjacent layers by physically increasing the distance between them as the van der Waals force is proportional to $1/r^6$ where r is the distance between the layers [97]. The van der Waals force is also expected to vanish for interlayer spacing above 5 Å. The distance between the layers can be increased by intercalating the layers using external species like ions, salts, surfactants, organic molecules and polymers, etc. Layered materials generously allow the external species like ions, molecules etc. to enter into the spacing between the layers, forming what is called inclusion complexes. Intercalation, mostly by ionic species, increases the spacing between the layers, which weakens the van der Waals forces and reduces the energy barrier to exfoliation. Intercalation of TMDCs by lithium and further exfoliation were demonstrated in 1970s by Morrison, Frindt and co-workers [12]. Such exfoliation methods were reported to produce microgram quantities of monolayers. In this technique, the bulk powder is submerged in a lithium-containing compound like n-butyllithium for sufficiently long time to allow lithium ion to fully intercalate into the material. This is then followed by exposure to water where the lithium ion reacts vigorously with water causing hydrogen gas to evolve between the layers. This release of gas causes the layers to be separated resulting in exfoliation in water. Eda et al. have attempted exfoliation of MoS_2 by immersing the bulk crystals of the same in butyllithium solution in hexane for 2 days [97]. The resultant Li_xMoS_2 was filtered and washed with plenty of hexane to remove excess lithium. The remaining Li_xMoS_2 was dispersed in water and subjected to ultrasonication. The mixture was further centrifuged several times to remove the excess lithium in the form LiOH and the unexfoliated material. The entire reaction can be represented as below [97–101]:

$$MoS_2 + BuLi \rightarrow Li_XMos_2 + 1/2Bu - Bu \tag{10.10}$$

$$Li_xMoS_2 + xH_2O \rightarrow MoS_{2\,(monolayer)} + xLiOH + \frac{X}{2}H_2 \tag{10.11}$$

Similarly for WS_2, a similar reaction is valid:

$$WS_2 + BuLi \rightarrow Li_xWS_2 + 0.5\,Bu - Bu \tag{10.12}$$

$$Li_xWS_2 + xH_2O \rightarrow WS_{2\,(monolayer)} + xLiOH + \frac{X}{2}H_2 \tag{10.13}$$

The schematic of the Li intercalation into the layered bulk and subsequent exfoliation in water is shown in Fig. 10.23 below:

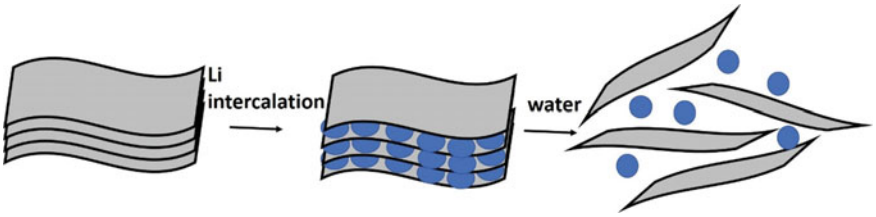

Fig. 10.23 Schematic showing Lithium intercalation and exfoliation

The majority of the exfoliated sheets were found to be mono-disperse with 300–800 nm in lateral dimensions and 1–1.2 nm thickness. Thin film was then prepared by filtering the diluted suspension through a 2.5 μm pore mixed cellulose membrane. The filter membrane with thin film was slowly introduced into water allowing the film to get delaminated from the membrane and floating freely on the surface of water. The floating film was scooped and transferred onto a substrate. Eda et al. have observed that the thermodynamically stable 2H MoS_2 undergoes phase transformation upon Li intercalation to the metastable octahedral 1 T MoS_2, which becomes metallic. After mild annealing at around 200ºC, they could retrieve the 2H phase partly, which becomes semiconducting again. Gu et al. have also reported a concentration of 1 mg/mL of MoS_2, obtained after lithium intercalation, when diluted with isopropyl alcohol [100]. Some other groups have also demonstrated Li–ion intercalation-based exfoliation for MoS_2, WS_2, $MoSe_2$ and SnS_2 [12, 99–101]. The major advantage of Li intercalation is that it results in high yield of monolayers. But unlike exfoliation in organic solvents, they are sensitive to ambient conditions where the flammability of the lithium compounds poses serious safety issues and hence requires the entire work to be carried out in inert atmosphere. Since this requirement makes whole process expensive, alternate ways for liquid exfoliation were explored.

Zheng et al. have attempted different techniques for ion intercalation [102]. Compared to Li, other alkali metal ions like Na and K are less explored for exfoliation studies. The ionic radius of Na and K is much larger than that of Li implying that Na and K intercalating between the layers can expand the gap between these layers to a larger extent that Li, thereby even strongly weakening the van der Waals forces. They also react with water more violently than Li and hence can be expected to aid in exfoliation. They have used a two-step expansion and intercalation method as shown in Fig. 10.24.

In the first step, the bulk powders are exposed to hydrazine vapour leading to the intercalation of N_2H_4 molecules. Decomposition and gasification of these molecules result in a significant expansion of the interlayer gap, causing the volume of the bulk to increase by more than 100 times. They are then intercalated by alkali naphthalenide (Li, Na and K) solution. Upon dipping in water, strong dispersion of layered TMDCs is obtained with much larger sized flakes of about 5–10 μm, than that obtained using solution-phase butyllithium intercalation. They have successfully applied this method to exfoliate various TMDCs like TiS_2, TaS_2, NbS_2, $NbSe_2$, $TiSe_2$, $MoSe_2$, etc.

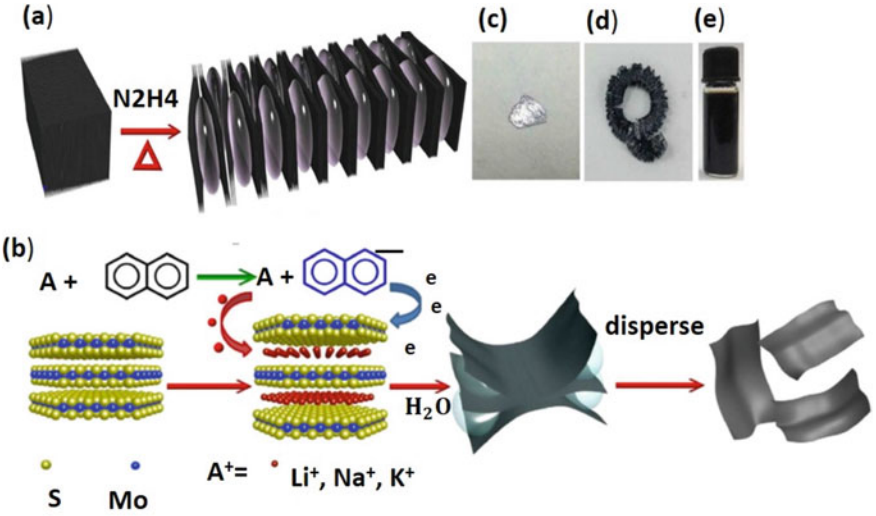

Fig. 10.24 Schematic representing **a** expansion of TMDs under exposure to hydrazine vapour and **b** intercalation of alkali naphthalenide and exfoliation, **c** photograph of bulk single-crystal MoS_2, **d** photograph of pre-exfoliated MoS_2, **e** photograph of Na exfoliated single-layer MoS_2 dispersion in water. Reproduced with permission from Springer Nature [102]

Surfactant-Based Intercalation

Though ion intercalation method has been successful in exfoliating layered materials, it suffers from some disadvantages—(1) the resulting monolayers are highly defective and highly distorted from 2H structure and (2) upon removal of the ions, there is strong restacking of the layers and they are sensitive to ambient conditions [12, 52, 103]. As mentioned before, the alternate route of exfoliation in organic solvents did not provide a high yield. Therefore, for large-scale production, the use of environment friendly alternate liquid medium route would be preferable. Some studies have dispersed layered materials in surfactant–water medium and demonstrated good success [103, 104]. Coleman group has dispersed graphite in sodium docecylbenzene sulfonate (SDBS) solution prepared in water [103]. They sonicated this dispersion in low power bath sonicator for 30 min followed by centrifugation. The large aggregates of the surfactants were allowed to settle and the supernatant was used for further analysis. Most of the graphene sheets were less than 5 layer thickness with a small amount of them with monolayer thickness. They observed high stability of the dispersion without reaggregation for a long duration. This was suggested to be due to the large potential barrier created by Coulombic repulsion between the surfactant coated sheets. Smith et al. have used an ionic surfactant to exfoliate MoS_2, which acts as ideal stabiliser due to its van der Waals binding to the exfoliated nanosheets and due to the electrostatic stabilisation [105]. They have estimated the number of layers to be within 2–9 layers. The obtained flake length was around 280–430 nm. They have extended this method also to exfoliate WS_2, $MoTe_2$,

$MoSe_2$, $NbSe_2$, $TaSe_2$ and BN. Though the concentrations obtained are less than that for Li intercalation method, the disadvantages with the latter method are not encountered here. Kang et al. have carried out exfoliation of ReS_2 in aqueous surfactant solution of sodium cholate (SC) in deionised water, by usual sonication followed by centrifugation [104]. The resultant ReS_2 nanolayers were polydisperse with respect to layer number and thickness. In order to improve this to sort out layer by layer, they adopted a novel isopycnic density gradient ultracentrifugation (iDGU) method as a follow-up procedure. They have modified the procedure to make them suitable for high-density 2D materials where they have added cesium chloride (CsCl) to the commonly used iodixanol to increase the maximum buoyant density. This enhanced the layer by layer dispersion of SC encapsulated ReS_2 nanosheets.

Besides the above intercalants, exfoliation through intercalation of organic molecules/polymers/biomolecules, etc. have also been attempted successfully [106–108].

Electrochemical Exfoliation

Electrochemical route is an efficient and mild method to intercalate and exfoliate layered materials into nanosheets and has been well explored by many groups [109–116]. The bulk material to be exfoliated is exposed to positive and negative cycles of voltage and hence subjecting it to oxidation and reduction reactions. This cycle of opposite polarity would facilitate the intercalation of opposite charged electrolyte species into the bulk materials. The basic setup required for this kind of exfoliation is a two-electrode system consisting of the bulk layered material acting as the anode, a counter electrode (mostly platinum) acting as the cathode, the electrolyte and a suitable power supply. Depending on the potential applied, electrochemical exfoliation can be divided into two categories, i.e., anodic and cathodic exfoliation [4, 110]. In anodic exfoliation, positive potential is applied to the electrode with the layered solid following which the anions of the electrolyte or that created during the electrolysis would intercalate into the layered material under the applied electric field. In the case of cathodic exfoliation, negative potential is applied to the electrode with the bulk material causing cations to intercalate into them. In the former aqueous solutions of acids like H_2SO_4, H_3PO_4 etc. and some ionic liquid–water mixtures are used as electrolytes. In the case of the latter, organic solvents like DMSO, propylene carbonate etc. containing lithium, alkylammonium salts etc. are generally used as electrolytes. The use of aqueous electrolytes has made the anodic exfoliation more preferable than the cathodic exfoliation. Different groups have adopted different architectures where bulk materials are used as electrodes in some studies while they are added to the electrolyte solution with platinum acting as the electrodes in some other studies.

Electrochemical exfoliation of graphene from graphite has been successfully demonstrated using ionic liquids and aqueous acids of H_2SO_4 or H_3PO_4 [112]. Liu et al. have used both the graphite rods for both the electrodes in their set up, dipping them in the ionic liquid/water solution. By applying a potential of 10–20 V for 30 min, the anode graphite rods got corroded and exfoliated to graphene nanosheets, forming

a black precipitate, which turned into homogenous solution [110]. An elaborate study on the performance of various ionic liquids and different concentrations of these ionic liquids was carried out in their study. Lu et al. also carried out one pot synthesis of graphene nanosheets in a similar setup by using ionic liquids/water mixture electrolytes [111]. In their study, platinum was used as counter-electrode while graphite rods and highly oriented pyrolytic graphite (HOPG) were used as anodes. Parvez et al. have shown the anodic exfoliation from graphite using aqueous electrolytes of inorganic salts like ammonium sulfate $(NH_4)_2SO_4$, sodium sulfate (Na_2SO_4) and potassium sulfate (K_2SO_4) [112]. Their study concluded that graphene sheets with the lowest defect density could be produced using this configuration. Zeng et al. have successfully exfoliated few layers of BN, $NbSe_2$, WSe_2, Bi_2Te_3, etc. using lithium intercalation [113]. Here, the slurry containing a mixture of layered materials, acetylene black and poly (vinylidene fluoride) (PVDF) binder are coated on copper foil acting as the cathode. Lithium foil was used as the anode with 1 M $LiPF_6$ in a mixture of ethylene carbonate (EC) and dimethyl carbonate (DMC) as the electrolyte. The whole lithium battery assembly with polypropylene (PP) film separator is assembled inside an Argon-filled glove box. Ejigu et al. have reported successful production of metallic 1 T-MoS_2 nanosheets by intercalating lithium into the bulk material through electrochemical route [114]. Here they have used an inert Li salt $(LiClO_4)$ in a mixture of DMC and EC, MoS_2 pellets or MoS_2 crystals as working electrode and platinum mesh as counter electrodes. The 1 T-MoS_2 sheets produced were demonstrated to be useful in hydrogen evolution reaction (HER) and for supercapacitor applications.

Similar to lithium intercalation, electrochemical exfoliation also proceeds through two main steps—(1) the bulk material swells macroscopically producing an expanded structure due to the intercalation of electrolyte followed by the production of gas and (2) exfoliation of the nanolayers due to the eruption of gas and the subsequent dispersion into the solution. The thickness of the nanosheets and the defect density produced, oxygen content, etc. can be controlled by varying the parameters and/or the electrolyte species [112]. Liu et al. also have exfoliated MoS_2 nanosheets using Na_2SO_4 salt as electrolyte [115]. They have claimed the production of large-area nanosheets of size about 50 μm with high quality, low degree of oxidation and with intrinsic structure. In their setup, the bulk MoS_2 crystal, platinum wire and 0.5 M Na_2SO_4 were acting as the working electrode, counter electrode and the electrolyte, respectively, with positive potential applied to the bulk crystal. A low potential of + 2 V was initially applied to wet the crystal for about 10 min, which was then increased to about + 10 V to exfoliate the nanosheets that became suspended in the solution. They have reported a yield of about 5–9% with the concentration in the range of 0.007–0.014 mg/mL. This study has suggested that by applying a positive bias to the working electrode, the •OH, •O radicals and/or SO_4^{2-} anions insert themselves into the bulk crystal and weaken the van der Waals forces between the layers. Oxidation of the radicals and/or the anions results in the release of O_2 and/or SO_2, which would largely expand the layers. The erupting gas would then delaminate the nanosheets, which remain suspended in the solution. Leong et al. have exfoliated WS_2 nanosheets electrochemically where glassy carbon and platinum are used as electrodes, and Na_2SO_4 is directly added to the aqueous dispersion of WS_2 [116].

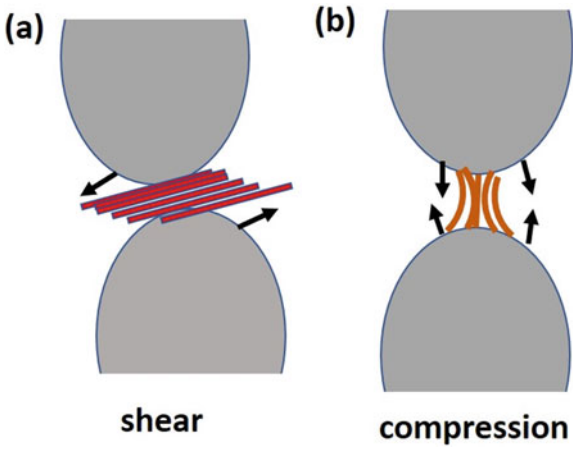

Fig. 10.25 Schematic showing the principle of ball milling based exfoliation

Ball Milling and Shear Milling Methods

A ball mill is a type of grinder used to grind and blend materials in the industries, laboratory researches on materials science, etc. Ball milling is a mechanochemical exfoliation method combining mechanical forces followed by ultrasonication, which has been successfully employed to isolate nanolayers of graphene, h-BN, MoS_2, WS_2, etc. [4, 17]. Ball milling imparts two kinds of forces, i.e., shear as well as compressive forces on the layered solids. Shear forces cleave off the layers from the top/bottom surface whereas the compression forces peel off the layers from the edges. Subsequent sonication breaks the bigger crystallites into smaller size (Fig. 10.25). This method employs either high energy or low energy ball milling where the former dominantly causes through plane fracture than the delamination of the flakes, and hence causing severe defects in the exfoliated layers. Control of the defect production is attempted by modifying the milling conditions and the interactions of correct guest molecules. Ball milling can be of different types—planetary ball milling, wet (liquid) ball milling, etc. In liquid ball milling, the ball to bulk powder ratio, the size of the milling balls, milling duration, the type of liquid chosen etc. affect the efficiency of exfoliation.

By using a combination of low energy ball milling and ultrasonication in surfactant solutions of sodium dodecyl sulfate–water (SDS) and by tuning the duration of ball milling, Yao et al. have reported high concentrations of about 0.9 $mgmL^{-1}$ for graphene, 0.8 $mgmL^{-1}$ for MoS_2 and 1.2 $mgmL^{-1}$ for BN [117]. SDS surfactant is also used by Knierke et al. to exfoliate graphene successfully [118]. Damm et al. have shown that stirred milling is an improved version of planetary ball milling where the smaller bead size (mostly 1 mm or smaller) allows a better temperature control during processing [119]. By using stirred media milling for exfoliation of graphene in surfactant-free NMP liquid, a yield of about 73 mg/h is obtained for graphene, which is higher than the quantity 33 mg/h obtained using ultrasonication. Lee et al. prepared hydroxyl group functionalised BN nanosheets by ball milling the bulk BN

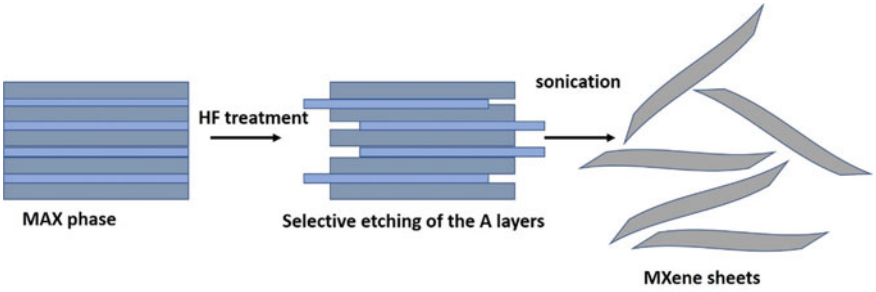

Fig. 10.26 Schematic showing the synthesise of MXene sheets from MAX phase

powder in the presence of sodium hydroxide [120]. They reported the production of OH-BN nanoplatelets with an average size of 1.5 μm, with negligible damage and a yield of around 18%.

Though ball milling is an alternate cheap and effective method for large-scale synthesis of nanosheets, it suffers from the disadvantage of introducing impurities. It also requires long processing hours, even up to 24 h, and mostly a follow up by ultrasonication. Yao et al. further improved the exfoliation procedure by employing a combination of grinding and sonication [91]. In their study, less energy shear forces are applied on the bulk MoS_2 by grinding them in NMP solvent, followed by ultrasonication in ethanol/water mixture. The grinding time is varied from 30 min to 3 h. They have reported concentrations of monolayer and few layer MoS_2 in aqueous solutions as high as 26.7 mg/mL. Nguyen et al. have modified this procedure by grinding in a variety of solvents with boiling points and surface tension lower than that of NMP, due to the problems faced using high boiling point solvents [121]. The solvents investigated are acetone, acetonitrile, hexane, cyclohexane, benzene, isopropyl alcohol, methanol and toluene. They have ground bulk MoS_2 in 0.5 mL of the chosen solvent using a mortar and pestle for about 30 min. The evaporated solvent during grinding was replenished by adding additional solvent in doses of about 0.1 mL. The powder was left to dry in a vacuum oven overnight at around 60ºC. The dried powder was then re-dispersed in ethanol and probe sonicated along with stirring, for about 90 min. The well-dispersed solution was centrifuged at around 4000 rpm for about 30 min, in about two steps. The supernatant containing nanoflakes was collected. Verification of the concentration of the flakes for all solvents showed that the use of isopropyl alcohol, acetone, methanol, benzene and toluene did not lead to measurable values. Their results further suggest that even though larger size and best quality flakes were obtained for NMP, acetonitrile (ACN) can be considered to be an alternative for NMP for exfoliating MoS_2, yielding the high concentration. Added advantage was that ACN was found to be removed from MoS_2 surface after grinding, unlike the case of NMP, which was found to be sticking on the surface of MoS_2. Nguyen et al. observed that the grinding step and the solvent used for grinding play a crucial role in determining the yield. Xu et al. have carried out shear exfoliation of BP in NMP by using a kitchen blender and a laboratory shear mixer at a shear

rate higher than 1.25×10^4 s^{-1}. They have obtained high quality, highly crystalline phosphorene nanoflakes [122]. Application of shear force on MoS_2 bulk powders in ethanol/water cosolvent followed by subjecting them to 1 hour of turbulence in a laboratory mixer with four rotating blades was reported by Yuan et al. [123]. They focused on ethanol in order to choose a green route to the exfoliation process. They have reported the best yield at 45% volume ratio of ethanol/water and at the initial concentration of 10 mg/mL of bulk MoS_2 powder. Their study concluded that with an increase in shearing mixing to a speed of 10,000 rpm and the number of cycles to 10, they obtained a yield of around 30%. Woomer et al. have investigated the efficiency of BP exfoliation in 18 solvents and have validated the same using HSP and Hildebrand parameters. They have demonstrated a large-scale production of monolayer, bilayer and few layer phosphorene to about 10 g scale [124]. Black phosphorous crystals were initially ground in a mortar and pestle and sonicated them for 13–16 h in a low-power bath sonicator under inert atmosphere. They have reported the best result while using benzonitrile achieving a mean concentration of about 0.11 mg/mL. From the measurements of concentrations of BP flakes for various solvents, they have inferred that the optimum conditions of the solvent necessary for BP are almost similar to other 2D materials like TMDCs and BN.

Synthesis of MXenes

Titanium carbide MXene was prepared in a typical procedure as follows [125]: A mixture of titanium hydrate, aluminium and graphite powder was thoroughly mixed in a required stoichiometric ratio using ball milling for about 20–80 h, and pelletised. The pellet was then sintered at high temperature of around 1350 ºC in argon atmosphere. The resulting pellet in MAX phase was pulverised, immersed and stirred in hydrofluoric acid (HF). The mixture was then centrifuged and washed with DI water for about 20 h. Gogotsi group has used different raw materials like TiC, Ti and Al to synthesise T_3AlC_2 precursors [49, 126]. There are reports synthesizing Ti_3AlC_2 using Ti, Al and C, Ti, Al_4C_3 and C or even TiO_2, Al and C. Though in the initial studies, pressure was applied on MAX powders to get fully dense samples, this step was removed in the later studies as the powder samples were even advantageous for further milling processes. In some studies, the A layer from the MAX phase was also etched using LiF/HCl combination [126]. Under this condition, delamination of the MXene sheets can occur simultaneously due to the intercalation of Li in between the MXene layers. MXenes can also be intercalated with different organic compounds such as dimethyl sulfoxide (DMSO), tetraalkylammonium hydroxides, etc. or inorganic salts, to exfoliate and produce the MXene sheets. A schematic showing the synthesise of MXene sheets from MAX phase is shown below (Fig. 10.26):

10.4 Characterisation Methods

Though many techniques like scanning electron microscopy (SEM), energy dispersive X-ray analysis (EDAX), transmission electron microscopy (TEM), X-ray diffraction measurements (XRD), X-ray photoelectron spectroscopy (XPS) are used to characterise the exfoliated flakes, UV–vis absorption spectrometry, atomic force microscopy (AFM), optical imaging, Raman spectroscopy and photoluminescent spectroscopy (PL) are the most important techniques that are used for estimating the layer thickness and the concentration of the yield. Hence only these techniques will be discussed in this chapter.

10.4.1 Atomic Force Microscopy (AFM) and Optical Imaging

Locating and identifying the nanolayers and estimating their layer thickness are the primary steps to be executed after exfoliation before proceeding into device fabrication. AFM is a primary tool to estimate the layer thickness as it physically measures the step height produced by the nanolayers. Verification of the morphology of the flakes on a substrate provides the roughness profile from which the step height is determined. The layer thickness values and, hence, the number of layers are estimated from the step height. Some examples of the AFM images of MoS_2 and WSe_2 are shown in Fig. 10.27a, c along with their corresponding optical images in Fig. 10.27b, d [55, 127].

Optical imaging is the simple and non-destructive step to characterise the nanolayers. It basically depends on the variation in the optical contrast between a nanolayer and the substrate brought about by the change in the layer thickness. The choice of the substrate is one of the major factors influencing the optical contrast. The SiO_2/Si substrates are most commonly used to locate and visualise the monolayer to few layer flakes [15]. The optical contrast is calculated within the Fresnel's formalism, as a function of SiO_2 thickness and the wavelength of the light used for illumination. The thickness of the SiO_2 wafer has to be around 270 nm or 90 nm such that a clear optical colour contrast of the flakes is obtained [57, 128, 129].

The 2D/dielectric/Si structure produces multiple reflections of light at the air-2D, 2D-dielectric, dielectric-Si interfaces, as shown in Fig. 10.27e. The colour of the dielectric-coated substrate depends on the interference effect from the reflections at the two surfaces of the dielectric. The presence of the mono/few layer thickness flakes modifies this interference effect thereby introducing optical contrast. Several methods have been applied to improve the optical contrast and to estimate the thickness, such as the use of narrow band illumination, collection of reflection spectra, measurement of total colour difference, ratio of colour difference, etc. [57, 128, 129].

Li et al. have demonstrated a simple technique to estimate the layer thickness. They have shown that the optical contrast between the nanolayers and the substrate can be obtained from the brightness profiles of their colour images or the grayscale

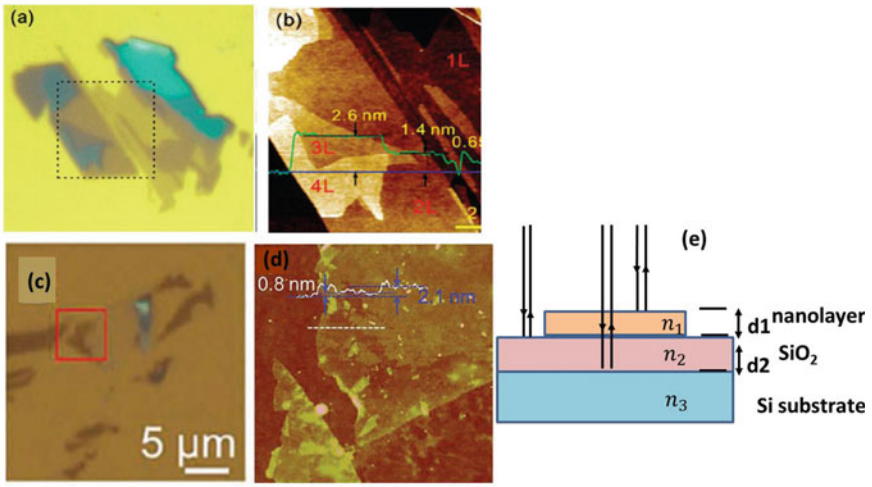

Fig. 10.27 **a** Optical imaging of a few layer MoS_2 flakes with a box marked of area 8 μm × 8 μm and **b**their AFM image (shown in box in this figure with corresponding step heights ("Reprinted (adapted) with permission from (ACS Nano, 2010, 4, 2695). Copyright (2018) American Chemical Society"), **c** optical image of 1L WSe_2 and **d** AFM image of the area shown in red square in (**c**) (Li, H.; Lu, G.; Wang, Y.; Yin, Z.; Cong, C.; He Q.; Wang, L.; Ding, F.; Yu, T. and Zhang, H. P. Mechanical Exfoliation and Characterization of Single- and Few-Layer Nanosheets of WSe_2, TaS_2 and $TaSe_2$. Small. 2013. 9. No. 11. 1974. Copyright Wiley–VCH Verlag GmBH & Co. KGaA. Reproduced with permission), **e** Schematic showing the multiple reflections at each interface

images of red, blue and green (R, G, B) components. The optical contrast C of the nanosheet and that of the substrate C_S was obtained from the images using a free software (image). The contrast difference C_D is obtained by taking the difference between C and C_S. Similarly, for grayscale images, the contrast difference C_{DR}, C_{DG} and C_{DB} for R, G, B channel can be obtained from the difference between the contrast C_R, C_G and C_B of the nanosheet with C_{SR}, C_{SG} and C_{SB} of the substrate. They have obtained contrast values of 162.3 and 118.6, respectively, for a six layer (6L) and eight layer (8L) MoS_2 nanolayers, and about 120.4 for 90 nm thick SiO_2/Si substrate. Hence a contrast difference of 41.9 for 8L and –1.8 for 6L MoS_2 flakes (Fig. 10.28a, b). They have further made elaborate studies for estimating the dependency of optical contrast on the exposure times. Their study also estimates systematically the contrast difference of MoS_2 flakes with thickness ranging from 1 to 5 L, on a 300 nm SiO_2/Si substrate (Fig. 10.28c–q). Detailed analysis of estimation of the number of layers in the flakes is also carried out by Ottaviano et al. and Benameur et al. [57, 129]. A similar optical microscope image of 1 to 6 L of MoS_2 flakes is shown in Fig. 10.29a. It can be clearly seen that a monolayer is almost transparent with minimum contrast with the substrate while the thicker layers showing increasing contrast. Ottaviano et al. have plotted the optical contrast for the red, blue and green components and their average values as a function of thickness for a few layers MoS_2, as shown in Fig. 10.29b–e. This result shows that the contrast is not a monotonic function of the

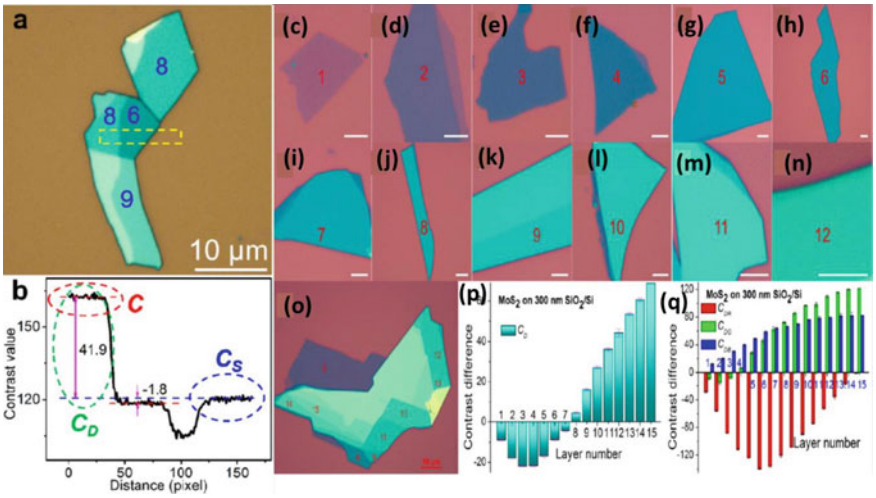

Fig. 10.28 **a** Optical images of a few layer MoS_2 flakes on 90 nm thick SiO_2 substrate, **b** their contrast profile **c–o** optical images of 1L-15 L MoS_2 on 300 nm SiO_2/Si, p) C_D values and q) C_{DR}, C_{DG} and C_{DB} values of these layers on 300 nm SiO_2, ("Reprinted (adapted) with permission from (ACS Nano, 2013, 7, 10,344). Copyright (2018) American Chemical Society")

layer thickness. It shows clear change from a monolayer to a few layer thickness, beyond which the distinction in the contrast appears to vanish.

10.4.2 Raman Spectroscopy

Apart from AFM and optical imaging, Raman spectroscopic measurements have been considered to be a major tool to estimate the layer thickness. They can also be used to identify crystal phases and they are very sensitive to the angle between the crystalline orientation and the incident Raman laser light. A typical Raman analysis for layer thickness measurement is shown in Fig. 10.30. Non-resonant Raman spectrum of MoS_2 is only characterised by two Raman active modes—the E^1_{2g} mode at around 383 cm^{-1} in the bulk corresponding to the in-plane vibrations of two S atoms with respect to Mo atoms, and the A_{1g} mode around 408 cm^{-1} representing the out-of-pane vibrations of the S atoms above and below the MoS_2 basal plane (Fig. 10.30a, c) [59, 127, 130, 131]. Many studies have reported that these peak positions are very sensitive to layer thinning where the E^1_{2g} mode is observed to stiffen and the A_{1g} mode to soften (Fig. 10.30b). The difference between the two peak frequencies is reduced from about 25 cm^{-1} in the bulk to about 19 cm^{-1} in the monolayer. For MoS_2, this has become a reliable measure to identify monolayers. Lee et al. have systematically measured the peak shift with an increase in layer thickness from monolayer and have shown the saturation of this shift beyond a certain number of

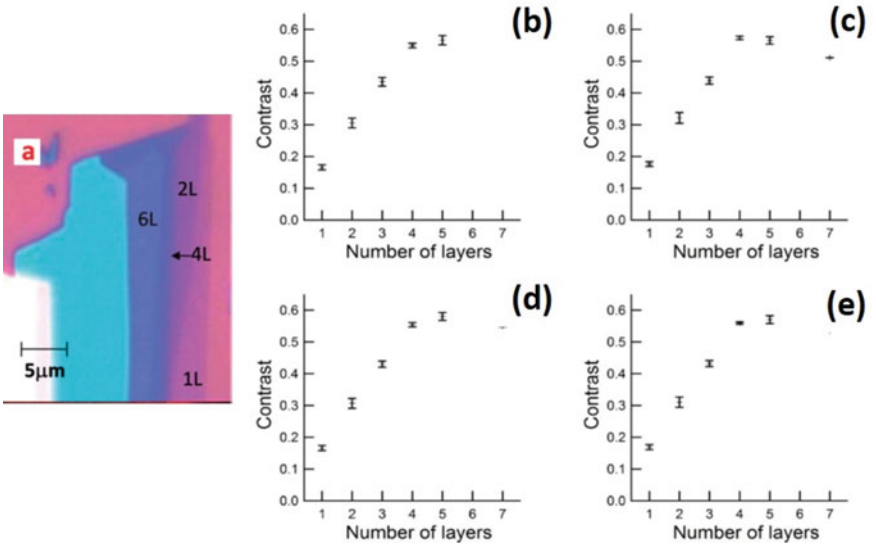

Fig. 10.29 **a** Optical image of a few layer MoS_2 flakes ("Reprinted (adapted) with permission from (Nano Lett. 2010, 10, 1271). Copyright (2018) American Chemical Society") and **b**, **c**, **d** and **e** red, blue, green components and their average contrast values respectively, estimated theoretically for a few layers thick MoS_2 nanoflakes. (Reproduced with permission from IOP Publishers [57]

layers with no change in the difference in the peak frequencies (Fig. 10.30b) [127]. According to classical harmonic oscillator model, when layer thickness increases from monolayer to bulk, both the modes should stiffen as the stacked layers are expected to hinder the vibrations and thereby increasing the force constant. Though the out-of-plane vibrational mode follows this expectation, the in-plane vibration mode behaves opposite, showing softening, indicating that stacking of the layers affects the intralayer bonding and their vibrational modes. It was suggested that the stacking induced structural changes in the intra-bonding in combination with the strong dielectric screening of the long range Coulombic interactions could be causing a redshift of the E^1_{2g} modes [30, 59, 127, 130–133].

Similar studies were made for other TMDCs like WS_2 etc. A typical thickness-dependent Raman spectrum for WS_2 is shown in Fig. 10.31a [30]. In the case of ReS_2, Rahman et al. report no change in Raman peak frequencies for these vibrational modes, due to the weak interlayer coupling between the layers that is mentioned before in this chapter (Fig. 10.31b) [37]. There are 18 vibrational modes for ReS_2 as shown in Fig. 10.31b, out of which the peaks 1 and 2 at 136.8 and 144.5 cm^{-1} are the out-of-plane A_g like vibrations of Re atoms. The peaks numbered 3, 4, 5 and 6 at 153.6, 163.4, 218.2 and 238.1 cm^{-1} are the E_g like in-plane vibrations of Re atoms. Their measured Raman spectrum shows negligible peak shift with change in layer thickness. On the contrary, some others demonstrate the presence of interlayer interaction accompanied by the observation in shift in Raman peak frequencies (Fig. 10.31c) [42]. The change in intensity and/or the intensity ratio of the

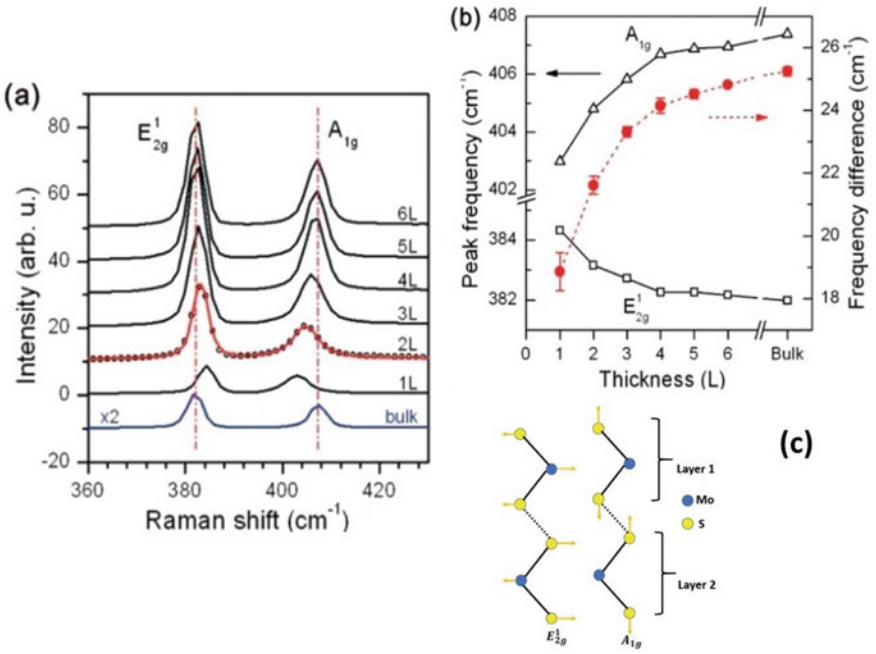

Fig. 10.30 **a** Raman spectrum of MoS_2 monolayer to bulk, **b** shift in peak frequencies and their difference as a function of layer thickness ("Reprinted (adapted) with permission from (ACS Nano, 2010, 4, 2695). Copyright (2018) American Chemical Society") and **c** In-plane and out-of-plane vibrational modes of MoS_2

peaks and the change in the peak width are also indicators of layer thickness. Raman spectrum is also sensitive to stress, strain and pressure applied to these nanolayers. In this chapter, these points are not discussed as the focus is only on the identification of layer thickness using Raman spectrum.

10.4.3 UV–Vis Absorption Spectrum

UV–vis absorption spectrum is a main tool employed to estimate the concentration of the dispersions of nanoflakes that are exfoliated through the liquid phase, using Beers law. As the band gap gets modified with number of layers for most of the layered materials like TMDs, the absorption spectrum also shows bands corresponding to the layer thickness. A typical transition from valence band to conduction band corresponding to different excitonic peaks is shown in Fig. 10.31a. The absorption spectra for LPE of MoS_2 for different centrifugal forces are shown in Fig. 10.32b with the excitonic positions marked, corresponding to that seen in Fig. 10.32a [77]. The lack of inversion symmetry together with strong spin–orbit interaction and the interlayer

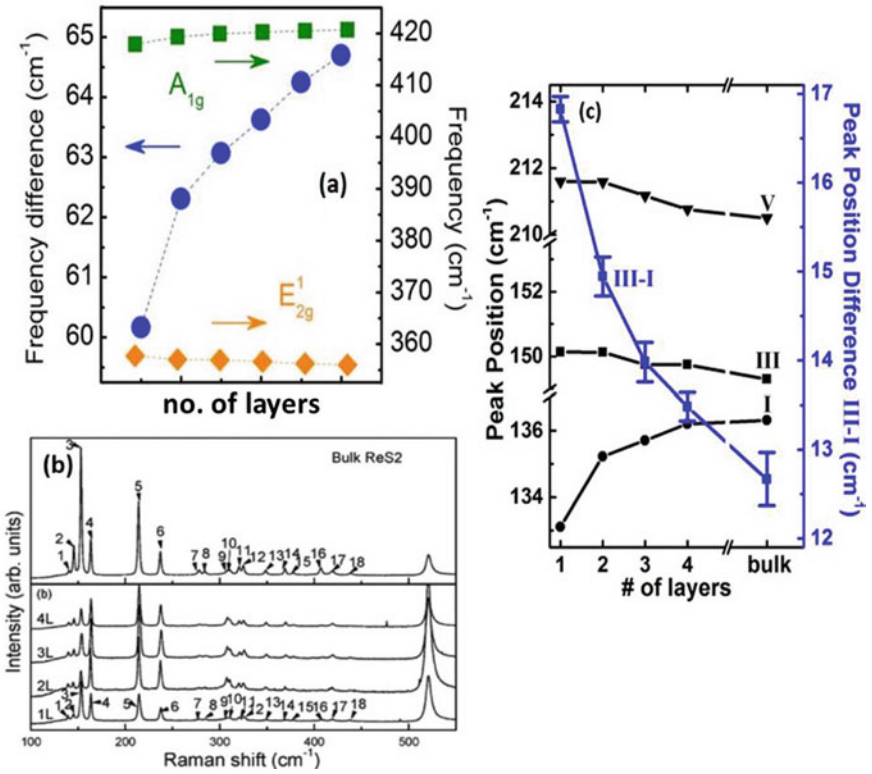

Fig. 10.31 **a** Peak positions of WS_2 (Reproduced with permission from [Nanoscale 2013, 5, 9677–9683]—Published by The Royal Society of Chemistry, **b** Raman spectrum of ReS_2 (Rahman, M.; Davey, K. and Qiao, S. Z. Advent of 2D Rhenium Disulfide (ReS_2): Fundamentals to Applications. Adv. Funct. Mater. 2017, 27, 1,606,129(1–21) copyright Wiley–VCH Verlag GmBH & Co. KGaA Reproduced with permission) and **c** peak position shift of ReS_2 peaks, all with change in number of layers (n) (Reprinted (adapted) with permission from (Nano Lett. 2015, 15, 5667). Copyright (2019) American Chemical Society")

coupling lift the degeneracy between in spin levels in the valence band and conduction bands at K point in the Brillouin zone [134, 135]. For MoS_2, two clear bands at 627 nm and 670 nm are observed corresponding to direct excitonic transitions between the two valence band maximum levels to the conduction band minimum at the Brillouin zone K point, as shown in Fig. 10.32a. These two resonances are known as A and B excitons. The energy difference between the two excitons defines the valence band splitting at this point. Similarly, the two bands around 460 and 410 nm, respectively, are the C and D excitons due to the direct transition from deep valence band to conduction band [121, 136–139]. Jia et al. have shown the shift in peak positions of A, B and C excitons to lower energies, with an increase in layer thickness, showing thickness-dependent behaviour (Fig. 10.32c) [136]. Similarly, the

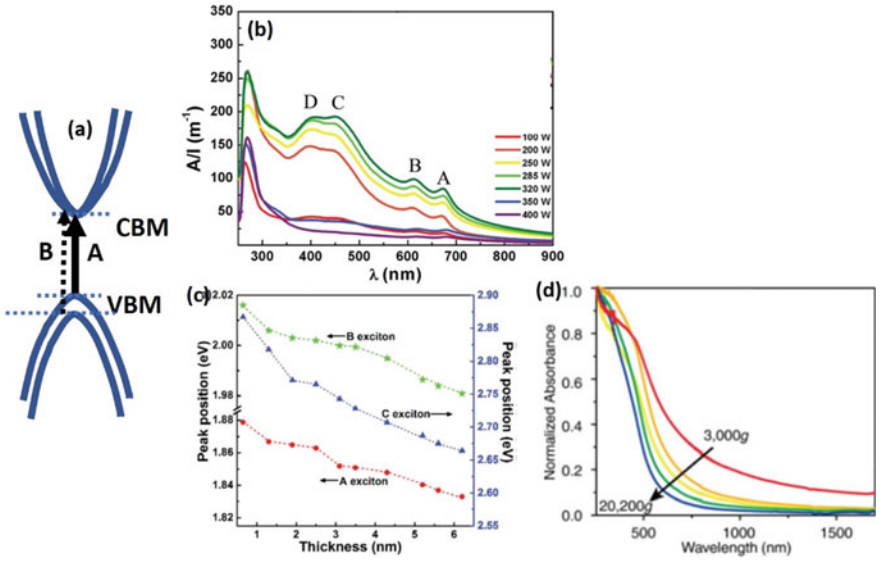

Fig. 10.32 **a** Schematic showing A and B exciton transition, **b** absorption spectrum of MoS_2 flakes varying as a function of ultrasonic power (Reproduced with permission from [RSC Adv., 2014, 4, 50981]—Published by The Royal Society of Chemistry, **c** layer thickness-dependent optical absorption spectrum of BP flakes at different centrifugal rates (Reproduced with permission from [J. Mater. Chem. C, 2016, 4, 8822]—Published by the Royal Society of Chemistry, **d** absorption spectrum of phosphorene at different centrifugation rates (Reprinted (adapted) with permission from (ACS Nano, 2015, 9, 8869). Copyright (2018) American Chemical Society").

typical absorption spectra of BP after liquid exfoliation under different centrifugation rates and hence different layer thicknesses are shown in Fig. 10.32d [140].

10.4.4 Photoluminescence (PL) Spectroscopy

Another optical method that can offer signature changes with change in layer thickness is photoluminescence (PL) spectroscopy. Figure 10.33a shows the PL emission corresponding to A and B excitonic transitions of MoS_2 for varying thickness from monolayer like to bulk like, under excitation with 532 nm laser [97].

Due to direct band gap transition, there is enhancement of PL emissions for MoS_2 for lowest thickness (monolayer like) while it is seen to be negligible for larger thickness (approaching bulk) due to its indirect band gap. This shows a clear and strong response of PL to layer thickness change. Similar observations are made by other studies also [35]. On the contrary, it can be seen from Fig. 10.33b that the PL emission is maximum for bulk ReS_2 which reduces with thinning of the layers [31]. This is because of the direct band gap for bulk and the weak coupling between the layers. Liu et al. have shown an increase in PL signal of monolayer phosphorene

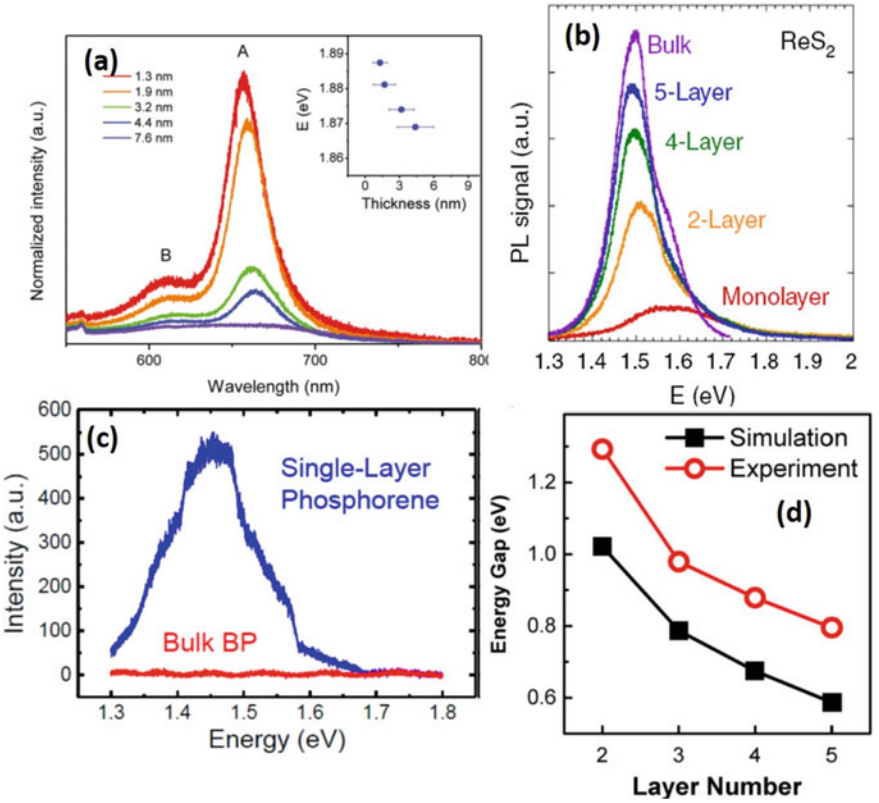

Fig. 10.33 PL change as a function of **a** MoS_2 layer thickness, inset-energy of A exciton as a function of thickness (Reprinted (adapted) with permission from (Nano Lett., 2011, 11, 5111). Copyright (2018) American Chemical Society"), **b** ReS_2 layer thickness. Reproduced with permission from Springer Nature [35]), **c** monolayer phosphorene and of bulk BP (Reprinted (adapted) with permission from (ACS Nano 2014, 8, 4033). Copyright (2019) American Chemical Society") and **d** theoretical and PL based change in band gap with layer thickness measured for phosphorene (Reproduced with permission from Springer Nature [npj 2D Materials and Applications 2017, 5(1–13)]

compared with that of the bulk BP when the former is mechanically exfoliated from the latter (Fig. 10.33c) [141]. The PL spectra also help in the estimation of the band gap that is varying with thickness. The inset in Fig. 10.33a, d shows the variation in band gap with layer thickness of MoS_2 and BP, respectively [97, 142].

10.5 Applications of 2D Nanolayers

Some of the common applications of 2D materials are in the areas of nanoelectronics like field-effect transistors (FETs) and in energy-related applications like photovoltaic devices/solar cells and supercapacitors, which will be discussed in this chapter.

10.5.1 Field-Effect Transistors (FETs)

FETs are three-terminal devices that act like switches and are operated by the electric field applied to the gate electrode. For practical purposes, devices with ON/OFF ratio above 10^4 with a high saturation drain current are necessary for power gain in radio frequency (RF) FET [56]. For this purpose, semiconductors that offer currents with good ON/OFF ratio are required. At room temperature, many semiconductors possess relatively low charge density that is not sufficient to produce high output currents required for FETs. In this point, the 2D materials score high over other semiconductors because, the 2D nature of the layered materials confines the charge carriers to atomically thin surface and prevents scattering observed in 3D solids, thereby allowing high mobility. The absence of dangling bonds on the surface of 2D semiconductors providing sharp band edges with minimal trap states and their flat topography are ideally suited for compatibility with the present complementary metal-oxide semiconductor (CMOS) technology that drives the electronic industry [1, 12, 19]. These factors enable them to be considered as ideal candidates for active materials in FETs, allowing transistors to push their scaling limits and operation speeds beyond Si-based transistors [9].

The basic requirement for the fabrication of FET device is the formation of channel on these flakes. After the isolation of the flakes, channels of the size in the range of a few microns are generally formed with the help of electron beam lithography techniques, followed by deposition of metal pads to act as source and drain electrodes. The devices can be fabricated either in the bottom gate or in the top gate configurations [56, 143]. In most of the studies on bottom gate FETs, mostly heavily doped Si itself is used as the gate electrode with SiO_2 acting as the dielectric. In the case of top gate configurations, polymer dielectrics or any high k dielectrics are deposited over the nanolayers above which the metal electrodes are coated to form the gate electrode. Radisavijevec et al. have employed a top gate structure with HfO_2 dielectric on a single layer of MoS_2 which is shown in Fig. 10.34a with its optical image in Fig. 10.34b and the corresponding transfer characteristics in Fig. 10.34c [56].

The transfer characteristics clearly show the n-type behaviour of MoS_2 FET. The advantage of using a top gate configuration is that they can also act as passivating layers for the nanoflakes, preventing them from degradation due to ambient exposure. The electron mobility of around 200 cm^2/Vs and a ON/OFF ratio as high as 1×10^8 are reported for this device. In another study, they could improve the mobility to 380

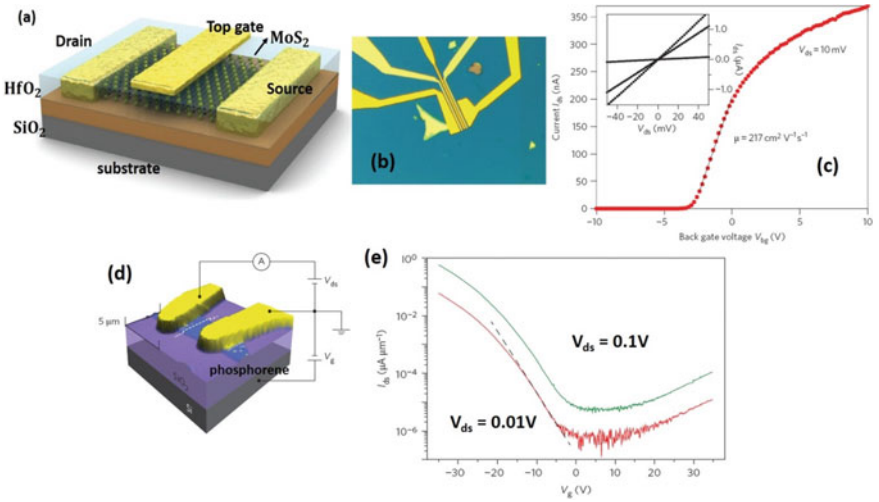

Fig. 10.34 **a** Schematic of a top gate FET with MoS_2 monolayer, **b** its optical image and **c** typical transfer characteristics of this FET(inset-output characteristics) (Reproduced with permission from Springer Nature [56]), **d** schematic and **e** transfer characteristics of a bottom gate FET with phosphorene flakes (Reproduced with permission from Springer Nature [143]

cm^2/Vs where they have demonstrated a small signal power amplifier using MoS_2 transistors [10]. Wang et al. have also reported a mobility of around 320 cm^2/Vs at 77 K, using a h-BN tunnelling layer between the Ni/Au contacts and the MoS_2 flakes [9]. Krasnozhon et al. have reported a mobility of around 70 cm^2/Vs and have demonstrated the use of this transistor at GHz frequencies [144]. Li et al. have demonstrated a bottom gate *p*-type FETs with hole mobility of around 1000 cm^2/Vs using 10 nm thick phosphorene nanolayers [143]. The typical bottom gate device configuration and the transfer characteristics using BP are shown in Fig. 10.34d, e, respectively. Studies are also reported on the use of these FETs for many applications like gas sensing, radiation detection, bio-sensors, photodetection, etc. [60, 62].

When the exfoliated flakes are large enough, channels can be formed by simply masking through shadow masks, instead of employing the tedious lithography techniques. Optical image of a typical MoS_2 flake exfoliated through the scotch-tape method is shown in Fig. 10.35a, across which a 25 μm wire is fixed under optical microscope to act as shadow mask. Electrical characteristics are measured across this channel by applying suitable potentials. A typical I–V characteristics measured across such a flake are shown in Fig. 10.35b [145].

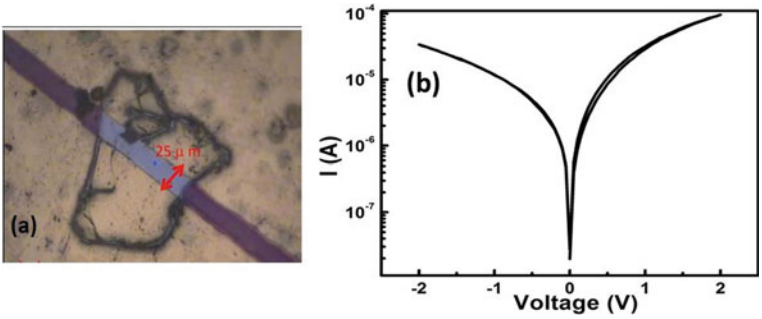

Fig. 10.35 **a** Optical image of a MoS_2 flake with a 25 μm channel across it ("Reprinted from [J. Appl. physics 2015, 117, 135,701 (1–9)] with the permission of AIP publishing"), **b** *I*–*V* measured across this flake

10.5.2 Photovoltaic Devices/Solar Cells

Due to their tunable band gap with layer thickness, 2D materials have recently enrolled as interesting members of the materials that are used for solar cell/photovoltaic device applications. Layered materials like MoS_2, phosphorene, indium selenide (InSe) etc. are tending to become prominent members in this field. Tunability in the band gap with layer thickness allows them to be useful in harvesting solar radiations in desired wavelengths, especially in the IR and near-IR regions, where 40% of the solar spectrum is available. Many studies have used them in combination with other materials that are harvesting in the visible region to act as complementary to them. The high conductivity of these materials enhances the charge carriers to reach their respective electrodes to flow as high current, thereby increasing the efficiency of the solar cells. Graphene has even shown to be performing like a transparent conductive oxide. Wang et al. have shown that by using graphene as anode, they could obtain around 83% of the efficiency of the solar cells that could be obtained using ITO [146]. Many studies deal with the large area deposition of 2D materials like CVD, PLD, sputtering etc. for solar cell applications. Since this chapter deals with exfoliation routes for 2D nanolayers, we will focus on the photovoltaic cells incorporating nanolayers of 2D materials prepared by exfoliation routes.

There are a number of studies on application of MoS_2 nanolayers for solar cells. Capasso et al. exploited few layer MoS_2 flakes as buffer layer in a lead halide perovskite solar cell as per the configuration glass/FTO/compact TiO_2/mesoporous TiO_2/$CH_3NH_3PbI_3$ (perovskite) /MoS_2/Spiro-OMeTAD/Au [147]. MoS_2 plays dual role to act as protective layer, preventing shunt contact with perovskite and Au electrode as well as the hole transporting layer from the perovskite to spiro-OMeTAD. The efficiency obtained was about 13.3% with MoS_2. Though the efficiency reported was comparable for the devices with and without MoS_2 buffer layer, they observed a stable performance of this device over about 550 h. They also confirmed the hole transporting property of MoS_2 by constructing a device without Spiro-OMeTAD, i.e., glass/FTO/compact TiO_2/mesoporous TiO_2/$CH_3NH_3PbI_3$ (perovskite)/MoS_2/Au

and compared the performance of this device with that without hole transporting layer (HTL). They found that the efficiency increased from about 1.5% for the latter to about 4.5% for the former. As stability in the performance is a major issue of concern with perovskite solar cells, the stability reported here is highly useful as it can pave the way for improving the same without losing the performance. MoS_2 nanolayers are also used as hole transport layers in bulk heterojunction polymer solar cells with the device structure as shown in Fig. 10.36a [148]. They have reported a J_{sc} of 15.9 mA/cm^2, V_{OC} of 0.72 V, fill factor (FF) of 71% and an efficiency of 8.11%. Yun et al. fabricated a bulk heterojunction solar cells with P3HT:PCBM and PBDTTT-CF:PCBM composites, using exfoliated and partially oxidised MoS_2 nanosheets as hole extraction layer, showing an efficiency of around 6.8% [149]. Yue et al. have obtained about 7.9% efficiency using MoS_2/carbon nanotube composite as counter electrode in a TiO_2/N719-based dye sensitised solar cell [150]. Liu et al. have demonstrated about 6.0% efficiency on a dye sensitised solar cell with MoS_2/graphene composite as counter electrode [151]. Many studies are also focussing on to employ phosphorene as active layers. Yang et al. have synthesised ultra-small BP nanosheets, named as BPQDs, and incorporated them in polyaniline layer (PANI), to act as photocathode (Fig. 10.36b) [43]. This photocathode exhibited NIR absorption, acting complementary to the visible region absorption by TiO_2/N719 dye photoanode and hence exposed to illumination on both sides, i.e., 100 mW/cm^2 in the front and about 45.6 mW/cm^2 at the rear. Such NIR absorption is expected to enhance efficiency. The typical energy level diagram of this device and the electron transfer process are shown in Fig. 10.36c. Under illumination, the photogenerated electrons in the N719 dye are transferred to the conduction band of TiO_2. The oxidised dye then gets reduced by accepting electrons from the donor in the redox couples. The photogenerated electrons in the BPQDs are transferred to BPQDs/electrolyte interface to oxidise the acceptor in the redox couples. They have reported an efficiency of about 6.8% and the short circuit current (J_{sc}) of 24.31 mA/cm^2 (Fig. 10.36c). This J_{sc} is about 120% higher than that obtained without BPQDs.

Deng et al. have attempted a *p–n* junction diode by forming heterostructures of mechanically exfoliated phosphorene layers with CVD grown MoS_2 monolayer [152]. They have demonstrated that this heterostructure can work as photovoltaic device with external quantum efficiency of 0.3%, when illuminated with 633 nm. Though this value is very low, it shows the potential of these materials for such applications. Chen et al. have employed the synthesised BPQDs as hole-transporting materials (HTM) in a hybrid perovskite solar cell as shown in Fig. 10.37a [153]. The energy levels of BPQDs are well suited to act as HTM as shown in Fig. 10.37b. They have reported improvement in efficiency from 14.1% for the device without BPQDs to 16.69% with BPQDs. The J–V characteristics of this device are shown in Fig. 10.37c.

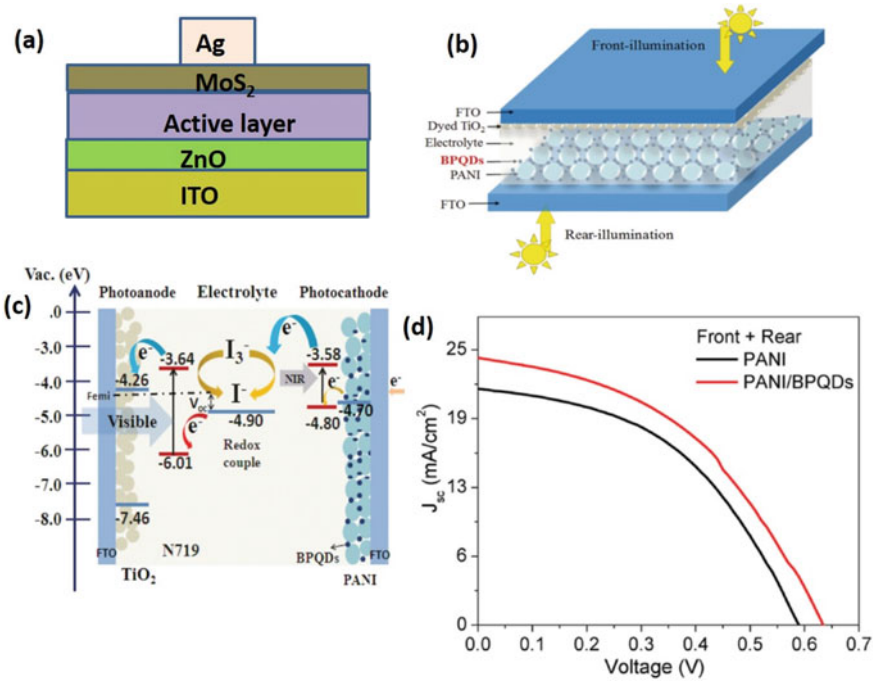

Fig. 10.36 **a** Device structure using MoS_2 HTL, **b** Device structure of a BPQD/PANI-based DSSC and **c** corresponding energy level diagram and **d** *J*–*V* characteristics of this device under illumination. **b**, **c** and **d** Yang, Y.; Gao, J.; Zhang, Z.; Xiao,S.; Xie, H.; Sun, Z.; Wang, J.H.; Zhou, C. H.; Wang, Y. W.; Guo, X. Y.; Chu, P.K. and Yu, X. F. Black Phosphorus Based Photocathodes in Wide band Bifacial Dye-Sensitized Solar Cells. Adv. Mater. 2016. 28. 8937. Copyright Wiley–VCH Verlag GmBH & Co. KGaA. Reproduced with permission).

10.5.3 Supercapacitors

Supercapacitors, basically electrochemical capacitors, have caught the global attention as potential energy storage and power devices, especially in smartphones, hybrid electric vehicles, smart grids, etc.[32]. They have earned this attention due to the high power density, fast charging/discharging and excellent stability in the performance over increased number of cycles they offer. Here, the solvated ions from the electrolyte accumulate at the electrode–electrolyte interface due to polarisation, forming a double electric layer resulting in the electric double layer capacitance (EDLC). The absence of chemical reactions unlike battery leads to the fast charging/discharging cycles. A typical assembly of a two-electrode symmetric supercapacitor is shown in Fig. 10.38a. High conductivity and large surface area are the basic requirements of the electrode materials in a supercapacitor to deliver best performance. Due to the capacity to offer large surface to volume ratio and to exhibit excellent electrochemical properties, 2D materials are the best candidates to be used as active electrodes

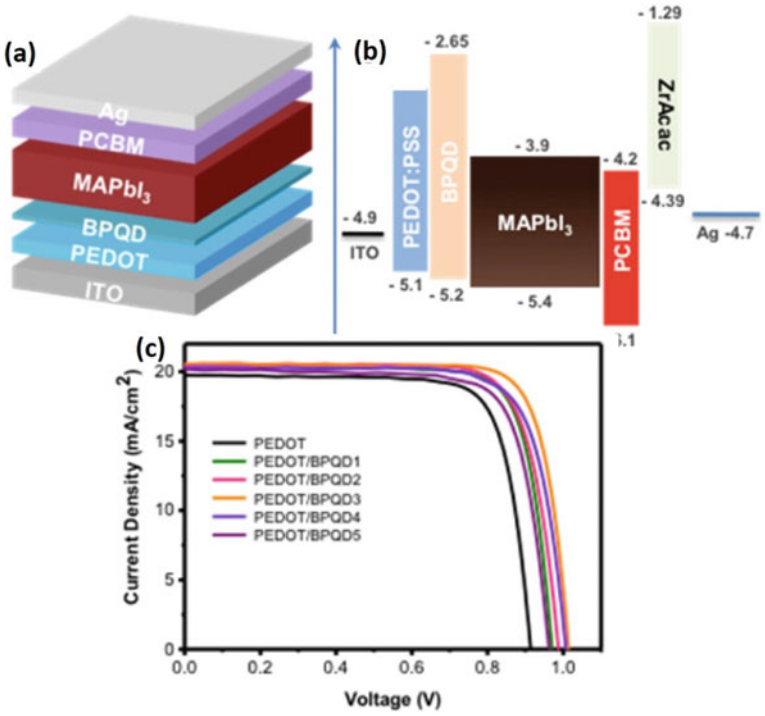

Fig. 10.37 **a** Device structure of BPQD HTM-based perovskite solar cell, **b** corresponding energy level diagram and **c** J–V characteristics of this device ("Reprinted (adapted) with permission from (J. Phys. Chem. Lett., 2017, 8, 591). Copyright (2018) American Chemical Society")

in supercapacitors. Discovery of graphene, fulfilling these basic requirements, has turned the global interest to replace carbon-based electrode materials with graphene. The advantage offered by the 2D nature of graphene is that the electrolyte can seep into the gap between the layers due to the weak van der Waals forces, thereby coming into contact with the entire surface area of each layer. This results in enormous EDLC, thereby improving the performance of the devices. A number of studies are reported in this direction with good success [154–156].

Yang et al. have demonstrated a graphene-based supercapacitor with specific capacitance of around 300 F/g and 100 F/g using pure ionic liquid 1-ethyl-3-methylimidazolium tetrafluoroborate ($EMIMBF_4$) and 1.0 M $LiPF_6$ electrolytes, respectively, at current densities of around 1A/g [154]. Maiti et al. have prepared holey graphene aerogel, which is shown in Fig. 10.38b and developed two electrode symmetric supercapacitors using these aerogels as electrodes [155]. They have reported an area capacity of about 35 mF/cm^2 at a discharging current rate of 10 mA/cm^2. Though specific capacitance for supercapacitors is generally provided as a gravimetric capacitance (measure of Farads per unit gram (F/g)), Maiti et al. have used the parameter F/cm^2 to represent the areal capacitance, as thin sheets are

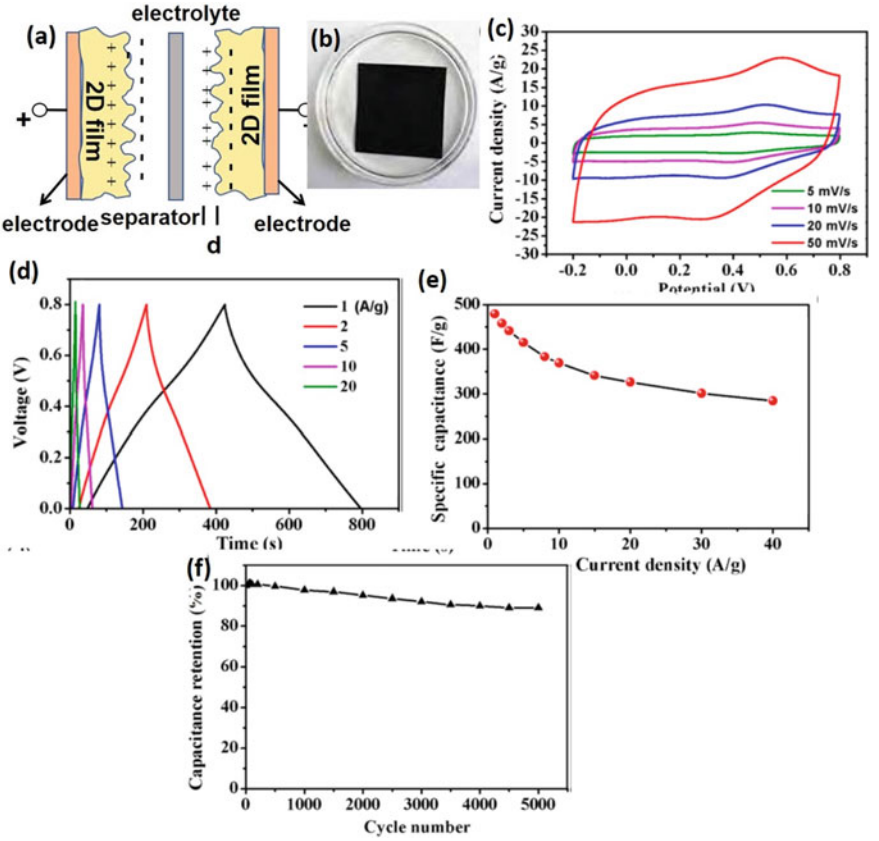

Fig. 10.38 **a** Supercapacitor device assembly, **b** graphene gel (Maiti, U. N.; Lim, J.; Lee, K. E.; Lee, W. J. and Kim, S. O. Three-Dimensional Shape Engineered, Interfacial Gelation of Reduced Graphene Oxide for High Rate, Large Capacity Supercapacitors. Adv. Mater. 2014. *26*. 615. Copyright Wiley–VCH Verlag GmbH & Co. KGaA. Reproduced with permission), **c** CV curves, **d** charge–discharge cycles, **e** specific capacitance as a function of discharging current and **f** capacitance retention curve of graphene-based supercapacitor. **c**–**f** ("Reprinted (adapted) with permission from (ACS Appl. Mater. Interfaces, 2017, 9, 22,588). Copyright (2018) American Chemical Society")

being used. Recently, Zhao et al. have reported a RGO-based supercapacitor with improved gravimetric specific capacitance of around 450 F/g [156]. Here they have prepared a mixture of an aqueous dispersion of liquid crystalline GO (LC-GO) with salt and urea and coated the mixture on Au-coated plastic substrates (current collectors) by doctor blade method. After drying, the solidified GO sheets, mediated by NaCl and urea are hydrothermally reduced forming nanoporous and rumpling N-doped RGO sheets. They have reported a high volumetric specific capacitance of 693 F/cm^3 at 1A/g in 1 M H_2SO_4 in a symmetric cell configuration. The typical CV,

charge/discharge cycles, specific capacitance as a function of current density and the retention cycles are shown in Fig. 10.38c–f.

Re-aggregation of the graphene nanosheets has been observed to be a serious bottleneck affecting the performance of the supercapcitors, resulting in a lesser specific capacitance than that is predicted theoretically. Attempts to functionalise graphene sheets to widen the interlayer gap and minimise re-aggregation have also resulted in conductivity loss. There are many other layered materials being attempted as the electrode materials. These materials are either used individually or in combination with graphene and/or other 2D materials like MoS_2, VS_2 etc. and many conducting polymers [157, 158]. MXenes are now considered as better replacements for graphene due to their high conductivity, in-spite of having functional groups attached to them during their synthesis. Recently, Yang et al. have attempted a composite of MXene with RGO and have reported an improved areal capacitance of around 800 F/cm^2 at a scan rate of 10 mV/s [159].

Apart from these applications, 2D materials are proving to be potential candidates for batteries, piezogenerators, thermoelectric devices, gas sensing, etc.[160–163]. Rao group and others have demonstrated their significant contributions in water splitting devices [164–167].

10.6 Conclusions

The production of nanolayers of some of the graphene analogous materials through different routes has been discussed. Though mechanical exfoliation is a simple process requiring simply a scotch tape, it suffers from limitations in reproducibility and scalability. Liquid phase exfoliation (LPE) has been shown to be a better alternative, which can result in yields as high as 1–40 mg/mL depending on the bulk material. Various solvents with high boiling points have been found to result in good yield. The green routes for the production of nanolayers, by using a simple mixture of water and alcohol or by using supercritical CO_2 have been an attractive alternative as it is environment friendly and cost-effective. Lithium intercalation or other alkali metal intercalations have been found to result in high yield but they suffer from the change in the phase of the flakes and the restacking of the same. Surfactant intercalation has been shown to offer stable dispersion of nanoflakes, preventing restacking of the same. Optical microscopy, AFM and vibrational techniques like Raman spectroscopy have been demonstrated to be useful tools for identifying layer thickness and change in electronic properties. Though LPE method results in scalable production, they generally suffer from some of the disadvantages, leading to defective layers and limitations in their size. They also result in large size distributions, which can be solved to some extent by carrying our size selected exfoliation with centrifugation at different steps. The layer thickness-dependent electronic properties demand strong control over the thickness for practical applications of the nanolayers. This is a difficult task to achieve in both mechanical as well as liquid exfoliation methods. Therefore, further improvements are being attempted to improve LPE to increase

the yield in order to produce to industrial scale (typically in the kilograms range) in a cost-effective and environment friendly manner. The method also needs to be extended to a wider range of layered materials. The resultant nanoflakes should be adaptable to the usage in device applications.

Liquid exfoliation could prove useful for chemical functionalisation of various materials that could enhance its applications in gas sensing, targeted drug delivery etc. Their other diverse range of properties makes them well suited for applications in electronics, photonics, energy harvesting and storage applications like thermoelectric, piezoelectric and photovoltaic devices, batteries, supercapacitors, etc. They can be envisaged as strong candidates to take over the nanotechnology world completely in future. The fascinating behaviour and the rich physics offered by these 2D materials as well as the relatively simpler methods of production motivate the research community to look for further new and interesting layered materials.

Acknowledgements The authors wish to thank Dr. Rekha Rao from Solid State Physics Division (SSPD), Bhabha Atomic Research Centre (BARC), Mumbai, for constant discussion and experiments/investigations on 2D materials. The authors would also like to thank Dr. Uday Narain Maity, Asst. Prof, IIT Guwahati, for valuable information on MXenes and supercapacitors. The authors would like to thank Mr. Ram Ashish Yadav, Homi Bhabha National Institute (HBNI) and SSPD, BARC, for helping in making figures and the references list.

References

1. Liu X, Qu D, Li HM, Moon I, Ahmed F, Kim C, Lee M, Choi Y, Cho JH, Hone JC, Yoo WJ (2017) Modulation of Quantum Tunnelling via a Vertical Two-Dimensional Black Phosphorus and Molybdenum Disulphide p−n Junction. ACS Nano 11, 9143–9150
2. Bhimanapati RG, Lin Z, Meunier V, Jung Y, Cha J, Das S, Xiao D, Son Y, Strano MS, Cooper VR, Liang L, Louie SG, Ringe E, Zhou W, Kim SS, Naik RR, Sumpter BG, Terrones H, Xia F, Wang Y, Zhu Z, Akinwande D, Alem N, Schuller JA, Schaak RE, Terrones M, Robinson JA (2015) Recent Advances in Two-Dimensional Materials beyond Graphene. ACS Nano 9:11509–11539
3. Novoselov KS, Geim AK, Morozov SV, Jiang D, Zhang Y, Dubonos SV, Grigorieva IV, Firsov A (2004) Electric Field Effect in Atomically Thin Carbon Films. Science 306:666–669
4. Tao H, Zhang Y, Gao Y, Sun Z, Yan C, Texter J (2017) Scalable exfoliation and dispersion of two-dimensional materials – an update. Phys Chem Chem Phys 19:921–960
5. Balendhran, S.; Walia S.; Nili, H.; Ou, J. Z.; Zhuiykov, S.; Kaner, R. B.; Sriram, S.; Bhaskaran, M. and Kalantar-zadeh, K. Two-Dimensional Molybdenum Trioxide and
6. Dichalcogenides. *Adv. Funct. Mater*., *2013, 23, 3952–3970.*
7. Wang G, Bao L, Pei T, Ma R, Zhang YY, Sun L, Zhang G, Yang H, Li J, Gu C, Du S, Pantelides ST, Schrimpf RD, Gao HJ (2016) Introduction of Interfacial Charges to Black Phosphorus for a Family of Planar Devices. Nano Lett 16:6870–6878
8. Nicolosi, V.; Chhowalla, M.; Kanatzidis, M. G.; Strano, M. S.; Coleman, J. N. Liquid Exfoliation of Layered Materials. *Science, 2013, 340, 1226419(1–18).*
9. Boukhvalov, D. W.; Katsnelson , M. I. and Lichtenstein, A. I. Hydrogen on graphene: Electronic structure, total energy, structural distortions and magnetism from first-principles calculations. *Phys. Rev. B*, *2008, 77, 035427(1–7).*

10. Wang J, Yao Q, Huang CW, Zou X, Liao L, Chen S, Fan Z, Zhang K, Wu W, Xiao X, Jiang C, Wu WW (2016) High Mobility MoS_2 Transistor with Low Schottky Barrier Contact by Using Atomic Thick h-BN as a Tunneling Layer. Adv Mater 28:8302–8308
11. Radisavljevic, B.; Whitwick, M. B. and Kis, A. Small-signal amplifier based on single-layer MoS_2. *Appl. Phys. Lett*., *2012, 101, 043103(1–4).*
12. Zhang, Y.; Rubio, A. and Lay, G. L. Emergent elemental two-dimensional materials beyond graphene. *J. Phys. D: Appl. Phys.2017, 50, 053004(1–11).*
13. Wang QH, Zadeh KK, Kis A, Coleman JN, Strano MS (2012) Electronics and optoelectronics of two-dimensional transition metal dichalcogenides. Nat Nanotechnol 7:699–712
14. Mas-Balleste R, Gomez-Navarro C, Gomez-Herrero J, Zamora F (2011) 2D materials: to graphene and beyond. Nanoscale 3:20–30
15. Miro´, P.; Audiffred, M. and Heine, T. An atlas of two-dimensional materials. *Chem. Soc. Rev., 2014, 43, 6537–6554.*
16. Butler SZ, Hollen SM, Cao L, Yi Cui Y, Gupta JA, Gutierrez HR, Heinz TF, Hong SS, Huang J, Ismach AF, Johnston-Halperin E, Kuno M, Plashnitsa VV, Robinson RD, Ruoff RS, Salahuddin S, Shan J, Shi L, Spencer MG, Terrones M, Windl W, Goldberger JE (2013) Progress, Challenges, and Opportunities in Two-Dimensional Materials Beyond Graphene. ACS Nano 7:2898–2926
17. Liu, J.; Cao, H.; Jiang, B.; Xue, Y. and Fu. L. Newborn 2D materials for flexible energy conversion and storage. *Sci China Mater 2016, 59(6), 459–474.*
18. Shi L, Zhao T (2017) Recent advances in inorganic 2D materials and their applications in lithium and sodium batteries. J. Mater. Chem. A 5:3735–3758
19. Kumar, A. and Ahluwalia, P. K. Electronic structure of transition metal dichalcogenides
20. monolayers 1H-MX_2 (M = Mo, W; X = S, Se, Te) from ab-initio theory: new direct band gap semiconductors. *Eur. Phys. J. B 2012, 85, 186(1–7).*
21. Chhowalla M, Shin HS, Eda G, Li LJ, Loh KP, Zhang H (2013) The chemistry of two-dimensional layered transition metal dichalcogenide nanosheets. Nat Chem 5:263–275
22. Wang S, Sawada H, Allen CS, Kirkland AI, Warner JH (2017) Orientation dependent interlayer stacking structure in bilayer MoS_2 domains. Nanoscale 9:13060–13068
23. Liu Q, Li L, Li Y, Gao Z, Chen Z, Lu J (2012) Tuning Electronic Structure of Bilayer MoS_2 by Vertical Electric Field: A First-Principles Investigation. J Phys Chem C 116:21556–21562
24. He, J.; Hummer, K. and Franchini, C. Stacking effects on the electronic and optical properties of bilayer transition metal dichalcogenides MoS_2, $MoSe_2$, WS_2, and WSe_2. *Phys. Rev.* B, *2014, 89, 075409(1–11).*
25. Peng, T.; Huai-Hong, G.; Teng, Y.; and Zhi-Dong, Z. Stacking stability of MoS_2 bilayer: An *abinitio* study. *Chin. Phys. B 2014, 23, 106801(1–6).*
26. Liu, K.; Zhang, L.; Cao, T.; Jin, C.; Qiu, D.; Zhou, Q.; Alex Zettl, A.; Yang, P.; Louie, S. G. and Wang, F. Evolution of interlayer coupling in twisted molybdenum disulfide bilayers. *Nature Communications*, *2014, 5:4966/DOI:*https://doi.org/10.1038/ncommns5966(1-6*).*
27. Xia M, Li B, Yin K, Capellini G, Niu G, Gong Y, Wu Zhou W, Ajayan PM, Xie Y (2015) Spectroscopic Signatures of AA' and AB Stacking of Chemical Vapor Deposited Bilayer MoS_2. ACS Nano 9:12246–12254
28. Voiry D, Mohite A, Chhowalla M (2015) Phase engineering of transition metal dichalcogenides. Chem Soc Rev 44:2702–2712
29. Ly TH, Zhao J, Kim H, Han GH, Nam H, Lee YH (2016) Vertically Conductive MoS_2 Spiral Pyramid. Adv Mater 28:7723–7728
30. Guo, Y.; Wei, Y.; Li, H. and Zhai, T. Layer Structured Materials for Advanced Energy Storage and Conversion. *Small 2017, 1701649(1–22).*
31. Wang X, Shen X, Wang Z, Yu R, Chen L (2014) Atomic-Scale Clarification of Structural Transition of MoS_2 upon Sodium Intercalation. ACS Nano 8:11394–11400
32. Zhao W, Ghorannevis Z, Amara AK, Pang JR, Toh M, Zhang X, Kloc C, Tan PH, Eda G (2013) Lattice dynamics in mono- and few-layer sheets of WS_2 and WSe_2. Nanoscale 5:9677–9683
33. Jang, H.; Ryder, C. R.; Wood, J. D.; Hersam, M. C. and Cahill, D. G. 3D Anisotropic Thermal Conductivity of Exfoliated Rhenium Disulfide. *Adv. Mater. 2017, 29, 1700650(1–6).*

34. Late DJ, Rout DS, Chakravarty D, Ratha S (2015) Emerging energy applications of two-dimensional layered materials. Can Chem Trans 3:118–157
35. Kang Y, Han S (2017) An origin of unintentional doping in transition metal dichalcogenides: the role of hydrogen impurities. Nanoscale 9:4265–4271
36. Zhao W, Ghorannevis Z, Chu L, Toh M, Kloc C, Tan P-H, Eda G (2013) Evolution of electronic structure in atomically thin sheets of WS_2 and WSe_2. ACS Nano 7:791–797
37. Splendiani A, Sun L, Zhang Y, Li T, Kim J, Chim CY, Galli G, Wang F (2010) Emerging Photoluminescence in Monolayer MoS_2. Nano Lett 10:1271–1275
38. Tongay, S.; Sahin, H.; Ko, C.; Luce, A.; Fan, W.; Liu, K.; Zhou, J. Huang, Y. S.; Ho, C. H. Yan, J.; Ogletree, D. F.; Aloni, S.; Ji, J. Shushen Li, S.; Li, J.; Peeters, F. M. and Wu, J. . Monolayer behaviour in bulk ReS_2 due to electronic and vibrational decoupling. *Nature Communications*, *2014, 5,3252(1–13).*
39. Rahman, M.; Davey, K. and Qiao, S. Z. Advent of 2D Rhenium Disulfide (ReS_2): Fundamentals to Applications. *Adv. Funct. Mater. 2017, 27, 1606129(1–21).*
40. He R, Yan JA, Yin Z, Ye Z, Ye G, Cheng J, Li J, Lui CH (2016) Coupling and Stacking Order of ReS_2 Atomic Layers Revealed by Ultralow-Frequency Raman Spectroscopy. Nano Lett 16:1404–1409
41. Gehlmann, M.; Aguilera, I.; Bihlmayer, G.; Nemšák, S.; Nagler, P.; Gospodarič, P.; Zamborlini, G.; Eschbach, M.; Feyer, V.; Kronast, F.; czak, E. M.; Korn, T.; Plucinski, L.; Schüller, C.; Blügel, S. and Schneider, C. M. Direct Observation of the Band Gap Transition in Atomically Thin ReS_2. *Nano Lett. 2017, 17, 5187−5192.*
42. Webb, J. L.; Hart, L. S.; Wolverson, D.; Chen, C.; Avila, J. and Asensio, M. C. Electronic band structure of ReS_2 by high-resolution angle-resolved photoemission spectroscopy. *Phys. Rev. B, 2017, 96, 115205 (1–8).*
43. Arora A, Noky J, Drüppel M, Jariwala B, Deilmann T, Schneider R, Schmidt R, Pozo Zamudio OD, Stiehm T, Bhattacharya A, Krüger P, Vasconcellos SMD, Rohlfing M, Bratschitsch R (2017) Highly Anisotropic in-Plane Excitons in Atomically Thin and Bulk like 1T′-$ReSe_2$. Nano Lett 17:3202–3207
44. Chenet DA, Aslan OB, Huang PY, van der Fan C, Zande AM, Heinz TF, T. F. and Hone, J. C. (2015) In-Plane Anisotropy in Mono- and Few-Layer ReS_2 Probed by Raman Spectroscopy and Scanning Transmission Electron Microscopy. Nano Lett 15:5667–5672
45. Yang Y, Gao J, Zhang Z, Xiao S, Xie H, Sun Z, Wang JH, Zhou CH, Wang YW, Guo XY, Chu PK, Yu XF (2016) Black Phosphorus Based Photocathodes in Wide band Bifacial Dye-Sensitized Solar Cells. Adv Mater 28:8937–8944
46. Pang, J.; Bachmatiuk, A.; Yin, Y.; Trzebicka, B.; Zhao, L.; Fu, L.; Mendes, R. G.; Gemming, T.; Liu, Z. and Rummeli, M. H. Applications of Phosphorene and Black Phosphorus in Energy Conversion and Storage Devices. *Adv. Energy Mater. 2017, 1702093(1–43).*
47. Cai, Y.; Zhang, G. And Zhang, Y. W. Layer-dependent Band Alignment and Work Function of Few-Layer Phosphorene. *Scientific Reports*, *2014, 4, 6677(1–6).*
48. Ji, J.; Song, X.; Liu, J.; Yan, Z.; Huo, C.; Zhang, S.; Su, M. Liao, L.;Wang, W.; Ni, Z.; Hao,Y and Zeng, H. Two-dimensional antimonene single crystals grown by van der Waals epitaxy. *Nature Communications*, 2016, 7:13352(1–9).
49. Zhang S, Zhou W, Ma Y, Ji J, Cai B, Yang SA, Zhu Z, Chen Z, Zeng H (2017) Antimonene Oxides: Emerging Tunable Direct Bandgap Semiconductor and Novel Topological Insulator. Nano Lett 17:3434–3440
50. Deschênes, M. F..; Waller, O.Menteş T. O.; Locatelli, A.; Mukherjee, S.; Genuzio, F.; Levesque, P. L.; Hébert, A.; Martel, R and Moutanabbir, O. Synthesis of Antimonene on Germanium. *Nano Lett.2017, 17, 4970−4975.*
51. Alhabeb M, Maleski K, Anasori B, Lelyukh P, Clark L, Sin S, Gogotsi Y (2017) Guidelines for Synthesis and Processing of Two-Dimensional Titanium Carbide ($Ti3C_2T_x$ MXene). Chem Mater 29:7633–7644
52. Ding L, Wei Y, Wang Y, Chen H, Caro J, Wang H (2017) A Two-Dimensional Lamellar Membrane: MXene Nanosheet Stacks. Angew Chem 129:1–6

53. Niu L, Coleman JN, Zhang H, Shin H, Chhowalla M, Zheng Z (2016) Production of Two-Dimensional Nanomaterials via Liquid-Based Direct Exfoliation. Small 12(3):272–293
54. Yang Q, Xu Z, Fang B, Huang T, Chen CS, H., Liu, Y., Gopalsamy, K., Gao, W. and Gao, C. (2017) MXene/graphene hybrid fibers for high performance flexible supercapacitors. J. Mater. Chem. A 5:22113–22119
55. Maleski K, Mochalin VN, Gogotsi Y (2017) Dispersions of Two-Dimensional Titanium Carbide MXene in Organic Solvents. Chem Mater 29:1632–1640
56. Huang Y, Sutter E, Shi NN, Zheng J, Yang T, Englund D, Gao HJ, Sutter P (2015) Reliable Exfoliation of Large-Area High-Quality Flakes of Graphene and Other Two-Dimensional Materials. ACS Nano 9:10612–10620
57. Li H, Lu G, Wang Y, Yin Z, Cong C, He Q, Wang L, Ding F, Yu T, Zhang HP (2013) Mechanical Exfoliation and Characterization of Single- and Few-Layer Nanosheets of WSe_2, TaS_2 and $TaSe_2$. Small 9(11):1974–1981
58. Radisavljevic B, Radenovic A, Brivio J, Giacometti V, Kis A (2011) Single-layer MoS_2 Transistors. Nat Nanotechnol 6:147–150
59. Ottaviano, L.; Palleschi, S.; Perrozzi, F.; D'Olimpio, G.; Priante, F.; Donarelli, M.; Benass, P.; Nardone, M.; Gonchigsuren, M.; Gombosuren, M.; Lucia, A.; Moccia, G. and Cacioppo, O. A. Mechanical exfoliation and layer number identification of MoS_2 revisited. *2D Mater., 2017, 4, 045013(1–15).*
60. Du Y, Liu H, Deng Y, Ye PD (2014) Device Perspective for Black Phosphorus Field-Effect Transistors: Contact Resistance, Ambipolar Behavior, and Scaling. ACS Nano 8:10035–10040
61. Li, H.; Zhang, Q.; Yap, C. C. R.; Beng Kang Tay, Edwin, T. H. T Olivier, A and Baillargeat, D. From Bulk to Monolayer MoS_2: Evolution of Raman Scattering. *Adv. Funct. Mater., 2012, 22, 1385–1390.*
62. Yin Z, Li H, Li H, Jiang L, Shi Y, Sun Y, Lu G, Chen ZQ, X. and Zhang, H. (2012) Single-Layer MoS_2 Phototransistors. ACS Nano 6:74–80
63. Late DJ, Huang YK, Liu B, Acharya J, Shirodkar SN, Luo J, Yan A, Charles D, Waghmare UV, Dravid VP, Rao CNR (2013) Sensing Behavior of Atomically Thin-Layered MoS_2 Transistors. ACS Nano 7:4879–4891
64. Castellanos-Gomez A, Poot M, Steele GA, van der Zant HSJ, Agraït N, Rubio-Bollinger G (2012) Elastic Properties of Freely Suspended MoS_2 Nanosheets. Adv Mater 24:772–775
65. Budania, P.; Baine, P. T.; Montgomery, J. H.; McNeill, D. W. Neil Mitchell, S. J. N.; Modreanu. M. and Hurley, P. K. Comparison between Scotch tape and gel-assisted mechanical exfoliation techniques for preparation of 2D transition metal dichalcogenideflakes, *Micro & Nano Letters, 2017, 12, 970–973.*
66. Desai, S. B.; Madhvapathy, S. R.; Amani, M.; Kiriya, D.; Hettick , M. Tosun, M.; Zhou, Y.; Dubey, M.; Ager III, J. W.; Chrzan, D and Javey, A. Gold-Mediated Exfoliation of Ultralarge Optoelectronically Perfect Monolayers. *Adv. Mater. 2016, 28, 4053–4058.*
67. Zaretski, A. V.; Moetazedi, H.; Kong ,C.;, Sawyer, E. J.; Savagatrup, S.; Valle, E.; O'Connor, T. F.; Printz, A. D. and Lipomi, D. J. Metal-assisted exfoliation (MAE): green, roll to-roll compatible method for transferring graphene to flexible substrates. *Nanotechnology 2015, 26, 045301(1–7).*
68. Lewis EA, Brent JR, Derby B, Haigh SJ, Lewis DJ (2017) Solution processing of two-dimensional black phosphorus. Chem Commun 53:1445–1458
69. Papageorgiou DG, Kinloch IA, Young RJ (2017) Mechanical properties of graphene and graphene-based nano composites. Prog Mater Sci 90:75–127
70. Shen J, He Y, Wu J, Gao C, Keyshar K, Zhang X, Yang Y, Ye M, Vajtai R, Lou J, Ajayan PM (2015) Liquid Phase Exfoliation of Two-Dimensional Materials by Directly Probing and Matching Surface Tension Components. Nano Lett 15:5449–5454
71. Bang, B. J. H. and Suslick, K. S. Applications of Ultrasound to the Synthesis of
72. Materials N (2010) Adv Mater 22:1039–1059
73. Suslick, K. S. Applications of Ultrasound to Materials Chemistry. *MRS Bulletin, April* 1995.
74. Štengl, V.; Henych, H.; Slušná, M. and Ecorchard, P. Ultrasound exfoliation of inorganic analogues of Graphene. *Nanoscale Research Letters 2014, 9:167(1–14).*

75. Hummers JR, W. S and Offema, R. E. Preparation of Graphitic Oxide. *Contribution from the baroid division, National Lead Company.*
76. Hernandez, Y.; Nicolosi, V.; Lotya, M.; Blighe, F. M.; Zhenyu Sun, Z.; De, S.; McGovern, I. T.; Holland, B.; Byrne, M.; Gun'ko, Y. K.; John, J. Boland, J. J.; Niraj, P.; Duesberg, G.; Krishnamurthy, S.; Goodhue, R.; Hutchison, J.; Scardeci, V.; Ferrari, A. C and Coleman J. N. High-yield production of graphene by liquid-phase exfoliation of graphite. *Nature Nanotechnology, 2008, 3, 563–568.*
77. Hernandez Y, Lotya M, Rickard D, Bergin SD, Coleman JN (2010) Measurement of multicomponent solubility parameters for graphene facilitates solvent discovery. Langmuir 26:3208–3213
78. Coleman JN (2013) Liquid Exfoliation of Defect-Free Graphene. Accounts Chemical Research 46:14–22
79. Bergin SD, Sun Z, Rickard D, Streich PV, Hamilton JP, Coleman JN (2009) Multicomponent Solubility Parameters for Single-Walled Carbon Nanotube Solvent Mixtures. ACS Nano 3:2340–2350
80. Qiao W, Yan S, He X, Song X, Li Z, Zhang X, Zhong W, Du Y (2014) Effects of ultrasonic cavitation intensity on the efficient liquid-exfoliation of MoS_2 nanosheets. RSC Adv 4:50981–50987
81. Khan U, O'Neill A, Porwal H, May P, Nawaz K, Coleman JN (2012) Size selection of dispersed, exfoliated graphene flakes by controlled centrifugation. CA R B O N 5:470–475
82. O'Neill A, Khan U, Coleman JN (2012) Preparation of High Concentration Dispersions of Exfoliated MoS_2 with Increased Flake Size. Chem Mater 24:2414–2421
83. Giordani, S.; Bergin, S. D.; Nicolosi, V.; Lebedkin, S.;. Kappes, M. M.; Blau, W. J.and Coleman, J. N. Debundling of Single-Walled Nanotubes by Dilution: Observation of Large Populations of Individual Nanotubes in Amide Solvent Dispersions. *J. Phys. Chem. B 2006, 110, 15708–15718.*
84. Bergin, S. D.; Nicolosi, V.; Giordani, S.; Gromard, A. D.; Carpenter, L.; Blau, W. J. and Coleman, J. N. Exfoliation in ecstasy: liquid crystal formation and concentration-dependent debundling observed for single-wall nanotubes dispersed in the liquid drug γ –butyrolactone. *Nanotechnology 2007, 18, 455705(1–10).*
85. Lee K, Kim HY, Lotya M, Coleman JN, Kim GT, Duesberg GS (2011) Electrical characteristics of molybdenum disulphide flakes produced by liquid exfoliation. Adv Mater 23:4178–4182
86. Bourlinos, A. B.; Georgakilas, V.; Zboril, R.; Steriotis, T.A. and Stubos, A. K. Liquid-Phase Exfoliation of Graphite Towards Solubilized Graphenes. *Small 2009, 5, No, 1841–1845.*
87. Hanlon, D.; Backes, C.; Doherty, E.; Cucinotta, C. S.; Berner, N. C.; Boland, C.; Lee, K.; Harvey, A.; Lynch, P.; Gholamvand, Z.; Zhang, S.; Wang, K.; Moynihan, G.; Pokle, A.; Ramasse, Q. M.; McEvoy, N.; Blau, W. J.; Wang, J.; Abellan, G.; Hauke, F.; Hirsch, A.; Sanvito, S.; O'Regan, D. D.; Duesberg, G. S.; Nicolosi, V. and Coleman, J. N., Liquid exfoliation of solvent-stabilized few-layer black phosphorous for applications beyond electronics, *Nature Communications, 6:8563/DOI:10:1038/ncommns9563*
88. Kang J, Wood JD, Wells SA, Lee JH, Liu X, Chen KS, Hersam MC (2015) Solvent Exfoliation of Electronic-Grade, Two-Dimensional Black Phosphorus. ACS Nano 9:3596–3604
89. Ren, X.; Li, Z.; Huang, Z.; Sang, D.; Qiao, H.; Qi, X.; Li, J.; Zhong, J. and Zhang, H. Environmentally Robust Black Phosphorus Nanosheets in Solution: Application for Self-Powered Photodetector. *Adv. Funct. Mater., 2017, 27, 16068349(1–8).*
90. O'Neill A, Khan U, Nirmalraj PN, Boland J, Coleman JN (2011) Graphene Dispersion and Exfoliation in Low Boiling Point Solvents. J Phys Chem C 115:5422–5428
91. Choi, E. Y.; Choi, W. S.; Young Boo Lee, Y. B. and Noh, Y. Y. Production of graphene by exfoliation of graphite in a volatile organic solvent. *Nanotechnology 2011, 22, 365601(1–6).*
92. Zhou KG, Mao NN, Wang HX, Peng Y, Zhang HL (2011) A Mixed-Solvent Strategy for Efficient Exfoliation of Inorganic Graphene Analogues. Angew Chem Int Ed 50:10839–10842
93. Halim U, Zheng CR, Chen Y, Lin Z, Jiang S, Cheng R, Huang Y, Duan X (2013) Nat Commun 4:2213. https://doi.org/10.1038/ncommns3213

94. Yao Y, Tolentino L, Yang Z, Song X, Zhang W, Chen Y, Wong C (2013) High-Concentration Aqueous Dispersions of MoS_2. Adv Funct Mater 23:3577–3583
95. Wang, Y.; Liu, Y.; Zhang, J.; Wu, J.; Xu, H.; Wen, X.; Zhang, X.; Tiwary, C. S.; Wei Yang, Vajtai, R.; Zhang, Y.; Chopra, N.; Odeh, I. N.; Wu,Y and Ajayan, P. M. Cryo-mediated exfoliation and fracturing of layered materials into 2D quantum dots. *Sci. Adv. 2017, 3:e1701500(1–7)*.
96. Serhatkulu GK, Dilek C, Gulari E (2006) Supercritical CO_2 intercalation of layered silicates. J. of Supercritical Fluids 39:264–270
97. Rangappa D, Sone K, Wang M, Gautam UK, Golberg D, Itoh H, Ichihara M, Honma I (2010) Rapid and Direct Conversion of Graphite Crystals into High-Yielding, Good-Quality Graphene by Supercritical Fluid Exfoliation. Chem Eur J 16:6488–6494
98. Pu NW, Wang CA, Sung Y, Liua YM, Ger MD (2009) Production of few-layer graphene by supercritical CO_2 exfoliation of graphite. Mater Lett 63:1987–1989
99. Qi, Y.; Wang, N.; Xu, Q.; Li, H.; Zhou, P.; Lu. X and Zhao, G. A green route to fabricate MoS2 nanosheets in water–ethanol–CO_2. *Chem. Commun., 2015,51, 6658–6868.*
100. Eda G, Yamaguchi H, Voiry D, Fujita T, Chen M, Chhowalla M (2011) Photoluminescence from Chemically Exfoliated MoS_2. Nano Lett 12:5111–5116
101. Liu, Y. D.; Ren, L.; Qi, X.; Yang, L. W.; Hao ,G. L.; Li, J.; Wei, X. L.; J. X. Zhong, J. X. Preparation, characterization and photoelectrochemical property of ultrathin MoS_2 nanosheets via hydrothermal intercalation and exfoliation route. *Journal of Alloys and Compounds 2013,571, 37–42.*
102. Xu BH, Lin BZ, Chen ZZ, Li XL, Wang Q (2009) Preparation and electrical conductivity of polypyrrole/WS_2 layered Nanocomposites. J Colloid Interface Sci 330:220–226
103. Gu X, Cui W, Li H, Wu Z, Zeng Z, Lee ST, Zhang H, Sun B (2013) A Solution-Processed Hole Extraction Layer Made from Ultrathin MoS_2 Nanosheets for Efficient Organic Solar Cells. Adv Energy Mater 3:1262–1268
104. Fan X, Xu P, Zhou D, Sun Y, Li YC, Nguyen MAT, Terrones M, Mallouk TE (2015) Fast and Efficient Preparation of Exfoliated 2H MoS_2 Nanosheets by Sonication-Assisted Lithium Intercalation and Infrared Laser-Induced 1T to 2H Phase Reversion. Nano Lett 15:5956–5960
105. Zheng, J.; Zhang, H.; Dong, S.; Liu, Y.; Nai, C. T.; Shin, H. S.; Jeong, H. Y. Liu ,B. & Loh, K. P. High yield exfoliation of two-dimensional chalcogenides using sodium naphthalenide. *Nature Communications 2014 , 5, 2995(1–7).*
106. Lotya, M.; Hernandez, Y.;, P. J.; Ronan J. Smith, R. J.; Nicolosi, V.; Karlsson, L. S.; Blighe, F. M.; De, S.; Wang, Z.; McGovern, I.T.; Duesberg, G. S. and Coleman, J. N. Liquid Phase Production of Graphene by Exfoliation of Graphite in Surfactant/Water Solutions. *J. Am. Chem. Soc. 2009, 131, 3611–3620.*
107. Kang, J.; Sangwan, V. K.; Wood, J. D. Liu, X.; Balla, I.; Lam, D and Hersam, M. C. Layer-by-Layer Sorting of Rhenium Disulfide via High-Density Isopycnic Density Gradient Ultracentrifugation. *Nano Lett., 2016, 16, 7216−7223.*
108. Smith RJ, King PJ, Lotya M, Wirtz C, Khan U, De S, O'Neill A, Duesberg GS, Grunlan JC, Moriarty G, Chen J, Wang J, Minett AI, Nicolosi V, Coleman J (2011) N. Adv Mater 23:3944–3948
109. Murugan AV, Quintin M, Delville M-H, Campet G, Viswanath AK, Gopinath CS, Vijayamohana K (2006) Synthesis and characterization of organic-inorganic poly(3,4-ethlyenedioxythiophene)/MoS_2 nanocomposite via in situ oxidative polymerization. J Mater Res 21:112–118
110. Bissessur R, Haines RI, Bruning R (2003) Intercalation of tetraazamacrocycles into molybdenum disulfide. J Mater Chem 13:44–49
111. Satheeshkumar, E.; Bandyopadhyay, A.; Sreedhara, M. B.; Pati, S. K.; Rao,C. N. R. and M. Yoshimara, One-step simultaneous ecfoliation and covalent functionalization of MoS_2 by amino acids-induced solution process, ChemNanoMat, https://doi.org/10.1002/cnma.201600363.
112. Wu W, Zhang C, Hou S (2017) Electrochemical exfoliation of graphene and graphene analogous 2D nanosheets. J Mater Sci 52:10649–10660

113. Liu BN, Luo F, Wu H, Liu Y, Zhang C, Chen J (2008) One-Step Ionic-Liquid-Assisted Electrochemical Synthesis of Ionic-Liquid-Functionalized Graphene Sheets Directly from Graphite. Adv Funct Mater 18:1518–1525
114. Lu J, Yang J, Wang J, Lim A, Wang S, Loh KP (2009) One-Pot Synthesis of Fluorescent Carbon Nanoribbons, Nanoparticles, and Graphene by the Exfoliation of Graphite in Ionic Liquids. ACS Nano 3:2367–2375
115. Parvez K, Wu ZS, Li R, Liu X, Graf R, Feng X, Mullen K (2014) Exfoliation of Graphite into Graphene in Aqueous Solutions of Inorganic Salts. J Am Chem Soc 136:6083–6091
116. Zeng Z, Sun T, Zhu J, Huang X, Yin Z, Lu G, Fan Z, Yan Q, Hng HH, Zhang H (2012) An Effective Method for the Fabrication of Few-Layer-Thick Inorganic Nanosheets. Angew Chem Int Ed 51:1–6
117. Ejigu, A.; Kinloch, I. A.; Prestat, E and Robert A. W. Dryfe, R .A.W. A simple electrochemical route to metallic phase trilayer MoS_2: evaluation as electrocatalysts and supercapacitors. *J. Mater. Chem. A, 2017, 5, 11316–11330.*
118. Liu N, Kim P, Kim JH, Ye JH, Kim S, Lee CJ (2014) Large-Area Atomically Thin MoS_2 Nanosheets Prepared Using Electrochemical Exfoliation. ACS Nano 8:6902–6910
119. Leong SX, Mayorga-Martinez CC, Chia X, Luxa J (2017) Sofer, Z and Pumera, M, 2H $\rightarrow$ 1T Phase Change in Direct Synthesis of WS_2 Nanosheets via Solution-Based Electrochemical Exfoliation and Their Catalytic Properties. ACS Appl Mater Interfaces 9:26350–26356
120. Yao, Y.; Lin, Z.; Li, Z. Xiaojuan Song, X.; Moon, K. S. and Wong, C. Large-scale production of two-dimensional nanosheets. *J. Mater. Chem., 2012, 22, 13494–13499.*
121. Knieke, C.; Berger. A.; Voigt, M.; Taylor, R. N. K.; Jonas Ro¨hrl, J and Peukert, W. Scalable production of graphene sheets by mechanical delamination. *Carbon, 2010, 48, 3196–3204.*
122. Damm C, Nacken TJ, Peukert W (2015) Quantitative evaluation of delamination of graphite by wet media milling. Carbon 81:284–294
123. Lee D, Lee B, Park KH, Ryu HJ, Jeon S, Hong SH (2015) Scalable Exfoliation Process for Highly Soluble Boron nitride Nanoplatelets by Hydroxide-Assisted Ball Milling. Nano Lett 15:1238–1244
124. Nguyen, E. P.; Carey, B. J.; Torben Daeneke, T.; Ou, J. Z. Latham, K.; Zhuiykov, S and Kalantar-zadeh, K. Investigation of Two-Solvent Grinding-Assisted Liquid Phase Exfoliation of Layered MoS_2. *Chem. Mater., 2015, 27, 53−59.*
125. Xu, F.; G,B.; Chen, J.; Xin, L.; Ma, H. Zhu, C.; Xia, W.; Min, H.; Li, Z.; Li, S.; Yu, K.; Wu, L.; Cui,Y.; Sun, L and Zhu, Y. Scalable shear-exfoliation of high-quality phosphorene nanoflakes with reliable electrochemical cycleability in nano batteries. *BNL-112615–2016-JA.*
126. Yuan H, Liu X, Ma L, Gong P, Yang Z, Wang H, Wang J, Yang S (2016) High efficiency shear exfoliation for producing high-quality, few-layered MoS_2 nanosheets in a green ethanol/water system. RSC Adv 6:82763–82773
127. Woomer AH, Farnsworth TW, Wells HuJ, R. A., Donley, C. L. and Warren, S. C. (2015) Phosphorene: Synthesis, Scale-Up, and Quantitative Optical Spectroscopy. ACS Nano 9:8869–8884
128. Rasid, Z. A. M.; Omar, M. F.; Nazeri, M. F. M.; A'ziz, M. A. A. and Szota, M. Low Cost Synthesis Method of Two-Dimensional Titanium Carbide MXene. *IOP Conf. Series: Materials Science and Engineering, 2017, 209, 012001(1–6).*
129. Maleski, K.; Mochalin, V. N. and Yury Gogotsi. Dispersions of Two-Dimensional Titanium Carbide MXene in Organic Solvents. *Chem. Mater., 2017, 29, 1632−1640.*
130. Lee C, Yan H, Brus LE, Heinz TF, T. F., Hone, J. and Ryu, S. (2010) Anomalous Lattice Vibrations of Single and Few-Layer MoS_2. ACS Nano 4:2695–2700
131. Li H, Wu J, Huang X, Lu G, Yang J, Lu X, Xiong Q, Zhang H (2013) Rapid and Reliable Thickness Identification of Two-Dimensional Nanosheets Using Optical Microscopy. ACS Nano 7:10344–10354
132. Benameur, M. M.; Radisavljevic, B.; Heron, J. S.; Sahoo, S.; Berger, H. and Kis, A. Visibility of dichalcogenide nanolayers. *Nanotechnology, 2011, 22. 125706 (1–5).*
133. Molina-S´anchez, A. and Wirtz, L. Phonons in single-layer and few-layer MoS_2 and WS_2. *Phys. Rev. B, 2011, 84, 155413 (1–8).*

134. Li S, Miyazaki H, Song H, Kuramochi H, Nakaharai S, Tsukagoshi K (2012) Quantitative Raman Spectrum and Reliable Thickness Identification for Atomic Layers on Insulating Substrates. ACS Nano 6:7381–7388
135. Berkdemir, A.; Gutie´rrez, H. R.; Botello-Me´ndez, A. R.; Perea-Lo´pez, N.;Elı´as, A. L.; Chen-Ing Chia, Wang, B.; Vincent H. Crespi, V. H.; Lo´pez-Urı´as, F.; Charlier, J. C.; Terrones, H. and Terrones, M. Identification of individual and few layers of WS_2 using Raman Spectroscopy. Scientific Reports 2013, 3, 1755(1–8) .
136. Qiao XF, Jiang-Bin Wu, J. B., Zhou, L., Jingsi Qiao, J., Wei Shi, W., Chen, T., Zhang, X., Zhang, J., Ji, W. and Ping-Heng Tan, P. H. (2016) Polytypism and unexpected strong interlayer coupling in two-dimensional layered ReS_2. Nanoscale 8:8324–8332
137. Mertens, J.; Shi, Y.; Molina-Sanchez, A.; Wirtz, L.; Yang, H. Y. and Baumberg, J.J. Excitons in a mirror: Formation of "optical bilayers" using MoS_2 monolayers on gold substrates. *Appl. Phys. Lett.*, *2014, 104, 191105(1–4).*
138. Qiu, D. Y.; da Jornada, F. H. and Louie, S. G. Optical Spectrum of MoS_2: Many-Body Effects and Diversity of Exciton States. *Phys. Rev. Lett.*, *2013,111, 216805(1–5).*
139. Jia GY, Liu Y, Gong JY, Lei DY, Wang DL, Huang ZX (2016) Excitonic quantum confinement modified optical conductivity of monolayer and few-layered MoS_2. J. Mater. Chem. C 4:8822–8828
140. Li BL, Zou HL, Lu L, Yang Y, Lei JL, Luo HQ, Li NB (2015) Size-Dependent Optical Absorption of Layered MoS_2 and DNA Oligonucleotides Induced Dispersion Behavior for Label-Free Detection of Single-Nucleotide Polymorphism. Adv Funct Mater 25:3541–3550
141. Shinde, S. M.; Dhakal, K. P.; Chen, X.; Yun, W. S.; Lee, J. D.;Kim, H. and Ahn, J. H. Stacking-controllable interlayer coupling and symmetric configuration of multilayered MoS_2. NPG *Asia Materials 2018,10, e468(1–13).*
142. Gopalakrishnan D, Damien D, Shaijumon MM (2014) MoS_2 quantum dot-interspersed exfoliated MoS_2 nanosheets. ACS Nano 8:5297–5303
143. Woomer AH, Farnsworth TW, Hu J, Wells RA, Donley CL, Warren SC (2015) Phosphorene: Synthesis, Scale-Up, and Quantitative Optical Spectroscopy. ACS Nano 9:8869–8884
144. Han Liu, H.; Adam T. Neal, A. T.; Zhu, Z.; Luo, Z.; Xu, X.; Toma´nek, D. and Ye, P. D. Phosphorene: An Unexplored 2D Semiconductor with a High Hole Mobility. *ACS Nano 2013,8,4033–4041.*
145. Akhtar, M.; Anderson, G.; Zhao, R.; Alruqi, A.; Mroczkowska, J. E.; Sumanasekera, G. and Jasinski, J.B. Recent advances in synthesis, properties, and applications of Phosphorene. *npj 2D Materials and Applications 2017, 5(1–13).*
146. Li L, Yu Y, Ye GJ, Ge Q, Ou X, Wu H, Feng D, Chen XH, Zhang Y (2014) Black phosphorus field-effect transistors. Nat Nanotechnol 9:372–377
147. Krasnozhon D, Lembke D, Nyffeler C, Leblebici Y, Kis A (2014) MoS_2 transistors operating at Gigahertz frequencies. Nano Lett 14:5905–5911
148. Karmakar, D.; Halder, R.; N. Padma, N.; Abraham, G.; Vaibhav, K.;Ghosh, M.;Kaur, M.; Bhattacharya, D. and Rao, T. V. C. Optimal electron irradiation as a tool for functionalization of MoS_2: Theoretical and experimental investigation. *J. Appl. physics 2015, 117, 135701 (1–9).*
149. Wang Y, Tong SW, Xu XF, Özyilmaz B, Loh KP (2011) Interface Engineering of Layer-by-Layer Stacked Graphene Anodes for High-Performance Organic Solar Cells. Adv Mater 23:1514–1518
150. Capasso, A.; Matteocci, F.; Najafi, L.; Prato, M.; Buha, J.; Cinà, L.; Pellegrini, V.; Carlo, A. D. and Bonaccorso, F. Few-Layer MoS_2 Flakes as Active Buffer Layer for Stable Perovskite Solar Cells. *Adv. Energy Mater. 2016, 6, 1600920(1–12).*
151. Gu, X.; Cui, W.; Li, H.; Wu, Z.; Zeng, Z,; Lee, S. T,;Zhang, H.and Sun, B. A Solution-Processed Hole Extraction Layer Made from Ultrathin MoS_2 nanosheets for Efficient Organic Solar Cells. *Adv. Energy Mater. 2013, 3, 1262–1268.*
152. Yun J, Noh Y, Lee C, Na S, Lee S, Jo SM, Joh H, Kim DY (2014) Exfoliated and Partially Oxidized MoS_2 Nanosheets by One-Pot Reaction for Efficient and Stable Organic Solar Cells. Small 10:2319–2324

153. Yue G, Zhang W, Wu J, Jiang Q (2013) Glucose aided synthesis of molybdenum sulfide/carbon nanotubes composites as counter electrode for high performance dye-sensitized solar cells. Electrochim Acta 112:655–662
154. Liu CJ, Tai SY, Chou SW, Yu YC, Chang KD, Wang S, Chien FSS, Lin JY, Lin TW (2012) Facile synthesis of MoS_2/graphene nanocomposite with high catalytic activity toward triiodide reduction in dye-sensitized solar cells. J Mater Chem 22:21057–21064
155. Deng Y, Luo Z, Conrad NJ, Liu H, Gong Y, Najmaei S, Ajayan PM, Lou J, Xu X, Ye PD (2014) Black Phosphorus Monolayer MoS_2 van der Waals Heterojunction p-n Diode. ACS Nano 8:8292–8299
156. Chen W, Li K, Wang Y, Feng X, Liao Z, Su Q, Lin X, He Z (2017) Black Phosphorus Quantum Dots for Hole Extraction of Typical Planar Hybrid Perovskite Solar Cells. J Phys Chem Lett 8:591–598
157. Yang, H.; Kannappan, S.; Pandian, A. S.; Jang, J. H.; Lee, Y. S. and Lu, W. Graphene supercapacitor with both high power and energy density. Nanotechnology 2017, 28, 445401 (1–10).
158. Maiti UN, Lim J, Lee KE, Lee WJ, Kim SO (2014) Three-Dimensional Shape Engineered, Interfacial Gelation of Reduced Graphene Oxide for High Rate. Large Capacity Supercapacitors. Adv. Mater. 26:615–619
159. Zhao Y, Liu J, Wang B, Sha J, Li Y, Zheng D, Amjadipour M, MacLeod J, Motta N (2017) Supercapacitor Electrodes with Remarkable Specific Capacitance Converted from Hybrid Graphene Oxide/NaCl/Urea Films. ACS Appl Mater Interfaces 9:22588–22596
160. Marri SR, Ratha S, Rout CS, Behera JN (2017) 3D cuboidal vanadium diselenide embedded reduced graphene oxide hybrid structures with enhanced supercapacitor properties. Chem Commun 53:228–231
161. Sarkar D, Das D, Das S, Kumar A, Patil S, Nanda KK, Sarma DD, Shukla A (2019) Expanding interlayer spacing in MoS_2 for realizing an advanced supercapacitor. ACS, Energy Lett 4:1602–1609
162. Yang Q, Xu Z, Fang B, Huang T, Cai S, Chen H, Liu Y, Gopalsamy K, Gao W, Gao C (2017) MXene/graphene hybrid fibers for high performance flexible supercapacitors. J. Mater. Chem. A 5:22113–22119
163. Cui, C.; Xue, F.; Hu, W-J. and Li, L-J., Two dimensional materials with piezoelectric and ferroelectric functionalities, *npj 2D Materials and Applications*, *2018*, *2:18;doi:*https://doi.org/10.1038/s41699-018-0063-5
164. Kong S, Wu T, Yuan M, Huang Z, Meng Q, Jiang Q, Zhuang W, Jiang P, Bao X (2017) Dramatically enhanced thermoelectric performance of MoS_2 by introducing MoO_2 nanoinclusions. J. Mater. Chem. A 5:2004–2011
165. Goel, N.; Kumar, R.; Jain, S. K.; Rajamani, S.; Roul, B.; Gupta, G.; Kumar, M. and Krupanidhi, S. B. A high performance hydrogen sensor based on a reverse-biased MoS_2/GaN heterojunction, *Nanotechnology, 2019, 30, 314001 (1–10).*
166. Kumar, R.; Kulriya, P. K.; Mishra, M.; Singh, F.; Gupta, G. and Kumar, M., Highly selective and reversible NO_2 gas sensor using vertically aligned MoS_2 flake networks, *Nanotechnology, 2018, 29, 464001 (1–9).*
167. Pramoda K, Ayyub MM, Singh NK, Chhetri M, Gupta U, Soni A, Rao CNR (2018) Covalently bonded MoS_2-Borocarbonitride nanocomposites generated by using surface functionalities on the nanosheets and their remarkable HER activity. J Phys Chem C 122:13376–13384
168. Pramoda K, Gupta U, Chhetri M, Bandyopadhyay A, Pati SK, Rao CNR (2017) Nanocomposites of C_3N_4 with layers of MoS_2 and nitrogenated RGO, obtained by covalent cross-linking; synthesis, characterization, and HER activity. ACS Appl Mater Interfaces 9:10664–10672
169. Huang Y, Sun Y, Zheng X, Aoki T, Pattengale B, Huang J, He X, Bian W, Younan S, Williams N, Hu J (2019) Atomically engineering activation sites onto metallic 1T-MoS_2 catalysts for enhanced electrochemical hydrogen evolution. Nat Commun 10:982, https://doi.org/10.1038/s41467-019-08877-9.
170. Gao MR, Chan MK, Sun Y (2015) Edge-terminated molybdenum disulphide with a 9.4 Å interlayer spacing for electrochemical hydrogen production. Nat Commun 6:7493. https://doi.org/10.1038/ncomms8493.

Chapter 11
Drying of Tiny Colloidal Droplets: A Novel Synthesis Strategy for Nano-structured Micro-granules

Debasis Sen, Jitendra Bahadur, and Avik Das

Abstract Colloids are ubiquitous, and they form an interesting branch of soft-matter science owing to the nature of interactions among the constituent phases. The stability of a colloidal dispersion is governed by various intriguing competitive forces, such as electrostatic, entropic, van der Waals interactions, etc., among its dispersed phases. If continuous medium of colloidal dispersion starts disappearing, e.g. evaporation of water from aqueous colloids, the interaction among the constituent particles gets significantly altered. In fact, the phenomenon of quick evaporation of suspension droplets, known as spray drying, is widely used in several industries including food and pharmaceutical industries. Since last decade, this novel technique has re-embellished itself in nano-science and nano-technology promising ample scope for synthesis of advanced materials. Fast-evaporating tiny colloidal droplets exhibit spectacular behaviour due to sudden transition from liquid to powder state associated with evaporation-induced assembly of the nanostructures. Using such evaporative technique, various hierarchically structured micro/meso/macroporous granules can be synthesized. The quick evaporation of the solvent owing to large available surface area of the atomized droplets, makes the process one-step and energy-efficient. The morphology of the synthesized nano-structured micro-granules can be tuned from spherical to non-spherical, such as doughnut, multi-faceted doughnut, etc. The reason behind such morphological transition is primarily associated with buckling of elastic shell that forms during evaporative assembly. These granules, owing to their characteristic structure and porosity, promise for potential technological applications too. Understanding the mesoscopic structure and correlation among the constituent nanostructures in a granule is indeed crucial. In this regard, small-angle neutron/X-ray scattering and scanning electron microscopy have been found to be effective tools in probing such correlated nano-structured granules. In this chapter, the synthesis strategy of such novel nano-structured micro-granules, their mesoscopic characterization will be elaborated.

D. Sen (✉) · J. Bahadur · A. Das
Solid State Physics Division, Bhabha Atomic Research Centre, Mumbai 400085, India
e-mail: debasis@barc.gov.in

Homi Bhabha National Institute, Anushaktinagar, Mumbai 400094, India

A. K. Tyagi and R. S. Ningthoujam (eds.), *Handbook on Synthesis Strategies for Advanced Materials*, Indian Institute of Metals Series,
https://doi.org/10.1007/978-981-16-1803-1_11

Keywords Evaporation-induced assembly · Colloids · Spray drying · Porous · Micro-granules · SAXS · SANS

11.1 Introduction

Granular materials are ubiquitous in our daily life. Sand is a common example of such naturally occurring material. In general, granular material is defined as a conglomeration of discrete solid particles. They behave in a significantly different way than conventional solids, liquids or gases, which has inspired many to characterize such materials as a new form of matter. Apart from various scientific interests owing to their complex flow properties, these materials play an important role in many industries, such as mining, agriculture, civil engineering, pharmaceutical manufacturing, etc. Often the granular materials that we are regularly habituated are of macroscopic length scale. Since the last couple of decades, much attention has been paid to synthesize granular materials having smaller dimension, e.g. micrometric or sub-micrometric length scale. Of course, one extreme of this field is populated by fascinating field of nanoparticles. Thus, bottom-up approach happens to be more effective compared to top-down approach to realize such micro-granules with nanoparticles as building blocks. It is easily understandable that such nano-structured micro-granules possess several inherent interesting structural features. Due to the presence of constituent nanoparticles, the granules are expected to have large available surface area. Further, the granules are inherently micro/meso porous in nature owing to the formation of the nanoparticle interstices. Such pores facilitate a percolation path for fluid transport through these granules.

Various strategies have been made to realize such nano-structured micro-granules including various low temperature chemical routes [1–4]. However, in many cases, such methods suffer from various issues including up-scalability for laboratory to commercial production, energy efficiency and total time duration of synthesis. Most of these shortcomings regarding the synthesis of such micro-granules could be overcome by following idea from an age-old industrial technique which is known as ‘spray drying’. This technique is well known, particularly in food and pharmaceutical industries, since long time. In this process, powder particles are obtained from drying of atomized droplets of liquid solution. Milk and coffee powder are common examples of spray-dried materials used in everyday life. Since the last decade, this technique has re-embellished itself in the field of nano-science and technology by producing various novel nano-structured micro-granules [5, 6]. The main principle behind this novel one-step technique is based on interlocking of colloidal particles in drying micrometric droplets through evaporation-induced assembly (EIA) owing to the dynamic interplay between several competitive forces arising due to the modification of potential landscape as solvent evaporates. At this juncture, it is worth mentioning that such assembly process is also often seen around us, as in the case of formation of ring when a drop of coffee gets dried [7] in a cup. Unlike drying

of bulk suspension, evaporation of solvent in spray drying becomes more energy-efficient owing to availability of large surface area of the atomized droplets. However, simultaneous involvement of several dynamic physicochemical parameters, such as volume fraction [8], interparticle interaction [9, 10], diffusion of the particles [11, 12] in the drying droplet, hydrodynamic effects, etc., impose a challenge to decipher the exact role of individual parameter in order to tune the granule morphology and interparticle correlation in the granules.

11.2 Synthesis of Micro-granules by Spray Drying

In a practical situation, such evaporation-induced assembly is achieved through usage of a spray dryer. '*Spray*' and '*Drying*', these two words together simply define the one-step facile process involving a phase separation of colloidal suspension from its solvent and interlocking of the dispersed phase through drying of sprayed liquid droplets into a hot chamber associated with air suction. Figure 11.1 depicts the schematic diagram of the different components of a typical spray dryer. A liquid stream of colloidal suspension is fed by peristaltic/syringe pump to an atomizer, which atomizes the feed solution into tiny droplets. The transformation of bulk

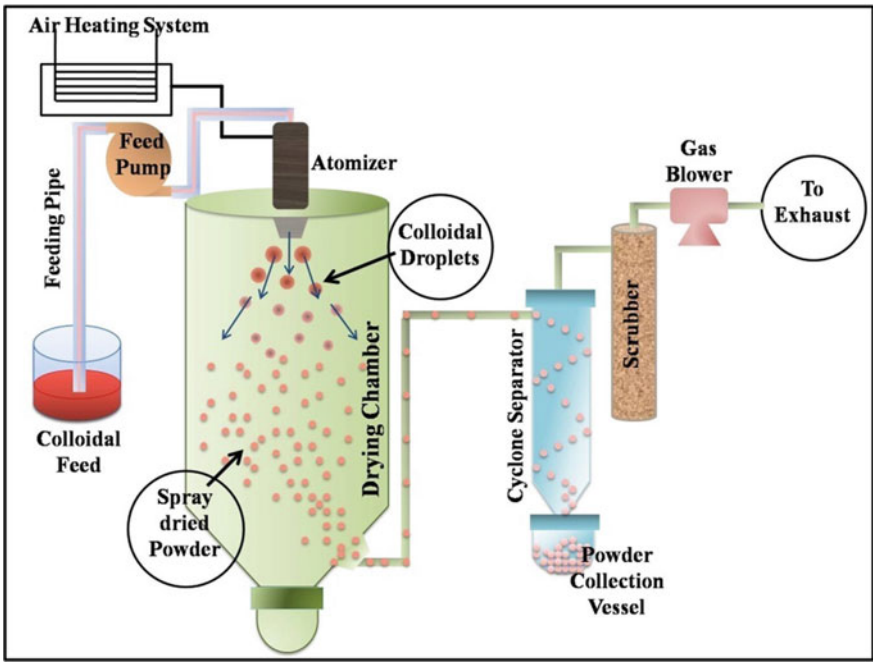

Fig. 11.1 Schematic diagram of a typical spray dryer for realizing micro-granules from colloidal dispersion

liquid into tiny droplets (typically 10–200 μm sizes) increases surface-to-volume ratio significantly, which enables more heat transfer in shorter duration of time. Controlling the atomization process, i.e. the fission of bulk liquid into large number of droplets is extremely crucial for a spray dryer as this particular process plays an important role in deciding the size distribution of the synthesized powder granules. The atomization process is familiar in everyday life which include shower heads, perfume sprays, etc. In spray drying process, normally such atomization process involves air-compressed nozzles. In air spray atomization, fluid emerging from a nozzle at low speed is surrounded by a high-speed stream of air. Friction between the liquid and air accelerates and disrupts the fluid stream and causes atomization. The energy source for air atomization is air pressure. Figure 11.2 illustrates how a stream of feed solution gets atomized while passing through an orifice. The atomized droplet size is a function of the type of atomizer nozzle and spray parameters including the feed flow rate, feed pressure, specific gravity of the feed, surface tension and viscosity of the feed [13]. However, the effective droplet size (D) can be approximated by

$$D = C P^{-n} M^{l} \eta^{w} \sigma_s^{s} \rho^{-t} \tag{11.1}$$

where 'P' is the atomization pressure, 'M' is the liquid feed rate, 'η' is the viscosity of the liquid, 'σ_s' is the surface tension, 'ρ' is the density of liquid and 'C', 'n', 'l', 'w', 's', 't' being positive constants. Apart from air-compressed nebulizer, other types of atomizer also exist, such as electrostatic atomizer or ultrasonic atomizer.

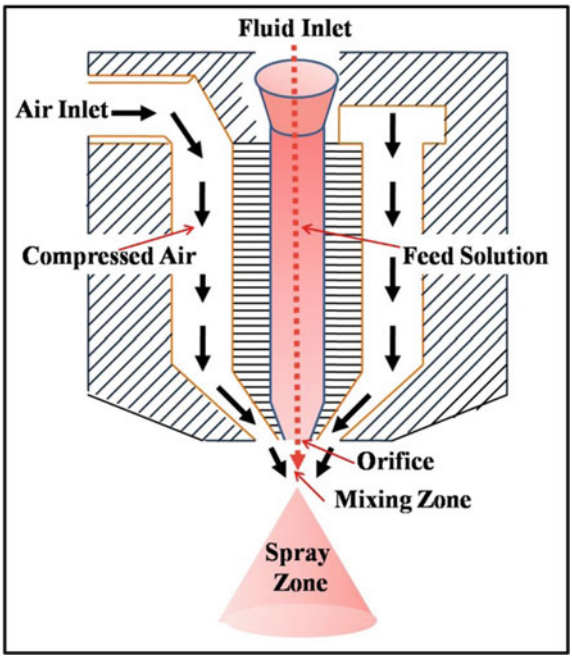

Fig. 11.2 Illustrates the atomization process of fluid by compressed air at the orifice of the nozzle

Electrostatic atomization exposes a fluid to a high electric field between the atomizer and the ground. The charge transfers to the fluid, and repulsive forces between the atomizer and the fluid tear the droplets from the atomizer. Ultrasonic atomization relies on an electromechanical device that vibrates at a very high frequency (20 kHz–10 MHz). Fluid passes over the vibrating surface, and the vibration causes the fluid to break into droplets. Ultrasonic atomizers have advantage of producing narrow size distribution of droplets as compared to polydisperse droplets produced by air-compressed atomizers. An electromechanical device made of two piezoelectric crystals that vibrate at a very high frequency governs the ultrasonic atomizer. However, ultrasonic atomization technology is primarily effective for low-viscosity Newtonian fluids. In subsequent stage of atomization, the droplets are brought into contact of hot gas in the spraying chamber. The evaporative assembly of the dispersed particles occurs in this part. The drying chamber is kept evacuated to ensure efficient evaporation and heat transfer from the hot gas to the droplets. The efficient drying at lower temperature makes the process economic. The solvent vaporizes in contact with hot gas leaving behind the micro-granules. The drying time should be less than the value of L/v, where 'L' denotes the length of the chamber and 'v' being the aspiration speed. The micro-granules are generally collected in cyclone separator by drawing the gas stream containing the evaporated moisture. It is worthy to mention that the rate of evaporation of the solvent molecules has a significant role to play which defines the morphology of the resultant powder and will be discussed later.

11.3 Colloidal Self-assembly During Spray Drying

It should be noted that for synthesis of the nano-structured micro-granules through spray drying, the starting ingredient is primarily a stable colloidal dispersion or sol, which is made up of dispersed phase and dispersion liquid. However, onset of evaporation during this one-step process suddenly starts altering the stability landscape owing to the continuous removal of solvent from the droplets. Thus, in order to understand the consequence of the spray drying process, it is required to discuss in brief about the stability of a colloidal dispersion where tiny dispersed particles have a typical dimension between 1 and 100 nm. The stability of a colloidal dispersion is defined by the particles remaining suspended in dispersion medium. To maintain the stability, it is required to prevent the aggregation of the colloidal particles which collide with each other through Brownian motion. For a charge stabilized system, this is generally achieved by increasing the surface charge associated with the particles. The stability of such a colloidal system is thus governed by the force balance between attractive van der Waals force and the repulsive electrostatic force. The DLVO theory (after Boris Derjaguin and Lev Landau, Evert Verwey and Theodoor Overbeek) tries to explain such stability by combining the effects of attractive and repulsive components. The typical variation of potential energy profile with interparticle distance is shown in Fig. 11.3. The combination of short-range attractive van der Waals and long-range repulsive screen Coulomb forces results in a deep attractive well, which is

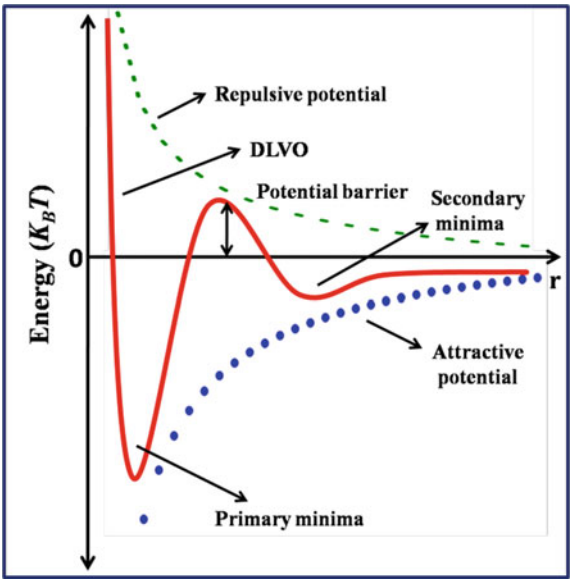

Fig. 11.3 Typical DLVO potential energy profile between two colloidal particles as function of interparticle separation (r)

referred as the primary minimum. At larger distances, the colloidal particles remain stable in secondary minimum in balance with attractive and repulsive forces. When the colloids come closer to each other, repulsive force shoots up resulting in energy profile maxima, called potential barrier. This barrier prevents the aggregation of colloids in the dispersed liquid phase. However, any external force can help them to overcome the potential hill to jump into the deep attractive well vis-à-vis primary energy minimum configuration. This is where the evaporation of liquid phase of the tiny droplets has significant role to play. As soon as the droplets come in contact with hot gas, the evaporation of solvent molecules commences creating a capillary pool among the dispersed particles. The attractive capillary force serves as the necessary external drive to overcome the potential barrier, and subsequently, the particles get interlocked into a deep potential well. Thus, the drying of the colloidal droplets inside the spray drying chamber induces self-assembly of nanoparticles resulting into nano-structured micro-granules. At larger distances, the energy profile goes through a maximum, and subsequently, passes through a barrier and then a shallow minimum, which is referred to as the secondary minimum. It should be noted that during the evaporation of solvent from a tiny colloidal droplet, the distance between particles starts to decrease due to capillary force. If the capillary forces are strong enough, attractive force can overcome the barrier leading to interlocking of particle into a deep potential well. This suggests that such induced assembly during the evaporation of solvent from tiny colloidal droplets can be a great way to realize nano-structured granules constituting interlocked nanostructures.

Let us discuss about physicochemical parameters that influence the drying rate of a droplet. The first factor which affects the drying is the phase change from liquid to vapour, i.e. the rate at which molecules escape the liquid–air interface [14]. The

second factor is the transport of the vapour molecules away from the droplet surface in the surrounding air. This transport can be purely diffusive [15], or a combination of diffusive and convective transport. The third rate-limiting factor is the evaporative cooling and heat transfer to the liquid–air interface [16]. The drying of droplets under atmospheric condition is mostly governed by the diffusive transport of vapour. The shrinkage of the isolated spherical droplet during drying under atmospheric condition is governed by the following equation [17]:

$$R_0{}^2 - R^2(t) = \frac{2D_V m_V}{\rho kT}(P_s - P_\infty)t \tag{11.2}$$

where 'R_0', '$R(t)$' is radius of droplet at $t = 0$ and t, respectively; 'D_v' and 'm_v' are diffusion coefficient and molecular mass of water vapour, respectively. 'ρ' is the mass density of water. 'P_s' is the saturation vapour pressure at the surface of the droplet, and 'P_∞' is the vapour pressure at a distance very far from the droplet, 'k' is Boltzmann constant and 'T' is absolute temperature. The shrinkage rate of the droplet deviates from Eq. (11.2) when it contains disperse or dissolved phase. Equation (11.2) suggests that typical drying time of an isolated water droplet of micrometer size in vacuum ($P_\infty \sim 0$) is extremely small and is typically less than millisecond order. However, in reality in a spray dryer, there are plenty of droplets instead of a single droplet. These droplets make 'P_∞' significant, and drying time is relatively more than that for a drying of a single droplet in vacuum.

It is important to discuss how the self-assembly of colloids takes place during drying of contact-free spray droplets. Here, only two dominant processes are considered that play crucial role in the assembly of colloids during drying. The first process is shrinkage of droplet which depends on rate of drying that depends on the temperature, aspiration rate, etc. The second process is the diffusion of colloids inside the droplet. These two phenomena are competing in nature as far as the assembly nature of the particles is concerned. The shrinkage of the droplet results into the accumulation of the colloids near droplet surface, whereas diffusion of colloids makes the concentration of the colloids uniform throughout droplet. A dimensionless parameter, known as Peclet number (P_e) is defined as follows:

$$P_e = \frac{\tau_{\text{mix}}}{\tau_{\text{dry}}} = \frac{R^2}{D\tau_{\text{dry}}} \tag{11.3}$$

where 'τ_{dry}' is the drying time of the droplet and 'τ_{mix}' is the mixing time, i.e. diffusion time of the colloidal particles from the droplet surface to its centre. 'R' is the radius of the droplet. 'D' is the diffusion coefficient of colloidal particles (radius r) in the droplet. The diffusion coefficient for Newtonian fluids can be expressed using Einstein-Stokes, as $D = \frac{kT}{6\pi\eta r}$. The case when $P_e << 1$ implies that the diffusion of colloids is faster than the shrinkage rate of droplet. In this case, concentration of the colloids remains uniform across the droplet, and the droplet shrinks isotropically throughout the drying process resulting into spherical granule [10, 18, 19]. This

scenario is considered as slow drying, and no buckling of the drying colloidal droplet is expected in contrast to the fast-drying regime. Under the slow-drying regime using mass balance during drying, one can derive a relation between the droplet radius and volume fraction of colloids.

$$R^3(t)\phi(t) = {R_0}^3\phi_0 \tag{11.4}$$

where 'R_0' and 'ϕ_0' are the radius of the droplet and volume fraction of the colloids before drying, respectively. '$R(t)$' and '$\phi(t)$' are instantaneous radius and volume fraction of colloids at time 't', respectively.

Peclet number $P_e >> 1$ implies that diffusion of colloids is slower compared to the shrinkage rate of the droplet leading to preferential accumulation of colloids at air–water interface of the droplet. A visco-elastic shell of the colloids is formed during drying followed by a visco-elastic to elastic transition that takes place due to the interlocking of the colloidal particles. The mechanical response of the elastic shell, under further compression of the droplet, may cause buckling of the shell resulting into complex morphology of the granules [20, 21], such as doughnut-shaped granules. The buckling of the shell indeed depends on its elastic properties and relative thickness [21]. Such drying scenario for $P_e >> 1$ is regarded as fast-drying regime. A scenario of slow and fast-drying processes is shown schematically in Fig. 11.4. It should be noted that if the initial droplets are polydisperse in nature, the Eq. (11.4) suggests that an isotropic drying will make the size distribution of the granules much narrower (Fig. 11.5) compared to the size distribution of the initial droplets. Further, the size distribution of the granules obtained by anisotropic drying will be broader compared to that obtained by isotropic drying (Fig. 11.5). So, accurate measurements of droplet size distribution and the granular size distribution (either

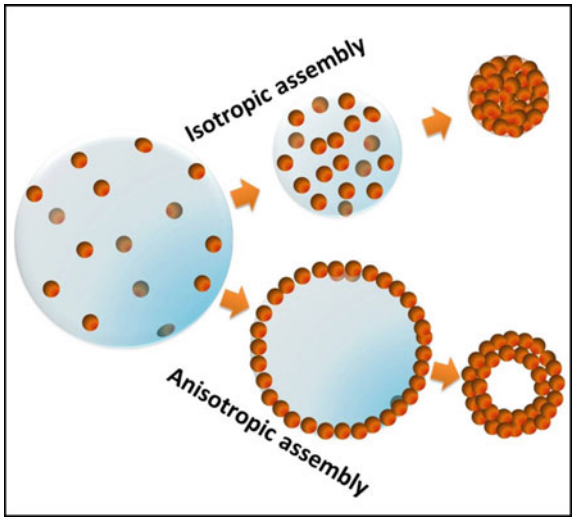

Fig. 11.4 Schematic representation of isotropic assembly at slow drying and anisotropic assembly at fast-drying scenario

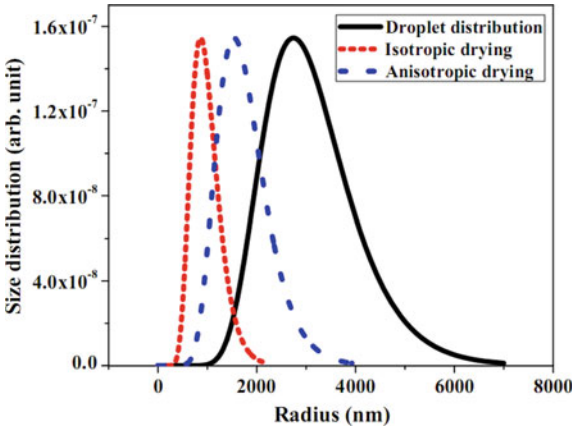

Fig. 11.5 Schematic representation of initial droplet size distribution and final granular size distribution under isotropic and anisotropic assembly scenario

by electron microscopy or by scattering techniques) can hint, in principle, about the nature of drying, isotropic or anisotropic. The jamming of colloids gives rise to the formation of mesopores owing to the presence of interstices between the jammed colloids. The pore size and specific surface area depend on the size of colloids and nature of jamming [22]. The spray drying technique can also be used to obtain pores with tunable size and porosity. The soft template such as polymer, surfactant and bacteria with hard colloids, such as silica, can be used to obtain the composite granules. The removal of the softer component results into templated pores [23] in the self-assembled granules. Figure 11.6 illustrates the template mechanism during drying of droplet under slow-drying regime.

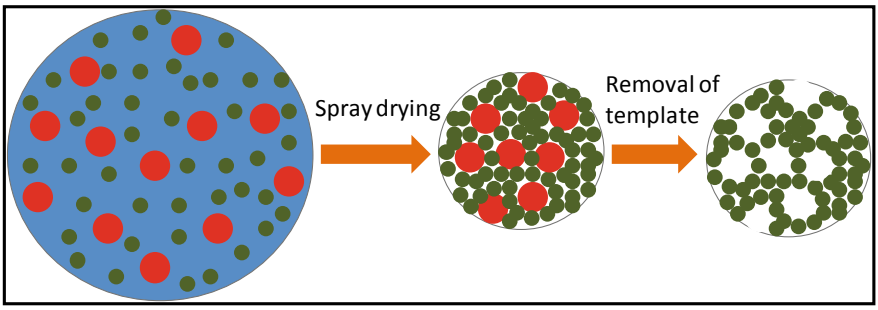

Fig. 11.6 Schematic representation of template mechanism during spray drying

11.4 Characterization Techniques

Often use of multiple characterization techniques become indispensable to gain insight into hierarchical structure of the assembled granules. The direct techniques like electron microscopy provide topological information of granules such as its shape and size. Electron microscopy, in particular, scanning electron microscopy (SEM) is the most suitable tool for investigating granules of micron size and below. However, internal structure of the granules such as packing fraction of colloids and nature of jamming cannot be probed using SEM. Further, standard transmission electron microscopy (TEM) is also not a very effective tool for getting internal structure of the granules due to limited penetration of electrons through the micron size granules. Moreover, real-time measurements during assembly of colloids are not feasible using microscopy techniques. Small-angle scattering (SAS) [24–26] using neutron and X-rays is an ideal technique to probe self-assembled granules having hierarchical structure [27]. Basic principle of microscopy and small-angle scattering technique is compared in Fig. 11.7. Microscopy techniques give information about object in real space whereas the scattering experiment provides information in reciprocal space. The microscopy and SAS methods are complementary techniques to probe the hierarchical nanostructures. We will describe SAS technique in a more detailed manner.

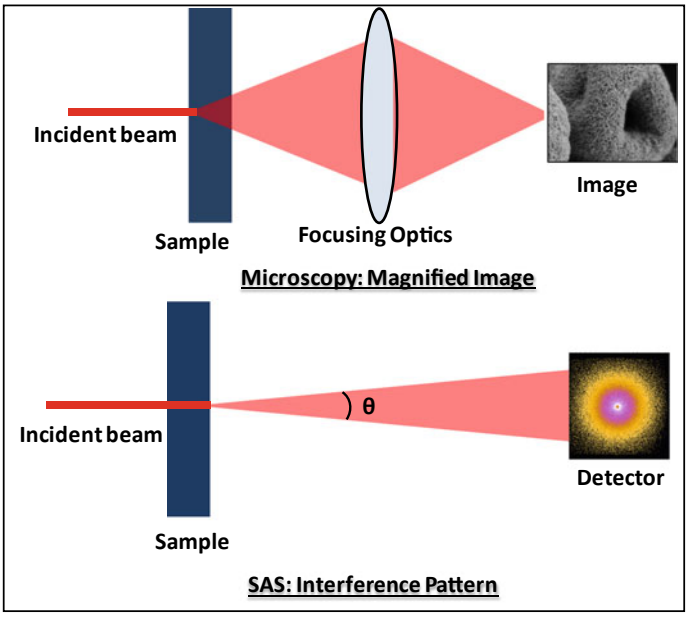

Fig. 11.7 Comparison of basic principle of the microscopy and small-angle scattering techniques

SAS provides structural information on inhomogeneities of mesoscopic dimension (1–1000 nm); structural features include size, shape, dimensionality and interparticle spatial correlation. The radiations such as X-rays, neutron and electrons interact with matter differently. Electrons being a charged particle interacts with matter strongly, hence, penetration of electron in the matter is less. This makes electrons as a local probe of the matter. Neutron is a neutral particle and hence it interacts with matter weakly. The penetration power of the neutron is quite high that makes it bulk probe of the matter. The X-ray interacts with matter via electromagnetic forces, the penetration power of X-rays falls in between that of electron and neutron.

X-rays and neutrons can be used as probe for SAS depending on the contrast it offers between the object and matrix where the objects are embedded. The strength of scattering of X-rays and neutron by an atom is quantified as scattering length. For X-ray, scattering length for each element scatters proportionally to its number of electrons. This indicates that scattering profile measured in an X-ray experiment will be primarily defined by the scattering from heavy Z elements. Neutron scattering lengths are determined by the quantum mechanics of the neutron–nucleus interaction and they vary irregularly across the periodic table. The basic differences between X-rays and neutrons as a probe for material are tabulated in Table 11.1.

In a SAS experiment, neutron/X-ray is incident on the sample with wave vector '$\boldsymbol{K_i}$' and is scattered into the state with wave vector '$\boldsymbol{K_f}$'. The intensity of scattered neutron/X-rays is thus measured as a function of momentum transfer (see Fig. 11.8): $\boldsymbol{q} = (\boldsymbol{K}_f - \boldsymbol{K}_i)$ where $\boldsymbol{q}$ is known as the wave vector transfer. The magnitude of a wave vector is defined as its wave number: $|\boldsymbol{K}| = K = 2\pi/\lambda$, where λ is the wavelength. For elastic scattering process $|\boldsymbol{K}_f| = |\boldsymbol{K}_i| = K$ and the magnitude of wave vector transfer '$\boldsymbol{q}$' is given by $|\boldsymbol{q}| = q = \frac{4\pi}{\lambda} sin\theta$, where '$2\theta$' is the scattering angle. The detailed theory of small-angle scattering and its analysis procedure can be found in literatures [24–26, 28]. The scattering intensity from a two-phase particulate system can be expressed as,

Table 11.1 Comparison of the various scattering parameters for Neutron and X-ray

Parameter	Neutron	X-ray
Intensity	Low	High
Hydrogen-sensitivity	High	None
Isotope-sensitivity	Strong	None
Heavy elements	Low	High
Spin-sensitivity	Strong	Average
Penetration depth	High	Low
Sample size/amount	Large	Small
Measurement time	Long	Short
Interaction	Nuclear (No systematic variation with Z), Magnetic	Electron (varies as Z^2)
Radiation damage	Negligible	High

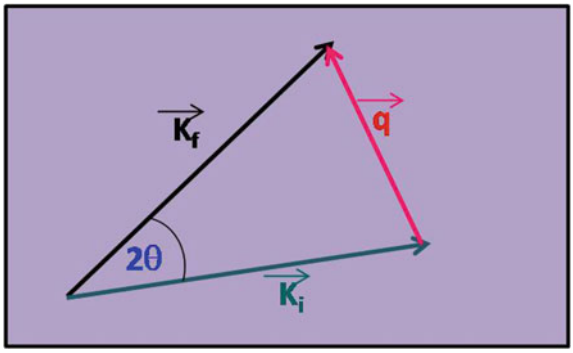

Fig. 11.8 The scattering law for elastic scattering scenario

$$I(q) = NV_p^2(\Delta\rho)^2 P(q)S(q) \tag{11.5}$$

where 'N' is the number density of scattering objects, 'V_p' is the particle volume and '$(\Delta\rho)^2$' is the contrast factor. The term '$P(q)$' is a dimensionless function known as form factor that describes scattering from a single particle and is dependent on both its shape and size. Analytical expressions for '$P(q)$' have been available in the literatures for most common shapes [25, 28]. Form factors of sphere of radius R can be written as $P(q, R) = 9\left[\frac{sin(qR)-(qR)cos(qR)}{(qR)^3}\right]^2$. The form factors of sphere of radius 20 nm, disk of radius 20 nm and cylinder of cross-section radius 20 nm and length 500 nm are shown in Fig. 11.9a. It is clear from this figure that functionality of the scattering profile significantly depends on the shape of scattering object. The slope of the scattering profile (log–log scale), in a particular q-range, shows ~q^{-1} and q^{-2} scattering behaviour for cylindrical and disk-shaped objects, respectively.

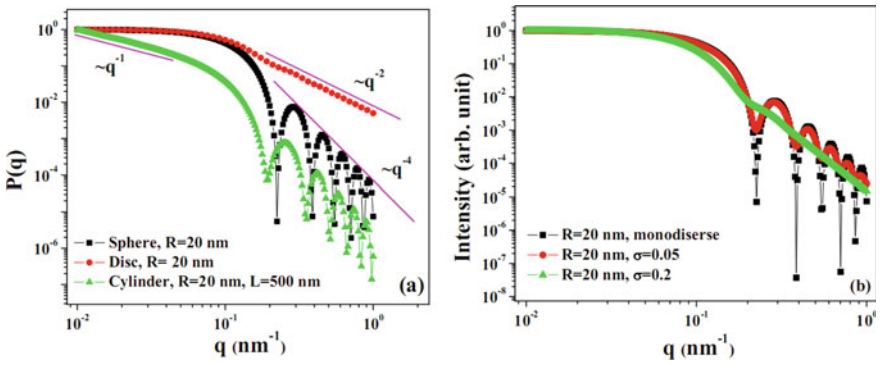

Fig. 11.9 **a** Form factor corresponding to different shapes of the particles is shown. Radius of sphere R = 20 nm, disc radius R = 20 nm, length L and radius of cylinder are 20 nm and 500 nm, respectively. **b** Effect of polydispersity on the scattering profiles

The scattering from spherical objects shows ~q^{-4} Porod scattering behaviour at high-q. The scattering intensity for a dilute system, where the distance between particles is much higher than their sizes, depends only on the form factor. In such a situation, interference between scattering from different particles may be neglected, and the measured signal carries information on the shape and size of individual particle. As the concentration of particle increases, the interference effects between scattering particles in the sample becomes important and is described by another dimensionless function '$S(q)$' that is called structure factor. '$S(q)$' depends on the spatial arrangements of the scattering objects, i.e. the correlations in their position and interactions. Its formula is given by:

$$S(q) = 1 + 4N\pi \int \left[(g(r) - 1) r^2 \frac{sin(qr)}{qr} dr \right] \tag{11.6}$$

where '$g(r)$' is the particle pair distribution function which describes the spatial distribution of the particles as a function of the average separation distance, 'r'. Analytical expressions for the structure factors have been derived for hard sphere interaction [29], sticky hard spheres between particles [28, 30, 31]. Similarly, for charged particle, structure factor has been derived using screen Coulomb interaction. Please note that Eq. 11.5 is valid for monodisperse particles only. For an ensemble of polydisperse particles, under local monodisperse approximation [32], the expression of the scattering intensity can be written as,

$$\mathrm{I(q)} = \mathrm{N}(\Delta\rho)^2 \int \mathrm{V_p}^2(\mathrm{R})\mathrm{P(q,\,R)D(R)S(q,\,R)dR} \tag{11.7}$$

where, '$D(R)$' is the size distribution of the particles.

The structure factor $S(q) \sim 1$ for dilute ensemble of polydisperse particles and the Eq. 11.7, in this case, can be written as:

$$\mathrm{I(q)} = \mathrm{N}(\Delta\rho)^2 \int \mathrm{V_p}^2(\mathrm{R})\mathrm{P(q,\,R)D(R)dR} \tag{11.8}$$

The effect of the polydispersity on the scattering profiles from an ensemble of spheres possessing lognormal size distribution

$$D(R) = \frac{1}{\sqrt{2\pi\sigma^2 r^2}} \exp\left(\frac{-\left(\ln\left(R/\mu\right)\right)^2}{2\sigma^2} \right) \tag{11.9}$$

is shown in Fig. 11.3b. μ is the median of the size distribution and σ is called polydispersity index that varies between 0 and 1. It is evident that sharp oscillations in the scattering profiles get smeared as the polydispersity index increases (Fig. 11.9b).

Figure 11.10a depicts both the form factor and structure factor as a function of q; the intensity obtained by multiplication of these two factors using Eq. 11.5 is also

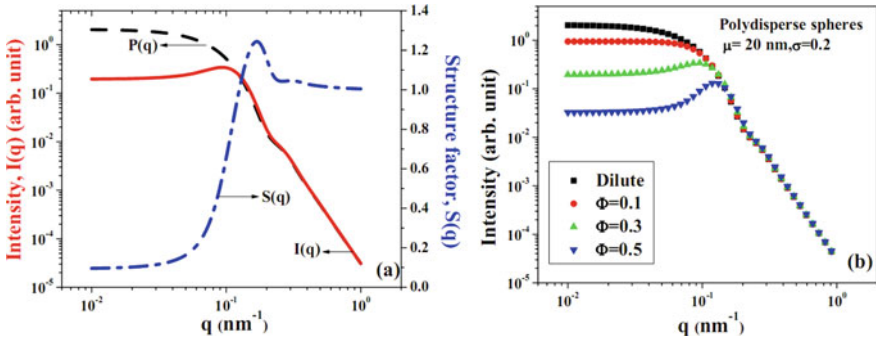

Fig. 11.10 **a** Scattering intensity is shown as multiplication of form factor and structure factor. **b** Effect of concentration of particle on the scattering profiles is depicted. Structure factor corresponding to the hard sphere interaction [29] under local monodisperse approximation [32] is used for modelling the data

shown. Polydisperse sphere with $\mu = 20$ nm and $\sigma = 0.2$ is assumed for calculation of '$P(q)$'. Hard sphere type interparticle interaction was considered for the simulation of the structure factor '$S(q)$'. It is observed from Fig. 11.5a that low-q intensity is governed by structure factor whereas the high-q scattering is dominated by the form factor. Figure 11.10b shows the scattering profiles as a function of volume fraction of the particle. The scattering intensity at low-q decreases with increasing volume fraction, a correlation peak starts building up at higher volume fraction $\phi \sim 0.3$ and it becomes sharp and shifts to high-q as ϕ increases to 0.5. The average distance between particles 'd_p' in a concentrated system is approximately related to peak position q_{peak} as $d_p \sim 2\pi/q_{\text{peak}}$.

In general, the granules obtained by spray drying process possess hierarchical structure of the jammed colloid. SAS profile in a wide-q-range can provide information about such the granule and the jamming nature of colloids. It should be mentioned that accessing scattering data over such a wide-q-range always remains a challenge due to limited q window of a particular instrument. In general, usage of conventional pin-hole small-angle scattering instrument [33] as well as double crystal-based ultra-small-angle scattering instrument [34] becomes necessary for investigating such granules. A simplistic model has been shown below to describe the scattering intensity from such assembled granule [35, 36]:

$$I(q) = C_g I_g(q) + C_{jc} I_{jc}(q) \tag{11.10}$$

where '$I_g(q)$' is the scattering contribution due to overall assembled granules and '$I_{jc}(q)$' is scattering contribution due to jammed colloids. 'C_g' and 'C_{jc}' are scale factor for granule and jammed colloid scattering contributions, respectively. It is to be noted that above equation is valid only if size of granules is quite large (order of the magnitude) compared to the size of individual colloidal particles.

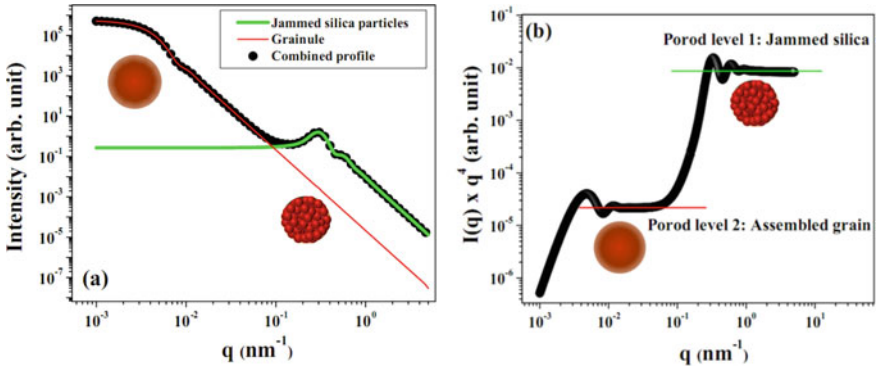

Fig. 11.11 Simulated small-angle scattering profile for assembled silica granules obtained by spray drying **a** $I(q)$ versus q. **b** $I(q) \times q^4$ versus q, i.e. in Porod representation

The first term in Eq. 11.10 gives information regarding the shape and size of the assembled granules, whereas second term in Eq. 11.10 provides information about the individual colloids such as its shape, size and nature of jamming. An ensemble of polydisperse spherical granules with $\mu = 500$ nm and $\sigma = 0.2$ has been taken as model for granule scattering $I_g(q)$. Randomly jammed colloids interacting via hard sphere interaction with a volume fraction $\phi \sim 0.54$ is taken as model to express $I_{\text{jc}}(q)$. Figure 11.11a shows simulated scattering profiles $I_g(q)$ and $I_{\text{jc}}(q)$ corresponding to scattering from over all granule and correlated colloids, respectively. The combined scattering intensity, i.e. sum of these scattering contributions is also shown in Fig. 11.11a in double logarithmic scale. The two-level structure is evident in Fig. 11.11b where data is plotted in Porod representation, i.e. $I(q) \times q^4$ versus q. Two constant levels in Porod plot indicate the presence of two-level structure in well-separated length scales. The Porod level at high-q is due to the scattering from individual colloid, whereas the Porod level at low-q is attributed to the scattering from overall granules.

11.5 A Few Illustrative Examples

11.5.1 Nano-structured Silica Micro-granules with Spherical and Doughnut Morphology

Silica micro-spheres as inorganic supports have become increasingly important for a variety of applications, including isolation of nucleic acids, cell separation and immuno- and DNA-based assays. They offer combined advantage of a broad platform and unique properties of a silica substrate. Silica micro-granules can be synthesized by spray drying technique with silica nano-suspension as starting material. The shape

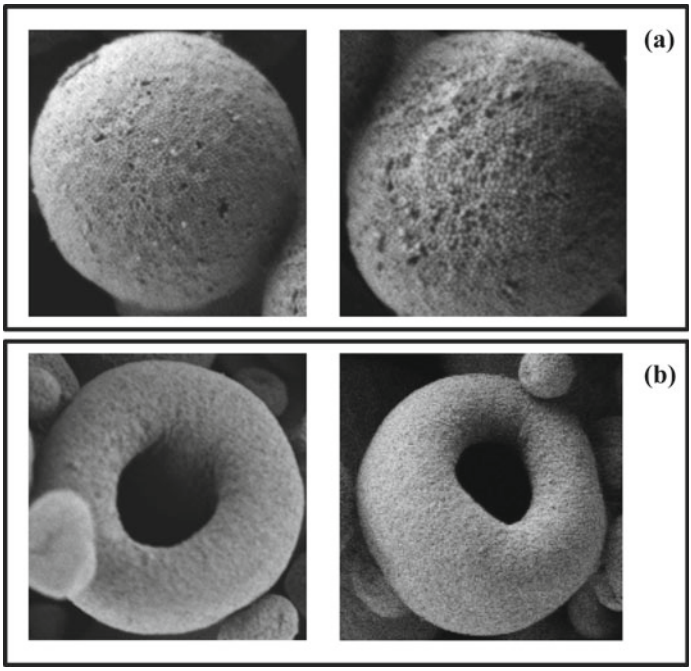

Fig. 11.12 FESEM micrographs showing: **a** spherical and **b** doughnut-shaped nano-structured silica granules. Reproduced with permission from Ref. No. 40 (Adapted with permission from (Biswas et al. Langmuir 2016. **32**(10): p. 2464–2473) Copyright (2016) American Chemical Society)

of the granules can be tuned by controlling the physicochemical conditions during spray drying [37]. Figure 11.12a, b shows spherical and doughnut-shaped granules, respectively. The formation of doughnut-shaped granules may be explained due to buckling of the shell formed during the rapid anisotropic drying as mentioned earlier [13, 20, 37–39].

It may be recalled from the earlier section that the Peclet number (P_e), signifying the nature of assembly, is given by $P_e = \frac{\tau_{\text{mix}}}{\tau_{\text{dry}}} = \frac{R^2}{D\tau_{\text{dry}}}$, where the diffusion coefficient of the nanoparticles in the droplet is 'D'. An increase in drying rate decreases 'τ_{dry}'. This in turn increases 'P_e'. It has been observed experimentally that gradual increase in drying rate results in increase in hollowness and subsequent bucking into doughnut shape [40]. The quantitative information on silica-silica correlation in the granules may be obtained from detail analysis of small-angle scattering profiles (Fig. 11.13). The correlation peak ~0.2 nm^{-1} in SAS profiles appears due to interparticle interference among the jammed silica particles in the granules.

These nanoporous silica granules have been found potential sorbents for cationic dyes such as methylene blue [41]. It needs to be mentioned that after sorption, the granules settle faster (Fig. 11.14), and thus allows easy decantation of the solvent in contrast to the situation with bare nanoparticles. It has been found [22, 42] that incorporation of such granules in ultra-filtration polysulphone membrane enhances

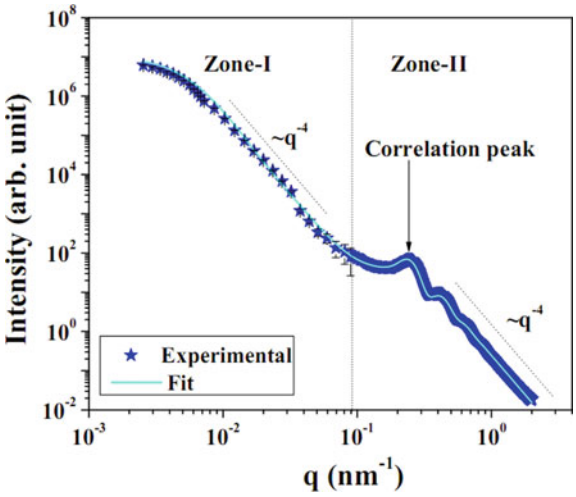

Fig. 11.13 Combined SAXS (Zone-I) and medium resolution SANS (Zone-II) data for nanostructured silica micro-granules. Reproduced with permission from Ref. No. 40 (Adapted with permission from (Langmuir 2016. **32**(10): p. 2464–2473) Copyright (2016) American Chemical Society)

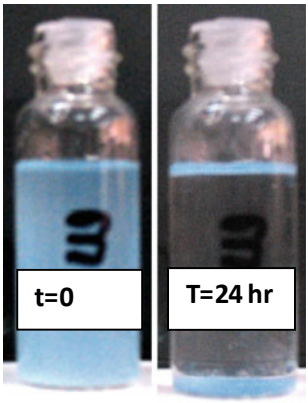

Fig. 11.14 The sorption of methylene blue dye by the granules from aqueous solution. The micro-granules, being heavier than bare nanoparticles, settle fast allowing easy decantation of the solvent after sorption. [41] Reproduced with permission from Ref. (Adapted with permission from Colloids and Surfaces A: Physicochem. Eng. Aspects 520 (2017) 279–288)

the pure water permeability quite significantly without affecting its rejection characteristics. This is probably because of the fact that the incorporated granules can offer suitable porous channels across membrane surface which were otherwise not accessible because of the tapering of the pore channels in casted membranes.

11.5.2 Macro/Meso Porous Silica Micro-spheres Using Template Mechanism

It is discussed earlier that spray drying is an effective technique to achieve macro/meso porous materials using template mechanism. Herein, an example of fabrication of macroporous silica granules has been shown which was obtained using *E. coli* bacteria as a template. *E. coli* are one of the primary bacterial contaminations in drinking water in most of the underdeveloped/developing countries including India. A unique approach is adopted to obtain silica-based macroporous micrometric granules for potential application of filtration of *E. coli* bacteria from drinking water using spray drying technique.

Initial silica dispersion (Visa Chemicals, Mumbai, India) was diluted in pure water (Milli-Q, Millipore). 2wt % silica dispersion and varying *E. coli* (0, 2, 4 and 6% in weight), soft component, were taken for spray drying. The inlet temperature was kept at 170 °C and the aspiration rate was kept at ~47m^3/h. The dried powders were collected from the cyclone separators. Removal of the imprinted materials was done by incineration in muffle furnace at 300 °C for 10 h. The powders, with 0, 2, 4 and 6% of *E. coli,* are designated as S0, S2, S4 and S6, respectively.

The SEM micrographs of samples S0–S6 are shown in Fig. 11.15a–c. It is evident that spray drying of the only silica colloids results into doughnut type granules as explained in previous section. The imprinting of *E. coli* in silica granule is also evident from the figure. The macroporosity of the spray-dried granules increases with increasing concentration of the *E. coli* in the initial dispersion used for spray drying. Interestingly, deformation of the assembled granules is increased at higher concentration of *E. coli.* It has been observed from Zeta potential measurements [9] that both silica and *E. coli* possess negative charge, and thus forms a repulsive system. During drying process of mixed colloids, the bigger size component diffusion is slow, and hence it remains primarily on the surface of the droplet during drying. Thus, the shell formed during drying consists of silica as well as *E. coli* leading to inhomogeneous shell. Subsequent compression of the droplet leads to the multi-faceted doughnut-shaped granule through buckling of elastic shell. The buckling gets enhanced with increase in softer component on the shell [39].

The arrest of buckling of the droplet containing mixed colloids requires prevention of shell formation or increase in elastic strength of the formed shell. In order to tune this aspect, *E. coli* cells were treated to impart a cationic charge on the cell surface using polyethylenimine (PEI) (Average MW ~ 7.5×10^5). *E. coli* cells were treated with PEI 0.2, 1 and 2%, respectively. The Zeta potential measurements show that charge on *E. coli* becomes positive due to PEI coating and magnitude of charge increases with increasing coating thickness [9]. The spray drying of the 2wt% silica and PEI-treated *E. coli* have been performed with identical drying parameters used previously. The dried granules obtained for 0.2, 1.0 and 2.0 wt% PEI-treated *E. coli* have been designated as ST1, ST2 and ST3, respectively. Figure 11.15d–f show the micrographs of spray-dried granules obtained for

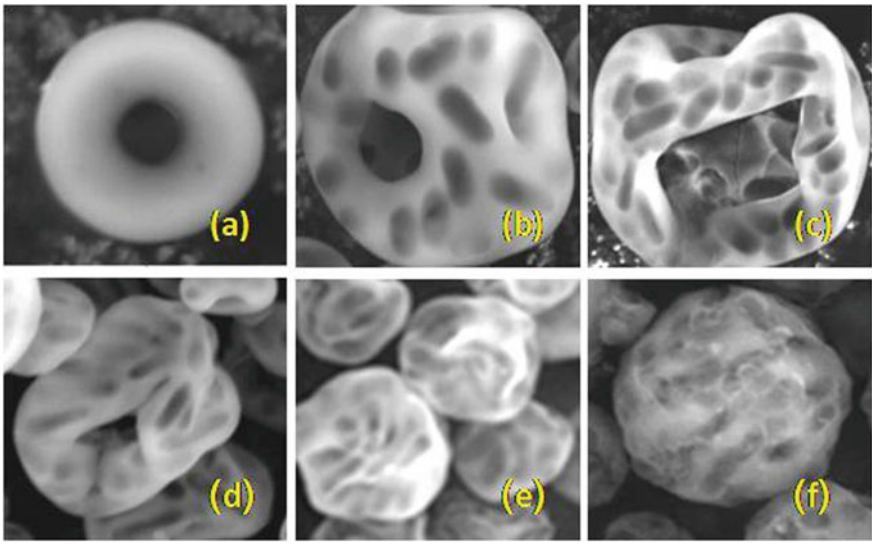

Fig. 11.15 SEM micrographs of **a** 2wt% silica, **b** 2wt% silica + 2wt% E. coli, **c** 2wt% silica + 6wt% E. coli. Reproduced with permission from Ref. No. 20 (From D. Sen et al., Buckling-driven morphological transformation of droplets of a mixed colloidal suspension during evaporation-induced self-assembly by spray drying. EPJ-E, 2010. 31(4): p. 393–402 with kind permission of The European Physical Journal (EPJ)) **d** 2wt% silica + 6wt% E. coli coated with 0.2% PEI, **e** 2wt% silica + 6wt% E. coli coated with 1.0% PEI and **f** 2wt% silica + 6wt% E. coli coated with 2.0% PEI. Reproduced with permission from Ref. No. 9 (Reproduced from Ref. 9 with permission from the Royal Society of Chemistry)

mixed colloids containing PEI-treated *E. coli*. It is evident from the figure that deformation of the granules significantly reduces with increasing PEI coating. The silica nanoparticles coat the surface modified *E. coli* bacteria due to the attractive force between them. Thus, the formed shell, exposed to the air-water interface, primarily contains silica coated reinforced *E. coli* and that results in its improved elastic properties. The increase in the elastic strength of the shell causes arrest of buckling of drying droplet resulting in spherical granules. A schematic of the assembly mechanism is shown in Fig. 11.16.

In order to get the quantitative information about the macroporous assembled granules, SANS measurements have been carried out in a wide-q-range (Fig. 11.17). The data were analysed using three length scale model. First contribution originates from the jammed silica in the granules, while the second contribution arises due to scattering from the *E. coli* templated pores. The third contribution is due to the scattering from the overall granular shape. Table 11.2 shows the important fitting parameters as obtained from analysis.

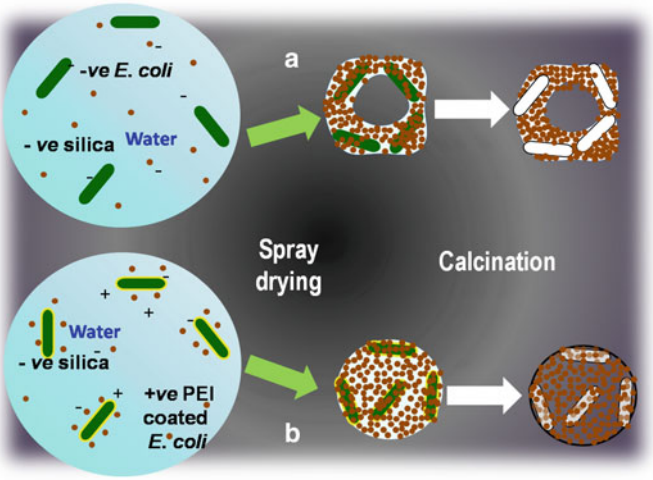

Fig. 11.16 Schematic representation of the assembly process of silica and E. coli. **a** Both silica and E. coli have negative surface charges and the system is repulsive. The assembled grains are deformed. **b** Silica is negative as in earlier case, but the E. coli surface is coated with PEI to impart positive charge on the E. coli surface. The assembled grains are spherical in this case and no buckling has occurred. [9] Reproduced with permission from Ref. No. 9 (Reproduced from Ref. with permission from the Royal Society of Chemistry)

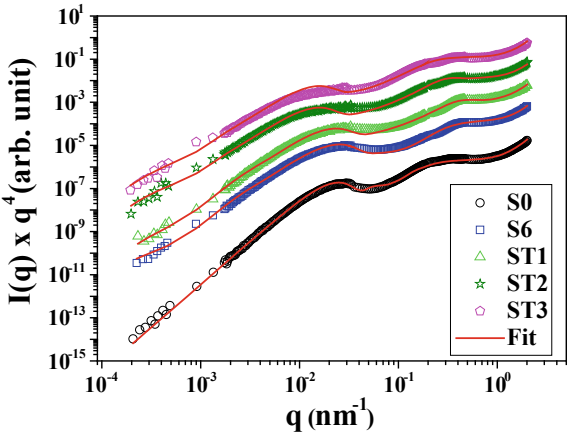

Fig. 11.17 SANS profiles (Porod representation) of the E. coli template macroporous granules over a wide-*q*-range ([9] Reproduced from Ref. with permission from the Royal Society of Chemistry)

11.5.3 TiO_2/SiO_2 Nano-composites Via Spray Drying of Mixed Colloids

Spray drying technique has unique advantage because of its ability to mix colloids of similar size uniformly during the drying process. An example of fabrication of TiO_2/SiO_2 composite micro-spheres has been discussed below. TiO_2-based materials

Table 11.2 Structural parameters obtained from SANS analysis. [9] Reproduced with permission from Ref. No. 9 (Reproduced from Ref. with permission from the Royal Society of Chemistry)

Sample	Assembled granule size distribution		Templated cylindrical macro pore		
	Mean radius (R_{granule}) (nm)	$\frac{\Delta R_{grain}}{R_{grain}}$	*Length* (L_{pore}) (nm)	*Average radius* (R_{pore}) (nm)	$\frac{\Delta R_{pore}}{R_{pore}}$
S0	200	0.099	–	–	
S6	2394	0.658	2000	102	0.205
ST1	2266	0.533	2050	115	0.209
ST2	2266	0.533	2600	167	0.305
ST3	2159	0.531	2600	167	0.305

are quite important due to their photocatalytic properties [43]. It is known that TiO_2 has three allotropes, namely, Anatase, Brookite and Rutile [44]. It is well established that anatase phase of TiO_2 is a more efficient photocatalyst as compared to its other allotropes [45]. However, the thermodynamic stability depends on particle size [46]. For particle size below ~14 nm, anatase phase is more stable than rutile phase. If TiO_2 nano-crystals are heated, crystal growth leads to alteration of phase stabilities and, ultimately, conversion of anatase phase to rutile phase takes place. Such phase transformation of anatase to rutile is considered to be one of the drawbacks for photocatalytic applications. Moreover, photocatalytic application of the TiO_2 requires a good dispersion of TiO_2 nanoparticles, as its efficiency increases because of availability of more surface area for reaction. Here, spray drying technique has been used to fabricate a TiO_2/SiO_2 composite that is stable against the anatase to rutile phase transformation. The incorporation of TiO_2 nanoparticles in the silica matrix leads to higher active surface area for the catalytic reaction.

A stable dispersion of the TiO_2 and SiO_2 has been mixed in the weight ratio of 2:1 for spray drying. The atomization pressure for the droplet generation was kept at 2.0 kg/cm^2 and inlet temperature during drying was fixed at 170 °C. Solution feed rate was kept as 2 ml/min and aspiration rate was fixed at 50 m^3/h. The spray drying has also been carried out on the individual dispersions of SiO_2 and TiO_2. The average size of the silica and titania colloids was determined using SAXS measurements [24, 25]. The average size of silica colloid was found to be ~16 nm, whereas the TiO_2 colloids possess biomodal size distribution with average size of 6 and 17 nm [47]. Figure 11.18 shows the SEM micrographs of the composite micro-spheres in low and high magnification. Nice spherical-shaped granules of micrometer size is achieved which is similar to the morphology of the TiO_2 and SiO_2 granules [47]. The energy dispersive X-ray (EDX) analysis was also carried out on the composite sphere which confirms the formation of TiO_2/SiO_2 composite (Fig. 11.18c).

Combined SANS profiles of the SiO_2, TiO_2 and TiO_2/SiO_2 micro-spheres have been depicted in Fig. 11.19a. Scattering profiles are also shown in Porod representation ($I(q)q^4$ versus q) as depicted in Fig. 11.19b. It is evident from the figure that the assembled granules possess hierarchical length scale structure, and existence of two

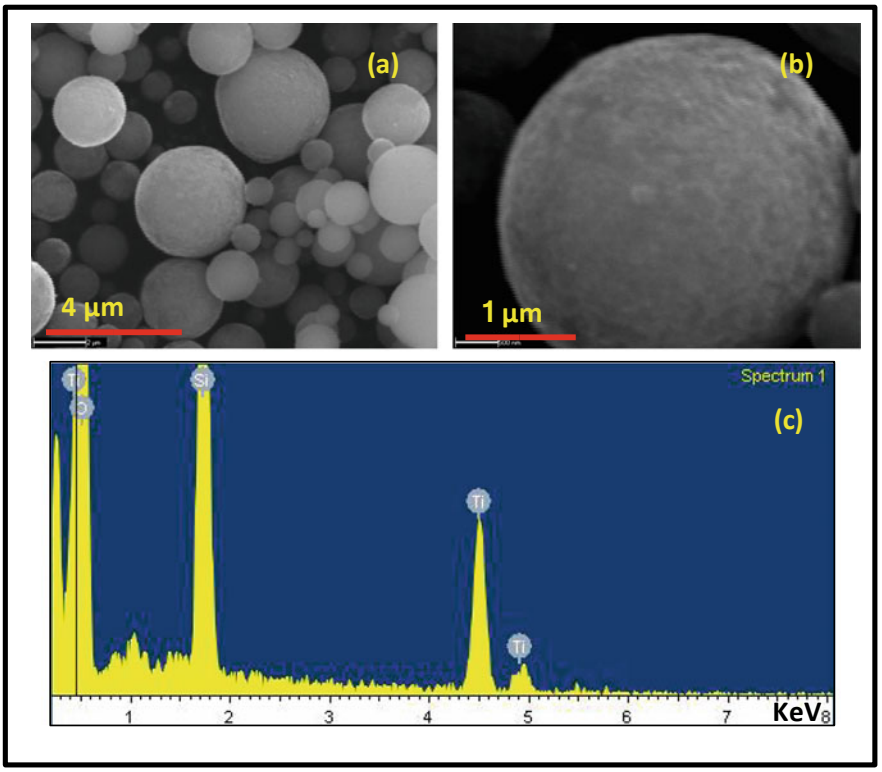

Fig. 11.18 TiO_2/SiO_2 micro-spheres: **a** in low and **b** high magnification (Adapted with permission from [47] Reproduced with permission from Ref. (Langmuir, 2012. 28(31): p. 11, 343–11, 353) Copyright (2012) American Chemical Society). The EDX spectrum of the composite is shown in (**c**)

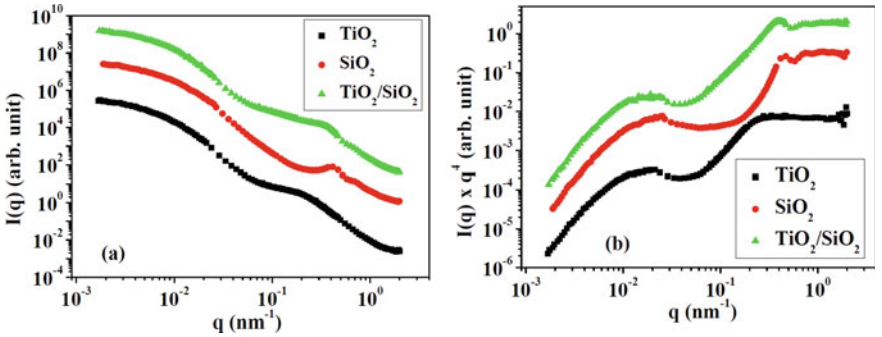

Fig. 11.19 SANS profiles of TiO_2, SiO_2 and TiO_2/SiO_2 composite micro-sphere is shown in two representations. **a** $I(q)$ versus q and **b** $I(q) \times q^4$ versus q. [47] Reproduced with permission from Ref. (Adapted with permission from (Langmuir, 2012. 28(31): p. 11,343–11,353) Copyright (2012) American Chemical Society)

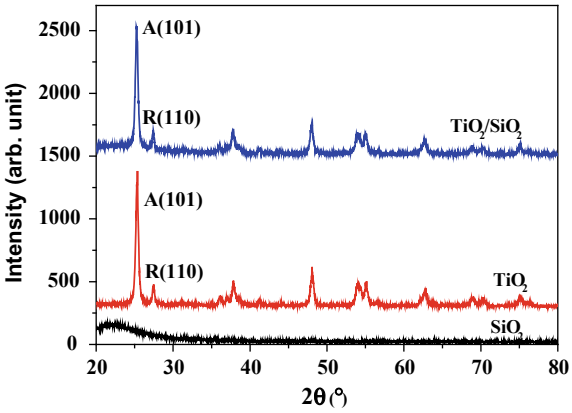

Fig. 11.20 XRD patterns of the TiO_2, SiO_2 and the composite micro-spheres. [47] Reproduced with permission from Ref. (Reprinted with permission from (Langmuir, 2012. 28(31): p. 11, 343–11, 353) Copyright (2012) American Chemical Society)

Porod levels is evident. The SANS profile of silica micro-spheres shows a distinct correlation peak at $q \sim 0.45$ nm^{-1} corresponding to jammed silica nanoparticles, the oscillations in the scattering profiles is due to low polydispersity in the size of colloids. A relatively broader hump is observed in the SANS profile of TiO_2 micro-spheres because of relatively larger polydispersity in the size of TiO_2 colloids. SANS profile of the composite shows a silica correlation peak which is broader than that for SiO_2 granules. The X-ray diffraction (XRD) profiles have been recorded for all the samples and it is shown in Fig. 11.20. A broad hump is observed for the silica micro-sphere indicating the amorphous nature of the silica nanoparticles.

The TiO_2 micro-sphere shows the diffraction peaks indicating its crystalline nature. The phase identification reveals that both anatase and rutile phase exist in 85:15 weight ratio [47]. The position of (101) and (110) planes corresponding to anatase and rutile phase, respectively, is marked in the figure. The XRD measurements were performed on TiO_2 and composite that were heat-treated at different temperatures. The evolution of (101) and (110) planes of the anatase and rutile phase as a function of temperature is shown in Fig. 11.21. It is evident that anatase to rutile phase transformation occurs beyond 600 °C for TiO_2 micro-sphere. However, no phase transformation takes place in case of composite micro-sphere. This suggests that composite granules are thermally stable against anatase to rutile phase transformation. The growth of TiO_2 nano-crystal is hindered in the composite granules as it is surrounded by SiO_2 nanoparticles; this leads to arrest of phase transformation at higher annealing temperature. Thus, spray drying technique using binary colloidal systems is a one-step method to fabricate composite granules with improved properties. The structure and dispersion properties can be tuned by ratios of size of colloids and its concentration.

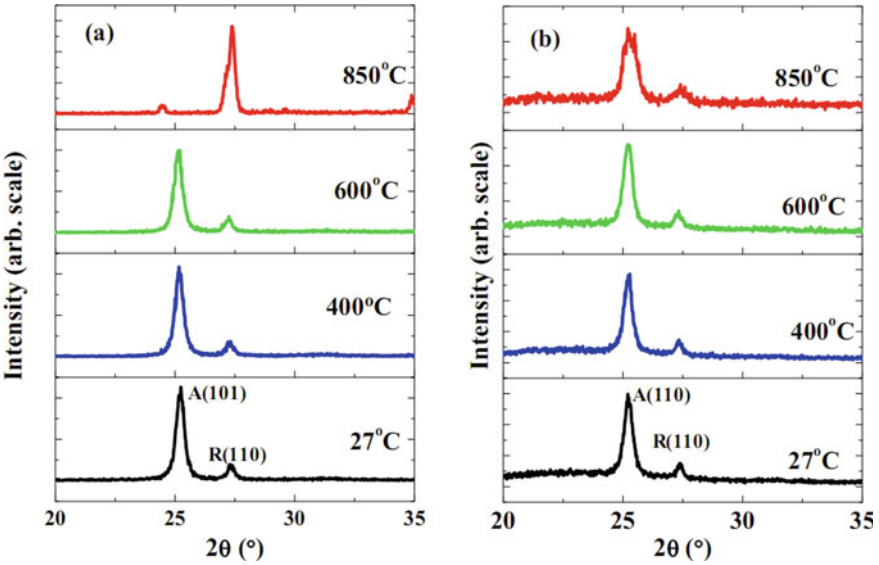

Fig. 11.21 XRD pattern of the TiO_2 and TiO_2/SiO_2 composite as a function of temperature. [47] Reproduced with permission from Ref. (Adapted with permission from (Langmuir, 2012. 28(31): p. 11,343–11,353) Copyright (2012) American Chemical Society)

11.5.4 Formation of Nano-composite Micro-spheres with Core–Shell Spatial Distribution

Spatial distribution of the building blocks during assembly may be controlled, and granules in the form of Janus [48] or Core–Shell [49] morphology can be synthesized in one-step process. Here, an example of core–shell micro-granules has been discussed, where contrasting interfacial interaction of two types of nanoparticles with solvent has been exploited during evaporation-induced self-assembly by spray drying. A mixed colloidal solutions of carbon black (from M/s. Hi-Tech Carbon of grade N-330) and silica (LUDOX® SM30 from M/s. Sigma Aldrich) nanoparticles are taken as feed to spray drying. The reason behind choosing carbon and silica is that they possess opposite polarity of water-affinity. Carbon being hydrophobic hates water molecules, whereas silica is hydrophilic in nature. The colloidal particles in mixed suspension remain dispersed in spatially random manner in water. However, after the colloidal suspension is sprayed inside the drying chamber, the fluid starts evaporating out of the droplet in radially outward direction. The movement of water molecules builds up a competition between hydrophilic and hydrophobic components. The water-loving component moves in radially outward direction along with water molecules, but water-repelling component tries to propel against the motion of water molecules and occupy water-depleted region. Thus, the contrasting interfacial interaction with solvent molecules creates a spatial distribution of hydrophilic and hydrophobic components in the drying droplet. The hydrophobic particles, i.e.

Fig. 11.22 Schematic representation of nano-composite core–shell micro-granules of carbon and silica. FESEM micrographs show silica-wrapped core–shell micro-granules and the carbon core after leaching. [42, 43] Reproduced with permission from Ref. (Reproduced from Ref. with permission from the Royal Society of Chemistry)

carbon nanoparticles assemble near the core, while hydrophilic particles, i.e. silica nanoparticles occupy the peripheral region of the droplet. In the course of drying, nano-structured carbon gets encapsulated by porous nano-structured shell of silica [42]. The schematic in Fig. 11.22 depicts how the contrasting interfacial interaction of nanoparticles with solvent has been utilized during evaporation-induced self-assembly to encapsulate nano-structured porous carbon core inside nano-structured porous silica shell.

SANS and SAXS measurements have been carried out to characterize the hierarchical mesoscopic structure of the spray-dried micro-granules. Combining SANS and SAXS (Fig. 11.23), a wide wave vector transfer range of three decades (0.003–2.5 nm^{-1}) has been accessed to map the positional correlation and particle form factor in mesoscopic length scale domain. In complementary to scattering investigations, field emission scanning electron microscopy (FESEM) has also been used to directly image the micro-granules in order to corroborate the results inferred from scattering.

The granules show unique features as far as application in water filtration is concerned. The hydrophilic shell of highly correlated nano-silica offers a wetting surface for convenient incorporation in polymeric ultra-filtration membrane. In addition to this, water transport occurs through the interstitial nano-pores towards the meso porous carbon core. It is to be noted that for decades, activated carbon is being used as water purification filter, because of its high specific surface area enabling adsorption of various organic compounds. Carbon is widely used in every household water filter for its high efficiency in maintaining the taste and odour of drinking water. In modern method of household drinking water purification, polymeric semi-permeable ultra-filtration membranes are also being exploited in separating colloidal

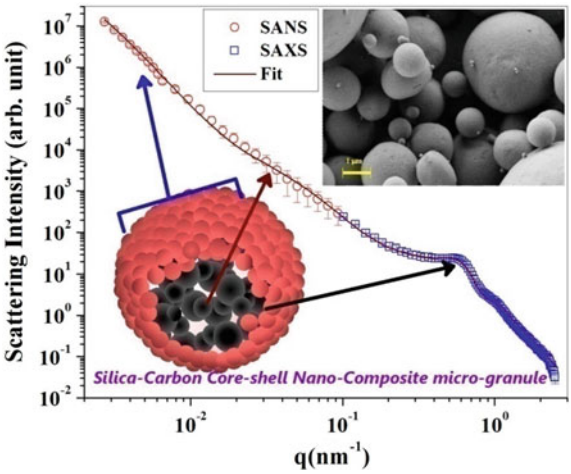

Fig. 11.23 Combined SANS and SAXS profile of the silica–carbon composite spray-dried granules. The inset shows the electron micrographs of the silica-wrapped spray-dried granules. [42, 43] Reproduced with permission from Ref. (Reproduced from Ref. with permission from the Royal Society of Chemistry)

and suspended matters from water [50, 51]. The carbon–silica nano-composite micro-granule, because of its core–shell morphology, is easy to incorporate into ultra-filtration membrane, and thus allow us to combine two separate filtration unit into a single one. The incorporation of these granules into a polymeric membrane has been accomplished and the performance is tested [42, 51]. Results reveal significant enhancement of water permeability (up to ~18%) through the micro-granules-incorporated membranes, and the rejection of PEO-100 K from water is almost 100% which has a huge impact as far as membrane separation characteristics are concerned. This is due to available interstitial pore channels and large specific surface of mesopores present in the micro-granules. The synthesized composite membrane, in comparison to standard polymeric membrane, can be utilized to gain the benefits of superior adsorption properties of mesoporous carbon combining with its own ultra-filtration separation characteristics with enhanced flux. Use of such silica–carbon composite membrane will make a household water filter substantially compact as the need for separate charcoal column, used in a standard filter, will become redundant.

11.6 Future Outlook

The representative studies discussed in this chapter show that the evaporation-induced assembly through spray drying technique is indeed a novel route to realize nano-structured micro-granules with interesting shape and pore structure. At this juncture, it is relevant to discuss the future prospects and associated challenges of this novel bottom-up technique. There are several aspects in this field which needs to be brought into closer scrutiny in order to understand this complex assembly procedure which crucially depends on several physicochemical parameters. Understanding the nature

of assembly of anisotropic colloids is highly desirable. Such assembly may ultimately result into a facile route in realizing porous granules with aligned ordered pore channels in the granules. Further, evaporative assembly of the anisotropic colloids can also be coupled with electric or magnetic field in realizing tunable architecture of granules. Apart from synthesis, the challenge remains in establishing an appropriate methodology in analysing small-angle scattering data from such granules with complex internal structure. Here, it is interesting to mention that random jamming of anisotropic particles is an interesting problem in general, and the established theory about the interparticle correlation in such concentrated system of anisotropic particles may be verified. Creation of Janus and core–shell granules by controlling the interparticle interaction during assembly still remains a challenge. Atomization, using three-fluid nozzle, of mixture of two colloids with contrasting hydrophilic and hydrophobic characteristics and proper tuning of interparticle interactions may result in such interesting morphology of the granules and thus needs attention. The inherent procedure of spray drying technique often involves hydrodynamic parameters apart from the thermodynamic parameters. Thus, it indeed remains a challenge to differentiate the individual role of these parameters in tuning the shape of the granules as well as the internal correlation of the nanoparticles. It is discernible from the above sections that such porous granules have several potentials for technological use including filtration and remediation depending on their shape and internal structure. Thus, challenge remains to optimize the synthesis parameters to tune the shape of the granules in addition to realizing extremely narrow distribution of their size. It is worthy to mention that in standard spray drying process, the coalescence of the droplets in the chamber at high feed rate remains an issue. Thus, experiments on levitated single drying colloidal droplets in an ultrasonic levitator may be useful in this regard while deciphering the role of various competitive physicochemical parameters. Further, it is worth mentioning that the effects of confinement on various chemical reaction equilibrium in nanoporous materials is an emerging field, and thus these porous granules may be used as host materials for such chemical reaction.

In short, evaporation-induced assembly of the colloidal particles in contact-free droplets can be realized through spray drying in order to obtain nano-structured micro-granules. The granular shape, internal correlation, porosity, etc., can be tuned by proper control of the governing parameters, including drying rate, viscosity, surface tension, size of colloids, interparticle interaction, etc. Such porous granules promise several technological applications.

References

1. Caruso F, Caruso RA, Möhwald H (1999) Production of hollow microspheres from nanostructured composite particles. Chem Mater 11(11):3309–3314
2. Martinez CJ, Hockey B, Montgomery CB, Semancik S (2005) Porous tin oxide nanostructured microspheres for sensor application. Langmuir 21(17):7937–7944
3. He Y (2005) Nanostructured CeO_2 microspheres synthesized by a novel surfactant-free emulsion. Powder Technol 155(1):1–4

4. He Y, Yu X, Zhao X (2007) Synthesis of hollow CuS nanostructured microspheres with novel surface morphologies. Mater Lett 61:3014–3016
5. Iskandar F, Mikrajuddin, Okuyama K (2001) In Situ production of spherical silica particles containing self-organized mesopores. Nano Lett 1:231–234
6. Martinez CJ, Hockey B, Montgomery CB, Semancik S (2006) Preparation of functional nanostructured particles by spray drying. Adv Powder Technol 17(6):587–611
7. Yunker PJ, Still T, Lohr MA, Yodh AG (2011) Suppression of the coffee-ring effect by shape-dependent capillary interactions. Nature 476:308–311
8. Sen D, Mazumder S, Melo JS, Khan A, Bhattyacharya S, D'Souza SF (2009) Evaporation driven self-assembly of a colloidal dispersion during spray drying: volume fraction dependent morphological transition. Langmuir 25(12):6690–6695
9. Sen D, Melo JS, Bahadur J, Mazumder S, Bhattacharya S, D'Souza SF, Frielinghaus H, Goerigk G, Loidl R (2011) Arrest of morphological transformation during evaporation-induced self-assembly of mixed colloids in micrometric droplets by charge tuning. Soft Matter 7(11):5423–5429
10. Sen D, Khan A, Bahadur J, Mazumder S, Sapra BK (2010) Use of small-angle neutron scattering to investigate modifications of internal structure in self-assembled grains of nanoparticles synthesized by spray drying. J Colloid Interface Sci 347(1):25–30
11. Bahadur J, Sen D, Mazumder S, Santoro G, Yu S, Roth S, Melnichenko Y (2015) Colloidal nanoparticle interaction transition during solvent evaporation investigated by in-situ small-angle X-ray scattering. Langmuir 31(16):4612–4618
12. Sen D, Bahadur J, Mazumder S, Santoro G, Yu S, Roth SV (2014) Probing evaporation induced assembly across a drying colloidal droplet using in situ small-angle X-ray scattering at the synchrotron source. Soft Matter 10(10):1621–1627
13. Masters K (1991) Spray drying handbook, 5th edn. Longman Scientific and Technical, Harlow
14. Cazabat AM, Guena G (2010) Evaporation of macroscopic sessile droplets. Soft Matter 6(12):2591–2612
15. Popov YO (2005) Evaporative deposition patterns: spatial dimensions of the deposit. Phys Rev E 71(3): 036313
16. Dunn GJ, Wilson SK, Duffy BR, David S, Sefiane K (2009) The strong influence of substrate conductivity on droplet evaporation. J Fluid Mech 623:329–351
17. Frohn A, Roth N (2000) Dynamics of droplets. Springer, Berlin
18. Sen D, Spalla O, Tache O, Haltebourg P, Thill A (2007) Slow drying of a spray of nanoparticles dispersion. In situ SAXS investigation. Langmuir 23(8):4296–4302
19. Bahadur J, Sen D, Mazumder S, Paul B, Khan A, Ghosh G (2010) Evaporation-induced self assembly of nanoparticles in non-buckling regime: volume fraction dependent packing. J Colloid Interface Sci 351(2):357–364
20. Sen D, Melo JS, Bahadur J, Mazumder S, Bhattacharya S, Ghosh G, Dutta D, D'Souza SF (2010) Buckling-driven morphological transformation of droplets of a mixed colloidal suspension during evaporation-induced self-assembly by spray drying. Eur Phys J E 31(4):393–402
21. Tsapis N, Dufresne ER, Sinha SS, Riera CS, Hutchinson JW, Mahadevan L, Weitz DA (2005) Onset of buckling in drying droplets of colloidal suspensions. Phys Rev Lett 94(1):0183021–0183024
22. Sen D, Ghosh AK, Mazumder S, Bindal RC, Tewari PK (2014) Novel polysulfone-spray-dried silica composite membrane for water purification: Preparation, characterization and performance evaluation. Sep Purif Technol 123:79–86
23. Biswas P, Sen D, Mazumder S, Melo JS, Basak CB, Dasgupta K (2017) Porous nano-structured micro-granules from silica-milk bi-colloidal suspension: synthesis and characterization. Colloids Surf B-Biointerfaces 154:421–428
24. Glatter O, Kratky O (1982) Small angle X-ray scattering. Academic Press, New York
25. Guinier A, Fournet G, Walker BC, Yudowith LK (1955) Small angle scattering of X-rays. Wiley, New York
26. Windsor C (1988) An introduction to small-angle neutron scattering. J Appl Crystallogr 21(6):582–588

27. Boissiere C, Grosso D, Amenitsch H, Gibaud A, Coupé A, Baccile N, Sanchez C (2003) First in-situ SAXS studies of the mesostructuration of spherical silica and titania particles during spray-drying process. Chem Commun 2798–2799
28. Pedersen JS (1997) Analysis of small-angle scattering data from colloids and polymer solutions: modeling and least-squares fitting. Adv Colloid Interface Sci 70(Supplement C):171–210
29. Kinning DJ, Thomas EL (1984) Hard-sphere interactions between spherical domains in diblock copolymers. Macromolecules 17(9):1712–1718
30. Menon SVG, Manohar C, Rao KS (1991) A new interpretation of the sticky hard sphere model. J Chem Phys 95:9186–9190
31. Baxter RJ (1968) Percus-Yevick equation for hard spheres with surface adhesion. J Chem Phys 49:2770
32. Pedersen J (1994) Determination of size distribution from small-angle scattering data for systems with effective hard-sphere interactions. J Appl Crystallogr 27(4):595–608
33. Aswal VK, Goyal PS (2000) Small-angle neutron scattering diffractometer at Dhruva reactor. Current Science, 2000. **79**(7).
34. Mazumder S, Sen D, Saravanan T, Vijayaraghavan PR (2001) A medium resolution double crystal based small-angle neutron scattering instrument at Trombay. Curr Sci 81(3):257–262
35. Thill A, Spalla O (2005) Influence of templating latex on spray dried nanocomposite powders studied by small angle scattering. J Colloid Interface Sci 291(2):477–488
36. Sen D, Spalla O, Belloni L, Charpentier T, Thill A (2006) Temperature effects on the composition and microstructure of spray-dried nanocomposite powders. Langmuir 22(8):3798–3806
37. Bahadur J, Sen D, Mazumder S, Paul B, Bhatt H, Singh SG (2012) Control of buckling in colloidal droplets during evaporation-induced assembly of nanoparticles. Langmuir 28(3):1914–1923
38. Sen D, Bahadur J, Mazumder S, Verma G, Hassan PA, Bhattacharya S, Vijai K, Doshi P (2012) Nanocomposite silica surfactant microcapsules by evaporation induced self assembly: tuning the morphological buckling by modifying viscosity and surface charge. Soft Matter 8(6):1955–1963
39. Bahadur J, Sen D, Mazumder S, Bhattacharya S, Frieinghaus H, Goerigk G (2011) Origin of buckling phenomenon during drying of micrometer-sized colloidal droplets. Langmuir 27(13):8404–8414
40. Biswas P, Sen D, Mazumder S, Basak CB, Doshi P (2016) Temperature mediated morphological transition during drying of spray colloidal droplets. Langmuir 32(10):2464–2473
41. Biswas P, Sen D, Mazumder S, Ramkumar J (2017) Porous microcapsules comprised interlocked nano-particles by evaporation-induced assembly: evaluation of dye sorption. Colloids Surf A-Physicoche Eng Aspects 520:279–288
42. Das A, Sen D, Mazumder S, Ghosh AK, Basak CB, Dasgupta K (2015) Formation of nanostructured core-shell micro-granules by evaporation induced assembly. RSC Adv 5:85052–85060
43. Shen X, Zhang J, Tian B, Anpo M (2012) Tartaric acid-assisted preparation and photocatalytic performance of titania nanoparticles with controllable phases of anatase and brookite. J Mater Sci 47(15):5743–5751
44. Reyes-Coronado D, RodrÃguez-Gattorno G, Espinosa-Pesqueira ME, Cab C, Coss RD, Oskam G (2008) Phase-pure TiO_2 nanoparticles: anatase, brookite and rutile. Nanotechnology 19(14):145605
45. Sclafani A, Palmisano L, Schiavello M (1990) Influence of the preparation methods of titanium dioxide on the photocatalytic degradation of phenol in aqueous dispersion. J Phys Chem 94:829
46. Zhang H, Banfield JF (1998) Thermodynamic analysis of phase stability of nanocrystalline titania. J Mater Chem 8:2073
47. Bahadur J, Sen D, Mazumder S, Sastry PU, Paul B, Bhatt H, Singh SG (2012) One-step fabrication of thermally stable TiO_2/SiO_2 nanocomposite microspheres by evaporation-induced self-assembly. Langmuir 28(31):11343–11353
48. Gangwal S, Cayre OJ, Bazant MZ, Velev OD (2008) Induced-charge electrophoresis of metallodielectric particles. Phys Rev Lett 100(5):058302

49. Klein MK, Saenger NR, Schuetter SP, Zumbusch A (2014) Shape-tunable core-shell microparticles. Langmuir 30(42):12457–12464
50. Upadhyayula VKK, Deng S, Mitchell MC, Smith GB (2009) Application of carbon nanotube technology for removal of contaminants in drinking water: a review. Sci Total Environ 408(1):1–13
51. Das A, Sen D, Mazumder S, Ghosh AK (2017) Nano-structured silica coated mesoporous carbon micro-granules for potential application in water filtration. AIP Conf Proc 1832(1):050094

Chapter 12
Amphiphilic Self-Assembly in the Synthesis and Processing of Nanomaterials

Bijaideep Dutta, K. C. Barick, Gunjan Verma, Sipra Choudhury, R. Ganguly, and P. A. Hassan

Abstract In recent years, the self-assembly of amphiphiles has been exploited to create nanostructures with controlled architecture and morphology. Maneuvering the intermolecular interactions between organic molecules offers attractive routes to tune the morphology of self-assembled structures. These structures can act as templates or nanoreactors for the creation of different inorganic materials. Amphiphiles have a significant role in regulating the nucleation and growth process of nanomaterials during liquid-phase synthesis. Dynamic equilibrium structures of micelles are employed in fine-tuning the colloidal stability, size distribution, and morphology of a variety of inorganic materials, polymers, etc. The synthesis of inorganic materials in the presence of organic additives offers nanostructured composites with superior properties. Microemulsions are employed as nanoreactors for the synthesis of size-controlled nanoparticles of lipids, polymers, metals, etc. The application of block copolymers in the production and ordering of nanomaterials is gaining increasing attention. Molecular self-assembly has become a key tool in the fabrication of a variety of materials with potential applications in biomaterials development, as carriers for drug delivery and templates for ordered nanostructures. Thus, this chapter focuses on the principles of the self-assembly process, its role in controlling the structure of materials and its applications in the emerging areas of materials development.

Keywords Self-assembly · Amphiphiles · Surfactants · Nanomaterials · Composite · Thin film

B. Dutta · K. C. Barick · G. Verma · S. Choudhury · R. Ganguly · P. A. Hassan (✉)
Chemistry Division, Bhabha Atomic Research Centre, Mumbai, India
e-mail: hassan@barc.gov.in

Homi Bhabha National Institute, Mumbai 40094, India

A. K. Tyagi and R. S. Ningthoujam (eds.), *Handbook on Synthesis Strategies for Advanced Materials*, Indian Institute of Metals Series,
https://doi.org/10.1007/978-981-16-1803-1_12

12.1 Introduction

Amphiphiles undergo spontaneous association into longer and meticulous arrangements. In this process, molecular building blocks organize into a well-ordered structure, by virtue of specific mutual interactions [1, 2]. Self-assembly processes, related to amphiphilic molecules, offer a unique platform for developing new nanomaterials for advanced scientific applications [3]. Nature created the maturation of biomolecules from the primordial by self-assembly and eventually shaped a colossal amount of complex biological systems. In biological systems, self-assembly is omnipresent and the assembled structures have their exclusive cellular functions. Thus, the self-assembly processes of amphiphiles have drawn significant interest for the past few decades due to their explicit biological system mimicking competence such as assembly of proteins and lipids apace with comprehensive utilization in biological applications. Contemporary advancements in the area of nanotechnology accelerated the amalgamation of elementary processes of self-association with the progressive concept for the design of hierarchical nanostructures. Inauguration of stimuli-responsive amphiphilic assembly–disassembly mechanism grants new methods for producing diverse bionanotechnology applications. Hence, studying amphiphilic self-assembly is imperative to the present effort of nanotechnology as this process caters to the direction of creating molecular building blocks [4–7].

12.2 Self-Assembly of Amphiphiles

Amphiphiles are natural or synthesized molecules that contain two distinct parts; namely, a hydrophilic part (*water-loving*, polar) designated as "head" group and a hydrophobic part (*fat-loving*, 'tail" group), which are able to aggregate into various nanostructures [8]. In conventional amphiphiles, the *fat-loving* tail often consists of a long hydrocarbon chain (either saturated or unsaturated), whereas the *water-loving* head can be ionic (cationic/anionic) or nonionic in nature. Typical hydrophilic head groups of the nonionic surfactants are polyhydroxyl or polyether units. Unlike ionic surfactants, these surfactants do not dissociate upon dissolving in an aqueous medium and possess a wide range of properties based on the ratio of hydrophilic-lipophilic balance (HLB). The most common nonionic surfactants are polyglycerol alkyl ethers, ester-linked molecules, Spans (sorbitan esters), Brij and Tweens, etc. Cationic surfactants are composed of a positively charged headgroup and a halide counterpart. Cetyltrimethylammonium bromide (CTAB) and dodecyltrimethylammonium bromide (DTAB) are widely used cationic amphiphiles. Anionic surfactants generally consist of negatively charged headgroups (carboxylate, sulfate, sulfonate and phosphate) and positively charged counterparts (Na^+, K^+ or NH_4^+ ions). Sodium bis(2-ethylhexyl) sulfosuccinate, with the trade name Aerosol-OT (AOT) and sodium dodecyl sulfate (SDS) are common examples of anionic surfactant. In zwitterionic amphiphiles such as phospholipid phosphatidylcholine, the headgroups have both

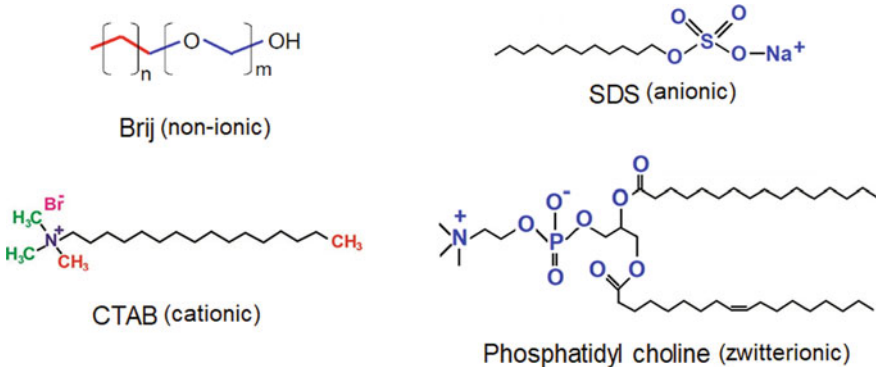

Fig. 12.1 Structures of a few common surfactants under different categories

positive and negative charge moieties. The chemical structures of some surfactants are shown in Fig. 12.1.

When dissolved in water, the polar head group of the surfactant interacts with the water, whereas the nonpolar tail migrates toward the interface (either toward air or nonpolar liquid). Thus, the interruption of cohesive energy at the interface helps the formation of micelles, vesicles, lamellae, etc. Micelles are equilibrium assemblies of amphiphile/ surfactant molecules dispersed in a liquid medium. Micelles are formed when the concentration of amphiphile reaches above a threshold value known as the critical micelle concentration (CMC). In a normal micelle, polar or ionic heads create an outer shell in association with water, whereas nonpolar hydrophobic tails are seized in the interior. The amphiphilic molecules can also form micelles in nonpolar organic mediums. These micelle aggregates are termed as inverse or reverse micelles. In inverse (reverse) micelles, the polar head groups are situated at the core, while the tails extend outwards to the solvent medium. In addition to micelles, amphiphiles help in the formation of microemulsions which are clear and thermodynamically stable liquid dispersions containing water, oil and surfactant. Often, in microemulsions, the aggregates are much larger in size. There are mainly three varieties of microemulsions such as direct (oil dispersed in water, o/w), reversed (water dispersed in oil, w/o), and bicontinuous. They have large liquid cores surrounded by a surfactant monolayer which stabilizes the dispersion. The microemulsion domains are typically studied by making ternary-phase diagrams mainly consisting of two immiscible liquids and a surfactant. Most of the microemulsions use water and oil as two immiscible liquids. The shape of micelles is mainly spherical. However, other shapes like bilayers, ellipsoids, and cylinders also exist. In a few cases, micelles can grow very long and entangle like long-chain polymer. The amphiphiles do not always associate with micelles and in some cases, they associate into extended flat lamellae without forming a closed structure (so-called lamellar structure). Closed bilayer structures are known as vesicles which encircle an aqueous pool and are surrounded by an aqueous solution. It composes of a bilayer of amphipathic molecules, in which the hydrophilic heads of the outer layer are exposed to the outer side, whereas the hydrophilic heads

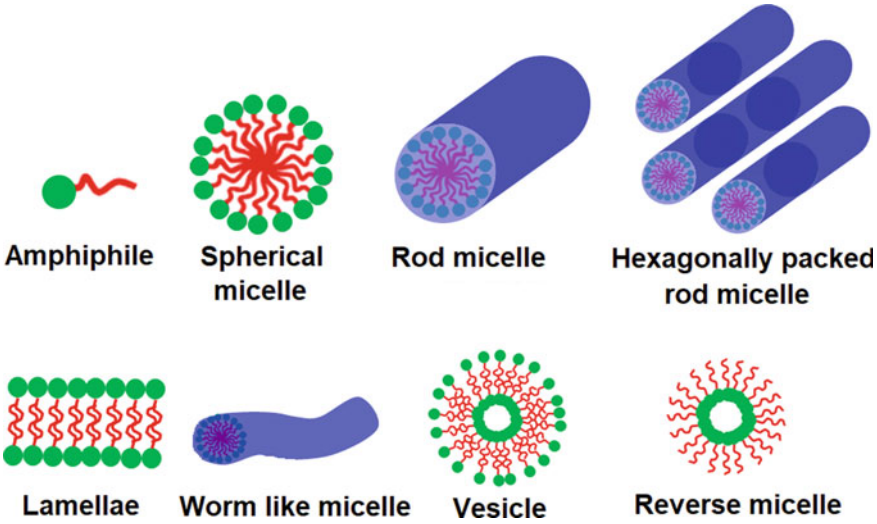

Fig. 12.2 Schematic representation of different structures formed by amphiphiles

of the inner layer make the inner hydrophilic core. The hydrophobic tails are situated in between the bilayers of two concentric circles. The schematic representation of micelles, vesicles, and lamellae is shown in Fig. 12.2. The formation of these self-assembled structures based on critical packing parameters is discussed in the following section.

12.2.1 Morphological Control of Self-Assembled Structures

12.2.1.1 Surfactant Assemblies

The self-association of amphiphilic molecules results in a large variety of structures such as spherical micelles, anisotropic micelles, bilayers, vesicles, liposomes, microemulsions, liquid crystalline dispersions, etc. The morphology of these aggregates is governed by the interaction of hydrophilic and hydrophobic forces responsible for the self-assembly process [9, 10]. The hydrophobic effect due to the hydrocarbon tails favors the self-assembly process. On the other hand, the solvation of the hydrophilic head group restricts the packing of amphiphilic molecules and hence opposes the self-assembly. The electrostatic repulsion between the head groups of ionic surfactants also contributes toward limiting the growth of self-assembled structure. In general, the stability of association structures in solution depends on the hydration of the polar head groups and insertion of the nonpolar tail in the solvent. The amphiphile self-assemble into various supramolecular structures mainly due to the combined effect of various noncovalent interactions such as solvation,

hydrogen bonding, hydrophobic effect, etc. The other important interparticle interaction involved in amphiphile self-assembly, specifically with ionic amphiphiles self-assembly is denoted by the Derjaguin, Landau, Vervey, and Overbeek (DLVO) theory [11]. This theory is the key foundation to rationalize the interfacial forces acted among charged amphiphiles and explain their agglomeration behavior in solution [12]. Further, the geometry (size and shape) of self-assembled structures depends on various additional factors like surfactant concentration, nature of surfactant, ionic strength of the medium, nature of the counterion, temperature, pH and nature of the additives, etc. The prediction of the geometry of a self-assembled structure in a surfactant-water system was a subject of major interest in the past. Consequently, some models have been proposed, which are helpful in predicting the shape of self-assembled structures in the surfactant-water system. The morphology of self-assemblies is satisfactorily explained by the geometric packing models [13, 14]. According to this model, the three main factors that dictate the geometry of a surfactant aggregate are length (l) and the volume (v) of the hydrophobic chain and the effective interfacial (head group) area (a_o) of the surfactant molecule. For a hydrocarbon chain, the length (l) and volume (v) of the surfactant tail can be found by the Tanford formulae using the following equations:

$$v = 27.4 + 26.9n\ (\text{Å})^3 \tag{12.1}$$

$$1 = 1.5 + 1.265n\ (\text{Å}) \tag{12.2}$$

"n" represents is the number of carbon atoms in the linear alkyl chain.

The head group area of the surfactant molecule can be obtained from surface tension (γ) data using Gibbs adsorption isotherm. Surfactants are amphiphilic in nature and in their presence, the surface tension of water decreases due to the adsorption of molecules at the surface. A steady reduction in γ followed by a linear decrease can be seen in the plot of γ versus log C (concentration of surfactant). Once CMC is attained, no change in γ occurs. From the slope of the linear portion of γ versus -logC plot, the surface excess concentration Γ (number of moles of surfactants per unit area (m^2) at the interface) can be determined using Gibb's equation.

According to the Gibbs relationship, at constant temperature, the surface tension γ and the surface excess (Γ) for a single surfactant component can be simply expressed as follows:

$$d\gamma \big/ d\log C = -2.303\Gamma RT \tag{12.3}$$

where C, R, and T represent the surfactant concentration, gas constant, and absolute temperature, respectively.

The area per molecule can be obtained from Γ, by using the relation,

$$\text{Area per molecules } (a_o) = 1 \big/ \Gamma N_A \left(m^2\right) \tag{12.4}$$

$$\text{or } 10^{18}/\Gamma N_A(\text{nm}^2) \tag{12.5}$$

where N_A is Avogadro's number. For ionic surfactants having carboxylate, sulfate, headgroups, etc., the area per surfactant is usually in the range of 0.4 nm^2, while for nonionic surfactants it is much higher (1–2 nm^2). Israelachivili and coworkers [14] suggested that the geometry of aggregated structures formed in the solution is a resultant of the optimum packing of molecules into aggregates. The optimum packing of surfactants into a surfactant assembly can be defined by a dimensionless parameter known as the critical packing parameter. The critical packing parameter (N) depends on the length (l) and volume (v) of the hydrophobic part, and the effective head group area (a_o) of the surfactant molecule.

$$N = v/a_o 1 \tag{12.6}$$

The packing parameter for different geometries of aggregates is different as per simple geometric calculations. For instance, the volume and surface area of a spherical micelle of radius, R and aggregation number, N can be expressed as

$$4/3\pi R^3 = Nv \tag{12.7}$$

$$4\pi R^2 = Na_o \tag{12.8}$$

Here v and a_o are the volume and headgroup area of the single surfactant molecule.

Since the maximum radius of a spherical micelle can be the length of the hydrocarbon part, l. by rearranging the Eqs. 12.5 and 12.6, we get

$$R = 3v/a_o \leq 1 \tag{12.9}$$

or in in the form of packing parameter, we can write it as

$$v/a_o 1 \leq 1/3 \tag{12.10}$$

Therefore, if the value of N is less than 1/3, the aggregates will preferably result in spherical geometry. In a similar manner, if the packing parameter is calculated for cylindrical geometry, N will be between 1/3 and 1/2, while for curved bilayer or vesicles, it is 1/2. For flat bilayers, the packing parameter approaches 1, whereas, for reverse micelles, the value of N is > 1.

In the case of vesicles, bilayers etc., there is another factor known as curvature energy, which is very crucial in controlling the geometry of the aggregates. As per the model of Helfrich [15], the free energy (F) per unit area (A) of a bilayer is related to the bilayer curvature by the equation

$$F/A = 1/2\kappa_s(c_1 + c_2 - c_s)^2 \tag{12.11}$$

where c_1 and c_2 represent two principal curvatures of the bilayer and c_s represents spontaneous curvature. The rigidity of the bilayer is related to κ_s, the bending modulus which is of the order of $k\beta T$, where $k\beta$ is Boltzmann constant. The different aggregate structure which can be anticipated from the packing parameter is shown in Fig. 12.3.

It is worth mentioning that the packing considerations of the surfactant molecule are built in the spontaneous curvature of the bilayers. For instance, if the interaction between the polar head groups of the surfactant results in a smaller packing area as compared to the hydrophobic tail interactions, the surfactant monolayer will tend to curve in such a way that the polar headgroups are on the inner side of the monolayer. On the other hand, if the interaction between the headgroups leads to the larger packing in comparison to the tail–tail interaction, the polar headgroups arrange themselves on the outer side of the monolayer.

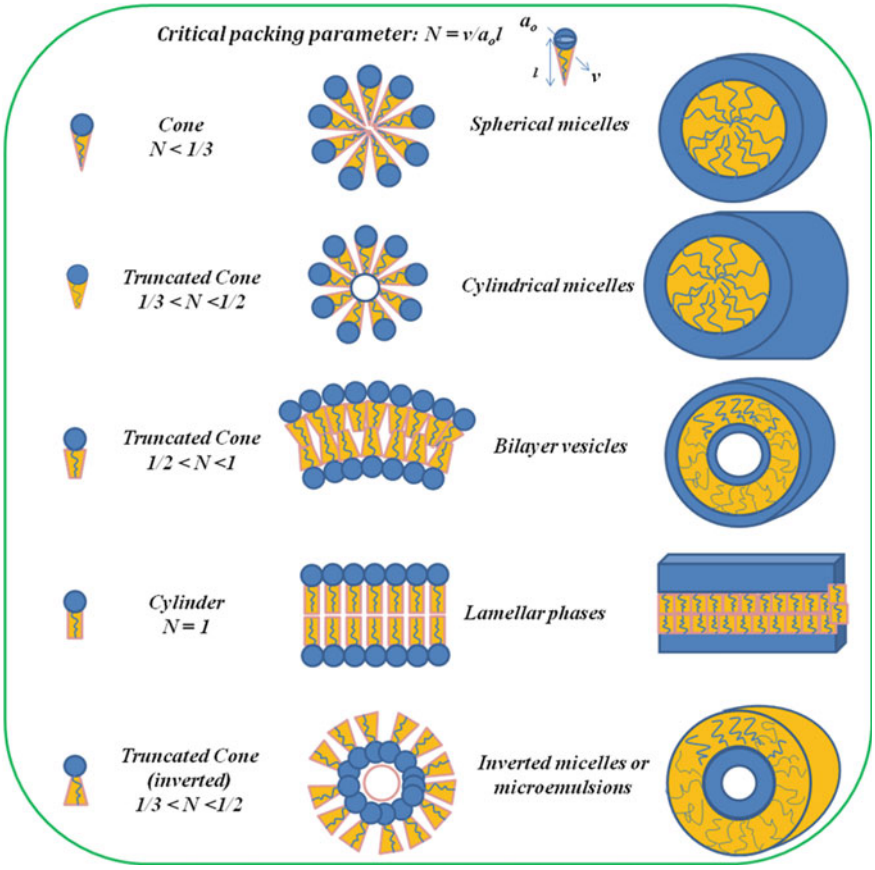

Fig. 12.3 Different aggregate structures which can be predicted from critical packing factor

12.2.1.2 Block Copolymer

The concept of amphiphile can be extended to macromolecular polymer-based amphiphiles by linking hydrophilic/hydrophobic polymer blocks. Block copolymers are mainly macromolecular compounds having two or more chemically dissimilar blocks conjugated to each other by covalent bonds. These materials exhibit amphiphilic character when the two blocks show different polarities [16]. The investigation of self-assembly characteristics of these compounds is an interesting research area to explore due to their rich structural polymorphism and different applications such as lithography for microelectronics, photovoltaics, drug delivery, nanostructure formation, etc. [16–19]. Further, block copolymer self-assembly can produce well-ordered structures of different morphologies such as spheres, cylinders, lamellae, vesicles, bicontinuous structures, and many other complexes or hierarchical assemblies [20]. Depending on the absolute and relative block lengths, the nature and architecture of the blocks, these copolymers form a diverse set of nanostructures that range from discrete micelles to vesicles to even gel-forming continuous network structures [16]. Recent progress in the synthesis route facilitate the preparation of block copolymers with desired molecular weights, compositions and architectures [16]. Like conventional surfactants, the self-assembly of these compounds in an aqueous medium is entropy driven arising out of gain in entropy due to destruction of water structures around the hydrophobic blocks [16].

Figure 12.4 shows a typical phase diagram of a block copolymer–water two-component system. At low and very high block copolymer concentrations normal and reverse micelles are formed. Liquid crystalline structures with different microstructures are formed at copolymer concentrations in between these two extremes [21]. Micelles formed are usually core–shell types with the core comprising hydrophobic blocks and the corona comprising the hydrophilic blocks.

Self-assembly behavior of many of these block copolymers is strongly dependent on temperature because of the differential solubility of the different blocks [22]. The solubility of the blocks in general decreases with an increase in temperature and they show phase separation at characteristic temperatures called cloud points

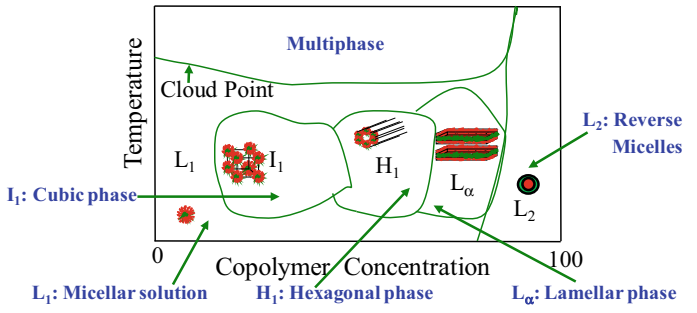

Fig. 12.4 Typical phase diagram of a block copolymer–water two-component system

[22]. Besides, micellar structural changes from spherical to rod-like or to disk-like shapes or to layered vesicle-like structures are also observed on approaching the phase separation temperatures [23]. These are attributed to changing critical packing parameters of the self-assembled structures as a function of temperature. Some of the block copolymers also exhibit critical behavior because of the onset of micellar attractive interaction and resulting micellar cluster formation on the verge of phase separation [24].

Self-assembly characteristics of block copolymers in water are also sensitive to the presence of additives that modulate the solubility characteristics of the blocks. Water structure making salts, hydrophobic solvents and solvents like glycerol increases the hydrophobicity of the copolymers and promotes the formation of aggregates [25]. Water structure breaking salts and solvents like ethanol, on the other hand, have disrupting influence on the self-assembled structure formation [25]. Triblock copolymers like Pluronics form a rich set of self-assembled structures in water-block copolymer–oil three-component systems [21].

12.2.2 Kinetics of Micellization of Amphiphiles

The primary requirement for the formation of self-assembly of amphiphile is the lowest free energy state at equilibrium. Generally, the self-assembly of the structure of amphiphile has lower entropy than the individual counterparts. Thus, the self-assembly of amphiphilic molecules is governed by the interfacial energy of the micellar core with solvent and the conformational distortion energy of the soluble chains and the favorable increase in entropy of the solvent molecules. Micelles are generally considered as spherically aggregated inert structures of amphiphile molecules. However, they are in dynamic equilibrium with individual amphiphile which is continuously replaced among bulk and micelles. Further, the micelles themselves undergo dissolution and reforming. Therefore, there are two relaxation processes occurred in micelle solutions [26]. The fast relaxation process of relaxation time, τ_1 (order of microseconds) is related to the exchange of amphiphile monomers among micelles and the surrounding bulk phase through the collision process. The second slow relaxation time, τ_2 (in the order of milliseconds to minutes) is associated with the process of complete disruption of micelles. The micellar relaxation kinetics are dependent on the concentration of micelle, temperature, and pressure of the micellar solution. A schematic illustration of the two relaxation times, τ_1 and τ_2 related to micelle formation is shown in Fig. 12.5.

Hadgiivanova et al. [27] demonstrated a new free-energy-based theoretical approximation to the kinetics of amphiphile micellization, where the different stages of aggregation are considered as constrained path ways on a single free energy landscape. They have identified three stages of micelle formation such as nucleation, growth, and relaxation steps of well-separated time. The first stage is involved with homogeneous nucleation of micelles, which are dependent on the concentration of surfactant, rate of nucleation, and critical size of nuclei. The first stage is much longer

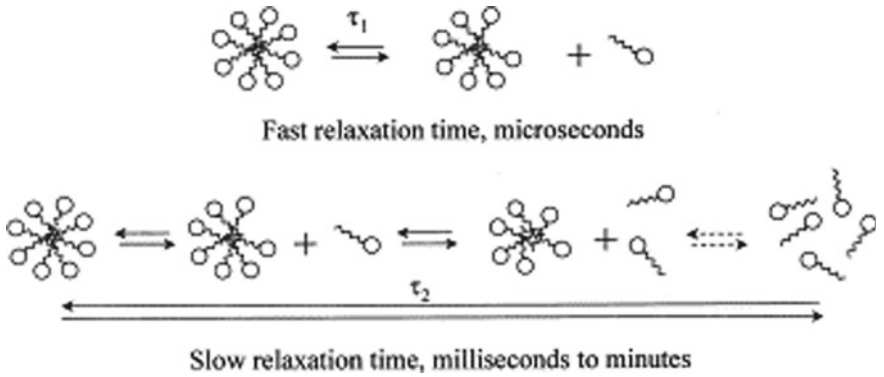

Fig. 12.5 Schematic illustration of the two relaxation times, τ_1 and τ_2 for an amphiphile solution above CMC (reproduced with permission A. Patist et al., Colloids Surf. A: Physicochem. Eng. Asp. 176 (2001) 3–16, Copyright © 2001 Elsevier Science B. V. [26]

than the other two as it is an activated process. The growth stage is diffusion limited for the concentration of surfactant slightly higher than CMC and it is either diffusion limited or kinetically limited for higher concentrations. Depending on the surfactant concentration, the micelle size may be either bigger or smaller than its equilibrium size at the end of the growth stage. In the relaxation stage, micelles relax to the equilibrium size by fission (a decrease in aggregate size) or fusion (an enhancement in aggregate concentration) process.

Kinetics of formation of block copolymer self-assembled aggregates is slower by a few orders of magnitude than that of ionic surfactants owing to their higher molecular mass [28]. Many of the aqueous block copolymer systems thus exhibit time-dependent micellar structural changes and even leads to the formation of kinetically arrested metastable systems [29, 30]. Quite expectedly such tendencies increase with an increase in hydrophobicity and molecular weight of the copolymers making their kinetics of aggregate formation increasingly sluggish.

12.3 Principle of Nanomaterials Synthesis

The nanostructured materials deal with the property-decisive phenomenon that happens in typically the size range of 1–100 nm. The most important part to be focused on is to what the accord between their structures and compositions is, and how their interface supervises the property of the material as a whole [31]. Mainly two different types of methods are often used for producing nanostructures. The first one is the bottom-up method where the material is manufactured from atomic or molecular species through chemical reactions, which enables the particles to grow in size to produce nano-sized structures. These nanostructures can sometimes form in parallel and be nearly identical, with no long-range order. [32, 33]. An opposite

approach is to break a bulk material into smaller pieces using chemical, mechanical or other forms of energy, called the top-down method [34]. In this, lithographic techniques are used to design materials. Materials science desires a handy policy to link these two approaches and to permit the production of materials with a satisfactory resolution [35, 36]. There are many instances of self-assembly connecting top-down and bottom-up constructions [37]. However, bottom-up self-assembly is surprisingly beneficial because it grants the accumulation of structures too small to be manipulated independently into the ordered arrangements or patterns. Researchers have developed varieties of soft-chemical approaches based on bottom-up self-assembly to formulate nanoparticles of well-defined composition, shape, and size. These soft-chemical approaches for the preparation of nanomaterials include the coprecipitation method, sol–gel process, hydrothermal synthesis, high-temperature reactions, microwave irradiation synthesis and polyol method, sonochemical synthesis, microemulsion, etc. [38–40]. In all these synthesis methodologies, the formation of nanoparticles undergoes two important processes, namely nucleation and growth.

12.3.1 Nucleation

In soft-chemical approaches, the nucleation process kicks off the evolution of a new phase from a solution. The atoms or molecules of the reactants reshuffle into a cluster of products, which has the ability to grow irreversibly to a macroscopically bigger size. The cluster or group is entitled as a nucleus or critical nuclei [41]. When nucleation occurs without the presence of foreign particles or crystals in the solution, it is termed as homogeneous nucleation. On the other hand, if the nucleation is induced by the existence of any foreign particles in the solution, it is termed as heterogeneous nucleation. These two together are termed as primary nucleation. In contrary to primary nucleation, secondary nucleation comes into the picture when crystals of the same substance induce nucleation.

The main driving force behind nucleation and subsequent growth of a crystal is supersaturation. This depends on the chemical potential of a molecule in solution (μ_s) and that in the bulk of the crystal phase (μ_c) as follows:

$$\Delta\mu = \mu_s - \mu_c \tag{12.12}$$

Thus, using thermodynamics we can write from Eq. (12.12):

$$\Delta\mu = k_\beta T \ln S \tag{12.13}$$

where T is the absolute temperature, k is the Boltzmann constant and S is the supersaturation ratio [42]. The solution is termed as supersaturated, when $\Delta\mu > 0$, thereby confirming the possibility of nucleation and/or growth, whereas $\Delta\mu < 0$ suggests

that the solution is under saturated and dissolution will take place. Now, this supersaturation ratio can have different forms based on the system under consideration. The mathematical expression for the degree of supersaturation is given below:

$$S = \frac{\Pi a_i^{n_i}}{\Pi a_{i,e}^{n_i}} \tag{12.14}$$

where n_i is the number of *i*th ions in the molecule of the crystal, and a_i and $a_{i,e}$ are the activities of the *i*th species in supersaturated solution and in equilibrium state, respectively.

Now, let us look at the thermodynamics of homogeneous nuclei formation. Figure 12.6 shows the (a) free energy diagram for nucleation explaining the existence of a "critical nucleus" and (b) a representative plot of nucleation rate, J as a function of supersaturation, S showing critical supersaturation. The total free energy of nanoparticles is the summation of the bulk free energy (ΔG_v) and surface free energy (ΔG_S), as shown in Fig. 12.6a [43]. Thus, for a spherical particle with surface energy γ, radius r, and the free energy of the bulk crystal G_v, the total free energy ΔG is given by Eq. 12.5. The bulk free energy (ΔG_v) depends on the degree of supersaturation and is given by Eq. 12.16, where k_β is Boltzmann's constant, S is the supersaturation ratio and V is its molar volume.

$$\Delta G = 4\pi r^2 \gamma + \frac{4}{3}\pi r^3 \Delta G_v \tag{12.15}$$

$$\Delta G_v = \frac{-k_\beta T \ln(S)}{V} \tag{12.16}$$

The surface free energy and crystal free energy are always positive and negative, respectively. Thus, a maximum free energy can be found which a nucleus will surpass to produce a stable nucleus. This critical value of radius can be obtained by equating the first derivative of ΔG with respect to r equal to zero. The critical radius which indicates the minimum size at which a particle can form in the solution without getting dissolved is given in Eq. 12.18. It is evident from the equation that the possibility of nucleation in a given system increases with the increase in supersaturation as critical radius decrease [44].

$$\Delta G_{crit} = \frac{4}{3}\gamma \pi r_{crit}^2 = \Delta G_{crit}^{\text{homo}} \tag{12.17}$$

$$r_{crit} = -\frac{2\gamma}{\Delta G_v} = \frac{2\gamma V}{k_\beta T \ln S} \tag{12.18}$$

The rate of nucleation, J which is defined as the number of nuclei formed per unit time per unit volume is expressed by an Arrhenius-type equation (Eq. 12.19) with the activation barrier equal to ΔG_{crit}:

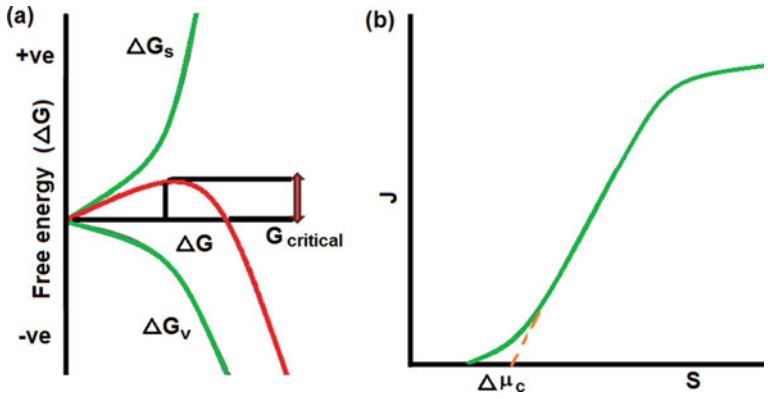

Fig. 12.6 **a** Schematic representation of the free energy diagram for nucleation explaining the existence of a "critical nucleus" and **b** a representative plot of nucleation rate, J as a function of supersaturation, S showing critical supersaturation

$$J = Ae^{-\Delta G_{crit}/k_\beta T} \tag{12.19}$$

From a representative plot of J as a function of S (Fig. 12.6b), we can clearly see that up to a certain value of supersaturation, nucleation rate is essentially zero and then it starts increasing exponentially from there. This critical supersaturation ($\Delta\mu_c$) point describes the allegedly metastable zone showing crystal growth can advance without having collateral nucleation.

Equation 12.17 and 12.18 have shown us that the ΔG_{crit} and r_{crit} both are highly dependent on the surface free energy parameter, i.e., γ. Thus, any change in this parameter will have a certain effect on the nucleation process. Presence of foreign substances decreases the value of ΔG_{crit} and r_{crit} at constant supersaturation and making nucleation more favorable [45]. Decrease in γ also declines the value of critical supersaturation, thus making the heterogeneous nucleation much more feasible than homogeneous nucleation at low supersaturated states. Now, this reduction in surface free energy is maximum when the foreign substance and the crystallizing substance are identical which leads to secondary nucleation.

12.3.2 Growth

Crystal growth is another intricate process where an atom or molecule is deposited over the surface of the crystal, which leads to the increase of size. This growth process can either be reaction limited or diffusion limited. Most of the cases have shown to be diffusion controlled only where temperature and concentration gradient has played a major role in defining the rate of growth as the new material is added to the surface of the particle [46]. There are various theories of nucleation and growth

of nanoparticles available in the literature. We will be discussing a few here to get an overall idea about the same.

(a) LaMer mechanism
The inaugural idea of nucleation and growth was given by LaMer [47] where he separated the nucleation and growth into two different stages (Fig. 12.7). He investigated the preparation of sulfur sols from the decomposition of sodium thiosulphate and proposed two distinct steps where nucleation is the formation of free sulfur from thiosulphate and growth is the formation of sulfur sols. The full process is further fractioned into three parts. (A) at first, the concentration of the free monomer is raised in solution, (B) the second part is the "burst nucleation" that reduces the free monomer concentration and at this point, nucleation is almost arrested due to very low monomer concentration, (C) the third portion is diffusion mediated growth in the solution. Changes in the reactant concentration during all three stages are depicted in Fig. 12.7 [48, 49].

(b) Ostwald ripening
In 1900 another theory was published to describe the growth phenomenon of crystal in solution which was termed as Ostwald ripening [50]. In his theory, he described the crystal growth where smaller particles are being consumed by larger particles and the main cause behind this is the solubility of nanoparticles in size-dependent manner. Greater solubility and the surface energy of smaller nanoparticles in solution enforce them to redissolve and grow larger ones even larger. A detailed mathematical explanation of Ostwald ripening is described by different research groups [51, 52]. Digestive ripening is basically just the

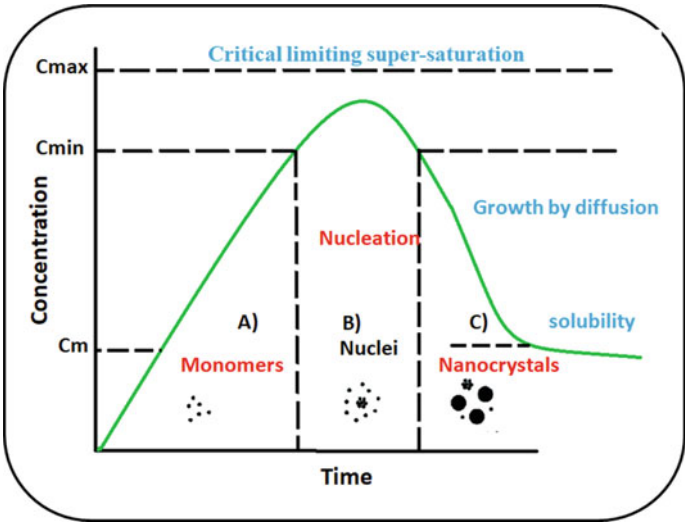

Fig. 12.7 Schematic illustration of the changes in reactant concentration as per LaMer mechanism of nucleation and growth

opposite of Ostwald ripening where larger particles redissolve and smaller particles grow [53].

(c) Finke–Watzky mechanism
Another mechanism was proposed for describing nucleation and growth of nanoparticles which is called as the Finke–Watzky two-step mechanism. In this nonclassical process, nucleation and growth both occur simultaneously [54]. This model fits well in various systems including the synthesis of iridium, platinum, ruthenium, and rhodium [55–57].

12.3.3 Role of Surfactants in Nanomaterials Synthesis

Irrespective of the synthesis approach, the preparation of nanomaterials always comprises nucleation and growth processes. The separation between them is tremendously difficult in the aqueous-based chemical synthesis approaches. The polydispersity of nanoparticles is remarkably decreased when nucleation and growth steps are well separated, which is extremely difficult to achieve. As far as thermodynamics is concerned, without any stabilizer the agglomeration of smaller particles in solution is inevitable. This agglomeration can take place at any stage of synthesis and thus making it a subject of investigation. Mainly two kinds of stabilization can be imparted to nanoparticles. First, electrostatic stabilization by means of repulsion between charged species at the surface and secondly, steric stabilization by virtue of surface fictionalization or capping the surface by long-chain moieties such as surfactants and polymers [58]. The second one is quite common and mostly followed due to its easy fabrication and chemical stability in a wide pH range [59].

Various surfactant molecules are used for the stabilization of nanoparticles in solution and the prevention of nanoparticles aggregation in solution by forming robust coating around the particles during synthesis or post-synthesis process. In addition to this, surfactant amphiphiles are also used as templates or nanoreactors for the synthesis of different shaped controlled nanoparticles [60]. The tuning of the nucleation process with the assistance of surfactant amphiphiles has a significant degree of control over the size distribution of the synthesized nanoparticles. Therefore, nanoparticles synthesis by surfactant self-assembly has been extensively used due to its superior ability in controlling the structural morphology and size of nanoparticles [61–63]. Specifically, nanoparticles–amphiphiles soft interactions are accountable for nanoparticles functionalization, colloidal and chemical stability procedures.

12.4 Self-Assemblies as a Template for Nanomaterials Synthesis

12.4.1 Surfactant Assisted Synthesis

Self-assembly process is ubiquitous in nature. There are several examples in living organisms, where the self-assembly process fabricates unique structures. For example, in bones, teeth, spines, shells, etc., the biomineralization takes place through a self-assembly process on a protein scaffold. In these structures, the organic template and inorganic minerals interact at molecular level and results in the structures with remarkable properties in spite of having very soft templates and brittle minerals as the constituting elements. The use of synthetic templates, inspired by nature is evolving as one of the promising routes for the fabrication of novel materials with controlled architecture inspired by nature. Recently, there is a growing interest in the preparation of hollow inorganic nanomaterials having well-defined geometrical features because of their characteristic properties such as controlled geometry and pore size, low density, huge specific area, and high mechanical and thermal stability. Owing to their fascinating properties, these hollow nanomaterials have tremendous potential for diverse technological applications ranging from everyday materials and processes, medical and health care, energy applications, electronics, and information technology applications to environmental remediation. A number of materials have been involved in pharmaceutical formulations, cosmetics, paint industry, catalysis, as well as for dyes and ink. The geometrical parameters of nanostructures including size, shape, composition, architecture, and surface area are some of the most important parameters to define various important properties of inorganic nanomaterials. Hence a lot of efforts have been made to exploit the fabrication of well-defined inorganic nanostructures using various methods involving physical as well as chemical routes. The involvement of sacrificial templates such as polymeric nanoparticles, self-assembled structures, etc., in the fabrication of nanomaterials with controlled size, morphology, and surface properties have also emerged as a growing field.

The self-assembly templating method has revolutionized the fabrication of smaller well-defined hollow nanomaterials having diameters in the nanometer range. Self-assemblies of amphiphilic molecules are one of the most promising templates to synthesize nanomaterials having defined architecture and high surface area. As discussed above, the self-association of amphiphilic molecules such as ionic/nonionic surfactants results in different structures and the morphology of these self-assembled structures is decided by a number of factors including, surfactant concentration, temperature, and nature of surfactant molecule as well as additives, if any. Self-assembled structures are dynamic in nature and are very receptive to the changes made in the constituting solutions. Hence, their microstructure and properties can be tuned easily by changing the concentration of surfactant, addition of inorganic electrolytes or organic additives as well as by varying the pH and temperature of the medium. For example, in the case of ionic micelles, the addition of inorganic electrolytes decreases intermicellar repulsion as it screens the charge at the micelle surface. This changes

the packing parameter, which in turn changes the morphology of the aggregates. Organic hydrotropes (hydrotropes are used to solubilize hydrophobic compounds in water medium by means other than micellar solubilization) are very effective in inducing the morphological changes in ionic aggregates by decreasing the surface charge at the micellar surface. The swelling of the micelles also takes place due to the solubilization of organic additives in the hydrophobic cores of the aggregates. Similarly, the change in the temperature of the solution results in the alteration of the head group area of the ionic and nonionic surfactants. As a consequence, the packing parameter of the surfactant changes and results in a change in the size and shape of the aggregates [64–69]. Hence, one of the major advantages of using self-assemblies as templates is that the morphology and porosity of the materials can be tuned to the desired extent by tuning the parameters affecting the microstructure of self-assemblies. Amphiphilic block copolymers have also been broadly employed for designing hollow nanostructures and ordered mesoporous materials. The polymeric micelles have a core composed of a hydrophobic block of copolymers and corona made up of the hydrophilic group of copolymers. The core of the micelles acts as a template of the hollow nanostructures and corona acts as a reservoir of the inorganic precursors [70].

The synthesis of inorganic materials, such as silica, titania, alumina, hydroxyapatite, metal oxide, metal phosphate, etc., using self-assembled structures as a template, has been a topic of tremendous importance [71]. There are several reports in which the employment of self-assembly during synthesis has resulted in materials with controlled geometry, and defined porous structure and are found to be very promising for diverse applications. MCM-41, belonging to the family of silicates is a well-known porous material with very high surface areas of the order of 1000 m^2/g with a pore size ranging from 2 to 20 nm and ordered arrays of cylindrical mesopores with very regular pore morphology [72]. During the synthesis of MCM-41, the hexagonal arrays of rod-like micelles of cationic surfactant, cetyltrimethylammonium bromide are employed as a template. The synthesis of material takes place at the surface of the templates and during calcination, the organic template is removed leaving a highly ordered porous material. Due to the large surface area of these materials, the possibility of reactant molecules reacting with the catalyst surface increases. These materials are widely used for catalytic applications. Since, the discovery of mesoporous molecular sieves by Kuroda et al., known as KSW-1 [73] and FSM-16, [74] and by Exxon Mobil, called M41S [72] a great deal of attention has been given to the investigation of mesoporous silica materials due to their wide range of applications. Recently, hollow silica spheres (HSS) with significant inner spaces, high specific surface area, mesoporous structure, and amorphous shell were synthesized using cetyltrimethylammonium bromide micelles as a soft template. The composite membrane prepared by mixing HSS with waterborne polyurethane showed improved water vapor permeability, water resistance, and mechanical performance [75]. In another study, hollow silica nanospheres with a highly uniform size were prepared using a micellar template with a core–shell-corona architecture composed of a triblock copolymer, poly (styrene-b-2-vinyl pyridine-b-ethylene oxide). The empty space in the hollow particle could be regulated by the size of the core regulated by

the chain length of the polystyrene block, while the shell thickness of nanospheres could be tuned by altering the concentration of the inorganic precursors [76].

Porous hydroxyapatite has attracted increasing interest because of its biocompatibility, bioactivity, osteointegration, osteoconductivity, and composition similarity with human bones and teeth. Hydroxyapatite is an inorganic material belonging to the apatite group, which is comprised of calcium, phosphate, and hydroxide. The chemical formula of hydroxyapatite is $Ca_5(PO_4)_3(OH)$, which is commonly written as $Ca_{10}(PO_4)_6(OH)_2$ suggesting the presence of two entities in the crystal unit cell. Bone is a hybrid structure comprised of inorganic needle-shaped carbonated and calcium-deficient hydroxyapatite nanocrystals and the organic part is mainly composed of the collagen matrix. The collagen matrix controls the nanoscale structure of hydroxyapatite and dictates its properties. Inspired by biomineralization, a great deal of attention has been paid by the chemists to the biomimetic synthesis of hydroxyapatite having controlled dimensional, morphological, and architectural features by using nanostructured self-assemblies as templates. The involvement of synthetic polymers and surfactant assemblies similar to that of collagen matrix during synthesis of hydroxyapatite could mimic biomineralization and leads to materials with characteristic morphology and porosity. Due to its excellent properties, synthetic hydroxyapatite has been extensively used in a range of biomedical applications including repairing and regeneration of damaged bones, as a filler for bone defects, and to replace amputated bones and as a bone graft. Hydroxyapatite has also been applied as a coating material to prosthetic implants in order to provide biocompatibility and bioactivity to implants.

The morphology and porosity of hydroxyapatite play an important role in making it a suitable material for biomedical applications. The presence of pores in hydroxyapatite supports the in-growth of bone tissue and full assimilation with the bones. Recently, porous hydroxyapatite is also being considered as a potential carrier for various molecules such as drugs, osteogenic agents, etc., which are used in treating bone infection, diseases, etc. There are several reports, which show the preparation of hydroxyapatite with controllable properties and porous structure using self-assemblies as templates. Stupp and coworkers employed ordered nanofibrous self-assemblies of peptide amphiphiles [77, 78] as nucleating centers for the mineralization of hydroxyapatite. They have also synthesized apatite-based materials using homopolymer poly(amino acids) and synthetic polyelectrolytes [79]. Self-assemblies of surfactants, as well as block copolymers, have been found very promising in dictating the geometry and porosity of hydroxyapatite. The usage of spherical micelles of cationic surfactant cetrimide as a template during synthesis resulted in spherical particles of hydroxyapatite, while in the presence of rod-like micelles of cetyltrimethylammonium bromide, the hydroxyapatite nanoparticles formed were rod-shaped [80–82]. Similarly, well-aligned hydroxyapatite nanorods were formed due to the templating by hexagonal liquid crystalline phase of a nonionic surfactant, Triton X-100, [83]. Several groups have also prepared hydroxyapatite nanostructures using self-assemblies as a template for drug delivery applications. Calcium-deficient hydroxyapatite hollow nanorods having mesopores on their surface were prepared using P123 and tween-60 as templates. The nanorods showed enhanced protein load

and sustained release behavior with a cumulative release of 84.2% over a period of 72 h [84]. In another study, hydroxyapatite hollow nanoparticles (HA HNPs) prepared using core–shell micelles composed of pluronic P123 and Tween-60 showed much higher drug loading for vancomycin drug as compared to nanoparticles prepared in the absence of micelles. In the presence of citric acid used as a cosurfactant, the morphology of the HA HNPs changed from nanospheres to nanotubes and the drug loading efficiency improved further due to the presence of a layer of citrate molecules on the hydroxyapatite surface [85]. An anticancer drug paclitaxel loaded in hydroxyapatite-collagen composites showed enhanced toxicity toward highly metastatic MDA-MB-231 cells in comparison to that of poorly metastatic MCF-7 cells through in-vitro studies. However, the collagen-containing free paclitaxel in the absence of hydroxyapatite was nontoxic toward both the cancer cells suggesting that hydroxyapatite-collagen composite could be employed as a promising drug carrier for paclitaxel [86]. The textural properties of hollow mesoporous carbonated HAp microsphere (CHAM) fabricated using sodium dodecyl sulfate (SDS) mediated precipitation can be controlled by changing the concentration of SDS. The CHAMs showed excellent biodegradability, high loading efficiency for cis-diammineplatinum (II) dichloride and a pH-dependent sustained release of drug. In vitro studies showed that drug-loaded CHAMs have high toxicity toward human squamous cell carcinoma [87].

Mesoporous "transition metal oxides" in particular, titania (TiO_2) have also drawn the attention due to the their intrinsic optical and electronic properties. The mesoporous titania shows extraordinary performance in applications such as photocatalysis and optical devices, which has made it to play a substantial role in solar-energy-based photovoltaic devices. Similarly, the high surface area, larger pore volume, and ordered pore structure of mesoporous TiO_2 make them desirable for various applications. For example, mesoporous TiO_2 (anatase phase) is highly desirable in photovoltaic applications as the photoanodes as high surface area mesoporous TiO_2 maximizes the dye-loading capacity and results in high photovoltaic efficiency [87]. There are several reports presenting the surfactant template-assisted synthesis of mesoporous TiO_2 [88]. Several liquid-crystalline phases of ionic/nonionic surfactants are being employed as a template during the synthesis of mesoporous TiO_2 [89].

12.4.2 Block Copolymer Mediated Nanomaterial Synthesis

Numerous nano-sized self-assembled structures that are formed by block copolymers are good templating agents for generating nanostructured materials with desired and tunable structural properties. Various types of nanostructures formed by using these materials as templates are discussed here. Of late, block copolymer micellar systems are the preferred choice over those of classical surfactants for use as nanocontainers to form metal nanoparticles because of their better kinetic stability and a more robust core-corona structure, which provide better stability to the nano particles against

Ostwald ripening [16, 90, 91]. By incorporating coordination properties in the constituting blocks, we can also induce selectivity in nano particle formation [16, 90, 91]. When physically adsorbed on metal nanoparticles, these block copolymers can stabilize them and in addition, can facilitate their integration into different systems where hydrophobic surface poses a problem [92]. Some block copolymers act as reductants thus avoiding the use of environmentally hazardous reagents and the material properties can be tuned by simply changing the composition of the block copolymers [93]. The presence of block copolymers like Pluronic F127 helps in promoting the formation of nanonetwork and dendritic metal structures with tunable surface properties [94]. In these cases, the copolymer used at a concentration below its CMC indicating that the formation and growth of metal nanostructure occurred along the unaggregated free copolymer chains. Finally, metal nanoparticles formed and dispersed in block copolymer three-dimensional liquid crystalline structures can make nanocomposite materials with suitable mechanical, optical, and electrical properties [95, 96].

According to IUPAC notation, a mesoporous material consists of pores with diameters in the range of 2–50 nm. Apart from silica, which is the most commonly used material for this, other materials like alumina, carbon niobium, tantalum, titanium, zirconium, cerium, and tin too reported to form mesoporous structure [97, 98]. Mesoporous materials have tremendous applications in drug delivery, catalysis, biosensing, ion exchange, optics, and photovoltaics. Block copolymers are widely used to form mesoporous oxides because of their nontoxic and biodegradable nature.

Traditionally, top-down lithographic techniques were used to form structural patterns at nanoscale. These methods are expensive and are inherently slow in pattern writing. Bottom-up self-assembly processes involving block copolymers are thus being considered as a suitable alternative to these traditional methods. Selective etching of one block from the self-assembled structures formed in block copolymer films can be used to form templates for making nanopatterns of magnetic and metal nanoparticles for application in photovoltaics, biosensing, etc. [99].

12.5 Microemulsions as Nanoreactors for Synthesis of Nanomaterials

Schulman et al. proposed the word microemulsion in 1959 [100]. It is a special case of reverse micelles. Reverse micelles are formed when surfactant molecules are dispersed in organic solvents [101]. These spherical aggregates having polar head groups pointed toward the core can also be formed in presence of water molecules. However, larger aggregates are generally appeared in presence of water molecules. If the water to surfactant ratio is greater than 15 ($W^\circ > 15$), then aggregates formed contain a large amount of water molecules, which are termed as microemulsions [102]. Microemulsions are easily differentiated from emulsions through their transparency, low viscosity, and thermodynamic stability. Microemulsions consist of two immiscible liquid (oil and water) phases, where one phase is dispersed in the other

by an interfacial film of surfactant molecules. In microemulsions, both immiscible phases are brought into a macroscopically homogeneous and thermodynamically stable single phase with the help of interfacial surfactants film accumulated at the oil–water interface. Microemulsion contains at minimum three components, such as water (a polar phase), oil (a nonpolar phase), and a surfactant. In many cases, a cosurfactant or cosolvent is added to form a microemulsion. Based on the content of these components and hydrophilic-lipophilic balance (HLB) value, the microdroplets exist in the form of oil-swollen micelles dispersed in water as oil-in-water (O/W) microemulsion (Fig. 12.8a) or water-swollen micelles dispersed in oil as for water-in-oil (W/O) microemulsion, also known as reverse microemulsion (Fig. 12.8b). It is well established that the W/O microemulsions are formed when surfactants with low HLB values (3–6) are used, whereas the formation of O/W microemulsions occurred with surfactants with high HLBs (8–18). On the other hand, microdomains of oil and water are interdispersed within the system in case of bicontinuous microemulsion (Fig. 12.8c). Among these, nano-sized water droplets dispersed in an oil phase have been extensively studied as nanoreactors for aqueous reactions wherein particle formation takes place and size of the droplets decide the size of nanoparticles as well as their polydispersity [103–106]. Other factors such as surface-active agent, the concentration of aqueous reactants, and temperature played important role in controlling of particles size.

The formation of microemulsion in a three-component system of water, oil, and surfactant can be depicted as shown in Fig. 12.9. Water-in-oil microemulsion can be prepared by dispersing water in a hydrocarbon-based continuous phase and positioned to the oil apex of the triangular phase diagram of water/oil/surfactant. In this region, thermodynamically guided surfactant molecules self-assembled to form reverse micelles. However, these micelles are in dynamic equilibrium with individual amphiphiles. They frequently collide through Brownian motion and merge to produce dimers, which may exchange contents and then separated. Thus, the inorganic/organic precursor loaded inside the micelles mixed thoroughly. This exchange process is central to the synthesis of nanoparticles in the core of reverse micelles.

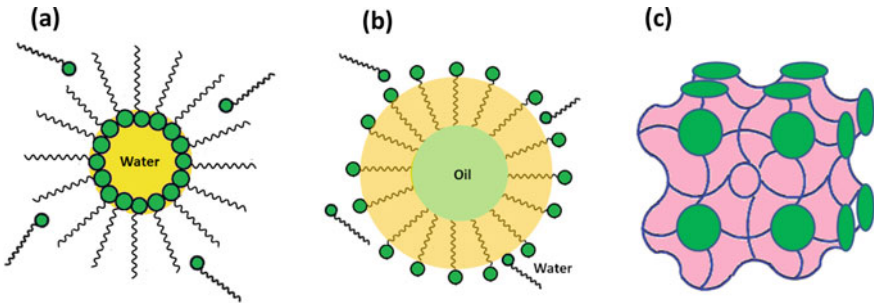

Fig. 12.8 **a** Schematic illustration of water-in-oil (W/O) microemulsion, **b** oil-in-water (O/W) microemulsion, and **c** bicontinuous microemulsion

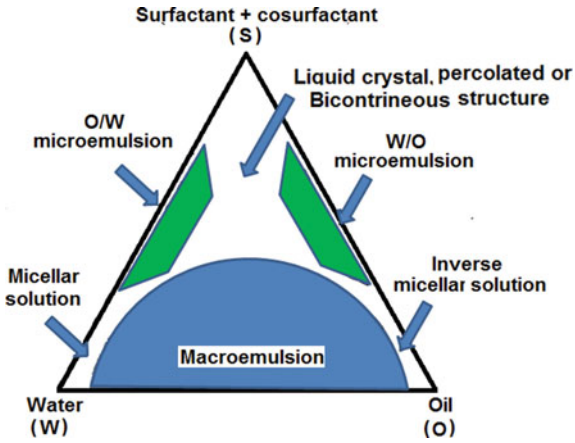

Fig. 12.9 A hypothetical phase diagram of a microemulsion system comprising of oil (O), water (W), and surfactant + cosurfactant (S)

Thus, the reverse micelles mainly act as "nanoreactors" and offer the desired condition for controlled nucleation and growth of particles [107]. In the latter stages of growth, the surfactant layer forms a robust coating on the surface of nanoparticles; thereby reduce the nanoparticle aggregation through steric stabilization [108].

The first step of nanoparticle synthesis in a microemulsion is the reaction between the reactant and the precipitating agent or the two reactants trapped in the core of the microemulsion. There are mainly two approaches for the synthesis of nanoparticles using microemulsion; "Single microemulsion method" and "Double microemulsion method" [109]. Nanoparticle production in a single microemulsion method can be either "energy triggering" or "one micro emulsion plus reactant" method. In the energy triggering method, the reaction is started by applying a triggering agent into the single microemulsion having a precursor. For instance, Kurihara et al. used pulse radiolysis and laser photolysis to trigger the synthesis of gold nanoparticles in water-in-oil microemulsions [110]. In the second approach, the reaction is started directly by introducing one reactant into the microemulsion containing another reactant, i.e., in one microemulsion plus reactant method. In the double microemulsion methods, two reactants that are dissolved in the aqueous nanodroplets of two different microemulsions are permitted to mix through the fusion–fission events. Thus, this method mainly depends on the fusion–fission events between the nanodroplet as shown in (Fig. 12.10).

In general, reactants exchange and mixing occur through the collision of water droplets in microemulsion. The reactants exchange takes place very fast and precipitation reaction occurs in the nanodroplets, followed by subsequent nucleation, growth, and coagulation process to form final nanoparticles. Rauscher et al. [111] demonstrated a typical time-dependent study of the precipitation reaction of $CaCO_3$ in the microemulsion system.

Various metal, magnetic, and semiconductor nanoparticles were successfully prepared by using microemulsion methods. Among the metallic nanoparticles, platinum, palladium, iridium, and rhodium nanoparticles were successfully synthesized

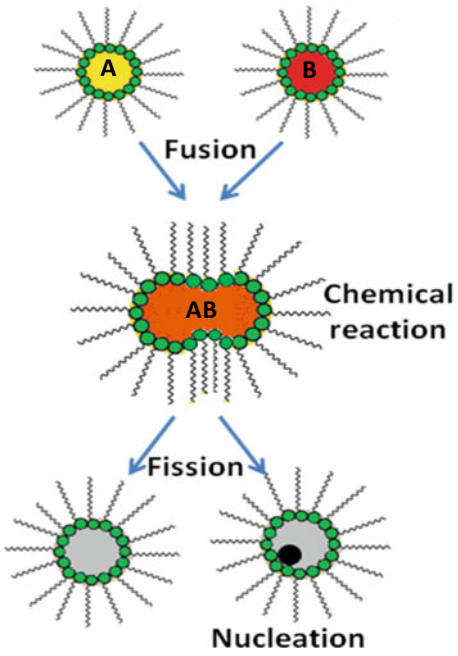

Fig. 12.10 Fusion and fission processes in microemulsion-mediated nanoparticles synthesis

from the microemulsions method [112]. For example, Pal et al. [113] synthesized Pt nanoparticles (<5 nm) by reducing H_2PtCl_6 using $NaBH_4$ in w/o microemulsions of water/TritonX-100/cyclohexene/1-hexanol. Martínez-Rodríguez et al. [114] prepared of shape-controlled Pt nanoparticles using a water-in-oil microemulsion method. They have reported that the shape/surface morphology of Pt nanoparticles is dependent on the concentration of HCl in the water phase of microemulsion. Chen et al. [115] synthesized palladium nanoparticles by reducing Pd salt in aerosol-OT (AOT)/isooctane microemulsion using hydrazine. Kurihara et al. [110] prepared Au nanoparticles by reducing chloroauric acid in w/o microemulsions and reported many advantages of nanoparticles synthesis in the microemulsion method than those in homogeneous solutions. Mihaly et al. synthesized bare and thiol-coated Au nanoparticles through microemulsion assisted photoreduction method using ternary water/Brij 30/*n*-heptane system [116]. Barnickel and Wokaum [116] successfully prepared Ag and Au colloidal nanoparticles by reduction of $AgNO_3$ and $HAuCl_4$ in a dodecyl heptaethyleneglycolether and hexane microemulsions. Qiu et al. [117] reported the preparation of spherical Cu nanoparticles in SDS/isopentanol/cyclohexane/water microemulsions with $NaBH_4$. Bimetallic alloy nanoparticles of Cu-Pt and Pd-Au were also prepared in water-in-oil (w/o) microemulsions of water/CTAB/isooctane/*n*-butanol through the simultaneous reduction of H_2PtCl_6 and $CuCl_2$ using hydrazine at room temperature [118, 119]. Metallic magnetic nanoparticles were also prepared by using microemulsion methods. For instance, Duxin et al. [120] obtained body-centered cubic α-Fe using

anionic surfactants (AOT), whereas Wilcoxon and Provencio [121] prepared face-centered cubic α-Fe using nonionic surfactant (nonylphenol polyethoxylate). Tanori et al. [122] developed magnetic mixed metals (alloys) by using mixed metal precursors in the microemulsion method. Xia et al. [123] discussed the formation of Ag–Ni core–shell nanoparticles by reducing $AgNO_3$ and of $Ni(NO_3)_2$ using $NaBH_4$ in water/polyoxyethylene (4) nonylphenol and polyoxyethylene (7) nonylphenol/*n*-heptane W/O microemulsions. Highly monodispersed ultra-small magnetic oxide nanoparticles were also prepared microemulsions method [124–127]. For instance, Inouye et al. prepared magnetic iron oxide nanoparticles by oxidation of Fe^{2+} salts in an AOT/isooctane system. Lu et al. developed a water-in-oil microemulsion route for synthesizing of Fe_3O_4 nanoparticles using different kinds of surfactant, *n*-heptane, and *n*-hexanol [126]. Liu et al. prepared $CoFe_2O_4$ nanoparticles using sodium dodecylbenzenesulfonate microemulsions in presence of hydrazine [127]. Other magnetic oxides such as $MnFe_2O_4$, $(Mn,Zn)Fe_2O_4$, $(Ni, Zn)Fe_2O_4$, $ZnFe_2O_4$, $Ca_{0.5}Sr_{0.5}MnO_3$, and $BaFe_{12}O_{19}$ were also prepared by various research groups using microemulsion methods [125, 128–131]. In addition, different non-magnetic metal oxide nanoparticles such as Fe_2O_3, SiO_2, ZrO_2, TiO_2, and GeO_2 were also developed using this method [132–141]. For instance, Esquena et al. [133] prepared SiO_2 nanoparticles by addition of $Si(OC_2H_4)_4$ to the solubilized aqueous ammonia solution in AOT and ployoxyethylated nonulphenyl ether W/O microemulsions. Li et al. [140] prepared TiO_2 nanoparticles by microemulsion-mediated hydration method having well-controlled structure and high photoactivity. Geng et al. [135] prepared zirconia nanoparticles in water-in-oil microemulsions of water/cyclohexane/Triton X-100/hexyl alcohol. Han et al. [137] developed size-controlled NiO nanoparticles in W/O microemulsion of Triton X-100/*n*-hexanol/cyclohexane/water. The reverse microemulsion process is also used for the preparation of core–shell nanoparticles. In this synthesis process, the thickness of the shell is usually tuned by different reaction conditions such as time, temperature, concentration of precursor, etc. [142, 143].

A large variety of semiconductor nanoparticles including CdS, ZnS, PbS, CuS, Cu_2S, and CdSe [144–150] were successfully prepared through the microemulsion route. For instance, Agostiano et al. [144] prepared CdS nanoparticles by mixing two microemulsions formed by cetyltrimethylammonium bromide (CTAB), pentanol, n-hexane, and water having $Cd(NO_3)_2$ and Na_2S. Petit et al. [145] prepared CdS nanoparticles in AOT and triton reverse micelles having cadmium lauryl sulfate and cadmium AOT surfactants. Manyar et al. [149] fabricated ZnS nanoparticles using four-component "water in oil" microemulsions containing CTAB, cosurfactant (pentanol or butanol), n-hexane, and water. Ethayaraja et al. [151] synthesized CdS-ZnS core–shell semiconductor nanoparticles using different water-in-oil microemulsions and demonstrated a two-stage mechanism for the preparation of core–shell nanoparticle.

Organic nanoparticles such as whey protein and polymer nanoparticles were synthesized by the microemulsion method. Zhang and Zhong [152] synthesized whey protein nanoparticles with higher heating stability by using microemulsions as nanoreactors. Guo et al. [153] investigated polymerization of styrene in microemulsion of SDS/pentanol/water adding water soluble (potassium peroxodisulfate) as

well as oil soluble (2,2′-azoisobutyronitrile) initiators. Palani et al. [154] explored the polymerization of methyl methacrylate (MMA) through MMA/ethylene glycol dimethacrylate/water microemulsion using acylamide as amphiphile. Microemulsion systems were also employed to synthesize organic nanoparticles of cholesterol, Rhovanil, retinol, Rhodiarome etc. [155, 156]. In an interesting review, Margulis-Goshen and Magdassi [157] discussed various approaches used to prepare organic nanoparticles from microemulsions. Microemulsion not only served as nanoreactors for particle formation but also prevent the agglomeration of nanoparticles as surfactants form a robust coating on particle surface when the particle size reaches that of the water pool.

Microemulsions served as good candidates for drug delivery. Microemulsions are found to improve the therapeutic efficacy of drug molecules and minimize the toxic side effects. It offers several other benefits such as increased absorption, long shelf life, improved clinical potency, decreased toxicity, and ease of preparation and administration. Specifically, the administration of drug molecules through microemulsions is easier for children and adults who have difficulty in swallowing powder or tablet forms of drugs. Thus, microemulsions have been widely used as carriers for the delivery of drug molecules through the oral route. Further, microemulsions have a low viscosity which makes their administration by an intravenous route much easier. Microemulsions are also used for transdermal drug delivery because of their higher solubilization capacity for both hydrophobic and hydrophilic drugs. For example, antifungal hydrophobic agents such as miconazole, ketoconazole, and itraconazole have been delivered via microemulsions-based formulation [158].

12.6 Langmuir–Blodgett Approach for Mesostructured Composites and Thin Films

In today's material science and electronic industries, suitable organic materials in their structured and organized states are of prime importance, as downsizing inorganic material beyond a certain point changes their properties completely. In this respect, Langmuir–Blodgett (LB) technique provides the desired control on the order at the molecular level. Hence, it is a potential technique for the construction of future organic as well as inorganic materials (from organic precursors) for various applications as the molecular orientation and packing can be highly controlled by using various organic amphiphilic molecules with suitably designed architecture and functionality.

Irving Langmuir [159] developed experimental and theoretical concepts which form the basis for the modern understanding of sizes and shapes of molecules in monolayers and their orientation at the interface. He has demonstrated that amphiphilic molecules (having hydrophilic and hydrophobic groups) accumulate on the water surface and form a monolayer where the hydrophilic group (e.g., -COOH, $-NH_2$, -OH) immersed in the water surface and hydrophobic group (long-chain

hydrocarbon) remains above the surface. His early work concentrated on floating monomolecular layer (Langmuir films) at the air–water interface. Later in 1919 under his guidance, Katherine Blodgett [160] had been able to develop, a technique to transfer the monomolecular film from a water surface onto a solid substrate. This is universally known as Langmuir–Blodgett technique. Around 1965 Hans Kuhn [161] and his colleagues began work on the organization of monolayers and their spectroscopic and other physical properties.

The most common technique for studying Langmuir monolayer has been to measure pressure-area isotherm, which is the change in surface pressure as a function of surface area per molecule at a constant temperature. When a long amphiphilic molecule such as fatty acid dissolved in a volatile solvent is spread onto the water surface, the solvent evaporates and molecules remain dispersed as a layer at the air–water interface. By the addition of the surface-active reagent (fatty acid or amine) the surface tension of the water is lowered. The monomolecular layer of the surface-active reagent on the surface of the water exerts a film pressure (π), depending on the surface concentration, such that $\pi = \gamma_0 - \gamma$ where, $\gamma_0 =$ surface tension of the pure water and $\gamma =$ surface tension of the monolayer covered water.

The pressure area ($\pi - A$) isotherm of the monolayer of amphiphilic molecule (fatty organic compound) at the air–water interface (Langmuir films) frequently show features suggesting phase transition [162]. Figure 12.11 shows the (a) schematic of surface pressure-area isotherm of a long-chain fatty acid (e.g., stearic acid) with their various phases, (b) different packing of the molecules in monolayer at various phases, and (c) multilayer structure of the molecules after the collapse at the air–water interface. If a solution of stearic acid is spread on the water surface, surface pressure area isotherm shows various phases, i.e., gas, liquid and solid which has an analogy with the pressure–volume isotherms in three dimensions. In the gas phase (at very low surface pressures), the molecules are almost flat on the water surface. The steepest part of the $\pi - A$ isotherm is associated with a solid and closed-packed region. The intermediate pressure region has been identified as the liquid phase with the hydrophobic hydrocarbon chains start to interact with each other and being lifted away from the water surface. Beyond the closed packed region for a smaller area per molecule, there is collapse and molecules may be forced out of the monolayers. The value of the collapse pressure for a simple fatty acid can be in excess of 50 mN/m which would be equivalent to about 200 atm [163] when extrapolated to three dimensions.

Figure 12.12 shows (a) schematic of LB trough and (b) surface pressure area isotherm of arachidic acid measured using the LB method. When the monolayer on the water surface is compressed with the barrier, the monolayer can be either expanded, partly expanded, or close-packed state at the air–water interface depending on the surface pressure. The structure of the monolayers depends on the nature of the subphase especially for films of fatty acids (or amines) under ionizing conditions when the ionized head group is complexed to its counter cation (or anion). This factor is important in understanding the nature of multilayer LB films as the dissociation of the fatty acid carboxylic group or fatty amine group in presence of different

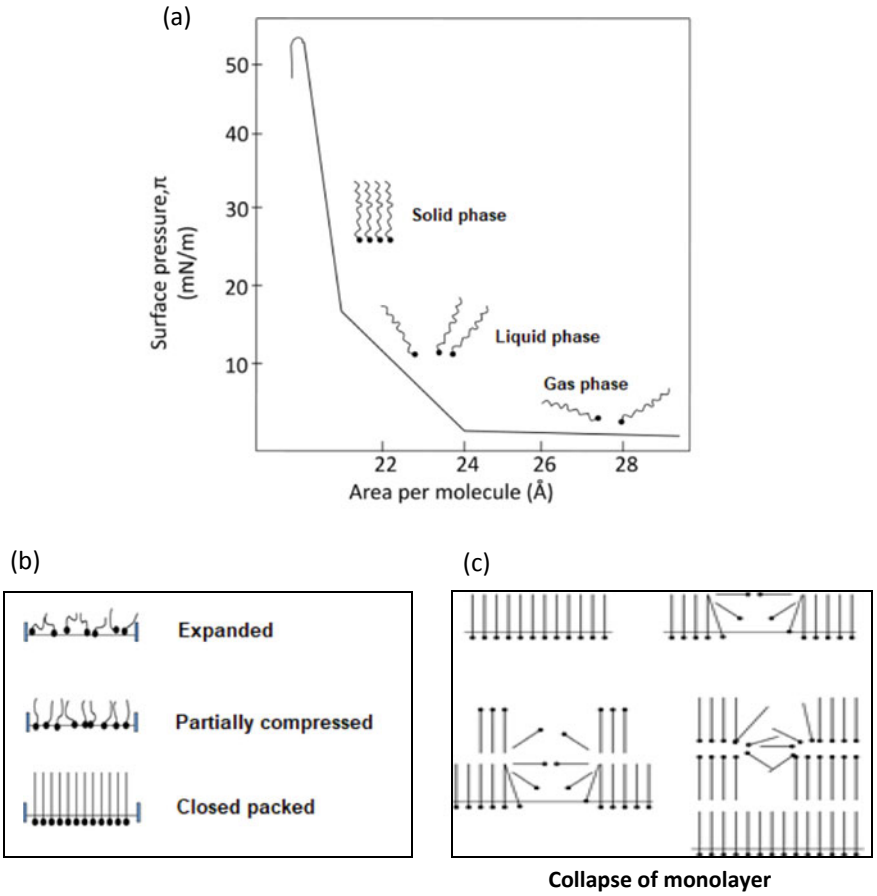

Fig. 12.11 **a** Schematic of surface pressure area isotherm of a long-chain fatty acid (e.g., stearic acid) with their various phases, **b** different packing of the molecules in monolayer at various phases and **c** multilayer structure of the molecules after the collapse at the air–water interface

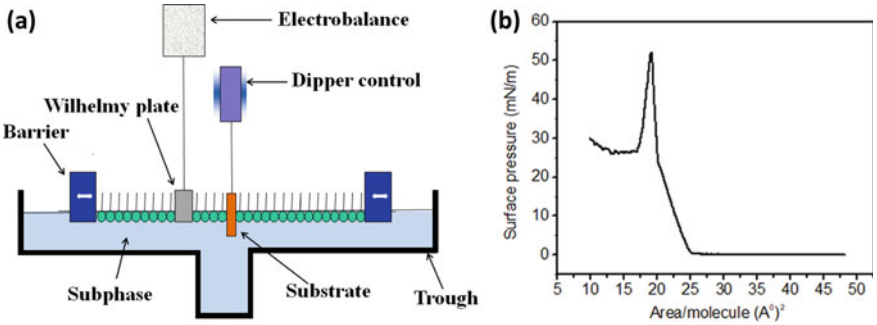

Fig. 12.12 **a** Schematic of LB trough and **b** surface pressure area isotherm of arachidic acid measured using LB trough

multivalent cation or anionic complexes in the subphase depends on the pH of the solution.

$R\text{-}COOH + H_2O \rightarrow R\text{-}COO^-$, $R\text{-}NH_3 + H_2O \rightarrow R\text{-}NH_4^+$ (where R is the long hydrocarbon chain).

In order to form LB multilayer films (Fig. 12.13), a suitable substrate is passed through a compressed monolayer, at a controlled speed to deposit layer by layer on the substrate from the air–water interface. The nature of subsequently deposited layers depends on the surface quality and composition of the substrate. The surface pressure is kept constant during the deposition. The first monolayer is deposited onto a hydrophilic substrate when the substrate rises up through the air–water interface. From the subsequent dipping, two more monolayers are deposited on the first monolayer. The deposition made in a head-to-head and tail-to-tail configuration is referred to as Y-type. There are two more deposition modes X and Z, where deposition occurs as the substrate is being inserted into the subphase or only as the substrate is being removed through air–water interface, respectively. The deposition process can be quantified through transfer ratio (TR) which is given by

$$\text{TR} = \frac{\text{Area of the monolayer removed from the surface at constant pressure}}{\text{Area of substrate immeresed in water}}$$

To investigate the orientation of the molecules and structure of LB films, various analytical techniques such as X-ray diffraction, Fourier transform infrared spectroscopy, X-ray photoelectron spectroscopy, and atomic force microscopy have been used.

It is vital to understand the nature of the stacking of the monolayers in the multilayer LB films in order to obtain the physical–chemical basis for the structure.

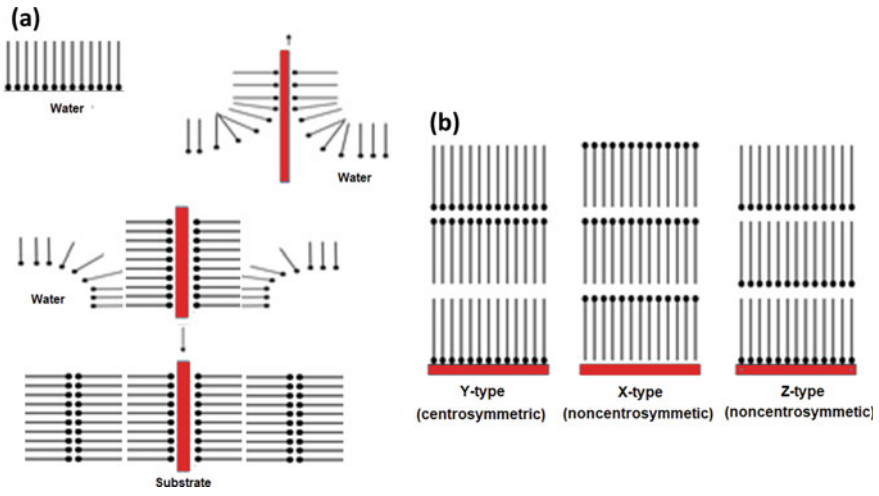

Fig. 12.13 **a** Deposition of multilayers by Langmuir Blodgett technique **b** various type of deposition mode

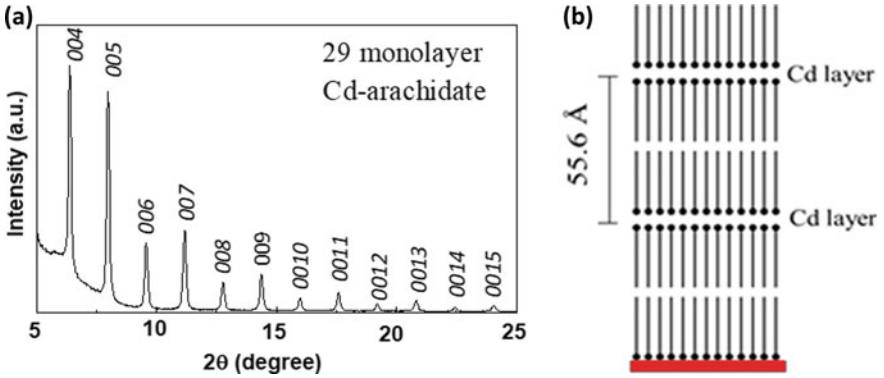

Fig. 12.14 X-ray diffraction pattern of 29 monolayers LB film of cadmium arachidate (C20 fatty acid) indicating 00 l reflections obtained with Cu K_α radiation ($\lambda = 1.5405$ Å). The film was deposited at a constant surface pressure of 30 mN/m using $CdCl_2$ solution (20^{-4} M, pH = 6.5)

Evidence for the multilayer structure may be obtained directly from X-ray diffraction studies of these films. Figure 12.14 represents the diffraction pattern of a multilayer Cd-arachidonate film showing the characteristic odd–even intensity oscillations of the *00 l* reflections. The d value obtained from the 00 l lines using Bragg's law equation is 55.6 Å, which is close to the value of bilayer thickness with hydrocarbon chains and the metal ions. The unit-cell c-parameter of LB films of metal salts of fatty acid changes by ~5.0 Å if the carbon atoms in the fatty acid are doubled [164]. The projected C–C distance along the c-axis is 1.25 Å obtained for all trans configurations assuming a perpendicular orientation of the chains, a tetrahedral angle between the carbon atoms and a C–C distance of 1.54 Å.

Initially, Langmuir–Blodgett technique was used for depositing organic amphiphilic molecules. Pure organic multilayer LB film was made by charge transfer complexes such as molecular electron donor, tetrathiafulvalene and acceptor, tetracyanoquinodimethane derivatives. These films are conducting in nature. Conducting polymers based on polycarbazole, polyaniline, polypyrrole, and polythiophene were organized by LB technique. Metal ion incorporation in the LB film is known for stabilizing of Langmuir monolayer in presence of divalent metal ions such as Cd, Pb, Mn, etc. Organometallic compounds like ferrocene, metal porphyrin, and metal phthalocyanine have been organized by the LB technique [165]. The inorganic–organic hybrid materials such as polyoxometallates incorporated in dimethyldioctadecylammonium can be prepared in a layered structure by the LB technique. These hybrid materials have a great impact in areas of catalysis, medicine, etc.

Langmuir monolayers, due to their simple two-dimensional nature, have been employed as templates that facilitates the crystallization of organic and inorganic materials [166–168]. Functional groups of amphiphilic molecules of Langmuir monolayer act as nucleation or/and growth centers, which control the morphology and orientation of crystal-axis of the crystals grown. Using Langmuir monolayer as a template, the oriented crystals of various inorganic salts such as NaCl, $CaCO_3$,

$BaSO_4$, $SrSO_4$, ice, CdS, PbS, and silver propionate have been successfully grown at the air–water interface. Crystals of Prussian blue analogues are difficult to grow in bulk. However oriented crystals of magnetic Prussian blue analogues have also been deposited at the air–water interface using octadecyl amine (ODA) monolayer as the template. Protonated amine head groups of ODA monolayer acted as the sites for the growth of oriented crystalline film of Prussian blue analogues.

Figure 12.15 shows schematically the growth of oriented crystallization of nickel (II) hexacyanoferrate (III) (NiHCF) in an LB trough at the air–water interface under the ODA monolayer. Initially, when ODA is spread on a (1.5×10^{-4}) M $NiCl_2$ solution, a stable monolayer is formed. A few drops of concentrated $K_3Fe(CN)_6$ solution were put through a micro syringe to the $NiCl_2$ forming greenish-yellow crystalline film of NiHCF after sixteen hours at the water interface. This crystalline film is transferred to a solid substrate by LB technique and from the X-ray diffraction studies, parallel alignment of the {100} crystal plane of Ni-hexacyanoferrate to the ODA surface has been observed [166]. Similar to NiHCF crystallization, growth of cobalt (II) hexacyanoferrate (III) (CoHCF) single crystals and other transition metal hexacyanochromates was observed under the Langmuir monolayer [167, 168]. Other crystals of the Prussian blue family which are generally difficult to grow in the bulk, can be grown at the air–water interface using the ODA monolayer as the template.

Langmuir–Blodgett (LB) technique has been used for preparing ultrathin metal oxides recently [169–175] as an alternative method for metal oxide thin film formation. Usually, by LB technique, a uniform and ordered thin films of various organic materials based on amphiphilic molecules are prepared. To make metal oxide thin

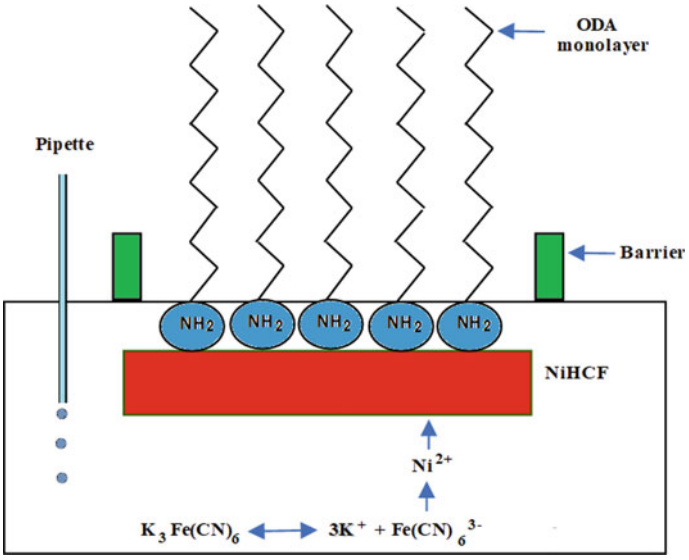

Fig. 12.15 Schematic illustration of oriented crystallization of Prussian blue analogue, nickel (II) hexacyanoferrate (III) under Langmuir monolayer

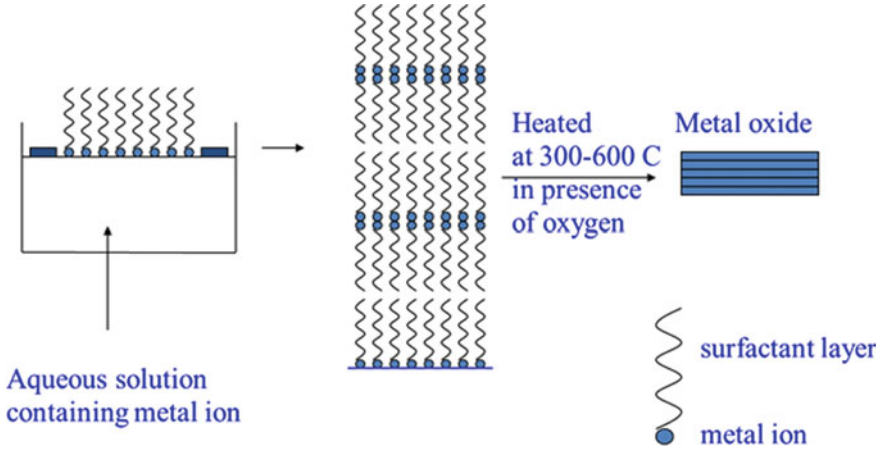

Fig. 12.16 Schematic of metal oxide thin film preparation by using LB technique

films, initially uniform and ordered multilayer LB films of metal salts of amphiphilic molecules are deposited on substrates and then decomposed by heating in the presence of oxygen. Metal ions form thin oxides on the substrate after the dissociation of the salts, decomposition/desorption of long hydrocarbon chain while heating. Thin films of metal oxides such as SnO_2, TiO_2, WO_3, and PdO [169–175] have been prepared by deposition of multilayer films of their corresponding anionic salt and ODA complex, from the air–water interface and subsequent decomposition of multilayer LB films (Fig. 12.16). These metal oxide films prepared from LB precursors have been used for gas sensing, photosensitization, and electrochromism [171–175].

12.7 Conclusions and Future Perspectives

Amphiphiles molecules have a strong affinity to self-assemble in selective solvents into various structures including lamellae, micelles, and vesicles. Diverse morphologies with an internal feature in the nanometer-length scale can be produced by the assembly of small molecules. Such association is occurred by various noncovalent interactions and hence can be modified by varying the environmental conditions such as solvent dielectric constant, pH, temperature, ionic strength, etc. This offers an attractive strategy to develop nanomaterials with tailored properties. The principle of self-assembly process and guiding rules to control the morphology of the assemblies is provided in this chapter. Various of liquid-phase synthesis methodologies of nanomaterials, and the role of amphiphiles in controlling the nucleation and growth process of nanoparticles has also been addressed in detail. The dynamics of these equilibrium structures and their influence on material synthesis are also presented. Applications of a variety of amphiphilic assemblies such as micelles,

microemulsions, block copolymers, etc. in modulating the microstructure of nanoparticles are discussed. The role of amphiphiles in developing thin-film materials with controlled thickness and internal structure using Langmuir–Blodgett approach is being discussed. In summary, self-assembly has been recognized as a novel route for the development of nanomaterials. The future of nanotechnology lies in the large-scale production of materials with controlled structure and order over multiple length scales, and self-assembly could play a promising role in realizing this goal.

References

1. Alivisatos AP (1998) From molecules to materials: Current trends and future directions. Adv Mater 10:1297–1336
2. Barick KC, Bahadur D (2010) Self-assembly of colloidal nanoscale particles: Fabrication, properties and applications. J Nanosci Nanotechnol 10:668–689
3. Glotzer SC, Solomon MJ (2007) Anisotropy of building blocks and their assembly into complex structures. Nat Mater 6:557–562
4. Israelachvili JN (1985) Thermodynamic and geometric aspects of amphiphile aggregation into micelles, vesicles and bilayers, and the interactions between them. In: Degiorgio V, Corti M (eds) Physics of amphiphiles: micelles, vesicles and microemulsions. North-Holland, Amsterdam, The Netherlands, pp 24–58
5. Domb C, Lebowitz JL, Gompper G, Schick M (1994) Self-assembling amphiphilic systems. Academic Press, London, UK, Phase Transitions and Critical Phenomena
6. Wang C, Wang Z, Zhang X (2012) Amphiphilic building blocks for self-assembly: from amphiphiles to supra-amphiphiles. Acc Chem Res 45:608–618
7. Feynman RP (1960) There's Plenty of Room at the Bottom. Eng Sci 23:22–36
8. Lombardo D, Kiselev MA, Magazù S, Calandra P (2015) Amphiphiles self-assembly: basic concepts and future perspectives of supramolecular approaches. Adv Cond Matter Phys 2015:151683
9. Rosen MJ (1989) Surfactants and interfacial phenomena, 2nd edn. Wiley, New York, NY, USA
10. Israelachvili JN (1992) Intermolecular and surface forces, 2nd edn. Academic Press, New York, USA
11. Hunter RJ (1986) Foundations of Colloid Science, Vol. I, Oxford University Press, Oxford
12. Belloni L (2000) Colloidal interactions. J Phys Cond Matter 12:549–587
13. Tanford C (1980) In The hydrophobic effect: formation of micelles and biological membranes, 2nd edn. John Wiley and Sons, New York
14. Israelachvili JN, Mitchell DJ, Ninham BW (1976) Theory of self-assembly of hydrocarbon amphiphiles into micelles and bilayers. J Chem Soc Faraday Trans 2 72:1525–1568
15. Helfrich W (1985) Effect of thermal undulations on the rigidity of fluid membranes and interfaces. J Phys (Paris) 46:1263–1268
16. Riess G (2003) Micellization of block copolymers. Prog Polym Sci 28:1107–1170
17. Otsuka H, Nagasaki Y, Kataoka K (2001) Self-assembly of block copolymers. Mater Today 4:30–36
18. Jeong B, Bae YH, Lee DS, Kim SW (1997) Biodegradable block copolymers as injectable drug-delivery systems. Nature 388:860–862
19. Hawker CJ, Russell TP (2005) Block Copolymer Lithography: Merging Bottom-Up with Top-Down Processes. MRS Bull 30:952–966
20. Mai Y, Eisenberg A (2012) Self-assembly of block copolymers. Chem Soc Rev 41:5969–5985

21. Alexandridis P, Olsson U, Lindman B (1998) A record nine different phases (four cubic, two hexagonal, and one lamellar lyotropic liquid crystalline and two micellar solutions) in a ternary isothermal system of an amphiphilic block copolymer and selective solvents (water and oil). Langmuir 14:2627–2638
22. Alexandridis P, Holzwarth JF, Hatton TA (1994) micellization of poly(ethylene oxide)-poly(propylene oxide)-poly(ethylene oxide) triblock copolymers in aqueous solutions: thermodynamics of copolymer association. Macromolecules 27:2414–2425
23. Khimani M, Ganguly R, Aswal VK, Nath S, Bahadur P (2012) Solubilization of parabens in aqueous pluronic solutions: Investigating the micellar growth and interaction as a function of paraben composition. J Phys Chem B 116:14943–14950
24. Ganguly R, Choudhury N, Aswal VK, Hassan PA (2009) Pluronic L64 micelles near cloud point: investigating the role of micellar growth and interaction in critical concentration fluctuation and percolation. J Phys Chem B 113:668–675
25. Ivanova R, Lindman B, Alexandridis P (2000) Effect of glycols on the self-assembly of amphiphilic block copolymers in water. 1. Phase diagrams and structure identification. Langmuir 16:3660–3675
26. Patist A, Oh SG, Leung R, Shah DO (2001) Kinetics of micellization: its significance to technological processes. Colloids Surf A: Physicochem Eng Asp 176:3–16
27. Hadgiivanova R, Diamant H, Andelman D (2011) Kinetics of surfactant micellization: A free energy approach. J Phys Chem B 115:7268–7280
28. Desai PR, Jain NJ, Sharma RK, Bahadur P (2001) Effect of additives on the micellization of PEO/PPO/PEO block copolymer F127 in aqueous solution. Colloids Surf A: Physicochem Eng Asp 178:57–69
29. Kositza MJ, Bohne C, Alexandridis P, Hatton TA, Holzwarth JF (1999) Dynamics of micro- and macrophase separation of amphiphilic block-copolymers in aqueous solution. Macromol 32:5539–5551
30. Ganguly R, Kumbhakar M, Aswal VK (2009) Time dependent growth of the block copolymer p123 micelles near cloud point: employing heat cycling as a tool to form kinetically stable wormlike micelles. J Phys Chem B 113:9441–9446
31. Jones W, Rao CNR (2002) Supramolecular organization and materials design. Cambridge University Press, Cambridge, UK
32. Lieber CM (2003) Nanoscale science and technology: building a big future from small things. MRS Bull 28:486–491
33. Hecht S (2003) Welding, organizing, and planting organic molecules on substrate surfaces-promising approaches towards nanoarchitectonics from the bottom up. Angew Chem Int Ed 42:24–26
34. Whitesides GM, Grzybowski B (2002) Self-assembly at all scales. Science 295:2418–2421
35. de Wild M, Berner S, Suzuki H, Rarnoino L, Baratoff A, Jung TA (2003) Molecular assembly and self-assembly: molecular nanoscience for future technologies. Chimia 56:500–505
36. Zhang S (2003) Building from the bottom up. Mater Today 6:20–27
37. Walt DR (2002) Nanomaterials: Top-to-bottom functional design. Nat Mater 1:17–18
38. Laurent S, Forge D, Port M, Roch A, Robic C, Elst LV, Muller RN (2008) Magnetic iron oxide nanoparticles: Synthesis, stabilization, vectorization, physicochemical characterizations, and biological applications. Chem Rev 108(9):2064–2110
39. Eastoe J, Hollamby MJ, Hudson L (2006) Recent advances in nanoparticle synthesis with reversed micelles. Adv Colloid Interf Sci 128-130:5–15
40. Wani IA (2014) Nanomaterials, novel preparation routes and characterizations. In: Shah MA, Bhat MA, Davim JP (eds) Nanotechnology applications for improvements in energy efficiency and environment management, Chapter 1. IGI Global Publisher, Hershey, PA, pp 1–40
41. Kashchiev D (2000) Nucleation: basic theory with applications. Butterworth-Heinemann, Oxford
42. Karpinski PH, Wey JS (2002) Precipitation processes. In: Myerson AS (ed) Handbook of industrial crystallization, 2nd ed. Chapter 6, Butterworth-Heinemann: Stoneham, MA, pp. 141–160

43. Kwon SG, Hyeon T (2011) Formation mechanisms of uniform nanocrystals via hot-injection and heat-up methods. Small 7:2685–2702
44. Thanh NTK, Maclean N, Mahiddine S (2014) Mechanisms of nucleation and growth of nanoparticles in solution. Chem Rev 114:7610–7630
45. Kashchiev D, van Rosmalen GM (2003) Review: Nucleation in solutions revisited. Cryst Res Technol 38:555–574
46. Livingston JD (1959) Critical particle size for precipitation hardening. Trans Metall Soc A I M E 215:566–571
47. LaMer VK, Dinegar RH (1950) Theory, production and mechanism of formation of monodispersed hydrosols. J Am Chem Soc 72:4847–4854
48. Sugimoto T, Shiba F, Sekiguchi T, Itoh H (2000) Spontaneous nucleation of monodisperse silver halide particles from homogeneous gelatin solution I: Silver chloride. Colloids Surf A 164:183–203
49. Sugimoto T, Shiba F (2000) Spontaneous nucleation of monodisperse silver halide particles from homogeneous gelatin solution II: Silver bromide. Colloids Surf A 164:205–215
50. Ostwald W (1900) Über die vermeintliche isomerie des roten und gelben quecksilberoxyds und die oberflächenspannung fester körper. Z Phys Chem 34:495–503
51. Lifshitz I, Slyozov V (1961) The kinetics of precipitation from supersaturated solid solutions. J Phys Chem Solids 19:35–50
52. Wagner C (1961) Theorie der Alterung von Niederschlagen durch Umlösen (Ostwald-Reifung). Ber Bunsenges Phys Chem 65:581–591
53. Lee W, Kim MG, Choi J, Park J, Ko SJ, Oh SJ, Cheon J (2005) Redox-transmetalation process as a generalized synthetic strategy for core-shell magnetic nanoparticles. J Am Chem Soc 127:16090–16097
54. Watzky MA, Finke RG (1997) Nanocluster size-control and "magic number" investigations. experimental tests of the "living-metal polymer" concept and of mechanism-based size-control predictions leading to the syntheses of iridium (0) nanoclusters centering about four sequential magic numbers. Chem Mater 9:3083–3095
55. Watzky MA, Finney EE, Finke RG (2008) Transition-metal nanocluster size vs formation time and the catalytically effective nucleus number: A mechanism-based treatment. J Am Chem Soc 130:11959–11969
56. Besson C, Finney EE, Finke RG (2005) A mechanism for transition-metal nanoparticle self-assembly. J Am Chem Soc 127:8179–8184
57. Yao S, Yuan Y, Xiao C, Li W, Kou Y, Dyson PJ, Yan N, Asakura H, Teramura K, Tanaka TJ (2012) Insights into the formation mechanism of rhodium nanocubes. Phys Chem C 116:15076–15086
58. Bramley AS, Hounslow MJ, Ryall RL (1996) Aggregation during precipitation from solution: A method for extracting rates from experimental data. J Coll Interf Sci 183:155–165
59. Reetz MT, Helbig W, Quaiser SA, Stimming U, Breuer N, Vogel R (1995) Visualization of surfactants on nanostructured palladium clusters by a combination of STM and high-resolution TEM. Science 267:367–369
60. Pileni M-P (2003) The role of soft colloidal templates in controlling the size and shape of inorganic nanocrystals. Nat Mater 2:145–150
61. Jana NR, Gearheart L, Murphy CJ (2001) Wet chemical synthesis of silver nanorods and nanowires of controllable aspect ratio. Chem Commun 617–618
62. Kovalenco MV, Bodnarchuk MI, Lechner RT, Heeser G, Schaffler F, Heiss W (2007) Fatty acid salts as stabilizers in size and shape-controlled nanocrystal synthesis: the case of inverse spinel iron oxide. J Am Chem Soc 129:6352–6353
63. Liu L, Wei T, Guan X, Zi X, He H, Dai H (2009) Size and morphology adjustment of PVP-stabilized silver and gold nanocrystals synthesized by hydrodynamic assisted self-assembly. J Chem C 113:8595–8600
64. Garg G, Hassan PA, Aswal VK, Kulshreshtha SK (2005) Tuning the structure of SDS micelles by substituted anilinium ions. J Phys Chem B 109:1340–1346

65. Aswal VK, Goyal PS (2000) Counterions in the growth of ionic micelles in aqueous electrolyte solutions: A small-angle neutron scattering study. Phys Rev E 61:2947–2953
66. Bhattacharjee J, Verma G, Aswal VK, Date AA, Nagarsenker MS, Hassan PA (2010) Tween 80-sodium deoxycholate mixed micelles: Structural characterization and application in doxorubicin delivery. J Phys Chem B 114:16414–16421
67. Kadama Y, Bharatiya B, Hassan PA, Verma G, Aswal VK, Bahadur P (2010) Effect of an amphiphilic diol (Surfynol®) on the micellar characteristics of PEO–PPO–PEO block copolymers in aqueous solutions. Colloid Surf A: Physicochem Eng Asp 363:110–118
68. Verma G, Paliwal P, Kumar S, Aswal VK, Hassan PA (2015) Effect of di-(2-ethylhexyl)phosphoric acid on microstructure, cloud point and uranyl ion binding competence of Triton X-100 micelles. Colloid Surf A: Physicochem Eng Asp 468:262–270
69. Garg G, Hassan PA, Kulshreshtha SK (2006) Dynamic light scattering studies of rod-like micelles in dilute and semi-dilute regime. Colloid Surf A: Physicochem Eng Asp 275:161–167
70. Sasidharan M, Nakashima K (2014) Core–shell–corona polymeric micelles as a versatile template for synthesis of inorganic hollow nanospheres. Acc Chem Res 47:157–167
71. Eckhardt B, Ortel E, Bernsmeier D, Polte J, Strasser P, Vainio U, Emmerling F, Kraehnert R (2013) Micelle-templated oxides and carbonates of zinc, cobalt, and aluminum and a generalized strategy for their synthesis. Chem Mater 25:2749–2758
72. Kresge CT, Leonowicz ME, Roth WJ, Vartuli JC, Beck JS (1992) Ordered mesoporous molecular sieves synthesized by a liquid-crystal template mechanism. Nature 359:710–712
73. Yanagisawa T, Shimizu T, Kuroda K, Kato C (1990) The preparation of alkyltrimethylammonium-kanemite complexes and their conversion to microporous materials. Bull Chem Soc Jpn 63:988–992
74. Inagaki S, Fukushima Y, Kuroda K (1993) Synthesis of highly ordered mesoporous materials from a layered polysilicate. J Chem Soc Chem Commun 680–682
75. Bao Y, Wang T, Kang Q, Shi C, Ma J (2017) Micelle-template synthesis of hollow silica spheres for improving water vapor permeability of waterborne polyurethane membrane. Sci Rep 7:46638
76. Khanal A, Inoue Y, Yada M, Nakashima K (2007) Synthesis of silica hollow nanoparticles templated by polymeric micelle with core-shell-corona structure. J Am Chem Soc 129:1534–1535
77. Zhang S, Greenfield MA, Mata A, Palmer LC, Bitton R, Mantei JR, Aparicio C, de la Cruz MO, Stupp SI (2010) A self-assembly pathway to aligned monodomain gels. Nature Mater 9:594–601
78. Newcomb CJ, Bitton R, Velichko YS, Snead ML, Stupp SI (2012) The role of nanoscale architecture in supramolecular templating of biomimetic hydroxyapatite mineralization. Small 8:2195–2202
79. Stupp SI, Braun PV (1997) Molecular manipulation of microstructures: Biomaterials, ceramics, and semiconductors. Science 277:1242–1248
80. Verma G, Barick KC, Manoj N, Sahu AK, Hassan PA (2013) Rod-like micelle templated synthesis of porous hydroxyapatite. Ceram Int 39:8995–9002
81. Shanthi PMSL, Mangalaraja RV, Uthirakumar AP, Velmathi S, Balasubramanian T, Ashok M (2010) Synthesis and characterization of porous shell-like nano hydroxyapatite using cetrimide as template. J Colloid Interface Sci 350:39–43
82. Shiba K, Motozuka S, Yamaguchi T, Ogawa N, Otsuka Y, Ohnuma K, Kataoka T, Tagaya M (2016) Effect of cationic surfactant micelles on hydroxyapatite nanocrystal formation: An investigation into the inorganic–organic interfacial interactions. Cryst Growth De 16:1463–1471
83. Zhang J, Jiang D, Zhang J, Lin Q, Huang Z (2010) Synthesis of organized hydroxyapatite (HA) using Triton X-100. Ceram Int 36:2441–2447
84. Yin S, Ren W, Sun J, Zhang Y, Li M, Deng K (2016) Hollow CDHA nanorods with mesopores on surface: Bi-micelle-templating method, dissolvability, cytocompatibility and protein delivery. Adv Powder Technol 27:199–206

85. Ye F, Guo H, Zhang H, He X (2010) Polymeric micelle-templated synthesis of hydroxyapatite hollow nanoparticles for a drug delivery system. Acta Biomater 6:2212–2218
86. Watanabe K, Nishio Y, Makiura R, Nakahira A, Kojima C (2013) Paclitaxel-loaded hydroxyapatite/collagen hybrid gels as drug delivery systems for metastatic cancer cells. Int J Pharma 446:81–86
87. Qiao W, Lan X, Tsoi JKH, Chen Z, Su RYX, Yeung KWK, Matinlinna JP (2017) Biomimetic hollow mesoporous hydroxyapatite microsphere with controlled morphology, entrapment efficiency and degradability for cancer therapy. RSC Adv 7:44788–44798
88. Calleja G, Serrano DP, Sanz R, Pizarro P, García A (2004) Study on the synthesis of high-surface-area mesoporous TiO_2 in the presence of nonionic surfactants. Ind Eng Chem Res 43:2485–2492
89. Antonelli DM, Ying JY (1995) Synthesis of hexagonally packed mesoporous TiO_2 by a modified sol-gel method. Angew Chem Int Ed 34:2014–2017
90. Löf D, Schillén K, Torres MF, Müller AJ (2007) Rheological study of the shape transition of block copolymer-nonionic surfactant mixed micelles. Langmuir 23:11000–11006
91. Antonietti M, Wenz E, Bronstein L, Seregina M (1995) Synthesis and characterization of noble metal colloids in block copolymer micelles. Adv Mater 7:1000–1005
92. Kim JK, Yang SY, Lee Y, Kim Y (2010) Functional nanomaterials based on block copolymer self-assembly. Prog Polym Sci 35:1325–1349
93. Euliss LE, Grancharov SG, O'Brien S, Deming TJ, Stucky GD, Murray CB, Held GA (2003) Cooperative assembly of magnetic nanoparticles and block copolypeptides in aqueous media. Nano Lett 3:1489–1493
94. Sakai T, Alexandridis P (2004) Single-step synthesis and stabilization of metal nanoparticles in aqueous Pluronic block copolymer solutions at ambient temperature. Langmuir 20:8426–8430
95. Wang L, Yamauchi Y (2009) Block copolymer mediated synthesis of dendritic platinum nanoparticles. J Am Chem Soc 131:9152–9153
96. Luyan W, Xiao C, Jie Z, Zhenming S, Jikuan Z, Zhenwen S (2004) Controllable morphology formation of gold nano- and micro-plates in amphiphilic block copolymer-based liquid crystalline phase. Chem Lett 33:720–721
97. Yang P, Zhao D, Margolese DI, Chmelka BF, Stucky GD (1998) Generalized syntheses of large-pore mesoporous metal oxides with semicrystalline frameworks. Nature 396:152–155
98. Zhao D, Huo Q, Feng J, Chmelka BF, Stucky GD (1998) Nonionic triblock and star diblock copolymer and oligomeric surfactant syntheses of highly ordered, hydrothermally stable, mesoporous silica structures. J Am Chem Soc 120:6024–6036
99. Park M, Harrison C, Chaikin PM, Register RA, Adamson DH (1997) Block copolymer lithography: periodic arrays of ~10^{11} holes in 1 square centimeter. Science 276:1401–1404
100. Schulman JH, Stoekenius W, Prince LM (1959) Mechanism of formation and structure of microemulsions by electron microscopy. J Phys Chem 63:1677–1680
101. Pileni MP (ed) (1989) Structure and reactivity in reverse micelles, Amsterdam, Elsevier
102. Luisi PL, Majid LJ, Fendler JH (1986) Solubilization of enzymes and nucleic acids in hydrocarbon micellar solution. Crit Rev Biochem 20:409–474
103. Eastoe J, Hollamby MJ, Hudson L (2006) Recent advances in nanoparticle synthesis with reversed micelles. Adv Colloid Interf Sci 128:5–15
104. Destree C, Debuigne F, George S, Champagne B, Guillaume M, Ghijsen J, Nagy JB (2008) J complexes of retinol formed within the nanoparticles prepared from microemulsions. Colloid Polym Sci 286:1463–1470
105. Zhong-min O, Hiroshi Y, Keisaku K (2007) Preparation and optical properties of organic nanoparticles of porphyrin without self-aggregation. J Photochem Photobio A: Chem 189:7–14
106. Wanzhong Z, Xueliang Q, Jianguo C (2006) Synthesis and characterization of silver nanoparticles in AOT microemulsion system. Chem Phys 330:495–500
107. Malik MA, Wani MY, Hashim MA (2012) Microemulsion method: A novel route to synthesize organic and inorganic nanomaterials: 1st Nano Update. Arabian J Chem 5:397–417

108. Lopez-Quintela MA, Tojo C, Blanco MC, Garcia Rio LG, Leis JR (2004) Microemulsion dynamics and reactions in microemulsions. Curr Opin Colloid Interf Sci 9:264–278
109. Osseo-Asare K, Arriagada FJ (1990) Synthesis of nanosize particles in reverse microemulsion, In: Ceramic Powder Sci. III, Messing GL, Hirano S, Hausner, H (eds), American Ceramic Society, Westerville, OH, pp 3–16
110. Kurihara K, Kizling J, Stenius P, Fendler JH (1983) Laser and pulse radiolytically induced colloidal gold formation in water-in-oil microemulsions. J Am Chem Soc 105:2574–2579
111. Rauscher F, Veit P, Sundmacher K (2005) Analysis of a technical grade w/o-microemulsion and its application for the precipitation of calcium carbonate nanoparticles. Colloid Surf A: Physicochem Eng Asp 254:183–191
112. Boutonnet M, Kizling J, Stenius P, Maire G (1982) The preparation of monodisperse colloidal metal particles from microemulsions. Colloid Surf 5:209–225
113. Pal A, Shah S, Belochapkine S, Tanner D, Magner E, Devi S (2009) Room temperature synthesis of platinum nanoparticles in water-in-oil microemulsion. Colloid Surf A: Physicochem Eng Asp 337:205–207
114. Martínez-Rodríguez RA, Vidal-Iglesias FJ, Solla-Gullón J, Cabrera CR, Feliu JM (2014) Synthesis of Pt nanoparticles in water-in-oil microemulsion: effect of HCl on their surface structure. J Am Chem Soc 136:1280–1283
115. Chen DH, Wang CC, Huang TC (1999) Preparation of palladium ultrafine particles in reverse micelles. J Coll Interf Sci 210:123–129
116. Barnickel P, Wokaum A (1990) Synthesis of metal colloids in inverse microemulsions. Mol Phys 69:1–9
117. Qiu S, Dong J, Chen G (1999) Preparation of Cu nanoparticles from water-in-oil microemulsions. J Coll Interf Sci 216:230–234
118. Weihua W, Xuelin T, Kai C, Gengyu C (2006) Synthesis and characterization of Pt–Cu bimetallic alloy nanoparticles by reverse micelles method. Colloid Surf A: Physicochem Eng Asp 273:35–42
119. Li T, Zhou H, Huang J, Yin J, Chen Z, Liu D, Zhang N, Kuang Y (2014) Facile preparation of Pd–Au bimetallic nanoparticles via in-situ self-assembly in reverse microemulsion and their electrocatalytic properties. Colloid Surf A 463:55–62
120. Duxin N, Stephan O, Petit C, Bonville P, Colliex C, Pileni MP (1997) Pure α-Fe coated by an $Fe_{1-x}B_x$ alloy. Chem Mater 9:2096–2100
121. Wilcoxon JP, Provencio PP (1999) Use of surfactant micelles to control the structure phase of nanosize iron clusters. J Phys Chem B 103:9809–9812
122. Tanori J, Duxin N, Petit C, Lisiecki I, Veillet P, Pileni MP (1995) Synthesis of nanosize metallic and alloyed particles in ordered phases. Colloid Polym Sci 273:886–892
123. Xia L, Hu X, Kang X, Zhao H, Sun M, Cihen X (2010) A one-step facile synthesis of Ag-Ni core-shell nanoparticles in water-in-oil microemulsions. Colloid Surf A: Physicochem Eng Asp 367:96–101
124. Inouye K, Endo R, Otsuka Y, Miyashiro K, Kaneko K, Ishikawa T (1982) Oxygenation of ferrous ions in reversed micelle and reversed microemulsion. J Phys Chem 86:1465–1469
125. Carpenter EE, Connor CJO, Harris VG (1999) Atomic structure and magnetic properties of $MnFe_2O_4$ nanoparticles produced by reverse micelle synthesis. J Appl Phys 85:5175–5177
126. Lu T, Wang J, Yin J, Wang A, Wang X, Zhang T (2013) Surfactant effects on the microstructures of Fe_3O_4 nanoparticles synthesized by microemulsion method. Colloid Surf A: Physicochem Eng Asp 436:675–683
127. Liu C, Rondinone AJ, Zhang ZJ (2000) Synthesis of magnetic spinel ferrite $CoFe_2O_4$ nanoparticles from ferric salt and characterization of the size-dependent superparamagnetic properties. Pure Appl Chem 72:37–45
128. Liu C, Zou BS, Rondinone AJ, Zhang ZJ (2000) Chemical control of superparamagnetic properties of magnesium and cobalt spinel ferrite nanoparticles through atomic level magnetic couplings. J Am Chem Soc 122:6263–6267
129. Yener DO, Giesche H (2001) Synthesis of pure and manganese nickel and zinc-doped ferrite particles in water-in-oil microemulsions. J Am Ceram Soc 84:1987–1995

130. Alejandra L, Reinhard S (2006) Synthesis of manganite perovskite nanoparticles in w/o-microemulsion. Mater Res Bull 41:333–339
131. Xu P, Han X, Wang M (2007) synthesis and magnetic properties of $BaFe_{12}O_{19}$ hexaferrite nanoparticles by a reverse microemulsion technique. J Phys Chem C 111:5866–5870
132. Finnie KS, Bertlett JR, Barbe CJA, Kong L (2007) Formation of silica nanoparticles in microemulsions. Langmuir 23:3017–3024
133. Esquena J, Tadros TF, Kostareios K, Solans C (1997) Preparation of narrow size distribution silica particles using microemulsions. Langmuir 13:6400–6406
134. Lopez-Perez JA, Lopez-Quintela MA, Mira J, Rivas J, Charles SW (1997) Advances in the preparation of magnetic nanoparticles by the microemulsion method. J Phys Chem B 101:8045–8047
135. Geng CL, Zhu ZF, Yu WJ (2008) Influence of cosurfactant on the structure and properties of ZrO_2 nano-powders prepared in microemulsion system. Key Eng Mater 368–372:729–731
136. Wright JB, Lam K, Hansen D, Burrell RE (1999) Efficacy of topical silver against fungal burn wound pathogens. Am J Infect Control 27:344–350
137. Han DY, Yang HY, Shen CB, Zhou X, Wang FH (2004) Synthesis and size control of NiO nanoparticles by water-in-oil microemulsion. Powder Technol 147:113–116
138. Anyaogu KC, Fedorov AV, Neckers DC (2008) Synthesis, characterization, and antifouling potential of functionalized copper nanoparticles. Langmuir 24:4340–4346
139. Li GL, Wang GH (1999) Synthesis of nanometer-sized TiO_2 particles by a microemulsion method. Nanostruct Mater 11:663–668
140. Li X, Zheng W, He G, Zhao R, Liu D (2014) Morphology Control of TiO_2 nanoparticle in microemulsion and its photocatalytic property. ACS Sustain Chem. Eng. 2:288–295
141. Zou X, Liu BB, Wu W, Li DM, Li QJ, Li ZP, Liu B, Mao HK (2013) Synthesis of hollow ß-phase GeO_2 in microemulsion. Adv Mater Res 669:360–365
142. Zhang M, Cushing BL, O'Connor CJ (2008) Synthesis and characterization of monodisperse ultra-thin silica-coated magnetic nanoparticles. Nanotechnology 19:085601
143. Joshi HM, De M, Richter F, He J, Prasad PV, Dravid VP (2012) Effect of silica shell thickness of Fe_3O_4-SiO_x core-shell nanostructures on MRI contrast. Contrast Media Mol Imaging 7:460–468
144. Agostiano A, Catalano M, Curri ML, Monica MD, Manna L, Vasanelli L (2000) Synthesis and structural characterisation of CdS nanoparticles prepared in a four-components "water-in-oil" microemulsion. Micron 3:253–258
145. Petit C, Lixon P, Pileni MP (1990) Synthesis of cadmium sulfide in situ in reverse micelles. 2. Influence of the interface on the growth of the particles. J Phys Chem 94:1598–1603
146. Robinson BH, Towey TF, Zourab S, Visser AJWG, Van Hoek A (1991) Characterization of cadmium sulphide colloids in reverse micelles. Colloid Surf 61:175–188
147. Eastoe J, Warne M (1996) Nanoparticles and polymer synthesis in microemulsions. Curr Opin Colloid Interf Sci 1:800–805
148. Haram SK, Mahadeshwar AR, Dixit SG (1996) Synthesis and characterization of copper sulphate nanoparticles in triton-X 100 water-in-oil microemulsion. J Phys Chem 100:5868–5873
149. Manyar HG, Iliade P, Bertinetti L, Coluccia S, Berlier G (2011) Structural and spectroscopic investigation of ZnS nanoparticles grown in quaternary reverse micelles. J Colloid Interface Sci 354:511–516
150. Eastoe J, Cox AR (1995) Formation of PbS nanoclusters using reversed micelles of lead and sodium Aerosol-OT. Colloid Surf A Physicochem Eng Asp 101:63–76
151. Ethayaraja M, Ravikumar C, Muthukumaran D, Dutta K, Bandyopadhyaya R (2007) CdS-ZnS core-shell nanoparticle formation: Experiment, mechanism, and simulation. J Phys Chem C 111:3246–3252
152. Zhang W, Zhong Q (2009) microemulsions as nanoreactors to produce whey protein nanoparticles with enhanced heat stability by sequential enzymatic cross-linking and thermal pretreatments. J Agric Food Chem 57:9181–9189

153. Guo JS, El-Aasser MS, Vanderhoff JW (1989) Microemulsion polymerization of styrene. J Polym Sci Part A: Polym Chem 27:691–710
154. Palani RW, Sasthav WR, Cheung HM (1991) Formation of porous polymeric structures by the polymerization of single-phase microemulsions formulated with methyl methacrylate and acrylic acid. Langmuir 7:2586–2591
155. Destree C, Nagy JB (2006) Mechanism of formation of inorganic and organic nanoparticles from microemulsions. Adv Colloid Interf Sci 123:353–367
156. Destrée C, Ghijsen J, Nagy JB (2007) Preparation of organic nanoparticles using microemulsions: their potential use in transdermal delivery. Langmuir 23:1965–1973
157. Margulis-Goshen K, Magdassi S (2012) Organic nanoparticles from microemulsions: Formation and applications. Cur Opin Colloid Interf Sci 17:290–296
158. Puranajoti P, Patil RT, Sheth PD, Bommareddy G, Dondeti P, Egbaria K (2002) Design and development of topical microemulsion for poorly water-soluble antifungal agents. J Appl Res Clin Exp Ther 2:1
159. Langmuir I (1917) The constitution and fundamental properties of solids and liquids. II. Liquids. J Am Chem Soc 39:1848–1906
160. Blodgett KB (1935) Films built by depositing successive monomolecular layers on a solid surface. J Am Chem Soc 57:1007–1022
161. Khun H (1965) Versuche zur herstellung einfacher organisierter systeme von molekülen. Pure Appl Chem 11:345–358
162. Gains GL (1966) Insoluble monolayers at liquid-gas interface. Wiley, New York
163. Harkins WD (1952) The physical chemistry of surface films. Reinhold Publishing Co., New York
164. Ganguly P, Paranjape DV, Patil KR, Chaudhari SK (1992) A new structural model for Langmuir-Blodgett films of metal salts of fatty acids. Langmuir 8:2365–2367
165. Roberts G (Ed.) (1990) Langmuir-Blodgett films. Springer, New York
166. Choudhury S, Bagkar N, Dey GK, Subramanian H, Yakhmi JV (2002) Crystallisation of prussian blue analogues at the air-water interface using octadecyl amine monolayer as a template. Langmuir 18:7409–7414
167. Choudhury S, Dey GK, Yakhmi JV (2003) Growth of cubic crystals of cobalt-hexacyanoferrate under the octadecyl amine monolayer. J Cryst Growth 258:197–203
168. Bagkar N, Choudhury S, Kim K-H, Chowdhury P, Lee S-I, Yakhmi JV (2006) Crystalline thin films of transition metal hexacyanochromates grown under Langmuir monolayer. Thin Solid Films 513:325–330
169. Choudhury S, Betty CA, Girija KG, Kulshreshtha SK (2006) Room temperature gas sensitivity of ultrathin SnO_2 films prepared from Langmuir-Blodgett film precursors. Appl Phys Lett 89:071914
170. Choudhury S, Betty CA, Girija KG (2008) On the preparation of ultra-thin tin dioxide by Langmuir-Blodgett film deposition. Thin Solid Films 517:923–928
171. Choudhury S, Betty CA, Girija KG (2010) Room temperature ammonia gas selectivity studies on SnO_2 ultra thin film prepared by Langmuir-Blodgett technique. AIP Conf Proc 1313:304–306
172. Choudhury S, Sasikala R, Saxena V, Aswal DK, Bhattacharya D (2012) A new route for the fabrication of ultrathin film of PdO-TiO_2 composite photocatalyst. Dalton Trans 41:12090–12095
173. Choudhury S, Betty CA (2013) A heterostructured SnO_2-TiO_2 thin film prepared by Langmuir-Blodgett technique. Mat Chem Phys 141:440–444
174. Kondalkar VV, Mali SS, Kharade RR, Mane RM, Patil PS, Hong CK, Kim JH, Choudhury S, Bhosale PN (2015) Langmuir-Blodgett self organized nanocrystalline tungsten oxide thin films for electrochromic performance. RSC Adv 5:26923–26931
175. Choudhury S, Betty CA, Bhattacharyya K, Saxena V, Bhattacharya D (2016) Nanostructured PdO thin film from Langmuir-Blodgett precursor for room temperature H_2 gas sensing. ACS Appl Mater Interf 8:16997–17003

176. Bagheri S, Hir ZAM, Yousefi AT, Hamid SBA (2015) Progress on mesoporous titanium dioxide: Synthesis, modification and applications. Microporous Mesoporous Mater 218:206–222
177. Mihaly M, Fleancu MC, Olteanu NL, Bojin D, Meghea A, Enachescu M (2012) Synthesis of gold nanoparticles by microemulsion assisted photoreduction method. Comptes Rendus Chimie 15:1012–1021

Chapter 13
Synthesis of Functionalized Noble Metal Nanoparticles

Abhishek Das and Nandita Maiti

Abstract Noble metals, for instance, silver and gold, have been extensively mined and utilized by mankind since time immemorial. Newer noble metals such as platinum group metals, namely platinum and palladium, became available for application with the advancement of metallurgy. The inert chemical nature and corrosion resistivity of the noble metals was the major attraction for their deployment in diverse technological avenues. With the advent of nanotechnology, further interest was created among researchers for the investigation of interesting structural, photophysical and catalytic properties. In this chapter, the advancement in the field of synthesis and application of surface-functionalized noble metals have been discussed. The different methods of nanoparticles synthesis such as chemical, radiolytic and photochemical have been discussed with few examples to draw out the advantages as well as disadvantages of one method in comparison to another. The importance and utility of the characterization techniques, which are usually used by researchers such as optical absorption, electron microscopy, etc., have been discussed. The observation of surface plasmon in noble metal nanoparticles and its role in quantitative analysis, as well as probing surface reactions, by surface-enhanced Raman scattering, have been explained by way of illustrations and examples. The interaction of plasmonic nanoparticles resulting in the variation in colour of the colloidal particles has been illustrated with examples of colorimetric sensing of analytes. The role of noble metal nanoparticles in heterogenous catalysis has also been discussed in this chapter.

Keywords Noble metal nanoparticles · Synthesis · Functionalization · Applications · Surface Plasmons · Surface-enhanced Raman scattering (SERS) · Colorimetric detection · Surface catalysis

A. Das · N. Maiti (✉)
Radiation & Photochemistry Division, Bhabha Atomic Research Centre, Mumbai 400085, India
e-mail: nanditab@barc.gov.in

A. Das
e-mail: abhidas@barc.gov.in

N. Maiti
Homi Bhabha National Institute, Mumbai 400094, India

A. K. Tyagi and R. S. Ningthoujam (eds.), *Handbook on Synthesis Strategies for Advanced Materials*, Indian Institute of Metals Series,
https://doi.org/10.1007/978-981-16-1803-1_13

13.1 Introduction

The word "noble" imparts a sense of detachment from the masses yet instils exquisiteness. Noble metals (NM) like gold (Au) and silver (Ag) are different from other metals in terms of reactivity. In fact, these metals tend to retain their intrinsic shine for a longer time. The inert nature of noble metal arises from its high standard reduction potential. These noble metals, viz., gold and silver exist in nature mostly in their elemental form [1, 2] as pure metal or alloy. Purification of ore metal to pure metal involves cyanidation followed by electrolytic extraction [3]. Extraction of noble metal in pure elemental form is an age-old process. In 1959, renowned physicist Richard Feynman presented a talk entitled, "There's Plenty of Room at the Bottom: An Invitation to Enter a New Field of Physics" [4], in which a number of interesting ramifications of manipulating matter on an atomic scale were discussed. With the discovery of sophisticated imaging techniques [5], for example, transmission electron microscopy (TEM), atomic force microscopy (AFM) and scanning electron microscopy (SEM), the synthesis of noble metal nanoparticles (NPs) gained popularity among scientists owing to their interesting surface chemistry as well as unique optical properties. In this chapter, efforts have been made to bring out various popular and rare synthetic approaches along with some noteworthy applications of functionalized noble metal NPs. With the aim to recognize and also appreciate the properties of noble metal NPs, it is essential to be informed about the bulk properties of the noble metals.

Gold is one of the first discovered metals. Throughout the history of mankind, gold has been considered a precious metal in many cultures across the world. This may be due to the fact that gold resists atmospheric oxidation due to its high standard reduction potential of 1.5 V [6]. Bulk gold metal is characterized by its lustrous yellow glow, high malleability [7], high ductility and high reflectivity. The yellow colour of gold metal has its origin in the interband transition which takes place in the visible region of the electromagnetic spectrum owing to the relativistic effects [8]. Apart from the above physical properties, gold exists in the oxidation states ranging from -1 to $+6$ [9–11], with $+1$ and $+3$ being the more dominant states [12].

Silver, unlike gold, is less abundant in nature in pure elemental form as it is more reactive than gold, with the standard reduction potential of 0.80 V [6]. Hydrogen sulphide readily available in the environment, from decomposed organic matter, tarnishes the shine of silver and blackens it with a layer of silver sulphide. The black layer of silver sulphide can be removed by chemical reduction [13]. Interestingly, silver occurs in the elemental form mostly along with gold in a natural alloy known as electrum, with a silver content of 8–10% [14], which makes electrum less dense than pure gold. Earlier in Egypt, gold was separated from silver in electrum by heating the alloy with sea salt[15]. Later, the salt of silver was reduced to obtain pure elemental silver. Unlike gold and copper (Cu), silver metal has the brightest white shine which makes it useful for the fabrication of a perfect mirror. Roman first devised the method to deposit silver on glass, which was later revived in the nineteenth century by Justus von Liebig [16]. This reaction is a variation of Tollen's reaction for testing aldehyde

[17]. Apart from virtual image formation in mirrors, silver is also associated with the development of photography [18]. Ag NPs are readily formed upon exposure of silver bromide to light. These negatives on polymer films are developed to produce a photograph, which is again another form of an image. Silver is known to exist in 0 to + 3 oxidation states with +1 being the most common [19]. Silver also contributes to the health aspect of human life. Silver-coated utensils are found to show antibiotic activity [20]. The anti-microbial activity of silver is not clearly understood, yet there are some proposed theories explaining the mechanism. Silver ions undergo oxidation at the surface of the cell membrane, which may form complexes due to their "soft" or more polarizable nature and disrupt the normal physiological functioning of the cell [21].

Platinum group metals (PGM), for instance, platinum (Pt), palladium (Pd), osmium (Os), etc., are also considered noble metals owing to their elevated chemical inertness and high oxidation resistance [22, 23]. Unlike gold and silver that is found naturally in elemental form, PGMs occur in nature in the form of arsenide or sulphide, viz., (Pt,Pd,Ni)S, (Pt,Pd)S, $Pt(AsS)_2$, PtS, $PtAs_2$, etc., which are generally extracted by hydrometallurgical methods [24]. Ores are generally concentrated by froth floatation followed by oxidation of the concentrate by smelting and reduction of the oxides in the converter. The PGM concentrate is then processed in a base metal refinery by pressure oxidation leach or dissolution–precipitation, molecular recognition technology and solvent extraction and ion exchange, where PGMs are separated from the base metals. The main challenge in PGMs extraction is the escalating content of chrome in the feed and the premature collapse of the refractory lining in the smelter. This is overcome by the Kell method of extraction [25]. PGMs are often used for applications in automotive, jewellery, electronics, catalysts, etc. [26]. The most noted application of platinum includes catalytic converters of automobiles where inert platinum surface coating facilitates heterogeneous catalytic oxidation of carbon monoxide [27]. Palladium metal is well known for its application in hydrogenation reactions [28].

In this chapter, the various methods of synthesis of noble metal NPs along with their physical, chemical properties as well as their applications have been discussed.

13.2 Synthetic Strategies

Noble metal NPs show interesting physico-chemical properties that depend on the shape and size of the particles [29–38]. The most important activity in the area of nanoscience involves the NPs synthesis and its functionalization. Researchers are involved in the development of various synthetic protocols for the preparation of functionalized metal NPs that can be used as molecular markers [39–42] and are also applicable in the areas of catalysis [43–45], sensors [46–49], etc. The synthesis of anisotropic NPs is also being investigated due to their unusual electronic, optical, catalytic and sensing properties [50–53]. The simplest approach towards the synthesis of colloidal metal NPs is achieved by the following methods: the "top-down method"

as well as the "bottom-up method" [54]. The top-down process involves the breaking down of the bulk metal by mechanical means, viz., nanolithography, micromachining, ion implantation, inert gas condensation, laser pyrolysis, high energy ball milling, melt mixing, pulse vapour deposition, flash spray pyrolysis, electrospraying, etc. [55, 56]. The resulting metal NPs are then stabilized by various protecting agents. This method, however, has a few drawbacks, namely the difficulty in obtaining a narrow distribution of particles size. The bottom-up methods, on the other hand, involve the wet chemical route of the NP preparation. In this approach, the NPs are prepared either by chemically reducing the metal salts or using electrochemical reduction and/or the controlled decomposition of metastable organometallic compounds in solution. Precise control over the growth of the primarily formed NPs is usually achieved with various stabilizers, viz., donor ligands, polymers, surfactants, etc. The mechanism behind the bottom-up approach involves a stepwise formation of NPs that consists of nucleation, growth and agglomeration [57–60] and is shown in Scheme 13.1. In this chapter, the bottom-up approach for preparing the noble metal NPs is discussed. The metal ion reduction followed by the NP formation can be achieved in numerous ways of which a few are listed as follows:

(a) Chemical reduction method
(b) Radiolytic reduction method
(c) Photochemical reduction method

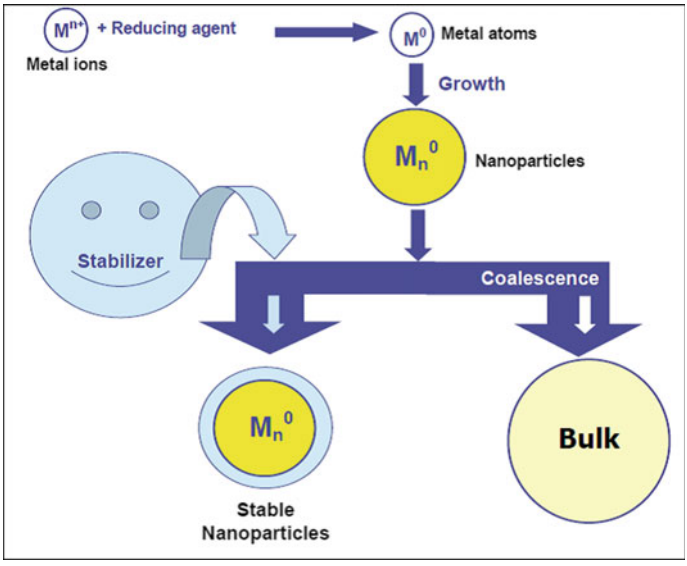

Scheme 13.1. Mechanism showing the bottom-up approach involving the stepwise formation of NPs consisting of nucleation, growth and agglomeration

Methods of Characterization of Synthesized Nanoparticles

Synthesized NPs are generally characterized by optical spectroscopy, microscopy, diffraction, electrophoresis and light scattering techniques.

In UV–visible (UV–vis) absorption spectroscopy, the noble metal or plasmonic NPs are characterized by the appearance of the surface plasmon resonance (SPR) band. The origin of the colour in noble metal NPs is fundamentally different from that in bulk metal. Noble metals are the only group among the transition elements in the periodic table that show colour in their elemental form [61]. The selection rule for the electronic transition is $\Delta l = \pm 1$, $\Delta S = 0$, where l is the azimuthal quantum number of subshells involved in the transition and S is the total spin of all the electrons [62]. In transition metal complexes, a strong colour is observed due to the d–d transition, where the selection rule is relaxed as the orbital character of the d-orbitals is lost due to mixing with ligand orbitals. But in pure elements such kind of mixing is not possible, resulting in mostly colourless transition metals, an exception being gold and copper. The origin of colour in noble metal lies in their electronic arrangement [61, 63]. The origin of colour in NPs of gold and silver is completely different from the above-mentioned discussion. Plasma is known as a state of matter where charged and uncharged matter co-exist, with overall electro neutrality [64]. Free electrons exist in the background of positive ionic cores in metals, which is also plasma. When electromagnetic radiation, i.e., photons, interacts with the metallic surface, it polarizes the electron cloud on the surface giving rise to "lossy" particles called polaritons [65]. Absorption of some of these polaritons leads to the intraband transition as discussed above, giving rise to the colour response of the metal. The rest of the polaritons are scattered back as photons.

In 1908, Gustav Mie proposed the Mie theory of light scattering by a homogenous sphere [66]. As a special case, light interacting with a particle comparatively much smaller than the incident electromagnetic radiation wavelength was discussed. It was proposed that under such a condition, the particle experiences a uniform electric field. For example, a metal NP of ~10 nm in size when excited with electromagnetic radiation of wavelength 520 nm experiences a uniform electric field. A gold NP of size ~10 nm contains about 30,000 atoms, out of which only ~40% constitute the surface. The electrons of the metal NP undergo polarization under such an electric field. The polarization of this electron gas forms a polariton that oscillates and scatters light, synchronously with electromagnetic radiation. The natural oscillation frequency of plasma, known as plasma frequency, is an intrinsic property of a metal. Under resonance conditions when the incident electromagnetic radiation frequency matches the metal plasma frequency, a built-up of electrons occurs and maximum damping of oscillation is observed. This phenomenon is known as SPR [67], wherein the surface electrons oscillate collectively as shown by a schematic illustration in Fig. 13.1. At this frequency of light, the metal NPs absorb light to give colour. Gold and silver in the nanometric domain show the SPR band in the visible region. The electron density of both gold and silver is very close, despite having different atomic numbers. As a result, their plasma frequency is expected to lie close to each other. On the contrary, their SPR frequencies are quite different. The SPR peak of Ag NPs emerges at about

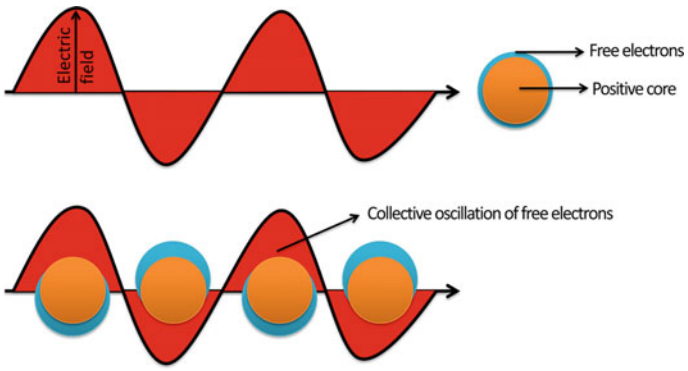

Fig. 13.1 Schematic diagram showing the collective and coherent oscillation of quasi-free electrons present in a metal NP exposed to the uniform electric field of incident radiation

400 nm whereas that of Au NPs appears around 520 nm. This is because the intraband transition of gold, which lies in the visible region, perturbs the SPR band of gold and shifts it from 400 to 520 nm. The SPR band of Ag NPs remains unaffected as its intraband transition lies in the UV region. Like gold, Cu NPs also show an SPR band at around 650 nm. The SPR band of Pd and Pt NPs does not appear in the visible region. For sizes of NPs from 2 to 20 nm, dipolar oscillations constitute the SPR band whereas upon increasing the size of the NPs multi-polar modes start contributing to the SPR band, due to the non-uniformity of the electric field as experienced by the particle. Thus, upon increasing the size of the NPs, the SPR band gets broader and red-shifted.

The presence of the SPR band in metal NPs explains the colour of Au, Ag and Cu NPs. Au NPs of size roughly ~5–10 nm show intense red colour. As the size of the particles increase, the colour changes from red, purple and blue. Similarly, Ag NPs show yellow colour for small particles, which turns grey with increasing size. Although this SPR phenomenon was understood recently, due to scientific advancement and technological progress, Au NPs were found to be used since the Roman age. Lycurgus cup [68, 69] shows red colour in transmitted light owing to the presence of Au NPs of size ~70 nm, trapped in the glass matrix. Interestingly, this was discovered by accidental contamination of minutely ground gold dust.

UV–vis (optical) absorption spectroscopy is used to identify the approximate size of the sphere-shaped NPs [70]. In the case of anisotropic NPs, two SPR bands are observed, transverse and longitudinal. The transverse mode corresponds to the plasmon across the minor axis and appears at a lower wavelength, whereas the longitudinal mode corresponds to the plasmon across the major axis and appears at a higher wavelength. Mulvaney et al. [71] have shown that for Au nanorods (NRs), variation in the aspect ratio leads to the shift of the SPR bands corresponding to the longitudinal and transverse modes.

TEM is used to record the morphology of the particles, i.e., the size and shape of the NPs [72]. Even though TEM is considered a non-invasive technique, an electron

beam is often found to locally heat the particles, leading to their fusion with time [73]. Different materials in a TEM image can be distinguished from the contrast of the image that depends on the material electron density [74]. The lattice spacing of materials can also be visualized by TEM in the form of lattice fringes [72]. In order to record a TEM image of noble metal NPs, a drop of solution is placed on the copper mesh grids, which is then air-dried. SEM technique is also used for studying the morphology of NPs at a lower magnification than TEM. It is often used to establish the particles size distribution [75]. Apart from TEM and SEM, AFM is another microscopic technique that uses the change in deflection of laser light, which is incident on the cantilever of the AFM tip, as a function of force between the AFM tip and the sample [76]. AFM can be used to measure the depth of the NPs (deposited on silicon or mica wafer) along the Z-axis. The size of the NPs in the XY plane is not the real size of the particles as it is influenced by the tip features.

X-ray diffraction (XRD) method is used to validate the formation of noble metal NPs [77–79]. Sometimes silver oxide [80] or silver chloride [81] formation can be confirmed using XRD. The XRD technique also provides information concerning the crystallite size of the particles from the observed lattice contraction[82]. But in the case of NPs, the Scherrer formula [82] has limited use in effectively calculating the particle size because of inadequate crystallinity and overlapping XRD peaks.

Surface charge [83] is another parameter useful for knowing the stability of the synthesized NPs. Zeta potential [84] is the measure of effective surface charge on any NP and is measured by electrophoresis along with laser Doppler velocimetry [85–87]. Zeta potential essentially provides an estimate of the electrical double-layer thickness, which is the determining parameter for the stability of NPs in solution [88].

Dynamic light scattering (DLS) is also an important technique that gives information about the hydrodynamic radius of NPs in solution [89]. The principle of DLS is based on time-dependent fluctuation of Rayleigh scattering which is a function of the hydrodynamic size-dependent diffusion behaviour of a NP. The size obtained from TEM may vary with that obtained from the DLS technique as the size obtained from DLS is the average ensemble size which is insensitive to deviation from the spherical shape of NPs. Depolarized Fabry–Perot interferometry (FPI) [90] is a less commonly used method for the size determination of anisotropic NPs.

The above-mentioned characterization techniques are often used to evaluate the quality as well as quantity of the NPs after synthesis. In the following sections, examples of characterization of noble metal NPs are presented for a better understanding of readers.

13.2.1 Chemical Reduction

The chemical reduction method is a rapid and simple approach for the metal NPs synthesis in the form of colloidal dispersions that remain stable in aqueous or organic solvents. The metal NPs with varying sizes and shapes can be prepared

using this approach. This process involves the initial creation of nuclei, induced by the commonly used reducing agents like sodium borohydride ($NaBH_4$) [91, 92], hydrazine [93], sodium citrate [94, 95], hydroxylamine hydrochloride [96], ascorbic acid [97], anionic ligands [98], etc. Some solvents like formamide [99, 100], N, N′-dimethylformamide (DMF) [101], formaldehyde [102], phenols [103, 104], methanol [105], ethanol [106–108], iso-propanal [109], ethylene glycol [110], etc. can act both as solvents as well as reducing agents. Various other methods of synthesis of composite nanomaterials are based on the dispersion of the NPs in a polymeric matrix. This method of synthesis of composite nanomaterials is of growing importance owing to their wide variety of applications. The frequently used polymers for the preparation of colloidal NPs are poly(vinylpyrrolidone) (PVP) [111, 112], poly(ethylene glycol) (PEG) [113–115], poly(methacrylic acid) (PMAA) [116], polymethylmethacrylate (PMMA) [117], polyacrylamide [118–122], etc. The type of reducing agent employed for the synthesis of NPs has been found to greatly affect the size of the resultant particles. It has been observed in the case of silver that stronger reductants such as $NaBH_4$ lead to the formation of smaller nuclei in the "seed" while employing weaker reductants such as citrate lead to the wider size distribution of particles owing to a slow reduction rate [123]. During the ripening process with strong reducing agents, the nuclei grow to produce the colloidal metal NPs with a narrow size distribution. The creation of nuclei is followed by a growth stage. The growth can be controlled using a stabilizer or it may result in the development of aggregated particles in the absence of a stabilizer. The reductant may also act as a stabilizer so as to avoid the agglomeration of the particles. A few commonly used synthetic protocols are discussed below.

13.2.1.1 Sodium Borohydride Reduction

In this method, the Ag NPs synthesis involves chemically reducing the Ag ions by $NaBH_4$ [91]. Briefly, 10 mg of $NaBH_4$ is added to 100 mL (N_2 saturated) $AgNO_3$ solution (100 μM). The solution is then shaken vigorously. The appearance of a clear yellow coloured solution confirms the formation of Ag NPs. The solution pH is ~9 owing to the hydrolysis of the excess amount of $NaBH_4$. The redox reaction is as follows:

$$2AgNO_3 + 2NaBH_4 + 6\,H_2O \rightarrow 2Ag + 2NaNO_3 + 2H_3BO_3 + 7\,H_2O \tag{13.1}$$

N_2 purging before the addition of $NaBH_4$ is necessary in order to eliminate O_2 and to circumvent the oxidation of Ag particles.

$$4Ag + O_2 + 2H_2O \rightarrow 4Ag^+ + 4OH^- \tag{13.2}$$

In the beginning, zerovalent Ag NPs are produced that owing to the occurrence of excess BH_4^- gets chemisorbed on the surface of particles causing deposition of

surplus electrons on the Ag particles. In this case, the Ag NPs are ionic in nature providing them hydrophilic character.

The alternative approach for the preparation of colloidal Ag NPs is according to the modified Creighton's method [92]. In brief, 10 mL of $AgNO_3$ (1 mM) solution is added gradually to 30 mL of 2 mM $NaBH_4$ (ice-cold) solution with slow stirring. The reaction is executed in an ice bath with continuous stirring. The colour of the solution changes steadily to pale yellow. Stirring is sustained till the solution is cooled down to room temperature (RT). The Ag NPs prepared by the modified Creighton's method leads to the development of monodisperse particles with a characteristic peak with an absorption maximum at 390 nm as displayed in Fig. 13.2. These particles are ideal for surface modification and functionalization. The alkaline pH (9) of the Ag NPs facilitates the dissolution of adsorbate molecules even with low solubility. The alteration in the SPR absorption band after surface modification/functionalization can be investigated using optical absorption spectroscopy. The size and shape of the NPs thus formed can be monitored using transmission electron microscopy (TEM), atomic force microscopy (AFM) and scanning electron microscopy (SEM) techniques. The representative TEM and AFM photographs of the Ag NPs formed by the modified Creighton procedure are shown in Figs. 13.3 and 13.4, respectively. The figures clearly display the development of spherical particles with ~15–20 nm average size.

The addition of 0.03 M HCl to borohydride stabilized NPs led to the formation of AgCl/Ag NPs [124]. The contrast in TEM image originating from the difference in electron density of Ag and AgCl NPs, as displayed in Fig. 13.5, along with the (SAED) selected area electron diffraction pattern led to the identification of AgCl/Ag hybrid particles.

Platinum (Pt) NPs can also be prepared by reducing Pt ions with $NaBH_4$ in the presence of a protecting agent [125–127]. Pt NPs were synthesized by reducing chloroplatinic acid by $NaBH_4$ in the presence of mercaptosuccinic acid as a stabilizer [128]. The above method led to the development of well-separated Pt particles of size ~2.5 nm, which was characterized by TEM and is shown in Fig. 13.6.

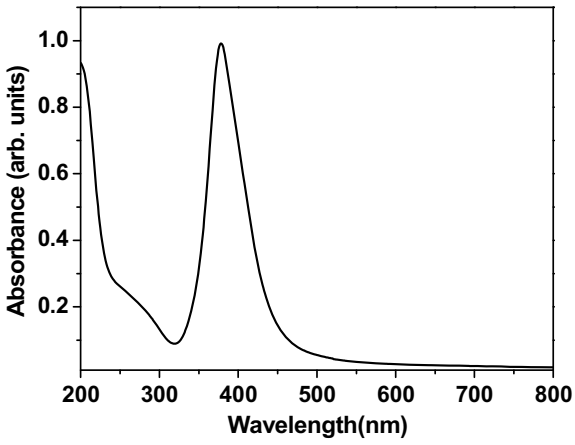

Fig. 13.2 SPR band of borohydride stabilized Ag NPs

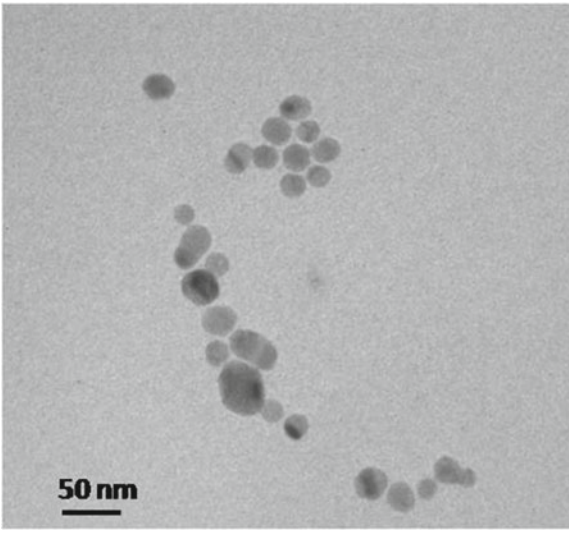

Fig. 13.3 TEM image of borohydride stabilized Ag NPs

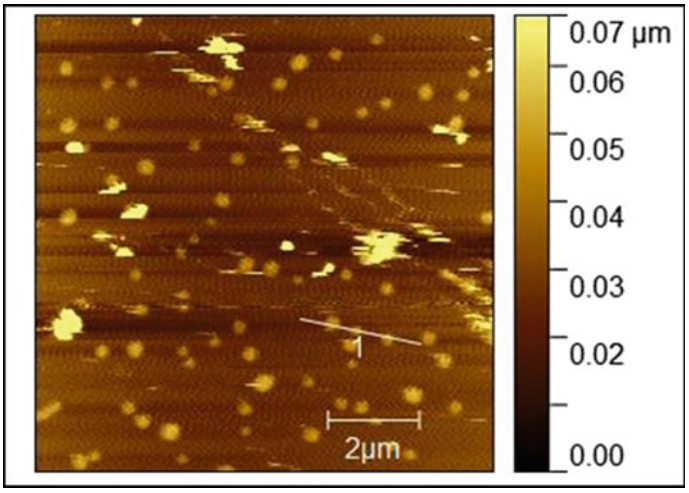

Fig. 13.4 AFM image of borohydride stabilized Ag NPs

Palladium (Pd) NPs stabilized by citrate can be synthesized by reducing palladium chloride with sodium borohydride at room temperature [129]. The Pd particles obtained were 6.5 nm in size. The Pd NPs were then loaded on polystyrene (PS) microspheres to make composite materials. The main idea behind the use of PS microsphere is to easily recover the composites after each catalytic cycle. The TEM image and associated histogram of the Pd NPs as well as the TEM photograph of

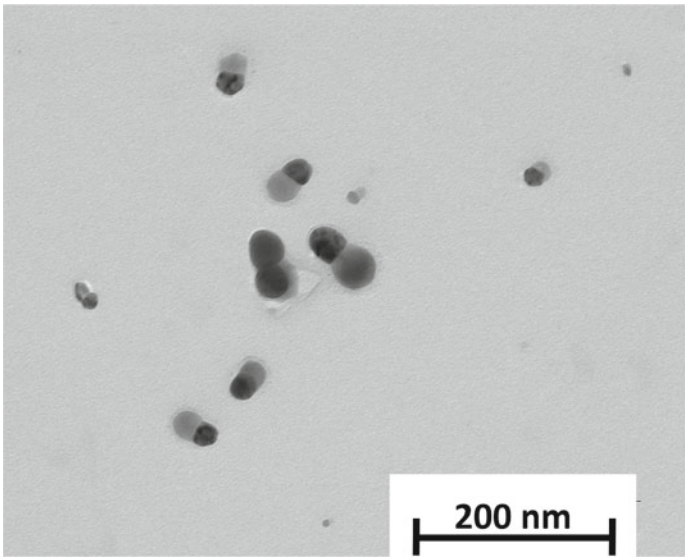

Fig. 13.5 TEM image of borohydride stabilized AgCl/Ag NPs

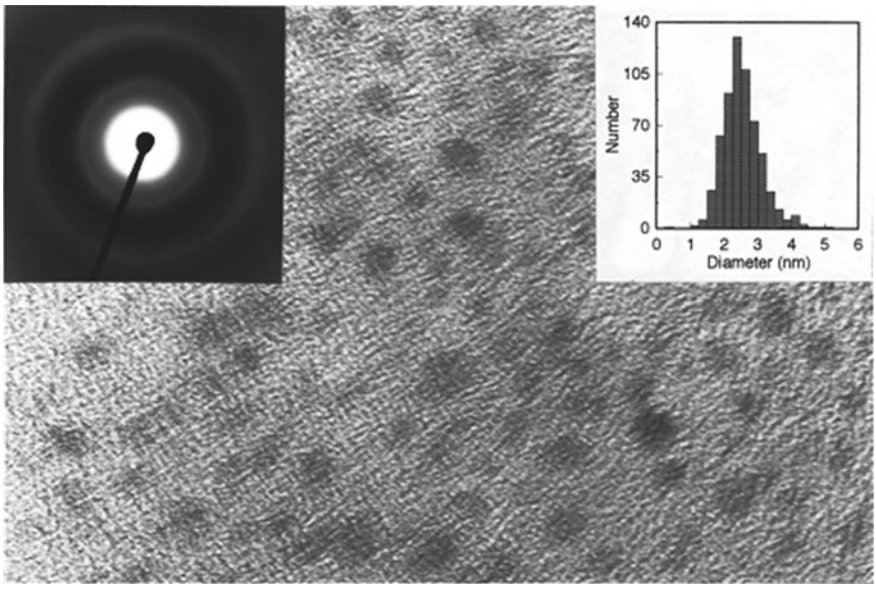

Fig. 13.6 HRTEM photograph of Pt NPs, synthesized in aqueous medium by reducing chloroplatinic acid with $NaBH_4$ in the presence of mercaptosuccinic acid. Inset displays the electron diffraction pattern and size distribution of particles. Reprinted and adapted with permission from Ref. [128] Copyright 2001 American Chemical Society

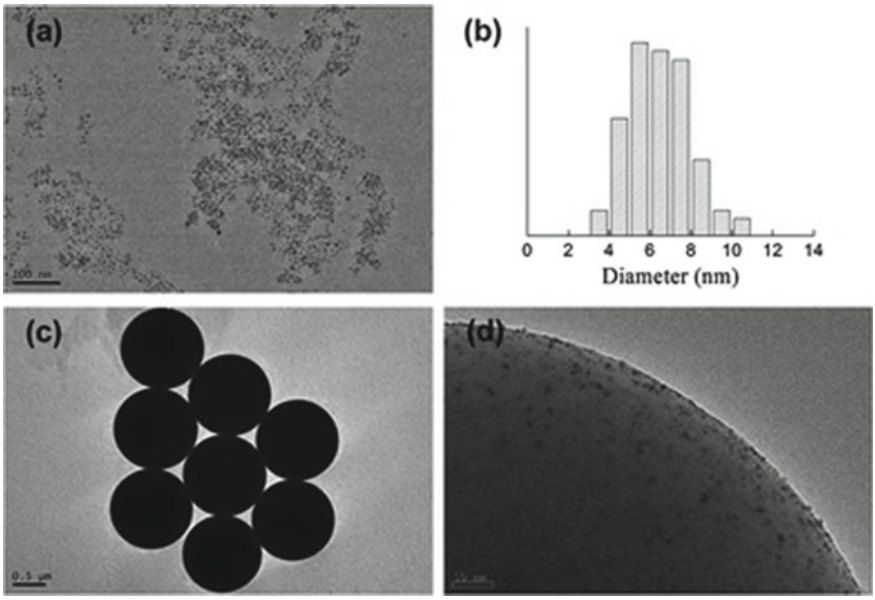

Fig. 13.7 TEM image of Pd NPs displaying the size (average) of **a** ~6.5 nm and **b** histogram with size distribution; TEM photographs of Pd/PS composites with different magnification; low **c** and high (**d**). Reprinted with permission from Ref. [129] Copyright 2015 Royal Chemical Society

Pd/PS nanocomposites is displayed in Fig. 13.7. The catalytic application of Pd NPs is discussed later.

13.2.1.2 Sodium Citrate Reduction

A rapid and simple method of Ag NPs preparation involves reducing $AgNO_3$ with sodium citrate by Lee and Meisel technique [94]. In brief, 100 mL aqueous solution of $AgNO_3$ (1 mM) is boiled, 3 mL of sodium citrate (1% wt/v) solution is then added dropwise with continuous stirring and the heating sustained for further 5 min until the colour of the solution turns intense yellow. The solution is subsequently cooled down to RT. The particles thus formed have high polydispersity and show the characteristic SPR absorption band with a maximum of about 400 nm.

For the preparation of Ag NPs with controlled shape and size, the balance involving nucleation and growth is of great importance. The modified Lee Meisel method [130] for the controlled preparation of quasi-spherical Ag NPs depends on combining the original Lee Meisel method and the seed-induced growth involving the reduction of $AgNO_3$ by heating with sodium citrate. Here, the citrate-capped Ag NPs having sizes varying up to 80 nm can be obtained through a single step or stepwise growth mechanism with the use of 4 nm Ag particles that are spherical in shape as the starting seeds. The major problems involving the development of NRs

and secondary nucleation through the growth process can be efficiently overcome by adjusting the experimental conditions, viz., the amount of seed, reaction temperature and tuning of pH. It is established that, regardless of the homogeneity of seeds, the ratio of monomer versus seed plays a crucial part in influencing the shape and size of the final particles. With the aim to restrain the formation of NRs and events related to the second or further nucleation, the monomer to seed ratio needs to be kept moderately low. These crucial factors, i.e. the reaction temperature, the amount of seed and pH alteration are necessary for the fabrication of size- and shape-controlled Ag NPs. Schematic illustration of a single step followed by the stepwise seed-induced growth of Ag NPs is displayed in Scheme 13.2. The optical absorption spectrum of the synthesized Ag NPs solution and the TEM photograph of the particles are given in Fig. 13.8a. The representative SEM photographs of the Ag NPs prepared by the Lee Meisel method and through seed-induced growth with 10, 5, 3, 1.5 and 0.75 mL of Ag seeds, respectively, are shown in Fig. 13.9.

Synthesis of Au NPs can be carried out using the modified Turkevich method [131]. In this method, 100 mL aqueous solution with 0.01 g of chloroauric acid is heated at first, followed by the dropwise addition of 3 mL of 1% (w/v) solution of sodium citrate with continuous stirring. Heating is then sustained for a further 15 min until the solution colour turns intense red. The solution is subsequently cooled down to RT. The Au NPs show a characteristic SPR peak with a maximum of 520 nm as shown in Fig. 13.10 and the particles remain stable for several weeks. The size (~20 nm) and spherical shape of the particles are clearly seen from the representative TEM and AFM photographs in Figs. 13.11 and 13.12, respectively.

Pt NPs can also be synthesized by reducing the Pt ions with sodium citrate by refluxing at 100 °C for 8 h, in the presence of inorganic salts as a stabilizer [132]. Different sizes of Pt NPs can be obtained by altering the ratios of Pt ion and citrate ion as well as Pt ion and the inorganic salt used as a stabilizer. The representative TEM photographs of the Pt NPs are displayed in Fig. 13.13.

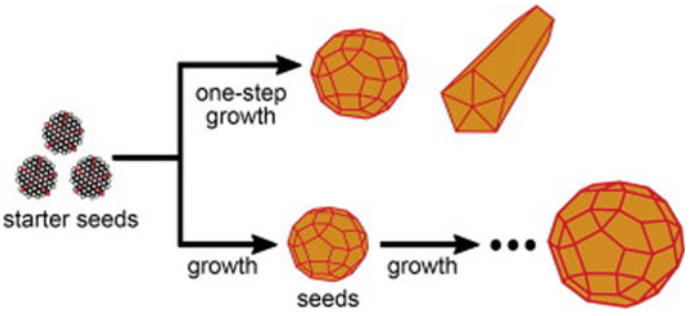

Scheme 13.2. Schematic representation showing a single step and stepwise seed-induced growth of Ag NPs (Lee Meisel method). Boundaries with twinning are demarcated with red lines. Reprinted with permission from Ref. [130] Copyright 2013 Elsevier

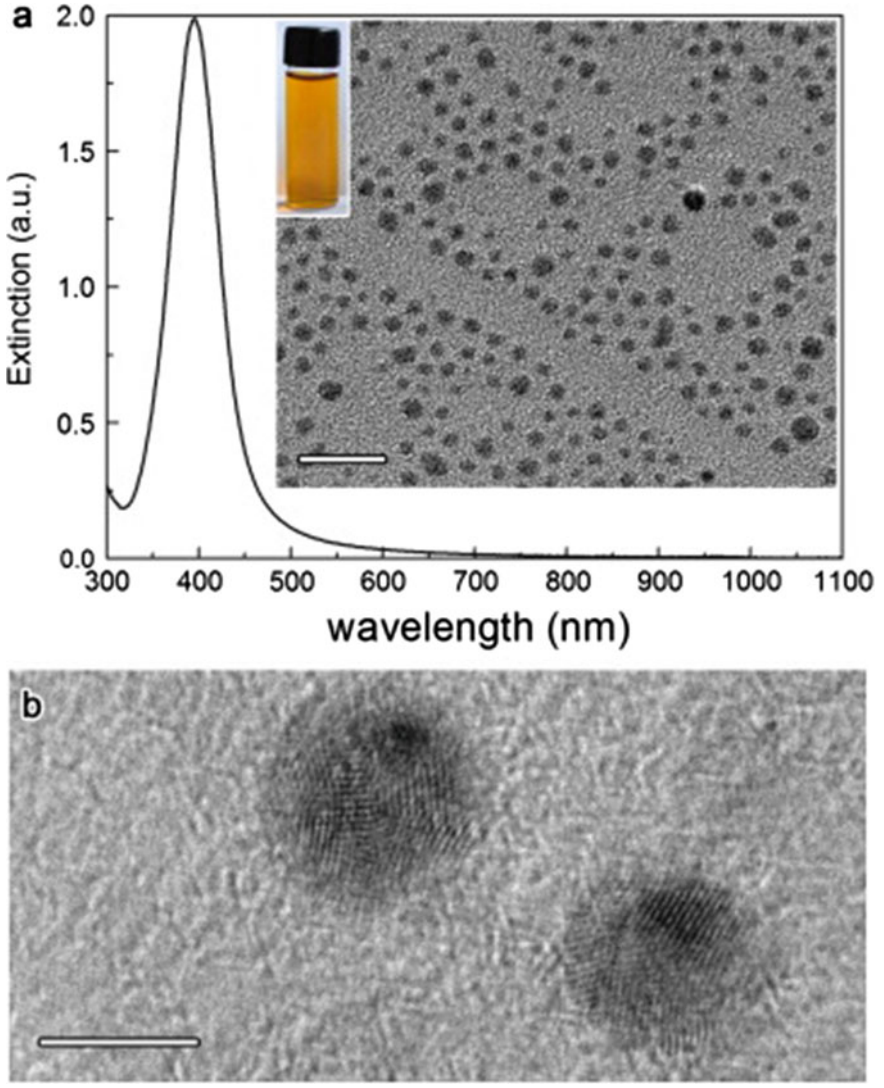

Fig. 13.8 **a** UV–vis absorption spectrum of the synthesized Ag NPs; An inset showing the photograph of the colloidal Ag NPs and its TEM image with the scale bar of 20 nm. **b** HRTEM photograph of the colloidal Ag NPs displayed in panel a with a scale bar of 5 nm. Reprinted with permission from Ref. [130] Copyright 2013 Elsevier

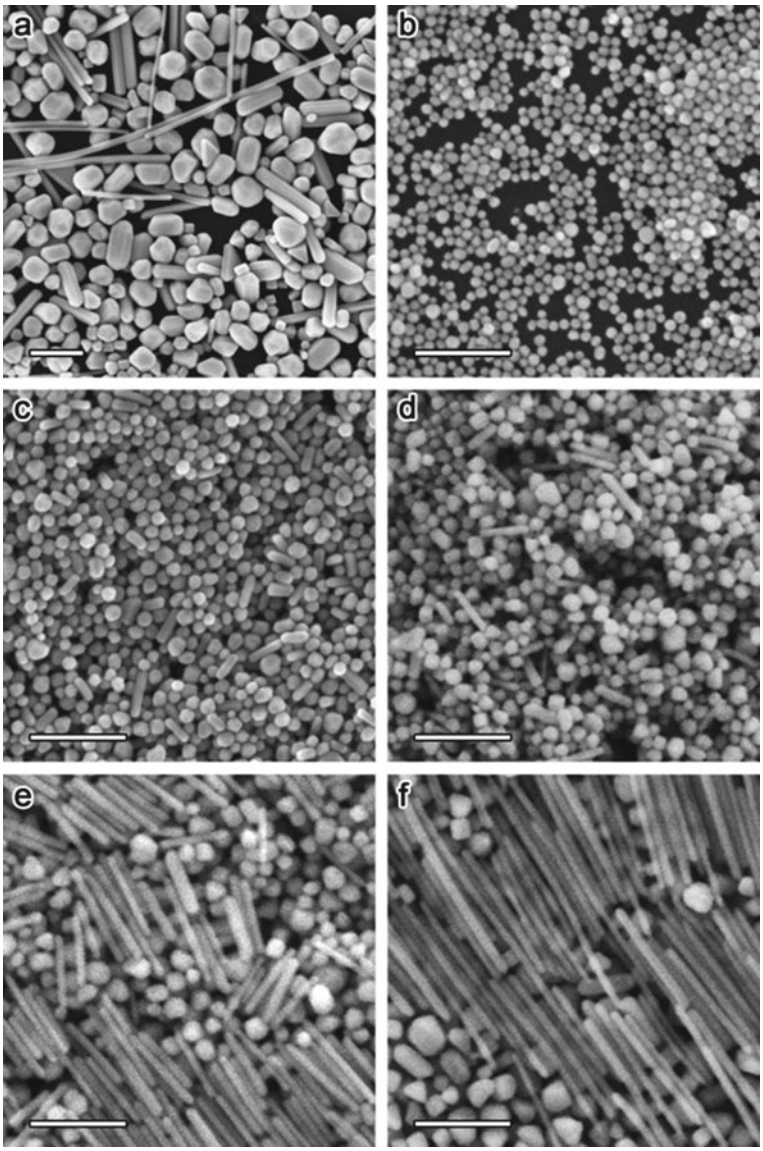

Fig. 13.9 SEM photographs of **a** the synthesized Ag NPs. **b–f** The synthesized Ag NPs displaying seed-induced growth with 0.75 to 10 mL of Ag seeds as per Ref [130]. Scale bars of 0.2 μm. Reprinted with permission from Ref. [130] Copyright 2013 Elsevier

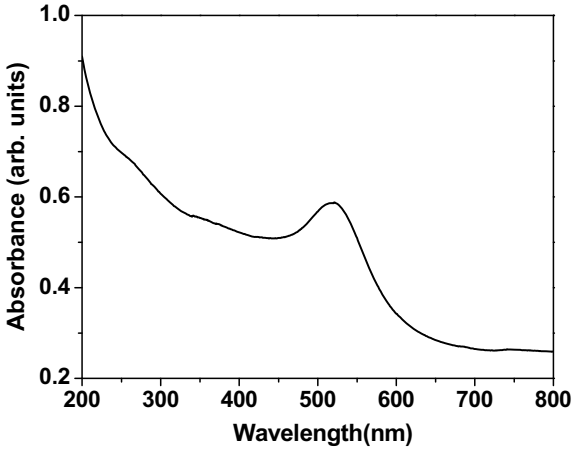

Fig. 13.10 SPR band of citrate stabilized Au NPs

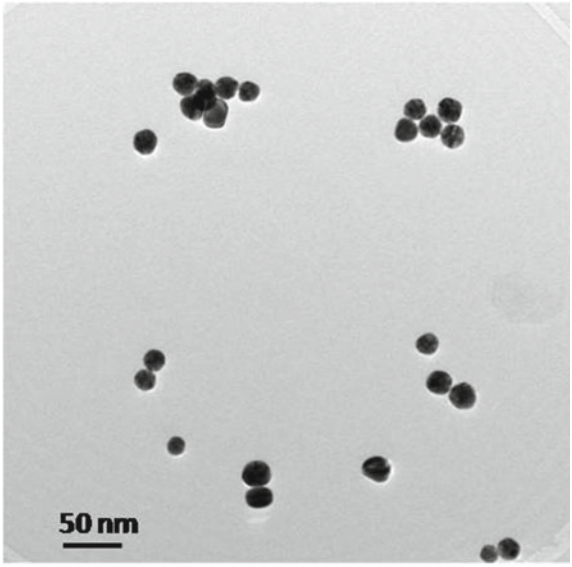

Fig. 13.11 TEM image of Au NPs prepared using modified Turkevich method

13.2.1.3 Functionalized Silver and Gold Nanoparticles

Amino Acids as Reducing Agent

Amino acids have been largely used for the preparation of Au NPs [133, 134] and Ag NPs [135]. Maruyama et al. [136] have shown that out of the 20 essential amino acids, about 9 amino acids such as alanine, asparagines, aspartic acid, glycine, histidine, phenylalanine, tryptophan, tyrosine and valine can efficiently reduce as well

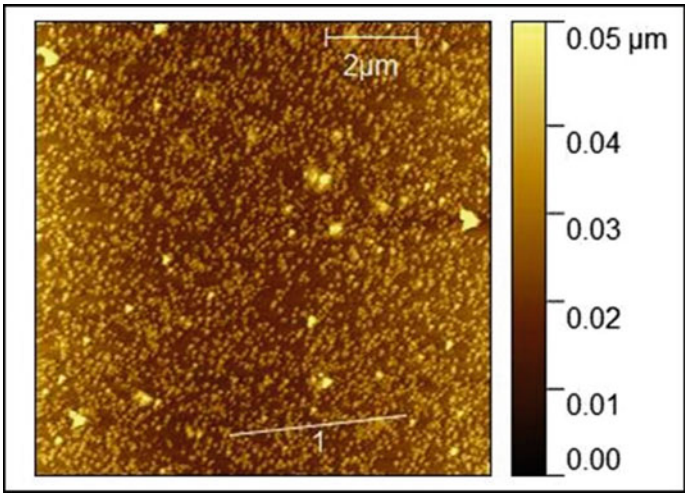

Fig. 13.12 AFM image of Au NPs prepared using modified Turkevich method

as stabilize the Au NPs. The stabilization of the metal particles by amino acids is attributed to the negative charge of the carboxylic groups [133, 134].

Tryptophan, phenylalanine and tyrosine show fluorescence, which adds another facet to the functionality of zwitterionic amino acids. Many amino acids including tryptophan were reported to be utilized as capping agents for functionalization of citrate or borohydride-capped Au or Ag NPs [135]. Tryptophan (Trp) has also been used for the preparation of Ag particles in the presence of other stabilizing agents. The reducing power of Trp is intermediate between borohydride and citrate. This makes Trp a suitable reductant for studying the development and growth of noble metal NPs.

The zwitterionic property of amino acids can be imparted to Au NPs by using Trp as a reducing agent as well as a stabilizer in a buffer medium [133]. Visual monitoring of the colour change in the reaction mixture containing Au ions and Trp in buffered aqueous medium at various pH revealed that the particles synthesized at pH 6 and above were stable, as shown in Fig. 13.14. It can be seen that at pH 3 and 4, the colourless solution of Au ions and Trp at first turned reddish, and then it turned purple as the reaction progressed and finally precipitated at the end of the reaction. In the case of pH 5 onwards, colourless reagents first turned orange-yellow, and finally red as the Au NPs were formed. This orange-yellow colour formation as observed above may be due to the complex formation between Au and Trp. At lower pH, the primary amine group of Trp due to protonation is available to a lesser extent for complex formation. Trp-Au complex then gets reduced by decarboxylation [133, 137] which is monitored by the evolution of carbon dioxide by gas chromatography, as shown in Fig. 13.15.

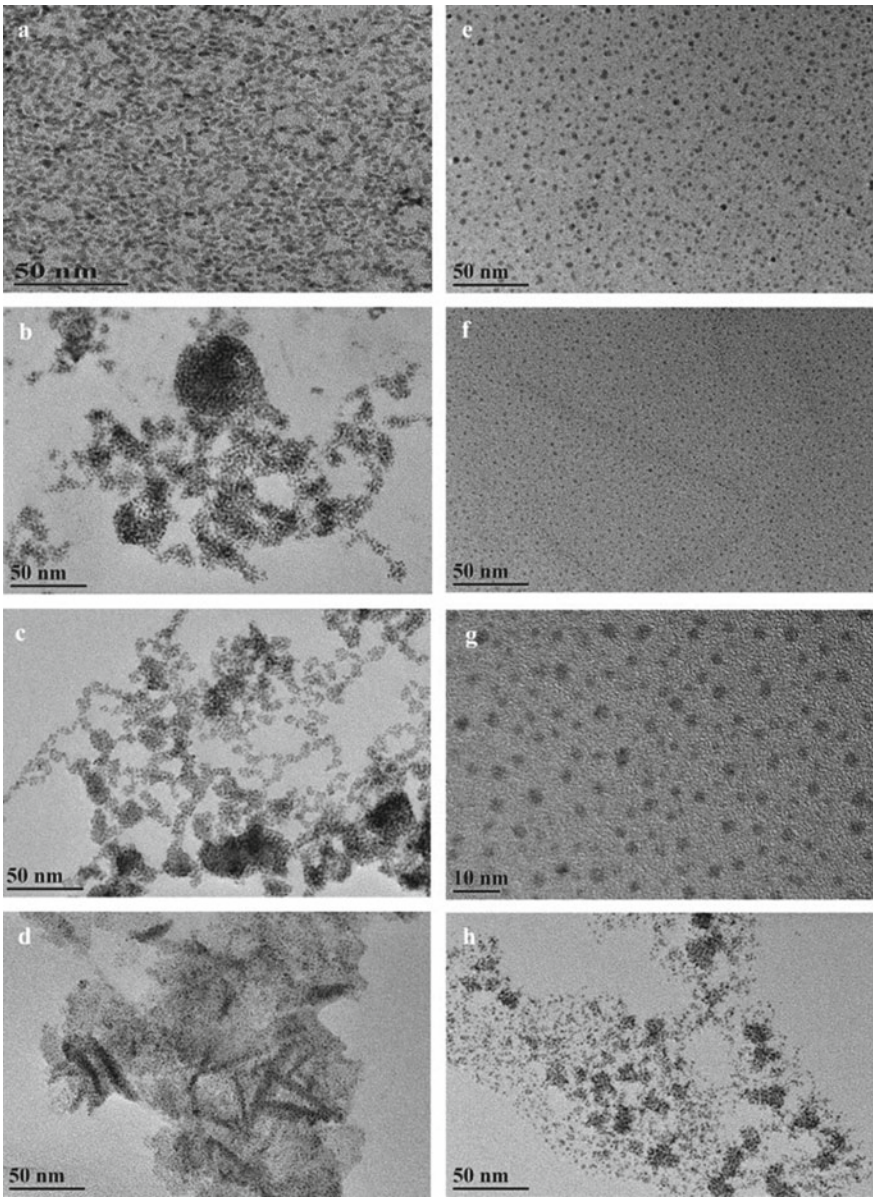

Fig. 13.13 TEM images of Pt NPs prepared by altering the ratio of trisodium citrate (Cyt) and Pt ions in solution in the presence of electrolytes as per Ref. [132]. Reprinted with permission from Ref. [132] Copyright 2014 Elsevier

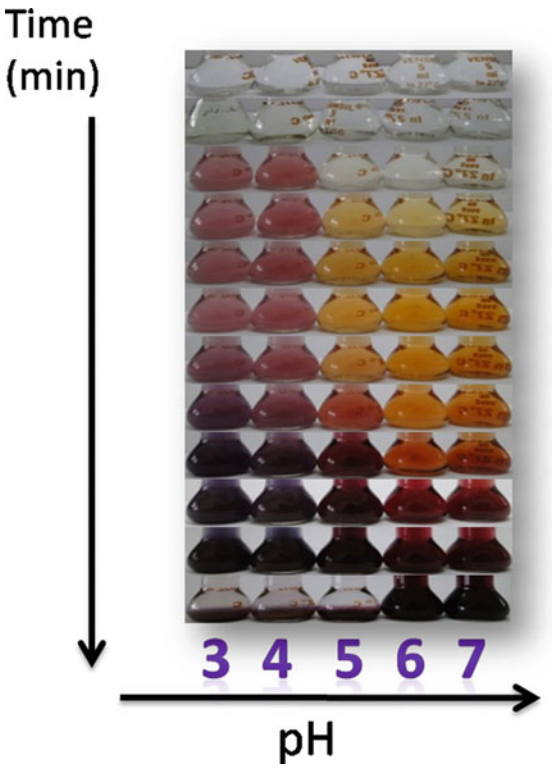

Fig. 13.14 Visual monitoring of colour change in the reaction mixture containing Au ions and Trp in buffered aqueous medium at various pH with time. Reprinted and adapted with permission from Ref. [133] Copyright 2015 Elsevier

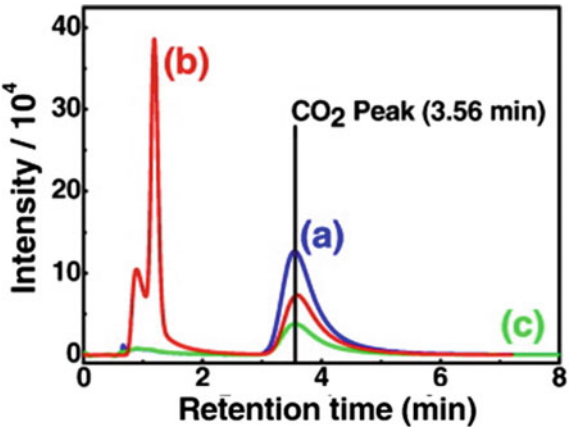

Fig. 13.15 Gas chromatograph of the evolved CO_2 during synthesis of Trp functionalized Au NPs; **a** sample, **b** standard and **c** blank. Reprinted with permission from Ref. [133] Copyright 2015 Elsevier

Chiral amino acids, viz., free cysteine and cysteine-containing peptides have been reported to impart chirality to Au NPs, which is manifested in their circular dichroism spectra as well as TEM image [138].

Formamide as Reducing Agent

Ag NPs synthesis in formamide [99] as stabilizing and reducing agent in the absence of any external reductant is discussed below. The growth of the Ag NPs depends on the Ag ions concentration. In the absence of a stabilizer, Ag films are deposited on the walls of the glass container. However, in the presence of a stabilizer such as poly(N-vinyl-2-pyrrolidone) (PVP) or colloidal silica (SiO_2), a clear dispersion is observed, which enables the formation of stable Ag NPs by complexation with PVP or SiO_2. The time-dependent (TD) UV–vis absorption spectrophotometry, TEM and AFM techniques are used to monitor the formation of Ag NPs. The TD optical absorption spectrum of Ag NPs in formamide with $AgNO_3$ (2 mM) and PVP (1% wt/v) is displayed in Fig. 13.16a. From the figure, gradual augmentation in the SPR band intensity at 425 nm is observed that indicates the incessant formation of NPs. In about an hour, there is relative slowing down in particle formation and the SPR band remains symmetric with an insignificant change in its width. This shows that the particles size remains almost uniform. The SPR band of Ag NPs in formamide in 1% PVP shows a maximum at 425 nm and is shifted to the red relative to the absorption maximum of Ag NPs in water. This red shift in the SPR band is possibly due to formamide having a higher refractive index than water. Kinetic traces displaying the Ag particles formation in formamide for varying concentrations of Ag ions in 1% PVP is displayed in Fig. 13.16b. From the figure, the growth rate of the particles is observed to be enhanced with increasing concentrations of Ag ions.

The surface topography of the Ag NPs, prepared in the presence of different stabilizers, is investigated using TEM. The TEM samples are prepared by inserting

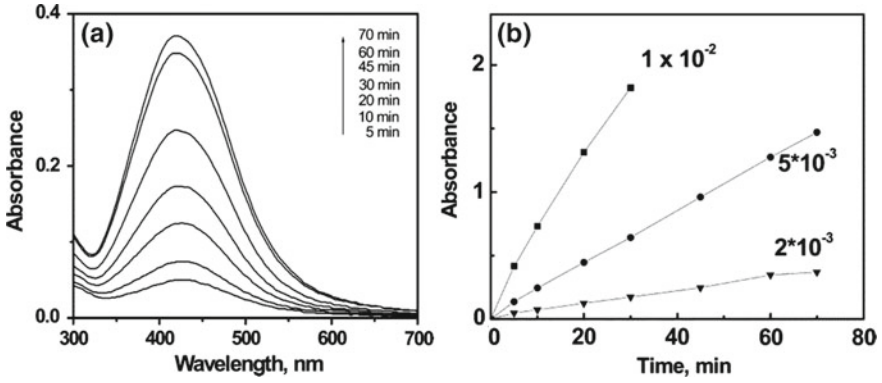

Fig. 13.16 **a** TD optical absorption spectrum of Ag NPs formed by reducing $AgNO_3$ (2×10^{-3} M) in formamide with PVP (1% wt/v). **b** Kinetic traces displaying the development of Ag NPs in formamide with constant (1 wt %/v) PVP concentration and increasing concentrations of Ag ion. Reprinted with permission from Ref. [99] Copyright 2005 American Chemical Society

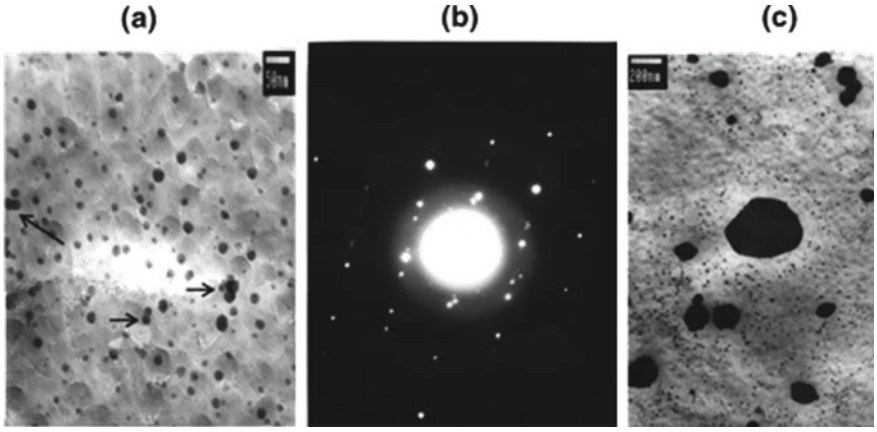

Fig. 13.17 TEM images of Ag NPs in formamide (**a**) for 5×10^{-3} M Ag ions concentration with PVP (1% wt/v) [displaying twinned particles]; **b** typical electron diffraction pattern of a twinned particle; and **c** huge flat particles having distinct geometric shapes. Reprinted with permission from Ref. [99] Copyright 2005 American Chemical Society

a drop of colloidal Ag NPs solution on the copper grid (carbon-coated) and drying at RT. Since formamide is extremely viscous with a high boiling point, it takes a long time to dry these samples. A characteristic TEM photograph for a colloidal Ag NPs solution containing PVP (1% wt/v) is displayed in Fig. 13.17. The mean size of the particles in PVP (1%) is about 25 nm as shown in Fig. 13.17a. Twinning of the particles is also observed at certain places as confirmed from the diffraction pattern (Fig. 13.17b). Twinning is a phenomenon that is common for face-centred cubic (fcc) structures. The TEM images as seen from Fig. 13.14c reveal that during the drying process, the Ag film arrangement takes place encircling many particles and assuming a disk type shape.

The morphology of the Ag NPs without an added stabilizer is probed by AFM. For this purpose, glass slides are suspended in the solution for ~24 h leading to the arrangement of Ag films on the glass surface. Once the films are formed, the slides are taken out, washed with water and air-dried before examining the same with AFM. Fig. 13.18 shows the AFM image of the polygonal particles with the size of 100 nm. The glass slides, prepared by this procedure, show TD optical properties that depend on the packing density of the Ag particles.

Polyols as Reducing Agent

Polygonal (triangular) Ag nanoprisms (NPRs) [139] can be synthesized by the reduction of silver perchlorate with formamide in the presence of polyethylene glycol (PEG) at RT. Briefly, an aqueous solution of silver perchlorate is added to formamide with PEG [0.1–1% (wt/v)] of varying concentrations. The solution is then uniformly mixed and allowed to stand. The solution immediately turns grey in colour. Glass slides are then suspended in the formamide solution with PEG. The film formation

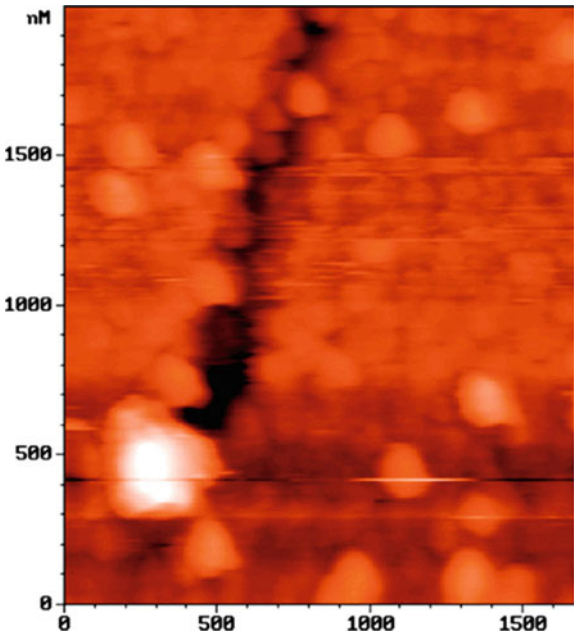

Fig. 13.18 AFM photograph of Ag NPs prepared by reducing 5 mM Ag ions in neat formamide. Reprinted with permission from Ref. [99] Copyright 2005 American Chemical Society

was found to take place on the glass slides with time. The slides are dipped in the solution for about 17 h and then these slides are removed, washed with water and dried at RT. These slides are protected from light; both during and after the film formation. The reduction of Ag ions by formamide results in the array deposition of triangle-shaped Ag NPs on the glass walls of the container. AFM images are recorded to study the morphology of the Ag films. The representative image as shown in Fig. 13.19 indicates the arrangement of triangular-shaped particles. It is observed that PEG results in the formation of triangle-shaped particles with distinct orientations. The structures displayed in the figure are representative of the entire film. The presence of particles with spherical or ellipsoidal/polygonal shape at random places contributes to less than a few percent of the surface. In addition, a three-dimensional AFM image is also shown in the figure, which reveals the film thickness. For the Ag films, since the reduction and aggregation processes are simultaneous, it is not possible to characterize the films with UV–vis (optical) absorption spectroscopy. Therefore, in order to record the optical absorption of Ag NPs, a different methodology is usually adopted. PVP, a polymer accomplished of stabilizing and complexing the Ag NPs, is added to the reaction mixture of Ag in formamide that contains PEG. It is observed that PVP inhibits the Ag particles aggregation resulting in a stable clear dispersion of Ag NPs. Thus, the Ag particles are prepared in formamide containing 1:1 ratio of PVP and PEG. In Fig. 13.20, the optical absorption spectrum of colloidal Ag NPs in formamide in the presence of both PEG and PVP is shown. It is seen from Fig. 13.20a, b that with increasing concentrations of Ag^+, the SPR band gets red-shifted with time. At first, only a single band is observed at 420 nm that corresponds

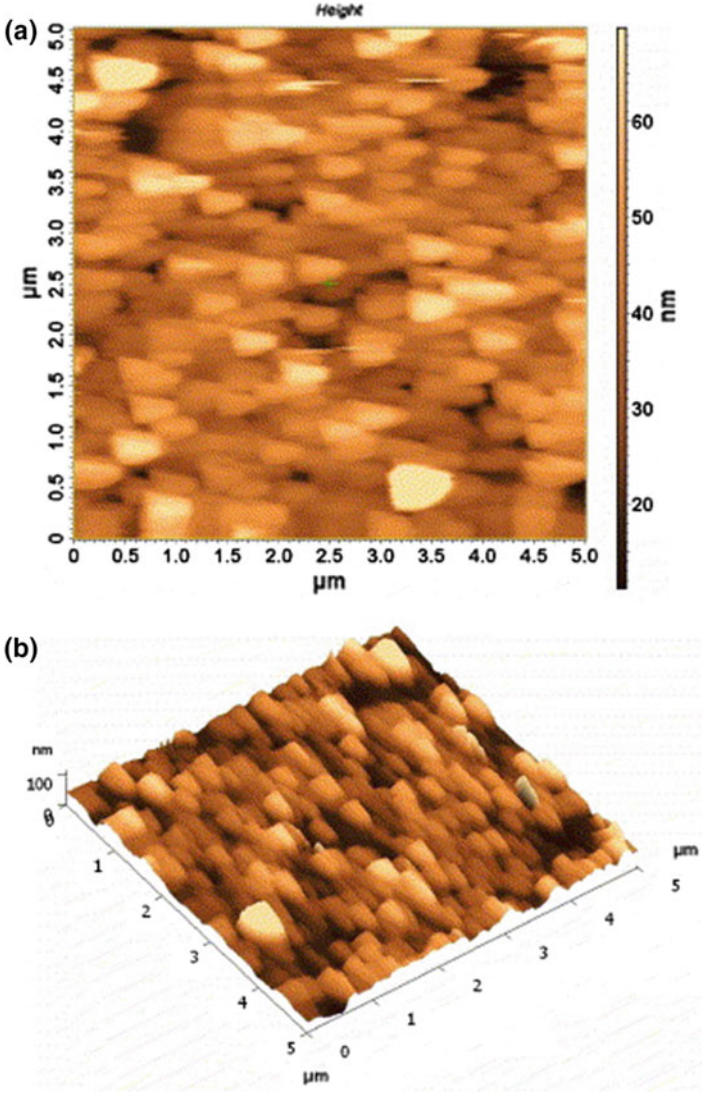

Fig. 13.19 **a** AFM photograph (5 × 5 μm) displaying the Ag NPRs array obtained by reducing Ag ions (10 mM) in formamide [1% PEG (wt/v)]. **b** 3D AFM photograph. Reprinted with permission from Ref. [139] Copyright 2005 Elsevier

to the out-of-plane (oop) dipole resonance of Ag (NSPs) nanospheres. This band steadily shifts towards a higher wavelength with the progress of the reaction and ultimately shows a peak with a maximum of 510 nm. Thus, in the presence of (1:1) PEG and PVP, the formation of both Ag NSPs and Ag NPRs is observed.

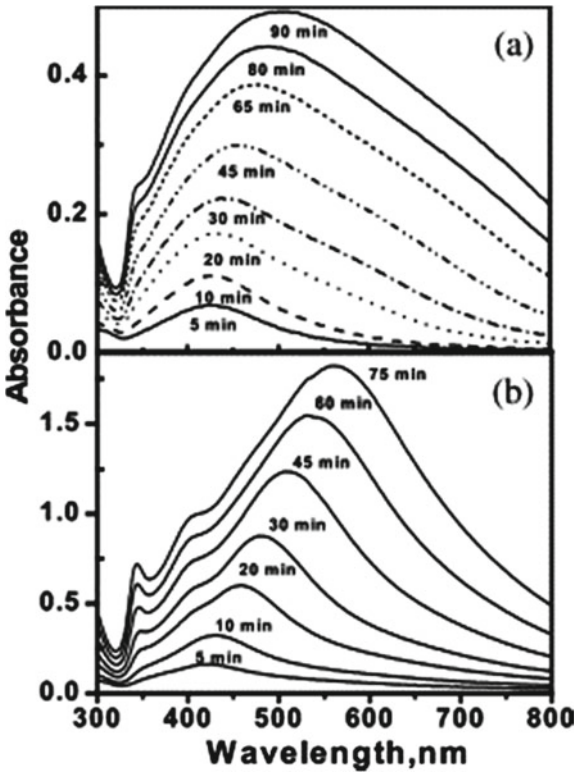

Fig. 13.20 Time-dependent (TD) optical absorption spectrum displaying the development of NSPs and NPRs obtained from **a** 2 mM $AgNO_3$ in formamide with 1% (wt/v) of PEG and PVP); **b** 4 mM $AgNO_3$ in formamide with 1% (wt/v) of PEG and PVP. Reprinted with permission from Ref. [139] Copyright 2005 Elsevier

Pt, Pt/Ag, Pd and Pd/Ag NPs can be synthesized from the metal precursors in ethylene glycol and glycerol in the presence of PVP using the microwave technique [140]. The formation of Pt, Pt/Ag, Pd and Pd/Ag NPs using microwave irradiation was monitored by UV–vis absorption spectroscopy, XRD and dynamic light scattering. X-ray diffraction (XRD) confirmed the formation of Pt, Pt/Ag, Pd and Pd/Ag NPs. It is observed that the mixed metal Pt/Ag and Pd/Ag NPs can be synthesized either by the amalgamation of the individual colloidal solutions or by co-reduction of the precursor metal salts.

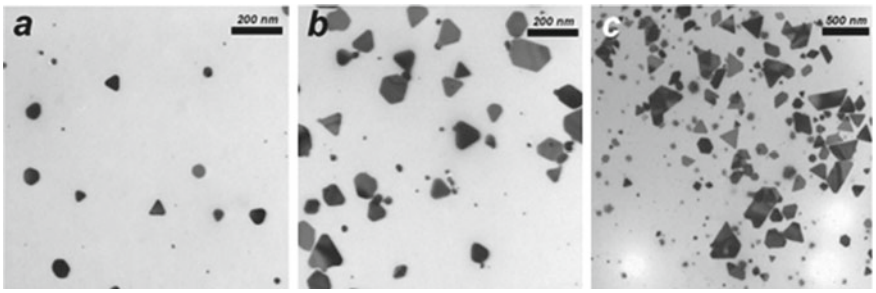

Fig. 13.21 TEM images displaying the development of Ag nanoprisms obtained by reducing high Ag^+ concentration (2×10^{-2} M) in DMF in the presence of PVP, at various time intervals: **a** 5, **b** 15 and **c** 60 min. Reprinted with permission from Ref. [141] Copyright 2002 American Chemical Society

N,N-Dimethyl Formamide as Solvent and Reducing Agent

Ag NPRs with polygonal shape (triangular) were prepared by heating $AgNO_3$ in N,N-dimethyl formamide (DMF) in the presence of poly(vinylpyrrolidone) [PVP] [141]. Here, DMF acts as a strong reductant. The proposed reaction is as follows:

$$HCONMe_2 + 2Ag^+ + H_2O \rightarrow 2Ag^0 + Me_2NCOOH + 2H^+ \qquad (13.3)$$

The reaction involves the formation of Ag NPs in addition to carbamic acid and an acidic environment. During this synthesis, a combination of NPRs and nanospheres are formed. The nanospheres can be separated through repeated centrifugation. The TEM images that show the growth of Ag NPRs as a function of time are displayed in Fig. 13.21. These images indicate that at first small spheres are produced, which then accumulate leading to the formation of particles with prism-like shapes. The formed NPRs then are converted into larger particles with time, and a broader range of shapes are observed (Fig. 13.21).

The UV−visible absorption spectrum of colloidal Ag NPs in DMF during the formation of NPRs is shown in Fig. 13.22. Initially, a single band centred at 410 nm is observed in the absorption spectrum that corresponds to the dipolar resonance of Ag NSPs. As the reaction progresses, this band is red-shifted, along with the appearance of other peaks. After 20 min of heating the reaction mixture, four peaks are seen, which are comparable to the ones predicted by Jin et al. [142], apart from an intense peak at 460 nm that is attributed to the existence of spherical particles (seen from TEM). Since the NSPs present in the colloidal dispersion are evidently smaller than the NPRs, they can be effortlessly removed by centrifugation. This method has the benefit that PVP prevents the aggregation of the particles all through the reaction.

A one-pot approach to synthesize triangular Ag NPRs was developed by Zhang et al. [143]. The size of the triangular Ag NPRs from 30 to 100 nm was adjusted by altering the amount of n-pentanol solution and sodium hydroxide in the ternary system containing water/PVP/n-pentanol. The n-pentanol solution and sodium

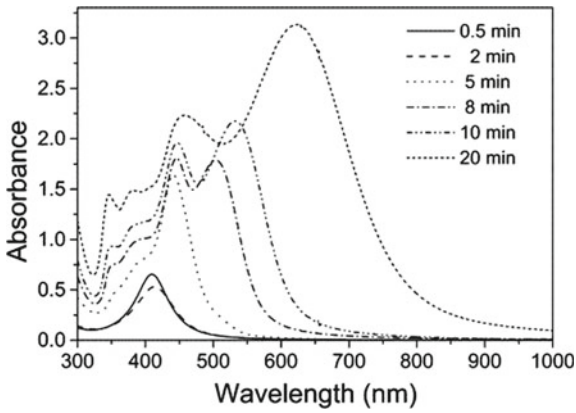

Fig. 13.22 Time evolution of the optical absorption spectrum showing the development of Ag nanoprisms in DMF medium. Reprinted with permission from Ref. [141] Copyright 2002 American Chemical Society

hydroxide led to the modification of the original pH of the ternary system. This resulted in the extremely reproducible synthesis of triangular NPRs. In order to have well-defined shapes of the NPs, formamide and N,N-dimethyl formamide (DMF) were both utilized to manage the system pH. The extinction spectrum of the triangular Ag NPRs was observed to be relatively narrow that made them suitable for different biological and chemical applications. The photographs of the Ag NPRs in ethanol dispersions of varying edge lengths (average) are displayed in Fig. 13.23a. These dispersions as seen from the figure differ in colour owing to their LSPR property ranging from pink, purple and blue. The dipole (in-plane) plasmon resonance peak of Ag NPRs gets shifted to the red with an enhancement in the (average) edge length of the NPRs. Fig. 13.23b shows the extinction spectrum of Ag NPRs with different (mean) edge lengths dispersed in ethanol. Each spectrum displays three distinct peaks; first strong peak at longer wavelength; second weak and broad band and third sharp weak peak at shorter wavelength. The three bands are attributed to in-plane (ip) dipole, (ip) quadrupole and out-of-plane (oop) quadrupole plasmon resonance bands [144]. It is observed from Fig. 13.23b, the dipole (ip) plasmon-resonance band gets blue shifted to a shorter wavelength with increasing amounts of the sodium hydroxide-pentanol solution. In Ag NPRs, the 111 reflection plane is prominent and appears at $2\theta = 38.2°$ and is shown in Fig. 13.23c. The figure displays that the preferred orientation of the Ag NPRs is the 111 plane. The surface morphology of the triangular Ag NPRs is also monitored using SEM. The SEM images as shown in Fig. 13.24a reveal that the Ag NPRs prepared using DMF have a definite shape with pointed corners but their sizes remain uneven. The use of formamide as displayed in Fig. 13.24b improves the shape (triangular) of the Ag NPRs, but the range of distribution in size gets expanded leading to broad extinction bands.

Chelating Agents as Reducing Agents

Au and Ag NPs can be synthesized using chelating agents [145, 146] such as ethylenediaminetetraacetic acid (EDTA). It is found that EDTA forms a complex

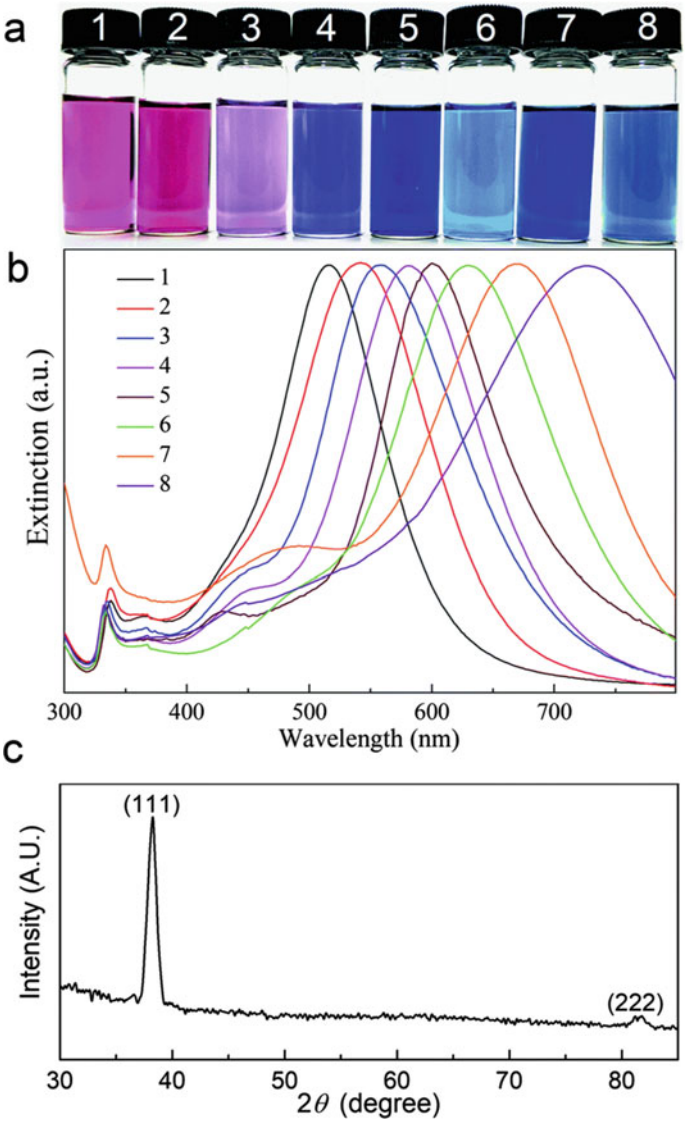

Figure 13.23. **a** Photographs and **b** extinction spectrum for the Ag NPRs in ethanol dispersions of varying edge lengths (average) of (1) 30, (2) 35, (3) 45, (4) 50, (5) 60, (6) 70, (7) 80 and (8) 100 nm. **c** XRD spectrum of the Ag NPRs. Reprinted with permission from Ref. [143] Copyright 2019 Royal Society of Chemistry

with metal ions [145] which helps in the controlled release of the metal ions for reduction. This phenomenon leads to the ligand concentration-dependent size control in noble metal NPs. The effect of different chelating agents such as nitrilotriacetic acid (NTA), triethylenetetramine-N,N,N',N'',N'''-hexaacetic acid (TTHA), EDTA, N-(2-hydroxyethyl)ethylenediaminetri-acetic acid (HEDTA) and iminodiacetic acid (IDA) on the surface activity of Ag NPs synthesized using the above ligands is investigated [98]. The denticity of the above ligands increases in the following order: IDA (3) < NTA (4) < HEDTA (5) < EDTA (6) < TTHA (10) where the maximum achievable denticity is given in parenthesis. In Fig. 13.25, the TEM image and the associated histogram of the chelating agent reduced Ag NPs is shown. It can be seen that the ligand with the smallest denticity (NTA) has the largest particle size. The NPs size was found to reduce with an increase in denticity. This observation indicates that after the initial formation of the NPs, the ligands get adsorbed on the surface of the particles, thereby controlling the growth of the particles size. Amongst NTA and HEDTA, it can be seen that although for both the ligands, the synthesized Ag NPs

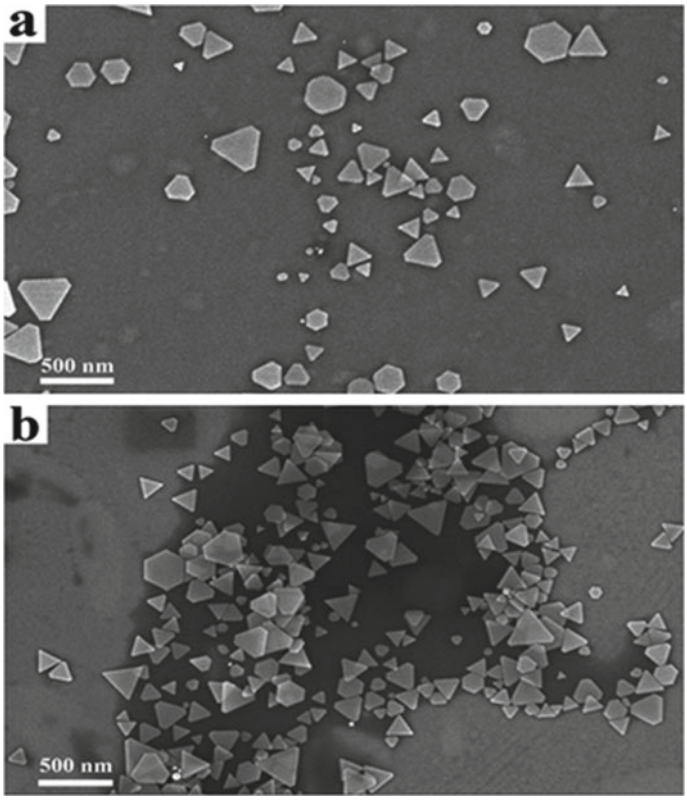

Fig. 13.24 SEM images of the Ag NPRs made from 0.6 g PVP and 3 mL of **a** DMF and **b** formamide. Reprinted with permission from Ref. [143] Copyright 2019 Royal Society of Chemistry

are fairly monodispersed, the NTA-capped Ag NPs are larger in size when compared to that of HEDTA-capped Ag NPs. This observation indicates that under similar conditions, ligands with lower denticity have poor control over the size of particles. HEDTA-capped Ag NPs are also found to show definite geometry, indicating strong adherence of the ligand to a selective crystal plane. In the case of TTHA, very high denticity results in the loss of size control and thus, Ag NPs with broad size distribution are formed. TTHA-capped Ag NPs are found to coalesce, which indicates poor stabilization by the ligand.

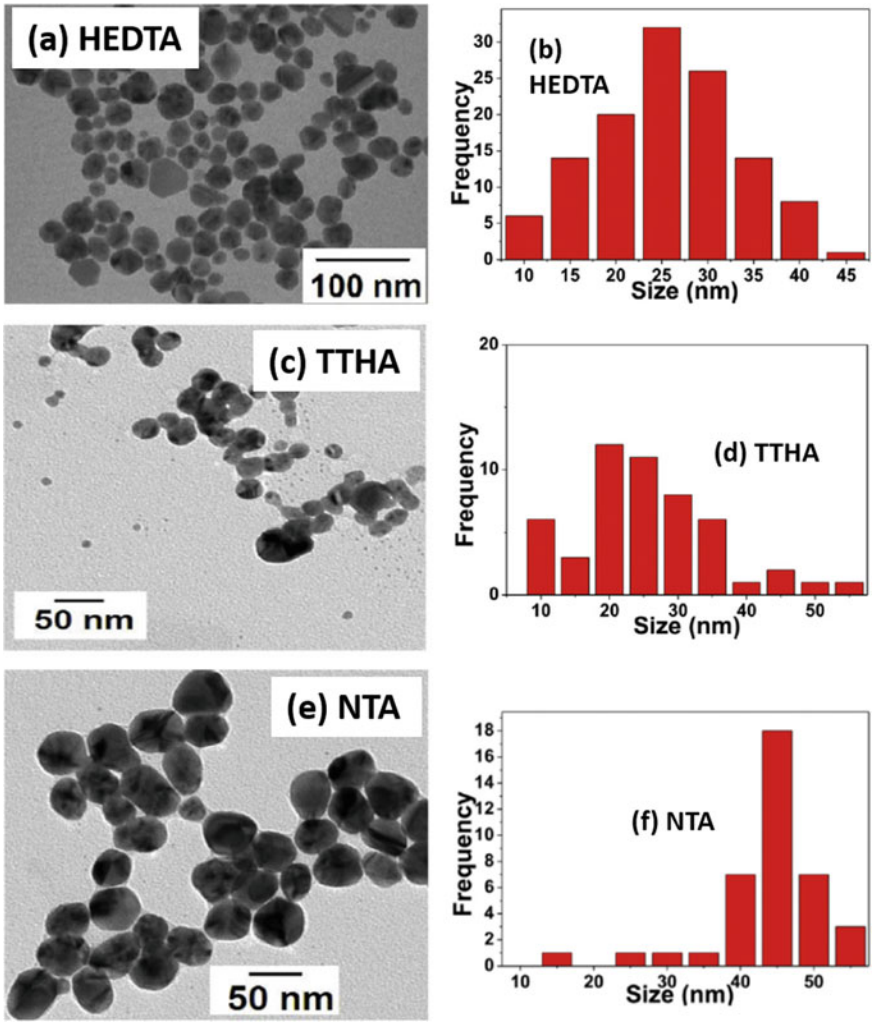

Fig. 13.25 TEM images and histogram of HEDTA, TTHA and NTA capped Ag NPs. Reprinted and adapted with permission from Ref. [98] Copyright 2014 Elsevier

Sugars as Reducing Agent

Ag and Au NPs functionalized with α-, β- and γ-cyclodextrin (CD) are prepared by the successive addition of $AgNO_3$ (1 mM) and $HAuCl_4 \cdot H_2O$ (1 mM) and NaOH to the aqueous solution of α-, β- and γ-CD (10 mM). In this method of preparation of functionalized Ag and Au NPs, α-, β- and γ-CD are used both as reductant as well as a stabilizer. The pH of the solution is maintained at $\geq$ 10. The solution initially appears colourless showing no development of Ag and Au NPs. The reaction mixture is then refluxed at ~60 °C for 10 min. During reflux, the colour of the solution starts to change and finally turns greenish-yellow and bright red demonstrating the development of Ag and Au NPs. The particles are then cooled to RT and used for additional characterization. The optical absorption spectrum of the synthesized Ag and Au NPs is shown in Fig. 13.26. The figure shows peaks with a maximum at 404 and 515 nm that correspond to the characteristic SPR bands of the Ag and Au NPs. The shape as well as the size of the NPs is obtained from TEM (Fig. 13.27) images that show the development of sphere-shaped particles with a size of 25 and 15 nm for Ag and Au NPs, respectively.

Au NPs can also be prepared using β-D-glucose as a reductant. The reaction occurs at RT in the presence of NaOH [147]. In another method, Au^{3+} ions are immobilized in Ca-Fe cross-linked alginate films and reduced using 0.05 M glucose in an aqueous medium by heating the solution for 5 min at 60 °C in a water bath [148]. The colour of the film varies from yellow to red after the reduction of Au^{3+} ions. The films showing maximum uptake of Au^{3+} ions are taken up for further studies. In Fig. 13.28, the TEM image of synthesized Au NPs shows clustering of the particles in the alginate matrix,

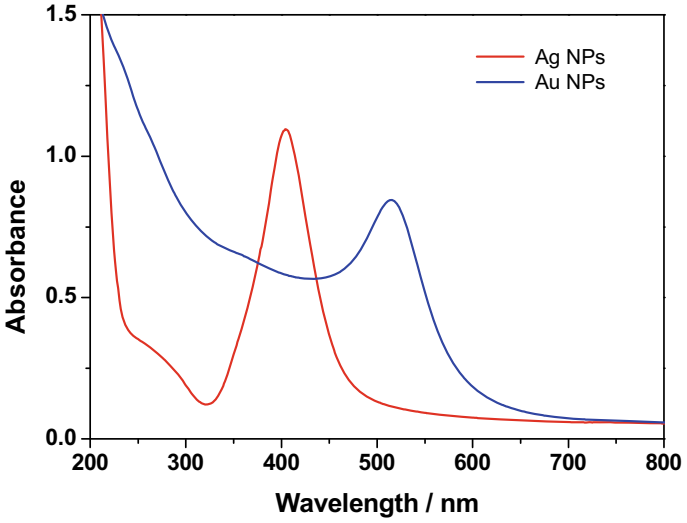

Fig. 13.26 SPR bands of γ-CD functionalized Ag and Au NPs

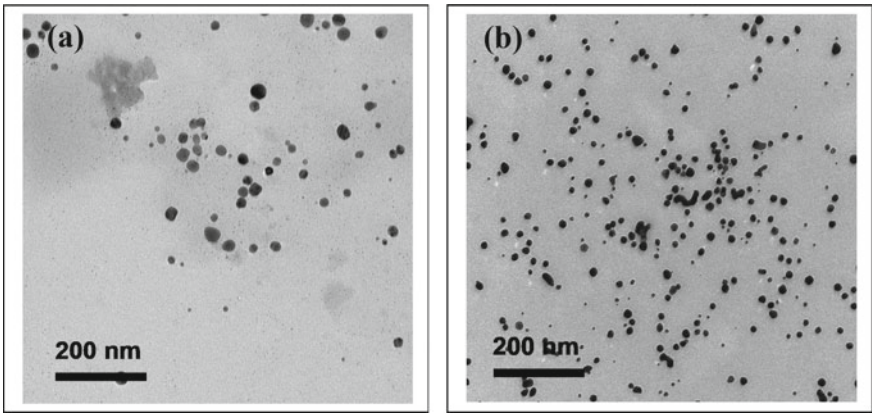

Fig. 13.27 TEM photographs of γ-CD-capped **a** Ag and **b** Au NPs

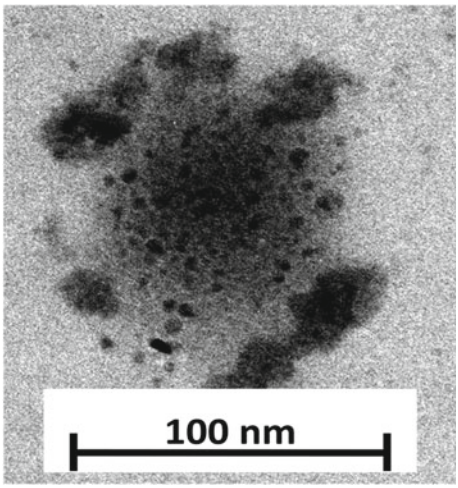

Fig. 13.28 TEM image of Au NPs loaded in Ca-Fe cross-linked alginate film

which is largely instrumental in the SERS activity exhibited by the films which will be discussed later.

13.2.2 Radiolytic Reduction

Radiolysis of water or any organic solvent by gamma (γ) radiation or electron produces primarily free radicals such as hydrated electrons (e^-_{aq}), $OH^\bullet$, $H^\bullet$ and H_2O_2 under N_2 atmosphere. e^-_{aq} and $H^\bullet$ are the primary reducing species responsible for reducing the noble metal ions or precursors to NPs [149, 150]. The standard reduction

potential of e^-_{aq} and $H^\bullet$ expressed as $E^0(H_2O/e^-_{aq})$ and $E^0(H^+/H^\bullet)$ are −2.87 V and −2.3 V, respectively [151]. No external reducing agent is required in this method. In fact, the reducing agent, i.e., the hydrated electron is generated in situ and the unreacted electrons are absorbed by the solvent via the recombination reaction. In contrast to the chemical methods, the lack of excess reducing agent in radiolytic synthesis eradicates the requirement of post-synthesis purification. The radiolytic reduction reaction takes place homogeneously, which leads to the narrow size distribution of particles [152].

In order to exclusively construct the environment for reducing radical-mediated reaction, potent oxidative radical $OH^\bullet$ must be scavenged using species such as secondary alcohols and formate anions. Radiolytic reduction reaction occurs spontaneously at RT as e^-_{aq} and $H^\bullet$ have very high diffusivity. The rate of reaction can only be controlled by varying the dose of the ionizing radiation. The dose rate controls the concentration of free radical generated, which in turn react with the metal precursors. The relation between the dose of ionizing radiation and the concentration of generated radical can be understood by a detailed study of the effects of the interaction of ionizing radiation with matter [153].

γ radiation, specifically, ^{60}Co source is generally used to carry out bulk reactions. In our laboratory, recently, Ag NPs were synthesized by reducing Ag ions by γ radiation in the presence of PVP as a stabilizer [154]. In this study, most of the critical controlling aspects of radiolytic synthesis have been covered. $AgClO_4$ solution of 3.0×10^{-2} M in the presence of 2-propanol (1 M) and varying concentrations of PVP was irradiated using ^{60}Co γ-radiation of dose rate 1 Gy/h. The development of Ag NPs was investigated using optical absorption spectroscopy, which is displayed in Fig. 13.29. It is known that perchlorate ions have lower reactivity towards the reducing radicals in comparison to nitrate ions. Thus, silver perchlorate was taken as a metal precursor to study other associated effects. In this study, nitrate ions did not show any shape alteration, which was otherwise observed by Kuo et al. [155]. Upon studying the effect of PVP as a stabilizer, it was observed that higher PVP concentration (0.1% w/v) promotes spherical Ag NPs formation, whereas lower concentration (0.01% w/v) leads to the development of anisotropic Ag NPs, which was characterized by the optical absorption spectroscopy. At higher concentrations of Ag ions, anisotropic NPs of a higher aspect ratio were obtained. At a lower concentration of Ag ions, the anisotropic effect was not observed. The appearance of the anisotropic particles at a higher concentration of Ag ions may be due to the higher concentration of Ag^0 seeds generated at a fixed dose. It was also observed that the adsorption of OH^- ions at higher pH affected the shape of the Ag NPs. Upon administration of a higher cumulative dose of ^{60}Co γ-radiation, Ag nanoplates were obtained, which is given in Fig. 13.30.

In another interesting work, radiolysis was used for the functionalization of Au NPs in DMF and water mixtures [156]. Thiol-functionalized polyoxometalates were subjected to in situ disulphide formation during radiolysis. This thiol or disulphide adsorption on the surface of Au NPs controlled the shape of the particles. Secondary alcohol added to the reaction mixture for scavenging the oxidizing radicals played

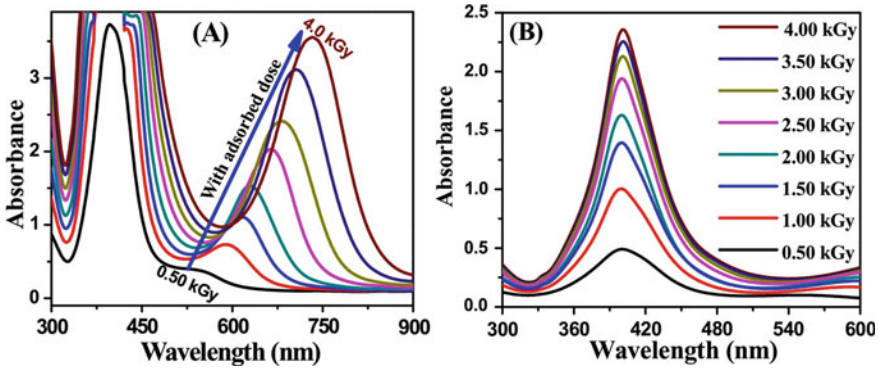

Fig. 13.29 Optical absorption spectrum of Ag NPs prepared with varying doses of γ radiation for the solution having $AgClO_4$ (30 mM), PVP (0.01% w/v) and 2-propanol (1 M) with a dose rate of 1 kGy hr^{-1}. Cuvette path length **a** 1 and **b** 0.1 cm. Reprinted with permission from Ref. [154] Copyright 2018 Elsevier

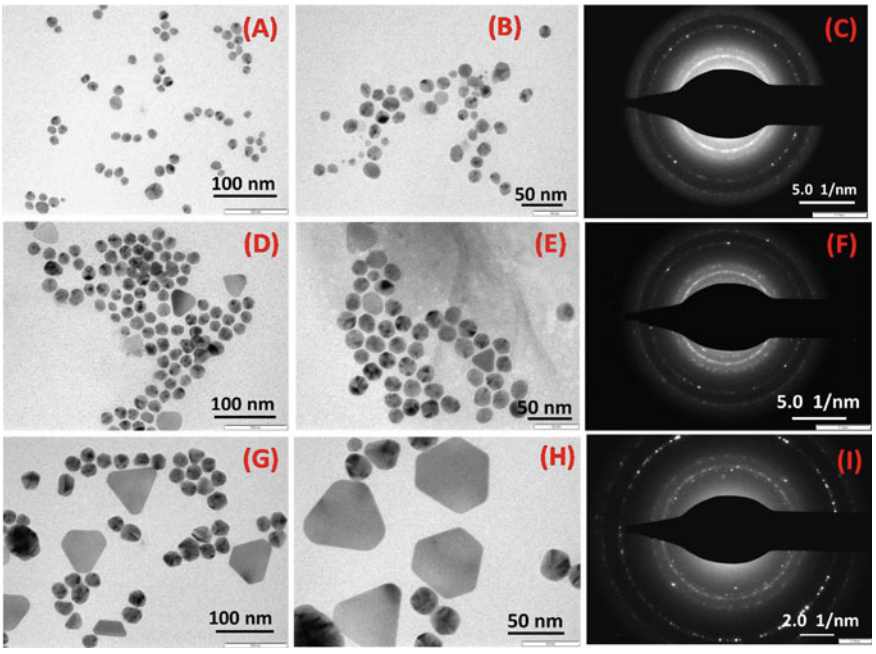

Fig. 13.30 TEM and SAED photographs of Ag NPs with varying doses of γ radiation (A–C) 0.5, (D–F) 2.0 and (G–I) 4.0 kGy for aqueous solutions containing $AgClO_4$ = 30 mM, PVP = 0.01% (w/v) and 2-propanol = 1 M with a dose rate of 1 kGy h^{-1}. Reprinted with permission from Ref. [154] Copyright 2018 Elsevier

a significant part in the disulphide formation [156]. The TEM images of different shapes of Au NPs obtained under different reaction conditions is given in Fig. 13.31.

Apart from γ radiolysis, the pulse radiolysis technique is also often used to study the synthesis of noble metal NPs by electron irradiation [157, 158]. Neither γ-radiation nor electrons interact directly with the solute molecules in a solution. Electrons, as well as γ-radiation, usually deposit their energy in the solvent, which leads to the formation of short-lived radicals. These short-lived free radicals interact with the solute molecules to generate transient species, which can be observed in microsecond (μs) time scales. In the pulse radiolysis technique, the time-resolved optical absorption spectrum of the transient chemical species at a fixed wavelength is recorded, which is triggered by the incoming electron pulse [159]. It is advisable to keep the temporal width of the electron pulse shorter than the decay time of the absorption spectra of the transient species at a fixed wavelength, preferably the absorption maxima. Synthesis of zerovalent metal atoms and their clusters using the pulse radiolytic technique is most important for fundamental research, basically to understand the reaction mechanism. The cost of production of NPs by the linear accelerator is very high and has limited applications.

Ag ions reduced by the hydrated electrons in ethylene glycol and glycerol medium using pulse radiolysis were investigated [160]. Ag_0 appeared both in ethylene glycol and glycerol at around 360 nm, after 1 to 1.5 μs of bombardment with the electron pulse. At longer times, i.e., beyond 4 μs, Ag_0 species was found to decay with the emergence of other cluster species of Ag such as Ag_2^+, which showed absorption at 310 nm. Prolonged irradiation with the electron pulse, resulted in the reduction of Ag ions by the hydrated electrons leading to the development of Ag NPs that showed SPR band at 410 nm [160]. Interestingly, excited metal cluster species-mediated reduction of metal ions can also be implemented using pulse radiolysis. The study of electron transfer from Tl_2^+ species to Ag^+ is reported. Similarly, Au^{3+} ions when irradiated with hydrated electrons form Au_0 species, which comproportionates in presence of excess Au^{3+} to form monovalent and divalent species of Au [161]. This makes Au_0 difficult to detect by nanosecond pulse radiolysis. In $Au(CN)^{2-}$ systems, where comproportionation is comparatively difficult than $AuCl_4^{3-}$, due to stronger complexation by cyanide, Au_0 species could be isolated at absorption maxima of 410 nm [162].

13.2.3 Photochemical Synthesis

Photochemical synthesis of noble metals is generally implemented by irradiating metal ions in the presence of a light-sensitive electron-donating agent [163]. Ag ions have a high tendency of forming Ag NPs when exposed to visible light [164]. This resulted in AgBr being an active ingredient of camera films. It is also reported that the seeds of Ag NPs autocatalyzes the formation of particles [165]. Au NPs can also be synthesized photochemically by using a photosensitizer that would generate

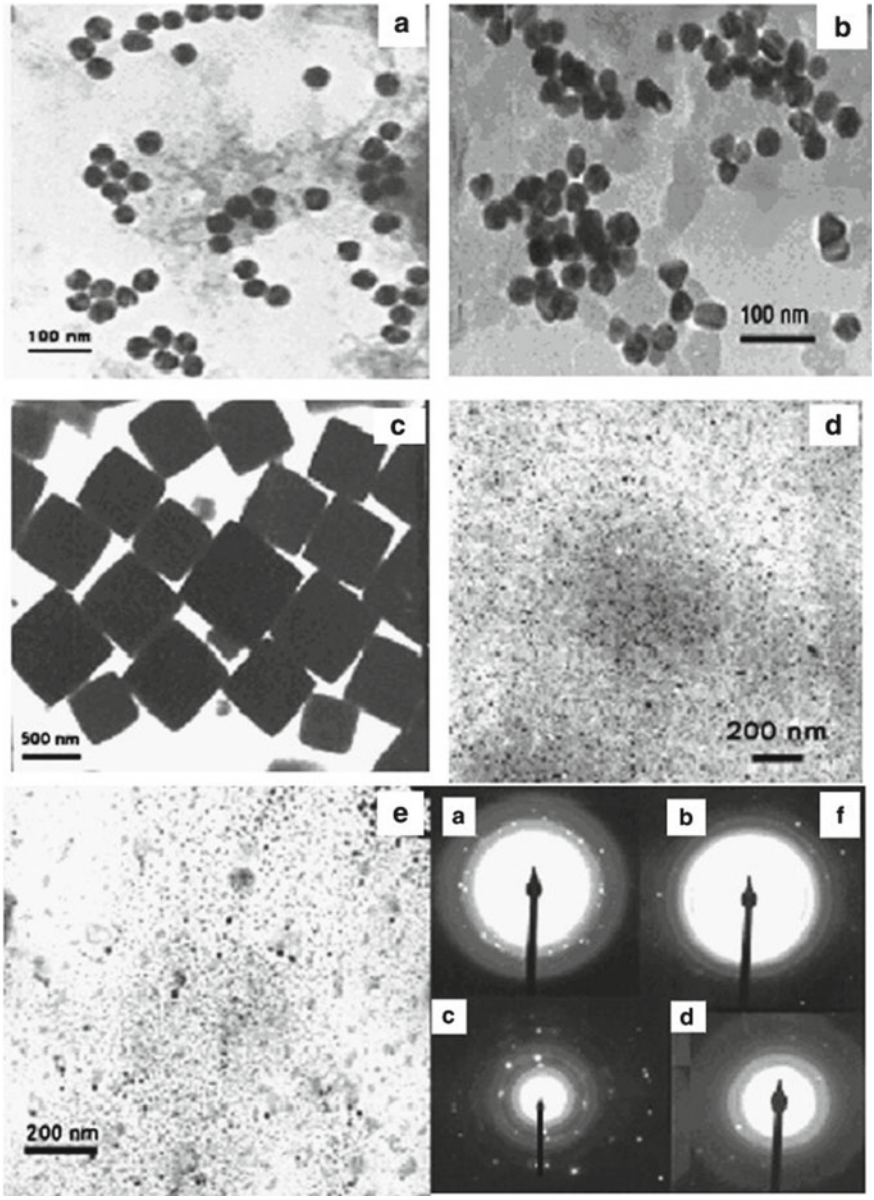

Fig. 13.31 TEM photographs of $[POM(SH_2)]^{4-}$ functionalized Au NPs acquired at different DMF/water ratios by γ-radiolysis **a** 3:1 **b** 2:1 and **c** 1:1 and by chemical reduction **d** 4:1 and **e** 1:1. **f** Electron diffraction patterns of the particles displayed in **a**-**d**. Reprinted with permission from Ref. [156] Copyright 2013 Elsevier

reducing radicals upon exposure to visible light [166]. Photochemical synthesis of Pt NPs is also known under UV irradiation [167].

Photochemical reduction of silver chloride in the presence of a dye is being pursued worldwide. AgCl NPs were partially reduced [168] by illumination under Xe Lamp, which led to the formation of Ag NPs decorated AgCl NPs. These Ag/AgCl NPs showed an excellent photocatalytic property. In another work, it was shown that blue-violet illumination of AgCl NPs led to the formation of Ag/AgCl NPs along with oxidative degradation of rhodamine 6G (R6G) [169]. There are other possible chemical methods [124, 170, 171] of synthesis of Ag/AgCl NPs apart from the above-mentioned photochemical methods [168]. Along with AgCl, TiO_2 has also been employed for the photoreduction of Ag^+ ions to Ag/AgCl@TiO_2 nanocomposite [172]. Ag NPs were found to be decorated on AgCl@TiO_2 support, as shown in Fig. 13.32. Ag NPs could be differentiated from AgCl by the interplanar distance of 111 plane of Ag as shown in Fig. 13.32.

Synthesis of Au NPs in the presence of ethylene glycol and PVP by photoreduction is also reported. A mechanism was suggested to describe the photoreduction, which claimed that light assisted in the excitation of Au^{3+} and reduction of Au^+ species [173]. The formation of Au NPs was monitored by the amplification in absorbance of the SPR band, which is shown in Fig. 13.33. Benzoquinone is a light-sensitive material that undergoes oxidation upon illumination by visible light [174] via a free radical mechanism. Such materials can act as photo-reduction agents for the preparation of Au NPs [175].

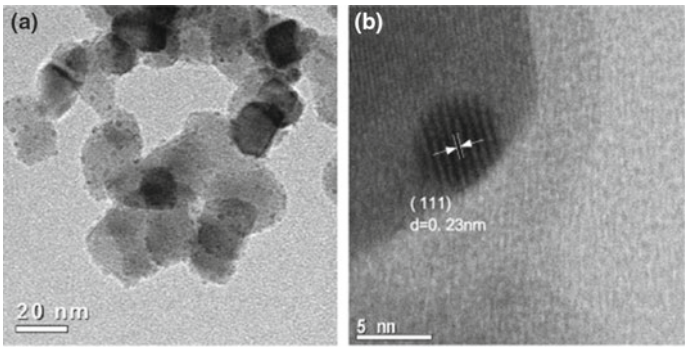

Fig. 13.32 TEM photograph of the synthesized Ag/AgCl@TiO_2-20 photocatalyst. Reprinted with permission from Ref. [172] Copyright 2012 Elsevier

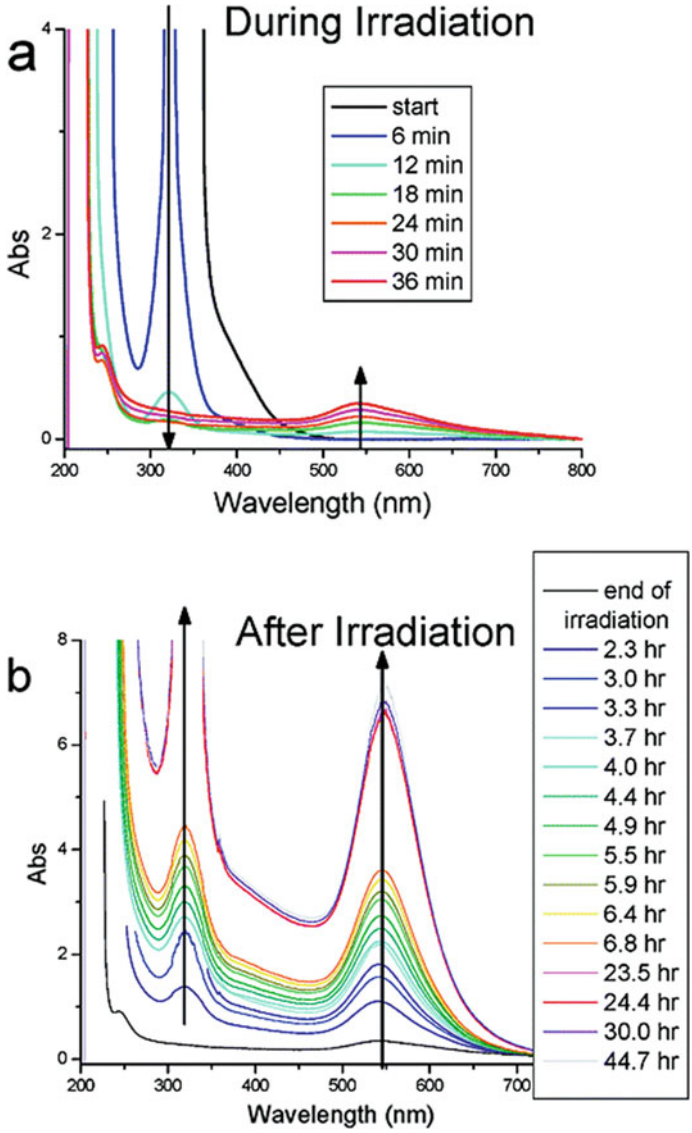

Fig. 13.33 **a** Optical absorption spectrum of the irradiated Au^{3+} solution through a xenon lamp with band-pass filters for different times. **b** Absorption spectrum of the samples at various intervals of time with interrupted irradiation. Growth of the NPs (545 nm) and Au^{3+} (323 nm) is observed. Both figures are from a sample containing $HAuCl_4$ (2.4 mM), PVP (0.01 M) and ethylene glycol (0.59 mol fraction). Reprinted with permission from Ref. [173] Copyright 2005 American Chemical Society

13.3 Applications of Functionalized Noble Metal Nanoparticles

Role of Plasmon in Colorimetry and SERS Applications

The unique SPR phenomenon in noble metal NPs is lately being implemented in different sensing studies. All these sensing applications are guided by inter-particle surface plasmon (SP) coupling [176]. Metal NPs exhibiting SPR are also called plasmonic NPs. Upon excitation of such plasmonic NPs by electromagnetic radiation of electric field E_0, an alternating electric field is produced in the neighbourhood of the surface of the particle, known as near field, E_{nf}, which decays with distance r away from the particle as $1/r^3$. When two plasmonic NPs are in close proximity to each other, each particle upon electromagnetic excitation experiences an electric field, E, which is a sum of E_0 and E_{nf} [177]. As a result, plasmons of both particles are coupled and a red-shifted coupled plasmon appears. This decrease in energy for plasmonic excitation can be ascribed to the amplification of the electric field at the junction of the particles. NPs are brought closer to each other by agglomeration [178]. Upon agglomeration, plasmonic NPs show a change in colour either due to plasmonic coupling [67] or due to charge transfer (CT) complex formation [179].

Colorimetric Sensing

The phenomenon of the appearance of a new plasmon band due to either agglomeration or CT is harnessed for colorimetric sensing applications. DNA recognition is one of the interesting applications of Au NPs-based colorimetric sensing [180]. Lately, a number of biologically important molecules such as heparin [181], melamine [182], methamphetamine [183], venlafaxine [184], etc. are detected using Au NPs as a probe. Similarly, Ag NPs are also used for the colorimetric detection of amoxicillin [185], hydrogen peroxide [186], etc.

Melamine is a compound that is rich in nitrogen (66%) and is often used as an adulterant in milk to enhance the protein content falsely in milk and dairy products [187]. Melamine is considered to be harmful if swallowed, inhaled or absorbed through the skin. The melamine-contaminated milk powder scandal occurred in China in the year 2008, where melamine adulteration was reported in infant formula. The presence of melamine in infant formula resulted in the formation of urinary stone in children leading to associated renal damage and increased child mortality. The methods (Kjeldahl and Dumas) used for the protein assessment in food samples actually evaluate the nitrogen content which is an indirect measure of the protein content. These methods are thus found to be unsuitable in distinguishing between the nitrogen of protein or non-protein source (melamine) [188, 189]. Therefore, detection of melamine in adulterated dairy products and food items by direct methods are essential.

A colorimetric detection protocol was developed in our laboratory to study the adulterant, melamine in real milk samples. This method of detection is inexpensive and has a fast response with a detection limit of 2 ppm, which is considered to be the safe limit for the adulterant. Here, firstly, colloidal Au NPs were prepared by the modified Turkevich procedure. Secondly, the adulterant, melamine was extracted from

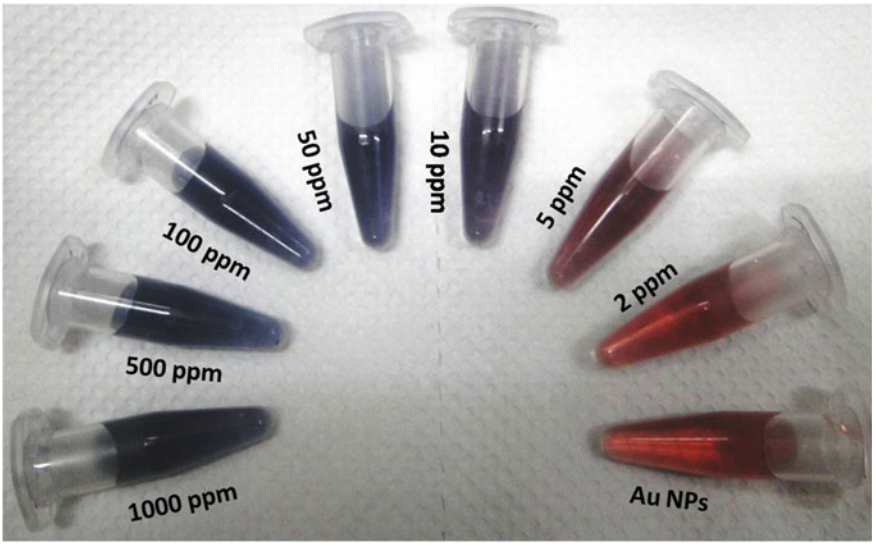

Fig. 13.34 Colour chart showing increasing concentrations of melamine added to Au NPs

powdered and liquid milk samples using the centrifugation method. The extracted melamine of different concentrations could be separated in the concentrate, which when added to colloidal Au NPs resulted in the transformation of colour from bright red to purple and finally to blue for high concentrations of melamine as shown in Fig. 13.34. The colour change observed in the case of Au NPs upon addition of melamine is possibly due to agglomeration of the particles caused by sorption of melamine on the surface of Au NPs leading to red shift in the SPR band (520 nm).

Plasmonic NPs-based colorimetric sensing can also be implemented on toxic heavy metal ions. Au nanoflowers (Au NFs) were synthesized at RT by mixing the requisite amount of NaOH (1 mM) with ethylene glycol. To this mixture, $HAuCl_4$ solution (0.5 mM) in the presence of PVP as stabilizer (0.1% w/v) was added [190]. The appearance of different colours as a function of time showed the development of stable dispersions of Au NPs. Synthesized Au NFs suspensions in ethylene glycol were violet in colour and demonstrated an intense absorption peak with a maximum at 570 nm (Fig. 13.35) attributed to the SPR band. Synthesized Au NFs were utilized for the detection of heavy toxic metal ions, Hg(II) and Pb(II) in an aqueous solution by colorimetry. The colour, as well as absorption spectrum at various time intervals, was monitored for the colloidal solution of Au NFs with the addition of Hg(II) and Pb(II) over a dynamic range of 1–10 μM, respectively. The Au NFs had a response time that was dependent on the metal ions concentration.

Adding Hg(II) to the colloidal Au NFs solution did not change either the colour or the absorption spectrum, till the optimum concentration of Hg(II) was $\geq$ 1 μM. When the Hg(II) concentration was 1 μM, the Au NFs changed colour within 4 h from violet to magenta. With an increase in the Hg(II) concentration from 5 to 10 μM, the

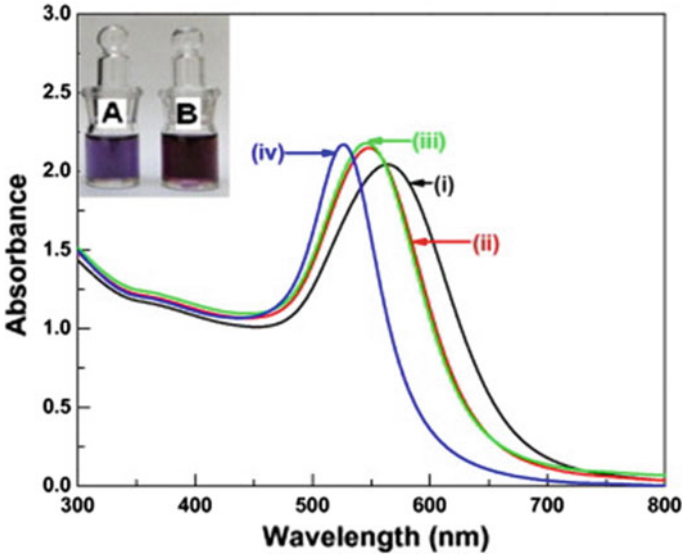

Fig. 13.35 Absorption spectrum of Au NFs with the addition of 10 μM Hg(II) ions at different times as per Ref. [190]. Inset displays the colour variation of colloidal Au NFs (**a**) before and (**b**) after the addition of Hg(II) ions. Reprinted with permission from Ref. [190] Copyright 2013 Elsevier

absorption spectrum gradually blue-shifted without much change in the absorbance. The colloidal dispersion changes colour within 30 min from violet to magenta and after 24 h to wine red (shown as an inset in Fig. 13.35). Similarly, for Pb(II) detection in colloidal Au NFs, varying concentrations of Pb(II) was added. In the presence of 10 μM Pb(II), the absorption spectrum underwent blue shifting with a decrease in its absorbance as shown in Fig. 13.36.

The detection procedure was also checked for other metal ions [Co(II), Cd(II), Cu(II), Mn(II), Zn(II), Na(I), Fe(II) and Fe(III)] of environmental relevance. The Hg(II), Pb(II) and other metal ions concentrations were fixed at 1 μM. Variation in the SPR band of the Au NFs with the metal ions addition was studied. From Fig. 13.37, it is observed that adding the metal ions of concentration about 10 μM [Co(II), Cd(II), Cu(II), Mn(II), Zn(II), Na(I), Fe(II), Fe(III)] to the Au NFs has a negligible effect on its SPR band. The feasibility of this method of detecting heavy metal ions, Hg(II) and Pb(II), at high concentration was established in real water samples.

SERS Applications

Electromagnetic (EM) radiation in the visible range can undergo scattering upon interaction with materials or substances, either by losing or gaining energy. EM radiations are transverse waves consisting of mutually perpendicular, propagating magnetic and electric fields [191]. The electric field component of EM radiation perturbs the electron charge cloud in a molecular or atomic orbital. An electronic

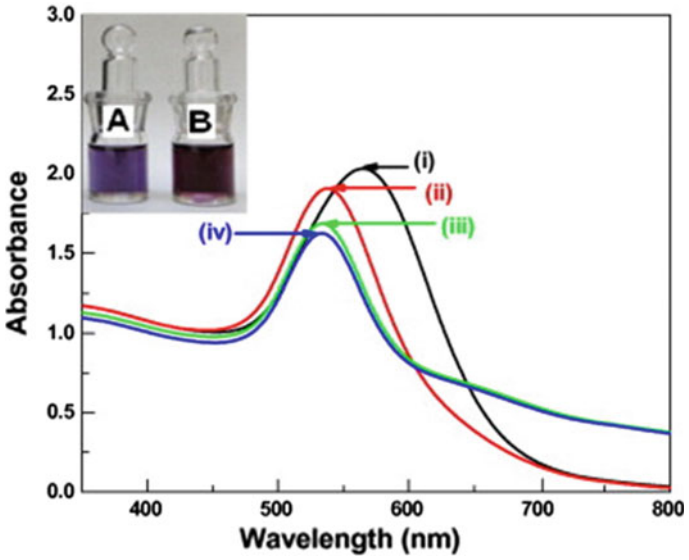

Fig. 13.36 Variation in the absorption spectrum of Au NFs with the addition of 10 μM Pb(II) ions at different times as per Ref. [190]. Inset displays the colour variation in the **a** absence and **b** presence of Pb(II) ions. Reprinted with permission from Ref. [190] Copyright 2013 Elsevier

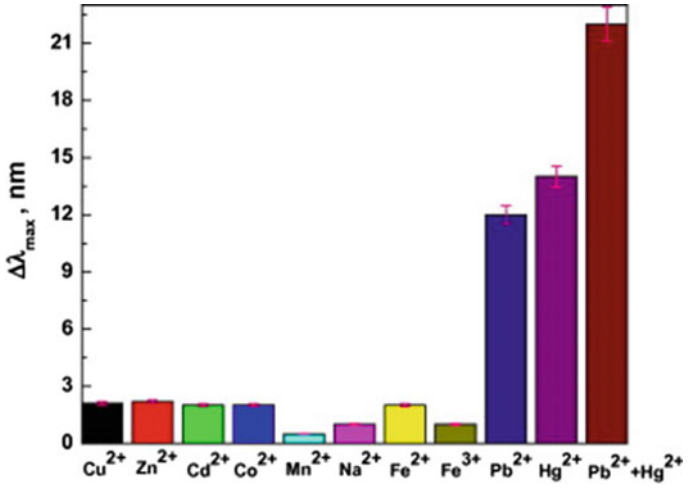

Fig. 13.37 Selectivity of the colloidal Au NFs for Pb(II) and Hg(II) ions relative to other metal ions. Each metal ion concentration was fixed at 1 μM. The time of incubation was 2 days. The standard deviations based on three sets of experiments are represented by the error bars. Reprinted with permission from Ref. [190] Copyright 2013 Elsevier

excitation to a higher state occurs when the contour of the distorted orbital geometrically matches the excited state with high energy. The above phenomenon leads to the observation of colour that can be monitored by UV–vis spectroscopy [192]. Another possibility is that the electric field may slightly polarize the electron charge cloud to form a transformed or altered orbital, which does not geometrically match the excited state orbital with higher energy. In such a scenario, no electronic transition occurs and the above mildly polarized transformed orbital is referred to as a virtual state that instantaneously releases the absorbed energy. This phenomenon is referred to as "scattering". Whenever the energy of the scattered radiation matches that of the incident radiation, the phenomenon is referred to as "Rayleigh scattering" [193]. Raman scattering is observed when the scattered radiation is of either higher or lower energy than the incident radiation [194]. The vibrational modes of a molecule in the ground electronic state are shown as Raman lines (Fig. 13.38).

Raman spectroscopy and infrared absorption spectroscopy [195] are complementary to each other. The low scattering cross-section (~10^{-30} cm^2) of the Raman technique [194] leads to the observation of Raman signal only in solid samples or highly concentrated solutions($\geq 10^{-2}$ M). Surface plasmons (SPs) assist in the improvement of the Raman signal of low concentrations of analyte adsorbed on plasmonic NPs by working as a confined excitation source of adsorbed molecules [196, 197]. An SP upon illumination behaves as an oscillating electric field similar to an electromagnetic radiation source. As a result, any molecule present on the surface of plasmonic NPs may get excited to a virtual state (polarized) by the SP. The radiation emitted by the excited adsorbed molecules can be seen in the far-field as Raman signal with

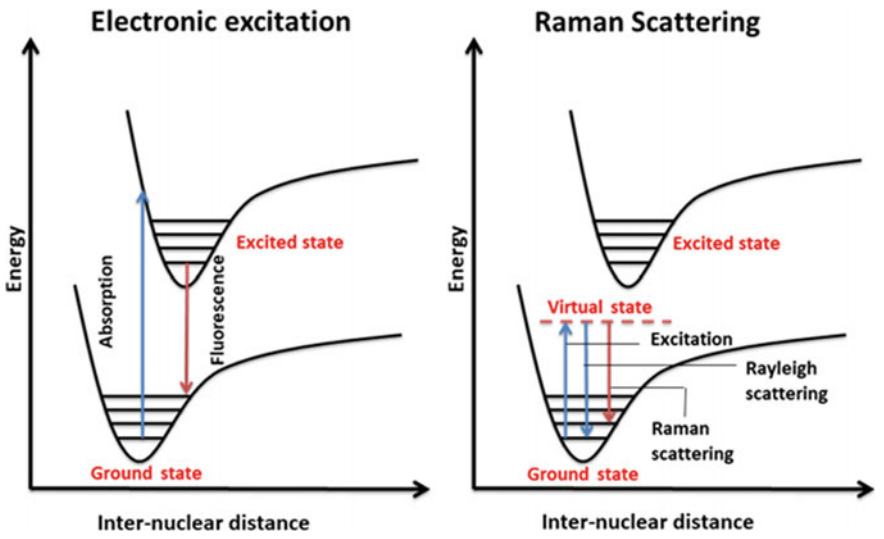

Fig. 13.38 Schematic illustration showing the phenomenon of electronic excitation and Raman scattering

signatures of metal–molecule interaction. This phenomenon of observation of vibrational bands of molecules adsorbed on plasmonic NPs is known as surface-enhanced Raman scattering (SERS) [135, 198–219]. Using this method very low sensing limit ($\leq \mu$M concentrations) can be attained [198, 215].

Apart from the determination of the concentration of analyte, the SERS technique is also being used for the determination of the orientation of analyte molecule on the metal NPs substrate [204, 211, 220]. The catalytic oxidation of 3-hydroxy anthranilic acid (HAA) on the surface of colloidal Ag NPs was investigated using time-dependent (TD) optical absorption (OA) spectroscopy and TDSERS [221]. In this study, the available thermal energy at room temperature alone was sufficient for the oxidation reaction. No external activation such as laser light source or heat was necessary for the catalytic oxidation reaction. HAA, a tryptophan aminophenol metabolite, is known for its anti-inflammatory and neuroprotective activity [222]. HAA is capable of undergoing intramolecular hydrogen bonding owing to the existence of carboxylic, hydroxyl and amino groups at ortho positions. The catalytic oxidation reaction of HAA to its azo-derivative on the surface of colloidal Ag NPs was monitored with time using the TDSERS and TDOA techniques.

The normal Raman spectrum of solid HAA is given in Fig. 13.39a. The calculated Raman vibrations of HAA [221] using B3LYP functional and aug-cc-pvdz basis set was used to assign the Raman bands of HAA solid. The Raman spectrum showed four strong bands at 1346, 1299, 783 and 627 cm^{-1} (Fig. 13.39a) that are ascribed to C-CO_2 stretch (str), C-NH_2 str, ring breathing and ring bending, respectively. Raman bands of medium intensity are seen at 457, 505, 1073, 1176, 1414 and 1551 cm^{-1}. These bands are ascribed to NH_2 rock, ph ring bend, ph CH bend, ph OH bend, ph C=C str and NH_2 scissoring (sci), respectively. Raman bands with low intensity are also seen at 588, 821, 908, 1010, 1098, 1222, 1619 and 1652 cm^{-1} that are assigned to ph OH bend, ph ring distortion, ph ring bend, ph CH twisting, ph CH bend, C–OH str, NH_2 sci and C=O str, respectively. Due to the poor solubility of HAA in water, its Raman spectrum could not be recorded in aqueous solution.

Immediately after adding HAA to Ag NPs colloidal solution, the SERS spectrum was recorded, which is shown in Fig. 13.39a. It is to be noted from the figure that the above SERS spectrum resembled the neat solid spectrum. The SERS spectrum of HAA (100 μM) was recorded with 514 nm excitation. The spectrum was found to evolve with time and is given in Fig. 13.39a. As seen from the figure, new peaks started appearing with time at 1487, 1444 and 1392 cm^{-1}. The intense peak seen at 1392 cm^{-1} is attributed to the symmetric (sym) CO_2^- str, which is known to appear when the analyte binds to the surface of the metal NPs through the carboxylate group [135, 203, 209]. The peaks at 1444 and 1487 cm^{-1} are found to grow steadily with time as shown in Fig. 13.39a. The peak at 1618 cm^{-1} (NH_2 sci mode) is found to disappear with time along with the simultaneous development of the intense peaks at 1487 and 1444 cm^{-1}. The gradual decrease of NH_2 sci vibration indicates that HAA undergoes a structural change to form an azo-derivative, which is evident from the emergence of two new peaks at 1487 and 1444 cm^{-1}, assigned to the ph C=C str in combination with N=N str (trans) and N=N str for the trans isomer, respectively. Apart from the above bands, the TDSERS spectrum also showed the formation and

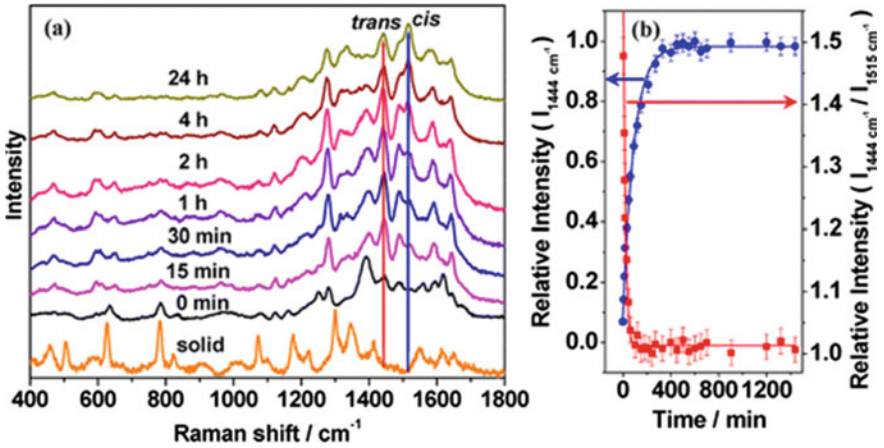

Fig. 13.39 **a** TDSERS spectra of HAA (100 μM) and **b** intensity increase of the 1444 cm^{-1} band attributed to N = N str mode of the trans azo derivative as a function of time and intensity decay of the 1444 cm^{-1} band relative to the 1515 cm^{-1} peak (cis N = N str) as a function of time (displaying error bar of 10%) (Reprinted with permission from Ref. [221] Copyright 2014 American Chemical Society)

development of the peaks at 1644, 1594 and 1276 cm^{-1} that are attributed to the ph C=C str, C=O str and C–N = N bend, respectively. The gradual increase in the Raman intensity at 592 and 1515 cm^{-1} assigned to the C–N = N–C torsion and N=N str vibrations is observed within a period of 15 min of initiation of the catalytic reaction on the colloidal Ag NPs surface. These modes correspond to the cis azo derivative. The development of the 1444 cm^{-1} band of the trans azo derivative followed by its decay due to the isomerization to the cis azo derivative as a function of time is displayed in Fig. 13.39b. It may be assumed that the initial formation of the trans azo isomer remains bonded to the surface of colloidal Ag NPs by the carboxylate group. Upon gradual isomerization to the cis form, the analyte remains bonded to the Ag NPs surface via the azo (N=N) group and not via carboxylate thus, resulting in an increase in the Raman intensity at 1515 cm^{-1} and total diminishing of the peak at 1392 cm^{-1}. The catalytic oxidation of HAA on the surface of colloidal Ag NPs is found to be complete within a day (24 h), reaching an equilibrium between the cis and trans azo derivatives.

The catalytic oxidation of HAA on the surface of colloidal Ag NPs is also investigated by TDOA spectroscopy. The TDOA spectrum of colloidal Ag NPs (Fig. 13.40) displays an intense peak having a maximum at 388 nm owing to the (bulk-like) BLSPR band. Upon adding HAA (100 μM) to the Ag NPs, the absorbance of the BLSPR band at 388 nm band is found to decrease with a concurrent manifestation of a band at 555 nm. The emergence of the red-shifted band is ascribed to the (surface-like) [217, 223–225] SLSPR band. This peak is formed as a result of surface sorption of the analyte molecule (HAA) on colloidal Ag NPs. The new band appearing at 555 nm gradually gets further shifted to higher wavelengths with peaks

at 565, 575, and 590 nm and the emergence of a broadband as well as a shoulder at 367 and 451 nm, within 10–15 min. The broad feature and the shoulder at 367 and 451 nm is credited to the π–π* and n–π* transition that corresponds to the trans azo conformer. With an increase in time, the azo derivative (trans) gradually isomerizes to its cis conformer. The TDOA spectrum, which is recorded after a period of 24 h of the initiation of the catalytic oxidation reaction on the colloidal Ag NPs surface, shows two bands having maxima at 466 and 367 nm that are ascribed to the n–π* and π–π* transitions of the azo (cis) conformer. No further change in the absorbance is observed. Thus, it is evident that the isomerization reaction is complete within a day (24 h), thus attaining an equilibrium between the cis and trans azo derivatives. Moreover, a peak that is red-shifted with a maximum at 590 nm is also observed, which appears due to aggregated Ag NPs. The absorption spectrum of 100 μM HAA in aqueous solution is shown as an inset in Fig. 13.40. The figure shows two peaks having maxima at 332 and 294 nm that corresponds to the n–π* and π–π* transition of HAA. It can be concluded from the TDOA spectrum that the activation energy for the catalytic oxidation reaction (azo formation) on the colloidal Ag NPs surface is relatively low (<0.025 eV). This is due to the fact that the catalytic (oxidation) reaction of HAA on the Ag NPs surface to the azo derivative (trans) and its isomerization reaction occurs at RT.

The catalytic oxidation of HAA on the colloidal Ag NPs surface to its trans azo derivative 2,2′-dihydroxy-6,6′-dicarboxylic-azobenzene (DHDCAB) and its successive isomerization to form the cis conformer is found to robustly depend on the prevailing external parameters, viz., pH (acidic/alkaline), temperature and

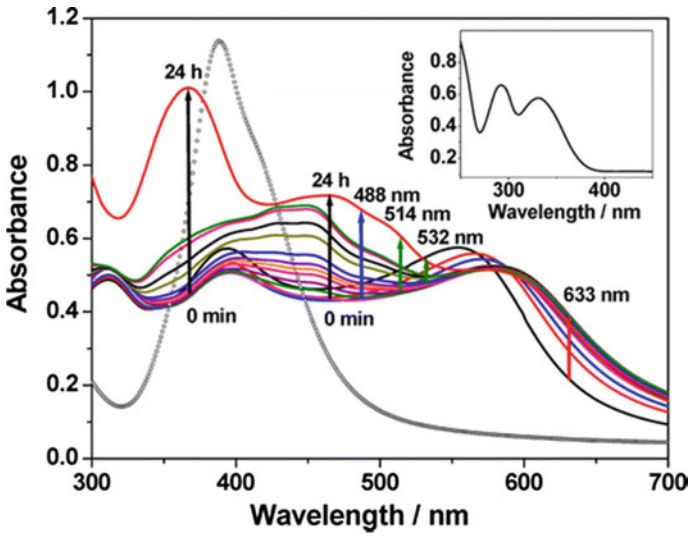

Fig. 13.40 TDOA spectrum of colloidal Ag NPs (○) and with the addition of HAA (100 μM). Inset displays the HAA (100 μM) absorption spectrum (Reprinted with permission from Ref. [221] Copyright 2014 American Chemical Society)

the surroundings (O_2, N_2, N_2O, etc.). The surface catalyzed oxidation and the isomerization reaction is summarized and shown in Scheme 13.3.

Selenourea (SeU) is an organoselenium diamide that is used for the production of selenium heterocycles, which show anti-inflammatory, anti-tumor and other medicinal properties. The oxygen and sulphur analogues of selenourea are less studied in comparison to their non-thiol counterparts, i.e. urea and thiourea, and relatively very few reports are available for SeU. The surface reactions and interaction of SeU with Ag and Au NPs are studied by the SERS technique [220]. It is observed that Au being soft compared to Ag exhibits a higher binding affinity for the soft Se atom than the N atom (borderline) of the amino (NH_2) group, whereas Ag shows a higher interaction affinity for the N atom. Raman and theoretical (DFT) results [220] indicate that SeU exists as the selenone conformer in neat solid and as selenol tautomer on colloidal Ag NPs surface. Both tautomeric forms, selenol and selenone, are simultaneously prevalent on colloidal Au NPs surface (Fig. 13.41).

Here, SeU is also used to form sandwich nanoassemblies within Au and Ag NPs. The SP-assisted SERS of Ag–SeU is found to be affected by the addition of Au NPs as shown in Fig. 13.42a. It is observed that gradually increasing the concentration of the Au NPs (12.5–50 μM), the SERS peaks at 1483 and 1655 cm^{-1} due to the CN str and NH_2 sci bands decrease in intensity and disappear totally upon addition of higher concentrations of Au NPs (100–250 μM). Moreover, the Ag–N str band appearing at 228 cm^{-1} steadily shifts to 239 cm^{-1} (shown as the shaded region in Fig. 13.42a. This alteration is possibly owing to the break in the Ag–N bond along with the creation of Au–Se. The SERS spectrum indicates a strong affinity of binding of the Au NPs

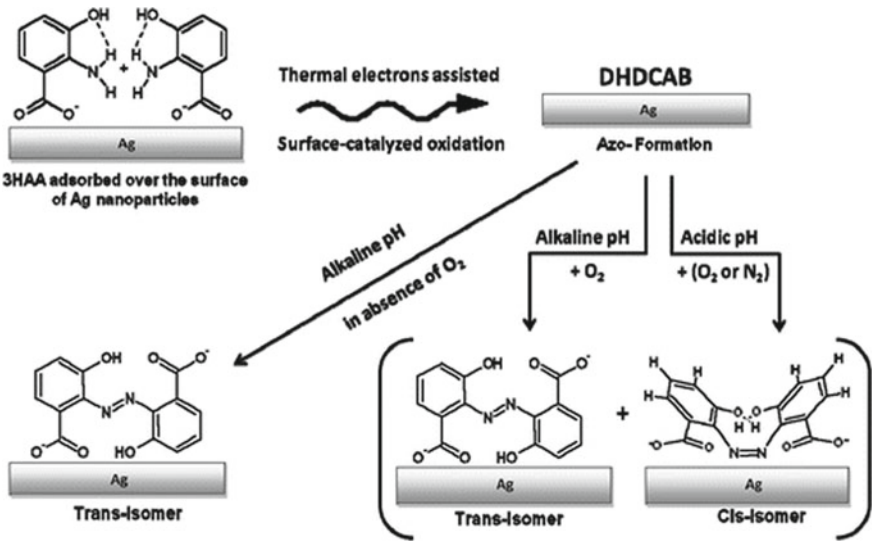

Scheme 13.3. Schematic representation of catalytic oxidation of HAA on the colloidal Ag NPs surface to form the trans azo derivative followed by its isomerization. (Reprinted with permission from Ref. [221] Copyright 2014 American Chemical Society.)

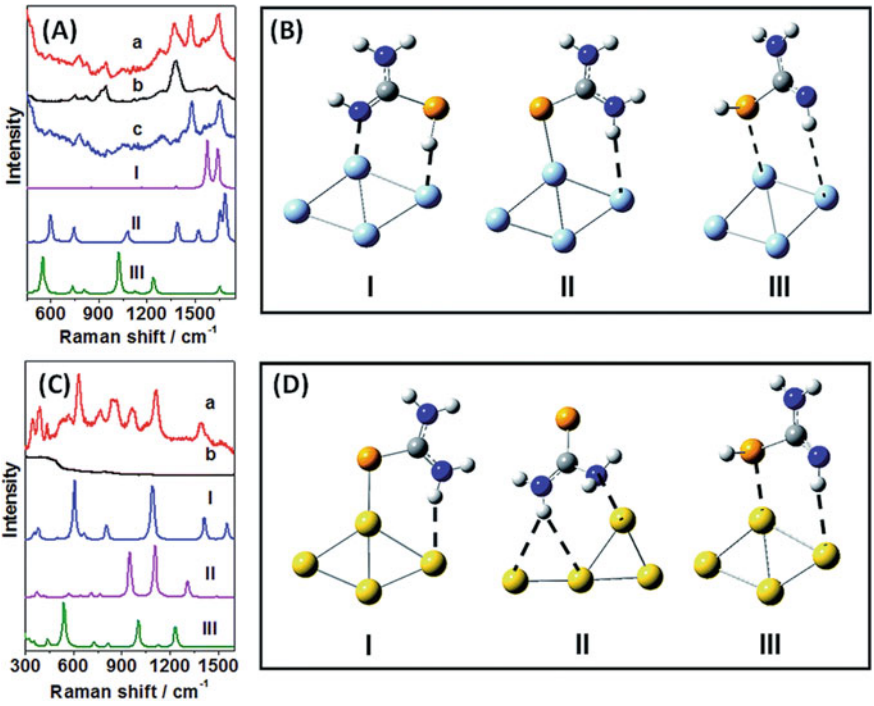

Fig. 13.41 **a** The SERS spectrum of **a** SeU bound to Ag, **b** colloidal Ag particles and **c** the subtracted (**a**, **b**) spectrum. Theoretically computed Raman spectrum of (I and III) selenol bound to Ag_4 and (II) selenone bound to Ag_4 and (**b**) the optimized structures. **c** The SERS spectrum of **a** SeU bound to Au and **b** colloidal Au particles. Computed Raman spectrum of (I and II) selenone bound to Au_4 and (III) selenol bound to Au_4 along with **d** the optimized structures. Reprinted with permission from Ref. [220] Copyright 2016 The Royal Society of Chemistry

towards the softer Se atom with the interaction being relatively stronger than the Ag NPs binding with the (borderline) N atom.

Addition of Ag NPs to Au–SeU is monitored by the SP-assisted SERS at 632 nm, which is shown in Fig. 13.42b. Upon gradual increase in the concentrations of Ag NPs (12.5–100 μM), the SERS band seen at 239 cm^{-1} (Au–Se str) and the bands at 346, 633, 966, 1112 (389), and 1395 cm^{-1} that are ascribed to N–C = Se bend, C = Se str, NH oop bend, NH_2 rock, and NCN bend, respectively, are found to gradually reduce in strength. These vibrations totally disappear upon adding 150 μM concentration of Ag NPs. The emergence of a weak band at 318 cm^{-1} is seen upon the addition of 50 μM concentration of Ag NPs. This band gradually gains intensity with an increase in the concentration of Ag NPs (shown as the shaded area in Fig. 13.42b). The above-mentioned vibration is assigned to the Se–Se str that emerges possibly owing to the catalytic oxidation of the selenol conformer to its diselenide on the surface of metal NPs. Even in literature, the Se–Se str mode of the diselenides [226] was observed at 290–330 cm^{-1} that is in consistent with our observations. The

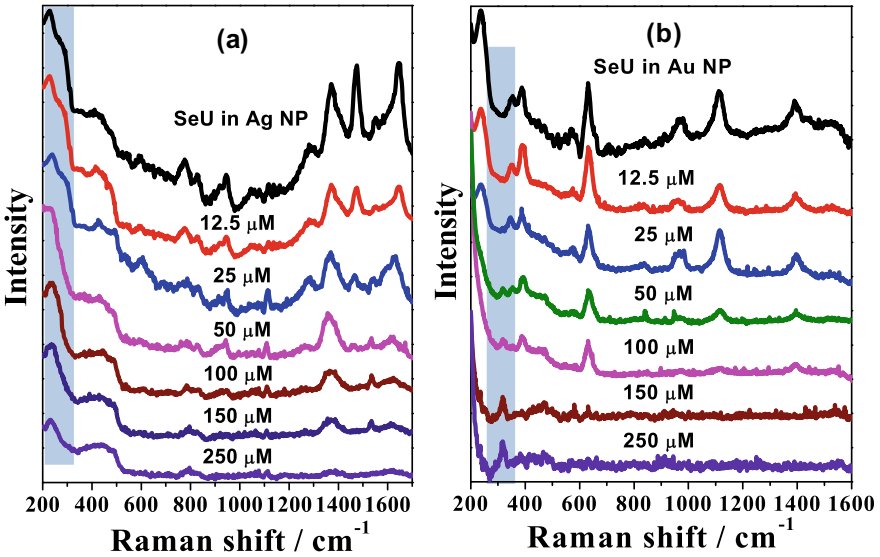

Fig. 13.42 The SERS spectrum of the nanoassemblies; **a** Ag–SeU–Au and **b** Au–SeU–Ag. Reprinted with permission from Ref. [220] Copyright 2016 The Royal Society of Chemistry

arrangement of the Ag–SeU–Au and Au–SeU–Ag nanoassemblies is schematically displayed in Fig. 13.43a and b. It is seen from the figure that on the colloidal Ag NPs surface, selenol tautomer is the major contributor, which on the addition of Au NPs leads to the arrangement of a sandwich Ag–SeU–Au nanoassembly. It is also seen from Fig. 13.43b that both the selenol and selenone conformers co-exists on the Au NPs surface, which upon Ag NPs addition leads to the diselenide formation as a result of catalytic oxidation of the selenol conformer.

Noble metal NPs immobilized in solid substrates can also be used for SERS-based sensing. Formamide-reduced Ag NPs deposited on glass substrates are used for SERS-based sensing of thioflavin T (TFT) [208]. Ca-Fe crosslinked Au NPs loaded alginate films are also used as SERS substrate [148]. It can be seen in Fig. 13.44 that upon reducing the concentration of crystal violet (CV) adsorbed on the Au NPs loaded alginate films, the SERS signal intensity decreases. The area under the peak at 1400 cm^{-1} is found to be proportional to the change in concentration of CV. This method is found to be successful in quantitative detection of CV in the range of concentration from 1 nM to 10 μM. The slight enhancement of overall SERS intensity from 10 to 1 μM CV can be ascribed to the formation of a monolayer on the Au NPs surface.

Hybrid Ag NPs such as Ag/AgCl NPs are found to show photocatalytic activity [168]. AgCl/Ag NPs formed by 0.03 M HCl solution due to the chlorination of Ag NPs is found to show light-induced surface reaction, which can be monitored by the SERS technique [124]. Sildenafil citrate (SC) is a renowned scheduled medicine used for treating erectile dysfunction [227]. SC exists in three known tautomeric forms that

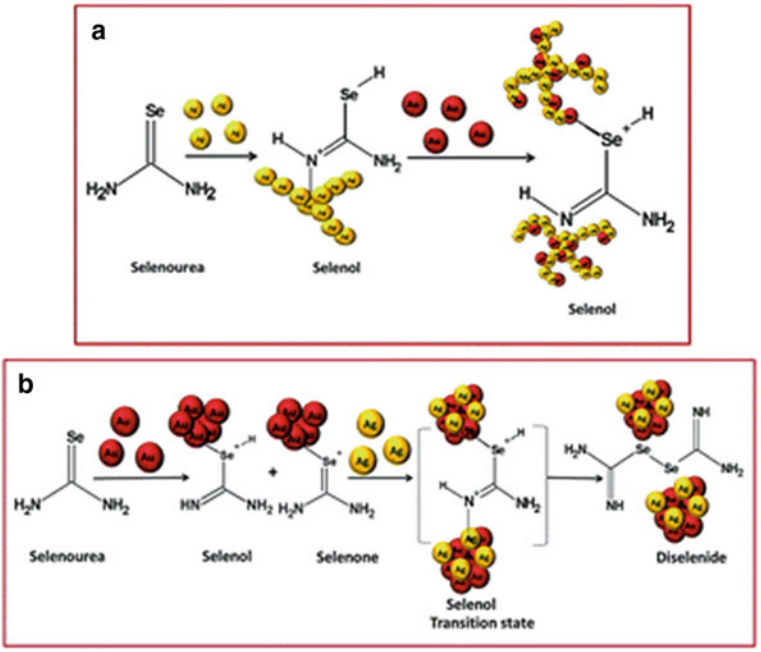

Fig. 13.43 Schematic illustration showing the creation of nanoassemblies; **a** Ag–SeU–Au and **b** Au–SeU–Ag. Reprinted with permission from Ref. [220] Copyright 2016 The Royal Society of Chemistry

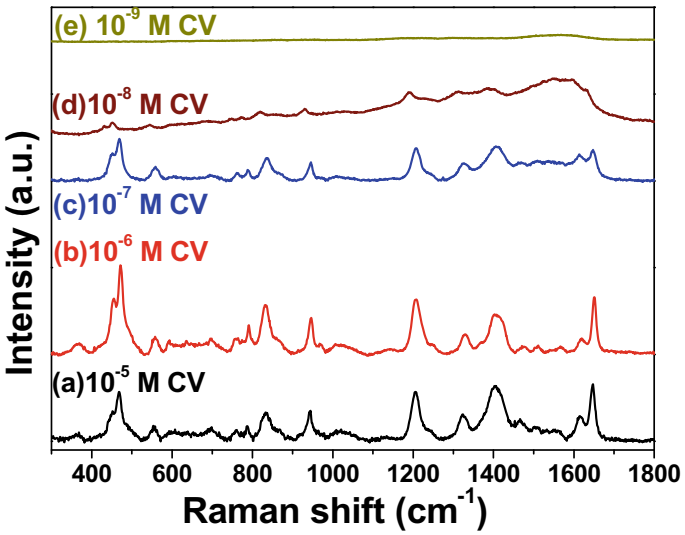

Fig. 13.44 SERS spectrum of varying CV concentrations (1 nM to 10 μM) adsorbed on Au NPs loaded crosslinked alginate film

are named 6H-PPO, 4H-PPO and enol [124]. Theoretical calculations suggest that SC remains as 6H-PPO in solid, which is also confirmed from the Raman spectrum. Varying concentrations of SC adsorbed on borohydride-capped Ag NPs are studied by UV–vis absorption spectroscopy that suggests that AgCl/Ag formation is influenced by the sorption of SC on Ag NPs. Here, the chlorinating agent HCl is added after adding SC to the Ag NPs. In the presence of high SC concentration (100 μM), HCl could not effectively oxidize Ag NPs to AgCl due to efficient functionalization of Ag NPs by SC, whereas in the presence of a low SC concentration of ≤ 1 μM, HCl could easily chlorinate the Ag NPs, forming AgCl NPs adjacent to each Ag NPs. 1 μM SC chemisorbed on AgCl/Ag NPs showed completely different SERS spectrum at 514 and 632 nm excitation and is shown in Fig. 13.45. This variation in SERS spectra is not observed when 10^{-4} M SC is adsorbed on Ag NPs. This phenomenon is attributed to the light-induced reduction of SC, which occurs as a result of the expansion of plasmon from Ag NPs to the conduction band of AgCl NPs. The above phenomenon is further confirmed by the pulse radiolysis method and the time-dependent density functional theoretical calculations (TD-DFT).

Pt as well as Pd NPs, similar to Ag and Au NPs also exhibit SERS activities for detection of analytes. Pd nanoparticles grown on Au surface are reported to show SERS activity. The SERS activity is mainly due to the Pd overlayer [228]. The SERS activity of Pd NPs of different sizes is displayed in Fig. 13.46.

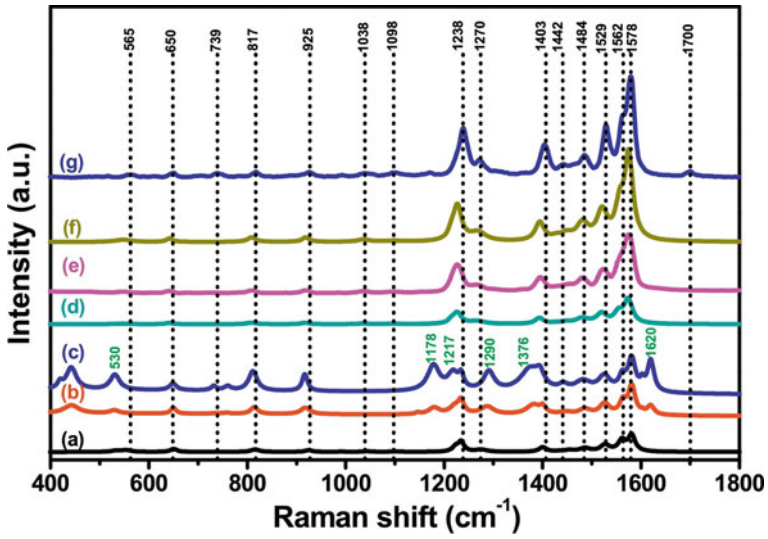

Fig. 13.45 Comparing the Raman/SERS spectrum of **a** 100 μM SC functionalized Ag NPs (SC-Ag) with λ_{ext}: 632 nm, **b** 10 μM SC-Ag with λ_{ext}: 632 nm, **c** 1 μM SC-Ag with λ_{ext}: 632 nm, **d** 100 μM SC-Ag with λ_{ext}: 514 nm, **e** 10 μM SC-Ag with λ_{ext}: 514 nm, **f** 1 μM SC-Ag with λ_{ext}: 514 nm, and **g** solid SC with λ_{ext}: 514 nm. Reprinted with permission from Ref. [124] Copyright 2019 Elsevier

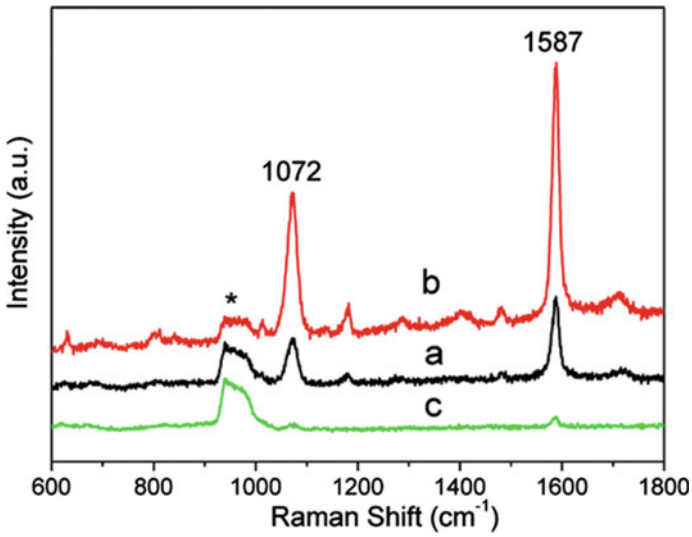

Fig. 13.46 SERS spectrum of 4-mercaptobenzoic acid chemisorbed on Pd NPs of sizes varying as **a** 110, **b** 62 and **c** 33 nm. The peak from the Si substrate is assigned "*". Reprinted with permission from Ref. [228] Copyright (2010) American Chemical Society

Structured substrates fabricated using Pt and Pd NPs showed SERS activity at 633 nm. Spherical voids on the metal surface are usually created that act as SERS hotspots. The fabrication is found to be quite reproducible [229]. Pd dendrites are also reported to show SERS activity [230].

Catalytic Activity

Multi-spiked Au NPs are synthesized at RT in ethylene glycol by controlling the pH with added NaOH without any external reducing agent [231]. These NPs with high monodispersity and a mean diameter of 75 ± 10 nm are obtained in good yield. The optical absorption spectrum of the multi-spiked Au NPs is tunable by the addition of PVP as a stabilizer. PVP addition enhances the stability of the particles. The catalytic activity of the PVP stabilized Au NPs is investigated to monitor the reduction reaction of o-nitro aniline. Here, the catalytic reduction reaction of o-nitro aniline to benzenediamine in the presence of $NaBH_4$ in excess is studied. The catalytic reaction rate is observed to be pseudo-first-order relative to the concentration of o-nitro aniline.

The addition of NaOH to the $HAuCl_4$ in ethylene glycol gradually changes the colour of the solution to deep violet from light yellow, indicating the development of Au NPs. The growth of the particles is monitored by recording the absorption spectrum as a function of time and is given in Fig. 13.47a. It is observed that the absorbance at λ_{max} reaches a maximum showing a high yield of the particles, which remain invariable with time, indicating that the $HAuCl_4$ are completely reduced. It is observed from the figure that the absorption band shows a time-dependent blue shift

along with the colour change to magenta and wine red gradually from bluish violet. The blue shift is possibly owing to the alteration in the contour or the adsorption characteristics of the stabilizer on the Au NPs surface. The shape or contour of the particles is characterized by TEM measurements. In Fig. 13.47b is shown the TEM image of the Au NPs taken after a day (24 h) of the initial reaction. The surface morphology of the particles shows a multi-spiked pattern both in the presence and absence of PVP. The particles were found to be stable for almost 3 months. The blue shift observed in the absorption band is attributed to the PVP chemisorbed on the Au NPs surface. The pattern seen in SAED confirmed the presence of multi-spiked Au NPs. Varying the Au^{3+} ions concentration (from 0.1 to 1 mM) and NaOH although changed the yield of the particles formed, but did not alter the SPR band of the particles.

The chemical reduction of nitro aniline with $NaBH_4$ without a catalyst is exceptionally sluggish. Hence, metal NPs were explored to study the catalytic reduction of nitro anilines. The reduction procedure of the nitro anilines can be effortlessly visualized with the discolouration of the yellow colour that is characteristic of the nitro aniline solution. In these experiments, the concentration of $NaBH_4$ is maintained higher than the concentration of nitro aniline, thereby treating the reduction reaction kinetics as pseudo-first-order relative to the concentration of nitro aniline. Moreover, excess amount of $NaBH_4$ accounts for the sluggish but noticeable reagent hydrolysis at pH 10. Here, the multi-spiked Au NPs prepared in ethylene glycol have been investigated for studying the catalytic reduction reaction. Since the concentration of Au NPs is maintained to be low in the reaction system, the o-nitro aniline absorption spectrum is not affected by the presence of Au NPs. The strong peaks that appear in the UV–vis absorption spectrum at 412 and 283 nm are characteristic of o-nitro aniline. In the absence of a catalyst, the spectrum reveals a very slow decrease in the absorbance of o-nitro aniline. However, adding Au NPs to the reaction mixture containing $NaBH_4$ in excess and o-nitro aniline, fast decay in the absorbance at 412 nm is observed. Furthermore, the gradual time-dependent red shift of the 283 nm peak to 289 nm indicated the steady formation of benzenediamine from o-nitro aniline as shown in Fig. 13.48a. The progress in the reduction reaction is investigated by recording the UV–vis absorption spectrum at various time intervals, t, with different Au NPs concentrations. It is observed that with the increase in the Au NPs concentration, the absorbance at 412 nm reduced steadily as shown in the inset of Fig. 13.48a. In Fig. 13.48b the reduction rate of o-nitro aniline is displayed. A reasonable linear correlation between $\ln(A_t/A_0)$ and time is observed (where A_t is the absorbance at different time intervals and A_0 is the absorbance at the initiation of the experiment), which indicates the reaction is pseudo-first-order. The observed rate constant (k_{obs}) can be directly approximated from the slope of the linear plots as given in the inset of Fig. 13.48b. The Au NPs catalyzed o-nitro aniline reduction reaction is elucidated by an electron relay mechanism [147, 232–234]. The metal surface catalyzes the transfer of electrons to the reactants from BH_4^- since the potential of the metals lies in between that of the electron acceptor (o-nitro aniline) and the electron donor (BH_4^-). The capture of the pre-solvated electrons by the Au NPs has also been explained using Cerenkov radiation [235]. The increase in the

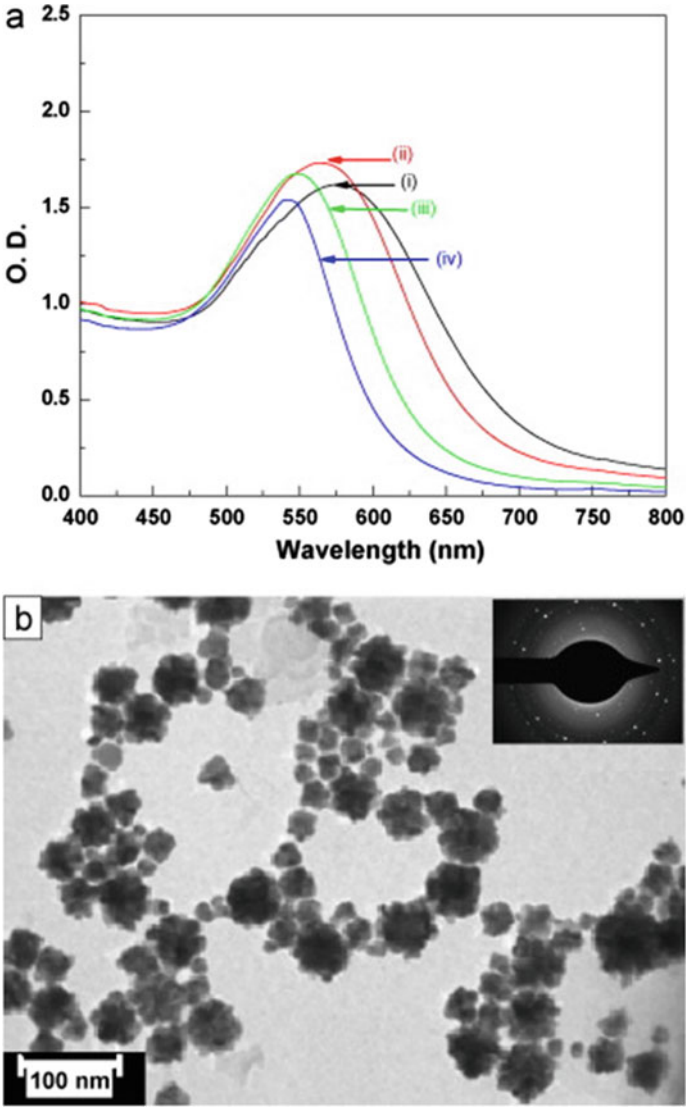

Fig. 13.47 **a** The time-dependent SPR band of Au NPs produced by mixing of $HAuCl_4$ (500 μM), NaOH (1 mM) and PVP (0.1% w/v) in ethylene glycol (neat) at time intervals of 3 min (i), 24 h (ii), 3 days (iii) and 17 days (iv). **b** TEM photograph of the multi-spiked Au NPs produced after 24 h of the initial reaction. Reprinted with permission from Ref. [231] Copyright 2012 Elsevier

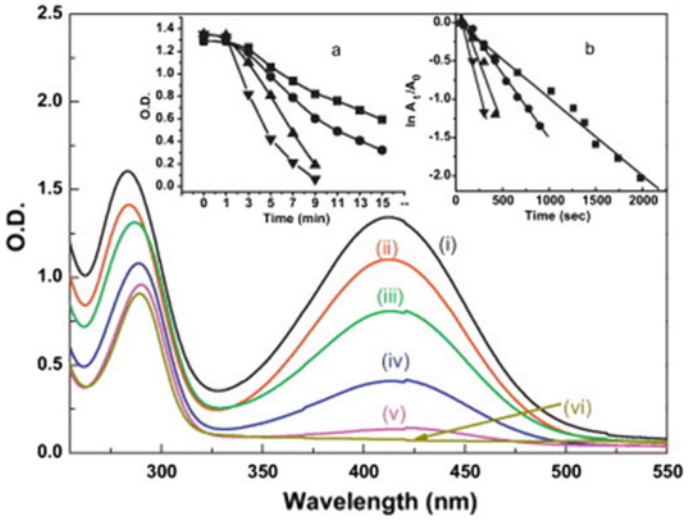

Fig. 13.48 The change in the optical absorption spectrum (time-dependent) of o-nitro aniline in the presence of $NaBH_4$ and 2.5 μg/mL Au NPs after (i) 1, (ii) 3, (iii) 5, (iv) 7, (v) 9 and (vi) 11 min. In the inset is shown **a** variation in the absorbance at 412 nm as a function of time and **b** the relative absorbance as a function of time (logarithmic plot). Reprinted with permission from Ref. [231] Copyright 2012 Elsevier

concentration of Au NPs from 1 to 2.7 μg/mL in the dispersion and maintaining all other parameters constant is found to amplify the reaction rate by a factor of 5.

The effect of ligands on the catalytic activity and its relationship with the surface coverage was also studied [98]. Ligands such as EDTA, HEDTA, TTHA, NTA and IDA are found to influence the available surface coverage of the Ag NPs.

Pt NPs show excellent promise in the field of heterogeneous catalysis. It is well known that Pt is used as a catalyst for the conversion of carbon monoxide to carbon dioxide. It is observed that Pt surface under realistic catalytic conditions, 300–538 K and 1–5 bar O_2, is prone to oxide formation [236]. This problem of oxide formation in Pt NPs can be easily averted. Pt NPs also play a vital role in various organic catalytic reactions such as hydrogenation [237], hydrosilylation [238], etc. Pd/PS nanocomposites are found to show the surface-assisted reduction of 4-nitro phenol by $NaBH_4$.

13.4 Conclusion and Future Prospects

During the past, new technologies in the field of nanoscience have prompted the development of new and improved materials necessary for biomedical applications with prime importance to diagnostics and therapy. Research is being undertaken for advancement in the areas of nanotechnology for developing nanocarriers for

drug delivery, photothermal treatment, cancer therapeutics, etc. where conventional methods lack specificity and do not efficiently discriminate between cancerous and normal cells. Moreover, nanoscale carriers for drug delivery offer great advantages, i.e. higher intracellular uptake over the conventional forms of drug delivery systems. Due to their miniature size, NPs can intermingle with the biomolecules both inside cells and at the surface, yielding targeted specificity for therapeutics and diagnostics. Designing novel nanocarriers that are conjugated with ligands such as antibodies may be favourable for targeted therapeutic strategy or drug delivery. Thus, a variety of NPs functionalized with diverse biomolecules are also being investigated for biomedical applications, viz., drug and gene delivery and silencing, radiotherapy, thermal ablation as well as imaging assays. Thus, the development of novel functionalized NPs for the above-mentioned biomedical applications is expected to revolutionize the field of targeted therapeutic strategy and treatment. However, during the process of designing these nanosized drug formulations for targeted therapy or drug delivery, a major concern regarding the short-term and long-term toxicity of these formulations should be addressed before these nanosized formulations are taken up for clinical trials.

Acknowledgements The authors thank Dr. A. K. Tyagi, Director, Chemistry Group, BARC and Dr. Awadhesh Kumar, Head, RPCD, BARC, for their kind encouragement and support.

References

1. Balcerzak M (2006) Noble metals, analytical chemistry of. In: Encyclopedia of analytical chemistry
2. Purcell TW, Peters JJ (1998) Sources of silver in the environment. Environ Toxicol Chem 17:539–546
3. Lottermoser BG (ed) (2007) Cyanidation wastes of gold-silver ores. In: Mine wastes: characterization, treatment, environmental impacts. Springer, Berlin, pp 183–199
4. "Plenty of room" revisited (2009) Nature nanotechnology 4:781
5. Luby Š, Lubyová M, Šiffalovič P, Jergel M, Majková E (2015) A brief history of nanoscience and foresight in nanotechnology. In: Bardosova M, Wagner T (eds) Nanomaterials and nanoarchitectures. Springer, Netherlands, Dordrecht, pp 63–86
6. Strehlow H, Milazzo G, Carioli S (1978) Tables of standard electrode potentials. Wiley, Chichester, New York (Brisbane, Toronto 1978. XVI + 419 Seiten. Preis: £ 17,50, Berichte der Bunsengesellschaft für physikalische Chemie, 82:1114–1114)
7. Kossoy A, Merk V, Simakov D, Leosson K, Kéna-Cohen S, Maier SA (2014) Optical and structural properties of ultra-thin gold films. Adv Opt Mater 3:71–77
8. Kolwas K, Derkachova A (2020) Impact of the interband transitions in gold and silver on the dynamics of propagating and localized surface plasmons. Nanomaterials (Basel) 10:1411
9. Jansen M (2008) The chemistry of gold as an anion. Chem Soc Rev 37:1826–1835
10. Lin J, Zhang S, Guan W, Yang G, Ma Y (2018) Gold with +4 and +6 oxidation states in AuF4 and AuF6. J Am Chem Soc 140:9545–9550
11. Preiß S, Förster C, Otto S, Bauer M, Müller P, Hinderberger D, Hashemi Haeri H, Carella L, Heinze K (2017) Structure and reactivity of a mononuclear gold(II) complex. Nat Chem 9:1249–1255

12. Rigoulet M, Massou S, Sosa Carrizo ED, Mallet-Ladeira S, Amgoune A, Miqueu K, Bourissou D (2019) Evidence for genuine hydrogen bonding in gold(I) complexes. Proc Natl Acad Sci 116:46
13. Palomar T, Ramírez Barat B, García E, Cano E (2016) A comparative study of cleaning methods for tarnished silver. J Cult Herit 17:20–26
14. William EM The Oxford handbook of greek and Roman Coinage. Oxford University Press
15. Notton JHF (1974) Ancient Egyptian gold refining. Gold Bull 7:50–56
16. Curtis HD (1911) Methods of silvering mirrors. Publ Astron Soc Pac 23:13–32
17. Benet WE, Lewis GS, Yang LZ, Hughes DEP (2011) The mechanism of the reaction of the Tollens reagent. J Chem Res 35:675–677
18. Hamilton JF (1973) The photographic process. Prog Solid State Chem 8:167–188
19. Bailar JC (1944) The oxidation states of silver. J Chem Educ 21:523
20. Pan K-Y, Chien C-H, Pu Y-C, Liu C-M, Hsu Y-J, Yeh J-W, Shih HC (2014) Studies on the annealing and antibacterial properties of the silver-embedded aluminum/silica nanospheres. Nanoscale Res Lett 9:307–307
21. Clement JL, Jarrett PS (1994) Antibacterial silver. Met Based Drugs 1:467–482
22. Xiao Z, Laplante AR (2004) Characterizing and recovering the platinum group minerals—a review. Miner Eng 17:961–979
23. Safarzadeh MS, Horton M, Van Rythoven AD (2018) Review of recovery of platinum group metals from copper leach residues and other resources. Miner Process Extr Metall Rev 39:1–17
24. Panda R, Jha MK, Pathak DD (2018) Commercial processes for the extraction of platinum group metals (PGMs). In: Kim H, Wesstrom B, Alam S, Ouchi T, Azimi G, Neelameggham NR, Wang S, Guan X (eds) Rare metal technology 2018. Springer International Publishing, Cham, pp 119–130
25. Liddell K, Newton T, Adams M, Muller B (2011) Energy consumption for Kell hydrometallurgical refining versus conventional pyrometallurgical smelting and refining of PGM concentrates. J South Afr Inst Min Metall 111:127–132
26. Hayes P (2003) Process principles in minerals and materials production. Publishing Co, Brisbane
27. Golunski SE (2007) Why use platinum in catalytic converters? Platinum Metals Rev 51:162
28. ĈErvenÝ L (1989) Palladium catalysts in hydrogenation reactions. Chem Eng Commun 83:31–63
29. Dreaden EC, Alkilany AM, Huang X, Murphy CJ, El-Sayed MA (2012) The golden age: gold nanoparticles for biomedicine. Chem Soc Rev 41:2740–2779
30. González AL, Noguez C, Beránek J, Barnard AS (2014) Size, shape, stability, and color of plasmonic silver nanoparticles. J Phys Chem C 118:9128–9136
31. Khodashenas B, Ghorbani HR (2019) Synthesis of silver nanoparticles with different shapes. Arab J Chem 12:1823–1838
32. Raza MA, Kanwal Z, Rauf A, Sabri AN, Riaz S, Naseem S (2016) Size-and shape-dependent antibacterial studies of silver nanoparticles synthesized by wet chemical routes. Nanomaterials (Basel) 6:74
33. Li J, Li JEJ, Zhang J, Wang X, Kawazoe N, Chen G (2016) Gold nanoparticle size and shape influence on osteogenesis of mesenchymal stem cells. Nanoscale 8:7992–8007
34. Wang S, Lu W, Tovmachenko O, Rai US, Yu H, Ray PC (2008) Challenge in understanding size and shape dependent toxicity of gold nanomaterials in human skin keratinocytes. Chem Phys Lett 463:145–149
35. Chen H, Kou X, Yang Z, Ni W, Wang J (2008) Shape-and size-dependent refractive index sensitivity of gold nanoparticles . Langmuir 24:5233–5237
36. Kelly KL, Coronado E, Zhao LL, Schatz GC (2003) The optical properties of metal nanoparticles: the influence of size, shape, and dielectric environment. J Phys Chem B 107:668–677
37. Grassian VH (2008) When size really matters: size-dependent properties and surface chemistry of metal and metal oxide nanoparticles in gas and liquid phase environments. J Phys Chem C 112:18303–18313

38. Cao S, Tao F, Tang Y, Li Y, Yu J (2016) Size- and shape-dependent catalytic performances of oxidation and reduction reactions on nanocatalysts. Chem Soc Rev 45:4747–4765
39. Conde J, Doria G, Baptista P (2012) Noble metal nanoparticles applications in cancer. J Drug Deliv 2012:751075–751075
40. Samanta A, Medintz IL (2016) Nanoparticles and DNA – a powerful and growing functional combination in bionanotechnology. Nanoscale 8:9037–9095
41. Mirabello V, Calatayud DG, Arrowsmith RL, Ge H, Pascu SI (2015) Metallic nanoparticles as synthetic building blocks for cancer diagnostics: from materials design to molecular imaging applications. J Mater Chem B 3:5657–5672
42. Pruneanu S, Coroş M, Pogacean F (2016) Bio-functionalized metallic nanoparticles with applications in medicine, pp 803–817
43. Astruc D (2020) Introduction: nanoparticles in catalysis. Chem Rev 120:461–463
44. Zhou Y, Jin C, Li Y, Shen W (2018) Dynamic behavior of metal nanoparticles for catalysis. Nano Today 20:101–120
45. Narayan N, Meiyazhagan A, Vajtai R (2019) Metal nanoparticles as green catalysts. Materials (Basel) 12:3602
46. Silva-De Hoyos LE, Sanchez-Mendieta V, Camacho-Lopez MA, Trujillo-Reyes J, Vilchis-Nestor AR (2020) Plasmonic and fluorescent sensors of metal ions in water based on biogenic gold nanoparticles. Arab J Chem 13:1975–1985
47. Deng W, Goldys EM (2014) Chemical sensing with nanoparticles as optical reporters: from noble metal nanoparticles to quantum dots and upconverting nanoparticles. Analyst 139:5321–5334
48. Hu P, Chen L, Kang X, Chen S (2016) Surface functionalization of metal nanoparticles by conjugated metal-ligand interfacial bonds: impacts on intraparticle charge transfer. Acc Chem Res 49:2251–2260
49. Ipe BI, Yoosaf K, Thomas KG (2006) Functionalized gold nanoparticles as phosphorescent nanomaterials and sensors. J Am Chem Soc 128:1907–1913
50. Paramasivam G, Kayambu N, Rabel AM, Sundramoorthy AK, Sundaramurthy A (2017) Anisotropic noble metal nanoparticles: Synthesis, surface functionalization and applications in biosensing, bioimaging, drug delivery and theranostics. Acta Biomater 49:45–65
51. Murphy CJ, Sau TK, Gole AM, Orendorff CJ, Gao J, Gou L, Hunyadi SE, Li T (2005) Anisotropic metal nanoparticles: synthesis, assembly, and optical applications. J Phys Chem B 109:13857–13870
52. Yang L, Zhou Z, Song J, Chen X (2019) Anisotropic nanomaterials for shape-dependent physicochemical and biomedical applications. Chem Soc Rev 48:5140–5176
53. Li N, Zhao P, Astruc D (2014) Anisotropic gold nanoparticles: synthesis, properties, applications, and toxicity. Angew Chem Int Ed 53:1756–1789
54. Jamkhande PG, Ghule NW, Bamer AH, Kalaskar MG (2019) Metal nanoparticles synthesis: an overview on methods of preparation, advantages and disadvantages, and applications. J Drug Deliv Sci Technol 53:101174
55. Dhand C, Dwivedi N, Loh XJ, Jie Ying AN, Verma NK, Beuerman RW, Lakshminarayanan R, Ramakrishna S (2015) Methods and strategies for the synthesis of diverse nanoparticles and their applications: a comprehensive overview. RSC Adv 5:105003–105037
56. Merkel TJ, Herlihy KP, Nunes J, Orgel RM, Rolland JP, DeSimone JM (2010) Scalable, shape-specific, top-down fabrication methods for the synthesis of engineered colloidal particles. Langmuir 26:13086–13096
57. Thanh NTK, Maclean N, Mahiddine S (2014) Mechanisms of nucleation and growth of nanoparticles in solution. Chem Rev 114:7610–7630
58. Lee SH, Jun B-H (2019) Silver nanoparticles: synthesis and application for nanomedicine. Int J Mol Sci 20:865
59. Yao Q, Yuan X, Fung V, Yu Y, Leong DT, Jiang D-E, Xie J (2017) Understanding seed-mediated growth of gold nanoclusters at molecular level. Nat Commun 8:927
60. Abedini A, Daud AR, Abdul Hamid MA, Kamil Othman N, Saion E (2013) A review on radiation-induced nucleation and growth of colloidal metallic nanoparticles. Nanoscale Res Lett 8:474

61. Gray DE (1957) American institute of physics handbook. McGraw-Hill Book Company Inc
62. Lee JD Concise inorganic chemistry, 5th edn. Wiley India
63. Pyykko P, Desclaux JP (1979) Relativity and the periodic system of elements. Acc Chem Res 12:276–281
64. Goldston RJ, Rutherford PH (2000) Introduction to plasma physics. Taylor & Frasis Group
65. Sanvitto D, Kéna-Cohen S (2016) The road towards polaritonic devices. Nat Mater 15:1061
66. Mie G (1908) Beiträge zur Optik trüber Medien, speziell kolloidaler Metallösungen. Ann Phys 330:377–445
67. Jain PK, El-Sayed MA (2010) Plasmonic coupling in noble metal nanostructures. Chem Phys Lett 487:153–164
68. Barchiesi D (2015) Lycurgus cup: inverse problem using photographs for characterization of matter. J Opt Soc Am A 32:1544–1555
69. Raddato C (2014) Lycurgus cup
70. Amendola V, Meneghetti M (2009) Size evaluation of gold nanoparticles by UV−vis spectroscopy. J Phys Chem C 113:4277–4285
71. Pérez-Juste J, Pastoriza-Santos I, Liz-Marzán LM, Mulvaney P (2005) Gold nanorods: synthesis, characterization and applications. Coord Chem Rev 249:1870–1901
72. Smith DJ (2015) Characterization of nanomaterials using transmission electron microscopy, nanocharacterisation, vol 2. The Royal Society of Chemistry, pp 1–29
73. Liu Y, Sun Y (2015) Electron beam induced evolution in Au, Ag, and interfaced heterogeneous Au/Ag nanoparticles. Nanoscale 7:13687–13693
74. Kikuchi J-i, Yasuhara K (2012) Transmission electron microscopy (TEM), supramolecular chemistry
75. Anuradha J, Abbasi T, Abbasi SA (2015) An eco-friendly method of synthesizing gold nanoparticles using an otherwise worthless weed pistia (Pistia stratiotes L.). J Adv Res 6:711–720
76. Darwich S, Mougin K, Rao A, Gnecco E, Jayaraman S, Haidara H (2011) Manipulation of gold colloidal nanoparticles with atomic force microscopy in dynamic mode: influence of particle-substrate chemistry and morphology, and of operating conditions. Beilstein J Nanotechnol 2:85–98
77. Jyoti K, Baunthiyal M, Singh A (2016) Characterization of silver nanoparticles synthesized using Urtica dioica Linn. leaves and their synergistic effects with antibiotics. J Radiat Res Appl Sci 9:217–227
78. Uppal MA, Kafizas A, Ewing MB, Parkin IP (2013) The room temperature formation of gold nanoparticles from the reaction of cyclohexanone and auric acid; a transition from dendritic particles to compact shapes and nanoplates. J Mater Chem A 1:7351–7359
79. Shah MA (2012) Growth of uniform nanoparticles of platinum by an economical approach at relatively low temperature. Scientia Iranica 19:964–966
80. Kayalvizhi T, Ravikumar S, Venkatachalam P (2016) Green synthesis of metallic silver nanoparticles using Curculigo orchioides rhizome extracts and evaluation of its antibacterial. Larvicidal Anticancer Act J Environ Eng 142:C4016002
81. Wang J, An C, Zhang M, Qin C, Ming X, Zhang Q (2012) Photochemical conversion of AgCl nanocubes to hybrid AgCl–Ag nanoparticles with high activity and long-term stability towards photocatalytic degradation of organic dyes. Can J Chem 90:858–864
82. Hall BD, Zanchet D, Ugarte D (2000) Estimating nanoparticle size from diffraction measurements. J Appl Crystallogr 33:1335–1341
83. Rasmussen MK, Pedersen JN, Marie R (2020) Size and surface charge characterization of nanoparticles with a salt gradient. Nat Commun 11:2337
84. Wang W, Ding X, Xu Q, Wang J, Wang L, Lou X (2016) Zeta-potential data reliability of gold nanoparticle biomolecular conjugates and its application in sensitive quantification of surface absorbed protein. Colloids Surf B 148:541–548
85. Wang A, Ng HP, Xu Y, Li Y, Zheng Y, Yu J, Han F, Peng F, Fu L (2014) Gold nanoparticles: synthesis, stability test, and application for the rice growth. J Nanomater 451232

86. Ivanov MR, Bednar HR, Haes AJ (2009) Investigations of the mechanism of gold nanoparticle stability and surface functionalization in capillary electrophoresis. ACS Nano 3:386–394
87. Lowry GV, Hill RJ, Harper S, Rawle AF, Hendren CO, Klaessig F, Nobbmann U, Sayre P, Rumble J (2016) Guidance to improve the scientific value of zeta-potential measurements in nanoEHS. Environ Sci Nano 3:953–965
88. Pfeiffer C, Rehbock C, Hühn D, Carrillo-Carrion C, de Aberasturi DJ, Merk V, Barcikowski S, Parak WJ (2014) Interaction of colloidal nanoparticles with their local environment: the (ionic) nanoenvironment around nanoparticles is different from bulk and determines the physico-chemical properties of the nanoparticles. J R Soc Interface 11:20130931
89. Stetefeld J, McKenna SA, Patel TR (2016) Dynamic light scattering: a practical guide and applications in biomedical sciences. Biophys Rev 8:409–427
90. Pecora R (2000) Dynamic light scattering measurement of nanometer particles in liquids. J Nanopart Res 2:123–131
91. Kapoor S (1998) Preparation, characterization, and surface modification of silver particles. Langmuir 14:1021–1025
92. Creighton JA, Blatchford CG, Albrecht MG (1979) Plasma resonance enhancement of Raman scattering by pyridine adsorbed on silver or gold sol particles of size comparable to the excitation wavelength. J Chem Soc, Faraday Trans 2: Mol Chem Phys 75:790–798
93. Gurusamy V, Krishnamoorthy R,. Gopal B, Veeraravagan V, Systematic NP (2017) investigation on hydrazine hydrate assisted reduction of silver nanoparticles and its antibacterial properties, Inorg Nano - Met Chem 47:761–767
94. Lee PC, Meisel D (1982) Adsorption and surface-enhanced Raman of dyes on silver and gold sols. J Phys Chem 86:3391–3395
95. Chadha R, Maiti N, Kapoor S (2014) Reduction and aggregation of silver ions in aqueous citrate solutions. Mater Sci Eng C 38:192–196
96. Leopold N, Lendl B (2003) A new method for fast preparation of highly surface-enhanced Raman scattering (SERS) active silver colloids at room temperature by reduction of silver nitrate with hydroxylamine hydrochloride. J Phys Chem B 107:5723–5727
97. Malassis L, Dreyfus R, Murphy RJ, Hough LA, Donnio B, Murray CB (2016) One-step green synthesis of gold and silver nanoparticles with ascorbic acid and their versatile surface post-functionalization. RSC Adv 6:33092–33100
98. Chadha R, Das A, Maiti N, Kapoor S (2014) Synthesis of silver nanoparticles: effects of anionic ligands on formation and catalytic activity. Mater Chem Phys 148:1124–1130
99. Sarkar A, Kapoor S, Mukherjee T (2005) Preparation, characterization, and surface modification of silver nanoparticles in formamide. J Phys Chem B 109:7698–7704
100. Sarkar A, Chadha R, Biswas N, Mukherjee T, Kapoor S (2009) Phase-transfer and film formation of silver nanoparticles. J Colloid Interface Sci 332:224–230
101. Pastoriza-Santos I, Liz-Marzán LM (2002) Formation of PVP-protected metal nanoparticles in DMF. Langmuir 18:2888–2894
102. Lei L, Song H, Zhao J, Yang Q, Chen Z (2019) Preparation of gold nanoparticles using pyridine-formaldehyde as a reducing agent and its application in high sensitivity colorimetric detection of Pb2+. Anal Methods 11:4362–4369
103. Jacob JA, Mahal HS, Biswas N, Mukherjee T, Kapoor S (2008) Role of phenol derivatives in the formation of silver nanoparticles. Langmuir 24:528–533
104. Jacob JA, Biswas N, Mukherjee T, Kapoor S (2011) Effect of plant-based phenol derivatives on the formation of Cu and Ag nanoparticles. Colloids Surf, B 87:49–53
105. Devi M, Devi S, Sharma V, Rana N, Bhatia RK, Bhatt AK (2020) Green synthesis of silver nanoparticles using methanolic fruit extract of Aegle marmelos and their antimicrobial potential against human bacterial pathogens. J Tradit Complement Med 10:158–165
106. Sudare T, Ueno T, Watthanaphanit A, Saito N (2015) Accelerated nanoparticles synthesis in alcohol–water-mixture-based solution plasma. Phys Chem Chem Phys 17:30255–30259
107. Liz-Marzán LM, Lado-Touriño I (1996) Reduction and stabilization of silver nanoparticles in ethanol by nonionic surfactants. Langmuir 12:3585–3589

108. Banihashemian SM, Hajghassem H, Nikfarjam A, Azizi Jarmoshti J, Abdul Rahman S, Boon Tong G (2019) Room temperature ethanol sensing by green synthesized silver nanoparticle decorated SWCNT. Mater Res Express 6:065602
109. Gordel M, Piela K, Kołkowski R, Koźlecki T, Buckle M, Samoć M (2015) End-to-end self-assembly of gold nanorods in isopropanol solution: experimental and theoretical studies. J Nanopart Res 17:477
110. Jacob JA, Kapoor S, Biswas N, Mukherjee T (2007) Size tunable synthesis of silver nanoparticles in water–ethylene glycol mixtures. Colloids Surf A 301:329–334
111. Gharibshahi L, Saion E, Gharibshahi E, Shaari AH, Matori KA (2017) Influence of Poly(vinylpyrrolidone) concentration on properties of silver nanoparticles manufactured by modified thermal treatment method. PLoS ONE 12:e0186094–e0186094
112. Kumar M, Devi P, Kumar A (2017) Structural analysis of PVP capped silver nanoparticles synthesized at room temperature for optical, electrical and gas sensing properties. J Mater Sci: Mater Electron 28:5014–5020
113. Mohamed EMA, Eisa WH, Abdel-Baset TA, Mahrous S (2017) Preparation and characterization of PEG-assisted growth of colloidal Ag nanoparticles. Int J Adv Sci Res 3:65–68
114. Shkilnyy A, Soucé M, Dubois P, Warmont F, Saboungi M-L, Chourpa I (2009) Poly(ethylene glycol)-stabilized silver nanoparticles for bioanalytical applications of SERS spectroscopy. Analyst 134:1868–1872
115. Ernest Ravindran RS, Subha V, Ilangovan R (2020) Silver nanoparticles blended PEG/PVA nanocomposites synthesis and characterization for food packaging. Arab J Chem 13:6056–6060
116. Baygazieva EK, Yesmurzayeva NN, Tatykhanova GS, Mun GA, Khutoryanskiy VV, Kudaibergenov SE (2014) Polymer protected gold nanoparticles: synthesis, characterization and application in catalysis. Int J Biol Chem 7(1)
117. Awad MA, Hendi AA, Ortashi KMO, Alanazi AB, Alzahrani BA, Soliman DA (2019) Greener synthesis, characterization, and antimicrobiological effects of helba silver nanoparticle-PMMA nanocomposite. Int J Polym Sci 2019:4379507
118. Bai J, Li Y, Du J, Wang S, Zheng J, Yang Q, Chen X (2007) One-pot synthesis of polyacrylamide-gold nanocomposite. Mater Chem Phys 106:412–415
119. Zhang W, Sun Y, Zhang L (2016) Fabrication of high efficient silver nanoparticle catalyst supported on poly (glycidyl methacrylate)–polyacrylamide. Ind Eng Chem Res 55:12398–12406
120. Tatarchuk VV, Dobrolyubova YO, Druzhinina IA, Zaikovskii VI, Gevko PN, Maksimovskii EA, Gromilov SA (2016) Facile synthesis of gold nanoparticles in aqueous acrylamide solution. Russ J Inorg Chem 61:535–543
121. Chen H, You T, Xu G, Gao Y, Zhang C, Yang N, Yin P (2018) Humidity-responsive nanocomposite of gold nanoparticles and polyacrylamide brushes grafted on Ag film: synthesis and application as plasmonic nanosensor. Sci China Mater 61:1201–1208
122. Song Y, Li Z, Wang L, Yao Y, Chen C, Cui K (2008) One-step preparation of hybrid materials of polyacrylamide networks and gold nanoparticles. Microsc Res Tech 71:409–412
123. Tyagi H, Kushwaha A, Kumar A, Aslam M (2016) A facile pH controlled citrate-based reduction method for gold nanoparticle synthesis at room temperature. Nanoscale Res Lett 11:362–362
124. Das A, Maiti N, Dhayagude AC, Pathak AK, Chadha R, Neogy S, Kapoor S (2019) A study of light induced surface reactions of sildenafil citrate on hybrid AgCl/Ag nanoparticle dimers by surface enhanced Raman scattering and pulse radiolysis techniques. Colloids Surfs A: Physicochem Eng Asp 582:123864
125. Nagao H, Ichiji M, Hirasawa I (2017) Synthesis of platinum nanoparticles by reductive crystallization using polyethyleneimine. Chem Eng Technol 40:1242–1246
126. Wu S, Zhu Z, Siepenkötter T, Guo X (2012) Platinum nanoparticles generated in spherical polyelectrolyte brushes and their high catalytic activity. Asia-Pac J Chem Eng 7:886–891

127. Salameh C, Bruma A, Malo S, Demirci UB, Miele P, Bernard S (2015) Monodisperse platinum nanoparticles supported on highly ordered mesoporous silicon nitride nanoblocks: superior catalytic activity for hydrogen generation from sodium borohydride. RSC Adv 5:58943–58951
128. Chen S, Kimura K (2001) Synthesis of thiolate-stabilized platinum nanoparticles in protolytic solvents as isolable colloids. J Phys Chem B 105:5397–5403
129. Li Y, Wu Z, Ye S (2015) Highly facile and efficient assembly of palladium nanoparticles on polystyrene microspheres and their application in catalysis. New J Chem 39:8108–8113
130. Wan Y, Guo Z, Jiang X, Fang K, Lu X, Zhang Y, Gu N (2013) Quasi-spherical silver nanoparticles: Aqueous synthesis and size control by the seed-mediated Lee-Meisel method. J Colloid Interface Sci 394:263–268
131. Kimling J, Maier M, Okenve B, Kotaidis V, Ballot H, Plech A (2006) Turkevich method for gold nanoparticle synthesis revisited. J Phys Chem B 110:15700–15707
132. Hou Z, Li M, Han M, Zeng J, Liao S (2014) Aqueous phase synthesis and characterizations of Pt nanoparticles by a modified citrate reduction method assisted by inorganic salt stabilization for PEMFCs. Electrochim Acta 134:187–192
133. Das A, Chadha R, Maiti N, Kapoor S (2015) Synthesis of pH sensitive gold nanoparticles for potential application in radiosensitization. Mater Sci Eng, C 55:34–41
134. Das A, Chadha R, Maiti N, Kapoor S (2014) Role of surfactant in the formation of gold nanoparticles in aqueous medium. J Nanoparticles 916429
135. Maiti N, Thomas S, Jacob JA, Chadha R, Mukherjee T, Kapoor S (2012) DFT and surface-enhanced Raman scattering study of tryptophan–silver complex. J Colloid Interface Sci 380:141–149
136. Maruyama T, Fujimoto Y, Maekawa T (2015) Synthesis of gold nanoparticles using various amino acids. J Colloid Interface Sci 447:254–257
137. Zaheer Z, Malik MA, Al-Nowaiser FM, Khan Z (2010) Preparation of silver nanoparticles using tryptophan and its formation mechanism. Colloids Surf, B 81:587–592
138. Lee H-E, Ahn H-Y, Mun J, Lee YY, Kim M, Cho NH, Chang K, Kim WS, Rho J, Nam KT (2018) Amino-acid- and peptide-directed synthesis of chiral plasmonic gold nanoparticles. Nature 556:360–365
139. Sarkar A, Kapoor S, Mukherjee T (2005) Synthesis of silver nanoprisms in formamide. J Colloid Interface Sci 287:496–500
140. Patel K, Kapoor S, Dave DP, Mukherjee T (2005) Synthesis of Pt, Pd, Pt/Ag and Pd/Ag nanoparticles by microwave-polyol method. J Chem Sci 117:311–316
141. Pastoriza-Santos I, Liz-Marzán LM (2002) Synthesis of silver nanoprisms in DMF. Nano Lett 2:903–905
142. Jin R, Cao Y, Mirkin CA, Kelly KL, Schatz GC, Zheng JG (2001) Photoinduced conversion of silver nanospheres to nanoprisms. Science 294:1901
143. Zhang Z, Yu J, Zhang J, Lian Y, Shi Z, Cheng Z, Gu M (2019) pH-controlled growth of triangular silver nanoprisms on a large scale. Nanoscale Adv 1:4904–4908
144. Zhang JH, Liu HY, Zhan P, Wang ZL, Ming NB (2007) Controlling the growth and assembly of silver nanoprisms. Adv Func Mater 17:1558–1566
145. Jiang D, Xie J, Chen M, Li D, Zhu J, Qin H (2011) Facile route to silver submicron-sized particles and their catalytic activity towards 4-nitrophenol reduction. J Alloy Compd 509:1975–1979
146. Dozol H, Mériguet G, Ancian B, Cabuil V, Xu H, Wang D, Abou-Hassan A (2013) On the synthesis of Au nanoparticles using EDTA as a reducing agent. J Phys Chem C 117:20958–20966
147. Liu J, Qin G, Raveendran P, Ikushima Y (2006) Facile "green" synthesis, characterization, and catalytic function of β-D-glucose-stabilized Au nanocrystals. Chem – Eur J 12:2131–2138
148. Himanshi AD, Chadha R, Maiti N, Neogy S, Kapoor S (2019) In-situ reduction of gold nanoparticles in alginate film matrix for application in surface enhanced Raman scattering. G P Glob Res J Chem 3:11–20

149. Rele M, Kapoor S, Mukherjee T (2002) Reduction, aggregation and physicochemical properties of silver nanoparticles in propan-2-ol:cyclohexane mixtures induced by a high energy electron beam. Mater Res Bull 37:2275–2283
150. Hegde S, Kapoor S, Joshi S, Mukherjee T (2006) Effect of ethylene glycol-bis(2-aminoethylether)-N, N, N′, N′-tetraacetic acid (EGTA) on the growth, stabilization and morphology of silver nanoparticles. Colloids Surf A 280:116–124
151. Belloni J, Mostafavi M, Remita H, Marignier J-L (1998) Marie-odile delcourt, radiation-induced synthesis of mono- and multi-metallic clusters and nanocolloids. New J Chem 22:1239–1255
152. Flores-Rojas GG, López-Saucedo F, Bucio E (2020) Gamma-irradiation applied in the synthesis of metallic and organic nanoparticles: a short review. Radiat Phys Chem 169:107962
153. Spinks JWT, Woods RJ (1990) An introduction to radiation chemistry. Wiley, United States
154. Dhayagude AC, Das A, Joshi SS, Kapoor S (2018) γ-Radiation induced synthesis of silver nanoparticles in aqueous poly (N-vinylpyrrolidone) solution. Colloids Surf A 556:148–156
155. Kuo CL, Hwang KC (2012) Nitrate Ion promoted formation of Ag nanowires in polyol processes: a new nanowire growth mechanism. Langmuir 28:3722–3729
156. Hegde S, Joshi S, Mukherjee T, Kapoor S (2013) Formation of gold nanoparticles via a thiol functionalized polyoxometalate. Mater Sci Eng C 33:2332–2337
157. Belloni J (1998) Contribution of radiation chemistry to the study of metal clusters. Radiat Res 150:S9–S20
158. Mulvaney P, Henglein A (1990) Long-lived nonmetallic silver clusters in aqueous solution: a pulse radiolysis study of their formation. J Phys Chem 94:4182–4188
159. Dorfman LM (1963) Pulse radiolysis: fast reaction studies in radiation chemistry. Science 141:493
160. Rele M, Kapoor S, Sharma G, Mukherjee T (2004) Reduction and aggregation of silver and thallium ions in viscous media. Phys Chem Chem Phys 6:590–595
161. Dey GR, El Omar AK, Jacob JA, Mostafavi M, Belloni J (2011) Mechanism of trivalent gold reduction and reactivity of transient divalent and monovalent gold ions studied by gamma and pulse radiolysis. J Phys Chem A 115:383–391
162. Ghosh-Mazumdar AS, Hart EJ (1968) A pulse radiolysis study of bivalent and zerovalent gold in aqueous solutions. Radiat Chemistry Am Chem Soc 193–209
163. Oster GK, Oster G (1959) Photoreduction of metal ions by visible light1. J Am Chem Soc 81:5543–5545
164. Król-Gracz A, Michalak E, Nowak PM, Dyonizy A (2011) Photo-induced chemical reduction of silver bromide to silver nanoparticles. Cent Eur J Chem 9:982
165. Sudeep PK, Kamat PV (2005) Photosensitized growth of silver nanoparticles under visible light irradiation: a mechanistic investigation. Chem Mater 17:5404–5410
166. McGilvray KL, Decan MR, Wang D, Scaiano JC (2006) Facile photochemical synthesis of unprotected aqueous gold nanoparticles. J Am Chem Soc 128:15980–15981
167. Luo X, Imae T (2007) Photochemical synthesis of crown-shaped platinum nanoparticles using aggregates of G4-NH2 PAMAM dendrimer as templates. J Mater Chem 17:567–571
168. Urakaev FK, Khan NV, Shalabaev ZS, Tatykaev BB, Nadirov RK, Burkitbaev MM (2020) Synthesis and photocatalytic properties of silver chloride/silver composite colloidal particles. Colloid J 82:76–80
169. Wang X, Liu X, Han Q, Guo P, Zhu J, Yin R (2020) Photo-assisted Ag/AgCl nanoparticle formation process can be used in the degradation of fluorescent dyes. Inorg Chem Commun 112:107716
170. Gawali P, Jadhav BL (2018) Synthesis of Ag/AgCl nanoparticles and their action on Human Serum albumin: a fluorescence study. Process Biochem 69:106–122
171. Devi TB, Ahmaruzzaman M, Begum S (2016) A rapid, facile and green synthesis of Ag@AgCl nanoparticles for the effective reduction of 2,4-dinitrophenyl hydrazine. New J Chem 40:1497–1506
172. Guo J-F, Ma B, Yin A, Fan K, Dai W-L (2012) Highly stable and efficient Ag/AgCl@TiO2 photocatalyst: Preparation, characterization, and application in the treatment of aqueous hazardous pollutants. J Hazard Mater 211–212:77–82

173. Eustis S, Hsu H-Y, El-Sayed MA (2005) Gold nanoparticle formation from photochemical reduction of Au3+ by continuous excitation in colloidal solutions. A Propos Mol Mech J Phys Chem B 109:4811–4815
174. Bruce JM (1967) Light-induced reactions of quinones. Q Rev Chem Soc 21:405–428
175. Ohara Y, Akazawa K, Shibata K, Hirota T, Kodama Y, Amemiya T, Wang JT (2020) Yamaguchi, Seed-mediated gold nanoparticle synthesis via photochemical reaction of benzoquinone. Colloids Surfs A: Physicochem Eng Asp 586:124209
176. Su KH, Wei QH, Zhang X, Mock JJ, Smith DR, Schultz S (2003) Interparticle coupling effects on plasmon resonances of nanogold particles. Nano Lett 3:1087–1090
177. Lal S, Grady NK, Goodrich GP, Halas NJ (2006) Profiling the near field of a plasmonic nanoparticle with Raman-based molecular rulers. Nano Lett 6:2338–2343
178. Zhu X, Zhang Q, Wang Y, Wei F (2016) Review on the nanoparticle fluidization science and technology. Chin J Chem Eng 24:9–22
179. Arenas JF, Woolley MS, Otero JC, Marcos JI (1996) Charge-transfer processes in surface-enhanced Raman scattering. Franck−condon active vibrations of pyrazine. J Phys Chem 100:3199–3206
180. Trantakis IA, Bolisetty S, Mezzenga R, Sturla SJ (2013) Reversible aggregation of DNA-decorated gold nanoparticles controlled by molecular recognition. Langmuir 29:10824–10830
181. Qu F, Liu Y, Lao H, Wang Y, You J (2017) Colorimetric detection of heparin with high sensitivity based on the aggregation of gold nanoparticles induced by polymer nanoparticles. New J Chem 41:10592–10597
182. Kumar N, Seth R, Kumar H (2014) Colorimetric detection of melamine in milk by citrate-stabilized gold nanoparticles. Anal Biochem 456:43–49
183. Yarbakht M, Nikkhah M (2016) Unmodified gold nanoparticles as a colorimetric probe for visual methamphetamine detection. J Exp Nanosci 11:593–601
184. Rawat KA, Basu H, Singhal RK, Kailasa SK (2015) Simultaneous colorimetric detection of four drugs in their pharmaceutical formulations using unmodified gold nanoparticles as a probe. RSC Adv 5:19924–19932
185. ul Ain N, Anis I, Ahmed F, Shah MR, Parveen S, Faizi S, Ahmed S (2018) Colorimetric detection of amoxicillin based on querecetagetin coated silver nanoparticles. Sens Actuators B: Chem 265:617–624
186. Zhang L, Li L (2016) Colorimetric detection of hydrogen peroxide using silver nanoparticles with three different morphologies. Anal Methods 8:6691–6695
187. Lin M (2009) A review of traditional and novel detection techniques for melamine and its analogues in foods and animal feed. Front Chem Eng China 3:427
188. Sun F, Ma W, Xu L, Zhu Y, Liu L, Peng C, Wang L, Kuang H, Xu C (2010) Analytical methods and recent developments in the detection of melamine. TrAC, Trends Anal Chem 29:1239–1249
189. Saint-Denis T, Goupy J (2004) Optimization of a nitrogen analyser based on the Dumas method. Anal Chim Acta 515:191–198
190. Nalawade P, Kapoor S (2013) Gold nanoflowers based colorimetric detection of Hg2+ and Pb2+ ions. Spectrochim Acta Part A Mol Biomol Spectrosc 116:132–135
191. Braeuer A (2015) Interaction of matter and electromagnetic radiation. In: Braeuer A (ed) Supercritical fluid science and technology. Elsevier, pp 41–192
192. Ultraviolet and visible absorption spectroscopy, characterization of materials
193. Xu R (2015) Light scattering: a review of particle characterization applications. Particuology 18:11–21
194. Bumbrah GS, Sharma RM (2016) Raman spectroscopy – Basic principle, instrumentation and selected applications for the characterization of drugs of abuse. Egypt J Forensic Sci 6:209–215
195. Berthomieu C, Hienerwadel R (2009) Fourier transform infrared (FTIR) spectroscopy. Photosynth Res 101:157–170
196. Schlücker S (2014) Surface-enhanced raman spectroscopy: concepts and chemical applications. Angew Chem Int Ed 53:4756–4795

197. Homola J, Yee SS, Gauglitz G (1999) Surface plasmon resonance sensors: review. Sens Actuators B Chem 54:3–15
198. Le Ru EC, Etchegoin PG (2012) Single-molecule surface-enhanced Raman spectroscopy. Annu Rev Phys Chem 63:65–87
199. Biswas N, Kapoor S, Mahal HS, Mukherjee T (2007) Adsorption of CGA on colloidal silver particles: DFT and SERS study. Chem Phys Lett 444:338–345
200. Biswas N, Thomas S, Sarkar A, Mukherjee T, Kapoor S (2009) Adsorption of methimazole on silver nanoparticles: FTIR, Raman, and surface-enhanced Raman scattering study aided by density functional theory. J Phys Chem C 113:7091–7100
201. Thomas S, Biswas N, Venkateswaran S, Kapoor S, Naumov S, Mukherjee T (2005) Studies on adsorption of 5-amino tetrazole on silver nanoparticles by SERS and DFT calculations. J Phys Chem A 109:9928–9934
202. Maiti N, Thomas S, Debnath A, Kapoor S (2016) Raman and XPS study on the interaction of taurine with silver nanoparticles. RSC Adv 6:56406–56411
203. Thomas S, Biswas N, Malkar VV, Mukherjee T, Kapoor S (2010) Studies on adsorption of carnosine on silver nanoparticles by SERS. Chem Phys Lett 491:59–64
204. Biswas N, Thomas S, Kapoor S, Mishra A, Wategaonkar S, Venkateswaran S, Mukherjee T (2006) Surface-enhanced resonance Raman scattering and density functional calculations of hemicyanine adsorbed on colloidal silver surface. J Phys Chem A 110:1805–1811
205. Biswas N, Thomas S, Sarkar A, Mukherjee T, Kapoor S (2009) Probing the adsorption mechanism in thiamazole bound to the silver surface with Surface-enhanced Raman Scattering and DFT. Chem Phys Lett 479:248–254
206. Biswas N, Thomas S, Kapoor S, Mishra A, Wategaonkar S, Mukherjee T (2008) Studies on adsorption of mono- and multi-chromophoric hemicyanine dyes on silver nanoparticles by surface-enhanced resonance Raman and theoretical calculations. J Chem Phys 129:184702
207. SenGupta S, Maiti N, Chadha R, Kapoor S (2014) Probing of different conformations of piperazine using Raman spectroscopy. Chem Phys 436–437:55–62
208. Maiti N, Chadha R, Das A, Kapoor S (2015) Adsorption and sub-nanomolar sensing of thioflavin T on colloidal gold nanoparticles, silver nanoparticles and silver-coated films studied using surface-enhanced Raman scattering. Spectrochim Acta Part A Mol Biomol Spectrosc 149:949–956
209. Thomas S, Maiti N, Mukherjee T, Kapoor S (2013) Investigation on the adsorption characteristics of anserine on the surface of colloidal silver nanoparticles. Spectrochim Acta Part A Mol Biomol Spectrosc 112:27–32
210. Chadha R, Maiti N, Kapoor S (2014) Interaction of anthranilic acid with silver nanoparticles: a Raman, surface-enhanced Raman scattering and density functional theoretical study. J Mol Struct 1076:35–41
211. Maiti N, Chadha R, Das A, Kapoor S (2016) Surface selective binding of 2,5-dimercapto-1,3,4-thiadiazole (DMTD) on silver and gold nanoparticles: a Raman and DFT study. RSC Adv 6:62529–62539
212. SenGupta S, Maiti N, Chadha R, Kapoor S (2015) Conformational analysis of morpholine studied using Raman spectroscopy and density functional theoretical calculations. Chem Phys Lett 639:1–6
213. Chadha R, Maiti N, Kapoor S (2013) Triplet and SERS study of crystal violet in presence of metal nanoparticles. Chem Phys Lett 579:68–72
214. Maiti N, Malkar VV, Mukherjee T, Kapoor S (2018) Investigating the interaction of aminopolycarboxylic acid (APCA) ligands with silver nanoparticles: a Raman, surface-enhanced Raman and density functional theoretical study. J Mol Struct 1156:592–601
215. Kumar N, Thomas S, Rao R, Maiti N, Kshirsagar RJ (2019) Surface-enhanced Raman scattering based sensing of trans-urocanic acid, an epidermal photoreceptor using silver nanoparticles aided by density functional theoretical calculations. J Raman Spectrosc 50:837–846
216. Kumar N, Thomas S, Rao R, Maiti N, Kshirsagar RJ (2019) Plasmon-induced dimerization of thiazolidine-2,4-dione on silver nanoparticles: revealed by surface-enhanced raman scattering study. J Phys Chem A 123:9770–9780

217. Chadha R, Das A, Kapoor S, Maiti N (2020) Surface-induced dimerization of 2-thiazoline-2-thiol on silver and gold nanoparticles: a surface enhanced Raman scattering (SERS) and density functional theoretical (DFT) study. J Mol Liq 114536
218. Dhayagude AC, Debnath AK, Joshi SS, Kapoor S, Maiti N (2020) Adsorption of l-selenomethionine and l-selenocystine on the surface of silver nanoparticles: a spectroscopic study. Nano Select (2020)
219. Mirajkar S, Dhayagude A, Maiti N, Suprasanna P, Kapoor S (2020) Distinguishing genomic DNA of Brassica juncea and Arabidopsis thaliana using surface-enhanced Raman scattering. J Raman Spectrosc 51:89–103
220. Dhayagude AC, Maiti N, Debnath AK, Joshi SS, Kapoor S (2016) Metal nanoparticle catalyzed charge rearrangement in selenourea probed by surface-enhanced Raman scattering. RSC Adv 6:17405–17414
221. Chadha R, Maiti N, Kapoor S (2014) Catalytic reactions on the surface of Ag nanoparticles: a photochemical effect and/or molecule property? J Phys Chem C 118:26227–26235
222. Krause D, Suh H-S, Tarassishin L, Cui QL, Durafourt BA, Choi N, Bauman A, Cosenza-Nashat M, Antel JP, Zhao M-L, Lee SC (2011) The Tryptophan metabolite 3-hydroxyanthranilic acid plays anti-inflammatory and neuroprotective roles during inflammation: role of hemeoxygenase-1. Am J Pathol 179:1360–1372
223. Le Ru EC, Galloway C, Etchegoin PG (2006) On the connection between optical absorption/extinction and SERS enhancements. Phys Chem Chem Phys 8:3083–3087
224. Das SK, Bhattacharya TS, Chowdhury J (2020) Deciphering the near-field response with the far-field wavelength-scanned SERS spectra of 4-mercaptopyridine adsorbed on gold nanocolloidal particles entrapped in Langmuir Reverse Schaefer film of 5CB liquid crystal molecules. Phys Chem Chem Phys 22:8719–8729
225. Dutta Roy S, Ghosh M, Chowdhury J (2018) near-field response on the far-field wavelength-scanned surface-enhanced raman spectroscopic study of methylene blue adsorbed on gold nanocolloidal particles. J Phys Chem C 122:10981–10991
226. Bandyopadhyay K, Vijayamohanan K, Venkataramanan M, Pradeep T (1999) Self-assembled monolayers of small aromatic disulfide and diselenide molecules on polycrystalline gold films: a comparative study of the geometrical constraint using temperature-dependent surface-enhanced Raman spectroscopy. X-Ray Photoelectron Spectrosc Electrochem Langmuir 15:5314–5322
227. Zhao H, Hasi W, Bao L, Han S, Sha X, Sun J, Lou X, Lin D, Lv Z (2017) Rapid detection of sildenafil drugs in liquid nutraceuticals based on surface-enhanced Raman spectroscopy technology. Chin J Chem 35:1522–1528
228. Chen H, Wei G, Ispas A, Hickey SG, Eychmüller A (2010) Synthesis of palladium nanoparticles and their applications for surface-enhanced raman scattering and electrocatalysis. J Phys Chem C 114:21976–21981
229. Abdelsalam ME, Mahajan S, Bartlett PN, Baumberg JJ, Russell AE (2007) SERS at structured palladium and platinum surfaces. J Am Chem Soc 129:7399–7406
230. Kannan P, Dolinska J, Maiyalagan T, Opallo M (2014) Facile and rapid synthesis of Pd nanodendrites for electrocatalysis and surface-enhanced Raman scattering applications. Nanoscale 6:11169–11176
231. Nalawade P, Mukherjee T, Kapoor S (2012) High-yield synthesis of multispiked gold nanoparticles: characterization and catalytic reactions. Colloids Surf, A 396:336–340
232. Hayakawa K, Yoshimura T, Esumi K (2003) Preparation of gold−dendrimer nanocomposites by laser irradiation and their catalytic reduction of 4-nitrophenol. Langmuir 19:5517–5521
233. Lu Y, Mei Y, Drechsler M, Ballauff M (2006) Thermosensitive Core-shell particles as carriers for Ag nanoparticles: modulating the catalytic activity by a phase transition in networks. Angew Chem Int Ed 45:813–816
234. Pradhan N, Pal A, Pal T (2001) Catalytic reduction of aromatic nitro compounds by coinage metal nanoparticles. Langmuir 17:1800–1802
235. Ghandi K, Wang F, Landry C, Mostafavi M (2018) Naked gold nanoparticles and hot electrons in water. Sci Rep 8:7258

236. van Spronsen MA, Frenken JWM, Groot IMN (2017) Observing the oxidation of platinum. Nat Commun 8:429
237. Rylander PN (1967) 18 - Carbocyclic aromatics. In: Rylander PN (ed) Catalytic hydrogenation over platinum metals. Academic Press, pp 309–330
238. Meister TK, Riener K, Gigler P, Stohrer J, Herrmann WA, Kühn FE (2016) Platinum catalysis revisited—unraveling principles of catalytic olefin hydrosilylation. ACS Catal 6:1274–1284

Chapter 14
Synthesis and Surface Functionalization of Nanostructured Biomaterials

Santosh L. Gawali, Bijaideep Dutta, Jagriti Gupta, P. A. Hassan, and K. C. Barick

Abstract Nanostructured biomaterials are finding their way into medicine, pharmaceutics and medical technology. Synthesis and processing parameters play a vital role in the creation of a biomaterial with the desired nanostructure. Especially in the development of nanostructured organic (polymers, hydrogel), inorganic (Au, SiO_2, ZnO, Fe_3O_4 and hydroxyapatite) as well as organic–inorganic hybrid biomaterials, the interface properties contribute decisively to the performance of the material. To achieve higher therapeutic efficacy, it is important to realize the relations of biomaterials with the biological structures (physical, chemical and biological characteristics). Thus, the designing of efficient modern biomaterials needs their surface to be modified with desired biocompatible molecules. Further, the conjugation of specific functional moieties on biomaterial surfaces offers stimuli-responsive shell that is vulnerable to exterior factors like pH, temperature and ionic strength. These surface-functionalized nanostructures act as smart carrier material for therapeutic agents such as drugs and biomolecules since they are small enough to evade their uptake by macrophage and offer enhanced absorption, retention and bioavailability of therapeutic agents. They can also be conjugated with receptors and imaging probes for cell-specific targeting as well as cellular imaging at the molecular level. In addition to therapeutic applications, these surface-functionalized biomaterials have tremendous applications in diagnosis, tissue engineering, and medical implants and devices.

Keywords Surface functionalization · Nanomaterials · Biomaterials · Therapeutics · Diagnostics · Tissue engineering · Device and implants

S. L. Gawali · B. Dutta · J. Gupta · P. A. Hassan · K. C. Barick (✉)
Chemistry Division, Bhabha Atomic Research Centre, Mumbai-400085, India
e-mail: kcbarick@barc.gov.in

S. L. Gawali · B. Dutta · P. A. Hassan · K. C. Barick
Homi Bhabha National Institute, Mumbai-400094, India

A. K. Tyagi and R. S. Ningthoujam (eds.), *Handbook on Synthesis Strategies for Advanced Materials*, Indian Institute of Metals Series,
https://doi.org/10.1007/978-981-16-1803-1_14

14.1 Introduction

Nanostructure is the structure with at least one of the dimensions in the nano-regime, usually from 1 to 100 nm. A variety of materials with nanostructures has been developed due to the rapid growth of nanoscience and nanotechnology. Generally, any material or a combination of materials irrespective of natural or synthetic having potential applications in the field of medicine, either therapeutic or diagnostic, are called biomaterials. These materials have the capacity of being in touch with biological mediums and tissues for extended periods of time without any adverse effect [1, 2]. In addition to the naturally occurring biomaterials, various organic (polymers, hydrogel), inorganic (metals, oxides and ceramics) and organic–inorganic hybrid biomaterials were developed by soft-chemical approaches. Among others, the development of biomaterials with nanostructure (nanostructured biomaterials, NBMs) is rapidly progressing as an integration of nanostructures into biomaterials not only provides exclusive chemical, physical and biological properties but also creates advanced materials that find promising applications in diagnosis, tissue engineering and drug delivery. Although NBMs have been used in many biomedical applications, the exact interaction between cells/tissue and NBMs is not so far clear.

The interaction of biomaterial with its environment is mainly determined by its surface chemistry and topography. The surface characteristics of NBMs contribute decisively to the performance of the material and play a tremendous role in bioapplications [3]. For example, the efficacy of synthetic implants in the human body is decided primarily by their surface distinctiveness such as surface microstructure, composition, morphology and properties. It is well reported that surfaces having nano-features in a well-organized manner significantly affect cellular and sub-cellular functions. The surface properties of NBMs can be altered to augment solubility, biocompatibility and cellular uptake. The restrictions of conventional drug carriers include reduced effective targeting, low bioavailability and budding cytotoxicity. The structural control at the nanoscale regime is the key factor in tailoring the bioavailability of the biomaterials. NBMs have been widely used as a carrier for the controlled release of drug molecules and synthetic matrices for tissue engineering. Various drug delivery systems can be developed using NBMs of different composition, size, shape and morphology. Further, the clinical applications of NBMs can be enhanced by functionalizing their exterior with suitable ligands.

Surface functionalization of NBMs with suitable ligands for binding drugs, biomolecules, targeting moieties, or fluorescent probes can be attained through various processes such as electrostatic binding, physical adsorption, covalent coupling and complementary recognition during synthesis (in-situ) or post-synthesis (ex-situ) processes. The surface modification is extremely essential for biological applications as the degree of adhesion of cells is tailored by non-specific adsorption of proteins. Further, prolonged stability of the NBMs in blood is crucial for targeted therapy and theranostic applications. Therefore, the development of novel NBMs for these applications requires complete characterization and optimization of their properties, and a thorough understanding of their interaction with biological systems.

14.2 Characteristics and Properties

Nanostructured materials exhibit significantly different optical, magnetic, mechanical and electrical properties compared to their bulk analogues. These materials have a superior specific surface area, which is beneficial for greater biochemical reactions. Further, NBMs possess physico-chemical properties similar to local tissue with nanometer hierarchical components. These unique properties enable NBMs to be a suitable candidate for biomedical applications. Especially, the design and selection of NBMs for specific applications depend on their long-term stability of structural (mechanical, physical and chemical) and biological properties. NBMs should not have adverse toxic effects and allergic symptoms to the body. The surface of NBMs, being precisely exposed to the living systems, plays a decisive role in biocompatibility. NBMs should have a high degree of compatibility when in touch with organs and tissues. The best possible way for enhancing the degree of tolerance is by maneuvering the surface properties of the biomaterials through surface alterations.

14.2.1 Structural Properties

The understanding of structural properties is fundamental to know the interaction of surfaces of NBMs with biomolecules, drugs as well as cells. The preferential gathering of biomolecules and cells at the surface is called adsorption which is basically a surface phenomenon. The nature of adsorption is generally determined by the strength by which these molecules are interacted/attached with the NBMs' surface. In general, there are two types of adsorption, namely physisorption and chemisorption. Physisorption (physical adsorption) is mainly long-range and weak van der Waals attraction energy in nature in the range of 10–50 kJ/mole. Generally, there is no activation barrier attached to it and it is fast and reversible in nature. However, chemisorption includes irreversible short-range and higher energy (200–400 kJ/mole) bonding between molecules and the surface. In addition to the protein and surface properties described above, adsorption also depends on the accessibility of molecules for interaction with the substrate. There are four major ways for transporting molecules to the surface: diffusion, convection, flow and combination of convection and diffusion. Other variables such as temperature, concentration and molecular size have a significant role in transporting drugs, biomolecules and cells to the NBMs' surfaces. The physical and chemical interactions of these molecules with the surface are greatly controlled by various parameters such as surface characteristics of NBMs, physiochemical response of biomolecules, drugs or cells and external factors like temperature, pH, ionic strength, etc. The NBMs used for bioapplications are mainly non-toxic materials with desired surface modifications to which biomolecules, molecular probes, drugs, etc., are conjugated. The NBMs' surface characteristic includes wettability (hydrophobicity/hydrophilicity), roughness, softness and chemical composition [4, 5]. The physiochemical properties of NBMs are

extremely reliant on the types, structures and orientations of the materials. With respect to surface charge, both positive and negative ions are used to coat on the surface of biomaterials for enhanced biocompatibility and cellular affinity [4].

The chemical stability as well as mechanical strength of NBMs are also important parameters for applications of NBMs, especially in implants and devices. Corrosion of NBMs in biological fluids affects both chemical stability as well as mechanical integrity [6]. The surface modification of NBMs is essential when degradation of materials occurs. NBMs with Young's modulus near to that of bone are generally suggested for implant [7]. The NBMs with desired characteristics such as high mechanical strength and wear resistance are primarily used for dental, orthopedic and cardiovascular implants.

14.2.2 Biological Properties

The binding of proteins at NBMs' surfaces has a crucial role in shaping the nature of the tissue–biomaterial interface and uses on nanomedicine [8, 9]. Proteins are comprised of distinct building blocks (amino acids) assembled into hierarchical structures. The heterogeneity in the amino acid side chain is displayed in protein surface characteristics. The charged and non-charged polar end form hydrophilic surface, whereas the non-polar non-charged side chain ends up with a hydrophobic surface. Hydrophobic surfaces are more prone to adsorption of protein compared to hydrophilic ones due to the occurrence of favorable hydrophobic interactions at the surface [9]. In addition to hydrophobic interaction, protein molecules can interact with the NBMs' surface through other forces, like ionic bonding and charge–transfer interactions. The interfacial behavior is mostly guided by the property of both the protein and the surface with which the biomolecules are interacting. The property of proteins that stimulate the surface action is linked to the sequence of amino acids which mainly controls the protein–NBMs surface interaction. Larger size molecules have more sites to interact with the surface. Similarly, molecules in their isoelectric point adsorb more easily. At the isoelectric point, reduction of repulsion between charged molecules leads to enhancement in protein binding. Not only the charge but also the charge distribution pattern governs the protein adsorption greatly. Stability of proteins and their unfolding rate also have an effect on surface interaction. Relatively less-stable proteins, i.e., those having less intramolecular cross-linking can unfold to larger amount and form more contact points with the surface. Likewise, molecules with higher unfolding rates enhance the probability of interaction with the surface by exposing more sites. Other properties of NBM surfaces which have an effect on the adsorption process are surface chemical composition (chemical composition of a surface will govern the types of intermolecular forces leading to interaction with proteins), various types of functional groups (such as carboxyl, hydroxyl, amine, thiol and other aromatic rings) present on the surface, etc. On a microscopic scale, surfaces of NBMs are not homogeneous. Thus, surface topography such as pores,

patches, domain and channels present on NBMs' surfaces can influence the interaction of biomolecules and proteins with the surface. Furthermore, chemical species existing in these textures have also affected the surface characteristics.

The adsorbed protein layer (so-called "protein corona") has many kinds of effects ranging from blood coagulation, platelet adhesion/activation to bacterial to cellular adhesion, etc. It also has an impact on NBMs' degradation. It is well recognized that the creation of protein corona on the NBMs' surface reduces their cellular uptake, targeting capability and biodistribution due to the changes in solubility, size and surface chemistry. For instance, dysopsonin proteins such as albumin and apolipoproteins aid in the prolonged flow of NBMs in the living system, while opsonin proteins such as IgG endorse phagocytosis [10]. NBMs are safe and effective for practical uses only when their physiological relation with living organisms is well-studied. Therefore, the understanding of the biological identity of NBMs and their physiological stability is important. In order to enhance, the physiological stability of NBMs and their circulation time in blood, poly(ethylene glycol) (PEG) is extensively used as a coating material due to its immunogenicity, almost zero surface charge, high water solubility, extensive hydrogen bonding and extreme protein-resistant characteristics [11, 12].

Biomaterials can be obtained either naturally or by synthesizing in a laboratory using different chemical approaches involving various metallic and non-metallic components as well as their hybrids. NBMs have potential applications in surgery, drug delivery and dental applications. These applications required NBMs to be highly biocompatible and hemocompatible [13]. The notion of biocompatibility is an enormous issue which is under investigation for a prolonged period of time. The exact meaning of biocompatibility varies from researcher to researcher typically. However, the competence of a biomaterial to execute its role as per the medical treatment selected with maximum efficiency in contact with the body without any local side effects is termed as biocompatibility. Approximately, all medical devices are prepared from several biomaterials, and thus inspecting of their compatibility with the biological system is required. Various kinds of efforts have been made to understand the dealings of these biomaterials with human tissue and how their mode of interactions affect the enactment of the imbedded devices [14, 15]. Biocompatibility test only on one type of cell line or tissue is never satisfactory as the human body is made up of so many types of tissue and is very much complex. After the in vitro testing is done, an in vivo experiment should be performed based on the intended use of the device material. Time for these testing can vary from weeks to several months based on the amount of data required before implantation. There may be some substances that leach out from NBMs' surface, and therefore all potentially harmful leachable materials should be removed and analyzed. NBMs ought to be non-toxic, unless otherwise they has been specially designed for any particular requirements like cancer treatment. To outline whether any material is biocompatible, or not, there are certain rules, regulations and protocols. The standard institute such as International Standards Organization (ISO) and American Society for Testing and Materials (ASTM) formulated a series of in vitro test standards. Although the in vitro tests cannot exclusively confirm the biocompatibility of a device or a material, they offer precious data

for the subsequent steps which are ideally in vivo tests followed by a human clinical trial. Having a consistent set of in vitro biocompatibility data can result in the cutback of animal uses and also facilitate setting the platform for human trials [16].

Blood ingredients usually do not interact with intact vascular endothelium. However, mechanical disruption of the blood vessel wall due to interaction with implants and particles may cause localized hemostatic responses [17]. The contact of blood with an unknown foreign element promotes the adsorption of protein and platelets. Hemocompatibility investigation is the estimation of critical interactions of foreign materials with blood to look for possible unfavorable effects arising from the exposure of the foreign element to blood cells and proteins. These adverse effects are common and can lead to serious health problems. Thus, hemocompatibility testing is very important for the introduction of new theranostic agents, medical implants/devices and medicines. Further, the deep knowledge and understanding of the interaction between nanostructures with biological components is essential for the practical applications of NBMs.

14.3 Different Types of Nanostructured Biomaterials: A Glimpse Toward Synthesis Aspects

Generally, any substance (not necessarily drug) or group of substances of a nano-sized dimension suitable for biomedical applications either as therapeutic, diagnostic agent or medical implants can be called NBMs. These materials have the capability to be in contact with biological fluids, cells and tissues for a long time, without any adverse side effects. Typically, these materials can be obtained either from nature or synthesized using different chemical methods. The development of NBMs finds many applications in diagnosis, tissue engineering, antimicrobial field, dental, surgical and medical implants [18–20]. These fields are highly interdisciplinary, requiring knowledge and expertise in chemistry, materials science, chemical engineering, biotechnology and medical sciences. Based on the material characteristics, NBMs can be classified into three major groups: organic biomaterials, inorganic biomaterials and organic–inorganic hybrid biomaterials. The ongoing advances in nanobiotechnology developed various methodologies to prepare NBMs from various materials, including ceramics, metals, metal oxides, composites, polymers, hydrogel, etc. Depending upon the preparation methods and origin, NBMs have unique physiochemical and structural features, which are vital for different applications in biomedical fields. Among the variety of available morphologies, nanostructured or nanoparticulate forms of biomaterials are widely employed as drug carriers and diagnostic agents as well as tissue engineering.

14.3.1 Organic Nanostructured Biomaterials

"Organic biomaterials" can be either natural or synthetic in origin. Often, they comprise naturally occurring biomaterials produced by an organism for itself. Polymers and hydrogels are two major classes of organic biomaterials. Various natural polymers such as chitin, starch, cellulose, chitosan, hyaluronic acid and dextrin are an interesting class of biomaterials which have gained considerable attention [21, 22]. All cellulose-forming organisms, namely algae, bacteria and higher plants, contain cellulose synthase proteins, which polymerize the glucan chains to form cellulose [22]. Similarly, the biosynthesis of chitin is catalyzed by the enzyme chitin synthase [23]. Most of these polymers are the main components of various natural products. For instance, lignin and chitin are the main ingredients of natural polysaccharides and represent the most abundant polymer in nature next to cellulose [24]. In 1996, researchers for the first time developed a methodology for the chemical synthesis of cellulose in a laboratory [25]. Polymeric biomaterials have numerous benefits over other biomaterials due to viable large-scale synthesis procedures, cost-effectiveness, easy processability for most of them and availability with preferred mechanical and physical properties. The polymer-based biomaterials are extensively synthesized by different mechanisms like radical polymerization, condensation polymerization and catalyzed polymerization. In radical polymerization, the reaction proceeds through a controlled reaction using free radicals, while condensation polymerization ends with the formation of well-defined products such as an ester, an amide or a urethane bond as a result of the polymerization process. However, enzymes act as a catalyst in a catalyzed polymerization process. Recently, the advancement of polymer nanoparticles (PNPs) has accorded a great amount of attention in drug delivery owing to their capability to improve solubility, bioavailability and pharmacokinetic properties of a drug molecule. It is also playing a key role in other fields such as photonics, electronics and environmental sciences. PNPs are mainly composed of biodegradable and biocompatible polymers of natural or synthetic origin. The most extensively used natural polymers for the preparation of PNPs are gelatin, chitosan, alginate and albumin. Among the synthetic polymers, polylactide (PLA), polyglycolide (PGA), poly (lactide co-glycolides) (PLGA), polyorthoesters, polycaprolactones, poly(methyl methacrylate) (PMMA) and polyacrylates are extensively explored. The properties of PNPs have to be revamped depending on the meticulous application.

Hydrogels are also a promising class of materials for biosensing, drug delivery, tissue engineering, etc. Hydrogels have a hydrophilic three-dimensional network structure with voids which made them competent in carrying hefty amounts of water via hydrogen bonding. On the other hand, it is a polymer network having the ability to swell and keep hold of a considerable fraction of water (>20%) within its construction [26]. The hydrophilic property of hydrogel minimizes non-specific adsorption of proteins, thereby imparting "non-fouling" characteristics. Many hydrogels are not homogenous in nature as different polymeric domains are created within the gel microstructure. Such features make these materials amenable for different industrial, biomedical and environmental applications. For instance, the elastic network

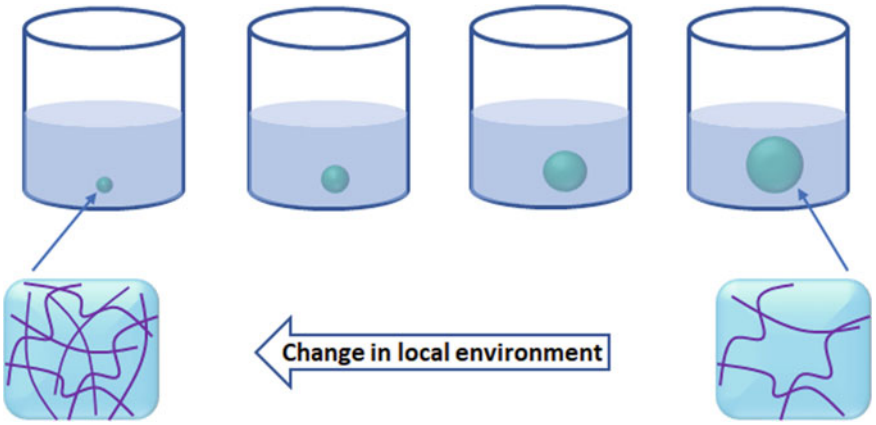

Fig. 14.1 Schematic representation of volume phase transition of a stimuli responsive hydrogel

structure of hydrogel can encapsulate various drugs and biomolecules. Further, the density of the network structure can be modified to provide better mechanical properties of the desired application. In addition, certain hydrogels undergo a volume phase transition (Fig. 14.1) depending on the change in the local environment such as light, temperature, pH, ionic strength and the presence of macromolecules [27–29]. Recently, the development of nano-sized hydrogels (hydrogel nanoparticles or nanogels) received considerable attention due to their prospective applications in drug delivery, biosensors and tissue engineering, etc. [30]. Interestingly, hydrogel nanoparticles have integrated characteristics of hydrogels (hydrophilicity, flexibility and biocompatibility) as well as nanoparticles (stability, long-term circulation and targeting ability) at the same time. Hydrogel nanoparticles can be made up of a variety of natural and synthetic polymers as well as their blending through chemical bonding or noncovalent physical cross-linking.

14.3.1.1 Synthesis Strategies of Organic Nanostructured Biomaterials

The method of preparation of PNPs plays a fundamental role in obtaining desired properties. The PNPs can be synthesized directly from a preformed polymer or polymerization of monomers using classical polymerization [31, 32]. Direct polymerization of monomers can be achieved by polymerization processes such as emulsion, microemulsion, miniemulsion, surfactant-free emulsion, interfacial polymerization and controlled/living radical polymerization. The preparation of PNPs from preformed polymers can be obtained through dialysis, salting out, solvent evaporation, nanoprecipitation and super-critical fluid technology. The schematic representation of different PNP preparation techniques is shown in Fig. 14.2. However, the choice of choosing an appropriate method for preparing PNPs depends on the types

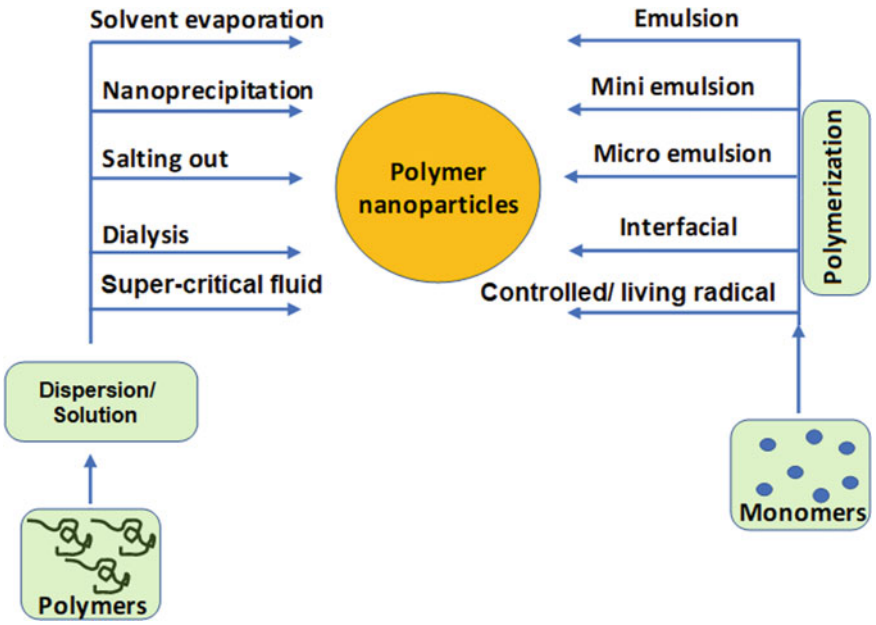

Fig. 14.2 Schematic representation of different polymer nanoparticle preparation techniques

of solvents and polymers used in the synthesis process, particle size requirement as well as area of application.

Mostly used techniques for the synthesis of PNPs are briefly reviewed here. The techniques used for the preparation of PNPs from preformed polymers did not engage any polymerization processes. Among others, solvent evaporation is extensively used to prepare nanoparticles of polymers from a preformed polymer (in the dispersed state) (Fig. 14.3a). In solvent evaporation, polymer solutions are first prepared in volatile solvents (acetone, chloroform, dichloromethane or ethyl acetate) and emulsions are formulated by two general methods: the first one namely single-emulsions, i.e., oil-in-water (o/w), secondly double-emulsions, i.e., (water-in-oil)-in-water, (w/o)/w using high-speed ultrasonication or homogenization. The emulsion is transformed into a nanoparticle suspension on the removal of the solvent by evaporation [33]. The solidified PNPs are usually gathered through ultracentrifugation followed by washing with water. Various stabilizers such as poly(vinyl pyrrolidine) (PVP), span, poloxamer, sucrose and sodium cholate are added during the preparation of PNPs via solvent evaporation. The mixing time and technique, polymer concentrations and nature of the solvent used in the making of emulsion strongly influence the properties of the PNPs made by solvent evaporation. The main drawback of this simple method is the necessity of a long time and the risk of possible coalescence of nanodroplets during the evaporation process.

The PNPs of desired properties can be synthesized by means of monomer polymerization. Emulsion polymerization is broadly employed for the preparation of

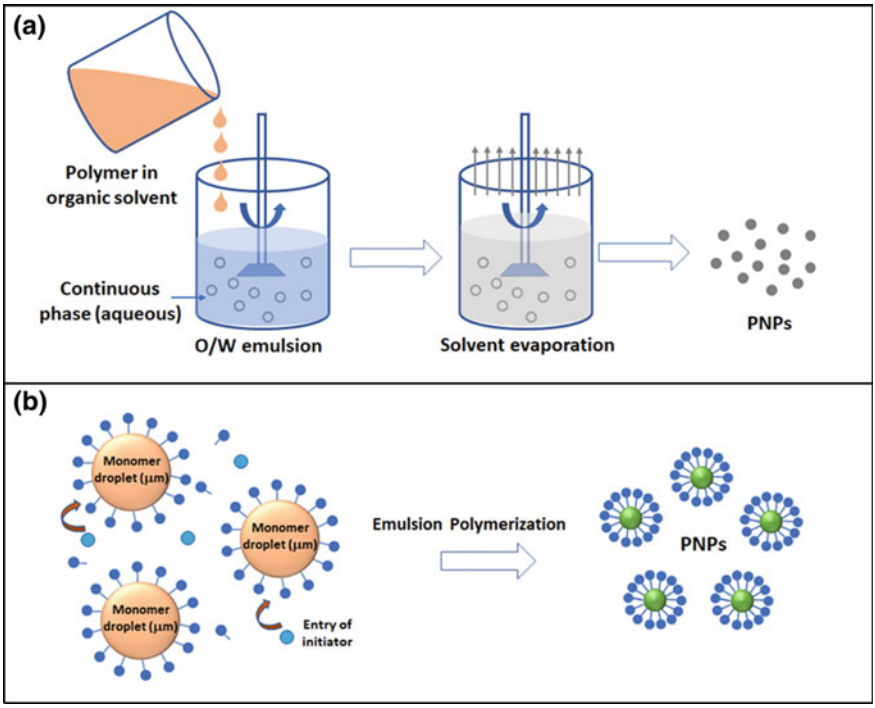

Fig. 14.3 Schematic presentation showing the preparation of PNPs by **a** solvent evaporation and **b** emulsion polymerization method

polymers from monomers (Fig. 14.3b). This method is broadly classified into two categories such as surfactant-free and conventional emulsion polymerization based on the use of surfactant [34]. In conventional emulsion polymerization, the components are water, a monomer with little water solubility, an initiator (water-soluble) and a surfactant. This polymerization process can be initiated by the use of initiators. Initiation reaction starts upon collision of monomer molecules dissolved in the continuous phase with an initiator molecule (i.e., ion or free radical). Application of high-energy radiation (γ-radiation, ultraviolet or strong visible light) can also lead to the conversion of monomer molecule into an initiator radical. Before or after the termination of reaction, the phase separation occurs and solid particles are generated. The PNPs of typical size ~ 100 nm can be obtained by this process. Different polymer nanoparticles formed by this method are PMMA, polystyrene (PS), poly(butylcyanoacrylate) and poly(ethylcyanoacrylate). The conventional emulsion polymerization process has become less important because of the heavy usage of toxic organic solvents, surfactants, monomers and initiator. These toxic components need to be removed However, the surfactants' removal is quite difficult and a time-taking process. Therefore, it is preferable to prepare PNPs without using added surfactants as an alternative method. The production of PNPs without using surfactant is known as emulsifier-free

polymerization or surfactant-free polymerization. The reagents used in this process are monomers (primarily acryl or vinyl monomers), initiator which is water-soluble and deionized water.

Hydrogel networks can be formed by the reaction of one or more hydrophilic monomeric components using multifunctional cross-linkers via single or multi-step procedures like polymerization. A variety of different polymerization methods such as copolymerization and cross-linking free-radical polymerizations have been utilized for the preparation of hydrogel networks. Further, these structures can also be formed by interacting polymers with suitable cross-linking agents to promote the formation of the network. In general, hydrogel nanoparticles are formed when hydrogel preparation is carried out at higher temperatures or by using stabilizing agents. Explicitly, the use of ionic surfactants has produced hydrogel nanoparticles via precipitation polymerization. The features of hydrogels are exceedingly reliant on the cross-linking network. Both naturally occurring polymers like proteins and synthetic polymers with water-loving characteristics may be used as starting materials for preparing hydrogel [35]. Among the naturally occurring polymers, chitosan, chitin and alginate have been widely used for making hydrogel nanoparticles. Similarly, from synthetic polymers, poly (vinyl alcohol), poly (ethyleneimine), poly (ethylene oxide) and poly-*N*-isopropylacrylamide are employed for the development of hydrogel nanoparticles. Recently, hydrogel nanoparticles have acknowledged an immense deal of attention in drug delivery due to their unique physiochemical properties [36]. The schematic representation of the synthesis of colloidal chitin nanogel and the drug loading in chitin nanogels are shown in Fig. 14.4 [37].

14.3.2 Inorganic Nanostructured Biomaterials

Due to the intrinsic physico-chemical and tunable surface properties, inorganic NBMs presents novel platforms to build sophisticated theranostic agents for superior detection and more efficient treatment of many diseases. In particular, inorganic nanoparticulates of metals (Au, Ag), oxides (SiO_2, TiO_2, ZnO, Fe_3O_4), hydroxyapatite (HAp) and layer double hydroxide (LDH) possessing unique physiochemical properties and non-toxicity are showing the way for developing advanced technology. The main attractive feature of using inorganic nanoparticles in bioapplications is due to their inherent physical properties, like superparamagnetism [38], surface plasmon resonance [39] and luminescence properties [40], which can be tailored by modifying the shape and size of particles. The other striking appeal arises from the huge surface-to-volume ratio of nanoparticles that provides an active site for conjugating imaging and therapeutic agents [41]. Owing to these characteristics, inorganic nanoparticles can provide an excellent platform for establishing multifaceted biomaterials for therapeutic and diagnostic applications. For instance, clinically approved inorganic nanoparticle-based agent ferumoxytol is used to cure iron deficiency anemia in humans, and ferucarbotran is used as a magnetic resonance imaging (MRI) contrast agent for revealing the small focal liver lesions [42]. The clinical trials are undergone

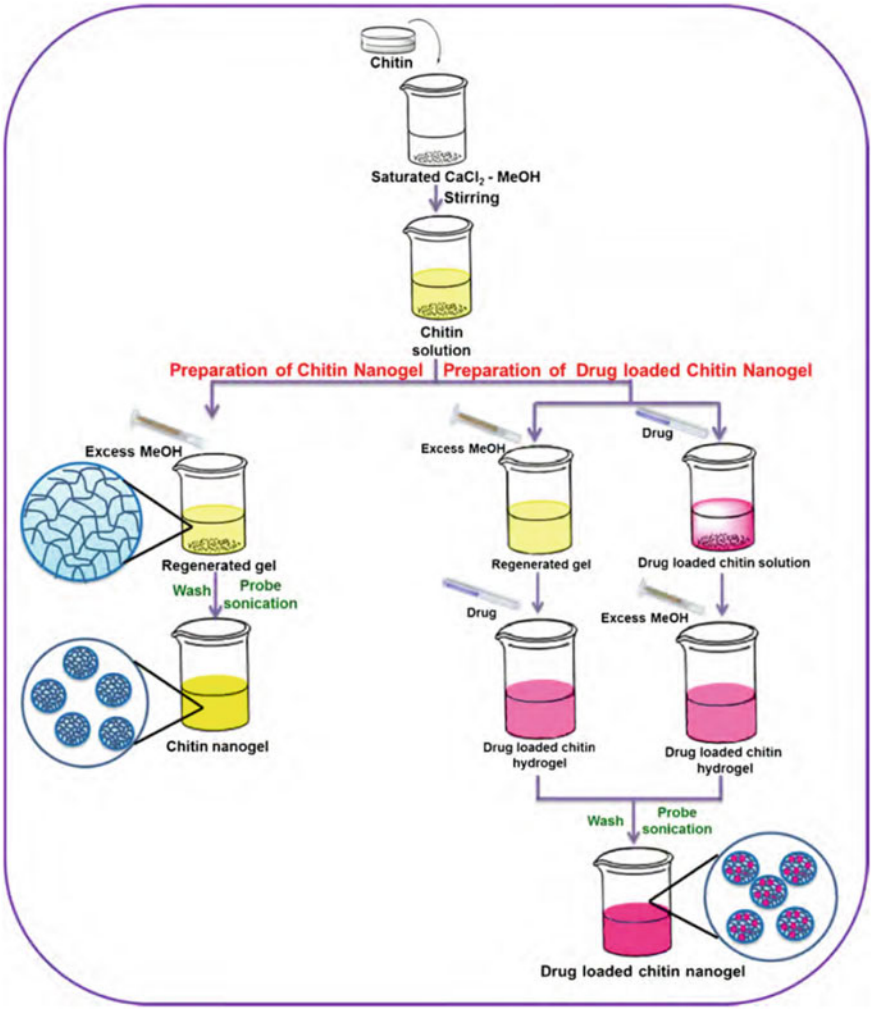

Fig. 14.4 Schematic representation of the synthesis of colloidal chitin nanogel and the drug loading in chitin nanogels (reproduced with permission from Priya et al., Carbohydrate Polymers 136 (2016) 609–617, Copyright ©2015 Elsevier Ltd. [37])

with various inorganic nanoparticles like aurimmune CYT-6091, an agent made up of gold nanoparticles bound with PEG and rhTNF (tumor necrosis factor) [43].

14.3.2.1 Synthesis Strategies of Inorganic Nanostructured Biomaterials

The synthesis strategies of inorganic NBMs can be broadly classified into two categories, such as top-down and bottom-up approaches. Mostly, the bottom-up chemical

processes are widely employed for the synthesis of NBMs. Among others, bottom-up chemical approaches commonly used in the synthesis of NBMS are colloidal precipitation (Fig. 14.5a), hydrothermal synthesis, thermal decomposition method (Fig. 14.5b), polyol method, microemulsions (Fig. 14.5c), sonochemical approach and sol–gel processing (Fig. 14.5d).

The colloidal precipitation method provides a dependable route to synthesize various types of inorganic nanoparticles. It relies on the precipitation of nanoparticles from an aqueous solution of metal ions under controlled temperature. Metal salts like nitrate, chloride and sulfate are used as starting materials for the synthesis of inorganic nanoparticles. The dissolved metal ions in water exist as metal hydrate and nanoparticles precipitated out by the addition of a base such as NaOH or NH_4OH at mild temperature (60–90 °C). By controlling the pH and temperature of the reaction medium, it is very much likely to obtain different shapes and sizes of nanoparticles. Gupta et al. prepared shape-controlled ZnO nanostructures via reflux of zinc precursor in ethanol using different concentrations of NaOH as catalyst [44]. They have demonstrated that the amount of OH^- ions in the reaction medium controls the shape of ZnO nanostructures. Verma et al. developed hydroxyapatite nanoparticles by precipitation method using rod-like micelles of cetyltrimethyl ammonium bromide (CTAB) and sodium salicylate [45]. Similarly, the co-precipitation method is used for the preparation of different complex hydroxide and oxide nanoparticles of metals. Using the co-precipitation method, Massart [46] first synthesized Fe_3O_4 nanoparticles by adding base to an aqueous solution of ferrous (Fe^{2+}) and ferric (Fe^{3+}) ions in an oxygen-free environment [47]. Basically, aqueous colloidal synthesis is the easiest method for synthesizing aqueous stable nanoparticles. The control of crystal growth in the chemical precipitation method is the vital challenge to prepare nano-sized particles. Barick and co-workers developed various surface-functionalized Fe_3O_4 nanoparticles of average sizes about 10 nm using co-precipitation method [38, 48–52].

Sol–gel method is a simple, cost-effective way to produce different materials with predetermined properties. It involves first conversion of a liquid (sol) into a gel state followed by successive post-treatment to obtain solid material. The steps involved in the sol–gel method are mixing, casting, gelation, aging, drying and densification. The major advantages of the sol–gel method are the high purity, economic viability and uniform nanostructure attainable at low temperatures. The sol–gel process occurs via hydrolysis and condensation reactions as follows:

Hydrolysis: $\text{M–O-R} + H_2O \rightarrow \text{M-OH} + \text{R-OH}$.

Water condensation: $\text{M-OH} + \text{M-OH} \rightarrow \text{M–O-M} + H_2O$.

Alcohol condensation: $\text{M–O-R} + \text{M-OH} \rightarrow \text{M–O-M} + \text{R-OH}$.

where M = Si, Zr, Ti, etc., and alkyl group R = CH_3, C_2H_5, etc.

For instance, Dubey et al. synthesized silica nanoparticles by the sol–gel route using tetraethylorthosilicate (TEOS) as a precursor and PVP as a stabilizer [53]. Bessekhouad et al. described the preparation of TiO_2 nanoparticles via sol–gel route using tetraisopropylorthotitanate as a starting precursor [54].

The hydrothermal method involves synthesis of metal oxide nanoparticles under high temperature and elevated pressure from aqueous solution of precursors. This

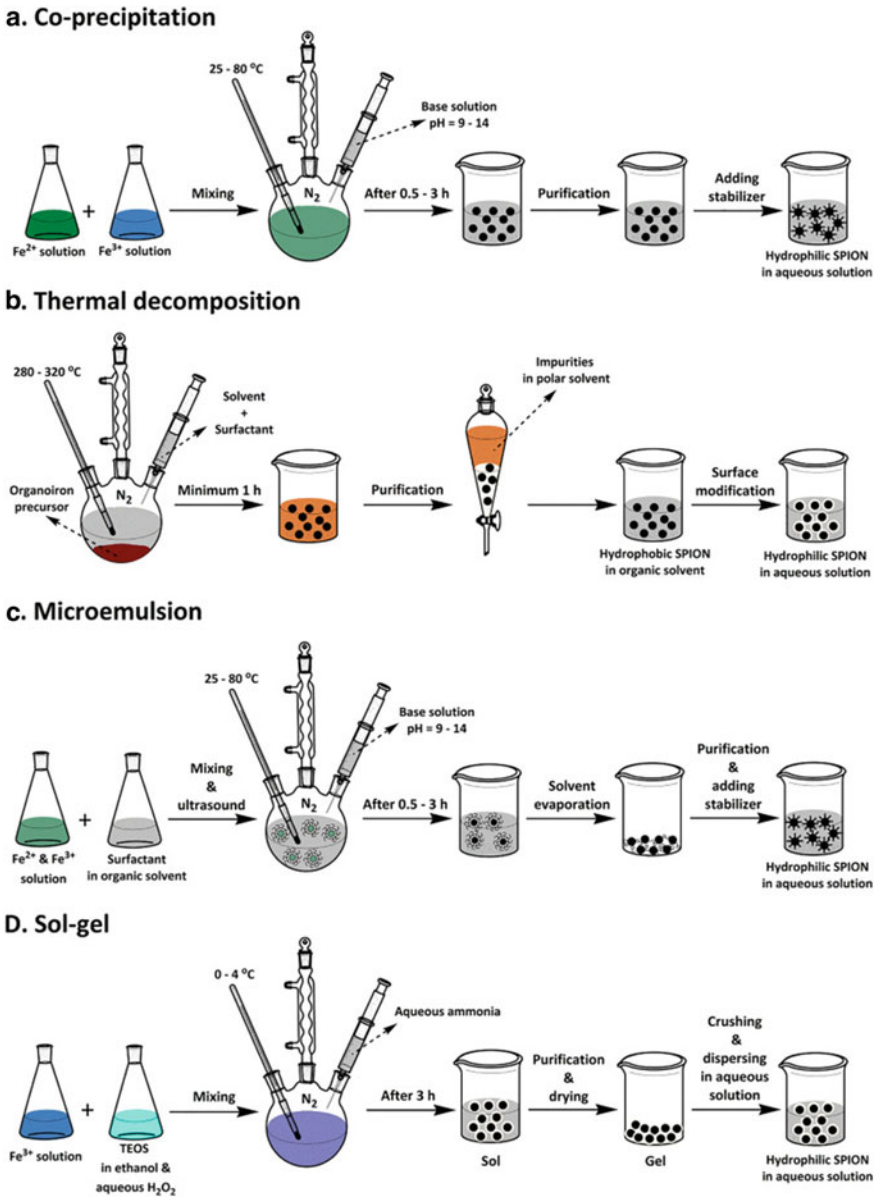

Fig. 14.5 Schematic representation of different routes for the production of superparamagnetic iron oxide (SPION) nanoparticles. **a** co-precipitation, **b** thermal decomposition, **c** reverse microemulsion and **d** sol–gel method (reproduced with permission from Dadfar et al., Adv. Drug Del. Rev. 138 (2019) 302–325, Copyright ©2019 Elsevier Ltd. [47])

reaction can be performed in a batch or continuous method. The batch hydrothermal process is used to perform in a system with preferred ratio phases, whereas the continuous method allows a superior rate of reaction to be attained at a shorter time period. This method is rationally inexpensive and has the capability to produce a large number of nanoparticles of optimized size, shape and composition. For instance, Gao et al. [55] developed carboxyl-modified Fe_3O_4 nanoparticles using the hydrothermal method. Recently, Sharma et al. prepared nano-sized pure and doped ZnO particles by the hydrothermal process at room temperature [56]. The preparation of nanoparticles using organic solvent instead of an aqueous solution under analogous conditions is termed as solvothermal method. Qiu et al. prepared core–shell Fe_3O_4@ZnO@mSiO_2 nanocarriers by the solvothermal method for the delivery of chemotherapeutic agent [57].

The polyol method is a robust strategy for the preparation of well-defined metal and metal oxide nanoparticles by dissolving the metal precursor in a polyol solvent (high-boiling, multivalent alcohols) and subsequently heating them for several hours at the refluxing temperature of the solvent. The polyol acts both as a solvent as well as a reducing agent and ligand to prevent aggregation particles. The choice of polyol used during synthesis is dictated by the optimum reflux temperature. Several kinds of polyols used for the preparation of nanoparticles by the polyol method are ethylene glycol, propylene glycol, diethylene glycol and triethylene glycol. Sun and Xia [58] prepared silver nanoparticles (cubes, wire and irregular shaped) of various dimensions via reduction of silver nitrate with ethylene glycol in the presence of PVP at 160 °C. They have observed that the size and structure of nanoparticles depend on various parameters like reaction temperature and concentration of precursor. Further, they prepared hollow gold nanoboxes using silver nanocubes as sacrificial templates. Barick et al. developed pure and metal-doped ZnO nanoassemblies by heating acetate precursors in diethylene glycol medium at 160–170 °C [59]. Fe_3O_4 nanoassemblies were also prepared by refluxing Fe-chloride precursors for 6 h in the presence of ethylenediamine and sodium acetate in ethylene glycol [60].

Nano-sized water droplets dispersed in the oil phase acted as nanoreactors for the preparation of nanoparticles in the microemulsion method [47, 61–63]. Both the metal ion and reducing agents are soluble in the water medium, where one microemulsion contains metal ion and the other contains the reducing agent. The precursor and reducing agents captured inside the reverse micelles are mixed thoroughly by the exchange process, which is primary to the preparation of nanoparticles in microemulsion. Therefore, precursors precipitated out in the aqueous phase are mainly situated at the core of micelles. Thus, the micelles in these systems provide an appropriate condition for controlled nucleation and growth of particles, which in the later stage form a robust coating on the nanoparticle. Various metal and metal oxide nanoparticles were effectively prepared by microemulsion methods. For instance, Zhang et al. developed hollow Fe_3O_4 nanospheres in reverse microemulsion using sodium dodecyl benzene sulfonate [61]. Lee et al. prepared highly crystalline γ-Fe_2O_3 nanoparticles of nano-sized by the microemulsion method at elevated temperature with iron (III) acetyl acetonate as a precursor [62]. Bose and Saha discussed the preparation of hydroxyapatite nanoparticles by a microemulsion method and

observed that the composition of microemulsion and synthesis parameters significantly control the phase purity of hydroxyapatite formation, and their surface area and morphology [63]. Ultrafine nanoparticles of diameter in the range of 5–50 nm can be synthesized by water-in-oil microemulsions.

The high-temperature thermal decomposition of organometallic precursor in high boiling point medium is known as "thermolysis". It produces excellent quality, highly crystalline, monodispersed inorganic nanoparticles [47, 64–67]. Specifically, in this process metastable organic compounds are decomposed in the organic medium at high temperature (260–320 °C) in the presence of surfactants. For instance, metastable organic compounds such as Fe (III) acetylacetonate [64, 65], Fe (III) oleate [66] and iron pentacarbonyl [67] are used for the synthesis of iron oxide nanoparticles. Barick et al. fabricated highly monodispersed Fe_3O_4 nanoparticles by thermal decomposition of Fe (III) acetylacetonate in the presence of laurylamine, lauric acid and 1, 12-dodacane diol in benzyl ether solvent at high temperature [64]. Hyeon et al. synthesized monodisperse maghemite nanocrystallites of high crystallinity by thermolysis of iron–oleic acid complexes [68]. Sun et al. demonstrated the synthesis of ultra-small Fe_3O_4 nanoparticles using iron (III) acetylacetonate by the thermal decomposition method [69]. Liu and Swihart reported controllable preparation of colloidal ZnO nanocrystals from thermal decomposition of zinc acetylacetonate precursor [70]. There are a few drawbacks to the thermal decomposition method. For instance, it employs costly organometallic compounds as precursors, high reaction temperature and tedious procedures. Further, surface engineering is essential for nanoparticles synthesized by this method to enable them water-dispersibility and biocompatibility.

A current advancement in the preparation of inorganic nanoparticles is the utilization of the sonochemical approach [71–74]. In this method, a high-energy ultrasonication is used to create acoustic cavitations which produce localized heating up to a temperature of ~ 5000 K. The nucleation and subsequent growth of nanoparticles take place at this temperature via collapsing of bubbles. Monodisperse metal and oxide nanoparticles of various shapes and sizes can be synthesized by this approach. For instance, Okits et al. prepared Au nanoparticles of different sizes by sonochemical reduction of Au^{3+} in an aqueous solution having 1-propanol and observed that the chemical effect of cavitation controls the particle size and the reduction process [72]. Mukh-Qasem and Gedanken reported the preparation of stable hydrosol of amorphous Fe_3O_4 nanoparticles by sonolysis of iron pentacarbonyl in the presence of sodium dodecyl sulfate [73]. Even though various metal and metal oxide nanoparticles are prepared by the sonochemical approach, large-scale synthesis is intricate to accomplish by this method.

14.3.3 Hybrid Nanostructured Biomaterials

Organic–inorganic hybrid biomaterials have received a great deal of attention due to their exceptional properties arising from the combinatorial effect of organic and

inorganic materials. Normally, hybrid materials exhibit higher mechanical, optical, magnetic and optoelectronic properties depending upon the materials involved. However, the overall properties of hybrid biomaterials rely on the individual constituents, their volume fraction, shape and size. Thus, they are extensively used in a variety of applications such as tissue engineering matrices, drug delivery and imaging. Most of these applications require good colloidal stability and biocompatibility of hybrid materials. Thus, it is most important to design and develop colloidally stable and biocompatible materials that optimize bio-interfaces with a suitable response. The researchers are seeking hybrid biomaterials having low mechanical disproportion and lesser side effects with good colloidal stability.

Recently, various research groups developed nanoparticle–hydrogel hybrid materials with enhanced adhesiveness, thermal response, mechanical properties and bioactivity [75–78]. The enhancement in these properties mainly arises due to the combination of two or more materials, Recently, the design of different supramolecular hydrogel–nanoparticle composites is proposed. For instance, the micro- or nanogels stabilized by using single/multiple nanoparticles through their noncovalent and covalent immobilization in hydrogel matrix were reported [79, 80]. Magnetic hydrogel composites were also developed by immobilizing magnetic nanoparticles into the hydrogel matrix by three different methods such as (a) blending, (b) in situ co-precipitation and (c) grafting method (Fig. 14.6) [80].

Inorganic–organic hybrid nano-sized layered double hydroxide (LDH) can be prepared by top-down exfoliation and bottom-up direct preparation routes. The most developed and widely used method for the synthesis of LDHs is top-down exfoliation. Exfoliation of layered materials is a simple two-step process: first, the intercalation of the layered materials with subsequent exfoliation steps to delaminate the layers. The bottom-up approach is normally a one-step process in which inorganic nanostructured materials were prepared directly from suitable precursors. Various methods were designed to create LDHs with diverse sizes such as exfoliation co-precipitation, electrodeposition methods and hydrothermal/solvothermal synthesis [81–84]. For example, Liang et al. reported the preparation of NiCo LDH nanoplates using a hydrothermal continuous flow reactor at high temperature and high pressure [82]. Recently, Jaśkaniec et al. [85] reported the preparation of hexagonal flakes of Ni–Fe LDH having high crystallinity by homogeneous precipitation route.

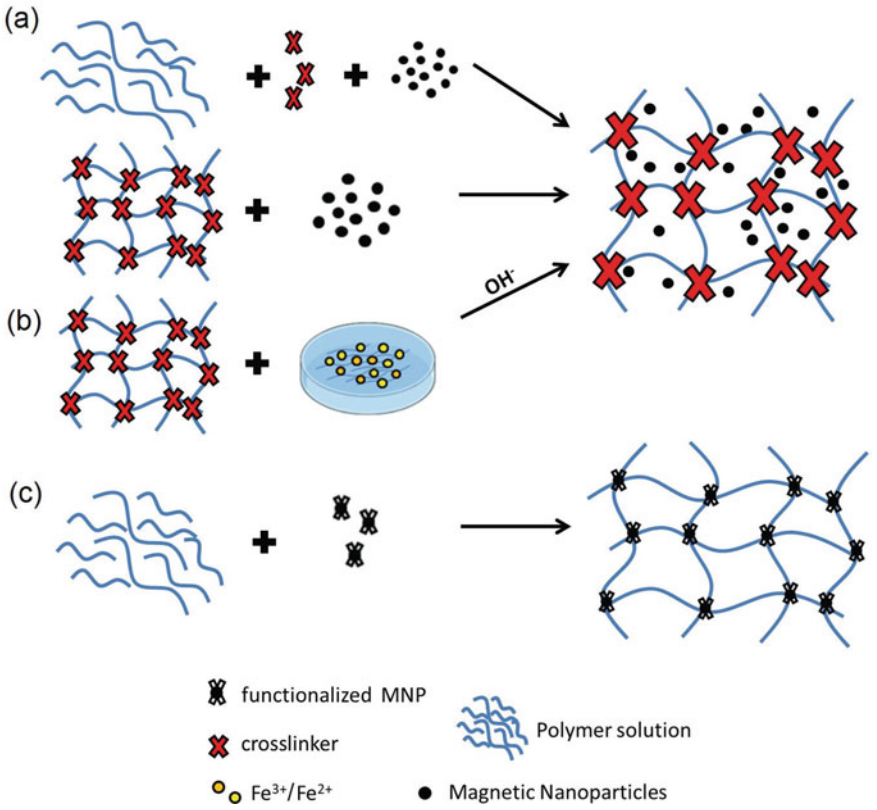

Fig. 14.6 Schematic representation of methods to prepare magnetic hydrogels. **a** blending; **b** in situ co-precipitation and **c** grafting method. Magnetic nanoparticle (MNP) is represented by black spheres. Red and white X symbols represent cross-linker and functional groups, respectively (adapted from Frachini and Petri., J. Braz. Chem. Soc. 30 (2019) 2010–2028 [80], an open-access article distributed under the terms of the Creative Commons Attribution License)

14.4 Surface Modification of Nanostructured Biomaterials

Designing surface functionalized NBMs is significantly important for potential biomedical applications. Most of the biomedical applications require NBMs to be chemically and colloidally stable in complex biological fluids. The surface properties like surface chemistry and surface charge mostly play important roles in upgrading of chemical and colloidal stability of NBMs [86, 87]. Further, the interaction of NBMs with the living matter at the cellular level is an important issue for their biomedical applications [88]. The interaction of proteins with NBMs' surface leads to an associated protein layer that mostly defines the biological identity of the NBMs. This protein corona determines the ability of NBMs to interact with the living organism and hence modifies their cellular internalization. Thus, there is a requirement to provide stealth

coatings on NBMs' surface with desired materials for prolonged circulation time in blood. Recently, surface modification has received considerable attention because of its significance in reduction of toxicity of materials at the nano level and prevention of opsonization in the biological medium [89]. Further, nanoparticles can be easily detected by the lymphatic system via the body's natural immune response to foreign substances. Therefore, suitable surface functionality needs to be introduced onto the nanoparticles to provide hydrophilicity characteristics that enhance their blood circulation time.

Surface modification not only enhances the stability, hydrophilicity, monodispersity and biocompatibility of materials but also provides different surface functional groups (-COOH-, -NH_2, -SH and so on) or charges that can be advantageous for the conjugation of biomolecules or drugs [90]. The interaction between atoms at the surface of nanoparticles with incoming ligands/coating agent is the key parameter for surface modification [91]. There are mainly two kinds of interaction such as noncovalent and covalent interactions that occur between nanoparticles and the coating agent during surface modification. The noncovalent modifications of nanoparticles occur through hydrophobic interaction, electrostatic attraction and van der Walls forces. However, sometimes, such conjugation between particles and coating agent is not adequate to form stable surfaces to overcome the barriers like multi-step washing during their preparation as well as long-term incubation in biological mediums. Therefore, it is essential to consider the influence of ionic strength and pH while employing a noncovalent approach for surface modification. In contrast, covalent modifications provide greater stability in the ionic and biological media through the use of immediate strong chemical conjugation between nanoparticles and coating agents (chemisorption). In general, surface modification can be achieved during their synthesis (in situ) or post-synthesis (ex situ) methodology [3, 51, 52, 92, 93]. Various surface coating agents, for example, long-chain polymers/organic molecules, biomolecules and inorganic materials, were widely used for surface modification of NBMs.

Organic molecules having chelating functional moieties like thiol, carboxylic, amine and phosphate groups can bind to nanoparticle surfaces to stabilize them as well as control their agglomeration [3, 38, 51, 52, 86, 94–99]. The organic molecules like citric acid, dimercaptosuccinic acid and tripolyphosphate conjugated to the surface of nanoparticles through chemical conjugation of some of its functional groups, whereas the remaining freely exposed groups furnished colloidal stability to particles in the aqueous medium. For instance, Nigam et al. prepared highly water-dispersible Fe_3O_4 nanoparticles via chemisorption of citrate molecules onto the surface of nanoparticles during the synthesis process [52]. The cyclic (sodium hexametaphosphate) and chain-like (sodium tripolyphosphate) phosphate molecules are also utilized for the preparation of aqueous stable and biocompatible Fe_3O_4 nanoparticles by Sharma et al. [97] and Majeed et al., respectively [51]. Gorbatsevich et al. synthesized aqueous-dispersible silica nanoparticles by hydrolytic polycondensation of tetraethoxysilane followed by modification through grafting of triethylene oxide moieties [98]. Tang et al. developed aqueous stable ZnO nanoparticles by one-pot polyol hydrolysis of zinc stearate in the presence of triethylene glycol (TREG).

They have demonstrated that the conjugation of in situ formed ester compound onto the surface of ZnO provides aqueous colloidal stability [99].

The coating of nanoparticles with long-chain polymers/copolymers or surfactants are widely used for colloidal stabilization [100–102]. Among others, the use of polyethylene glycol (PEG) and PEG-based copolymers, for instance, polyoxamer, poloxamine and polysorbate 80 as coating agents is most popular and highly effective with respect to in vivo applications [41, 102, 103]. Rana et al. [66] synthesized aqueous stable carboxyl PEGylated Fe_3O_4 nanoparticles by conjugating bifunctional PEG-diacid molecule, whereas Rezayan et al. [104] prepared Fe_3O_4 nanoparticles coated with carboxyl functionalized PEG through dopamine cross-linker. Barick et al. [64] developed water-dispersible triblock-copolymer, Pluronic 123 stabilized Fe_3O_4 nanoparticles via hydrophobic interaction. Rahme et al. [105] prepared water-stable Au nanoparticles by grafting of PEG-based thiol polymers onto the nanoparticle surface. These PEG-based polymers hinder the opsonization of nanoparticles and thereby prevent the undesired uptake of nanoparticles by the reticuloendothelial system (RES) [106]. Additionally, biopolymers such as carbohydrates (chitosans, dextran, gelatin, ethyl cellulose and alginate) and proteins (bovine serum albumin and lipoproteins) as well as other synthetic polymers such as polyvinyl alcohol (PVA), polyethylenimine (PEI), polyaniline and polyacrylic acid (PAA) are often used as coating agent during nanoparticles synthesis processes [50, 107–111].

The hydrophobic nanoparticles (HMNPs) are generally converted to water-dispersible through ligand addition and ligand exchange methods. In ligand addition method, an additional layer of the ligand is introduced onto the HMNPs surface, whereas the hydrophobic molecules conjugated to the nanoparticle surface are substituted by hydrophilic molecules in the ligand exchange method. Both short-chain organic molecules such as dopamine (DA), mercaptosuccinic acid (MSA), DMSA and lipoic acid, and long-chain dendron and polymer molecules were used for stabilizing HMNPs [112–117]. Moreover, the hydrophilic inorganic shell can also be introduced onto the surface of nanoparticles via the formation of a core–shell structure [118, 119]. For example, Lai et al. developed a colloidally stable Fe_3O_4/SiO_2 core/shell structure for multifunctional applications by introducing an inorganic SiO_2 shell [119]. Xu et al. developed Au-coated Fe_3O_4 nanoparticles via the formation of Au shell on Fe_3O_4 by reduction of $HAuCl_4$ in the presence of oleylamine and then transferred them into a water medium by using sodium citrate and CTAB [120]. Further, they have introduced an Ag shell onto the surface of Fe_3O_4/Au by the addition of $AgNO_3$ to the reaction container.

In addition to the colloidal stabilization of nanoparticles, surface passivation also creates sites for conjugation to different biomolecules such as proteins, enzymes and antibodies. Sapsford et al. discussed the abundant chemistry available on the conjugation of nanoparticles with biomolecules for the development of nanoprobes [121]. Generally, bioconjugation can be performed via covalent or noncovalent interactions between biomolecules and surface-modified nanoparticles. The nanoparticles having amine, carboxyl and thiol functional groups can be conjugated covalently with biomolecules and drugs directly or via a linker molecule. Rana et al. [122] developed folic acid conjugated Fe_3O_4 nanoparticles through amide linkage between amine

groups of nanoparticles and the carboxyl group of folic acid using carbodiimide cross-linker chemistry. Similarly, Dixit et al. [123] prepared folate receptor-targeted Au nanoparticles by conjugating PEG with nanoparticles through the disulfide group of thioctic acid. Recently, the cell membrane components like platelets, red blood cells (RBC), macrophage cells and stem cells bounded nanoparticles have been evolving as a potential platform for in vivo therapeutic and diagnostic applications [124–126]. Gao et al. [125] developed Au nanoparticles functionalized with cellular membranes originated directly from natural RBC to provide immunosuppressive functionalities for effective escaping of macrophage uptake. Similarly, RBC-functionalized Fe_3O_4 nanoparticles were also prepared in a similar way that shows enhanced circulation time and diminished accelerated blood clearance through CD47 marker (a cell surface glycoprotein) [126].

The noncovalent electrostatic attachment also offers rapid and facile bioconjugation between nanoparticles and biomolecules. It is the simplest process to conjugate biomolecules, which are solely dependent on the attraction among two opposing charged moieties. For instance, CTAB-modified Au nanoparticles having a high positive charge can be easily conjugated with negatively charged nucleic acids [127]. The ionic strength and pH value play a significant part in such charged mediated interaction between nanoparticles and biomolecules [128].

14.5 Applications of Nanostructured Biomaterials

The aptitude to introduce biological property into synthetic materials significantly upsurges the potential applications of NBMs. Millions of patients, world-wide, are benefited with biomaterials-based implants and devices, drug delivery systems and imaging agents. The advancement in understanding the disease and tissue regeneration in association with recent technology have created new openings for the use of functional biomaterials. Therefore, functionalized NBMs have received a great deal of attention in the biomedical community. The applications of NBMs in therapeutic and diagnostic, tissue engineering, and medical implants and devices are discussed below.

14.5.1 Therapeutic and Diagnostic Applications

NBMs are used in several therapeutic applications such as hyperthermia therapy, drug delivery, photothermal and photodynamic therapy, and diagnostic applications in magnetic resonance imaging (MRI) and computed tomography (CT). Drug delivery systems based on nanostructured materials have proved to be a great route for targeting drugs to tumor sites where conventional therapy is not much effective. These drug delivery systems are capable of delivering therapeutic agents which otherwise exhibit poor solubility and poor pharmacokinetics. The encapsulation efficiency

of drug molecules as well as their release characteristic primarily depends upon the ability to create novel NBMs.

Organic NBMs such as hydrogels and PNPs are extensively used as a carrier for drug delivery [129, 130]. PNPs made of pH-sensitive biodegradable and biocompatible polymers are used for oral delivery of drugs, which are poorly water-soluble [131]. One of the most significant ultimatums in drug delivery is to deliver therapeutics agents to the central nervous system (CNS) and brain. The PNPs of chitosan, chitosan-PEG and PLA-poloxamer 188 are used for CNS delivery of tacrine, caspase-3 inhibitor and breviscapin. [132–134]. The PNPs are susceptible to transcytosis across the blood brain barrier (BBB) mainly dictates the systemic delivery of the drugs to the CNS. This delivery process can be enhanced by conjugating cell-penetrating ligands and/or peptides onto PNPs surfaces [135]. Further, PNP-mediated targeted drug delivery can conquer the problems associated with conventional chemotherapy [136].

Like PNPs, hydrogels are used for oral drug delivery [137], gastrointestinal (GI) drug delivery [138] and ocular delivery [139] as well as for topical and transdermal applications [140, 141]. As compared to microgels, nanogels have high payload capacity owing to their high degree of porosity. Among others, nanogels made up of thermoresponsive polymers are widely investigated for the delivery of drugs [142–144]. For example, Cho et al. [143] developed thermosensitive poly (D,L-lactide-co-glycolide)-block-poly(ethylene glycol)-block-poly(D,L-lactide-co-glycolide) (PLGA-b-PEG-b-PLGA) nanogels for the delivery of feebly water-soluble drugs and biomolecules. Chen et al. [144] delivered an anticancer drug, placlitaxel, using pH and thermoresponsive self-assembled nanogel composed of mPEG-isopropylideneglycerol. Further, the nanogel can also be functionalized with targeting molecules such as peptides and receptors for tumor-specific targeting [145] of drug molecules. In addition to drug delivery, nanogels are also used for the delivery of siRNA and oligonucleotides [146, 147].

Inorganic NBMs such as Au and its compounds are widely used for various bioapplications including biosensors, bioimaging and photothermal therapy due to their tunable optical and electronic properties as well as easy chemical synthesis and functionalization [148–152]. By controlling the shape, size and surface morphology, the plasmon absorption wavelength of Au nanoparticles can be tuned to overlap with the spectral zone, where the depletion of photons by physiological fluids and tissues is low. Au nanoparticles with specific surface functionality can easily get conjugated with antibodies and peptides for active as well as passive drug delivery [153–156]. For instance, Zong et al. discussed the probable applications of peptide-modified gold nanoparticles in drug delivery and biosensing [155]. Chanda et al. employed bombesin peptide-tagged gold nanoparticles to aim the gastrin-releasing peptide receptor, which is overly expressed in various cancer cells such as breast, prostate and small-cell lung carcinoma [156]. Au nanoparticles can deliver biomolecules such as siRNA that are prone to enzymatic deterioration, as well as those that exhibit lesser intracellular uptake [157]. Gold nanoparticles are also widely used in photothermal and photodynamic therapy of cancer treatment [158]. Similarly, nanoparticulate of Ag and its compounds have also been used for various biomedical purposes such

as biosensors and therapeutic applications [159–161]. The inorganic oxides such as TiO_2 and ZnO nanoparticles are also used as a potential agent for photo-induced therapy [162].

The commonly used oxide materials for drug delivery are iron oxide, zinc oxide, silica nanoparticles, etc. [48–52, 57, 66, 87, 97, 122, 163]. The research on these oxide materials has achieved an immense deal of consideration due to their unique physico-chemical and biological properties, and non-toxicity. In these systems, the drug molecules are either physically rooted or bound onto the surface of nanoparticles by electrostatic/covalent immobilization. For instance, Cheng et al. [164] demonstrated the physical entrapment of cisplatin into the porous hollow nanoparticles (PHNPs) of Fe_3O_4 and investigated their release characteristics. Puvvada et al. [165] developed folic acid-tagged biocompatible ZnO hollow nanocarrier (HZnO) for précised delivery of paclitaxel and observed their preferential accumulation in breast cancer cells (MDA-MB-231). Further, ZnO nanoparticles have been reported to shown antitumor activity toward cancer cells [166]. Recently, Zhou et al. [167] discussed the uses of mesoporous silica nanoparticles as efficient delivery systems for feebly soluble drugs, anticancer agents and therapeutic genetic substances. The surface-functionalized Fe_3O_4 nanoparticles were also used for covalent binding of an anticancer drug via the formation of amide and azo bonds [168, 169]. In addition, a cationic anticancer drug such as doxorubicin hydrochloride has been effectively conjugated to negatively charged Fe_3O_4 nanoparticles through electrostatic forces [52, 94, 97]. Both electrostatic as well covalently conjugated drug molecules are used to release under the influence of temperature, light, pH, ultrasound and magnetic field [3, 170–173]. However, the drug delivery systems generated by covalent approaches give better stability to the drug molecules as well as their controlled release than those formed by noncovalent interaction.

Among the various magnetic nanoparticles, Fe_3O_4 nanoparticles have been extensively examined for their uses in hyperthermia therapy [38, 97, 174]. Barick and coworkers described the uses of different surface-functionalized Fe_3O_4 nanoparticles as a heating source for magnetic hyperthermia [38, 48–52, 93, 97, 174]. It is well reported that the heating efficiency of these nanoparticles relies on the concentration of particles, magnitude of applied AC magnetic field and frequency along with the physical parameters such nanoparticle size, size distribution and their magnetic moment [38]. Further, the heat produced during magnetic hyperthermia through the relaxation loss process can also increase the toxicity of anticancer drugs in some cancer cells that are otherwise resistant to drugs. In addition to drug delivery and hyperthermia therapy, Fe_3O_4 magnetic nanoparticles are also investigated as MRI contrast agents and several preparations have been permitted for clinical use [86, 174, 175]. Similarly, Au nanoparticles are also made to be used as a contrast agent for computed tomography (CT) imaging of cancer owing to its various benefits over conventional CT contrast agents based on iodine [176]. Further, multimodal imaging is required for the precise diagnosis of disease. In this aspect, Au nanoparticles are used for dual-mode CT/MR imaging applications [177].

14.5.2 Tissue Engineering Applications

Tissue engineering is an integrative research field devoted to the development or identification of appropriate materials to facilitate cell behavior and tissue function. The surface-functionalized NBMs play an essential constituent of tissue engineering. They are intended to grant direct mechanical interactions with cellular components and cell surface receptors, and served as temporary extra-cellular matrices (ECMs) for cell growth and eventual tissue regeneration. The main intention of tissue engineering is to reinstate tissue and organ functions with nominal host rejection. Further, the materials used for tissue engineering should be resorbed and replaced over time. Thus, the development of biomaterials with desired surface functionality is important for tissue regeneration by efficient transferring of therapeutic molecules and cell populations. Among others, regeneration of cartilage and bone has received a great deal of interest [178]. A broad range of inorganic materials similar in composition to bone such as β-tricalcium phosphate (TCP), calcium phosphate ceramics (hydroxyapatite (HAP) and biphasic calcium phosphate (BCP)), bioactive glasses and metal-based biomaterials are used as scaffolds for regeneration [179–182]. The three major steps involved in tissue engineering are transplantation of isolated bone cells (osteogenic) at the defected site, introduction of isolated tissue producing molecules and designing of 3D scaffold [183]. These scaffolds are temporary porous structures for boosting new tissue generation and provide support to cell growth during the regeneration process [184]. The well-designed 3D scaffold with the capability to imitate the ECM of bone promotes the generation of new tissue by enhancing cell adhesion and proliferation, which is dependent on the porosity, biomechanical and physical properties of scaffolds [185]. The biomaterial used for regeneration should have sufficient mechanical strength and it should be degradable at an equivalent rate to the growth of new tissue at the implementation site. The synthetic biomaterials are smart as they can be reproduced with the ability to manage structure, mechanical strength and degradation rate. However, the naturally produced materials have certain advantages due to the presence of embedded functional and structural molecules as well as favorable immune recognition by a beneficiary.

Recently, NBMs have been used in tissue engineering for enhanced mechanical and biological performances. The advantage of using NBMs in tissue engineering is mainly associated with its ultra-small size and huge surface-to-volume ratio. Thus, NBMs with specific surface characteristics can enhance cellular uptake by easily penetrating through cell membranes. Further, they can also impersonate the natural nanometer-sized ECM components of tissues. Among others, hydroxyapatite nanoparticles (HANPs) have been widely used in different forms and shapes as an ideal synthetic material in bone tissue engineering [186]. Various HANP-based composite materials having hydrogels and polymers have been developed for the revival of different parts of the bone systems, particularly those under major mechanical tension [187, 188]. Maji and Dasgupta [189] developed a nano-β-TCP integrated gelatin-chitosan-based composite matrix for bone renewal. Chen et al. [190] reported that biphasic calcium phosphate nanoparticles/collagen porous composite

loaded with dexamethasone have a strong affinity for bone tissue. Wang et al. [191] demonstrated that combining stem cells with nanostructured calcium phosphate biomaterials accelerates bone regeneration.

Other than calcium phosphate ceramics, Au, TiO_2, ZnO and Fe_3O_4 nanoparticles have also been used to improve the rate of cell growth for bone and cardiac tissue revival. It has been reported that Au nanoparticles support osteogenic differentiation of an osteoblast precursor cell as well as promote neuronal differentiation and maturation [192, 193]. Au nanoparticles are also found to control osteoclast construction from hematopoietic cells while granting protection to mitochondrial malfunction in osteoblastic cells [194, 195]. Kumar et al. [196] developed nano-TiO_2-doped chitosan scaffold and observed that chitosan and nano-TiO_2 interaction makes it highly porous and brittle for bone tissue engineering. Liu et al. [197] developed a scaffold where TiO_2 nanoparticles were 3D-printed with PLGA polymer to precisely map the nanostructured roughness of bone. Biocompatible hybrid chitosan-PEG-nanohydroxyapatite-ZnO composite scaffolds were also prepared by Bhowmick et al. [199] for the proliferation of osteoblast-like MG-63 cells [198]. Further, magnetite cationic liposomes (MCLs) were used to construct 3D tissue by magnetic force-based tissue engineering without scaffolds.

14.5.3 Devices and Implants

Biomaterials have been widely used since long in dental fillings and intraocular lens replacement. However, the recent developments in cellular and molecular biology, chemical sciences and engineering offer ample opportunity for their clinical use. Biomaterials are also used to physically swap hard or soft tissues that suffered damage or get destroyed in the course of some pathological process. Sometimes, body tissue undergoes infection, fracture and specific diseases which create disfigurement, pain or loss of specific function. Under these conditions, damaged tissue is used to be replaced (repair) with biomaterials. Among others, NBMs' implants and devices are extensively used in dental, orthopedic, ophthalmic and cardiovascular applications. The NBMs used for the above purposes should be biocompatible, resistant to corrosive biological conditions, sufficient mechanical strength and wear resistance. The commonly used biomaterials in medical devices and implants are metals, polymers, ceramics and composites. Metals are mostly exploited for load-bearing implants such as screws and wires to artificial joints for knees, hips and shoulders. Different metals as well as their alloys are also employed as implants in dental, maxillofacial and cardiovascular surgery. The most commonly used implants are silver, gold, stainless steels, titanium and titanium alloys. Various polymers such as polyethylene, polypropylene, polyethylene terephthalate, polyamides, polytetrafluoroethylene, polyesters, polyurethanes, poly(vinyl chloride) and PMMA are used in different medical applications varying from facial prostheses to tracheal tubes, from liver to kidney parts to heart components, and from hip to dentures and knee joints. Ceramic-based materials (zirconia, alumina and calcium phosphate) and composite

materials are used as restorative materials in dental applications. The composite materials have also found wide applications in bone repair and joint replacement. When these biomaterials are placed in the human body, the tissue responds toward the devices/implant in several ways depending on the material properties [200, 201].

The employment of implantable devices is an essential part of medical care. In the clinical field, the biomaterial is mostly used to prepare medical devices to safely reinstate a part or a function of the body in an economically and physiologically tolerable way [202]. The use of Ag nanoparticle-based antimicrobials coatings can endorse a long-lasting antibacterial effect on medical devices [203]. Kose et al. [204] recently developed Ag nanopowder coating which significantly reduces the bacterial colonization on coated titanium implants. In addition, the manufacturing of auto-sanitizing products for healthcare applications is extremely required to prevent infections associated with health care [205]. The use of NBMs as scaffolds can help in creating a constructive interaction between native bone and orthopedic implants. Moreover, nanotechnology has the capability to modernize medical diagnostics as well as orthopedic surgery [206].

14.6 Summary and Future Prospects

The unique physiochemical and biological properties of NBMs provide a strong platform for the development of nanotechnology-based novel biomedical applications. Among others, organic (polymer, hydrogels) and inorganic (Ag, Au, SiO_2, ZnO, TiO_2, Fe_3O_4, hydroxyapatite and LDH) as well as their hybrid NBMs have been fruitfully used in drug delivery, diagnosis, tissue engineering, and medical implants and devices. The synthesis methodology, structural and surface features of NBMs, and their interactions with the complex biological systems decide the performance of NBMs. In order to achieve better efficacy, surface modification of NBMs with biocompatible molecules having stimuli-responsive behavior, targeting and imaging capability is highly essential. Surface modification not only provides long-term colloidal stability, targeting and imaging capability to NBMs but also prevents the non-specific adsorption of proteins, which are crucial for the delivery of therapeutic molecules. At the same time, surface modification helps in direct biological and mechanical interactions of NBMs with cellular components and cell surface receptors, and serves as temporary ECMs for cell growth and eventual tissue regeneration.

In view of ongoing research activities across the globe, it may be expected that human beings will significantly benefit from nanotechnology and NBMs in near future. However, the effect of nanotoxicity on human health and the environment should be thoroughly understood. The biodistribution and release kinetics of NBMs used for therapeutic and diagnostic applications should also be investigated in detail. Further, complete characterization and optimization of NBMs properties as well as a thorough understanding of their interaction with biological systems is required.

References

1. Kalita SJ (2008) Nanostructured biomaterials. In: Seal S (ed) Functional nanostructures: nanostructure science and technology. Springer, New York, NY, pp 168–219
2. Helmus MN, Gibbons DF, Cebon D (2008) Biocompatibility: meeting a key functional requirement of next-generation medical devices. Toxicol Pathol 36:70–80
3. Chandra S, Barick KC, Bahadur D (2011) Oxide and hybrid nanostructures for therapeutic applications. Adv Drug Deliv Rev 63:1267–1281
4. Chang H, Wang Y (2011) Cell responses to surface and architecture of tissue engineering scaffolds. In: Eberli D (ed) Regenerative medicine and tissue engineering-cells and biomaterials, IntechOpen. https://doi.org/10.5772/21983
5. Xu LC, Siedlecki CA (2007) Effects of surface wettability and contact time on protein adhesion to biomaterial surfaces. Biomaterials 28:3273–3283
6. Thevenot P, Hu W, Tang L (2008) Surface chemistry influence implant biocompatibility. Curr Top Med Chem 8:270–280
7. Wang Y (2016) Bioadaptability: an innovative concept for biomaterials. J Mater Sci Technol 32:801–809
8. Kasemo B, Lausmaa J (1994) Material-tissue interfaces: the role of surface properties and processes. Environ Health Perspect 102:41–45
9. Mout R, Moyano DF, Rana S, Rotello VM (2012) Surface functionalization of nanoparticles for nanomedicine. Chem Soc Rev 41:2539–2544
10. Aggarwal P, Hall JB, McLeland CB, Dobrovolskaia MA, McNeil SE (2009) Nanoparticle interaction with plasma proteins as it relates to particle biodistribution, biocompatibility and therapeutic efficacy. Adv Drug Deliv Rev 61:428–437
11. Sun C, Du K, Fang C, Bhattarai N, Veiseh O, Kievit F, Stephen Z, Lee D, Ellenbogen RG, Ratner B, Zhang M (2010) PEG-mediated synthesis of highly dispersive multifunctional superparamagnetic nanoparticles: their physicochemical properties and function in vivo. ACS Nano 4:2402–2410
12. Torchilin VP, Trubetskoy VS (1995) Which polymers can make nanoparticulate drug carriers long-circulating? Adv Drug Deliv Rev 16:141–155
13. Wang YX, Robertson JL, Spillman WB Jr, Claus RO (2004) Effects of the chemical structure and the surface properties of polymeric biomaterials on their biocompatibility. Pharm Res 21:1362–1373
14. Anderson JM (2001) Biological responses to materials. Annual Rev Mater Res 31:81–110
15. Gad SC (2013) Standards and methods for assessing the safety and biocompatibility of biomaterials. In: Jaffe M, Hammond W, Tolias P, Arinzeh T (eds) Characterization of biomaterials, Woodhead Publishing, Cambridge, UK, pp 285–306
16. Muller U (2008) In vitro biocompatibility testing of biomaterials and medical devices. Med Device Technol 19:32–34
17. Jung F, Braune S, Lendlein A (2013) Haemocompatibility testing of biomaterials using human platelets, clinical hemorheology and microcirculation. Clin Hemorheol Microcirc 53:97–115
18. Park JB, Bronzino JD (2002) Biomaterials: principles and applications. CRC Press
19. Ratner BD, Hoffman AS, Schoen FJ, Lemwsons JE (eds) (1996) Biomaterials science. Academic Press, Orlando
20. Jiang T, Abdel-Fattah WI, Laurencin CT (2006) In vitro evaluation of chitosan/poly (lactic acidglycolic acid) sintered microsphere scaffolds for bone tissue engineering. Biomaterials 27:4894–4903
21. Dias GJ, Peplow PV, Teixeira F (2003) Osseous regeneration in the presence of oxidized cellulose and collagen. J Mater Sci Mater Med 14:739–745
22. Saxena IM, Brown RM Jr (2005) Cellulose biosynthesis: current views and evolving concepts. Ann Bot 96:9–21
23. Imai T, Watanabe T, Yui T, Sugiyama J (2003) The directionality of chitin biosynthesis: a revisit. Biochem J 374:755–760

24. Dutta PK, Dutta J, Tripathi VS (2004) Chitin and chitosan: chemistry, properties and applications. J Sci Ind Res 63:20–31
25. Pear JR, Kawagoe Y, Schreckengost WE, Delmer DP, Stalker DM (1996) Higher plants contain homologs of the bacterial cell a genes encoding the catalytic subunit of cellulose synthase. Proc Natl Acad Sci 93:12637–12642
26. Ahmed EM, Aggor FS, Awad AM, El-Aref AT (2013) An innovative method for preparation of nanometal hydroxide superabsorbent hydrogel. Carbohydr Polym 91:693–698
27. Ulijn RV, Bibi N, Jayawarna V, Thornton PD, Todd SJ, Mart RJ, Smith AM, Gough JE (2007) Bioresponsive hydrogels. Mater Today 10:40–48
28. Hoare T, Pelton R (2004) Highly pH and temperature responsive microgels functionalized with vinylacetic acid. Macromolecules 37:2544–2550
29. Hendrickson GR, Lyon LA (2009) Bioresponsive hydrogels for sensing applications. Soft Matter 5:29–35
30. Neamtu I, Rusu AG, Diaconu A, Nita LE, Chiriac AP (2017) Basic concepts and recent advances in nanogels as carriers for medical applications. J Drug Del 24:539–557
31. Nagavarma BVN, Yadav HKS, Ayaz A, Vasudha LS, Shivakumar HG (2012) Different techniques for preparation of polymeric nanoparticles-a review. Asian J Pharm Clin Res 5:16–23
32. Zhang G, Niu A, Peng S, Jiang M, Tu Y, Li M, Wu C (2001) Formation of novel polymeric nanoparticles. Acc Chem Res 34:249–256
33. Anton N, Benoit JP, Saulnier P (2008) Design and production of nanoparticles formulated from nano-emulsion templates-a review. J Control Rel 128:185–199
34. Thickett SC, Gilbert RG (2007) Emulsion polymerization: state of the art in kinetics and mechanisms. Polymer 48:6965–6991
35. Hennink WE, van Nostrum CF (2002) Novel crosslinking methods to design hydrogels. Adv Drug Del Rev 54:13–36
36. Hamidi M, Azadi A, Rafiei P (2018) Hydrogel nanoparticles in drug delivery. Adv Drug Del Rev 60:1638–1649
37. Priya MV, Sabitha M, Jayakumar R (2016) Colloidal chitin nanogels: A plethora of applications under one shell. Carbohydr Polym 136:609–617
38. Barick KC, Hassan PA (2012) Amino acid passivated Fe_3O_4 colloidal nanoparticles for thermal therapy. J Colloids Interface Sci 369:96–102
39. Cheng X, Sun R, Yin L, Chai Z, Shi H, Gao M (2017) Light-triggered assembly of gold nanoparticles for photothermal therapy and photoacoustic imaging of tumors in vivo. Adv Mater 29:1604894
40. Gao JH, Chen K, Xie RG, Xie J, Lee S, Cheng Z, Peng XG, Chen XY (2010) Ultrasmall near-infrared non-cadmium quantum dots for in vivo tumor imaging. Small 6:256–261
41. Nam J, Won N, Bang J, Jin H, Park J, Jung S, Jung S, Park Y, Kim S (2013) Surface engineering of inorganic nanoparticles for imaging and therapy. Adv Drug Del Rev 65:622–648
42. Bobo D, Robinson KJ, Islam J, Thurecht KJ, Corrie SR (2016) Nanoparticle-based medicines: a review of FDA-approved materials and clinical trials to date. Pharm Res 33:2373–2387
43. Pombo GK, Zarschler K, Barbaro L, Barreto JA, O'Malley W, Spiccia L, Stephan H, Graham B (2014) Zwitterionic-coated "stealth" nanoparticles for biomedical applications: recent advances in countering biomolecular corona formation and uptake by the mononuclear phagocyte system. Small 10:2516–2529
44. Gupta J, Barick KC, Bahadur D (2011) Defect mediated photocatalytic activity in shape-controlled ZnO nanostructures. J Alloys Comp 509:6725–6730
45. Verma G, Barick KC, Manoj N, Sahu AK, Hassan PA (2013) Rod-like micelle templated synthesis of porous hydroxyapatite. Ceramics Intern 39:8995–9002
46. Massart R (1981) Preparation of aqueous magnetic liquids in alkaline and acidic media. IEEE Trans Magn 17(2):1247–1248
47. Dadfar SM, Roemhild K, Drude NI, von Stillfried S, Knüchel R, Kiessling F, Lammers T (2019) Iron oxide nanoparticles: diagnostic, therapeutic and theranostic applications. Adv Drug Del Rev 138:302–325

48. Gawali SL, Barick BK, Barick KC, Hassan PA (2017) Effect of sugar alcohol on colloidal stabilization of magnetic nanoparticles for hyperthermia and drug delivery applications. J Alloys Comp 725:800–806
49. Rana S, Jadhav NV, Barick KC, Pandey BN, Hassan PA (2014) Polyaniline shell cross-linked Fe_3O_4 magnetic nanoparticles for heat activated killing of cancer cells. Dalton Trans 43:12263–12271
50. Rana S, Barick KC, Hassan PA (2015) Stimuli responsive carboxyl PEGylated Fe_3O_4 nanoparticles for therapeutic applications. J Nanofluids 4:421–427
51. Majeed J, Barick KC, Shetake NG, Pandey BN, Hassan PA, Tyagi AK (2015) Water-dispersible polyphosphate grafted Fe_3O_4 nanomagnets for cancer therapy. RSC Adv 5:86754–86762
52. Nigam S, Barick KC, Bahadur D (2011) Development of citrate-stabilized Fe_3O_4 nanoparticles: conjugation and release of doxorubicin for therapeutic applications. J Magn Magn Mater 323:237–243
53. Dubey RS, Rajesh YBRD, More MA (2015) Synthesis and characterization of sio_2 nanoparticles via sol-gel method for industrial applications. Mater Today Proc 2:3575–3579
54. Bessekhouad Y, Robert D, Weber JV (2003) Preparation of TiO_2 nanoparticles by sol-gel route Int. J Photoenergy 5:153–158
55. Gao R, Hao Y, Zhang L, Cui X, Liu D, Zhang M, Tang Y, Zheng Y (2016) A facile method for protein imprinting on directly carboxyl-functionalized magnetic nanoparticles using non-covalent template immobilization strategy. Chem Eng J 284:139–148
56. Sharma N, Kumar S, Kumar J (2018) Synthesis and structural properties of ZnO doped nanoparticles prepared by hydrothermal method. Integrated Ferroelect 186:115–119
57. Qiu H, Cui B, Li G, Yang J, Peng H, Wang Y, Li N, Gao R, Chang Z, Wang Y (2014) Novel Fe_3O_4@ZnO@$mSiO_2$ nanocarrier for targeted drug delivery and controllable release with microwave irradiation. J Phys Chem C 11:14929–14937
58. Sun Y, Xia Y (2002) Shape-controlled synthesis of gold and silver nanoparticles 298:2176–2179
59. Barick KC, Aslam M, Dravid VP, Bahadur D (2008) Self-aggregation and assembly of size-tunable transition metal doped ZnO nanocrystals. J Phys Chem C 112:15163–15170
60. Barick KC, Aslam M, Prasad PV, Dravid VP, Bahadur D (2009) Nanoscale assembly of amine functionalized colloidal iron oxide. J Magn Magn Mater 321:1529–1532
61. Zhang D, Tong Z, Li S, Zhang X, Ying A (2008) Fabrication and characterization of hollow Fe_3O_4 nanospheres in a microemulsion. Mater Lett 62:4053–4055
62. Lee Y, Lee J, Bae CJ, Park JG, Noh HJ, Park JH, Hyeon T (2005) Large-scale synthesis of uniform and crystalline magnetite nanoparticles using reverse micelles as nanoreactors under reflux conditions. Adv Funct Mater 15:503–509
63. Bose S, Saha SK (2003) Synthesis and characterization of hydroxyapatite nanopowders by emulsion technique. Chem Mater 15:4464–4469
64. Barick KC, Ekta SL, Gawali A, Sarkar A, Kunwar KI, Priyadarsini PA (2016) Hassan, Pluronic stabilized Fe_3O_4 magnetic nanoparticles for intracellular delivery of curcumin. RSC Adv 6:98674–98681
65. Ge R, Li X, Lin M, Wang D, Li S, Liu S, Tang Q, Liu Y, Jiang J, Liu L, Sun H, Zhang H, Yang B (2016) Fe_3O_4@polydopamine composite theranostic superparticles employing preassembled fe_3o_4 nanoparticles as the core. ACS Appl Mater Interfaces 8:22942–22952
66. Hwang J, Lee E, Kim J, Seo Y, Lee KH, Hong JW, Gilad AA, Park H, Choi J (2016) Effective delivery of immunosuppressive drug molecules by silica coated iron oxide nanoparticles. Colloids Surf B 142:290–296
67. Lin F, Doong R (2017) Catalytic nanoreactors of Au@Fe_3O_4 yolk-shell nanostructures with various Au sizes for efficient nitroarene reduction. J Phys Chem C 121:7844–7853
68. Hyeon T, Lee SS, Park J, Chung Y, Na HB (2001) Synthesis of highly crystalline and monodisperse maghemite nanocrystallites without a size-selection process. J Am Chem Soc 123:12798–12801

69. Sun SH, Zeng H (2002) Size-controlled synthesis of magnetite nanoparticles. J Am Chem Soc 124:8204–8205
70. Liu X, Swihart MT (2013) A general single-pot heating method for morphology, size and luminescence-controllable synthesis of colloidal ZnO nanocrystals. Nanoscale 5:8029–8036
71. Kumar RV, Koltypin Y, Xu XN, Yeshurun Y, Gedanken A, Felner I (2001) Fabrication of magnetite nanorods by ultrasound irradiation. J Appl Phys 89:6324–6328
72. Okitsu K, Ashokkumar M, Grieser F (2005) Sonochemical synthesis of gold nanoparticles: effects of ultrasound frequency. J Phys Chem B 109:20673–20675
73. Mukh-Qasem RA, Gedanken A (2005) Sonochemical synthesis of stable hydrosol of Fe_3O_4 nanoparticles. J Colloid Interface Sci 284:489–494
74. Zhanjiang Z, Jinpei L (2012) Synthesis and characterization of silver nanoparticles by a sonochemical method. Rare Metal Mater Eng 41:1700–1705
75. Jordan J, Jacob KI, Tannenbaum R, Sharaf MA, Jasiuk I (2005) Experimental trends in polymer nanocomposites—a review. Mater Sci Eng A 393:1–11
76. Liu Y, Meng H, Konst S, Sarmiento R, Rajachar R, Lee BP (2014) Injectable dopamine-modified poly(ethylene glycol) nanocomposite hydrogel with enhanced adhesive property and bioactivity. ACS Appl Mater Interfaces 6:16982–16992
77. Skelton S, Bostwick M, O'Connor K, Konst S, Casey S, Lee BP (2013) Biomimetic adhesive containing nanocomposite hydrogel with enhanced materials properties. Soft Matter 9:3825–3833
78. Marcelo G, López-González M, Mendicuti F, Tarazona MP, Valiente M (2014) Poly(N-isopropylacrylamide)/gold hybrid hydrogels prepared by catechol redox chemistry. Characterization and smart tunable catalytic activity. Macromolecules 47:6028–6036
79. Satarkar NS, Biswal D, Hilt JZ (2010) Hydrogel nanocomposites: a review of applications as remote controlled biomaterials. Soft Matter 6:2364–2371
80. Frachini ECG, Petri DFS (2019) Magneto-responsive hydrogels: preparation, characterization, biotechnological and environmental applications. J Braz Chem Soc 30:2010–2028
81. Vasti C, Pfaffen V, Ambroggio E, Galiano MR, Rojas R, Giacomelli CE (2017) A systematic approach to the synthesis of LDH nanoparticles by response surface methodology. Appl Clay Sci 137:151–159
82. Liang H, Meng F, Cabán-Acevedo M, Li L, Forticaux A, Xiu L, Wang Z, Jin S (2015) Hydrothermal continuous flow synthesis and exfoliation of NiCo layered double hydroxide nanosheets for enhanced oxygen evolution catalysis. Nano Lett 15:1421–1427
83. Huang P-P, Cao C-Y, Wei F, Sun Y-B, Song W-G (2015) MgAl layered double hydroxides with chloride and carbonate ions as interlayer anions for removal of arsenic and fluoride ions in water. RSC Adv 5:10412–10417
84. Lu X, Zhao C (2015) Electrodeposition of hierarchically structured three-dimensional nickel–iron electrodes for efficient oxygen evolution at high current densities. Nat Commun 6:6616
85. Jaśkaniec S, Hobbs C, Seral-Ascaso A, Coelho J, Browne MP, Tyndall D, Sasaki T, Nicolosi V (2018) Low-temperature synthesis and investigation into the formation mechanism of high quality Ni-Fe layered double hydroxides hexagonal platelets. Sci Rep 8:4179
86. Laurent S, Forge D, Port M, Roch A, Robic C, Elst LV, Muller RN (2008) Magnetic iron oxide nanoparticles: synthesis, stabilization, vectorization, physicochemical characterizations and biological applications. Chem Rev 108:2064–2110
87. Barick KC, Rana S, Hassan PA (2015) Surface modification of magnetic nanoparticles for therapeutic applications. J Surf Sci Technol 31:60–68
88. Ding J, Tao K, Li J, Song S, Sun K (2010) Cell-specific cytotoxicity of dextran-stabilized magnetite nanoparticles. Coll Surf B: Biointerf 79:184–190
89. Nel A, Xia T, Mädler L, Li N (2006) Toxic potential of materials at the nanolevel. Science 311:622–629
90. Shen L, Li B, Qiao Y (2008) Fe_3O_4 nanoparticles in targeted drug/gene delivery systems. Materials (Basel) 11:324
91. Li L, Gu W, Chen J, Chen W, Xu ZP (2014) Co-delivery of siRNAs and anti-cancer drugs using layered double hydroxide nanoparticles. Biomater 35:3331–3339

92. An P, Zuo F, Wu YP, Zhang JH, Zheng ZH, Ding XB, Peng YX (2012) Fast synthesis of dopamine coated Fe_3O_4 nanoparticles through ligand-exchange method. Chinese Chem Lett 23:1099–1102
93. Dutta B, Shetake NG, Barick BK, Barick KC, Pandey BN, Priyadarsini KI, Hassan PA (2018) pH sensitive surfactant-stabilized Fe_3O_4 magnetic nanocarriers for dual drug delivery. Colloids Surf B 162:163–171
94. Verma G, Barick KC, Shetake NG, Pandey BN, Hassan PA (2016) Citrate-functionalized hydroxyapatite nanoparticles for pH-responsive drug delivery. RSC Adv 6:77968–77976
95. Gawali SL, Dutta B, Barick KC, Hassan PA (2017) Surface engineering of iron oxide nanoparticles for cancer therapy. Biomed Res J 4:49–66
96. Verma G, Shetake NG, Barick KC, Pandey BN, Hassan PA, Priyadarsini KI (2018) Covalent immobilization of doxorubicin in glycine functionalized hydroxyapatite nanoparticles for pH-responsive release. New J Chem 42:6283–6292
97. Sharma P, Rana S, Barick KC, Kumar C, Salunke HG, Hassan PA (2014) Biocompatible phosphate anchored Fe_3O_4 nanocarriers for drug delivery and hyperthermia. New J Chem 38:5500–5508
98. Gorbatsevich OB, Kholodkov DN, Kurkin TS, Malakhova YN, Strel'tsov DR, Buzin AI, Kazakova VV, Muzafarov AM (2017) Synthesis and properties of water-soluble silica nanoparticles. Russ Chem Bull 66:409–417
99. Tang X, Choo ESG, Li L, Ding J, Xue J (2009) One-Pot Synthesis of Water-stable ZnO nanoparticles via a polyol hydrolysis route and their cell labeling applications. Langmuir 25:5271–5275
100. Khalkhali M, Rostamizadeh K, Sadighian S, Khoeini F, Naghibi M, Hamidi M (2015) The impact of polymer coatings on magnetite nanoparticles performance as MRI contrast agents: a comparative study. DARU J Pharm Sci 23:45
101. Labhasetwar V, Song C, Humphrey W, Shebuski R, Levy RJ (1998) Arterial uptake of biodegradable nanoparticles: effect of surface modifications. J Pharm Sci 87:1229–1234
102. Dutta B, Shetake NG, Gawali SL, Barick BK, Barick KC, Babu PD, Pandey BN, Priyadarsini KI, Hassan PA (2018) PEG mediated shape-selective synthesis of cubic Fe_3O_4 nanoparticles for cancer therapeutics. J Alloys Comp 737:347–355
103. Na HB, Lee IS, Seo H, Park YI, Lee JH, Kim S-W, Hyeon T (2007) Versatile PEG-derivatized phosphine oxide ligands for water-dispersible metal oxide nanocrystals. Chem Commun 5167–5169
104. Rezayan AH, Mousavi M, Kheirjou S, Amoabediny G, Ardestani MS, Mohammadnejad J (2016) Monodisperse magnetite (Fe_3O_4) nanoparticles modified with water soluble polymers for the diagnosis of breast cancer by MRI method. J Magn Magn Mater 420:210–217
105. Rahme K, Nolan MT, Doody T, McGlacken GP, Morris MA, O'Driscoll C, Holmes JD (2013) Highly stable PEGylated gold nanoparticles in water: applications in biology and catalysis. RSC Adv 3:21016–21024
106. Li S-D, Huang L (2010) Stealth nanoparticles: high density but sheddable PEG is a key for tumor targeting. J Control Release 145:178–181
107. Kayal S, Ramanujan RV (2010) Doxorubicin loaded PVA coated iron oxide nanoparticles for targeted drug delivery. Mater Sci Eng C 30:484–490
108. Wang R, Degirmenci V, Xin H, Li Y, Wang L, Chen J, Hu X, Zhang D (2018) PEI-coated Fe_3O_4 nanoparticles enable efficient delivery of therapeutic siRNA targeting REST into glioblastoma cells. Int J Mol Sci 19:2230
109. Palui G, Aldeek F, Wang W, Mattoussi H (2015) Strategies for interfacing inorganic nanocrystals with biological systems based on polymer-coating. Chem Soc Rev 44:193–227
110. Padwal P, Bandyopadhyaya R, Mehra S (2014) Polyacrylic acid-coated iron oxide nanoparticles for targeting drug resistance in mycobacteria. Langmuir 30:15266–15276
111. Yu F, Yang VC (2010) Size-tunable synthesis of stable superparamagnetic iron oxide nanoparticles for potential biomedical applications. J Biomed Mater Res A 92:1468–1475
112. Singh S, Barick KC, Bahadur D (2011) Surface engineered magnetic nanoparticles for removal of toxic metal ions and bacterial pathogens. J Hazard Mater 192:1539–1547

113. Gonçalves LC, Seabra AB, Pelegrino MT, de Araujo DR, Bernardesc JS, Hadda PS (2017) Superparamagnetic iron oxide nanoparticles dispersed in Pluronic F127 hydrogel: potential uses in topical applications. RSC Adv 7:14496–14503
114. Hofmann A, Thierbach S, Semisch A, Hartwig A, Taupitz M, Rühl E, Graf C (2010) Highly monodisperse water-dispersable iron oxide anoparticles for biomedical applications. J Mater Chem 20:7842–7853
115. ten Hove JB, Schijven LMI, Wang J, Velders AH (2018) Size-controlled and water-soluble gold nanoparticles using UV-induced ligand exchange and phase transfer. Chem Commun 54:13355–13358
116. Swami A, Kumar A, Sastry M (2003) Formation of water-dispersible gold nanoparticles using a technique based on surface-bound interdigitated bilayers. Langmuir 19:1168–1172
117. Moussodia R-O, Balan L, Merlin C, Mustin C, Schneider R (2010) Biocompatible and stable ZnO quantum dots generated by functionalization with siloxane-core PAMAM dendrons. J Mater Chem 20:1147–1155
118. Iqbal MZ, Ma X, Chen T (2015) Silica-coated super-paramagnetic iron oxide nanoparticles (SPIONPs): a new type contrast agent of T1 magnetic resonance imaging (MRI). J Mater Chem B 3:5172–5518
119. Lai CW, Wang YH, Lai CH, Yang MJ, Chen CY, Chou PT, Chan CS, Chi Y, Chen YC, Hsia JK (2008) Iridium-complex-functionalized Fe_3O_4/SiO_2 core/shell nanoparticles: a facile three-in-one system in magnetic resonance imaging, luminescence imaging, and photodynamic therapy. Small 4:218–224
120. Xu Z, Hou Y, Sun S (2007) Magnetic core/shell Fe_3O_4/Au and Fe_3O_4/Au/Ag nanoparticles with tunable plasmonic properties. J Am Chem Soc 129:8698–8699
121. Sapsford KE, Algar WR, Berti L, Gemmill KB, Casey BJ, Oh E, Stewart MH, Medintz IL (2013) Functionalizing nanoparticles with biological molecules: developing chemistries that facilitate nanotechnology. Chem Rev 113:1904–2074
122. Rana S, Shetake NG, Barick KC, Pandey BN, Salunke HG, Hassan PA (2016) Folic acid conjugated Fe_3O_4 magnetic nanoparticles for targeted delivery of doxorubicin. Dalton Trans 45:17401–17408
123. Dixit V, den Bossche JV, Sherman DM, Thompson DH, Andres RP (2006) Synthesis and grafting of thioctic acid-PEG-folate conjugates onto Au nanoparticles for selective targeting of folate receptor-positive tumor cells. Bioconjug Chem 17:603–609
124. Xuan M, Shao J, Dai L, He Q, Li J (2015) Macrophage cell membrane camouflaged mesoporous silica nanocapsules for in vivo cancer therapy. Adv Healthcare Mater 4:1645–1652
125. Gao W, Hu C-MJ, Fang RH, Luk BT, Su J, Zhang L (2013) Surface functionalization of gold nanoparticles with red blood cell membranes. Adv Mater 25:3549–3553
126. Rao L, Bu L-L, Xu J-H, Cai B, Yu G-T, Yu X, He Z, Huang Q, Li A, Guo S-S, Zhang W-F, Liu W, Sun Z-J, Wang H, Wang T-H, Zhao X-Z (2015) Red blood cell membrane as a biomimetic nanocoating for prolonged circulation time and reduced accelerated blood clearance. Small 11:6225–6236
127. Miao XM, Ning X, Li ZB, Cheng ZY (2016) Sensitive detection of miRNA by using hybridization chain reaction coupled with positively charged gold nanoparticles. Sci Rep 6:32358
128. Vincent A, Babu S, Heckert E, Dowding J, Hirst SM, Inerbaev TM, Self WT, Reilly CM, Masunov AE, Rahman TS, Seal S (2009) Protonated nanoparticle surface governing ligand tethering and cellular targeting. ACS Nano 3:1203–1211
129. El-Say KM, El-Sawy HS (2017) Polymeric nanoparticles: Promising platform for drug delivery]. Intern J Pharm 528:675–691
130. Hamidi M, Azadi A, Rafiei P (2008) Hydrogel nanoparticles in drug delivery. Adv Drug Del Rev 60:1638–1649
131. Wang XQ, Zhang Q (2012) PH-sensitive polymeric nanoparticles to improve oral bioavailability of peptide/protein drugs and poorly water-soluble drugs. Eur J Pharm Biopharm 82:219–229

132. Wilson B, Samanta MK, Santhi K, Kumar KPS, Ramasamy M, Suresh B (2010) Chitosan nanoparticles as a new delivery system for the anti-Alzheimer drug tacrine. Nanomed Nanotechnol Biol Med 6:144–152
133. Karatas H, Aktas Y, Gursoy-Ozdemir Y, Bodur E, Yemisci M, Caban S, Vural A, Pinarbasli O, Capan Y, Fernandez-Megia E, Novoa-Carballal R, Riguera R, Andrieux K, Couvreur P, Dalkara T (2009) A nanomedicine transports a peptide caspase-3 inhibitor across the blood-brain barrier and provides neuroprotection. J Neurosci 29:13761–13769
134. Liu M, Li H, Luo G, Liu Q, Wang Y (2008) Pharmacokinetics and biodistribution of surface modification polymeric nanoparticles. Arch Pharm Res 31:547–554
135. Patel T, Zhou J, Piepmeier JM, Saltzman WM (2012) Polymeric nanoparticles for drug delivery to the central nervous system. Adv Drug Deliv Rev 64:701–705
136. Ashley CE, Carnes EC, Phillips GK, Padilla D, Durfee PN, Brown PA, Hanna TN, Liu J, Phillips B, Carter MB, Carroll NJ, Jiang X, Dunphy DR, Willman CL, Petsev DN, Evans DG, Parikh AN, Chackerian B, Wharton W, Peabody DS, Brinker CJ (2011) The targeted delivery of multicomponent cargos to cancer cells by nanoporous particle-supported lipid bilayers. Nat Mater 10:389–397
137. Gutowska A, Bark JS, Kwon IC, Bae YH, Kim SW (1997) Squeezing hydrogels for controlled oral drug delivery. J Control Rel 48:141–148
138. Park H, Park K, Kim D (2006) Preparation and swelling behavior of chitosan-based superporous hydrogels for gastric retention application. J Biomed Mater Res A 76:144–150
139. Cohen S, Lobel E, Trevgoda A, Peled T (1997) A novel in situ-forming ophthalmic drug delivery system from alginates undergoing gelation in the eye. J Control Rel 44:201–208
140. Wang YY, Hong CT, Chiu WT, Fang JY (2001) In vitro and in vivo evaluations of topically applied capsaicin and nonivamide from hydro gels. Int J Pharm 224:89–104
141. Fang J-Y, Huang Y-B, Lin H-H, Tsai Y-H (1998) Transdermal iontophoresis of sodium nonivamide acetate. IV. Effect of polymer formulations. Int J Pharm 173:127–140
142. Molina M, Giulbudagian M, Calderón M (2014) Positively charged thermoresponsive nanogels for anticancer drug delivery. Macromol Chem Phys 215:2414–2419
143. Cho H, Gao J, Kwon GS (2016) PEG-b-PLA micelles and PLGA-b-PEG-b-PLGA sol-gels for drug delivery. J Control Rel 240:191–201
144. Chen D, Yu H, Sun K, Liu W, Wang H (2014) Dual thermoresponsive and pH-responsive self-assembled micellar nanogel for anticancer drug delivery. Drug Deliv 21:258–264
145. Murphy EA, Majeti BK, Mukthavaram R, Acevedo LM, Barnes LA, Cheresh DA (2011) Targeted nanogels: a versatile platform for drug delivery to tumors. Mol Cancer Ther 10:972–982
146. Blackburn WH, Dickerson EB, Smith MH, McDonald JF, Lyon LA (2009) Peptide-functionalized nanogels for targeted siRNA delivery. Bioconjugate Chem 20:960–968
147. Vinogradov SV, Batrakova EV, Kabanov AV (2004) Nanogels for oligonucleotide delivery to the brain. Bioconjug Chem 15:50–60
148. Patra CR, Bhattacharya R, Mukhopadhyay D, Mukherjee P (2010) Fabrication of gold nanoparticles for targeted therapy in pancreatic cancer. Adv Drug Del Rev 62:346–361
149. Lepinay S, Staff A, Ianoul A, Albert J (2014) Improved detection limits of protein optical fiber biosensors coated with gold nanoparticles. Biosens Bioelectron 52:337–344
150. Azzouzi S, Rotariu L, Benito AM, Maser WK, Ali MB, Bala C (2015) A novel amperometric biosensor based on gold nanoparticles anchored on reduced graphene oxide for sensitive detection of l-lactate tumor biomarker. Biosens Bioelectron 69:280–286
151. Sun IC, Na JH, Jeong SY, Kim DE, Kwon IC, Choi K, Ahn CH, Kim K (2014) Biocompatible glycol chitosan-coated gold nanoparticles for tumor-targeting CT imaging. Pharm Res 31:1418–1425
152. Choi WI, Sahu A, Kim YH, Tae G (2012) Photothermal cancer therapy and imaging based on gold nanorods. Ann Biomed Eng 40:534–546
153. Tiwari PM, Vig K, Dennis VA, Singh SR (2011) functionalized gold nanoparticles and their biomedical applications. Nanomaterials 1:31–63

154. Dykman LA, Khlebtsov NG (2014) Uptake of engineered gold nanoparticles into mammalian cells. Chem Rev 114:1258–1288
155. Zong J, Cobb SL, Cameron NR (2017) Peptide-functionalized gold nanoparticles: versatile biomaterials for diagnostic and therapeutic applications. Biomater Sci 5:872–886
156. Chanda N, Kattumuri V, Shukla R, Zambre A, Katti K, Upendran A, Kulkarni RR, Kan P, Fent GM, Casteel SW, Smith CJ, Boote E, Robertson JD, Cutler C, Lever JR, Katti KV, Kannan R (2010) Bombesin functionalized gold nanoparticles show in vitro and in vivo cancer receptor specificity. Proc Natl Acad Sci 107:8760–8765
157. Guo S, Huang Y, Jiang Q, Sun Y, Deng L, Liang Z, Du Q, Xing J, Zhao Y, Wang PC, Dong A, Liang X-J (2010) Enhanced gene delivery and siRNA silencing by gold nanoparticles coated with charge-reversal polyelectrolyte. ACS Nano 4:5505–5511
158. Yao C, Zhang L, Wang J, He Y, Xin J, Wang S, Xu H, Zhang Z (2016) Gold nanoparticle mediated phototherapy for cancer. J Nanomater 2016:5497136
159. Jun BH, Noh MS, Kim J, Kim G, Kang H, Kim MS, Seo YT, Baek J, Kim JH, Park J, Kim S (2010) Multifunctional silver-embedded magnetic nanoparticles as SERS nanoprobes and their applications. Small 6:119–125
160. Sanpui P, Chattopadhyay A, Ghosh SS (2011) Induction of apoptosis in cancer cells at low silver nanoparticle concentrations using chitosan nanocarriers. ACS Appl Mater Interfaces 3:218–228
161. Wei L, Lu J, Xu H, Patel A, Chen Z-S, Chen G (2015) Silver nanoparticles: synthesis, properties, and therapeutic applications. Drug Discov Today 20:595–601
162. Zhang H, Shan Y, Dong L (2014) A comparison of TiO_2 and ZnO nanoparticles as photosensitizers in photodynamic therapy for cancer. J Biomed Nanotechnol 10:1450–1457
163. Barick KC, Nigam S, Bahadur D (2010) Nanoscale assembly of mesoporous ZnO: a potential drug carrier. J Mater Chem 20:6446–6452
164. Cheng K, Peng S, Xu C, Sun S (2009) Porous hollow Fe_3O_4 nanoparticles for targeted delivery and controlled release of cisplatin. J Am Chem Soc 131:10637–10644
165. Puvvada N, Rajput S, Kumar BN et al (2015) Novel ZnO hollow-nanocarriers containing paclitaxel targeting folate-receptors in a malignant pH-microenvironment for effective monitoring and promoting breast tumor regression. Sci Rep 5:11760
166. Wang J, Lee JS, Kim D, Zhu L (2017) Exploration of zinc oxide nanoparticles as a multitarget and multifunctional anticancer nanomedicine. ACS Appl Mater Interfaces 9:39971–39984
167. Zhou Y, Quan G, Wu Q, Zhang X, Wu BB, Huang Y, Pan X, Wu C (2018) Mesoporous silica nanoparticles for drug and gene delivery. Acta Pharmaceutica Sin B 8:165–177
168. Purushotham S, Chang PEJ, Rumpel H, Kee IHC, Ng RTH, Chow PKH, Tan CK, Ramanujan RV (2009) Thermoresponsive core-shell magnetic nanoparticles for combined modalities of cancer therapy. Nanotechnol 20:305101
169. Chen FH, Gao Q, Ni JZ (2008) The grafting and release behavior of doxorubicin from Fe_3O_4@SiO_2 core-shell structure nanoparticles via an acid cleaving amide bond: the potential for magnetic targeting drug delivery. Nanotechnol 19:165103
170. Xu D, Xie R, Xu T, Guo X, Liu Q, Liu J, Lv W, Jing X, Zhang H, Wang J (2016) Combination therapeutics of doxorubicin with Fe_3O_4@chitosan@phytic acid nanoparticles for multi-responsive drug delivery. RSC Adv 6:88248–88254
171. Akbarzadeh A, Samiei M, Joo SW, Anzaby M, Hanifehpour Y, Nasrabadi HT, Davaran S (2012) Synthesis, characterization and in vitro studies of doxorubicin-loaded magnetic nanoparticles grafted to smart copolymers on A549 lung cancer cell line. J Nanobiotechnol 10:46
172. Mohammadi-Samani S, Miri R, Salmanpour M, Khalighian N, Sotoudeh S, Erfani N (2013) Preparation and assessment of chitosan-coated superparamagnetic Fe_3O_4 nanoparticles for controlled delivery of methotrexate. Res Pharm Sci 8:25–33
173. Ding W, Guo L (2013) Immobilized transferrin Fe_3O_4@SiO_2 nanoparticle with high doxorubicin loading for dual-targeted tumor drug delivery. Int J Nanomedicine 8:4631–4639
174. Barick KC, Singh S, Bahadur D, Lawande MA, Patkar DP, Hassan PA (2014) Carboxyl decorated Fe_3O_4 nanoparticles for MRI diagnosis and localized hyperthermia. J Colloid Interf Sci 418:120–125

175. Barick KC, Aslam M, Lin Y-P, Bahadur D, Prasad PV, Dravid VP (2009) Novel and efficient MR active colloidal Fe_3O_4 nanoassemblies. J Mater Chem 19:7023–7029
176. Peng C, Zheng L, Chen Q, Shen M, Guo R, Wang H, Shi X (2012) PEGylated dendrimer-entrapped gold nanoparticles for in vivo blood pool and tumor imaging by computed tomography. Biomaterials 33:1107–1119
177. Wen S, Li K, Cai H, Chen Q, Shen M, Huang Y, Shi X (2013) Multifunctional dendrimer-entrapped gold nanoparticles for dual mode CT/MR imaging applications. Biomaterials 34:1570–1580
178. Hutmacher DW (2000) Scaffolds in tissue engineering bone and cartilage. Biomaterials 21:2529–2543
179. Teixeira S, Fernandes H, Leusink A, van Blitterswijk C, Ferraz MP, Monteiro FJ, de Boer J (2010) In vivo evaluation of highly macroporous ceramic scaffolds for bone tissue engineering. J Biomed Mater Res A 93:567–575
180. Kim HJ, Park IK, Kim JH, Cho CS, Kim MS (2012) Gas foaming fabrication of porous biphasic calcium phosphate for bone regeneration. Tissue Eng Regen Med 9:63–68
181. Miguel BS, Kriauciunas R, Tosatti S, Ehrbar M, Ghayor C, Textor M, Weber FE (2010) Enhanced osteoblastic activity and bone regeneration using surface-modified porous bioactive glass scaffolds. J Biomed Mater Res A 94:1023–1033
182. Balla VK, Bodhak S, Bose S, Bandyopadhyay A (2010) Porous tantalum structures for bone implants: fabrication, mechanical and in vitro biological properties. Acta Biomater 6:3349–3359
183. Chen H, Truckenmüller R, Van Blitterswijk C, Moroni L (2013) Fabrication of nanofibrous scaffolds for tissue engineering applications BT-nanomaterials in tissue engineering. Woodhead Publishing Series in Biomaterials, Woodhead Publishing, pp 158–183
184. Hollister SP (2005) Porous scaffold design for tissue engineering. Nat Mater 4:518–524
185. Thein-Han WW, Saikhun J, Pholpramoo C, Misra RD, Kitiyanant Y (2009) Chitosan-gelatin scaffolds for tissue engineering: physico-chemical properties and biological response of buffalo embryonic stem cells and transfectant of GFP-buffalo embryonic stem cells. Acta Biomater 5:3453–3466
186. Saravanan S, Nethala S, Pattnaik S, Tripathi A, Moorthi A, Selvamurugan N (2011) Preparation, characterization and antimicrobial activity of a bio-composite scaffold containing chitosan/nano-hydroxyapatite/nano-silver for bone tissue engineering. Int J Biol Macromol 49:188–193
187. Li Z, Yunlan Su, Xie B, Wang H, Wen T, He C, Shen H, Decheng Wu, Wang D (2013) A tough hydrogel–hydroxyapatite bone-like composite fabricated in situ by the electrophoresis approach. J Mater Chem B 1:1755–1764
188. Peter M, Ganesh N, Selvamurugan N, Nair SV, Furuike T, Tamura H, Jayakumar R (2010) Preparation and characterization of chitosan-gelatin/nanohydroxyapatite composite scaffolds for tissue engineering applications. Carbohydr Polym 80:687–694
189. Maji K, Dasgupta S (2017) Effect of β-tricalcium phosphate nanoparticles additions on the properties of gelatin-chitosan scaffolds. Bioceram Dev Appl 7:2
190. Chen Y, Kawazoe N, Chen G (2018) Preparation of dexamethasone-loaded biphasic calcium phosphate nanoparticles/collagen porous composite scaffolds for bone tissue engineering. Acta Biomater 67:341–353
191. Wang P, Zhao L, Liu J, Weir MD, Zhou X, Xu HHK (2014) Bone tissue engineering via nanostructured calcium phosphate biomaterials and stem cells. Bone Res 2:14017
192. Boisselier E, Astruc D (2009) Gold nanoparticles in nanomedicine: preparations, imaging, diagnostics, therapies and toxicity. Chem Soc Rev 38:1759–1782
193. Baranes K, Shevach M, Shefi O, Dvir T (2016) Gold nanoparticle-decorated scaffolds promote neuronal differentiation and maturation. Nano Lett 16:2916–2920
194. Ko WK, Heo DN, Moon HJ, Lee SJ, Bae MS, Lee JB, Sun IC, Jeon HB, Park HK, Kwon IK (2015) The effect of gold nanoparticle size on osteogenic differentiation of adipose-derived stem cells. J Colloid Interf Sci 438:68–76

195. Suh KS, Lee YS, Seo SH, Kim YS, Choi EM (2013) Gold nanoparticles attenuates antimycin A-induced mitochondrial dysfunction in MC3T3-E1 osteoblastic cells. Biol Trace Elem Res 153:428–436
196. Kumar P (2018) Nano-TiO_2 doped chitosan scaffold for the bone tissue engineering applications. Int J Biomater 2018:6576157
197. Liu H, Slamovich EB, Webster TJ (2006) Less harmful acidic degradation of poly(lacticco-glycolic acid) bone tissue engineering scaffolds through titania nanoparticle addition. Int J Nanomed 1:541–545
198. Bhowmick A, Pramanik N, Manna PJ, Mitra T, Selvaraj TKR, Gnanamani A, Das M, Kundu PP (2015) Development of porous and antimicrobial CTS-PEG-HAP-ZnO nano-composites for bone tissue engineering. RSC Adv 5:99385–99393
199. Shimizu K, Ito A, Yoshida T, Yamada Y, Ueda M, Honda H (2007) Bone tissue engineering with human mesenchymal stem cell sheets constructed using magnetite nanoparticles and magnetic force. J Biomed Mater Res B: Appl Biomater 82:471–480
200. Ben-Nissan B, Heness G (2004) Innovative bioceramics. Mater Forum 27:104–114
201. LeGeros RZ (1988) Calcium phosphate materials in restorative dentistry: a review. Adv Dent Res 2:164–183
202. Bronzino JD (ed) (2000) The biomedical engineering handbook, vol 1, 2nd edn. CRC Press, Boca Raton, FL
203. Marassi V, Cristo LD, Smith SGJ, Ortelli S, Blosi M, Costa AL, Reschiglian P, Volkov Y, Prina-Mello A (2018) Silver nanoparticles as a medical device in healthcare settings: a five-step approach for candidate screening of coating agents. R Soc Open Sci 5:171113
204. Kose N, Çaylak R, Pekşen C, Kiremitçi A, Burukoglu D, Koparal S, Doğan A (2016) Silver ion doped ceramic nano-powder coated nails prevent infection in open fractures: in vivo study. Injury 47:320–324
205. Hazer DB, Sakar M, Dere Y, Altinkanat G, Ziyal MI, Hazer B (2016) Antimicrobial effect of polymer-based silver nanoparticle coated pedicle screws: experimental research on biofilm inhibition in rabbits. Spine (Phila Pa 1976) 41:E323-E329
206. Smith WR, Hudson PW, Ponce BA, Manoharan SRR (2018) Nanotechnology in orthopedics: a clinically oriented review. BMC Musculoskelet Disord 19:67

Chapter 15
Implications of Synthesis Methodology on Physicochemical and Biological Properties of Hydroxyapatite

Mural Quadros, Munira Momin, and Gunjan Verma

Abstract Hydroxyapatite (HAp) is a well-known ceramic biomaterial, which has widely been used in various biomedical applications. It has garnered the attention of researchers mainly due to its chemical and mechanical similarities with the apatite phase present in the bones and teeth of humans. Owing to its biological similarity, HAp has excellent biocompatibility and can trigger both osteoconduction and osteoinduction activities. Therefore, HAp has been employed in a wide range of therapeutic applications ranging from simple dental fillings, bioactive coatings on implants to strategically designed drug delivery systems, and even for tissue engineering applications. Synthesis methodology plays an important role in determining the physicochemical properties of HAp, which in turn affects its mechanical and biological performance. The desired characteristics of HAp can be achieved by choosing an appropriate method of synthesis with optimized reaction conditions. This chapter, in depth, will discuss the various methods of synthesizing HAp, along with their advantages and disadvantages and implications on physicochemical characteristics and biological performance.

Keywords Hydroxyapatite · Synthesis methods · Particle morphology · Chemical precipitation · Hydrothermal method · Drug delivery · Biomaterials

M. Quadros · G. Verma (✉)
Chemistry Division, Bhabha Atomic Research Centre, Mumbai 400 085, India
e-mail: gunjanv@barc.gov.in

M. Quadros · M. Momin
Dr. Bhanuben Nanavati College of Pharmacy, Vile Parle, Mumbai 400 056, India

G. Verma
Homi Bhabha National Institute, Mumbai 400 094, India

A. K. Tyagi and R. S. Ningthoujam (eds.), *Handbook on Synthesis Strategies for Advanced Materials*, Indian Institute of Metals Series,
https://doi.org/10.1007/978-981-16-1803-1_15

15.1 Introduction

HAp is the most commonly occurring calcium phosphate belonging to a class of mineral compounds, called apatite. It is represented by the chemical formula $Ca_{10}(PO_4)_6OH_2$ or $(Ca_5(PO_4)_3OH)$ with a calcium to phosphorous (Ca/P) molar ratio of 1.67. The crystal structure of stoichiometric HAp is monoclinic with P21/b space group, while non-stoichiometric HAp has a hexagonal structure with P63/m space group. Most of the methods of HAp synthesis results in to slightly non-stoichiometric HAp; therefore, they are observed to have hexagonal crystal structures [1, 2]. Biological apatite is also a non-stoichiometric form of HAp, characterized by Ca^{2+} deficiency but contains trace elements such as Na^+, Mg^{2+}, Zn^{2+}, Sr^{2+}, K^+, F^-, Cl^-, $CO_3{}^{2-}$, and Si [3]. Carbonated and calcium-deficient HAp nanocrystals form major inorganic constituents of the bone, whereas the organic part is mainly composed of the collagen matrix.

In recent times, a great deal of attention has been paid to develop synthetic HAp, as it possesses excellent properties such as biocompatibility, bio-integration, bioactivity, non-toxicity, and biological degradation, which makes it a promising candidate for various biomedical applications. HAp is a versatile biomaterial that can be used for bone cavity filling, repair and reconstruction of damaged and degenerative bones, bioactive coating of metallic implants, for tissue engineering applications, and more recently it has also been viewed as a drug delivery vehicle. Each of these applications requires a different set of physicochemical properties, which ultimately determine its biological performance. For instance, when used as a drug delivery vector, the size of HAp particles is a major determinant of its *in-vivo* pharmacokinetics, while the shape of the particle is another physical parameter, which has implications on its cellular uptake and bio-distribution [4]. In addition to this, homogenous dispersion and good colloidal stability of synthesized HAp are also key parameters to be considered for drug delivery applications. Besides these prerequisites, slow dissolution of the carrier material, the feasibility of high drug payload, and sustained release of the drug are some desired features of an ideal drug delivery system. On the other hand, while using HAp as a bioactive coat on metallic implants, it is required to be stable in biological fluid for a long period of time. The success of HAp-coated implant majorly depends on its durability, coating thickness, micro topography, and bond strength of HAp and implant. Further, the porous nature of HAp is also advantageous, as it helps in compact fixation of the implant by allowing in-growth of bone tissues and its integration with the living bones.

A wide variety of experimental techniques, including dry and wet chemical methods, have been used for the synthesis of HAp. Through several studies, it has been established that structural and morphological characteristics of synthetic HAp can be controlled by optimizing the reaction conditions. For example, the crystallinity of HAp particles, in general, depends on the reaction temperature, period of ageing, and calcination temperature. In almost all the methods of HAp synthesis including, chemical precipitation, hydrothermal, sol–gel, emulsion technique, etc., the crystallinity of HAp particles seems to increase with increasing temperature and ageing

time. Several research groups have successfully tailored the structural and morphological parameters of HAp nanostructures by experimenting with different synthesis methodologies and reaction parameters.

It is noteworthy to mention that different synthesis techniques result in HAp with varied architecture and properties, which may not be universally compatible for all types of biomedical applications. For example, biomimetic method, sol–gel method, electrochemical methods, and plasma spraying are the preferred techniques for coating implants. On the other hand, chemical precipitation being a simple process provides an opportunity to perform several modifications in HAp nanostructures during synthesis by involving functionalizing agents, targeting ligands, etc., along with optimizing reaction parameters to enhance its suitability for drug delivery applications. Therefore, an appropriate choice of synthesis methodology plays a pivotal role in determining the biomedical success of HAp. This chapter provides a comprehensive background on various techniques employed for the synthesis of HAp including their advantages and drawbacks. The effect of variable reaction parameters on the physicochemical properties of synthesized HAp will also be discussed and correlated with its biological performance. Thereby, we will be addressing the implications of different synthetic techniques on the development of HAp for various biomedical applications.

15.2 Classification of Synthesis Methodologies for HAp

With growing interest in HAp for biomedical applications, various methods have been devised for its synthesis. The synthesis methods of HAp can be broadly classified into two categories, viz., dry and wet chemical methods as shown in Fig. 15.1. Dry methods are simple processes as compared to wet methods. These methods have top-down approach and generally employ the application of external force such as temperature or pressure to aid the reaction. Due to their simplicity, dry methods are often used for large-scale production of HAp. However, the limitation of dry methods is poor control of the size and morphology of the synthesized HAp [5]. Wet chemical synthesis methods generally have bottom-up approach. During wet chemical synthesis, the desired characteristics of HAp in terms of size and morphology can be achieved by experimenting with reaction parameters such as reaction temperature, duration of reaction, and pH [5]. However, each method of synthesis has its own advantages and limitations, which will be discussed at length. Apart from conventional dry and wet chemical methods of synthesis, there are other methods that involve different trigger mechanisms for the precipitation of HAp, which have been categorized under miscellaneous methods.

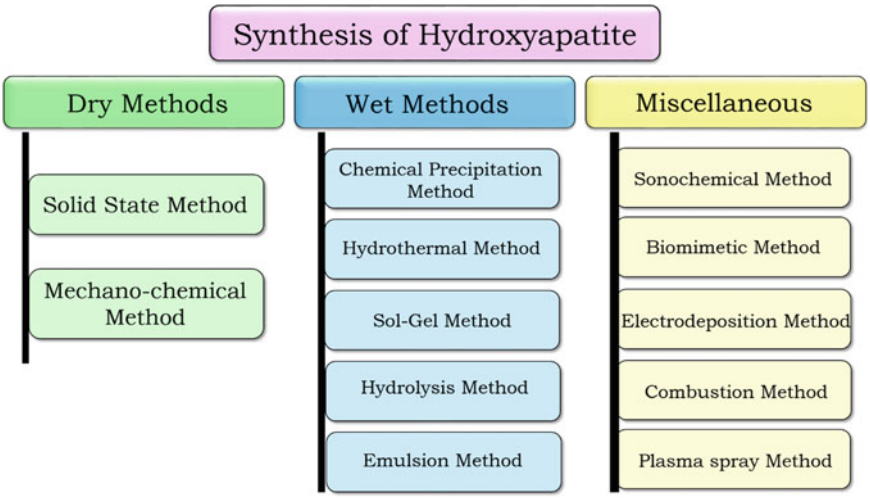

Fig. 15.1 Different approaches for the synthesis of hydroxyapatite

15.3 Synthesis Methodologies: Effect on Physicochemical and Biological Properties

Over the years, researchers have experimented with variable reaction parameters such as temperature, pH, and solvent and correlated them with the physicochemical properties of synthesized HAp such as size, shape, and crystallinity. Variation in these physicochemical properties is further reflected in the biological performance of HAp. Hence, it is very crucial to use appropriate methodology for the synthesis of HAp [5–7].

15.3.1 Dry Methods/Physical Methods

These are called dry methods as there is no involvement of any solvent during HAp formation. Dry methods can be further classified as solid state synthesis and mechano-chemical synthesis.

15.3.1.1 Solid State Method

Solid state technique is one of the simplest methods for the synthesis of HAp. This method involves diffusion of ions among the powdered raw materials to form HAp, thus it requires a high reaction temperature such as 1200–1300 °C for initiation of the reaction. Briefly, the starting materials, i.e., calcium and phosphate precursors

are weighed in a stoichiometric amount to maintain the Ca/P molar ratio of 1.67. The powders are mixed and ground together with a binder or solvent (e.g., acetone) that evaporates during the sintering phase or they are simply pressed into pellets before sintering [8]. Figure 15.2 shows a diagrammatic illustration of solid state method of synthesis of HAp. The choice and ratio of precursors as well as sintering temperature have a significant effect on HAp properties in terms of phase purity and particle size. Rao et al. experimented with varying ratios of tricalcium phosphate

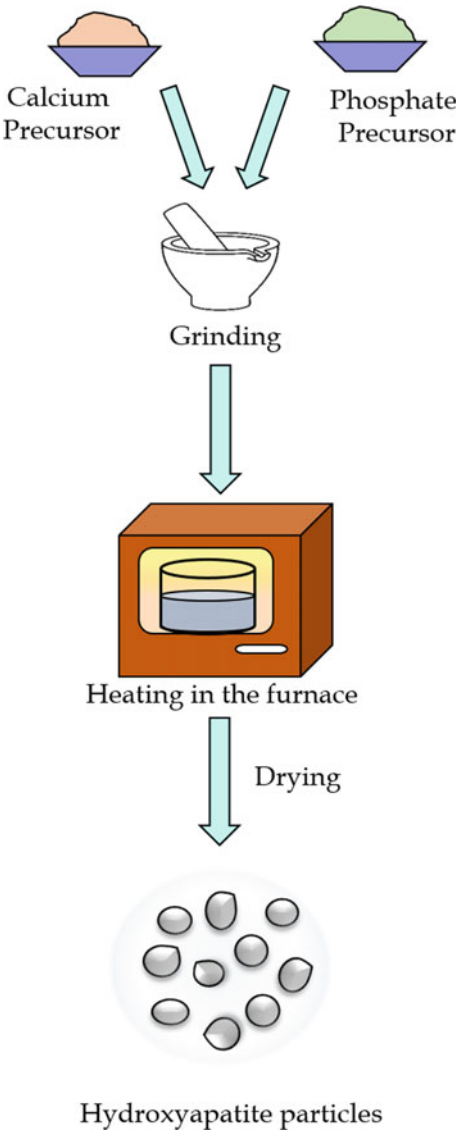

Fig. 15.2 Flow sheet of hydroxyapatite synthesis by solid state method

(TCP) and calcium hydroxide ($Ca(OH)_2$) at 1000 °C. They observed the presence of a biphasic mixture of HAp and TCP at low concentrations of $Ca(OH)_2$, while pure HAp was produced at equimolar ratios (3:3). However, a further increase in the concentration of $Ca(OH)_2$(3:4) led to the formation of a secondary calcium oxide (CaO) phase as an impurity [9]. Pramanik et al. demonstrated the need for sintering during the synthesis process. The presence of unreacted CaO was seen in unsintered samples, while samples sintered at 1250 °C exhibited monophasic HAp particles with a well-connected granular structure and average grain size of 7–8 μm [10]. The temperature used for sintering has also been observed to have an effect on the morphology of HAp, more specifically the particle size. Ezerskyte-Miseviciene et al. noted that particles ranging from 200 to 300 nm were formed when the sintering temperature was 800 °C, while beyond this temperature, the particle size increased up to 400 nm as observed by scanning electron microscopy studies. The difference in the particle size as a function of temperature was attributed to the agglomeration of particles [11]. Similar results were reported by Guo et al., as an increase in HAp particle size was observed with an increase in sintering temperature [12].

15.3.1.2 Mechano-Chemical Technique

The mechano-chemical method is another dry method used on a commercial scale for the synthesis of HAp. It is capable of producing nanoscale HAp powder with better control on morphology as compared to solid state synthesis method. This method majorly employs a rotating ball mill to mix the precursor reactants followed by annealing at elevated temperatures to form HAp. Figure 15.3 shows a diagrammatic illustration of solid state method of HAp synthesis. The collision between balls (usually made up of stainless steel or zirconia) or ball and wall of the mill exerts intense mechanical stress on the precursor powders resulting in mechanical deformation and increased local temperature. The high temperature coupled with structural deformation increases the reactivity of calcium and phosphate precursors to form HAp [13–15]. Other advantages of the mechano-chemical method include low reaction temperature and comparatively inexpensive equipment. Some parameters that need to be monitored during this process are period of milling, choice of precursors, mass to ball ratio, etc. Optimization of these parameters can result in desired morphology of the material. Silva et al. observed a change in crystallinity of HAp as a function of milling time when synthesizing HAp–titanium ceramic system. They noted a slight improvement in crystallinity as milling time was increased from 5 to 15 h; however, an increase in particle size was also observed indicating the formation of agglomerates [16]. Serraj et al. experimented with different calcium and phosphate precursors at various Ca/P ratios. They observed that the choice of precursors and ratio have a significant effect on the formation of the HAp phase [17]. The weight of precursor powders can also affect the reaction kinetics. For example, Briak-Ben Abdeslam et al. used calcium oxide and dicalcium phosphate dehydrate (DCPD) as calcium and phosphate precursors, respectively, and they noted that the

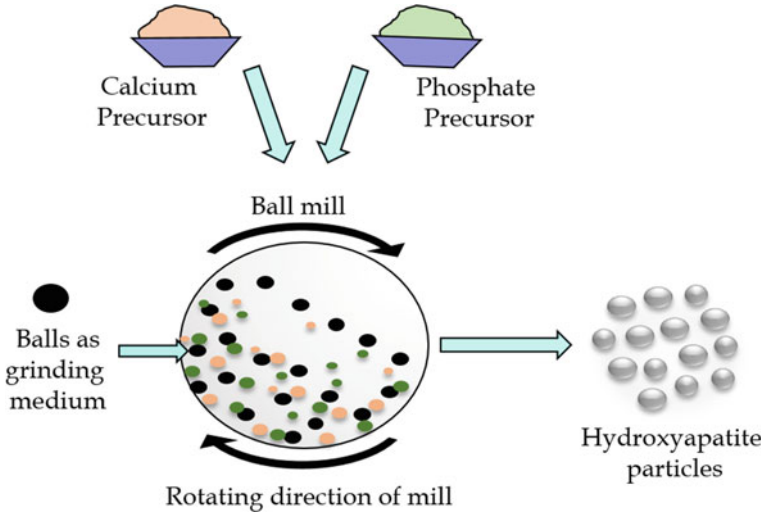

Fig. 15.3 Diagrammatic illustration of HAp synthesis by the mechano-chemical method

time for the complete disappearance of DCPD increased linearly with the mass of powder ground. The rate constant for conversion of 30 g DCPD was half of the one obtained for 15 g [18]. In another study, the same group co-related the influence of instrumental parameters with reaction kinetics. They concluded that the rate of reaction of DCPD was dependent on the rotation velocity of the mill, the eccentricity of the vial on the rotating disk, and the product of the total mass and surface area of the balls [19]. Another parameter that can be optimized to control the morphological parameters of HAp is annealing temperature; Fahami et al. demonstrated the thermal annealing process to be an important step in ensuring high crystallinity. The samples synthesized without annealing step exhibited a lesser degree of crystallinity as compared to the annealed samples [20, 21]. Although the mechano-chemical method is a dry process, Otsuka et al. theorized water of crystallization present in precursors to largely affect its activity. They showed that the mixture of DCPA and CaO, which contains 2.0 mol of crystalline water, less actively transformed into HAp as compared to DCPD and $Ca(OH)_2$ mixture that contained 3.0 mol of water [22]. In spite of having many advantages, the main drawback of the mechano-chemical method is the risk of contamination during the milling process due to high mechanical attrition. For instance, when milling was performed in a biocompatible polymeric vial, it provided better safety in terms of contamination as compared to metallic vials [23]. A comparative study of products prepared using metallic and polymeric vials indicated that HAp crystals synthesized in polymeric vials had more product efficiency and uniformity than those produced in metallic vials [24].

Although dry processes, like solid state and mechano-chemical methods, are very much feasible for large-scale industrial synthesis, they lack control on the size and morphology of the synthesized material as well the presence of heterogeneity in

the phase composition. Moreover, other disadvantages of dry processes are batch to batch variability and the presence of process impurities mainly from wear and tear of grinding equipment, e.g., ball mill. Due to these reasons, dry methods remain an unattractive synthesis option for HAp, especially for biomedical applications. To overcome these shortcomings, the use of wet chemical methods is gaining increasing popularity.

15.3.2 Wet Methods

During wet chemical synthesis, calcium and phosphate precursors are mixed in molar stoichiometric ratios in the presence of either water or other organic solvents and the reaction is carried out at elevated or room temperature. Generally, the pH of the reaction is maintained at an alkaline value of 8–11, throughout the reaction, followed by ageing, washing, and calcination of precipitated HAp particles. For any synthesis method, with an increase in the number of steps, the opportunities for optimizing the reaction parameters also increases, which in turn provides more control on the physicochemical properties of the product. By experimenting with different reaction parameters such as pH, temperature, ageing period, calcination temperature, choice of calcium and phosphate precursors, as well as the addition of organic modifiers during wet chemical processes, the physicochemical properties of synthesized HAp can be tuned to the desired extent. Wet chemical synthesis can be further classified as co-precipitation, sol–gel emulsification method, hydrothermal method, and hydrolysis method [25–27].

15.3.2.1 Co-Precipitation Method

Co-precipitation or chemical precipitation is the most conventional and most commonly used method for the synthesis of HAp and can be scaled up to produce HAp in large quantities at a reasonable cost [28]. It is one of the most applicable techniques with multiple reaction variables, which can be tuned easily to attain desired HAp morphology. Moreover, low reaction temperature, usually <100 °C, is another advantage of this process. The solubility of HAp in acidic pH and stability at alkaline pH form the basis of this method and can be explained as nucleation–aggregation–agglomeration followed by growth of HAp nanoparticles. The reactants are calcium and phosphate precursors, namely calcium hydroxide, calcium nitrate, or calcium carbonate as the calcium source, while orthophosphoric acid or diammonium hydrogen phosphate are used as phosphate precursors. The procedure of HAp synthesis during chemical precipitation begins with the gradual addition of phosphate precursor to a solution of calcium precursor at room temperature or slightly elevated temperature under constant stirring to avoid agglomeration. An alkaline pH of > 9.0 is maintained for the rest of the reaction followed by ageing at the desired reaction temperature to form mature HAp crystals. This is followed by multiple washings to

remove unreacted reagents and finally the drying of the product [29–31]. Figure 15.4 shows a diagrammatic illustration of the chemical precipitation method of HAp synthesis. Care should be exercised while weighing the reactants and during their addition so as to get the final stoichiometric molar ratio (Ca/P) of 1.67.

The careful management of reaction parameters such as pH, temperature, stirring speed, rate of reactant addition, time period for ageing, calcination temperature, and proper selection of precursor materials that are thought to be important parameters during synthesis as they directly affect the composition and physicochemical properties of the synthesized product is done [32]. Optimizing the reaction temperature is one of the simplest parameters to control the morphology of HAp. Bouyer

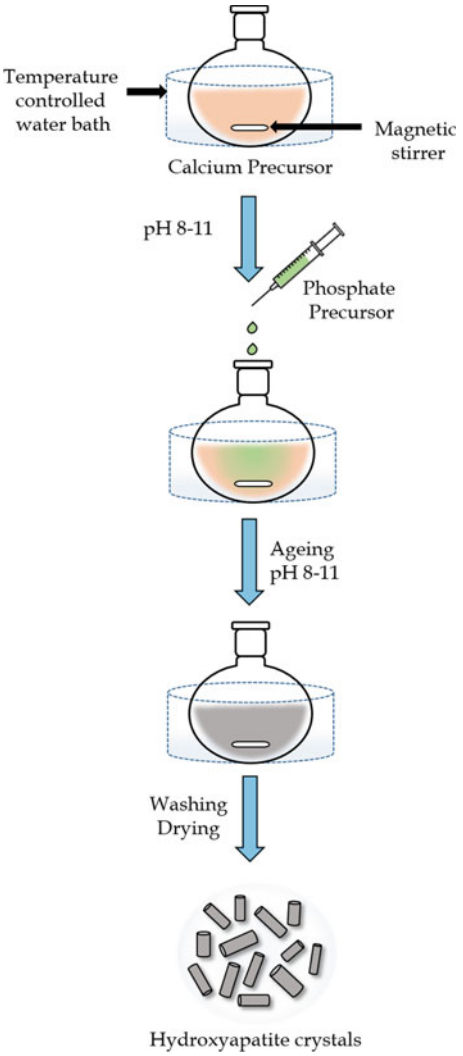

Fig. 15.4 Diagrammatic illustration of hydroxyapatite synthesis by chemical precipitation method

et al. observed that the increase in the synthesis temperature results in the transition of crystal morphology from needle to spherical shape. This transition of shape was attributed to temperature-dependent characteristics of crystalline materials, i.e., at low temperatures (<45 °C), crystal growth follows the c-axis of HAp structure. However, at higher temperature (>85 °C), they tend to grow uniformly around all axes, thus resulting in spherical crystals [33]. In another study, Bouyer et al. demonstrated that the rate of addition of reactants also affects HAp characteristics. With a high addition rate (2400 ml/min) of precipitating agents such as phosphoric acid, the pH of the reaction decreases drastically, resulting in incomplete dissociation of phosphoric acid, and due to the unavailability of sufficient phosphate ions, the formation of HAp is compromised. With the slow addition of phosphoric acid (100 ml/min), 100% calcium hydroxide was converted into HAp [33]. The period of ageing, also known as ripening time, is a crucial parameter in determining the crystallinity of HAp particles. Pang et al. demonstrated that the crystallinity of HAp increases with time and can be corroborated by clear and sharp diffraction peaks observed in X-ray diffraction patterns [34]. By controlling the concentration and pH of the reaction, HAp with various morphologies such as wires, platelets, and needles can also be obtained [35]. The co-precipitation method has also been modified to increase its efficiency. For instance, Peng et al. were able to synthesize HAp nanorods with a narrow particle size distribution by employing high-gravity precipitation technology. In this process, the calcium and phosphate precursors were pumped onto a rotating bed at a rotating speed of 1600 rpm. The high rotation speed generates a high-gravity environment, resulting in the formation of tiny liquid droplets enabling better contact of precursor reagents [36]. Overall, the controllable morphology, good reproducibility, and industrial scale-up feasibility coupled with reasonable cost makes chemical precipitation a very feasible method for the synthesis of HAp.

There are reports which suggest that the size and shape of nanoparticles influence their biological performance. For instance, Palazzo et al. demonstrated that HAp nanoparticles with plate morphology have 1.3 times higher loading efficiency for anticancer drugs (platinum–bisphosphonate complexes) than their needle-shaped counterparts. This selective preference of drug adsorption was theorized to be because of differences in drug-crystal plane interaction [37]. Iafisco et al. studied the influence of the size of HAp crystals synthesized by the chemical precipitation method on the time taken for its resorption when used as a subcutaneous implant. They observed that HAp with a particle size of 100 nm was completely resorbed within 4 weeks of implantation in mice, while the presence of HAp with size 50 nm was noted up to a period of 8 weeks. The longer resorption time of smaller particles was related to its high tendency to form large agglomerates with strong electrostatic interactions, which delays its breakdown for the resorption process [38]. Guo et al. demonstrated that nanostructured HAp exhibits better osteoblastic proliferation activity as compared to its microscale counterpart [39]. This interplay of size and osteoblastic activity can be ascribed to a higher surface area of nanostructured HAp for enhanced cellular adherence and proliferation [40]. The topology of the implant surface is a crucial interface that influences the reaction of tissue to the implant material. Osteoblast

cells "sense" surface morphology of implant by means of filopodia, a slender cytoplasmic projection of cell to collect spatial information. These protrusions also help the cell to adhere and move along the solid surface [41]. Zhou et al. synthesized HAp implants with different crystal morphologies, i.e., rod-like and spherical nanocrystals by using the chemical precipitation method. They noted that implants composed of spherical nanocrystals have a large number of filopodias indicating higher activity of osteoblast cells. This discrimination of osteoblastic cells towards spherical nanocrystals was attributed to higher contact points of the spherical surface as compared to rod-shaped morphology [42].

Since chemical precipitation is a simple and feasible process, several modifications can be performed on HAp during synthesis by addition of functionalizing agents, targeting ligands, polymers, etc. Along with optimizing reaction parameters, researchers have also incorporated various additives during precipitation to further improve the physicochemical characteristics of HAp. The colloidal stability of nanoparticles is a very crucial parameter, especially for drug delivery applications. HAp nanoparticles due to their high surface energy have a tendency to form aggregates. To avoid this, physical methods like mechanical stirring and sonication are employed during the synthesis and processing of HAp [43, 44]. However, these methods are temporary and do not provide long-term stabilization. Another approach for increasing colloidal stability is by modifying the surface of HAp with stabilizing agents [45]. Such surface modifications can be classified as electrostatic stabilization, steric stabilization, and a hybrid of both, i.e., electrosteric stabilization. Figure 15.5 depicts different approaches used for enhancing the colloidal stability of HAp nanostructures. Electrostatic stabilization involves surface modification with charged molecules, which induces electrostatic repulsion between nanoparticles and helps in imparting them colloidal stability [46]. Leah et al. demonstrated that modification of HAp surface with calcium, citrate, and phosphate ions confer electrostatic

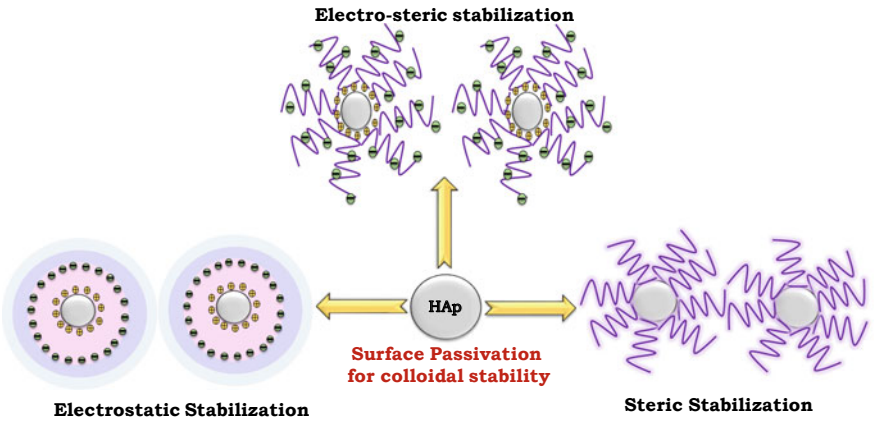

Fig. 15.5 Schematic illustration of different approaches used for enhancing colloidal stability of hydroxyapatite nanostructures

stabilization under physiological conditions [47]. Tan et al. added sodium citrate and sodium hexametaphosphate along with calcium precursors, which resulted in functionalized HAp nanoparticles, exhibiting colloidal stability in aqueous media, with no visible sedimentation or agglomeration for a period of 7 months [48]. Surface modification with alkyl phosphates exhibited electrostatic repulsion due to the presence of a larger number of surface P-OH groups on the HAp surface conferring greater negative electrophoretic mobility compared with the unmodified material [49, 50]. Steric stabilization can be achieved by using capping reagents or polymerization and esterification reactions on the HAp surface [51]. Huang et al. used block co-polymer F127 as a stabilizer to inhibit nanoparticle aggregation during synthesis of HAp by chemical precipitation method [52]. Electrosteric stabilization involves surface modification with molecules that provide both electrostatic and steric repulsion. Organic molecules like chitosan, gelatin, collagen, etc. form a protective barrier around the HAp nanoparticles, thus discouraging the Van der Waals interactions with adjacent particles. Additionally, the functional groups such as carboxyl and amine present in these molecules offer electrostatic stabilization. Zhou et al. modified HAp nanoparticles with polyphenols using the chemical precipitation method. These nanoparticles exhibited colloidal stability due to electrostatic repulsion between the particles (zeta potential: −26.1 mV) as well as the presence of steric barrier offered by branched polyphenolic structure [53]. In another study, HAp particles were coated with gelatin, and the thick gelatin layer on HAp particles resulted in increased stability through spatial stabilization, as well as through electrostatic repulsive interaction [54].

The chemical precipitation method not only allows easy incorporation of surface functionalizing moieties for providing colloidal stability to HAp nanoparticles, but also helps in improving its drug delivery efficiency. Through surface functionalization, a large number of organic molecules having functional groups such as hydroxyl, carboxyl, amine, and phosphate can be incorporated on the surface of HAp nanostructures, which provides binding sites for biomolecules and drugs. Several groups have incorporated different functionalities on HAp nanostructures during synthesis by chemical precipitation method and investigated their drug delivery behaviour. A high loading efficiency for DOX along with pH-responsive release was reported in citrate functionalized HAp nanoparticles as compared to pure HAp. The high drug loading was attributed to electrostatic interaction between the negatively charged citrate molecules and positively charged DOX [55]. Li et al. anchored polyacrylic acid (PAA) on the surface of HAp particles by chemical precipitation method for delivery of DOX. PAA acted as a pH-controlled switch, which retarded the release of DOX at physiological pH (pH 7.4) due to strong electrostatic interactions between DOX and PAA. However, under an acidic environment (pH 5.0), the electrostatic interactions weekend resulting in dissociation of DOX in the media [56]. The pH-responsive drug delivery systems are of great importance, in particular for cancer therapy. Due to the acidic microenvironment of tumour cells, a selective and targeted release of drugs can be achieved using pH-responsive drug carriers, which helps in reducing the potential side effects of drugs. In addition to this, HAp nanoparticles can be conjugated with site-specific ligands such as folic acid (FA), hyaluronic acid (HA), and transferrin, which are abundantly expressed on cancer cells. The incorporation of

these ligands increases the uptake probability of drug nanocarriers by the cancer cells, which are over-expressed with the receptors. This helps in decreasing the side effects of the drug on healthy tissues by mostly localizing the drug in cancerous tissue. Kong et al. used the chemical precipitation method to incorporate HA ligand on the surface of HAp nanoparticles to bind over-expressed CD44 receptors on cancer cells. They observed enhanced cellular uptake of nanocarriers in CD44 receptors over-expressed A549 cells as compared to U87 cells having low CD44 receptors expression [57, 58]. Verma et al. prepared glycine-coated HAp nanoparticles by co-precipitation method and functionalized them with FA. The results indicated higher uptake of DOX-loaded nanoparticles by KB cancer cells, which are over-expressed with folate receptors as compared to folate-receptor deficient, WRL-68 cells [59]. Similarly, Venkatasubbu et al. used folic acid as a targeting ligand for site-specific delivery of paclitaxel [60]. Along with drug delivery, HAp can also be used for the theranostic activity, i.e., therapeutics conjugated with diagnostics. The concurrent delivery of drug as well as imaging increases the accuracy and efficiency of HAp as a therapeutic agent. Therefore, researchers have attempted incorporating various molecules that are capable of being detected by magnetic resonance imaging, fluorescence imaging, positron emission tomography (PET), single-photon emission computed tomography (SPECT), etc. in HAp. Victor et al. fabricated a theranostic HAp system doped with neodymium by chemical precipitation method for the delivery of 4 acetyl salicylic acid to treat and simultaneously monitor colon cancer. The system was functionalized with alginic acid polymer to impart pH-responsive drug release in colonic alkaline medium. While neodymium doping conferred near-infrared fluorescence capability, thereby making simultaneous imaging possible [61]. In another study, Europium-doped HAp nanoparticles were fabricated as theranostic near-infrared luminescent carriers for delivery of DOX [62]. Et al. designed HAp nanoparticles labelled with radionuclides technetium-99 m and radium-223, for diagnostics and therapeutic activity, respectively [63]. Figure 15.6 shows the schematic diagram of different methodologies used for the fabrication of HAp-based nanostructures for targeted drug delivery and theranostics.

15.3.2.2 Hydrothermal Method

The hydrothermal method for HAp synthesis is the next most frequently used method. The hydrothermal method is similar to chemical precipitation, except that the ageing step is carried out under high pressure at a reaction temperature, normally between 90 °C–150 °C [64]. The high pressure and temperature accelerate the dissolution and crystallization process of precursors and HAp, respectively, which alter the crystal growth mechanism and habit. As a result, the HAp crystals formed using this method seem to have large and well-defined sizes with lesser chances of particle agglomeration [65]. The pressure and temperature can be optimized to allow the formation of HAp with controlled morphology [66]. If the solvent used is water, then it is termed as hydrothermal and in the presence of other organic solvents, it is called solvothermal. This is a simple process beginning with thorough mixing of calcium

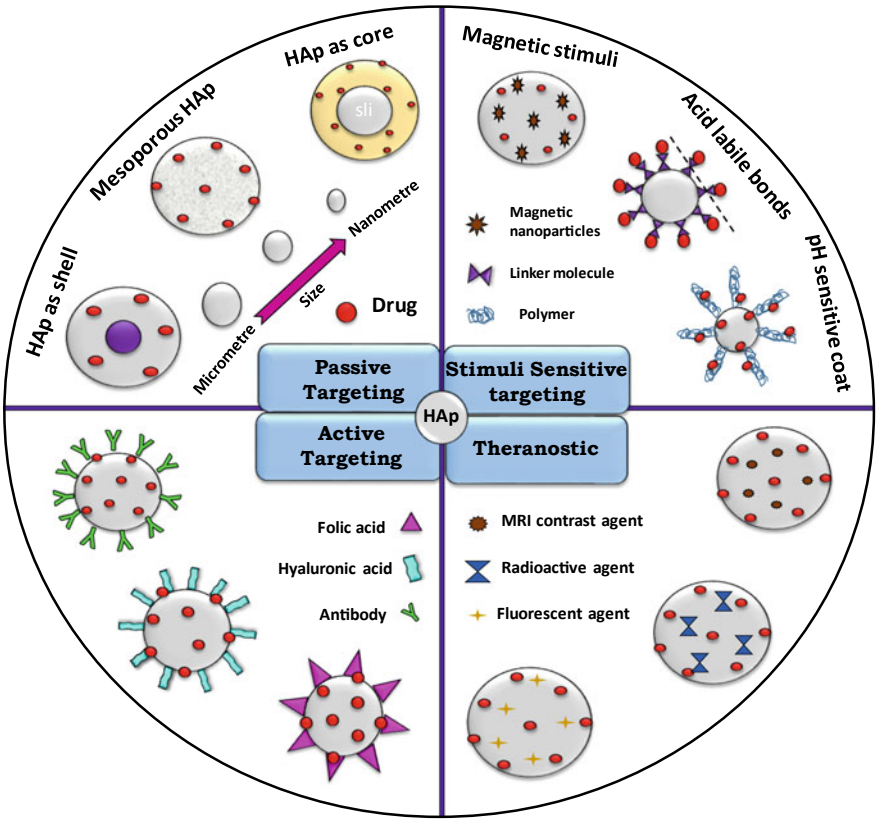

Fig. 15.6 Schematic diagram showing different methodologies for fabrication of HAp-based nanostructures for targeted drug delivery and theranostics

and phosphate precursors in the required stoichiometric amount. The mixture is then transferred to a Teflon-lined stainless steel hydrothermal autoclave and heated at the desired temperature for about 12 h, following which, the powder is calcined, washed, and dried to remove residual reactants [67–69]. The hydrothermal reaction inside the autoclave can be described in two steps, first formation of nuclei, i.e., nucleation in the supersaturated solution followed by its gradual growth to form the final product [70]. Figure 15.7 shows the diagrammatic illustration of HAp synthesis by hydrothermal method. The product obtained using this technique has high crystallinity and phase purity and is often seen to have rod-shaped morphology. The formation of rod-like particles using this technique is attributed to the slow growth of crystals in one-dimensional orientation [71]. However, using specific reaction conditions and in the presence of additives, other morphologies can also be obtained. The pH of the reaction is also considered as a prime factor in deciding the morphology of the HAp particles. At high pH, the degree of crystallinity is seen to increase, which can be attributed to the presence of an increased number of phosphate ions [72].

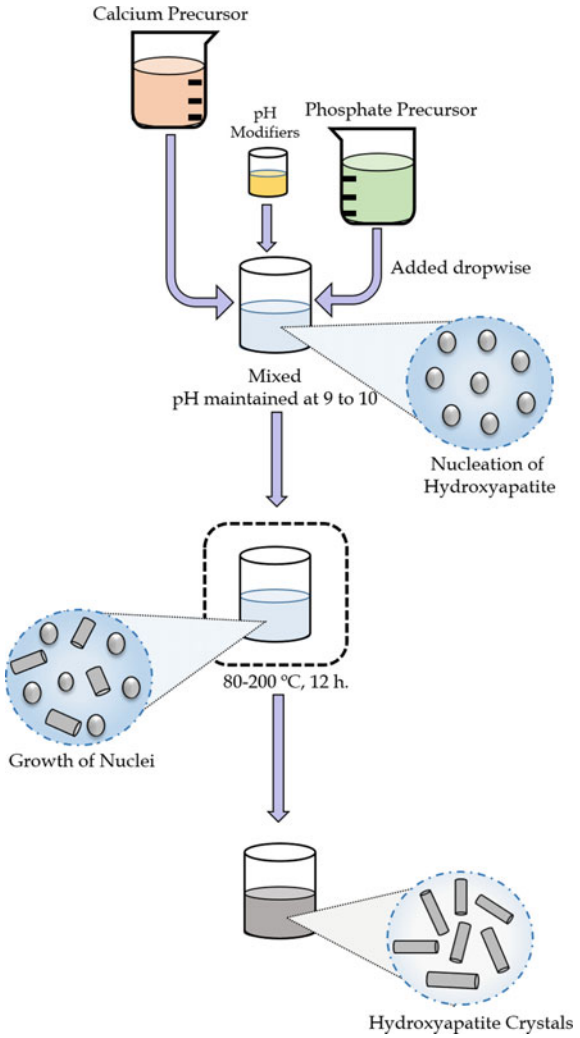

Fig. 15.7 Schematic representation of the synthesis of HAp by hydrothermal method

In order to synthesize more diverse structures, different types of additives have also been examined, which in a way regulate the morphology of HAp. Jiang et al. used ethylenediaminetetraacetic acid (EDTA) and citric acid as double chelating agents and fluoride ions as crystal growth inhibitor during the hydrothermal method of HAp synthesis, resulting in flower, shuttle, rod, whisker, and prismatic shaped microcrystals. The final shape of the HAp microcrystal was governed by the molar ratio of calcium ions with EDTA and citric acid [73]. When citric acid was incorporated in the reaction, the morphology of HAp particles transformed from nanosheets to nanorods with an increasing concentration of citric acid [74]. Whisker-like morphology was obtained by the introduction of additives like acetamide and urea, which gradually

raise the reaction pH, thereby increasing the rate of hydrolysis which causes supersaturation [75, 76]. In a study, Shojai et al. elucidated the role of urea to be more than just a pH modifier during the preparation of HAp. They theorized urea to form complexes with calcium ions, subsequently decreasing the number of nucleation sites, which allows the small crystallites to grow into larger particles [72].

As discussed in the chemical precipitation method, the surface functionalization enhances the drug delivery efficacy of HAp due to the presence of surface moieties. Another modification that can increase the drug delivery efficiency of HAp particles is the formation of hollow microspheres. The high surface area of HAp particles coupled with hollow structure provides more binding sites for drug attachment. Lin et al. demonstrated hollow microspheres prepared by the hydrothermal method enabled high loading of antimicrobial drug vancomycin than that of the traditional HAp nanoparticles [77]. In another study, Cipreste et al. used the surfactant-assisted hydrothermal method to synthesize folic acid functionalized HAp nanorods with gadolinium doping. The folic acid provided targeted ability, while gadolinium provides radiotherapy as well as acts as a magnetic resonance imaging contrast agent, therefore, functioning as a theranostic agent with the capability of radiotherapy and bio-imaging [78].

15.3.2.3 Sol–gel Method

The sol–gel method of HAp synthesis involves molecular interaction of calcium and phosphorus precursors thereby asserting greater control over the purity of the formed HAp phase [79, 80]. In general, sol–gel technique is a rather complex method with a series of steps; first, the hydrolyzed precursor solution (sol) is transformed into a 3D gel structure by poly-condensation or poly-esterification reaction. The gel is aged to allow conversion into a solid mass, and this period of ripening is generally long (24 h) due to the slow reaction of calcium and phosphorus precursors. Next, it is dried at temperatures greater than >800 °C, which collapses the network to form the final product [68, 81–83]. This method is also used for coating metallic implants with HAp. In this process, the surface to be coated is dipped into the precursor sol or the sol is spin coated on the implant. The sol is aged to form a gel, which is in turn heated at 500–1000 °C to form xerogel, i.e., dried gel with unhindered shrinkage and high porosity. Further, heating and sintering of xerogel at elevated temperatures results in the bonding of HAp to the metallic surface. This process is repeated until the coating of desired thickness is achieved [84]. Figure 15.8 shows the diagrammatic illustration of HAp synthesis by sol–gel method.

The reaction temperature plays an important role in regulating the phase impurity of HAp. By using sol–gel method, Santosh et al. synthesized HAp with the Ca/P ratio of 1.67 at temperatures below 600 °C, beyond which they observed the formation of calcium oxide (CaO) phase indicated by an increased Ca/P ratio of 1.75 [85, 86]. Since the presence of CaO impurity may possibly affect the biological performance of HAp, many attempts have been made to decrease or eliminate it. For instance, Jillavenkatesa et al. proposed neutralizing CaO with dilute hydrochloric acid to form

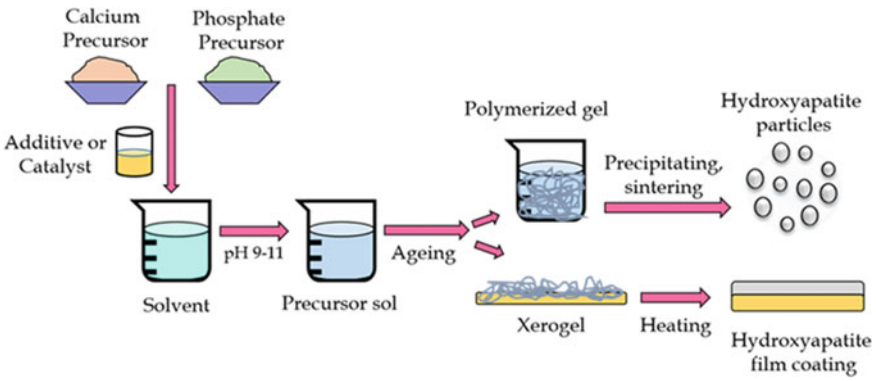

Fig. 15.8 Diagrammatic illustration of hydroxyapatite synthesis by sol–gel method

water-soluble calcium chloride that can be removed by filtration [87]. In another study, in order to avoid the use of alkoxide catalyst, ethanol was used, and the resulting HAp was stable up to 1200 °C without the formation of any by-products [88, 89]. The size and shape of HAp can also be controlled by optimizing the calcination temperature. Padmanabhan et al. observed that at 700 °C, the HAp crystals increase in size and elongate in an anisotropic direction, resulting in the formation of rod-shaped particles [90]. Also, the introduction of polyethylene glycol as an organic modifier was used to control the size of the particles by virtue of the interaction between the ether bonds of polyethylene glycol and HAp crystal [91]. HAp fibres have also been formed using sol–gel method, using calcium acetate and phosphorous pentoxide as the starting precursors [92]. The major limitation of sol–gel method for the synthesis of HAp is the poor hydrolysis of phosphates, since phosphate esters are very stable in water they cannot be hydrolyzed easily and hence require a metal-ion catalyst, which considerably increases the cost of the reaction. Another drawback is the long ageing period and sintering process. However, researchers have managed to cut down this time by 50-fold to 200-fold by avoiding ageing and using fast rotary evaporation instead [93]. Another alternative is to employ microwave-assisted drying that takes only 2 h if the temperature is around 150 °C [94].

Sol–gel method is widely used for coating of HAp on metallic or ceramic implants [95, 96]. Biomedical implants are medical devices, which are used to replace or support a damaged biological structure or simply enhance the structural integrity of an existing biological structure. Most implants are composed of metallic materials like stainless steel (316L) [97–99], cobalt [100–102], and titanium-based alloys [103–106]. These metal alloys are used as implant material due to their good structural and mechanical strength; however, their low biocompatibility and osteointegration ability limit their application. Moreover, on prolonged contact with physiological fluids, they may corrode or leach out metallic ions which, in turn, would elicit an immune response [107]. A most widely used approach to increase the biocompatibility of these implants is to create a barrier between the metallic and tissue interface, i.e., to coat the metal surface with biocompatible materials. In this context, HAp has

been extensively tested as a coating material for implants by virtue of its excellent biocompatibility, chemical stability, and osteo-conductivity. Upon implantation, it is crucial that the implant remains in the designated place throughout its intended lifespan, and any change in position is undesirable. Therefore, to avoid this, the patient's mobility is restricted for a period of about 100 days to allow the implant to fixate strongly with surrounding tissues. However, this period can be reduced to only 20 days by using HAp-coated implants [107]. The success of the HAp-coated implant majorly depends on its durability, coating thickness, microtopography, the bioactivity of surrounding tissue cells, and adhesion of bonding strength of HAp and implant.

Zhang et al. coated titanium (Ti) implant with HAp using sol–gel method, using triethyl phosphite and calcium nitrate as phosphorus and calcium precursors, respectively. The Ti implants were dipped in the sol and withdrawn at a speed of 20 mm/min. After drying at 80 °C to evaporate the residual solvent, the implants were annealed at 450 °C for 2 h. This process was repeated six times until a HAp coat of 1–2 μm was obtained. The biocompatibility and osteointegration of these HAp-coated implants were studied by immersing them in an SBF solution, which mimics the biological environment. Formation of apatite crystals was observed only on HA- coated implant as compared to an uncoated implant, thus indicating that HAp coat favours apatite formation possibly due to the release of calcium ions from HAp [108]. The bond strength of the HAp coat on the implant material is of critical importance to withstand the stress of the growing bone. The strength of the human bone is noted to be about ∼18 MPa; hence, it is ideal to have the coating on the implant with greater bond strength than 18 MPa. Piveteau et al. were able to attain an adhesion strength of >25 MPa using sol–gel coating method. In another study, dense and adhesive HAp coatings on SS implants were obtained using sol–gel method and heat treatment at 375–500 °C to obtain crystalline morphology. However, micro-cracks were observed at an annealing temperature of 500 °C resulting in compromised bonding strength of HAp-SS [109]. Considering theoretical aspects, implants such as hip prostheses experience a great amount of bending stress, and the HAp coats on such implants should, therefore, exhibit high bending strength. In such cases, thick HAp layers have a high risk of being damaged by forming surface cracks; therefore, thin HAp layers are more suitable for these purposes. Sol–gel method has the capability of producing thin ceramic coatings with a nano-range thickness of 70–200 nm [110]. Breme et al. fabricated thin HAp layers (1 μm) on Ti alloy substrate using sol–gel method with good cohesion with implant surface which was tested to be about 70 N mm^2 [107]. Owing to the molecular interaction of reactants, the sol–gel method has been also increasingly used for the incorporation of other elements like sodium [111], fluorine [112], cerium [113], strontium [114], zinc, chromium [115], and so on to form doped HAp. These elements are chosen intentionally to change the crystal lattice of HAp or simply for added biological activity. Incorporation of additives has also been observed to increase the bonding of HAp with the metal implant. For instance, the addition of fluoride ions increased the adherence of the HAp coat with Ti alloy up to 35%. This improvement in adherence was attributed to improved chemical bonding of Ti and fluoride containing HAp at the interface [116]. The surface morphology

of the implant plays an important role in the attachment of osteoblast cells. In a study, Feng et al. demonstrated that rough and porous implant surfaces aid in adherence and stimulation of osteoblast cells [117]. Additionally, the surface composition also determines osteoblast adhesion as hydroxyl groups favour osteoblast attachment and proliferation [118]. Feng et al. noted that adhesion of osteoblast cells on the HAp layer is via interaction with calcium ions [119]. The presence of hydroxyl groups promotes osteoblast proliferation and also increases the production of osteocalcin (a biomarker for osteoblast differentiation) [120]. HAp coatings prepared via sol–gel method displays rough and porous morphology, and thereby have enhanced biological activity.

15.3.2.4 Emulsion Method

Most chemical methods have poor control over the particle size of HAp and other microstructural heterogeneities. However, the synthesis of HAp via the emulsion method has been found to provide greater control on morphological parameters of HAp. Typically, emulsions are dispersions of two or more immiscible liquids, made miscible by the addition of surfactants at the critical micellar concentration (CMC) to form globular micelles. If the volume of water in oil is very low, it is called a microemulsion which has thermodynamic stability and is optically transparent. The emulsion method, particularly the microemulsion method for synthesis of HAp, is an effective method for regulating the size and size distribution of HAp particles as the growth of the particles is strictly restricted to the microreactors, i.e., the emulsion droplets. These microreactors also discourage the agglomeration of particles due to the presence of surfactants forming an interfacial barrier between aqueous and organic phases [121]. HAp synthesized by emulsion methods have been observed to have a smaller HAp particle size than the ones prepared by the co-precipitation method [122–124]. Moreover, the microemulsion globules act as nanosized reactors that favour the growth of spherical HAp particles instead of instinctive rod-like structures. The procedure for HAp synthesis using this method is fairly simple with stepwise mixing of organic, surfactant, and aqueous phase containing calcium and phosphate precursors. The solution is stirred thoroughly or homogenized while maintaining the pH between 9 to 11, which results in precipitation of HAp. This is further dried and calcined at elevated temperatures to remove excess reactants [125, 126]. Figure 15.9 provides a schematic representation of the synthesis of HAp by emulsion method and Table 15.1 renders the details of the chemical composition of emulsion systems employed for the synthesis of HAp nanoparticles.

Precise control on the size and shape of HAp can be obtained by varying primary parameters like surfactant type, surfactant concentration, water to oil ratio, synthesis temperature, reaction time, solvent type, and pH of the reaction. For example, Sun et al. demonstrated that as the molar ratio of solvent and surfactant increases, the length of HAp nanorods increases. This phenomenon was attributed to the increased flexibility of the interfacial film, allowing the growth of HAp nanorods [127]. Bakhtiari et al. demonstrated that by increasing the concentration of pore

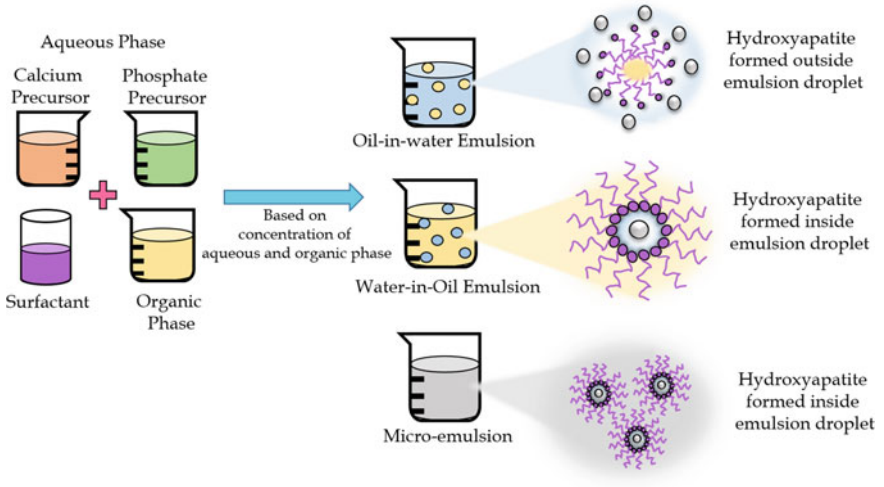

Fig. 15.9 Schematic representation of the synthesis of hydroxyapatite by emulsion method

Table 15.1 General composition of emulsion and microemulsion systems with reported hydroxyapatite particle size range

Organic solvents	Surfactant	Calcium and phosphate precursors	Size	Ref
1-dodecanethiol	CTAB	Calcium nitrate, Orthophosphoric acid	23–40 nm	[128]
Cyclohexane	Span-80	Calcium nitrate, Diammonium phosphate	70 nm	[125]
Iso-octane, n-caproic acid	Span-20, Tween-80	Calcium chloride,Diammonium phosphate	10 μm	[130]
N-butanol	TX-100, CTAB	Calcium nitrate, Diammonium phosphate	200 nm	[129]
Iso-octane	Sodium salt of dioctylsulfosuccinate	Calcium hydroxide, Orthophosphoric acid	100 nm	[122]
1-butanol, n-octane	CTAB	Monocalcium phosphate, Calcium chloride,	50–200 nm	[132]
Cyclohexane	Poly(oxyethylene) nonylphenol ether	Calcium chloride, Diammonium phosphate	20–40 nm	[123]

(continued)

Table 15.1 (continued)

Organic solvents	Surfactant	Calcium and phosphate precursors	Size	Ref
Ethanol, pure vegetable oil	Triton X-100	Calcium hydroxide, Orthophosphoric acid	10–50 μm	[124]
Petroleum ether	Ethoxylated lauryl alcohol (KB6ZA)	Calcium chloride, Diammonium phosphate	10 nm	[133]
Dodecane, ethanol	Pentaethyleneglycol dodecyl ether (C12E5)	Calcium hydroxide, Potassium dihydrogen phosphate	20–100 nm	[126]
Petroleum ether	Tomadol	Calcium nitrate, Diammonium phosphate	160 nm	[131]
Cyclohexane	Poly(oxyethylene) nonylphenol ethers	Calcium nitrate, Orthophosphoric acid	30–50 nm	[134]
Cyclohexane, n-octyl alcohol	CTAB	Calcium nitrate, Diammonium phosphate	100 nm	[135]
N-butanol, n-octane	CTAB	Calcium nitrate, Diammonium phosphate	30–90 nm	[136]
Cyclohexane	Poly(oxyethylene) nonyl phenol ethers	Calcium chloride, Diammonium phosphate	5–10 nm	[137]

expander, 1-dodecanethiol changed the morphology from rod-like micelles to spherical HAp structures [128]. A similar shape transition from rod to spherical was seen by increasing the pH of the reaction from neutral to alkaline [129]. In another study, the effect of reaction temperature was noted to have decreased the surface area of synthesized HAp from 227 to 98 m^2g^{-1} implying an increase in particle size [130]. The choice of calcium precursor also affects the quality of HAp produced. Chen et al. observed that when calcium nitrate was used as a calcium precursor, it transformed into β-tricalcium phosphate (β-TCP) impurity thus exhibiting low thermal stability at high temperatures. While the presence of β-TCP was not detected in HAp prepared using calcium hydroxide as a calcium precursor [131]. Although HAp synthesis by emulsion and microemulsion technique has been shown to offer control on the formation of homogenous nanoparticles with minimum agglomerations, the requirement of large quantities of organic solvents not only acts as a limitation for industrial scale-up but also stands as a non-green process.

15.3.2.5 Hydrolysis Method

The hydrolysis method for synthesizing HAp is one of the simplest methods as compared to other wet methods. As the name suggests, it involves hydrolysis of other calcium phosphate(CaP) phases such as dicalcium phosphate (DCPA), dibasic calcium phosphate dehydrate (DCPD) [1, 138, 139], and tricalcium phosphate (TCP) [26]. Acidic calcium phosphates like DCPA and DCPD are thermodynamically unstable above pH 6.0–7.0; therefore, they undergo transformation into more stable calcium phosphates, like HAp. The synthesis of HAp using the hydrolysis method follows two stages; the first is the dissolution of calcium phosphate precursor resulting in a supersaturated solution to form HAp, followed by precipitation of HAp with phosphate precursor. The synthesized HAp is then washed with deionized water and dried [140]. Hydrolysis of calcium phosphate precursor, α-TCP, has been commonly used for the synthesis of HAp. When used for bulk HAp synthesis, the procedure is characterized by an initial dissolution of the α-TCP powder, i.e., an induction period, followed by growth of HAp, where the transformation of α-TCP to HAp occurs [141].

The variable factors that govern the morphology of HAp are pH and temperature of the reaction [1]. Park et al. prepared whisker-shaped HAp from the hydrolysis of α-TCP at pH 9.0; however, at pH 11.5, it transformed into an ellipsoidal shape [142]. Ito et al. demonstrated that at high pH 11.0–13.0, HAp produced was in the form of bundled needles, while at comparatively low pH of 9.0–10.0, elongated HAp nanosheets were formed. This change in morphology in response to varying pH was attributed to the different mechanisms of DCP hydrolysis to form HAp [143]. Similar attempts have been made by incorporating additives that can act as morphology modulating agents. In one such scientific exploration, Shih et al. studied the effect of surfactant CTAB in HAp synthesis from precursor dicalcium phosphate dehydrate (DCPD). They observed that HAp nanoparticles decreased in size with increasing CTAB concentration, which was explained by the formation of CTAB micelles that inhibit the further growth of crystals [144]. Durucan et al. demonstrated the effect of temperature on HAp morphology. Smaller crystallites were formed at low temperatures, i.e., 37 °C as compared to those formed at 56 °C, which was attributed to microstructural coarsening at high temperatures [141]. A similar observation was noted by Fulmer et al., where the morphology of HAp formed by DCPD hydrolysis varied from needle-like at 25 °C to globular shape at 60 °C [145]. The type of solvent system used for the hydrolysis method has also been seen to affect reaction time and morphology of synthesized HAp. For example, HAp produced using a hydro-alcoholic solvent system with a polar solvent like ethanol was found to delay the hydrolysis of α-TCP, thereby increasing the reaction time up to 120 h. In this reaction, the high miscibility of ethanol with water was theorized to reduce the hydrolytic activity of water. Similarly, experimenting with other alcoholic solvents, a trend was observed, which correlated increasing solvent polarity with increasing reaction time. In other words, non-polar (hydrophobic) solvents form a biphasic system, as a result, they do not interfere with the ongoing hydrolytic process in the aqueous phase [146]. In the hydro-alcoholic solvent system, Sakamoto et al. observed the formation of long needle-shaped crystals in the presence of 1-octanol as compared to platelet crystals,

which were obtained when only water was used as a solvent. In order to further understand this phenomenon, 1-octanol was replaced with its alkane counterpart, i.e., n-octane, and the HAp crystals produced were smaller in size. Since the only difference between 1-octanol and n-octane is the presence of −OH group, it can be assigned to have some interaction with the aqueous phase resulting in inhibition of crystal growth. Similar results were obtained with other solvents without OH groups such as cyclooctane and toluene [147]. These examples suggest that the size and shape of HAp crystals can be controlled by solvent properties, i.e., hydrophobicity and the presence of −OH groups.

15.3.3 Miscellaneous Methods

In addition to the above methods, there are several other methods, such as sonochemical, biomimetic, combustion, plasma spray, and electrodeposition, which are widely being employed for the preparation of HAp for various biomedical applications.

15.3.3.1 Sonochemical Method

The sonochemical method is generally used when HAp particles are to be synthesized at the nanoscale. As the name suggests, this method involves powerful ultrasound radiation to accelerate the reaction of calcium and phosphate precursors. Therefore, HAp nanocrystals with highly crystalline, uniform, and narrow particle size distribution are synthesized at a rate that is 5.5 times greater than conventional techniques [148]. The ultrasonic energy is provided by the ultrasonic horn, a metallic bar with a tapered end, which is powered by an ultrasonic transducer. The principle of the sonochemical method is based on acoustic cavitation, i.e., formation and collapse of bubbles when subjected to intense sound. Here, calcium and phosphate precursors are theorized to be adsorbed onto or inside the bubble. On application of ultrasound, as the bubble collapses, enormous energy is released, which in turn heats the contents of the bubble [149]. This localized high energy in the form of temperature and pressure functions as a small chemical reactor accelerating the reaction of precursors to form HAp [150–152]. On comparing sonochemical method with conventional precipitation method under identical reaction conditions, Jevtic et al. observed co-precipitation method to form a multiphase system, consisting of various calcium phosphate phases such as calcium hydrogen phosphate hydrate, calcium phosphate, calcium phosphate hydroxide, and monetite, while HAp synthesized with the sonochemical method was monophasic in nature [150].

Some variables that can be optimized in sonochemical synthesis are ultrasound frequency, intensity, power and horn tip size, horn immersion depth, the volume of ultrasonicated solution, and duration of ultrasound [153, 154]. Kim et al. studied HAp synthesis by the sonochemical process using phosphoric acid and calcium hydroxide

as precursors. They observed that before the formation of monophasic HAp, dicalcium phosphate hydrate (DCPD) is formed as an intermediate at the beginning of the reaction, which disappears completely after 60 min of ultrasound irradiation. It can be conceived that prolonging the irradiation time increases the reactivity of DCPD to form monophasic HAp effectively [155]. Along with ultrasound radiation, increasing the reaction temperature up to 80 °C seems to further aid the dissolution and reactivity of precursors [154]. To control the morphology of HAp crystals, researchers have experimented with various additives. For instance, the addition of urea as a precipitating reagent resulted into platelet-shaped HAp crystals [156], while needle-shaped crystals obtained with carbamide were used as a precipitating agent [157]. The sonochemical method has been shown to significantly reduce agglomeration, which is one of the major drawbacks of other conventional methods. This has been assigned to the involvement of three consecutive processes in sonochemical synthesis; first, the shockwave caused by cavitation pushes the crystals away from each other to the extent of prohibiting their bonding together. Second, as the crystal nuclei grow in size, their surface area comparatively increases and they become more stable; therefore, they need not form agglomerate to decrease their surface energy. And the third is the mini reactors created by ultrasound, which inhibit aggregation through control of the local nucleus population [153]. To further decrease agglomeration, non-ionic dispersing agents like glycerol and glucose have also been incorporated, which adsorb on HAp nuclei via hydrogen bond and electrostatic interaction. Additionally, the HAp crystals preferentially grow along the c-axis resulting in whisker-like morphology [158]. Although the sonochemical method provides highly crystalline, nanoscale HAp crystals with a narrow size distribution, its scalability to industrial level remains a barrier, as the penetration capability of the power ultrasound in the liquid is limited, which is about 0.1 m when generally used for a batch size of 500 mL precursor mixture [159]. However, increasing the number of ultrasonic probes or making the mixture flow through probes in a tube can be thought of to use the sonochemical method for HAp synthesis at an industrial scale.

15.3.3.2 Biomimetic Method

The biomimetic method for HAp synthesis impersonates biological HAp formation [160]. The HAp produced with this technique mimics bone HAp that is known to be calcium deficient and has the presence of inorganic ions [161]. The biomimetic method is a fairly simple process, similar to that of the chemical precipitation method with exception of the first step, i.e., incubation of calcium and phosphate precursors in simulated body fluid (SBF) for the formation of fine precipitates also called "seeds". The SBF is prepared in such a way that it mimics the human body fluid, containing various inorganic ions with concentrations identical to those found in human blood plasma. Both calcium and phosphate precursors are dissolved in SBF separately, followed by dropwise addition of phosphate solution to calcium solution

under magnetic stirring. The pH of the reaction is maintained throughout at an alkaline range of 7–11. The precipitated HAp is then aged, washed, filtered, and calcined at elevated temperatures to improve the levels of crystallization seeds [162–164].

The quality of SBF used for the precipitation process is of utmost importance, as even a slight change in pH can severely affect the characteristics of synthesized HAp crystals such as phase purity and stability [162]. Tas et al. synthesized HAp powders using SBF solutions at physiological conditions of pH and temperature (i.e., 7.4 and 37 °C, respectively) [165]. Mavis et al. modified the SBF solution by varying the ionic strength in order to accelerate the precipitation of HAp [166]. For further increasing the precipitation rate, Demirtaş et al. employed microwave radiation to improve energy transfer throughout the volume of solution [167]. Similarly, Altınsoy et al. combined the biomimetic method with microwave irradiation to produce HAp with high purity, small particle sizes, and narrow size dispersion [168]. Another variable is the choice of calcium and phosphate precursors used, as they too affect the crystallinity and phase content. For instance, when calcium chloride was used as a calcium precursor, the chloride ions were seen to be incorporated in HAp and resulting into chloroapatite phase [162]. Similar to other synthesis methods, additional reagents, i.e., modifiers can be added in the biomimetic process to control HAp morphology. The addition of 2–6% polyethylene glycol (PEG) resulted in HAp with higher crystallinity than those produced without PEG [169, 170].

The biomimetic method is a widely used technique for coating implants to render them biocompatible with surrounding tissue [171]. Jiang et al. used the biomimetic method to coat nickel–titanium (NiTi) implants with HAp to reduce the leaching of Ni ions. The implants were first treated with aqueous HNO_3 followed by quick immersion in boiling NaOH solution to activate the surface before immersion in SBF. Briefly, a layer of titanium oxide (TiO_2) is formed on the surface due to the reaction of Ti with HNO_3. Next, the NaOH treatment results in many Ti-OH groups, which absorb calcium and phosphate ions from SBF, to precipitate a layer of HAp on the implant surface. The formation of HAp coat on implant resulted in the release of significantly less amount of Ni, when compared with its uncoated counterpart, suggesting that HAp forms a barrier between SBF and metal interface. Further, the incubation period, i.e., the period of implant being immersed in SBF was observed to determine the quality of the HAp coat. The incubation period of 3 days resulted in a discontinuous HAp layer, while a uniform film was observed after incubation of 5 days [172]. Zhang et al. synthesized spherical HAp micro-particles using the biomimetic method and using polymer polylactic acid as a physical scaffold to provide multiple nucleation sites for HAp [173].

15.3.3.3 Combustion Method

The principle of the combustion method is to generate a vigorous exothermic redox reaction between the oxidizer (e.g., nitrate) and fuel (e.g., citric acid) to increase the reactivity of calcium and phosphate precursors for the formation of HAp [174]. Its key features include quick synthesis, high purity, high homogeneity, and the

formation of ultrafine powder. The process is similar to that of sol–gel process, the fuel agent, e.g., citric acid is mixed with calcium and phosphate precursor solution (sol), and the pH of the solution is adjusted as 2–3 by nitric acid. The reaction mixture is heated to evaporate the solvent to form a gel, which is dried at 110–120 °C followed by calcination at 200 °C to form HAp following Eqs. (15.1) and (15.2) [175, 176]. Simply put, the reaction begins at a comparatively low temperature and rapidly rises during the combustion period followed by subsequent fast cooling. All these processes ensure the formation of numerous crystal nuclei resulting into fine particulates towards the end of the reaction [177].

$$9Ca(NO_3)_2 + 5C_6H_8O_7 \rightarrow 30CO_2 + 9N_2 + 20H_2O + 9CaO \tag{15.1}$$

$$10CaO + 6(NH_4)_2HPO_4 \rightarrow Ca_{10}(PO_4)_6(OH)_2 + 12NH_3 + 8H_2O \tag{15.2}$$

The ratio of oxidizer to fuel is of paramount importance in this method as it controls the exothermicity of the combustion. Sasikumar et al. used tartaric acid as fuel to produce submicron-size particles of HAp. The rationale for using tartaric acid was for two main reasons; first, it acted as a chelating agent preventing precipitation of calcium ions, so that it can be transformed into a gel. Secondly, a large amount of heat is evolved when tartrate gel undergoes combustion, which provides local heating to the precursors for the formation of HAp. Further, they optimized the metal ions to fuel ratio, i.e., calcium to tartaric acid ratio to be 1: 2 in order to avoid the formation of calcium phosphate phases other than HAp [178]. Similarly, succinic acid was also studied as a reducing agent, moreover, it also formed a polymer matrix to avoid precipitation of calcium ions [179]. Tas et al. synthesized HAp using urea as a fuel in less than 15 min reaction time. Urea decomposes into a gaseous mixture of nitrous oxides, which ignite spontaneously at 500 °C, thereby increasing the local temperature of dried gel to 1300 °C instantly. This high temperature increases the reactivity of calcium and phosphate precursors to form submicron-size (0.45 mm) HAp powder [180]. The concentration of nitric acid (oxidizer) also seems to affect the purity of the end product. Aghayan et al. demonstrated that at a lower nitric acid concentration (0.1–0.3 mol), both HAp and β-TCP were formed, while as the concentration of nitric acid is increased beyond 0.7 mol, the HAp phase was seen to be more predominant [181]. The combustion method can be considered for large-scale synthesis as the high exothermic chemical reaction becomes self-sustaining after only a short energy pulse initiating the reaction. Thus, the reduced synthesis energy and materials cost have the advantage of being extremely time and energy efficient [182].

15.3.3.4 Electrodeposition Method

Electrodeposition is based on the principle of electrophoresis, i.e., the application of an electric field to move charged molecules in a liquid medium towards an electrode.

This method is used to coat metallic implants using preformed HAp (electrophoretic deposition) or by a series of electrochemical reactions using calcium and phosphate precursors (electrochemical deposition). Both techniques offer uniform layers with high coating efficiency and easy control at a relatively low expense, thereby making it an industrially viable technique. The electrochemical method for deposition of HAp on a substrate involves immersion of electrodes (typically an anode and cathode) in an electrolyte containing calcium and phosphate precursors with/without SBF. The material to be coated forms one electrode, the pH is adjusted to 6–9, and a potential is applied across the electrodes using a potentiostat, which results in deposition of HAp on the implant surface. The freshly prepared HAp-coated implants are then sintered at high temperatures to densify and form a cohesive bond with the implant. The mechanism of deposition of HAp can be explained by two steps; first, nucleation of HAp at the metallic surface followed by growth of the HAp crystals to form a film. Chemically, it can be explained by a series of electrochemical half-reactions, acid–base reactions, and precipitation reactions shown in Eqs. 15.3–15.6. Briefly, the electrolysis of water at the cathode forms hydrogen gas and hydroxide ions, which increase the local pH around the cathode. Further, the hydroxide ions react with phosphate precursor, e.g., dihydrogen phosphate to form dicalcium phosphate, which later converts into HAp [183].

$$2\,H_2O + 2e^- = H_2 + 2OH^- \tag{15.3}$$

$$OH^- + H_2PO_4^- \rightleftharpoons H_2O + HPO_4^{2-} \tag{15.4}$$

$$Ca^{2+} + HPO_4^{2-} + 2H_2O \rightleftharpoons CaHPO_4.2H_2O \tag{15.5}$$

$$5CaHPO_4.2H_2O + 6\,OH^- \rightleftharpoons Ca_5(PO_4)_3OH + 2PO_4^{3-} + 15\,H_2O \tag{15.6}$$

As observed in other synthesis methods, the temperature of HAp synthesis and processing plays a major role in determining the morphology and composition of HAp coatings. Yuang et al. observed that coatings formed on stainless steel (SS) at 65 ℃ were more crystalline in nature than coatings deposited at 25 °C. Additionally, they also observed that the temperature of sintering post HAp formation determines the chemical composition of the coating layer as at high temperatures of about 600 °C, HAp decomposes into TCP. To avoid the formation of TCP, Yuang et al. employed a vacuum for the sintering process. Their results demonstrated the absence of TCP even at a sintering temperature of 800 ℃ [184]. The pH at the surface of the device can be tuned by controlling the current density that passes through the electrodes, which in turn would control the deposition rate and morphology of the HAp layer. In order to increase the cohesion of HAp to the implant, Stoch et al. fabricated an intermediate layer of calcium–silica between the Ti surface and HAp layer. They observed improved adhesive strength of HAp with implant due to the formation of $CaTiO_3$ and $CaSiO_3$ intermediates [185].

For electrophoretic coating, preformed HAp powder is suspended in an electrolyte (e.g. water, organic solvent, etc.) to form a colloidal suspension. On application of potential difference, the colloidal HAp particles migrate towards the counter charged electrode (coating substrate), on which the deposition needs to be performed. The HAp-coated implants are then sintered at high temperatures to allow bonding of HAp with the implant surface. Since coating occurs by movement of HAp particles towards the electrode, it is crucial that the HAp particles be colloidally stable as aggregated particles would result in the non-uniform coating. Using this technique, Wei et al. formed a thick layer of about 500 μm on the implant surface [186]. Eliaz et al. studied both electrochemical and electrophoretic deposition of HAp on implant surfaces. They observed that in the case of electrophoretic deposition, the applied potential and time affect the development of HAp coatings. The coating weight and thickness both were found to increase with the increase in applied potential and period of deposition, respectively. On the other hand, in the case of electrochemical deposition, the pH of the solution, applied cathodic potential, and bath temperature were found to influence the nature of coatings [187]. Some drawbacks of electrodeposition techniques are the involvement of the post-synthesis annealing process of HAp-coated implants, which result in the appearance of decomposition products such as tricalcium phosphate, tetracalcium phosphate, oxyhydroxyapatite, brushite, and so on. Huang et al. skipped the sintering step after electrochemical deposition of HAp and instead used the hydrothermal method. They observed the formation of needle-like and plate-like crystals on the Ti-6Al-4 V alloy substrate [188]. In order to have better nucleation conditions for HAp crystals on implants, Kar et al. pre-treated Ti implants with NaOH to increase the surface pH of Ti during electrodeposition. They observed that samples prepared by alkali pre-treatment had greater bond strength of 25 MPa as compared with samples without alkali treatment (19 MPa) [189].

15.3.3.5 Plasma Spray Method

The plasma spray technique is another widely adopted method for coating implants and similar substrates with HAp. It has the ability to construct sufficiently thick and adherent bioactive HAp coatings on implants [190–192]. This method involves spraying the precursor solutions through a thermal plasma jet, towards the substrate to be coated. The calcium and phosphate solutions undergo thermochemical reactions inside the plasma jet to form HAp. The HAp particles go through a series of complex thermal changes and melt to form a molten or semi-molten state while propagating through the plasma jet, which typically has a temperature of 10,000 K and can even be as high as 30,000 K [193]. The plasma jet accelerates and propels the molten HAp particles towards the substrate resulting in flattened splats that cover the substrate surface. Candidato et al. used an aqueous solution of calcium nitrate and triethyl phosphite as calcium and phosphate precursors to coat stainless steel substrates [194]. In some of the studies, suspensions containing HAp particles were directly injected into the plasma jet [195, 196]. Aruna et al. compared HAp coating produced by both solution precursor method and suspension method. They reported that although

both techniques produced HAp with similar crystallinity, the coating formed using HAp suspension exhibited marginally higher biocompatibility with osteoblast-like cells. Moreover, it also showed better corrosion and wear resistance compared to the solution precursor method [197]. The solution precursor method of plasma spray coating allows easier incorporation of dopant elements [198].

Livingstone et al. used the factorial design of experiments to analyse the effect of process parameters such as current, gas flow rate, and powder feed rate on the roughness, crystallinity, and purity of HAp coatings. They reported that high current and powder feed rate accompanied with a low gas flow rate of spray resulted in HAp coatings with high crystallinity [193]. Li et al. reported that the melting state of sprayed HAp particles can be varied from minor melting, semi-molten to fully molten state by varying the plasma power input. These melting state variations of HAp were reflected in the deposited coatings as their morphology changed from a porous loosed structure to a densified layer structure [199]. Candidato et al. reported a higher coating of the substrate with HAp while using a shorter spray distance [194].

The chemical stability, i.e., the durability of the implant is one of the crucial parameters that determine the performance of the implant, especially for implants meant for long-term use. In such cases, the coating of the implant with highly crystalline HAp was thought to be stable for a long period of time due to its low dissolution rate in physiological solutions. However, the use of highly crystalline HAp would not result in the formation of the biological apatite layer, which is formed by local supersaturation of calcium and phosphate ions near the implant surface. Without the formation of the apatite layer, the implant might fail and elicit an immune response. To avoid such a scenario, some amount of amorphous HAp is desirable as it would provide the necessary calcium and phosphate ions to form apatite by undergoing rapid dissolution. In this context, plasma spraying offers the formation of highly crystalline HAp embedded in an amorphous phase. Additionally, at plasma temperature, HAp is bound to undergo degradation to some extent into its more soluble phases such as ACP, TCP, and OCP. The thickness of the HAp coat on the implant surface needs to be in an optimal range, as very thick coatings result in its detachment from the implant surface, while very thin layers may have poor crystallinity, and as a result, the coating stability would be affected. Zhu et al. found that HAp coating of 10 μm has enough adhesion with the titanium substrate in order to be stable in the physiological medium [200]. Ji et al. fabricated a 200 μm-thick HAp coat on Ti substrate using the plasma spray method [201]. A major drawback of the plasma spray method is the presence of impurities resulting due to the decomposition of HAp at high temperatures. Unabia et al. reported a significant presence of tricalcium phosphate (TCP) along with traces of CaO [202]. Also, it produces a non-uniform coating to implants with heterogeneous structures [203].

15.4 Conclusion

Over the past decades, various synthesis methods have been introduced for the synthesis of HAp. These methods are broadly classified under two categories, namely dry and wet chemical methods. Dry methods are relatively simpler and can be used to produce HAp on a large scale; however, the poor control on HAp morphology, batch to batch variability, and the heterogeneity in the phase composition limit their usage for biomedical applications. On the other hand, wet chemical methods provide better control over the physicochemical properties of HAp by tuning the reaction parameters such as pH, temperature, calcination temperature, choice of calcium and phosphate precursor, and solvent type. The wet chemical process of HAp synthesis involves a number of methods, including chemical precipitation, hydrolysis, sol–gel technique, hydrothermal, and emulsion method. The feasibility of incorporation of surface modifiers on HAp nanoparticles during the chemical precipitation method is very advantageous in increasing the colloidal stability and drug delivery efficacy of HAp-based nanocarriers. Sol–gel method of synthesis is widely employed for coating HAp on metallic implants in order to render them biocompatibility and osteointegration. Though wet chemical methods have the advantage of synthesizing nanoscale HAp with precise control over the morphology and size, however, attaining intricate characteristics such as crystallinity, phase purity, and stoichiometry requires considerable time-consuming optimization of reaction parameters. Additionally, wide size distribution and particles agglomeration are other limitations that make wet chemical methods of synthesis very challenging for large-scale production. HAp synthesized by microemulsion method has shown to offer control over size distribution with minimum agglomerations; however, the requirement of large quantities of organic solvents not only acts as a limitation for industrial scale-up but also stands as a non-green process. In addition to the conventional method of synthesis, several other methods of HAp synthesis such as biomimetic, electrodeposition, sonochemical, and plasma spraying have acquired the attention of researchers, in particular for bioactive coating of metallic implants with HAp. Biomimetic and electrodeposition methods are considered to be very promising methods for implant coating as they allow complete access to the liquid medium to reach all the surfaces of the implant, i.e., both outer surfaces and inner surfaces at a low synthesis temperature. Overall, the biological performance of HAp depends upon its physicochemical properties; hence, it becomes very crucial to identify the appropriate method of synthesis with optimized reaction parameters to achieve the biomedical success of synthesized HAp.

Acknowledgements Dr. Gunjan Verma thanks Dr. A. K. Tyagi, Associate Director, Chemistry Group, BARC, and Dr. P. A. Hassan, Head, Nanotherapeutics and Biosensor Section, BARC, for their constant support and encouragement. Ms. Mural Quadros thanks Mrs. Ozilia Quadros for being a pillar of unwavering support, guidance, and motivation.

References

1. Morgan H, Wilson RM, Elliott JC, Dowker SEP, Anderson P (2000) Preparation and characterisation of monoclinic hydroxyapatite and its precipitated carbonate apatite intermediate. Biomaterials 21:617–627. https://doi.org/10.1016/S0142-9612(99)00225-2
2. Elliott JC, Mackie PE, Young RA (1973) Monoclinic hydroxyapatite. Science 80(180):1055–1057. https://doi.org/10.1126/science.180.4090.1055
3. Suetsugu Y, Tateishi T (2008) Implants and biomaterials (hydroxyapatite). Implants 10:1–10
4. Jindal AB (2017) The effect of particle shape on cellular interaction and drug delivery applications of micro- and nanoparticles. Int J Pharm 532:450–465. https://doi.org/10.1016/j.ijpharm.2017.09.028
5. Saxena V, Shukla I, Pandey LM (2019) Hydroxyapatite: an inorganic ceramic for biomedical applications. In: Holban AM, Grumezescu AM (eds) Materials for biomedical engineering: Nanobiomaterials in tissue engineering, Chapter 8. Elsevier Inc., pp 205–249 https://doi.org/10.1016/B978-0-12-816909-4.00008-7
6. Khalid H, Chaudhry AA (2020) Basics of hydroxyapatite-structure, synthesis, properties, and clinical applications. Elsevier Ltd. https://doi.org/10.1016/b978-0-08-102834-6.00004-5
7. Lu Y, Dong W, Ding J, Wang W, Wang A (2019) Hydroxyapatite nanomaterials: synthesis, properties, and functional applications. In: Wang A, Wang W (eds) Nanomaterials from clay minerals: A new approach to green functional materials micro and nano technologies, Chapter 10. Elsevier Inc., pp 485–536. https://doi.org/10.1016/b978-0-12-814533-3.00010-7
8. Koonawoot R, Saelee C, Thiansem S, Punyanitya S (2012) Synthesis control and characterization of hydroxyapatite ceramic using a solid state reaction. In: 1st Mae Fah Luang University International Conference, pp 2–6
9. Rao RR, Roopa HN, Kannan TS (1997) Solid state synthesis and thermal stability of HAP and HAP—β-TCP composite ceramic powders. J Mater Sci Mater Med 8:511–518. https://doi.org/10.1023/A:1018586412270
10. Pramanik S, Agarwal AK, Rai KN, Garg A (2007) Development of high strength hydroxyapatite by solid-state-sintering process. Ceram Int 33:419–426. https://doi.org/10.1016/j.ceramint.2005.10.025
11. Ezerskyte-Miseviciene A, Kareiva A (2019) Everything old is new again: a reinspection of solid-state method for the fabrication of high quality calcium hydroxyapatite bioceramics. Mendeleev Commun 29:273–275. https://doi.org/10.1016/j.mencom.2019.05.010
12. Guo X, Yan H, Zhao S, Li Z, Li Y, Liang X (2013) Effect of calcining temperature on particle size of hydroxyapatite synthesized by solid-state reaction at room temperature. Adv Powder Technol 24:1034–1038. https://doi.org/10.1016/j.apt.2013.03.002
13. Mochales C, Wilson RM, Dowker SEP, Ginebra MP (2011) Dry mechanosynthesis of nanocrystalline calcium deficient hydroxyapatite: structural characterisation. J Alloys Compd 509:7389–7394. https://doi.org/10.1016/j.jallcom.2011.04.033
14. Fathi MH, Zahrani EM (2008) Mechanochemical synthesis of fluoridated hydroxyapatite nanopowder. Int J Mod Phys B 22:3099–3106. https://doi.org/10.1142/S0217979208047961
15. Boudeville P, Pauvert B, Ginebra MP, Fernandez E, Planell JA (2001) Dry mechanochemical synthesis of apatites and other calcium phosphates. Key Eng Mater 192–195:115–118. https://doi.org/10.4028/www.scientific.net/kem.192-195.115
16. Silva CC, Graça MPF, Valente MA, Sombra ASB (2007) Crystallite size study of nanocrystalline hydroxyapatite and ceramic system with titanium oxide obtained by dry ball milling. J Mater Sci 42:3851–3855. https://doi.org/10.1007/s10853-006-0474-0
17. Serraj S, Boudeville P, Pauvert B, Terol A (2001) Effect on composition of dry mechanical grinding of calcium phosphate mixtures. J Biomed Mater Res 55:566–575. https://doi.org/10.1002/1097-4636(20010615)55:4%3c566::AID-JBM1050%3e3.0.CO;2-F
18. El Briak-BenAbdeslam H, Mochales C, Ginebra MP, Nurit J, Planell JA, Boudeville P (2003) Dry mechanochemical synthesis of hydroxyapatites from dicalcium phosphate dihydrate and calcium oxide: a kinetic study. J Biomed Mater Res Part A 67:927–937. https://doi.org/10.1002/jbm.a.10025

19. Mochales C, El Briak-BenAbdeslam H, Ginebra MP, Terol A, Planell JA, Boudeville P (2004) Dry mechanochemical synthesis of hydroxyapatites from DCPD and CaO: influence of instrumental parameters on the reaction kinetics. Biomaterials 25:1151–1158. https://doi.org/10.1016/j.biomaterials.2003.08.002
20. Fahami A, Ebrahimi-Kahrizsangi R, Nasiri-Tabrizi B (2011) Mechanochemical synthesis of hydroxyapatite/titanium nanocomposite. Solid State Sci 13:135–141. https://doi.org/10.1016/j.solidstatesciences.2010.10.026
21. Yeong B, Junmin X, Wang J (2001) Mechanochemical synthesis of hydroxyapatite from calcium oxide and brushite. J Am Ceram Soc 84:465–467. https://doi.org/10.1111/j.1151-2916.2001.tb00681.x
22. Otsuka M, Matsuda Y, Hsu J, Fox JL, Higuchi WI (1994) Mechanochemical synthesis of bioactive material: effect of environmental conditions on the phase transformation of calcium phosphates during grinding. Biomed Mater Eng 4:357–362. https://doi.org/10.3233/BME-1994-4502
23. Nasiri-Tabrizi B, Honarmandi P, Ebrahimi-Kahrizsangi R, Honarmandi P (2009) Synthesis of nanosize single-crystal hydroxyapatite via mechanochemical method. Mater Lett 63:543–546. https://doi.org/10.1016/j.matlet.2008.11.030
24. Honarmandi P, Honarmandi P, Shokuhfar A, Nasiri-Tabrizi B, Ebrahimi-Kahrizsangi R (2010) Milling media effects on synthesis, morphology and structural characteristics of single crystal hydroxyapatite nanoparticles. Adv Appl Ceram 109:117–122. https://doi.org/10.1179/174367509X12447975734230
25. Mohd Pu'ad NAS, Abdul Haq RH, Mohd Noh H, Abdullah HZ, Idris MI, Lee TC (2020) Synthesis method of hydroxyapatite: a review. Mater Today Proc 29(1):233–239. https://doi.org/10.1016/j.matpr.2020.05.536
26. Sadat-Shojai M, Khorasani MT, Dinpanah-Khoshdargi E, Jamshidi A (2013) Synthesis methods for nanosized hydroxyapatite with diverse structures. Acta Biomater 9:7591–7621. https://doi.org/10.1016/j.actbio.2013.04.012
27. Szcześ A, Hołysz L, Chibowski E (2017) Synthesis of hydroxyapatite for biomedical applications. Adv Colloid Interface Sci 249:321–330. https://doi.org/10.1016/j.cis.2017.04.007
28. Santos MH, de Oliveira M, de Freitas Souza LP, Mansur HS, Vasconcelos WL (2004) Synthesis control and characterization of hydroxyapatite prepared by wet precipitation process. Biomaterials Symposium - II SBPMAT, RIO DE JANEIRO - RJ 26-29 DE OUTUBRO/2003 Mat Res 7(4). https://doi.org/10.1590/s1516-14392004000400017
29. Kothapalli C, Wei M, Vasiliev A, Shaw MT (2004) Influence of temperature and concentration on the sintering behavior and mechanical properties of hydroxyapatite. Acta Mater 52:5655–5663. https://doi.org/10.1016/j.actamat.2004.08.027
30. Gentile P, Wilcock CJ, Miller CA, Moorehead R, Hatton PV (2015) Process optimisation to control the physico-chemical characteristics of biomimetic nanoscale hydroxyapatites prepared using wet chemical precipitation. Materials (Basel) 8:2297–2310. https://doi.org/10.3390/ma8052297
31. Mobasherpour I, Heshajin MS, Kazemzadeh A, Zakeri M (2007) Synthesis of nanocrystalline hydroxyapatite by using precipitation method. J Alloys Compd 430:330–333. https://doi.org/10.1016/j.jallcom.2006.05.018
32. Afshar A, Ghorbani M, Ehsani N, Saeri MR, Sorrell CC (2003) Some important factors in the wet precipitation process of hydroxyapatite. Mater Des 24:197–202. https://doi.org/10.1016/S0261-3069(03)00003-7
33. Bouyer E, Gitzhofer F, Boulos MI (2000) Morphological study of hydroxyapatite nanocrystal suspension. J Mater Sci Mater Med 11:523–531. https://doi.org/10.1023/A:1008918110156
34. Pang YX, Bao X (2003) Influence of temperature, ripening time and calcination on the morphology and crystallinity of hydroxyapatite nanoparticles. J Eur Ceram Soc 23:1697–1704. https://doi.org/10.1016/S0955-2219(02)00413-2
35. Han GS, Lee S, Kim DW, Kim DH, Noh JH, Park JH, Roy S, Ahn TK, Jung HS (2013) A simple method to control morphology of hydroxyapatite nano- and microcrystals by altering phase transition route. Cryst Growth Des 13:3414–3418. https://doi.org/10.1021/cg400308a

36. Peng H, Wang J, Lv S, Wen J, Chen JF (2015) Synthesis and characterization of hydroxyapatite nanoparticles prepared by a high-gravity precipitation method. Ceram Int 41:14340–14349. https://doi.org/10.1016/j.ceramint.2015.07.067
37. Palazzo B, Iafisco M, Laforgia M, Margiotta N, Natile G, Bianchi CL, Walsh D, Mann S, Roveri N (2007) Biomimetic hydroxyapatite-drug nanocrystals as potential bone substitutes with antitumor drug delivery properties. Adv Funct Mater 17:2180–2188. https://doi.org/10.1002/adfm.200600361
38. Iafisco M, Varoni E, Battistella E, Pietronave S, Prat M, Roveri N, Rimondini L (2010) The cooperative effect of size and crystallinity degree on the resorption of biomimetic hydroxyapatite for soft tissue augmentation. Int J Artif Organs 33:765–774. https://doi.org/10.1177/039139881003301101
39. Guo X, Gough JE, Xiao P, Liu J, Shen Z (2007) Fabrication of nanostructured hydroxyapatite and analysis of human osteoblastic cellular response. J Biomed Mater Res Part A 82A:1022–1032. https://doi.org/10.1002/jbm.a.31200
40. Mondal S, Dorozhkin SV, Pal U (2018) Recent progress on fabrication and drug delivery applications of nanostructured hydroxyapatite. Wiley Interdis Rev Nanomed Nanobiotechnology 10:1–32. https://doi.org/10.1002/wnan.1504
41. Wood W, Martin P (2002) Structures in focus—filopodia. Int J Biochem Cell Biol 34:726–730. https://doi.org/10.1016/S1357-2725(01)00172-8
42. Zhao Y, Zhang Y, Ning F, Guo D, Xu Z (2007) Synthesis and cellular biocompatibility of two kinds of HAP with different nanocrystal morphology. J Biomed Mater Res Part B Appl Biomater 83 B(1):121–126. https://doi.org/10.1002/jbm.b.30774
43. Sada E, Kumazawa H, Murakami Y (1991) Hydrothermal synthesis of crystalline hydroxyapatite ultrafine particles. Chem Eng Commun 103:57–64. https://doi.org/10.1080/00986449108910862
44. Fang Y, Agrawal DK, Roy DM, Roy R, Brown PW (1992) Ultrasonically accelerated synthesis of hydroxyapatite. J Mater Res 7:2294–2298. https://doi.org/10.1557/JMR.1992.2294
45. Borum-Nicholas L, Wilson OC (2003) Surface modification of hydroxyapatite. Part I. Dodecyl alcohol. Biomaterials 24(21):3671–3679. https://doi.org/10.1016/S0142-9612(03)00239-4
46. Tung MS (1983) Surface properties of hydroxyapatite in fluoride solution. Colloids Surf 6:283–285. https://doi.org/10.1016/0166-6622(83)80019-5
47. Leach SA (1960) Electrophoresis of synthetic hydroxyapatite. Arch Oral Biol 3:48–56. https://doi.org/10.1016/0003-9969(60)90018-2
48. Tan J, Chen M, Xia J (2009) Water-dispersible hydroxyapatite nanorods synthesized by a facile method. Appl Surf Sci 255:8774–8779. https://doi.org/10.1016/j.apsusc.2009.06.044
49. Tanaka H, Yasukawa A, Kandori K, Ishikawa T (1997) Surface modification of calcium hydroxyapatite with hexyl and decyl phosphates. Colloids Surf A Physicochem Eng Asp 125:53–62. https://doi.org/10.1016/S0927-7757(96)03876-9
50. Tanaka H, Yasukawa A, Kandori K, Ishikawa T (1997) Modification of calcium hydroxyapatite using alkyl phosphates. Langmuir 13:821–826. https://doi.org/10.1021/la960422f
51. Wang S, Wen S, Shen M, Guo R, Cao X, Wang J, Shi X (2011) Aminopropyltriethoxysilane-mediated surface functionalization of hydroxyapatite nanoparticles: synthesis, characterization, and in vitro toxicity assay. Int J Nanomedicine 6:3449–3459
52. Huang YT, Imura M, Nemoto Y, Cheng CH, Yamauchi Y (2011) Block-copolymer-assisted synthesis of hydroxyapatite nanoparticles with high surface area and uniform size. Sci Technol Adv Mater 12(4):045005. https://doi.org/10.1088/1468-6996/12/4/045005
53. Zhou R, Si S, Zhang Q (2012) Water-dispersible hydroxyapatite nanoparticles synthesized in aqueous solution containing grape seed extract. Appl Surf Sci 258:3578–3583. https://doi.org/10.1016/j.apsusc.2011.11.119
54. Chen M, Tan J, Lian Y, Liu D (2008) Preparation of Gelatin coated hydroxyapatite nanorods and the stability of its aqueous colloidal. Appl Surf Sci 254:2730–2735. https://doi.org/10.1016/j.apsusc.2007.10.011
55. Verma G, Barick KC, Shetake NG, Pandey BN, Hassan PA (2016) Citrate-functionalized hydroxyapatite nanoparticles for pH-responsive drug delivery. RSC Adv 6:77968–77976. https://doi.org/10.1039/c6ra10659e

56. Li D, Huang X, Wu Y, Li J, Cheng W, He J, Tian H, Huang Y (2016) Preparation of pH-responsive mesoporous hydroxyapatite nanoparticles for intracellular controlled release of an anticancer drug. Biomater Sci 4:272–280. https://doi.org/10.1039/c5bm00228a
57. Kong L, Mu Z, Yu Y, Zhang L, Hu J (2016) Polyethyleneimine-stabilized hydroxyapatite nanoparticles modified with hyaluronic acid for targeted drug delivery. RSC Adv 6:101790–101799. https://doi.org/10.1039/c6ra19351j
58. Xiong H, Du S, Ni J, Zhou J, Yao J (2016) Mitochondria and nuclei dual-targeted heterogeneous hydroxyapatite nanoparticles for enhancing therapeutic efficacy of doxorubicin. Biomaterials 94:70–83. https://doi.org/10.1016/j.biomaterials.2016.04.004
59. Verma G, Shetake NG, Pandrekar S, Pandey BN, Hassan PA, Priyadarsini KI (2020) Development of surface functionalized hydroxyapatite nanoparticles for enhanced specificity towards tumor cells. Eur J Pharm Sci 144:105206. https://doi.org/10.1016/j.ejps.2019.105206
60. Venkatasubbu GD, Ramasamy S, Avadhani GS, Ramakrishnan V, Kumar J (2013) Surface modification and paclitaxel drug delivery of folic acid modified polyethylene glycol functionalized hydroxyapatite nanoparticles. Powder Technol 235:437–442. https://doi.org/10.1016/j.powtec.2012.11.003
61. Victor SP, Paul W, Vineeth VM, Komeri R, Jayabalan M, Sharma CP (2016) Neodymium doped hydroxyapatite theranostic nanoplatforms for colon specific drug delivery applications. Colloids Surf B Biointerfaces 145:539–547. https://doi.org/10.1016/j.colsurfb.2016.05.067
62. Victor SP, Paul W, Jayabalan M, Sharma CP (2014) Supramolecular hydroxyapatite complexes as theranostic near-infrared luminescent drug carriers. CrystEngComm 16:9033–9042. https://doi.org/10.1039/C4CE01137F
63. Suchánková P, Kukleva E, Nykl E, Nykl P, Sakmár M, Vlk M, Kozempel J (2020) Hydroxyapatite and titanium dioxide nanoparticles: radiolabelling and in vitro stability of prospective theranostic nanocarriers for223 ra and99m tc. Nanomaterials 10:1–12. https://doi.org/10.3390/nano10091632
64. An L, Li W, Xu Y, Zeng D, Cheng Y, Wang G (2016) Controlled additive-free hydrothermal synthesis and characterization of uniform hydroxyapatite nanobelts. Ceram Int 42:3104–3112. https://doi.org/10.1016/j.ceramint.2015.10.099
65. Wang X, Zhuang J, Peng Q, Li Y (2006) Liquid-solid-solution synthesis of biomedical hydroxyapatite nanorods. Adv Mater 18:2031–2034. https://doi.org/10.1002/adma.200600033
66. Sierra-Pallares J, Huddle T, García-Serna J, Alonso E, Mato F, Shvets I, Luebben O, Cocero MJ, Lester E (2016) Understanding bottom-up continuous hydrothermal synthesis of nanoparticles using empirical measurement and computational simulation. Nano Res 9:3377–3387. https://doi.org/10.1007/s12274-016-1215-6
67. Wu SC, Tsou HK, Hsu HC, Hsu SK, Liou SP, Ho WF (2013) A hydrothermal synthesis of eggshell and fruit waste extract to produce nanosized hydroxyapatite. Ceram Int 39:8183–8188. https://doi.org/10.1016/j.ceramint.2013.03.094
68. Cushing BL, Kolesnichenko VL, O'Connor CJ (2004) Recent advances in the liquid-phase syntheses of inorganic nanoparticles. Chem Rev 104:3893–3946. https://doi.org/10.1021/cr030027b
69. Kien PT, Phu HD, Linh NVV, Quyen TN, Hoa NT (2018) Recent trends in hydroxyapatite (HA) synthesis and the synthesis report of nanostructure HA by hydrothermal reaction. Adv Exp Med Biol 1077:343–354. https://doi.org/10.1007/978-981-13-0947-2_18
70. Cao H, Zhang L, Zheng H, Wang Z (2010) Hydroxyapatite nanocrystals for biomedical applications. J Phys Chem C 114:18352–18357. https://doi.org/10.1021/jp106078b
71. Zhou H, Yang M, Hou S, Deng L (2017) Mesoporous hydroxyapatite nanoparticles hydrothermally synthesized in aqueous solution with hexametaphosphate and tea polyphenols. Mater Sci Eng C 71:439–445. https://doi.org/10.1016/j.msec.2016.10.040
72. Sadat-Shojai M, Atai M, Nodehi A (2011) Design of experiments (DOE) for the optimization of hydrothermal synthesis of hydroxyapatite nanoparticles. J Braz Chem Soc 22:571–582. https://doi.org/10.1590/S0103-50532011000300023

73. Jiang D, Li D, Xie J, Zhu J, Chen M, Lü X, Dang S (2010) Shape-controlled synthesis of F-substituted hydroxyapatite microcrystals in the presence of Na2EDTA and citric acid. J Colloid Interface Sci 350:30–38. https://doi.org/10.1016/j.jcis.2010.06.034
74. Daryan SH, Khavandi A, Javadpour J (2020) Surface engineered hollow hydroxyapatite microspheres: Hydrothermal synthesis and growth mechanisms. Solid State Sci 106:106301. https://doi.org/10.1016/j.solidstatesciences.2020.106301
75. Aizawa M, Ueno H, Itatani K, Okada I (2006) Syntheses of calcium-deficient apatite fibres by a homogeneous precipitation method and their characterizations. J Eur Ceram Soc 26:501–507. https://doi.org/10.1016/j.jeurceramsoc.2005.07.007
76. Zhang H, Darvell BW (2010) Synthesis and characterization of hydroxyapatite whiskers by hydrothermal homogeneous precipitation using acetamide. Acta Biomater 6:3216–3222. https://doi.org/10.1016/j.actbio.2010.02.011
77. Lin K, Chen L, Liu P, Zou Z, Zhang M, Shen Y, Qiao Y, Liu X, Chang J (2013) Hollow magnetic hydroxyapatite microspheres with hierarchically mesoporous microstructure for pH-responsive drug delivery. CrystEngComm 15:2999–3008. https://doi.org/10.1039/c3ce26683d
78. Cipreste MF, Peres AM, Cotta AAC, Aragón FH, Antunes ADM, Leal AS, Macedo WAA, Sousa EMBD (2016) Synthesis and characterization of ^{159}Gd-doped hydroxyapatite nanorods for bioapplications as theranostic systems. Mater Chem Phys 181:301–311. https://doi.org/10.1016/j.matchemphys.2016.06.063
79. Roopalakshmi S, Ravishankar R, Belaldavar S, Prasad RGSV, Phani AR (2017) Investigation of structural and morphological characteristic of hydroxyapatite synthesized by Sol-Gel process. Mater Today Proc 4:12026–12031. https://doi.org/10.1016/j.matpr.2017.09.126
80. Bigi A, Boanini E, Rubini K (2004) Hydroxyapatite gels and nanocrystals prepared through a sol-gel process. J Solid State Chem 177:3092–3098. https://doi.org/10.1016/j.jssc.2004.05.018
81. Sanosh KP, Chu MC, Balakrishnan A, Lee YJ, Kim TN, Cho SJ (2009) Synthesis of nano hydroxyapatite powder that simulate teeth particle morphology and composition. Curr Appl Phys 9:1459–1462. https://doi.org/10.1016/j.cap.2009.03.024
82. Ioiţescu A, Vlase G, Vlase T, Ilia G, Doca N (2009) Synthesis and characterization of hydroxyapatite obtained from different organic precursors by sol-gel method. J Therm Anal Calorim 96:937–942. https://doi.org/10.1007/s10973-009-0044-1
83. Hashimoto K, Toda Y, Miura K, Udagawa S, Kanazawa T (1995) Synthesis of hydroxyapatite by Sol-Gel method. Phosphorus Res Bull 5:25–30. https://doi.org/10.3363/prb1992.5.0_25
84. Gross KA, Chai CS, Kannangara GSK, Ben-Nissan B, Hanley L (1998) Thin hydroxyapatite coatings via sol – gel synthesis. J. Mater Sci: Mater Med 9:839–843. https://link.springer.com/article/10.1023/A:1008948228880
85. Sanosh KP, Chu MC, Balakrishnan A, Kim TN, Cho SJ (2009) Preparation and characterization of nano-hydroxyapatite powder using sol-gel technique. Bull Mater Sci 32:465–470. https://doi.org/10.1007/s12034-009-0069-x
86. Hsieh M-F, Perng L-H, Chin T-S, Perng H-G (2001) Phase purity of sol–gel-derived hydroxyapatite ceramic. Biomaterials 22:2601–2607. https://doi.org/10.1016/S0142-9612(00)00448-8
87. Jillavenkatesa A, Condrate RA (1998) Sol-gel processing of hydroxyapatite. J Mater Sci 33:4111–4119. https://doi.org/10.1023/A:1004436732282
88. Anee Kuriakose T, Kalkura SN, Palanichamy M, Arivuoli D, Dierks K, Bocelli G, Betzel C (2004) Synthesis of stoichiometric nano crystalline hydroxyapatite by ethanol-based sol-gel technique at low temperature. J Cryst Growth 263(1–4):517–523. https://doi.org/10.1016/j.jcrysgro.2003.11.057
89. Rajabi-Zamani AH, Behnamghader A, Kazemzadeh A (2008) Synthesis of nanocrystalline carbonated hydroxyapatite powder via nonalkoxide sol-gel method. Mater Sci Eng C 28:1326–1329. https://doi.org/10.1016/j.msec.2008.02.001
90. Padmanabhan SK, Balakrishnan A, Chu MC, Lee YJ, Kim TN, Cho SJ (2009) Sol-gel synthesis and characterization of hydroxyapatite nanorods. Particuology 7:466–470. https://doi.org/10.1016/j.partic.2009.06.008

91. Ruban Kumar A, Kalainathan S (2010) Sol-gel synthesis of nanostructured hydroxyapatite powder in presence of polyethylene glycol. Physica B: Condensed Matter 405(13):2799–2802. https://doi.org/10.1016/j.physb.2010.03.067
92. Ramanan SR, Venkatesh R (2004) A study of hydroxyapatite fibers prepared via sol-gel route. Mater Lett 58:3320–3323. https://doi.org/10.1016/j.matlet.2004.06.030
93. Ben-Arfa BAE, Salvado IMM, Ferreira JMF, Pullar RC (2017) Novel route for rapid sol-gel synthesis of hydroxyapatite, avoiding ageing and using fast drying with a 50-fold to 200-fold reduction in process time. Mater Sci Eng C 70:796–804. https://doi.org/10.1016/j.msec.2016.09.054
94. Robles-Águila MJ, Reyes-Avendaño JA, Mendoza ME (2017) Structural analysis of metal-doped (Mn, Fe Co, Ni, Cu, Zn) calcium hydroxyapatite synthetized by a sol-gel microwave-assisted method. Ceram Int 43:12705–12709. https://doi.org/10.1016/j.ceramint.2017.06.154
95. Liu DM, Troczynski T, Tseng WJ (2001) Water-based sol-gel synthesis of hydroxyapatite: process development. Biomaterials 22:1721–1730. https://doi.org/10.1016/S0142-9612(00)00332-X
96. Narayanan R, Seshadri SK, Kwon TY, Kim KH (2008) Calcium phosphate-based coatings on titanium and its alloys. J Biomed Mater Res Part B Appl Biomater 85B(1):279–299. https://doi.org/10.1002/jbm.b.30932
97. Pattanayak S, Panda S, Dhupal D (2020) Laser micro drilling of 316L stainless steel orthopedic implant: a study. J Manuf Process 52:220–234. https://doi.org/10.1016/j.jmapro.2020.01.042
98. Rezaei A, Golenji RB, Alipour F, Hadavi MM, Mobasherpour I (2020) Hydroxyapatite/hydroxyapatite-magnesium double-layer coatings as potential candidates for surface modification of 316 LVM stainless steel implants. Ceram Int 46:25374–25381. https://doi.org/10.1016/j.ceramint.2020.07.005
99. Cicek S, Karaca A, Torun I, Onses MS, Uzer B (2019) The relationship of surface roughness and wettability of 316L stainless steel implants with plastic deformation mechanisms. Mater Today Proc 7:389–393. https://doi.org/10.1016/j.matpr.2018.11.100
100. Revilla-León M, Sánchez-Rubio JL, Pérez-López J, Rubenstein J, Özcan M (2021) Discrepancy at the implant abutment-prosthesis interface of complete-arch cobalt-chromium implant frameworks fabricated by additive and subtractive technologies before and after ceramic veneering. J Prosthet Dent 125(5):795–803. https://doi.org/10.1016/j.prosdent.2020.03.018
101. Oda H, Itoh T, Sasaki W, Uchimura Y, Taguchi Y, Kaneko K, Sakamoto T, Goto I, Sakuma M, Ishida M, Kikuchi T, Terashita D, Otake H, Morino Y, Shinke T (2020) Cut-off value of strut-vessel distance for the resolution of acute incomplete stent apposition in the early phase using serial optical coherence tomography after cobalt-chromium everolimus-eluting stent implantation. J Cardiol 75:641–647. https://doi.org/10.1016/j.jjcc.2019.12.006
102. Naito Y, Hasegawa M, Tone S, Wakabayashi H, Sudo A (2020) Minimum 10-year follow-up of cementless total hip arthroplasty with a 32-mm cobalt-chromium head on highly cross-linked polyethylene and a tapered, fiber metal proximally coated femoral stem. J Arthroplasty https://doi.org/10.1016/j.arth.2020.08.055
103. Seah KHW, Thampuran R, Teoh SH (1998) The influence of pore morphology on corrosion. Corros Sci 40:547–556. https://doi.org/10.1016/S0010-938X(97)00152-2
104. Chen J, Hu G, Li T, Chen Y, Gao M, Li Q, Hao L, Jia Y, Wang L, Wang Y (2021) Fusion peptide engineered "statically-versatile" titanium implant simultaneously enhancing anti-infection, vascularization and osseointegration. Biomaterials 264:120446. https://doi.org/10.1016/j.biomaterials.2020.120446
105. Xiang G, Huang X, Wang T, Wang J, Zhao G, Wang H, Feng Y, Lei W, Hu X (2020) The impact of sitagliptin on macrophage polarity and angiogenesis in the osteointegration of titanium implants in type 2 diabetes. Biomed Pharmacother 126:110078. https://doi.org/10.1016/j.biopha.2020.110078
106. Toy VE, Dundar S, Bozoglan A (2020) The effects of a nonsteroidal anti-inflammatory drug on the degree of titanium implant osseointegration. J Oral Biol Craniofacial Res 10:333–336. https://doi.org/10.1016/j.jobcr.2020.06.006

107. Breme J, Zhou Y, Groh L (1995) Development of a titanium alloy suitable for an optimized coating with hydroxyapatite. Biomaterials 16:239–244. https://doi.org/10.1016/0142-9612(95)92123-N
108. Zhang JX, Guan RF, Zhang XP (2011) Synthesis and characterization of sol-gel hydroxyapatite coatings deposited on porous NiTi alloys. J Alloys Compd 509:4643–4648. https://doi.org/10.1016/j.jallcom.2011.01.196
109. Liu DM, Yang Q, Troczynski T (2002) Sol-gel hydroxyapatite coatings on stainless steel substrates. Biomaterials 23:691–698. https://doi.org/10.1016/S0142-9612(01)00157-0
110. Roest R, Latella BA, Heness G, Ben-Nissan B (2011) Adhesion of sol-gel derived hydroxyapatite nanocoatings on anodised pure titanium and titanium (Ti6Al4V) alloy substrates. Surf Coatings Technol 205:3520–3529. https://doi.org/10.1016/j.surfcoat.2010.12.030
111. Sopyan I, Pusparini E, Ramesh S, Tan CY, Ching YC, Wong YH, Abidin NIZ, Chandran H, Ramesh S, Bang LT (2017) Influence of sodium on the properties of sol-gel derived hydroxyapatite powder and porous scaffolds. Ceram Int 43:12263–12269. https://doi.org/10.1016/j.ceramint.2017.06.088
112. Cheng K, Shen G, Weng W, Han G, Ferreira JMF, Yang J (2001) Synthesis of hydroxyapatite/fluoroapatite solid solution by a sol-gel method. Mater Lett 51:37–41. https://doi.org/10.1016/S0167-577X(01)00261-0
113. Kaygili O, Dorozhkin SV, Keser S (2014) Synthesis and characterization of Ce-substituted hydroxyapatite by sol-gel method. Mater Sci Eng C 42:78–82. https://doi.org/10.1016/j.msec.2014.05.024
114. Zhang W, Cao N, Chai Y, Xu X, Wang Y (2014) Synthesis of nanosize single-crystal strontium hydroxyapatite via a simple sol-gel method. Ceram Int 40:16061–16064. https://doi.org/10.1016/j.ceramint.2014.07.103
115. Tautkus S, Ishikawa K, Ramanauskas R, Kareiva A (2020) Zinc and chromium co-doped calcium hydroxyapatite: sol-gel synthesis, characterization, behaviour in simulated body fluid and phase transformations. J Solid State Chem 284:121202. https://doi.org/10.1016/j.jssc.2020.121202
116. Zhang S, Xianting Z, Yongsheng W, Kui C, Wenjian W (2006) Adhesion strength of sol-gel derived fluoridated hydroxyapatite coatings. Surf Coatings Technol 200:6350–6354. https://doi.org/10.1016/j.surfcoat.2005.11.033
117. Anselme K (2000) Osteoblast adhesion on biomaterials. Biomaterials 21:667–681. https://doi.org/10.1016/S0142-9612(99)00242-2
118. Feng B, Weng J, Yang BC, Qu SX, Zhang XD (2003) Characterization of surface oxide films on titanium and adhesion of osteoblast. Biomaterials 24:4663–4670. https://doi.org/10.1016/S0142-9612(03)00366-1
119. Feng B, Weng J, Yang BC, Qu SX, Zhang XD (2004) Characterization of titanium surfaces with calcium and phosphate and osteoblast adhesion. Biomaterials 25:3421–3428. https://doi.org/10.1016/j.biomaterials.2003.10.044
120. Massaro C, Baker MA, Cosentino F, Ramires PA, Klose S, Milella E (2001) Surface and biological evaluation of hydroxyapatite-based coatings on titanium deposited by different techniques. J Biomed Mater Res 58:651–657. https://doi.org/10.1002/jbm.1065
121. Lai C, Tang SQ, Wang YJ, Wei K (2005) Formation of calcium phosphate nanoparticles in reverse microemulsions. Mater Lett 59:210–214. https://doi.org/10.1016/j.matlet.2004.08.037
122. Phillips MJ, Darr JA, Luklinska ZB, Rehman I (2003) Synthesis and characterization of nanobiomaterials with potential osteological applications. J Mater Sci Mater Med 14:875–882. https://doi.org/10.1023/A:1025682626383
123. Lim GK, Wang J, Ng SC, Chew CH, Gan LM (1997) Processing of hydroxyapatite via microemulsion and emulsion routes. Biomaterials 18:1433–1439. https://doi.org/10.1016/S0142-9612(97)00081-1
124. Murray MGS, Wang J, Ponton CB, Marquis PM (1995) An improvement in processing of hydroxyapatite ceramics. J Mater Sci 30:3061–3074. https://doi.org/10.1007/BF01209218

125. Ma X, Chen Y, Qian J, Yuan Y, Liu C (2016) Controllable synthesis of spherical hydroxyapatite nanoparticles using inverse microemulsion method. Mater Chem Phys 183:220–229. https://doi.org/10.1016/j.matchemphys.2016.08.021
126. Sonoda K, Furuzono T, Walsh D, Sato K, Tanaka J (2002) Influence of emulsion on crystal growth of hydroxyapatite. Solid State Ionics 151:321–327. https://doi.org/10.1016/S0167-2738(02)00730-0
127. Sun Y, Guo G, Wang Z, Guo H (2006) Synthesis of single-crystal HAP nanorods. Ceram Int 32:951–954. https://doi.org/10.1016/j.ceramint.2005.07.023
128. Bakhtiari L, Javadpour J, Rezaie HR, Erfan M, Mazinani B, Aminian A (2016) Pore size control in the synthesis of hydroxyapatite nanoparticles: the effect of pore expander content and the synthesis temperature. Ceram Int 42:11259–11264. https://doi.org/10.1016/j.ceramint.2016.04.041
129. Sun Y, Guo G, Tao D, Wang Z (2007) Reverse microemulsion-directed synthesis of hydroxyapatite nanoparticles under hydrothermal conditions. J Phys Chem Solids 68:373–377. https://doi.org/10.1016/j.jpcs.2006.11.026
130. Jarudilokkul S, Tanthapanichakoon W, Boonamnuayvittaya V (2007) Synthesis of hydroxyapatite nanoparticles using an emulsion liquid membrane system. Colloids Surf A Physicochem Eng Asp 296:149–153. https://doi.org/10.1016/j.colsurfa.2006.09.038
131. Chen CW, Riman RE, TenHuisen KS, Brown K (2004) Mechanochemical-hydrothermal synthesis of hydroxyapatite from nonionic surfactant emulsion precursors. J Cryst Growth 270:615–623. https://doi.org/10.1016/j.jcrysgro.2004.06.051
132. Koumoulidis GC, Katsoulidis AP, Ladavos AK, Pomonis PJ, Trapalis CC, Sdoukos AT, Vaimakis TC (2003) Preparation of hydroxyapatite via microemulsion route. J Colloid Interface Sci 259:254–260. https://doi.org/10.1016/S0021-9797(02)00233-3
133. Lim GK, Wang J, Ng SC, Gan LM (1999) Formation of nanocrystalline hydroxyapatite in nonionic surfactant emulsions. Langmuir 15:7472–7477. https://doi.org/10.1021/la981659+
134. Bose S, Saha SK (2003) Synthesis and characterization of hydroxyapatite nanopowders by emulsion technique. Chem Mater 15:4464–4469. https://doi.org/10.1021/cm0303437
135. Huang A, Dai H, Wu X, Zhao Z, Wu Y (2019) Synthesis and characterization of mesoporous hydroxyapatite powder by microemulsion technique. J Mater Res Technol 8:3158–3166. https://doi.org/10.1016/j.jmrt.2019.02.025
136. Yang C, Yang P, Wang W, Gai S, Wang J, Zhang M, Lin J (2009) Synthesis and characterization of Eu-doped hydroxyapatite through a microwave assisted microemulsion process. Solid State Sci 11:1923–1928. https://doi.org/10.1016/j.solidstatesciences.2009.07.013
137. Lim GK, Wang J, Ng SC, Gan LM (1996) Processing of fine hydroxyapatite powders via an inverse microemulsion route. Mater Lett 28:431–436. https://doi.org/10.1016/0167-577X(96)00095-X
138. Shih WJ, Chen YF, Wang MC, Hon MH (2004) Crystal growth and morphology of the nanosized hydroxyapatite powders synthesized from CaHPO4·2H2O and CaCO3 by hydrolysis method. J Cryst Growth 270:211–218. https://doi.org/10.1016/j.jcrysgro.2004.06.023
139. Monma H, Kamiya T (1987) Preparation of hydroxyapatite by the hydrolysis of brushite. J Mater Sci 22:4247–4250. https://doi.org/10.1007/BF01132015
140. Graham S, Brown PW (1996) Reactions of octacalcium phosphate to form hydroxyapatite. J Cryst Growth 165:106–115. https://doi.org/10.1016/0022-0248(95)00994-9
141. Durucan C, Brown PW (2000) A-Tricalcium phosphate hydrolysis to hydroxyapatite at and near physiological temperature. J Mater Sci Mater Med 11:365–371. https://doi.org/10.1023/A:1008934024440
142. Park HC, Baek DJ, Park YM, Yoon SY, Stevens R (2004) Thermal stability of hydroxyapatite whiskers derived from the hydrolysis of α-TCP. J Mater Sci 39:2531–2534. https://doi.org/10.1023/B:JMSC.0000020021.82216.6b
143. Ito H, Oaki Y, Imai H (2008) Selective synthesis of various nanoscale morphologies of hydroxyapatite via an intermediate phase. Cryst Growth Des 8:1055–1059. https://doi.org/10.1021/cg070443f

144. Shih WJ, Wang MC, Hon MH (2005) Morphology and crystallinity of the nanosized hydroxyapatite synthesized by hydrolysis using cetyltrimethylammonium bromide (CTAB) as a surfactant. J Cryst Growth 275:2339–2344. https://doi.org/10.1016/j.jcrysgro.2004.11.330
145. Fulmer MT, Brown PW (1998) Hydrolysis of dicalcium phosphate dihydrate to hydroxyapatite. J Mater Sci Mater Med 9:197–202. https://doi.org/10.1023/A:1008832006277
146. Nakahira A, Sakamoto K, Yamaguchi S, Kaneno M, Takeda S, Okazaki M (1999) Novel synthesis method of hydroxyapatite whiskers by hydrolysis of α-tricalcium phosphate in mixtures of water and organic solvent. J Am Ceram Soc 82:2029–2032. https://doi.org/10.1111/j.1151-2916.1999.tb02035.x
147. Sakamoto K, Yamaguchi S, Nakahira A, Kaneno M, Okazaki M, Ichihara J, Tsunawaki Y, Elliott JC (2002) Shape-controlled synthesis of hydroxyapatite from α-tricalcium bis(orthophosphate) in organic-aqueous binary systems. J Mater Sci 37:1033–1041. https://doi.org/10.1023/A:1014316401945
148. Rouhani P, Taghavinia N, Rouhani S (2010) Rapid growth of hydroxyapatite nanoparticles using ultrasonic irradiation. Ultrason Sonochem 17:853–856. https://doi.org/10.1016/j.ultsonch.2010.01.010
149. Han Y, Wang X, Li S (2009) A simple route to prepare stable hydroxyapatite nanoparticles suspension. J Nanoparticle Res 11:1235–1240. https://doi.org/10.1007/s11051-008-9507-8
150. Jevtic M, Mitric M, Škapin S, Jančar B, Ignjatovic N, Uskokovic D (2008) Crystal structure of hydroxyapatite nanorods synthesized by sonochemical homogeneous precipitation. Cryst Growth Des 8(7):2217–2222. https://doi.org/10.1021/cg7007304
151. McNamara WB, Didenko YT, Suslick KS (1999) Sonoluminescence temperatures during multi-bubble cavitation. Nature 401:772–775. https://doi.org/10.1038/44536
152. Li H, Li H, Guo Z, Liu Y (2006) The application of power ultrasound to reaction crystallization. Ultrason Sonochem 13:359–363. https://doi.org/10.1016/j.ultsonch.2006.01.002
153. Luque de Castro MD, Priego-Capote F (2007) Ultrasound-assisted crystallization (sonocrystallization). Ultrason Sonochem 14:717–724. https://doi.org/10.1016/j.ultsonch.2006.12.004
154. Giardina MA, Fanovich MA (2010) Synthesis of nanocrystalline hydroxyapatite from Ca(OH)2 and H3PO4 assisted by ultrasonic irradiation. Ceram Int 36:1961–1969. https://doi.org/10.1016/j.ceramint.2010.05.008
155. Kim W, Saito F (2001) Sonochemical synthesis of hydroxyapatite from H3PO4 solution with Ca(OH)2. Ultrason Sonochem 8:85–88. https://doi.org/10.1016/S1350-4177(00)00034-1
156. Kuznetsov AV, Fomin AS, Veresov AG, Putlyaev VI, Fadeeva IV, Barinov SM (2008) Hydroxyapatite of platelet morphology synthesized by ultrasonic precipitation from solution. Russ J Inorg Chem 53:1–5. https://doi.org/10.1134/S0036023608010014
157. Cao LY, Zhang CB, Huang JF (2005) Synthesis of hydroxyapatite nanoparticles in ultrasonic precipitation. Ceram Int 31:1041–1044. https://doi.org/10.1016/j.ceramint.2004.11.002
158. Zhang J, Zhan X, Wen X, Song B, Ma L, Peng W (2009) Effects of ultrasonic and dispersants on shape and composition of hydroxyapatite by reflux method. Inorg Mater 45:1362–1365. https://doi.org/10.1134/S0020168509120103
159. Li H, Wang J, Bao Y, Guo Z, Zhang M (2003) Rapid sonocrystallization in the salting-out process. J Cryst Growth 247:192–198. https://doi.org/10.1016/S0022-0248(02)01941-3
160. Cengiz B, Gokce Y, Yildiz N, Aktas Z, Calimli A (2008) Synthesis and characterization of hydroxyapatite nanoparticles. Colloids Surf A Physicochem Eng Asp 322:29–33. https://doi.org/10.1016/j.colsurfa.2008.02.011
161. Leena M, Rana D, Webster TJ, Ramalingam M (2016) Accelerated synthesis of biomimetic nano hydroxyapatite using simulated body fluid. Mater Chem Phys 180:166–172. https://doi.org/10.1016/j.matchemphys.2016.05.060
162. Yoruç ABH, Aydınoğlu A (2017) The precursors effects on biomimetic hydroxyapatite ceramic powders. Mater Sci Eng C 75:934–946. https://doi.org/10.1016/j.msec.2017.02.049
163. Moreno EC, Varughese K (1981) Crystal growth of calcium apatites from dilute solutions. J Cryst Growth 53:20–30. https://doi.org/10.1016/0022-0248(81)90052-X
164. Inskeep WP, Silvertooth JC (1988) Kinetics of hydroxyapatite precipitation at pH 7.4 to 8.4. Geochim Cosmochim Acta 52:1883–1893. https://doi.org/10.1016/0016-7037(88)90012-9

165. Cüneyt Tas A (2000) Synthesis of biomimetic Ca-hydroxyapatite powders at 37°C in synthetic body fluids. Biomaterials 21(14):1429–1438. https://doi.org/10.1016/S0142-9612(00)00019-3
166. Mavis B, Demirtaş TT, Gümüşderelioğlu M, Gündüz G, Çolak Ü (2009) Synthesis, characterization and osteoblastic activity of polycaprolactone nanofibers coated with biomimetic calcium phosphate. Acta Biomater 5:3098–3111. https://doi.org/10.1016/j.actbio.2009.04.037
167. Demirtaş TT, Kaynak G, Gumuşderelio¡lu M (2015) Bone-like hydroxyapatite precipitated from 10×SBF-like solution by microwave irradiation. Mater Sci Eng C 49:713–719. https://doi.org/10.1016/j.msec.2015.01.057
168. Türk S, Altınsoy G, ÇelebiEfe M, Ipek M, Özacar C (2017) Bindal, Microwave–assisted biomimetic synthesis of hydroxyapatite using different sources of calcium. Mater Sci Eng C 76:528–535. https://doi.org/10.1016/j.msec.2017.03.116
169. Qiu C, Xiao X, Liu R (2008) Biomimetic synthesis of spherical nano-hydroxyapatite in the presence of polyethylene glycol. Ceram Int 34:1747–1751. https://doi.org/10.1016/j.ceramint.2007.06.001
170. Chen Z, Wu B, Huang X, Li X, Lin Y (2018) Biomimetic synthesis of hydroxyapatite in presence of imidazole-4,5-dicarboxylic acid grafted chitosan for removing chromium(VI). J Nanotechnol Article ID 5431290. https://doi.org/10.1155/2018/5431290
171. Harun WSW, Asri RIM, Alias J, Zulkifli FH, Kadirgama K, Ghani SAC, Shariffuddin JHM (2018) A comprehensive review of hydroxyapatite-based coatings adhesion on metallic biomaterials. Ceram Int 44:1250–1268. https://doi.org/10.1016/j.ceramint.2017.10.162
172. Jiang HC, Rong LJ (2006) Effect of hydroxyapatite coating on nickel release of the porous NiTi shape memory alloy fabricated by SHS method. Surf. Coatings Technol 201:1017–1021. https://doi.org/10.1016/j.surfcoat.2006.01.015
173. Zhang R, Ma PX (1999) Porous poly(L-lactic acid)/apatite composites created by biomimetic process. J Biomed Mater Res 45:285–293. https://doi.org/10.1002/(sici)1097-4636(19990615)45:4%3c285::aid-jbm2%3e3.3.co;2-u
174. Ayers RA, Burkes DE, Gottoli G, Yi H-C, Zhim F, Yahia L, Moore JJ (2007) Combustion synthesis of porous biomaterials. J Biomed Mater Res Part A 81A:634–643. https://doi.org/10.1002/jbm.a.31017
175. Han Y, Li S, Wang X, Chen X (2004) Synthesis and sintering of nanocrystalline hydroxyapatite powders by citric acid sol-gel combustion method. Mater Res Bull 39:25–32. https://doi.org/10.1016/j.materresbull.2003.09.022
176. Sasikumar S, Vijayaraghavan R (2006) Low temperature synthesis of nanocrystalline hydroxyapatite from egg shells by combustion method. Trends Biomater Artif Organs 19:70–73
177. Ghosh SK, Roy SK, Kundu B, Datta S, Basu D (2011) Synthesis of nano-sized hydroxyapatite powders through solution combustion route under different reaction conditions. Mater Sci Eng B 176(1):14–21. https://doi.org/10.1016/j.mseb.2010.08.006
178. Sasikumar S, Vijayaraghavan R (2008) Effect of metal-ion-to-fuel ratio on the phase formation of bioceramic phosphates synthesized by self-propagating combustion. Sci Technol Adv Mater 9(3):035003. https://doi.org/10.1088/1468-6996/9/3/035003
179. Sasikumar S, Vijayaraghavan R (2008) Solution combustion synthesis of bioceramic calcium phosphates by single and mixed fuels-A comparative study. Ceram Int 34:1373–1379. https://doi.org/10.1016/j.ceramint.2007.03.009
180. Tas AC (2000) Combustion synthesis of calcium phosphate bioceramic powders. J Eur Ceram Soc 20(14–15):2389–2394. https://doi.org/10.1016/S0955-2219(00)00129-1
181. Aghayan MA, Rodríguez MA (2012) Influence of fuels and combustion aids on solution combustion synthesis of bi-phasic calcium phosphates (BCP). Mater Sci Eng C 32:2464–2468. https://doi.org/10.1016/j.msec.2012.07.027
182. Kingsley JJ, Patil KC (1988) A novel combustion process for the synthesis of fine particle α-alumina and related oxide materials. Mater Lett 6:427–432. https://doi.org/10.1016/0167-577X(88)90045-6

183. Redepenning J, Schlessinger T, Burnham S, Lippiello L, Miyano J (1996) Characterization of electrolytically prepared brushite and hydroxyapatite coatings on orthopedic alloys. J Biomed Mater Res 30:287–294. https://doi.org/10.1002/(SICI)1097-4636(199603)30:3%3c287::AID-JBM3%3e3.0.CO;2-M
184. Yuan Q, Golden TD (2009) Electrochemical study of hydroxyapatite coatings on stainless steel substrates. Thin Solid Films 518:55–60. https://doi.org/10.1016/j.tsf.2009.06.029
185. Stoch A, Brozek A, Kmita G, Stoch J, Jastrz W, Rakowska A (2001) Electrophoretic coating of hydroxyapatite on titanium implants. J Mol Struct 596:191–200. https://doi.org/10.1016/S0022-2860(01)00716-5
186. Wei M, Ruys AJ, Milthorpe BK, Sorrell CC (2005) Precipitation of hydroxyapatite nanoparticles: effects of precipitation method on electrophoretic deposition. J Mater Sci Mater Med 16:319–324. https://doi.org/10.1007/s10856-005-0630-0
187. Eliaz N, Sridhar TM, Mudali UK, Raj B (2005) Electrochemical and electrophoretic deposition of hydroxyapatite for orthopaedic applications. Surf Eng 21:238–242. https://doi.org/10.1179/174329405X50091
188. Huang LY, Xu KW, Lu J (2000) A study of the process and kinetics of electrochemical deposition and the hydrothermal synthesis of hydroxyapatite coatings. J Mater Sci Mater Med 11:667–673. https://doi.org/10.1023/A:1008934522363
189. Kar A, Raja KS, Misra M (2006) Electrodeposition of hydroxyapatite onto nanotubular TiO2 for implant applications. Surf Coatings Technol 201:3723–3731. https://doi.org/10.1016/j.surfcoat.2006.09.008
190. Singh J, Chatha SS, Singh H (2020) Characterization and corrosion behavior of plasma sprayed calcium silicate reinforced hydroxyapatite composite coatings for medical implant applications. Ceram Int https://doi.org/10.1016/j.ceramint.2020.08.189
191. Chen QY, Zou YL, Fu W, Bai XB, Ji GC, Yao HL, Wang HT, Wang F (2019) Wear behavior of plasma sprayed hydroxyapatite bioceramic coating in simulated body fluid. Ceram Int 45:4526–4534. https://doi.org/10.1016/j.ceramint.2018.11.137
192. Chambard M, Marsan O, Charvillat C, Grossin D, Fort P, Rey C, Gitzhofer F, Bertrand G (2019) Effect of the deposition route on the microstructure of plasma-sprayed hydroxyapatite coatings. Surf Coatings Technol 371:68–77. https://doi.org/10.1016/j.surfcoat.2019.01.027
193. Levingstone TJ, Ardhaoui M, Benyounis K, Looney L, Stokes JT (2015) Plasma sprayed hydroxyapatite coatings: understanding process relationships using design of experiment analysis. Surf Coatings Technol 283:29–36. https://doi.org/10.1016/j.surfcoat.2015.10.044
194. Candidato RT, Sokołowski P, Pawłowski L, Lecomte-Nana G, Constantinescu C, Denoirjean A (2017) Development of hydroxyapatite coatings by solution precursor plasma spray process and their microstructural characterization. Surf Coatings Technol 318:39–49. https://doi.org/10.1016/j.surfcoat.2016.10.072
195. Deram V, Minichiello C, Vannier RN, Le Maguer A, Pawlowski L, Murano D (2003) Microstructural characterizations of plasma sprayed hydroxyapatite coatings. Surf Coatings Technol 166:153–159. https://doi.org/10.1016/S0257-8972(02)00855-1
196. Gkomoza P, Vardavoulias M, Pantelis DI, Sarafoglou C (2019) Comparative study of structure and properties of thermal spray coatings using conventional and nanostructured hydroxyapatite powder, for applications in medical implants. Surf Coatings Technol 357:748–758. https://doi.org/10.1016/j.surfcoat.2018.10.044
197. Aruna ST, Kulkarni S, Chakraborty M, Kumar SS, Balaji N, Mandal C (2017) A comparative study on the synthesis and properties of suspension and solution precursor plasma sprayed hydroxyapatite coatings. Ceram Int 43:9715–9722. https://doi.org/10.1016/j.ceramint.2017.04.146
198. Unabia RB, Bonebeau S, Candidato RT, Jouin J, Noguera O, Pawłowski L (2019) Investigation on the structural and microstructural properties of copper-doped hydroxyapatite coatings deposited using solution precursor plasma spraying. J Eur Ceram Soc 39:4255–4263. https://doi.org/10.1016/j.jeurceramsoc.2019.06.034
199. Li H, Ma Y, Zhao Z, Tian Y (2019) Fatigue behavior of plasma sprayed structural-grade hydroxyapatite coating under simulated body fluids. Surf Coatings Technol 368:110–118. https://doi.org/10.1016/j.surfcoat.2019.04.028

200. Zhu X, Son DW, Ong JL, Kim K (2003) Characterization of hydrothermally treated anodic oxides containing Ca and P on titanium. J Mater Sci Mater Med 14:629–634. https://doi.org/10.1023/A:1024079109073
201. Ji H, Ponton CB, Marquis PM (1992) Microstructural characterization of hydroxyapatite coating on titanium. J Mater Sci Mater Med 3:283–287. https://doi.org/10.1007/BF00705294
202. Unabia RB, Bonebeau S, Candidato RT, Pawłowski L (2018) Preliminary study on copper-doped hydroxyapatite coatings obtained using solution precursor plasma spray process. Surf Coatings Technol 353:370–377. https://doi.org/10.1016/j.surfcoat.2018.09.008
203. Radin SR, Ducheyne P (1992) Plasma spraying induced changes of calcium phosphate ceramic characteristics and the effect on in vitro stability. J Mater Sci Mater Med 3:33–42. https://doi.org/10.1007/BF00702942

Chapter 16
Synthesis and Processing of Magnetic-Based Nanomaterials for Biomedical Applications

Arunima Rajan, R. K. Chandunika, Femy Raju, Rashmi Joshi, Niroj Kumar Sahu, and Raghumani Singh Ningthoujam

Abstract Recent developments in the design, synthesis, and processing of magnetic nanomaterials have gained immense attention for various biomedical applications. Magnetic nanomaterial-mediated therapy and diagnostic applications have opened up new avenues for cancer therapy in terms of non-toxicity, biocompatibility, chemical stability, size, shape, and composition. This chapter covers a detailed account of the synthesis methods (chemical and biological) and the surface functionalization process determining the physico-chemical properties of the nanomaterials favorable for biomedical applications. Finally, a detailed overview of distinctive applications of magnetic-based nanomaterials in the field of magnetic hyperthermia, photothermal therapy, drug delivery, bioimaging and biosensing has been provided.

Keywords Synthesis · Magnetic nanomaterials · Biomedical applications · Magnetic hyperthermia · Drug delivery · Bioimaging · Biosensing

Abbreviations

ACMF	Alternating current magnetic field‘
[bmim][BF4]	1-Butyl-3-methylimidazolium tetrafluoroborate
CL	Chemiluminescence
CNT	Carbon nanotube

A. Rajan · R. K. Chandunika · F. Raju · N. K. Sahu (✉)
Centre for Nanotechnology Research, Vellore Institute of Technology, Vellore 632014, India
e-mail: nirojs@vit.ac.in

A. Rajan · F. Raju
School of Advanced Sciences, Vellore Institute of Technology, Vellore 632014, India

R. Joshi · R. S. Ningthoujam (✉)
Chemistry Division, Bhabha Atomic Research Centre, Mumbai 400085, India
e-mail: rsn@barc.gov.in

Homi Bhabha National Institute, Mumbai 400094, India

A. K. Tyagi and R. S. Ningthoujam (eds.), *Handbook on Synthesis Strategies for Advanced Materials*, Indian Institute of Metals Series,
https://doi.org/10.1007/978-981-16-1803-1_16

CPE	Carbon paste electrode
^{c}RGD	Cyclic arginine-glycine-aspartate
CRP	C-reactive protein
CT	Computed tomography
CTAB	Cetyltrimethylammonium bromide
CV	Cyclic voltammetry
DMSA	Dimercaptosuccinic acid
DNA	Deoxyribonucleic acid
DOTA	1,4,7,10-Tetraazacyclododecane-1,4,7,10-tetraacetic acid
DOX	Doxorubicin
DPV	Differential pulse voltammetry
EC	Electrochemical
EPR	Enhanced permeability and retention
FDA	Food and Drug Administration
FITC	Fluorescein isothiocyanate
GO	Graphene oxide
IONPs	Iron oxide nanoparticles
IR	Infrared
LOD	Low limit of detection
LSPR	Localized surface plasmon resonance
MF	Magnetic field
MHT	Magnetic hyperthermia
MNPs	Magnetic Nanoparticles
MRI	Magnetic resonance imaging
MWA	Microwave-assisted
MWCNTs	Multi-walled carbon nanotubes
NIR	Near-infrared
NMR	Nuclear Magnetic Resonance
NOTA	1,4,7-Triazacyclononane-N,N′,N″-triacetic acid
NPs	Nanoparticles
PAA	Polyacrylic acid
PAA-b-PS	Poly (acrylic acid)-b-polystyrene
PANI	Polyaniline
PDA	Polydopamine
PEG	Polyethylene glycol
PEGDE	Pentaethylene glycol dodecyl ether
PEI	Polyethylenimine
PET	Positron emission tomography
PMMA	Poly(methyl methacrylate)
PS	Polystyrene
PTT	Photothermal therapy
PVA	Polyvinyl alcohol
PVP	Polyvinylpyrrolidine
QCM	Quartz-crystal microbalance
SAR	Specific absorption rate

SPIONs	Superparamagnetic iron oxide nanoparticles
SPR	Surface plasmon resonance
TEM	Transmission electron microscopy
TMA	Thiomalic acid
TOPSe	Trioctyl phosphine selenide

16.1 Introduction

The global pervasiveness of cancer is a major health concern posing serious threats in terms of mortality and incidence rates [1]. Nanomedicine employing efficient nanomaterials as therapeutic or diagnostic probes has been the prime focus of attention during the past two decades in the area of cancer nanotechnology [2]. Recent advancements in nanotechnology enabled the utilization of nanomaterials in two distinctive fields of therapy and diagnosis. The development of multifunctional nanomaterial platforms, capable of integrating therapy and diagnostics as a single entity, has been proving its effectiveness in terms of remarkable progress in cancer research [3]. Such nanomaterials are promising in terms of facilitating early diagnosis and delivering effective therapy owing to their outstanding physico-chemical and biological characteristics. Various organic/inorganic nanomaterials such as iron oxide [4], silica [5], quantum dots of carbon, ZnS, [6], carbon nanotubes [7], manganese oxide [8] and gold [9] have been used for diverse biomedical applications. Nanomaterials especially magnetic-based nanomaterials have occupied a pivotal position for targeting, imaging and synergistic therapies for cancer. Owing to small size, easy functionalization, ease of penetration, enhanced retention inside the targeted area, biocompatibility and biodegradability, magnetic nanoparticles (MNPs) or magnetic-based nanomaterials are being extensively researched for various cancer theranostic modalities such as magnetic hyperthermia, drug delivery, bioimaging and biosensing [10, 11]. The intrinsic magnetic properties and the ability to be driven by an externally applied magnetic field make MNPs excellent materials as contrast agents for magnetic resonance imaging (MRI) and as heating probes for thermal therapies. The ability of MNPs for incorporating one or more cancer drugs to accumulate in the tumor sites via the enhanced permeability and retention (EPR) effect is widely exploited for drug delivery applications [12, 13]. Among the various MNPs, multifunctional iron oxide nanoparticles (IONPs) still remain as the potential candidate to serve as dual-purpose nanoplatform for clinical theranostics [14, 15]. IONPs, approved by Food and Drug Administration (FDA), are commonly used as contrast agents for bioimaging applications [16]. IONPs, specifically magnetite (Fe_3O_4) and maghemite (γ-Fe_2O_3), and ferrites (MFe_2O_4 where M = Mn^{2+}, Zn^{2+}, Co^{2+}) are being exploited for combined biomedical approaches such as image-guided drug delivery and image-guided thermal therapy [17–19]. The functional aspects of IONPs are greatly influenced by the synthesis routes for developing the MNPs with desired size, shape, crystallinity and optimal magnetic properties including saturation magnetization

and superparamagnetism. Surface modification of nanoparticles (NPs) is crucial for ensuring the colloidal stability of NPs. Surface-modified NPs enhance the therapeutic properties of bare NPs beneficial for specific targeting, imaging and therapeutic purposes. Various strategies are being used for the preparation as well as surface modification of MNPs suitable for biomedical applications. For example, Khaledian et al. recently fabricated DOX-loaded polymer-encapsulated superparamagnetic IONPs for targeted co-delivery into tumor cells [20]. IONPs were prepared by the co-precipitation method and subsequent polymerization for developing PLA–PEG–FA co-polymer functionalized IONPs. Following this, the conjugation of DOX (drug) on the PLA–PEG–FA IONPs (nanocarrier) was conducted via an emulsion method. The targeted nano-system offers a synergistic chemo-thermal therapy.

Generally, MNPs of metal oxides (ferrites, hexa-ferrites, garnets and perovskites) are used as sources of heat under AC magnetic fields (ACMF) for hyperthermia application due to easy processing and stability in the biological microenvironment [21]. There are other sources of hyperthermia treatment using non-magnetic nanoparticles such as Au, Ag, Cu and CuS through surface plasma resonance (SPR), which is also included for comparison [22–25]. Generally, this type of treatment is called photothermal therapy (PTT). Even, 2D materials absorb light in near-infrared (NIR) range and can produce heat. 2D materials of carbides such as MXenes including Ti_3C_2, Nb_2C, Ta_3C_4 and Mo_2C have been reported for photothermal heating-based hyperthermia [26]. Some of the magnetic compounds of metal carbides, borides, nitrides and phosphides will be potential materials for hyperthermia-based treatment under ACMF [27–30].

The present chapter presents an outline of commonly used synthesis methods to generate monodispered highly stable MNPs with priority in terms of facile, low-cost, highly reproducible techniques. Later, a section covering the importance of surface modification/functionalization of NPs for enhancing the effectiveness for specific biomedical applications has been summarized. Finally, recent progress in the application of magnetic-based nanomaterials for several biomedical applications such as magnetic hyperthermia, drug delivery, bioimaging and biosensors have been addressed.

16.2 Synthesis Methods

Various synthesis routes have been employed to fabricate NPs with unique physicochemical characteristics such as size, shape, surface composition and stability. Synthesis protocols have to be selected with utmost care ensuring the development of NPs with required characteristics. Synthesis methods can be broadly categorized into chemical (aqueous phase route and non-aqueous phase routes) and biological routes as shown in Fig. 16.1 [31]. These belong to the bottom-up approach, where ions or atoms are precipitated to the nanosized particles [21]. There is another method known as the top-down approach, in which micron-sized particles are brought to nanosized particles by grinding, ball-milling or bombarding high-energy particles

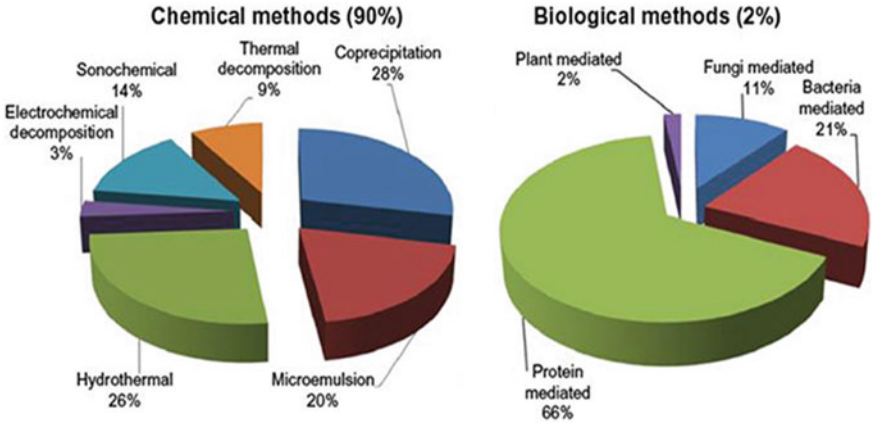

Fig. 16.1 Percentage estimation of the usage of various synthesis methods commonly employed to produce magnetic-based nanomaterials. Reproduced with permission from DOVE Medical Press [31]

on the target. The following section provides a brief overview of these commonly used synthesis routes for fabricating magnetic-based nanomaterials with a specific focus on biomedical applications.

16.2.1 Aqueous Phase Synthesis Routes

Aqueous synthesis routes are generally used to obtain hydrophilic NPs owing to the ease of control over the thermodynamics and kinetics of the growth reactions. Major aqueous phase synthesis routes are discussed in the following sections.

16.2.1.1 Precipitation or Co-Precipitation Method

In a chemical reaction, precipitation occurs when the ionic product is higher than the solubility product. Precipitation of $Fe(OH)_3$ can be obtained from an aqueous medium of 0.05 M $FeCl_3$ in 0.05 M HCl, as well as a solution of 0.05 M NaOH. At room temperature, the solubility product ($K_{sp} = [Fe^{3+}][OH^-]^3$) is found to be 1.6×10^{-39} [32]. If the ionic product in the solution increases, supersaturation occurs. The term co-precipitation is used when 2 or more metal ions are precipitated using counter ions. Fe_3O_4 MNPs can be precipitated using Fe^{3+}, Fe^{2+} ions in an alkaline medium such as NH_4OH, NaOH and KOH [33–37].

$$Fe^{3+}{}_{(aq)} + 3OH^-{}_{(aq)} \rightleftharpoons Fe(OH)_{3(solid/precipitate)} \tag{16.1}$$

$$2Fe^{3+}{}_{(aq)} + Fe^{2+}{}_{(aq)} + 8OH^{-}{}_{(aq)} \rightleftharpoons Fe_3O_{4(solid/precipitate)} + 4H_2O \quad (16.2)$$

Co-precipitation is one of the most facile and extensively used methods for synthesizing NPs owing to its high yield, easy reproducibility, high product purity and cost-effectiveness [33–38]. The co-precipitation reaction products are generally insoluble species formed under supersaturation conditions. The non-essentiality of hazardous organic solvents, high pressure and temperature make it an eco-friendly method for nanomaterial synthesis. This synthesis involving the addition of a mixture of metallic ions in an alkaline solution [NaOH, KOH, NH_4OH, or $N(CH_3)_4OH$] at a temperature below 100 °C was first proposed by Massart in 1981 [39]. Metal ferrite NPs by the co-precipitation method are fabricated by mixing solutions of ferric cation [Fe(III)] and M(II) salts (where M is a transition metal) in an alkaline solution forming particles of magnetic materials (known as precipitated particles) according to the reaction given as follows:

$$2Fe^{3+}{}_{(aq)} + M^{2+}{}_{(aq)} + 8OH^{-}{}_{(aq)} \rightleftharpoons MFe_2O_{4(solid/precipitate)} + 4H_2O \quad (16.3)$$

The processes involved in co-precipitation can be categorized into three steps: (1) preparation of a liquid phase solution of metal ions, (2) thermal treatment (if required) and (3) addition of a precipitating agent. The morphology, crystallinity and structure of the NPs are directly influenced by the thermal treatment, the precipitating agent and other factors such as foreign particles or molecules or ions (reducing or oxidizing), catalysts (homogenous and heterogenous types), types of capping agents and pH of the medium. The processes of nucleation, growth, coarsening and/or agglomeration occur simultaneously during a co-precipitation reaction. In the homogeneous precipitation process when species concentration attains critical supersaturation, rapid nucleation occurs and the diffusion of solutes to the surface on the crystal leads to the slow growth of nuclei. Monodispersed NPs are obtained when these two stages are ideally separated thereby avoiding nucleation during the period of growth [40, 41]. The size, shape and structural composition of obtained NPs could be fine-tuned by optimizing the reaction variables, viz., type of metal cation precursors, alkaline agent concentration and reaction temperature. Surfactants or functionalized polymers are used to protect the NPs from being oxidized in this protocol. Peternele et al. synthesized Fe_3O_4 and Fe_2O_3 phases of IONPs via co-precipitation using iron salts and alkali such as NaOH and NH_4OH as precipitants [42]. Transmission electron microscopy (TEM) analysis suggested that NPs precipitated from NH_4OH were more uniform than NPs precipitated from NaOH, and increasing the reaction temperature limits the aggregation of NPs thereby reducing the size of NPs. The mechanism and reaction pathway for synthesizing Fe_3O_4 NPs through the co-precipitation method have been proposed by Ahn et al. Formation of Fe_3O_4 can occur in two ways of nucleation, either by the (a) conversion of the akaganeite phase to goethite to hematite to maghemite and finally magnetite or by the (b) conversion of ferrous hydroxide to lepidocrocite to maghemite and finally magnetite. The pH of this reaction as well as the type of precursors determine the reaction pathway for the

formation of magnetite NPs [43]. Chen et al. reported $MnFe_2O_4$ NPs synthesized through co-precipitation exhibiting a decrease in both Curie temperature and saturation magnetization for small crystallite size particles [44]. Martina et al. employed a co-precipitation technique to produce superparamagnetic liposomes suitable for in vivo MRI imaging contrast agents [45]. The challenges such as tuning the size of particles and chemical homogeneity limit the application of this method in several circumstances.

Most of the MNPs prepared in an aqueous medium are associated with their corresponding hydroxides which will get agglomerated due to the hydrophilic nature as well as magnetic dipole interactions [46, 47]. Because of this, these particles are unstable for keeping them in the ambient atmosphere for a longer duration. It is necessary to use acetone to remove OH groups from particles. This makes compounds stable [48]. In the case of preparation of Fe_3O_4 nanoparticles, room temperature synthesis can be performed from the Fe^{3+} and Fe^{2+} ions (mole ratio of 2:1) in an alkaline medium (NaOH, NH_4OH). If N_2 gas is passed through the solution, the yield of MNPs can be increased [49]. Fe_3O_4 (magnetite) can be converted to γ-Fe_2O_3 (maghemite) by partial oxidation, whereas the opposite reaction can occur by partial reduction. Among iron oxides, α-Fe_2O_3 antiferromagnetic phase is thermodynamically stable. Fe_3O_4 or γ-Fe_2O_3 can be converted to α-Fe_2O_3 partially or fully after keeping them in an air or moisture environment. Magnetic and non-magnetic particles in solution can be separated using a magnet.

16.2.1.2 Hydrothermal or Solvothermal Method

The hydrothermal/solvothermal synthesis technique is the process of conducting chemical reactions in solvents, in which the solvent is heated to its critical point inside a sealed reactor (autoclave) under autogenous pressure. This method is performed under a temperature of 130–250 °C and a high vapor pressure of 0.3–4 MPa [50]. It has been widely accepted as a classic method for synthesizing inorganic and metal–organic nanomaterials. Water is employed as a solvent for the hydrothermal route whereas other solvents such as ammonia, alcohol, ethylene glycol and glycerol are used for solvothermal treatment. The solubility of salt precursors in hot water/other solvents is a major factor influencing this type of crystal synthesis method. The method is effective in making products of intermediate states, metastable states and other novel compounds. Above the critical temperature and pressure of solvent, many precursors that do not dissolve at normal atmosphere can be dissolved due to change in the dielectric constant of the solvent. The dielectric constants of water at room temperature are 78 and thus many polar salts can dissolve. Above the critical point, water can have dielectric constants in the range of 2–10, in which less-polar organic compounds can dissolve in water. Also, the solubility product is reduced and precipitation occurs faster. Nucleation and growth mechanisms are different in different temperatures and pressure in the hydrothermal or solvothermal method. In this way, compounds of desired phase and compositions (including different sizes and shapes of particles, metastable phase) can be prepared [51].

In the reaction mechanism, the crystallization process occurs via crystal nucleation and subsequent growth. The ions to be nucleated are formed in the reaction solution initially. Due to the temperature gradient along the top to bottom of the autoclave, a driving force is produced which transports the ions toward the low-temperature area. The process of transportation of ions continues until the solution becomes supersaturated. When the solution becomes supersaturated, nucleation occurs and the solute precipitates into clusters of crystals that are capable of growing to larger sizes. The kinetics of the reaction is controlled by the solvent which modifies the coordination of solvated species thereby inducing specific structures. Controlling the factors such as reaction time, temperature, metal salts precursors, surfactants (if any) and reducing agents is crucial for achieving precise control over size, shape and crystallinity. Gyergyek et al. compared the size distribution of IONPs synthesized via co-precipitation and hydrothermal method and found better control of size and shape with hydrothermal condition (180 °C) [52]. Chen et al. used iron–oleate and zinc–oleate precursors for synthesizing zinc-doped IONPs via the hydrothermal technique for MRI applications [53]. Li et al. reported hydrothermally synthesized spherical shaped 15 nm-sized PEI-coated IONPs for in vivo MRI of tumors [54]. However, the synthesis of nanocrystals with size < 10 nm is found to be difficult through this approach. Though the hydrothermal approach provides high crystalline mono-sized NPs, the reaction kinetics of crystallization can be further accelerated when coupled with microwaves.

16.2.1.3 Sonochemical Method

Sonochemical synthesis of NPs involves irradiating a liquid with high intensity of ultrasonic waves (20 kHz–10 MHz) in order to generate extreme pressure and temperature resulting in unique mechanisms and reaction pathways. Since acoustic wavelengths are longer compared to molecular dimensions, there exists no direct molecular-level interaction occurring between chemical species and ultrasound. Instead, it behaves as being exposed to alternating acoustic waves subjecting the liquid to dynamic tensile stress consequently changing the density of the liquid [55]. The ultrasonic waves break the chemical bonds by developing acoustic cavitation in the liquid leading to the generation, growth and collapse of microbubbles in the solution. These microbubbles are generated from the pre-existing impurities and oscillate according to the applied sound field. The bubbles grow to a certain size at the expense of ultrasonic energy, and accumulated energy in the bubble will be released in a very localized spot within a short time span leading to extremely high temperature (~5000 K) and pressure (~1000 bar) which facilitate high-energy chemical reactions [56, 57]. The heating and cooling rates are extremely fast (about 10^{10} K s^{-1}) leading to shock waves to the surrounding molecules of solvent or reaction. Figure 16.2 shows the schematic illustration of the development of acoustic cavitation in a liquid irradiated with high intensity ultrasonic wave: the formation, growth and implosive collapse followed by very fast cooling or rapid quenching [57]. This can produce free radicals ($H^{\cdot}$ and $OH^{\cdot}$) in case of aqueous medium, which can reduce noble metal ions

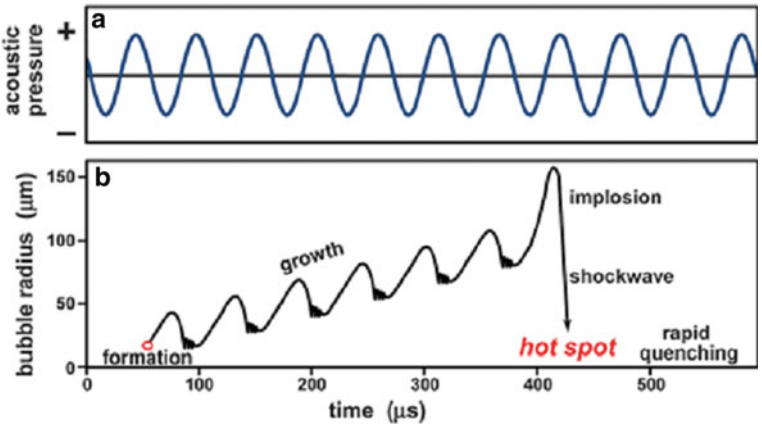

Fig. 16.2 Schematic representation of the development of acoustic cavitation in liquid irradiated with high-intensity ultrasound waves: formation, growth and implosive collapse followed by very fast cooling or rapid quenching. Reproduced with permission from RSC publisher [57]

to metal nanoparticles. The sonication duration, power and frequency of ultrasonication significantly affect the size and shape of the obtained particles. Sonochemical synthesis of nanomaterials can be classified as primary and secondary sonochemistry. In primary sonochemistry, free metal atoms from volatile precursors are produced via dissociation of bonds occurring at elevated temperatures created in the course of bubble collapsing. These atoms could be injected into liquid phase followed by nucleation to obtain NPs with the aid of suitable templates or stabilizing agents existing in the solution. This requires nonvolatile solvents because additional vapor absorbs the energy in the bubble. In secondary sonochemistry, nonvolatile precursors are used and sonochemical reactions may occur even outside the collapsing bubbles followed by diffusion into liquid phase initiating a set of reactions. Nanostructured noble metals are commonly prepared by dissolving nonvolatile precursors in a volatile solvent such as water or alcohols [57]. The radicals that could facilitate redox reactions are generated by collapsing bubbles induced by the ultrasonic field. For instance, Dolores et al. synthesized IONPs using ferrous–ferric salts in ethylene glycol solvent at distinctive ultrasound frequencies of 581, 861 and 1141 kHz with the equivalent acoustic power [58]. It was revealed that the generated hydroxyl radicals oxidized Fe^{2+} to Fe^{3+}. In addition, the rate of Fe^{3+} generation reduced in a linear manner with ultrasound frequency. Ultrasound waves used in the process initiate the reactions without external reagents and mass transfer occurs at both the microscopic and macroscopic levels. The mechanical effects generated by ultrasound enhance mass transfer within the medium which will further accelerate the chemical reactions and other different processes. By tuning the ultrasound power and frequency, better control on the size distribution of NPs can be obtained [59]. Moreover, the shape of NPs can also be controlled by this method. Monodispersed iron oxide nanocubes of 80 nm size using iron sulfate salts have been fabricated

by Abbas et al. [60]. This high-intensity ultrasonic waves offer a facile synthesis route for developing the NPs which are difficult to obtain using other conventional methods. Albeit, this eco-friendly method is still associated with major challenges such as scaling-up issues and energy efficiency.

16.2.1.4 Microemulsion Method

Amphiphiles are natural or synthetic molecules having a hydrophilic head group (functional group such as –COOH, $–SO_3$, $–NH_2$ and $–NH_3$) and hydrophobic tail group (long-chain hydrocarbons). These molecules are capable of self-assembling to distinctive nanostructures such as micelles, emulsions, nanotubes, vesicles, nanofibers and lamellae [61]. Such assembly is found in lipids and proteins of biological systems. Different shapes and sizes of self-assembly can be controlled by pH, ionic strengths, type of amphiphile molecules, temperature and dielectric constant. In reversed micelle, there is a nanoreactor where many chemical reactions can take place. Many NPs of metals (Ag, Au, Pt, Pd, Ni), alloys, core–shell structures and oxides (Fe_3O_4, NiO, TiO_2, $MnFe_2O_4$ and ZrO_2) can be prepared which can control nucleation as well as the growth of NPs. Oxide thin films can be prepared from amphiphiles and respective metal ions using the Langmuir Blodgett approach.

Microemulsions, developed by Hoar and Schulman in 1943, are clear homogeneous solutions in which two immiscible liquids (water and oil) coexist as a single phase due to the presence of surfactants [62]. Typically, surfactants with a hydrophilic head and a lipophilic tail are used. Two variants of microemulsions such as direct emulsion (oil dispersion in water) and reversed emulsion (water dispersion in oil) can be prepared for the synthesis of MNPs based on the hydrophilic–lipophilic balance of surfactants as well as the ratio of oil–water. Cetyltrimethylammonium bromide (CTAB) was used as a surfactant during the initial study by Schulman and is still the commonly used surfactant for this method. In addition to this, sodium bis(2-ethylhexyl)sulfosuccinate, pentaethylene glycol dodecyl ether (PEGDE) and Triton-x have also been used as surfactants. Later, in 1970 Friberg investigated the orientation of molecules through NMR and IR studies finding that the interfacial tension between molecules is minimized in the microemulsion and is thermodynamically stable [63]. For the synthesis of metal particles, a microemulsion solution consisting of dissolved metal salts is mixed with a second solution consisting of the reducing agent to form metallic particles via reduction. A reducing agent should be stable in an aqueous solution and non-reactive to other components in the microemulsion as it plays a major role in this process. Commonly used reducing agents for microemulsion methods are hydrazine dihydrochloride ($N_2H_4{\cdot}2HCl$) or hydrazine hydrate ($N_2H_4{\cdot}H_2O$). For synthesizing metal oxide NPs, this technique is similar to co-precipitation in which the hydroxides are precipitated by the addition of a microemulsion solution diluted with an oxidizing agent to the solution of aqueous metal ions. Another way to prepare metal oxide NPs is the formulation of 2 microemulsions in different beakers: the first microemusion contains metal ions (M^{n+}) and the second one has oxidizing agent or anions such as OH^-, VO_2^+

and VO_3^- (from NH_4OH, NaOH, KOH, NH_4VO_3). When both microemulsions are mixed, there is a fusion of two microemulsions leading to an interaction between metal ions and anions. Finally, metal oxides or metal hydroxides or metal vanadate are formed [64]. The obtained metal hydroxides are collected by centrifugation. Metal ferrites (MFe_2O_4 where M = Fe, Mn, Co, Zn) of 10–20 nm sized NPs have been synthesized by this method. Zereffa et al. synthesized silica-coated Fe_3O_4 NPs using the water-in-oil microemulsion technique using ferric nitrate and ferrous sulfate as iron salts [65]. Ammonia solution has been used as an oxidizing agent with Tween-80 (surfactant),1-butanol (co-surfactant) and n-heptane as the oil phase. Solution I constitutes iron salts dissolved in Tween-80/butan-1-ol/n-heptane. Solution II constitutes a mixture of SiO_2 solution with Tween-80/butan-1-ol/n-heptanes and ammonia. Both the solutions were mixed and stirred for 150 min under 1000 rpm at various temperatures of 30, 50 and 80 °C. Obtained $Fe_3O_4@SiO_2$ was rinsed with a mixture of DI water and acetone 2–3 times for removing excess ammonia and surfactants. Here, reactants in the aqueous solution acted as dispersed phase and 16 nm sized NPs were obtained. In another work by Singh et al., magnetite NPs were synthesized by the microemulsion method with particle size < 10 nm confirmed by transmission electron microscopy studies [66]. The metal salts of ferrous and ferric ammonium sulfate dispersed in sulphuric acid were mixed with the solution containing sodium hydroxide (reducing agent), CTAB and Triton- × 100 as surfactants. The mixed solution was thermally treated for 30 min duration at 80 °C to obtain magnetite phase NPs. This method facilitated the production of nanostructures of narrow size distribution with good reproducibility. Fe_3O_4/SiO_2 core–shell nanostructures of varying sizes of 31, 33, 43 and 55 nm were prepared using the water-in-oil reverse microemulsion method in the presence of Triton-X100 surfactant [67]. A cationic polymer layer was further conjugated to the core–shell structure and hence proved to be used as a carrier for anionic drug and nucleic acids. However, this synthesis method requires more stabilization and several washing procedures of the synthesized NPs prior to bioapplications. A hypothetical phase diagram of the microemulsion method is shown in Fig. 16.3 [68].

Depending on the water/oil ratio (reverse micelle route), different sizes and shapes of particles can be prepared. In order to prepare pure compounds or metals, the surfactants, oils and water, which are associated with particles, need to be removed. There are many ways to remove these such as warming, dissolving with other solvents and heating at higher temperatures (say above 500 °C).

16.2.1.5 Electrochemical Method

Electrochemical synthesis is a facile, cost-effective and efficient strategy for fabricating MNPs with various nanostructures such as nanospheres, nanorods and nanosheets in which fabrication is conducted in an electrochemical cell [69]. As the name implies, electrochemical synthesis is carried out by passing an electric current between electrodes in the electrolyte solution. Electrochemical synthesis takes place at an electrode–electrolyte interface, and material gets deposited on the

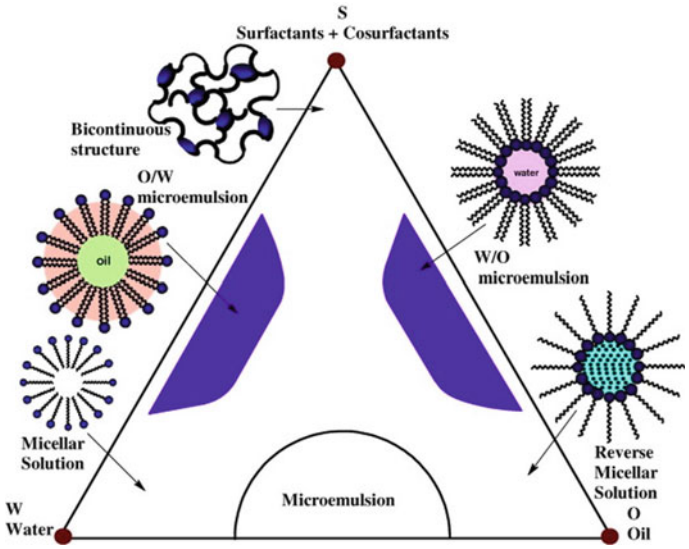

Fig. 16.3 Phase regions of microemulsion system. Adapted and reprinted with permission from Elsevier Publisher [68]

electrodes as thin films. It is one of the low-temperature synthesis methods, and the kinetics of the reaction can be controlled easily by the applied current. The choice of electrode, electrolyte, temperature, pH and composition of electrolyte affect the electrochemical process. In a typical synthesis, the reactants dissolved in the electrolyte will get deposited on the application of current. The experimental setup requires a potentiostat or a galvanostat and an electrochemical cell with either two or three electrode configurations, supporting electrolytes, solvents and precursor chemicals. The transfer of electron(s) from the electrode to the electrolyte (metal ions in the solution) or vice versa across the electrode/solution interface takes place to bring the chemical changes. For the synthesis of IONPs in an electrochemical cell, a sacrificial anode (iron) produces Fe^{3+}/Fe^{2+} ions whereas the cathode generates hydroxyl anions via electrolysis of water. Reetz et al. were the first to synthesize powdered Pd metallic NPs of size 4.8 nm by electrochemical synthesis [70]. Aghazadeh et al. synthesized ultra-fine-sized PVA-coated IONPs of 10 nm by tuning the applied current density through an electrochemical method using a two-electrode electrochemical cell [71]. The setup employs two graphite anodes which were placed in between a stainless-steel cathode as electrodes. An aqueous solution of iron salts such as ferrous chloride and ferric nitrate was used as electrolyte. After the addition of polymer (PVA) to the electrolyte solution, PVA was deposited on an iron oxide surface at the cathode with a current density of 10 mA/cm^2 for 30 min duration and at a temperature of 40 °C. The steel cathodes were washed using ethanol several times and deposited NPs were scraped from the cathode surface, dispersed in ethanol, centrifuged and dried. Fajaroh et al. employed electro-oxidation of iron in the water for synthesizing

magnetite Fe_3O_4 NPs [72]. Pure iron plate and PEG solution were used as the iron source and electrolyte, respectively. The electro-oxidation of iron takes place in the dilute solution of PEG under DC voltage for 4 h. Monodispersed spherical-shaped particles with diameter 62.5 nm were obtained. It was found that the size of obtained NPs could be regulated by varying the electrochemical cell parameters, and the method seems to be promising for the synthesis of metal ferrites. However, it has certain disadvantages associated with the poor structural properties of the material formed and inability to produce uniform particle shapes or sizes and the inherent limitation to only use conducting substrates. Figure 16.4 shows a depiction of the electrochemical synthesis of IONPs [73].

Morphology of particles (size, shape and hollowness of particles) can be regulated using the electrochemical route. One of the advantages of this route is homogenous electroplating of any shape of materials. Other advantages of electrochemical route over other synthesis methods include the following: (a) non-requirement of chemical oxidants or reductants due to the presence of precursors. The chemicals such as ions in solution undergo electron transfer directly on the electrode surface, (b) a large redox potential range of several volts is easily accessible by selecting an appropriate combination of electrode materials, solvents and supporting electrolytes. Such a large potential range of several volts involves very high energy either comparable or more than most of chemical bonds and activation energy involved in chemical reactions, leading to a controlled generation of highly energetic intermediates under mild experimental conditions and (c) a high selectivity and percentage yield can be obtained because of very precise control over potential and current.

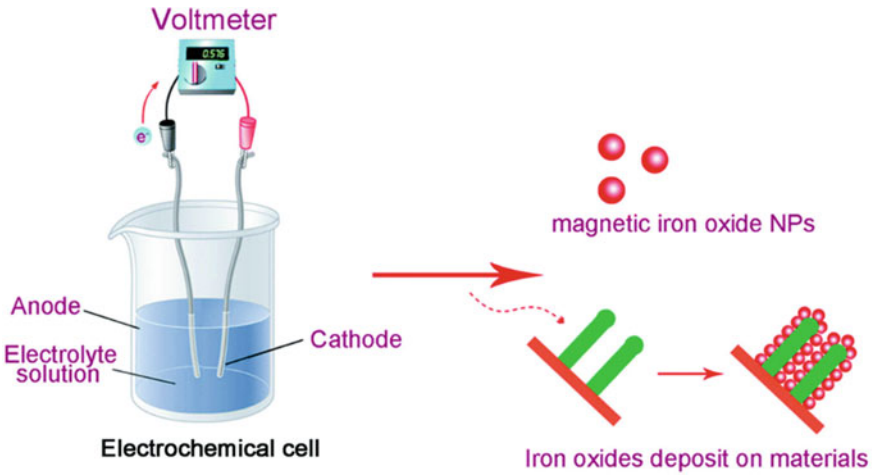

Fig. 16.4 Depiction of electrochemical fabrication of IONPs. Adapted and reprinted with permission from RSC Publisher [73]

16.2.1.6 Sol–Gel Method

The sol–gel method also termed as chemical solution deposition is a wet chemical route which involves the hydrolysis and polycondensation of metal alkoxide precursors resulting in gel formation (dispersion of metal oxide particles) which is then followed by drying and thermal treatment [74]. The sol–gel method proceeds via a series of various phases: (i) Formation of metal alkoxide or metal precursor solution, (ii) Gelation by polycondensation or polyesterification of the solution, (iii) Aging of the gel, (iv) Drying to remove water from the gel (very slow evaporation) in the temperature range of 50–100 °C and (v) Decomposition of gel by slow heat treatment up to 500 °C. Here, simultaneous oxidation and reduction occur in the temperature range 250–450 °C. Thus, a strain developed in particles is removed and finally, non-agglomerated fine particles in a nanosized range of metal oxide can be prepared. With a further increase of annealing temperature, particle size can be increased uniformly. The density of metal oxide obtained by compaction of powder and followed by sintering is higher than that of other synthesis methods. This is an advantage of the sol–gel route as compared to other synthesis routes. Precursors can be hydrolyzed with the aid of an acid or a base and the commonly used solvent is water. The colloidal gel can be obtained if a base is used for hydrolyzing, and polymeric gel can be obtained if an acid is used for hydrolyzing. The reaction occurs at room temperature and subsequent thermal treatment is required for the final crystalline formation. The reaction mechanism for the generation of Fe_3O_4 NPs via sol–gel using iron (III) aqueous solution occurs through different stages such as the formation of iron ($2Fe^{3+}$, Fe^{2+}) alkoxides, gelation in alkaline medium and decomposition. The obtained NPs show a narrow size distribution and are hydrophilic. Factors such as pH, precursor ratio, temperature, kinetics and gel properties influence the synthesis method. Instead of isopropyl alcohol, some precursors like citric acid, ethylene glycol, polyvinyl alcohol, glycerol and polyethylene glycol have also been used [75–77]. This can make cross-linking with metal ions to form a gel, which is of amorphous and cross-linking polymeric type. Takai et al. synthesized magnetite NPs using ferrous–ferric chloride salts via the sol–gel method [78]. The metal salts were dissolved in ethylene glycol and continuously stirred at 45 ℃ for 3 h to obtain a sol. The obtained sol was heated at 45 ℃ until a dark colored formation occurred. Later the gel was aged for 72 h and dried at 140 °C for 5 h and annealed at temperatures ranging from 200 to 400 ℃. The obtained magnetite NPs were in sizes of 2.20, 5.58 and 8.35 nm for the decomposition temperatures of 200, 300 and 400 °C, respectively. Jacintha et al. synthesized $MnFe_2O_4$ NPs employing natural polymers such as wheat flour and potato flour by the sol–gel method [79]. Manganese nitrate, ferric nitrate and sodium hydroxide are dissolved in deionized water upon stirring for 15 min to achieve a homogeneous solution. Subsequently, the polymer solution was added and stirred continuously at 50 °C for the formation of sol. The sol was then thermally treated to 90 °C to form a gel followed by aging for 2 days. It was then annealed at 600 °C to obtain $MnFe_2O_4$ nanoparticles. Crystallite sizes of 23.12 nm and 16.87 nm were obtained with wheat flour and potato flour, respectively. Recently, magnetic carbon dot-based heterostructures with 20–80 nm sizes synthesized using

the sol–gel technique have exhibited 37% cell death on tumor cells (human osteosarcoma) [80]. Recently, Li-Zn-Co-ferrite of 12 nm spherical-shaped NPs synthesized via the sol–gel method were taken in a CNT matrix for testing toward magnetic hyperthermia [81]. The as-prepared NPs were proven to conjugate antitumor drugs thereby exhibiting an enhanced therapeutic performance.

16.2.1.7 Solid State Reaction Method

In the solid-state reaction method, all precursors required for the formation of metal oxides in the form of oxides, carbonates and acetates are mixed using a pestle mortar. The mixture is heated at a higher temperature (800–900 °C) and subsequently cooled to room temperature. Then the powder is grounded and pellets are prepared. These pellets are then heated at a higher temperature at 1000 °C or above. Sometimes, intermediate grinding and palletization are required to get a proper stoichiometry and phase. Palletization helps in the diffusion of ions and direct contact between particles [82]. For example, when a mixture of MgO and Fe_2O_3 precursors are heated, $MgFe_2O_4$ compound can be formed, but in-homogeneities in phase may occur (partly, $MgFe_2O_4$, Fe_2O_3 and MgO). Intermediate grinding, palletization and heating help in getting a proper stoichiometry without other impurities. In some cases, an oxygen atmosphere is provided to get a proper stoichiometry and phase. In this way, many magnetic oxides such $A_{1-x}B_xO_3$ (A = La, B = Ca, Sr, Ba) and $A_{3-x}B_xMn_2O_7$ are prepared [83].

16.2.1.8 Combustion Method

In the combustion method, metal ions in the form of nitrates or oxy-nitrates as oxidants are treated with organic compounds such as urea, citric acid, ascorbic acid and glycine as fuel in a large capacity of a borosilicate glass beaker, and then the mixture is heated at 300–500 °C [84, 85]. The instantaneous reaction occurs due to a huge amount of exothermic reactions. Voluminous or porous metal oxides are observed inside the beaker and because of this, a large capacity of borosilicate glass beaker (2–5 L) is preferable for the preparation of 2–10 g of metal oxides. Such exothermic reaction produces a large evolution of gases such as CO, CO_2, N_2, H_2O and NO_x. It needs to take some precautions during preparation. The amount of heat generation can be obtained by a ratio (ϕ) of the net oxidizing valency of oxidants to the net reducing valency of fuel (O/F). This ratio is an important factor in getting a high yield of the product. Generally, a ratio of 1:1 is used.

For attaining this, metal precursors are dissolved in HNO_3 and glycine followed by the addition of citric acids or polyvinyl alcohols according to the O/F ratio. The solution is prepared by stirring which is kept for one day. Then it is heated very slowly up to 300–500 °C. There is a decomposition of metal–glycine complex with an exothermic reaction. This makes fine particles of metal oxides. Then it is further heated at 600–1000 °C to get the different sizes of particles. In this way, many

magnetic compounds such as ferrites, garnets and hexa-ferrites and $A_{1-x}B_xO_3$ (A = La, B = Ca, Sr, Ba) and $A_{3-x}B_xMn_2O_7$ are prepared [86–99].

16.2.2 Non-aqueous/Organic Phase Synthesis Routes

Non-aqueous/organic routes for synthesizing hydrophobic NPs are based on chemical reactions of metal precursors which are dissolved in high boiling point solvents at a higher temperature. Major non-aqueous synthesis routes are briefly explained in the following sections.

16.2.2.1 Thermal Decomposition Method

Thermal decomposition route is generally employed for synthesizing hydrophobic NPs with controlled physico-chemical attributes such as size, shape, morphology, chemical composition, crystallinity and magnetic properties. This method involves the decomposition of organometallic precursors in the presence of surfactants in high boiling point organic solvents at very high temperatures (240–350 °C) in an inert atmosphere. However, there are reports on the synthesis of nanocrystals in different atmospheres (reducing and oxidizing atmosphere). Such decomposition occurs owing to the chemical bond breakage in metal complex through an exothermic or endothermic or simultaneous exothermic and endothermic reaction in an inert atmosphere preventing undesirable phase formation. Commonly used organic solvents possessing high boiling points are phenyl ether (bp = 258 °C), benzyl ether (bp = 298 °C), octyl ether (bp = 292 °C), 1-eicosene (bp = 151 °C), 1-hexadecane (bp = 286 °C), 1-octadecene (bp = 315 °C), hexadecanodiol (bp = 72 °C) and trioctylamine (bp = 168 °C), and surfactants used are fatty acids, oleic acid, oleylamine (bp = 364 °C), linoleic acid (bp = 230 °C), Trioctylphosphine (TOP, bp = 408 °C), Trioctylphosphine oxide (TOPO, bp = 408 °C) and long-chain amines. This method is proved as one of the most effective approaches to obtain high-quality monodispersed NPs of various materials such as metals, alloys, metal oxides, metal chalcogenides, composites and core–shell. Maity et al. reported enhanced magnetic properties for thermally decomposed magnetite NPs with prolonged reaction duration (4 h) and higher temperature (330 °C) [100]. In addition, the obtained narrow-size particle distribution was attributed either to the selective binding of surfactant (oleic acid) to core NPs' surface or to the synthesis route involving a solvent-free reaction [100]. The compounds prepared by thermal decomposition in an organic solvent are highly crystalline.

Two types of synthesis approaches used in thermal decomposition are (a) rapid/hot injection mode and (b) direct heating mode. Rapid injection mode comprises initial heating of reaction solution consisting of surfactants and solvents to a certain temperature. Following this, a metal precursor solution is injected into the hot reaction system for facilitating a rapid nucleation process or short burst of nucleation at

the critical saturation. The size and shape of the crystalline phase depend on injection temperature, waiting time, metal to surfactant ratio, others such as reducing or oxidizing environment, co-surfactant, catalysts and nucleation site used in the reaction [101]. Hence, the growth process of NPs could be controlled in terms of reaction temperature as well as reaction duration, thereby assuring uniform growth and monodispersed NPs. Instantaneous supersaturation occurs in the case of the hot injection method compared to direct heating mode. Hyeon et al. prepared monodispersed crystalline γ-Fe_2O_3 NPs via rapid injection thermal decomposition of iron pentacarbonyl [$Fe(CO)_5$] in the presence of surfactants [102]. Nucleation of NPs is attained by the rapid injection of $Fe(CO)_5$ into the hot reaction solution (mixture of surfactant and solvent) heated above the precursor decomposition temperature. It has been proposed that nucleation ensuing from the thermal decomposition of iron pentacarbonyl started at a low temperature (100 °C). On the other hand, growth resulting from the decomposition of the iron–oleate complex takes place at an elevated temperature (300 °C). Distinctive nucleation and growth processes assist in obtaining extreme control over particle size as well as distribution. Bawendi and group in 1993 introduced this hot injection process to produce monodispersed highly crystalline cadmium chalcogenides [103]. In their work, organometallic precursors such as dimethyl cadmium and trioctyl phosphine selenide (TOPSe) have been injected into the reaction solution at 360 °C which induced a burst of nucleation followed by subsequent growth for the formation of monodispersed CdSe nanocrystals. It was inferred that precursors as well as capping agents grafted on the nanocrystal surface control both nucleation and growth rates thereby controlling the size and shape of NPs. Efficient exchange coupled/core–shell nanostructures beneficial for biomedical applications can also be prepared via the hot injection method. Here, the core will be synthesized initially followed by the injection of shell precursors into the solution in which the core is prepared. A major benefit of this method is that it allows the preparation of multiple shells via successive injection of shell precursors in a single pot.

The direct heating strategy of thermal decomposition route (commonly known as thermolysis) involves the complete mixing of metal precursors, surfactants and solvents in a certain ratio followed by slow heating at 100–360 °C depending on the required phase and morphology of crystalline compounds [104]. Under this high temperature, decomposition of metal precursors occurs followed by rapid burst nucleation leading to a steady growth process to form monodispersed NPs. Usually, organic metal precursors such as metal acetate, carbonyl and acetylacetonates are used. Lassenberger et al. studied the mixing of organometallic precursors such as iron pentacarbonyl ($Fe(CO)_5$) in the presence of oleic acid (capping agent) and dioctyl ether (solvent) and heating at 290 °C to form mono-sized IONPs of 3–4 nm [105]. Size and morphology can be controlled by optimizing the heating process and heating parameters. Long-chain surfactants such as oleic acid, oleylamine and octyl phosphonic acid significantly affect this type of synthesis routes. Owing to the strong coordination ability and improved thermal stability, decomposition of the formed intermediate products during this reaction could be difficult. At a specific reaction temperature, slow decomposition of such intermediates occurs which can potentially impact the size and morphology of NPs. This method is commonly employed

for the synthesis of ferrites such as manganese ferrite ($MnFe_2O_4$), nickel ferrite ($NiFe_2O_4$), cobalt ferrite ($CoFe_2O_4$), magnetite (Fe_3O_4) and their composites. Sun et al. have reported that monodispersed metal-ferrites such as $MnFe_2O_4$, $CoFe_2O_4$ and Fe_3O_4 with a narrow size distribution of 3–20 nm synthesized via the high-temperature thermal decomposition method possess greater potentials to be explored for prospective biomedical applications [106]. Corresponding metal acetylacetonate salts as precursors with 1,2- hexadecanediol in the presence of oleic acid and oleylamine have been employed for this high-temperature solution phase reaction. A diverse technique was adopted by Park et al. to synthesize monodispersed MNPs of the narrow size distribution of 5–22 nm using metal–oleate complex as a precursor in varying high boiling point solvents [107]. Even though the thermal decomposition method is capable of synthesizing highly monodispersed IONPs, the prepared NPs are hydrophobic in nature. Due to this hydrophobicity, subsequent phase transfer and surface modification procedures with the aid of several ligand exchange methods are required for their effective usage for biomedical applications.

Different shapes from spherical to cuboid Fe_3O_4 particles can be prepared based on Oswald repining methods. Here, smaller-sized particles got dissolved and deposited over larger particles. Figure 16.5 shows TEM images of monodispersed particles of Fe_3O_4 and particle size increases after addition of scarifying material of small-sized particles into already prepared particles by the concept of the core–shell model [104]. With the further addition of scarifying material of small-sized particles, particle size distribution is broad and sometimes, bimodal distribution occurs. With a decrease of particle size, there is a chance of occurrence of a mixed phase of Fe_3O_4 and γ-Fe_2O_3. This is confirmed by XANES and EXAFS [108].

MNPs of metallic Fe, Co, Ni, CoNi, FePd, FePt and their alloys have been prepared by thermal decomposition of respective metal precursors [109–112]. Sometimes, monodispersed particles (Co, Ni, CoNi (Fig. 16.6, [109]), Au, Ag, $NaYF_4$:RE (RE = rare-earths)) are prepared from the metal precursors either by the process of digestion, Oswald ripening or a combination during thermolysis. The formation of monodispersed particles may not be only due to the thermal decomposition of metal precursors (acetate, carbonyl). The precursors of metal chlorides, nitrate and oxides are used to prepare monodispersed particles. In the case of preparation of monodispersed particles $NaYF_4$:RE, the source of F is a mixture of NaF or NH_4F and NaOH in methanol and metal precursor can be of metal chloride or oxide [113–115].

16.2.2.2 Microwave-Assisted Method

The microwave-assisted method is one of the methods that can prepare materials within a short time [116]. When suitable frequency and power are applied to the reaction vessel containing reactants/precursors and solvents for a few minutes, the materials such as metals, alloys, oxides, sulfides, composites, biomaterials and non-metals (carbon allotropes, CNTs, graphene) can be prepared. Nanometre-sized regime particles can be synthesized. Heat generation in the reaction system under the microwave cavity is due to dielectric polarization and ionic conduction. Solvents such as water

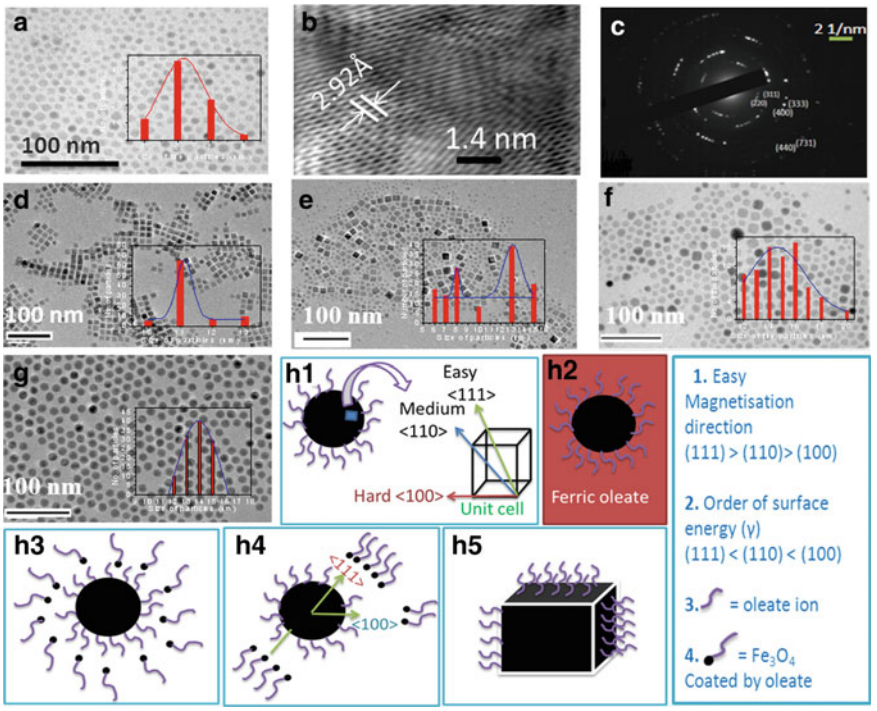

Fig. 16.5 Core Fe_3O_4 particles (heating rate of 4 °C/min): (A) TEM image, (B) HRTREM image and (C) SAED pattern. Core–shell Fe_3O_4@ Fe_3O_4 particles after adding (D) 1 mL and (E) 5 mL of ferric oleate (1 h heating duration) and (F) 5 mL of ferric oleate (8 h heating duration). (G) Core Fe_3O_4 particles synthesized with a heating rate of 1.3 °C per min. Graphical illustration of sphere to cube shape transformation of particles in the core–shell model (Ostwald ripening mechanism): (H1) slightly spherical oleate-coated particle along with magnetization axes of face-centered cube (Fe_3O_4 unit cell), (H2) particles in ferric oleate medium, (H3) formation of Fe_3O_4 small particles/cluster which surrounds a larger particle, (H4) faster growth/deposition along < 111 > direction as compared to < 100 > or < 220 > direction, (H5) cube-shaped particle formation. Reproduced with permission from Springer Nature Publisher [104]

and ethylene glycol are used to get uniform heating. This is different from conventional heating from heat sources. The role of solvents, reaction vessels, additives, MW frequencies and powers to achieve microwave synthesis are important parameters. In this method, uniform heating over particles can be obtained.

Compared to conventional heating techniques for NP synthesis, microwave-assisted (MWA) synthesis has been extremely effective in terms of higher yield, reduced particle size and dissolution enhancement. Here, microwaves (1 mm^{-1} m range of wavelengths and frequency of 300 MHz–300 GHz) are used as heat sources to stimulate the reaction for NP synthesis. Microwaves are capable of inducing nucleation or growth of NPs. This method is generally executed in combination with thermal decomposition method and hence this is considered as a non-aqueous route. However, microwaves can also be employed to accelerate aqueous-based

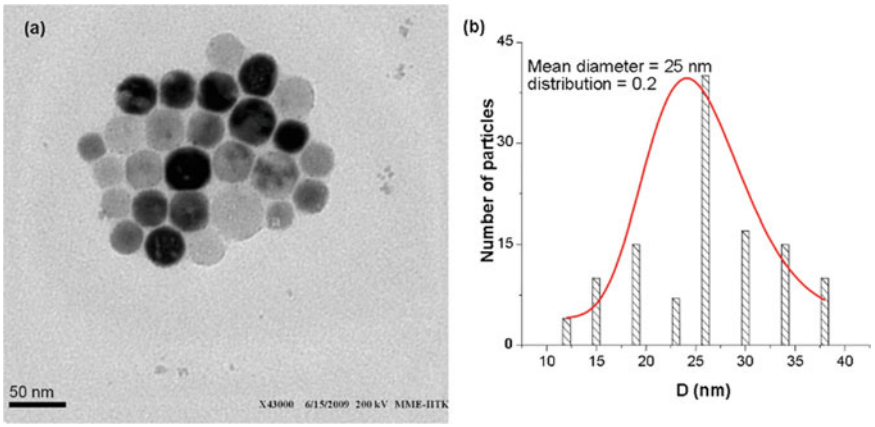

Fig. 16.6 **a** Bright-field TEM image of $Co_{50}Ni_{50}$ NPs and **b** its particle size distribution. Reproduced with permission from Elsevier Publisher [109]

approaches such as hydro/solvothermal and sol–gel. MWA offers the advantages of facileness, rapid heating, higher reaction rate, inexpensiveness, energy efficiency and eco-friendliness. Due to higher heating rates and precise heating control, this method produces highly crystalline uniform NPs with monodispersed size distribution. MWA uses a specially designed microwave synthesis reactor for controlling the reaction temperature, stirring rate and pressure inside the reactor. MWA works on the principle of exciting a material to induce dipole alignment by microwave electromagnetic waves. The heating effect of microwave occurs due to the interaction of the electric field component of a microwave with charged particles in the material via both conduction and polarization. Microwave irradiation directly activates molecules possessing a dipole (dipolar polarization mechanism) or ionic (ionic conduction mechanism) leading to a sudden upsurge in temperature. In general, microwaves interact with material or solvent with polar molecules. Nature and polarity of solvents play crucial roles in MWA for the formation of inorganic NPs. The polarity of the solvent regulates the reaction rate. The higher the solvent polarity, the higher will be the potentiality to couple with the microwaves for an increased temperature and reaction rate. Water is a widely used solvent for MWA synthesis of inorganic NPs owing to its polarity as well as the ability to absorb microwaves. Shorter reaction duration and uniform heat distribution arising from instantaneous interaction of microwaves with the material are major advantages over other methods. IONPs have been reported to be effectively synthesized by the MWA method [117]. Hu et al. synthesized monodispersed Fe_3O_4 NPs ($\sim$6 nm) using $Fe(acac)_3$ and 1,2-hexadecanediol in dibenzyl ether in the presence of oleic acid and [bmim][BF4] via MWA heating instantaneously at 220 °C for 5 min followed by 250 °C for another 5 min [118]. Komarneri et al. synthesized magnetite NPs with sizes ranging from 24 to 1000 nm exhibiting magnetization in the range of 59–89 emu/g under MWA heating by varying temperature (80–150 °C) and time (1–16 min). It was also inferred that the crystallinity of NPs was increased

as the temperature was raised by microwave heating [119]. In another study, simultaneous stirring and MWA heating reduced ferric chloride salt in the presence of dextran (surfactant) and hydrazine (reducing agent) to generate FITC–dextran-coated IONPs. Smaller-sized NPs of 21.5 nm size with excellent reproducibility were synthesized which exhibited improved response for applications such as MRI positive contrast agents and as optical probes (fluorescent imaging) [120]. In spite of the fact that the penetration depth of the microwave is confined, MWA is capable of achieving a higher yield with enhanced efficiency.

16.2.3 Biological Synthesis Routes

Biomineralization, in which biological systems produce finite size and shape-controlled solid inorganic materials, has rectified several problems associated with the conventional synthesis routes. Specific uptake of elements by the living organism from the environment results in developing highly ordered inorganic materials in the size regime of nanometeres to centimeters. Bio-reducing agents such as plant extracts, algae and bacteria render biological routes facile, inexpensive and eco-friendly. Among the different chemical synthesis routes, biological methods seem to be superior due to the absence of the usage of virulent materials for any adverse effects. Ferromagnetic materials have been reported to be biomineralized by a wide range of organisms such as insects, algae and birds [121]. Various bio-inspired nanomaterials such as liposomes, lipid NPs, bio-synthesized metal NPs, viral NPs and protein NPs have garnered immense attraction in cancer theranostics [122–127]. Bio-inspired NP mimicking natural elements in the body can be employed as an alternative biocompatible drug delivery system in cancer theranostics. Nanomaterial formation by the living systems is usually carried out under mild conditions supplied from the specific organelle which mediates the environment for nanomaterial growth. For instance, magnetotactic bacteria produce magnetite NPs termed as magnetosomes in a controlled manner with well-defined size and shapes. Magnetotactic bacteria use Earth's magnetic field for alignment and migration [128]. The bacteria derive the NPs from a specially isolated protein present in their bodies via intra/extracellular mineralization processes. These naturally synthesized NPs are characterized by chain-like structures possessing good crystallinity and better biocompatibility, advantageous for homogeneous distribution in tumors capable of producing a large amount of heat required for cancer therapies [129]. In addition to these applications, these types of NPs are proved to be suitable for efficient drug delivery and imaging applications. Zhou et al. prepared 16 nm-sized mesoporous magnetite NPs using yeast cells as templates [130]. Biologically synthesized multifunctional NPs with noble metal centers functionalized with various therapeutic and imaging agents possess improved theranostic activities against cancer [129]. Generally, the formation process of bio-inspired theranostic agents involves (a) screening of plant extracts for the synthesis of NPs, (b) optimization of physico-chemical parameters employed during biosynthesis, (c) conjugating with theranostic agents and (d) finally characterization of

nanocarriers using various analytical methods. Though this method is eco-friendly, a substantially slower rate of reaction kinetics limits the synthesis of iron oxide-based NPs. However, a positive outlook for bio-synthesized NPs may open up new horizons in the near future of cancer theranostics.

Recently, it is reported that MNPs of Fe_3O_4 and γ-Fe_2O_3 have been formed in cancer cells [131]. It is due to the generation of reactive oxygen species (H_2O_2) and the involvement of the glycolytic pathway in the cancer cells as compared to the normal cells. In vitro study confirms the significant increase of Fe and Zn concentrations in cancer cells after treatment with $FeCl_2$ and Zn gluconate. Under AC magnetic field, hyperthermia temperature can be achieved.

16.3 Surface Modification and Ligand Exchange Method

Surface modification to make particles water-dispersible can be done for biomedical applications. Two types of particles can be considered as follows.

- Bare particles.
- Particles having capping ligands.

In the case of bare particles, capping ligands (L) such as citric acids, oleic acid, dextran, PEG-diacids, glutathiol and chitin can be added to the bare particles (NPs) (mole ratio of L:NPs = 1:1, 2:1, 3:1,…) [64, 88, 91, 95, 132–139]. Water is used as a solvent for proper interaction at different pH = 5, 7, 8. Mixing can be done for 10–36 h under constant rotation. Then centrifugation will be done so that excess supernatant is removed. In this way, bare NPs become properly surface-functionalized. Chemical binding between the surface of particles and ligands can be investigated by many techniques such FTIR and TG–DTA. The use of proper ligands having long-chain hydrocarbons reduces agglomeration among particles.

In the case of particles having capping ligands, it needs to see whether particles are water-dispersible as well as biocompatible or not up to 250 μg/ml or beyond. In the case of hydrophobic ligands such as oleic acid, olylamine and linoleic acid, particles will not be dispersible [104, 132]. To make water dispersible, the following strategies can be done: (i) Ligand exchanges with hydrophilic ligands such as citric acid, PEG diacids and glutathiol, (ii) Substitution reaction at long-chain hydrocarbon molecule, (iii) Breaking of bonds at long-chain hydrocarbon molecule, (iv) Addition reaction at double bond containing molecule, etc. In the case of hydrophilic ligands, but not biocompatible, it needs to exchange with biocompatible ligands. For example, CTAB-coated NPs are highly toxic, but by exchanging CTAB with biocompatible ligands such as citric acid and PEG, particles become water-dispersible as well as biocompatible. After proper surface functionalization, hydrodynamic radius needs to be investigated using DLS and surface charge using zeta potentials. The hydrodynamic size should not be more than 500 nm for biological applications. Zeta potential

should not be very high (< 5 mV). Otherwise, particles will affect other surrounding environment in blood and cells.

To get efficient internalization of nanoparticles in cells, the surface of particles should be partly hydrophobic as well as partly hydrophilic in nature, since layers of cells have hydrophobic lipids. To make particles targeted to cells, other molecules such as folic acids, iRGD peptides and glucose need to be added on the surface of the particles [134]. Such molecules are overexpressed in such cells. To track nanoparticles in the whole body, extra molecules or nanoparticles or radioisotopes need to be added tover the surface of he nanoparticles. Sometimes, if drug molecules are required to deliver to the target cells, it requires loading of drug molecules efficiently, followed by the release of drug molecules by electrostatic forces or hyperthermia temperature or pH response. Carrier nanoparticles such as mesoporous, liposomes, micelles, hollow Au and carbon nanotubes have been used.

Bare NPs within the biological medium have a tendency to agglomerate for reducing their large surface area to volume ratio and to get oxidized due to their high chemical activity. Thus, the stability of NPs should be ensured during therapeutical applications for effective outcomes. Moreover, NPs when injected into the bloodstream quickly follow opsonization (binding of plasma proteins) which deteriorates their functionality. Interactions with proteins in the biological media cover the NP surface forming a protein corona which changes the transport as well as the biodistribution properties of the particles. Hence to overcome these issues, surface modifications are performed on NPs by either coating using biocompatibile polymeric or non-polymeric materials or conjugating using biomolecules. Coating with effective surfactants not only prevents the NPs from aggregation but also modifies the surface chemistry of NPs beneficial for interactions with proteins, cells or tissues within the biological media. This coating layer can also provide colloidal stability thereby acting as a pathway between particle and target site on cells and can minimize direct exposure to the biological environment. Surface-modified NPs can further assist in improving cell proliferation and viability, cellular uptake, target specificity and preventing opsonization prior to in vitro/in vivo/clinical applications. In the case of magnetic nanostructures, coatings minimize the exchange coupling effect and short-range dipolar interactions between the particles. Biocompatible stabilizers such as PEG and its derivatives are commonly used as effective coatings to form a protective shield around the NPs [140, 141]. Moreover, surface modification with suitable biocompatible materials is important in order to obtain monodispersed nanosized particles and stable ferro fluids advantageous for magnetic-based theranostics. These coatings on the surface of NPs facilitate proper binding to the surface receptors at the diseased area. Owing to their nanoscale size and physico-chemical properties, surface-modified NPs can be employed as probes and magnetic delivery vectors appropriate for theranostic applications [15, 142]. In order to prevent opsonization, to increase the ability to evade the reticuloendothelial system and to favor biodistribution and bioelimination, the suitable coating and its anchoring at its surface have to be tailored and the average hydrodynamic size should be within 10–100 nm size for high blood circulation times which is suitable for in vivo delivery. Polymers such as polyethylene glycol (PEG), polyvinyl alcohol (PVA), polyethylenimine

(PEI), polyvinylpyrrolidine (PVP), natural surfactants such as dextran, chitosan, gelatin, ethyl cellulose, albumin, starch, lipids, proteins, dendrimers, polyacrylamide, polysaccharides, bisphosphonates and aminosilane have been used for surface modification of NPs to target tumor cells [143–145]. Interaction of MNPs with cells such as adhesion and internalization varies according to the coatings applied. In addition, surfactants such as sodium oleate, cetyl trimethyl ammonium bromide (CTAB), sodium carboxymethylcellulose and dodecylamine are also used for aqueous synthesis routes to enhance the dispersibility of NPs [146, 147]. Surface engineering using antibodies, aptamers, peptides and small molecules allows to specifically target different receptors overexpressed on cells [148].

Surface modification can be accomplished during the synthesis or post-synthesis of NPs through physical or chemical adsorption on the particle surface, chemical grafting or ligand exchange. Surface modification along with nucleation and growth processes during the synthesis (in situ) has a profound influence on NPs' crystal structure and morphology. Post-synthesis surface modification can yield core–shell nanostructures using inorganic materials such as gold, silica and organic dye molecules [149]. These coatings render certain additional beneficial properties to the NPs such as plasmonic features of gold and ensure protection from the biological medium. For instance, a thin gold layer modified on the surface of IONPs dissipates more heat as compared to bare IONPs, beneficial for thermal therapy applications [150].

The process of surface modification follows either non-covalent or covalent approaches. The non-covalent approach refers to a physical absorption phenomenon in which ligand adsorption occurs on NPs' surface through non-covalent forces such as electrostatic/hydrogen bonding/hydrophobic interactions. One of the examples of this type of non-covalent surface modification is steric stabilization in which polymers are used as capping agents/surfactants to produce monodispersed NPs. The polymer layer bonded on to the NP surface acts as a diffusion barrier to the growing species leading to diffusion-limited nuclei growth. This diffusion-limited growth could suppress the size distribution of the initial nuclei resulting in monodispersed NPs. Polymers not only stabilize individual NPs but also inhibit agglomeration due to steric repulsive forces between particles maintaining the NP dispersion stable. Moreover, polymers yield high-density functional groups which could be derivatized afterwards with suitable ligands/biomolecules for bioconjugation.

Covalent approaches based on the formation of covalent bonds provide the advantages of robust linkage and coating stability. In this approach, organic/inorganic surfactants get attached to the surface of NPs via end functional groups either by chemisorption or covalent bonding. This protective layer facilitates further functionalization with specific binding agents or ligands or various drugs or functional groups. For instance, surface functionalization performed on water-dispersible Fe_3O_4 NPs by conjugating with glycine and thereby cross-linking with carboxyl groups to form carboxyl-decorated Fe_3O_4 has shown to be used for thermal therapy as well as for diagnostic applications [151]. Biocompatible coatings possessing varying end functional groups such as –OH, $–NH_2$ and –COOH have been exploited generally for the covalent approach. Mahdavi et al. demonstrated that oleic acid gets coated on magnetite via chemisorption, attributed to the carboxylic group (COO–) present in

the oleic acid molecules [152]. Suitable surfactants such as polymers/ligands to get binded should be selected appropriately depending on core material characteristics. Coating/surface functionalization of NPs is performed to ensure physical stability and linkage to specific molecules prior to in vivo applications. A schematic representation of various precursor salts and coating materials/biological molecules used for different synthesis and surface functionalization of MNP biomedical applications is shown in Fig. 16.7 [153].

For the utilization of magnetic colloids for biological applications, MNPs need to be water-dispersible. Otherwise, the MNPs must undergo a prior ligand exchange process to make the MNPs water-dispersible. The ligand exchange method is an effective surface engineering procedure based on the phase transfer of MNPs. The selected ligand replaces the coating layer on the surface of NPs ensuring the colloidal stability of MNPs achieved during surface functionalization. The ligand to be used should possess equal or higher affinity compared to the coating material toward the NPs for a full or partial replacement. Hydrophobic surfactants on the surface of NPs (synthesized via non-aqueous approaches) could be replaced with hydrophilic ligands of certain small molecules such as tetramethylammonium 11-aminoundecanoate to form an aqueous phase before injecting into a biological medium. Ligand exchange performed in a non-aqueous phase of a gold cluster containing triphenylphosphine was initially reported by Schmid et al. [154]. Similarly, Yu et al. executed the phase transfer of oleic acid-coated Fe_3O_4 NPs via ligand exchange with the aid of an amphiphilic co-polymer of poly(maleic anhydride-alt-1-octadecene) and PEG. The co-polymer constitutes side chain each of hydrophobic C16 alkane as well as hydrophilic PEG groups. The hydrophobic C16 side chain coordinates with the alkane groups of oleic acid via hydrophobic–hydrophobic interactions whereas the hydrophilic PEG chains being exposed outside make the NPs hydrophilic. Hence, the free carboxylic groups present in PEG could be further used for bioconjugation [155]. Later, Mao et al. reported aqueous phase transformation of co-polymer (polylactide and PEG)-coated gold (Au) NPs via the hydrogen bond ligand exchange

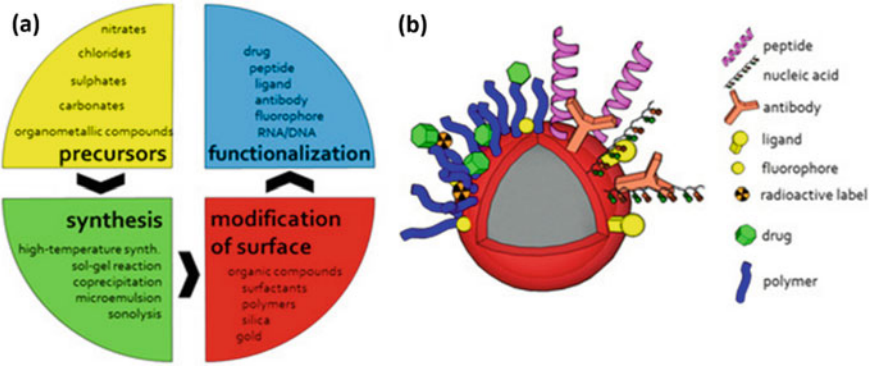

Fig. 16.7 Schematic depicting synthesis and surface modification/functionalization of MNPs. Adapted and reprinted with permission from MDPI, Basel, Switzerland [153]

selection process. During this process, NPs were treated with NaOH in the presence of citrate at 40 °C for the degradation of polylactide. During this treatment, the hydrogen bond formed between PEG brushes and citrate drives the Au NPs to cross the hydrophilic–hydrophobic interface after the complete degradation of the polylactide brushes which transfers the NPs to the aqueous phase [156]. A two-step ligand exchange process has been performed for strongly water-dispersed MNPs for biomedical applications by Hatakeyama et al. Thiomalic acid (TMA) was selected as a temporary ligand which is soluble in both oil and water to remove fatty acids. Later, citric acids have been used as secondary ligands for TMA-exchanged MNPs to remove TMA from the surface of MNPs to obtain highly water-dispersed MNPs [157]. Grafting the NPs' surface with active targeting ligands has been demonstrated to improve tumor targeting and retention of the NPs. In a recent work, Hou et al. employed a block co-polymer named poly (acrylic acid)-b-polystyrene (PAA-b-PS) for surface grafting on oleic acid-coated Fe_3O_4 NPs for ligand exchange. The carboxyl group present in PAA polymer (hydrophilic) binds to the surface of IONPs replacing monovalent oleic acid molecules through multivalent coordination whereas the PS units provide dispersibility in organic solvents. By adjusting the pH of the aqueous phase, the oil/water interfacial interaction has changed and resulted in the deformation of NPs readily to be used as T_2-weighted MRI [158]. The ligand exchange process should ensure that the coating agents should be displaced completely or should not interfere with the adsorption on the surface of NPs.

Monodispersed Fe_3O_4 nanoparticles coated with oleic acids are hydrophobic in nature. After proper surface functionalization, particles can become water dispersible. A simple representation of surface functionalization to nanoparticles has been carried out using methyl oleate as nanoparticles coated with oleate. Figure 16.8 shows the reaction pathways of (a) addition of thioglycolic acid to the double bond of methyl oleate, (b) addition of aspartic acid to oxirane derivatives of methyl oleate and (c) synthesis of aminophosphonate from aldehyde obtained from methyl oleate [104]. These are characterized by FTIR and NMR spectroscopy.

16.4 Biomedical Applications of Nanomaterials

The potentiality of nanomaterials in invading the bloodstream for specific targeting has undergone the most investigation recently in the field of cancer nanomedicine. Nanomaterial-mediated biomedical applications for cancer are mostly oriented toward imaging, sensing, drug delivery and thermal therapies. Figure 16.9 depicts a schematic illustration of functional nanomaterials used for various biomedical applications [159]. The concept of using multifunctional magnetic-based nanomaterials opens up improved therapeutic efficacy with minimal side effects ensuring safe execution for clinical use. This section will explain the therapeutic and diagnostic nanomaterials capable of killing tumor cells and the possible mechanisms of nanomaterial-mediated thermal therapy.

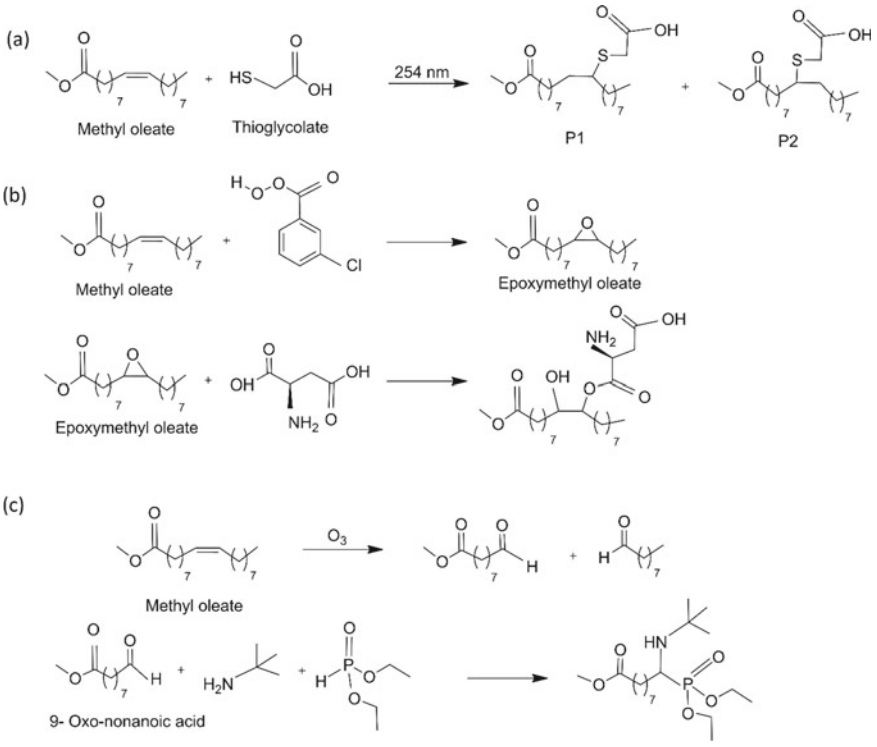

Fig. 16.8 The reaction pathways of (**a**) addition of thioglycolic acid to the double bond of methyl oleate, (**b**) addition of aspartic acid to oxirane derivatives of methyl oleate and (**c**) synthesis of aminophosphonate from aldehyde obtained from methyl oleate

16.4.1 Magnetic Nanomaterial-Based Thermal Therapy

Thermal therapy using nanomaterials as heat sources has paved the way for promising trends in thermotherapeutical biomedical applications. These nanomaterials should be (a) in the size regime of 10–100 nm for longer circulating times in the bloodstream and effective nanoparticle incorporation into cells, (b) dispersible in biocompatible liquids for easy penetration into the body, (c) with minimum side effects on the normal behavior of the host biosystem in the absence of any external stimulus and (d) dissipating heat in an efficient manner when externally excited [160, 161]. This section provides an account of the nanomaterials used for thermal therapy emphasizing magnetic hyperthermia and photothermal therapy, both being a promising therapeutic tool to combat cancer. Thermal therapy, termed as hyperthermia, exposes cancer cells to a higher temperature of 41–46 °C for a specified time duration leading to effective cellular destruction. Since cancer cells are highly susceptible to heat than normal cells, this thermal therapy by elevating the temperature in the tumor area

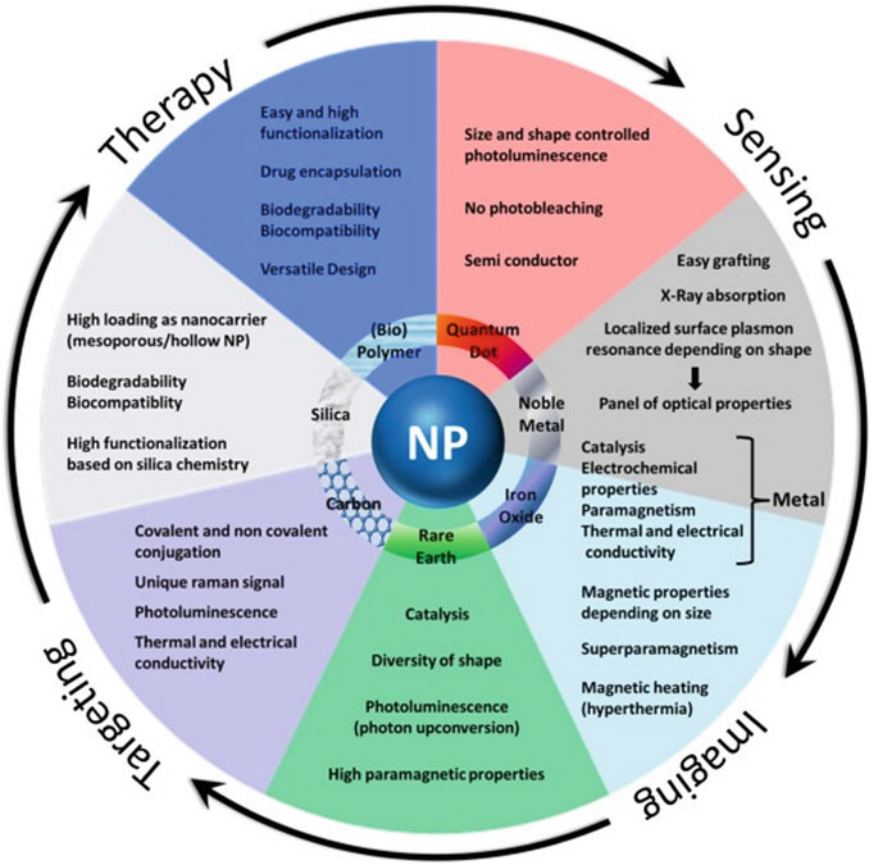

Fig. 16.9 Functional nanomaterials used for various biomedical applications. Adapted and reprinted with permission from Elsevier Publisher [159]

promotes cellular death via denaturation of intracellular protein and/or via disruption of the cell membrane. Generation of intracellular heat occurs within tumor sites by the introduction of suitable NPs (magnetic/plasmonic particles) using either an alternating magnetic field or electromagnetic wave (photon). The primary mechanism of nanomaterial-mediated thermal therapy is based on the heat dissipation via absorption of infrared light (photothermal therapy, PTT) or via magnetically induced heating (magnetic hyperthermia). Both modes have exhibited improved therapeutic efficiency in in vivo and a few clinical trials. Generally, thermal therapy possesses trivial side effects in comparison with conventional chemo/radiotherapy.

16.4.1.1 Magnetic Hyperthermia (MHT)

Biocompatible MNP-mediated MHT is an innovative, efficient and safer thermotherapeutic approach for cancer. MHT is an effective tool for therapeutic temperature enhancement employing MNPs under an external AC magnetic field (ACMF). Such NPs, also termed as tumor-specified nanoheaters, when subjected to ACMF, dissipate heat to the specific tumor tissues for controlled homogeneous heating without affecting normal cells which makes MHT distinct from other conventional cancer modalities. This makes localized heating to tumor. The use of MNPs was initially proposed by Gilchrist in 1957 [162]. Maghemite ferromagnetic particles of particle sizes varying from 20 to 100 nm were utilized for heating cancer tissues exposed to an external alternating current magnetic field with a frequency of 1.2 MHz. Applied magnetic field parameters used for MHT to achieve the therapeutic limit should be in the Brezovich limit (product of magnetic field amplitude and frequency $< 5 \times 10^9$ Am^{-1} s^{-1}) [163]. In the history of thermal therapies, MHT has gained spectacular success due to its potential applications in medicine. MHT, assuring specificity to the target area, improved colloidal stability of MNPs and minimal adverse effects to the surrounding healthy tissues, has garnered recognition as a prospective cancer therapy [160, 161]. MHT came out with successful results when experimented in animal tumor models which led to the pathway for future clinical trials [164, 165]. Superparamagnetic NPs are highly exploited in MHT owing to their size as well as the innate property of substantial magnetization value and magnetic susceptibility under ACMF and nullifying its magnetization completely upon field removal. Such NPs prevent aggregation and avoid detrimental conditions resulting in thrombus formation [166]. Moreover, these NPs are able to generate heat via relaxation processes at physiologically relevant magnetic fields.

In general, heat generation occurs in magnetic materials under an ACMF that can be categorized into (1) eddy current loss, (2) hysteresis loss and (3) susceptibility loss (Nèel relaxation loss and Brownian relaxation loss). Eddy current loss can be neglected in the MHT context since such losses occur in bulk magnetic materials. Hysteresis loss results from the delay of a magnetic material where the magnetic moment at some frequency fails to retrace its path instantaneously with an ACMF resulting in hysteresis loops. Hysteresis loop due to this irreversible magnetization process thus results in heat losses. Hysteresis heat loss is considered to be the basis of heat dissipation for ferromagnetic particles. Optimal heat loss can be calculated from the area of such hysteresis loops. Current research focuses on single domain superparamagnetic NPs for MHT in which the heat dissipation is due to susceptibility losses such as Nèel relaxation loss and Brownian relaxation loss as well as hysteresis loss. Nèel relaxation (internal rotation) induced by an external ACMF occurs due to the oscillations of the magnetic moments thereby changing the moment direction keeping the physical orientation of particles fixed whereas Brownian relaxation (external rotation) is caused by the physical rotation of the particles itself in a medium they are placed. The former mechanism primarily depends on the magnetic anisotropy energy of MNPs whereas the latter is based on the local environment such as viscosity of the medium in which MNPs are dispersed. These internal and

external rotations of particles can lead to a phase lag between the applied magnetic field and the magnetic moment direction resulting in heat loss. Brownian relaxation has a small contribution in a viscous medium. The amount of heat dissipated is evaluated in terms of specific absorption rate (SAR), and it is expressed in W g^{-1} of MNPs. The larger the amount of heat generated by the MNPs, the larger will be the SAR value. The power dissipation rate of MNPs is a function of MNP size, shape, composition, magnetic interactions and applied magnetic field parameters. Elucidating and optimizing these variables are vital for future clinical applications. The success of MHT application underlies on developing biocompatible and superparamagnetic NPs with suitably functionalized surfaces exhibiting the highest saturation magnetization thereby assuring effective heating under an oscillating magnetic field.

Generally, Nèel's spin relaxation of superparamagnetic NPs takes 10^{-9}–10^{-10} s [40, 160]. It is to be noted that a 200–300 kHz frequency is used in MHT. The experimental time window will be 5–3 × 10^{-6} s. During the time window, the net magnetic moment of superparamagnetic particles can be measured, and thus hysteresis loss is associated in superparamagnetic particles under 200–300 kHz frequency and 100–300 magnetic field or 100–400 A current. The experimental time window for VSM or SQUID is 1 s–60 s that is not able to see a magnetic moment of superparamagnetic particles. Only zero moment can be seen due to fast relaxation from + z to – z direction within 10^{-9}–10^{-10} s.

Brownian relaxation (τ_B) of particles in a fluid having the dynamic viscosity (η) at absolute temperature (T) can be represented by Eq. (16.4).

$$\tau_B = \frac{4\pi\eta r_h^3}{k_B T} \tag{16.4}$$

r_h is the hydrodynamic radius of the particle. τ_B varies from μs to ms and even to hours depending on hydrodynamic radius and temperature.

Nèel relaxation (T_N) of superparamagnetic particles is represented by Eq. (16.5).

$$\tau_N = \tau_o e^{\Delta E/k_B T} \tag{16.5}$$

τ_o is 10^{-9} s, ΔE is the anisotropic energy barrier (the product of anisotropic energy constant (K) and volume (V) of particle = KV), k_B is Boltzmann's constant and T is absolute temperature. Equation (16.2) suggests that Nèel's relaxation is fast for the smaller nanoparticles.

Hysteresis loss of magnetic particles in ACMF is represented by Eq. (16.6).

$$\text{Area under curve} = f \int M dH \tag{16.6}$$

f is the frequency of the AC magnetic field, M is magnetization and H is the applied magnetic field. The ratio of magnetization (M) to the applied magnetic field (H) gives

magnetic susceptibility (χ), which represents the type of magnetic materials (diamagnetic, paramagnetic, antiferromagnetic and ferromagnetic particles). For diamagnetic particles, χ has the negative value, where the other remaining particles have a positive value. In the AC magnetic field, χ is represented by Eq. (16.7).

$$\chi = \chi' + i\chi'' \tag{16.7}$$

where χ' is a real part of susceptibility and χ'' is an imaginary part of susceptibility, which is represented by Eq. (16.8).

$$\chi'' = \frac{\omega\tau}{1 + (\omega\tau^2)} \tag{16.8}$$

τ is the total relaxation contributed by Brownian (τ_B) and Nèel's relaxations (τ_N).

According to Faraday's and Lenz's laws, eddy current loss (ED) from conducting materials having μ (the permeability of a material), d (the diameter of the particle) and ρ (resistivity of the material) is represented by Eq. (16.9).

$$\text{ED} = \frac{(\mu\pi d f H_0)^2}{20\rho} \tag{16.9}$$

Total heat/power dissipation from particles is represented by Eq. (16.10).

$$P = \mu_0\pi\chi'' f \mathrm{H}_0^2 \tag{16.10}$$

μ_0 is the permeability of free space.

The specific absorption rate (SAR) in ACMF is represented by Eq. (16.11) and its unit is W g^{-1}.

$$SAR = c\frac{\Delta T}{\Delta t}\frac{1}{m_{magn}} \tag{16.11}$$

ΔT/Δt is obtained from the slope of the time-dependent temperature curve at the initial time, c is the specific heat capacity of combined superparamagnetic particles and the solvent and m_{magn} is calculated by the ratio of the amount of MNPs or Fe per total amount of MNPs or Fe and solvent.

In addition to magnetite (Fe_3O_4), ferrites such as $CoFe_2O_4$, $NiFe_2O_4$, $ZnFe_2O_4$, $CuFe_2O_4$, $MnFe_2O_4$ $MgFe_2O_4$ and alloys such as FePt and NiCu have been used for MHT [167–172]. In addition, anisotropic magnetic Janus nanostructures such as Fe_3O_4–Pd and carbon-coated Fe–Co exhibited excellent magneto-thermal properties [173, 174]. Pure metals (Fe, Co, Ni) are not suitable for MHT applications due to their extreme sensitivity to oxidation and toxicity. However, iron oxides such as magnetite

and maghemite less prone to oxidation can provide a stable magnetic response and are biocompatible being advantageous for MHT applications.

Studies reported that heat induction can be enhanced through proper synthesis and surface modification strategy. The sol–gel route has been employed for reducing Ni and Cu to produce Ni–Cu NPs for self-regulating MHT [175]. It has been demonstrated that 50–87 nm sized spherical-shaped Ni–Cu NPs dissipate SAR in the range of 6–80 W/g. Wang et al. PVP-functionalized Fe_3O_4 nanotubes with an outer diameter of 200 ± 20 nm and length of 400 ± 20 nm synthesized through hydrothermal synthesis that exhibited highest SAR of 5050 W/g beneficial for MHT [176]. Various superparamagnetic core–shell nanostructures have been synthesized to achieve higher SAR values. For instance, $Zn_{0.4}Co_{0.6}Fe_2O_4$ as core and $Zn_{0.4}Mn_{0.6}Fe_2O_4$ as shell to form a core–shell structure synthesized via thermal decomposition method exhibited an enhanced SAR of 3866 W/g which is 1.7 times greater than the SAR obtained from individual counterparts [177]. Xie et al. reported IONPs synthesized via co-precipitation method followed by conjugating the surface of NPs with polymers such as PMMA and PAA constituting novel Janus structure (PMMA/Fe_3O_4/PAA) [178]. These NPs were tested for in vitro MHT on 4T1 breast cancer cells under ACMF (445 kHz, 35A) and exhibited ~ 35% cell inhibition whereas DOX-loaded Janus NPs under ACMF showed a more pronounced cell inhibition rate of ~ 78%. In addition, in vivo MHT demonstrated the improved antitumor effect in DOX-loaded Janus NPs suggesting the effectiveness of synergistic chemo-thermal therapy. Polycaprolactone-coated superparamagnetic IONPs synthesized using a single precursor (ferrous chloride) have shown 60% cell death during in vitro MHT when treated on HepG2 human cancer cells upon ACMF [179]. The current research direction is focused toward MHT conjunction with other cancer therapies such as photothermal therapy (PTT) or chemotherapy to achieve a synergistic therapeutic effect.

SAR values of Fe_3O_4, PEG-coated Fe_3O_4 and Oleic acid (OA)-coated Fe_3O_4 are estimated to be 40.52, 31.39 and 25.5 W/g, respectively [180]. Figure 16.10 shows the heat generation from these particles at different applied currents [180]. The magnetic field (H) at 100, 200, 300, 400, 500 and 600 A correspond to 83.8, 167.6, 251.4, 335.2, 419 and 502.8 Oe, respectively. With the increase of magnetic field, the heat generation increases. This suggests that the role of hysteresis loss is important in heat generation.

Fe_3O_4 NPs coated with OA exhibit internalization with cancer cells (WEHI 164 cells), and more killing of cancer cells through apoptosis under ACMF is observed and this could be seen from confocal microscopy images (Fig. 16.11) [132].

In vivo study provides the decrease of tumor size with respect to control in BALB/c mice (Fig. 16.12) [181]. A decrease in tumor size can be seen from a decrease in luminescent intensity of WEHI 164 cells expressing the luciferase gene as compared to the control. Human trials have been reported using magnetic nanoparticles under AC magnetic nanoparticles in Germany and Japan [182–184].

Using magnetic-luminescence magnetic nanoparticles (nanocomposite, YVO_4:10Eu/Fe_3O_4), localization or internalization of nanoparticles in cancer

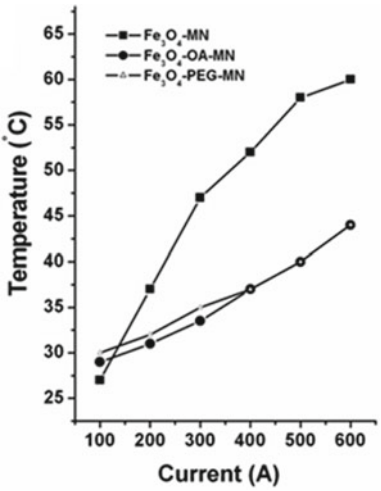

Fig. 16.10 The heat generated from Fe_3O_4 MNPs (bare MN), oleic acid (OA)-coated MN and PEG-coated MN at different currents. Adapted and reprinted with permission from RSC Publisher [180]

cells as well as more killing of cancer cells are reported (Figs. 16.13 and 16.14) [185].

16.4.1.2 Photothermal Therapy

Photothermal therapy (PTT) employing photo absorbers in the near-infrared (NIR) region is an effective therapeutic tool for localized cancer therapy. Therapy makes use of light-induced heating NPs as NIR photo absorbers which can convert light energy into heat eventually elevating the temperature inside the tumor tissues to induce thermal ablation beneficial for thermal therapy applications. NPs absorb the light photons which then convert to heat sufficient for cell apoptosis. PTT ensures the incorporation of NPs into the tumors for high heat dissipation at a lower laser light intensity and minimal adverse effects to the surrounding healthy cells. PTT treatment is primarily dependent on size, shape and optical properties of NPs as well as the wavelength, energy, power density and diameter of laser beam delivered to the diseased tissue [186–190]. Though tissues and cells possess inherent natural photothermal agents such as hemoglobin and cytochromes, their absorption efficiency is very inferior. Therefore, NPs exhibiting strong absorption in the NIR region are used as PTT photo absorbers for facilitating heat production and therefore, the optical absorption efficiency and biocompatibility of plasmonic NPs are of prime importance. NPs should be selected depending upon the nature of the tumor as well as the laser source. During the illumination of NPs with a laser beam, the incident photons can be absorbed and scattered by the NPs. The absorbed incident photons by the NPs cause either phonon emission or photon emission of different frequencies. Phonon emission is responsible for heat production whereas photon emission can lead to luminescence. The efficient utilization of NPs for PPT requires

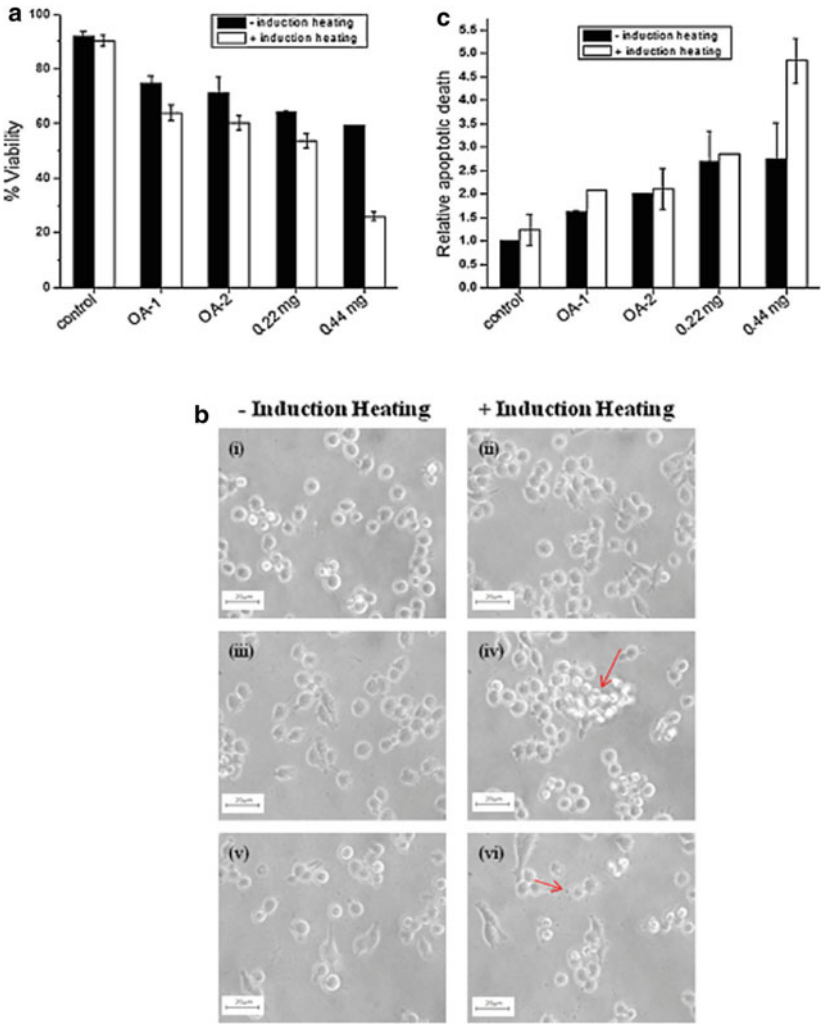

Fig. 16.11 (A) Cell viability (%) of WEHI 164 cells treated with (0.22 or 0.44 mg) of MN-OA (0.5) for 3 h with/without induction heating (400 A, 10 min.). Cells were also treated with corresponding vehicle controls for which 4.4 μl of OA was dispersed in sodium carbonate and 50 μl (OA-1) and 100 μl (OA-2) of the resultant stock was used for treatment. The viability of untreated control (tumor cells not treated with MN-OA) was found to be 90 ± 2%. Error bars represent standard error, n = 6 (B) The effect of different amounts of MN-OA(0.5) treatment on the morphological features of WEHI 164 cells, with or without induction heating. (i–ii) Untreated controls, (iii–iv) cells treated with 0.22 mg and (v–vi) 0.44 mg of MN-OA(0.5). The arrow in B (iv) indicates detached cells and in B (vi) indicates cell rupture and debris. (C) The effect of MN-OA treatment with or without induction heating on apoptotic cell death in tumor cells. The WEHI 164 cells were treated with (0.22 mg or 0.44 mg) of MN-OA(0.5) and corresponding vehicle controls (OA-1 and OA-2) for 3 h followed with or without induction heating. After 24 h, cells were harvested by trypsinization, and apoptosis assay was performed using cell death detection ELISA PLUS kit. Relative apoptotic cell death was expressed which is a ratio of absorbance in treated samples to untreated control. Error bars represent standard error, n = 4. Adapted and reprinted with permission from Elsevier Publisher [132]

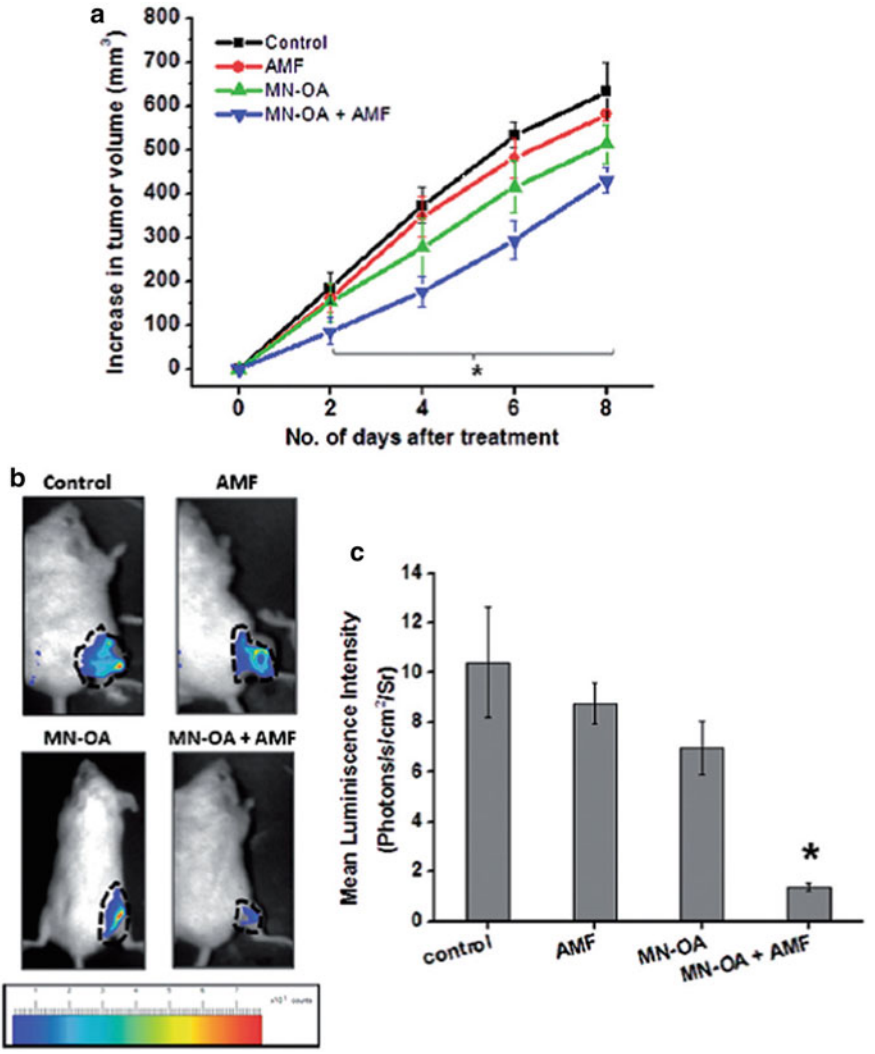

Fig. 16.12 Tumor regression studies. (**a**) Tumors were subjected to MHT and tumor volume was measured by digital Vernier caliper. Graph represents the increase in tumor volume measured on different days after starting the therapy. (**b**) WEHI 164 cells expressing the luciferase gene were transplanted in female BALB/c mice to obtain tumors and further subjected to MHT. The luminescence intensity of tumors was measured on day 8 after treatment, using in vivo live animal imaging system. Data is presented as Mean ± SD, N = 5 and * indicates that values are significant at $P < 0.05$. (**c**) Images captured by live in vivo animal imaging system on day 8 after initiating the treatment. Adapted and reprinted with permission from Taylor & Francis Group Publisher [181]

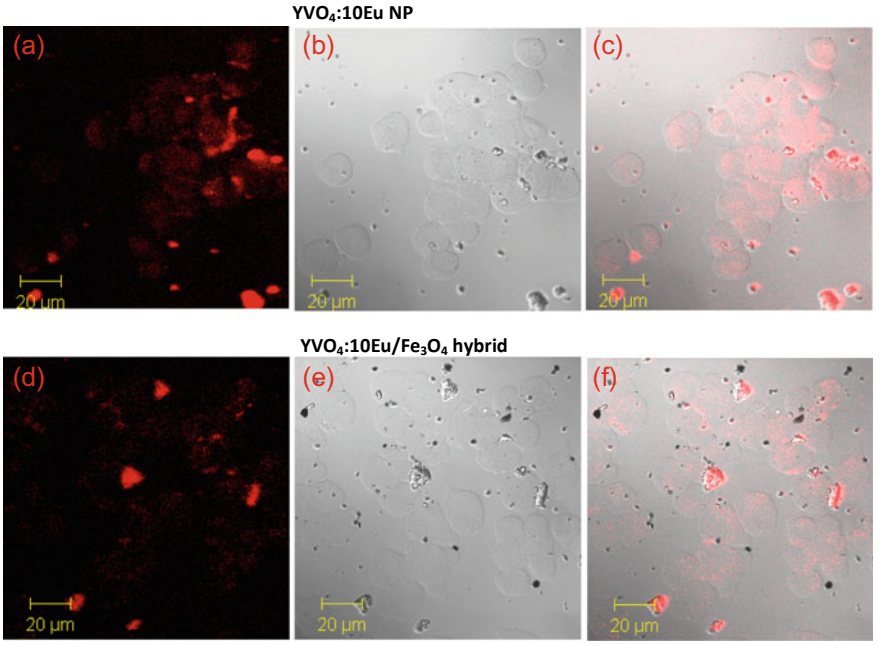

Fig. 16.13 Internalization of YVO_4:10Eu (**a**–**c**) and YVO_4:10Eu/Fe_3O_4 (**d**–**f**) in WEHI 164 tumor cells studied by confocal laser scanning microscopy. **a** and **d** correspond to luminescence measured at 364 nm excitation wavelength and 575–615 nm emission wavelength. **b** and **e** correspond to bright-field imaging and **c** and **f** correspond to merged images. Red color corresponds to the luminescence from YVO_4@Eu. Adapted and reprinted with permission from RSC Publisher [185]

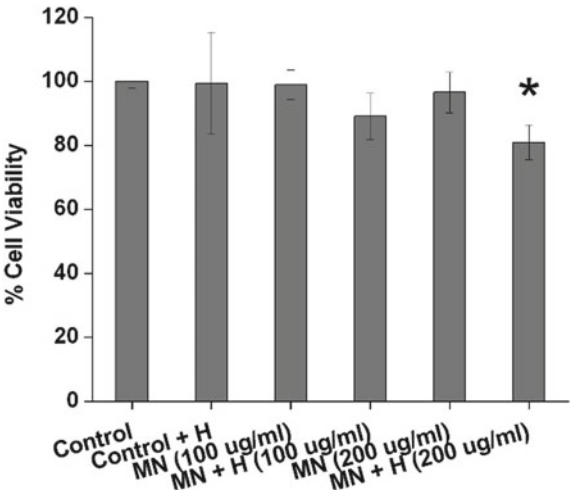

Fig. 16.14 Cell viability of WEHI 164 tumor cells after treatment with different concentrations of YVO_4:10Eu/Fe_3O_4 in the presence and absence of induction heating (H). *indicates that the values are significant at $P < 0.05$. Adapted and reprinted with permission from RSC Publisher [185]

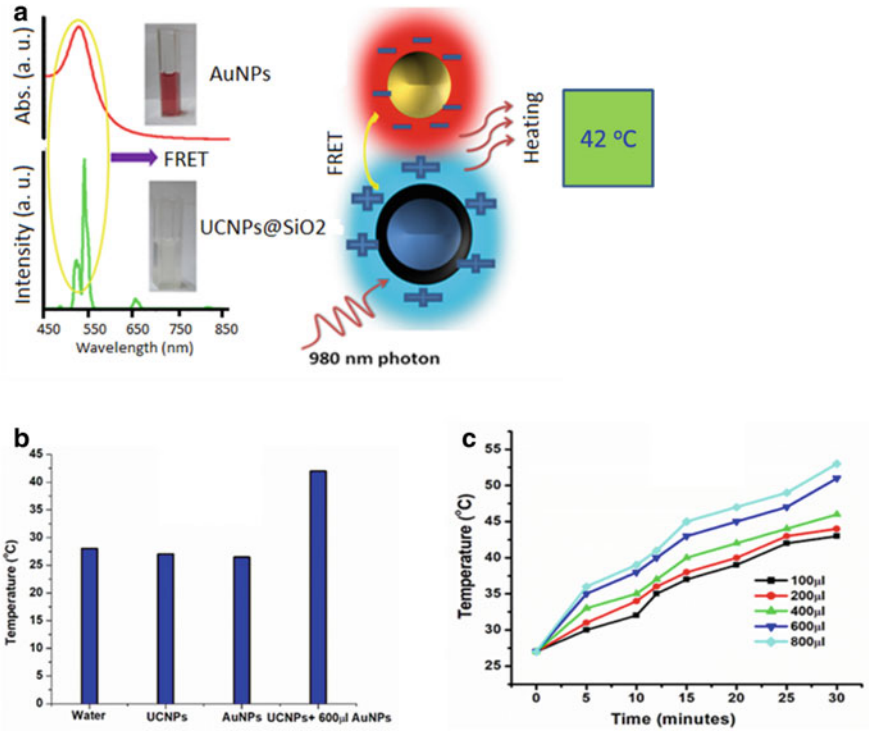

Fig. 16.15 (**a**) FRET responsible spectral overlap of UC green band of UCNPs@SiO_2 and absorption of AuNPs with their illustration inducing heat through FRET. (**b**) Temperature gain for 15 min heating via 980 nm NIR laser radiation (power 600 mW). (**c**) Time-dependent temperature gain under NIR laser excitation for different particle concentrations of AuNPs in hybrid NCC. Adapted and reprinted with permission from ACS Publisher [113]

larger absorption efficiency (high heat dissipation) and lower luminescence quantum yields. Absorption efficiency can be calculated as the ratio of the number of absorbed photons to the total number of incident photons with the NPs. NPs should possess a large absorption coefficient, minimal toxicity, ease of functionalization and better solubility in biocompatible liquids. The synthesis methods for the formation of light-induced nanostructures can be altered for fine-tuning the absorption band of NPs to the desired wavelength range to enhance the specificity and response of PTT. NPs such as noble metals, CuS, semiconductors, rare earth ion-doped NPs, carbon-based NPs and organic NPs can be utilized for PTT. Though noble metals such as gold (Au), copper (Cu), platinum (Pt) and silver (Ag) exhibit plasmonic resonances in near-NIR region, Au is preferred as the primary choice for PTT applications. Au is the single noble metal exhibiting localized surface plasmon resonance (LSPR) in the NIR region beneficial for cancer therapy [191]. Au nanoshells were reported for the tumor regression for in vivo PTT without any significant rate of increase in the stem cells [192]. Hong et al. demonstrated PEGylated Au nanoclusters (AuNCs)

conjugated with AS1411 for achieving cancer-targeted PTT and anti-proliferation activity [193]. Wang et al. explored different Au nanostructures such as nanorods, nanocages and nanohexapods for photothermal therapy for cancer [194]. It has been elucidated that Au nanohexapods are prospective materials for cancer theranostics compared to others and exhibited the highest cell uptake with minimum cytotoxicity in vitro. Further, incorporation of drug carrier into NIR photo absorbers has recently been investigated for enhanced selectivity and therapeutic efficiency with minimizing photothermal damage to normal tissues. Nanocage-like Au structures as a drug carrier have proven to be potential for clinical PTT [195]. Phan et al. synthesized high NIR-absorbed polypyrrole-coated FePt NPs via the thermal decomposition method and performed in vitro PTT with breast cancer cells [196]. A laser of power density 1 W cm^{-2} for 5 min when exposed elevated the temperature from 39.3 °C to 71 °C for varying concentrations of NPs. Liu et al. proved that PEG-modified graphene-iron oxide-Au NPs combining the photothermal properties of graphene, magnetic properties of iron oxide and LSPR of Au NPs can enhance the therapeutic efficacy [197]. Moreover, the PTT is often combined with MHT for an enhanced synergistic cancer therapy. For instance, Espinosa et al. synthesized Fe_3O_4 nanocubes via the thermal decomposition method and experimented for a combined MHT-PTT therapy in vivo. Combined NIR laser exposure and ACMF exhibited an enhanced dual therapy when treated on mice bearing solid tumors [198]. Recently, polydopamine (PDA)-coated magnetite NPs synthesized via hydrothermal method have been exposed to laser power of 2 W/cm^2 for in vitro PTT on hepatocellular carcinoma HepG2 cells [199]. Reduced cell viability has been observed for the cells treated with increased NP concentration after laser exposure to 5 min. Further drug conjugation on NPs has been found to cause an enhanced cell death than bare NPs. This implies chemo-PTT dual therapy is more effective compared to individual modalities.

Heating can be produced by florescent resonance energy transfer (FRET) by using upconversion luminescence (UCNPs)—gold nanoparticles hybrid (NCC) [113]. Here, $NaYF_4$:Er-Yb (upconversion luminescence) nanoparticles absorb NIR light at 980 nm and produce light at the visible range. This visible light is absorbed by suitable Au nanoparticles through the SPR process (SPR = surface plasmon resonance). Figure 16.15 shows heat generation of NCC by addition of Au NPs in a fixed amount of UCNPs. With an increase of Au NPs, amount of the heat generation increases.

16.4.2 Magnetic Nanomaterials for Drug Delivery

Nanocarrier-based drug delivery is attracting research interest due to the controlled release of drugs, desired NPs size and its specificity toward the target site. Various organic materials such as polymeric NPs, micelles and liposomes have previously demonstrated to be beneficial for effectual clinical impacts [200]. However, magnetic nanomaterial-based drug delivery system has significant advantages such as reducing the problems associated with the usage of bare drugs and specifically targeting the

diseased areas sparing normal cells [201]. Intrinsic magnetic properties and the ability to be guided with the aid of external ACMF in combination with their drug loading ability enable the MNP drug delivery system to become a subject of intense research [202]. Generally, the drug gets binded to the MNPs either via covalent attachment or adsorption in case of porous structure or electrostatic interaction with functional groups. Targeted delivery of MNPs can be of two types—passive and active targeting. Passive targeting is achieved by the selective accumulation of NPs into the targeted area via the leaky microvasculature of tumor as a result of the enhanced permeation and retention (EPR) phenomena. In general, the majority of tumors have vascular pore sizes around 380–780 nm, and this may differ depending on the growth and type of tumor [203]. Thus, for targeted passive delivery, the particle size should be below the capillary diameter of the tumor site. Clearance of NPs via healthy capillaries is another major concern. NPs < 6 nm can be rapidly cleared from kidneys whereas larger NPs > 200 nm end up with phagocytic uptake [204]. In addition, less accumulation of NPs for large tumors and short circulation times limits passive targeting. Better protocols are required for a high concentration of nanocarriers to be accumulated in tumor tissues with a minimal amount to be accumulated in the liver and spleen for their effective clearance. Since passive targeting provides delivering a wide range of nanocarriers, active targeting employs targeting ligands to facilitate enhanced targeted delivery of the therapeutic agents to the specific surface receptors at the tumor sites. Stimuli-responsive magnetic vectors have been employed for conjugating drugs for active targeting. Active targeting is based on the conjugation of biochemical ligands such as proteins, peptides, folic acid, polysaccharides (hyaluronic acid) and DNA to the magnetic vectors owing to their high specificity and affinity toward specific surface receptors [205]. For drug delivery, magnetic vectors are sensitive to external stimuli such as temperature, pH, light, electric field and magnetic field for drug release.

Since the 1970s, the use of magnetic nanoparticles for chemotherapy has been evolving. The first preclinical trial with MNPs has been conducted by Lübbe et al. in 1996 [206]. Since then, many researches have been conducted on magnetic vectors for the potential use of drug delivery. MNP-conjugated drug carriers already commercialized are TargetMAG-doxorubicin, FluidMAG and MagNaGel [207]. The main advantages of the use of magnetic nanoparticles are they can be guided, visualized (like in MRI) and heated (hyperthermia) with the help of a magnetic field. The major factor for drug delivery is surface chemistry to increase the half-life in the bloodstream by avoiding the immune system. Conjugation/coating with hydrophilic polymers such as PEG on MNPs' surface enhance longer circulation avoiding opsonization [208]. IONPs are commonly employed as drug carriers owing to their ease of preparation and superior magnetic properties. Kakwere et al. synthesized 20 nm iron oxide nanocubes for conjugating an anticancer drug, doxorubicin (DOX) [209]. IONPs have been surface-functionalized with a thermoresponsive polymer shell (poly(N-isopropylacrylamide)). DOX release as a result of heat dissipation with the aid of external ACMF was observed and the release was more than 90%, when the temperature was raised to 50 °C. Drugs can be released from the carrier through pH response. Generally, cancer cells have lower pH (5–6) as compared to normal

cells (pH = 7.4). In another study by Zhang et al., iron oxide nanoflowers coated with carbon shells were tested for loading acetaminophen drug [210]. The drugs were trapped inside the pores of the carbon shell by hydrogen bond formation. The drug loading efficiency was increased by the increase in pore volume of the material. With a pore diameter of 65 nm, the loading percentage was around 30% and burst release of 74% in 2 h and 80% after 4 h at 37 °C were obtained. Cheng et al. fabricated porous hollow Fe_3O_4 nanoparticles with a hydrodynamic diameter of 20 nm for DOX release [211]. The release was studied in two different pH of 7.4 (physiological pH) and 5 (cancerous cell pH). The DOX release % after 24 h was only 30% in pH 7.4 and 80% in pH 5 at 37 °C. Other ferrite NPs such as MFe_2O_4 where M = Mn, Zi, Ni and Co have also been investigated for drug delivery application. For example, Ravichandran et al. fabricated a 25 nm size core–shell structure of $MnFe_2O_4$@Au for the anticancer doxorubicin drug [212]. The nanoparticle has been coated with folic acid for conjugation of DOX molecules on the surface. Loading efficiency of 97.5% and release of 79.6% at pH 5.4 were observed. MNP-based drug carriers are expected to continue for specific targeting and safe image-guided delivery for the future theranostic applications.

16.4.3 Magnetic Nanomaterials for Bioimaging

For the last several decades, MNPs have been studied for imaging purposes. Magnetic resonance imaging (MRI) is one of the most widely used diagnostic imaging techniques for clinical nanomedicine providing a cross-sectional view of the body. This method is a non-invasive imaging tool commonly used for visualizing the structure and function of tissues. MRI provides an enhanced image contrast of soft tissues compared to other imaging modalities. MRI works on the basis of proton alignment and its interactions in the presence of a high strength magnetic field. Under a very strong magnetic field, protons present in the tissues get perturbed. Contrast agents alter longitudinal (T1) or transverse (T2) relaxation times which are monitored by MRI. Depending on T1 and T2 relaxation processes, contrast agents are named T1 and T2 contrast agents. T1 contrast agents shorten T1 relaxation time generating bright images, whereas T2 contrast agents or negative contrast agents shorten T2 relaxation time generating dark images. In order to obtain an accurate interpretation, positive and negative contrasts have to be used to obtain complementary information. Recently, the use of superparamagnetic iron oxide nanoparticles (SPIONs) as an MRI contrast agent has a significant advantage of differentiating the pathogenic cells from the healthy cells [213]. SPIONs act as negative contrast agents showing a darker image in MRI by shortening the transversal relaxation time (T2) of the surrounding water protons. Increased relaxivity value results in enhanced image contrast even at a lower concentration of SPIONs. Zhou et al. employed the thermal decomposition method for synthesizing small iron oxide nanocubes coated with DMSA with varying sizes in the range from 7 to 21 nm and obtained transversal relaxivity (r2) of 76 mM^{-1} s^{-1}–298 mM^{-1} s^{-1} [214]. In another work by Orza et al., PEI-coated

Fe_3O_4 nanorods have been synthesized. NPs exhibited an improved MRI contrast effect in terms of T2 relaxivity value enhancement from 670.6 to 905.5 mM^{-1} s^{-1} for nanorods of size varying from 25 to 50 nm, respectively [215]. In addition to IONPs, MNPs such as $MnFe_2O_4$ [216, 217], $CoFe_2O_4$ [216], $NiFe_2O_4$ [216] and $ZnFe_2O_4$ [218] have been used for MRI applications. In recent years, several studies revealed the application of iron oxide as T1 contrast agents as a substitute to gadolinium-based T1 contrast agents for reducing the associated toxicity [219]. Macher et al. developed ultrathin iron oxide nanowhiskers (20 × 2 nm) and obtained longitudinal relaxivity r1 of 6.13 mM^{-1} s^{-1} when used as a T1 contrast agent for MRI [220]. This work suggests the potential of nanowhiskers to serve as T1 MRI contrast agents. Zhou et al. developed magnetite hexagonal-shaped nanoplates as strong T1 and T2 contrast agents by tuning the size and composition [221]. In this case, morphology and high magnetic moment of NPs led to the strong T2 effect and increased water proton interaction in the [110] facet of iron oxide resulting in a strong T1 effect. It was also found that T1–T2 dual-mode contrast agents can be controlled by the thickness of the nanoplates.

Medical imaging techniques include positron emission tomography (PET), computed tomography (CT), MRI and optical imaging. Since single imaging modality cannot provide all the information, combining different techniques has been recently under investigation. The PET-MRI multimodel image uses a combination of radioactive metal ions with chelating ligands such as 1,4,7-triazacyclononane-N,N′,N″-triacetic acid (NOTA) and 1,4,7,10-tetraazacyclododecane-1,4,7,10-tetraacetic acid (DOTA) for providing a high-resolution image [222]. For tumor imaging, ^{64}Cu-NOTA and ^{c}RGD are coupled on the surface of multifunctional iron oxide NPs. CT which is the most common imaging technique provides high temporal resolution and low sensitivity when compared to MR imaging. CT uses iodine, bismuth, gold, lanthanides and tantalum as contrast agents. Unlike PET-MRI, conjugating iodinate molecules onto the magnetic nanoparticle is complicated. Optical imaging is used to verify biomarkers and its principle is based on the detection of light. Deep tissue imaging is not possible in this technique since light has limited penetration. This technique uses organic fluorescent dyes such as fluorescein isothiocyanate (FITC) and Cy 5.5. For a combined optical-MRI, these fluorescent dyes are conjugated with MNPs [223]. Cy5.5 labeled IONPs have been used for brain tumor imaging [224]. Some other magnetic probes for optical-MRI are the encapsulation of dyes for enhancing the signal intensity [225] or the use of quantum dots instead of dyes [226].

16.4.4 Magnetic Nanomaterials for Biosensors

A biosensor is a device which combines a biorecognition element to capture the target molecules and a transducing element to transfer a measurable signal proportional to the interaction between the target molecules. Based on the types of transducers, biosensors are classified as thermal, piezoelectric, optical and electrochemical

sensors. Owing to the prospective development brought about by nanotechnology in the field of biosensing, MNPs have been utilized to enhance selectivity and sensitivity. MNPs offer several advantages in sensing strategies such as low limit of detection (LOD), enhanced sensitivity, less analyzing time and high signal-to-noise ratio compared to non-magnetic-based sensors [227]. MNPs are used either directly by integrating MNPs into the transducer materials or/and dispersed in the samples to be detected followed by attracting toward active detection surface of biosensor under an external MF. Electrochemical (EC) biosensors measure EC signals originated by the interaction of electrodes and analytes in the form of voltage or current or impedance. The electrodes are coated with biochemical materials in order to improve the signal intensity [228]. Due to their high sensitivity, easy operation and low cost, EC biosensors are used in environmental, clinical, pharmaceutical and biological fields [229]. Based on the working principle, electrochemical sensors can be classified as voltammetric, potentiometric, amperometric, capacitive and chemiresistive [230]. MNPs have been used to improve the sensitivity due to their easy preparation, biocompatible and superparamagnetic properties. The most commonly used mode of detection is voltammetry. Surface-functionalized Fe_3O_4 NPs are used commonly in biosensor applications. In biosensors, core–shell structured MNPs are widely used for the attachment of binding ligands and to improve stabilization in solution [231]. For example, $Fe_3O_4@SiO_2$ is widely used to modify electrode surfaces owing to its large surface area, good response in conductivity and increased electroactive interaction sites [232, 233]. Carbon-based materials such as graphene oxide (GO) and carbon nanotubes (CNTs) are also widely used to functionalize MNPs. Carbon-coated MNPs have improved characteristics in terms of large surface area, thermal and chemical stability, catalytic activity and electro-conductivity [234]. Recently, Beitollahi et al. synthesized $GO/Fe_3O_4@SiO_2$ core–shell nanocomposite sensors for the detection of dopamine and uric acid [235]. For analysis, the concentration ranges of dopamine and uric acid taken are 0.1–600.0 μM and 0.75–300.0 μM, respectively. The detection limit obtained by $GO/Fe_3O_4@SiO_2$ core–shell modified electrode was 8.9×10^{-8} M for dopamine and 5.7×10^{-7} M for uric acid. The sensor exhibited good analytical performance, and two different well-defined anodic peaks were obtained for dopamine and uric acid. In another study by Arvand et al., multi-walled carbon nanotube (MWCNT)-decorated magnetic core–shell structure $Fe_3O_4@SiO_2$/MWCNT-CPE was fabricated to determine uric acid [236]. The electrochemical behavior of uric acid on an unmodified carbon electrode, an MWCNT-electrode and $Fe_3O_4@SiO_2$/MWCNT-CPE modified electrode was investigated by cyclic voltammetry. The anodic peak current of the magnetic nanoparticle-modified electrode was found to be 4.6 times higher than that of the unmodified electrode and 2.7 times higher than the MWCNT-modified electrode. The increased sensitivity was ascribed to a larger electroactive surface area and fast electron-transfer kinetics in $Fe_3O_4@SiO_2$/MWCNT-CPE. Magnetic nanocomposites based on Au NPs are also widely used as biosensor materials due to their easy preparation, strong absorption, improved biocompatibility and good conductivity. Recently, Saljooqi et al. fabricated a modified glassy carbon electrode by using the magnetic nanocomposite of $Fe_3O_4@SiO_2$-PANI-Au for the detection of quercetin in food and biological fluids

[237]. The modified electrode detected queretin in the range of 1.0×10^{-8}–1.5×10^{-5} mol L^{-1} with the limitation of 3.8×10^{-9} mol L^{-1}. Furthermore, the sensor was also studied on biological (human serum and urine) samples, apple juice, radish leaves and teas with the detectable concentration range of 1.0×10^{-8} molL^{-1} or 5.0×10^{-6} molL^{-1}. In another study, Gan et al. use Fe_3O_4/Au magnetic nanoparticles to modify a screen-printed carbon electrode to determine the organophosphorus pesticides in Chinese cabbages, and its electrochemical properties were investigated by cyclic voltammetry (CV) and differential pulse voltammetry (DPV) [238]. The sensor performance was comparable to gas chromatography, and it exhibited better performance in terms of fast response and sensitivity for detecting organophosphorus pesticides. The detectable concentration of dimethoate in cabbage is in the range of 1.0×10^{-3}–10 ng.mL^{-1} with a detection limit of 5.6×10^{-4} ng.mL^{-1}. Compared with the other sensors, the recovery rate obtained is 88–105%. In addition, other MNPs such as $CoFe_2O_4$ NPs have also been utilized as electrochemical biosensors like $CoFe_2O_4$ NPs [239, 240].

Optical devices have also been employed as sensors for the detection of several analytes due to their low manufacturing cost, reduced interferences and low signal-to-noise ratio. Optical sensors can be used in food, environmental and clinical samples [241–243]. Different principles of detection used in optical sensors are chemiluminescence (CL), reflectance, fluorescence spectroscopy, interferometry and light scattering. CL-detection is the most commonly used technique, and for quantitative analysis, the systems' selectivity and emission intensity can be improved by the use of MNPs as a catalyst in the reaction [244]. The surface plasmon resonance (SPR)-based optical sensor is the most widely used to investigate the interactions between two molecules, such as antibody-antigen, DNA/RNA and protein–nucleic acid interactions. It has high assay sensitivity and can target analytes at a very low nanomolar concentration range. Generally, Au and Ag nanoparticle-conjugated MNPs at the size range of 10–15 nm are used for SPR sensors. Theoretically, by increasing the particle size, the SPR effect can be increased but it may decrease the colloidal stability of the nanoparticles. Sun et al. reported SPR biosensors based on hollow polydopamine-Ag capped Fe_3O_4 NPs reduced with graphene oxide to detect rabbit IgG [245]. The comparative analysis with the conventional SPR biosensor shows that Ag/Fe_3O_4 biosensor showed detection at 132 times lower concentration and 8 times lower than immuno-sandwich assay. In another study by Chen et al., core–shell structured Au/magnetic nanoparticle SPR-based biosensors were developed for the detection of thrombin with the LOD of 0.6 nM [246]. Piezoelectric biosensors work on the principle of quartz-crystal microbalance (QCM). The QCM has a quartz-crystal disk, and it vibrates under the influence of an electric field. The frequency of vibration changes as molecules adsorb or desorb from the surface of the crystal. The mass of the absorbed molecule on the surface is proportional to the frequency. QCM sensors are inexpensive, small and capable of giving a rapid response even at the change of 1 ng. MNPs with piezoelectric properties can increase the active surface area and decrease the noise in conventional QCM sensors. Zhou et al. developed Au NPs-coated SiO_2/Fe_3O_4 nanoparticle-based immunosensors for

the detection of C-reactive protein (CRP) in serum [247]. The CRP detection of Au-Fe_3O_4@SiO_2 QCM is comparable with ELISA methodology, and the sensor surface can be regenerated and used repeatedly. Still, more research is required on the use of magnetic nanoparticle piezoelectric sensors to improve the sensitivity and stability of the sensors.

16.5 Conclusions

Successful progress in the field of multifunctional magnetic nanoplatforms possesses broad potential applications in cancer nanomedicine. Substantial improvements are being incorporated into the synthesis methods to yield more stable monodispersed NPs with controlled size, shape, chemical composition and surface functionalization pertinent for biomedical applications. Various synthesis protocols to produce magnetic-based nanomaterials, their surface functionalization along with the associated challenges for distinctive biomedical applications have been summarized. Further, the application of magnetic-based nanomaterials in distinctive biomedical applications such as MHT, PTT, drug delivery, bioimaging and biosensing have been discussed in detail.

References

1. Siegel RL, Miller KD, Jemal A (2020) Cancer statistics. CA: A Cancer Journal for Clinicians 70:7–30
2. Shi J, Kantoff PW, Wooster R, Farokhzad OC (2017) Cancer nanomedicine: progress, challenges and opportunities. Nat Rev Can 17:20–37
3. Mrówczyński R (2018) Polydopamine-Based Multifunctional (Nano)materials for Cancer Therapy. ACS App. Mat. & Inter. 10:7541–7561
4. Ling Y, Wei K, Luo Y, Gao X, Zhong S (2011) Dual docetaxel/superparamagnetic iron oxide loaded nanoparticles for both targeting magnetic resonance imaging and cancer therapy. Biomat 32:7139–7150
5. Park JH, Gu L, von Maltzahn G, Ruoslahti E, Bhatia SN, Sailor MJ (2009) Biodegradable luminescent porous silicon nanoparticles for in vivo applications. Nat Mat 8:331–336
6. Savla R, Taratula O, Garbuzenko O, Minko T (2011) Tumor targeted quantum dot-mucin 1 aptamer-doxorubicin conjugate for imaging and treatment of cancer. J. Cont. Rel. 153:16–22
7. Liu Z, Chen K, Davis C, Sherlock S, Cao Q, Chen X et al (2008) Drug delivery with carbon nanotubes for in vivo cancer treatment. Canc. Res. 68:6652–6660
8. Bae KH, Lee K, Kim C, Park TG (2011) Surface functionalized hollow manganese oxide nanoparticles for cancer targeted siRNA delivery and magnetic resonance imaging. Biomat 32:176–184
9. Huang P, Bao L, Zhang C, Lin J, Luo T, Yang D et al (2011) Folic acid-conjugated Silica-modified gold nanorods for X-ray/CT imaging-guided dual-mode radiation and photo-thermal therapy. Biomat 32:9796–9809
10. Wu M, Huang S (2017) Magnetic nanoparticles in cancer diagnosis, drug delivery and treatment. Mol. & Clin. Onc. 7:738–746

11. Liu X, Zhang Y, Wang Y, Zhu W, Li G, Ma X et al (2020) Comprehensive understanding of magnetic hyperthermia for improving antitumor therapeutic efficacy. Ther 10:3793–3815
12. Golombek SK, May JN, Theek B, Appold L, Drude N, Kiessling F et al (2018) Tumor targeting via EPR: Strategies to enhance patient responses. Adv. Drug. Del. Rev. 130:17–38
13. Hervault A, Thanh NTK (2014) Magnetic nanoparticle-based therapeutic agents for thermo-chemotherapy treatment of cancer. Nanoscale 6:11553–11573
14. Ramachandra KSA, Thomas RG, Unnithan AR, Saravanakumar B, Jeong YY, Park CH et al (2016) Multifunctional Nanocarpets for Cancer Theranostics: Remotely Controlled Graphene Nanoheaters for Thermo-Chemosensitisation and Magnetic Resonance Imaging. Sci Rep 6:20543
15. Zhao S, Yu X, Qian Y, Chen W, Shen J (2020) Multifunctional magnetic iron oxide nanoparticles: an advanced platform for cancer theranostics. Theranostics 10:6278–6309
16. Thakor AS, Jokerst JV, Ghanouni P, Campbell JL, Mittra E, Gambhir SS (2016) Clinically Approved Nanoparticle Imaging Agents. Journal of nuclear medicine : official publication, Society of Nuclear Medicine 57:1833–1837
17. Mohammed L, Gomaa HG, Ragab D, Zhu J (2017) Magnetic nanoparticles for environmental and biomedical applications: A review. Particuology 30:1–14
18. Figuerola A, Di CR, Manna L, Pellegrino T (2010) From iron oxide nanoparticles towards advanced iron-based inorganic materials designed for biomedical applications. Pharmacol Res 62:126–143
19. Wu W, Wu Z, Yu T, Jiang C, Kim WS (2015) Recent progress on magnetic iron oxide nanoparticles: synthesis, surface functional strategies and biomedical applications. Sci Technol Adv Mater 16:023501
20. Khaledian M, Nourbakhsh MS, Saber R, Hashemzadeh H, Darvishi MH (2020) Preparation and Evaluation of Doxorubicin-Loaded PLA-PEG-FA Copolymer Containing Superparamagnetic Iron Oxide Nanoparticles (SPIONs) for Cancer Treatment: Combination Therapy with Hyperthermia and Chemotherapy. Int J Nanomedicine 15:6167–6182
21. Ningthoujam RS, Vatsa RK, Kumar A, Pandey BN (2012) Functionalized magnetic nanoparticles: concepts, synthesis and application in cancer hyperthermia. In: Banerjee S, Tyagi AK (eds). Elsevier Inc., USA. Chapter 6, 229–260.
22. Vines JB, Yoon J-Y, Ryu N-E, Lim D-J, Park H (2019) Gold Nanoparticles for Photothermal Cancer Therapy. Front Chem 7:167
23. Shi J, Wang L, Zhang J, Ma R, Gao J, Liu Y, Zhang C, Zhang Z (2014) A tumor-targeting near-infrared laser-triggered drug delivery system based on GO@Ag nanoparticles for chemo-photothermal therapy and X-ray imaging. Biomat 35:5847–5861
24. Nam J, Won N, Jin H, Chung H, Kim S (2009) pH-Induced Aggregation of Gold Nanoparticles for Photothermal Cancer Therapy. J Am Chem Soc 131:13639–13645
25. Chakravarty R, Chakraborty S, Ningthoujam RS, Nair KVV, Sharma KS, Ballal A, Guleria A, Kunwar A, Sarma HD, Vatsa RK, Dash A (2016) Industrial-scale synthesis of intrinsically radiolabeled ^{64}CuS nanoparticles for use in positron emission tomography (PET) imaging of cancer. Ind Eng Chem Res 55:12407–12419
26. Feng W, Wang R, Zhou Y, Ding L, Gao X, Zhou B, Hu P, Chen Y (2019) Ultrathin molybdenum Carbide MXene with fast biodegradability for highly efficient theory-oriented photonic tumor hyperthermia. Adv Funct Mater 29:901942
27. Ningthoujam RS, Vatsa RK, Prajapat CL, Yashwant G, Ravikumar G (2010) Interaction between amorphous ferromagnetic Co–Fe–B particles in conducting silver matrix prepared by chemical reduction route. J. Alloys Comp. (Letters) L40:492
28. Meffre A, Mehdaoui B, Kelsen V, Fazzini PF, Carrey J, Lachaize S, Respaud M, Chaudret B (2012) A Simple Chemical Route toward Monodisperse Iron Carbide Nanoparticles Displaying Tunable Magnetic and Unprecedented Hyperthermia Properties. Nano Lett 12:4722–4728
29. Hamayun MA, Abramchuk M, Alnasir H, Khan M, Pak C, Lenhert S, Ghazanfari L, Shatruk M, Manzoor S (2018) Magnetic and magnetothermal studies of iron boride (FeB) nanoparticles. J Magn Magn Mater 451:407–413

30. Ningthoujam RS, Gajbhiye NS (2010) Magnetization studies on ε- $Fe_{2.4}Co_{0.6}N$ nanoparticles. Mater Res Bull 45:499
31. Ali A, Zafar H, Zia M, Haq U I, Phull A R, Ali J S et al (2016) Synthesis, characterization, applications, and challenges of iron oxide nanoparticles. Nanotechnol sci appl 9:49–67
32. Michelle M, Joseph M, Renee F (2008) Determining the solubility product of Fe(OH)3: An equilibrium study with environmental significance. J Chem Educ 85:254
33. Patil RM, Shete PB, Thorat ND, Otari SV, Barick KC, Prasad AI, Ningthoujam RS, Tiwale BM, Pawar SH (2014) Superparamagnetic iron oxide/chitosan core/shells for hyperthermia application: Improved colloidal stability and biocompatibility. J Magn Magn Mater 355:22–30
34. Patil RM, Shete PB, Thorat ND, Otari SV, Prasad AI, Ningthoujam RS, Tiwale B, Pawar SH (2014) Non-aqueous to aqueous phase transfer of oleic acid coated iron oxide nanoparticles for hyperthermia application. RSC Adv 4:4515–4522
35. Prasad AI, Parchur AK, Juluri RR, Jadhav N, Pandey BN, Ningthoujam RS, Vatsa RK (2013) Bi-functional properties of Fe3O4@YPO4: Eu hybrid nanoparticles: Hyperthermia application. Dalton Trans 42:4885–4896
36. Parchur AK, Ansari AA, Singh BP, Hasan TN, Syed NA, Rai SB, Ningthoujam RS (2014) Enhanced luminescence of CaMoO4: Eu by core@shell formation and its hyperthermia study after hybrid formation with Fe3O4: Cytotoxicity assessing on human liver cancer cells and mesanchymal stem cells. Integr Biol 6:53–64
37. Shete PK, Patil RM, Ningthoujam RS, Ghosh S, Pawar SH (2013) Magnetic core shell structures for magnetic fluid hyperthermia therapy application. New J Chem 37:3784–3792
38. Ningombam GS, Ningthoujam RS, Kalkura SN, Singh NR (2018) Induction heating efficiency of water dispersible Mn0.5Fe2.5O4@YVO4:Eu3+ magnetic-luminescent nanocomposites in acceptable AC magnetic field: Haemocompatibility and cytotoxicity studies. J Phys Chem B 122:6862–6871
39. Massart R (1981) Preparation of aqueous magnetic liquids in alkaline and acidic media. IEEE Trans Magn 17:1247–1248
40. Faraji M, Yamini Y, Rezaee M (2010) Magnetic nanoparticles: Synthesis, stabilization, functionalization, characterization, and applications. J Iran Chem Soc 7:1–37
41. Joshi R, Singh BP, Ningthoujam RS (2020) Confirmation of highly stable 10 nm sized Fe3O4 nanoparticle formation at room temperature and understanding of heat-generation under AC magnetic fields for potential application in hyperthermia. AIP Adv 10:105033
42. Peternele WS, Monge FV, Fascineli ML, Rodrigues da SJ, Silva RC, Lucci CM et al (2014) Experimental investigation of the coprecipitation method: An approach to obtain magnetite and maghemite nanoparticles with improved properties. J Nanomater 682985
43. Ahn T, Kim JH, Yang HM, Lee JW, Kim JD (2012) Formation pathways of magnetite nanoparticles by coprecipitation method. J Phy Chem C 116:6069–6076
44. Chen JP, Sorensen CM, Klabunde KJ, Hadjipanayis GC, Devlin E, Kostikas A (1996) Size-dependent magnetic properties of MnFe2O4 fine particles synthesized by coprecipitation. Phys Rev B 54:9288–9296
45. Martina MS, Fortin JP, Ménager C, Clément O, Barratt G, Grabielle MC et al (2005) Generation of superparamagnetic liposomes revealed as highly efficient MRI contrast agents for in vivo imaging. J Am Chem Soc 127:10676–10685
46. Chakraborty S, Sharma KS, Rajeswari A, Vimalnath KV, Sarma HD, Pandey U, Jagannath, Ningthoujam RS, Vatsa RK, Dash A (2015) Radiolanthanide-loaded agglomerated Fe3O4 nanoparticles for possible use in the treatment of arthritis: formulation, characterization and evaluation in rats. J Mater Chem B 3:5455–5466
47. Singhal P, Pulhani V, Ali SM, Ningthoujam RS (2019) Sorption of different metal ions on magnetic nanoparticles and their effect on nanoparticles settlement. Environ Nanotechnol Monitor Manag 11:100202
48. Joshi R, Singh BP, Ningthoujam RS (2020) Confirmation of highly stable 10 nm sized Fe3O4 nanoparticle formation at room temperature and understanding of heat-generation under AC magnetic fields for potential application in hyperthermia. AIP Adv 10:105033

49. Majeed J, Pradhan L, Ningthoujam RS, Vatsa RK, Bahadur D, Tyagi AK (2014) Enhanced specific absorption rate in silanol functionalized Fe3O4 core - shell nanoparticles: study of Fe leaching in Fe3O4 and hyperthermia in L929 and HeLa cells. Colloids Surf, B 122:396–403
50. Shabestari Khiabani S, Farshbaf M, Akbarzadeh A, Davaran S (2017) Magnetic nanoparticles: preparation methods, applications in cancer diagnosis and cancer therapy. Artificial cells, nanomedicine, and biotechnology 45:6–17
51. Li J, Wu Q, Wu J (2015) Synthesis of nanoparticles via solvothermal and hydrothermal methods. Handbook of nanoparticles © Springer International Publishing Switzerland
52. Gyergyek S, Makovec D, Jagodič M, Drofenik M, Schenk K, Jordan O et al (2017) Hydrothermal growth of IONPs with a uniform size distribution for magnetically induced hyperthermia: Structural, colloidal and magnetic properties. J All Comp 694:261–271
53. Chen F, Bu W, Lu C, Chen G, Chen M, Shen X et al (2011) Hydrothermal synthesis of a highly sensitive T2-weigthed MRI contrast agent: zinc-doped superparamagnetic iron oxide nanocrystals. J Nanosci Nanotechnol 11(12):10438–10443
54. Li J, Zheng L, Cai H, Sun W, Shen M, Zhang G et al (2013) Polyethyleneimine-mediated synthesis of folic acid-targeted iron oxide nanoparticles for in vivo tumor MR imaging. Biomaterials 34:8382–8392
55. Bang JH, Suslick KS (2010) Applications of ultrasound to the synthesis of nanostructured materials. Adv Mater 22:1039–1059
56. Patil AB, Bhanage BM (2016) Sonochemistry: A greener protocol for nanoparticles synthesis. In: Aliofkhazraei M (ed) Handbook of nanoparticles. Springer International Publishing, Cham, pp 143–166
57. Xu H, Zeiger BW, Suslick KS (2013) Sonochemical synthesis of nanomaterials. Chem Soc Rev 42:2555–2567
58. Dolores R, Raquel S, Adianez GL (2015) Sonochemical synthesis of iron oxide nanoparticles loaded with folate and cisplatin: Effect of ultrasonic frequency. Ultrason Sonochem 23:391–398
59. Ashokkumar M (2016) Advantages, disadvantages and challenges of ultrasonic technology, pp 41–42
60. Abbas M, Takahashi M, Kim C (2012) Facile sonochemical synthesis of high-moment magnetite (Fe3O4) nanocube. J Nanopart Res 15:1354
61. Zemb TN, Klossek M, Lopian T, Marcus J, Schöettl S, Horinek D, Prevost SF, Touraud D, Diat O, Marčelja S, Kunz W (2016) How to explain microemulsions formed by solvent mixtures without conventional surfactants. Proceedings of National Academy of Sciences 113:4260–4265
62. Hoar TP, Schulman JH (1943) Transparent water-in-oil dispersions: the oleopathic hydro-micelle. Nature 152:102–103
63. Gillberg G, Lehtinen H, Friberg S (1970) NMR and IR investigation of the conditions determining the stability of microemulsions. J Colloid Interface Sci 33:40–53
64. Luwang MN, Ningthoujam RS, Srivastava SK, Vatsa RK (2011) Preparation of white light emitting YVO4:Ln3+ and silica-coated YVO4:Ln3+ (Ln3+ = Eu3+, Dy3+, Tm3+) nanoparticles by CTAB/n-butanol/hexane/water microemulsion route: Energy transfer and site symmetry studies. J Mater Chem 21:5326
65. Asab G, Zereffa EA, Abdo ST (2020) Synthesis of silica-coated Fe3O4 nanoparticles by microemulsion method: Characterization and evaluation of antimicrobial activity. Int J Biomater 2020:4783612
66. Singh P, Upadhyay C (2018) Fine tuning of size and morphology of magnetite nanoparticles synthesized by microemulsion. AIP Conf Proc 1953:030051
67. Nayeem J, Al-Bari MAA, Mahiuddin M, Rahman MA, Mefford OT, Ahmad H et al (2020) Silica coating of iron oxide magnetic nanoparticles by reverse microemulsion method and their functionalization with cationic polymer P(NIPAm-co-AMPTMA) for antibacterial vancomycin immobilization. Colloids Surf Physicochem Eng Aspects 25857
68. Malik MA, Wani MY, Hashim MA (2012) Microemulsion method: A novel route to synthesize organic and inorganic nanomaterials: 1st Nano Update. Arab J Chem 5:397–417

69. Li GR, Xu H, Lu XF, Feng JX, Tong YX, Su CY (2013) Electrochemical synthesis of nanostructured materials for electrochemical energy conversion and storage. Nanoscale 5:4056–4069
70. Reetz MT, Helbig W (1994) Size-selective synthesis of nanostructured transition metal clusters. J Am Chem Soc 116:7401–7402
71. Aghazadeh M, Karimzadeh I, Ganjali MR (2017) Electrochemical evaluation of the performance of cathodically grown ultra-fine magnetite nanoparticles as electrode material for supercapacitor applications. J Mater Sci: Mater Electron 28:13532–13539
72. Fajaroh F, Nazriati, Yahmin, Marfu'ah S, Sumari, Nur A (2018) Synthesis of Fe3O4 Nanoparticles using PEG Template by Electrochemical Method. J Phys Conf Ser 093:012022
73. Wu W, Jiang CZ, Roy VAL (2016) Designed synthesis and surface engineering strategies of magnetic iron oxide nanoparticles for biomedical applications. Nanoscale 8:19421–19474
74. Sikka S (2005) Handbook of sol-gel science and technology: Processing, characterization and applications. Kluwar Academic Publishers
75. Umare SS, Ningthoujam RS, Sharma SJ, Shrivastava S, Kurian S, Gajbhiye NS (2008) Mössbauer and magnetic studies on nanocrystalline NiFe2O4 particles prepared by ethylene glycol route. Hyperfine Interact 184:235
76. Ningthoujam RS, Gajbhiye NS, Sachil S (2009) Reduction mechanism of Ni2+ into Ni nanoparticles prepared from different precursors: Magnetic studies. Pramana J Phys 72:577
77. Gajbhiye NS, Bhattacharyya S, Balaji G, Ningthoujam RS, Das RK, Basak S, Weissmuller J (2005) Mössbauer and magnetic studies of MFe2O4 (M = Co, Ni). Hyperfine Interact 165:153
78. Takai Z, Mustafa M, Asman S, Sekak K (2019) Preparation and characterization of magnetite (Fe3O4) nanoparticles By Sol-Gel method. Int J Nanoelectronics Mater12:37–46
79. Jacintha A, Umapathy V, Neeraja P, S RJR (2017) Synthesis and comparative studies of MnFe2O4 nanoparticles with different natural polymers by sol–gel method: structural, morphological, optical, magnetic, catalytic and biological activities. J Nanostruct Chem 7:375–387
80. Borhan A, Herea DD, Gherca D, Stavila C, Minuti AE, Grigoras M et al (2020) Flash-cooling assisted sol-gel self-ignited synthesis of magnetic carbon dots-based heterostructure with antitumor properties. Mater Sci Eng C 117:111288
81. Dalal M, Greneche JM, Satpati B Ghzaiel TB, Mazaleyrat F, Ningthoujam RS et al (2017) Microwave absorption and the magnetic hyperthermia applications of Li0.3Zn0.3Co0.1Fe2.3O4 nanoparticles in multiwalled carbon nanotube matrix. ACS Appl Mater Interf 9:40831–40845
82. Carter RE (1961) Mechanism of solid-state reaction between magnesium oxide and aluminum oxide and between magnesium oxide and ferric oxide. J Am Ceram Soc 44:116–120
83. Sudhakar N, Ningthoujam RS, Gajbhiye NS, Rajeev KP (2007) Structural, magnetic and electron transport studies on nanocrystalline layered manganite La1.2Ba1.8Mn2O7 system. J Nanosci Nanotech 7:965
84. Shukla R, Tyagi AK (2010) Phase stability of rare-earth based mixed oxides in nano-regime: Role of synthesis in thermal and thermodynamic stability of nanomaterials, S. C. Parida. Trans. Tech publisher Materials Science Forum 653:131-152.
85. Shukla R, Dutta DP, Ramkumar J, Mandal BP, Tyagi AK (2013) Nanocrystalline functional oxide materials in handbook of nanomaterials by R. Vajtai; Springer Publisher, pp 517-552
86. Thorat ND, Shinde KP, Barick KC, Pawar SH, Betty CA, Ningthoujam RS (2012) Polyvinyl alcohol: an efficient fuel for synthesis of superparamagnetic LSMO nanoparticles for biomedical application. Dalton Trans 41:3060
87. Jadhav SV, Nikam DS, Khot VM, Thorat ND, Phadatare MR, Ningthoujam RS, Salunkhe AB, Pawar SH (2013) Studies on colloidal stability of PVP-coated LSMO nanoparticles for magnetic fluid hyperthermia. New J Chem 37:3121
88. Thorat ND, Khot VM, Salunkhe AB, Prasad AI, Ningthoujam RS, Pawar SH (2013) Surface functionalized La0.7Sr0.3MnO3nanoparticles with improved colloidal stability for hyperthermia applications. J Phys D 46:105003

89. Thorat ND, Khot VM, Salunkhe AB, Ningthoujam RS, Pawar SH (2013) Functionalization of La0.7Sr0.3MnO3 nanoparticles with polymer: Studies on enhanced hyperthermia and biocompatibility properties for biomedical applications. Colloids Surf Biointerf 104:40–47
90. Thorat ND, Otari SV, Patil RM, Bohara RA, Yadav HM, Koli VB, Chaurasia AK, Ningthoujam RS (2014) Synthesis, characterization and biocompatibility of chitosan functionalized superparamagnetic nanoparticles for heat activated curing of cancer cells. Dalton Trans 43:17343–17351
91. Thorat ND, Patil RM, Khot VM, Salunkhe AB, Prasad AI, Barick KC, Ningthoujam RS, Pawar SH (2013) Highly water dispersible surface functionalized LSMO nanoparticles for magnetic fluid hyperthermia application. New J Chem 37:2733
92. Ningthoujam RS, Umare SS, Sharma SJ, Shukla R, Kurian S, Vatsa RK, Tyagi AK, Tewari R, Dey GK, Gajbhiye NS (2008) Magnetic and Mössbauer studies on nanocrystalline Co1-xLixFe2O4 (x = 0, 0.2). Hyperfine Interact 184:227
93. Shukla R, Ningthoujam RS, Umare SS, Sharma SJ, Kurian S, Vatsa RK, Tyagi AK, Gajbhiye NS (2008) Decrease of superparamagnetic fraction at room temperature in ultrafine CoFe2O4 particles by Ag doping. Hyperfine Interact 184:217
94. Thorat ND, Otari SV, Bohara RA, Yadav HM, Khot VM, Salunkhe AB, Phdatre MR, Prasad AI,, Ningthoujam RS, Pawar SH (2014) Structured superparamagnetic nanoparticles for high performance mediator of magnetic fluid hyperthermia: Synthesis, colloidal stability and biocompatibility evaluation. Mater Sci Eng C 42:637–646
95. Thorat ND, Otari SC, Patil RM, Khot VM, Prasad AI, Ningthoujam RS, Pawar SH (2013) Enhanced colloidal stability of polymer coated La0.7Sr0.3MnO3 nanoparticles in physiological media for hyperthermia application. Colloids SurfB: Biointerf 111:264
96. Dalal M, Das A, Das D, Ningthoujam RS, Chakrabarti PK (2018) Studies of magnetic, Mössbauer spectroscopy, microwave absorption and hyperthermia behavior of Ni-Zn-Co-ferrite nanoparticles encapsulated in multi-walled carbon nanotubes. J Magn Magn Mater 460:12–27
97. Gajbhiye NS, Vijayalakshmi A, Weissmuller J (2002) Magnetic Properties of Nanosize Lead Hexaferrite Particles. Phys. Stat. Sol. (a) 189:685–689
98. Sankaranarayanan VK, Gajbhiye NS (1991) Spectrochemical investigations of ultrafine amorphous and crystalline rare earth iron garnets. J Solid State Chem 93:134–145
99. Jadhav NV, Prasad AI, Kumar A, Mishra R, Dhara S, Babu KR, Prajapat CL, Misra NL, Ningthoujam RS, Pandey BN, Vatsa RK (2013) Synthesis of oleic acid functionalized Fe3O4 magnetic nanoparticles and studying their interaction with tumor cells for potential hyperthermia applications. Colloids Surf, B 108:158–168
100. Maity D, Ding JUN, Xue JM (2008) Synthesis of magnetite nanoparticles by thermal decomposition: time, temperature, surfactant and solvent effects. Funct Mater Lett 01:189–193
101. Ningthoujam RS, Gautam A, Padma N (2017) Oleylamine as reducing agent in syntheses of magic-size clusters and monodisperse quantum dots: optical and photoconductivity studies. Phys Chem Chem Phys 19:2294–2303
102. Hyeon T, Lee SS, Park J, Chung Y, Na HB (2001) Synthesis of highly crystalline and monodisperse maghemite nanocrystallites without a size-selection process. J Am Chem Soc 123:12798–12801
103. Murray CB, Norris DJ, Bawendi MG (1993) Synthesis and characterization of nearly monodisperse CdE (E = sulfur, selenium, tellurium) semiconductor nanocrystallites. J Am Chem Soc 115:8706–8715
104. Sharma KS, Ningthoujam RS, Dubey AK, Chattopadhyay A, Phapale S, Juluri RR, Mukherjee S, Tewari R, Shetake NG, Pandey BN, Vatsa RK (2018) Synthesis and characterization of monodispersed water dispersible Fe3O4 nanoparticles and in vitro studies on human breast carcinoma cell line under hyperthermia condition. Sci Rep 8:14766
105. Lassenberger A, Grünewald TA, van Oostrum PDJ, Rennhofer H, Amenitsch H, Zirbs R et al (2017) Monodisperse iron oxide nanoparticles by thermal decomposition: Elucidating particle formation by second-resolved in situ small-angle X-ray scattering. Chem Mater 29:4511–4522
106. Sun S, Zeng H, Robinson DB, Raoux S, Rice PM, Wang SX et al (2004) Monodisperse MFe2O4 (M = Fe Co, Mn) nanoparticles. J Am Chem Soc 126:273–279

107. Park J, An K, Hwang Y, Park JG, Noh HJ, Kim JY et al (2004) Ultra-large-scale syntheses of monodisperse nanocrystals. Nat Mater 3:891–895
108. Piquer C, Laguna-Marco MA, Roca AG, Boada R, Guglieri C, Chaboy J (2014) Fe K-Edge X-ray absorption spectroscopy study of nanosized nominal magnetite. J Phys Chem C 118:1332–1346
109. Sharma S, Gajbhiye NS, Ningthoujam RS (2010) Synthesis and self-assembly of monodisperse CoxNi100-x (x = 50, 80) colloidal nanoparticles by homogenous nucleation. J. Colloids & Interface Science 351:323
110. Gajbhiye NS, Sharma S, Ningthoujam RS (2008) Synthesis of self-assembled monodisperse 3 nm FePd nanoparticles: phase transition, magnetic study and surface effect. J Appl Phys 104:123906
111. Sharma S, Ningthoujam RS, Gajbhiye NS (2013) Spin-glass-like behavior of surfactant capped Co50Ni50 nanoparticles. Chem Phys Lett 558:48–52
112. Sharma S, Gajbhiye NS, Ningthoujam RS (2010) Effect of annealing on magnetic properties of FePd and FePdPt nanoparticles. AIP Conference Proceeding 1313:125
113. Soni AK, Joshi R, Singh BP, Kumar NN, Ningthoujam RS (2019) Near-infrared- and magnetic-field-responsive NaYF4:Er3+/Yb3+@SiO2@AuNP@Fe3O4 nanocomposites for hyperthermia applications induced by fluorescence resonance energy transfer and surface plasmon absorption. ACS Appl. Nano Mater. 2:7350–7361
114. Soni AK, Yadav KK, Singh BP, Joshi R, Chakraborty S, Chakravarty R, Nagaraja NK, Singh DK, Kain V, Dash A, Ningthoujam RS (2020) Smart YPO4:Er-Yb nanophosphor for optical heating, hyperthermia, security ink, cancer endoradiotherapy and uranyl recovery. ACS Appl Nano Mater
115. Joshi R, Perala RS, Shelar SB, Ballal A, Singh BP, Ningthoujam RS (2020) Super bright red upconversion in NaErF4:0.5%Tm@NaYF4:20%Yb nanoparticles for anti-counterfeit and bio-imaging applications. ACS Appl Mater Interf
116. Motshekga SC, Pillai SK, Ray SS, Jalama K, Krause RWM (2012) Recent trends in the microwave-assisted synthesis of metal oxide nanoparticles supported on carbon nanotubes and their applications. J Nanomater 691503
117. Aivazoglou E, Metaxa E, Hristoforou E (2017) Microwave-assisted synthesis of iron oxide nanoparticles in biocompatible organic environment. AIP Adv 8:048201
118. Hu H, Yang H, Huang P, Cui D, Peng Y, Zhang J et al (2010) Unique role of ionic liquid in microwave-assisted synthesis of monodisperse magnetite nanoparticles. Chem Commun 46:3866–3868
119. Komarneni S, Hu W, Noh YD, Van Orden A, Feng S, Wei C et al (2012) Magnetite syntheses from room temperature to 150°C with and without microwaves. Ceram Int 38:2563–2568
120. Bhavesh R, Lechuga VA, Ruiz CJ, Herranz F (2015) T1 -MRI fluorescent iron oxide nanoparticles by microwave assisted synthesis. Nanomaterials 5:1880–1890
121. Zhu X, Hitchcock AP, Bazylinski DA, Denes P, Joseph J, Lins U et al (2016) Measuring spectroscopy and magnetism of extracted and intracellular magnetosomes using soft X-ray ptychography. Proc Natl Acad Sci 113:E8219
122. Patra CR, Mukherjee S, Kotcherlakota R (2014) Biosynthesized silver nanoparticles: a step forward for cancer theranostics? Nanomedicine 9:1445–1448
123. Lim EK, Kim T, Paik S, Haam S, Huh Y-M, Lee K (2015) Nanomaterials for theranostics: Recent advances and future challenges. Chem Rev 115:327–394
124. Gao L, Fan K, Yan X (2017) Iron oxide nanozyme: A multifunctional enzyme mimetic for biomedical applications. Theranostics 7:3207–3227
125. Gaddam RR, Mukherjee S, Punugupati N, Vasudevan D, Patra CR, Narayan R et al (2017) Facile synthesis of carbon dot and residual carbon nanobeads: Implications for ion sensing, medicinal and biological applications. Mater Sci Eng, C 73:643–652
126. Silva CO, Pinho JO, Lopes JM, Almeida AJ, Gaspar MM, Reis C (2019) Current trends in cancer nanotheranostics: Metallic, polymeric, and lipid-based systems. Pharmaceutics 11:22
127. Mukherjee A, Waters A, Babic I, Nurmemmedov E, Glassy M, Kesari S et al (2018) Antibody drug conjugates: Progress, pitfalls, and promises. Hum Antibodies 27:1–10

128. Dickerson MB, Sandhage KH, Naik RR (2008) Protein- and peptide-directed syntheses of inorganic materials. Chem Rev 108:4935–4978
129. Vargas G, Cypriano J, Correa T, Leão P, Bazylinski DA, Abreu F (2018) Applications of magnetotactic bacteria, magnetosomes and magnetosome crystals in biotechnology and nanotechnology: Mini-review. Molecules 23:2438
130. Zhou W, He W, Zhong S, Wang Y, Zhao H, Li Z et al (2009) Biosynthesis and magnetic properties of mesoporous Fe3O4 composites. J Magn Magn Mater 321:1025–1028
131. Kaushik S, Thomas J, Panwar V, Ali H, Chopra V, Sharma A, Tomar R, Ghosh D (2020) In situ biosynthesized superparamagnetic iron oxide nanoparticles (SPIONS) induce efficient hyperthermia in cancer cells. ACS Appl Bio Mater 3:779–788
132. Jadhav NV, Prasad AI, Kumar A, Mishra R, Dhara S, Babu KR, Prajapat CL, Misra NL, Ningthoujam RS, Pandey BN, Vatsa RK (2013) Synthesis of oleic acid functionalized Fe3O4 magnetic nanoparticles and studying their interaction with tumor cells for potential hyperthermia applications. Colloids Surf Biointerf 108:158–168
133. Barick KC, Sharma A, Shetake NG, Ningthoujam RS, Vatsa RK, Babu PD, Pandey BN, Hassan PA (2015) Covalent bridging of surface functionalized Fe3O4 and YPO4: Eu nanostructures for simultaneous imaging and therapy. Dalton Trans 44:14686–14696
134. Bhattacharya S, Roychowdhury A, Tiwari V, Prasad AI, Ningthoujam RS, Patel A, Das D, Nayar S (2015) Effect of biomimetic templates on the magneto-structural properties of Fe3O4 nanoparticles. RSC Adv 5:13777–13786
135. Nikam DS,Jadhav SV, Khot VM, Ningthoujam RS, Hong CK, Mali SS, Pawar SH (2014) Colloidal stability of polyethylene glycol functionalized Co0.5Zn0.5Fe2O4 nanoparticles: effect of pH, sample and salt concentration for hyperthermia application. RSC Adv 4:12662
136. Shete PB, Patil RM, Thorat ND, Prasad A, Ningthoujam RS, Ghosh SJ, Pawar SH (2014) Magnetic chitosan nanocomposite for hyperthermia therapy application: Preparation, characterization and in vitro experiments. Appl Surf Sci 288:149–157
137. Khot VM, Salunkhe AB, Thorat ND, Ningthoujam RS, Pawar SH (2013) Induction heating studies of dextran coated MgFe2O4 nanoparticles for magnetic hyperthermia. Dalton Trans 42:1249–1258
138. Parchur AK, Kaurav N, Ansari AA, Prasad AI, Ningthoujam RS, Rai SB (2013) CaMoO4:Tb@Fe3O4 hybrid nanoparticles for luminescence and hyperthermia applications. AIP Conf Proc 1512:184
139. Mallick A, Mahapatra AS, Mitra A, Greneche JM, Ningthoujam RS, Chakrabarti PK (2018) Magnetic properties and bio-medical applications in hyperthermia of lithium zinc ferrite nanoparticles integrated with reduced graphene oxide. J Appl Phys 123:055103
140. Suk JS, Xu Q, Kim N, Hanes J, Ensign LM (2016) PEGylation as a strategy for improving nanoparticle-based drug and gene delivery. Adv Drug Deliv Rev 99:28–51
141. Rajan SA, Sharma M, Sahu NK (2020) Water-to-PEG variation: Morphology and hyperthermic behaviour of iron oxide. J Supercond Novel Magn 33:1603–1609
142. Zhu N, Ji H, Yu P, Niu J, Farooq MU, Akram MW et al (2018) Surface modification of magnetic iron oxide nanoparticles. Nanomaterials (Basel) 8:810
143. Muthiah M, Park I K, Cho C (2013) Surface modification of iron oxide nanoparticles by biocompatible polymers for tissue imaging and targeting. Biotechnol Adv 31:1224-1236
144. Rajan A, Sharma M, Sahu NK (2020) Assessing magnetic and inductive thermal properties of various surfactants functionalised Fe3O4 nanoparticles for hyperthermia. Sci Rep 10:15045
145. Rajan A, Sahu NK (2020) Inductive calorimetric assessment of iron oxide nanooctahedrons for magnetic fluid hyperthermia. Colloids Surf Physicochem Eng Aspects 603:125210Muthiah, M.; Park, I. K.; Cho, C. Surface Modification of Iron Oxide Nanoparticles by Biocompatible Polymers for Tissue Imaging and Targeting. *Biotechnology Advances* **2013**.
146. Wang Z, Choi F, Acosta E (2017) Effect of surfactants on zero-valent iron nanoparticles (NZVI) reactivity. J Surfactants Detergents 20
147. Chakraborty T, Chakraborty I, Ghosh S (2006) Sodium carboxymethylcellulose−CTAB interaction: A detailed thermodynamic study of polymer−surfactant interaction with opposite charges. Langmuir 22:9905–9913

148. Reverdatto S, Burz DS, Shekhtman A (2015) Peptide aptamers: development and applications. Curr Top Med Chem 15:1082–1101
149. Zuo B, Li W, Wu X, Wang S, Deng Q, Huang M (2020) Recent advances in the synthesis, surface modifications and applications of core-shell magnetic mesoporous silica nanospheres. Chem Asian J 15:1248–1265
150. Nassireslami E, Ajdarzade M (2018) Gold coated superparamagnetic iron oxide nanoparticles as effective nanoparticles to eradicate breast cancer cells via photothermal therapy. Adv Pharm Bull 8:201–209
151. Barick K, Hassan PA (2011) Glycine passivated Fe3O4 nanoparticles for thermal therapy. J Colloid Interface Sci 369:96–102
152. Mahdavi M, Ahmad MB, Haron MJ, Namvar F, Nadi B, Rahman MZA et al (2013) Synthesis, surface modification and characterisation of biocompatible magnetic iron oxide nanoparticles for biomedical applications. Molecules 18:7533–7548
153. Kudr J, Haddad Y, Richtera L, Heger Z, Cernak M, Adam V et al (2017) Magnetic nanoparticles: From design and synthesis to real world applications. Nanomaterials (Basel) 7:243
154. Schmid G, Klein N, Korste L, Kreibig U, Schönauer D (1988) Large transition metal clusters—VI. Ligand exchange reactions on Au55(PPh3)12Cl6—the formation of a water soluble Au55 cluster. Polyhedron 7:605–608
155. Yu WW, Chang E, Sayes CM, Drezek R, Colvin VL (2006) Aqueous dispersion of monodisperse magnetic iron oxide nanocrystals through phase transfer. Nanotechnology 17:4483–4487
156. Mao Z, Guo J, Bai SNTL, Xia H, Huang Y et al (2009) Hydrogen-bond-selective phase transfer of nanoparticles across liquid/gel interfaces. Angew Chem Int Ed 48:4953–4956
157. Hatakeyama M, Kishi H, Kita Y, Imai K, Nishio K, Karasawa S et al (2011) A two-step ligand exchange reaction generates highly water-dispersed magnetic nanoparticles for biomedical applications. J Mater Chem 21:5959–5966
158. Hou Z, Ren M, Wang K, Yang Y, Xu J, Zhu J (2020) Deformable block copolymer microparticles by controllable localization of pH-responsive nanoparticles. Macromolecules 53:473–481
159. DeCrozals G, Bonnet R, Farre C, Chaix C (2016) Nanoparticles with multiple properties for biomedical applications: A strategic guide. Nano Today 11:435–463
160. Joshi R, Perala R, Srivastava M, Singh BP, Ningthoujam R (2019) Heat generation from magnetic fluids under alternating current magnetic field or induction coil for hyperthermia-based cancer therapy: Basic principle. Journal of Radiation and Cancer Research 10:156–164
161. Rajan A, Sahu NK (2020) Review on magnetic nanoparticle-mediated hyperthermia for cancer therapy. J Nanopart Res 22:319
162. Gilchrist RK, Medal R, Shorey WD, Hanselman RC, Parrott JC, Taylor CB (1957) Selective inductive heating of lymph nodes. Ann Surg 146:596–606
163. Atkinson WJ, Brezovich IA, Chakraborty DP (1984) Usable frequencies in hyperthermia with thermal seeds. IEEE Trans Biomed Eng BME-31:70–75
164. Maier-Hauff K, Rothe R, Scholz R, Gneveckow U, Wust P, Thiesen B et al (2007) Intracranial thermotherapy using magnetic nanoparticles combined with external beam radiotherapy: Results of a feasibility study on patients with glioblastoma multiforme. J Neurooncol 81:53–60
165. Maier-Hauff K, Ulrich F, Nestler D, Niehoff H, Wust P, Thiesen B et al (2011) Efficacy and safety of intratumoral thermotherapy using magnetic iron-oxide nanoparticles combined with external beam radiotherapy on patients with recurrent glioblastoma multiforme. J Neurooncol 103:317–324
166. Dennis CL, Ivkov R (2013) Physics of heat generation using magnetic nanoparticles for hyperthermia. Int J Hyperth 29:715–729
167. Sahu NK, Gupta J, Bahadur D (2015) PEGylated FePt–Fe3O4 composite nanoassemblies (CNAs): in vitro hyperthermia, drug delivery and generation of reactive oxygen species (ROS). Dalton Trans 44:9103–9113

168. Kumar S, Daverey A, Sahu NK, Bahadur D (2013) In vitro evaluation of PEGylated mesoporous MgFe2O4 magnetic nanoassemblies (MMNs) for chemo-thermal therapy. Journal of Materials Chemistry B 1:3652–3660
169. Kotoulas A, Dendrinou-Samara C, Sarafidis C, Kehagias T, Arvanitidis J, Vourlias G et al (2017) Carbon-encapsulated cobalt nanoparticles: synthesis, properties, and magnetic particle hyperthermia efficiency. J Nanopart Res 19:399
170. Sharifi I, Shokrollahi H, Amiri S (2012) Ferrite-based magnetic nanofluids used in hyperthermia applications. J Magn Magn Mater 324:903–915
171. Mazario E, Menéndez N, Herrasti P, Cañete M, Connord V, Carrey J (2013) Magnetic hyperthermia properties of electrosynthesized cobalt ferrite nanoparticles. J Phys Chem C 117:11405–11411
172. Stergar J, Ban I, Maver U (2019) The potential biomedical application of NiCu magnetic nanoparticles. Magnetochemistry 5:66
173. Ma X, Wang Y, Liu XL, Ma H, Li G, Li Y et al (2019) Fe3O4–Pd Janus nanoparticles with amplified dual-mode hyperthermia and enhanced ROS generation for breast cancer treatment. Nanoscale Horizons 4:1450–1459
174. Augustine S, Singh J, Srivastava M, Sharma M, Das A, Malhotra BD (2017) Recent advances in carbon based nanosystems for cancer theranostics. Biomaterials Science 5:901–952
175. Meneses-Brassea BP, Borrego EA, Blazer DS, Sanad MF, Pourmiri S, Gutierrez DA et al (2020) Ni-Cu nanoparticles and their feasibility for magnetic hyperthermia. Nanomaterials (Basel) 10:1988
176. Wang X, Pan F, Xiang Z, Jia W, Lu W (2020) Magnetic Fe3O4@PVP nanotubes with high heating efficiency for MRI-guided magnetic hyperthermia applications. Mater Lett 262:127187
177. Lee J-H, Jang J-T, Choi J-S, Moon SH, Noh S-H, Kim J-W et al (2011) Exchange-coupled magnetic nanoparticles for efficient heat induction. Nat Nanotechnol 6:418–422
178. Xie L, Jin W, Zuo X, Ji S, Nan W, Chen H et al (2020) Construction of small-sized superparamagnetic Janus nanoparticles and their application in cancer combined chemotherapy and magnetic hyperthermia. Biomaterials Science 8:1431–1441
179. Hedayatnasab Z, Dabbagh A, Abnisa F, Wan Daud WMA (2020) Polycaprolactone-coated superparamagnetic iron oxide nanoparticles for in vitro magnetic hyperthermia therapy of cancer. Euro Polym J 133:109789
180. Ghosh R, Pradhan L, Devi YP, Meena SS, Tewari R, Kumar A, Sharma S, Gajbhiye NS, Vatsa RK, Pandey BN, Ningthoujam RS (2011) Induction heating studies of Fe3O4 magnetic nanoparticles capped with oleic acid and polyethylene glycol for hyperthermia. J Mater Chem 21:13388
181. Shetake NG, Kumar A, Gaikwad S, Ray P, Desai S, Ningthoujam RS, Vatsa RK, Pandey BN (2015) Magnetic nanoparticle-mediated hyperthermia therapy induces tumour growth inhibition by apoptosis and Hsp90/AKT modulation. Int J Hyperthermia 31:909–9019
182. Maier-Hauff K, Ulrich F, Nestler D, Niehoff H, Wust P, Thiesen B, Orawa H, Budach V, Jordan A (2011) Efficacy and safety of intratumoral thermotherapy using magnetic iron-oxide nanoparticles combined with external beam radiotherapy on patients with recurrent glioblastoma multiforme. J Neurooncol 103:317–324
183. Gneveckow U, Jordan A, Scholz R, Brüß V, Waldöfner N, Ricke J, Feussner A, Hildebrandt B, Rau B, Wust P (2004) Description and characterization of the novel hyperthermia- and thermoablationsystem MFH ® 300F for clinical magnetic fluid hyperthermia. Med Phys 31:1444
184. Müller S (2009) Magnetic fluid hyperthermia therapy for malignantbrain tumors—an ethical discussion, nanomedicine: Nanotechnology. Biology, and Medicine 5:387–393
185. Singh LP, Jadhav NV, Sharma S, Pandey BN, Srivastava SK, Ningthoujam RS (2015) Hybrid nanomaterials YVO4:Eu/Fe3O4 for optical imaging and hyperthermia in cancer cells. J. Mater. Chem. C 3:1965–1975
186. Leung JP, Wu S, Chou KC, Signorell R (2013) Investigation of sub-100 nm gold nanoparticles for laser-induced thermotherapy of cancer. Nanomaterials (Basel) 3:86–106

187. Hubenthal F, Hendrich C, Träger F (2010) Damping of the localized surface plasmon polariton resonance of gold nanoparticles. Appl Phys B 100:225–230
188. Shanmugam V, Selvakumar S, Yeh CS (2014) Near-infrared light-responsive nanomaterials in cancer therapeutics. Chem Soc Rev 43:6254–6287
189. Jaque D, Martínez Maestro L, del Rosal B, Haro-Gonzalez P, Benayas A, Plaza JL et al (2014) Nanoparticles for photothermal therapies. Nanoscale 6:9494–9530
190. Khan A, Sahu NK (2020) 6 - Remotely stimulated nanomedicine for breast cancer therapy. In: Thorat ND, Bauer J (eds) Nanomedicines for breast cancer theranostics. Elsevier, pp 107–30
191. Soni AK, Joshi R, Singh BP, Kumar NN, Ningthoujam RS (2019) Near-infrared- and magnetic-field-responsive NaYF4:Er3+/Yb3+@SiO2@AuNP@Fe3O4 nanocomposites for hyperthermia applications induced by fluorescence resonance energy transfer and surface plasmon absorption. ACS Appl Nano Mater 2:7350–7361.5678
192. Atkinson RL, Zhang M, Diagaradjane P, Peddibhotla S, Contreras A, Hilsenbeck SG et al (2010) Thermal enhancement with optically activated gold nanoshells sensitizes breast cancer stem cells to radiation therapy. Sci Transl Med 2:55ra79–55ra79
193. Hong EJ, Kim YS, Choi DG, Shim MS (2018) Cancer-targeted photothermal therapy using aptamer-conjugated gold nanoparticles. J Ind Eng Chem 67:429–436
194. Wang Y, Black KCL, Luehmann H, Li W, Zhang Y, Cai X et al (2013) Comparison study of gold nanohexapods, Nanorods, and Nanocages for Photothermal Cancer Treatment. ACS Nano 7:2068–2077
195. Thakor AS, Jokerst J, Zavaleta C, Massoud TF, Gambhir SS (2011) Gold nanoparticles: A revival in precious metal administration to patients. Nano Lett 11:4029–4036
196. Phan TTV, Bui NQ, Moorthy MS, Lee KD, Oh J (2017) Synthesis and In vitro performance of polypyrrole-coated iron-platinum nanoparticles for photothermal therapy and photoacoustic imaging. Nanoscale Res Lett 12:570
197. Liu Z, Robinson JT, Sun X, Dai H (2008) PEGylated nanographene oxide for delivery of water-insoluble cancer drugs. J Am Chem Soc 130:10876–10877
198. Espinosa A, Di CR, Kolosnjaj-Tabi J, Flaud P, Pellegrino T, Wilhelm C (2016) Duality of iron oxide nanoparticles in cancer therapy: amplification of heating efficiency by magnetic hyperthermia and photothermal bimodal treatment. ACS Nano 10:2436–2446
199. Jędrzak A, Grześkowiak BF, Golba K, Coy E, Synoradzki K, Jurga S et al (2020) Magnetite nanoparticles and spheres for chemo- and photothermal therapy of hepatocellular carcinoma in vitro. Int J Nanomedicine 15:7923–7936
200. Patra JK, Das G, Fraceto LF, Campos EVR, Rodriguez-Torres MDP, Acosta-Torres LS et al (2018) Nano based drug delivery systems: recent developments and future prospects. J Nanobiotechnology 201:16–71
201. De Jong WH, Borm PJA (2008) Drug delivery and nanoparticles:applications and hazards. Int J Nanomedicine 3:133–149
202. Huang J, Li Y, Orza A, Lu Q, Guo P, Wang L et al (2016) Magnetic nanoparticle facilitated drug delivery for cancer therapy with targeted and image-guided approaches. Adv Funct Mater 26:3818–3836
203. Hobbs SK, Monsky WL, Yuan F, Roberts WG, Griffith L, Torchilin VP et al (1998) Regulation of transport pathways in tumor vessels: Role of tumor type and microenvironment. Proc Natl Acad Sci 95:4607
204. de la Puente P, Azab AK (2017) Nanoparticle delivery systems, general approaches, and their implementation in multiple myeloma. Eur J Haematol 98:529–541
205. Brigger I, Dubernet C, Couvreur P (2012) Nanoparticles in cancer therapy and diagnosis. Adv Drug Deliv Rev 64:24–36
206. Lübbe AS, Bergemann C, Huhnt W, Fricke T, Riess H, Brock JW et al (1996) Preclinical experiences with magnetic drug targeting: tolerance and efficacy. Cancer Res 56:4694–4701
207. Arruebo M, Fernández-Pacheco R, Ibarra MR, Santamaría J (2007) Magnetic nanoparticles for drug delivery. Nano Today 2:22–32
208. Gref R, Minamitake Y, Peracchia MT, Trubetskoy VS, Torchilin VP, Langer R (1994) Biodegradable long-circulating polymeric nanospheres. Science (New York, NY) 263:1600–1603

209. Kakwere H, Leal MP, Materia ME, Curcio A, Guardia P, Niculaes D et al (2015) Functionalization of strongly interacting magnetic nanocubes with (Thermo) responsive coating and their application in hyperthermia and heat-triggered drug delivery. ACS Appl Mater Interfaces 7:10132–10145
210. Zhang C, Mo Z, Teng G, Wang B, Guo R, Zhang P (2013) Superparamagnetic functional C@Fe3O4 nanoflowers: development and application in acetaminophen delivery. Journal of Materials Chemistry B 1:5908–5915
211. Cheng K, Peng S, Xu C, Sun S (2009) Porous hollow Fe3O4 nanoparticles for targeted delivery and controlled release of cisplatin. J Am Chem Soc 131:10637–10644
212. MR, SV, Ramirez JT, AV, LL (2018) Biofunctionalized MnFe2O4@Au core–shell nanoparticles for pH-responsive drug delivery and hyperthermal agent for cancer therapy. Artif Cells, Nanomed Biotechnol 46:S993-S1003
213. Dulińska-Litewka J, Łazarczyk A, Hałubiec P, Szafrański O, Karnas K, Karewicz A (2019) Superparamagnetic iron oxide nanoparticles-current and prospective medical applications. Materials (Basel) 12:617
214. Zhou Z, Zhu X, Wu D, Chen Q, Huang D, Sun C et al (2015) Anisotropic shaped iron oxide nanostructures: controlled synthesis and proton relaxation shortening effects. Chem Mater 27:3505–3515
215. Orza A, Wu H, Xu Y, Lu Q, Mao H (2017) One-step facile synthesis of highly magnetic and surface functionalized iron oxide nanorods for biomarker-targeted applications. ACS Appl Mater Interfaces 9:20719–20727
216. Lee JH, Huh YM, Jun YW, Seo J-W, Jang J-T, Song HT et al (2007) Artificially engineered magnetic nanoparticles for ultra-sensitive molecular imaging. Nat Med 3:9–95
217. Deng H, Li X, Peng Q, Wang X, Chen J, Li Y (2005) Monodisperse magnetic single-crystal ferrite microspheres. Angew Chem Int Ed 44:2782–2785
218. Jang J-T, Nah H, Lee J-H, Moon SH, Dr MG, Prof J (2009) Critical enhancements of MRI contrast and hyperthermic effects by dopant-controlled magnetic nanoparticles. Angew Chem 121:1260–1264
219. Bao Y, Sherwood JA, Sun Z (2018) Magnetic iron oxide nanoparticles as T1 contrast agents for magnetic resonance imaging. J Mater Chem C 6:1280–1290
220. Macher T, Totenhagen J, Sherwood J, Qin Y, Gurler D, Bolding MS et al (2015) Ultrathin iron oxide nanowhiskers as positive contrast agents for magnetic resonance imaging. Adv Funct Mater 25:490–494
221. Zhou Z, Zhao Z, Zhang H, Wang Z, Chen X, Wang R et al (2014) Interplay between longitudinal and transverse contrasts in Fe3O4 nanoplates with (111) exposed surfaces. ACS Nano 8:7976–7985
222. Forte E, Fiorenza D, Torino E, Costagliola di Polidoro A, Cavaliere C, Netti PA et al (2019) Radiolabeled PET/MRI nanoparticles for tumor imaging. J Clin Med 9:89
223. Na HB, Lee IS, Seo H, Park YI, Lee JH, Kim S-W et al (2007) Versatile PEG-derivatized phosphine oxide ligands for water-dispersible metal oxide nanocrystals. Chem Commun 5167–5169
224. Kircher M, Mahmood U, King R, Weissleder R, Josephson L (2004) A multimodal nanoparticle for preoperative magnetic resonance imaging and intraoperative optical brain tumor delineation. Cancer Res 63:8122–8125
225. Lee J-H, Jun Y-W, Yeon S-I, Shin J-S, Cheon J (2006) Dual-mode nanoparticle probes for high-performance magnetic resonance and fluorescence imaging of neuroblastoma. Angew Chem Int Ed Engl 45:8160–8162
226. Kim S, Lim YT, Soltesz EG, De Grand AM, Lee J, Nakayama A et al (2004) Near-infrared fluorescent type II quantum dots for sentinel lymph node mapping. Nat Biotechnol 22:93–97
227. Justino CIL, Rocha-Santos TAP, Cardoso S, Duarte AC (2013) Strategies for enhancing the analytical performance of nanomaterial-based sensors. TrAC, Trends Anal Chem 47:27–36
228. Xu Y, Wang E (2012) Electrochemical biosensors based on magnetic micro/nano particles. Electrochim Acta 84:62–73

229. Aguilar-Arteaga K, Rodriguez JA, Barrado E (2010) Magnetic solids in analytical chemistry: A review. Anal Chim Acta 674:157–165
230. Duarte K, Justino CIL, Freitas AC, Duarte AC, Rocha-Santos TAP (2014) Direct-reading methods for analysis of volatile organic compounds and nanoparticles in workplace air. TrAC, Trends Anal Chem 53:21–32
231. Chen D, Deng J, Liang J, Xie J, Hu C, Huang K (2013) A core–shell molecularly imprinted polymer grafted onto a magnetic glassy carbon electrode as a selective sensor for the determination of metronidazole. Sens Actuators, B Chem 183:594–600
232. Wang X, You Z, Sha H, Sun Z, Sun W (2014) Electrochemical myoglobin biosensor based on carbon ionic liquid electrode modified with Fe3O4@SiO2 microsphere. J Solid State Electrochem 18:207–213
233. Jiang J, Lin X, Ding D, Diao G (2018) Enzyme-free homogeneous electrochemical biosensor for DNA assay using toehold-triggered strand displacement reaction coupled with host-guest recognition of Fe3O4@SiO2@β-CD nanocomposites. Biosens Bioelectron 114:37–43
234. Hu Y, Zhang Z, Zhang H, Luo L, Yao S (2012) Selective and sensitive molecularly imprinted sol–gel film-based electrochemical sensor combining mercaptoacetic acid-modified PbS nanoparticles with Fe3O4@Au–multi-walled carbon nanotubes–chitosan. J Solid State Electrochem 16:857–867
235. Beitollahi H, Nejad FG, Shakeri S (2017) GO/Fe3O4@SiO2 core–shell nanocomposite-modified graphite screen-printed electrode for sensitive and selective electrochemical sensing of dopamine and uric acid. Anal Methods 9:5541–5549
236. Arvand M, Hassannezhad M (2014) Magnetic core–shell Fe3O4@SiO2/MWCNT nanocomposite modified carbon paste electrode for amplified electrochemical sensing of uric acid. Mater Sci Eng, C 36:160–167
237. Saljooqi A, Shamspur T, Mostafavi A (2020) Fe3O4@SiO2-PANI-Au nanocomposite prepared for electrochemical determination of quercetin in food samples and biological fluids. Electroanalysis 32:581–587
238. Gan N, Yang X, Xie D, Wu Y, Wen W (2010) A disposable organophosphorus pesticides enzyme biosensor based on magnetic composite nano-particles modified screen printed carbon electrode. Sensors (Basel, Switzerland) 10:625–638
239. Fu X-H (2008) Magnetic-controlled non-competitive enzyme-linked voltammetric immunoassay for carcinoembryonic antigen. Biochem Eng J 39:267–275
240. Pita M, Tam TK, Minko S, Katz E (2009) Dual magnetobiochemical logic control of electrochemical processes based on local interfacial pH changes. ACS Appl Mater Interfaces 1:1166–1168
241. Justino CIL, Rocha-Santos TA, Duarte AC, Rocha-Santos TA (2010) Review of analytical figures of merit of sensors and biosensors in clinical applications. TrAC, Trends Anal Chem 29:1172–1183
242. Elosúa C, Vidondo I, Arregui FJ, Bariain C, Luquin A, Laguna M et al (2013) Lossy mode resonance optical fiber sensor to detect organic vapors. Sens Actuators, B Chem 187:65–71
243. Silva LIB, Ferreira FDP, Freitas AC, Rocha-Santos TAP, Duarte AC (2010) Optical fibre-based micro-analyser for indirect measurements of volatile amines levels in fish. Food Chem 123:806–813
244. Iranifam M (2013) Analytical applications of chemiluminescence-detection systems assisted by magnetic microparticles and nanoparticles. TrAC, Trends Anal Chem 51:51–70
245. Li S, Wu Q, Ma P, Zhang Y, Song D, Wang X et al (2017) A sensitive SPR biosensor based on hollow gold nanospheres and improved sandwich assay with PDA-Ag@Fe3O4 /rGO. Talanta 180:156–161
246. Chen H, Qi F, Zhou H, Jia S, Gao Y, Koh K et al (2015) Fe3O4@Au nanoparticles as a means of signal enhancement in surface plasmon resonance spectroscopy for thrombin detection. Sens Actuators, B Chem 212:505–511
247. Zhou J, Gan N, Li T, Zhou H, Li X, Cao Y et al (2013) Ultratrace detection of C-reactive protein by a piezoelectric immunosensor based on Fe3O4@SiO2 magnetic capture nanoprobes and HRP-antibody co-immobilized nano gold as signal tags. Sens Actuators B Chem 178:494–500

Chapter 17
Role of Synthesis in Evolution of Catalyst: Bulk, Dispersed to Single Atom

Mrinal R. Pai, Sushma. A. Rawool, Rajendra V. Singh, Atindra Mohan Banerjee, and A. K. Tripathi

Abstract The quantity of information available on subject such as synthesis and catalysis is vast. However, it is significant to integrate both subjects and present a comprehensive article. The present chapter is a small contribution to acclaim the role of synthesis in the development of catalysis industry and research. Three main categories of catalysts that evolved over the years are bulk, dispersed or supported and single atom catalysts (SACs)—which is an ultimate possible form of the dispersed catalysts. With the advancement in research on synthetic techniques, the dream of dispersion of single atoms on support could be realized by managing the associated high surface energy, which is a chief obstacle causing agglomeration and migration of metal ions. SACs are promising catalysts with exceptionally high activity, selectivity and turn over number. The catalyst industry is heavily dependent on bulk and dispersed catalysts, while SAC is at research stage. This chapter aims to give a brief account of all three classes and synthetic methods used to prepare industrial catalysts. It also gives an overview of novel/modified methodologies used to prepare nanoparticles of mixed metal bulk oxides and supported catalysts at large scale. Atomic layer deposition, wet chemical co-precipitation route, photo-deposition and atom trapping are four different approaches adopted to synthesize SACs are also discussed. Finally, it emphasizes synthesis–activity correlations by using examples from our laboratory on thermal reactions ranging from low-temperature CO oxidation, CO + N_2O to high-temperature sulfuric acid decomposition catalytic reactions.

Keywords Synthesis · Bulk oxides · Dispersed · Single atom catalyst · CO + N_2O · Sulfuric acid decomposition

M. R. Pai (✉) · Sushma. A. Rawool · R. V. Singh · A. M. Banerjee · A. K. Tripathi
Chemistry Division, Bhabha Atomic Research Centre, Mumbai 400085, India
e-mail: mrinalr@barc.gov.in

Homi Bhabha National Institute, Mumbai 400094, India

A. K. Tyagi and R. S. Ningthoujam (eds.), *Handbook on Synthesis Strategies for Advanced Materials*, Indian Institute of Metals Series,
https://doi.org/10.1007/978-981-16-1803-1_17

17.1 Introduction

Catalysis is a prominent realm of applied chemistry regulated by chemical engineering principles leading to a significant contribution (30-40%) in the world's GDP [1–3]. The advent of catalysts has brought a revolution in chemical industry by opening new possibilities for many important reactions, which were difficult to realize under normal temperature and pressure conditions. In addition, catalysts have immense applications in energy and environment sector. Catalysts are class of materials that improve the rate of forward and reverse reactions, or it can be said that they allow the reactants to reach the equilibrium faster, without itself undergoing any morphological or compositional change. However, this is an overrated statement. After several cycles, the catalytic activity deteriorates; the surface characteristics and bulk properties alter mainly due to the adsorption of reaction intermediates and thermal shocks. Leaching of the active sites along with evolution of gaseous products during a catalytic reaction is a very common drawback associated with metal-supported catalysts. Thus, practically catalyst was defined as "a catalyst is a substance that changes the rate of a chemical reaction without itself appearing in the products" by Ostwald in 1895, almost 60 years after the standard definition given by Berzelius of ideal catalyst. A more refined definition by IUPAC (1976) was, "a catalyst is a substance that, being present in small proportions, increases the rate of attainment of chemical equilibrium without itself undergoing chemical change" [1–4].

The scope of the present article is limited to heterogeneous catalysis (gas or liquid phase reactants and solid catalyst) in which reactions proceed at interface by adsorption of one or more reactant molecules on the catalyst surface. Adsorption on catalyst surface concentrates and activates the reactant molecules, facilitates close interaction leading to breaking and formation of new bonds. Conductors (metals, alloys), semiconductors (oxides, chalcogenides) and insulators (metal oxides, solid acids or bases, heteropolyacids, clays zeolites) are the three main categories of compounds, which are employed as catalysts depending on the application. The reactive chemistry of these compounds guides their catalytic property. For instance, metals have shown potential in catalyzing hydrogenation, dehydrogenation and hydrogenolysis reactions. Semiconductors; metal oxides such as Fe_2O_3, NiO, CuO, etc. serve as oxidation catalyst while sulfides carry out desulfurization reactions. Dehydration and isomerization reactions can occur on insulator oxides such as Al_2O_3, MgO, SiO_2 etc. Solid acids/bases catalyze organic reactions involving carbocation or anions as intermediates. Thus, suggesting that all cannot catalyze all reactions. A compound is qualified to catalyze a particular reaction, for which it has compatible chemistry with reactant molecules. Mostly, catalysts have application in oil refining, automobiles, bulk chemicals, fine chemicals, fertilizers, polymers, detergents, textiles, pharmaceuticals and energy and environment sectors. Many sections of these industries are using one or more reactions in which catalysts are essential. It has been estimated that at least 80% of chemical products are generated through the involvement of a catalytic process at some stage or other. Catalytic converter installed in all modern

automobiles to control the exhaust emissions is one of the widely known applications [5, 6]. Haber's process catalyst brought revolution in fertilizer industry [7]. Electrocatalysts coated on electrode surface play a vital role in fuel cells, where dissociation and reaction of fuel molecules take place and that govern their overall functioning is another example from innumerable applications [8].

Normally, performance of catalyst in a catalytic reaction is gauged by its activity, selectivity and turn over number [9]. Catalytic activity is identified by percent conversion (total number of moles of product formed per mole of reactant × 100) in a given period. Conversion should reach theoretical thermodynamic yield possible under given conditions of temperature and pressure. The faster the catalyst approaches toward thermodynamic yield, better is the catalyst. Figure 17.1 compares the simulated conversion calculated via thermochemical equilibrium modeling with experimental results for catalytic methane decomposition (CMD) reactions over activated char and biochar catalysts [10]. The experimental values are much lower than simulated values and led researchers to investigate the plausible reasons hampering to achieve the simulated thermodynamic yield. Industrialists search for catalysts enable to attain the thermodynamic yield in minimum possible time under reduced temperature and pressure conditions for an economically viable process. A complete understanding of a catalytic reaction involves a great deal of chemical kinetics, thermodynamics and surface chemistry explained in dedicated monographs and books [11–16].

Designing a catalyst for a particular process is a mainstream research area and innumerable laboratories in fact several institutes are dedicated to catalysis research worldwide. A variety of tailor-made catalytic materials are required for specific

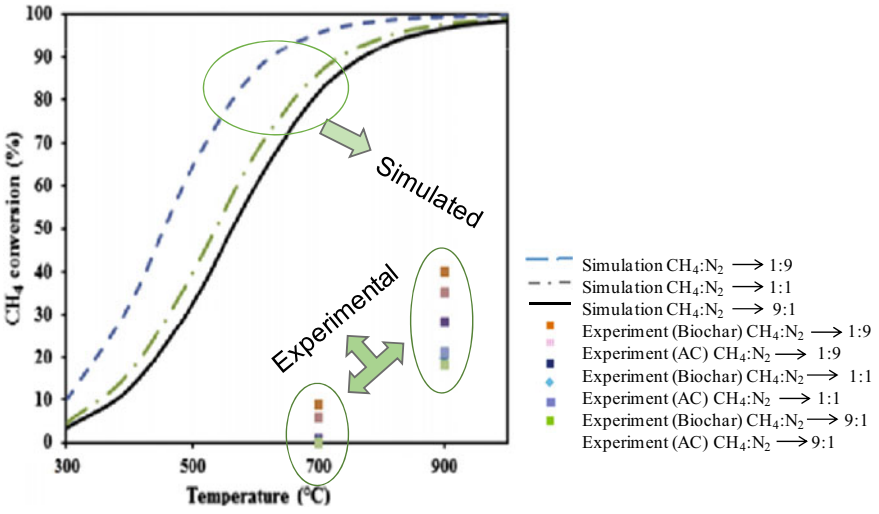

Fig. 17.1 Percent conversion of methane observed experimentally and compared with simulated equilibrium values as a function of temperature. Reprinted from Ref. [10] with permission from Elsevier

applications, which can perform the desired task selectively, efficiently and at the same time during the long operational times In order to design such dedicated rationally designed catalysts, it is important to have a thorough understanding of their physico-chemical properties. The first step in designing of catalyst is to screen the potential candidate that fulfills the essential thermodynamic criteria necessary for the required application. Next is to develop that candidate catalyst by pruning its bulk and surface characteristics—using appropriate modification strategies—for enhancing its catalytic properties. The modified developed catalyst is finally tested and evaluated for catalytic activity and compared with the parent compound. Bulk and surface properties play an important role in deciding the catalytic performance of a catalyst. Adsorption of reactants takes place on surface of catalyst in heterogeneous reactions, thus modification in surface area, porosity and distribution of active sites on surface or surface composition results in considerable improvement of reaction kinetics by lowering the activation energy. Surface of a catalyst may not adhere to the chemical formula by which that compound is known. For instance, $Cu_{0.02}Ti_{0.98}O_{2-\delta}$ may have more than 0.02 mol percent Cu on surface [17]. Chemical composition on surface is mainly governed by unsatisfied valence of metal ions and vice-versa. Particle size, N_2-BET (based on van der Waal interactions) and metal (based on chemisorption) surface area are other important characteristics of catalyst surface and are crucial for its catalytic activity. The active sites for any catalytic reaction reside on surface and depend on the above characteristics of surface. In case of thermal reactions catalyzed by mixed or simple oxides, the crystal type, orientation of planes, flexibility of lattice, non-stoichiometry and defects play an important role in determining the oxide O^{2-} ion mobility at high temperatures. Several mechanisms such as Mars van kreveleen, Eley Rideal etc. are proposed [18–20] based on evidences from in situ experimental probes to explain the participation of lattice oxygen during redox reactions at higher temperatures. For photocatalytic processes, semiconductors mainly are employed to harness the photon energy and thus referred as photocatalysts, are the core of photocatalytic process. The optical and electronic qualities of the photocatalyst control the channeling and utilization of the absorbed solar photons into energy conversion reactions. The valence orbitals of cations and anions forming crystal lattice combine and based on this, band structure can be elucidated using first principles. At the same time, the crystallite size and crystallinity are also very important for deciding the yield of photocatalytic reactions as these have direct implications on path of photogenerated photons from bulk to surface. The role of synthesis in designing and determining the efficiency of photocatalysts will be dealt in details in the next chapter.

The basic chemistry of a catalyst is intrinsic to its chemical constitution and that will not vary from one synthesis method to another. However, a synthesis methodology does control the surface and bulk properties to certain or may be large extent in specific cases. Extensive understanding of a relationship between the structural and morphological characteristics with the catalytic properties is extremely important for developing a desired catalyst. Since, the advent of catalysts a constant pursuit for improvisation has led researchers to invent newer technologies for the synthesis of superior catalysts with desired control on composition, structure and morphology. The synthesis of catalyst involves several steps where every step is

crucial in deciding its surface and bulk characteristics. Thus, catalysts must be synthesized under accurate and carefully controlled conditions [21–23].

Aim and scope

The present chapter has two main aspects. First, it gives an account of existing and emerging synthetic techniques adopted to modify the bulk and surface, of potential catalyst candidates. Oxides (simple/mixed metal) and metal-supported are two main catalyst categories that would be focus of the present article. This also includes advancements in synthetic protocols for the preparation of catalyst in bulk powder/granular, dispersed on support and dispersion of active component to the extent of single atoms on support referred as single atom catalysts. The second part will emphasize the role of synthesis in evolution of catalysts and catalytic processes. Here, several catalytic thermal reactions investigated in our research group will be discussed to exemplify how catalyst development is reliant on exploration of synthesis methodologies. Our studies focus on how catalyst synthesis, plays a crucial role in establishing the desired composition and structure of the catalytic materials active for low to moderate temperature CO oxidation, CO + N_2O to high-temperature sulfuric acid decomposition catalytic applications. This segment illustrates synthesis–catalytic activity correlations.

17.2 Bulk Catalysts

A large number of simple oxides, mixed metal oxides, unsupported metals etc. are used as heterogeneous catalysts in industries [24, 25] for the production of chemicals (organic and inorganic), crude oil refining and petrochemistry, environmental protection, energy conversion process (Table 17.1). Simply, oxides can be classified into stoichiometric and non-stoichiometric based on their thermal stability. Oxides such as Al_2O_3, SiO_2, ZrO_2 etc. are thermally stable, do not deviate from their stochiometery on heating are called stoichiometric. While non-stoichiometric oxides tend to loose or gain oxygen on heating, for example, ZnO, Fe_2O_3 etc. Non-stochiometric oxides can be either simple oxides or multi-metal also referred as mixed metal oxides. The stability of simple oxides against melting (or sublimation) or dissociation is of great importance in catalysis. Many transition metal oxides have rather low melting points. These oxides can be stabilized thermally by the formation of multicomponent mixed oxides systems. V_2O_5, contact process catalyst is known for its high catalytic activity but its use is limited by its low melting at 695 °C. V_2O_5 in combination with number of rare earth and other metal ions forms homophasic new chemical identities, vanadates, such as lanthanum vanadate, $LaVO_4$, thorium metavanadate, $Th(VO_3)_4$, thorium pyrovanadate, ThV_2O_7 and thorium orthovanadate, $Th_3(VO_3)_4$. These compounds are thermally stable with very high melting point (minimum 1000 °C) and have shown potential for catalyzing CO oxidation reaction [26–30].

Table 17.1 List of conventional synthesis methods used to prepare selected bulk and supported catalysts employed in various industrial processes [12, 13, 24, 25, 36]

S. No	Catalyst	Processes	Synthesis method	Operating conditions
Metal oxides				
1	Fe_3O_4 (K_2O, Al_2O_3)	Ammonia synthesis	Fusion	450–500 °C, 250–400 bar
2	Pt/Rh nets	Oxidation of NH_3 to NO (nitric acid)	Fusion	Around 900 °C
3	Bauxite, Al_2O_3	Claus process (sulfur) $2H_2S + SO_2 \rightarrow 3S + 2H_2O$	Sol–gel	300–350 °C
4	$CuCr_2O_4$	Esters to alcohols	Precipitation	250–300 °C, 250–500 bar
5	Fe_3O_4 (Cr, K oxide)	Ethylbenzene to styrene	Fusion	500–600 °C, 1.4 bar
6	Pt/Rh nets	Methane to HCN	Fusion	800–1400 °C, 1 bar
Mixed metal oxides				
7	ZnO–Cr_2O_3	Methanol synthesis	Co-precipitation	250–400 °C, 200–300 bar
8	CuO–ZnO–Cr_2O_3	$CO + 2H_2 \rightarrow CH_3OH$	Co-precipitation	230–280 °C, 60 bar
9	Fe/Cr oxides	CO conversion: $CO + H_2O \rightleftharpoons H_2 + CO_2$	Co-precipitation	350–450 °C
10	Cu/Zn oxides	CO conversion: $CO + H_2O \rightleftharpoons H_2 + CO_2$	Co-precipitation	140–260 °C
11	Bi/Mo oxides	Propene to acrolein	Co-precipitation	350–450 °C, 1.5 bar
12	Al_2O_3/SiO_2; zeolites	Cracking of kerosene	Hydrothermal	500–550 °C, 1–20 bar
13	V_2O_5–$K_2S_2O_7$	SO_2 oxidation	Fusion	400–500 °C
Supported catalysts				
14	V_2O_5/support	Oxidation of SO_2 to SO_3	Impregnation	400–500 °C
15	V_2O_5/support	Benzene or butene to maleic anhydride	Impregnation	400–450 °C, 1–2 bar
16	MoO_3/Al_2O_3	Demethylation of toluene to benzene	Impregnation	500–600 °C, 20–40 bar
17	Ni/Al_2O_3	Steam reforming of methane $H_2O + CH_4 \rightarrow 3H_2 + CO$	Precipitation	750–950 °C, 30–35 bar

(continued)

Table 17.1 (continued)

S. No	Catalyst	Processes	Synthesis method	Operating conditions
18	Ni/Al_2O_3	Methanization $CO + 3H_2 \rightarrow CH_4 + H_2O$	Precipitation	500–700 °C, 20–40 bar
19	Co or Ni on Al_2O_3	Nitriles to amines	Impregnation	100–200 °C, 200–400 bar
20	Cr_2O_3/SiO_2	Polymerization of ethene to polyethylene	Impregnation	50–150 °C, 20–80 bar
21	H_3PO_4/SiO_2	*Alkylation*: Ethylbenzene from benzene and ethylene	Impregnation	300 °C, 40–60 bar
22	H_3PO_4/kieselguhr	Oligomerization of olefins to prepare gasoline	Impregnation	200–240 °C, 20–60 bar
23	$V_2O_5–K_2S_2O_7/SiO_2$	*o*-Xylene or naphthalene to phthalic anhydride formation	Impregnation	400–450 °C, 1.2 bar
24	V_2O_5/TiO_2	*o*-Xylene or naphthalene to phthalic anhydride formation	Impregnation	400–450 °C, 1.2 bar
25	H_3PO_4/activated carbon	Oligomerization of olefins to form gasoline	Impregnation	200–240 °C, 20–60 bar

Perovskites, scheelites, pyrochlores, spinels etc. are of considerable interest not only form stable oxyions but also perform better than constituent oxides. The crystal structure, lattice distortion, defects, multi-valence, oxygen non-stochiometry help in enhancing the oxygen ion mobility makes it more labile at lower temperatures. Electronic transfers may lead to valence exchange between two metal ions, for example, iron cobaltite may contain Co^{2+} and Fe^{3+}, instead of Co^{3+} and Fe^{2+}. This leads to variation in the oxygen content over a small range, close to stoichiometry corresponding to the given spinel phase. Mixed oxides either as solid solution or as poly phases have been used extensively as complete oxidation and partial oxidation catalysts [20, 31, 32]. For example, molybdates are used as catalysts for a number of selective oxidation reactions. Bismuth molybdate catalyzes the oxidation of olefins whereas iron molybdate catalyzes the oxidation of alcohol to aldehydes [33]. In complex mixed oxides such as Fe–Mo–O system, bulk oxygen is very mobile as compared with constituent oxides. The mobility of bulk oxygen depends upon the ease of desorption of surface oxygen, and gets enhanced, if metal—surface oxygen bond strength (q_s) is low. When constituent components of a complex oxide catalyst give a new chemical compound, the later has a value of q_s, which is not the sum of the values of q_s for the components. Thus complex mixed oxides generally have a lower q_s and higher mobility of oxygen, as compared with constituent metal oxides [11, 34]. For instance, when potassium sulfate is added to V_2O_5, it results in loosening of the

V–O bond. Similarly, high mobility of the bulk oxygen in V–Mo–O system [35] is attributed to a lowering in value of q_s for V–Mo–O mixed oxide as compared with that of corresponding constituent oxides. Thus, by virtue of improved thermal stability and lattice mobility, mixed metal oxides are preferred and more recommended over simple oxides as catalysts.

17.2.1 Preparation of Bulk Catalysts

For industrial applications, tons of catalysts per day are required to be produced. From Table 17.1, bulk oxides such as Fe/Cr oxide are used for CO oxidation, ZnO–Cr_2O_3 and Cu–Cr–Zn–O for methanol synthesis, spinel $CuCr_2O_4$ for ester to alcohol conversion, Bi–Mo–O, MoO_3, V_2O_5, Fe_3O_4 and Cr_2O_3 are also used as active component for many catalytic reactions, Al_2O_3, TiO_2, SiO_2 and are used as supports [12, 13, 24, 25, 36]. These oxides are synthesized in bulk as these are inexpensive. Precipitation is one of the most common methods used to prepare the oxides and also pure support materials. Stoichiometric amounts of one or more metal salts solutions are mixed and the co-precipitated under specific conditions to yield hydroxides or carbonates, which are further, dried, shaped, calcined in air to yield oxide powders. The precipitation conditions can affect the crystallinity, particle size, porosity and composition. Iron-chromium oxide used as catalyst for high-temperature CO oxidation is produced by co-precipitation, Fe_3O_4 required for styrene production, and CuO–ZnO–Al_2O_3 from their respective nitrates is prepared by co-precipitation for methanol synthesis. However, each compound precipitates at different rates that cause microscopic inhomogeneity.

Unsupported metals were also used as bulk catalysts such as Pt–Rh gauge catalyzed oxidation of ammonia. Pt–Rh gauge was prepared by fusion of pre-molten precursors. The famous Fe_2O_3 catalyst of Haber's process for ammonia synthesis (Table 17.1) was also prepared by fusion methodology in which iron ore was melted in an electric furnace at 1600 °C in the presence of process promoters such as alumina and silica. While other promoters viz; CaO and KNO_3 or K_2CO_3 are added later during oxidation step at 1600–2000 °C. The melt is then cooled, crushed and sieved into several size fractions. Fine particles are discarded and again fed to melt for recycling. Molten V_2O_5 is fused with $K_2S_2O_7$ to yield V_2O_5–$K_2S_2O_7$ catalyst for SO_2 oxidation reaction. Fusion catalysts generally have low surface area in range of 1–2 m^2/g. Among bulk non-supported metal catalysts, Raney nickel is the most established for hydrogenation and dehydrogenation reactions. It is also referred as skeletal metal ore sponge catalysts. These are having metal crystallites anchored on skeletal metal sponge. The metal sponges are prepared by leaching the alloys using caustic soda. In 1921, Murray Raney performed independent research, prepared an alloy of Ni/Si in 1:1 ratio and treated it with sodium hydroxide, which was found to be five times more active than the best catalyst used in the hydrogenation of cottonseed oil. Subsequently, Raney produced a 1:1 Ni/Al alloy following a procedure similar to the one used for the nickel–silicon catalyst, leached it by concentrated NaOH and

most of the aluminum dissolved, leading to a porous sponge-like metal with very high surface area (30–120 m^2/g) and catalytic activity. 2–15 nm sized microcrystallites agglomerated to form macropores of sponges. In the porous network of the spongy metal, black Ni crystallites are supported on Ni–Al cores. The choice of Ni–Al ratio was accidental without much scientific basis. However, this is the preferred alloy composition for the production of Raney nickel catalysts currently in use. Raney catalysts are often referred as skeletal catalysts or active base metal catalysts too. There are many other Raney catalysts used commercially, such as Raney Cu–Zn catalysts for methanol synthesis and water–gas shift reactions, Raney Cu–Zn–Cd catalysts for selective hydrogenation of α, β-unsaturated aldehydes and ketones and Raney Cu for methyl formate production. Due to spongy nature, these are highly reactive and catch fire in air (pyrophoric), thus stored as wet catalysts.

Melting procedures show limitations for the preparation of high-temperature refractory materials. Wet chemistry, however, provided a new approach to synthesize homogeneous ceramic materials called sol–gel method. It is a versatile method widely used in industry for the preparation of amorphous high surface area catalysts and carriers such as SiO_2, TiO_2, etc. also offer nanocrystalline homophasic refractory materials such as spinel, $MgAl_2O_4$. There are several parameters in each step, which influences and controls the morphology of the final product. It involves hydrolysis of the metal precursor in the acidic or basic mediums, followed by polycondensation of the hydrolyzed products. In this way, hydrogel—a metastable open structure polymer—is formed in which metal nanoparticles are retained. The gel is aged, dried and calcined for the final product. Depending on the drying and preparation procedure, pore size and porosity of the products can be tailored. Supercritical drying results in mesoporous aerogel (pore size 2–10 nm) with large surface area, while slow drying at ambient conditions results in microporous xerogel with a narrow pore size distribution, which is comparable to that of zeolites. During heat treatment, different product forms can be acquired such as powder, monoliths, thin films or membranes. For practical application, the catalyst powder is cast into different shapes by kneading or by extrusion or by pressing into tablets with help of additives. An overview of different shapes in which commercial catalysts are functional [37] is given in Fig. 17.2.

Flame hydrolysis method is used for the preparation of dense non-porous supports with high thermal stability and surface area such as fumed silica, alumina, TiO_2. The precursors, hydrogen and air are fed into flame, where the precursor is hydrolyzed to hydroxide formation. P25 TiO_2 is synthesized using aerosol flame pyrolysis process having a particle size of 21 nm and 50 m^2/g surface area [38]. The hydroxides are later recovered, calcined to oxides. Alumino silicates are prepared by hydrothermal route.

Fig. 17.2 Various shapes of catalysts for practical applications. **a** Granules **b** Extrudates **c** Pellets **d** Cylinders **e** Spheres **f** Monolith **g** Rings. *Reproduced with permission from Ref.* [37] *Copyright 2018 MDPI*

17.2.2 Preparation of Mixed Metal Oxides (MMO) Nanoparticles

With increasing demand for catalysts and catalytic reactions, continuous advancement in synthetic procedures was made. Researchers have investigated and developed both physical and chemical methods for the preparation of MMO nanoparticles [39–49]. Figure 17.3 presents a flowchart summarizing all possible methods for the preparation of MMO nanoparticles. The details of most of the chemical methods adopted for the preparation of nanomaterials are dealt with other chapters of the present book.

Physical methods for the preparation of MMO mainly are based on aerosols that include gas condensation techniques, [39–41] spray pyrolysis, [42, 43] thermochemical decomposition of metal–organic precursors in flame reactors [44, 45]. Among physical methods, perhaps flame spray pyrolysis (FSP) was found to be most useful and extensively used for the preparation of MMO nanoparticles. This method was developed and patented by University of Michigan [50]. Tal materials Inc. adopted flame spray pyrolysis method for commercial production of inexpensive MMO nanopowders. FSP is collective term for preparation techniques such as aerosol thermolysis, evaporative decomposition of solutions, plasma vaporization of solutions, aerosol decomposition, flame pyrolysis, etc. Here, the appropriate salts or precursors in form of sol, solution or suspension can be used, whichever is

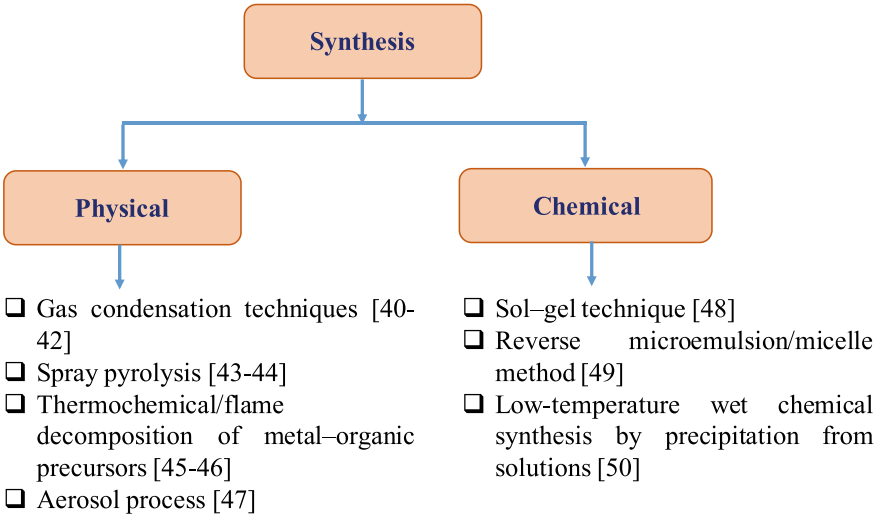

Fig. 17.3 Flowchart showing the methods for the preparation of MMO nanoparticles

conveniently available. These precursors can be automized by various methods such as including pressure, two-fluid, electrostatic and ultrasonic atomizers resulting in 2–15 μm droplets depending on atomization rate and droplet velocities. Pramanik et al. [51] reported a new polymer matrix-based precursor solution for the synthesis of a variety of nanosized MMO such as Spinels $MgAl_2O_4$, $CuFe_2O_4$, $NiFe_2O_4$, $CoFe_2O_4$, $ZnFe_2O_4$, also orthoferrites such as $LaFeO_3$, $NdFeO_3$, $GdFeO_3$ powders using thermolysis/flame pyrolysis.

Other physical methods such a mechanical milling and laser ablation follow top-down approaches are single step, easy to execute and does not require toxic/hazardous chemicals or solvents. The fundamental principle is energy imparted to material through either collisions among reactants and metal balls or laser energy to break the larger particles into smaller ones. The mechanical milling or say ball milling methods cannot be employed for reduction in particle size infinitely. Shin et al. [52] reported an investigation on wet ball milling of Al_2O_3 powders using zirconia balls with varying speed and ball sizes. They revealed that for a given speed, there is an optimum size of balls, which can yield minimum particle size. The optimum ball diameter deceases as the rotation speed of ball milling increases. This is obvious also as the speed increases, the kinetic energy increases which shift the ball size toward smaller size. Also for a given rotation speed and optimum ball diameter, with an increase in amount of sample from 1 to 35 g, the milling efficiency decreases. Thus, mechanical procedure by ball milling will not reduce the particle size infinitely; in fact, it is limited by sample amount, particle size, rotation speed and ball diameter.

17.3 Dispersed Catalysts

Table 17.1 shows another category of catalysts called dispersed or supported catalysts used in industry, where active component is dispersed over support such as supported V_2O_5 for SO_2 oxidation used in contact process, MoO_3 supported on Al_2O_3 for demethylation, hydrocracking processes, Ni/Al_2O_3 for steam reforming and so on so forth. Here, the active component is carried by most often less reactive oxides such as stoichiometric oxides, Al_2O_3, SiO_2 etc. In a heterogeneous catalytic reaction, adsorption/desorption of reactants/intermediates/product species takes place on surface of the catalyst. Thus, efficiency of a process is largely determined by the surface properties such as surface area, crystallite size, porosity of a catalyst. To increase the surface area, crystallite size has to be sacrificed. A correlation between the specific surface area and crystallite size of nickel metal shows that for preparation of reasonably high surface area Ni catalyst, particle size has to be decreased below 10 nm [53]. To carry such small nanoparticles, a support is required.

Porous supports are preferred in order to allow high loading of highly dispersed metal particles. Supported catalysts fulfill the following two requirements: i. Reduces cost of catalyst, the amount of active component dispersed is much less as compared with bulk catalysts, more economical in case of precious metal (Pt, Au, Ag, Rh, Ru) supported catalysts, ii. Improves the quality of catalyst. Supported catalysts also propose to immobilize the organometallic complex or enzyme on an inert support thus, allowing easy recovery of active phase after reaction and solves one of the major issues of homogeneous catalysis. The invention of supported catalysts, advancement in field of heterogeneous catalysis has rendered affordable and superior noble metal catalysts to industry for various applications. Actual credit goes to researchers who have invested serious efforts and interest in preparation procedures of catalyst and have investigated the influence of preparation parameters in detail on catalyst properties and eventually activity [54, 55].

Impregnation and precipitation are two very successful methodologies to disperse active component on a support. However, both are extremely different in their approach. One is impregnation in which active component is dispersed by ion exchange on an already selected optimal design support with well-defined surface area and porosity. After interaction with metal precursor, the samples are dried, calcined and undergo reduction step. Other is precipitation route in which support particles allows nucleation or crystallization of active component into fine particles from its precursor. Precipitation can be carried out by co-precipitation, homogeneous deposition precipitation and precipitation at constant pH techniques [53]. The supported catalysts can take a powder or granular form or the form of a pre-shaped support (Fig. 17.2).

Impregnation route is more advantageous as compared with precipitation as this route provides choice for support with desired pore structure, surface area, shape, size and mechanical strength. Thus, impregnation route offers tailor-made catalysts with respect to support such that it can manipulate mass transport properties. For example, in automobile industry, the catalytic converters (to catalytically convert

harmful gases of automobile exhaust into harmless products) utilize monoliths as carriers for the active noble metals using impregnation route. These monolith supports are specifically designed to overcome mass transfer and mechanical stability issues and, therefore, have unique pore as well as geometrical structure. The development of impregnation route facilitated the anchoring of active components on such supports. Impregnation method as the name suggests, precursor of the active component containing thermally unstable anions (nitrates, acetates, hydroxides, carbonates, chlorides) or cations (ammonium) is allowed to interact with the pre-shaped or powder support, either by exchanging with surface OH or gets adsorbed over it. For reaction, the concentration of hydroxyl groups on surface of support matters, which can be controlled by pretreating the support under different conditions. While in case of interaction through adsorption, surface charge is very crucial. The pH value at which surface is electrically neutral is called point of zero charge (PZC). For pH more than PZC, the surface is negatively charged, and for pH values <PZC, the surface acquires positive charge. Depending on the cation or anion of the precursor to be adsorbed, the pH is maintained for maximum adsorption. PZC for alumina and silica is 8–9 and 3, respectively. For the synthesis of dispersed alumina or silica catalysts, one has to select appropriate pH for modifying the surface charge of carrier depending on the cationic or anionic precursors. It is important to mention that the exact PZC values of carrier depend on its chemical nature also on its source and method of preparation. Also, it may happen that the carrier may not be stable and dissolve at some inappropriate pH value say >12 for alumina. If the adsorption of $[Pt(NH_3)_4]^{2+}$ on silica gel and alumina supports with increasing pH is compared, then it was observed clearly that silica gel adsorbs Pt ions more than alumina. Since, PZC of silica is 3, so as soon as pH 3 is crossed, its surface charge becomes negative and Pt adsorption takes place upto pH of 9. In case of alumina PZC is much higher (8–9) than silica and could not adsorb Pt species unless pH was raised more than 8. On similar lines, it is predictable that adsorption of anionic Pt species such as $[Pt(Cl)_6]^{2-}$ would follow reverse, will be more for alumina than silica. Thus, to prepare Pt/alumina catalysts, by ion exchange, $[Pt(Cl)_6]^{2-}$ and for Pt/silica-supported catalysts, $[Pt(NH_3)_4]^{2+}$ precursor should be preferred.

Another main highlight of impregnated catalysts is distribution profiles of active phase on support. The distribution of active phase may or may not be uniform and it may acquire different forms. Figure 17.4 shows different distribution profiles possible by impregnation. These are termed as uniform, egg-shell, egg-white and egg-yolk. Each profile is beneficial for specific reactions. By modifying the parameters of drying step or pretreatment step of support during synthesis, the distribution profile of supported impregnated catalysts can be tailored [56–58]. For reactions, where catalyst is susceptible to pore-mouth poisoning, it is advisable to anchor the active sites in the interior of catalysts as in egg-yolk profile. Similarly, to prevent leaching of precious metals during reaction, it can be placed in the interior of catalysts.

Under normal conditions, adsorption of H_2PtCl_6 over alumina will yield egg shell type of profile, however, in the presence of some poison such as citric acid, it will be adsorbed preferably on the outer surface, and H_2PtCl_6 will then be adsorbed on inside ring leading to egg-yolk profile (Fig. 17.4d). Drying after adsorption is

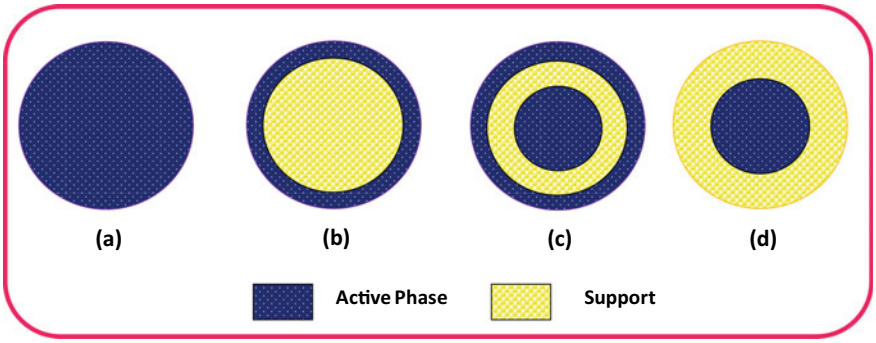

Fig. 17.4 Shapes of distribution profiles of active phase over support obtained in impregnated catalysts

very critical in determining the homogeneous dispersion of active phase. In drying step, the solution inside pores will be dried and precipitation of active phase will take place. Fast drying may lead to fast evaporation of the precursor, with inhomogeneous distribution. Slow drying with well-crystallizing precursors will result in egg-shell profile. The use of more viscous, less crystallizing precursor and slow drying leads to homogeneous dispersion [56]. In case of structured monoliths, microwave or freeze-drying is applied for homogeneous distribution [57, 58]. However, conventional stationary air drying resulted in increased concentration of Ni ions at the entry and exit of monoliths, which was not suitable for the application.

Impregnation technique is well established and recommended for lower metal loadings with high dispersion of small crystallites. However, for higher loadings and high dispersions, the procedure has to be repeated many times till required loading is achieved. Precipitation method has this advantage; in this method, the metal precursor solution is supersaturated to induce nucleation and crystal growth of metal particles. If both support and metal precursors are taken together and allowed to co-precipitate, it is referred as co-precipitation. In case metal precursor solution is allowed to supersaturate on existing support, it is called homogeneous deposition precipitation (HDP) [53, 59]. Both co-precipitation and HDP techniques offer advantage of higher loadings with high dispersion. The HDP can be carried out either under influence of increasing pH or constant pH conditions [59–61]. The details of these methods are given in several review articles as well as books [62–64].

Besides these methods, there are more recent and advanced methodologies to prepare supported catalysts such as melt filtration, colloidal route and vapor deposition [65–67]. Mehrabadi et al. [67] have provided a thorough survey of different methods for preparation of most popular and extensively applied Pt catalysts on four different supports, TiO_2, Al_2O_3, SiO_2 and carbon. A histogram presentation was prepared after survey of around 1500 studies published during the period from 2015 to 2017. Since particle size achieved of the metal particles is one of the criteria predicting the efficacy of the catalyst, so particle size obtained from different preparation routes of these four different catalysts from 1500 studies is presented. It

compares the different emerging routes with traditional routes. Strong electrostatic attractions (SEA) and charge enhanced dry impregnation are newer approaches to modify conventional impregnation route [67].

17.4 Single Atom Catalysts (SAC)

Supported metal catalysts are widely used in industry for various heterogeneous catalytic processes. The particle size of metal ions is a key aspect that influences the catalyticperformance. Figure 17.5 shows the effect of particle size on conversion and surface energy of supported catalysts.

Downsizing the metal ions increases the number of active sites on surface and offers more active sites for a catalytic reaction. Decrease in particle size increases the specific activity of catalyst by providing low coordination unsaturated environment, quantum size effects and associative metal support interactions [68–70]. Progress through numerous modifications in synthetic procedures and optimization of synthetic parameters to the finest resolution created supported catalysts with nanosize as well as sub-nanosized metal particles/clusters. Despite nanosized, the supported catalysts still suffer with existence of range of nanosized metals dispersed, instead of uniform sized particles. This brings heterogeneity on the catalyst surface as

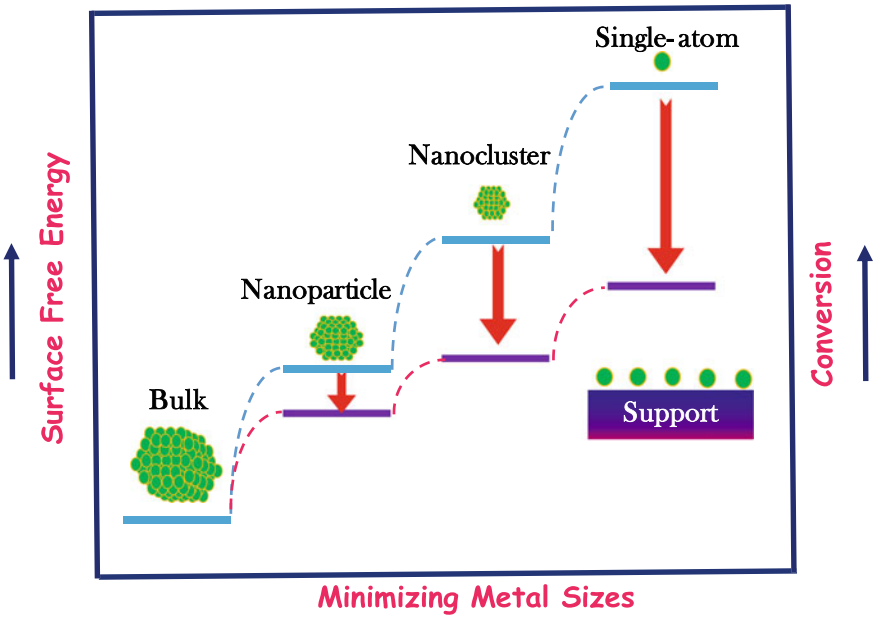

Fig. 17.5 A schematic depicting the effect of particle size of active phase on catalytic conversion and surface energy

active sites contain multiple active centers that may set aside undesired side reactions, and thus deteriorates the catalyst performance.

In view of above considerations, the ideal scenario would be uniform distribution of single atoms of metal on the support. This is the ultimate goal of fine dispersion for supported catalysts, also referred as single atom catalysts (SACs) [71–74]. SACs have huge potential due to their superior catalytic properties and, therefore, are new frontier area in catalysis research. The advantages of single atom catalysts are; drastic improvement in catalytic performance, facilitates understanding of catalytic mechanisms, and have huge potential in bringing down the cost of commercial noble metal catalysts in industry. The first and foremost challenge in the development of SAC is their synthesis, and the second is development of tools to characterize them. Recent studies [74–77] have shown technological advancements toward the synthesis of SACs with indubitable characterization. The very first synthesis of single atom catalysts was reported by Qiao et al. [73]. Single Pt atoms were successfully anchored on FeO_x support using co-precipitation method under carefully optimized pH and temperature conditions also reported exceptionally high catalytic activity and stability for CO oxidation reaction. It was simulated using density functional theory and revealed that partially vacant 5d orbital of Pt plays role in decreasing the activation barrier for CO oxidation reaction. The morphology and distribution of single atoms/metal clusters are characterized using subangstrom resolution, aberration-corrected scanning transmission electron microscopy (STEM) in the catalysts. High-angle annular dark-field (HAADF) helps in identifying the heavy atoms at atomic resolution.

Chief obstacle in preparation of SAC is the high surface energy associated with single atom, which causes migration and agglomeration of the atoms. Therefore, role of support is very important to achieve dispersion and stabilization of single atom. Support that has defect sites or other specified sites where metal particles can be anchored are preferred. Some of the strategies for the synthesis of SACs are summarized below.

17.4.1 Atomic Layer Deposition (ALD) Method

Atomic layer deposition (ALD) method is a sophisticated technique used for the deposition of a catalyst in the nanometer and subnanometer range in a controlled manner by changing the number of deposition cycles [78]. However, long processing time and relatively high cost are the demerits of this method. ALD has been used for the deposition of the SACs. This method offers the control over the size, morphology, density and the amount of deposited metal. ALD is divided into four steps: (i) exposure of the metal precursors, (ii) precursor or by-product removal from the chamber by evacuation or purging, (iii) exposure of reactant species and (iv) removal of the reactants and by-product from chamber by evacuation or purging [79]. Sun and coworkers [80] implemented the ALD method for the deposition of the Pt single metal atom on the surface of the graphene used as a support. Deposition was carried out by using

(methylcyclopentadienyl)-trimethylplatinum ($MeCpPtMe_3$) and oxygen as precursors, and nitrogen as purge gas. Figure 17.6 shows the schematic representation of the reactions expressed by Eqs. 17.1 and 17.2:

Equation 17.1:

$$\text{Pt-O*} + (\text{MeCp})\text{Pt}(\text{CH}_3)_3 \Longrightarrow (\text{CH}_3)_2\text{Pt}(\text{MeCp})^* + \text{CO}_2\uparrow + \text{H}_2\text{O}\uparrow + \text{fragments}$$

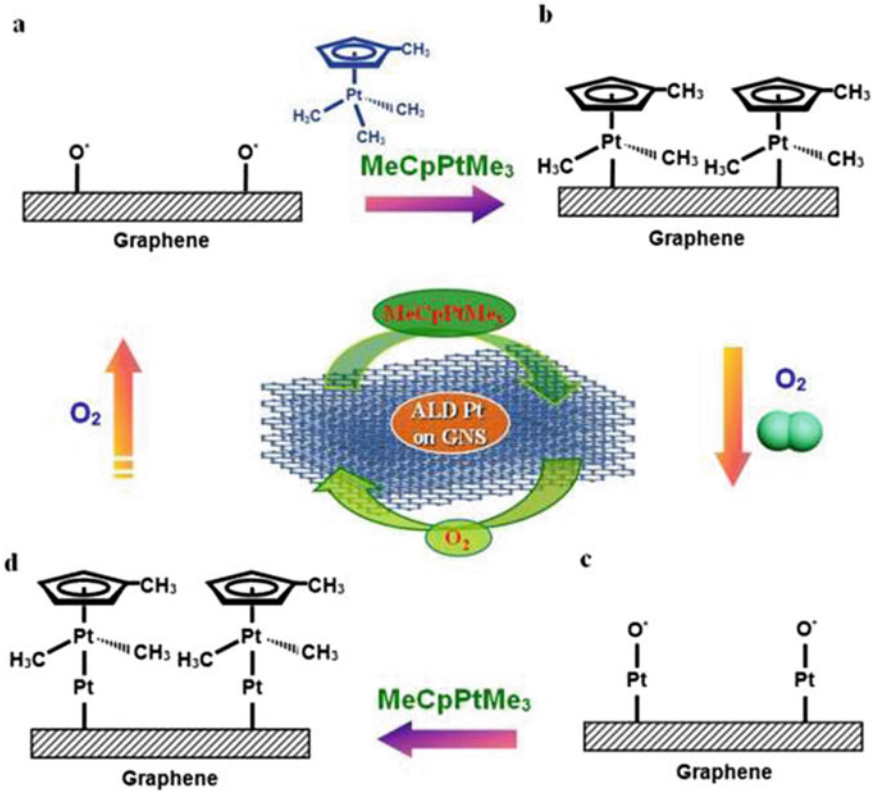

Fig. 17.6 Schematic representation of the ALD process for Pt deposition on graphene nanosheets (GNS), **a** existence of the monolayer of functional groups possessing oxygen ions on the surface of the graphene nanosheets, **b** during exposure of the $MeCpPtMe_3$, some of the ligands reacts with the adsorbed oxygen on the surface leading to the generation of Pt containing monolayer, **c** exposure of oxygen leading to the formation of the adsorbed oxygen layer on the surface. Process **b** and **c** constitute a complete ALD cycle. By varying the ALD cycles, **d** a Pt deposition in a controlled way can be achieved. (* and Pt-O* represent an active surface species and oxygen molecules or dissociated oxygen ions adsorbed on the Pt surface). *Reproduced with permission from Ref.* [80], *with the permission from Springer Nature*

Equation 17.2:

$$(CH_3)_2Pt(MeCp)^* + O_2 \Longrightarrow Pt\text{-}O^* + CO_2\uparrow + H_2O\uparrow + \text{fragments}$$

where, * and Pt-O* correspond to the active surface species, and oxygen molecules adsorbed on the Pt surface, respectively. The ALD cycle composed of two processes. First is exposure of the $MeCpPtMe_3$, where precursor ligands reacted with the adsorbed oxygen to form CO_2, H_2O and hydrocarbon fragments as shown in Fig. 17.6 and Eq. 17.1. The limited oxygen supply prevented the oxidation of all ligands and helps to form Pt monolayer. In the second process, a new layer of the adsorbed oxygen formed on the surface of Pt on the exposure of the oxygen. The amount of Pt was accurately controlled by the number of ALD cycles. The catalytic activity for methanol oxidation reaction using Pt SACs was found to be 10 times higher than that of commercial Pt/C catalyst.

17.4.2 Wet-Chemical Route

The surface defects present on the surface of the support offer the site for the attachment of the single atom. The metal–support interaction prevents the aggregation of the single atoms. Co-precipitation method is the most commonly employed method. The temperature and pH are the important parameters during synthesis of SACs by this method. Qiao et al. [73] synthesized the atomically dispersed Pt over FeOx by co-precipitation method. Here, simple strategy of dispersion of lower metal loadings leads to better dispersion on high surface area nanocrystalline support (290 m^2g^{-1}) was adopted to successfully anchor the Pt ions on to the defects sites of the FeO_x support. 0.17 wt% of Pt with Pt/Fe ratio of 1/1430 was dispersed to prepare Pt_1/FeO_x SAC using co-precipitation method. SACs were compared with conventional catalysts with similar loading (Pt loading of 2.5 wt% with a Pt/Fe atomic ratio of 1/95) to establish and affirm their superiority catalytic activity. These methods are widely used for the synthesis of the SACs as it is easy to operate and no requirement of any special equipment. Moses-De Busk et al. [81] have dispersed single atom of Pt over the support by wet impregnation method. In this method, Θ-Al_2O_3 dispersed in an aqueous solution of the chloroplatinic acid and then the water was evaporated to get a powder, which was calcined at 450 °C. With the help of computational studies, it was deciphered that Pt was situated between two oxygen atoms of support. Characterization using STEM, IR and EXAFS data show that the samples are supported single Pt atoms. Based on their investigations, they concluded that the conventional Langmuir–Hinshelwood mechanism is not applicable for CO oxidation on single atom and proposed a variation of L–H mechanism for CO oxidation reaction on SACs.

17.4.3 Photodeposition Method

This method involves the utilization of light energy for the deposition of the metal atom. This method is better than the conventional calcination methods as it prevents the agglomeration of atoms to give cost-effective nanoparticles. Liu et al. [82] dispersed Pd atomically over ultrathin TiO_2 nanosheets up to 1.5 wt% (referred as Pd_1/TiO_2) under UV light photodeposition. Ultrathin nanosheets of TiO_2 were synthesized using $TiCl_4$ and ethylene glycol (EG) as the precursors. It was observed that the TiO_2 nanosheets were coated with ethylene glycolate. The ethylene glycol radicals were generated during UV irradiation that helped in removal of the Cl^- ions from the Pd precursor. To load Pd atom, H_2PdCl_4 dispersed in water and then irradiated under UV source. As a result of this Pd atom was stabilized by forming Pd–O bonds over TiO_2 nanosheets. Pd_1/TiO_2 exhibited high catalytic activity and stability for styrene hydrogenation reaction as compared the commercial Pd/C catalyst.

17.4.4 Atom Trapping Strategy

Pt nanoparticles agglomerate into large particles undergoing aging treatment at high temperature in air. This process is called as Ostwald ripening. Carrillo et al. [83] found that the PdO could trap mobile PtO_2 to form Pt–Pd alloy, thus, prohibiting the sintering of the Pt nanoparticles. By taking inspiration from this work, Jones et al. [84] synthesized the atomically dispersed Pt over CeO_2. For this, 1 wt% Pt/La-Al_2O_3 and CeO_2 was physically mixed in 2:1 weight ratio and then subjected to the aging treatment at 800°C in air flow. During aging treatment, the vapor of mobile PtO_2 was emitted from alumina and got deposited over surface of ceria to form the atomically dispersed Pt/CeO_2 catalysts.

17.5 Thermal Reactions

Mixed metal oxides are suitable catalyst systems for oxidation or reduction processes. In our laboratory, we continually prepared and improvised oxide-based catalysts for CO oxidation, $CO + N_2O$ reactions and SO_2 oxidation reactions. Here, in this section, highlights of our work are presented to emphasize the role of synthesis in improvising the catalyst performance and stability.

17.5.1 CO Oxidation

First example is about strategy to improve the thermal stability of active bulk catalyst, V_2O_5. It is known to be a good catalyst [85] for many inorganic and organic reactions but it melts at 658 °C whereas lower valent oxides like VO_2 and V_2O_3 melt at 1640 °C and 1970 °C, respectively, but they were catalytically inactive. Therefore, a way of stabilizing such low melting oxide can be in the form of oxy anions. As vanadium exhibits multiple oxidation states right from 2 to 5, its mixed oxides can exist as varied anionic species like $VO^-{}_3$ (metavanadate with perovskite structure), $V_2O_7{}^{4-}$ (pyrovanadate with pyrochlore structure) and $VO_4{}^{3-}$ (orthovanadate with scheelite structure). ThO_2 is thermally stable. Thus, combination of catalytically active, V_2O_5 and thermally stable, ThO_2 in different stoichiometric ratios resulted in ternary compounds, viz; thorium metavanadate, $Th(VO_3)_4$ and thorium pyrovanadate, ThV_2O_7 and thorium orthovanadate, $Th_3(VO_3)_4$ where vanadium is in +5 and Th exists in +4 valence state. Both $Th(VO_3)_4$ and ThV_2O_7 are stable up to 1000 °C and have stable structure. The structural aspects of these three oxides systems were available in literature but as far as catalytic properties are concerned almost nil or scanty information was available. In our laboratory, we, thus, entered into a totally unexplored area of research on thorium vanadates, synthesized, characterized and evaluated temperature-dependent catalytic activities of these oxides for CO oxidation. These multi-metal oxides were found to exhibit the improved thermal stability as well as catalytic activity [26–30]. Several nominal compositions of La/Mn substituted non-stoichiometric $Th_3(VO_3)_4$ and pyrovanadates were found to be active in temperature window of 300–400 °C. Since, catalytic activity in case of oxides is determined by the crystal structure of the phase obtained and also mixed phase composition, our studies on La and Mn substituted Thorium vanadates could establish the structure–activity correlations. The thorium vanadates in our studies were prepared by ceramic route, which has drawback of insufficient homogeneous mixing. For enhancing the catalytic activity, synthetic procedures were modified allowing mixing of metal ions at atomic level by mixing nitrate solutions of metal ions in appropriate stoichiometry. Solution route fabricated pure phase mixed oxides, prevented the segregation of secondary phases due to homogeneous mixing and reactions. A new series of perovskites with Fe substitution at B site, $La_{0.8}Sr_{0.2}Mn_{1-x}Fe_xO_{3-\delta}$ (LSMF) samples with x values from 0 to 1.0 were also synthesized by solution route using nitrate precursors and compared with their solid-state analogues, and finally calcining at 900 °C and 1400 °C, respectively [86, 87]. Since the metal ions come in close contact in solution route, their diffusivity during lattice reorganization is enhanced, leading to single phase formation at lower calcination temperatures. Thus, samples prepared by nitrate route yield the pure phase orthorhombic Fe substituted, LSMF samples at 900 °C while solid state route required 1400 °C. As expected, the solution route LSMF (x = 0.2–0.4) samples produced 15–16 nm crystallites as compared with 49–50 nm through solid state route [86]. LSMF2 sample exhibited 100% conversion at 400 °C as compared with ~60% conversion when prepared by ceramic route. This was also augmented by increased reducibility of the sample at

lower temperature shown in their temperature programmed reduction (TPR) profiles. The results of comparative study of same compositions prepared by different routes, revealed that the particle morphology is a crucial factor in determining the catalytic performance. The substitution-induced micro-structural defects and the synergistic effects due to presence of multivalent Fe and Mn ions at b-site, play an important role in determining and uplifting the catalytic behavior of the substituted perovskites.

17.5.2 N_2O Reduction

Nitrous oxide (N_2O) poses threat to environment as it contributes to global warming causing stratospheric ozone destruction**.** N_2O emissions can be converted to harmless gases catalytically by supported metals, zeolites, pure or mixed oxides [88]. Here, we present the sequence of adaptations in our approach to enhance the catalytic activity for CO + N_2O reaction. To begin with bulk layered perovskite, lanthanum titanate, $La_2Ti_2O_7$ with Fe substitution at B-site were prepared by citrate gel combustion (GC) route using metal nitrate precursors and compared with conventional solid-state (SS) synthesis [89, 90]. Among complete series of $La_2Ti_{2(1-x)}Fe_{2x}O_{7-\delta}$, nominal composition of $La_2Ti_{1.2}Fe_{0.8}O_{7-\delta}$ (LF4) was found to be most active for CO + N_2O reaction, where activity was credited to substitution induced non-stoichiometry defects and short-range crystallographic shears, which increased the lability of lattice oxygen at lower temperatures, thus improving the catalyst activity [89]. Gel combustion synthesis lowered the reaction temperature considerably . 100% conversion was achieved at 325 °C with onset at 200 °C while with solid-state samples, conversion initiated at 275 °C and a temperature of 550 °C was required for 100% conversion using 40–60% Fe substituted samples. Thus, lowering of particle size and increased surface area by GC route improved the reaction kinetics. The role of Fe substitution was further investigated by monitoring the CO + N_2O reaction *insitu* using FTIR as probe. As a result of aliovalent, Fe^{3+} substitution, additional active sites in form of anionic vacancies/defects or pores are created, where CO and N_2O gases are chemisorbed. *Insitu* IR shows a band of 1337 cm^{-1} at 200 °C over LF4 sample, and 1230 cm^{-1} over unsubstituted LTO surface attributed to carbonate formation. Normally, the adsorption at defect site such as anionic vacancy or pores in LF4 leads to more stronger adsorption at higher wave number (1337 cm^{-1}), as compared with normal terrace sites as in LTO (1230 cm^{-1}) [90]. The intensity of band due to gaseous phase CO_2 at 2342 cm^{-1} correlates well with the carbonate formation. The presence of easily reducible Fe^{3+} ions and highly mobile lattice oxygen assists the binding of CO with two surface oxygen, thus forming carbonate (CO_3^{2-}) species over iron-substituted sample. The carbonate formation facilitates the reduction of pre-adsorbed N_2O on LF4 surface. However, the unsubstituted, parent lanthanum titanate, $La_2Ti_2O_7$, are stoichiometric oxide and, therefore, deficient in such reactive sites on the surface. Thus, reactants were physisorbed not chemisorbed as suggested by the absence of *insitu* carbonate formation. Based on *insitu* FTIR investigations and catalytic activity results, following mechanism over Fe-substituted LF4 sample was

proposed. It follows a redox mechanism here, where the surface is initially reduced by CO, and then, the reduced surface is oxidized by dissociative N_2O chemisorptions (Scheme 1). While, in case of unsubstituted lanthanum titanate, $La_2Ti_2O_7$, an associative mechanism was observed.

Dispersed catalysts

With an objective to further decrease the temperature required for the 100% conversion, for CO + N_2O reaction, fine powders of metal ions (Ni, Co and Pt) were dispersed on Fe substituted/unsubstituted lanthanum titanate, $La_2Ti_{2(1-x)}Fe_{2x}O_{7-\delta}$ oxides as supports. Two compositions of $La_2Ti_{2(1-x)}Fe_{2x}O_{7-\delta}$ oxides in which x = 0 and 0.4 (LTO and most active LF4 from previous section) were chosen to act as support for dispersion of Ni, Co and Pt metal ions. Lanthanum titanate, $La_2Ti_2O_7$, or modified Fe substituted, $La_2Ti_{1.6}Fe_{0.4}O_{7-\delta}$ are layered perovskites with several advantages as support as compared to alumina or other traditional supports. $La_2Ti_2O_7$ is stable toward reduction and oxidation atmosphere up to 1000 °C. $La_2Ti_2O_7$ is a monoclinic layered perovskite, which is capable of compensating for small fluctuations in the oxygen content of automobile exhaust by virtue of the mobile lattice oxygen and reducible B-site cations. Thus, metal dispersed on perovskite surface can migrate between the B-site in the perovskite structure and the metal particle lattice site in the real catalyst when exposed to fluctuation of the oxygen content of the emission exhaust. Perovskite surface offers stability to dispersed metal ions during prolonged use and prevents the aging, agglomeration and subsequent deterioration of catalyst performance [88] unlike the conventional catalysts, Pt/Al_2O_3, Pd/Al_2O_3. Thus, here some important observations and findings are given that are obtained after dispersing metals (Pt, Ni, Co) on unconventional layered perovskites as supports.

Support samples $La_2Ti_2O_7$ (LT) and $La_2Ti_{1.2}Fe_{0.8}O_{7-\delta}$ (LF4) were synthesized by gel combustion route (GC) followed by dispersion of metal using wet impregnation method resulting in M-$La_2Ti_{2(1-x)}Fe_{2x}O_{7-\delta}$ oxides (M = Ni, Pt and Co; x = 0 and 0.4) compositions characterized by XRD, SEM, TEM, XPS, TPDRO and AAS. Reduction behavior of these supported perovskite catalysts was monitored by recording multiple TPR-TPO cycles and further analyzed for CO + N_2O as well as N_2O decomposition catalytic reactions. The course of adsorption of CO, N_2O and CO + N_2O, formation of intermediate species on the surface of self-supported catalyst pellets during the

$$CO\ (g) + * \longrightarrow CO*$$

$$*\text{-}CO + O* + O^{2-} \longrightarrow *\text{-}CO_3{}^{2-} + * \longrightarrow CO_2 + *\text{-}O + 2e$$

$$N_2O\ (g) + * \longrightarrow N_2 + *\text{-}O$$

$$CO\ (g)/*\text{-}CO + O* \longrightarrow CO_2 + *$$

Scheme 1. Reactive sites on catalyst surface facilitated carbonate formation and N_2O decomposition as shown in above mechanism proposed for CO + N_2O reaction proceeding via $CO_3{}^{2-}$ formation over Fe-substituted Lanthanum Titanate, LF(0.6)GC, sample

catalytic reaction was monitored by *insitu* FTIR to provide insights about the reaction mechanism involved. XRD patterns of Ni, CO and Pt dispersed on $La_2Ti_{1.2}Fe_{0.8}O_{7-\delta}$ sample revealed the formation of single phase of rhombohedral $LaFeO_3$ (JC-PDS No. 37–1493) with unit cell parameters a = 5.566 Å, b = 7.854 Å, and c = 5.56 Å, Vol = 242.81 $Å^3$. No additional XRD reflections due to metal ions were observed for M-LTO/LF4 samples suggesting that metal ions are finely dispersed on surface and were left undetected by XRD. Oxygen excess layered perovskite, $A_2B_2O_7$ support was subjected to consecutive four to five reduction-oxidation cycles. Each temperature programmed reduction (TPR) cycle was followed by a temperature programmed oxidation (TPO cycle). It was found that $A_2B_2O_7$ support reorganizes to ABO_3 type perovskite lattice on reduction (TPR) and reverse was observed for TPO cycle. This shows that support lattice facilitates easy removal and uptake of oxygen, due to its capability of reorganizing within same composition. After metal dispersion, additional low-temperature peaks at ~ 150 °C and 280 °C were also observed in first and second TPR cycles of Pt-LFGC and Ni-LFGC samples attributed to reduction of Pt and Ni, respectively (Fig. 17.7). TPR profiles suggest strong metal–support interactions. During first cycle, due to strong interactions and linkages of M–O–LT

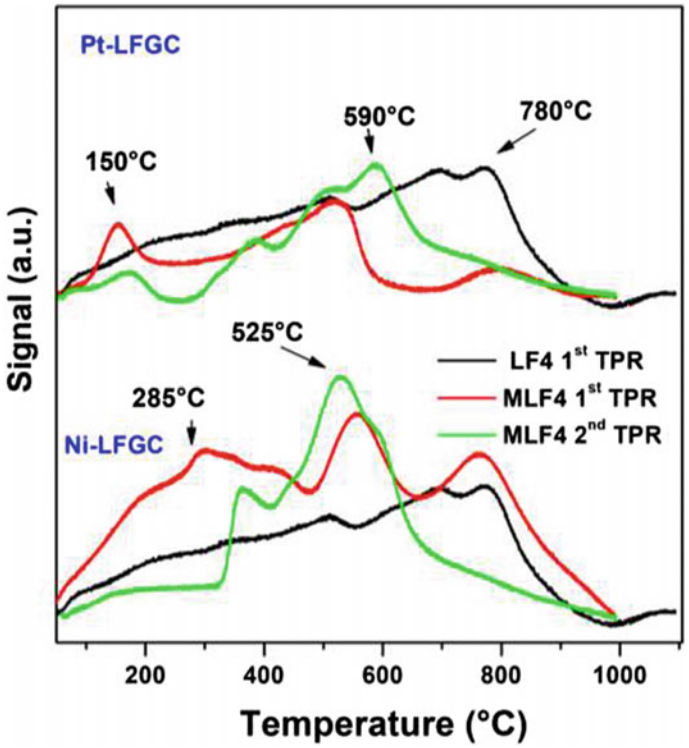

Fig. 17.7 Metal support interactions are evident by multiple TPR/TPO profiles of $Pt/La_2Ti_{1.2}Fe_{0.8}O_{7-\delta}$ and $Ni/La_2Ti_{1.2}Fe_{0.8}O_{7-\delta}$ supported catalysts

type, a sluggish profile with poor reduction kinetics was observed. However, during second cycle, metal ion bonds with support weakened and show distinct reduction peaks (Fig. 17.7). All these samples were found to be active and the decreasing order of catalytic activity was NiO-LT (PT-LT) > NiO-LF4 > PtO-LT > Ni-LF4 > Ni-LT > CoO-LT > Co-LT (Fig. 17.8). For the $CO + N_2O \rightarrow CO_2 + N_2$ reaction, the maximum conversion was observed with NiO dispersed on LT support where sample showed activity at 250 °C and attained 100% conversion at 300 °C. Metal dispersed LT/LF4 samples have exhibited considerably enhanced activity, as against support alone. Negligible conversion was observed for LTO at 300 °C. In case of LF4, conversion was initiated at 300 °C and 100% was reached at 400–410 °C. TEM image of NiO/LT sample (Fig. 17.9) confirmed uniform dispersion of amorphous NiO particles with average size of ~10–12 nm on crystalline $La_2Ti_2O_7$ support. Electron diffraction images (inset of Fig. 17.9) show two different patterns, one is

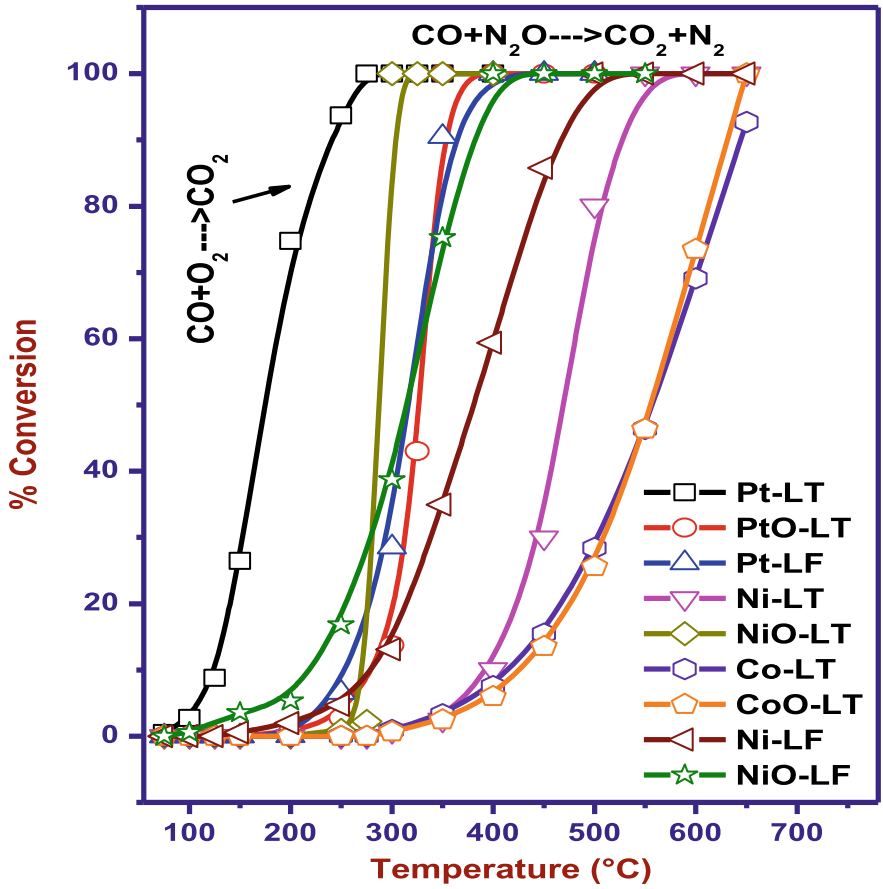

Fig. 17.8 The temperature-dependent catalytic activity of M-$La_2Ti_{2(1-x)}Fe_{2x}O_{7-\delta}$ oxides for $CO + N_2O$ reaction

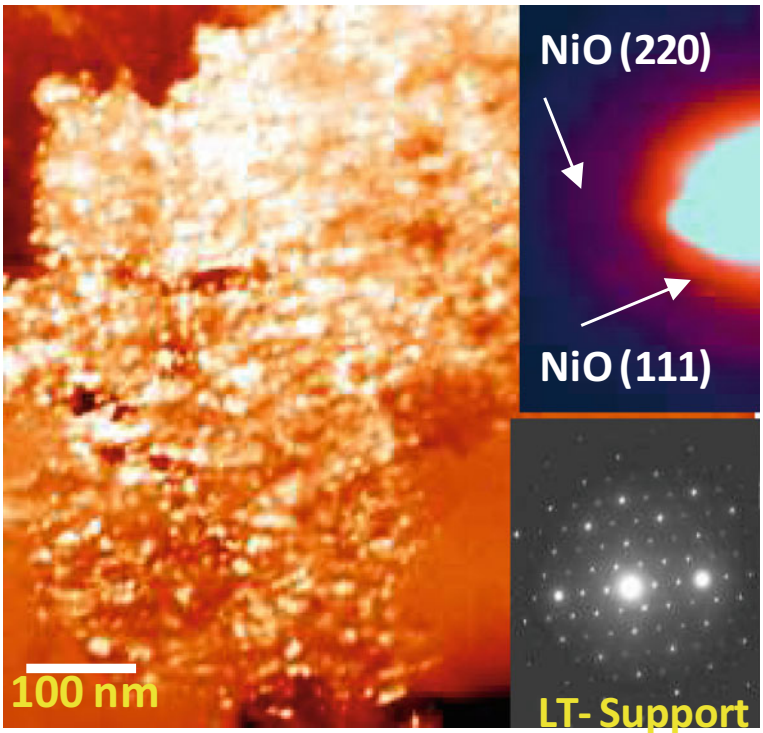

Fig. 17.9 TEM/ED image of NiO dispersed on lanthanum titanate support (white spots correspond to the NiO nanoparticles). Inset shows electron diffraction patterns corresponding to nanocrystalline NiO and lanthanum titanate crystalline support

showing diffused rings due to 220 and 111 planes of amorphous NiO dispersed on support, other consists of well-defined dots attributed to crystalline monoclinic lanthanum titanate support. Highly dispersed NiO nanoparticles are responsible for the considerable rise in activity over NiO/LT sample as compared with other samples. Pt-LTGC exhibited considerable enhancement in catalytic activity for CO oxidation reaction with onset at 75 °C and complete 100% conversion at 275 °C (Fig. 17.8). Temperature-dependent *insitu* IR results show the adsorption and conversion of CO to CO_2 via carbonate formation evident at 1585 cm^{-1} in temperature range of 250–300 °C (Fig. 17.10). Metal dispersed samples also facilitated the adsorption and decomposition of N_2O alone considerably at 300° as observed on NiO-LTGC surface (Fig. 17.11), in contrast to support samples, LT and LF4 where no decomposition was observed even at 350 °C. Overall, conclusion is that dispersion of Ni and Pt metal ions by impregnation on $La_2Ti_2O_7$ and LF4 support modifies the characteristics of bulk LT/LF4 catalysts considerably and makes them superior catalysts for N_2O decomposition reaction.

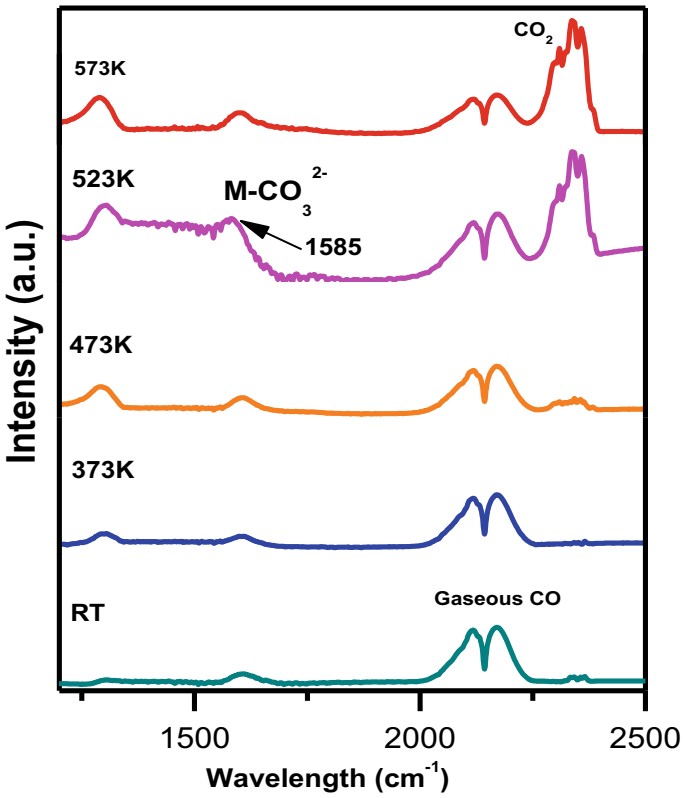

Fig. 17.10 To monitor the adsorption of CO as a function of temperature on surface of NiO-LTGC catalyst using *insitu* FTIR spectroscopy

17.5.3 H_2SO_4 Decomposition

Another very useful thermal reaction for which we have developed catalysts is sulfuric acid decomposition reaction. It is one of the most challenging and endothermic steps of sulfur-based thermochemical cycles [91, 92]. Thermochemical water splitting cycles are designed based on Hess's law of chemical thermodynamics. Water splitting into hydrogen and oxygen is achieved via chemical reactions using intermediate elements and compounds, which are recycled. The sum of all the reactions is equivalent to the dissociation of the water molecule. Sulfuric acid decomposition takes place in following two steps:

$$H_2SO_4(l) \rightarrow H_2O(l) + SO_3(g)(450^\circ C) \tag{17.3}$$

$$SO_3(g) \rightarrow SO_2(g) + 1/2O_2(g)\ (800 - 900^\circ C) \tag{17.4}$$

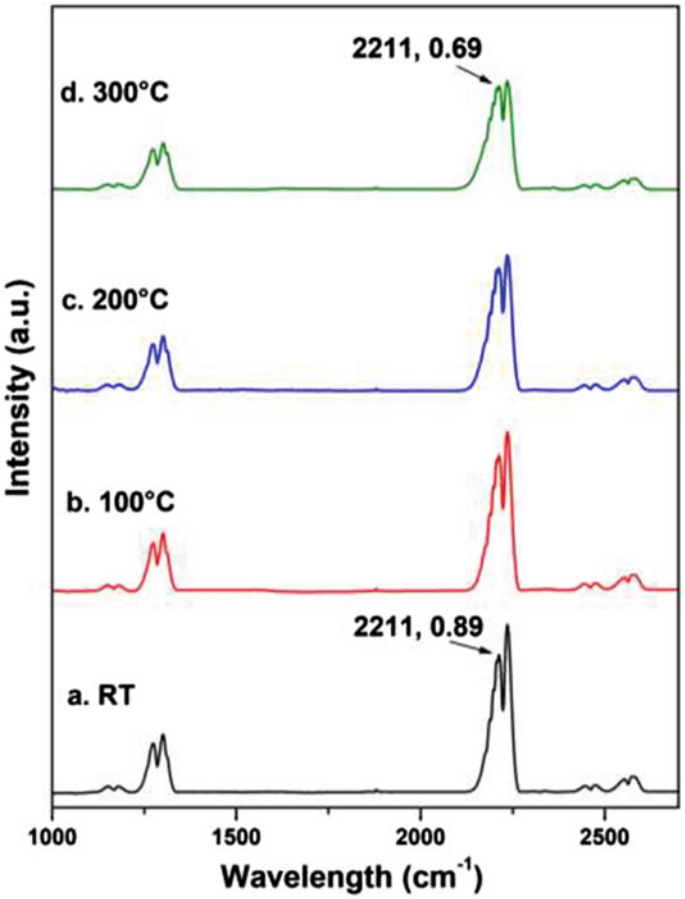

Fig. 17.11 To monitor the adsorption of N_2O as a function of temperature on surface of NiO-LTGC catalyst using *insitu* FTIR spectroscopy

First is simple thermal decomposition of sulfuric acid into its anhydride by loss of water at ~450 °C, while second is the reduction of SO_3 to SO_2, with evolution of oxygen is a catalytic reaction. Figure 17.12 shows the calculated thermodynamic yield and experimental yield in the absence of catalyst obtained at different temperatures [93]. Without catalyst, almost negligible yield is obtained around 1073 K. It has slow kinetics in the absence of catalyst. Some of the reported noble metal-based catalysts employed for sulfuric acid decomposition include supported platinum catalysts such as (Pt/Al_2O_3, Pt/TiO_2 and Pt/ZrO_2) [94], (Pt/TiO_2 (rutile) [95], ($Pt/BaSO_4$) [96] and theoretical studies on supported metal particles (Pd, Pt, Rh, Ir and Ru supported on titania) [97]. Metal oxide catalysts are active and can be a substitute for noble metal catalysts as they fulfill the essential requirement of materials with better chemical, thermal stability and modified catalytic properties. Long back in 1977,

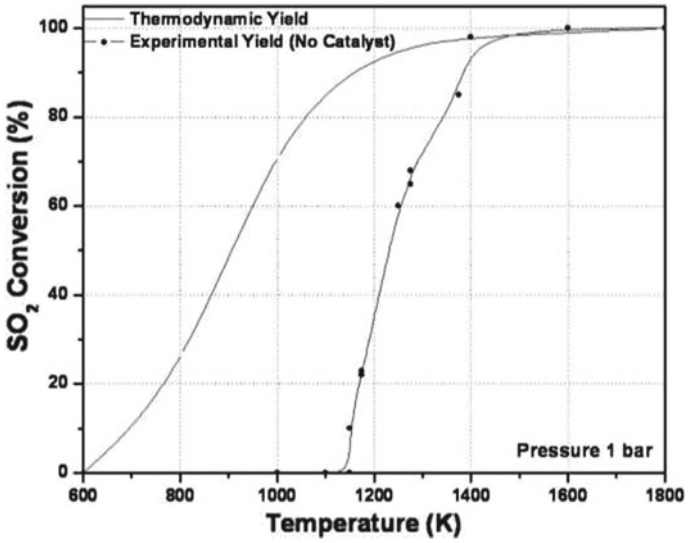

Fig. 17.12 Comparison of thermodynamic yield and experimental yield in the absence of catalyst as a function of temperature obtained in H_2SO_4 decomposition reaction. Reprinted from Ref. [93], with permission from Elsevier

Dokiya et al. [98] first reported the use of several metal oxide catalysts for sulfuric acid decomposition, where Fe_2O_3 was found to be the most active catalyst. Thus, to explore the potential of cheap Fe-based catalysts, development of Fe-based catalysts started at our end. To begin with, studies on Cr doped Fe_2O_3-based powder catalysts were undertaken [99–105].

Bulk catalysts: A series of iron-chromium binary mixed oxides ($Fe_{2(1-x)}Cr_{2x}O_3$: $0 \leq x \leq 1.0$) $Fe_{2x}Cr_{1-x}O_3$ were synthesized using ceramic route. Highly crystalline powders are obtained by this method and if proper intermittent grinding and heating are done, the product obtained is also homogeneous. One of the disadvantages of this method is that the powders obtained are in micron range as high-temperature heating causes sintering and grain growth. The catalytic activity of Cr substituted sample during prolonged duration was found to be better than unsubstituted iron oxide [101]. This was also further established by reproducible TPR/TPO cycles. The maximum conversion was obtained at 800 °C with the onset of formation of SO_2 at 600 °C. Solid solution of 20% Cr substitution in Fe_2O_3 lattice has not only enhanced reproducibility toward repeated reduction–oxidation cycles but also prevented the deactivation of the catalyst during use in sulfuric acid decomposition reaction. $Fe_{1.8}Cr_{0.2}O_3$ was found to be promising active and stable mixed oxide catalyst for the above reaction. For, further improvement in catalytic and mass transfer properties considering fixed bed reactor, granular $Fe_{1.8}Cr_{0.2}O_3$ and Fe_2O_3 catalysts were prepared by co-precipitation route as described in Scheme 2. The main difference in the two routes is the proximity of the reacting species. Several parameters, such as pH, mixing rates, temperature and concentration have to be controlled to produce satisfactory results. The composition

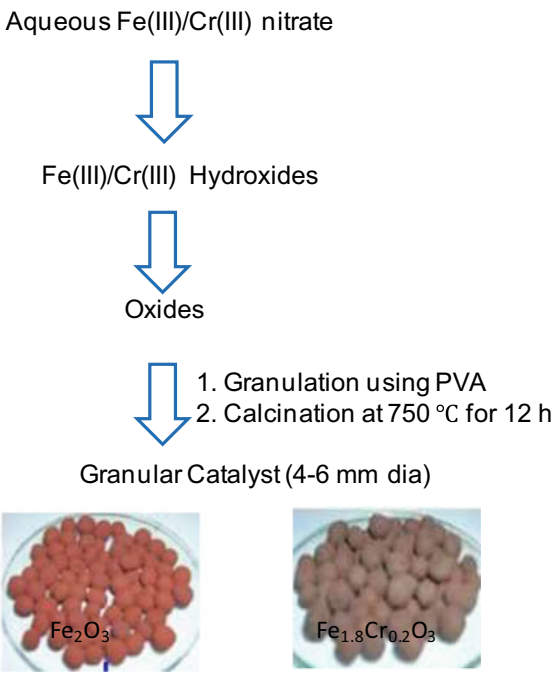

Scheme 2. Synthesis methodology followed to prepare granular Fe_2O_3 and Cr doped iron oxide catalysts

control, purity and morphology of the resulting product are good. However, different rates of precipitation of each individual compound may lead to microscopic inhomogeneity. Co-precipitated granular catalysts, $Fe_{1.8}Cr_{0.2}O_3$ and Fe_2O_3, were tested for their efficacy in actual reactor conditions where inert gas will not be used to facilitate the elution of product gases. The activity was evaluated in an indigenously designed and fabricated dual-tube quartz catalytic reactor [101, 103], which served as an integrated boiler, preheater and decomposer having no high-temperature connections at larger scale of ~20 g. The concept of this dual-tube type of catalytic reactor can also be enhanced to an engineering scale for pilot plants.

The SO_2 yield as measured with chemical titrimetric method increased with rise in temperature with a maximum activity of 76% and 82% for Fe_2O_3 and $Fe_{1.8}Cr_{0.2}O_3$ at ~825 °C. However, the SO_2 yield was higher for the Cr-doped samples than the pristine Fe_2O_3 throughout the 100 h run [101].

Fe_2O_3 and 10% Cr-doped Fe_2O_3 catalyst pellets or granules were tested as catalyst for sulfuric acid decomposition reaction for 100 h at 800 °C and a sulfuric acid flux of 0.63 ml/min (WHSV of 3.4 g acid g^{-1} catalyst h^{-1}), in an indigenously constructed quartz dual tube catalytic reactor, which served as an integrated boiler, preheater and decomposer [102]. No decrease in catalytic activity was observed during this long-term experiment, although the doped sample exhibited slightly higher catalytic activity throughout. However, in the temperature-dependent catalytic runs, the Cr-doped sample showed much higher intrinsic activity at lower temperatures (<775 °C). Both the catalysts exhibited a loss in catalytic activity when subjected to very high

flow of sulfuric acid of 2–10 ml/min. Bulk Fe_2O_3-based catalysts both in powder and granular form suffer limitations of limited mass transfer.

Dispersed Fe_2O_3-based catalysts

One of the challenges in supported catalyst is to rationally design the catalysts such that it possesses essential activity, selectivity and stability. For this, selection of support is very critical. Jin et al. [106] reported an excellent example of rational catalyst design of bimetallic CuPd-graphene nanocatalysts in which a deliberate attempt to match the lattice of active metals with support phase (graphene) was done. It resulted in exceptionally improved catalytic properties for facile conversion of biomass-derived polyols to lactic acid, owing to electron density overlap of the support and dispersed phase. We in our laboratory with an objective to further improve the prowess of sulfuric acid decomposition catalyst-dispersed Fe_2O_3 nanoparticles on a support [103–105]. With an aim to investigate the metal–support interactions; Fe_2O_3 was dispersed on different supports such as TiO_2, CeO_2, ZrO_2 and SiO_2 using equilibrium–adsorption method [104]. Basically, support lowers the associated surface energy and prevents agglomeration and migration of metal nanoparticles. The role of suitable carrier here is to immobilize the iron oxide particles in the maximum possible dispersed state and preserve the nanostructured morphology of catalyst during long operational conditions of high temperature and corrosive exposure by sulfuric acid. Figure 17.13 shows the catalytic activities of Fe_2O_3 supported catalysts. Role of different synthetic route supports and mesh size in development of sulfuric acid decomposition catalyst is highlighted. CeO_2 and ZrO_2 underwent sintering during calcination step at 1000 °C and yielded low surface area supported catalysts. Anatase TiO_2 formed a solid solution at 1000 °C resulted in pseudo-brookite Fe_2TiO_5 dispersed over TiO_2. Among all supports, silica-supported Fe_2O_3 was found to be most active (Fig. 17.13). Silica owing to its high surface area (~249 m^2/g) facilitated homogeneous distribution of nanosized iron oxide (~2–3 nm) as evident by TEM mages. Surface area of SiO_2 decreased to ~149 m^2/g after dispersion indicating that Fe_2O_3 has diffused inside the pores. Other supports such as ZrO_2, CeO_2 resulted into heterogeneous distribution, evident by mapping along line distribution of Fe_2O_3 in TEM images. Although same synthesis methodology was adopted, different supports produced catalysts with varied characteristics and catalytic activity. Among different loadings, 15 wt % was found to be most optimum with ~74% conversion at 850 °C as shown in Fig. 17.13. The amorphous SiO_2 stabilized crystalline Fe_2O_3 through Fe–O–Si linkages evident by XPS and TPR studies. In XPS, the presence of peaks at ~712.8 eV can be attributed to Fe^{3+} bound to the SiO_2 support. A lower intensity peak of O 2p at the highest BE value of ~533.5 eV assigned to chemisorbed surface oxygen or surface adsorbed water or hydroxyl moieties, which progressively increased with increase in Fe_2O_3 loadings indicated that the peak could be assigned to O^{2-} present in dispersed Fe_2O_3. TPR profile characteristics provided evidence for reduction of Fe^{3+} to Fe^0 present in Fe–O–Si linkages. The amount of Fe^{3+} species reduced in first TPR cycle, increased in 2, 3 and 4th TPR cycles during multiple TPR/TPO runs. Increase in intensity of Fe^{3+} is possible only if we consider metal support interactions. During

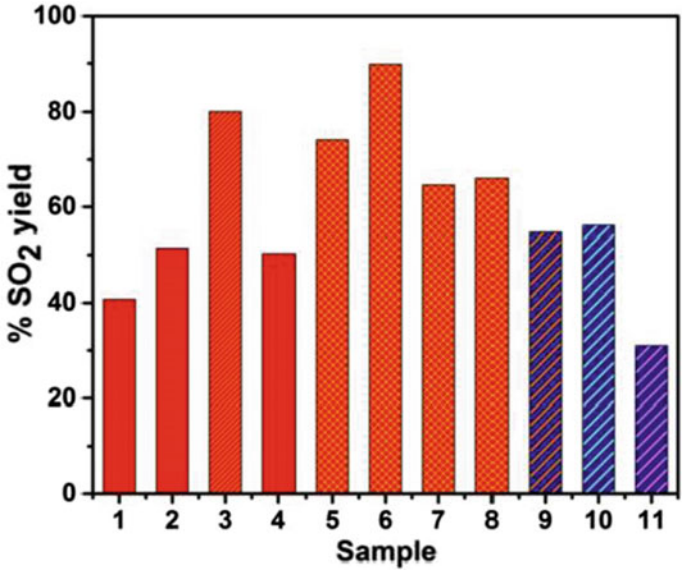

1- (5wt %)Fe_2O_3/SiO_2 (80-45 mesh)Eq.Adsorption method

2-(10wt %)Fe_2O_3/SiO_2 (80-45 mesh)Eq.Adsorption method

3-(15wt %)Fe_2O_3/SiO_2(80-45 mesh)Eq.Adsorption method

4-(20wt %)Fe_2O_3/SiO_2 (80-45 mesh)Eq.Adsorption method

5-(15wt %)Fe_2O_3/SiO_2(45-20 mesh) Eq.Adsorption method

6-(15wt %)Fe_2O_3/SiO_2(45-20 mesh) Polyol

7-(15wt %)Fe_2O_3/SiO_2(45-20 mesh) Solvothermal

8-(15wt %)Fe_2O_3/SiO_2(45-20 mesh) Wet impregnation

9-(15wt %)Fe_2O_3/TiO_2(45-20mesh)Eq.Adsorption method

10-(15wt %)Fe_2O_3/ZrO_2(45-20 mesh)Eq.Adsorption method

11-(15wt %)Fe_2O_3/CeO_2(45-20 mesh)Eq.Adsorption method

Fig. 17.13 Effect of synthesis, mesh size, loading and support on catalytic activity of Fe_2O_3 dispersed catalysts for sulfuric acid decomposition reaction at 800 °C

first cycle, SiO_2 inhibits the reduction of Fe^{3+} species anchored over it, and a sluggish reduction profile of Fe^{3+} to Fe^0 was observed. Subsequently, more and more free Fe_2O_3 segregated on surface and intensity of reduction peak increased. The presence of peaks due to Fe_2SiO_4 in the XRD of spent TPR sample confirms the participation of support in reduction of active iron oxide nanophase. These metal–support interactions facilitated sulfation of support and its facile decomposition. Although, SiO_2 could not prevent completely the agglomeration of Fe_2O_3 particles, but enabled Fe_2O_3 to sustain through the corrosive environment during the long operational times

(~100 h). A feature specific to SiO_2 was that it was immune to sulfation under experimental conditions in sharp contrast to what was observed for other supports such as ZrO_2, TiO_2 and CeO_2 [104].

To study the role of synthesis on catalytic activity and stability, the most active Fe_2O_3 (15wt%)/SiO_2 combination was synthesized by other methods also such as polyol (P), solvothermal (ST) and wet-impregnation (WI) methods in addition to equilibrium–adsorption method and evaluated for sulfuric acid decomposition (Fig. 17.13). The different procedures yielded catalysts with varying crystal structure, porosity, morphology and redox properties. These were examined by XRD, Mössbauer spectroscopy, N_2-BET surface area, SAXS, ED-XRF, HR-TEM, TPR/O and XPS techniques. Due to their varying effect, on bulk and surface properties, catalytic activities were also affected. Figure 17.13 exhibits that the catalytic activity was maximum by polyol > wet impregnation ~solvothermal at 800 °C. Polyol and WI yielded surface area of 125 m^2/g, while ST was lower of ~75 m^2/g. Pore confinement and high calcination temperature are two main reasons for reduction in surface area. SAXS profiles of all samples show that maximum fraction of Fe_2O_3 has aggregated inside mesopores using polyol method. The mesopores with pore radius of 12.9 nm existing on SiO_2 were filled by Fe_2O_3 to a maximum extent using polyol methodology and that has favorable effect on its catalytic properties. Interestingly, different methods yielded different morphology, polyol yielded rod-shaped α phase of Fe_2O_3 and that goes well with filling up of mesopores observation from SAXS results too, WI yielded elliptical shape and ST method resulted in spherical Fe_2O_3 probably due to high pressures in autoclave. TPR shows maximum hydrogen consumption by polyol > WI > ST, thus suggesting more reducible species on surface and better catalyst for redox reactions. Ethylene glycol is a high boiling solvent used in polyol method, allows formation of highly crystalline nanomaterials [105] and is one of the major advantages of synthesis by polyol method. Dispersion of highly crystalline and stable phases is suitable for high temperature catalytic applications as in the present case of sulfuric acid decomposition reaction. Thus, through polyol method, most active and stable supported catalyst was fabricated. It has facilitated homogeneous distribution of nano-crystalline rod-shaped α-Fe_2O_3 over mesoporous SiO_2 with Fe–O–Si linkages, which is favorable for high temperature sulfuric acid decomposition reaction. Mesh size is important from the back pressure exerted by particulate catalyst in fixed bed reactor. Lower the mesh size, bigger is the particle size and will have lower contact time with reactant gases, thus 45-mesh yield poor activity as compared with 80–90 mesh (Fig. 17.13).

17.6 Conclusions

In this chapter, we have described three main categories of catalysts that developed over the years in search of improvisation: bulk, dispersed and single atom. The general features of the three categories are described. An overview of preparation methods that developed for the synthesis of both bulk and supported industrial

catalysts is given above. Novel methods to prepare nanosized mixed metal oxides at large scale are also described. The above article highlights how advancement in synthesis practices helped in addressing optimum usage of active phase, active site engineering, morphology and cost of active component (precious metals). Single atom catalyst (SAC) is an emerging and promising science. It is ultimate form of dispersed catalyst with exceptionally high catalytic activity, selectivity and turn over number. Sophisticated atomic layer deposition, wet chemical co-precipitation technique based on carefully tuning the pH, temperature and loading amount in order to lower the associated surface energy and prevent agglomeration and other approaches such as photo-deposition and atom trapping are presently adopted to prepare SACs. Thermal reactions such as CO oxidation, $CO + N_2O$ and sulfuric acid decomposition performed in our research group are discussed to illustrate that mobility of lattice oxygen, adsorption on surface-active sites, extent of crystallinity, pore confinement, dispersed phase–support interactions, shape and size of dispersed phase—all can be tailored by adopting suitable method of preparation. By using selected examples, we attempted to correlate synthesis-induced modifications with catalytic properties. Finally, based on above, it can be concluded that catalysis science is an artwork and most workable catalytic formulations can be created by the finest synthesis process.

Acknowledgements Authors sincerely thank Dr. A. K. Tyagi, Outstanding Scientist, Director, Chemistry Group and Head, Chemistry Division, BARC for his keen interest, support and encouragement. MRP sincerely thank her mentor and PhD guide, Dr. N. M. Gupta, former Head, Applied Chemistry Division, BARC for introducing to the exciting field of heterogeneous catalysis.

References

1. Schmal M (2016) Heterogeneous catalysis and its industrial applications. Springer International Publishing
2. Thomas JM, Thomas WJ (2014) Principles and practice of heterogeneous catalysis, 2nd edn. Wiley-VCH, Weinheim, Germany
3. Ross J (2018) Contemporary catalysis, fundamentals and current applications, 1st edn. Elsevier
4. Védrine JC (2017) Heterogeneous catalysis on metal oxides. Catalysts 7:341
5. Mabilon G, Durand D, Prigent M (1991) Kinetics of the physico-chemical and catalytic activity evolution of a Pt-Rh catalyst in automotive exhaust gas. In: Crucq A (ed), Catalysis and automotive pollution control II. Elsevier, Amsterdam, pp 569
6. Shinjoh H, Muraki H, Fujitani Y (1991) Effect of severe thermal aging on noble metal catalysts. In: Crucq A (ed) Catalysis and automotive pollution control II. Elsevier, Amsterdam, pp 617
7. Leigh GJ, Haber-Bosch (2004) Other industrial processes. In: Smith BE, Richards RL, Newton WE (eds) Catalysts for nitrogen fixation. Nitrogen fixation: origins, applications, and research progress, vol 1. Springer, Dordrecht
8. Staffell I, Scamman D, Abad AV, Balcombe P, Dodds PE, Ekins P, Shah N, Ward KR (2019) The role of hydrogen and fuel cells in the global energy system. Energy Environ Sci 12:463
9. Kozuch S, Martin JML (2012) Turning over. Definitions in catalytic cycles. ACS Catal 2:2787
10. Patel S, Kundu S, Halder P, Marzbali MH, Chiang K, Surapaneni A, Shah K (2020) Production of hydrogen by catalytic methane decomposition using biochar and activated char produced from biosolids pyrolysis. Int J Hydrogen Energy 45:29978

11. Golodets GI (1983) Heterogeneous catalytic reactions involving molecular oxygen, studies in surface science and catalysis, vol 15. Elsevier, Amsterdam
12. Hagen J (2015) Industrial catalysis: a practical approach, 3rd edn. Wiley-VCH Verlag GmbH & Co, KGaA
13. Satterfield CN (1993) Heterogeneous catalysis in industrial processes. McGraw-Hill, Singapore
14. Ross JRH (2011) Heterogeneous catalysis 1st edn. In: Fundamentals and applications, Elsevier
15. Somorjai GA (1994) Introduction to surface chemistry and catalysis, John Wiley & Sons, Inc., New York, pp 444
16. Bond GC (1972) Principles of catalysis, 2nd edn. The chemical society, Burlington House, London
17. Pai MR, Banerjee AM, Rawool SA, Singhal A, Nayak C, Ehrman SH, Tripathi AK, Bharadwaj SR (2016) A comprehensive study on sunlight driven photocatalytic hydrogen generation using low cost nanocrystalline Cu-Ti oxides. Sol Energy Mater Sol Cells 154:104
18. Widmann D, Behman RJ (2018) Dynamic surface composition in a Mars-van Krevelen type reaction: CO oxidation on Au/TiO_2. J Catalysis 357:263
19. Mars P, van Krevelen DW (1954) Oxidation carried out by means of vandium oxide catalysts. Chem Eng Sci Suppl 3:41
20. Dadyburjor DB, Jewur SS, Ruckenstein E (1979) Selective oxidation of hydrocarbons on composite oxides. Catal Rev Sci Eng 19:293
21. Schmidt F (2001) New catalyst preparation technologies—observed from an industrial viewpoint. Appl Catal A Gen 221:15
22. Regalbuto J (2007) Catalyst preparation, science and engineering, CRC Press, Boca Raton, FL
23. Saab R, Polychronopoulou K, Zheng L, Kumar S, Schiffer A (2020) Synthesis and performance evaluation of hydrocracking catalysts: A review. J Ind Eng Chem 89:83
24. Bartholomew CH, Farrauto RJ (2006) Fundamentals of industrial catalytic processes. John Wiley & Sons Inc., Hoboken, NJ
25. Deutschmann O, Knözinger H, Kochloefl K, Turek T (2011) Ullmann's encyclopedia of industrial chemistry, heterogeneous catalysis and solid catalysts, 7th edn. Wiley-VCH Verlag GmbH, Weinheim
26. Pai MR, Wani BN, Belapurkar AD, Gupta NM (2004) Role of substitution in catalytic activity of La–Th–V–O mixed oxides for the reaction of methanol. J Mol Catal A: Chemical 223:275
27. Pai MR, Wani BN, Gupta NM (2002) Synthesis, characterization and thermal behavior of Th-Mn-VO oxides. J Mater Sci Lett 21:1187
28. Pai MR, Wani BN, Gupta NM (2005) Effect of La substitution on thermal stability of ThV_2O_7. Thermochim Acta 425(1-2):109
29. Pai MR, Wani BN, Gupta NM (2006) The role of substitution-induced micro-structural defects on the redox behavior and catalytic activity of LaxTh1− x (VO3− δ) 4 mixed oxide catalysts. J Phys Chem Solids 67:1502
30. Achary SN, Pai MR, Mishra R, Tyagi AK (2008) Crystal structure of thorium metavanadate (Th $(VO_3)_4$). J Alloys Compd 453:332
31. Sokolovski VD (1990) Principles of oxidative catalysis on solid oxides. Catal Rev-Sci Eng 32:1
32. Grasselli RK, Burrington JD (1981) Selective oxidation and ammoxidation of propylene by heterogeneous catalysis. Adv Catal 30:133
33. Courty P, Ajot H, Delmon B (1973) Acad CR Sci Ser C 276:1147
34. Sazonov VA, Popovskii VV, Boreskov GK (1968) Kinetica i Kataliz 9:307
35. Pankratyev YD, Tichy J (1975) Binding energy of oxygen with a Vanadium-Molybdenum oxide on silica catalyst. React Kin Catal Lett 2:319
36. Dunn JP, Koppula PR, Stenger HG, Wachs IE (1998) Oxidation of sulfur dioxide to sulfur trioxide over supported vanadia catalysts. Appl Catal B Environ 19:103
37. Bingre R, Louis B, Nguyen P (2018) An overview on zeolite shaping technology and solutions to overcome diffusion limitations. Catalysts 8(4):163

38. Li WG, Hu YJ, Jiang H, Li CZ (2019) Aerosol spray pyrolysis synthesis of porous anatase TiO_2 microspheres with tailored photocatalytic activity. Acta Metall Sin (Engl Lett) 32(3):286
39. Siegel RW, Ramaswami S, Hahn H, Zongquan L, Ting L, Grousky R (1988) Synthesis, characterization, and properties of nanophase TiO_2. J Mater Res 3:1367
40. El-Shall MS, Slack W, Vann W, Kane D, Hanely D (1994) Synthesis of nanoscale metal oxide particles using laser vaporization/condensation in a diffusion cloud chamber. J Phys Chem 98(12):3067
41. Edelstein AS, (1994) Nanoparticles from a supersaturated vapor. In: Hadjipanayis GC, Siegel RW (eds) Nanophase Materials. Springer Netherlands, pp 73–80
42. Kodas TT (1989) Aerosol spray pyrolysis synthesis techniques. Adv Mater 6:180
43. Messing GL, Zhang SC, Jayanthi GV (1993) Ceramic powder synthesis by spray pyrolysis. J Am Ceram Soc 76(11):2707
44. Chow GM, Gonsalves KE (1996) (eds) Nanotechnology, molecularly designed materials. American chemical society, Washington, DC, pp 64–78
45. Skandan G, Chen Y-J, Glumac N, Kear BH (1999) Synthesis of oxide nanoparticles in low pressure flames. Nanostructured Materials 11(2):149–158
46. Khaleel A, Richards RM (2001) Ceramics. In: Klabunde KJ (ed) Nanoscale materials in chemistry. Wiley- Interscience, New York, pp 85–120
47. Mehrotra RC, Singh A (1997) Recent trends in metal alkoxide chemistry. In: Karlin KD (ed) Progress in inorganic chemistry. John Wiley&Sons Inc., pp 239
48. Herrig H, Hempelmann R (1996) A colloidal approach to nanometre-sized mixed oxide ceramic powders. Mater Lett 27:287
49. Thimmaiah S, Rajamathi M, Singh N, Bera P, Meldrum F, Chandershekhar N, Seshadsi R (2001) A solvothermal route to capped nanoparticles of g-Fe_2O_3 and $CoFe_2O_4$. J Mater Chem 11:3215
50. Laine RM, Waldner K, Bickmore C, Treadwell DR (1999) Ultrafine powders by flame spray pyrolysis. US Patent, 5, 958, 361
51. Pramanik P, Roy JC, Sen A, Pati RK (2001) Novel chemical methods for preparation of nano-sized oxide ceramics. In: International symposium on metastable, mechanically alloyed and nanocrystaline materials; Proceedings of ISMANAM-2000, Oxford, UK, Material Science Forum, vols 360–362, 623–630
52. Shin H, Lee S, Jung HS, Kim J-B (2013) Effect of ball size and powder loading in the milling efficiency of a laboratory-scale wet ball mill. Ceram Int 39(8):8963
53. Anderson JA, García MF (2005) Catalysis science series- volume 5: supported metals in catalysis. Imperial College press
54. Geus JW, van Dillen AJ (2008) Preparation of supported catalysts by deposition–precipitation. In: Ertl G, Knozinger H, Schüth F, Weitkamp J (eds) Handbook of heterogeneous Catalysis, vol 1. Wiley-VCH Verlag GmbH& Co. KGaA, Weinheim, Germany, pp 428
55. Geus JW, van Veen JR (1999) Catalysis, an integrated approach to homogeneous, heterogeneous and industrial catalysis. In: Moulijn JA, van Leeuwen PWNM, van Santen RA (eds) Elsevier, Amsterdam, pp 467
56. Van Dillen AJ, Terorde RJAM, Lensveld DJ, Geus JW, de Jong KP (2003) Synthesis of supported catalysts by impregnation and drying using aqueous chelated metal complexes. J Catal 216:257
57. Nijhuis TA, Beers AEW, Vergunst T, Hoek I, Kapteijn F, Moulijn JA (2001) Preparation of monolithic catalysts. Catal Rev Sci Eng 43:345
58. Vergunst T, Linders MJG, Kapteijn F, Moulijn JA (2001) Carbon-based monolithic structures. Catal Rev Sci Eng 43:291
59. Geus JW (1983) Production and thermal pretreatment supported catalysts. Stud Surf Sci Catal 16:1
60. van der Grift CJG, Boon AQM, van Veldhuizen AJW, Trommar HGJ, Geus JW, Quinson JF, Brun M (1990) Preparation and characterization of porous silica spheres containing a copper (oxide) catalyst. Appl Catal 65:225

61. Mul G, Hirschon AS (2001) Effect of preparation procedures on the activity of supported palladium/lanthanum methanol decomposition catalysts. Catal Today 65:59
62. Liu X, Khinast JG, Glasser BJ (2008) A parametric investigation of impregnation and drying of supported catalysts. Chem Eng Sci 63:4517
63. Schwarz JA, Contescu C, Contescu A (1995) Methods for preparation of catalytic materials. Chem Rev 95(3):477
64. Geenen PV, Boss HJ, Pott GT (1982) A study of the vapor-phase epoxidation of propylene and ethylene on silver and silver-gold alloy catalysts. J Catal 77:499
65. Munnik P, de Jongh PE, de Jong KP (2015) Recent developments in the synthesis of supported catalysts. Chem Rev 115:6687
66. Geus JW, van Dillen AJ (1999) Preparation of supported catalysts by deposition-precipitation. In: Ertl G, Knözinger H, Weitkamp J (eds) Preparation of solid catalysts. Wiley-VCH Verlag GmbH, pp 460–487
67. Mehrabadi BAT, Eskandari S, Khan U, White RD, Regalbuto JR (2017) A review of preparation methods for supported metal catalysts. Adv Catal 61:1
68. Haruta M, Kobayashi T, Sano H, Yamada N (1987) Novel gold catalysts for the oxidation of carbon monoxide at a temperature far below 0°C. Chem Lett 16(2):405
69. Somorjai GA, Park JY (2008) Molecular surface chemistry by metal single crystals and nanoparticles from vacuum to high pressure. Chem Soc Rev 37:2155
70. Crespo-Quesada M, Yarulin A, Jin M, Xia Y, Kiwi-Minsker L (2011) Structure sensitivity of alkynol hydrogenation on shape- and size-controlled palladium nanocrystals: Which sites are most active and selective? J Am Chem Soc 133:12787
71. Yang X-F, Wang A, Qiao B, LI J, Liu J, Zhang T (2013) Single-atom catalysts: A new Frontier in heterogeneous catalysis. Acc Chem Res 46:1740
72. Wang G, Su J, Gong Y, Zhou M, Li J (2010) Chemistry on single atoms: spontaneous hydrogen production from reactions of transition-metal atoms with methanol at cryogenic temperatures. Angew Chem Int Ed 49(7):1302
73. Qiao B, Wang A, Yang X, Allard LF, Jiang Z, Cui Y, Liu J, Li J, Zhang T (2011) Single-atom catalysis of CO oxidation using Pt_1/FeO_x. Nat Chem 3:634
74. Lu J, Aydin C, Browning ND, Gates BC (2012) Imaging isolated gold atom catalytic sites in zeolite NaY. Angew Chem Int Ed 51(24):5842-5846, https://doi.org/10.1002/anie.201107391
75. Heiz U, Sanchez A, Abbet S, Schneider WD (1999) Catalytic oxidation of carbon monoxide on monodispersed platinum clusters: each atom counts. J Am Chem Soc 121:3214
76. Kaden WE, Wu T, Kunkel WA, Anderson SL (2009) Electronic structure controls reactivity of size-selected Pd clusters adsorbed on TiO_2 surfaces. Science. Science 326:826-829, 10.1126/science.1180297
77. Abbet S, Sanchez A, Heiz U, Schneider WD, Ferrari AM, Pacchioni G, Rosch N (2000) Acetylene cyclotrimerization on supported size-selected Pdn clusters ($1 <= n <= 30$): one atom is enough!. J Am Chem Soc 122:3453
78. Wang Q, Zhang D, Chen Y, Fu W-F, Lv X-J (2019) Single-atom catalysts for photocatalytic reactions. ACS Sustain Chem Eng 7:6430
79. Asim N, Ahmadi S, Alghoul MA, Hammadi FY, Saeedfar K, Sopian K (2014) Research and development aspects on chemical preparation techniques of photoanodes for dye sensitized solar cells. Int J Photoenergy 2014:518156
80. Sun S, Zhang G, Gauquelin N, Chen N, Zhou J, Yang S, Chen W, Meng X, Geng D, Banis MN, Li R, Ye S, Knights S, Botton GA, Sham T-K, Sun X (2013) Single-atom catalysis using Pt/graphene achieved through atomic layer deposition. Sci Rep 3:1775
81. Moses-DeBusk M, Yoon M, Allard LF, Mullins DR, Wu Z, Yang X, Veith G, Stocks GM, Narula CK (2013) CO oxidation on supported single Pt atoms: Experimental and ab Initio density functional studies of CO interaction with Pt Atom on θ-Al_2O_3(010) surface. J Am Chem Soc 135:12634
82. Liu P, Zhao Y, Qin R, Mo S, Chen G, Gu L, Chevrier DM, Zhang P, Guo Q, Zang D, Wu B, Fu G, Zheng N (2016) Photochemical route for synthesizing atomically dispersed palladium catalysts. Science 352(6287):797

83. Carrillo C, Johns TR, Xiong H, DeLaRiva A, Challa SR, Goeke RS, Artyushkova K, Li W, Kim CH, Datye AK (2014) Trapping of mobile Pt species by PdO nanoparticles under oxidizing conditions. J Phys Chem Lett 5(12):2089
84. Jones J, Xiong H, DeLaRiva AT, Peterson EJ, Pham H, Challa SR, Qi G, Oh S, Wiebenga MH, Hernández XIP, Wang Y, Datye AK (2016) Thermally stable singe-atom platinum-on-ceria catalysts via atom tapping. Science 353(6295):150
85. Weckhuysen BM, Keller DE (2003) Chemistry, spectroscopy and the role of supported vanadium oxides in heterogeneous catalysis. Catal Today 78:25
86. Pai MR, Wani BN, Sreedhar B, Singh S, Gupta NM (2006) Catalytic and redox properties of nano-sized $La_{0.8}Sr_{0.2}Mn_{1-x}Fe_xO_{3-\delta}$ mixed oxides synthesized by different routes. J Mol Catal A: Chem 246:128
87. Pai MR, Wani BN, Bharadwaj SR (2006) Synthesis, characterization and redox behavior of nano-size $La_{0.8}Sr_{0.2}Mn_{0.8}Fe_{0.2}O_{3-\delta}$. J Ind Chem Soc 83:336-341
88. Nishihata Y, Mizuki J, Akao T, Tanaka H, Uenishi M, Kimura M, Okamoto T, Hamada N (2002) Self-regeneration of a Pd-perovskite catalyst for automotive emissions control. Nature 418:164
89. Kartha KK, Pai MR, Banerjee AM, Pai RV, Meena SS, Bharadwaj SR (2011) Modified surface and bulk properties of Fe-substituted lanthanum titanates enhances catalytic activity for CO+ N_2O reaction. J Mol Catal A 335:158
90. Pai MR, Banerjee AM, Kartha K, Pai RV, Kamble VS, Bharadwaj SR (2010) Mechanism of CO + N_2O reaction via transient CO_3^{2-} species over crystalline Fe-Substituted lanthanum titanates. J Phys Chem B 114:6943
91. Kodama T, Gokon N (2007) Thermochemical cycles for high temperature solar hydrogen production. Chem Rev 107:4048
92. Onuki K, Kubo S, Terada A, Sakaba N, Hino R (2009) Thermochemical water-splitting cycle using iodine and sulfur. Energy Environ Sci 2:491
93. Barbarossa V, Brutti S, Diamanti M, Sau S, De Maria G (2006) Catalytic thermal decomposition of sulphuric acid in sulphur–iodine cycle for hydrogen production. Int J Hydrogen Energy 31:883
94. Ginosar DM, Petkovic LM, Glenn AW, Burch KC (2007) Stability of supported platinum sulfuric acid decomposition catalysts for use in thermochemical water splitting cycles. Int J Hydrogen Energy 32(4):482
95. Petkovic LM, Ginosar DM, Rollins HW, Burch KC, Pinhero PJ, Farrell HH (2008) Pt/TiO_2 (rutile) catalysts for sulfuric acid decomposition in sulfur-based thermochemical water-splitting cycles Appl Catal A 338:27
96. Nagaraja BM, Jung KD, Ahn BS, Abimanyu H, Yoo KS (2009) Catalytic decomposition of SO_3 over $Pt/BaSO_4$ materials in sulfur-iodine cycle for hydrogen production. Ind Eng Chem Res 48:1451
97. Rashkeev SN, Ginosar DM, Petkovic LM, Farrell HH (2009) Catalytic activity of supported metal particles for sulfuric acid decomposition reaction. Catal Today 139:291
98. Dokiya M, Kameyama T, Fukuda K, Kotera Y (1977) The study of thermochemical hydrogen preparation—III: an oxygen-evolving step through the thermal splitting of sulfuric acid. Bull Chem Soc Jpn 50:2657
99. Banerjee AM, Pai MR, Meena SS, Tripathi AK, Bharadwaj SR (2011) Catalytic activities of cobalt, nickel and copper ferrospinels for sulfuric acid decomposition: the high temperature step in the sulfur based thermochemical water splitting cycles. Int J Hydrogen Energy 36:4768
100. Banerjee AM, Pai MR, Tewari R, Naina Raje, Tripathi AK, Bharadwaj SR, Das D (2015) A comprehensive study on Pt/Al_2O_3 granular catalyst used for sulfuric acid decomposition step in sulfur–iodine thermochemical cycle: Changes in catalyst structure, morphology and metal-support interaction. Appl Catal B: Environ 162:327-337
101. Banerjee AM, Pai MR, Bhattacharya K, Tripathi AK, Kamble VS, Bharadwaj SR, Kulshreshtha SK (2008) Catalytic decomposition of sulfuric acid on mixed Cr/Fe oxide samples and its application in sulfur–iodine cycle for hydrogen production. Int J Hydrogen Energy 33(1):319

102. Banerjee AM, Shirole AR, Pai MR, Tripathi AK, Bharadwaj SR, Das D, Sinha PK (2012) Catalytic activities of Fe_2O_3 and chromium doped Fe_2O_3 for sulfuric acid decomposition reaction in an integrated boiler, preheater, and catalytic decomposer. Appl Catal B Environ 127:36
103. Nadar A, Banerjee AM, Pai MR, Meena SS, Pai RV, Tewari R, Yusuf SM, Tripathi AK, Bharadwaj SR (2017) Nanostructured Fe_2O_3 dispersed on SiO_2 as catalyst for high temperature sulfuric acid decomposition—Structural and morphological modifications on catalytic use and relevance of Fe_2O_3-SiO_2 interactions. Appl Catal B Environ 217:154
104. Nadar A, Banerjee AM, Pai MR, Pai RV, Meena SS, Tewari R, Tripathi AK (2018) Catalytic properties of dispersed iron oxides Fe_2O_3/MO_2 (M= Zr, Ce, Ti and Si) for sulfuric acid decomposition reaction: Role of support. Int J Hydrogen Energy 43:37
105. Nadar A, Banerjee AM, Pai MR, Meena SS, Patra AK, Sastry PU, Singh R, Singh MK, Tripathi AK (2021) Immobilization of crystalline Fe_2O_3 nanoparticles over SiO_2 for creating an active and stable catalyst: A demand for high temperature sulfuric acid decomposition. Appl Catal B Environ 283:119610
106. Jin X, Dang L, Lohrman J, Subramaniam B, Ren S, Chaudhari RV (2013) Lattice-matched bimetallic CuPd-graphene nanocatalysts for facile conversion of biomass-derived polyols to chemicals. ACS Nano 7(2):1309

Chapter 18
Synthesis—Activity Correlations Established for TiO_2 Based Photocatalysts

Sushma A. Rawool, Mrinal R. Pai, Rajendra V. Singh, Atindra Mohan Banerjee, and Arvind K. Tripathi

Abstract Photocatalysis is one of the promising technologies that can harvest solar energy for various applications: production of solar fuels, removal of pollutants, water purification, etc. The success of process is primarily dependent on the performance of the photocatalyst. Conventionally, bulk titanium dioxide (TiO_2) was considered as a robust, cheap, and UV light active photocatalyst. In last few decades, newer synthesis methodologies helped in evolution of TiO_2 as a photocatalyst. The photocatalytic properties of nano (0D, 1D, 2D), single atom, defected TiO_2 are unique. Present chapter deals with the photocatalytic reactions and impact of the synthesis methodologies on photocatalytic properties of the TiO_2. It is mainly divided in three parts. First part of chapter introduces the general scheme of processes involved, thermodynamic selection criteria and suitability of a photocatalyst. A brief overview of selected promising photocatalytic systems from literature is given. Second part provides synthetic protocols to prepare bulk, nano titania of different dimensions, and single atom dispersed photocatalysts. It discusses variation of the electric, optical, and surface properties based on the dimensionality and nature of the catalyst. The synthesis method—physicochemical property—photocatalytic activity correlations for TiO_2 based photocatalysts involved in different applications are established. Finally, the developments in our laboratory towards improving the sunlight driven photocatalytic hydrogen yield by introducing various modifications in TiO_2 are discussed.

Keywords Photocatalysis · Nano TiO_2 · Single atom · Hydrogen · Synthesis

S. A. Rawool · M. R. Pai (✉) · R. V. Singh · A. M. Banerjee · A. K. Tripathi
Chemistry Division, Bhabha Atomic Research Centre, Mumbai 400085, India
e-mail: mrinalr@barc.gov.in

Homi Bhabha National Institute, Anushaktinagar, Mumbai 400094, India

A. K. Tyagi and R. S. Ningthoujam (eds.), *Handbook on Synthesis Strategies for Advanced Materials*, Indian Institute of Metals Series,
https://doi.org/10.1007/978-981-16-1803-1_18

18.1 Introduction

Energy requirements of world's population are majorly fulfilled by the non-renewable fossil fuels. The world's energy demand is growing continuously due to ever increasing urbanization and industrialization. The use of fossil fuels is limited by its scarcity and emissions of greenhouse gases (GHG) on combustion. Thus, extensive research is going on to replace fossil fuels with sustainable, environment friendly fuels [1].

Solar energy is one of the most abundant sources of renewable energy with 1.73×10^5 terawatts (TW) power irradiating earth continuously. This amounts to four orders of magnitude higher than the current global human energy consumption (18.5 TW) and therefore can easily suffice the global demands. However, the variance in solar flux with season, time, and geographical location is a major limitation in its application. Intermittency issues can be resolved either by storage or conversion into another form. Photovoltaic cells convert solar energy directly into useful electrical output. Photovoltaic cells though efficient, but costlier than the fossil fuels and also its transportation to the remote places is challenging [2].

Another approach found suitable to harvest solar energy is to store it in form of solar fuels; hydrogen from water and hydrocarbons from CO_2 reduction. Among fuels, hydrogen has very high calorific value, yields 141.8 kJg^{-1} (three times that of gasoline ~40 kJg^{-1}) on combustion accompanied with water vapor and devoid of any GHG emissions. Photocatalytic water splitting is a process in which solar energy is utilized to split water molecules and produce hydrogen as energy carrier. Absorption and conversion of solar energy with the help of a photocatalyst is an effective technique for the generation of sustainable fuels at room temperature. Thermally, the water splitting is not feasible as it requires temperature more than 2500 K. Conversion of CO_2 into hydrocarbons photocatalytically is another thrust area as it offers a practical solution to tackle the adverse climatic change occurred due to rising levels of CO_2 in atmosphere [3]. These CO_2 derived hydrocarbons can be utilized further as a fuel in a closed cycle [4]. Dye degradation, abatement of volatile organic compounds (VOCs) present in atmosphere to harmless products, and water purification are some other important applications of photocatalysis.

18.1.1 Background

Photocatalytic water splitting is a chemical reaction driven by solar energy used to dissociate water molecules into H_2 and O_2 in presence of a photocatalyst. It mimics photosynthesis by green plants hence referred as artificial photosynthesis. Verne, in 1874 predicted that hydrogen will be futuristic fuel and would be produced from water and solar energy, therefore termed water as 'future coal' [5]. Ciamicin, in 1912 [6], suggested the application of sunlight for photochemical reactions involving generation of O_2 and CH_4 from water and CO_2, respectively. Bard, [7] referred

water splitting by sunlight as "holy grail". During 1972, Fujishima and Honda [8] performed an historical experiment in which photoelectrochemical water splitting was demonstrated over n- type TiO_2 (rutile) electrode under light illumination. When light shines on TiO_2 electrode, electrons and holes are produced, the electrons travel to the platinum counter electrode and reduce water to produce H_2. The holes on the TiO_2 electrode oxidize water to give O_2. At the same time in 1978, first report on photoelectrochemical CO_2 conversion to formic acid, formaldehyde, and methane under UV–visible light illumination using single crystal gallium phosphide were reported by Halmann et al. [9]. Inoue et al. [10] in 1979 reported the photocatalytic CO_2 conversion using different metal oxides/non-oxides like WO_3, TiO_2, CdS, GaP, SiC, and ZnO under UV–visible light illumination. Subsequently, large number of investigations was carried out in the field of photocatalytic hydrogen generation and CO_2 conversion, using different metal oxide and non-oxide semiconductors.

18.1.2 Processes Involved

Photocatalytic reactions can be homogeneous as well as heterogeneous in nature. Till date several kinds of homogeneous catalysts [11–13] such as Pt, Ni, Fe, and Co complexes as well as heterogeneous catalysts [14–16] such as metal oxide, nitride, sulfide, and oxysulfide are well studied for photocatalytic reactions. In order to scale up the reaction and for efficient utilization of the solar energy heterogeneous catalysis is more advantageous as compared to homogeneous catalysis. The scope of present chapter is limited to heterogeneous photocatalysis. In heterogeneous photocatalysis, sequence of processes that take place during light illumination is described here and pictorially shown in Fig. 18.1. (i) Absorption of light and generation of charge carriers e^- and h^+. When a semiconductor is illuminated with a light source (energy equal or more than band gap) it absorbs photons and charge carriers are generated. (ii) Separation of charges takes place by transfer of electron from valence band (VB) to conduction band (CB) leaving behind hole in the VB, (iii) transfer of electron and hole to the surface of the semiconductor, and (iv) utilization of electron and hole to carry out the reduction and oxidation reactions, respectively.

The electron and hole thus generated can be used to drive reduction and oxidation of the reactant molecules. These reactions are similar to an electrolysis where reduction and oxidation occurs at different electrodes. Thus in powdered photocatalyst each particle behaves as a small electrochemical cell.

18.1.3 Thermodynamic Criterion for Selection

Reduction potential (E^0 V vs. Normal hydrogen electrode (NHE) at pH 7) required to form various compounds are given below:

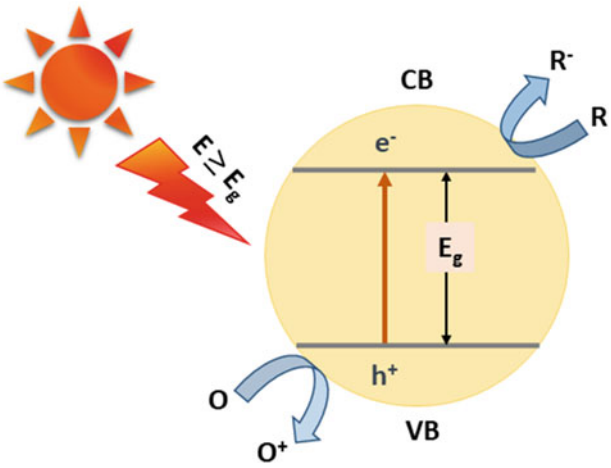

Fig. 18.1 Schematic representation of photocatalytic reaction using TiO_2 (CB: conduction band, VB: valence band, R: chemical undergoing reduction reaction, and O: chemical undergoing oxidation reaction, Eg: band gap of semiconductor)

$$CO_2 + e^- \rightarrow CO_2^- \quad E^0 = -1.90\,V \tag{18.1}$$

$$CO_2 + 2H^+ + 2e^- \rightarrow HCOOH \quad E^0 = -0.61\,V \tag{18.2}$$

$$CO_2 + 2H^+ + 2e^- \rightarrow CO + H_2O \quad E^0 = -0.53\,V \tag{18.3}$$

$$CO_2 + 4H^+ + 4e^- \rightarrow HCHO + H_2O \quad E^0 = -0.48\,V \tag{18.4}$$

$$CO_2 + 6H^+ + 6e^- \rightarrow CH_3OH + H_2O \quad E^0 = -0.38\,V \tag{18.5}$$

$$CO_2 + 8H^+ + 8e^- \rightarrow CH_4 + 2H_2O \quad E^0 = -0.24\,V \tag{18.6}$$

$$2H^+ + 2e^- \rightarrow H_2 \quad E^0 = -0.41\,V \tag{18.7}$$

$$2H_2O \rightarrow O_2 + 4H^+ + 4e^- \quad E^0 = +0.81\,V \tag{18.8}$$

Based on the above reduction potentials and the band potentials (VB and CB) a semiconductor possess, it is selected to be a photocatalyst for a CO_2 reduction and hydrogen generation. For example, for water splitting, a photocatalyst should fulfill following minimum thermodynamic requirements.

(i) The conduction band minima must be more negative than the reduction potential of water, i.e., 0 V vs. NHE at pH = 0 and maxima of the valence band must be more positive than the oxidation potential of water, i.e., 1.23 V vs. NHE at pH = 0. Therefore, the minimum band gap required to bring the overall water splitting is 1.23 eV which corresponds to the wavelength ~1100 nm. However, there is a barrier that the electron needs to overcome during the charge transfer process between photocatalyst and water molecules. Hence, energy greater than 1.23 eV is needed to drive the reaction. A photocatalyst having a band gap around 2 eV is preferred. This energy corresponds to wavelength in visible region thus making it possible to carry out reaction using solar energy.

(ii) The photogenerated e^{-}-h^{+} pair transfer rate must be faster than their recombination rate.

(iii) A photocatalyst should not undergo corrosion during reaction, and it must be stable at least up to ten years of use.

(iv) The intermediates and the product formed during evolution of H_2 and O_2 may recombine back to give reactants. Photocatalyst should not promote such kind of back reactions.

18.1.4 Evaluation of Photocatalytic Activity

Photocatalytic activity generally expressed as number of moles of hydrogen produced per gram of photocatalyst per unit time. Amount of hydrogen evolved depends on many factors such as flux of light, reaction time, reactor geometry, and illumination area. If experimental parameters such as type of light source and reaction cell are different, then it is difficult to compare the H_2 yield from lab to lab. Hence, determination of quantum efficiency (ratio of number of electrons produced to the number of photons absorbed by the system) is important. It is difficult to determine the number of photons absorbed by the photocatalyst, but it is possible to determine the number of photons incident on it by a luxmeter. Hence, the determined quantum efficiency is the **apparent quantum efficiency** (AQE, η). AQE is expected to be lower than the real QE because it takes into account only the incident photons which are higher in number than the absorbed photons. AQE is calculated by using following equation:

$$\eta(\%)\frac{2 \times \text{Number of } H_2 \text{ molecules evolved}}{N} \times 100 \tag{18.9}$$

where N is number of photons incident on the reactor.

Solar to fuel efficiency (SFE): The other parameter to evaluate the efficiency of the catalyst is solar to fuel efficiency (SFE). It is given as follows:

$$\text{SFE} = \frac{r\text{H}_2 \times \Delta H}{P_{sun} \times \text{S}} \times 100 \tag{18.10}$$

where rH_2 is the hydrogen production rate (mol/h), P_{sun} is the solar light energy flux (W/m^2), ΔH is enthalpy of water splitting reaction and S is the illumination area of the reactor (m^2).

18.1.5 Overview of the Literature Reports for Photocatalytic Hydrogen Generation

Researchers have put tremendous efforts in finding a photocatalyst formulation that can demonstrate water splitting with required AQE and can sustain hydrogen yield for long durations. In search of low cost, active semiconductor materials with optimized properties, such as minimized overpotentials for catalysis, narrow band levels for visible-light absorption, and stability, various metal oxide and non-oxides, are extensively investigated and reported in last few decades. Out of which few systems have shown promising results as listed in Table 18.1.

There are innumerable semiconductors of different classes such as metal oxides, sulfides, nitrides, and oxynitrides developed for various photocatalytic applications. Among all types, TiO_2 has gained tremendous attention as it is chemically stable, environmentally friendly, non-toxic, and inexpensive. The valence band of TiO_2 is comprised of O 2*p* states, while conduction band is composed of titanium 3*d* states. The band edge potentials, crystal structure, electronic, and optical properties of TiO_2 are such that it can carry out different photocatalytic reactions and makes it a promising photocatalyst [15].

18.1.6 Aim and Scope

TiO_2 is considered to be cheap, robust, nontoxic, and stable conventional photocatalyst. Over the decades it has been evolved into nano titania of different dimensions and as a support for single atom dispersed catalysts with unique photocatalytic properties. The present chapter illustrates the role of synthesis in development of TiO_2 photocatalysts for various applications. It is mainly divided in three segments. First part of chapter introduces general features of photocatalytic reactions and emphasizes its importance in harvesting solar energy for various applications. Second part discusses the impact of synthesis methods for the generation of nano TiO_2 with different dimension and effect of different morphology and shape of nanoparticles on the photocatalytic activity of TiO_2. It also discusses different synthesis strategies employed with examples to overcome the disadvantages of TiO_2—such as poor light absorption in visible region of sunlight and inefficient separation of charge carriers—leading to improved photocatalytic properties. It also establishes synthesis—photocatalytic activity correlations in nano and single atom TiO_2 based photocatalysts. Third and

Table 18.1 Photocatalyst systems, hydrogen yield obtained, light source, and other experimental conditions are listed below [17–28]

Sr. no	Photocatalyst	Co-catalyst	Light source	Reaction conditions	H_2 yield	AQE/SFE	Reference
1	$(Ga_{(1-x)}Zn_x)(N_{(1-x)}O_x)$ [17]	$Rh_{2-y}Cr_yO_3$	High pressure Hg lamp (450 W) with aq $NaNO_2$ as filter ($\lambda > 400$ nm)	300 mg photocatalyst dispersed in 370 ml of aqueous H_2SO_4, pH adjusted to 4.5	H_2: 927 μmol/h O_2: 460 μmol/h	AQE 5.9% at 420–440 nm	[17]
2	CdS [18]	Pt-PdS	Xe-lamp (300 W, $\lambda > 420$ nm)	300 mg of photocatalysts powder suspended in 200 mL of 0.5 M Na_2S-0.5 M Na_2SO_3 solution	8.77 mmol/h	AQE 93%	[18]
3	Black TiO_2 [19]	Pt	Solar simulator	20 mg photocatalyst dispersed in 1:1 water: methanol solution	10 mmol/h/g	SFE 24%	[19]
4	CoO [20]	No cocatalyst	Solar simulator	25 mg photocatalyst dispersed in water	20 ml in 30 min	SFE 5%	[20]
5	Carbon/TiO_2/Carbon nanotube [21]	Pt	Solar simulator (AM 1.5G filter)	10 mg photocatalyst dispersed in 120 ml of 1:1 water: ethanol solution	37.6 mmol/h/g	AQE = 95% at $\lambda <$ 340 nm& 1.5% at 430 nm	[21]
6	Carbon dots/g-C_3N_4 [22]	No cocatalyst	Xe-lamp (300 W, $\lambda > 420$ nm)	80 mg photocatalyst dispersed in 150 ml water	H_2: 45.3 μmol/h O_2: 22.7 μmol/h	SFE 2% AQE 16%	[22]
7	La/$NaTaO_3$ [23]	NiO	High pressure Hg lamp (400 W)	1 g of catalyst dispersed in 390 ml of pure water	H_2: 19.8 mmol/h O_2: 9.66 mmol/h	AQE 56% (at 270 nm)	[23]

(continued)

Table 18.1 (continued)

Sr. no	Photocatalyst	Co-catalyst	Light source	Reaction conditions	H_2 yield	AQE/SFE	Reference
8	Hf doped (Na, K)TaO_3 [24]	No cocatalyst	High pressure Hg lamp (350 W)	0.1 g dispersed in 350 ml pure water	H_2: 4.96 mmol/h O_2: 2.46 mmol/h	Not given	[24]
		No cocatalyst	High pressure Hg lamp (350 W)	0.1 g dispersed in 300 ml pure water and 50 ml of methanol	25.6 mmol/h	Not given	
9	ZrO_2–TaON and WO_3 [25]	Pt	Xe lamp, (300 W, 420 < λ < 800 nm)	100 mg of Pt/WO_3 and 50 mg of Pt/ZrO_2/TaON; 100 ml NaI	H_2: 32.6 μmol/h O_2: 15.6 μmol/h (420 < λ < 800 nm)	AQE 6.3% at 420.5 nm	[25]
10	$BiVO_4$:In, Mo [26]	RuO_2	Hg arc lamp (500 W)	0.3 g of photocatalyst in 100 ml of water	H_2: 17 μmol/h	AQE 3.2% (at 420–800 nm)	[26]
11	GaN:Mg/InGaN:Mg [27]	Rh/Cr_2O_3	Xe lamp (300 W, AM 1.5G, 26 suns)	0.48 mg sample deposited over 3 cm^2 glass plate and immersed in water	H_2: 3.46 mol/h/g O_2: 1.69 mol/h/g	AQE: 12.3% (400–475 nm), SFE: 1.8%	[27]
12	$SrTiO_3$:Al [28]	Rh/CrOx, CoOOH	Xe lamp (300 W)	0.1 g sample dispersed in 100 ml of water	H_2: 3.54 mmol/h/g O_2: 1.78 mmol/h/g	AQE = 96% at (350–360 nm), SFE: 0.65%	[28]

last part briefly presents the synthesis strategies and modifications adopted in our laboratory to enhance the solar hydrogen yield using TiO_2 based photocatalysts.

18.2 Bulk TiO_2 as a Photocatalyst

Anatase, rutile, and brookite phase are three polymorphs of TiO_2 which occurs naturally [29, 30]. Both anatase and rutile phases of TiO_2 show tetragonal crystal system consist of chains of distorted TiO_6 octahedral structure. Along with these polymorphs, TiO_2 can exist in α-PbO_2-type structure (orthorhombic structure) at high pressure around 0.8 to 10 GPa [31]. At pressure higher than 20 GPa, formation of baddelleyite with ZrO_2 structure and cotunnite with $PbCl_2$ structure has been reported [32, 33]. In addition, TiO_2 (I) ramsdellite, [34] TiO_2 (B) monoclinic [35], and TiO_2 (H) hollandite [36] are also reported. TiO_2 (I) ramsdellite was synthesized by soft chemical method in which lithium ions extracted and oxidized from $Li_{0.5}TiO_2$ using 1 M HCl. Hydrothermal method has been reported for the synthesis of TiO_2 (B) (monoclinic) [35]. TiO_2 (H) hollandite was synthesized by oxidation–ion extraction process using hollandite $K_{0.21}TiO_2$ [36]. Table 18.2 lists the synthetic procedures adopted to prepare polymorphs of TiO_2 and their typical structure.

Rutile is thermodynamically stable phase among the three naturally occurring polymorphs of TiO_2, whereas the other two phases, i.e., anatase and brookite are the metastable states. Anatase phase gets transformed into rutile phase above 600 °C [37]. TiO_6 octahedra is more distorted in anatase phase in comparison to the rutile phase. Structural difference in anatase and rutile results in different electronic band alignment. Anatase and rutile possess the band gap of 3.2 and 3.0 eV, respectively. Pristine Brookite form is difficult to synthesize hence scarcely reported [38]. Formation of different phases depends on the synthesis conditions as shown in Table 18.1. In ancient times TiO_2 were used as a white pigment [39]. Before knowing the photocatalytic properties of TiO_2, it was reported for dye bleaching in vacuum as well as in oxygen atmosphere in 1938 [40]. In this report, TiO_2 was referred as photosensitizer. It remains unaltered during UV light irradiation and produces the active oxygen species that causes bleaching of dye [40]. Also, in 1956 the photooxidation properties of TiO_2 were invaded [41], and it was concluded that the anatase phase was more photocatalytically active as compared to the rutile phase of TiO_2. The photocatalytic properties of TiO_2 came into light after the historical experiment by Fujishima and Honda in 1972 [8]. In which photon assisted splitting of water was demonstrated using a photoanode made up of single crystal wafer of n-type rutile phase of TiO_2 under UV light illumination. Since then, many modifications were done to further improvise the photocatalytic properties of TiO_2.

Bulk materials with micrometer sized particles show the low surface area, and photogenerated electron–hole pair needs to travel larger distance, thus limits the photocatalytic activity. Downsize of the micron particle to the nanometer scale opens up new avenue for exploring the different physico-chemical properties of the material. The electronic, surface, and optical properties of the material affected while

Table 18.2 Synthesis methods, crystal structure, space group, and band gap of different polymorphs of TiO_2 are listed below

Phase of TiO_2	Synthesis method	Crystal system	Space group	Band gap (eV)	References
Anatase	Sol gel, Hydrothermal method	Tetragonal	$I4_1/amd$	3.2	[16, 29, 30]
Rutile	Sol gel, Hydrothermal method	Tetragonal	$P4_2/mnm$	3.0	[16, 29, 30]
Brookite	Hydrothermal method	Orthorhombic	Pbca	3.3	[16, 30]
α-PbO_2-type phase	High pressure around 0.8–10 Gpa	Orthorhombic	Pbcn	NA	[31]
Baddelleyite	At pressure higher than 20 Gpa	Monoclinic with ZrO_2 structure	$P2_1/c$	NA	[32]
Cotunnite	At pressure higher than 20 GPa	With $PbCl_2$ structure	Pnma	NA	[33]
TiO_2 (R) (ramsdellite)	Li ion extraction and oxidation from the ramsdellite-type $Li_{0.5}TiO_2$ by 1 M HCl treatment	Orthorhombic	Pbnm	3.34	[34]
TiO_2 (B) (monoclinic)	Hydrothermal synthesis	Monoclinic	C2/m	NA	[35]
TiO_2 (H) (hollandite)	Oxidation–ion extraction process using hollandite $K_{0.21}TiO_2$	Tetragonal	*I4/m*	NA	[36]

*NA: the data on band gap value was not found for pure phase to the best of our knowledge

moving from micron size bulk particle to the nano size dimension to the single atom. As TiO_2 is evolved from bulk to nanoparticles to nanoclusters, its absorption characteristic (λmax) also decreased from 400 to 250–300 nm [42]. Anpo et al. [43] in 1987 first time reported the impact of the particle size on photocatalytic properties. Along with increase in particle size with calcination temperature, significant change in the absorption and photoluminescence spectra was also observed. It was found that the quantum yield for photocatalytic hydrogenation reaction of unsaturated hydrocarbons with H_2O increased significantly for small particles having particle size below 10 nm.

In case of small particle size, the photogenerated charge carriers have to travel shorter distance from bulk to the surface active sites. This resulted in decrease in recombination probability of the charge carriers and thus improved photocatalytic performance. Along with particle size, crystallinity and surface area are the important factors which govern the photocatalytic properties of the photocatalyst. During synthesis of nanoparticles, defects in addition to grain boundaries form which can act as a recombination centers for photogenerated e^--h^+ pair. Generally, calcination at high temperature is needed to eliminate the grain boundaries and annihilate the defects. With increase in calcination temperature particle size increases and also the crystallinity of the material, but it leads to decrease in surface area of the material as a result of agglomeration of the nanoparticles at high calcination temperature. Therefore, optimization of the surface area, particle size along with crystallinity of the nanoparticles is necessary to improve the photocatalytic conversion. In our earlier study, we synthesized indium titanate by solvothermal method at 220 °C using titanium isopropoxide and indium acetate as titanium and indium precursors, respectively [44]. The correlation between photocatalytic activity for hydrogen generation and surface area and crystallinity of nanoparticles of the indium titanate were established. It was found that with increase in calcination temperature the photocatalytic activity increased and reached maximum for nanoparticles calcined at 800 °C having a surface area of $\sim$38 m^2 g^{-1} with optimum crystallinity. While on further increase in calcination temperature beyond 800 °C, photocatalytic activity deteriorated.

18.3 Nano TiO_2

Nanomaterial is defined as the material possessing at least one of the dimensions in the 1–100 nm range. Pokropivny and Skorokhod classified the nanomaterials as 0D, 1D, 2D and 3D [45]. Nanomaterials are classified as zero dimensional (0D), one dimensional (1D), two dimensional (2D), and three dimensional (3D) on the basis of dimensions. Zero dimensional nanomaterials (0D) include spherical nanoparticles. One dimensional nanomaterials (1D) include nanowires, nanotubes, nanorods, and nanobelts. Two dimensional nanomaterials (2D) include nanosheets, whereas three dimensional nanomaterials (3D) includes bulk powders, bundles of nanowires and nanotubes, and multi-nanolayers and porous nanostructure.

TiO_2 nanoparticles were synthesized in different forms. Synthesis methods have significant influence on the dimension of the nanomaterials. Also, the electrical, optical, and surface properties of the nanomaterials can be altered by adopting different synthesis methods. As explained in the previous chapter, the synthesis methods of nanomaterials are divided into two parts: chemical methods and physical methods. Chemical methods include bottom-up approach and the physical methods deals with the top-down approach. As explained in the previous chapter, physical methods include gas condensation techniques, spray pyrolysis, ball milling, and aerosol processes, and flame decomposition of metal-organic precursor and chemical methods include sol–gel method, reverse microemulsion/micelle method, and wet

chemical synthesis methods. Physical methods are preferred over chemical methods as the material can be synthesized in a large quantity. However, the demerit of physical methods is that one can generate particles of sizes in tens of nanometers only. Whereas using chemical methods the particle size can be tuned to even less than 10 nm and can approach atomic scale [46]. However, the demerit of chemical methods is that it produces nanoparticles in small quantities. Physical vapor synthesis, laser pyrolysis, mechanical milling, spray pyrolysis, and sol–gel methods are some of the synthesis methods adopted to industrially scale up the nanoparticle production [47]. Most researchers compare the photocatalytic activity of their photocatalysts with commercially available Degussa P25 as a benchmark and have reported the compared activities. Degussa (Evonik) P25 is a commercially available TiO_2 photocatalyst containing crystalline phases of anatase, rutile and amorphous phase in the proportion of 78:14:8, respectively and this formulation was found to be possessing very high photocatalytic activity for many reactions [48]. P25 is white color titania powder, in which both high temperature (rutile) and a low temperature phase (anatase) coexists. Moreover, it is not a mechanical mixture of both the phases, then curiosity arises to know about the synthetic method which has resulted in both high and low temperature phases at the same time. P25 is synthesized using aerosol flame pyrolysis process having particle size of 21 nm and 50 $m^2\ g^{-1}$ surface areas [49].

Among all the methods, chemical methods are well suited for the synthesis of nanoparticles for photocatalytic application as the control over size, phase, and surface area is easy to achieve [46]. The synthesis of TiO_2 nanoparticles with different dimensions by using chemical methods and the role of synthesis methods in altering the physico-chemical and photocatalytic properties of TiO_2 is explained in next sections of this chapter.

18.3.1 Zero Dimensional TiO_2

Chemical methods, like sol gel, hydrothermal, and solvothermal methods are generally used for the synthesis of nano and microspheres of TiO_2. Cargnello et al. [46] summarized the synthesis methods used to prepare quasi-zero-dimensional TiO_2 nanocrystals.

We also attempted to synthesize 0D TiO_2 nanoparticles and observed that photocatalytic activity dramatically changes on varying the synthesis conditions. Here, sol–gel method was selected for the synthesis of 0D TiO_2 nanoparticles. Synthesis of TiO_2 nanoparticles was done under acidic condition and in presence of non-ionic ligand like ethylene glycol. TiO_2-E was synthesized using tetrabutyl titanate as titanium precursor and ethylene glycol as non-ionic ligand. In similar way, TiO_2-1 and TiO_2-2 were synthesized using same protocol as TiO_2-E but without ethylene glycol for comparison. Unlike TiO_2-1, TiO_2-2 was synthesized under acidic conditions. Faceted nanoparticles were formed and seen in TEM images of TiO_2-E sample synthesized using ethylene glycol. While in case of TiO_2-1 sample, irregular shaped particle was observed. Extended X-ray absorption fine structure (EXAFS) studies

revealed that the Ti–O and Ti–Ti bond lengths were higher with lower disorder in TiO_2-E as compared to other TiO_2 samples. All the samples were evaluated for photocatalytic H_2 generation. TiO_2-E showed highest activity for H_2 generation at the rate of 476 μmol h^{-1} g^{-1} under sunlight illumination achieving 2.2% AQE (Fig. 18.2). Dispersal of 1 w/w% Pt as cocatalyst over surface of TiO_2-E, rate of H_2 generation further enhanced to 3382 μmol h^{-1} g^{-1} under sunlight illumination with AQE 15.9%. The improvement in the photocatalytic activity of TiO_2-E was attributed to the presence of crystalline anatase phase with increased surface area and porosity and modified local structure (increased bond length and reduction in lattice disorder as revealed by EXAFS) of TiO_2.

During 2013, Pan et al. [50] synthesized the defect free TiO_2 nanosheets decorated with 0D quantum dots of anatase TiO_2 using hydrothermal route. In this work, a solution of tetrabutyl titanate and hydrofluoric acid (HF) solution was hydrothermally treated at 180 °C by varying the reaction time (t = 24, 72 and 168 h). It was found that the 24 h of hydrothermal treatment produces nanosheets and 72 and 168 h

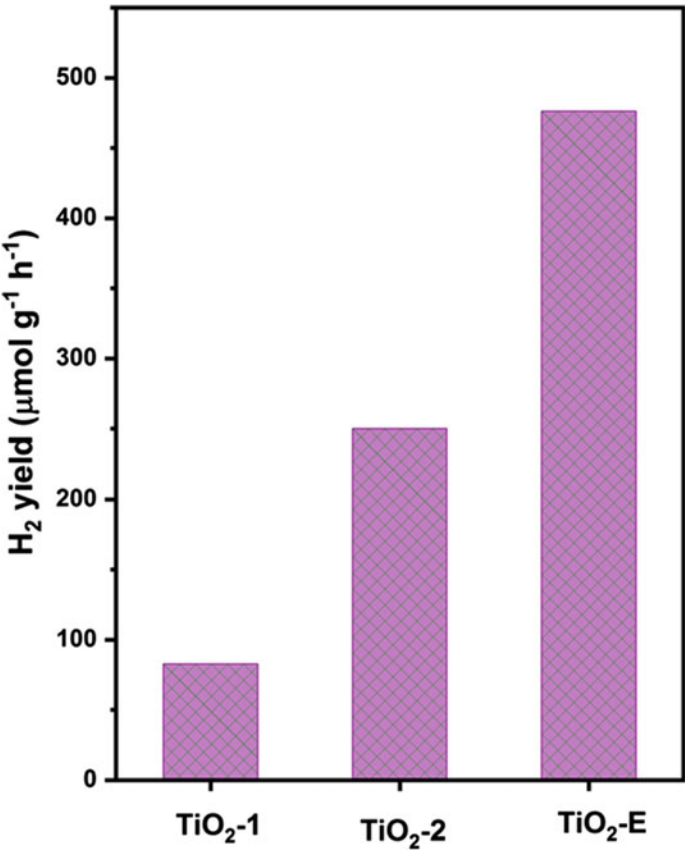

Fig. 18.2 Comparison of photocatalytic hydrogen yield evolved over different TiO_2 samples

treatment produces nanosheets decorated with the nanodots of 1.5–3 nm size and with further increase in hydrothermal treatment time, concentration of nanodots increased. Band gap of 72 and 168 h treated samples was blue shifted in comparison to the clean nanosheets (24 h). The photocatalytic performance for Rhodamine B (RhB) dye degradation was evaluated for different samples. It was found that the catalytic activity was highest for 168 h sample having more number of TiO_2 quantum dots. In order to get rid of surface defects, the sample was hydrothermally treated in water at 100 °C for 24 h or calcined at 500 °C. Improvement in photoactivity for Rhodamine B dye degradation after hydrothermal as well as calcination treatment was observed. The nanosheets decorated with quantum dots provided a new charge transfer pathway as compared to the pure nanosheets. The transfer of the photogenerated electron occurred from {001} facets of nanosheets to the quantum dots, thus reduced the recombination of charges and improved the photocatalytic activity. This suggested that tailoring of local surface structure is an effective synthetic strategy to improve the activity.

Inducing surface/sub-surface defects improved the light absorption as well as charge separation properties of quantum dots of rutile TiO_2 as reported by Li et al. [51]. 10 nm sized rutile particles were synthesized by direct hydrolysis of $TiCl_4$ solution and calcination at 473 and 673 K. Rapid hydrolysis and evaporation steps in the presence of high concentration of chloride ions resulted into formation of nanoparticles instead of nanorods and also generated defects in the nanoparticles. The presence of defects improved the visible light absorption as compared to other rutile synthesized by hydrothermal route. Among all samples, 473 K calcined sample exhibited highest photocatalytic hydrogen generation at 1954 $\mu mol\ h^{-1}\ g^{-1}$ under simulated solar light using 1 wt% Pt as cocatalyst. An upward shift of 0.3 eV in the valence band edge was observed in the sample calcined at 473 K thus, enhancing photoresponse in visible region. The improved photocatalytic activity of 10 nm rutile TiO_2 synthesized by hydrolysis route was attributed to the existence of the surface defects, i.e., hydroxyl group on the surface which resulted into narrowing of band gap and improved charge carrier separation.

18.3.2 One Dimensional TiO_2

1D TiO_2 nanomaterials include nanorods, nanowires, nanotubes, and nanobelts. Sol–gel template method, hydrothermal method, solvothermal method, and electrochemical oxidation are used for the synthesis of nanorods, nanowires, and nanotubes. Wang et al. [52] reviewed the synthesis and growth mechanism of 1D nanomaterials and also includes the morphology assisted properties and application of the 1D TiO_2 nanomaterials. For the synthesis of 1D structure, hydrothermal method is the most commonly used. Hydrothermal synthesis of TiO_2 nanorods offers several advantages such as i. formation of product at relatively lower temperature thus preventing agglomeration of the nanorods, ii. high purity of the product due to recrystallization

in the hydrothermal solution, and iii. TiO_2 with different morphology and structure can be easily synthesized by changing the reaction conditions [53].

1D nanorods with different exposed crystal facets have gained tremendous attention, as the electron and hole can be driven to the different facets to carry out the reduction and oxidation reaction, respectively. This occurs because of the different atomic arrangement at the exposed facets which resulted into different surface energy levels of the conduction bands and valence bands. Yang et al. [53] synthesized the nanorods of TiO_2 having rutile, anatase, and brookite phase with different facets by hydrothermal synthesis using peroxide titanic acid (PTA). It was found that pH of the solution plays a critical role in deciding the crystal phase of TiO_2. The amount of hydroxyl group and their position in the complex decides the formation of the different phases at different pH. Rutile phase TiO_2 nanorods formed when the pH of PTA was lower than 10, due to the presence of neutral $Ti_2O_5(OH)_2(H_2O)_4$ or cationic $Ti_2O_5(H_2O)_6^{2+}$ condensing complexes. At lower pH, number of hydroxyl group were less and thus corner shared bonding was preferred, thus rutile phase was dominant. At pH higher than 10, anatase phase was formed due to the presence of anionic $Ti_2O_5(OH)_4(H_2O)_2^{2-}$ condensing species. The anionic species contained a greater number of hydroxyl groups which enhanced the probability of edge sharing and crystallization of anatase phase. Whereas, at pH 10 the presence of neutral species facilitated both edge sharing and corner sharing leading to crystallization of brookite phase. Figure 18.3 shows the TEM images of the nanorods synthesized at different pH conditions. Rutile TiO_2 nanorods efficient in photocatalytic oxidation of methylene blue dye while brookite phase was active for chromium ion reduction. The improved oxidation ability of rutile phase was attributed to the better spatial separation of charge carriers on different facets, while the shift of the conduction band towards cathodic potential improved the reduction ability of brookite nanorods.

Alkaline hydrothermal method is a simple and easily scalable method for the production of the 1D TiO_2 nanotubes. Peng et al. [54] synthesized the 1D TiO_2 by alkaline hydrothermal method using TiO_2 nanoparticles (P25 TiO_2) as Ti precursor and reported the impact of the synthesis conditions such as NaOH concentration, temperature, and amount of TiO_2 precursor on photocatalytic hydrogen generation using 3-factor 3-level Box Behnken design (BBD). In this synthesis method, P25 TiO_2 nanoparticles were added to NaOH solution and subjected to the hydrothermal

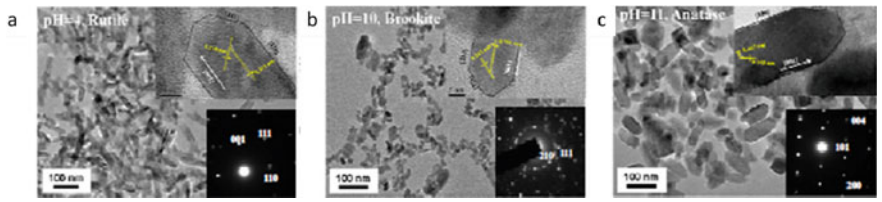

Fig. 18.3 TEM images of TiO_2 nanorods synthesized at pH equal to **a** 4, **b** 10, and **c** 11. Inset shows the HR-TEM images and SAED pattern. Reproduced with permission from Ref. [53]. Copyright 2015 American Chemical Society

treatment for 48 h. The BDD model illustrated that the reaction temperature and NaOH concentration during synthesis has substantial effect on the TiO_2 phase, crystallite size, specific surface area, band gap, and thus on photocatalytic activity. It was observed that maximum hydrogen generation was produced at the rate of 475 μmol h^{-1} under UV irradiation using 10 mg of 1D TiO_2 having anatase phase with crystallite size of around 20 nm.

18.3.3 Two Dimensional TiO_2

Exposed {001} faceted anatase TiO_2 nanosheets have attracted tremendous attention in the field of photocatalysis. The sequence of average surface energies of anatase TiO_2 is 0.90 J m^{-2} for {001} > 0.53 J m^{-2} for {100} > 0.44 J m^{-2} for {101} [55, 56]. Nanosheets can be synthesized using hydrothermal, solvothermal, chemical vapor deposition (CVD) and sol gel method [57]. Most commonly used method for synthesis of 2D TiO_2 is hydrothermal as it is simple and easy to scale up. Han et al. [58] synthesized the single crystal of anatase TiO_2 nanosheets by hydrothermal treatment using tetrabutyl titanate [$Ti(OBu)_4$] as titanium precursor and HF as a capping agent. It was revealed that the F^- ions played crucial role in formation of exposed {001} facets and also the temperature of the reaction determined the size as well as thickness of the TiO_2 nanosheets. Figure 18.4 shows the TEM images of the TiO_2 nanosheets having 77% average percentage of (001) facets. Under optimum conditions such as reaction temperature 200 °C, 5 ml of $Ti(OBu)_4$, and 0.8 ml of HF, the TiO_2 nanosheets with average percentage of 89% of (001) facets having average size of 130 nm and thickness of nearly 8 nm could be synthesized. The as synthesized

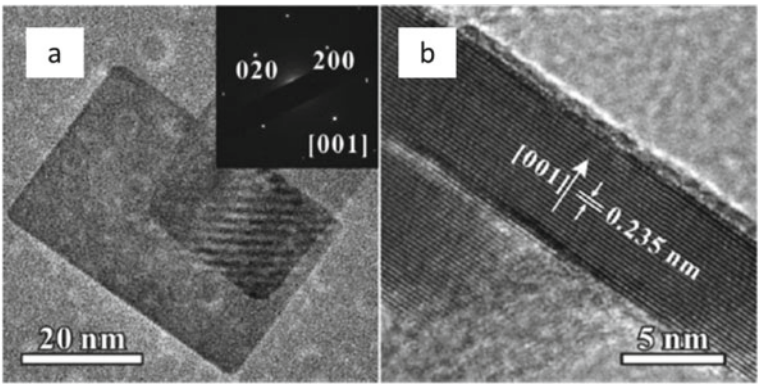

Fig. 18.4 **a** TEM image (inset shows selected area electron diffraction, SAED pattern) and **b** HR-TEM image of vertical nanosheets of TiO_2 synthesized by hydrothermal method at temperature 180 °C using 5 mL of $Ti(OBu)_4$ and 0.6 mL of HF, having 77% of average percentage of (001) facets. Reproduced with permission from Ref. [58]. Copyright, 2009 American Chemical Society

nanosheets with 89% exposed (001) facets showed improved photocatalytic activity for the methyl orange degradation.

Another strategy adapted was the synthesis of porous 2D nanomaterials with copious in-plane pores. The well-defined microstructural porous 2D nanomaterials offer benefits that are obtained by combining the property of both 2D nanomaterials and porous materials and thus improved photocatalytic properties. Song et al. [59] synthesized the 2D hollow nanoplates of anatase phase of TiO_2 by hard template method. In this case, α-Fe_2O_3 was used as a template. The ratio of anatase and rutile phase was adjusted by changing the calcination temperature. 2D hollow TiO_2 nanoplates showed improved catalytic activity for rhodamine B dye degradation, and it was attributed to the high specific surface area of 59 $m^2\ g^{-1}$ and increased number of active centers.

18.3.4 Three Dimensional TiO_2

Three dimensional TiO_2 nanomaterials (3D) include bulk powders, bundles of nanowires and nanotubes, and multi-nanolayers and porous nanostructure. Mesoporous TiO_2 structure has received tremendous interest because of the high surface area, large pore volume, tunable pore structure, and nano-confined effects [60]. These properties are advantageous in the field of catalysis as the high surface area provides, more number of surface active sites for better adsorption of reactant or intermediate formed during the process and porous structure further helps in the enhancement of reactants and products diffusion, thus facilitate the reaction kinetics.

Polshettiwar and co-workers [61] reported a solution deposition method for deposition of TiO_2 over the fibers of nanosilica (KCC-1 as a support). This synthesis protocol was developed as an alternative to the costly and complex atomic layer deposition technique. In this method, KCC-1 was used as a support and the titanium butoxide as a titanium precursor. The hydrolysis of the titanium salt was brought over the surface of the KCC-1 in the solution deposition technique. It was revealed that the high surface area, accessible active sites, and formation of Si–O–Ti increased hydrogen yield to 26.4 mmol h^{-1} per g of TiO_2 under UV light irradiation. Polshettiwar and co-workers [62] also probed the formation mechanism of TiO_2 coated fibrous nanosilica using solid-state ^{1}H, $^{47,49}Ti$ and ^{29}Si NMR, and *insitu* FTIR studies. The proposed mechanism included following steps: a. silanols present on the surface of silica deprotonated in the presence of ammonia and titanium butoxide hydrolysed to titanium hydroxide, b. lone pair of ammonia donated to Ti^{4+}ion of titanium hydroxide, c. hydroxide ions released and subsequently Si–O-Ti oxo-bridges generated by condensation of dehydroxylated titanium ions with the deprotonated silanols, d. oxy-anion of titanols formed and Ti–O-Ti generated by the reaction of oxy-anion of tiatanols with ammonia-activated titanium hydroxide molecules, and the continuation of above steps till titanium hydroxide was utilized to form titanium hydroxide coating over silica. At the time of calcination, titanols get converted into TiO_2 over the silica support.

TiO_2 hollow shells with well-defined inner cavity offer advantages such as improved diffusion of the reactants to the surface-active sites and enhanced light absorption due to multiple reflections of light within inner cavity. Eskanderloo et al. [63] reported a synthesis of hollow shell using a droplet-based microfluidic approach. In this, a single emulsion technique was used for the emulsification of oil phase having titanium butoxide (TBT), UV-curable resin ethoxylated trimethylolpropane triacrylate (ETPTA), 2-hydroxy-2-methyl-1-phenyl-1-propanone (HMPP), and aqueous phase containing 1 wt.% triblock copolymer Pluronic F108. The emulsion droplets formed undergo a phase separation, and hydrolysis of TBT takes place at the interface of the emulsion which leads to the formation of the TiO_2 shell. This shell gets ruptured and released ETPTA core and formed hollow shell of anatase TiO_2 after the post-treatments with UV, washing with isopropanol and thermal treatment. Schematic representation of different steps during the synthesis of hollow sphere of TiO_2 along with their optical microscopic images recorded at different time interval is given in Fig. 18.5a. This leads to the formation of the TiO_2 hollow shell with uniform size about 50 μm and well-defined inner cavity of around 18–20 μm. The hollow shell showed better light absorption efficiency as compared to the hollow sphere because of the multiple light reflections within inner cavity. Also, the hollow shell of TiO_2 provides high surface area and improved contact between the photocatalyst and reactant molecules. Also, Pt deposition within and outside the hollow shell showed better photocatalytic activity for methylene blue degradation than the hollow sphere or hollow shell decorated with Pt only on outer surface.

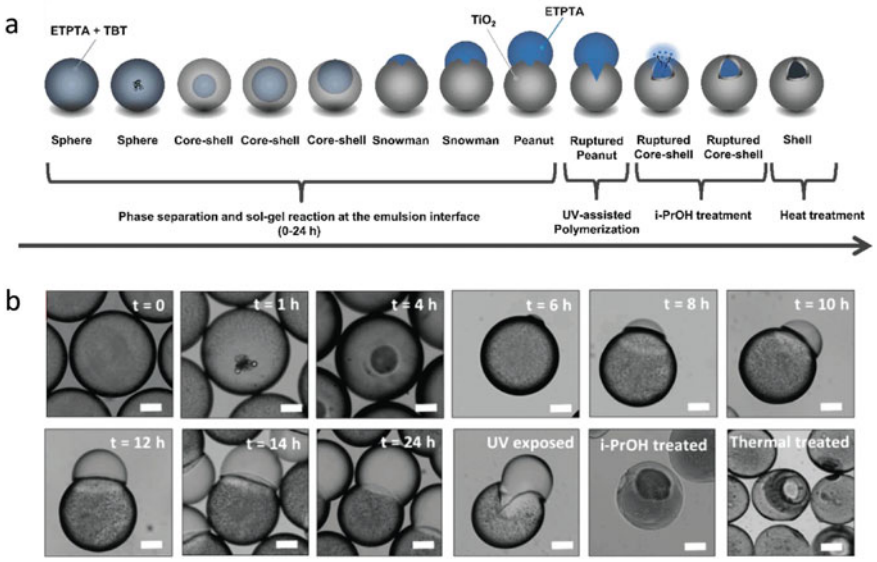

Fig. 18.5 **a** Schematic illustration of different steps during the synthesis of hollow sphere of TiO_2 **b** optical microscopic images recorded at different time intervals and steps. Reproduced with permission from Ref. [63]. Copyright 2018 Elsevier

Mesocrystals signifies the new class of nanostructured solids. A mesocrystal is defined as a superstructure of crystalline nanoparticles with external crystal faces on the scale of some hundred nanometers to micrometers [64]. Jiao et al. [65] developed a protocol for one-pot synthesis of the mesocrystals of TiO_2 with exposed {101} facets and hollow single crystal of TiO_2. In this work, hydrothermal synthesis was performed using titanium sulfate as precursor of Ti and Na_3PO_4 and HF as a morphology controlling co-mediators. The solid and hollow crystal was obtained by varying the concentration of HF used during synthesis. To understand the factors affecting the formation of hollow and mesocrystal, different additives were added systematically during hydrothermal synthesis. The presence of F^- and $PO_3{}^{4-}$ ions leads to the formation of micron meter sized crystals and 10 nm sized nanoparticles, respectively. From this, it was concluded that the presence of both F^- and $PO_3{}^{4-}$ is necessary for the growth of the hollow crystals with exposed {101} facets. The SEM and TEM images of the solid anatase TiO_2 single crystals, hollow anatase TiO_2 single crystal, and hollow anatase TiO_2 mesocrystals with exposed {101} facets are given in Fig. 18.6. Specific surface area of the solid single crystals, hollow single crystals, and hollow mesocrystals synthesized in this work were found to be 17, 35, and 42 $m^2\ g^{-1}$, respectively. It was revealed that the hollow TiO_2 structure and the mesocrystal showed highest H_2 generation and CO_2 conversion to methane as compared to the solid single crystal TiO_2. The position of the CB and VB band edges were derived from UV–vis DRS spectra and valence band XPS spectra (Fig. 18.6g). It was found that the CB and VB edges of hollow mesocrystals were higher as compared to the hollow and solid single crystal. Hence the photogenerated electrons in the CB of mesocrystals possess the higher reduction ability as compared to the solid and hollow single crystals, thus improved photocatalytic activity. The author attributed the improvement in activity to the presence of surface terminated $PO_3{}^{4-}$ species which resulted into increase in the band gap and the co-existence of major {101} and minor high-index facets on the hollow single crystals and mesocrystals which could improve the transfer of charges on different facets.

18.4 Modifications in TiO_2

Application of TiO_2 as photocatalyst is limited by its inability to absorb visible light wavelengths of sunlight and high rate of recombination reaction [16, 29, 37]. Metal loading, cationic and anionic doping, composite formation and dye sensitization are most commonly used strategies to improve the photoresponse of TiO_2 towards visible wavelengths as discussed below.

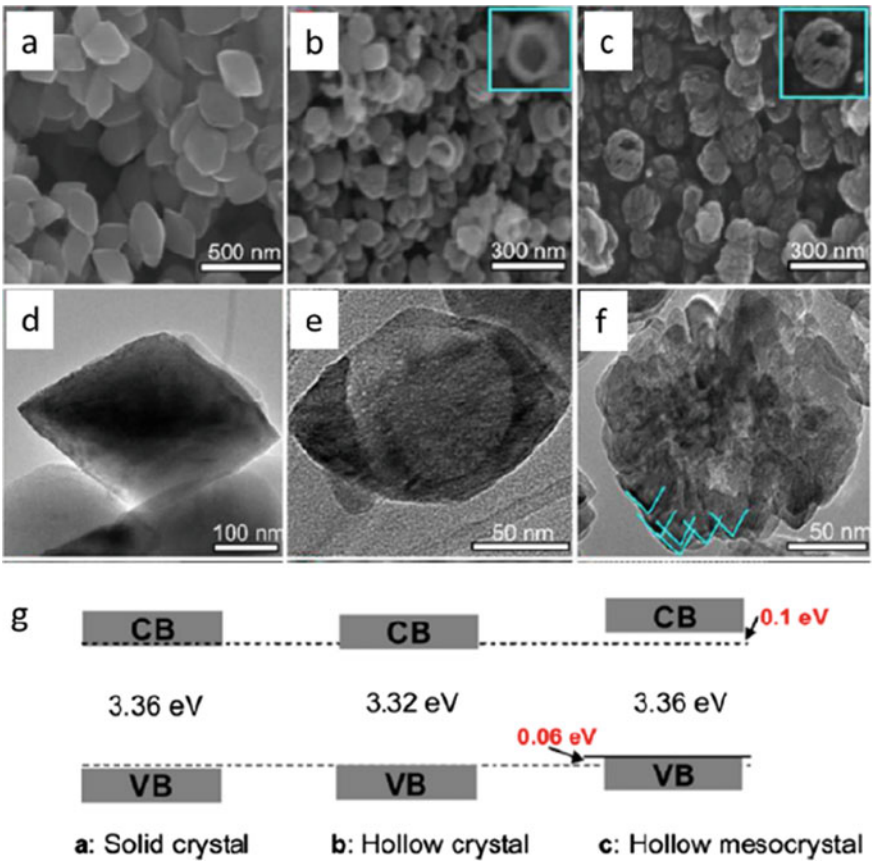

Fig. 18.6 SEM and TEM images of (**a**) and (**d**) solid anatase TiO_2 single crystals synthesized using 500 mM HF concentration, (**b**) and (**e**) hollow anatase TiO_2 single crystal synthesized using 400 mM HF concentration and (**c**) and (**f**) hollow anatase TiO_2 mesocrystals with exposed {101} facets synthesized using 300 mM HF concentration, and **g**. schematic of band structure derived from the valence band XPS spectra and the DRS data. Reproduced with permission from Ref. [65]. Copyright 2012 American Chemical Society

18.4.1 Cationic Doping

Dopant is a foreign element which replaces the crystal lattice point of the host material [37]. Doping of cation creates impurity levels within the band gap by changing the electronic structure of semiconductor. These levels may be donor level above the valence band or the acceptor level below the conduction band [66], thus helps in overall reduction of band gap. Along with improvement in light absorption in visible region, the presence of dopant in the TiO_2 lattice also helps to improve the electrical conductivity.

The effect of doping of higher valent ion (W^{6+}, Ta^{5+}), undoped and doping with (Ge^{4+}), and doping with lower valent ion (Mg^{2+}) on the electrical conductivity of 0.5% Pt/TiO_2 was studied by Akubuiro et al. [67]. Figure 18.7 shows the influence of high and low valent doping and undoped 0.5% Pt/TiO_2 on electrical conductivity under different gas environment. It was revealed that incorporation of higher valent cations into TiO_2 lattice improved the electrical conductivity as compared lower valent ions. However, electrical conductivity was unaffected by doping with isovalent ions such as Ge^{4+}. The doping with higher valence cations introduced excess electrons to

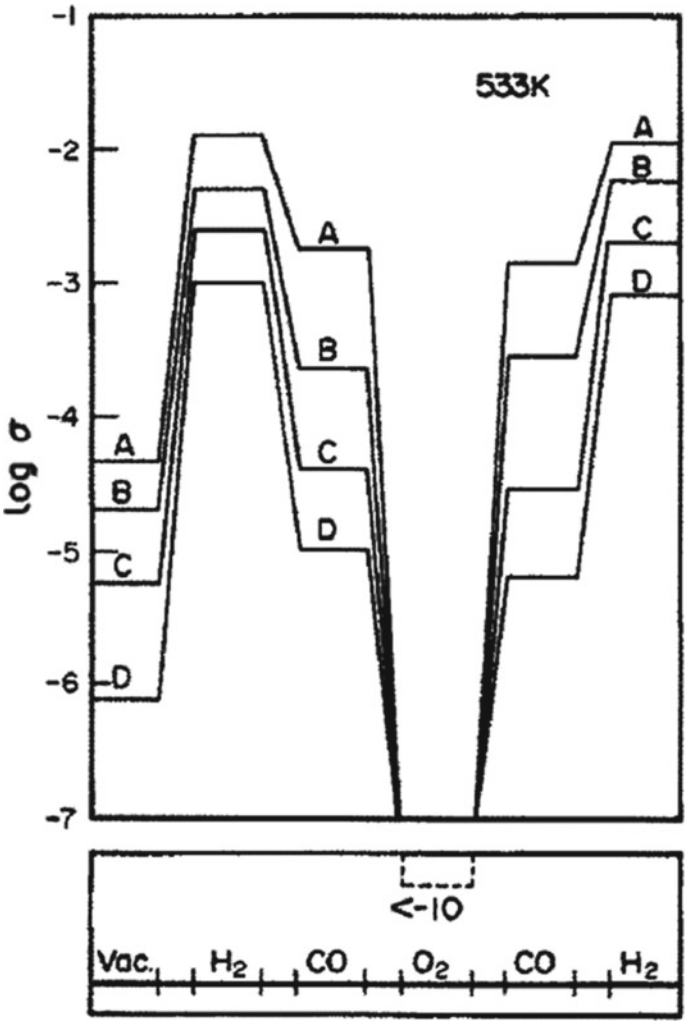

Fig. 18.7 Effect of gas cycles of sequences on electrical conductivity of 0.5% Pt/TiO_2, doped with **A** W^{6+}, **B** Ta^{5+}, **C** undoped and **D** Mg^{2+}. Reproduced with permission from Ref. [67] Copyright 1989 Elsevier

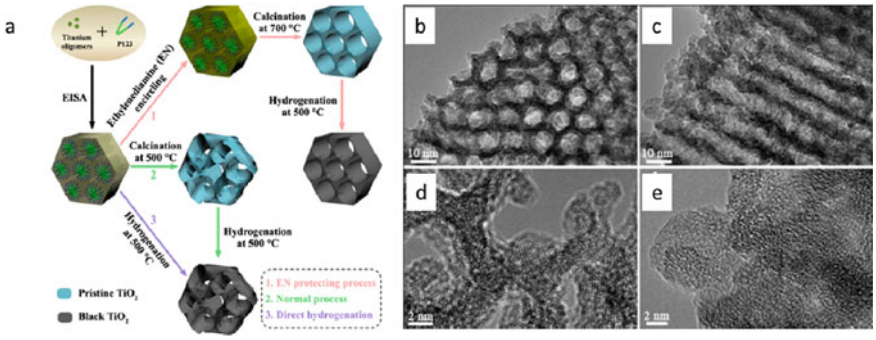

Fig. 18.8 **a** Schematic illustration of synthesis of OMBT, TEM images along **b** [100] and **c** [110] planes, **d** and **e** HR-TEM images of the OMBT. Reproduced with permission from Ref. [70]. Copyright 2014 American Chemical Society

TiO_2, thus resulting in increased n-type semiconductivity whereas doping with lower valence cations resulted in introduction of positive holes in TiO_2 lattice resulting in decreased n-type semiconductivity, while electronic structure of TiO_2 was retained on isovalent doping.

Also, the presence of point defects in TiO_2 plays an important role in deciding the electrical conductivity of TiO_2 [29]. Point defects in TiO_2 can be generated by different reduction methods. Reduction methods include use of H_2 gas, treatment with inert gases like Ar, N_2, and He, reducing agents such as $NaBH_4$, metallothermic reduction involving metals for reduction viz; Al, Mg, Zn etc., bombardment with high energy particle (such as electron beam, proton beam, hydrogen plasma), electrochemical reduction, etc. More details are available in literature [68, 69].

Self doping with Ti^{3+} is also an effective way to improve visible light absorption of TiO_2. Zhou et al. [70] reported facile synthesis of the ordered mesoporous black TiO_2 (referred as OMBT). An evaporation-induced self-assembly method in combination with an ethylenediamine encircling process followed by hydrogenation was employed for synthesis of OMBT (Fig. 18.8a). In order to understand the role of ethylenediamine encircling process, synthesis was carried out by alternate routes 2 and 3 (Fig. 18.8a). During direct calcination at 500 °C (route 2), the ordered porous structure was collapsed. After hydrogenation, porous structure further collapsed also some of anatase transformed to rutile phase. The ordered mesoporous structure was collapsed due to intrinsic crystal growth and sintering at high calcination temperature, while in route 3, as synthesized product was directly calcined in presence of H_2 at 500 °C. It resulted in formation of mixed phase product with reduced surface area (62 $m^2\ g^{-1}$). From this, it was concluded that ethylenediamine encircling process, allows the formation of the highly crystalline ordered mesoporous TiO_2 with anatase phase, high surface area, and large pore size. Because of the presence of large pore size and high surface area, hydrogen diffusion and its interaction with surface was facilitated. And also, the transformation of anatase to rutile phase and crystal growth during hydrogenation process at 500 °C was prevented. Specific surface area of OMBT was

124 m^2 g^{-1}. The OMBT showed highest photocatalytic hydrogen generation at the rate of 136.2 μmol h^{-1} using 100 mg of photocatalyst under simulated solar light illumination among all the samples. The improved light absorption from UV to IR region and photocatalytic hydrogen production was attributed to the presence of Ti^{3+} point defects.

18.4.2 pn *Heterojunction*

pn heterojunctions are commonly used to restrict recombination reaction by facilitating the separation of photoinduced charges at interfacial contact and also to decrease the effective band gap. A composite of two dissimilar semiconductors (p and n) shows modified properties as compared to the individual semiconductors. This is attributed to the heterojunctions formed at the interface of p and n semiconductors. Depending on the band positions and band gap, the valence band (VB) and conduction band (CB) of p are aligned with the VB and CB of n type semiconductor in three different manners classified as type (I), type (II), and type (III) as shown in Fig. 18.9. The band alignment at heterojunction facilitates the efficient transfer and separation of charge carriers [71].

A composite consisting of two different semiconductors has the following advantages (i) allows reduction and oxidation reactions to occur at different sites (ii) enhanced light absorption in visible region can be achieved by combining TiO_2 with low band gap semiconductors, and (iii) helps in better separation of electron and hole, and decrease in rate of recombination reaction. Among solid–solid interfaces, semiconductor—semiconductor heterojunction, semiconductor—carbon heterojunction, and semiconductor—metal heterojunction have gained much interest. Interfacial contact between the semiconductors is important for the facile charge transfer, and this helps in lowering the recombination rate of charge carriers. Thus, to construct intimate contact between the semiconductors, it is important to select appropriate synthesis methods.

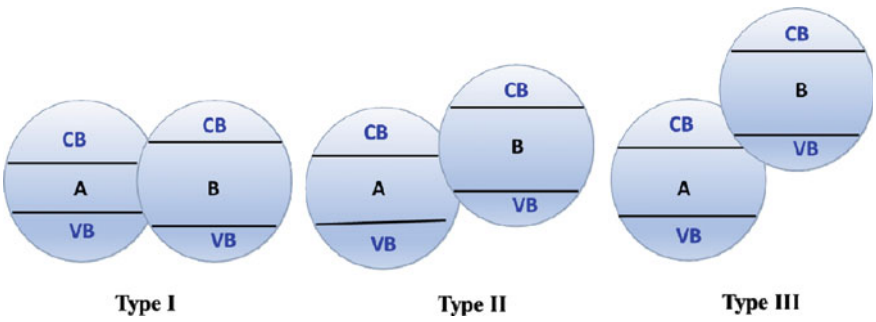

Fig. 18.9 Different types of *pn* heterojunctions (CB: conduction band, VB: valence band)

18.4.3 Semiconductor—Metal Heterojunctions

The light absorption and charge separation properties of TiO_2 can be improved by forming effective metal-semiconductor heterojunction. A Schottky barrier is formed at the interface of metal and semiconductor which helps in the separation of photogenerated charge carriers [72]. Also, the surface plasmon resonance (SPR) effect shown by metal nanoparticles further helps in absorption in the visible region [72, 73]. The metal nanoparticles dispersed on the surface of the semiconductor offer surface active sites and act as a cocatalyst during the reaction. The photocatalytic activity is strongly affected by the size, shape, and spatial distribution of the metal nanoparticles; therefore, it is necessary to design a synthesis methodology to control the properties of the metal nanoparticles. Methodologies like photodeposition method, wet impregnation method, chemical reduction, chemical vapor deposition, deposition–precipitation, electrodeposition, atomic-layer deposition, sputtering, and physical mixing were explored to load metal over the semiconductor surface [74, 75]. Among all these methods, photodeposition is an attractive method because it allows the deposition of metal nanoparticles at the active centers present on the surface using light energy. Loading of Pt nanoparticles to improve the photocatalytic activity for hydrogen generation is a common practice.

Recently, Jiang et al. [76] tuned the absorption of the plasmonic band in the near IR region by changing the size and shape of the metal nanoparticles. To harvest visible and NIR region, Au nanocubes and Au nanocages having plasmonic bands in visible and NIR region, respectively, were deposited on TiO_2 nanosheets (referred as Au cube/cage–TiO_2). Non-plasmonic Pd nanocubes were also deposited on TiO_2 nanosheets as a cocatalyst. Anatase TiO_2 nanosheets having average edge of 200 nm and thickness of 5–7 nm with 95% of percentage of (001) facets over the surface, were synthesized by hydrothermal method. Au nanocubes and Au nanocages were deposited by ligand-exchange method. The capping agent cetyltrimethylammonium bromide (CTAB) present on the Au nanocubes and Au nanocages surface were replaced by the 3-mercaptopropionic acid (MPA). Thiol and carboxylic groups present in MPA shows stronger interaction for Au and TiO_2, respectively. To form the hybrid structure, the Au nanocubes, nanocages, and TiO_2 were sonicated with MPA solution. Proper interfacial contact is necessary for the transfer of electron from Au to TiO_2. Thus, to further improve the interfacial contact between the two, evacuation followed by annealing was performed. Subsequent to loading of Au nanocubes and nanocages, Pd nanocubes were also deposited over it. The sample showed the extended absorption upto NIR region as Au nanocubes and nanocages absorbs in visible and NIR region, respectively. The sample showed the enhanced photocatalytic activity for hydrogen generation under NIR light illumination. The photogenerated electrons get transferred from Au metal to the TiO_2 photocatalyst, while Pd nanocubes acted as a cocatalyst to trap the charge carriers. This strategy resulted in development of efficient catalyst with improved properties for hydrogen generation.

18.5 Single Atom Catalysts (SACs)

Single atom catalysts (SACs) recently have gained tremendous attention over nanomaterials, nanoclusters, and bulk materials. SAC is an ultimate form of the dispersed catalysts with distinct properties leading to exceptionally high activity and stability. SACs offer a rational use of metals (advantageous in case of precious metals) with high efficiency of utilization of atom, distinctive electronic structure, and active sites with unsaturated coordination [77]. Zhang and co-workers [78] in 2011 deposited single atoms of Pt over FeOx support by co-precipitation method. Presence of Pt-O-Fe bonds suggested enhanced metal-support interactions with improved catalytic activity and stability for CO oxidation reaction. Since then, the SACs have attracted huge attention for its application in different fields.

Decoration of the single atom on the surface of the support is an important step in the synthesis of the SACs [79]. Also, the prevention of aggregation of the single atoms during the synthesis as well as while carrying out the catalytic reaction is a challenge in SACs. Different synthesis methodologies have been adopted to overcome the challenges associated with it. Atomic layer deposition, coprecipitation, photodeposition and atom trapping approach are the methodologies adopted to synthesize SACs. These methods are described in previous chapter by Pai et al. of the present book.

Long et al. [80] introduced isolated Cu atoms in the Pd lattice deposited over TiO_2 nanosheets by aqueous solution synthesis and evaluated its performance for photocatalytic CO_2 conversion. K_2PdCl_4 and $CuCl_2$ were used as precursors for Pd and Cu ions, respectively. Pd_xCu_1 alloy nanocrystals were crystallized *insitu* over the TiO_2 nanosheets by aqueous solution synthesis. The improved activity for CO_2 conversion was assigned to the increased CO_2 adsorption and activation along with suppressed hydrogen generation due to presence of the paired Cu-Pd sites with tunable d-band centers of Cu sites. Pd_7Cu_1–TiO_2 photocatalyst showed high selectivity (96%) for CH_4 generation at the rate of 19.6 μmol g_{cat}^{-1} h^{-1}.

Similarly, Sui et al. [81] deposited single atom of Pt selectively over the (101) facet of the nanosized TiO_2 single crystal (referred as x-Pt/TiO_2-A where x is the Pt loading in weight percent) by photodeposition method. Single atom decorated Pt catalysts were found to be active and stable for photocatalytic hydrogen generation. Also, its photocatalytic activity was compared with the commercially available anatase nanoparticles with similar surface area (referred as TiO_2-0). Figure 18.10a shows the High angle annular dark field-Scanning transmission electron microscopy (HAADF-STEM) images of the 0.6Pt_1/TiO_2-A. It confirmed the dispersion of atomic size Pt on TiO_2-A surface. It was found that the Pt deposited preferentially over the (101) facets of the TiO_2-A. Figure 18.10b shows the representative model of Pt dispersion over nanosized TiO_2 single crystal. The size distribution in 0.6Pt_1/TiO_2-A showed that 72% single atoms, 16% nanoclusters of 0.4–1 nm, and 12% particles were in the region of 1–2 nm size. Also, it was found that size distribution altered after loading same amount of Pt over TiO_2-0. In TiO_2-0 maximum, Pt particles were found to be of greater than 2 nm (Fig. 18.10c). The photocatalytic hydrogen generation

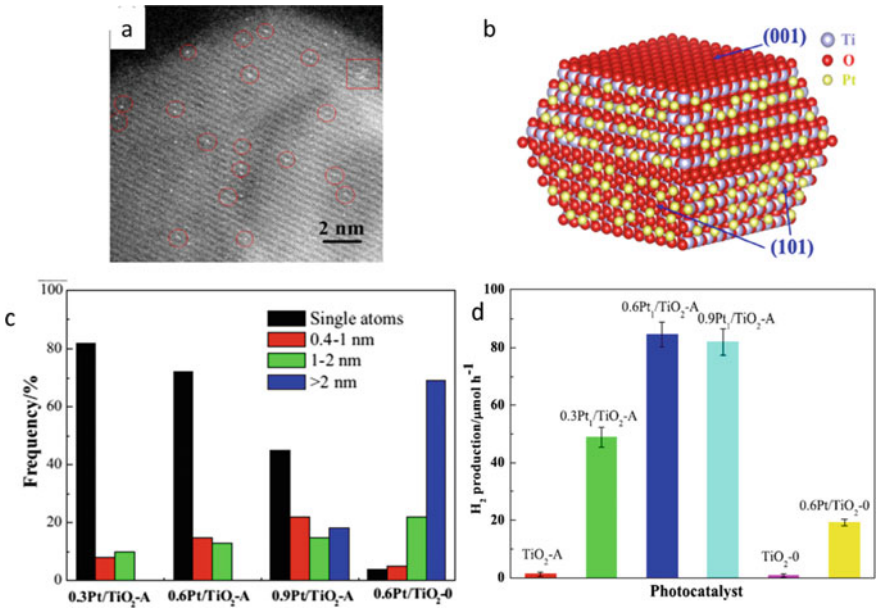

Fig. 18.10 **a** HAADF-STEM images of the $0.6Pt_1/TiO_2$-A, **b** representation of the Pt_1/TiO_2-A sample, **c** distribution of particle size of Pt deposited over different samples, and **d** photocatalytic hydrogen generation using different samples. Reproduced with permission from Ref. [81]. Copyright 2017 Elsevier

using the different samples were evaluated and shown in Fig. 18.10d. The presence of Pt enhances the photocatalytic activity for hydrogen generation of both TiO_2-A and TiO_2-0. Highest hydrogen generation of 84.5 μmol h^{-1} was observed using $0.6Pt_1/TiO_2$-A having Pt loading of 0.6 wt%. It was observed that on increasing the Pt loading beyond 0.6 wt%, photocatalytic activity decreased. Also, the H_2 yield on $0.6Pt_1/TiO_2$-A was 4.5-fold greater than that of the $0.6Pt_1/TiO_2$-0 though having the similar Pt loading over TiO_2-A and TiO_2-0. It was also revealed that the $0.6Pt_1/TiO_2$-0 possessed optimum amount of exposed (001) and (101) facets as it showed enhanced photocatalytic hydrogen yield as compared to the sample with higher percentage of (001) or (101) facets. Thus, dispersion of Pt at atomic level along with optimum percentages of exposed (001) and (101) facets play a crucial role in modifying the photocatalytic properties of TiO_2.

18.6 Development of TiO_2 Based Photocatalysts

A brief account of the developmental activities taken place in our laboratory during last few years is given here. It is needless to mention that success of photocatalytic water splitting process primarily depends on the properties of photocatalyst.

In continuous search of efficient catalytic systems and surge for improving hydrogen yield, we investigated and reported photocatalytic properties of several oxide semiconductors [44, 82–92]. The development in TiO_2 based photocatalysts falls under the purview of present chapter and will be discussed here. Several titania based In_2TiO_5, Cu doped TiO_2, nanocomposites of NiO-TiO_2, CuO-TiO_2, and carbon-TiO_2 heterostructures were developed, and their properties were investigated by us. Various investigative studies were undertaken to induce alterations in the lattice and structure, which are manifested in light absorption, band structure, and photocatalytic properties of titanium oxide. Strategies such as cationic doping by Cu in TiO_2, composite formation with NiO and CuO inducing *p-n* heterojunctions, carbon incorporation in bulk TiO_2 (C@TiO_2) to improve electronic conductivity were adopted to develop a promising photocatalyst. Photocatalysts were characterized by X-ray diffraction, X-ray photoelectron spectroscopy, N_2-BET, Raman spectroscopy, inductively coupled plasma-optical emission spectroscopy, high resolution transmission electron microscopy/selected area electron spectroscopy, and diffuse reflectance UV–visible spectroscopy. Photocatalytic properties of samples were investigated under sunlight, visible, and UV–visible irradiation. The emission spectra of both light sources along with reaction assemblies are shown in our earlier publications [83, 85, 86]. Density functional theory calculations were performed, and life time of $e^-/h^+$from PL decay curves was measured to support the activity trend. The present section briefly discusses the significant results obtained from these studies.

18.6.1 Type-II pn Heterojunction

NiO is *p*-type semiconductor and shows absorption in the visible region because of d-d transition, whereas TiO_2 is *n*-type semiconductor having a band gap of 3.2 eV. A combination of both *p*-type and *n*-type semiconductor forms *pn* heterojunction at the interface of the two and will generate electric field which can be utilized to drive the electron and hole in the opposite direction. Thus, pn junction formation helps in separation of charge carriers and retards the recombination of the charges.

To prepare NiO-TiO_2 composites, sol-gel method is preferred over other methods as it is simple and cost-effective process required low temperature, easy to incorporate the dopant ions, and produced fine powders [93]. Titanium isopropoxide and nickel nitrate hexahydrate were used as Ti and Ni precursor, respectively. In this preparation both Ni and Ti precursors were mixed in 1:1 molar ratio of Ni:Ti and allowed to form the gel under acidic conditions. Then the gel was dried by evaporating the solvent and the dried sample was calcined at different temperature to get desired crystallinity and phase composition [85]. Figure 18.11 shows the schematic of synthesis methodology adopted for the synthesis of NiO and TiO_2 heterojunction. While carrying out the synthesis it was observed that not only the calcination temperature but gel drying temperature also has significant impact on formation of a binary phase (NiO and TiO_2), devoid of undesired $NiTiO_3$ phase. Figure 18.11 shows the XRD pattern of different samples synthesized by varying the gel drying temperature from 90 to

150 °C as well as the calcination temperature. LT and HT are abbreviations denoting the samples synthesized by keeping the gel drying temperature at 90 °C and 150 °C, respectively. Composite samples showed presence of both cubic NiO and anatase phase of TiO_2 along with $NiTiO_3$ phase. It was found that the amount of $NiTiO_3$ phase was maximum in the sample synthesized by drying the gel at 150 °C than the sample obtained by drying the gel at 90 °C, even though the calcination temperature was kept the same in both the cases (Fig. 18.11). From this study, it was revealed that higher gel drying temperature, i.e., 150 °C favored formation of $NiTiO_3$ phase. To study the impact of the presence of different phases on photocatalytic properties, hydrogen generation from water splitting reaction was carried out. The following trend in activity was observed: NTC11-LT 600 °C, 10 h > NTC11 600 °C, 3 h > NTC11-HT 600 °C, 10 h > NTC11 500 °C, and 5 h. The deterioration in activity coincides with the appearance of the $NiTiO_3$ phase in the samples. For comparison, pure phase of $NiTiO_3$ was also synthesized using solid state and sol gel method. Both the samples synthesized by two different routes showed very poor activity nearly 2.2 μmol of H_2 g^{-1} h^{-1} under sunlight illumination.

To further understand the effect of crystallinity and phase composition, sample synthesized by drying the gel at 90 °C calcined at two different temperatures 500 and 600 °C and also the duration of calcination time was varied from 3 to 10 h. It was observed that the sample calcined at 600 °C for 10 h consisted of maximum amount of $NiTiO_3$ phase along with small amount of rutile as compared to the sample calcined at 600 °C for 3 h. Thus, it was inferred that rutile phase of TiO_2 reacted preferentially with NiO to form $NiTiO_3$ phase [85]. The poor crystallinity of the sample calcined at 500 °C was one of the factors resulting in lowering of the activity as compared to the sample obtained by carrying out calcination at 600 °C. From the above experiments, it was evident that synthesis parameters such as gel drying temperature and calcination temperature and also duration of calcination are crucial in determining the phase composition, crystallinity of the sample and eventually photocatalytic activities are affected. The highest H_2 generation was observed using sample synthesized by drying the gel at 90 °C and calcining it at 600 °C for 10 h. This sample was referred as NiO-TiO_2 (1:1)—LT 600 °C for 10 h or NTC11 for convenience. Under these synthesis conditions, a heterojunction formed between NiO and TiO_2 having appropriate crystallinity and with minimum amount of $NiTiO_3$. H_2 yield at the rate of 204 μmol g^{-1} h^{-1} under sunlight illumination with AQE of 5.4% and SFE of 0.8% was observed using the sample NTC11 (Fig. 18.11c). Also, it showed stable photocatalytic activity for 60 h of irradiation under sunlight.

On further characterization of NTC11 sample, it was observed that both the phases of NiO and TiO_2 co-exist together. Figure 18.12 shows scanning transmission electron microscopy-high angle annular dark field (STEM-HAADF) images of the NTC11 samples. The bright and dark contrast represents the presence of TiO_2 and NiO, respectively. Electron energy loss spectroscopy (EELS) confirms that the NiO and TiO_2 are in close contact (Fig. 18.12b). Also, the band alignment at the interface of NiO and TiO_2 in the NTC11 sample was derived using valence band XPS spectra and DRS measurement data which indicated that the effective band gap at the interface of NiO-TiO_2 in NTC11 was lower, i. e., 2.67 eV as compared to the pristine

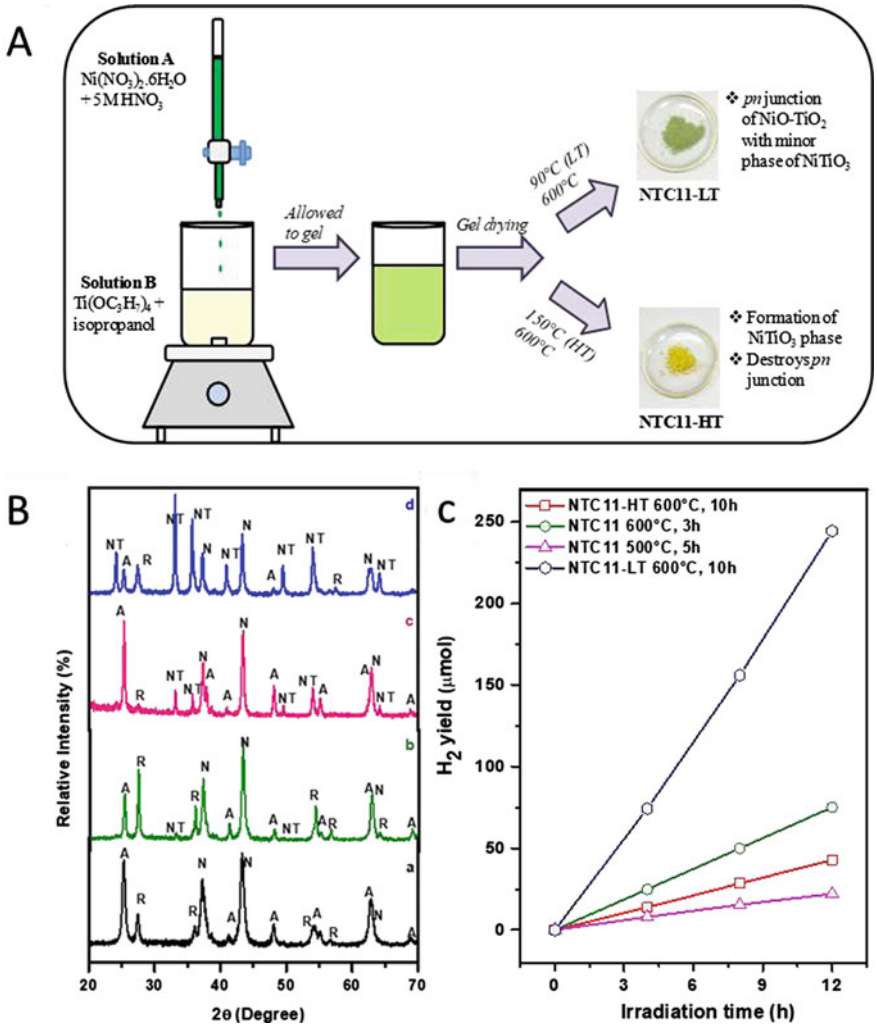

Fig. 18.11 **A** Schematic representation of the synthesis of composite samples of NiO and TiO_2, **B** XRD patterns of the samples synthesized by varying the synthesis conditions such as gel drying temperature and calcination conditions NTC11 obtained after **a.** drying the gel at 90 °C (LT) and further calcined at 500 °C for 5 h (named as NTC11 500 °C, 5 h), **b** drying the gel at 90 °C (LT) and further calcined at 600 °C for 3 h (named as NTC11 600 °C, 3 h), **c** drying the gel at 90 °C (LT) and further calcined at 600 °C for 10 h (named as NTC11-LT 600 °C, 10 h), 10 h or also referred as NTC11 for convenience and **d** drying the gel at higher temperature of 150 °C (HT) and was calcined at 600 °C for 10 h (named as NTC11-HT 600 °C, 10 h). (A: Anatase phase of TiO_2, R: Rutile phase of TiO_2, N: NiO and NT $NiTiO_3$) and **C** Comparison of photocatalytic hydrogen yield using different samples. Reproducedwith permission from Ref. [85] Copyright 2018 Elsevier

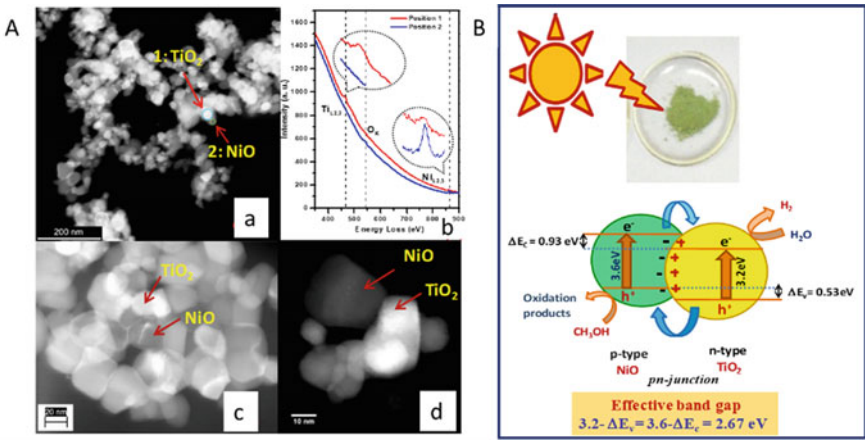

Fig. 18.12 Low **a** and high **c**-**d** resolution scanning transmission electron microscopy-high angle annular dark field (STEM-HAADF) images of NTC11 accompanied by electron energy loss spectroscopy (EELS) **b** of the selected area indicated as positions 1 and 2. **B** Schematic representation of the proposed mechanism for photocatalytic hydrogen generation. Reproduced with permission from Ref. [85]. Copyright 2018 Elsevier

NiO (band gap of 3.6 eV) and TiO_2 (band gap of 3.2 eV) (Fig. 18.12). Based on the above facts the mechanism was proposed as shown in Fig. 18.12B. The improved crystallinity and surface area, minimum amount of $NiTiO_3$, suitable type II band alignment at the interface, enhanced light absorption and lower recombination of charges, contributed positively for the highest H_2 production in composite NTC11 sample.

18.6.2 Carbon@TiO_2 Composites

Carbon-semiconductor heterojunction is similar to the metal–semiconductor heterojunction. A series of carbon and TiO_2 composites (referred as C@TiO_2) were prepared by varying the amount of carbon from 0.14 to 14.7 wt% using ethylene glycol and tetrabutyltitanate as precursors for carbon and titanium, respectively. An organic-inorganic polymer was formed on mixing the two precursors which was calcined under inert atmosphere and resulted in C@TiO_2 composite samples with TiO_2 as major phase. All the C@TiO_2 composite samples showed improved light absorption in the visible region as compared to pristine TiO_2 sample. Presence of carbon prevented the growth of TiO_2 nanoparticles as evident by the increase in crystallite size with an increase in carbon content. Among all samples, C@TiO_2 composite with carbon loading of 3.8 wt% showed highest H_2 yield @ 1360 μmol of H_2 h^{-1} g^{-1} under sunlight. Beyond 3.8 wt%, photo catalytic activity deteriorated. Excess carbon content could hinder the light absorption of TiO_2, thus lowering the

activity for hydrogen generation. Optimum amount of carbon enhanced the surface area, light absorption properties, imparted favorable morphology and chemical interaction of C with Ti helped in limiting the recombination reaction and improving the photocatalytic hydrogen yield over C@TiO_2 composites.

18.6.3 Cationic Doping

Incorporation of cationic dopants introduces donor or acceptor levels within the band gap of TiO_2 and helps in enhancing visible light photoresponse. Thus, a series of Cu substituted TiO_2 $Cu_xTi_{1-x}O_{2-\delta}$ (x = 0, 0.02, 0.06, 0.1, 0.2, 0.5) catalysts were synthesized by sol–gel using appropriate amounts of cupric acetate and titanium isopropoxide. It was observed that TiO_2 lattice could tolerate upto 6 mol% of Cu ions resulting in single-phase compositions in which Cu^{2+}occupied Ti^{4+}sites in TiO_2 lattice. The modifications in bond length, coordination number, and disorder in the lattice caused due to Cu incorporation were investigated by X-ray absorption spectroscopy at Cu edge [86, 87], while incorporation of Cu equal to or greater than 10 mol%, resulted in a biphasic mixture consisting of TiO_2 and CuO phases. Among all the samples, 2 mol% Cu doped TiO_2 (referred as CuTi2) has shown maximum H_2 yield under sunlight illumination. Cu incorporation has imparted favorable electronic and optical properties. With an increase in Cu content the absorption in the visible region increases. Figure 18.13 shows the DRS spectra of the samples recorded in the region of 200–1000 nm. EXAFS studies revealed that doping of Cu into TiO_2 lattice generated oxygen vacancies and lengthened Ti–O bonds. Doped samples

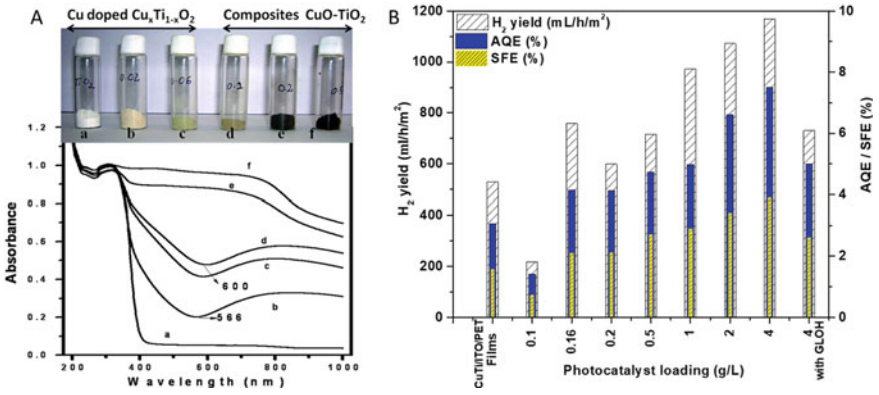

Fig. 18.13 DRS absorption spectra of samples synthesized by varying the amount of Cu in TiO_2. **a** TiO_2, **b** CuTi(2), **c** CuTi(6), **d** CuTi(1–9), **e** CuTi(2–8), and **f** CuTi(5–5), **B** Comparison of AQE and SFE over CuTi(2) at different catalyst loadings, sacrificial agents (methanol and glycerol (GlOH)), and form of catalysts. Reproduced with permission from Ref. [86]. Copyright 2016 Elsevier

have shown lengthened Ti–O bonds, introduced oxygen ion vacancies, and distortion in TiO_2 lattice. Along with this, XPS studies of fresh and spent photocatalysts revealed that during light illumination CuO present on surface was reduced to Cu_2O by photogenerated electrons. Based on exsitu investigations from XPS and other experimental evidences, a mechanistic scheme involving the $Cu^{2+}$and Cu^{+} species was also proposed [86]. Apart from development of photocatalysts, we also monitored the effect of various experimental parameters such as amount of photocatalyst, amount of sacrificial reagent, form of catalyst (powder/films), alignment of photoreactor with respect to light source, effect of variation of flux of sunlight in different months and day, on photocatalytic activity of most active CuTi(2) sample as shown in Fig. 18.13c [86, 87]. Also, we attempted to improve the catalytic efficiency as well as scale up the reaction for practical use by spreading the catalysts over the indium tin oxide coated on polyethylene terephthalate (ITO-PET) films [86, 87]. For preparing films of CuTi(2), doctor-blade technique was used to coat ITO-PET substrates. It was found that the films resulted in better efficiency of 3.06% for photocatalytic hydrogen generation rather than dispersed in the powder form (1.41%) (Fig. 18.13B). Also, the easy processing, handling, and recovery of catalyst are the additional advantages offer by spreading of catalyst over the film.

The most active TiO_2 samples obtained after above modifications without co-catalyst are compared under sunlight (Fig. 18.14). We summarize here that cationic dopants, formations of pn heterojunctions, and dispersal of carbon are effective in improving the optical and photocatalytic properties of TiO_2 for its application in conversion of solar energy to solar fuels.

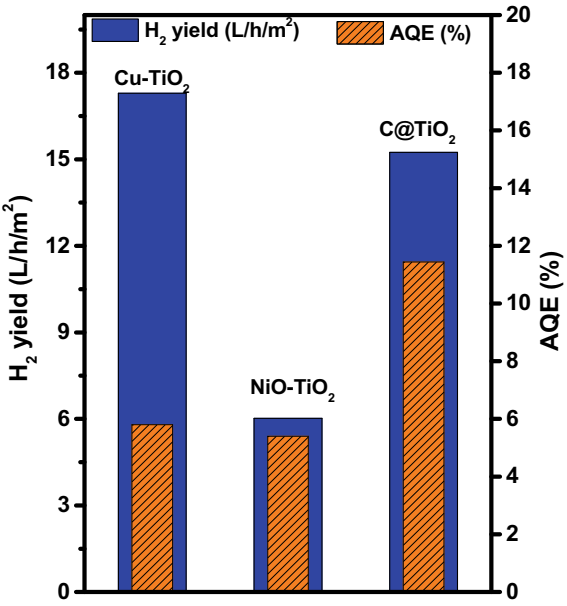

Fig. 18.14 Comparison of photocatalytic H_2 generation terms of L h^{-1} m^{-2} and AQE of the Cu-TiO_2, NiO-TiO_2 composite, and C@TiO_2 composite samples recorded under sunlight illumination. *Note* The experiments were carried out under direct sunlight illumination. Flux variations are taken care by AQE measurements

Experimental conditions: 50 to 100 mg of the catalyst dispersed in water + methanol solutions (15 mol of 33% v/v of methanol) in a 81 ml volume quartz reactor with geometric illumination area of 20 cm^2). Reaction mixture was evacuated and irradiated under direct sunlight on terrace of our institute. Hydrogen yield was monitored intermittently using GC equipped with thermal conductivity detector.

Conclusions and future perspective

Present chapter acclaimed the role of synthesis in evolution of TiO_2 based catalysts over the decades for various photocatalytic applications. First part of chapter deals with the photocatalytic processes, role of photocatalyst, their selection criteria, and overview of the selected promising photocatalysts. Second part illustrated the role of synthetic methods/conditions in modifying the morphology and structural characteristics of TiO_2 such as surface area, particle size, shape, phase, crystallinity, exposed facets, and defects. The synthesis driven modifications enhanced the photocatalytic properties of TiO_2 nanomaterials for various applications. Some typical examples in each category of 0D, 1D, 2D, and single atom TiO_2 based photocatalysts were discussed to establish the synthesis-property correlations. Different methodologies such as metal doping, and heterojunction formation is also discussed by which electric, optical, and surface properties of TiO_2 was improved further. Last section of the above chapter presents the research work undertaken in our laboratory to improve the photocatalytic properties of TiO_2 based photocatalysts for sunlight assisted photocatalytic hydrogen generation. We conclude here that an understanding of the synthesis methodologies is crucial for growth of TiO_2 or other catalysts for photocatalytic applications.

Acknowledgements The authors sincerely thank Dr. A. K. Tyagi, Director, Chemistry Group, BARC for his support and encouragement.

References

1. Khalil M, Gunlazuardi J, Ivandini TA, Umar A (2019) Photocatalytic conversion of CO_2 using earth-abundant catalysts: a review on mechanism and catalytic performance. Renew Sustain Energy Rev 113:109246. https://doi.org/10.1016/j.rser.2019.109246
2. Green MA, Emery K, Hishikawa Y, Warta W, Dunlop ED (2015) Solar cell efficiency tables (version 46). Prog Photovolt Res Appl 23:805–812
3. Zhang Y, Xia B, Ran J, Davey K, Qiao SZ (2020) Atomic-level reactive sites for semiconductor-based photocatalytic CO2 reduction. Adv Energ Mater 10(9):1903879
4. Sato S, Arai T, Morikawa T (2015) Toward solar-driven photocatalytic CO_2 reduction using water as an electron donor. Inorg Chem 54:5105–5113
5. Jules V (1874) The mysterious island; Pierre-Jules Hetzel Publisher: Paris, France
6. Ciamician G (1912) The photochemistry of the future. Science 36:385–394
7. Bard AJ, Fox MA (1995) Artificial Photosynthesis: Solar Splitting of Water to Hydrogen and Oxygen. Acc Chem Res 28:141–145
8. Fujishima A, Honda K (1972) Electrochemical photolysis of water at a semiconductor electrode. Nature 238:37–38

9. Halmann M (1978) Photoelectrochemical reduction of aqueous carbon dioxide on p-type gallium phosphide in liquid junction solar cells. Nature 275:115-116
10. Inoue T, Fujishima A, Konishi S, Honda K (1979) Photoelectrocatalytic reduction of carbon dioxide in aqueous suspensions of semiconductor powders. Nature 277:637–638
11. Fukuzumi S, Jung J, Yamada Y, Kojima T, Nam W (2016) Homogeneous and heterogeneous photocatalytic water oxidation by persulfate. Chem Asian J 11(8):1138–1150
12. Hennig H (1999) Homogeneous photo catalysis by transition metal complexes. Coord Chem Rev 182:101–123
13. Du P, Eisenberg R (2012) Catalysts made of earth-abundant elements (Co, Ni, Fe) for water splitting: recent progress and future challenges. Energy Environ Sci 5:6012–6021
14. Corredor J, Rivero MJ, Rangel CM, Gloaguen F, Ortiz I (2019) Comprehensive review and future perspectives on the photocatalytic hydrogen production. J Chem Technol Biotechnol 94:3049–3063
15. Chen S, Takata T, Domen K (2017) Particulate photocatalysts for overall water splitting. Nat Rev Mater 2:17050. https://doi.org/10.1038/natrevmats.2017.50
16. Shimura K, Yoshida H (2011) Heterogeneous photocatalytic hydrogen production from water and biomass derivatives. Energy Environ Sci 4:2467–2481
17. Maeda K, Teramura K, Domen K (2008) Effect of post-calcination on photocatalytic activity of $(Ga_{1-x}Zn_x)(N_{1-x}O_x)$ solid solution for overall water splitting under visible light. J Catal 254:198–204
18. Yan H, Yang J, Ma G, Wu G, Zong X, Lei Z, Shi J, Li C (2009) Visible-light-driven hydrogen production with extremely high quantum efficiency on Pt–PdS/CdS photocatalyst. J Catal 266:165–168
19. Chen X, Liu L, Yu PY, Mao SS (2011) Increasing solar absorption for photocatalysis with black hydrogenated titanium dioxide nanocrystals. Science 331:746–750
20. Liao L, Zhang Q, Su Z, Zhao Z, Wang Y, Li Y, Lu X, Wei D, Feng G, Yu Q, Cai X, Zhao J, Ren Z, Fang H, Robles-Hernandez F, Baldelli S, Bao J (2014) Efficient solar water-splitting using a nanocrystalline CoO photocatalyst. Nat Nanotechnol 9:69–73
21. Zhao C, Luo H, Chen F, Zhang P, Yi L, You K (2014) A novel composite of TiO_2 nanotubes with remarkably high efficiency for hydrogen production in solar-driven water splitting. Energy Environ Sci 7:1700–1707
22. Liu J, Liu Y, Liu N, Han Y, Zhang X, Huang H, Lifshitz Y, Lee S-T, Zhong J, Kang Z (2015) Metal-free efficient photocatalyst for stable visible water splitting via a two-electron pathway. Science 347:970–974
23. Kato H, Asakura K, Kudo A (2003) Highly efficient water splitting into H_2 and O_2 over Lanthanum-Doped $NaTaO_3$ photocatalysts with high crystallinity and surface nanostructure. J Am Chem Soc 125:3082–3089
24. Sun J, Chen G, Li Y, Jin R, Wang Q, Pei J (2011) Novel (Na, K)TaO_3 single crystal nanocubes: molten salt synthesis, invariable energy level doping and excellent photocatalytic performance. Energy Environ Sci 4:4052–4060
25. Maeda K, Higashi M, Lu D, Abe R, Domen K (2010) Efficient nonsacrificial water splitting through two-step photoexcitation by visible light using a modified oxynitride as a hydrogen evolution photocatalyst. J Am Chem Soc 132:5858–5868
26. Jo JW, Kang JH, Kong K, Lee SY, Park H, Lee Y, Buonassisi T, Gleason KK, Lee JS (2015) Phase transition-induced band edge engineering of $BiVO_4$ to split pure water under visible light. Proc Natl Acad Sci USA 112:13774–13778. https://doi.org/10.1073/pnas.1509674112
27. Kibria MG, Chowdhury FA, Zhao S, AlOtaibi B, Trudeau ML, Guo H, Mi Z (2015) Visible light-driven efficient overall water splitting using p-type metal-nitride nanowire arrays. Nat Commun 6(6797):1–8
28. Takata T, Jiang J, Sakata Y, Nakabayashi M, Shibata N, Nandal V, Seki K, Hisatomi T, Domen K (2020) Photocatalytic water splitting with a quantum efficiency of almost unity. Nature 581:411–414
29. Ali I, Suhail M, Alothman ZA, Alwarthan A (2018) Recent advances in syntheses, properties and applications of TiO_2 nanostructures. RSC Adv 8:30125–30147

30. Verma R, Gangwar J, Srivastava AK (2017) Multiphase TiO_2 nanostructures: a review of efficient synthesis, growth mechanism, probing capabilities, and applications in bio-safety and health. RSC Adv 7:44199–44224
31. Haines J, Leger JM (1993) X-ray diffraction study of TiO_2 up to 49 GPa. Phys B 192:233–237
32. Ahuja R, Dubrovinsky LS (2002) Cotunnite-structured titanium dioxide and the hardest known oxide. High Press. Res. 22:429–433
33. Nishio-Hamane D, Shimizu A, Nakahira R, Niwa K, Sano-Furukawa A, Okada T, Yagi T, Kikegawa T (2010) The stability and equation of state for the cotunnite phase of TiO_2 up to 70 GPa. Phys. Chem. Minerals 37:129–136
34. Takahashi Y, Kijima N, Akimoto J (2006) Synthesis, structural change upon heating, and electronic structure of ramsdellite-type TiO_2. Chem Mater 18(3):748–752. https://doi.org/10.1021/cm0521370
35. León-Ríos S, González RE, Fuentes S, Ángel EC, Echeverría A, Serrano AE, Demergasso CS, Zárate RA (2016) One-dimensional TiO_2-B crystals synthesised by hydrothermal process and their antibacterial behaviour on Escherichia coli. J Nanomater. Article ID 7213672, 8 pages. https://doi.org/10.1155/2016/7213672
36. Pérez-Flores JC, Baehtz C, Kuhna A, García-Alvaradoa F (2014) Hollandite-type TiO_2: a new negative electrode material for sodium-ion batteries. J Mater Chem A 2:1825–1833
37. Kudo A, Miseki Y (2009) Heterogeneous photocatalyst materials for water splitting. Chem Soc Rev 38:253–278
38. Noman MT, Ashraf MA, Ali A (2019) Synthesis and applications of nano-TiO_2: a review. Environ Sci Pollut Res 26:3262–3291
39. Hashimoto K, Irie H, Fujishima A (2005) TiO_2 Photocatalysis: a historical overview and future prospects. Jpn J Appl Phys 44:8269–8285
40. Goodeve CF, Kitchener JA (1938) The mechanism of photosensitisation by solids. Trans Faraday Soc 34:902–908
41. Gaya UI (2014) Principles of heterogeneous photocatalysis. In book: Heterogeneous photocatalysis using inorganic semiconductor solids, Springer, Dordrecht, 1–41
42. Mori K, Yamashita H, Anpo M (2012) Photocatalytic reduction of CO_2 with H_2O on various titanium oxide photocatalysts. RSC Adv 2:3165–3172
43. Anpo M, Shima T, Kodama S, Kubokawa Y (1987) Photocatalytic hydrogenation of propyne with water on small-particle titania: size quantization effects and reaction intermediates. J Phys Chem 91(16):4305–4310
44. Pai MR, Singhal AM, Banerjee AM, Tewari R, Dey GK, Tyagi AK, Bharadwaj SR (2012) Synthesis, characterization and photocatalytic H_2 generation over ternary indium titanate nanoparticles. J Nanosci Nanotechnol 12:1957–1966. https://doi.org/10.1166/jnn.2012.5187
45. Pokropivny VV, Skorokhod VV (2007) Classification of nanostructures by dimensionality and concept of surface forms engineering in nanomaterial science. Mater Sci Eng C 27:990
46. Cargnello M, Gordon TR, Murray CB (2014) Solution-Phase Synthesis of Titanium Dioxide Nanoparticles and Nanocrystals. Chem Rev 114(19):9319–9345
47. Robichaud CO, Uyar AE, Darby MR, Zucker LG, Wiesner MR (2009) Estimates of upper bounds and trends in nano-TiO_2 production as a basis for exposure assessment. Environ Sci Technol 43(12):4227–4233
48. Ohtani B, Prieto-Mahaney OO, Li D, Abe R (2010) What is Degussa (Evonik) P25? Crystalline composition analysis, reconstruction from isolated pure particles and photocatalytic activity test. J Photochem Photobiol A Chem 216(2–3):179–182
49. Li W-G, Hu Y-J, Jiang H, Li C-Z (2019) Aerosol spray pyrolysis synthesis of porous anatase TiO_2 microspheres with tailored photocatalytic activity. Acta Metall Sin (Engl Lett) 32:286–296. https://doi.org/10.1007/s40195-018-0788-3
50. Pan L, Zou J-J, Wang S, Huang Z-F, Yu A, Wang L, Zhang X (2013) Quantum dot self-decorated TiO_2 nanosheets. Chem Commun 49:6593–6595. https://doi.org/10.1039/C3CC42152J
51. Li L, Yan J, Wang T, Zhao Z-J, Zhang J, Gong J, Guan N (2015) Sub-10 nm rutile titanium dioxide nanoparticles for efficient visible-light-driven photocatalytic hydrogen production. Nat Commun 6:5881. https://doi.org/10.1038/ncomms6881

52. Wang X, Li Z, Shi J, Yu Y (2014) One-Dimensional Titanium dioxide nanomaterials: nanowires, nanorods, and nanobelts. Chem Rev 114(19):9346–9384
53. Yang Z, Wang B, Cui H, An H, Pan Y, Zhai J (2015) Synthesis of crystal-controlled TiO_2 nanorods by a hydrothermal method: Rutile and brookite as highly active photocatalysts. J Phys Chem C 119(29):16905–16912
54. Peng T, Zhang J, Ray S, Bagh FSG, Fakhouri H, Arefi-Khonsari F, Lalman JA (2019) Optimizing one-dimensional TiO_2 for photocatalytic hydrogen production from a water-ethanol mixture and other electron donors. J Environ Chem Eng 7(1):102868. https://doi.org/10.1016/j.jece.2018.102868
55. Lazzeri M, Vittadini A, Selloni A (2002) Erratum: structure and energetics of stoichiometric TiO_2 anatase surfaces [Phys Rev B 63:155409 (2001)] Phys Rev B 65:119901. https://doi.org/10.1103/PhysRevB.63.155409
56. Diebold U (2003) The surface science of titanium dioxide. Surf Sci Rep 48:53–229
57. Sajan CP, Wageh S, Al-Ghamdi AA, Yu J, Cao S (2016) TiO2 nanosheets with exposed 001 facets for photocatalytic applications. Nano Res 9:3–27
58. Han X, Kuang Q, Jin M, Xie Z, Zheng L (2009) Synthesis of titania nanosheets with a high percentage of exposed (001) facets and related photocatalytic properties. J Am Chem Soc 131:3152–3153
59. Song C, Wang L, Gao F, Lu Q (2016) Two-dimensional hollow TiO_2 nanoplates with enhanced photocatalytic activity. Chem Eur J 22:6368–6373
60. Zhang W, Tian Y, He H, Xu L, Li W, Zhao D (2020) Recent advances in the synthesis of hierarchically mesoporous TiO_2 materials for energy and environmental applications. Natl Sci Rev 7:1702-1725
61. Bayal N, Singh R, Polshettiwar V (2017) Nanostructured silica–titania hybrid using dendritic fibrous nanosilica as a photocatalyst. Chemsuschem 10(10):2182–2191
62. Singh R, Bayal N, Maity A, Pradeep DJ, Trébosc J, Madhu PK, Lafon O, Polshettiwar V (2018) Probing the interfaces in nanosilica supported TiO_2 photocatalysts by solid-state NMR and In-situ FTIR. ChemNanoMat 4:1231–1239
63. Eskandarloo H, Zaferani M, Kierulf A, Abbaspourrad A (2018) Shape-controlled fabrication of TiO_2 hollow shells toward photocatalytic application. Appl Catal B: Environ 227:519–529
64. Sturm EV (née Rosseeva), Cölfen H (2016) Mesocrystals: structural and morphogenetic aspects. Chem Soc Rev 45:5821–5833. https://doi.org/10.1039/C6CS00208K
65. Jiao W, Wang L, Liu G, (Max) Lu GQ, Cheng H-M (2012) Hollow anatase TiO_2 single crystals and mesocrystals with dominant {101} facets for improved photocatalysis activity and tuned reaction preference. ACS Catal 2(9):1854–1859. https://doi.org/10.1021/cs300229e
66. Yuan L, Han C, Yang M, Xu Y (2016) Photocatalytic water splitting for solar hydrogen generation: fundamentals and recent advancements. Int Rev Phys Chem 35:1–36
67. Akubuiro EC, Verykios XE (1989) Effects of altervalent cation doping on electrical conductivity of platinized titania. J Phys Chem Solids 50(1):17–26
68. Chen X, Liu L, Huang F (2015) Black titanium dioxide (TiO_2) nanomaterials. Chem Soc Rev 44:1861–1885
69. Chatzitakis A, Sartori S (2019) Recent advances in the use of black TiO_2 for production of hydrogen and other solar fuels. ChemPhysChem 20:1272–1281
70. Zhou W, Li W, Wang J-Q, Qu Y, Yang Y, Xie Y, Zhang K, Wang L, Fu H, Zhao D (2014) Ordered mesoporous black TiO_2 as highly efficient hydrogen evolution photocatalyst. J Am Chem Soc 136(26):9280–9283
71. Marschall R (2014) Semiconductor composites: Strategies for enhancing charge carrier separation to improve photocatalytic activity. Adv Funct Mater 24(17):2421–2440
72. Gupta B, Melvin AA, Matthews T, Dash S, Tyagi AK (2016) TiO_2 modification by gold (Au) for photocatalytic hydrogen (H_2) production. Renew Sustain Energy Rev 58:1366–1375
73. Hou W, Cronin SB (2013) A review of surface plasmon resonance-enhanced photocatalysis. Adv Funct Mater 23:1612–1619
74. Fu Y-S, Li J, Li J (2019) Metal/Semiconductor nanocomposites for photocatalysis: fundamentals, structures, applications and properties. Nanomaterials 9:359

75. Wenderich K, Mul G (2016) Methods, mechanism, and applications of photodeposition in photocatalysis: a review. Chem Rev 116:14587–14619
76. Jiang W, Bai S, Wang L, Wang X, Yang L, Li Y, Liu D, Wang X, Li Z, Jiang J, Xiong Y (2016) Integration of multiple plasmonic and co-catalyst nanostructures on TiO_2 nanosheets for visible-near-Infrared photocatalytic hydrogen evolution. Small 12:1640–1648
77. Gao C, Low J, Long R, Kong T, Zhu J, Xiong Y (2020) Heterogeneous single-atom photocatalysts: fundamentals and applications. Chem Rev 120(21):12175–12216
78. Qiao B, Wang A, Yang X, Allard LF, Jiang Z, Cui Y, Liu J, Li J, Zhang T (2011) Single-atom catalysis of CO oxidation using Pt1/FeOx. Nat Chem 3:634–641
79. Wang Q, Zhang D, Chen Y, Fu W-F, Lv X-J (2019) Single-atom catalysts for photocatalytic reactions. ACS Sustainable Chem Eng 7:6430–6443
80. Long R, Li Y, Liu Y, Chen S, Zheng X, Gao C, He C, Chen N, Qi Z, Song L, Jiang J, Zhu J, Xiong Y (2017) Isolation of Cu atoms in Pd lattice: forming highly selective sites for photocatalytic conversion of CO_2 to CH_4. J Am Chem Soc 139(12):4486–4492
81. Sui Y, Liu S, Li T, Liu Q, Jiang T, Guo Y, Luo J-L (2017) Atomically dispersed Pt on specific TiO_2 facets for photocatalytic H_2 evolution. J Catal 353:250–255
82. Pai MR, Banerjee AM, Tripathi AK, Bharadwaj SR (2012). In: Banerjee S, Tyagi AK (eds) Functional materials: preparations, processing and applications. Elsevier, USA, pp 579–606
83. Pai MR, Majeed J, Banerjee AM, Arya A, Bhattacharya S, Rao R, Bharadwaj SR (2012) Role of Nd^{3+} ions in modifying the band structure and photocatalytic properties of substituted indium titanates, $In_{2(1-x)}Nd_{2x}TiO_5$ oxides. J Phys Chem C 116:1458–1471
84. Banerjee AM, Pai MR, Arya A, Bharadwaj SR (2015) Photocatalytic H_2 generation over In_2TiO_5, Ni substituted In_2TiO_5 and $NiTiO_3$ – a combined theoretical and experimental study. RSC Adv 5:61218–61229
85. Rawool SA, Pai MR, Banerjee AM, Arya A, Ningthoujam RS, Tewari R, Rao R, Chalke B, Ayyub P, Tripathi AK, Bharadwaj SR (2018) *pn* Heterojunctions in NiO:TiO_2 composites with type-II band alignment assisting sunlight driven photocatalytic H_2 generation. Appl Catal B: Environ 221:443–458
86. Pai MR, Banerjee AM, Rawool SA, Singhal A, Nayak C, Ehrman SH, Tripathi AK, Bharadwaj SR (2016)A comprehensive study on sunlight driven photocatalytic hydrogen generation using low cost nanocrystalline Cu-Ti oxides. Sol Energy Mater Sol Cells 154:104–120. https://doi.org/10.1016/j.solmat.2016.04.036
87. Rawool SA, Pai MR, Banerjee AM, Bapat RD, Nayak C, Tripathi AK (2018) Lab scale optimization of various factors for photocatalytic hydrogen generation over low cost $Cu_{0.02}Ti_{0.98}O_{2-\delta}$ photocatalyst under UV/Visible irradiation and sunlight. Int J Hydrogen Energy 43:1271–1284. https://doi.org/10.1016/j.ijhydene.2017.11.090
88. Pai MR, Banerjee AM, Bharadwaj SR (2015) Effect of transition metal ion doping on photocatalytic properties of In-Ti oxides. J Mater Res 30:3259–3266
89. Singh N, Pai MR, Kaur G, Divya, Satsangi VR, Dass S, Shrivastav R (2019) $Zn_{1-x}Fe_xO_y$ nanocomposites for renewable hydrogen produced efficiently via photoelectrochemical *vis-a-vis* photocatalytic splitting of water. SN Appl Sci 1:611. https://doi.org/10.1007/s42452-019-0597-y
90. Sharma S, Pai MR, Kaur G, Divya, Satsangi VR, Dass S, Shrivastav R (2019) Efficient hydrogen generation on CuO core/Ag-TiO_2 shell nano-hetero-structures by photocatalytic splitting of water. Renewable Energy 136:1202–1216. https://doi.org/10.1016/j.renene.2018.09.091
91. Pai MR, Banerjee AM, Bharadwaj SR, Kulshreshtha SK (2007) Synthesis, characterization, thermal stability and redox behavior of $In^{3+}{}_2Ti^{4+}{}_{1-x}Tm^{3+}{}_xO_{5-\delta}$, (Tm = Fe^{3+} and Cr^{3+}, $0.0 \leq x \leq 0.2$) mixed-oxide catalysts. J Mater Res 22:1787–1796. https://doi.org/10.1557/jmr.2007.0240
92. Banerjee AM, Pai MR, Jagannath, Bharadwaj SR (2011) Influence of Ni substitution on redox properties of $In_{2(1-x)}TiO_{5-\delta}$. Thermochim Acta 516:40-45
93. Kumar A, Yadav N, Bhatt M, Mishra NK, Chaudhary P, Singh R (2015) Sol-Gel derived nanomaterials and its applications: a review. Res J Chem Sci 5(12):98–105

Chapter 19
Lasers in Materials Processing and Synthesis

Sisir K. Sarkar

Abstract The laser is a central technology within photonics having a great economic impact. Laser material processing has currently flourished into a full-scale discipline. The present article conveys the basic essence of the subject with a few examples but definitely not a comprehensive review. Here, the purpose is to bring scientists, engineers, and manufacturers on a common platform to overview the understandings of current developments of laser applications in material science and also of the various new possibilities. We will first explore some processing segments of the industry, namely, lasers in cutting, drilling, marking, engraving, and then follow it up with further developments such as laser shock peening and laser surface treatment. In recent times the market is witnessing a paradigm shift with newer applications of laser annealing for thin films, additive materials deposition, and rapid prototyping. Various strategies are discussed based on non-equilibrium processes at interfaces and chemistry for the synthesis of materials including nanoparticles, nanocomposite films, and nano patterning. The advent of ultrashort lasers and their commercial availability has opened up novel applications in the processing industry.

Keywords Laser material interaction · Materials processing and synthesis · Ultrafast laser · Laser chemistry · Laser Isotope Separation · Chemical vapor deposition · Nano and nanostructured materials · Laser-Induced Graphene · Laser photochemical technology

19.1 Introduction

Albert Einstein in his paper on the theory of quantum and radiation described an effect which is known as stimulated emission of radiation [1]. A new light source that originated based on this process was named LASER, which is an acronym of

S. K. Sarkar (✉)
Bhabha Atomic Research Centre, Mumbai 400085, India

National Centre for Free Radical Research, Savitribai Phule Pune University, Pune-411007, India

A. K. Tyagi and R. S. Ningthoujam (eds.), *Handbook on Synthesis Strategies for Advanced Materials*, Indian Institute of Metals Series,
https://doi.org/10.1007/978-981-16-1803-1_19

Light Amplification by Stimulated Emission of Radiation. Therefore, a theoretical foundation was made in 1917 for today's several billion-dollar industries.

After about 43 years, the theoretical knowledge was realized experimentally and the first laser was "born" on May 16, 1960. Theodore Maiman, working at Hughes Research Laboratories, USA, built the first laser with a ruby rod, emitting red light pulses at 693.4 nm. It took another seven years to employ this laser for the first industrial applications for drilling a hole into a diamond. The hole drilled had the dimension of 4.7 mm in diameter by 2 mm deep and was accomplished in 15 min. This feat was remarkable since a similar application was needed one day at that time.

The laser is a central technology within photonics having a great economic impact and it can be classified as "general-purpose technology". Laser technology has progressed by a series of important innovations and a large number of lasers have been developed over the last sixty years. Advances in lasers have widened the applications of this technology, many of which have shaped remarkable enhancements in the performance of technologies utilizing lasers. It has altogether transformed medicine, opened up communication through the internet, and plays a pivotal role in linking economic, cultural, and political aspects of society worldwide. Nurturing global awareness about light-based technologies can offer solutions to challenges in agriculture, education, energy, health care, and security.

The application of lasers in material science and technology has flourished into a full-scale discipline. This area is attracting the attention of scientists, engineers, and manufacturers equally. Scientists are looking at the basic laser material interaction, while others are exploring it as a device to make faster, cheaper, and cleaner manufacturing processes. All these efforts are also opening up newer technologies and manufacturing processes. The most recognized application areas are machining which includes drilling, cutting and shaping, welding, recrystallization, glazing, and surface treatments. Chemical processing which includes reaction, material deposition, micro-patterning, and extended-area processing has applications in material science, optoelectronics, and sensor technology. Progressively, they are being used in biotechnology, medicine, and also in the restoration/conservation of artworks.

The present article conveys the basic essence of the subject with a few examples but definitely not a comprehensive review. There are many excellent books and review articles on various aspects of the field available in the literature [2–11]. Here, the purpose is to bring scientists, engineers, and manufacturers on a common platform to overview the understandings of current developments of laser applications in material science and also of the various new possibilities. We will first explore some processing segments of the industry, namely, lasers in cutting, drilling, marking, engraving, and then follow it up with further developments such as laser shock peening and laser surface treatment. In recent times, the market is witnessing a paradigm shift with newer applications of laser annealing for thin films, additive materials deposition, and rapid prototyping. Next, various strategies will be discussed based on non-equilibrium processes at interfaces and chemistry for synthesis of materials including nanoparticles, nanocomposite films, and nano patterning. The advent of ultrashort lasers and their commercial availability has opened up novel applications in the processing industry [2].

19.2 Back to the Basics: Light Industry

Lasers are photon energy sources with unique properties. For a detailed understanding of the subject, refer to many excellent books in the literature [12–17]. The basic laser system consists of the lasing medium, the resonator optics, the pumping system, and the cooling system if required (Fig. 19.1) [10]. The lasing medium according to its energy level structure generates the primary wavelength of the output beam. The lasing mediums, such as crystals or gas mixtures, are pumped by various methods such as flash lamp, electrical discharge or diode laser stack. Population inversion is achieved in the lasing medium by exciting with the proper pumping system and photons are generated within the optical resonator due to stimulated emission. The optical resonator design governs the photon energy to a narrow range, and only those photons along the optical axis of the resonator can be continuously amplified. The front mirror allows a certain fraction of laser energy to come out of the resonator as laser output. The output beam may pass through further optics to be adapted to specific applications such as polarizer, beam expander and lens, and beam scanner, etc. The use of nonlinear optical elements can generate different wavelengths from the primary wavelength. The Nd:YAG (neodymium-doped yttrium aluminum garnet) laser emitting 1.06 μm wavelength can be frequency doubled (532 nm) or tripled (355 nm) by inserting nonlinear crystals inside the resonator cavity.

Understanding the physics of laser-material interaction is crucial for gaining insight into material processing. When a laser beam hits the target material, its energy being partitioned in three different ways, namely, reflection, transmission, and absorption. The absorbed energy is utilized for heating or dissociating the material. From the microscopic viewpoint, first, the free electrons absorb the laser energy and then the absorbed energy gets transferred to the lattice ions via the associated electron network as illustrated in Fig. 19.2 [10].

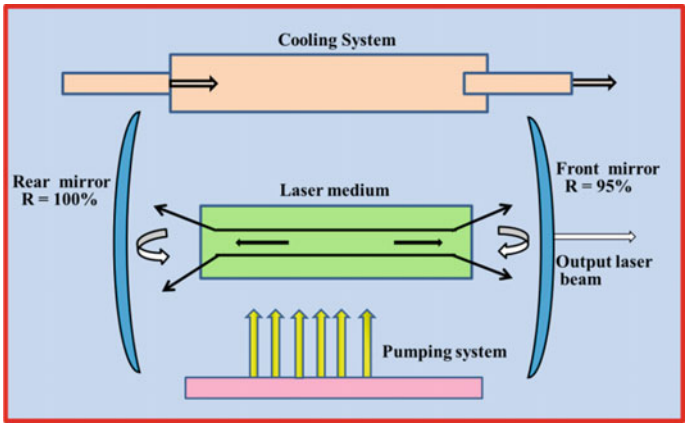

Fig. 19.1 Configuration of a basic laser system

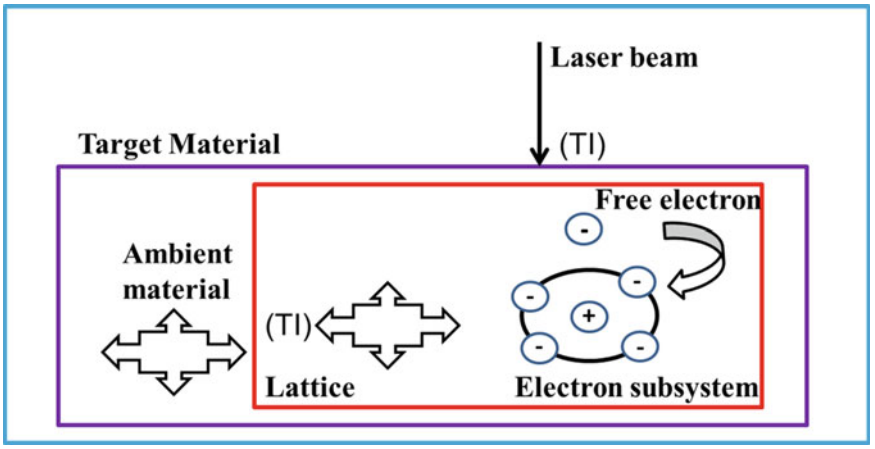

Fig. 19.2 Laser material interaction and energy absorption by the target material

At sufficiently high laser intensities, the material surface rapidly attains melting and vaporization temperature, and at the same time, heat is being dissipated into the material via thermal conduction. This leads to the melting and vaporization of the target material. By raising the intensities further, the vaporized materials start losing their electrons and plasma is formed which is a cloud of ions and electrons. Rapidly expanding vapor/plasma above the target generates a strong shock wave along with the thermal effects.

The heat penetration depth D through which the heat can be transported within the laser pulse duration is estimated as: $D = [4 \times \alpha \times t_p]^{1/2}$, where α is the diffusivity of materials, and t_p is the laser pulse duration. The well-known Lambert's law provides the transmission of laser energy in the target material, I(z)

$$I(z) = I_0.\left[\exp\left(-a\,.\,z\right)\right]$$

where I_0 is the incident laser intensity at the surface, a is the wavelength-dependent absorption coefficient and z is the distance from the surface. Metals are mostly opaque to all laser wavelengths and a is in the range of 10^5 cm^{-1}, which indicates that laser energy decays to 1/e of the energy at the surface within a depth of 0.1 μm. Liquids, glasses, and many nonmetals have different a values, and therefore, laser energy during its transmission may be absorbed over a much longer distance.

The three quantities: A the surface absorptivity, R the reflection, and T the transmission are related through the relation: A = 1 − R – T. For opaque material, it simplifies to A = 1 – R since T being zero. It may be noted that reflection and absorption are dependent on various parameters like wavelength, temperature, and surface condition. Thus, copper having an absorptivity of 2% for 10.6 μm CO_2 laser can have much higher absorptivity of about 60% for UV laser. At elevated temperatures, absorption usually increases due to more availability of free electrons.

19.3 Analysis of Material Processing System

From the discussion above, it is obvious that laser material interaction can be complex, involving a wide range of phenomena like thermal conduction, fluid dynamics, melting, vaporization, plasma, and shock wave formation. It is possible to get insight into the underlying physics in laser material processing by modeling. However, without going into the actual modeling, as a process engineer or manager, one can get a relatively complete picture following the four-factor analysis of time, spatial, frequency, and magnitude.

19.3.1 Time Attribute

CW laser has the capability of power modulations such as ramping up or down the power, focusing control, and energy-motion synchronization which are very attractive features for laser processing system. Though the CW laser delivers an average power ranging from W to tens of kW, its peak power is relatively lower compared to pulsed lasers.

There are several types of pulsed lasers delivering typically from millisecond to nanosecond pulses. One way to produce such pulses from several tens to hundreds of nanoseconds (10^{-9} s) is by a technique known as Q-switching. In this mode, the cavity is rapidly changed from a low-Q to a high-Q state, where Q represents the ratio of energy stored to the energy dissipated within the cavity. Material processing by such Q-switched solid-state lasers and CO_2 lasers is benefited from their high peak power and reduction of thermal diffusion. Even shorter pulse durations can be achieved with other techniques and their application will be discussed in the later section. Currently, large varieties of pulsed lasers can deliver pulse energies from nJ to over 100 J and can have kHz–MHz repetition rate. From the basic parameters of pulse energy, duration, and repetition rate, the peak power and the average power of the laser can be calculated. Peak laser intensity is obtained, dividing the pulse energy by pulse duration and beam area. With the availability of several orders of pulse duration, the pulsed laser can achieve peak laser intensities much in excess of 10^8 W/cm^2, while CW lasers normally provide laser intensities less than 10^8 W/cm^2.

19.3.2 Spatial Attribute

For laser material processing, the spatial distribution of the beam is of importance which governs the thermal field on the target. Normally, the output laser beam from the resonator cavity can have one or several modes, which are called *transverse electromagnetic mode* (TEM). The lowest order TEM_{00} mode has Gaussian beam distribution and is quite useful for processing. For a material with absorption A (= 1

– R), processed with a Gaussian beam of radius r, the spatial distribution of absorbed laser intensity on the material surface is given by

$$I(x,\ y,\ t)\ =\ (1-R)\ x\ I_0(t)\ x\ \exp\left[-\left(x^2+\ y^2\right)/\ r^2\right]$$

where $I_0(t) = 2P(t)/\pi r^2$ is the average laser intensity and P(t) being the time-dependent laser power. In general, the transmission of laser energy at depth z is expressed as

$$I(x,\ y,\ z,\ t)\ =\ A\ x\ I_0(t)\ x\ \exp\left(-az\right)\ SP(x,\ y)$$

where A = fraction of laser energy absorbed by the material surface, $I_0(t)$ = initial distribution of temporal intensity, a = absorption coefficient, and SP = spatial distribution of intensity. Other beam shapes like hat-top profile having uniform laser intensity at the center are also being employed.

Laser beam radius is estimated as the length from the beam center within which 86.4% $[(1 - 1/e^2)]$ of total energy resides. By using a focusing lens, the beam radius can be reduced and the beam radius at the focus is called the focused spot size. For lower intensity laser, an energy profiler can be used to directly measure the intensity distribution. However, it is difficult to measure spot size smaller than tens of microns or when the laser power is high. By burning holes in appropriate thin sheet material, the spot size is measured for high-power laser. A more accurate solution is obtained in case of a Gaussian beam by combining the experimental measurements with optical calculations. More than three measurements at different locations are measured to obtain (Z_n, D_n), n = 1, 2, 3… where D_n is the beam size at location Z_n. The propagation of laser beam in the air is expressed as

$$D_n^2 =\ D_0^2 + \left[\ 4M^2\lambda\ /\ \pi\ \right]^2\left[\ (Z_n - Z_0)^2/\ D_0^2\right];\ \ n\ =1, 2, 3\ldots$$

where D_0 is the beam waist, Z_0 is the beam waist location, and M^2 is the beam quality parameter. M^2 can be determined by measuring D_0, Z_0, and (Z_n, D_n), and then it is possible to determine the spot size at any location along the optical axis. Knowing M^2, one can also calculate the beam divergence and depth of focus (DOF), which is the range of distance over which the spot size changed from the focused spot size by 5 percent. Figure 19.3 illustrates the propagation, the beam waist, and the DOF of a laser beam [8].

Laser material processing is claimed to be noncontact because the highest intensity is at the focus while laser optics are some distance away from the target. It is not always convenient to change the focus in processing. The limited depth of focus limits laser machining to relatively thin materials (usually < 15 mm). In material processing, one has the option of moving either the beam or the job and also both of them if the need arises. An XY or XYZ motorized stage is commonly used. Laser beams can be quickly scanned across specified locations by computer controlled

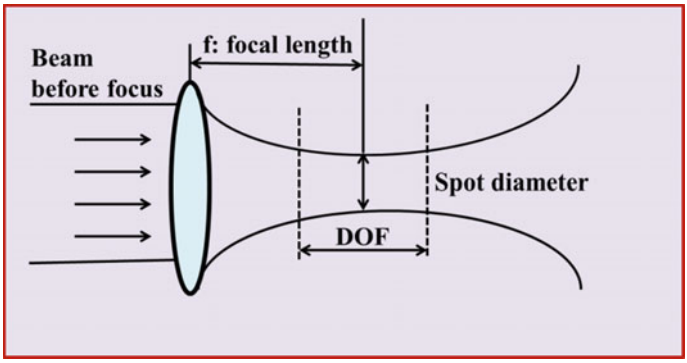

Fig. 19.3 The depth of focus of laser light

reflection optics. This makes high-speed marking or drilling possible. The spatial resolution of laser material processing is influenced by the focused spot size. Shorter wavelength lasers are thus used for precision machining tasks.

19.3.3 Frequency Attribute

Since interaction of materials is a function of laser frequency, the processing frequency is one of the important parameters in deciding the outcome. The frequency governs the energy associated with the laser photon. Lasers being monochromatic have very narrow spectral width, while conventional energy sources have wide and complex spectral distributions. For circular beams, the focal spot size is given by $D_{min} = 2.44\ f \times \lambda / D$, where f is the focal length of the lens, λ is the wavelength, and D is the unfocused beam diameter. Therefore, shorter wavelength lasers are preferred for high-precision applications. The ablation of organic polymers by UV laser can have different mechanisms compared to visible or infrared laser ablation. While the UV laser ablation proceeds mainly through photodissociation, the visible and infrared laser ablation occurs via photothermal route.

Metals normally having high absorption at UV, the absorption decreases with increasing wavelength (CO_2 laser 10.6 μm). Liquids and nonmetals like ceramics have strong absorption at UV, then it decreases in visible and again increases in the infrared region. Almost all materials absorb strongly in the vacuum UV region. Based on this understanding, different materials need to use lasers of different wavelengths for efficient energy coupling. Absorption also depends on temperature, purity, and surface condition. Defects or impurities in transparent media may strongly absorb the laser energy, and thus create a local thermal point and finally break down the transparent condition. At high enough laser intensity, multiphoton absorption may occur; material reacts nonlinearly to the irradiation. Once the surface temperature rises,

absorption tends to increase, which forms a positive feedback. In this meaning, very high laser intensity may be regarded as wavelength-independent material processing.

19.3.4 Magnitude Attribute

The characteristic magnitudes of laser energy are power (watt), pulse energy (Joule), and intensity (unit: W/m^2). The interaction is governed by energy intensity when the interaction between the laser and the material is not continuous. The variation of laser pulse energy can be from nJ to well above 1 J, pulse duration from several femtoseconds (fs $= 10^{-15}$ s) to about 1 s, and the spot size from micrometer to over 1 cm. As indicated earlier for pulsed lasers, the laser intensity is equal to $E_0/(t_p \times \pi r^2)$, where E_0 is pulse energy, t_p is pulse duration, and r is beam radius. For laser pulse energy of 0.1 J, if the pulse repetition rate can vary in the range from 1 Hz to 4 kHz, then the average power is 0.1−400 W. Let's vary the pulse duration and the irradiation area and then compute the peak intensity. With r = 0.5 μm, the peak intensity of a 10 fs pulse is 10^{22} W/cm^2, the intensity of a μs pulse is 10^7 W/cm^2, and the intensity of a ms pulse is only 10^4 W/cm^2. From this, it is quite clear that laser intensity can be flexibly controlled over a very wide range.

Depending on the absorbed laser intensity, different physical phenomena are involved [2]. Applications at various laser intensities and deposition times are shown in Fig. 19.4 [10] and Table 19.1 [2, 4, 10]. We tacitly assume that only one photon is absorbed by one electron at a specific time at normal laser intensities, but when the laser intensity is extremely high, as in the case of ultrafast lasers (pulse duration $< 10^{-12}$ s), more than one photon can be absorbed by one electron simultaneously. This is termed as multiphoton absorption. Material optical property is then highly nonlinear and is very different from single-photon absorption. Material can act as if

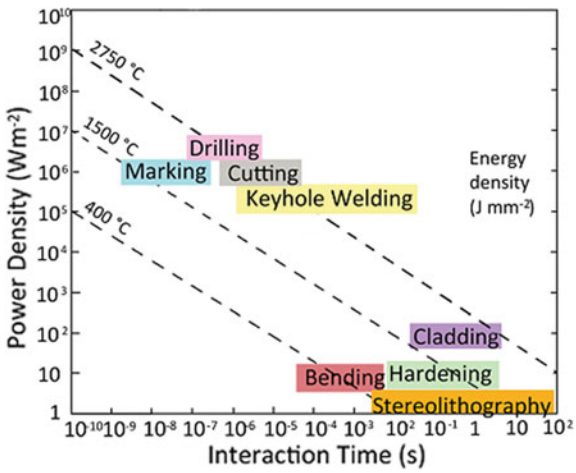

Fig. 19.4 Correlation of the laser power density and interaction time deciding the material processing map. This was reproduced with permission from the Laser Institute of America [9]

Table 19.1 Applications of lasers in material processing [2, 4, 9]

Applications	Intensity (W/cm^2) and laser material interaction
Laser surface transformation hardening, laser forming, laser assisted machining, etc	$<10^5$ W/cm^2, target heated below melting temperature, phase transformation may occur that can harden the material, elevated temperature can soften the material. Pulse duration > 10^{-3} s, CW lasers are used
Laser welding, laser cladding and alloying, rapid tooling, and laser machining	From 10^6 W/cm^2 to 10^8 W/cm^2, material melts, some vaporization and plasma formation possible. Pulse duration > 10^{-3} s, CW lasers are used
Higher intensity laser machining like marking, grooving, drilling, and cutting	From 10^7 W/cm^2 to 10^9 W/cm^2, material melts and strong vaporization occurs, shock wave and plasma formation possible. Pulse duration normally < 10^{-3} s, 10^{-9} to 10^{-6} s pulse duration are common, while for micromachining even shorter pulses are used. CW lasers or pulsed lasers are used
Laser shock processing, laser surface cleaning	Intensity > 10^9 W/cm^2 and pulse duration < 10^{-7} s, very intense surface vaporization induces strong shock pressure toward the target

it were irradiated by a frequency doubled or tripled laser source. In a sense, we can say that an extremely high magnitude of laser intensity can be equivalent to shorter wavelength experiments. From the above discussion, it is seen that four attributes analysis is quite useful in laser material processing.

19.4 Application Areas

A laser material processing system consists of the laser source, the beam delivery system, the motion and material handling system, and the process control system. Some systems may integrate the sensing unit to improve process quality. The individual laser material interaction for specific jobs is discussed below (Fig. 19.5) [10].

19.4.1 Laser Drilling

Laser drilling is one of the initial applications of laser machining processes. It is a process by which holes are formed by the removal of material through laser material interaction. Graduating from drilling hole in diamonds, now a days, it has found successful applications in automobile, aerospace, electronic, medical, and consumer

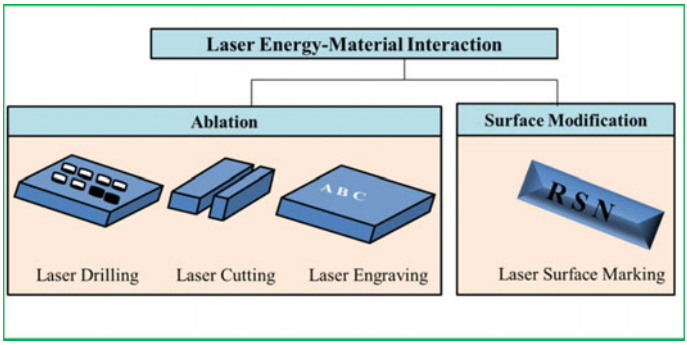

Fig. 19.5 Typical laser material processing areas

goods industries. One recognized example is the laser drilling of airfoil cooling holes of aircraft engines.

Lasers used for drilling require higher laser intensities than the intensities used in laser cutting. With finite pulse energy, high laser intensity can be achieved by tight focus and by short pulse duration. Normally, pulsed Nd:YAG lasers or pulsed CO_2 lasers are used. Similar to laser cutting, CO_2 lasers are a better fit for nonmetals and Nd:YAG lasers are better suited for metals. The laser pulse duration is normally less than 1 ms. The average power of the laser may not be as high as that used in laser cutting, but the achievable laser intensity is higher than laser cutting due to shorter pulse duration and smaller spot size. Lasers can drill very small holes with high accuracy and high repeatability. The diameters of holes range from several microns to about 1 mm. For extremely small diameter holes, tighter focus is needed and green or UV lasers, such as frequency doubled or tripled Q-switched Nd:YAG lasers, are used. When the pulse duration is short and the pulse repetition rate is high, the laser can drill even when the part is moving, resulting in high drilling speed.

19.4.2 Laser Cutting

Important process parameters in laser cutting are power, spot size, stand-off distance, focus position, scanning speed, gas pressure, gas flow rate and direction, and gas composition. The quality of laser cutting depends on both the material and the laser. With suitable control of the process parameters, high quality cutting can be achieved.

The lasers used in laser cutting are mainly CO_2, Nd:YAG, and excimer lasers. Industrial lasers for cutting typically have power levels from 50 W to 5 kW, although higher powers are used to cut thick sections. With robust technology of producing higher average powers with cheaper cost / W, CO_2 lasers are being used for the majority of cutting operations, particularly for nonmetals. The Nd:YAG laser emitting at1.06 μm having better absorption with metals than CO_2 lasers can have smaller focused spot size and also be fiber-coupled onto the target. All these advantages

have made the YAG laser a better choice for metal cutting industry. Excimer lasers emitting in the ultraviolet (193 nm: ArF, 248 nm:KrF or 308 nm: XeCl) are quite effective for nonmetals, metals, polymers, and semiconductors. Because of their shorter wavelengths, these UV lasers have better spatial resolution and are used for high-precision cutting jobs. Recently, advanced technology of diode lasers and diode-pumped conventional lasers not only have made these lasers compact, but also increased their average power and they are quickly replacing the bulky conventional lasers in the market.

In laser micromachining, a much wider variety of lasers with short pulse durations and high pulse repetition rates are used, such as frequency doubled (Green 532 nm) and tripled (UV 355 nm) Nd:YAG laser, copper vapor lasers, ultrashort pulsed lasers, and excimer lasers. The shorter wavelength and shorter pulse duration help to increase spatial resolution and reduce the heat-affected zone in laser cutting. The higher pulse repetition rate at smaller pulse energy makes it easier to get a smoother machined edge. But the average power of these systems is much lower than industrial lasers, typically < 50 W. High-power industrial lasers are commonly used to cut through larger thickness parts with sufficient speed, while micromachining lasers are used to generate small features with high precision.

19.4.3 Laser Marking and Engraving

Laser marking is a thermal process that creates permanent contrasting marks in target materials by scanning or projecting intense laser energy onto the material. In some cases, a shallow layer from the target is removed to make the marks, while in other cases, strong laser irradiation can create a color contrasting from non-irradiated area. Lasers are also used to engrave features into materials such as wood or stone products. Laser marking holds around 20% market share of all laser applications and represents the largest number of installations among all laser applications. Lasers can mark almost any kind of material and are used for showing production information, gemstone identification, engraving artistic features, imprinting complex logos, etc. Lasers used for marking and engraving are again pulsed CO_2, Nd:YAG, and excimer lasers.

In general, there are two fundamental marking schemes: one is marking through beam scanning or direct writing, and the other is marking through mask projection. In beam scanning or direct writing method, the focused laser beam is scanned across the target, and material is ablated as discrete dots or continuous curves. In the mask projection method, a mask with desired features is put into the laser beam path. Laser energy is thus modulated when it passes through the mask and a feature is created on the target. The mask can contact the target directly or can be away from the target and be projected onto the target by optics. This method has been used in the IT industry to produce very minute and complex features with the assistance of chemical etching. Beam scanning marking has more flexibility than mask projection marking, while mask projection marking can be much faster than beam scanning marking.

19.5 More Applications

We have seen already that laser energy is flexible, accurate, easy to control, and has a wide range of freedom in spatial, temporal, magnitude, and frequency of laser. In this section, we will present some more applications other than the already described above processes.

19.5.1 Laser Hardening

In laser hardening, a laser beam scanning across the metal surface can rapidly heat the top thin layer of the metal during laser irradiation without melting, and after the irradiation, it quickly cools down due to heat conduction into the bulk material. This is equivalent to the quenching process in conventional thermal treatment. When favorable phase transformation occurs in this laser quenching process, such as in the case of carbon steels, the top surface hardness increases strikingly. Commonly used systems are Nd:YAG, diode, and CO_2 lasers. The hardened depth can be varied up to 1.5 mm and the surface hardness can be improved by more than 50%. Laser hardening can selectively harden the target, such as the cutting edges, guide tracks, grooves, interior surfaces, dot hardening at naps, and blind holes. The neighboring area remains uninfluenced during laser hardening. By suitable overlapping, a larger area can be treated.

19.5.2 Laser Glazing

In laser glazing, the laser beam scans over the surface to produce a thin melt layer while the interior of the work piece remains cold. Re-solidification occurs very rapidly once the laser beam passes by, thus the surface is quickly quenched. As a result, a surface with special microstructure is produced that may be useful for improved performance such as increased resistance to corrosion. The surface layer usually has finer grains and may even be amorphous. Laser glazing of cast iron and aluminum bronze has demonstrated much enhanced corrosion resistance.

19.5.3 Laser Cladding

Laser cladding normally involves covering a relatively low performance material with a high-performance material for enhancing the wear resistance and check corrosion. In laser cladding, the overlay material is spread over the substrate or continuously fed to the target surface. A thin top layer is melted which bonds with the overlay material

metallurgically. The difference with laser alloying is that the overlay material doesn't intermix with the substrate. Cladding allows the bulk of the part to be made with low-cost material and coat it with a suitable material to gain desired properties and a good surface finish. Compared to conventional cladding processes, such as plasma spraying, laser cladding has the advantage of low porosity, better uniformity, and good dimensional control of the cladding alloy.

19.5.4 Laser Shock Peening

High intensity (>GW/cm^2) laser ablation of materials generates plasma that has high temperature and high pressure. In open air, this pressure can be as high as sub GPa and the expansion of such high-pressure plasma imparts shock waves into the surrounding media. With the assistance of a fluid layer which confines the expansion of the plasma, 5 to 10 times stronger shock pressure can be induced. This multi-GPa shock pressure can be imparted onto the target material and the target is thus called laser shock peened (LSP).

Laser shock processing can harden the metal surface and induce in-plane compressive residual stress distribution. The compressive residual stress refrains from crack propagation and greatly increases the fatigue life of treated parts. LSP when compared to mechanical shot peening, especially for irregular shapes, provides a profound layer of compressive residual stress and is a more flexible process. LSP can increase the fatigue life of aluminum alloy by more than 30 times and increase its hardness by 80%. Materials such as aluminum and aluminum alloys, iron and steel, copper, and nickel have been successfully treated. Laser shock processing has become the specified process to increase the fatigue lives of aircraft engine blades.

Conventional laser shock processing requires laser systems that can deliver high pulse energy (~50 J) with a very short pulse duration (~50 ns) with a Q-switched Nd:YAG laser. Such laser systems are expensive and the repetition rate is low (several pulses per minute). This situation is improving with cheaper high-power systems becoming commercially available. On the other hand, this technique can be extended to low pulse energy lasers with short pulse duration and tight focus. Two key requirements for successful processing are laser intensity >GW/cm^2 and short enough pulse duration (<50 ns). It is shown that the efficiency of the process can be more than 300 percent by treating the sample with a 50 ns pulsed UV laser.

There are many other laser material processing applications, in which difficult problems are solved by lasers, such as laser-assisted machining of super alloys and ceramics, laser-assisted etching, laser surface cleaning, and laser coating removal. In laser-assisted machining, the laser is used to locally heat the work piece prior to the cutting tool in an attempt to improve the machinability of difficult materials such as super alloys and ceramics. Etching rate is sensitive to temperature, thus laser beam can be used to enhance the etching rate locally. This is, in fact, one way of direct writing on the material. With the combination of laser heating and chemical etching, semiconductor devices can be etched 10 to 100 times faster than conventional

procedures. Laser-induced shock waves can be used to clean very minute particles on a silicon wafer, and laser ablation has also been used to remove rust or peel-off coatings by affecting a very thin surface layer.

19.6 Shifting of Landscape

In recent times, the laser materials processing market is witnessing a paradigm shift boosted by a multitude of advances—in Europe and in Asia-Pacific (APAC) countries such as India, Japan, China, and South Korea. Figure 19.6 shows the materials processing accounts in the total laser market compiled by European Photonics Industry Consortium (EPIC) [8]. This consortium keeps track of potential users in various sectors like avionics, automotive, electronics, medical, jewelry, etc.

High-power lasers govern the materials processing sector. The umbrella of mature laser technology encompasses a variety of lasers - nanosecond, picosecond or femtosecond; ultraviolet, green; CO_2, diode-pumped solid-state (DPSS), and fiber lasers. Now with so many choices at hand, the processing industry has to decide whether there is a strategic laser that can be customized to cater several applications or one suitable laser per application.

Traditionally, laser materials processing has been subtractive meaning materials are removed from the work piece. Of late laser additive processing, also known as 3D printing, is complementing to these operations. Though initially, additive processing

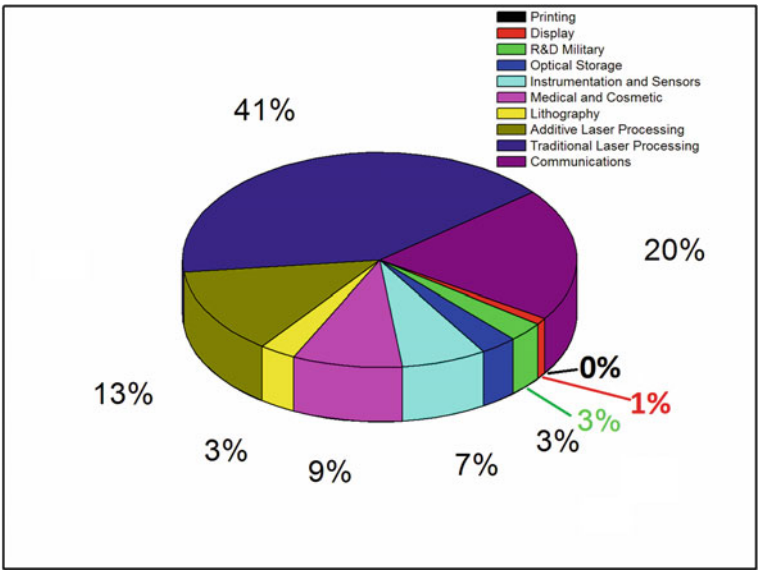

Fig. 19.6 Materials processing accounts in the total laser market compiled by EPIC

remained as the curiosity, it has now picked up to generate 13% of total revenues in 2014. Now several years on, this area is showing annual growth of 20% and is estimated to contribute 30% of revenues by 2020 [18].

19.6.1 Rapid Prototyping and Additive Manufacturing

Rapid prototyping is finding applications in designing either prototypes or quick fabrication of complex parts in low volume without the requirement of complex tooling. The process can be one of the two, namely, stereo-lithography using a photo-sensitive epoxy polymer or selective laser melting using ceramic or metal powder. The first one uses a low-power UV laser to selectively harden the polymer in a bath to form the part, while the latter builds up the part with a CO_2 laser or 1-μm fiber laser. In both of these processes, a 3D Computer Aided Design model is sliced into many layers and then moved to the respective tool. Layer-by-layer processing is done by directing the laser beam with a galvanometric scanner head. After each layer processing, polymer or powder is deposited on top of the part, and then the next laser processing step is initiated to complete the job.

19.7 Ultrafast Laser Processing of Materials

Ultrafast lasers have been developed for quite some time and are becoming more user-friendly and cost-effective. While the technology is advancing beyond the attosecond (1 as $= 10^{-18}$ s) regime, presently the lasers in the nano, pico, and femtosecond time regimes have been routinely used for processing various materials. Ultrafast pulses are unique having exceedingly large peak intensities and interact with materials faster than heat diffusion and lattice disorder time. These two characteristics permit ultrafast lasers to both control and manipulate the states of materials very precisely [19].

The advances made in chirped pulse amplification process facilitated the building of ultrafast lasers. Figure 19.7 shows the schematic of such laser system with the crucial steps of first the beam stretching, then amplifying, and finally compressing the beam back [10].

The fs-pulse controls the kinetics of melting and re-solidification of the target material. Under fs-pulse irradiation, the material undergoes several regimes of excitation and relaxation, before returning to its initial equilibrium state. These are (i) carrier excitation, (ii) thermalization (iii) carrier removal, and (iv) thermal and structural effects. The fs-laser pulses can generate huge electric fields, which are even greater than the binding coulomb fields of electrons in the atom (10^9 V/m). High peak pulse energies result in nonlinear absorption within short absorption depths, limiting the volume of laser energy deposition.

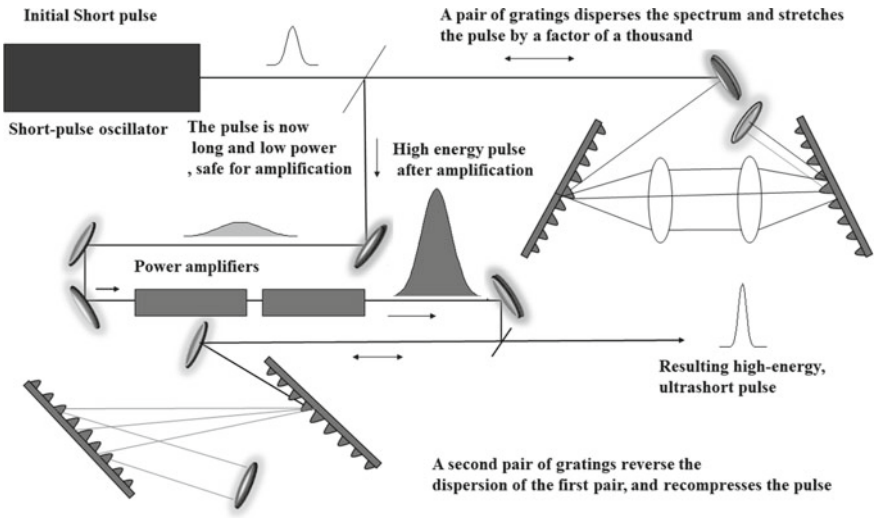

Fig. 19.7 Schematic of ultrashort pulse laser system

It is interesting to discuss the interaction dynamics of ultrafast pulse irradiation of semiconductors. First; the pulse delivers energy to the material at a faster rate than the electron–phonon coupling relaxation time. Thus, the laser energy is supplied only to the electrons and the ions remained completely "cold." Only after the pulse is turned off, thermal energy gets transferred to the lattice. Therefore, laser-semiconductor interactions can be described by unique processes of decoupled optical absorption and lattice thermalization. Second, high peak intensities of ultrashort pulse facilitate multiphoton absorption processes.

Compared to the above ultrafast process, when ns laser pulse interacts with a material, we have already seen that during the excitation process, the excited electrons transfer their energy to the lattice. Thus, during the entire excitation process, electrons and the lattice remain in equilibrium and the material gets heated to its melting temperature. The ns absorption process being linear resulted in a much longer absorption depth and generates a smaller temperature gradient over a longer distance between the molten layer and the solid material. Consequently, the melt duration is longer, and the re-solidification front speed is slower, resulting in a crystalline structure such as in case of silicon. In case of negligible absorption of material at the employed laser wavelength, both ultrafast and ns lasers can induce multiphoton processes. However, ns lasers with lower peak powers ablate materials via thermal mechanism. This thermal ablation resulted in a poor quality job characterized by a large heat-affected zone (HAZ) which can also favor melt re-deposition and generate shockwaves leaving behind defects like chipping and cracks.

Due to the flexibility, speed, and precision, ultrafast lasers are finding large-scale applications in micromachining. It should be mentioned that they are also being

utilized as material characterization tools such as surface-enhanced Raman spectroscopy (SERS) [17] and laser-induced breakdown spectroscopy (LIBS), besides providing the basic understanding of the dynamics of ultrafast chemical processes pioneered by Zewail [20].

19.8 Lasers in Materials Synthesis

Laser chemistry brings to mind the intention that in principle it should be possible to provide lasers tuned to a given energy level of atoms/molecules so that one can break the required specific bonds, make specific additions at a particular location, and prompt specific rearrangements eliminating the wasteful side reactions. Chemists are so excited about these possibilities that some of them have been talking about the arrival of laser alchemy. But laser chemistry is not alchemy—at least not yet, because they are not powerful enough to achieve nuclear transmutation. So far they have been used to cause changes only on the periphery of the atom—by enlarging the orbits of electrons, breaking molecular bonds, and making molecules rotate and vibrate faster. But even these achievements constitute a major breakthrough.

The first milestone in laser chemistry was achieved in 1972 when fairly powerful UV and IR lasers came into the market. The development of laser isotope separation (LIS) demonstrated the new potential of lasers in chemistry and material science [21–23]. Further progress was made by the ground-breaking works of Zewail leading to femtochemistry, which revealed the dynamics of ultrafast chemical processes and also helped in realizing the long-cherished dream of controlling the chemical reactions [24, 25].

The laser-induced synthesis of materials has the root in laser chemistry. The initial works in material science as discussed in earlier sections were confined to mechanical processing of materials. However, more knowledge-intensive information on laser-matter interaction accumulated over time and they were used for the production of new materials. Laser ablation of a substance in a vacuum or in a liquid is used to produce nanomaterials. A large variety of novel materials including carbon nanotubes, fullerenes, and graphene were synthesized by laser. Deposition of thin films can be carried out with great accuracy by laser ablation since one nm thickness film can be obtained with only several hundred laser pulses. It is quite easy to instantaneously alter the composition of the deposited film by simply switching the laser beam from one target to another. As discussed earlier, pulsed lasers readily produce highly non-equilibrium conditions favorable for synthesizing new materials and also permit access to new states of matter that enhances our understanding based upon bulk phase diagrams. These states are short-lived, dynamically evolving, and at the same time, they pose challenging problems to theoretical researchers.

In essence, it can be put as the chemist is able to reach into the molecular structures with his hands and rearranging the structure at will. Laser chemistry has blossomed into a full-scale discipline so much so that, we must restrict our attention to infrared laser chemistry, leaving mostly any excited electronic state photochemistry. Within

this restriction, various types of laser-driven reaction can be addressed from purely thermal to bond-specific reaction in a phenomenological way [26–30]:

1. Laser pyrolysis, where the laser is used as Bunsen burner, with the difference of providing homogeneous chemistry at high temperatures.
2. Laser enhancement of chemical reaction, where the reaction rate can be accelerated by one or two quanta of excitation.
3. Molecule-specific reactions, where laser not only triggers the reaction, but also supplies all the energy required thermodynamically to complete the reaction, e.g., isotope separation, ultrapurification, etc.
4. Bond specific chemistry, where the normal thermochemical route of a chemical reaction can be changed by the laser.

19.9 Selectivity of Photoexcitation

Before overviewing the above reactions, we should understand the types of selectivity expected from photoexcitation and also develop some methodology to establish for IR laser specific reactions from thermal ones.

The rate of excitation for a molecule, $W_{exc}{}^{nm}$, for the stimulated transition m ← n is given by $W_{exc}{}^{nm} = \sigma_{nm} I(\nu_{nm})$ where σ_{nm} and $I(\nu_{nm})$ are the absorption cross section and radiation intensity at the resonant frequency ν_{nm}. Owing to the small magnitude of the infrared quanta, the population of the corresponding vibrationally excited state by thermal equilibrium is not as a rule negligibly small compared with the population induced by the radiation. Until the advent of high-power IR lasers, there had been no IR-source with sufficiently high intensity to be capable of generating excited species at a higher rate than in thermal equilibration processes. Till then, only IR-spectroscopy existed, but no IR-photochemistry. Under the influence of an intense IR laser pulse, energy can be deposited at a very fast rate (1–10 eV during $10^{-8} - 10^{-12}$ s amounting to 10^{13} eV/s) which can far exceed the relaxation rate W_{relax}. For such a strong deposition $W_{exc} = \sigma_{abs} I > \tau_{pulse} > W_{relax}$, considerable excitation of the internal degrees of freedom is possible without any heating. Therefore, by considering different relaxation processes, we can obtain different kinds of selectivity. Typically, there are three kinds of relaxation processes:

(i) intramolecular vibrational energy redistribution (IVR) among vibrational modes with a typical time scale of $\tau_{stochastic} \approx 10^{-13} - 10^{-11}$ s.
(ii) inter-molecular vibrational–vibrational (v-v) energy transfer $\tau_{v\text{-}v} \approx 10^{-9} - 10^{-6}$ s.
(iii) vibrational–rotational/translational (V-R/T) energy transfer with $\tau_{V\text{-}R/T} \approx 10^{-6} - 10^{-3}$ s.

Since the first process is intramolecular, it may occur without collisions, while the other two processes are governed by collisions. Thus, the times τ_{VV} and τ_{VT} are mostly dependent on the particular experimental conditions.

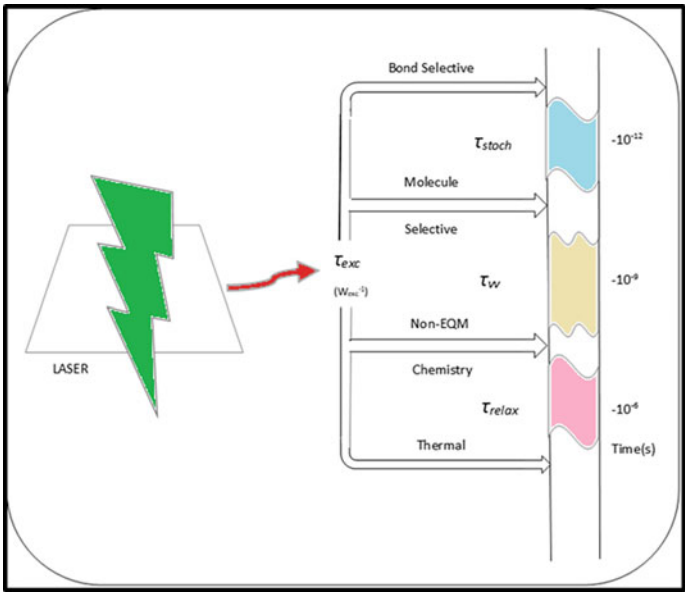

Fig. 19.8 Hierarchy of relaxation times vis-à-vis laser excitation rate and various laser chemical process

Now depending on the magnitude of $\tau_{exc}(\equiv W_{exc}^{-1})$ relative to various $\tau_{relaxation}$, in principle, it is possible to achieve four different types of chemistry (Fig. 19.8) [21]. They are considered below:

[A] Under the condition: $\tau_{exc} << \tau_{stoch}$, it is possible to realize mode (bond)-selective excitation of molecules in a non-equilibrium state under the influence of intense IR laser field. With such excitation, a certain mode or functional group of a molecule attains a higher vibrational temperature than the remaining modes or functional groups. Apparently, success can be obtained with the use of ultrafast laser pulse and appropriate choice of large molecules.

[B] Under a more moderate condition: $\tau_{stoch} << \tau_{exc} << \tau_{vv}$, it is possible to achieve molecule-specific chemistry. The molecules which are resonant with the IR field attain a higher vibrational temperature than the remaining molecules. But all the molecules in the mixture retain their initial translational temperature. This type of molecule-selective chemistry has been developed extensively, which started in landmark experiments on laser isotope separation.

[C] Further moderating the condition: $\tau_{vv} << \tau_{exc} << \tau_{VT}$, vibrational equilibrium can be established among all the components in the mixture, but the vibrational excitation does not degrade to heat by that time. This is possible when no molecular component in the mixture has a very fast VT rate. In such case, non-selective vibrational chemistry during the time $\leq \tau_{VT}$ can take place due to the difference between the vibrational and translational temperatures in the mixture. Based on this principle, indirect activation of molecules can

be achieved through efficient vibrational energy transfer from the chemically passive sensitizer molecule that absorbs the laser radiation. This method is successfully utilized for the investigation of dissociation kinetics.

[D] Finally, under the condition: $\tau_{VT} << \tau_{exc}$, there is equilibrium thermal excitation of all the molecules in the reactor volume, but there is no heat transfer to the reactor wall. In this case, pulsed thermal homogeneous heating of molecular gas occurs.

From the above understanding, it is apparent that a methodological difference has to be ascertained for the contribution of laser-specific reaction over thermal one. A few criteria for distinguishing the two modes are given below:

1. demonstrate isotopic selectivity in a mixture.
2. time resolve the evolution of reaction products with a resolution comparable or less than the mean collision time.
3. in case the reaction follows two routes, demonstrate that specific vibrational excitation accelerates two routes by different amounts.

In the context of various material synthesis strategies, however, we will particularly examine laser pyrolysis and molecule-selective chemistry schemes in the following sections.

19.10 Laser Pyrolysis

Laser initiated bulk reaction (case D) can be categorised as "black-box" vessels for efficient synthesis and chemical process control. CW laser irradiation of a substance at high sample pressure ($p \geq 10$ torr) or collisional energy transfer (from chemically inert laser absorbing molecule like sulphur hexafluoride) inevitably leads to equilibrium thermal heating owing to V-T relaxation. Here, laser serves as a Bunsen burner and naturally gives rise to thermochemistry. Still, laser-driven reactions could be very different from the corresponding ones, in which, an equivalent amount of translational energy is deposited by a conventional heat source. In these reactions, the key to understanding the mechanism may be that the laser induces high-temperature chemistry away from the vessel walls or homogeneous chemistry, whereas conventional high-temperature chemistry often has a dominant heterogeneous component. This technique has many advantages over hot flow tube reactors such as use of very simple apparatus, small sample size, and strictly homogeneous pyrolysis.

Remarkably specific yields of unusual products have been found: (i) icosaborane ($B_{20}H_{16}$) from irradiation of diborane (B_2H_6) with 1.5 W CW CO_2 laser and (ii) high yield of paraformaldehyde from CO_2 laser radiation of ethylene/air mixture. SF_6 has been used to provide vehicle for absorption of CW infrared laser radiation in those instances where the reactants are transparent to such radiation, thereby generating controlled temperatures from 500 to 1500 K. Since SF_6 is quite stable up to 1500 K and has a reasonably fast vibrational-translational (V-T) relaxation time, the

absorbed energy is rapidly (within millisecond) transferred to the ambient gas. Many gases like CH_4, C_2F_6, and t-butylchloride are decomposed by this laser-powered homogeneous pyrolysis technique to give various unique products [31]. Interesting studies on telomerization of C_2F_4 and CF_3I induced by TEA CO_2 laser were carried out in conventional and waveguide photoreactors. The product distribution in two cases differed and was understood in terms of perfluoroalkyl radical concentration generated in the irradiated volume and their various competing rate constants [32].

19.10.1 Synthesis of Defined Solids and Catalysts with Lasers

Catalytically active solids of adjustable composition can be obtained by laser pyrolysis of various gas mixtures (Fig. 19.9). Rapid heating of well-mixed gaseous reagents by the laser beam produced very small solid particles with homogeneous structure and large surface area. Figure 19.10 shows the yield of alkanes and alkenes obtained from the Fischer–Tropsch synthesis with such Fe/Si/C catalysts. Whereas with saturated hydrocarbons, mainly, methane is formed, with olefins, considerably longer chains are obtained. By adjusting the composition of the laser-synthesized catalysts, better selectivity and preferential formation of the valued light olefins (C_2-C_4) can be achieved [33]. In a similar process, powders of specialty ceramics

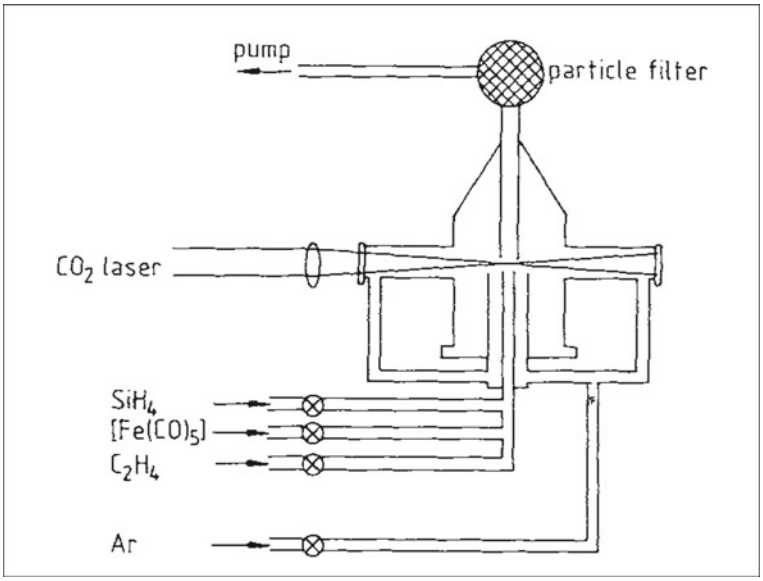

Fig. 19.9 Synthesis of Fe/Si/C catalysts by CO_2 laser pyrolysis. Partial pressures of the gaseous components and the laser intensities can be varied to produce catalysts with varying properties. This was reproduced with permission from Wiley Publisher [33]

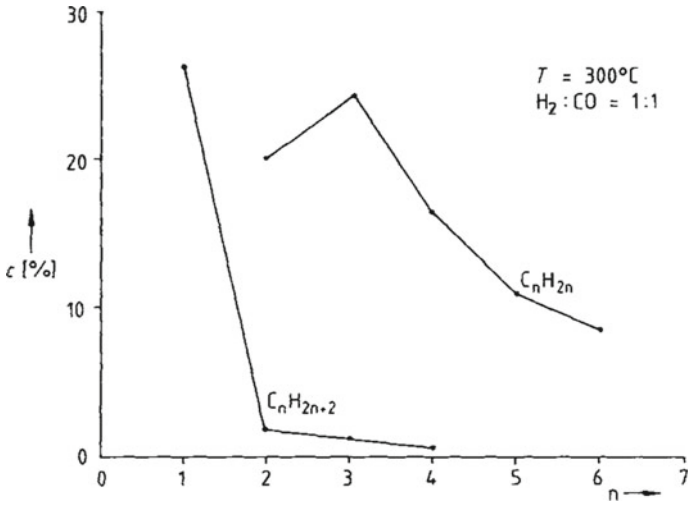

Fig. 19.10 Yield of alkanes and alkenes obtained from the Fischer–Tropsch synthesis with laser-produced Fe/Si/C catalysts. The amount of product in % is c and n is the number of C atoms. This was reproduced with permission from Wiley Publisher [33]

with defined composition can be obtained [34–36]. Irradiation of $Fe(CO)_5/SiH_4$, NH_3/SiH_4, $(Me_3Si)_2/NH_3$ or$SiH_4/NH_3/CH_4$ gas mixtures with a CO_2 laser leads to particularly fine, pure, spherical, relatively non-clumping, and uniform sized Si/Fe, Si_3N_4, and Si/C/N grains for the production of special ceramics.

19.10.2 Laser-Induced Powder Generation

Ceramic materials are extremely useful materials for manufacturing high-performance engine parts, such as the turbine, combustion chamber's inner walls, injector nozzles, caps and rings for pistons, and rotors for turbo-chargers. Normally, these materials are brittle and sometimes fail disastrously. However, they can be strengthened by proper sintering to fuse them into dense parts. This can be achieved if the starting powder has the following requisite properties:

1. Uniform particle size distribution (<0.5 μm)
2. The particles must be free of contaminants, agglomerates, and multiple polymorphic phases
3. The particles must have spherical morphology, i.e., the microstructure must be equiaxed

Conventionally, materials like Si_3N_4 and SiC are produced by using: (a) high-temperature vapor phase reactions in tube furnaces, (b) nitriding or carbiding of

Si, and (c) DC arc plasma techniques. However, none of these processes produce particles with all the above specifications.

Ceramic powders of Si_3N_4 and SiC with improved properties such as low density, high-temperature strength, hardness, corrosion resistances were synthesized by Haggerty et al. by laser-induced chemical reactions [37]. Various mixtures of the reactant gases, such as SiH_4/CH_4 or SiH_4/C_2H_4 for SiC and SiH_4/NH_3 for Si_3N_4, were flowed vertically across a horizontally propagating CO_2 laser beam. Representative reactions are given below:

1. $SiH_4\ (g) + CH_4\ (g) \rightarrow SiC\ (s) + 4\ H_2\ (g)$
2. $SiH_4\ (g) + C_2H_4\ (g) \rightarrow 2\ SiC\ (s) + 6\ H_2\ (g)$
3. $SiH_4\ (g) + 4NH_3\ (g) \rightarrow Si_3N_4\ (s) + 12\ H_2\ (g)$

The absorption coefficient of SiH_4at 10P(20) CO_2 laser line (944.18 cm^{-1}) attains a maximum value at about 0.025 atm, while the absorption coefficient of NH_3 goes to a minimum at about 0.25 atm pressure. Considering these facts, a 10:1 NH_3 to SiH_4 mixture at a total pressure of 1 atm was irradiated, where about 70% of the laser energy gets absorbed within a few cm lengths of the mixture, making the synthesis process quite efficient. This method produced 5–20 nm sized Si_3N_4 and SiC particles with a narrow size distribution. Morphologically, the shapes are generally spherical with a large surface area up to 200 m^2/gm and no aggregation or internal porosity. Based on this, a plant for low-cost production of tens of kilograms of nanometric-sized powder has been operated with 2.5 kW CO_2 transverse flow laser. The plant has a production rate of 500gm/hr while operating continuously for several hours [38].

To date, oxides such as titanium oxide (TiO_2) and titanium vanadium oxide ($Ti_{1-x}V_xO_2$) and non-oxides such as SiC, Si_3N_4 and $Si_xC_yN_z$ ternary compounds with continuously adjustable between pure carbide and pure nitride have been synthesized. Synthesis of niobium, tungsten, and tantalum-doped TiO_2, SnO_2, and ZnS has also been carried out by such laser-assisted process.

19.10.3 Synthesis of Metastable Materials

The synthesis of metastable materials can be carried out depending on the high heating and cooling rates achievable with lasers. The cooling rates achieved in standard splat cooling or melts pinning techniques (about 10^6 K/s) can easily be obtained with scanned cw-laser-heated surfaces. This rate can be further enhanced to about $10^{10} - 10^{12}$ K/s using Q-switched or mode-locked pulsed lasers. With such enormous cooling rates, it was possible to make glassy alloys for the first time. Binary alloys consisting of two transition metals, and for combinations of metals with group-IV elements were made and detailed investigations have been performed. Among the binary transition metal systems, glasses of Cu–Ti, Co–Ti, Cr–Ti, V–Ti, Au–Ti, and Ag–Cu have many interesting features [39]. The most studied system of binary alloys consisting of metals and group-IV elements is the silicides. However, such

glass formation will not be possible if the glass is unstable at ambient temperatures and if single-phase crystallization is possible from the melt.

19.11 Molecule-Selective Chemistry

Tunable and intense infrared radiation can be interacted with one species which may be one component in a gaseous mixture or even one isotope in a chemically pure compound (case B, Sect. 19.9). These molecules undergo multiphoton excitation and lead to stable products by irreversible dissociation or isomerization in the ground electronic state. When standard chemical and physical methods of purifications fail, such selective molecular photodissociation can be used to purify materials.

As already stated, photochemical and photophysical approaches to the separation of isotopes present major challenges in laser research in chemistry. We will present a brief account of the vast amount of work concentrating mainly on those aspects studied in our laboratory.

19.11.1 Laser Ultra-Purification

The selective photochemical removal of impurities with lasers is exemplified by the purification of gaseous SiH_4 (the starting material for the preparation of pure silicon for semiconductor production) from compounds such as AsH_3, PH_3, and B_2H_6, which are difficult to remove chemically. Contamination of such p- and n-charge carriers, even at a ratio of $1{:}10^9$, can negatively influence the functioning of integrated circuits. The beauty of the process is that, laser acts only on the impurities, whereas in conventional methods, the entire material is subjected to the purification process. Thus, laser radiation at $\lambda = 193$ nm is absorbed four orders of magnitude more strongly by PH_3 and AsH_3 and two orders of magnitude more strongly by B_2H_6 than by SiH_4. For purifying an impure (1%) sample, only 1% of the SiH_4 gets photolyzed while more than 99% AsH_3, and 40% PH_3 and B_2H_6 are removed [40–42]. The end products of this photolysis are readily separable solid polymers or gaseous compounds. Laboratory experiments show that the purification process even proceeds efficiently at atmospheric pressure, so that, for impurities of several ppm, typical absorption cross sections of 10^{-17} cm^2 and reactor lengths of several meters, more than 50% of the laser light is absorbed. Extremely high-purity silane is important for the economic production of electricity from sunlight, since the efficiency of silicon solar cells depends strongly on the impurities present. Further examples of efficient purification of gases are the separation of $COCl_2$ from BCl_3 and of CCl_4 from $AsC1_3$ and the destruction of dioxin.

Lanthanides and actinides can be efficiently separated and purified by exciting the narrow absorption bands of their compounds in the visible and UV [43]. The excitation is still selective even for higher absorber densities in the liquid phase. The

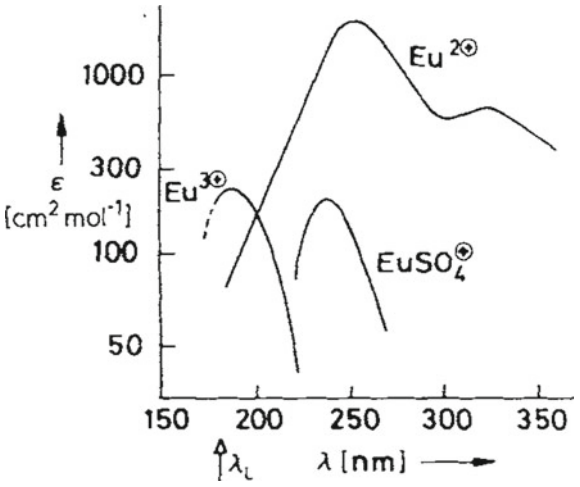

Fig. 19.11 Laser-induced separation of lanthanides. The absorption spectra of europium in various oxidation states show that the Eu^{3+}ions can be selectively reduced in the liquid phase with 193 nm ArF laser. The Eu^{2+} ions formed are precipitated as $EuSO_4$ after reaction with sulfate ions. This was reproduced with permission from Wiley Publisher [33]

new oxidation states formed by the photoredox processes enable the compounds to be readily separated. Figure 19.11 shows the separation of europium as an example, whereby the hydroxyl radical has to be scavenged, e.g., by isopropanol, to avoid the reverse reaction [33]. The quantum yield for Eu^{3+} photoreduction at 193 nm was given as 5% at 90% conversion, whereby up to a three-100-fold enrichment of europium was measured in the precipitate after irradiation of binary europium/lanthanide mixtures.

$$Eu^{3+} + H_2O \rightarrow Eu^{2+} + H^+ + OH$$
$$Eu^{2+} + SO_4^{2-} \rightarrow EuSO_4$$

H_2S in CO/H_2 synthesis gas was photolyzed selectively with an ArF laser and the sulfur released was removed by adsorption on a metal surface [38]. In this way, sulfur impurities could be reduced from 10 to 1 ppm. A spectroscopic selectivity (excitation only of H_2S in the synthesis gas) of 10^7 was measured in the wavelength range 210–220 nm. Quantum yields of H_2S decomposition of 0.4 (1 atm) to 1.0 (10 torr) were achieved. In particular, the use of a laser is interesting for the removal of "fine impurities" (< I ppmH_2S), since catalysts based on copper (e.g., those used for the production of methanol from synthesis gas) have lifetimes of about one year if the H_2S impurities in the CO/H_2 mixture can be reduced to less than I ppm.

19.11.2 Organic Synthesis with Lasers

The photolytic ring opening of 7-dehydrocholesterol (7-DHC) (Fig. 19.12) to give vitamin D_3, via previtamin D_3 (P_3), has long been employed for the large-scale

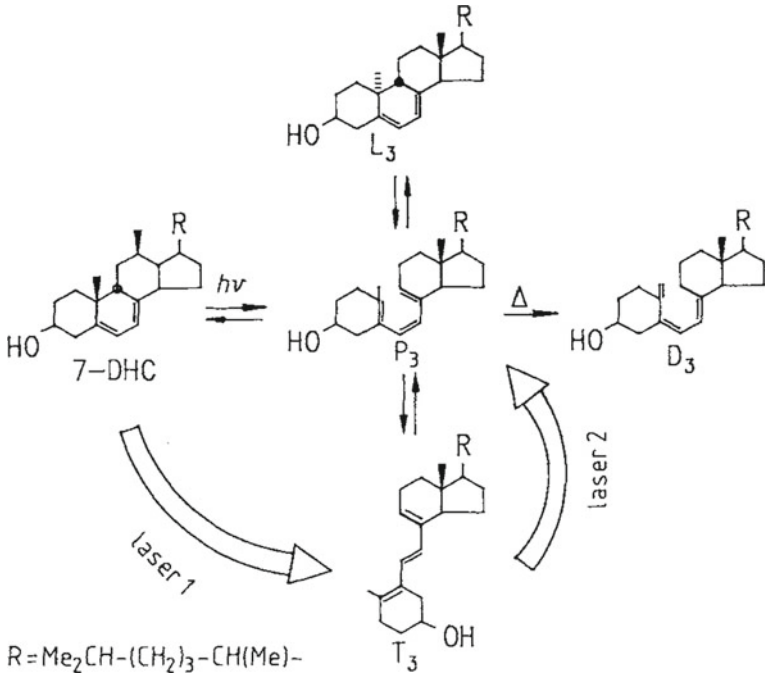

Fig. 19.12 Scheme for the synthesis of vitamin D_3. This was reproduced with permission from ACS Publisher [39]

synthesis of vitamin D_3. The three isomers: lumisterol (L_3), tachysterol (T_3), and P_3 can be interconverted by irradiation with UV light, whereby the photostationary composition depends strongly on wavelength. Table 19.2 and Fig. 19.12 show that the use of two laser wavelengths rather than irradiation with a Hg lamp leads to a considerable improvement in the yield of the desired vitamin D_3 precursor P_3 [33, 45, 46]. Irradiation with short UV light pulses in the picosecond range decreases the photolysis of P_3, and improves the ratio of P_3 to the undesired T_3 by another factor of 3.

Table 19.2 Photostationary composition of the mixture on irradiation of the vitamin D_3 precursor [45]

Light Source	% 7-DHC	% T_3	% L_3	% P_3
Low pressure Hg lamp	1.5	75.0	2.5	20.0
Medium pressure Hg lamp	3.4	26.0	17.0	53.0
248 nm KrF laser	2.9	71.0	–	26.0
308 nmXeCl laser	13.0	3.4	42.0	35.0
KrF + N_2 laser (337 nm)	0.1	11.0	9.0	80.0

The results of the laser experiments allow improvements in the conventional photochemical process, namely, the KrF laser (248 nm) and the N_2 laser (337 nm) are replaced by a low-pressure Hg lamp (254 nm) and a medium-pressure Hg lamp equipped with a suitable filter, respectively. In the production of special vitamin D_3 metabolites for medical diagnostics, an increase in yield by a factor of 5 is achieved by the use of lasers [47].

19.11.3 Laser Isotope Separation (LIS)

The main aim is to develop an effective isotope separation route for uranium-235, the fissile isotope of uranium which is used as fuel in light water moderated nuclear reactors. Additionally, a potential market exists for lighter element isotopes like deuterium, 6-lithium, 10-boron in energy production sectors. Non-radioactive tracers like 13-carbon, 15-nitogen, 17 & 18-oxygen, 34-sulphur, etc., are very useful in medical, analytical, and environmental studies. When compared with the current methods of isotope separation, LIS has the potential to deliver a product with higher enrichment per stage, energy economy, and savings in capital investment.

Mostly, all laser enrichment processes have three similar requirements: (1) the isotopic species must have well-resolved spectroscopic absorption features with a discernable isotope shift. The dense collection of electronic transitions in the visible or UV spectrum of gaseous atoms or molecules, display very little isotope shifts arising out of dissimilar nuclear mass, size, shape, and spin. Such isotope shift varies from $1:10^5$ to $1:10^8$ of electronic transition energy. Whereas the vibrational transitions of molecules in the infrared spectral region are directly linked to the reduced mass of the constituent atoms. In this case, the relative isotope shift is usually in the range of 1:100 to 1:1000. (2) the processing laser must be monochromatic and tunable so that selective excitation of the desired isotope can be performed. (3) an extraction step must be there which can efficiently remove the desired isotope. The step could be electrical, magnetic, optical or chemical that operates preferentially on the excited species before various processes of isotopic scrambling like relaxation, collisional energy and/or charge transfer can take place. The last one is the most rigorous condition for practical implementation of any LIS process. Based on the above criteria, several strategies have been investigated on a laboratory scale: (a) single-step electronic excitation via $h\nu_1$; (b) two-step electronic excitation with $h\nu_3$ via vibrational state excitation with $h\nu_2$; and (c) multiple- photon (n) excitation via $nh\nu_4$ in the ground electronic state (Fig. 19.13) [48]. Few isotope selective experimental results are presented in Table 19.3.

It may be worth mentioning that naturally occurring carbon isotope 13-C has an abundance of 1.11% and is required to be enriched at a much higher level for its use. The current technology of enrichment is based on a cryogenic distillation of carbon monoxide has inherent drawbacks of low separation factor (1.0076), high energy expenditure, huge distillation tower, and very long time for equilibrium attainment leading to a high production cost. In order to meet a projected 100-fold increase

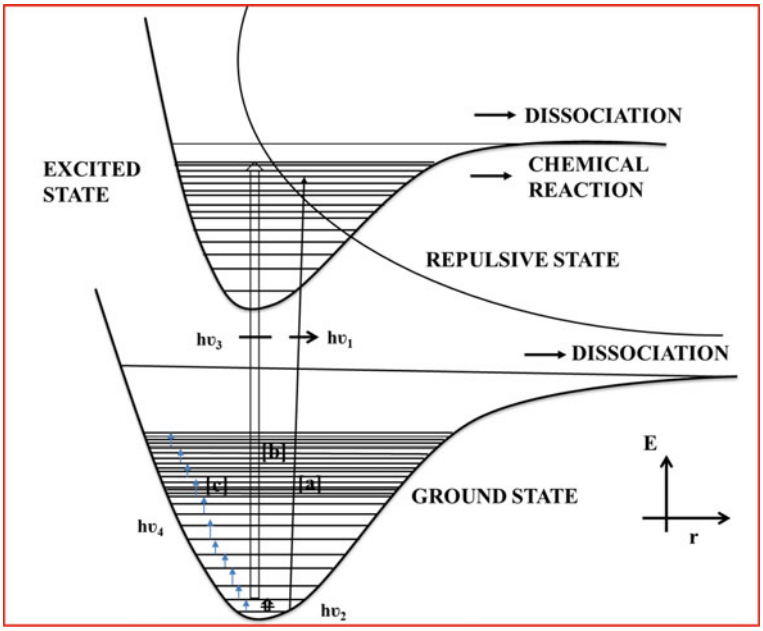

Fig. 19.13 Selective excitation schemes in LIS: **a** single step electronic excitation via $h\nu_1$; **b** two-step electronic excitation with $h\nu_3$ via vibrational state excitation with $h\nu_2$; and **c** multiple-photon excitation via $nh\nu_4$ in the ground electronic state

in demand at lower cost, BARC has developed an energy-efficient LIS process to produce 50% and ≥ 90% enrichment level products in single and two-stage processes, respectively (Table 19.3; 48, 49). A prototype facility has been built for demonstrating plant scale technology, consisting of a 5 J commercial pulsed CO_2 laser, photochemical reactor based on multipass refocussing Herriott cell and product separator, with computerized process monitoring and control.

19.12 Laser Chemical Vapor Deposition (LCVD)

LCVD is a well-established strategy for obtaining thin film deposition on a substrate by inducing chemical reactions of various materials by laser [50]. This technique can be of two types depending on the reaction mechanism: (1) pyrolytic and (2) photolytic. In pyrolytic process, usually Nd:YAG or CO_2 laser is employed to create a hot zone. In this zone, thermally induced chemical reactions take place producing the film material that is finally chemisorbed onto the substrate. The precursors for this process must be selected carefully so that the chemical reactions can occur below the substrate melting point.

Table 19.3 Isotope selective laser photochemistry at Bhabha Atomic Research Centre [48, 49]

Isotopes Pressure (Torr)		Typical results		
		Laser line	Fluence (J/cm^2)	Selectivity
Sulphur 34 / 32	SF_6 1.0	10 P(20) CO_2 laser	2.0	10
Uranium 235/238	$UO_2(hfacac)_2$.THF Molecular Beam	10 P(4) CO_2 laser	0.08	1.2
Carbon 13 / 12	CF_3Cl 15.0	9 P(18) CO_2 laser	3.0	80
Carbon 13 / 12	CF_2HCl 100.0	9 P(20) CO_2 laser	4.0	60
Stage 1	CF_3Br/Cl_2(1:4) 50.0	9 P(32) CO_2 laser	4.5	65
Stage 2	CF_3Cl/Br_2 (1:6) 20.0	9 P(8) CO_2 laser	1.7	200
Deuterium D / H	CHF_3/Ar (1:2) 75.0	10 R(10) CO_2 laser	30.0	> 40
Tritium T / H	CHF_3/Ar (1:2.5) 28.0 (0.2 ppm CTF_3)	9 R(8)-9 R(14) CO_2 laser	65.0	38
T / D	$CDCl_3$/Ar (1:5) 12.0	828 cm^{-1} NH_3 laser	21.0	5000.0

On the contrary, photolytic LCVD depends on the interactions of the laser beam directly with the reactants. After absorbing the laser photons, the reactant molecules dissociate to yield a final product which gets deposited on the surface of the substrate. Normally, the UV and visible lasers are used in this scheme because the photon energy is in excess of bond dissociation energy. The precursors and the processing laser are carefully chosen so that the precursors have a satisfactory absorption coefficient at the laser wavelength. It is apparent that the photolytic LCVD technique offers deposition of films at lower temperature compared to conventional deposition techniques. This is a beneficial feature for the semiconductor devices fabrication, since at lower temperature, impurity redistribution and thermally induced residual stress are minimized.

Further LCVD process looks promising by eliminating several disadvantages of other film-depositing techniques like plasma-assisted deposition, chemical vapor deposition (CVD), molecular beam epitaxy (MBE), etc. Some of the advantages are (i) better deposition rate (ii) spatial resolution and control, and (iii) least damage to film/substrate materials.

19.12.1 Metal Films

For preparing metal film, metal alkyls are a promising starting material. Most exhaustive studies have been made on photolytic LCVD of $Cd(CH_3)_2$and $Al_2(CH_3)_6$. Based on their well-known photochemistry, these molecules undergo single-photon excitation and dissociation with a UV Ar+-laser

$$Cd(CH_3)_2 + h\nu(257\ \text{nm},\ Ar + \text{-laser}) \rightarrow Cd\left(^1S_0\right) + 2CH_3$$

Photolysis can be affected in the gas phase and also on the surface, and the generated free methyl radicals subsequently dimerize to form ethane. With UV intensities of about 10^4 W/cm^2, reasonable deposition rates for Cd of up to 0.1 μm/s have been obtained and direct writing with line widths as fine as 0.7 μm has also been established.

Both pyrolytic and photolytic LCVD have been employed to obtain very good quality aluminum film from $Al_2(CH_3)_6$ [51]. Direct writing of aluminum lines with deposition rates up to 0.1 μm/s and line widths of 2–3 μm was demonstrated. Further studies have been carried with photolytic LCVD on $Ga(CH_3)_3$, $In(CH_3)_3$, $Te_2(CH_3)_2$, $Zn(CH_3)_2$, and $Zn(C_2H_5)_2$ [52].

19.12.2 Deposition from Metal Carbonyls

Metal carbonyls are attractive candidates for making extended thin film of metals by photolytic decomposition of $Ni(CO)_4$, $Fe(CO)_5$, $Cr(CO)_6$, $Mo(CO)_6$, and $W(CO)_6$. Typically, metal carbonyls undergo fragmentation process below 350 nm. Using cw- and low-power pulsed laser, single-photon sequential elimination of CO ligands can be affected

- $M(CO)_m + h\nu \rightarrow M(CO)^*_{m-1} + CO$,
- $M(CO)^*_{m-1} + h\nu \rightarrow M(CO)^*_{m-2} + CO$,
- $M(CO)^* + h\nu \rightarrow M^* + CO$,

where the star indicates electronically excited molecule/fragments. Removal of the remaining ligands after absorption of one or two photons can also be induced by collisions. Pulsed laser excitation at higher power can lead to multiple-photon dissociation releasing all CO groups together instead of single-photon sequential elimination of CO ligands.

The literature in this area has been well documented in reference [4]. Metal films of Cr, Mo, and W were deposited on Si substrates using Ar^+-laser radiation at 257 nm. The temperature rise of the substrate was estimated to be less than 50 K with the employed laser powers. Deposits were analyzed by Auger technique to get information on surface photo dissociation and dissociative chemisorption processes.

19.13 Chemical Transformations in Bulk and Within Thin Film Materials

Chemical transformations inside organic materials using light encompass photodecomposition, polymerization, and photochromic reactions. Among these, photopolymerization has become an active area of research and development in polymer science and technology. A well-known instance is the transformation of methyl methacrylate (MMA) into PMMA by using UV or visible radiation. Various techniques employing laser direct writing, interference and laser-light projection are used for localized polymerization. Additionally, multiple-photon-induced photopolymerization has opened new prospects in 3D-photoprocessing. Frequency-multiplied Nd:YAG and excimer lasers are mainly used for the fabrication of 3D optical data storage, optical waveguides, and photonic bandgap structures. The other significant applications of laser-induced chemical transformations include the following:

(i) Laser lithography: Hg-lamps ($\lambda = 436$ nm or 365 nm) were employed earlier in optical lithography for microelectronic chip fabrication. They are presently substituted by ArF / KrF excimer lasers [53]. For the fabrication of low-resolution patterns, maskless techniques are gaining increasing importance. For the next generation, optical lithography and extreme ultraviolet (EUV) radiation at 13.5 nm is being developed [54].

(ii) Stereo lithography: Using a CAD program and laser-beam interference for layer-by-layer polymerization, 3D periodic structures have been fabricated [55]. Based on two-photon absorption, 780 nm Ti:sapphire laser radiation ($\varphi = 44$ mJ/cm^2, $\tau_p = 60$ fs, rep rate $= 90$ MHz), can induce polymerization in viscous liquids like acrylate, epoxy, silica sol–gel, etc. The feature sizes obtained are well below 100 nm [56]. The technique has been employed for the fabrication of many devices and, in particular, for 3D photonic crystal structures [57].

19.14 Pulsed Laser Synthesis of Nanomaterials

Different nanostructured materials have been synthesized by pulsed laser synthesis (PLS) using a host of gas, liquid, and solid precursors [58, 59]. This versatile technique has the potential for industrial manufacturing since high pressure or temperature conditions are not required. Various experimental setups are used to optimize the product yield and size homogeneity depending on the starting materials and the processing lasers. Typically, the processing laser beam is focused (i) within a gaseous precursor filled reactor, (ii) in colloidal solution, and (iii) on a solid target positioned in a pure solution.

19.14.1 Synthesis by Pulsed Laser Ablation (PLA)

Synthesis of inorganic and carbon-based materials can be carried out by ablation [60] which is a top-down synthesis procedure for nanotubes, nanowires, nanoribbons, and quantum dots. The procedure is conveniently categorized into the liquid phase and gas phase with pulsed laser ablation (LP/GP-PLA). The processing laser beam is focused on the target inside the reactor containing liquid–solid or gas–solid interfaces. The generated plume of nanoparticles from the ablated target material subsequently reacts with the liquid or gas. The synthesized material can conveniently be doped by selecting a precursor containing the dopant element [61].

19.14.1.1 Synthesis by GP-PLA

The GP-PLA is nothing but laser chemical vapor deposition LCVD technique which has been already discussed (Sect. 19.9). The gas in GP- PLA is used simply to control the plasma plume dynamics. This setup with low laser power in conjunction with an external temperature arrangement is used to produce nanomaterials such as carbon nanotubes (CNT) [62]. With increased laser power, produced plasma itself provides the high temperature needed for the synthesis of some nanomaterials [63].

19.14.1.2 Synthesis by LP-PLA

Laser irradiation of the solid target positioned in a liquid medium kept inside the reactor undergoes vaporization followed by the formation of a plume containing ions, atoms, molecules, clusters, and particles. The generated species react with the liquid molecules, producing novel nanostructures consisting of both target and liquid atoms. The liquid layer and high temperature/pressure generated by the focused laser beam create a confinement situation. This confinement offers a suitable condition for the formation of metastable phases, which, in turn, helps in various nanostructures synthesis [64]. The choice of the solid target, the liquid, laser power, and wavelength are the crucial parameters in producing nanostructured materials of specific properties and sizes. The synthesized nanomaterials can be collected by filtration from the colloidal suspension or by evaporation of the homogenous mixture of soluble nanoparticles.

19.14.1.3 Synthesis by Pulsed Laser-Induced Breakdown (PLIB)

A pulsed infrared laser is focused inside a reactor containing a liquid hydrocarbon such as toluene and benzene to achieve breakdown [65]. The strong electric field generated by the focused laser prompts the ionization of the hydrocarbon. In the ionized volume, the free electrons are further accelerated by the intense field.

These accelerated electrons collide with the hydrocarbon molecules eject more electrons and results in avalanche multiplication, which induces the breakdown of the hydrocarbon.

19.14.1.4 Synthesis by Pulsed Laser Photolysis (PLP)

The synthesis method is suitable for both carbon-based and organic materials [66], and inorganic nanoparticles [67, 68]. Pulsed Laser Photolysisis carried out by irradiating room temperature colloidal suspension with UV or IR pulsed laser. Nanoparticles of FePt were synthesized by irradiating a solution containing iron acetylacetonate and platinum acetylacetonate. By changing the laser energy, it is possible to control the size and the ratio of the metals. Photochemical reaction pathways have been proposed for such nanostructures formation.

19.14.1.5 Synthesis by Pulsed Laser Deposition (PLD)

PLD is employed for the thin film synthesis of semiconductors [69, 70], heterostructures of complex-oxide [71], and ceramics [72–74]. Generally, the high-power laser is focused inside a vacuum chamber to vaporize the bulk target onto a substrate kept near the target. The laser-ablated material produces the plasma plume which contains neutrals and ionic species and these species get deposited on the substrate. For deposition of oxides, the chamber can be filled with appropriate pressure of oxygen.

19.14.1.6 Synthesis of Graphene Quantum Dots (GQD)

Of late, considerable attention has been received by Graphene Quantum dots (GQDs). They have many novel properties like excitation-dependent photoluminescence, resistance to photobleaching, biocompatibility, and low toxicity. They are basically planar nanoflakes (2–20 nm) of graphene material which is a few atomic layers thick and have a high surface-to-volume ratio. They have potential applications in photodynamic therapy, drug delivery, bio-imaging, and photocatalysis [75, 76]. However, the synthesis of good quality GQDs with narrow size distributions and high yield is still challenging. Recently, a new method using pulsed laser for the synthesis of intrinsically luminescent GQDs has been reported [77].

19.14.1.7 Synthesis Using PLS of Boron Nitride Nanostructures

Nanostructures of boron nitride (BN) have currently attracted many investigations due to its various interesting properties, like hardness, low thermal expansion, good thermal conductivity, better thermal shock resistance, high electrical resistance, and

Table 19.4 Pulsed laser synthesis of boron nitride nanostructures [80]

Target	Methodology	Synthesized nanostructure	Literature
h-BN/acetone	LP-PLA	Nanofibers	[73]
h-BN/acetone	LP-PLA	Nanotubes	[73]
BN	Plasma-assisted PLD	Nanocapsules	[66]
h-BN	PLD	Nanosheets	[67]
h-BN	PLD	Thin Films	[68]
h-BN	Ion assisted PLD		[72]

chemical inertness [78–80]. Further, the synthesis procedure has been initiated for obtaining various forms of BN, such as cubic (c-BN), hexagonal (h-BN), and boron nitride nanotubes (BNT), which are having many potential applications.

A large number of reports are available in the literature on the synthesis of BN nanostructures using various techniques [72–74, 78, 79]. Table 19.4 summarizes the different experimental procedures.

Recently, nanostructures of c-BN and h-BN in high yields were synthesized using PLS in the gas phase [75]. The characteristic particles produced have a size of 20–100 nm range and a composition of boron to nitrogen = 1. Borazine vapor was irradiated with two wavelengths simultaneously (1064 and 532 nm) generated from the same pulsed Nd:YAG laser for an hour in a high vacuum reactor. Product material was collected on a substrate placed inside the reactor.

The Raman spectrum (Fig. 19.14a) revealed two sharp peaks at 803 and 1356 cm^{-1}, and two broad bands at ca. 1000 and ca. 1400 cm^{-1}. The sharp ones are assigned to the h-BN and the two broad bands correspond to c- BN. This indicates that both the form were simultaneously synthesized. The porous nature of the nanostructures of BN with nanocrystals of 20–100 nm covering the silicon substrate is quite evident from the SEM and TEM images (Fig. 19.14b).

19.14.2 Laser for Biomaterial Coatings

Laser has brought revolutionary progress in the field of biomaterials, where ceramics are employed for quality betterment of our life. Specially developed ceramics are used for the reconstruction and repair of bone defects or traumatic diseases [81]. Hydroxyapatite (HAP) has emerged as an important bioceramic which forms good bonding with the surrounding bone tissues after implantation. It has found application in both dentistry and orthopedics [82]. However, bulk HAP is not suitable for load-bearing applications and large bony defects since it is brittle and weak. Therefore, bone fillers use HAP in granular form and it is coated for osteointegration of various cement-less titanium-based implant devices.

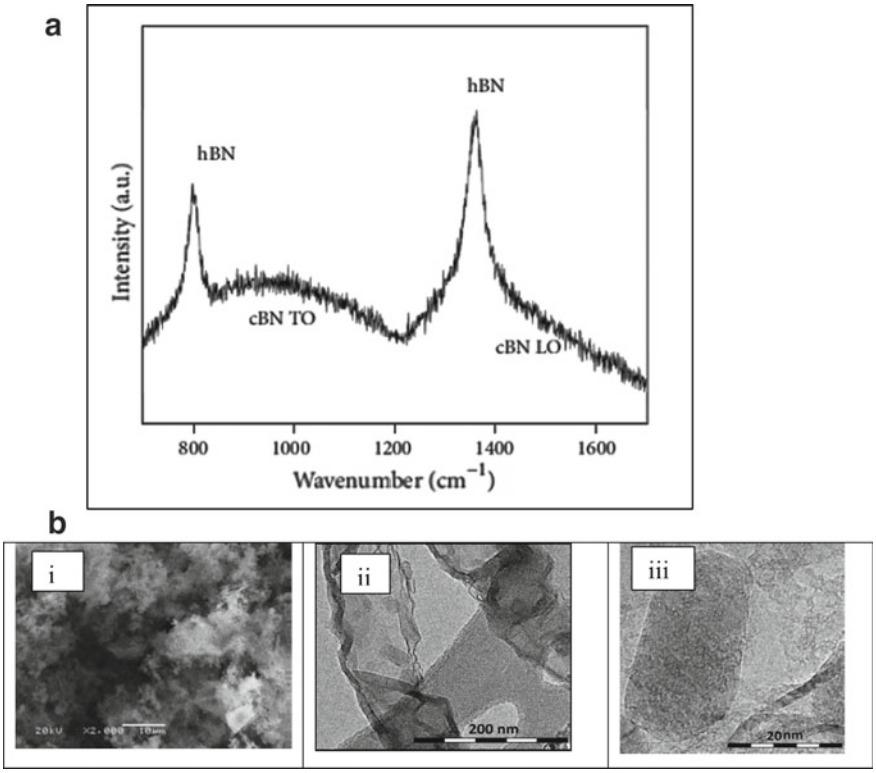

Fig. 19.14 **a** Characteristic two bands at 803 cm^{-1}and 1356 cm^{-1}revealed in Raman spectrum assigned to hexagonal BN and **b** (i) BN nanostructures as seen in SEM images; (ii) BN nanostructures (20–100 nm) as seen in TEM image; (iii) synthesized cubic BN nanostructures revealed in TEM image. This was reproduced with the permission from Hindawi Publisher [80]

The first method developed for making a calcium phosphate coating on metallic implants was by plasma spraying [83]. Currently, three laser-based methods are developed for coating metallic substrates with bioceramics. LCVD (Sect. 19.12) technique has been successfully employed to deposit simple ceramics such as silicon nitrides, silicon oxides, chromium oxide, or boron carbide on metallic substrates. The other two techniques are laser ablation and laser cladding. Between them, laser ablation has become more advanced and routinely used to coat commercial orthopedic spine screws and dental implants. Both corners and sidewalls of implants can receive uniform coating by this technique [84, 85].

19.15 Laser-Induced Graphene

The wonder material of the twenty-first century, graphene, has been investigated extensively right from the basics to the applications [86]. In quest of material having a large area and matching morphologies, native two-dimensional (2D) forms of graphene were improved as graphene foams. Several routes have been worked out to produce graphene foams by wet-chemical and chemical vapor deposition methods. These methods require high-temperature furnaces, pure gases, and strong acids and oxidants. However, the growing need for attractive applications has prompted the technologist and manufacturer for macroscale production of graphene material. Recently, laser synthesis has come to lead the way by producing what is known as Laser-Induced Graphene (LIG).

Irradiating polyimide (PI) plastic films using a commercial laser scribing system in air leads to the formation of LIG. This simple technique being a one-step method eliminates high temperature, solvent or subsequent treatments. Produced LIG has atomic arrangements comprising of several five-and seven-membered rings. This can be considered as "kinetic graphene", because this synthesis route does not provide any annealing which normally favors the rearrangement to the ideal all six-membered ring form [87].

It is quite apparent that the conversion of PI to LIG goes via photothermal route caused by the high temperature and pressure produced by focused laser irradiation. In this case, LIG offers about 340 m^2/g of surface area with a hierarchical structure along with plentiful wrinkles. This is quite comparable to that of 3D graphene prepared by the wet-chemistry procedure. The aberration-corrected scanning transmission electron microscopy images unveil an unusual polycrystalline character of LIG. Instead of the conventional hexagon lattice, the carbon of LIG exists in a hybrid lattice of pentagon-heptagon and hexagon. The irradiation parameters are crucial in determining the physical and chemical properties of LIG. Generally with increased laser power, one can get thicker LIG, which, in turn, enhances the conductivity. Using a 4.8 W laser, irradiation product LIG attains its highest crystallinity with fewer defects and maximum domain size. It may be noted that laser fluence of about 5.5 J/cm^2converts PI into LIG quite efficiently. The control of LIG morphology can be achieved by the image density. The image density is governed by the pulses and the lines per inch (PPI and LPI). Typically, with 100 μm laser spot size and an image density of 1000 PPI × 1000 LPI, LIG adopts an in-plane porous structure. By decreasing the image density (500 PPI × 500 LPI) and the laser spot size (60 μm), LIG converts to out-of-plane fibers (LIGF) and forms a vertically aligned forest morphology [88].

With hectic investigations all over the world, LIG has already established wide applications in catalysis, sensors, microfluidics, renewable energy devices, water purification, etc. Moreover, there are exciting possibilities for preparing LIG from natural products which can be used for the fabrication of biodegradable devices for reducing e-waste. With these emergent advancements, the transfer of technology to commercially synthesize LIGis expected very soon [89–92].

19.16 Conclusions and Future Perspectives

The attractive features associated with laser do not come without disadvantages. The single, most important disadvantage is their high cost. Laser photons are generally expensive ingredients. Normally, the capital and operating costs of lasers are relatively high in comparison to the cost of processing and synthesizing chemicals.

In this brief overview, we have shown that laser material processing has slowly but steadily become indispensable engineering solution for a large number of applications. Traditionally, laser materials processing has been subtractive, meaning materials are removed from the workpiece. Recently, laser additive processing, the 3D printing, is complementing these operations. Though initially, additive processing remained as curiosity, it has now picked up and showing annual growth of 20% and is estimated to contribute 30% of laser system revenues by 2020 (Sect. 19.6). Moreover, the appearance of new applications and markets for lasers has created strong incentives for further investment in innovation in lasers. All of this feedback and self-reinforcing dynamics are classic features of general-purpose technology.

Periodic assessments of the potential for exploiting lasers in the chemical industry are being made as the development of laser technology and the exploration of new and exciting laser photochemical synthesis processes are continued as discussed from Sect. 19.8 onwards. All these expertise will provide an infrastructure for future thrust areas of "laser photochemical technology" and affect the chemical industry in three broad areas as envisaged presently:

(i) Laser-based processes that offer lower costs, improved yields, higher product purity, and fewer unwanted side products.
(ii) Laser-based analytical methods have already achieved the ultimate in sensitivity: detection of single atom in the gas phase and single molecule in solution. These new analytical methods will change the way product specifications are defined currently and will provide new opportunities for process monitoring and control.
(iii) In addition, reaction diagnostics using lasers provide the detailed mechanistic and kinetic information required to design new processes and synthesize new materials. During the last ten years, lasers have been put to use for controlling chemical reactions as well, often with additional selectivity provided by the unique properties of laser radiation.

It may be worth mentioning that nuclear engineering is a potential field for such application requiring enriched fuel, moderator, synthesizing new strategic materials by isotopic tailoring of structural material (90-Zr), burnable poisons like (157-Gd and 155-Gd). A brief description of several isotope separation efforts is given in Sect. 19.11.3. Laser processes are being employed in reprocessing of spent nuclear fuel and recovering noble metals like Ru, Rh, Pd, other elements Sr, Cs, etc., and long-lived elements Am, Cm, Np, etc. Additionally, reactor technology requires developing new materials with low neutron absorption cross section. It is required not only to improve the neutron economy, but also to suppress the activation and

disintegration of materials due to α-particle decay. The interesting materials to be developed are 50-Ti, 53-Cr, 56,57,58-Fe, and 96,97-Mo.

In the material processing field, there are numerous opportunities for laser processes. Some of them are laser welding of end plug of reactor fuel clad tube, development of graded overlay of stellite on SS 304, laser cladded refurbishment of Ni superalloy based turbine blades. These techniques are also unique in the sense that remote handling/operation is possible, for example, cutting of zircaloy fuel pins for extraction of fuel pellets, cutting of end plates of irradiated fuel bundles, welding of miniature radiotherapy capsule, and cutting thick concrete blocks for possible decontamination/decommissioning of the radioactive facility.

Judging from the development since the days of drilling holes in diamonds, it is quite clear that laser application is a dynamic field, and even today new and interesting technology is being pursued throughout the world. Therefore, assessment of evolving technology must also be a continuing activity, not only to recognize the impact of the scientific achievements themselves, but also to keep the entire processing endeavor in step with a changing worldwide economic and political environment.

Acknowledgements The author acknowledges the works of many researchers in the field on which the article is based and apologies for not representing many other works. He is also grateful to the Department of Atomic Energy for grant of Raja Ramanna Fellowship to work at National Centre for Free Radical Research, Savitribai Phule Pune University, and Bhabha Atomic Research Centre for continuing support for his research activities.

References

1. Einstein A (1971) The quantum theory of radiation. Phys Z 18:121
2. Letokhov VS (1983) Non linear laser chemistry. Springer, Berlin
3. Svelto O (2010) Principles of lasers, 5th edn. Springer, US
4. Siegman AE (1986) Lasers. University Science Books
5. Silfvast WT (2004) Laser fundamentals, 2nd edn. Cambridge University Press (2004)
6. Thyagarajan K, Ghatak AK (1981) Lasers, theory and applications. Plenum Press, New York
7. Sarkar SK (2017) Material processing by laser: shifting landscape. SMC Bull 8:1
8. Steen WM (2010) Laser material processing, 4th edn. Jyotirmoy Mazumder. Springer, London (2010)
9. Bäuerle D (2011) Laser processing and chemistry, 4th edn. Springer, Berlin (2011)
10. Suder WJ, Williams SW (2012) Investigation of the effects of basic laser material interaction parameters in laser welding. J Laser Appl 24:032009
11. Demtroder W (2004) Laser spectroscopy: basic concepts and Instrumentation, 3rd edn. Springer, Berlin
12. EPIC Laser Market Report (2015) A European perspective, Jose Pozo, European Photonics Industry Consortium (EPIC)
13. Sugioka K, Cheng Y (eds) (2013) Ultrafast laser processing: from micro to nanoscale. CRC Press, Taylor & Francis Group, USA
14. Zewail AH (1999) Femtochemistry: atomic-scale dynamics of the chemical bond using ultrafast lasers. Nobel lecture
15. Letokhov VS, Moore CB (1977) In: Moore CB (ed) Chemical & biochemical applications of lasers, vol 3. Academic Press, New York

16. Mathi P, Nayak AK, Parhtasarathy V, Sarkar SK (2006) In: Kaneco S (ed) Laser enrichment of light and middle mass isotopes : prospects and challenges. Photo/electrochemistry & photobiology in environment energy and fuel, pp 227–257
17. Lawrence Livermore National Laboratory (2000) Laser technology follows in lawrence's footsteps. Hargrove S (ed). Sci Technol Rev 13–17
18. Dantus M, Rosker J, Zewail AH (1987) Real-time femtosecond probing of "transition states" in chemical reactions. J Chem Phys 87:2395
19. Scherer NF, Khundkar KR, Bernstein RB, Zewail AH (1987) Real-time picosecond clocking of the collision complex in a bimolecular reaction: The birth of OH from H+CO2. J Chem Phys 87:1451
20. Lupo DW, Quack M (1987) IR-laser photochemistry. Chem Rev 87:181
21. Sarkar SK, Mittal JP (1999) Laser selective chemistry. In: Agarwala RP (ed) Laser in materials science. Trans Tech Publication Ltd, Switzerland, pp 1–46
22. Sarkar SK (2000) Free electon laser photochemistry : Current developments and future prospects. PINSA – 66A 71
23. Sarkar SK, Mittal JP (2002) Breaking bonds to order - a dream still alive. Asian Chem Lett 6:1
24. Singh AK, Konaradi J, Sarkar SK , Materny A (2008) Mode selective excitation using coherent control spectroscopy. Am Inst Phys (AIP) Proc 1075:64
25. Shaub WM, Bauer SH (1975) Laser-powered homogeneous pyrolysis. Int J Chem Kinet 7:509
26. Sarkar SK, Nayak AK (1995) TEA CO2 laser-induced telomerization chemistry in conventional and waveguide photoreactors. J Photochem Photobiol A: Chem 87:75
27. Kleinermannsand K, Wolfrum J (1987) Laser chemistry-what is its current status?. Angew Chem Int Ed Engl 26:38
28. Rice GW, Woodin RL (1984) Laser synthesis of powders from large molecules. Proc SPIE Int Soc Opt Eng 458:98
29. Cannon WR, Danforth SC, Flint JH, Haggerty JS, Marra RA (1982) Sinterable ceramic powders from laser-driven reactions: I, process description and modeling . J Am Ceram Soc 65:324
30. Cannon WR, Danforth SC, Haggerty JS, Marra RA (1982) Sinterable ceramic powders from laser-driven reactions: II, powder characteristics and process variables. J Am Ceram Soc 65:330
31. Flint JH, Haggerty JS (1984) Ceramic powders from laser driven reactions. Proc SPIE Int Soc Opt Eng 458:108
32. Garifo L (1995) Laser Focus World 30
33. von Allmen M, Blatter A (1995) Laser-beam interactions with materials, 2nd edn. Springer series in materials science, vol. 2 Springer, Berlin
34. Clark JH, Anderson RG (1978) Silane purification via laser-induced chemistry. Appl Phys Lett 32:46
35. Hartford A (1980) Laser purification of silane: impurity reduction to the sub-part-per-million level. J Appl Pliys 51:4471
36. Geiser EM, Johnson RW (1981) US. Pat. 4287038
37. Donohue T (1977) Photochemical separation of europium from lanthanide mixtures in aqueous solution. J Chem Phys 67:5402
38. Chen HL, Borzileri C (1980) Laser cleanup of H2S from synthesis gas. IEEE J Quantum Electron QE 16:1229
39. Malatesta V, Willis C, Hackett PA (1981) Laser photochemical production of vitamin D. J Am Chem Soc 103:6781
40. Dauben WG, Phillips RB (1982) Wavelength-controlled production of previtamin D3. J Am Chem Soc 104:858
41. Hackett PA, Willis C, Gauthier M, Alcock AJ (1984) Viable commercial ventures involving laser chemistry production: two medium-scale processes. Proc SPIE Int Soc Opt Eng 458:65
42. Sarkar SK, Parthasarathy V (2007) Molecular laser isotope separation programme at BARC. BARC Report E/014
43. Sarkar SK (2010) Science and technology of isotope enrichment. J Indian Chem Soc 87:195–203

44. Mazumder J, Kar A (1995) Theory and application of laser chemical vapour deposition. Springer Science+Business Media, New York
45. Suzuki N, Anayama C, Masu K, Tsubouchi K, Mikoshiba N (1986) Pyrolysis and photolysis of trimethylaluminum. Jpn J Appl Phys 25:1236
46. Eden JG (1991) Photochemical vapor deposition. In: Thin film processes. Academic, London
47. Ohfuji T, Ogawa T, Kuhara K, Sasago M (1996) Prospect and challenges of ArF excimer laser lithography processes and materials. J Vac Sci Technol B 14:4203
48. Nakamura D, Tamaru K, Akiyama T, Takahashi A, Okada T (2008) Investigation of debris dynamics from laser-produced tin plasma for EUV lithography light source. Appl Phys A 92:767
49. Lai ND, Zheng TS, Do DB, Lin JH, Hsu CC (2010) Fabrication of desired three-dimensional structures by holographic assembly technique. Appl Phys A 100:171
50. Haske W, Chen VW, Hales JM, Dong W, Barlow S, Marder SR, Perry JW (2007) 65 nm feature sizes using visible wavelength 3-D multiphoton lithography. Optics. Express 15:3426
51. Farsari M, Ovsianikov A, Vamvakaki M, Sakellari I, Gray D, Chichkov BN, Fotakis C (2008) Fabrication of three-dimensional photonic crystal structures containing an active nonlinear optical chromophore. Appl Phys A 93:11
52. Shirk MD (1998) A review of ultrashort pulsed laser ablation of materials. Molian PA. J Laser Appl 10:18–28
53. Zeng H, Du X-W, Singh SC, Kulinich SA, Yang S, He J, Cai W (2012) Nanomaterials via laser ablation/Irradiation in liquid: A review. Adv Funct Mater 22:1333-1353
54. Patil P, Phase D, Kulkarni S, Ghaisas S, Kulkarni S, Kanetkar S, Ogale S, Bhide V (1987) Pulsed-laser-induced reactive quenching at liquid-solid interface: Aqueous oxidation of iron. Phys Rev Lett 58:238–241
55. Smith MJ, Sher M-J, Franta B, Lin Y-T, Mazur E, Gradečak S (2014) Improving dopant incorporation during femtosecond-laser doping of Si with a Se thin-film dopant precursor. Appl Phys A 114:1009–1016
56. Pola J, Urbanová M, Bastl Z, Plzák Z, Šubrt J, Vorlíček V, Gregora I, Crowley C, Taylor R (1997) Laser photolysis of liquid benzene and toluene: Graphitic and polymeric carbon formation at ambient temperature. Carbon 35:605–611
57. Scott CD, Arepalli S, Nikolaev P, Smalley RE (2001) Growth mechanisms for single-wall carbon nanotubes in a laser-ablation process. Appl Phys A Mater Sci Process 72:573–580
58. Li Yang L (2007) Self-assembly and ordering nanomaterials by liquid-phase pulsed laser ablation. PhD thesis. University of Bristol
59. Toyota K, Nakashima S, Okada T (2000) Near-infrared laser-induced breakdown of liquid benzene. Chem Phys Lett 323:323–328
60. Wesolowski MJ, Kuzmin S, Wales B, Sanderson JH, Duley WW (2013) Self-assembly of thin carbon micro-shells through pulsed laser irradiation of a ferrocene/benzene solution. J Mater Sci 48:6212–6217
61. Nkosi SS, Mwakikunga BW, Sideras-Haddad E, Forbes A (2012) Synthesis and characterization of potential iron-platinum drugs and supplements by laser liquid photolysis. Nanotechnol Sci Appl 5:27–36
62. Kim CH, Im HS, Cho YJ, Jung CS, Jang DM, Myung Y (2012) High-yield gas-phase laser photolysis synthesis of germanium nanocrystals for high-performance photodetectors and lithium ion batteries. Phys Chem C 116:26190
63. Lin H, Rumaiz AK, Schulz M, Wang D, Rock R, Huang CP, Shah I (2008) Photocatalytic activity of pulsed laser deposited TiO2 thin films materials. Mater Sci Eng B 151:133–139
64. Chen J, Wang L, Su X, Kong L, Liu G, Zhang X (2010) In GaZnO semiconductor thin film fabricated using pulsed laser deposition. Opt Express 18:1398
65. Christen H, Eres G (2008) Recent advances in pulsed-laser deposition of complex oxides. J Phys: Condens Matter 20:264005
66. Komatsu S, Shimizu Y, Moriyoshi Y, Okada K, Mitomo M (2002) Preparation of boron nitride nanocapsules by plasma-assisted pulsed laser deposition. J Appl Phys 91:6181

67. Sajjad M, Morell G, Feng P (2013) Advance in novel boron nitride nanosheets to nanoelectronic device applications. ACS Appl Mater Interfaces 5:5051–5056
68. Sajjad M, Feng P (2011) Low temperature synthesis of c-BN films. Appl Phys Lett 99:253109
69. Zhu S, Zhang J, Qiao C, Tang S, Li Y, Yuan W (2011) Strongly green-photo luminescent graphene quantum dots for bioimaging applications. Chem Commun 47:6858–6860
70. Peng J, Gao W, Gupta BK, Liu Z, Romero-Aburto R, Ge L (2012) Graphene quantum dots derived from carbon fibers. Nano Lett 12:844–849
71. Habiba K, Makarov VI, Avalos J, Guinel MJF, Weiner BR, Morell G (2013) Luminescent graphene quantum dots fabricated by pulsed laser synthesis. Carbon 64:341–350
72. Reisse G, Weissmantel S (1999) Pulsed laser deposition of hexagonal and cubic boron nitride films. Appl Phys A: Mater Sci Process 69:S749–753
73. Eason R (2007) Pulsed laser deposition of thin films: application-led growth of functional materials. Wiley, Hoboken, New Jersey
74. Hidalgo A, Makarov V, Morell G, Weiner B (2013) High-yield synthesis of cubic and hexagonal boron nitride nanoparticles by laser chemical vapor decomposition of borazine. Dataset Pap Nanotechnol 281672–281676
75. Hench LL, Wilson J (eds) (1993) An introduction to bioceramics. World Scientific, Singapore, p 1
76. LeGeros RZ (1988) Calcium phosphate materials in restorative dentistry: a review. Adv Dent Res 2:164–180
77. De Groot K, Geesink R, Klein CPAT (1987) Plasma sprayed coatings of hydroxyapatite. J Biomed Mater Res 21:1735–1781
78. Roy M, Bandyopadhyay A, Bose S (2008) Laser surface modification of electrophoretically deposited hydroxyapatite coating on titanium. J Am Ceram Soc 91:3517–3521
79. Roy M, Krishna BV, Bandyopadhyay A, Bose S (2008) Laser processing of bioactive tricalcium phosphate coating on titanium for load-bearing implants . Acta Biomater 4:324–333
80. Lin J, Peng Z, Liu Y, Ruiz-Zepeda F, Ye R, Samuel ELG, Yacaman MJ, Yakobson BI, Tour JM (2015) Laser-induced porous graphene films from commercial polymers. Nat Commun 5:5714
81. Duy LX, Peng Z, Li Y, Zhang J, Ji Y, Tour JM (2018) Laser-induced graphene fibers. Carbon 126:472–479
82. Ruquan Y, James DK, Tour JM (2018) Laser-induced graphene. Acc Chem Res 51:1609
83. Ruquan Y, James DK, Tour JM (2019) Laser-induced graphene: From discovery to translation. Tour Adv Mater 31:1803621
84. Luong DX, Yang K, Yoon J, Singh SP, Wang T, Arnusch CJ, Tour JM (2019) Laser-induced graphene composites as multifunctional surfaces. ACS Nano 13:2579–2586
85. Kannatey-Asibu E (2009) Principles of laser materials processing. Wiley, Hoboken, New Jersey, USA (2009)
86. Ossi PM (ed) (2018) Advances in the application of lasers in materials science. Springer Nature, Switzerland AG
87. Castillejo M, Ossi PM, Zhigilei L (eds) (2014) Lasers in materials science. Springer series in materials science, vol 191
88. Schaaf P (ed) (2010) Laser processing of materials fundamentals, applications and developments. Springer, Berlin
89. Akinlabi ET, Mahamood RM, Akinlabi SA (2016) Advanced manufacturing techniques using laser material processing. Engineering science reference, USA (2016)
90. Parthasarathy V, Bajaj PN, Sarkar SK (2007) Laser enrichment of isotopes. In: Lackner M (ed) Lasers in chemistry. Wiley-VCH Publications
91. Sarkar SK, Ahmed M, Mukadam MD, Yusuf SM (2016) Investigation of graphite oxide and reduced graphene oxide: magnetic properties revisited. Asian J Mat Chem 1:66–74
92. Stanford MG, Yang K, Chyan Y, Kittrell C, Tour JM (2019) Laser-induced graphene for flexible and embeddable gas sensors. ACS Nano 13:3474

Chapter 20
Ultra Fast Electrically Exploding Wire Method for Production of Raw Material for Additive Manufacturing Based 3D Printing

Rohit Shukla and Archana Sharma

Abstract 3D printing nowadays is considered as a very smart method for producing structures with very fine and intricate internal features. The process is now going through a very fast scientific development, and laser based 3D printing tools are already available to the users. Strong and intense laser pulses are bombarded at well-defined locations on a 2D plane covered by particles through a proper alignment process controlled by computers as per the instructions given to it. These intense laser pulses cause the melting of the target which is composed of scattered small particles. Because of this melting and subsequent cooling, these particles start making metallic bonds with the substrate which is already solidified cold metal. This way, three dimensional growth of the structure using fine granules of metals can be achieved. Since the process depends upon the metal granules and intensity of the laser, hence, a fine degree of structure growth control can be obtained in the case of dissimilar material being used for the construction of the model or structure. If alloys are fed as raw material into the printing system then an alloy structure can be obtained through this 3D printing. High power portable lasers which can be focused onto very tiny spots may give additional advantages such as achievement of the temperatures in a very controlled fashion so that almost all the possible combinations of alloy manufacturing can be incorporated into a single system of 3D printing requiring different melting points in constituent metals. Not only laser based printing but also electron beam based printing can be used in this manufacturing process. Vacuum may be an additional requirement of the environment in which such electron beam based additive manufacturing is contemplated. In order to have better control of the structure fabrication process, the computer-based monitoring and controlling of various parameters will be helpful for the advanced manufacturing process.

R. Shukla · A. Sharma (✉)
Pulsed Power & Electro-Magnetic Division, Beam Technology Development Group, Bhabha Atomic Research Centre, Mumbai 400085, India
e-mail: arsharma@barc.gov.in

Homi Bhabha National Institute, Mumbai 400094, India

R. Shukla
e-mail: rshukla@barc.gov.in

A. K. Tyagi and R. S. Ningthoujam (eds.), *Handbook on Synthesis Strategies for Advanced Materials*, Indian Institute of Metals Series,
https://doi.org/10.1007/978-981-16-1803-1_20

Keywords Nanoparticles · Action integral · Compact pulsed power system · High voltage · Additive manufacturing

20.1 Introduction

Production and characterization of nanoparticles produced using electrical explosion of metal wire is well reported by Kotov [1], Das et al. [2]. Nanoparticle production for very interesting application points of view in various media is studied by Nazarenko et al. [3, 4] In another article [6] Nazarenko et al. have reported the effect of various gas environments (reactive gas and non-reactive gas combinations) for the nanoparticle production by electrical exploding wire scheme. They have suggested less than 2% reactive gas for metal nanopowder production which otherwise leads to the oxide formation. Károly Lázár et al. [6] have reported the iron nanopowder reaction in different media using electrical explosion of wire. An interesting, molecular dynamics based simulation is presented by Kryzhevich et al. [7] for exploding wire based nanoparticle production. Earlier Go Kawamura et al. [8] have reported oxygen resistant copper based nanoparticles by wire explosion. Chung et al. [9] have presented a superior oxygen stability copper silver nanoparticle layers sintered by flash lights to achieve the electrical conductivity close to copper. Suitable environment study and findings are reported for tungsten carbide nanopowder production in this method by Ranjan et al. [10]. Taek-Kyun Jung et al. have reported production of nickel nanopowder by exploding wire method [11], and earlier [12] titanium nitride nanopowder production is reported in electrical explosion in nitrogen environment. Beketev et al. [13] have studied magnetic nanoparticles production by electrical explosion of iron wires.

20.1.1 Concept of Pulsed-Power Plasma Method

In order to generate ultrafine nanopowder of the size less than 10 nm, the capacitor bank discharges into the wire has to be optimized such that the energy inside the wire is dissipated at very fast rate which means that before the plasma formation takes place the considerable amount of energy is given to the wire. Because of the conducting nature of the plasma, further resistance (I^2R) heating becomes practically impossible and hence the burst phase is relatively less violent. Higher the energy given to the atoms, higher is the kinetic energy or the pressure in plasma state. Because of this generated high pressure, the atoms form very fine coagulation in the form of nanoparticles.

In the case of the generation of micron sized particles, a very simple scheme of melting is followed similar to the electrically exploded nanoparticle system. In this case, the wire is fed longer in the dimensions and is allowed to reach only to the melt state or liquid state, and the thrust is given by the return conductor current to

form the droplets of the tens to even hundreds of microns in size. The thrust is J X B thrust (J is the current density, and B is the magnetic field) or the repulsive force or hoop force acting between current carrying conductors with current in opposite directions. In this way, only a single pulse power system can support the fabrication of micron-sized to nano-sized particle synthesis of any metal. As this method of particle synthesis is based on the electrical conductivity and phase-transformation based on heating (resistive), therefore any conducting metal can be used as a feed material and its particle size can be easily controlled and hence well determined. As alloys are constructed mostly from metal atoms, they show finite or considerable electrical conductivity constructed from most of the metals therefore they can also equally efficiently be used for the production of particles from micron to nano size.

We have used copper, zinc, aluminum, Iron and Tungsten for producing nanoparticles during this method.

20.1.2 Merits and Demerits of This Method

Certainly any process of commercial/academic interest needs to be compared with the other processes being used for the similar jobs. Therefore, this process also needs to be compared with other methods.

Now as explained that getting nano-sized particles as well as micron sized particles required different types of approaches to obtain the desired extreme size particles results, a proper experimental approach which is achieved comfortably may give a broad spectrum of the sizes in between these two extremes. For this purpose, in order to meet both the ends a simple and single pulsed power system is used, which is so portable that a single person can handle it and operate it safely. Its mobility also allows it to arrange the whole setup at a place where the particle consumption is taking place. This reduces coagulation probability because of very less transit time especially in the case of very fine nano-powder. Losses during transit, if any, can also be further minimized by connecting powder generator output to its consumption unit directly. For high voltage insulation between two units (particle generator to particle consumption units) conveyor duct or transmission duct of insulator material will be a good choice for the operator. A normal supply available even in households can be used for the purpose because capacitor banks are slowly charged with low wattage power supply, but they deliver higher powers during the electrical discharges. Based on the simplicity, versatility and portability, the device plays a very important role in commercial/academic terms also apart from the safety aspects.

20.2 Characterization and Other Properties

For the characterization of Nano powder X Ray Diffraction (XRD) Scanning electron microscopy (SEM) and Photon Cross Correlation Spectroscopy (**PCCS**) techniques have been used. The results have revealed that faster discharges are capable of producing nanosized metal particles. Some of the images and the results are attached in the figures in this chapter.

Coating the metal nanopowder on the fabric has been accomplished. A cluster coating is successfully obtained by the method followed and particles produced by this method. The size of the particles forming clusters on the fabric is confirmed in the nano form and can solve the purpose.

Now it has also been shown in the experiments that non optimized dimensions of the wire lead to the production of larger size of particles which implies that the pressure at the burst phase is relatively lower and hence particles of larger size are produced.

In the case of production of larger (micron sized) particles produced by melting of wire and driving by J X B forces, the analysis part has been done mostly on the optical microscopes.

20.3 Application of Advance Materials Prepared By This Route

Various metals like copper, silver, zinc, Iron and tungsten have been used in our experiments. Of course for the largest particles as discussed above the feeder wire dimensions can be increased first in terms of width and then in terms of length also. A challenging metal with conducting nature and not producing nanopowder by this technique is still being found out.

Usually nanoparticles are the particles with the size below 100 nm. There are the methods by which nanoparticles may be generated in quite a good amount of quantity and hence support the construction of materials using additive manufacturing techniques which may be laser based or electron beam based for fusing these particles. Plasma based techniques have successfully been implemented for the production of bulk nanoparticles and the consumption rate of laser based additive manufacturing can be fulfilled easily by the plasma based production technique. In this context Bhabha Atomic Research Centre, Visakhapatnam, has developed a miniaturized machine for the continuous production of nanopowder by using electrically exploding wire technique. It has been understood during the experiments that if the current discharges through the exploding conductor are very quick and intense, then the energy being dissipated in the metal plasma formation can be sufficiently high to generate fine nano particles. For this purpose up to 180 kA (short circuit current) has been dissipated for exploding metal wire of copper, silver, zinc, Iron and tungsten at size of nearly half a millimeter diameter, and the system is compact and portable and

can generate nanoparticles, repetitively. Because of this inherent advantage of portability and repeatability of the nanopowder generator, nearly 50 mg of nanopowder is produced every 6 s. In a similar pattern, generating larger size the particles of metal has also been experimented by exploding wire technique but limiting to the liquid state. The system is optimized in such a way that the liquid metal experiences hoop force or JXB force at the time of melting. This ensures that the metal droplets are formed and thrown away from its initial location and are collected on the bottom of the chamber in which the melting or discharge is taking place. With the same electrical parameters of the capacitor bank, which are used for the nanopowder generation of nearly 50 mg material, 500 mg of larger sized (micron sized) particles of the same metal has been produced in a different chamber fitting. The procedure gives the flexibility to the operator or the user so that depending upon the requirement of additive manufacturing one can feed either nanopowder or micron sized powder depending upon the size and the surface finish of the product.

20.4 Nanoparticle Production

It is noteworthy that while producing the nanoparticles from the electrically exploding wire method any metal can be fed which has optimized dimensions according to the pulsed power machine and hence the process is similar for all metals. This fact greatly introduces the flexibility of the process selection for ablative manufacturing feed material. Therefore, pure metals as well alloys can directly be used for ablative manufacturing. One need not worry about the availability of alloys in the form of powder feed. The nanoparticle generator based on the electrically exploding wire is only dependent upon the resistivity parameter of various phases of the material. It has been experimented using this powder generator and is found that copper nanopowder of less than 10 nm particle size is being produced by the machine with good reproducibility.

In Fig. 20.1, the repetitive metal nanoparticle generator is shown. Electrical schematic is shown in Fig. 20.2 in which the reaction chamber boundary is shown with the blue circle. Inside this chamber, the repetitive wire loading assembly/mechanism is also fitted.

Figures 20.3 and 20.4 are showing the size distribution of copper nano powder produced by the system. Similarly Figs. 20.5 and 20.6 are showing the particle size distribution produced by aluminum wire in this method. It has been done using the PCCS technique of analysis. Coagulation on nanoparticles is remarkably seen in the case of aluminum metal.

Figure 20.7 is a typical current waveform of the current pulse obtained during capacitor bank discharge inside optimized wire. The calibration of the current measurement probe is 100 kA per Volt for the study undertaken. Single pulse discharge is another indication of optimized wire dimensions being used inside the system.

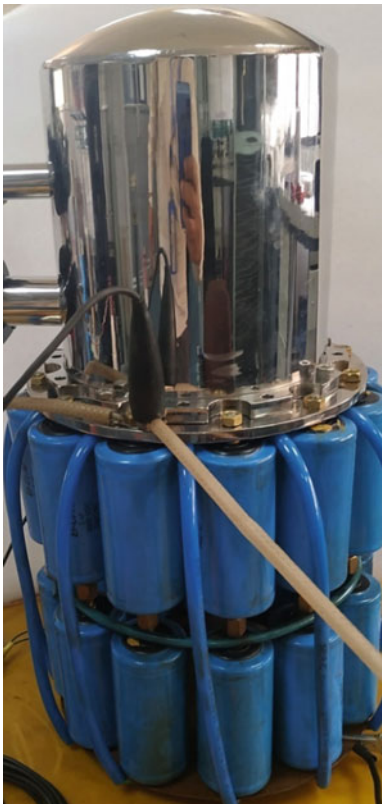

Fig. 20.1 Repetitive metal nanoparticle generator

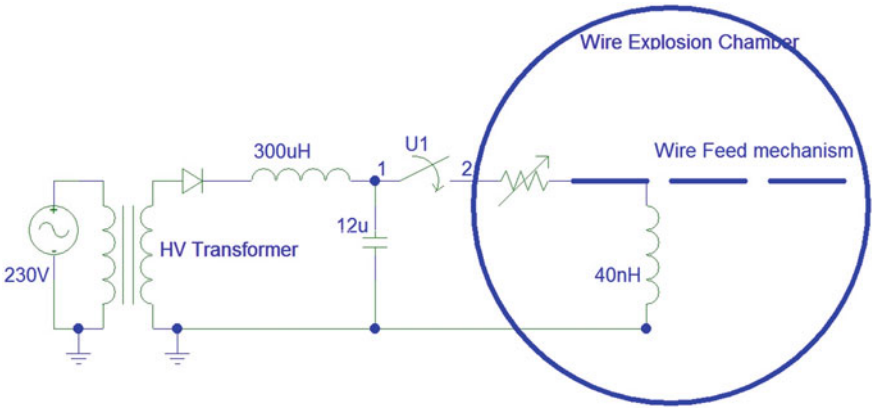

Fig. 20.2 Electrical schematic for compact pulsed power system for metal particle generation

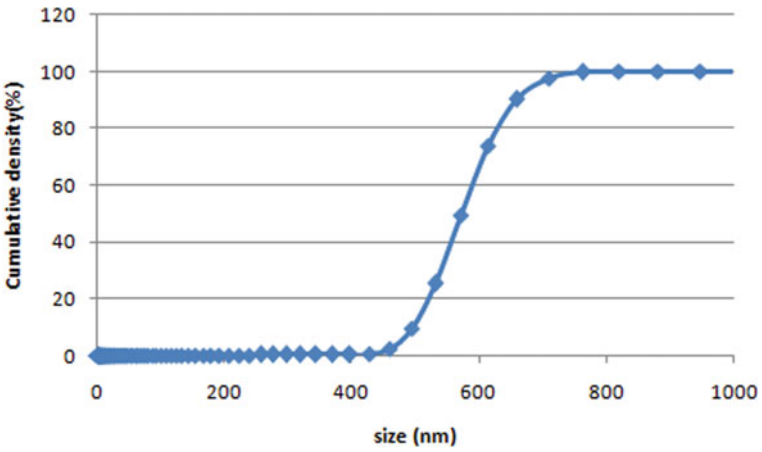

Fig. 20.3 Al powder (coagulation) produced by ultrafast wire explosion collected after 30 min (Cumulative Density)

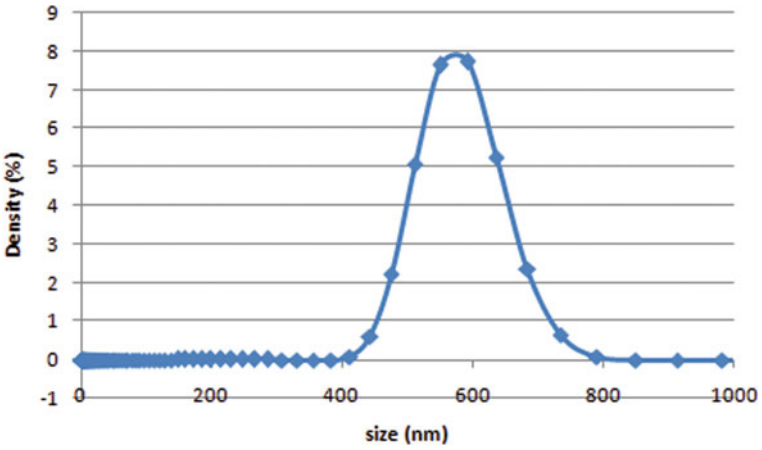

Fig. 20.4 Al powder (coagulation) produced by ultrafast wire explosion collected after 30 min (Density)

In recent covid-19 pandemic times, some reports suggested that the coating of Personal Protective Equipment (PPE) fabric material can be conducted using metals in the nanopowder form in order to increase the efficacy of the PPE kit in fight against various infections. For this purpose recently copper, zinc and aluminum nanopowders were produced using this ultra fast system and coating over the clothes was successfully conducted for the demonstration of the technique and process. Clusters of the nanoparticles are distributed over the cloth surface indicating a non-uniform coating by metal particles. Some of the images of the coating conducted by

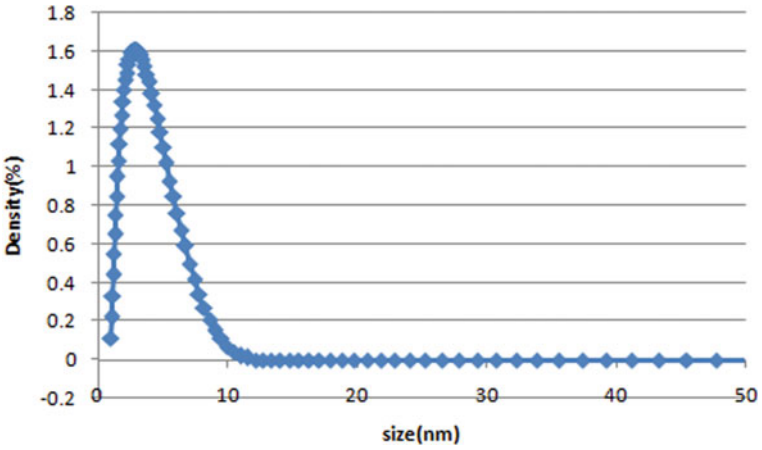

Fig. 20.5 Copper nanopowder (distribution) produced by ultrafast wire explosion

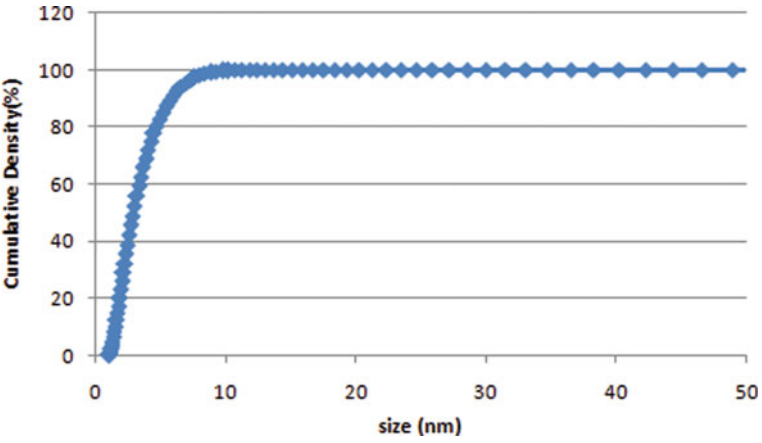

Fig. 20.6 Copper nanopowder (cumulative) produced by ultrafast wire explosion

the aforesaid method are shown in Fig. 20.8. SEM analysis of the PPE fabric is also conducted, and similar results are observed.

Zinc oxide nanopowder produced by the generator is shown in Fig. 20.9 which is collected in a plastic bag. This experiment was conducted in a normal air environment and hence no inert gas environment was used. But in the case of Fig. 20.10, the inert gas environment of Argon was used inside the chamber and hence the pure zinc metal nanopowder is visible after opening the chamber. It is collected all over the internal surfaces.

The images of the particles generated in the case of Micron size production are shown in the attached Fig. 20.11 which is obtained from similar discharge of the capacitor bank but with wire heating up to liquid state only.

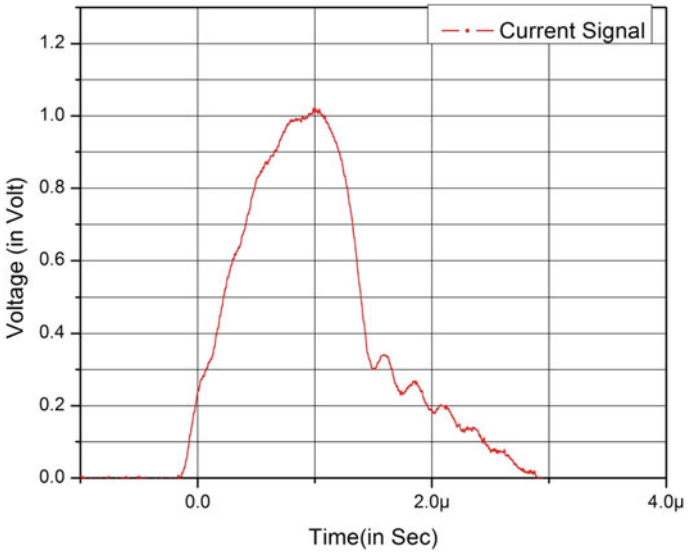

Fig. 20.7 A typical current discharge curve from the nanoparticle generator (1 V corresponds to 100kA)

Fig. 20.8 Personal Protective Equipment (PPE) fabric coated with copper nanopowder produced by electrically exploded wire

20.5 Tailoring of Particle Size

The important point is that the action integral data for burst in pure metals are reported by Tucker and Toth [14] in a capacitor bank discharge machine in particular current rise rate. As far as the nanoparticle generator is concerned for the generation of the

Fig. 20.9 Zinc oxide nanopowder produced using pulsed power

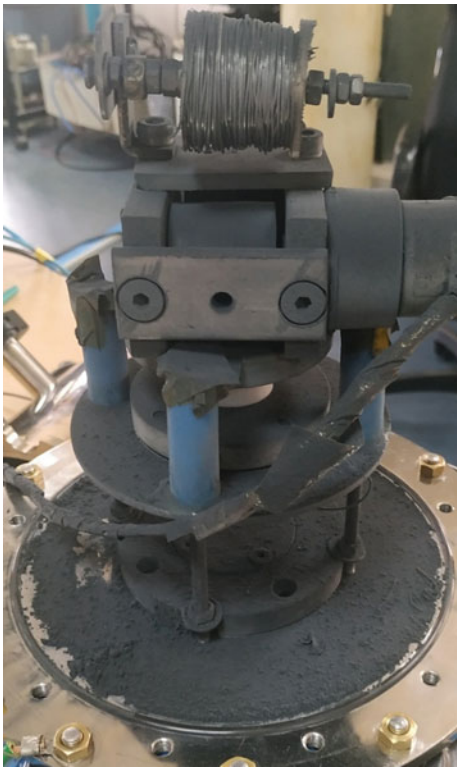

Fig. 20.10 Zinc metal nanopowder produced using pulsed power system

particles below 10 nm using electrically exploding wire method, the energy dissipation in the form of electrical energy inside the wire material should be conducted at a considerably fast rate. Since the conductivity of the wire reduces, till the wire reaches plasma state through the liquid and the vapor states starting from solid state, the energy dissipation rate or heating rate is quite fast up to the onset of plasma state but as soon as the plasma state is reached, the conductivity of the metal increases

Fig. 20.11 Micron sized particles of zinc produced from pulsed power system

abruptly and this reduces further heating of the wire metal and subsequent dissipation of electrical energy in the wire. Hence it becomes very difficult from this stage onwards to further increase the temperature of the wire metal. However, it is reported in the literature [15, 16] that the faster current rates can raise the temperature of the wire metal relatively higher than that compared with the slower current rates. It may be partially considered as a kind of thermal inertia in reaching the plasma state or conducting state at faster current discharge rates and some higher amount of energy compared to the ionization energy of the metal can be given to the metal atoms.

20.6 Effect of Various Parameters on Powder Properties

20.6.1 Effect of Medium

As plasma is highly reactive, the produced metal plasma reacts with the surrounding after the discharge. In order to form oxides, oxygen inside the reaction chamber is required. If pure metal nanopowder is desired then filling the reaction chamber with non-reactive gases is the required condition. It has been observed that experiments in air lead to the formation of oxides while experimenting with aluminum and zinc. Copper in the Argon environment yielded pure metal powder.

Interestingly in the formation of micron size particles it is observed that even in an air atmosphere, copper micro particles are produced in the pure form. It is also noteworthy that since this is a high voltage discharge method of production of particles from the metal wire, the system needs to be filled with some insulating media otherwise the electrical discharge may take place in surrounding media and this may lead to a loss of electrical energy in undesirable processes of discharge. It suggests that the gas pressure of the system should not be in the Paschen-minimum region of the breakdown curve. Rather a higher insulation strength of gas is suggested to be used in the process.

20.6.2 Pressure Control

If high pressure gases of inert nature are filled in the reaction chamber or discharge chamber then the particles produced after explosion will not travel longer distances and this is due to enhanced drag resistance offered by the surrounding media. This way the reaction chamber diameter dimensions may be restricted to the smaller values. Successful operation of the system up to three or four atmospheric pressures inside the reaction chamber has been observed. When inert gas is used in the case of nanoparticle formation, then it has been further observed that the continuity between electrode in repetitive shots is well maintained subsequently helping to conduct repetitive shorts whereas in the case of oxide or nitride nanopowder formation the nanopowder, which gets deposited over the electrodes, may be insulating if the fill gas is reactive. So the accumulation of nanopowder over the electrodes leads to poor electrical connections between the running feed wires in between these two electrodes. Now in this situation, the electrical energy tries to find out some other ways to discharge, which is not through the wire, like from the surfaces or the system starts malfunctioning and gets stopped for the subsequent discharges. This affects the performance of the system. So in repetitive operation it is recommended, based on the experimental evidence, that an inert gas environment is the most suited environment for the production of metal nanopowder. It is also suggested that other reactions of chemical interest may be conducted separately after pure nanopowder is continuously produced in the chamber.

20.6.3 Production of Nanoparticles Inside the Liquid

Since the pulsed power system is very fast and in the sub-microsecond regime of operation, the nanoparticle producing discharges can be done in the liquid submerged conditions as well. This will additionally require the structural integrity analysis in consideration as the pressure generated in the burst phase will be transmitted to the boundaries more intensely and rapidly than that in the case of air/gas. Repetitive wire feed system is the component which is in the close proximity of the metal wire explosion zone and is most vulnerable to the pressures. Hence a proper protection of the system from repetitive shock pressures will be required in the planning and design stage.

20.7 Conclusions

A repetitive operation of a portable and miniaturized capacitor bank is reported earlier [17]. The bank is further augmented with energy and automation in order to be used for the production of metal particles from nanometer size to micron size in a single electrical unit. The discharge chambers are different as per the required size of the particles. This portability leads to further exploration of applications of particles in other fields. The optical isolation of the system from high voltage and confined production of the particles has another feature of enhanced electrical safety chemical safety. In future the particles produced in the bulk quantity are to be fed to the laser or other like electron beam based 3D printing or additive manufacturing setups.

References

1. Kotov YA (2003) Electric Explosion of Wires as a Method for Preparation of Nanopowders. J Nanopart Res 5:539550. https://doi.org/10.1023/B:NANO.0000006069.45073.0b
2. Rashmita D, Basanta Kumar Das, Rohit Shukla, T Prabaharan and Anurag Shyam "Analysis of electrical explosion of wire systems for the production of nanopowder" Sadhana Vol. 37, Part 5, October 2012, pp. 629–635.
3. Nazarenko O (2007) Nanopowders produced by electrical explosion of wires. In: Proceedings of European Congress of Chemical Engineering (ECCE-6) Copenhagen, 16–20 September 2007
4. Nazarenko OB, Ilyin AP (2008) Nanopowders production by electrical explosion of wires: environmental applications" Proceedings of the 3rd Environmental Physics Conference, 19–23 Feb. 2008, Aswan, Egypt
5. Nazarenko OB, Ilyin AP, Tikhonov DV (2014) Effect of the Gas Composition at the Electrical Explosion of Wires on the Nanopowders Properties" Advanced Materials Research, Vol. 872 (2014) pp 142–149 Online available since 2013/Dec/19 at www.scientific.net © (2014) Trans Tech Publications. Switzerland
6. Lázár K, Varga LK, Kis VK, Fekete T, Klencsár Z, Stichleutner S, Szabó L, Harsányi I (2018) Electric explosion of steel wires for production of nanoparticles: Reactions with the liquid

media, Journal of Alloys and Compounds, Volume 763:759–770, ISSN 0925–8388,https://doi.org/10.1016/j.jallcom.2018.05.326. (http://www.sciencedirect.com/science/article/pii/S092538818320632)
7. Kryzhevich DS, Zolnikov KP, Korchuganov AV, Psakhie SG (2017) Nanopowder synthesis based on electric explosion technology" AIP Conference Proceedings 1893, 030125. https://doi.org/10.1063/1.5007583 Published Online: 26 October 2017
8. Kawamura G, Alvarez S, Stewart IE, Catenacci M, Chen Z, Ha YC (2015) Production of Oxidation-Resistant Cu-Based Nanoparticles by Wire Explosion. Sci. Rep. 5, 18333. https://doi.org/10.1038/srep18333
9. Chung WH, Hwang YT, Lee SH, Kim HS. "Electrical wire explosion process of copper/silver hybrid nano-particle ink and its sintering via flash white light to achieve high electrical conductivity." Nanotechnology. 2016 May 20;27(20):205704. doi: https://doi.org/10.1088/0957-4484/27/20/205704. Epub 2016 Apr 12. PMID: 27070756.
10. Ranjan P (2020) Formation of tungsten carbide nanoparticles by wire explosion process. Int J Appl Ceram Technol 17:304310. https://doi.org/10.1111/ijac.13350
11. Jung T-K (2011) Hyo-Soo Lee and Min-Ha Lee "Fabrication of Ni nanopowder using wire explosion process and its characterization" Rev. Adv Mater Sci 28:171–174
12. Wonbaek Kim, Je-shin Park, Chang-yul Suh, Sung-wook Cho, Sujeong Lee and In-Jin Shon "Synthesis of TiN Nanoparticles by Explosion of Ti Wire in Nitrogen Gas" Materials Transactions, Vol. 50, No. 12 (2009) pp. 2897 to 2899
13. Beketov IV, Safronov AP, Medvedev AI, Alonso J, Kurlyandskaya GV, Bhagat SM (2012) Iron oxide nanoparticles fabricated by electric explosion of wire: focus on magnetic nanofluids" AIP ADVANCES 2, 022154
14. Tucker TJ, Toth RP. "EBW1: a computer code for the prediction of the behavior of electrical circuits containing exploding wire elements" Albuquerque (NM): Sandia National Laboratories; 1975 Apr. Report No.: SAND-75–0041.
15. LChemezova LI, Mesyats GA, Sedoi VS, Semin BN, Valevich VV (1998) The integral of specific current action and the specific energy input under fast electrical explosion. In: IEEE 18th international symposium on discharges and electrical insulation in vacuum Eindhoven 1998
16. Rohit S, Anurag S (2014) "Note: Compact, reusable inductive-storage-cum-opening-switch based 1.5 GW single-shot pulsed power generator" Review of Scientific Instruments 85, 036101. https://doi.org/10.1063/1.4867079
17. Shukla R, Shyam A (2008) Note: Repetitive operation of the capacitor bank of the low-voltage miniature plasma focus at 50 Hz. Review of Scientific Instruments 84(10), 106112